FATIGUE PROPERTIES OF METAL INERT GAS AND FRICTION STIR WELDED ALUMINIUM ALLOY 5383-H321

by

GARETH RICHARD BRADLEY

A thesis submitted to the University of Plymouth
in partial fulfilment for the degree of

Doctor of Philosophy

Department of Mechanical & Marine Engineering
Faculty of Technology

In collaboration with

Corus Research, Development and Technology

October 2003

Contents

List of Figures

List of Tables

Nomenclature

The following nomenclature is used throughout this dissertation unless indicated otherwise.

2θ	diffraction angle
$2\theta_0$	strain free diffraction angle
a	crack depth
AA	aluminium alloy
B	short crack growth scaling constant
c	surface half-crack length
	c_f final crack size
	$c_{f\varepsilon}$ transition crack length from predominantly plane strain to plane stress
	$c_{f\sigma}$ final crack length
	c_i initial crack size
	c_t SCG to LCG transition crack size
C	Paris law constant
	C_ε Paris law constant for LCG under predominantly plane strain
	C_σ Paris law constant for LCG under predominantly plane stress
CT	compact tension (long crack growth test specimens)
CW	clockwise direction
d	lattice spacing
d_0	strain free lattice spacing
da	crack increment
dc	crack increment
dN	load cycle increment
E	elastic modulus
EDM	electrical discharge machining
EM	electro-magnetic resonance test frame
FEA	finite element analysis
FS	friction stir (welding)
	SP single pass (FS weld)
	DP double pass (FS weld)
	DPA advancing side (of FS DP weld)
	DPR retreating side (of FS DP weld)
GMAW	gas metal arc welding
HV	Vickers hardness
	$HV_{0.1}$ Vickers microhardness, 0.1 Kg force loading
	HV_{100} Vickers microhardness, 100g force loading
	HV_{200} Vickers microhardness, 200g force loading
HAZ	heat affected zone (MIG & FS welds)
K_c	critical stress intensity factor

K_{cl} stress intensity factor at crack closure
- K_{max} maximum stress intensity factor
- K_{min} minimum stress intensity factor

K_t stress concentration factor

K_I mode I stress intensity factor

LC long crack
- LCG long crack growth

LEFM Linear elastic fracture mechanics

LS long short plane of the AA plate

LT long transverse plane of the AA plate

m Paris law constant
- m_ε Paris law constant for LCG under predominantly plane strain
- m_σ Paris law constant for LCG under predominantly plane stress

MIG metal inert gas (weld)
- LI low input (MIG weld)
- HI high input (MIG weld)

MT middle tension (long crack growth test specimens)

n short crack growth scaling constant

N number of load cycles
- N_i number of cycles attributable to crack initiation
- N_{lcg} number of load cycles attributable to LCG
  - $N_{lcg\,T}$ total number of load cycles attributable to LCG
  - $N_{lcg\,\varepsilon}$ number of load cycles attributable to LCG under plane strain
  - $N_{lcg\,\sigma}$ number of load cycles attributable to LCG under plane stress
- N_{scg} number of load cycles attributable to SCG
- N_T total number of cycles to failure or a predetermined length

O annealed condition (with respect to the temper of aluminium alloys)

P load

PFD partial fusion defect (fusion defect in FS SP welds)

PP parent plate (AA 5383-H321 or 5083-H321)
- |- loading direction transverse to the rolling direction of the plate
- // loading direction parallel to the rolling direction of the plate

r_c cyclic plastic zone size

r_{pr} reversible plastic zone size

R stress ratio, $\sigma_{min}/\sigma_{max}$ or K_{min}/K_{max}

SC short crack
- CSC chemically small (short crack)
- MCSC mechanically small (short crack)
- MSSC microstructurally small (short crack)
- PSC physically small (short crack)

	SCG	short crack growth
SCF		stress concentration factor
SH		servo-hydraulic test frame
ST		short transverse plane of the AA plate
t		plate thickness
T_m		melting temperature
TMAZ		thermo-mechanically affected zone (FS welds)
Y		geometric configuration factor
ΔK		stress intensity factor range
	ΔK_{eff}	effective stress intensity factor range
	ΔK_{th}	threshold stress intensity factor range (long crack) independent of R (the lowest value of ΔK_0 below which fatigue cracks do not advance at any R)
	ΔK_0	threshold stress intensity factor range (long crack) dependent on R
ΔP		load range
$\Delta\sigma$		stress range
ε		strain
	$\varepsilon_{failure}$	strain at failure
	ε_{max}	maximum strain
	ε_{Pmax}	maximum principal strain
	ε_{min}	minimum strain
	ε_{Pmin}	minimum principal strain
	ε_{TS}	strain at σ_{TS}
	ε_y	yield strain
θ		weld toe angle
ρ		weld toe radius
σ		stress
	σ_a	stress amplitude
	σ_{max}	maximum stress
	σ_{Pmax}	maximum principal stress
	σ_{min}	minimum stress
	σ_{op}	crack opening stress
	σ_{Pmin}	minimum principal stress
	σ_R	stress range
	σ_{TS}	tensile strength
	σ_y	yield stress
	$\sigma_{0.1\%}$	0.1% proof stress
	$\sigma_{0.2\%}$	0.2% proof stress
	$\sigma_{failure}$	failure stress
	σ^{∞}	remotely applied stress
ν		Poisson's ratio

Acknowledgements

The author wishes to acknowledge the assistance afforded by the following:

Engineering and Physical Sciences Research Council (EPSRC) for financial support.

Corus Research, Development and Technology, IJmuiden and Rotherham, for financial support.

MN James and DC Plane, Department of Mechanical and Marine Engineering, University of Plymouth, for supervision.

LW Wei, formerly of the University of Plymouth, for finite element analyses and assistance.

DJ Hughes, PJ Webster and G Mills, University of Salford and DG Hattingh, Port Elizabeth Technikon for assistance with synchrotron strain scanning.

TJ Hurd, J Pool, MF de Vaan, BL Doeve and S Moldenhauer, Corus Research, Development and Technology, IJmuiden for assistance, notably with metallurgical investigations.

S Webster, C Lindley, J Daley and F Coombes, Corus Research, Development and Technology, Rotherham for assistance, notably with Talysurf measurements.

R Moate and P Bond, University of Plymouth, for assistance with electron-microscopy.

D Short, T Richards, B Lord, R Crocker and N Fewings, University of Plymouth for assistance.

P Threadgill, TWI for assistance.

PM Mackenzie, Department of Mechanical Engineering, University of Strathclyde, Glasgow for advice.

Author's Declaration

At no time during the registration for the degree of Doctor of Philosophy has the author been registered for any other University award.

This study was financed with the aid of a studentship from the Engineering and Physical Sciences Research Council and industrial support from Corus.

A programme of advanced study was undertaken that included attendance at short courses in "Light Metals and Alloys" and an "Introduction to Metallurgy" and a seminar on "Project Management & Presentation Skills".

The work was regularly presented to Corus in both oral and written formats.

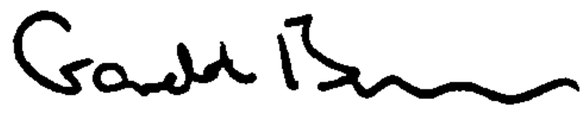

31st October, 2003

1. Abstract

FATIGUE PROPERTIES OF METAL INERT GAS AND FRICTION STIR WELDED ALUMINIUM ALLOY 5383-H321

GARETH RICHARD BRADLEY

The following dissertation details the development of a simple defect-tolerant based model for determining the fatigue properties of a 5383-H321 aluminium alloy and metal inert gas and friction stir welded butt joints in the same alloy. The model considers the fatigue life to consist of three regimes, crack initiation and short and long crack growth, in contrast to the typical defect-tolerant approaches which only consider the long crack growth period.

Crack initiation was considered to consist of an initial short crack, present prior to fatigue loading, identical in length to the crack initiator. The short crack growth rate was considered to be a function of the crack length and stress amplitude, whilst the long crack growth regime was described through the Paris equation, $dc/dN = C(\Delta K)^m$. The model also considers the effect on the crack initiation and growth rates of the microstructure, macrostructure and residual stresses, with the latter being determined both through the conventional hole-drilling approach and the emerging technique of synchrotron strain scanning.

The accuracy of the model was verified through integration of the short and long crack growth regimes, with the predicted lifespan being compared to results obtained from S-N testing of identical welded specimens. A good correlation between the experimental and theoretical results was observed for the parent material and friction stir welded joints for lives in the region 10^5-10^6 cycles, although the approach, in its current format, appeared less suitable for determining the fatigue properties of the MIG welded joints.

2. Introduction

The applications for aluminium alloys are increasing due to their low density, and for a number of alloys their high strength, typically resulting in a reduction in fuel consumption when utilised in the transport industry. Other properties which are also considered beneficial in the transport and other industries are their corrosion resistance, durability, recyclability and thermal and electrical conductivity. At the time of writing many fatigue design codes for welded joints in aluminium are factored from steel codes, although as the structural use of aluminium increases it is preferable that dedicated codes are developed. Advances in welding techniques, notably friction stir welding, mean that the current codes are unsuitable for assessing the fatigue capabilities of joints produced by these processes. Factoring of design codes is also undesirable as welded joints in steel and aluminium exhibit different properties that factoring of the stresses does not take into consideration. Welded joints in steel are more likely to exhibit undercuts and slag inclusions, these may be considered to be crack like defects, whereas welded joints in aluminium, although porosity is more common, frequently exhibit a significant crack initiation period. The crack initiation period, which may consist of more than 95% of the fatigue life, may be considered to consist of short crack growth, cracks that grow at stress intensities below the long crack threshold and/or at accelerated rates when quantified by the stress intensity factor range.

2.1 Welding Processes

Due to the affinity of aluminium for oxygen, it cannot be successfully arc welded in an air environment. If fusion welded in a normal atmosphere oxidisation readily occurs and this results in slag inclusion, whilst hydrogen contamination results in porosity in the weld, both resulting in a reduction in the joints strength. To overcome these problems one of the commonest ways of welding aluminium has been to use the electric arc process whilst shielding the weld pool with an inert gas, so called metal inert gas welding. This method produces good welds, although annealing of the plate in the vicinity of the weld, porosity in the weld metal, the stress concentrating effects of the weld bead and high residual stresses are detrimental to the weld properties. More recently solid-state methods, that are suitable for welding aluminium alloys, have been developed, one of these being friction stir welding. It is claimed that friction stir welding results in lower residual stresses and fewer defects, thereby enhancing the weld properties.

2.1.1 Metal Inert Gas Welding

The concept of MIG welding was developed in the 1920s, but commercial exploitation did not begin until 1948. Initially it involved a high current density, small diameter metal electrode and inert gas for arc shielding. It was primarily used for welding aluminium, and the term MIG (Metal arc Inert Gas) welding was employed. With advancements in the

process, the term gas metal arc welding (GMAW) is now becoming a more common description, because both inert and reactive gases, particularly CO_2, are now employed[1].

MIG welding is a well-established way of joining various aluminium alloys, although some alloys, notably those in the 2XXX and 7XXX series, are difficult to fusion weld. MIG welding employs an electric arc, struck between the filler rod and the material being welded, to generate localised heat. The heat melts both the parent plate and the filler metal, mixing of the two occurs, and upon cooling fusion of them occurs. The filler wire is continually fed through to the weld pool; this is generally automated, thereby maintaining the arc length and the supply of filler material. Due to the reactive nature of aluminium, the arc is shrouded by an inert gas, generally argon, protecting the base metal from contact with oxygen, nitrogen or hydrogen. Figure 2.1 and Figure 2.2 show a typical automated MIG welding set up.

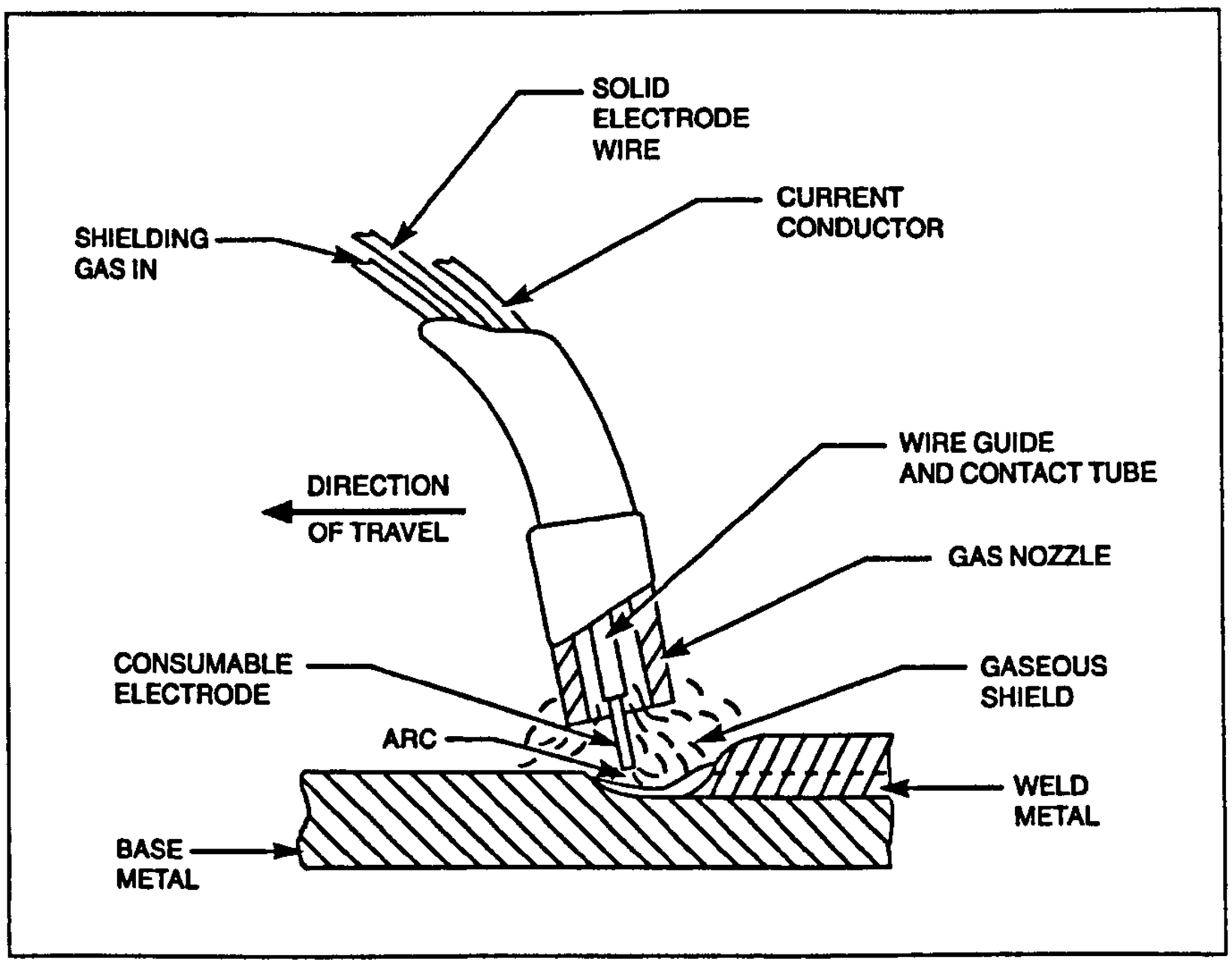

Figure 2.1: Gas metal arc welding process[1].

[1] O'Brien, RL (1997)

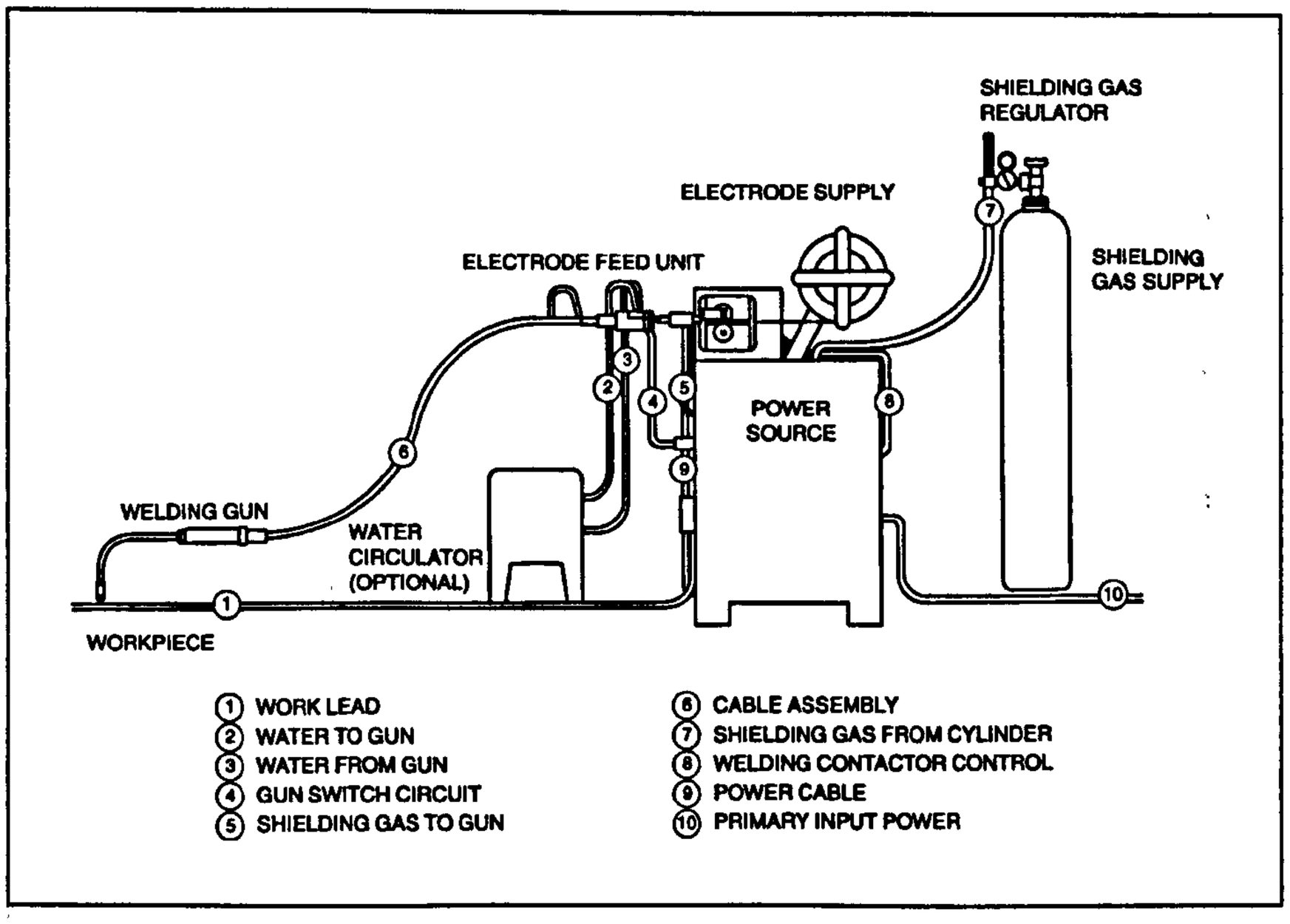

Figure 2.2: Gas metal arc equipment[1].

Although MIG welding is a well-established method for joining aluminium, it has several shortcomings. Weld porosity is more commonly detected in MIG welds in aluminium when compared to those undertaken in steel; this is due to the high solubility of hydrogen in the molten aluminium weld pool, but low solubility in solid aluminium[2]. The higher thermal conductivity and expansion coefficients, and lower modulus of elasticity, result in greater shrinkage and distortion, again when compared to steel. A loss of strength also occurs in the heat affected zone (HAZ), in heat-treated alloys through over-ageing and in strain hardened alloys through annealing, resulting in the material properties differing between the weld metal, HAZ and parent plate.

The MIG weld pool solidifies to form a "reinforced" area around the joint, commonly termed the weld bead. The weld bead leads to stress concentration effects and the failure of MIG welds frequently occurs due to crack initiation and growth along the weld toe. Within the weld bead, grain growth on cooling results in large columnar grains growing from the fusion zone into the weld bead and within the bead large equiaxed grains; large grains are generally considered to be detrimental to a material's mechanical properties. To reduce the stress concentration effect removal of the weld bead can be undertaken, but the process is both time consuming, expensive and may expose pores that then act as surface defects. Similarly, the effect of microstructural changes can be reduced through the application of thermal processes.

---

[1] O'Brien, RL (1997)
[2] Dickerson, PB (1993)

Residual stresses form due to the contraction of the weld metal on cooling and the restraint used during the process. These are tensile and may attain yield magnitude or greater at, and near to, the weld toe, in both the direction of, and transverse to, the weld[1]. The effect of residual stresses induced by the welding process, and the duration of this effect with respect to relaxation, on the mechanical performance of the weld is not fully understood at the present time, although they are generally considered to be adverse[2].

2.1.2 Friction Stir Welding

TWI (formerly The Welding Institute) developed friction stir welding in 1991. The solid state process involves plastic deformation and welding of the material, but, being a solid state process, at a temperature below the melting point. The combination of heat, generated by adiabatic shearing and friction, and the consequent plastic deformation are the main causes of fusion. Although a relatively new process, it has shown considerable potential for welding what were considered difficult-to-weld materials and dissimilar ones. The resultant welds are claimed to exhibit improved static and dynamic mechanical properties when compared to other welding techniques. A diagrammatic representation of the process is shown in Figure 2.3.

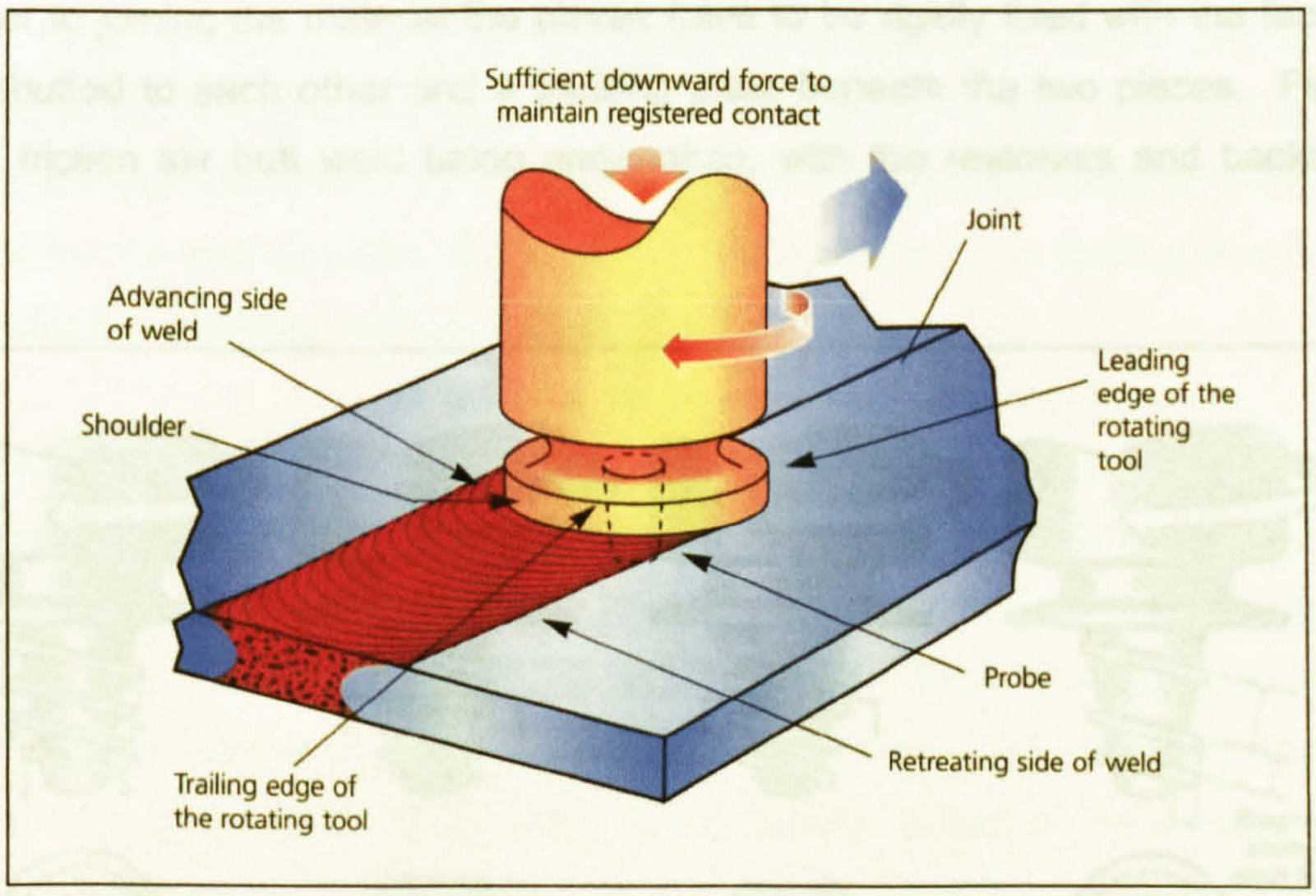

Figure 2.3: Friction stir welding[3]

[1] Harrison, JD (1981)
[2] Iida, K; Takanashi, M (1998)
[3] Johnson, R; Kallee, S (1999)

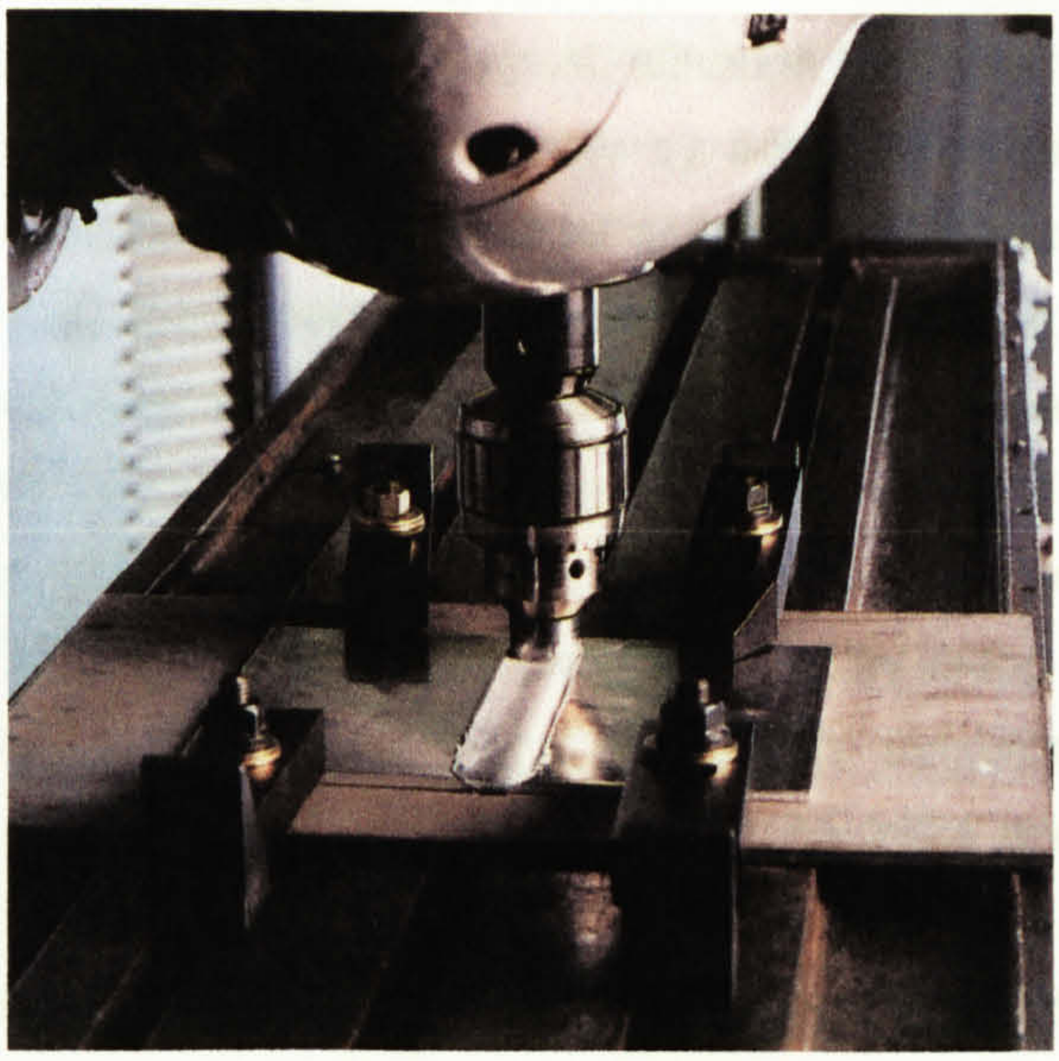

Figure 2.4: Close up of friction stir welding at the Edison Welding Institute[1]

The friction stir process is suitable for butt, lap and T joints, requiring little material preparation, no filler material and in the case of materials like aluminium, no shielding gas. Prior to joining the material the pieces have to be rigidly fixed with the faces to be welded abutted to each other and a backing plate beneath the two pieces. Figure 2.4 shows a friction stir butt weld being undertaken, with the restraints and backing plate evident.

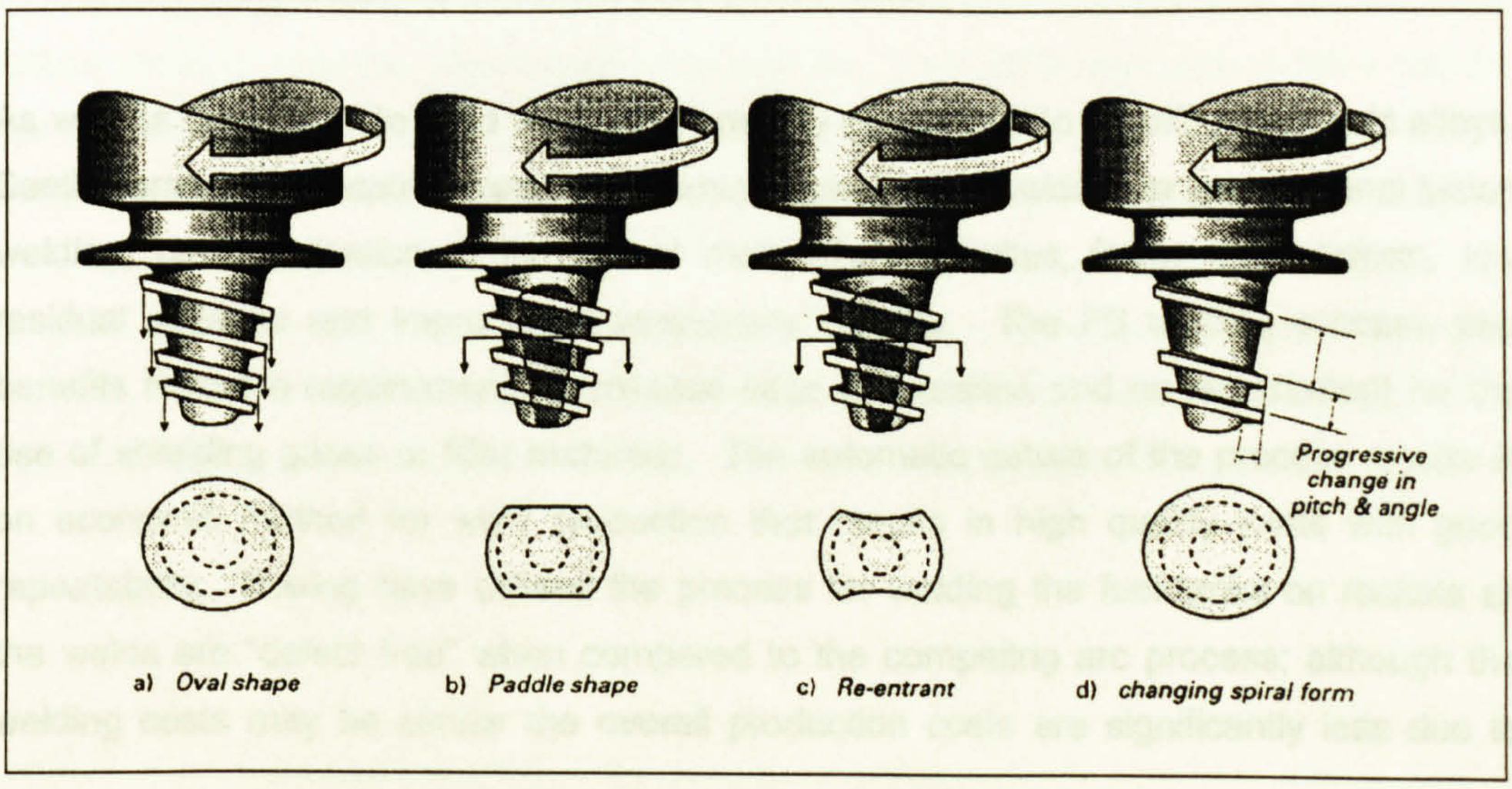

Figure 2.5: Whorl™ friction stir welding tool profiles[2]

[1] O'Brien, RL (1997)
[2] Thomas, WM (1998)

A specially shaped rotating tool, typical geometries of which are shown in Figure 2.5, is plunged between the abutting faces of the joint, although for thicker sections a pilot hole may be required. The heat generated, mainly by adiabatic shearing and to a lesser extent through friction between the tool shoulder and pin and the parent material, result in a plasticised area around the immersed region of the tool. Initially it was thought that the main generator of heat was due to friction between the tool pin and shoulder and the material to be welded[1], but adiabatic shearing is now considered to be the main heat source. During the process temperatures of up to 0.8 of the material's melting temperature (T_m) were measured by type K thermocouples by Wang et al[2] in an AA 6061-T6 weld, whilst microstructures suggesting a comparable maximum temperature have been reported by Li et al[3] in a FS weld between an AA 2024 and AA 6061. Recent advances to the process include force control over the tool, this resulting in a more uniform weld microstructure and allowing thinner materials to be welded[4].

Once the tool has penetrated the work piece, the heat and rotational movement of the pin result in plasticisation of the surrounding material. Initially the material is extruded at the surface, but as the tool shoulder contacts the plate the plasticised material is compressed between the shoulder, parent material and backing plate. The tool is then moved along the joint; Li[2], when welding AA 2024 to 6061, employed rotational speeds of 400-1200 rpm and traverse speeds of 1 $mm.s^{-1}$, whilst Ericsson and Sandström[5] employed rotational speeds of 2200-2500 rpm and transverse speeds of 700-1400 $mm.min^{-1}$ when welding 4 mm thick AA 6082. As the tool traverses the joint, the material is heated and plasticised by the leading edge of the tool and transported to the trailing face of the pin, where, upon consolidation, it forms a solid-phase weld.

As well as being able to weld what are generally considered to be difficult to weld alloys, Seetharaman et al[6] state several other advantages for FS welds over conventional fusion welding; better retention of the parent material's properties, fewer weld defects, low residual stresses and improved dimensionally stability. The FS welding process also benefits from the requirements of minimal edge preparation and no requirement for the use of shielding gases or filler materials. The automatic nature of the process results in an economic method for weld production that results in high quality joints with good repeatability. Boeing have utilised the process for welding the fuel tanks on rockets as the welds are "defect free" when compared to the competing arc process; although the welding costs may be similar the overall production costs are significantly less due to

---

[1] Thomas, WM (1998)
[2] Tang, W et al (1998)
[3] Li, Y et al (1999)
[4] Talwar, R et al (2000)
[5] Ericsson, M; Sandström R (2002)
[6] Seetharaman, V et al (2000)

there being no weld defects that require repairing[1]. Boeing have claimed reductions of 71% in weld cycle time and 81% in labour and cost reductions from $24 per foot (£48,000 Km^{-1}) to $0.14 per foot (£280 Km^{-1}) when comparing a circumferentially bolted joint with a FSW one[1]. In a similar approach Hitachi have employed the process to fabricate aluminium rail cars, with them making savings on the welding process as the resulting joints require no post-processing to rectify distortion[1].

2.2 Fatigue Properties

The classical approach employed in determining the fatigue strength of various components is to develop cyclic stress range/life (S-N) or cyclic strain range/life (ε-N) curves. Testing is typically undertaken on smooth specimens under laboratory conditions, with various techniques being employed to account for the stress ratio, type of loading, stress concentrations etc., although either full size or scaled components may also be employed. Due to the high percentage of the fatigue life considered to consist of crack initiation and/or short crack growth the stress/life and strain/life approaches may be considered to be a measure of the materials resistance to crack initiation.

In contrast to the stress/life or strain/life approach, defect-tolerant design, which is increasingly being employed for fatigue-critical applications, relies upon being able to accurately predict the number of cycles, or time, for a defect to grow from an initial size to some critical dimension. A linear elastic fracture mechanics (LEFM) approach is generally employed, therefore the technique is reliant on small scale yielding, with various methods having been developed to take into consideration aspects such as the mean stress, residual stresses, stress concentrations etc. The LEFM approach dictates that the crack propagation under consideration pertains to long cracks, with the technique therefore relying on the initial defect resulting in long crack growth; if the defect does not exhibit small scale yielding an estimate of the crack initiation period is necessary. The long crack growth rates frequently of interest to engineers fall within the linear region, on a log/log scale, of crack growth rate/stress intensity factor range plots, often described as the Paris regime, with the growth rates typically described by the Paris equation, (2.1).

$$\left(\frac{dc}{dN}\right)_{lcg} = C.(\Delta K)^m \qquad (2.1)$$

where: $(dc/dN)_{lcg}$ = long crack growth rate.

ΔK = stress intensity factor range.

C and m = scaling constants.

[1] Threadgill, P (2003)

The Paris equation will generally return an accurate assessment on the fatigue life of a cracked specimen, but it does not take into consideration the crack initiation or short crack growth period, the result being a conservative estimate of the fatigue life in an uncracked specimen. Therefore, as the resolution of flaw detection increases, the ability to predict the behaviour of what are termed short cracks becomes a requirement. Short cracks do not typically conform to the LEFM required for accurate analysis utilising the Paris equation, with accelerated crack growth, and frequent arrest, often being observed at stress intensities below the long crack threshold and accelerated growth being observed above the threshold stress intensity factor. The determination of short crack growth rates have tended to be empirically based, making prediction both time consuming and expensive, but in recent studies it has been suggested short crack growth rates may be considered to be a function of the crack length when the stress amplitude, yield or tensile strength and maximum applied strain are taken into consideration:

$$\left(\frac{dc}{dN}\right)_{scg} = f\left(\sigma_a, \sigma_y, \sigma_{TS}, \varepsilon_{max}, c\right) \tag{2.2}$$

$$\left(\frac{dc}{dN}\right)_{scg} = B.\left(\frac{\sigma_a}{\sigma_{y\ or\ TS}}\right)^n .c \tag{2.3}$$

$$\left(\frac{dc}{dN}\right)_{scg} = B.\left(\frac{\sigma_a}{\sigma_{y\ or\ TS}}\varepsilon_{max}\right)^n .c \tag{2.4}$$

where: $(dc/dN)_{scg}$ = short crack growth rate.

σ_a = stress amplitude.

σ_y = yield stress.

σ_{TS} = tensile strength.

c = crack length.

ε_{max} = maximum applied strain.

B and n = scaling constants.

Although a combination of equations (2.1) and (2.3) or (2.4) will provide an accurate assessment of the fatigue life of an uncracked specimen, engineering structures are generally fabricated and the processes employed present further problems. Both metal inert gas and friction stir welding result in a change in the microstructure from the parent material, and although the microstructure is often considered to have a nominal effect on long crack growth rates in the Paris regime, it is considered to be more influential with respect to short crack growth rates. To take into account of the effect of the microstructure on the short crack growth rate either measurements of the growth rate should be conducted in a comparable microstructure to that where crack initiation and short crack growth occur, or the growth rate should be adjusted to take their effect into consideration.

Residual stresses also influence the fatigue properties, with welding processes known to result in residual stresses that may be up to the yield strength in magnitude and acting both locally and throughout the structure. The defect-tolerant approach to determining the fatigue life requires both an accurate assessment of their magnitude and redistribution under loading to be known, with these typically being taken into consideration through modification of the mean stress.

The welding processes also result in a change in the external geometry of the structure that result in stress concentrating effects, with the weld bead of metal inert gas welds being a notable example, although the surface finish that results from friction stir welding has a similar, albeit less severe, effect.

3. Geometry, Microstructure and Mechanical Properties

3.1 Abstract

The following section details the geometry, microstructure, microhardness and tensile properties of AA 5383-H321 8 mm thick plate and metal inert gas (MIG) and friction stir (FS) welded butt joints in this alloy. Two types of welds within each category are described; high and low input (HI and LI respectively) MIG welds and single and double pass (SP and DP respectively) FS welds.

Details of the external geometry of the welds are discussed; the weld bead in the case of the MIG welds and the friction band and backing plate sides and first and second pass sides in the case of the single and double pass friction stir welds respectively.

Microstructure of the parent plate and welds are described, notably the weld bead and heat affected zone (HAZ) in the MIG welds and thermo-mechanically affected zone (TMAZ), including the weld nugget, and HAZ in the friction stir welds.

The mechanical properties of the parent plate and welds were determined through microhardness and tensile testing and these results are presented.

3.2 Literature Review

Dickerson[1] states that aluminium has several chemical and physical properties that influence its welding characteristics, although it can be joined by more methods than any other metal. The specific properties that affect the welding of aluminium and its alloys are its oxide characteristics, the solubility of hydrogen in molten aluminium, its thermal, electrical and non-magnetic characteristics, its lack of colour change when heated and its alloys wide range of mechanical properties and melting points[1].

The fatigue properties of materials are influenced by numerous factors and the macrostructure and microstructure of welded joints have a significant influence on the fatigue strength. Stress concentrators increase the likelihood of crack initiation and accelerated crack growth. The weld bead, in the case of MIG welds, and the surface topography, in the case of FS welds, act as stress concentrators and hence influence the fatigue properties. The heat generated by both the MIG and FS processes affects the microstructure of the material in the region of the weld. Within the weld bead, in the case of MIG welds, slow cooling of the molten weld metal results in the formation of large grains, generally considered detrimental to the mechanical properties of a metal. In contrast, the small grain structure found within FS weld nuggets would generally be considered beneficial to the mechanical properties. Annealing, of both strain hardened (through recrystallisation and a reduction in lattice distortions[2]) and heat treatable (through precipitation caused by over-ageing[3]) aluminium alloys occurs, the change in microstructure affecting both crack initiation and propagation rates.

---

[1] Dickerson, PB (1993)
[2] Altenpohl, D (1982)
[3] Lancaster, JF (1999)

3.2.1 Metal Inert Gas Welds in Aluminium Alloys

The welding of non-heat treatable alloys causes microstructural damage in the HAZ. This results in recovery, recrystallisation and grain growth; therefore, the loss in strength is not as severe as that found in the heat treatable alloys where strengthening precipitates may dissolve or coarsen[1]. The weakest part of a weld in non-heat treatable aluminium alloys is generally the weld metal, in contrast to most heat treatable alloys where the HAZ has the lowest strength[1]. The welding procedure and fusion process has a minimal effect on the transverse tensile strength of a butt weld, although they will affect the size of the HAZ[2].

The weld metal microstructure of non-heat treatable aluminium alloys consists of columnar, epitaxial grains with a cellular or columnar-dendritic substructure that has interdendritic eutectic constituents, Mg_2Al_3, for 5XXX alloys[1], although Mondolfo[3] states that this should be Mg_5Al_8 as Mg_2Al_3 is outside the limits of existence according to the aluminium~magnesium phase diagram.

The type of grain growth that occurs as the molten weld metal solidifies is depicted in Figure 3.1. Figure 3.1 (f) depicts five temperature gradients, a - e, versus constitutional supercooling; the resulting grain structures, from each of the temperature gradients, are depicted in Figure 3.1 (a - e). For non-planar growth to occur, a negative temperature gradient, the temperature decreasing from the solid-liquid interface into the liquid, is generally required, but negative temperature gradients do not exist in welds[4]. In a single component system, pure metal, the positive temperature gradient that exists prevents non-planar growth occurring, but constitutional supercooling can occur in alloys, allowing non-planar solidification, even though a positive temperature gradient exists[4]. For the five temperature gradients shown in Figure 3.1 (f), the lesser the gradient, the greater the degree of supercooling. For gradient (a), the temperature gradient is greater than that of the liquidus and thus only planar growth can occur[4]. For gradient (e), the liquidus temperature is so much greater than that of the liquid that equiaxed dendrites can form ahead of the solid-liquid interface[4]. The intermediate temperature gradients allow cellular, cellular dendritic and columnar dendritic for gradients (b), (c) and (d) respectively[4].

The types of grain structure found within welds depends upon the welding parameters, energy input, velocity of welding etc.[4], although typical grain structures, with respect to the solidification rate around the weld pool, are depicted in Figure 3.2[5]. Constitutional

---

[1] Cross, CE (1993)
[2] Dickerson, PB (1993)
[3] Mondolfo, LF (1976)
[4] Solomon, HD (1993)
[5] Matsuda, F et al (1969) *referenced by Solomon, HD (1993)*

supercooling within the weld pool results in the formation of equiaxed dendrites ahead of the solid-liquid interface, Figure 3.1 (e); the weld bead, excluding the weld/parent metal interface regions, consists of this type of grain structure. At the interface between the weld pool and the parent material the degree of supercooling is less than found in the weld pool and columnar dendritic growth occurs, Figure 3.1 (d), from the parent material into the weld pool. If no supercooling occurs between the weld pool and parent material interface, planar grain growth, Figure 3.1 (a), from the parent material into the weld pool will occur.

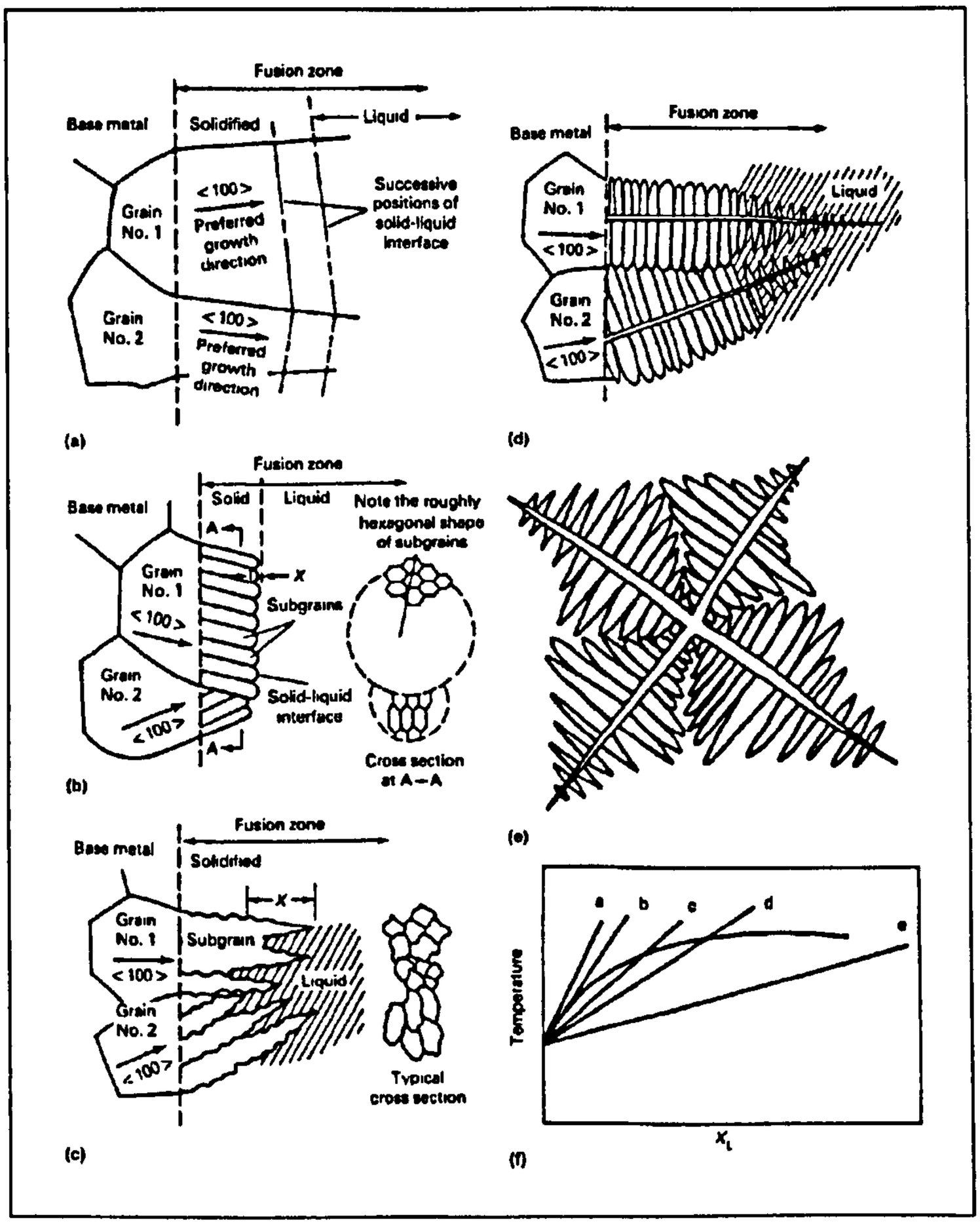

Figure 3.1: Schematics showing microstructure of solid liquid interface modes of solidification and the temperature gradients that generate each of the different modes; (a) planar growth, (b) cellular growth, (c) cellular dendritic growth, (d) columnar dendritic growth, (e) equiaxed dendrite and (f) five temperature gradients versus constitutional supercooling[1].

[1] Savage, WF et al (1976) *referenced by Solomon, HD (1993)*

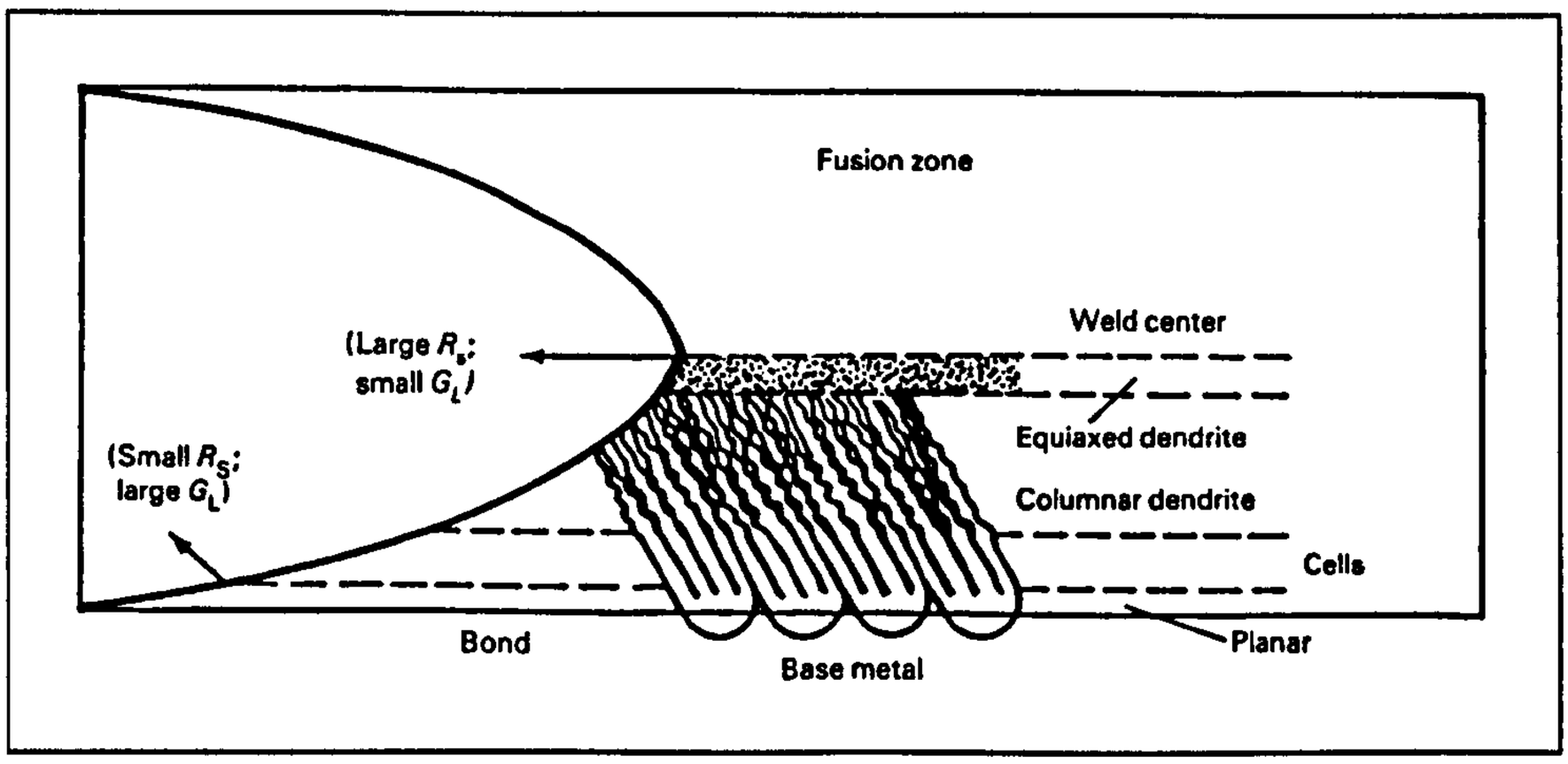

Figure 3.2: Schematic showing variation of microstructure in response to variation of the solidification rate around the weld pool (R_S = solidification rate , G_L = free energy of the liquid phase)[1].

3.2.1.1 Hardness Profile and Heat Affected Zone

Calcraft et al[2] measured the size of the HAZ in a MIG welded AA 5383-H116 through microhardness measurements as shown in Figure 3.3. The parent material had a hardness of 98.5 $HV_{0.1}$, whilst that of the weld, the filler material being AA 5356, was 74.5 $HV_{0.1}$ and that of the HAZ being 85.5 $HV_{0.1}$. The HAZ was noted to extend from 3.8 - 4.2 mm from the weld toe, 12 - 12.4 mm from the weld centre, the hardness of the parent material being attained at a distance of 9 - 9.8 mm from the weld toe, 17.6 mm from the weld centreline.

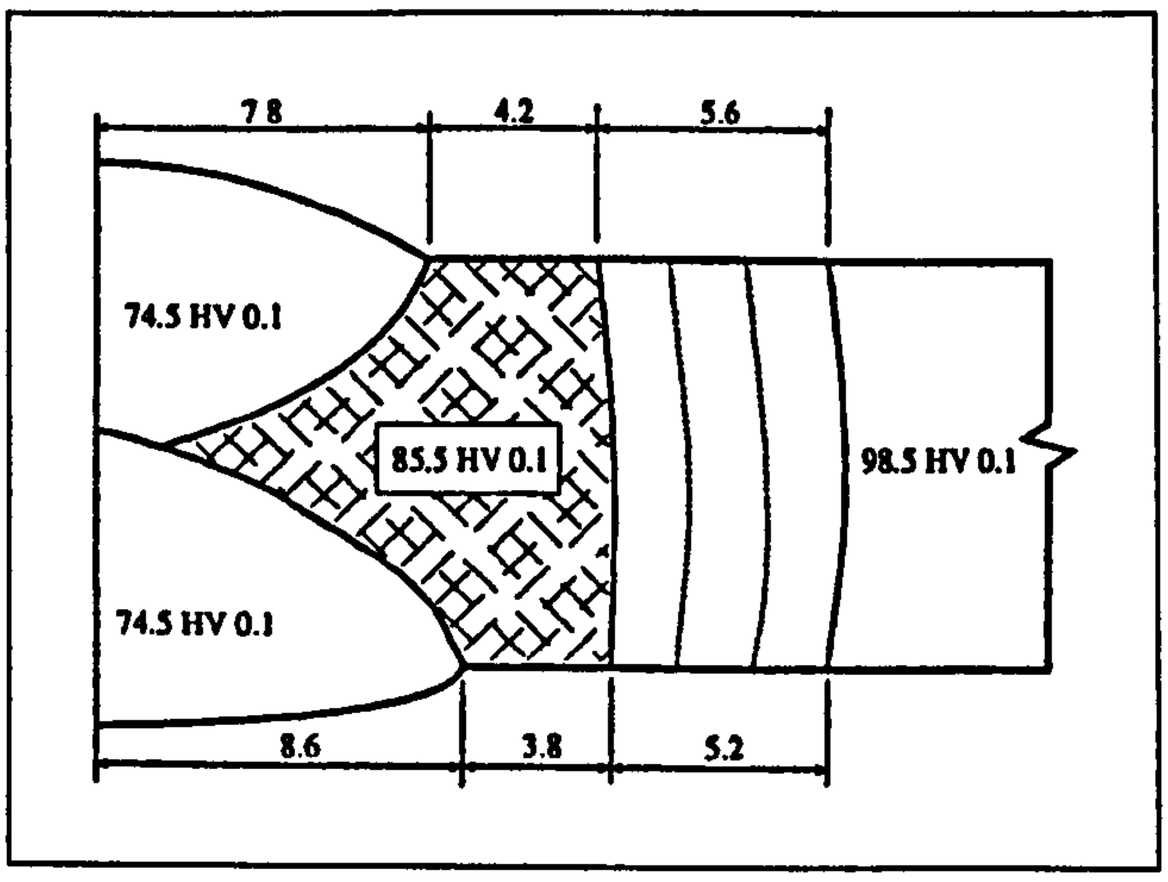

Figure 3.3: Microhardness profile of the weld and HAZ in a MIG butt weld in AA 5383-H116.

[1] Matsuda, F et al (1969) *referenced by Solomon, HD (1993)*
[2] Calcraft, RC et al (1999)

3.2.1.2 Effects of the Weld Profile

The MIG welding process results in a change in the profile of the pieces being fabricated. This change is generally termed the weld bead, and various aspects of its geometry are known to affect the fatigue properties of MIG welded joints. The term "reinforcement" is frequently used to describe the weld bead, although its effect in cyclic loading is to reduce, rather than reinforce, the strength of the joint due to its stress concentrating nature. Automatic welding processes are favoured over manual welds for several reasons, one of these being the increase in control over the weld geometry. Gurney[1] states that the high cycle fatigue strength of automatic welds was lower than that obtained from manual welds, due to the poor profile of the weld reinforcement, although advancements in the process since this publication are likely to have reduced or reversed this. The weld profile factors that are known to influence the fatigue properties of a welded joint are the weld toe radius and angle and, according to Chapetti and Otegui[2], the waviness of the toe (detailed in Section 5.3.1.2.1, Weld Toe Profile Modification, pages 248 - 250). A typical geometry for a MIG, as-welded, profile is shown in Figure 3.4, where ρ is the weld toe radius and θ the weld toe angle (weld toe angles are also frequently detailed as what would be the equivalent of $180° - \theta$ in Figure 3.4). Both Sanders et al[3] and Kelsey and Nordmark[4] state that the overriding factor in the fatigue life of (MIG) welded joints is the weld profile. To overcome the adverse effects of the profile, weld dressing, involving improvement of the profile with respect to the fatigue strength, have been implemented as a solution, although the process tends to be both expensive and time consuming.

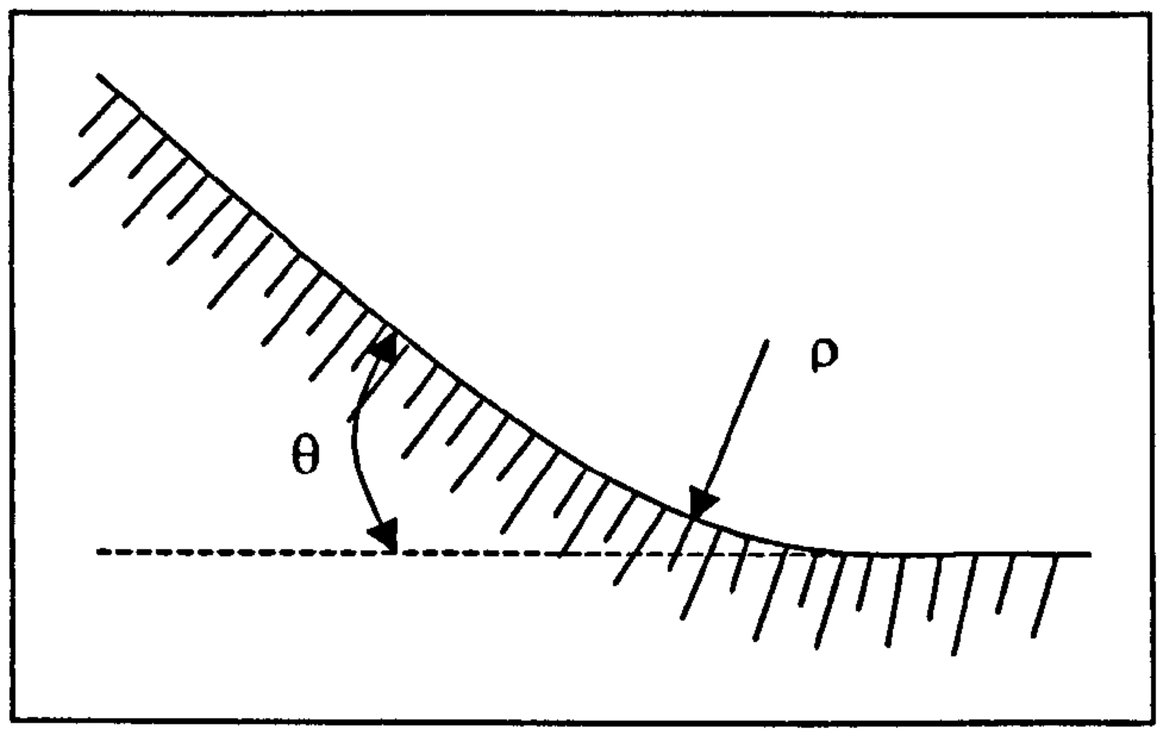

Figure 3.4: Weld toe profile, where θ and ρ are the weld toe angle and radius respectively.

[1] Gurney, TR (1979)
[2] Chapetti, MD; Otegui, JL (1997)
[3] Sanders Jr, WW et al (1965)
[4] Kelsey, RA; Nordmark, GE (1979)

Weld toe angles and radii were measured by Aabø and Thuestad[1] in both fillet and butt welded joints in an AlMg4.5Mn alloy, the results for the butt welds being shown in Table 3.1.

Aluminium alloy	Welding position	Mean toe radius (mm)	Mean reinforcement angle (°)	Min. toe radius (mm)	Max. reinforcement angle (°)
AlMg4.5Mn	Flat	1.2	30	0.3	43
	Horizontal-vertical	0.7	23	0.1	68
	Vertical	2.3	16	0.2	58

Table 3.1: Butt weld toe profiles[1]

Niu and Glinka[2], in their method for calculating the weight function and subsequent stress intensity factors, K_I, for a T-butt weld, stated that the K_I for a crack in a welded joint is dependent upon the overall geometry of the joint, weld profile and type of loading. The authors investigated the effects that the weld toe radius, ρ, and angle, θ, had on crack initiation and crack growth. Their results implied that the weld toe radius had a greater effect on the stress field in the close vicinity of the weld toe and therefore on crack initiation, whilst the weld angle affected the stress field further from the toe and therefore had a greater influence on crack growth[2]. Through a finite element analysis they determined the stress distribution through the thickness of the plate for four weld toe radii to plate thickness, t, ratios; values ranged from 3.8 - 2.6 times the nominal stress distribution at the surface for ρ/t ranging from 0.2 - 0.067 respectively, the weld toe angle being considered constant at an angle of 45°. Similarly, the effect of the weld toe angle on the through thickness stress distribution was determined for three angles, ρ/t being considered constant at 0.067. The stress distribution at the surface, ranged from 3.3 times the nominal distribution for an angle of 60° to 2.6 times for an angle of 30°. The effects resulting from the radii were considered influential at depths of less than 2% of the plate thickness, in contrast, those from the toe angle were considered influential up to a depth of 10% of the plate thickness. They suggest that these differences result in the weld toe radius having a greater effect on the stress field in the close vicinity of the weld toe and therefore on crack initiation, while the weld angle affects the stress field further from the toe and therefore has a greater influence on crack growth. K_I were calculated at, and distant to, the weld toe, as shown in Figure 3.5, taking into consideration both the weld angle and radius. For ρ/t values ranging from 0.2 - 0.067 the K_I at the weld toe was 3.2 - 2.3 times greater than that found for the same crack when it had increased in length to 0.1t and was considered to be influential to a depth of 6% of the thickness. For angles ranging from 30° - 60° the K_I at the weld toe was found to be 2.5 - 3.2 greater than that

[1] Aabø, S; Thuestad, JG (1985)
[2] Niu, X; Glinka, G (1987)

found for the same crack when it had increased in length to 0.3t and was considered influential to a depth of 30% of the thickness. The K_I were noted to act over a much greater distance than the stress fields and, as they are a function of both stress and geometry, both these factors should be considered.

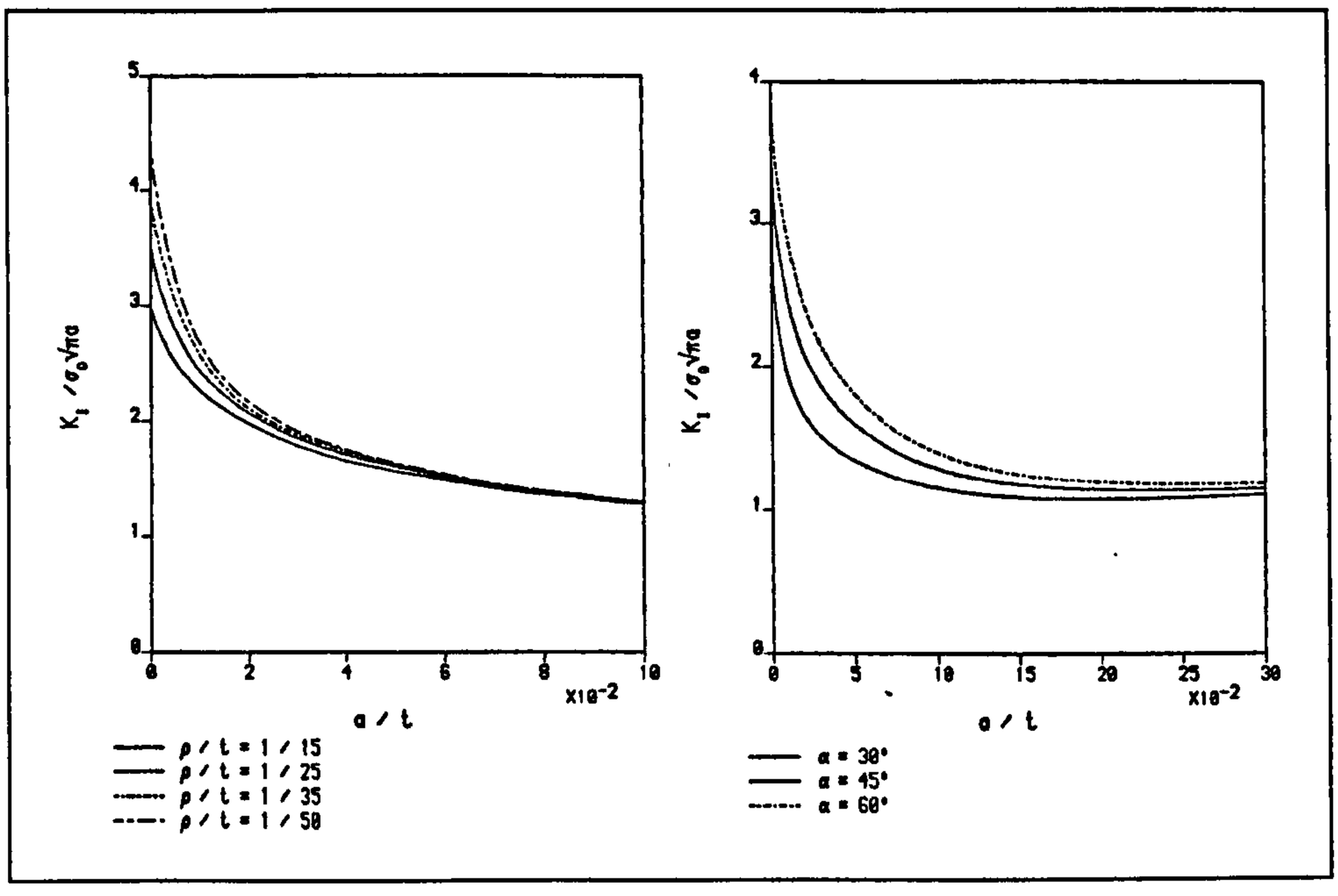

Figure 3.5: Effect of the weld toe radius, θ = 45°, (left) and of the weld toe angle, ρ/t = 0.067, (right) on the stress intensity factor, K_I, for an edge crack in a T-butt joint under bending load[1].

Further details with respect to the effect of the weld profile on the fatigue properties of welded joints are given in Section 5.3.1.2, Weld Profile (pages 241 - 250).

3.2.1.3 Porosity in Aluminium Welds

The main cause of porosity in aluminium welds is hydrogen contamination, hydrogen being the only gas with any significant solubility in aluminium. The ratio of the maximum solubility of hydrogen in superheated liquid aluminium to the solubility in liquid aluminium at the solidification temperature is 36 times greater than that of iron[2]. The main sources of contamination are hydrogen contained within both the filler and parent material, hydrogen bearing contamination of both the filler and parent material surfaces and hydrogen or water vapour in the shielding gas[2]. The main source of porosity in commercial welding is from surface contamination[2]. Once the hydrogen is absorbed into the weld pool, the formation of pores is controlled by solidification morphology, hydrogen pressure, solubility considerations, and nucleation and growth kinetics[2]. Pore growth

---

[1] Niu, X; Glinka, G (1987)
[2] Devletian, JH; Wood, WE (1983)

occurs to minimise the surface energy of the bubble in the weld pool, with growth occurring through either further hydrogen diffusion or coalescence with a neighbouring pore. Factors affecting pore growth rates include[1]:

i. Cooling/solidification rate of the weld.
ii. Diffusion of hydrogen.
iii. Concentration of hydrogen in the molten weld metal.
iv. Concentration of stable nuclei (cell walls, grain boundaries, interdendritic spacings, oxide and other inclusions, etc.).

Other variables affecting concentration of porosity include the composition of the alloy; the addition of 6% magnesium nearly doubles the solubility of hydrogen in aluminium, although a subsequent increase in the threshold level for porosity formation results in the amount of porosity decreasing[1]. The welding direction and subsequent shape of the weld bead also influence the amount of porosity in the weld. Narrow welds that have a high crown tend to trap porosity due to the distance the pores must travel before escaping to the surface[1]. Other welding parameters considered to affect the porosity found in aluminium welds include the weld current and speed, arc length, atmospheric pressure and shielding gas composition[1].

Ashton et al[2] considered the effect of porosity on butt welded joints in an AA 5086-H116, porosity levels ranged from 0.03 - 4.2% by volume. The tensile elongation was found to be susceptible to small increases porosity with a reduction of 50% being observed as the porosity volume increased from 0.03 - 4.2%. The tensile strength was less affected, with a significant reduction not being noted until the porosity level increased above 1.1%; at porosity levels of 4.2% a reduction of 15% was measured. Yield strength was only slightly affected by porosity levels of up to 4%.

Lawrence et al[3] studied the effect of porosity on the fatigue performance of butt welded AA 5083/5183, base/filler metal. Welds were grouped into four grades depending on the level of porosity, determined as a percentage of the area, ranging from sound welds to high porosity welds and tests were undertaken on both as-welded (AW) and reinforcement removed (RR) specimens. Porosity levels were measured on the fracture surface, with the porosity being graded as either macroporosity, pore diameter ≥ 0.01" (≥ 254 μm), and microporosity, pore diameter < 0.01" (< 254 μm). Minimum and maximum porosity levels were as shown in Table 3.2.

---

[1] Devletian, JH; Wood, WE (1983)
[2] Ashton, RF et al (1975)
[3] Lawrence, FV et al (1975)

	AW 3/8" (9.525 mm) thickness			AW 1" (25.4 mm) thickness		
	Porosity density by area (%)					
	macro	micro	total	macro	micro	total
Min.	0	0	0	0	0	0
Max.	24.80	21.60	42.02	5.63	26.1	27.56
	RR 3/8" (9.525 mm) thickness			**RR 1" (25.4 mm) thickness**		
	Porosity density by area (%)					
	macro	macro	macro	macro	macro	macro
Min.	0	2.29	2.95	0	1.14	4.69
Max.	5.85	25.80	29.58	4.87	44.58	49.04

Table 3.2: Range of porosity levels measured in AA 5083 MIG welds.

Of 28 fatigue tests completed on the 3/8" thickness AW specimens 26 failed at the weld toe, none due to porosity, whereas for the RR specimens 11 of the 12 failures were due to porosity. The 1" thickness AW specimens exhibited failure at the weld toe for 22 of the 27 tests, in contrast to this, of the 18 RR specimens tested, 14 failed due to porosity[1]. The authors concluded that there was little influence of porosity on the fatigue strength of the 3/8" AW specimens and only a small influence on the AW 1" welds. The dominant fatigue notch was described as being the weld toe, finite element analysis returning values of K_t of 1.7 - 2.0 for the 3/8" welds and 1.3 - 1.7 for the 1" welds[1]. For the RR specimens there was a moderate effect on the fatigue properties due to porosity, although the RR welds had better fatigue properties than the AW specimens except in cases of very high porosity. Pores resulting in failure of the RR welds were located just below the surface, the authors stating that the stress concentration factor (SCF) due to a pore would be at a maximum for this position[1].

[1] Lawrence, FV et al (1975)

3.2.2 Friction Stir Welds in Aluminium Alloys

TWI recommends that the following microstructural classification, depicted in Figure 3.6, is employed for friction stir welds[1].

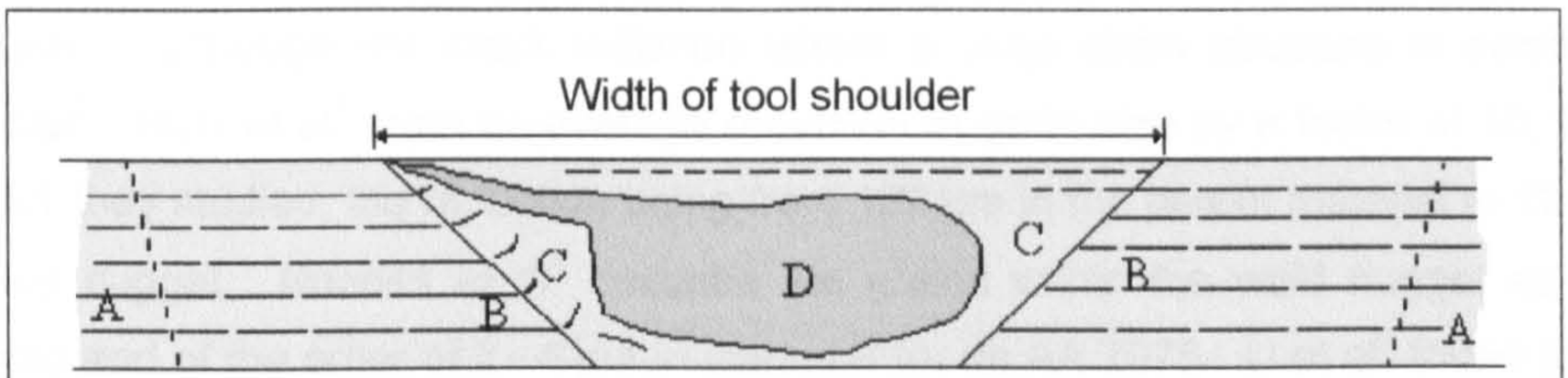

A. Parent metal unaffected by weld.
B. Heat affected zone (HAZ).
C. Unrecrystallised area found in aluminium alloys.
D. Recrystallised nugget found in aluminium alloys.
C+D Thermomechanically affected zone (TMAZ).

Figure 3.6: Microstructural classification of friction stir welds[1].

The unaffected material, or parent metal, is remote from the weld and although it may have experienced a thermal cycle from the process, this will not have affected its microstructure or mechanical properties. The HAZ lies closer to the weld centreline and the thermal cycle will have modified its microstructure and/or mechanical properties. Unlike the thermomechanically affected zone (TMAZ), the region does not undergo plastic deformation and the changes in properties are comparable to those in the HAZ observed for other thermal processes.

The TMAZ is a result of both plastic deformation and thermal exposure. In the case of aluminium, it is possible to have significant plastic strain at high temperature without recrystallisation occurring[2]. The majority of authors, for example[3,4,5,6], state that the result of this is the formation of a dynamically recrystallised region, the weld nugget, whilst the remainder of the TMAZ experiences plastic deformation, but not recrystallisation. Yang[7] studied FS welds in AA 7475-T6 and considered the finely grained structure of the nugget to be a dynamically recovered subgrain structure, rather than a dynamically recrystallised one. Frigaard et al[8], studying FS welds in AA 6082 and AA 7108, concluded that dynamic recovery was also the most likely mechanism to account for the microstructural features of the weld nugget. The weld nugget is not typically found in other materials that

---

[1] TWI (2000a)
[2] TWI (1999)
[3] Karlsson, J et al (1998)
[4] Murr, LE et al (1997)
[5] Murr, LE et al (1998a)
[6] Strangwood, M et al (1999)
[7] Yang, HS (1998)
[8] Frigaard, Ø et al (1999)

have been welded by the FS technique, the TMAZ being completely recrystallised, resulting in the absence of the weld nugget[1].

Grain sizes in the weld nugget are significantly smaller than the parent material; this should be beneficial with respect to various mechanical properties, including fatigue crack propagation, although not crack initiation where a large grain structure is considered beneficial[2]. Murr et al[3] state an average reduction in grain size by a factor of 10, for the AA 6061 they studied, the reduction being from 100 µm in the parent material to 10 µm in the weld nugget. Rhodes et al[4] describe the grains within the weld nugget as being equiaxed and of the order of 2 - 4 µm in diameter for an AA 7075. Li et al[5] found that the equiaxed grains of the weld nugget, for a FS weld between an AA 2024 and AA 6061, varied from 1 - 15 µm depending upon their location within the nugget. The authors suggested that the temperature difference between the tool shoulder (friction band) side and the backing plate side and between the tool centreline and the edge of the weld nugget were the cause of the grain size variations[5]. Flores et al[6] reported that the dislocation density was significantly lower and no dislocation cells were present in FS welded AA 1100. A reduction in dislocation density in the weld nugget has also been observed by Liu et al[7] and Murr et al[8] in FS welded AA 6061.

A series of concentric rings, shown in Figure 3.7[9] and Figure 3.8[10], are also reported by several authors, for example[10,11,12,13]; Magnusson and Källman[14] claim that the rings are related to the thread of the tool and are seen as a sign of good weld quality. Threadgill[9] detailed the macrostructure of friction stir welds in AA 7075-T7351, AA 2014A-T6 and AA 5083-H321. All exhibited a series of concentric rings, sometimes referred to as "onion rings", at the centre of the weld nugget, as shown in Figure 3.7, although he states that this feature is not visible with all alloys. The shape of the nugget is described as being very variable[9]. Appendages, evident in Figure 3.7, are described as being frequently evident, of a complex shape, and extending from the weld nugget to as far as the tool shoulder[9]. No comment is made about the microstructure of the appendages, or the cause of their formation, although the TWI microstructural classification of friction stir welds in aluminium alloys, shown in Figure 3.6, suggests that they are part of the weld nugget and their microstructure is comparable to that found in the weld nugget. The

---

[1] TWI (1999)
[2] Suresh, S (1998)
[3] Murr et al (1998a)
[4] Rhodes, CG et al (1997)
[5] LI, Y et al (1999)
[6] Flores, OV et al (1998)
[7] Liu, G et al (1997)
[8] Murr, LE et al (1998b)
[9] Threadgill, P (1997)
[10] Dalle Donne, C; Biallas, G (1998)
[11] Biallas, G et al (1999)
[12] Hashimoto, T et al (1998)
[13] Larsson, H et al (2000)
[14] Magnusson, L; Källman, L (2000)

shape of the weld nugget is also variable, depending on the alloy and process conditions; its diameter detailed as being slightly greater than that of the tool, but significantly less than the tool shoulder diameter[1]. Dalle Donne and Biallas[2] describe variations in the microstructure of friction stir welds in AA 2024-T3 due to modifications to the tool, although details of the modifications were not described. A concentric ring type inner structure was described for the tool B nugget, although this became less evident with increasing weld traverse and rotation speed, as shown in Figure 3.8.

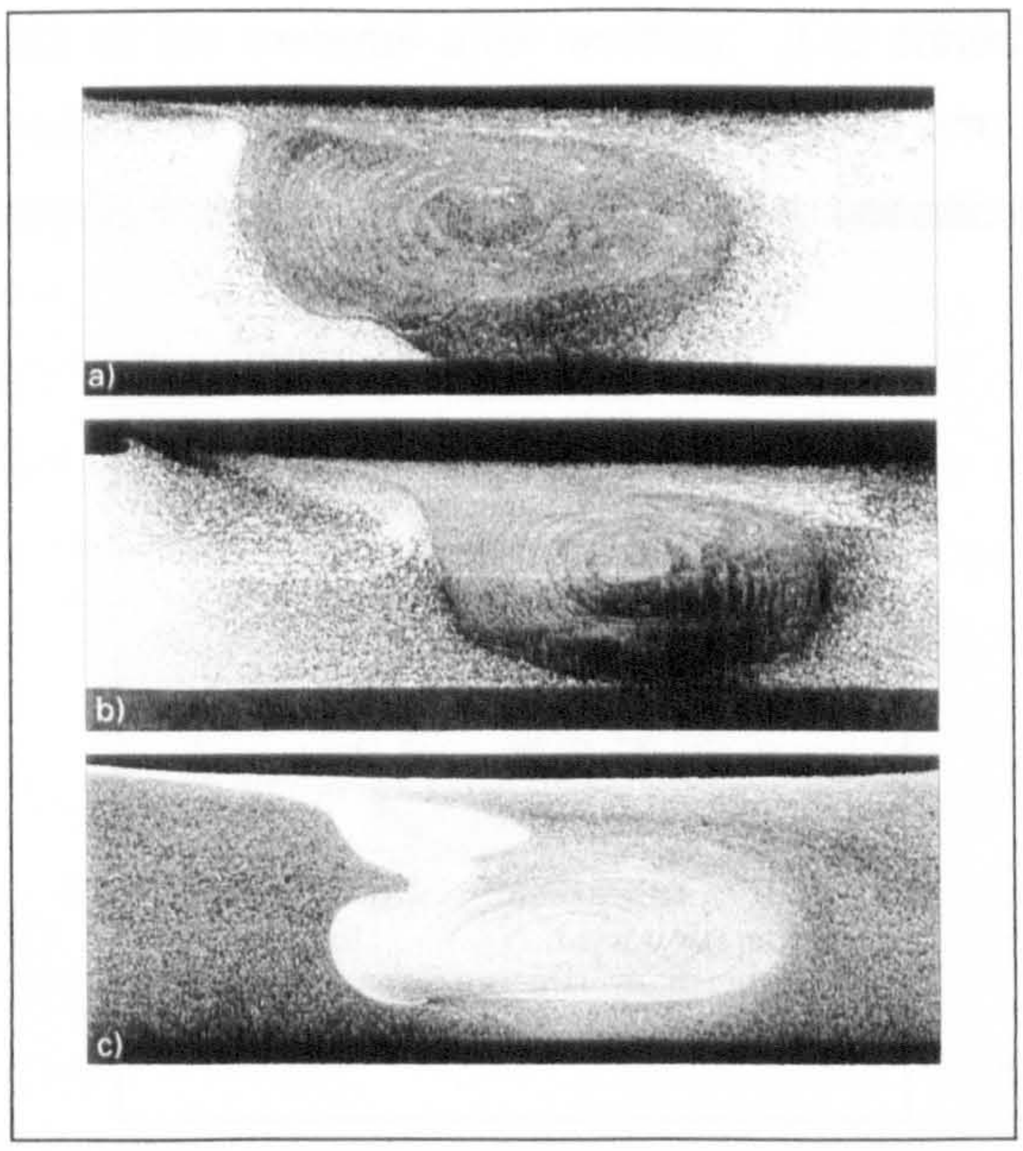

Figure 3.7: Typical macrosections from friction stir welds in 6.4 mm thick materials: a) AA 7075-T7351, b) AA 2014-T6 and c) AA 5083-H321[1].

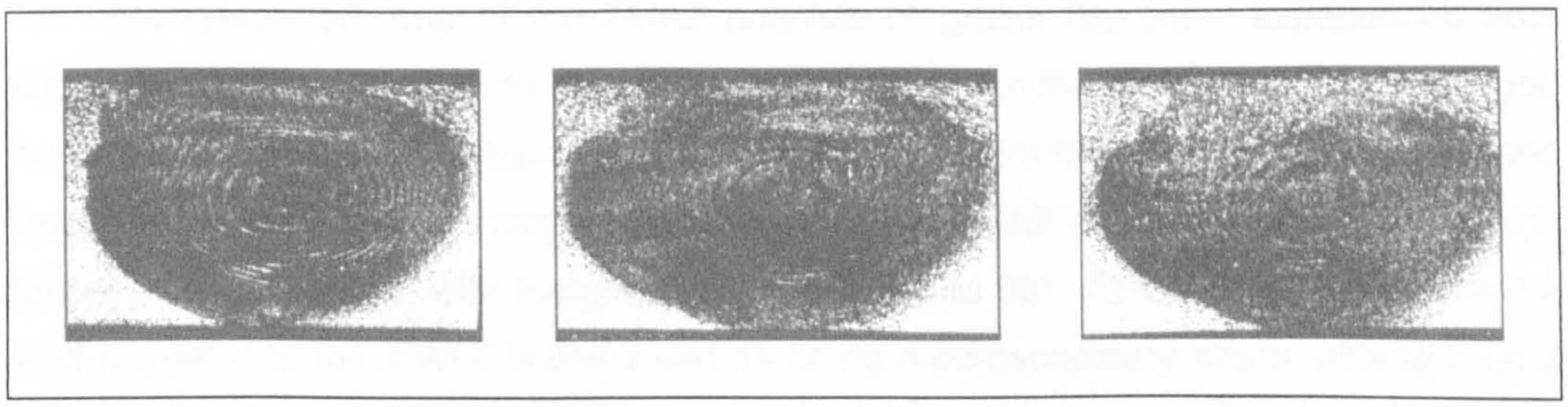

Figure 3.8: Variation of nugget structure with lateral and rotational speed, increasing from left to right, in a friction stir weld of 4 mm AA 2024-T3[2].

Subsequent work by Dalle Donne et al[3] and Biallas et al[4] describe the rings as being concentric tube shaped interfaces that are generated due to stirring. The tubes forming a

---

[1] Threadgill, P (1997)
[2] Dalle Donne, C; Biallas, G (1998)
[3] Dalle Donne, C et al (2000)
[4] Biallas, G et al (1999)

helical structure of decreasing radii, shown in Figure 3.9, which appear as a series of concentric rings when the surface is observed. It is stated that the rings disappear as the rotational speed is increased and that non-threaded tools did not produce the rings. Larsson et al[1], studying FS welds in AA 5083 and AA 6082, suggests that the rings are the result of periodic variations in crystallographic orientation of grains, or the relative orientation of adjacent grains, and not differences in grain size. Leonard[2] examined the microstructure of a FS weld at mid-section, but from the tool shoulder side, and observed a series of advancing semi-circles that were similar in appearance to the ridges found on the friction band surface of the material after welding. It is stated that the semi-circles consisted of bands of alternate coarser, ~6 μm, and finer, ~5 μm, grains. Biallas et al[3] state that the nugget structure had not been related to any specific mechanical properties of the weld.

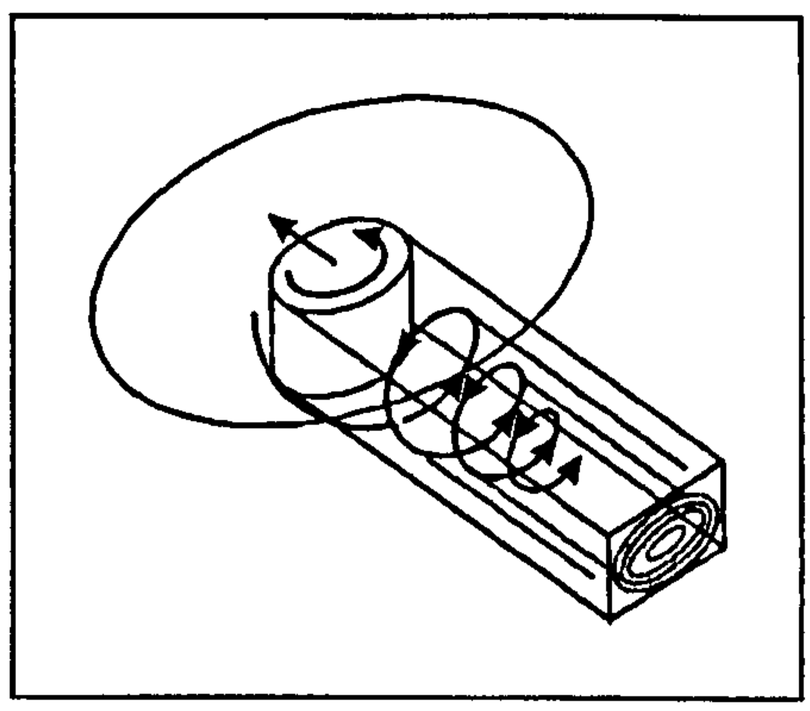

Figure 3.9: Diagrammatic representation of the formation of concentric rings in the weld nugget[3].

The unrecrystallised area of the TMAZ consists of grains that have experienced both plastic deformation and thermal exposure, although, unlike the grains in the weld nugget, the grains are of a similar size to those found in the parent material. Both Leonard[2] and Threadgill[4] describe the unrecrystallised grains of the TMAZ as having undergone a high degree of plastic strain, with the grains rotated by up to 90°. The transition between the weld nugget and the TMAZ is described as being macroscopically sharp, although on a microscopic scale a transition zone was evident[2]. Strangwood et al[5] describe the unrecrystallised grains of the TMAZ as being rotated by up to 90° and retaining the elongated nature of the parent material. A transition region, described as being adjacent to the fully recrystallised nugget, contained grains that exhibited varying degrees of break-up, recovery and recrystallisation[5].

---

[1] Larsson, H et al (1998)
[2] Leonard, AJ (2000)
[3] Biallas, G et al (1999)
[4] Threadgill, P (1997)
[5] Strangwood, M et al (1999)

The HAZ, as with the other microstructural features, is affected by the processing parameters, but is typically trapezoidal in shape, as shown in Figure 3.6[1] for a single pass weld. The greater width occurs beneath the tool shoulder due to the heat generated because of friction between the parent material and the tool shoulder. The extent of the HAZ can be determined both through observation of the microstructure and hardness measurements. As the main contributor to heat is adiabatic shearing, it is probable that the maximum temperatures, measurements of up to 0.8 T_m being recorded by Li et al[2], will occur near to the pin and beneath the outer edge of the tool shoulder, but the high thermal conductivity of aluminium will also result in temperatures able to induce microstructural and mechanical changes away from the tool shoulder. Threadgill[4] states that in both age and strain hardened alloys the hardness decreases in the HAZ due to either overageing and/or lowering of the dislocation density.

Hardness profiles, of both strain hardened and heat treated FS welded aluminium alloys, are shown in Figure 3.10[3] and Figure 3.11[4]. The hardness traverses across the welds exhibit similar trends, with an increase in the hardness at the centre of the weld, when compared to the value returned for the annealed material. Minimum hardness values are returned at the edge of the friction band, with the values between the edge of the friction band and centre being equal to those returned by the annealed material. From the edge of the friction band, moving away from the centre, the hardness gradually increases until it attains the magnitude of the parent material. The increased values found at the centre of the weld are returned by the weld nugget and would generally be associated with the small grain size, although the low dislocation density would be expected to offset the increase in hardness to some degree. The minimum hardness values, found at the edge of the friction band, may be assumed to be due to the temperature in this region attaining or exceeding that required to cause annealing, due in part to frictional heating. The outer edge of the tool shoulder, having the greatest velocity, will result in frictional heating being at a maximum. From the minimum hardness values there is a gradual increase as the distance from the edge of the friction band increases until the hardness of the parent plate is attained, this region representing the HAZ.

From Figure 3.10[3] and Figure 3.11[4] it was evident that AA 5083 in the O condition, fully annealed, showed no decrease in hardness, although a slight increase was evident through the weld nugget. Liu et al[5] undertook a series of butt welds and simulated welds in 6.3 mm thick AA 6061-T6 plate. Microhardness measurements showed a slightly reduced range of values in the weld region nearest to the friction band side, 50 - 60 HV_{100}, in comparison to those recorded near to the backing plate side of the weld, 52 - 70

---

[1] TWI (2000a)
[2] Li, Y et al (1999)
[3] Threadgill, P (1997)
[4] Karlsson, J et al (1998)
[5] Liu, G et al (1997)

HV_{100}. The base metal hardness was 85 - 100 HV_{100}. It was stated that this was a result of the higher temperatures experienced at the top of the weld and, although not stated, it has been presumed that the higher temperatures resulted from frictional heating occurring between the tool shoulder and aluminium plate.

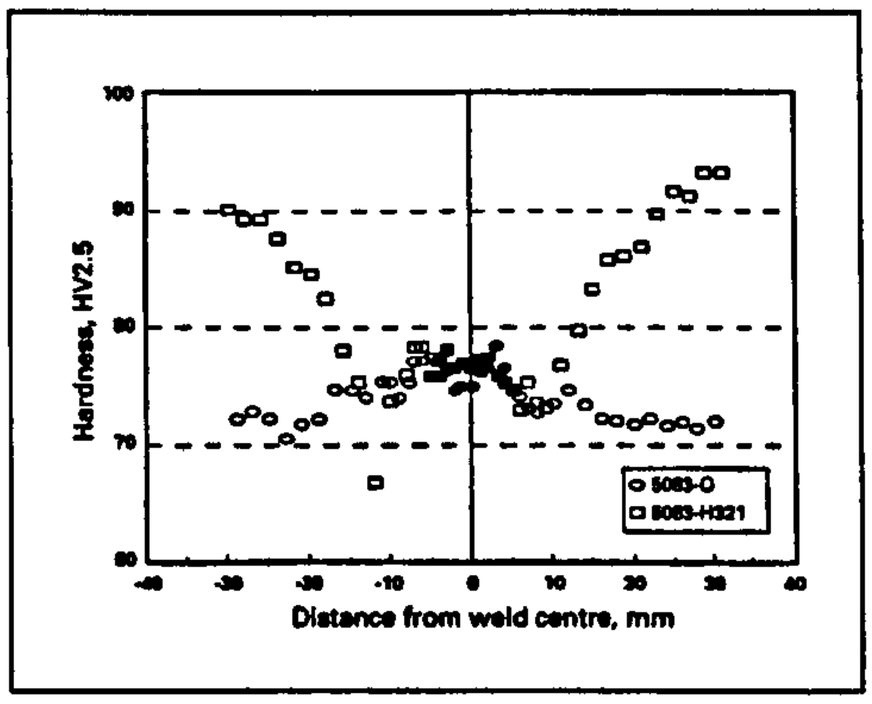

Figure 3.10: Hardness values for AA 5083-O and 5083-H321[1].

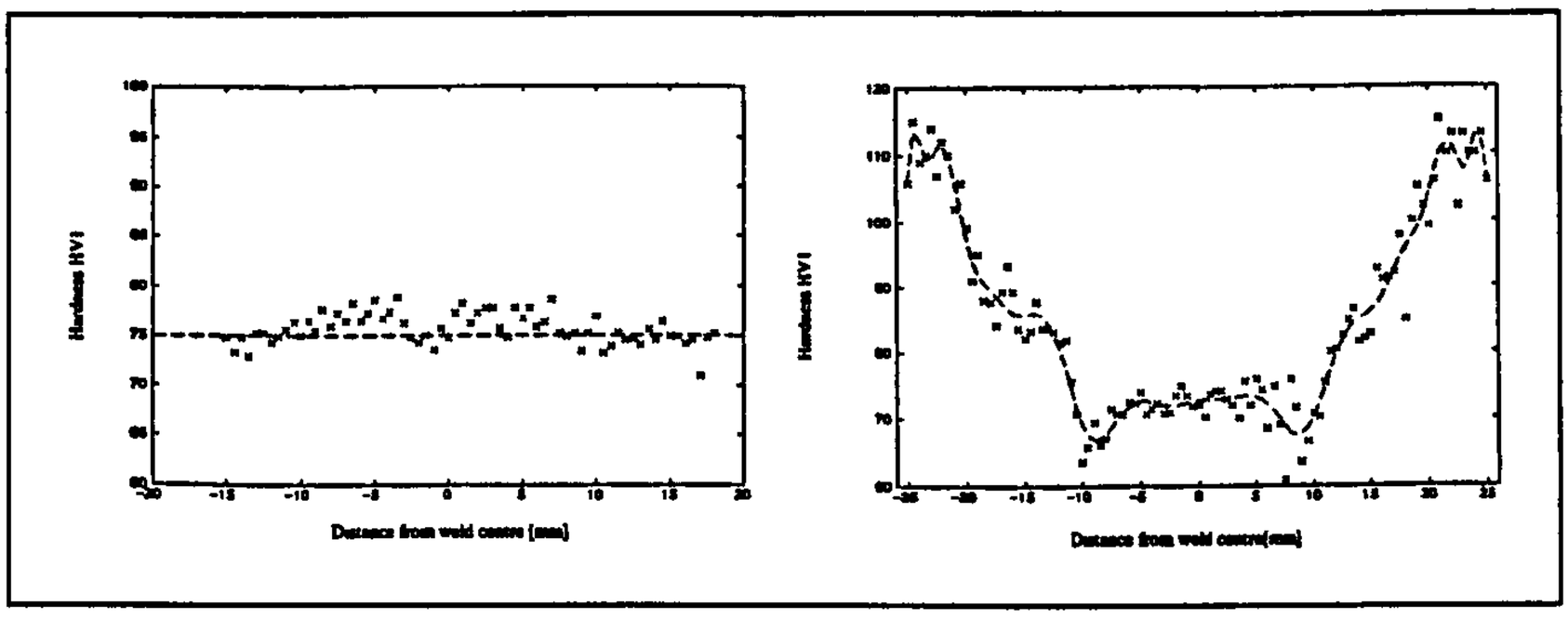

Figure 3.11: Microhardness profiles for friction stir welds in AA 5083-O (left) and AA 6082-T6 (right)[2].

[1] Threadgill, P (1997)
[2] Karlsson, J et al (1998)

3.3 Aluminium Alloy 5383-H321 Composition

5383-H321 aluminium alloy plates, 1000 x 250 x 8 mm (length x width x thickness), were butt welded along the length to produce a welded plate of 1000 x 500 x 8 mm. The rolling direction of the plate was parallel to the direction of the weld run. Four different welding processes were employed:

Metal inert gas – low input (MIG LI)
Metal inert gas – high input (MIG HI)
Friction stir welding – single pass (FS SP)
Friction stir welding – double pass (FS DP)

The welding was undertaken by TWI, Cambridge, England. All the welds underwent radiographic examination to minimise the possibility of unforeseen defects being present.

Due to a limited amount of AA 5383-H321 material being available the long crack growth analysis of the MIG LI weld was undertaken with a comparable weld in AA 5083-H321, an alloy which has similar properties to the AA 5383-H321.

The nominal composition of the batch of 5383-H321 alloy employed, as reported by the manufacturer, was as shown in Table 3.3[1]:

Element	%	Element	%
Aluminium	Balance	Boron	0.0028
Silicon	0.1120	Sodium	0.0001
Iron	0.1247	Zirconium	0.0310
Copper	0.0830	Lead	0.0020
Manganese	0.8213	Nickel	0.0030
Magnesium	4.7540	Beryllium	0.0013
Chromium	0.0807	Vanadium	0.0030
Zinc	0.2180	Calcium	0.0005
Titanium	0.0297	Lithium	0.0002

Table 3.3: Composition of AA 5383-H321.

Spark source optical emission spectroscopy analysis of both the AA 5383-H321 and AA 5083-H321 employed returned the compositional values shown in Table 3.4[2]; any variation between the results shown for the AA 5383-H321 in Table 3.3 and Table 3.4 were probably due to the techniques employed in the analysis.

---

[1] Moldenhauer, S (1999)
[2] Scientifics Ltd. (2001)

Element	5383-H321 (%)	5083-H321 (%)
Silicon	0.12	0.25
Iron	0.09	0.15
Copper	0.09	0.06
Manganese	0.78	0.60
Magnesium	4.43	4.20
Chromium	0.09	0.09
Nickel	< 0.01	< 0.01
Zinc	0.21	0.09
Lead	0.01	0.01
Tin	0.01	0.01
Titanium	0.03	0.02

Table 3.4: Composition of AA 5383-H321 and AA 5083-H321[1]

The following is quoted from Chapter 3, "Aluminium-Magnesium, Aluminium-Manganese Alloys", of Aluminium Alloys – Structure and Properties[2]:

"The magnesium in the commercial alloys ranges all the way from 0.5 to 12 - 13% Mg, the low-magnesium alloys having the best formability, the high-magnesium reasonably good castability and high strength. It is normal practice to prepare these alloys from the higher grades of aluminium (99.7 or better) to obtain maximum corrosion resistance and reflectivity; thus the iron and silicon contents are usually lower than in other aluminium alloys. Iron and zirconium are sometimes added to increase the recrystallisation temperature; silicon to improve the fluidity; manganese or chromium to correct for the corroding effect of iron. Copper is added (albeit seldom) to reduce pitting corrosion by enhancing general corrosion; zinc has little or no effect on corrosion but enhances castability and strength. In the early days antimony was added, and to its oxide was attributed the corrosion resistance of seawater, but later experiments disproved antimony's effectiveness. Titanium and titanium plus boron are often added as grain refiners; beryllium and sometimes lithium to reduce oxidation of magnesium at high temperature, and especially in the molten state. Lead has been added to improve machinability, supposedly without loss of strength or corrosion resistance."

[1] Scientifics Ltd. (2001)
[2] Mondolfo, LF (1976)

3.4 Welding Procedures

Two types of MIG welds, low and high input (LI and HI respectively), and two FS welds, single and double pass (SP and DP respectively), were produced. It was initially intended that the fatigue properties of the two processes, MIG and FS, would be compared on an energy input basis; the MIG LI and FS SP and the MIG HI and FS DP welds. Unfortunately, at the time of writing, there was no satisfactory method for determining the energy input of friction stir welds and therefore the fatigue properties have been considered on an individual basis.

3.4.1 MIG Welds

The filler metal for both MIG welds was AA 5183, the nominal composition of which is shown in Table 3.5[1]:

Element	5183 (%)
Silicon	0.4 - 0.7
Iron	0.4
Copper	0.1
Manganese	0.5 - 1.0
Magnesium	4.3 - 5.2
Chromium	0.05 - 0.25
Zinc	0.25
Beryllium	< 0.0008
Titanium	0.15

Table 3.5: Nominal composition of AA 5183 filler wire.

3.4.1.1 Low Input

Prior to both the first and second weld runs the plates were back gouged using a milling cutter as shown in Figure 3.12. The plates were prepared and cleaned with a scraper and acetone.

Welding was undertaken with AA 5183 filler rod of 1.2 mm diameter, shielding was provided by argon gas at a flow rate of 20 $l.min^{-1}$ and a mechanised process was employed. Other welding details were as shown in Table 3.6[2].

[1] ASM (1993)
[2] All MIG LI welding details/specifications from TWI (1998a)

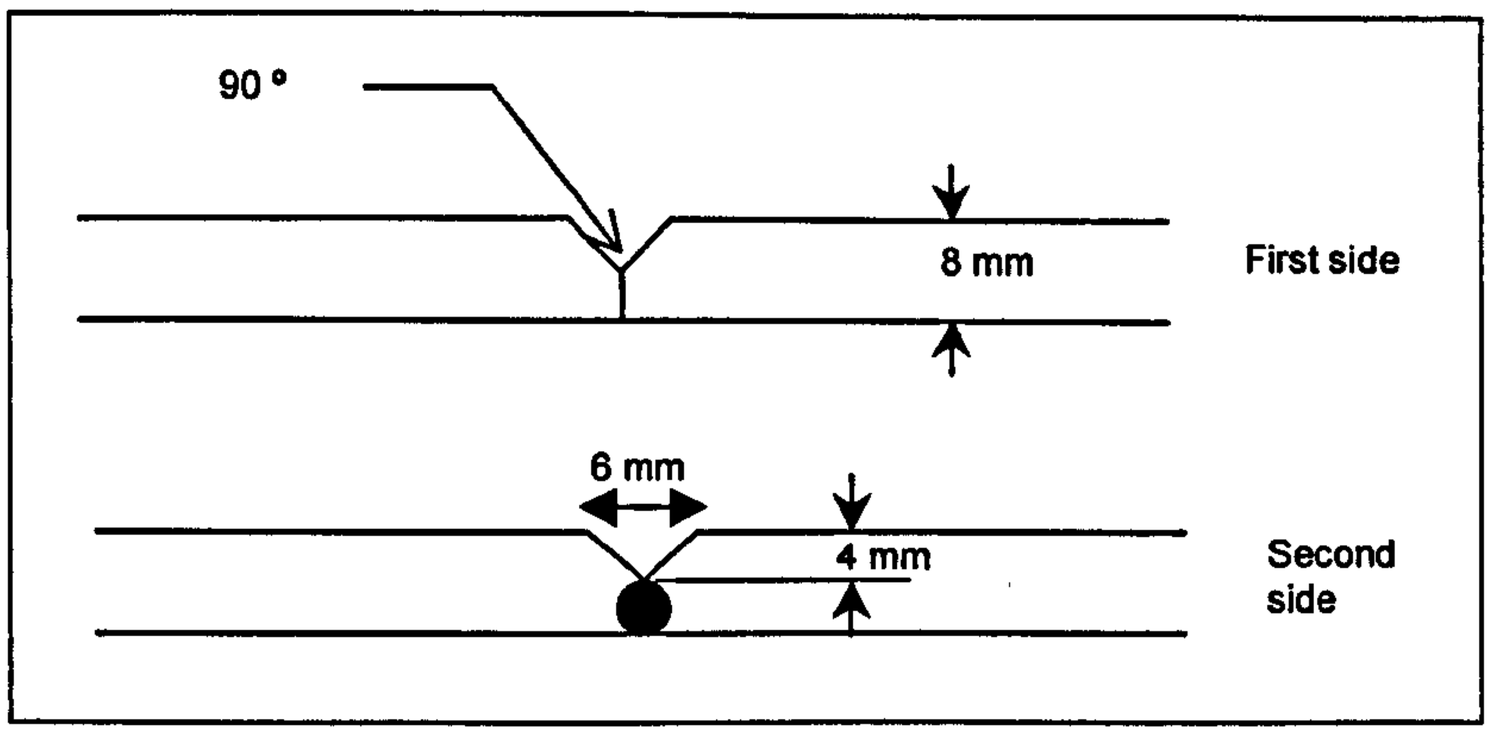

Figure 3.12: MIG LI back gouging prior to welding[1].

Run number	Process	Filler size	Current (A)	Voltage (V)	Type of current and polarity	Travel speed ($mm.min^{-1}$)	Heat input ($KJ.mm^{-1}$)
1	MIG	1.2	202	22.3	DC +ve	600	0.36
2	MIG	1.2	202	23	DC +ve	600	0.36

Table 3.6: Welding specifications for MIG LI welds.

3.4.1.2 High Input

Unlike the low input process, no back gouging was performed prior to welding. Two mechanised runs were undertaken with the two plates butted together. The plates were prepared and cleaned with a scraper and acetone.

Welding was undertaken with AA 5183 filler rod of 1.2 mm diameter, shielding was provided by argon gas at a flow rate of 20 $l.min^{-1}$. Other welding details were as shown in Table 3.7[2]

Run number	Process	Filler size	Current (A)	Voltage (V)	Type of current and polarity	Travel speed ($mm.min^{-1}$)	Heat input ($KJ.mm^{-1}$)
1	MIG	1.2	288	27	DC +ve	600	0.56
2	MIG	1.2	290	27.1	DC +ve	600	0.56

Table 3.7: Welding specifications for MIG HI welds.

3.4.2 FS Welds

The friction stir welds were undertaken with a tool comparable to that shown in Figure 3.13, with the tool shoulder angle, E, ≈ 7°, radius, F, = 1 mm and diameter, D, = 25 mm. TWI tools employ left hand threads so that rotation of the tool forces material from the top

[1] All MIG LI welding details/specifications from TWI (1998a)
[2] All MIG HI welding details/specifications from TWI (1998b)

to the bottom through the augering action of the threads (some machines rotate in the opposite direction and therefore need right hand threads)[1]. Other tool details were as described for each weld process.

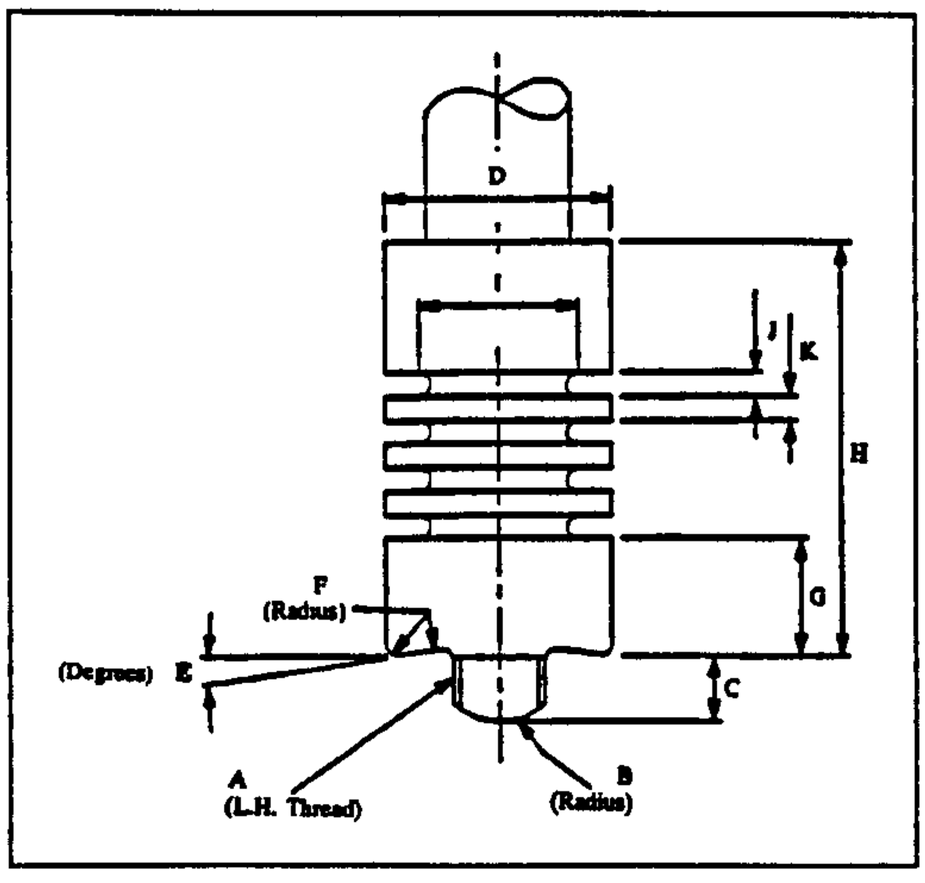

Figure 3.13: Friction stir weld 5651 tool profile[1].

3.4.2.1 Single Pass

Welding details for the friction stir single pass welded plate were as shown in Table 3.8[2,3].

Process	Downward force (KN)	Travel speed ($mm.min^{-1}$)	Tool rotation direction	Rotational speed (rpm)	Tool tilt	Heel plunge depth (mm)
FS SP	15 (approximately for an 8 mm plate thickness)	70	Clockwise	500	2.5°	0.2

Table 3.8: Welding specifications for FS SP welds.

With reference to Figure 3.13 the tool utilised for the SP welds had the following dimensions:

Pin diameter = 10 mm.

Pin length, C, = 7.9 mm.

Tip radius, B, = 7.5 mm.

Thread, A, = M10, 1.25 mm pitch.

---

[1] Threadgill, P (2002)
[2] Welding details/specifications from TWI (2000b)
[3] Welding details/specifications from TWI (2000c)

3.4.2.2 Double Pass

The double pass weld involved welding of one side to a depth of just over half the plate thickness, the plate was then turned over and the second side welded. Welding details for the friction stir double pass welded plate were as shown in Table 3.9[2,3].

Process	Downward force (KN)	Travel speed ($mm.min^{-1}$)	Tool rotation direction	Rotational speed (rpm)	Tool tilt	Heel plunge depth (mm)
FS DP	15 (approximately for an 8 mm plate thickness)	120	Clockwise (for both passes, when viewed from above the surface being welded)	500	2.5°	0.2

Table 3.9: Welding specifications for FS DP welds.

With reference to Figure 3.13 the tool utilised for the DP welds had the following dimensions:

Pin diameter = 8 mm.

Pin length, C, = 5.9 mm.

Tip radius, B, = 6.0 mm.

Thread, A, = M8, 1.0 mm pitch.

3.5 Experimental Procedure

The various planes and surfaces of the specimens are designated in accordance with ASTM E616[1], as shown in Figure 3.14. The LT (rolled), LS and TS planes corresponding to the longitudinal, transverse and planar faces respectively.

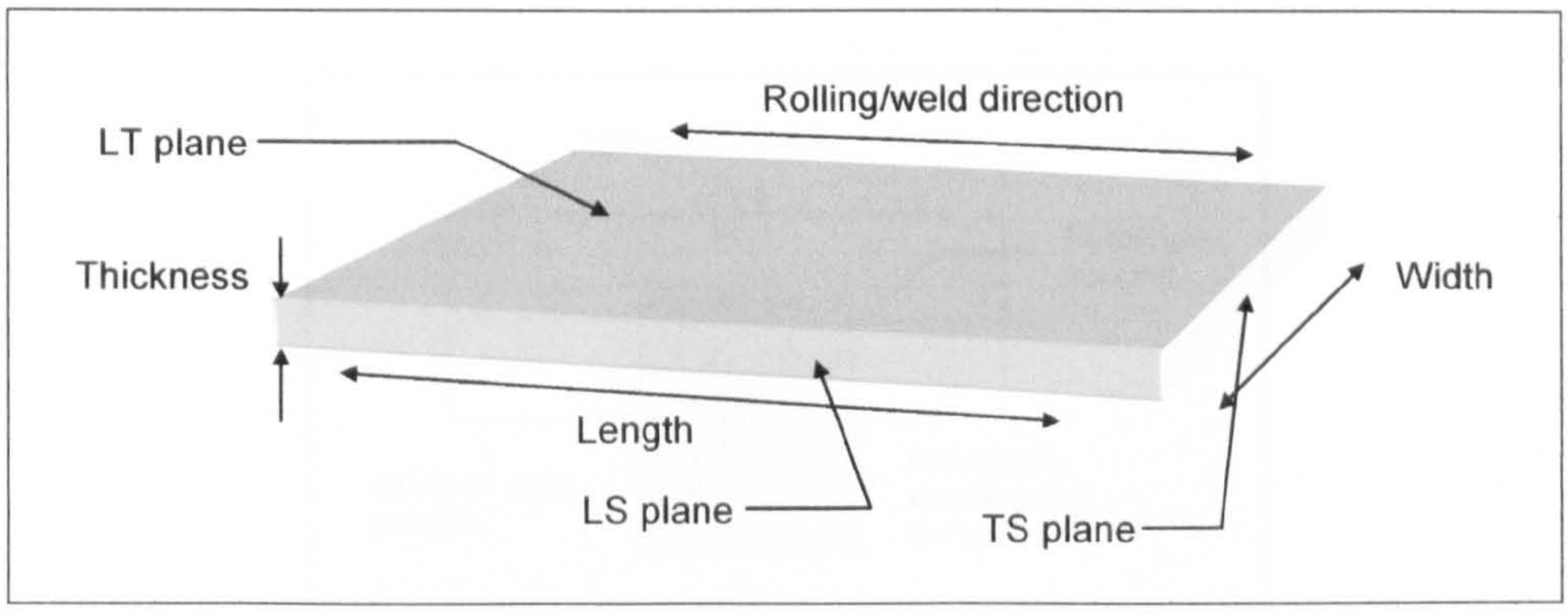

Figure 3.14: Schematic representation of the various planes and directions in the rolled AA 5383-H321 plate, in accordance with ASTM E616.

3.5.1 Planar Grinding, Polishing and Electro-etching

To reveal the microstructure of the AA 5383-H321 mechanical grinding/polishing, using a Motopol Grinder/Polisher 2000, and electro-etching were undertaken. The following regime was employed:

i. Planar grinding of the surface was undertaken with 600 grit followed by 1000 or 1200 grit SiC paper until a uniform surface finish was attained. Water was used for lubrication. Later specimens were further ground with a 2500 grit SiC paper as material removal rates were greater than those attained by the diamond compounds detailed in ii. Specimens were rinsed with distilled water between each grinding stage.

ii. Initial polishing was undertaken using 15 or 9 μm diamond compound followed by 3 μm and 1 μm diamond compounds for 3, 3 and 2 minutes respectively. Hyperez Fluid, Type W, was used for lubrication. Specimens were ultrasonically cleaned in acetone and rinsed with distilled water between each polishing stage.

iii. Final polishing was completed using a colloidal silica (SiO_2) or aluminium oxide (Al_2O_3) suspension for 20 to 30 seconds. Specimens were finally rinsed with distilled water and dried using a warm air blower.

iv. Electro-etching was undertaken in a fume cupboard using a cell as shown in Figure 3.15. The electrolyte consisted of a 2% solution of fluoroboric acid, HBF_4

[1] ASTM (1982)

(5 ml HBF_4 (40%) diluted with 100 ml of distilled H_2O). The cathode was made from stainless steel, the surface area of which was much greater than that of the anode (surface to be etched). The maximum surface area of the anode left exposed was 250 mm^2, for the production of the macrographs, the remainder being masked with either tape or Lacomit varnish. The specimens were electro-etched at a voltage of between 20 - 30 volts for a period of 2 - 3 minutes.

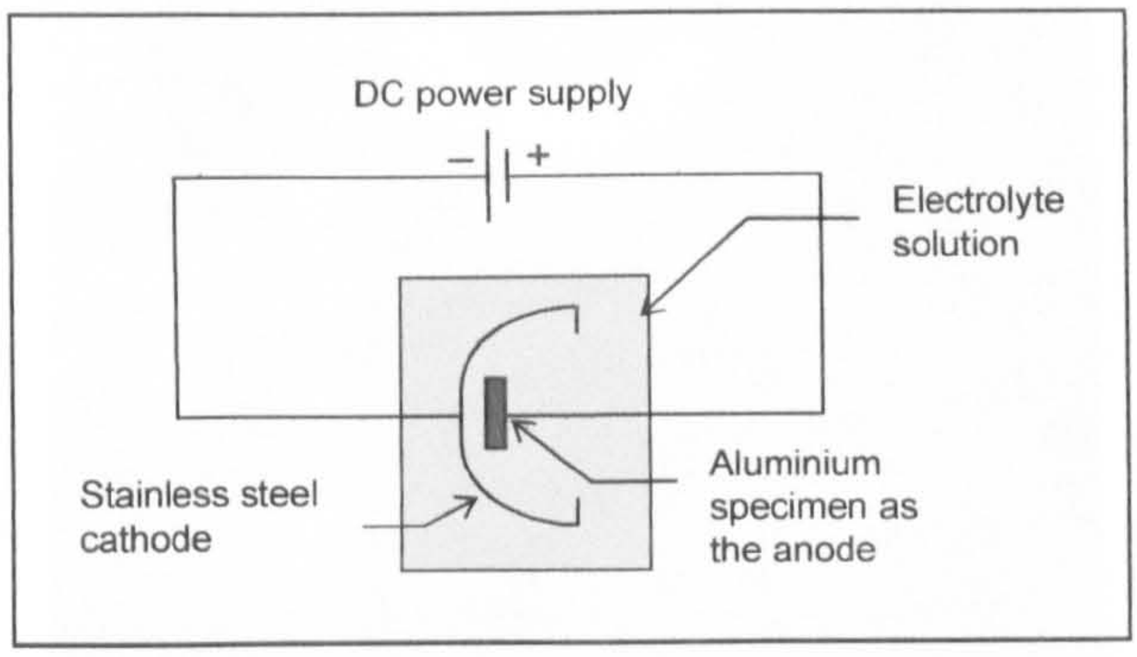

Figure 3.15: Diagrammatic representation of the electro-polishing procedure.

3.5.2 Surface Topography and Weld Geometry

The topography of the parent plate and FS welds was undertaken with Talysurf series 2 apparatus utilising a 2 μm diamond stylus.

The geometry of the MIG welds, notably the weld toe radius and angle, was determined through the use of a Nikon projector as shown in Figure 3.16. The weld toe angle was measured by rotating the cross hairs on the proctor screen and noting the angle displayed on the calibrated bezel. The toe radius was determined through tracing the weld toe outline and then using either a compass or series of curves of known radius.

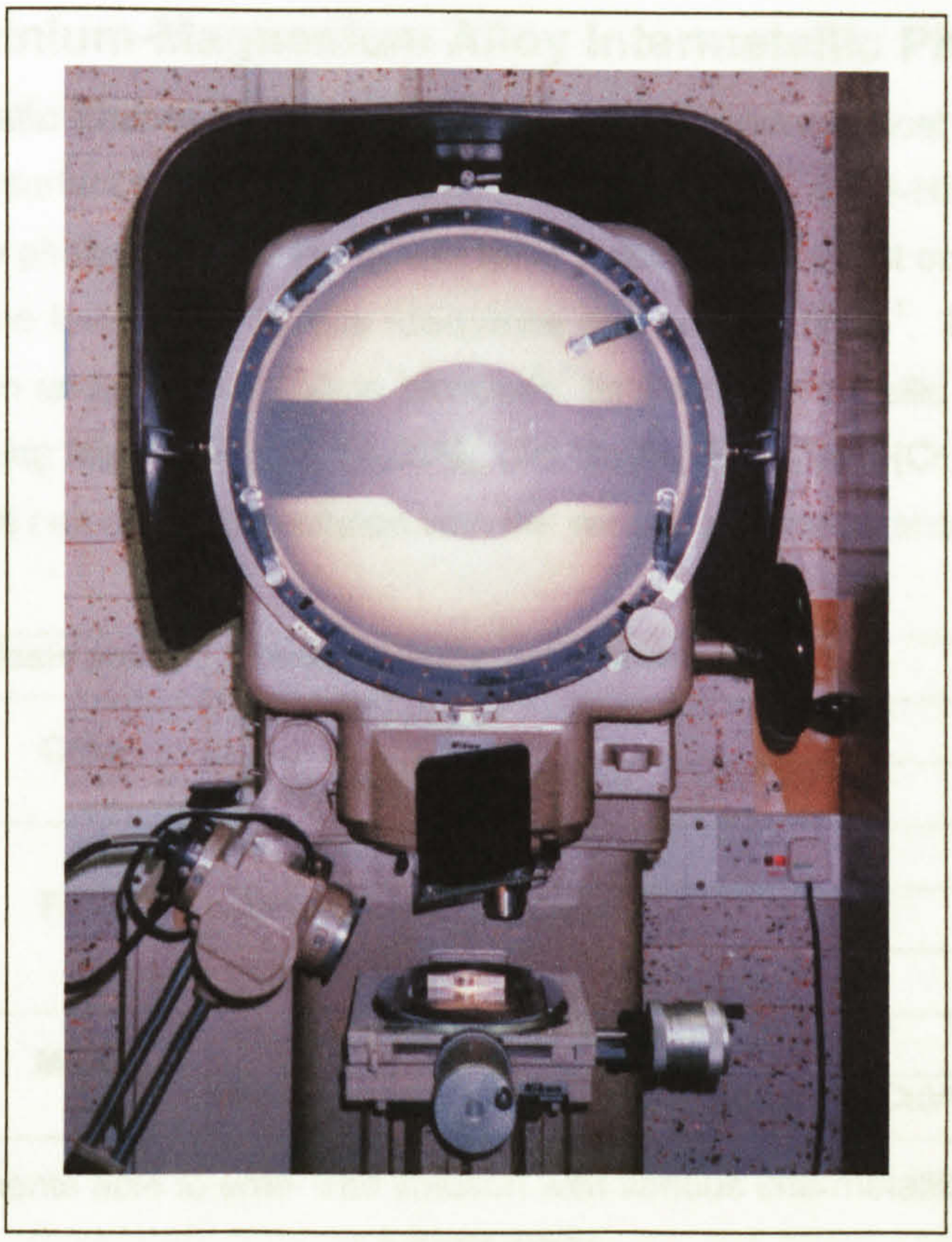

Figure 3.16: Nikon projector with the cross section of a MIG HI weld visible.

3.5.3 Determination of Microstructure

Macrographs were produced using a Meiji EMZ TR optical microscope, with oblique illumination. The electro-etched surface had sufficient relief under such lighting to show the macrostructure of the weld regions. Images were captured using a video camera and printed with a video printer. An Olympus BX60M optical microscope was used to view the microstructure using polarised light and images were captured on 400 ASA 35 mm colour film. Images used to calculate the grain size were captured using a video camera and measurements made using Image Tool software*. Initially, due to the limitations of the available equipment, grain sizes were determined by measuring ten individual grains and calculating the mean value. The results for the equiaxed grains were later verified using an eyepiece reticle in accordance with ASTM E112[1]. The colour microstructural images contained within 3.6 Geometry, Microstructure and Mechanical Properties (page 47) were obtained with a Reichert-Jung optical microscope and Leica QWin software.

---

* Image Tool Software 2.00 developed at the University of Texas Health Science Centre at San Antonio, Texas and available from the internet by anonymous ftp from ftp://maxrad6.uthscsa.edu

[1] ASTM (1996)

3.5.3.1 Aluminium-Magnesium Alloy Intermetallic Phases

Various intermetallic phases were evident, when viewed under optical light microscopy, on the polished surfaces of both the welded and parent AA 5383-H321, as shown in Figure 3.17. The phases are not thought to have a substantial effect on the strength, but they can affect the formability, fatigue resistance and surface finish[1]. For the AA 5383-H321 composition under consideration Mondolfo[1] lists the intermetallic phases that may be present as being Mg_5Al_8, Mg_2Si, Fe_2SiAl_8, $(Fe,Mn)Al_6$, $FeAl_3$ and $(Cr,Fe)Al_7$. Stevens[2] lists elements that can enter into solution with the various phases as shown Table 3.10.

Basic phase	Elements that enter into solution
$CrAl_7$	Iron as $(Cr,Fe)Al_7$
	Manganese as $(Cr,Mn)Al_7$
$FeAl_3$	Chromium as $(Fe,Cr)Al_3$
	Manganese as $(Fe,Mn)Al_3$
	Possibly copper
$MnAl_6$	Iron as $(Fe,Mn)Al_6$
	Isomorphous with (Fe,Cu) $(Al,Cu)_6$ or $(Fe,Cu)Al_6$

Table 3.10: Elements able to enter into solution with various intermetallic phases found in AA 5383-H321.

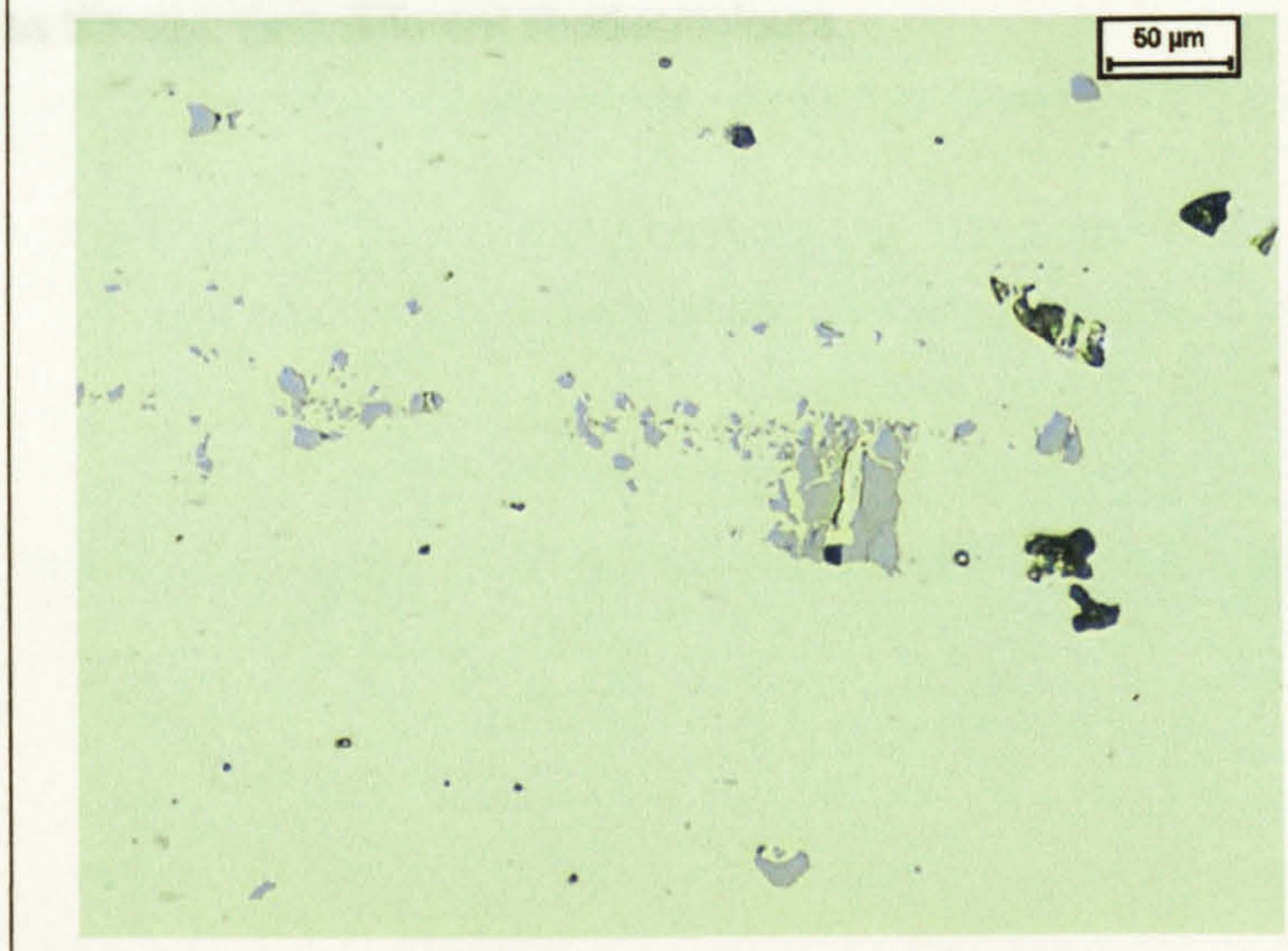

Figure 3.17: Optical micrograph of AA 5383-H321 phases, LT surface (rolled surface).

[1] Mondolfo, LF (1976)
[2] Stevens, RH (1985)

Two distinct intermetallic phases were evident when viewed under optical microscopy, a dark blue/black phase and a grey phase as shown Figure 3.17. Reference to Mondolfo[1] and Stevens[2] suggested that dark phase was Mg_2Si and the grey phase either $(Fe,Mn)Al_6$ or $FeAl_3$ (or one of their derivatives resulting from other elements entering into solution with either of these phases). Electron microscopic elemental analysis of the matrix confirmed that the main constituent elements of the alloy were Al and Mg as shown in Figure 3.18. Figure 3.19 established that the dark intermetallic phase consisted of Mg and Si, confirming that this was Mg_2Si. Al, Fe, Mn and Cr were recorded as being present in grey intermetallic phase, as shown in Figure 3.20, although this did not confirm the exact chemical composition of the phase it suggested that was either $(Fe,Mn)Al_6$ or $FeAl_3$. Although further analysis would allow an exact determination of the $(Fe,Mn)Al_6/FeAl_3$ phase, it was not considered necessary for the present research. Electron probe microanalysis (EPMA) of the LT surface of the AA 5383-H321 confirmed the composition of the intermetallic phases as shown in Figure 3.21. Calcraft et al[3] in their study of welding procedures and fatigue properties of AA 5383 also suggested that the main intermetallic phases were Mg_2Si and $(Fe,Mn)Al_6$ or $FeAl_3 + MnAl_6$,

The size and distribution of the Mg_2Si phase and the $FeAl_3/(Fe,Mn)Al_6$ phase were measured using a Reichert-Jung optical microscope and Leica QWin software, the surfaces having being prepared as described in i - iii of Section 3.5.1, Planar Grinding, Polishing and Electro-etching (page 36). The software determined the various phases and their sizes through their different shades/colours.

---

[1] Mondolfo, LF (1976)
[2] Stevens, RH (1985)
[3] Calcraft, RC et al (1999)

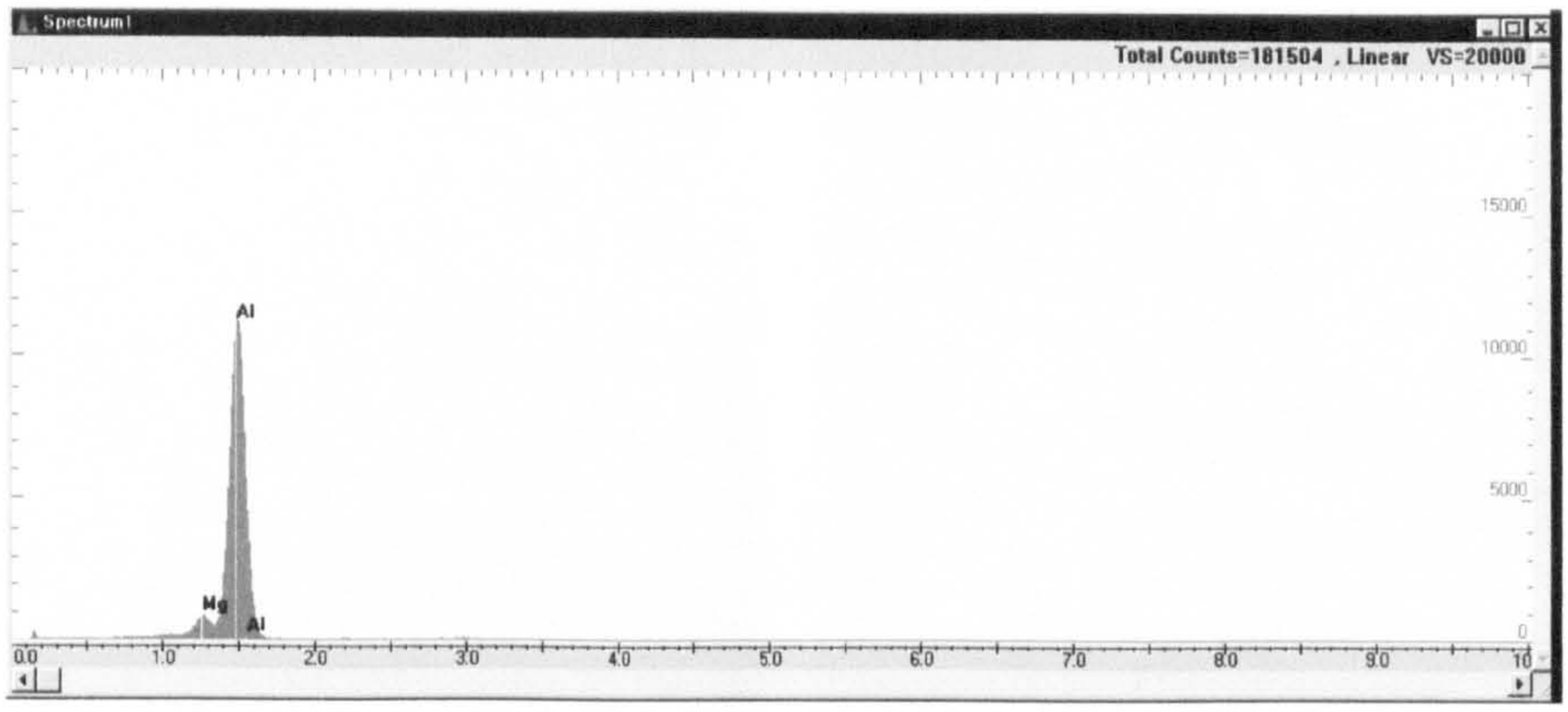

Figure 3.18: Al + Mg_5Al_8 matrix elemental mapping.

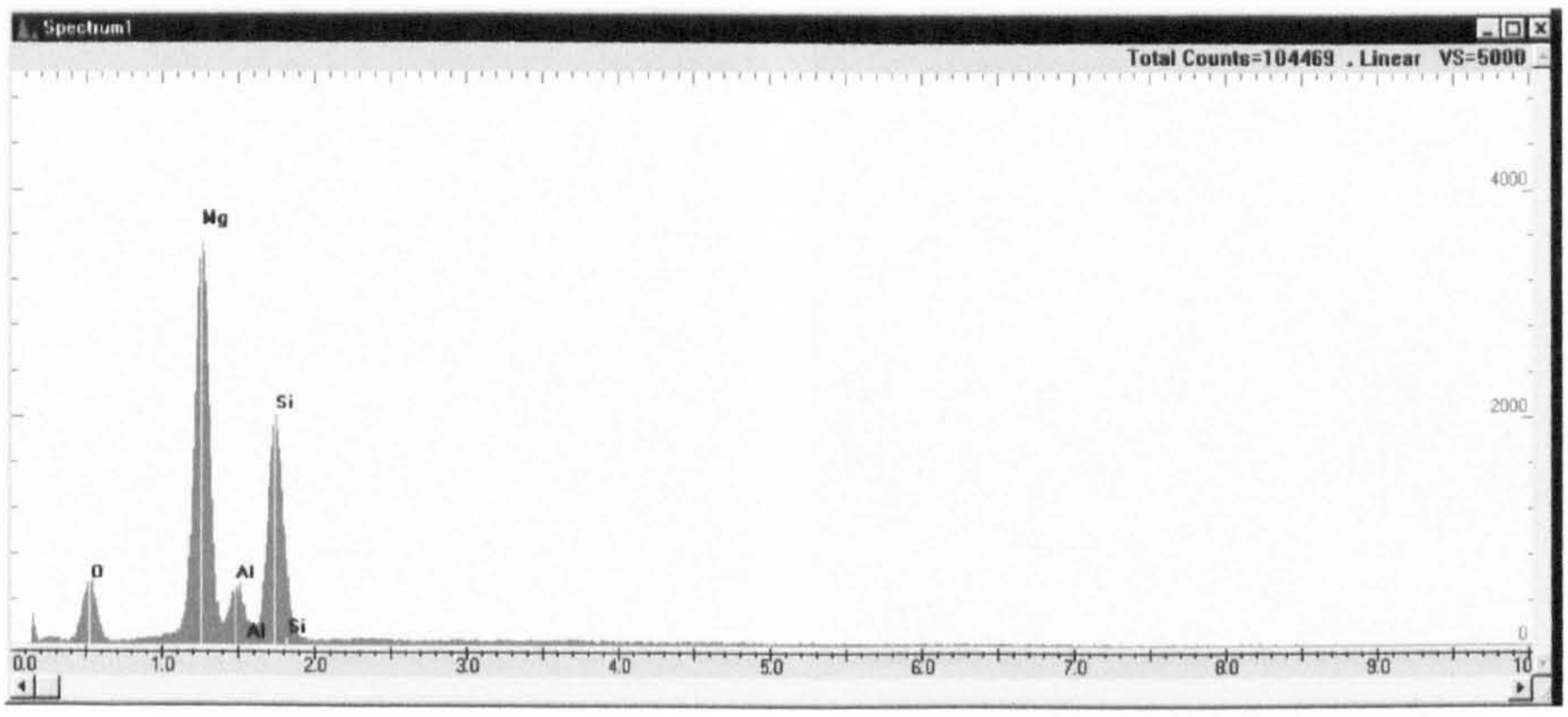

Figure 3.19: Mg_2Si intermetallic elemental mapping.

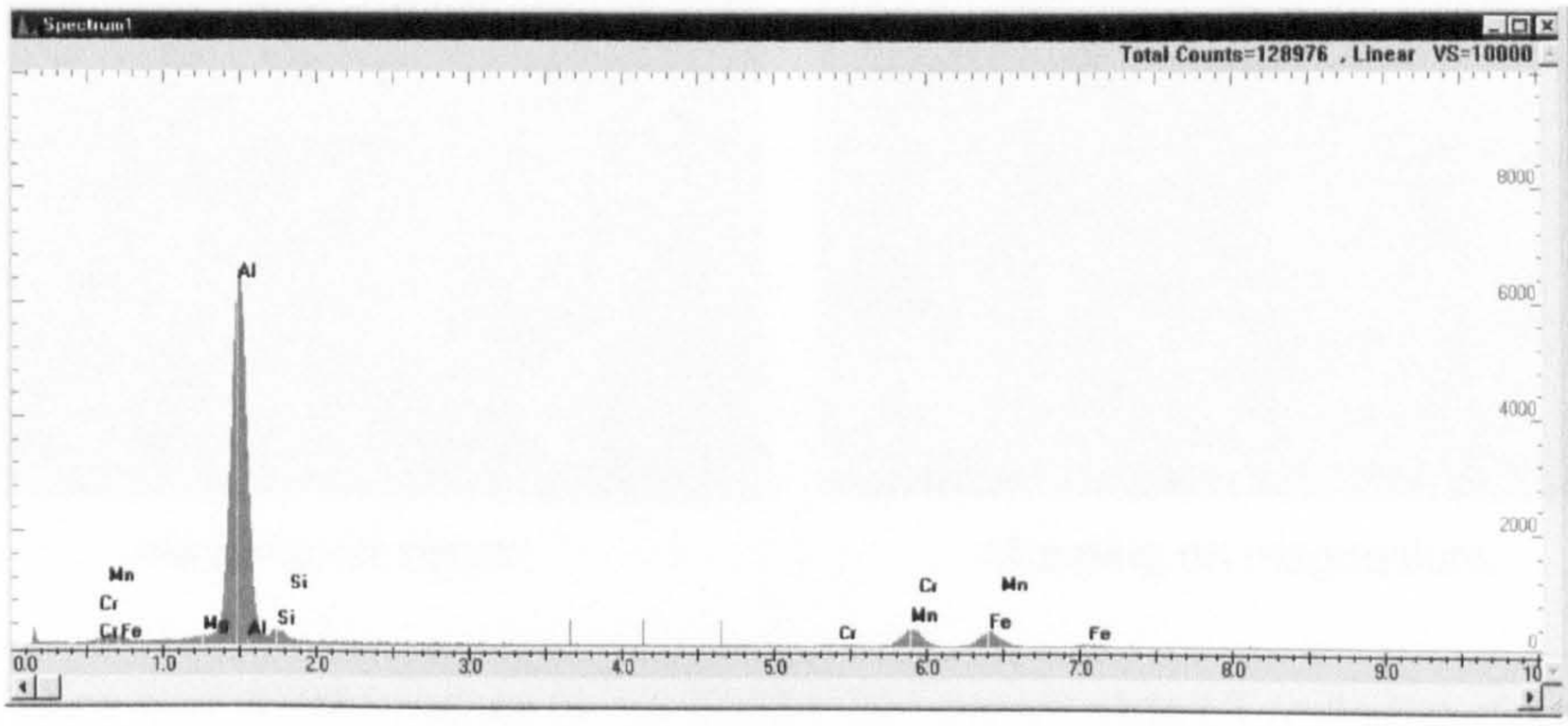

Figure 3.20: $FeAl_3$/$MnAl_6$ intermetallic elemental mapping.

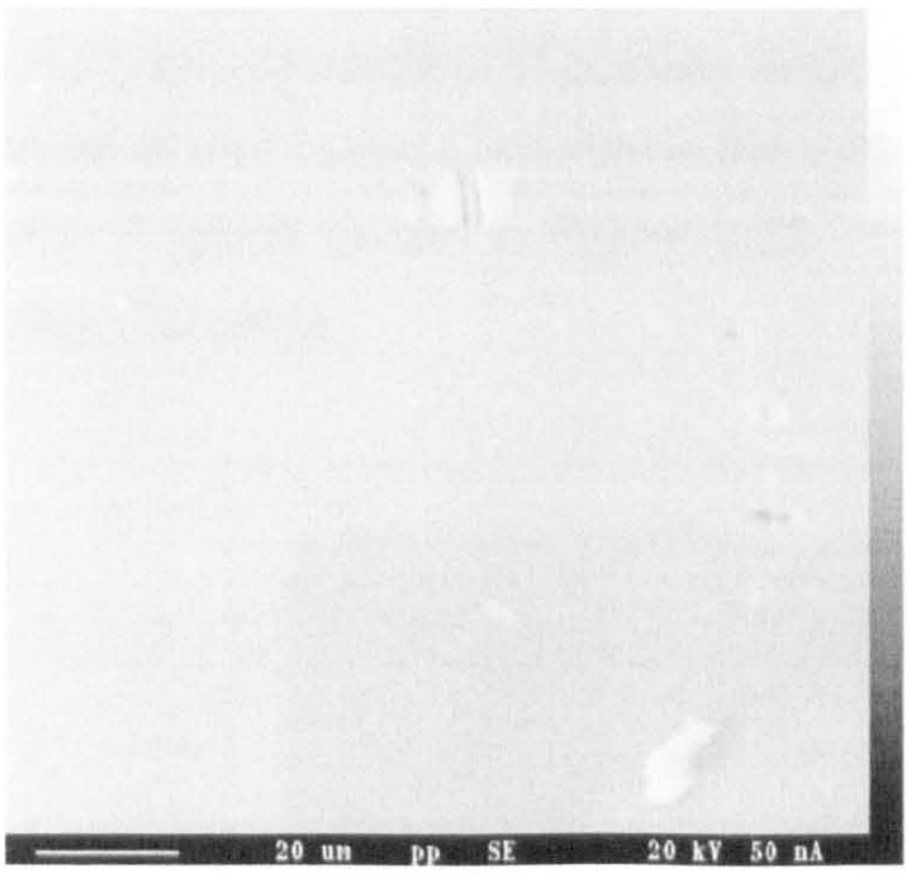

Secondary electron image.

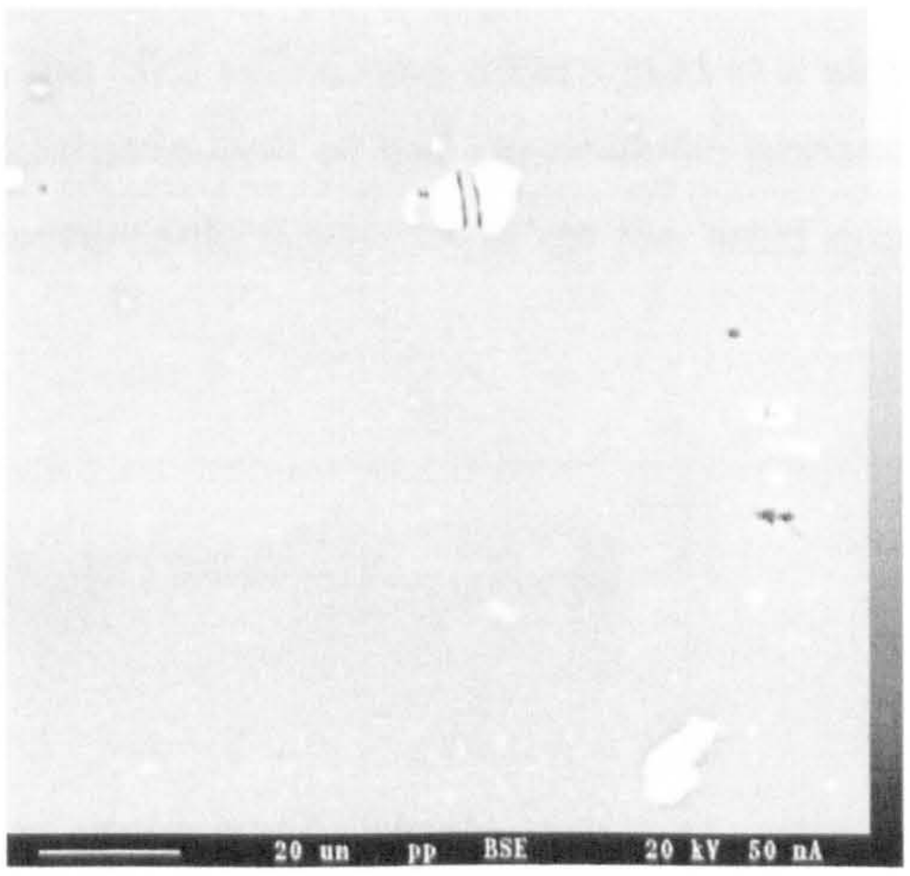

Composition contrast.

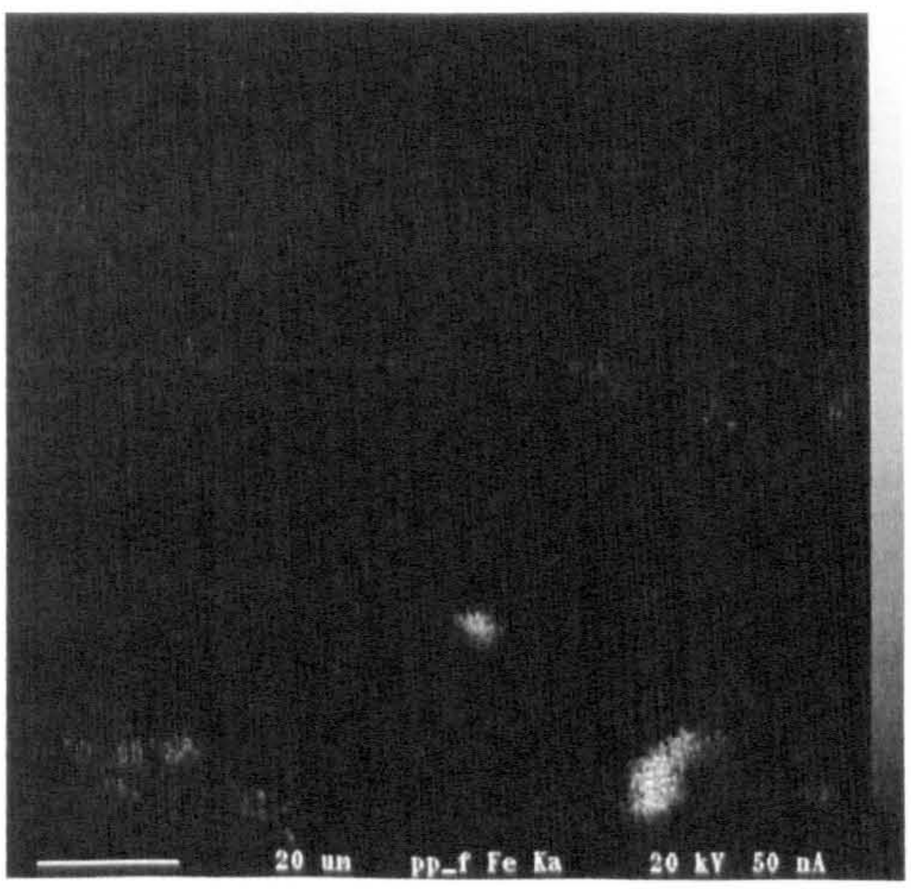

Mapping on iron.

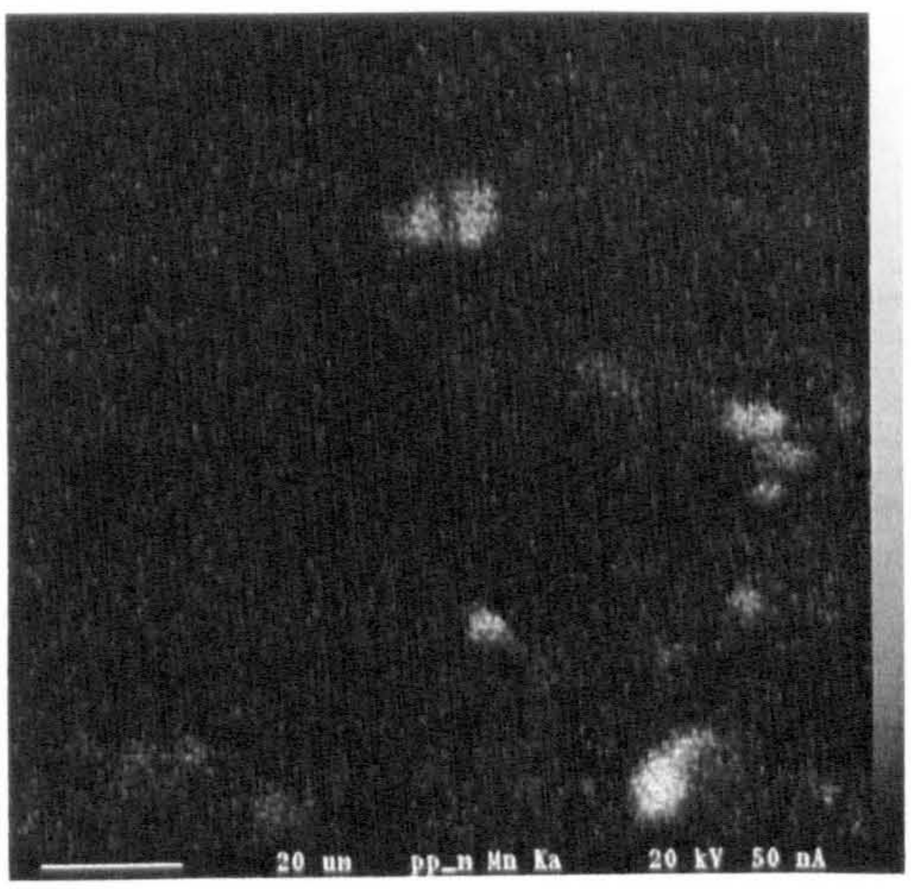

Mapping on manganese.

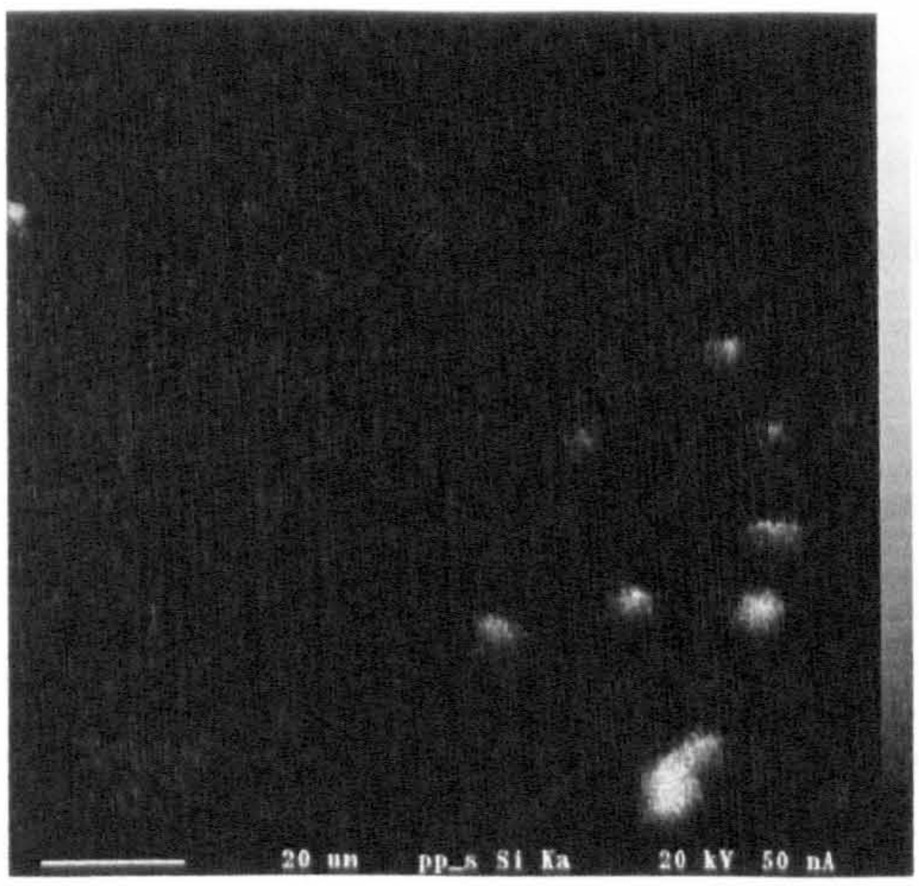

Mapping on silicon.

Mapping on magnesium.

Figure 3.21: EPMA results on AA 5383-H321 parent plate LT (rolled) surface.

3.5.3.2 Porosity

The size and distribution of porosity evident in the MIG welds was determined in a similar manner to that used to determine the size and distribution of the intermetallic phases, a typical image is shown in Figure 3.22. Measurements were made on the weld cross-section, TS plane.

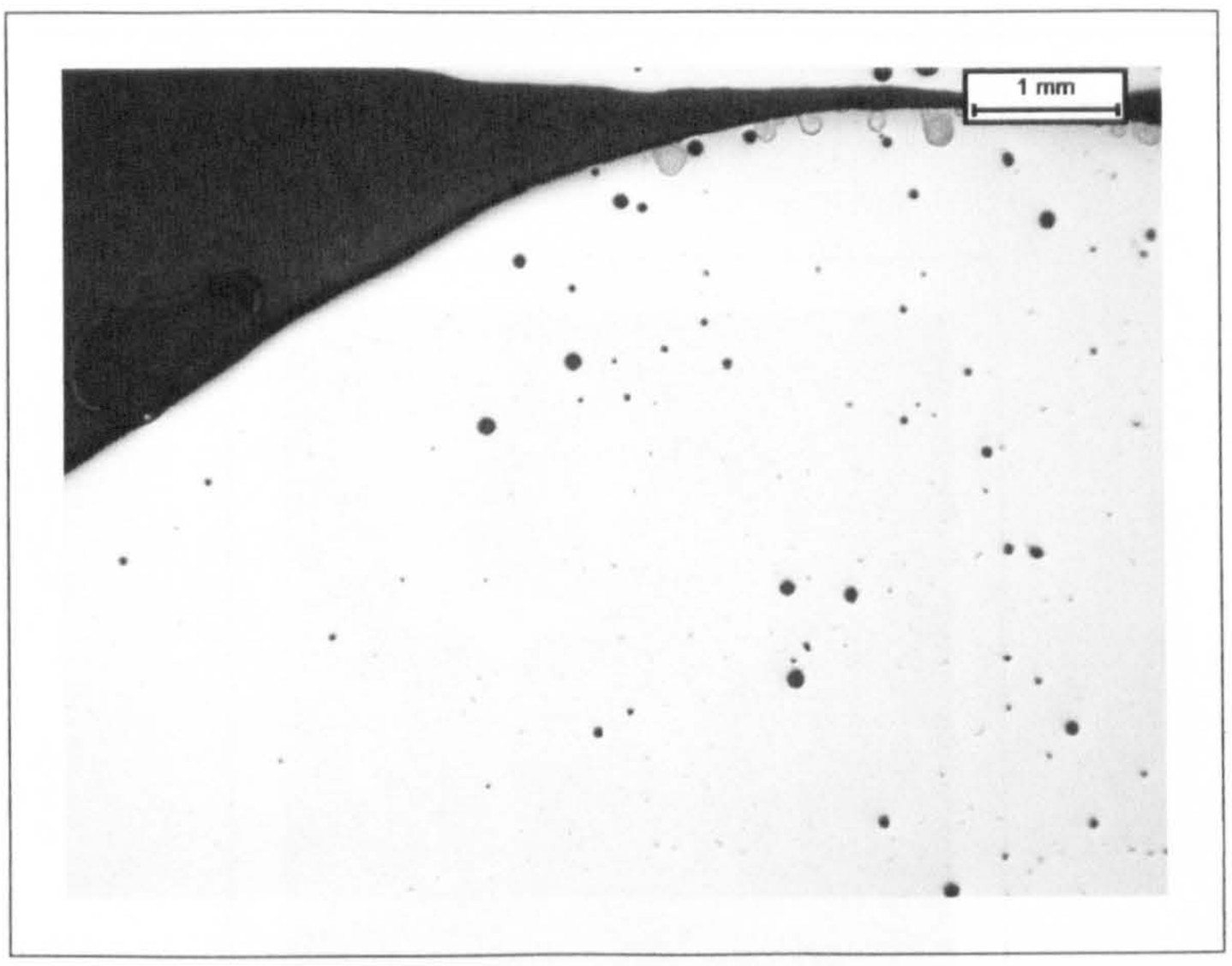

Figure 3.22: Optical microscopy image of porosity in MIG HI weld bead.

3.5.4 Uniaxial monotonic tensile testing

Uniaxial monotonic tensile testing of both the AA 5383-H321 and AA 5083-H321 parent plate, with loading being applied both transverse to (|-), and parallel to (//), the rolling direction, was undertaken. Testing was also undertaken on the MIG, LI and HI, and FS, SP and DP, AA 5383-H321 butt welds. The test coupon geometry is shown in Figure 3.23, with the weld direction, transverse to the 50 mm gauge length, being shown where appropriate. Testing was undertaken on an Instron 1175 test frame employing a 100 KN load cell and 50 mm clip gauge extensometer as shown in Figure 3.24, testing was undertaken at 5 $mm.min^{-1}$ crosshead extension. The mechanical properties were determined as the mean of two tests per specimen type, except for the Poisson's ratio which was determined from a single test undertaken on the AA 5383-H321. For the determination of Poisson's ratio one strain gauge was applied to the LT (rolled) surface parallel to the applied load, whilst a second gauge was applied at right angles to this, also on the LT surface. The contraction was measured parallel to the rolling direction.

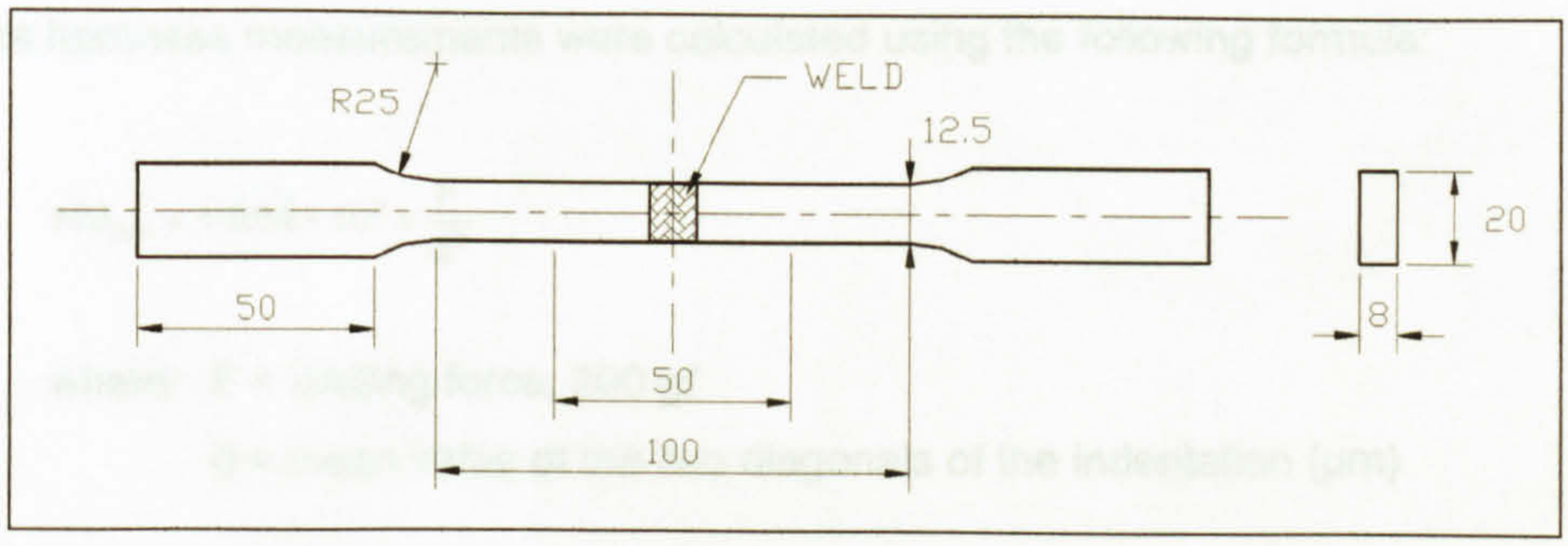

Figure 3.23: Tensile test coupon (all dimensions in mm).

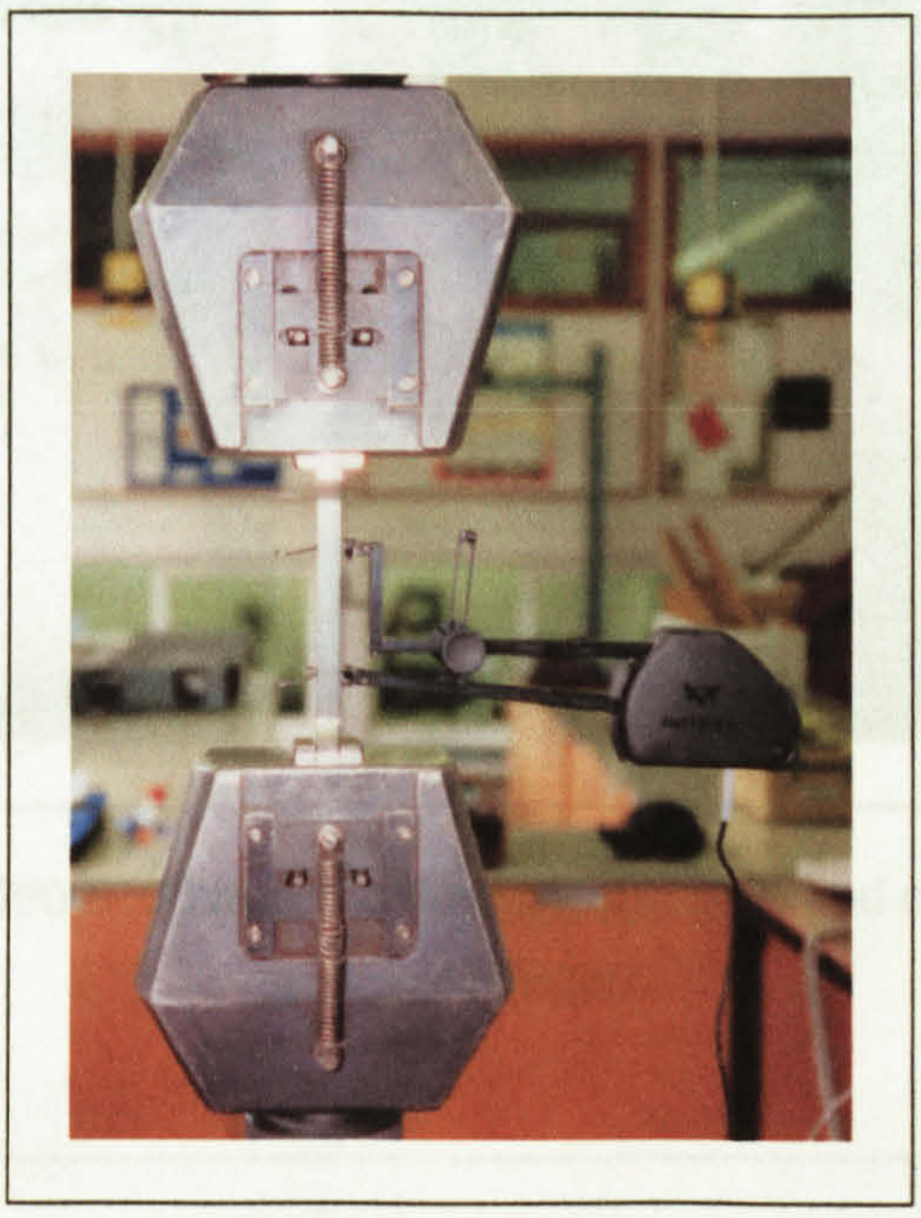

Figure 3.24: Monotonic uniaxial tensile testing.

3.5.5 Microhardness Testing

Microhardness testing was undertaken using a Buehler 1600-6100 microhardness tester, as shown in Figure 3.25, in accordance with ASTM E384[1]. Measurements on the welded specimens were made on the TS surface at the positions indicated in Figure 3.26. A load of 200 gf was employed and a loading time of 10 to 15 seconds. Ten measurements were made on the AA 5383-H321 parent plate, again on the TS surface.

[1] ASTM (1989)

Vickers hardness measurements were calculated using the following formula:

$$HV_{200} = 1.854 \times 10^3 \times \frac{F}{d^2} \qquad (3.1)$$

where: F = loading force, 200 gf

d = mean value of the two diagonals of the indentation (μm)

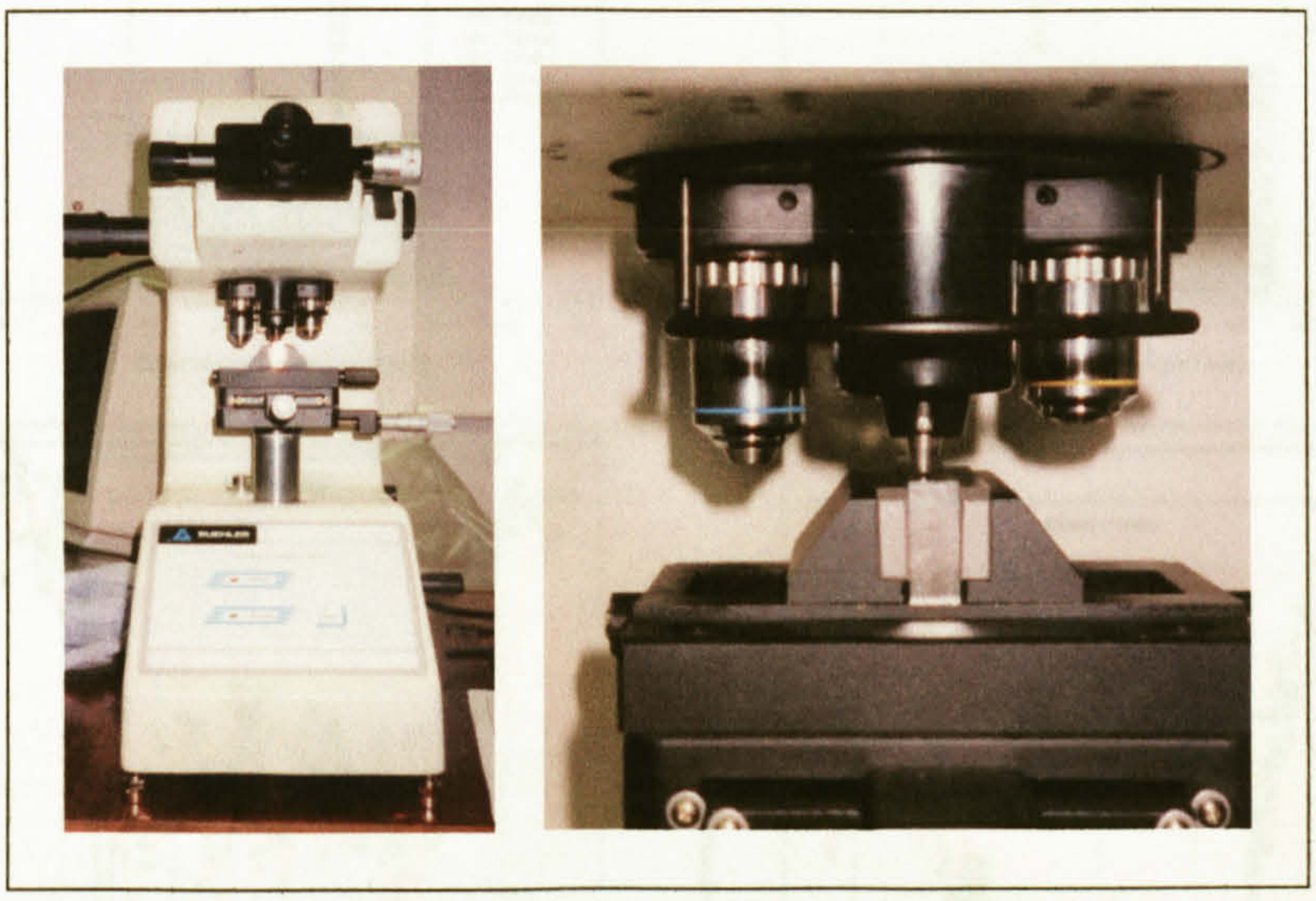

Figure 3.25: Buehler 1600-6100 microhardness tester (left) and close-up of indenter and specimen (right).

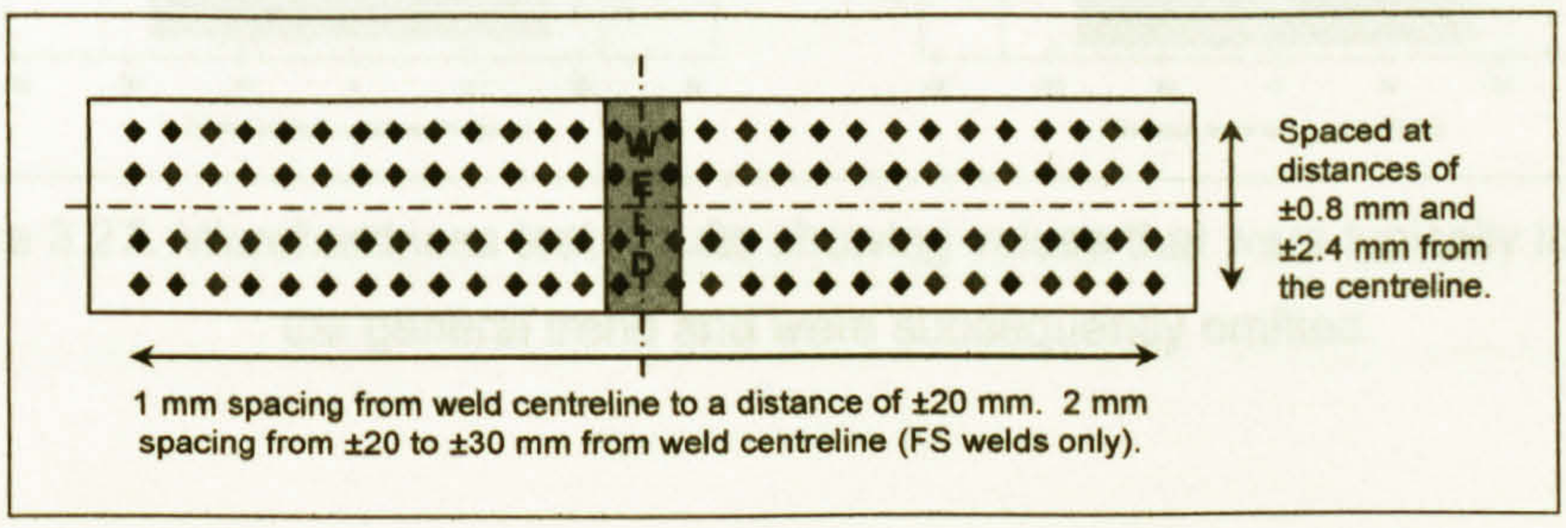

Figure 3.26: Positions of microhardness test indentations on the TS plane of the welded specimens.

Each weld sample exhibited one or more values that were substantially lower than the general trend, as shown in Figure 3.27. Initially it was thought that defects, such as porosity or partial fusion defects, within the weld may have been responsible, but the reduced values were also found outside of the weld area. Electro-etching of the indented surface was undertaken in an attempt to determine the cause, but the large surface area etched resulted in excessive material removal and difficulty observing the indentations, therefore the exact cause was not determined. These values have been excluded as they were not considered indicative of the underlying properties.

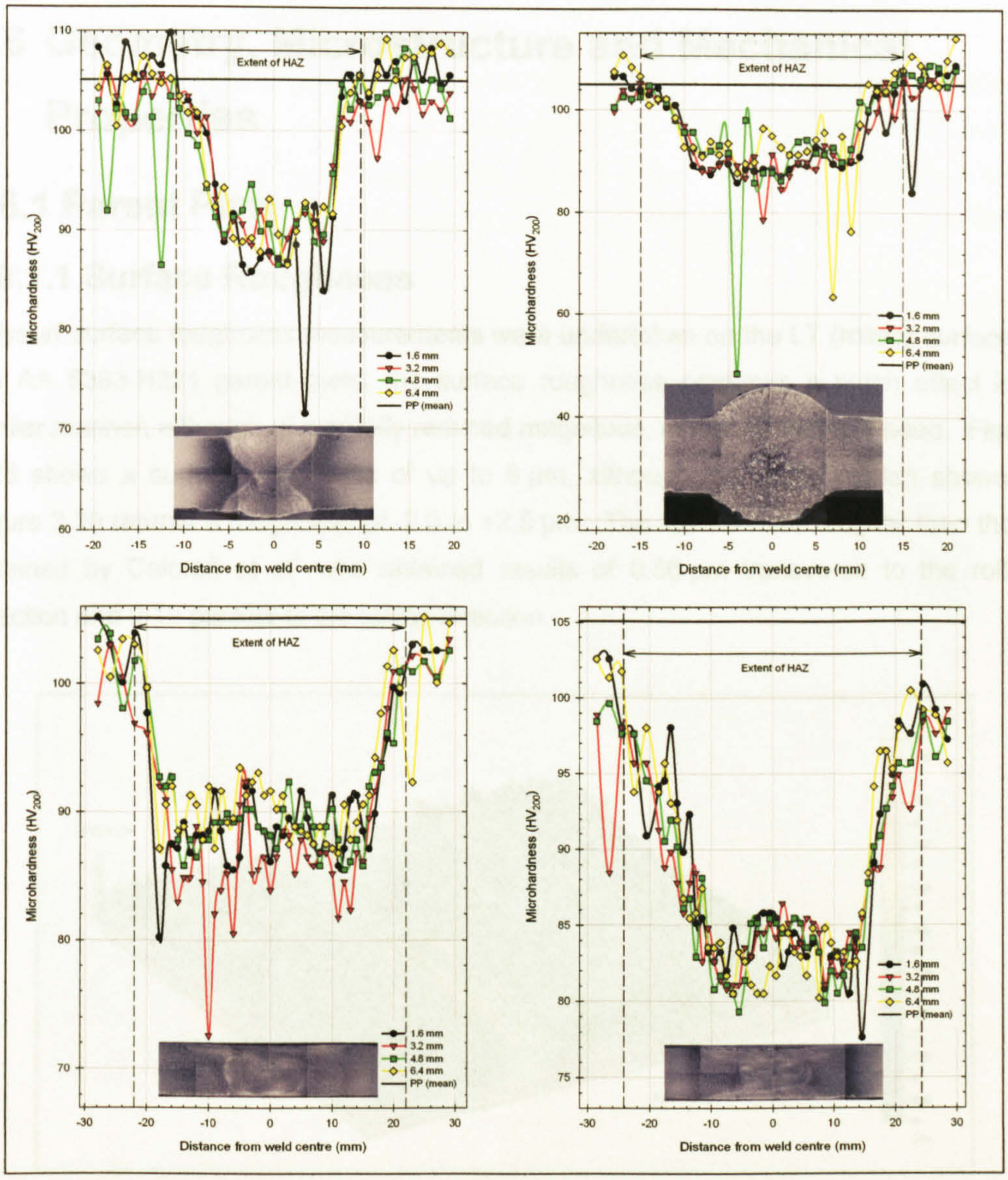

Figure 3.27: Microhardness test results showing values that were typically lower than the general trend and were subsequently omitted.

3.6 Geometry, Microstructure and Mechanical Properties

3.6.1 Parent Plate

3.6.1.1 Surface Roughness

Talysurf surface roughness measurements were undertaken on the LT (rolled) surface of the AA 5383-H321 parent plate; the surface roughness produces a notch effect in a similar manner, although of a greatly reduced magnitude, to that of the weld bead. Figure 3.28 shows a surface roughness of up to 9 µm, although the cross section shown in Figure 3.29 returns a roughness of -2.0 to +2.5 µm. The results were rougher than those obtained by Calcraft et al[1] who obtained results of 0.56 µm transverse to the rolling direction and 0.19 parallel to the rolling direction.

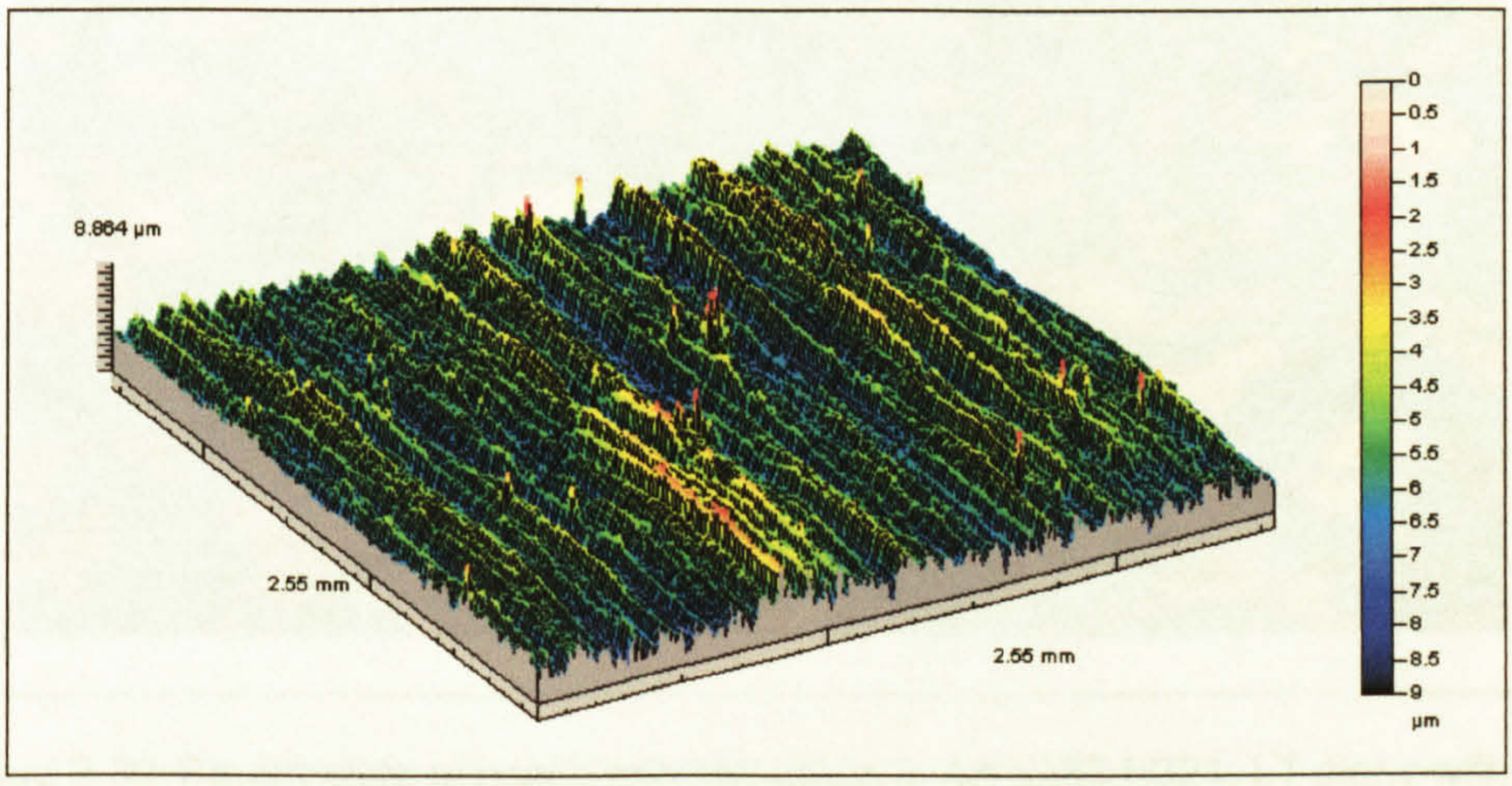

Figure 3.28: Three dimensional representation of the surface roughness of AA 5383-H321 plate obtained using Talysurf instrumentation, the rolling direction was from lower right to upper left.

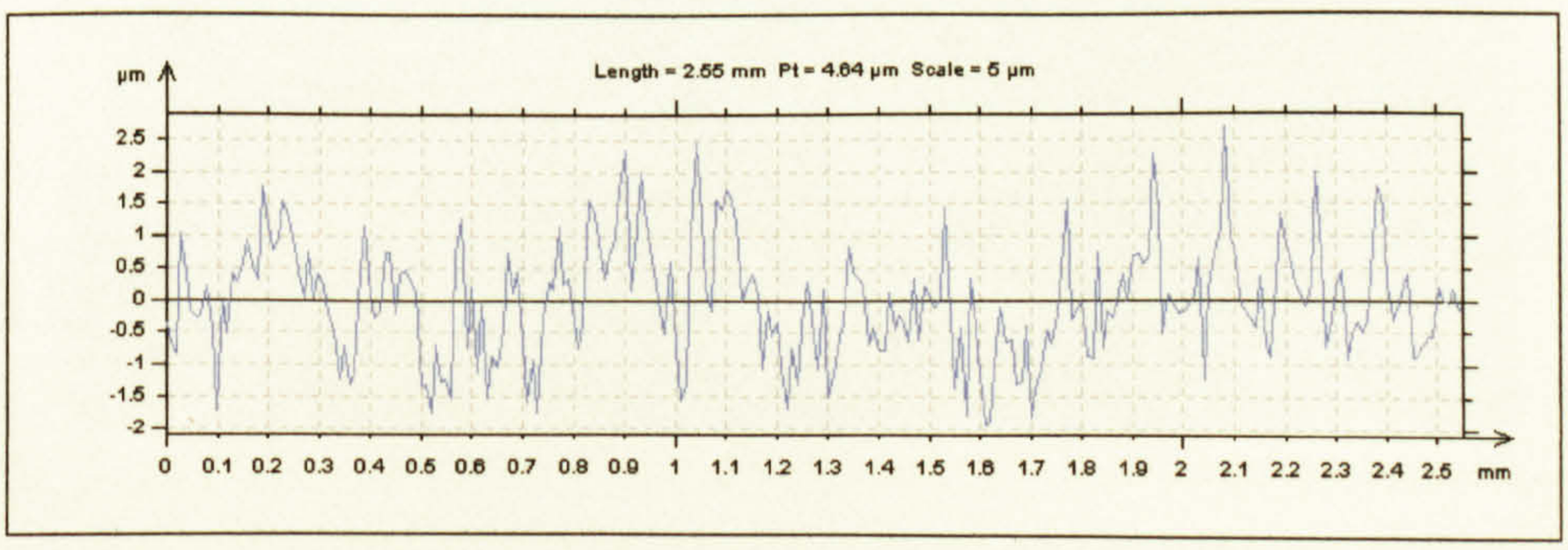

Figure 3.29: Cross section of surface roughness of AA 5383-H321 plate.

[1] Calcraft, RC et al (1999)

3.6.1.2 Microstructure

Figure 3.30 to Figure 3.32 show the microstructure of the AA 5383-H321 parent material, the planes related to those shown schematically in Figure 3.14. The pancake shaped grains being the result of the rolling process. The TS plane returned average grain sizes of approximately 15 - 25 µm in width with the length being approximately 2 - 4 times greater.

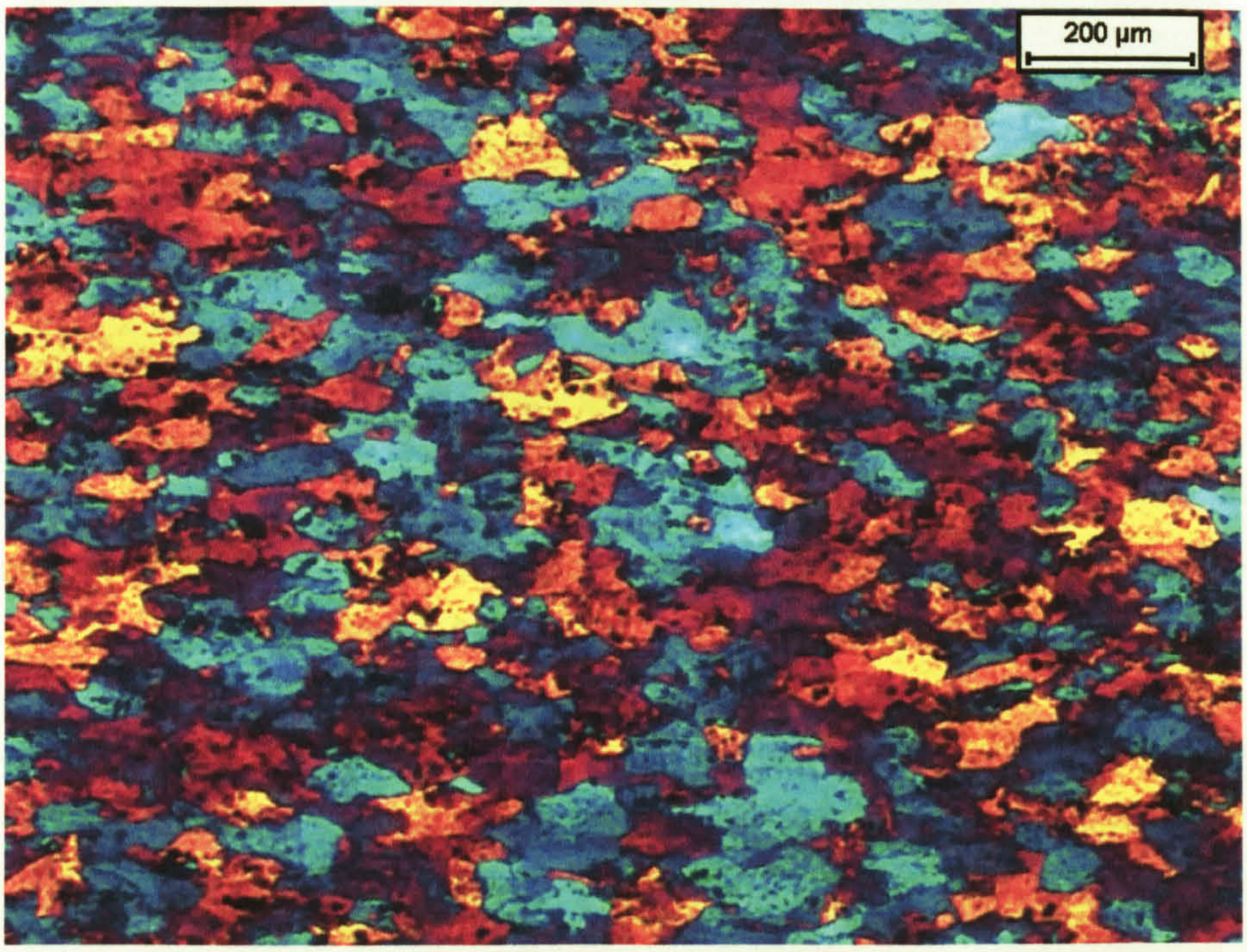

Figure 3.30: Parent plate pancake microstructure in AA 5383-H321; LT plane with the rolling having occurred in the horizontal direction

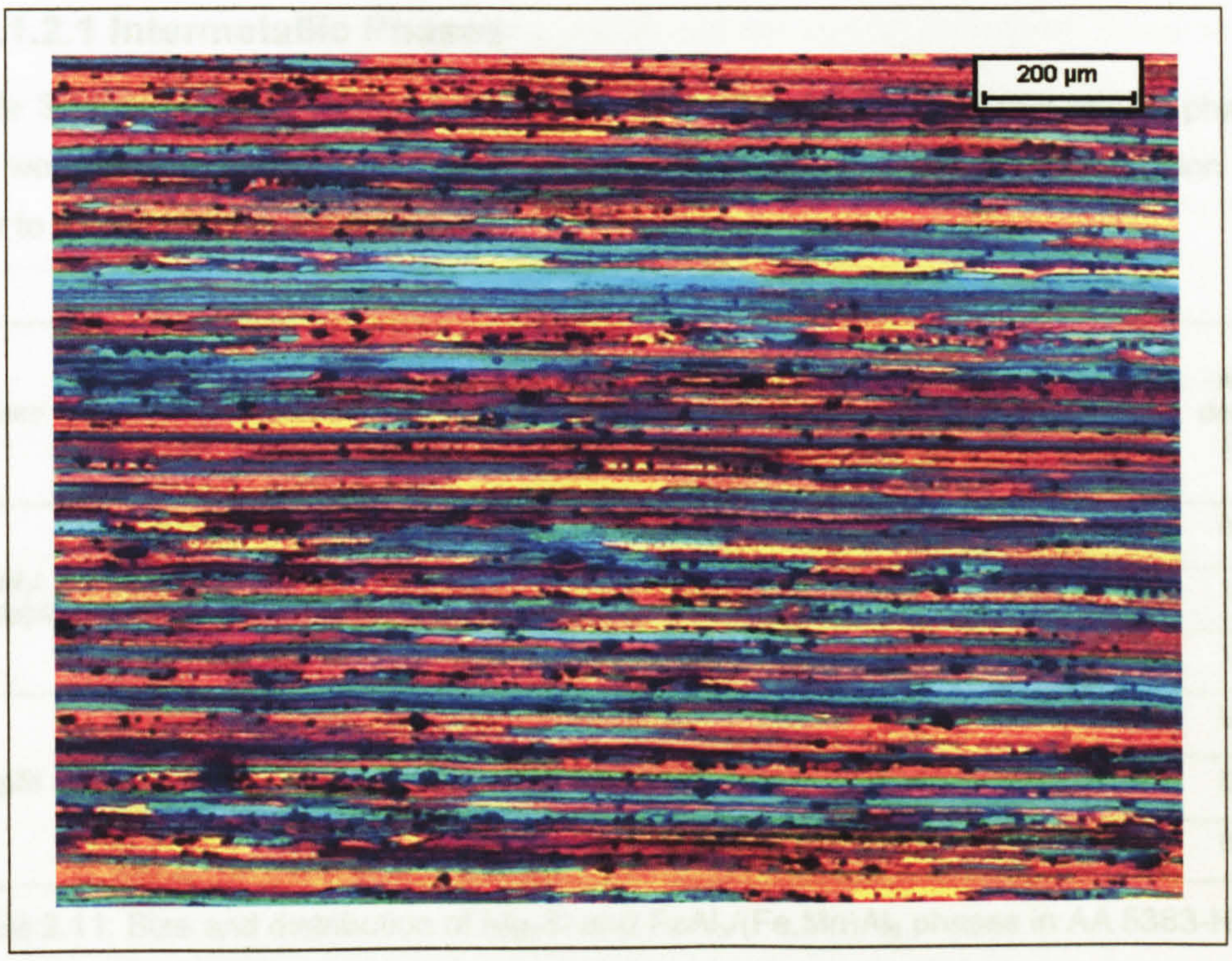

Figure 3.31: Parent plate pancake microstructure in AA 5383-H321; LS plane with the rolling having occurred in the horizontal direction.

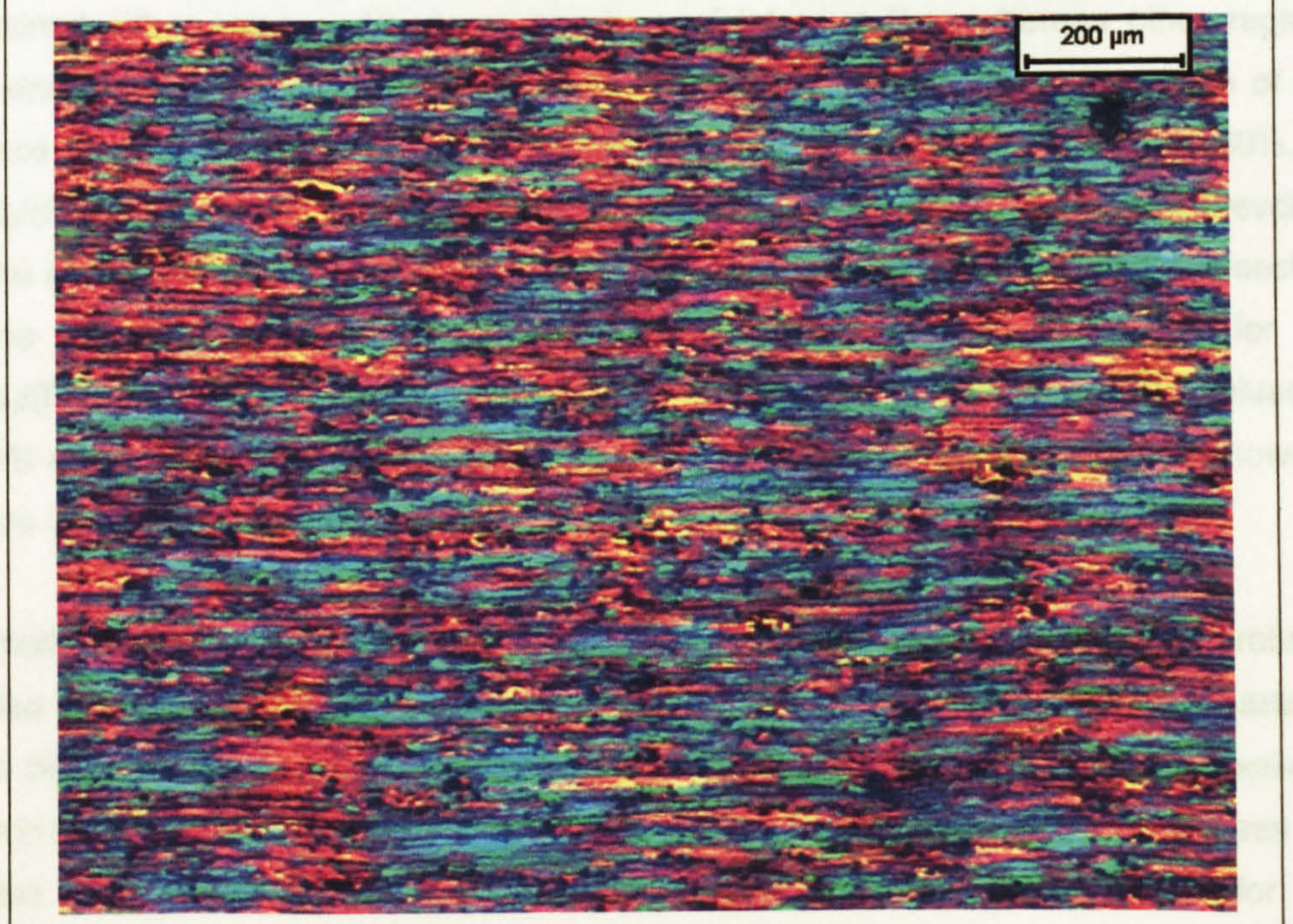

Figure 3.32: Parent plate pancake microstructure in AA 5383-H321; TS plane with the rolling having occurred in the horizontal direction.

3.6.1.2.1 Intermetallic Phases

Table 3.11 details the sizes and distribution of the Mg_2Si and $FeAl_3$/(Fe,Mn)Al_6 phases that were determined for both the LT (rolled) surface and the LS, both mid-section and near to the LT surface, plane.

Phase	Plane and position	Area examined (mm^2)	No. of particles	Phase size (μm^2)						Area density (%)
				Min	Max	Mean	Median	Std. Dev.	Total area	
$FeAl_3$/(Fe,Mn)Al_6	LS mid-section	3.533	2096	1.1	264	16.6	9.7	19.7	34695	0.98
	LS near edge	1.767	1093	1.1	185	16.6	9.7	19.5	17667	1.03
	LT (rolled surface)	1.767	1116	1.1	543	18.9	9.1	32.0	21063	1.19
Mg_2Si	LS mid-section	3.533	455	1.1	123	18.6	13.7	16.3	8461	0.24
	LS near edge	1.767	287	1.1	102	18.0	12.8	15.6	5151	0.29
	LT (rolled surface)	1.767	189	1.1	197	27.6	16.3	31.6	5214	0.30

Table 3.11: Size and distribution of Mg_2Si and $FeAl_3$/(Fe,Mn)Al_6 phases in AA 5383-H321 parent plate.

The distribution of secondary phases varied significantly, although this was more noticeable for the LT surface and for the $FeAl_3$/(Fe,Mn)Al_6 phase. Some regions contained either large and/or large numbers of intermetallics, whereas other regions contained relatively few. From Table 3.11 it can be seen that, as a percentage of the surface area measured, there was approximately four times less Mg_2Si, 0.24 - 0.30%, as $FeAl_3$/(Fe,Mn)Al_6, 0.98 - 1.19%, present. Both phases were noted to be more prevalent on the LT surface and the LS plane near to the LT edge in comparison to the mid-section of the LS plane, the values for the LT surface being 1.19% and 0.30% for the $FeAl_3$/(Fe,Mn)Al_6 and Mg_2Si respectively, the mid-section LS plane returning values of 0.98% and 0.24%. The variation in phase density was also evident visually, as shown in Figure 3.33 and Figure 3.34.

For both phases the smallest sized particles were recorded as 1.1 μm^2, this was probably related to the resolution of the microscope and/or software. The maximum sized particles were bigger for the $FeAl_3$/(Fe,Mn)Al_6 than the Mg_2Si, 264 μm^2 and 123 μm^2 respectively, for measurements made at the mid-section of the LS plane. For both the phases the largest particles found were on the LT surface, 543 μm^2 and 197 μm^2 for the $FeAl_3$/(Fe,Mn)Al_6 and Mg_2Si respectively. The mean particle size for the $FeAl_3$/(Fe,Mn)Al_6 on the LT surface was 14% greater than that for the LS plane, but the mean Mg_2Si particle size was 48% greater than that found on the LS plane. The median values for the $FeAl_3$/(Fe,Mn)Al_6, 9.7 μm^2 for the LS plane and 9.1 μm^2 for the LT surface, suggest that the LT surface consists of a small number of large particles, hence the increase in

the mean size, and a large number of particles that are smaller than those found on the LS plane, hence the lower median value. For the Mg_2Si phase the LT surface returned values that were greater for both the mean and median values in contrast to the LS plane, suggesting that the particles are typically larger on the LT surface. The variation between the two phases may be explained to some extent by the effect the rolling process is having on them; the $FeAl_3$/$(Fe,Mn)Al_6$ particles initially being larger than the Mg_2Si ones, but being broken into smaller particles by the rolling process, this appears to be substantiated by Figure 3.33 to Figure 3.35.

It was also noted that the largest particles found on the LS plane, but near to the edge of the LT surface, were smaller than the largest particles found at the mid-section of the LS plane.

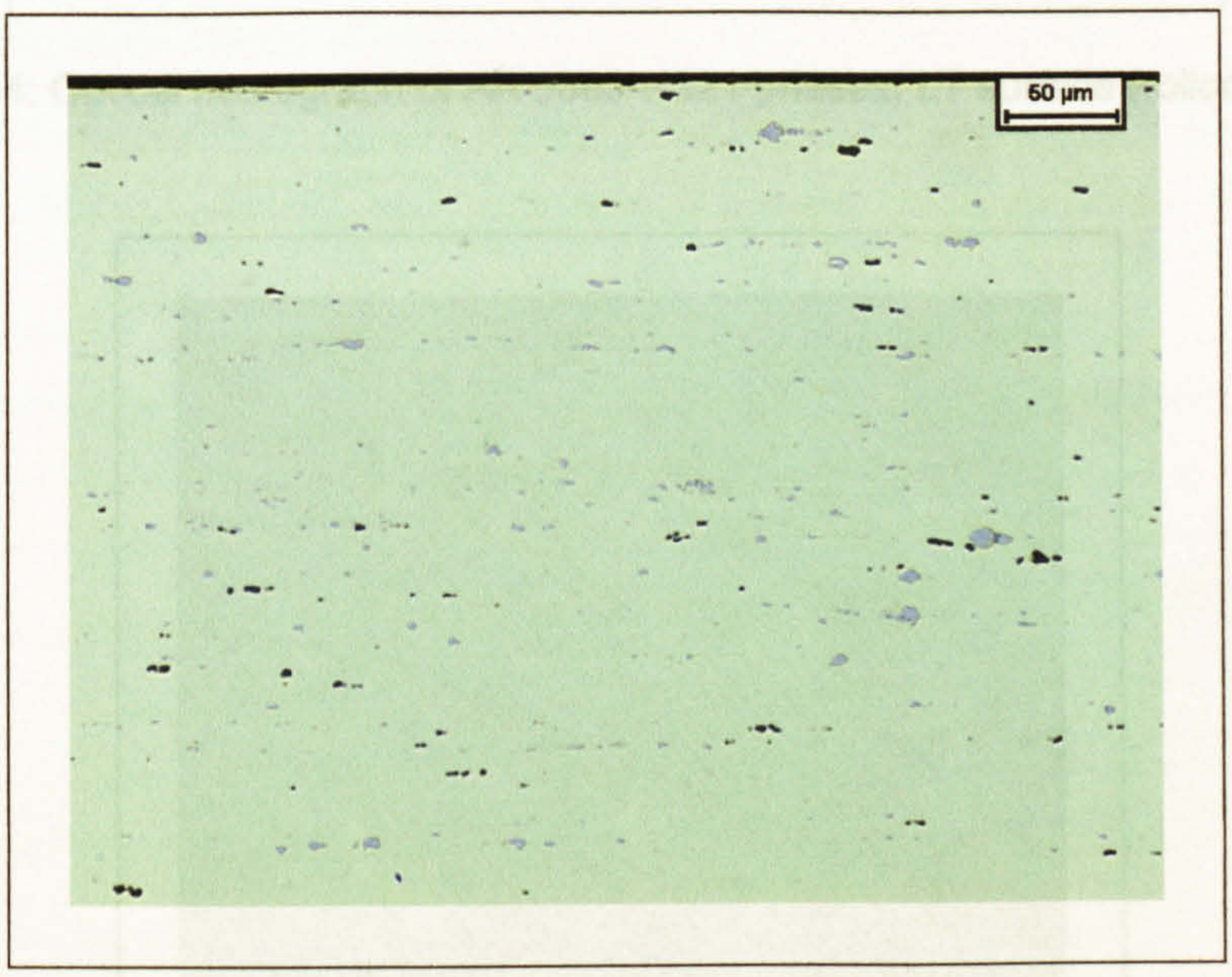

Figure 3.33: Optical micrograph of AA 5383-H321 phases, LS plane near to LT surface.

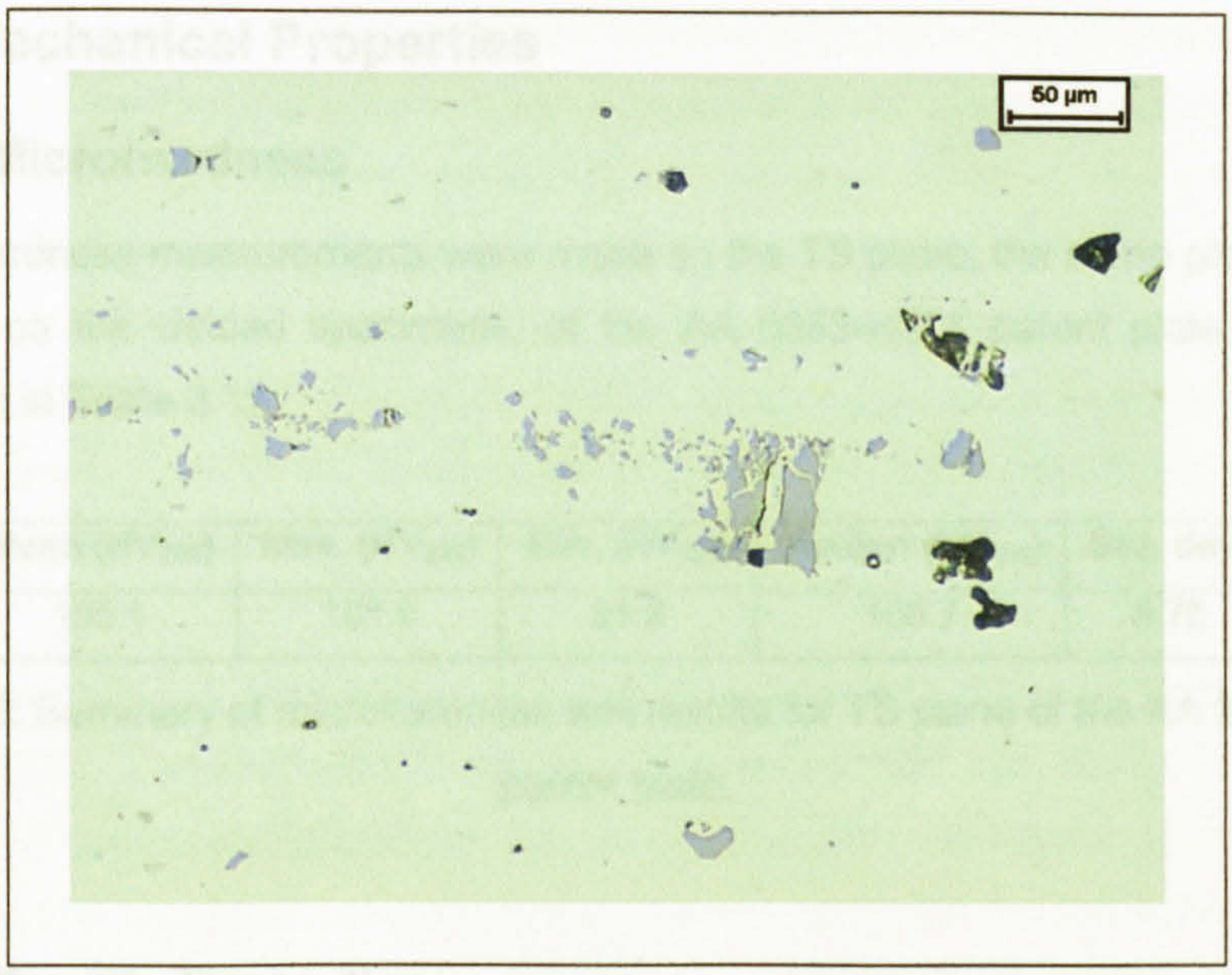

Figure 3.34: Optical micrograph of AA 5383-H321 phases, LT surface (rolled surface).

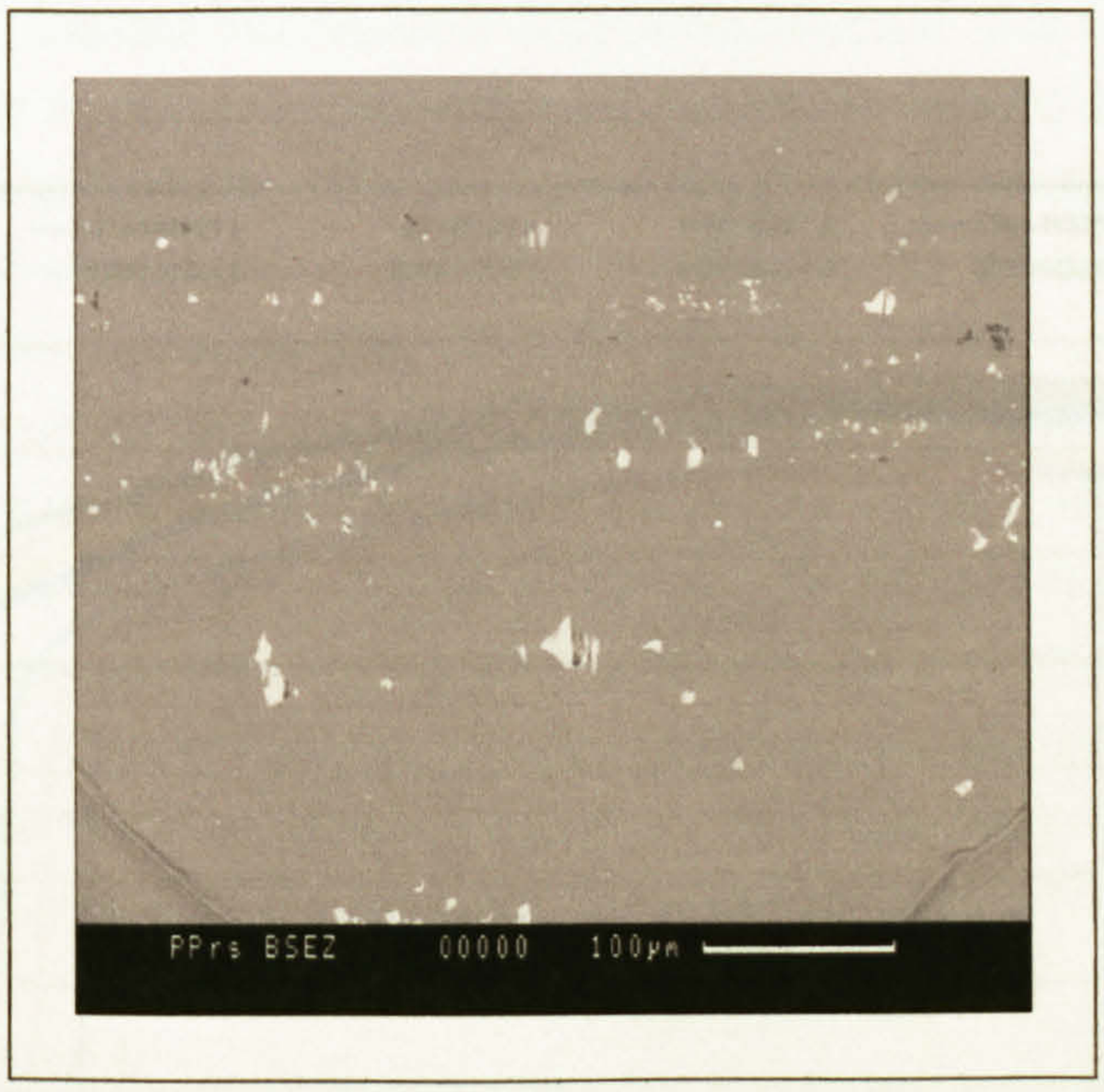

Figure 3.35: Electron micrograph of the AA 5383-H321 LT surface.

3.6.1.3 Mechanical Properties

3.6.1.3.1 Microhardness

Ten microhardness measurements were made on the TS plane, the same plane as those undertaken on the welded specimens, of the AA 5383-H321 parent plate, the results being shown in Table 3.12.

Mean (HV_{200})	Max. (HV_{200})	Min. (HV_{200})	Median (HV_{200})	Std. dev.
105.1	107.9	91.2	106.7	5.78

Table 3.12: Summary of microhardness test results for TS plane of the AA 5383-H321 parent plate.

3.6.1.3.2 Tensile Properties

The results from monotonic tensile testing of both AA 5383-H321 and AA 5083-H321 parent plate, both parallel (//) and transverse (|-) to the rolling direction, are shown in Figure 3.36.

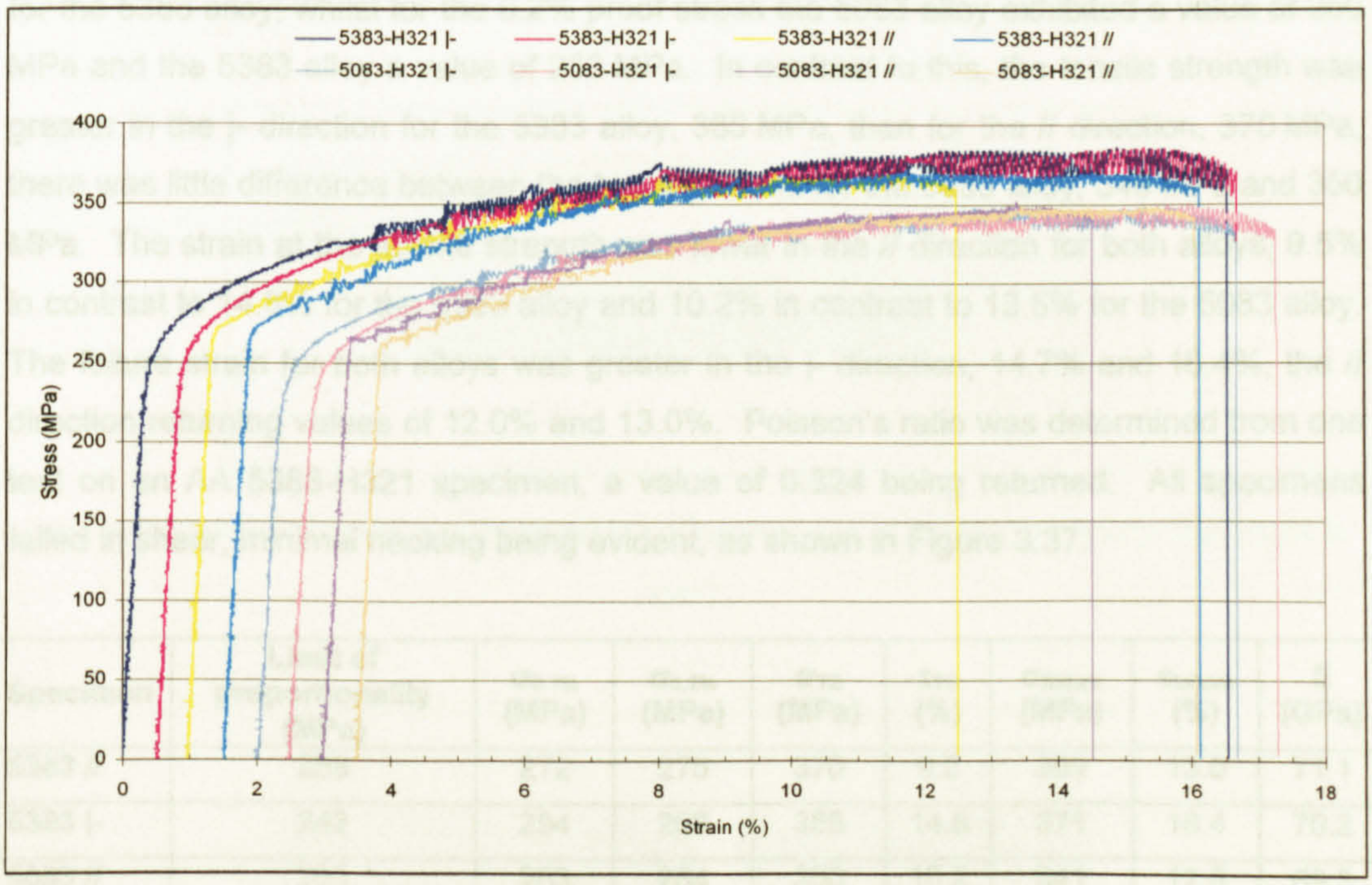

Figure 3.36: Stress/strain plots from monotonic uniaxial tensile tests of AA 5383-H321 and AA 5083-H321 8 mm thick plate.

From the stress-strain plots it can be seen that both alloys initially exhibited a linear elastic response, although the transformation from elastic to plastic deformation was dependent on the direction that the load was applied in relation to the rolling direction.

For both alloys, when the load was applied // to the rolling direction, a distinct yield point was evident, whereas a reducing tangent modulus was apparent when the loading was applied |- to the rolling direction. Application of the loading both // and |- to the rolling direction resulted in an uneven response of the stress/strain curve in the plastic region. This may have been due to either incremental yielding, close observation of the specimen during the test revealed the formation of shear bands, or dynamic recrystallisation. The uneven response of the stress/strain curve in the plastic region was noted to occur at a lower plastic strain for specimens loaded // to the rolling direction.

Table 3.13 summarises the mechanical properties of the two alloys for both the // and |- rolling directions. The 5383 alloy is considered to be a similar alloy to the 5083 alloy, but with enhanced mechanical properties, this was evident from the results obtained from the tensile tests. The elastic modulus for both alloys and directions ranged from 69 - 71 GPa, although the 5083 alloy with the rolling direction |- to the load returned a value 66 GPa. Both alloys returned greater values for both the limit of proportionality, 261 MPa and 268 MPa, and 0.2% proof stress, 264 MPa and 275 MPa, for the 5083 and 5383 alloys respectively, when the load was applied // to the rolling direction. |- to the rolling direction returned values for the limit of proportionality of 205 MPa for the 5083 alloy and 242 MPa for the 5383 alloy; whilst for the 0.2% proof stress the 5083 alloy exhibited a value of 250 MPa and the 5383 alloy a value of 263 MPa. In contrast to this, the tensile strength was greater in the |- direction for the 5383 alloy, 385 MPa, than for the // direction, 370 MPa, there was little difference between the two directions for the 5083 alloy, 348 MPa and 350 MPa. The strain at the tensile strength was lower in the // direction for both alloys, 9.5% in contrast to 14.8% for the 5383 alloy and 10.2% in contrast to 13.5% for the 5083 alloy. The failure strain for both alloys was greater in the |- direction, 14.7% and 16.4%, the // direction returning values of 12.0% and 13.0%. Poisson's ratio was determined from one test on an AA 5383-H321 specimen, a value of 0.324 being returned. All specimens failed in shear, minimal necking being evident, as shown in Figure 3.37.

Specimen	Limit of proportionality (MPa)	$\sigma_{0.1\%}$ (MPa)	$\sigma_{0.2\%}$ (MPa)	σ_{TS} (MPa)	ε_{TS} (%)	$\sigma_{failure}$ (MPa)	$\varepsilon_{failure}$ (%)	E (GPa)
5383 //	268	272	275	370	9.5	359	13.0	71.1
5383 |-	242	254	263	385	14.8	371	16.4	70.2
5083 //	261	263	264	350	10.2	341	12.0	69.3
5083 |-	205	238	250	348	13.5	338	14.7	65.5

Table 3.13: Mechanical properties of AA 5383-H321 and AA 5083-H321 parent plate (mean of two tests per specimen).

Poisson's ratio (AA 5383-H321), $\nu = 0.324$

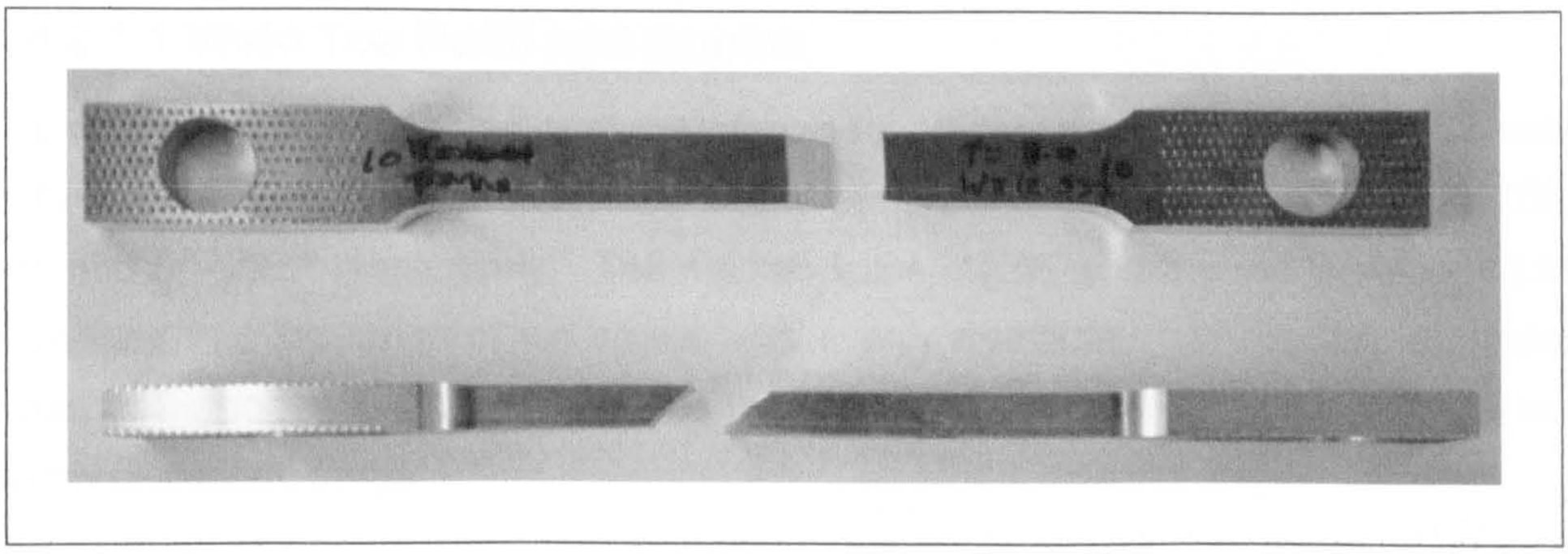

Figure 3.37: Shear failure resulting from monotonic uniaxial tensile testing of AA 5383-H321 8 mm thick plate.

3.6.2 MIG Low Input

3.6.2.1 Weld Geometry

A typical cross section of the MIG LI weld geometry is shown in Figure 3.38, views of the two weld beads are shown in Figure 3.39. From Figure 3.38 it was evident that the plate on the right side is slightly out of plane with that on the left, indicating lateral distortion in the welded section.

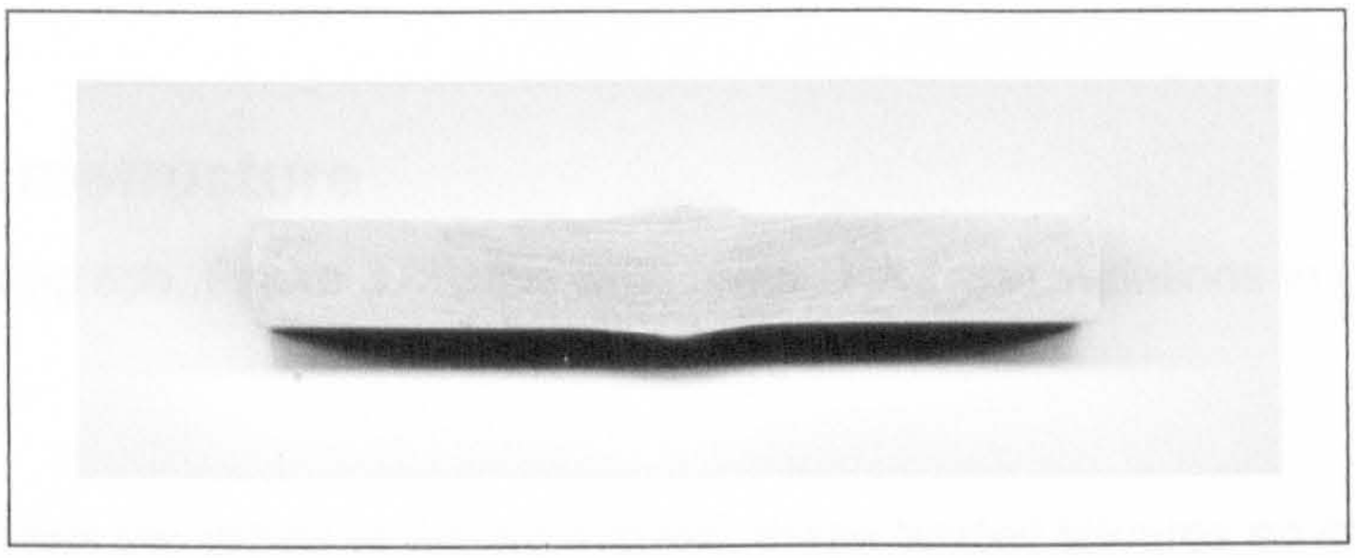

Figure 3.38: MIG LI weld bead geometry, 1st weld pass at the bottom (plate thickness 8 mm).

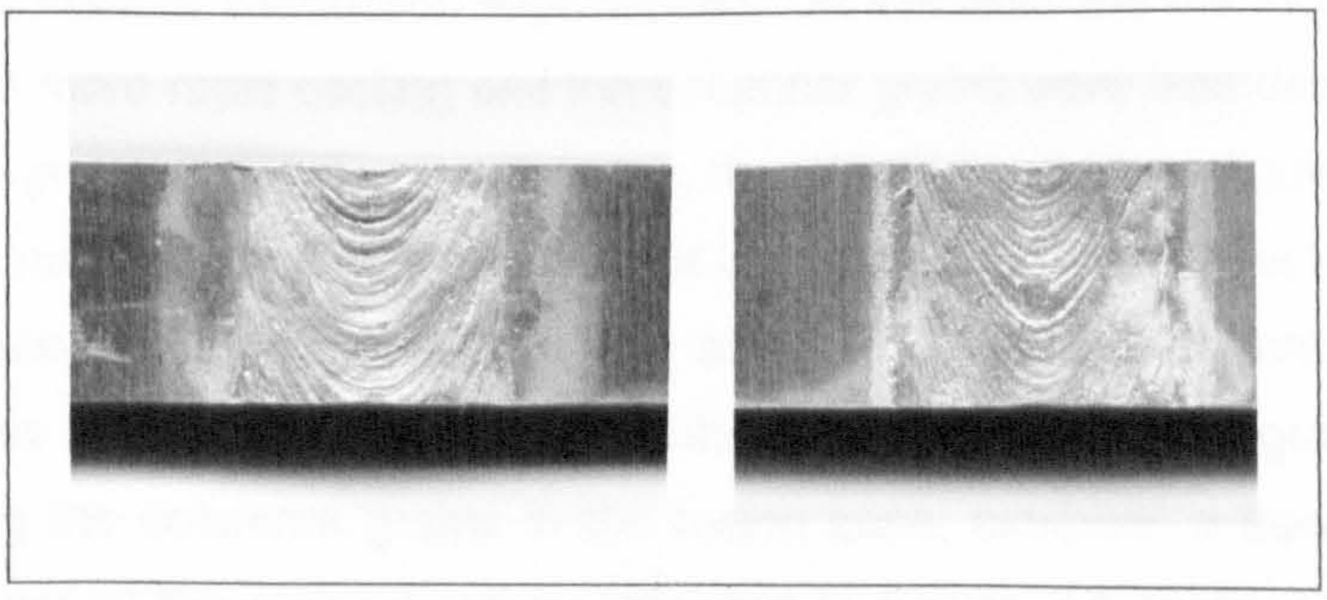

Figure 3.39: MIG LI weld beads, 1st run left, 2nd run right.

3.6.2.1.1 Weld Toe Radii and Angles

The weld toe radii and angles were determined for 12 positions, the results being shown in Table 3.14. Both the weld toe radius and angles varied significantly, from 1.030 - 4.080 mm and 6° - 26.5° respectively. The median value, 12.5°, and the mean value, 13.9°, suggested that the range of toe angles was evenly distributed. In contrast, the mean value for the toe radius, 2.381 mm, and the median value, 1.855 mm, suggested a less evenly distributed range.

Radius (mm)	Angle (°)	Radius (mm)	Angle (°)	Radius (mm)	Angle (°)
1.430	9	1.030	15	1.990	14
3.940	11	4.040	26.5	2.270	25
4.080	6	3.400	12	1.720	10.5
1.390	13	1.660	11.5	1.620	13

	Radius (mm)	Angle (°)
Minimum	1.030	6
Maximum	4.080	26.5
Mean	2.381	13.9
Median	1.855	12.5
Std. dev.	1.149	6.03

Table 3.14: MIG LI weld toe radii and angles.

3.6.2.2 Microstructure

From the macrograph, Figure 3.40, the weld metal, HAZ and variations in grain geometry are evident.

Figure 3.42 shows the grains in the weld metal, these tended towards an equiaxed shape with an average diameter of 100 µm (ASTM grain size 3.5G). The grains in the fusion zone were generally columnar in shape, shown in Figure 3.41 and Figure 3.43 to Figure 3.45, this being due to epitaxial growth from grains in the HAZ, coupled with the direction and gradient of thermal conduction experienced. At the weld toe the increased surface area resulted in more rapid cooling and the columnar grains were less developed, Figure 3.41 shows the grain structure at the weld toe, the initiation point for fatigue cracks; grains within the weld metal are shown on the right of the figure and those of the HAZ on the left. The figures clearly indicate the difference in size and the rapid transformation between the grains of the weld metal and the HAZ in the parent metal. All the grains in the weld metal, including the columnar grains in the fusion zone, exhibited a dendritic structure. The development of the microstructure, depicted in Figure 3.1 (page 17), of the weld metal at the fusion zone, is represented by (c), cellular dendritic growth, and (d), columnar dendritic growth, whilst the grains within the weld metal are represented by (e), equiaxed dendritic growth.

Figure 3.46 and Figure 3.47 depict grains within the HAZ, near and distant to the weld respectively. The grains were more equiaxed than those in the parent metal, although the grains in the HAZ became more elongated as the distance from the weld increased due to the reduction in the influence of the thermal cycle. Typical grain sizes in the HAZ were 20 µm in width and 50 µm in length, although more equiaxed grains were evident near to the weld, with an approximate diameter of 30 µm (ASTM grain size 7.5G). In comparison, grains in the weld bead were around 100 µm in diameter (ASTM grain size 3.5G) and those in the parent material 15 - 25 µm in width and 2 - 4 times greater in length. The HAZ extended approximately 10 mm from the weld centreline, 5 mm from the weld toe, although only slight changes in the pancake shaped grain structure of the parent material were evident at these distances from the weld. Major changes to the parent grain structure, the grains being near equiaxed, were evident up to distances of 2 mm from the weld toe, 7 mm from the weld centreline, although the exact distances varied through the thickness due to the weld geometry and back gouging.

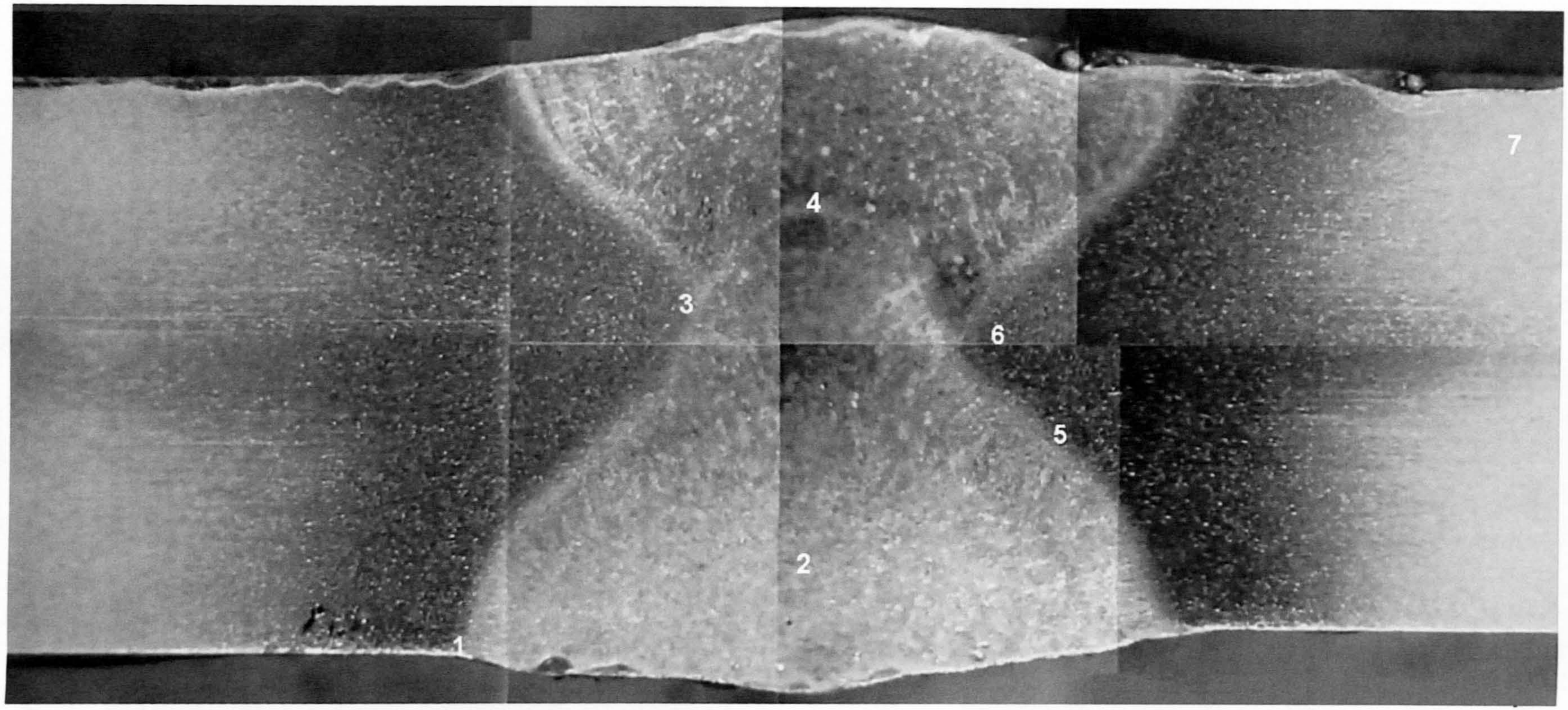

Figure 3.40: Macrograph of AA 5383-H321 MIG LI butt weld, plate thickness 8 mm, (numbers refer to the positions and orientations of the following micrographs).

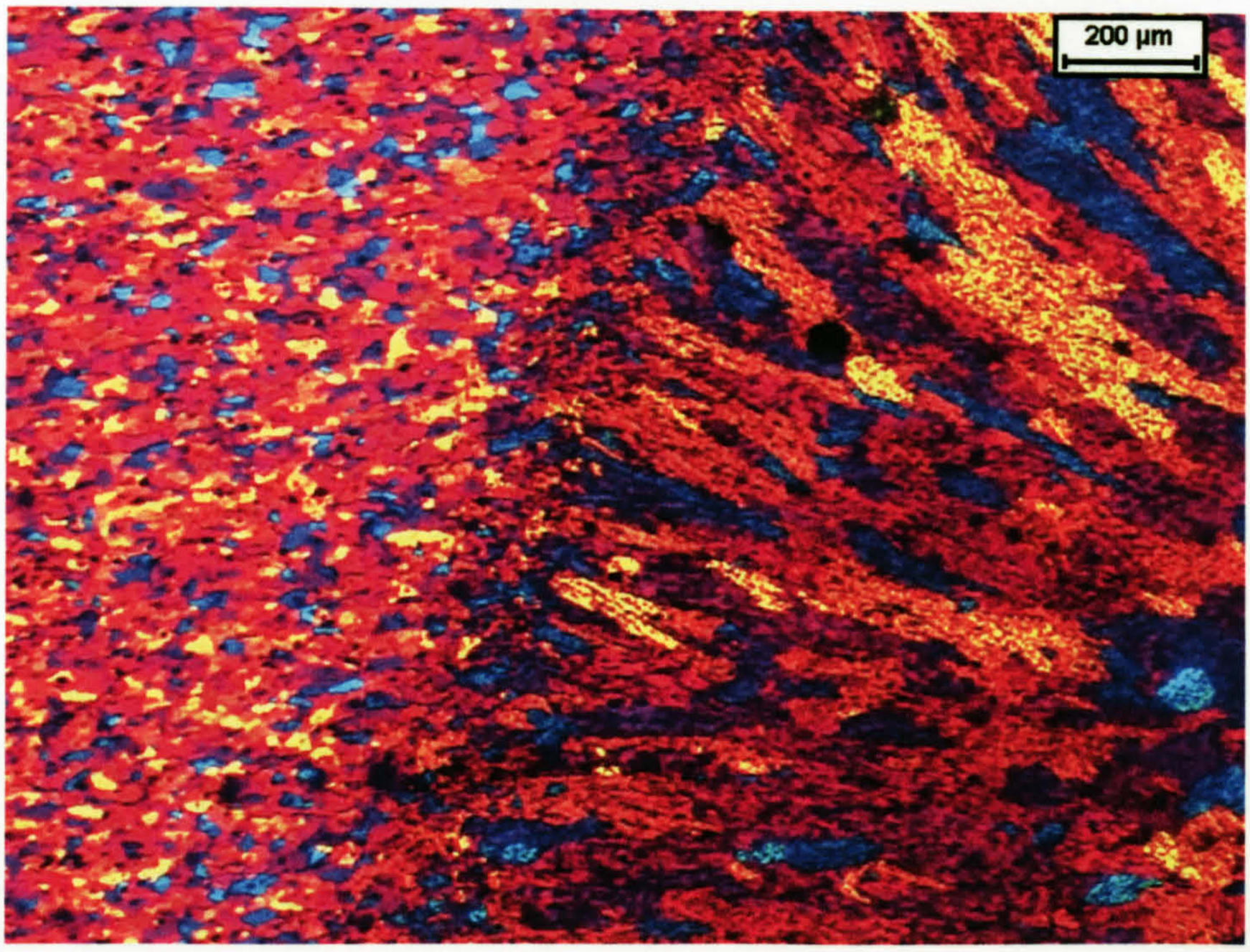

Figure 3.41: MIG LI grains at the HAZ (left) and weld toe (right) boundary, position 1 in Figure 3.40.

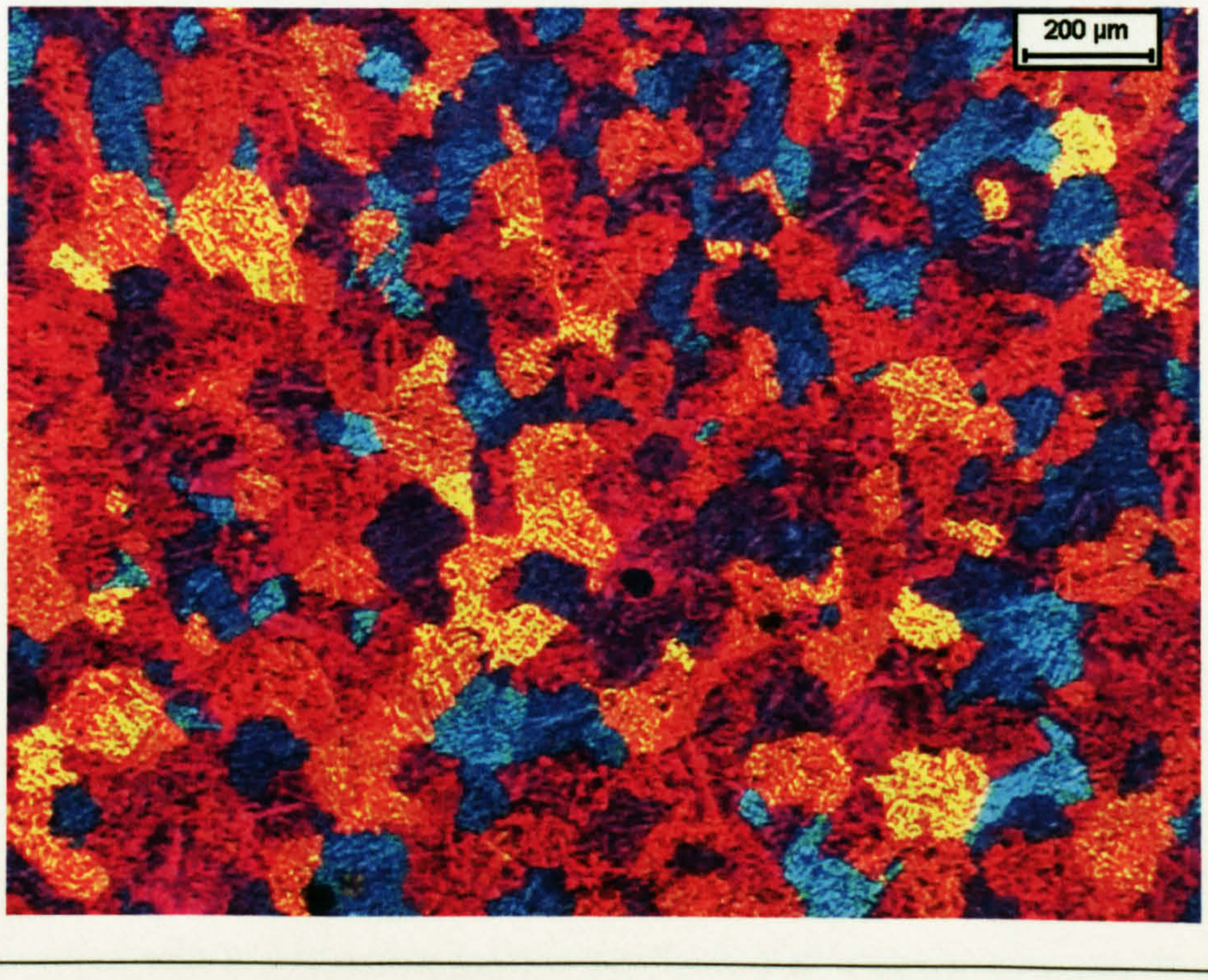

Figure 3.42: MIG LI grains in the weld metal, position 2 in Figure 3.40. Average grain size 100 µm, ASTM 3.5G.

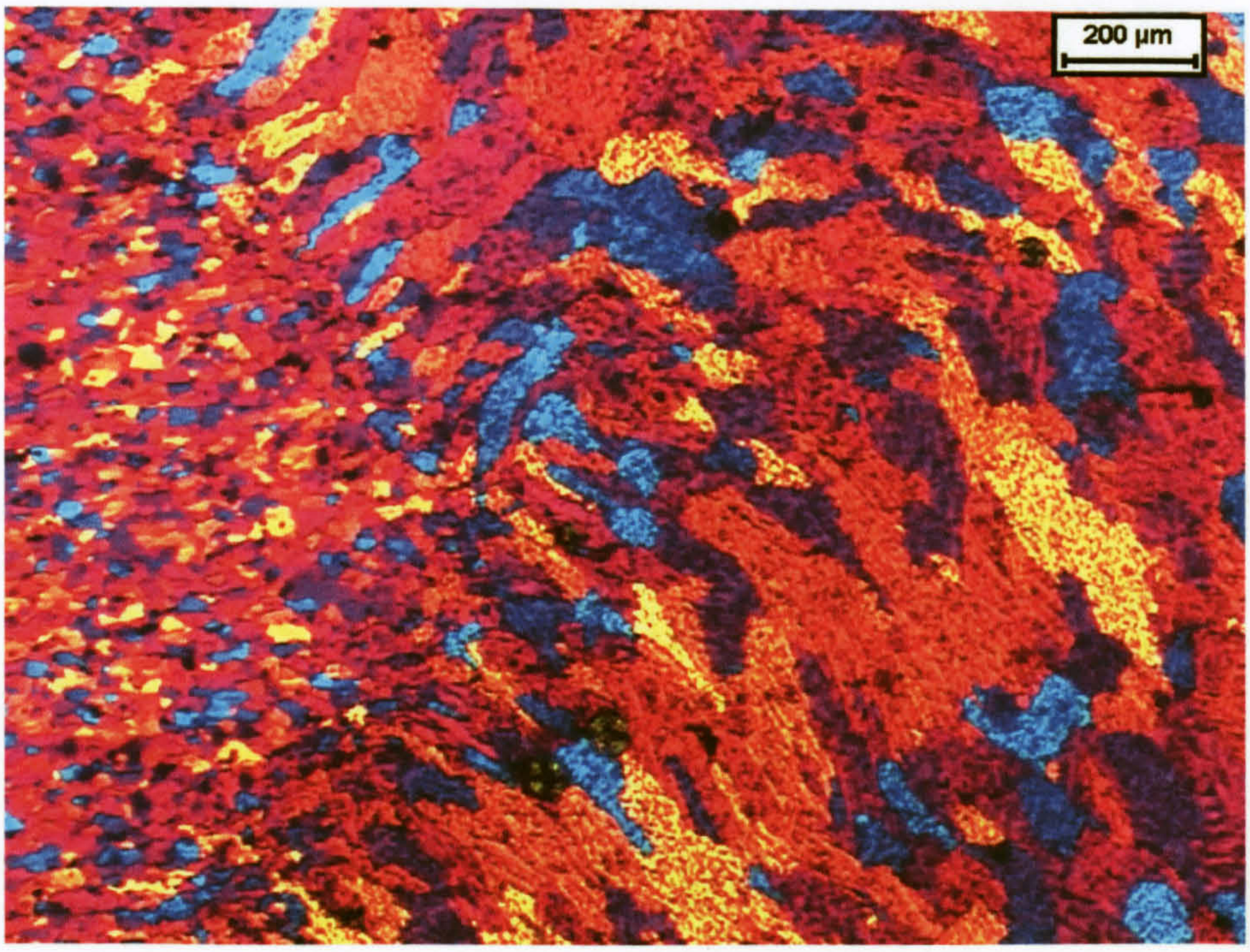

Figure 3.43: MIG LI grains at the boundary of both weld pools and the HAZ, position 3 in Figure 3.40.

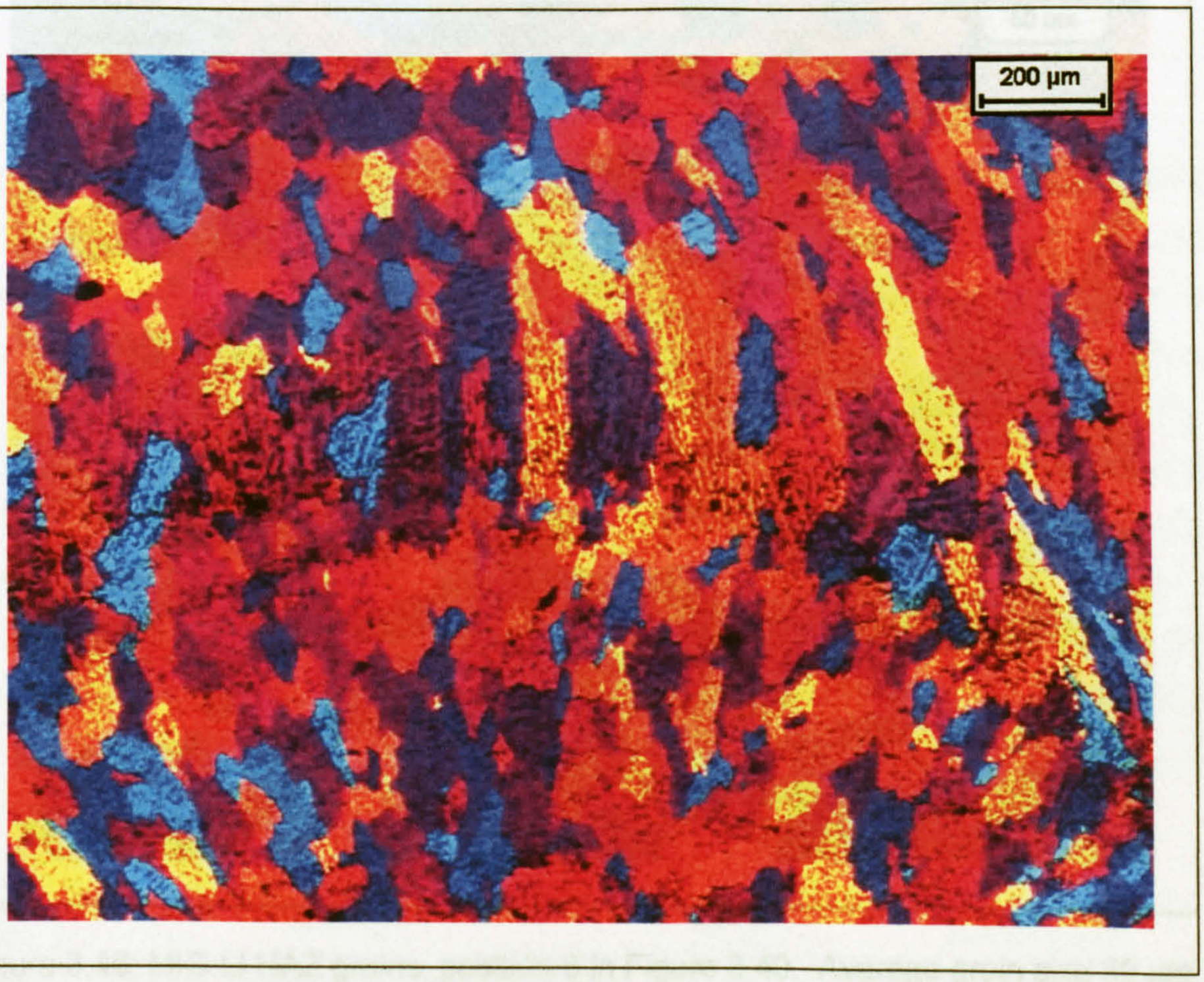

Figure 3.44: MIG LI grains at the weld metal, the second pass at the bottom, position 4 in Figure 3.40.

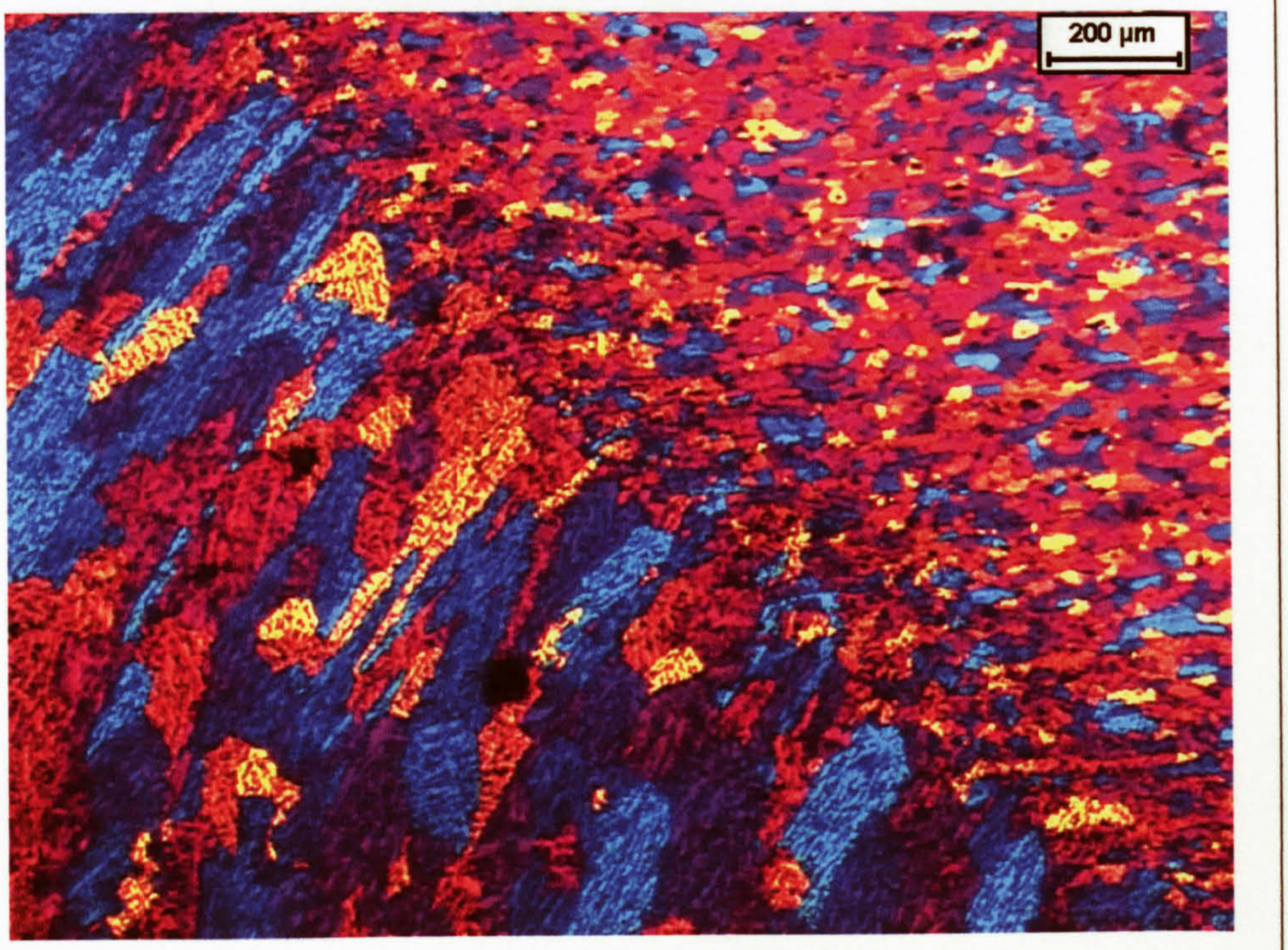

Figure 3.45: MIG LI grains at the HAZ/weld metal boundary, position 5 in Figure 3.40.

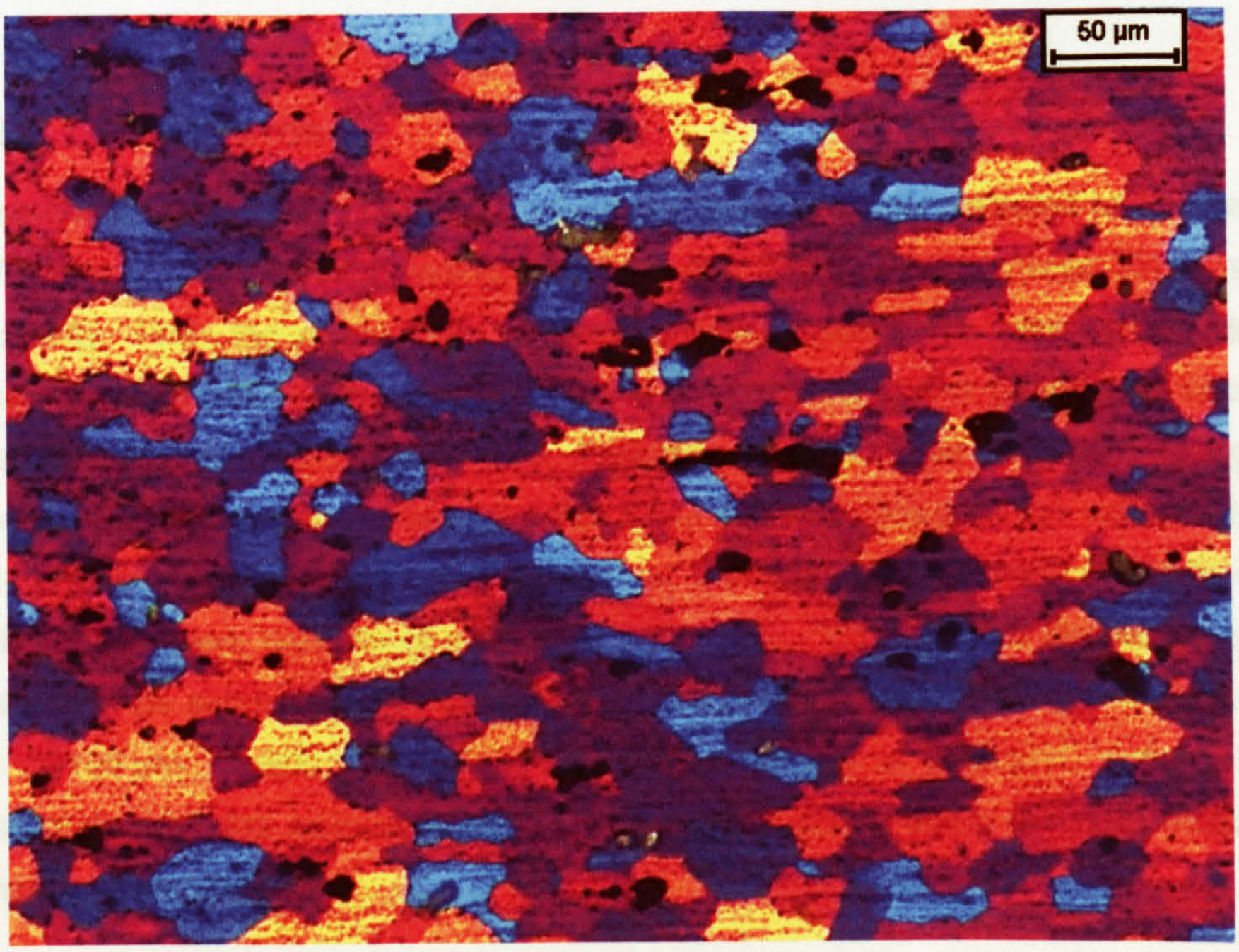

Figure 3.46: MIG LI HAZ grains, position 6 in Figure 3.40. Average grain size 30 µm, ASTM 7.5G.

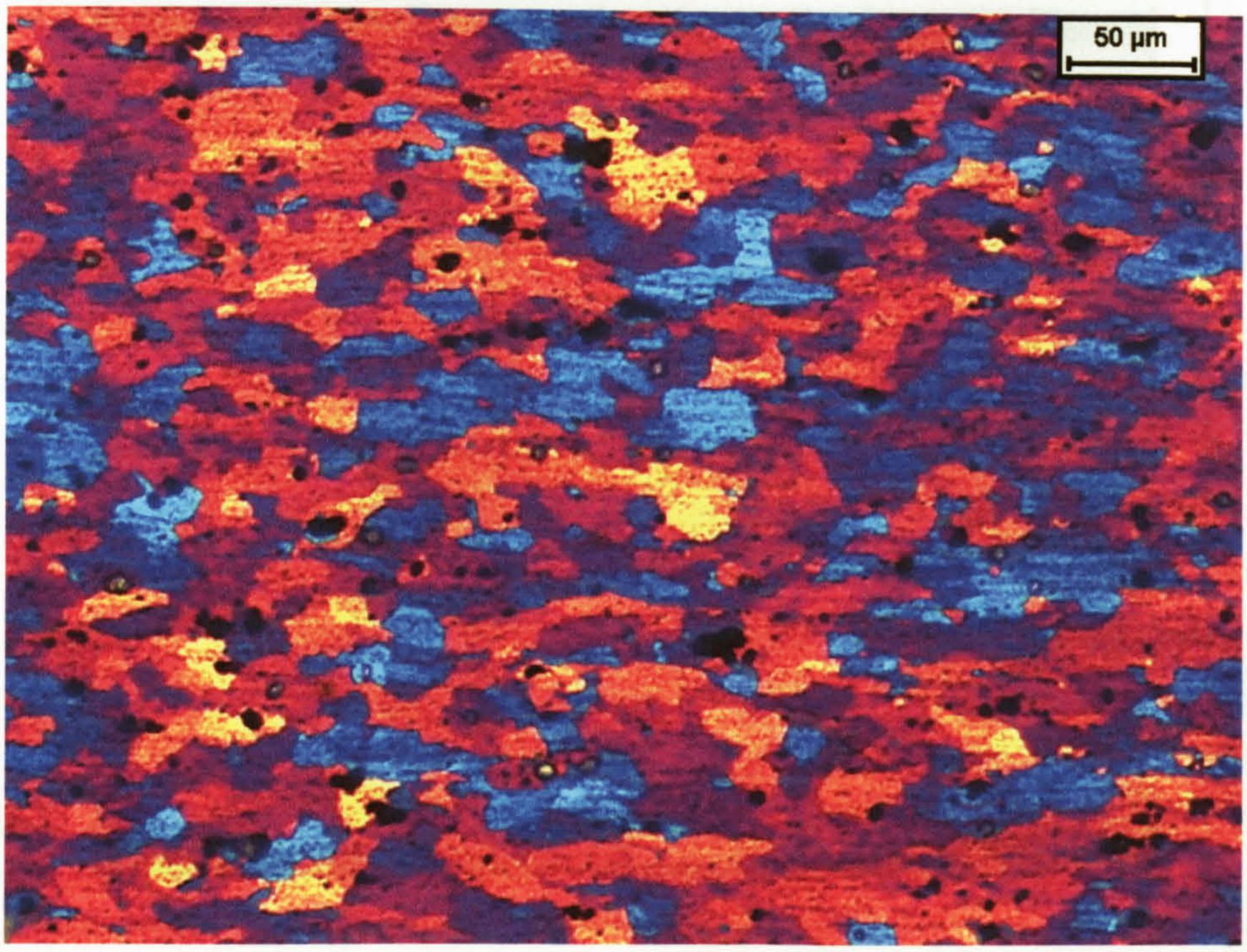

Figure 3.47: MIG LI HAZ, all the grains have been affected by the thermal cycle, but those on the left, nearer to the weld, have become much more equiaxed in comparison to those on the right, position 7 in Figure 3.40.

3.6.2.2.1 Weld Porosity

A cross-section of the MIG LI weld, as shown in Figure 3.48, was prepared as detailed in i - iii of Section 3.5.1, Planar Grinding, Polishing and Electro-etching (page 36) to reveal the porosity. From the image it can be seen that the largest pores were located near to the surface of the weld metal, suggesting that coalescence and/or growth had occurred as the pores moved towards the surface. Smaller pores tend to be distributed throughout the weld, although areas of minimal pores were noted, typically in the wake of larger pores. Although some pores were evident at the weld toe, the site of fatigue crack initiation, these were typically of a small to mean size. The size and distribution of the porosity was as summarised in Table 3.15. The measured pores ranged in area from 2000 - 32100 μm^2, radius 25 - 101 µm, with a mean value of 5463 μm^2, radius 42 µm. The area density was calculated as the total area of pores within the weld metal and returned a value of 0.30%.

No. of Pores	Area (μm^2)				Area density (%)	Radius (µm)		
	Max.	Min.	Mean	Total		Max.	Min.	Mean
35	32100	2000	5463	191200	0.30	101	25	42

Table 3.15: Size and distribution of porosity in a MIG LI weld.

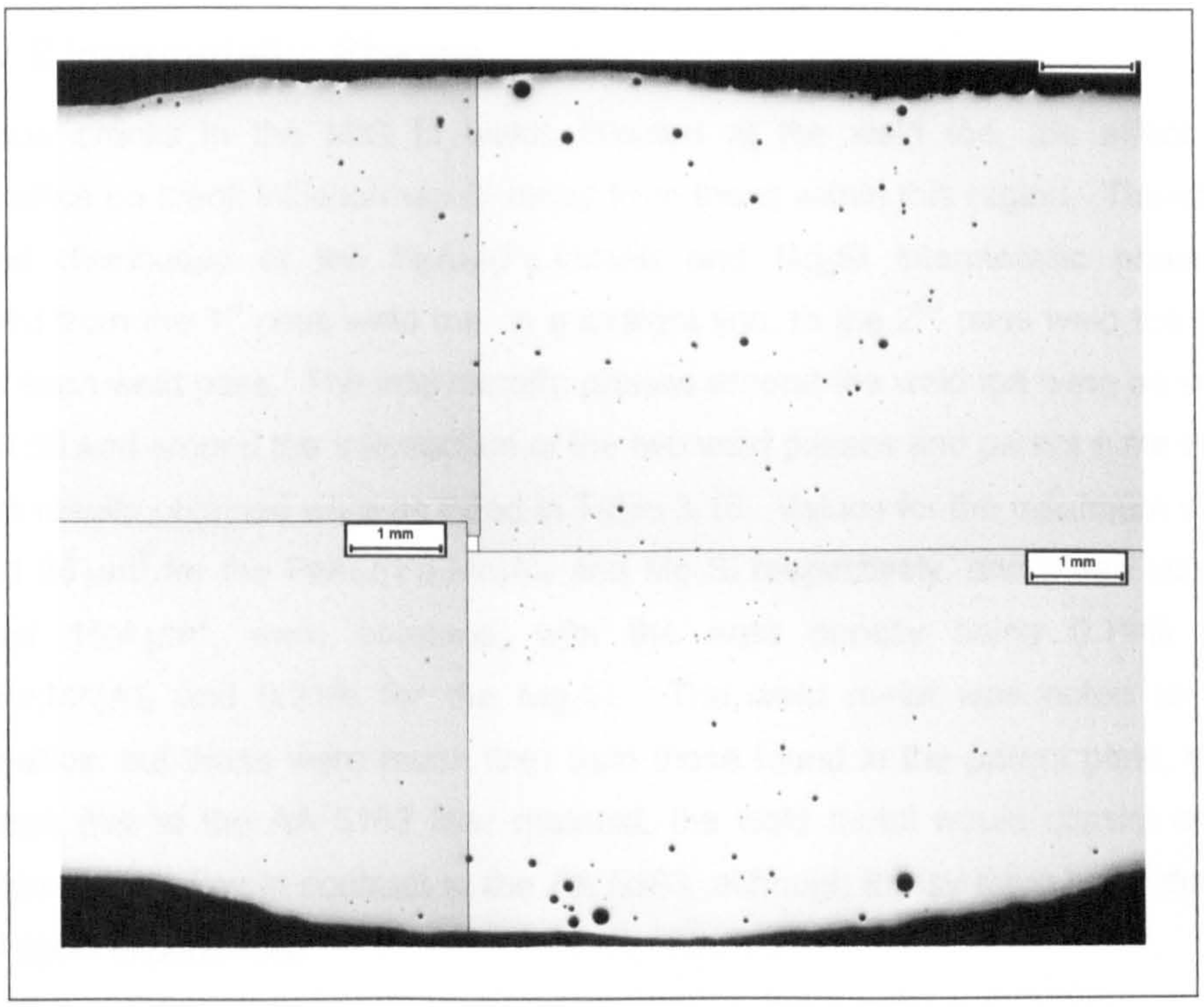

Figure 3.48: Weld porosity in MIG LI weld, second pass uppermost.

A pore was found in the MIG LI weld, as shown in Figure 3.49, in a specimen that had been produced for the measurement of short crack growth. The pore was in the weld metal, the maximum radius of pore on the machined surface of the specimen being 1.45 mm, and was not detected by the fabricator using radiographic examination.

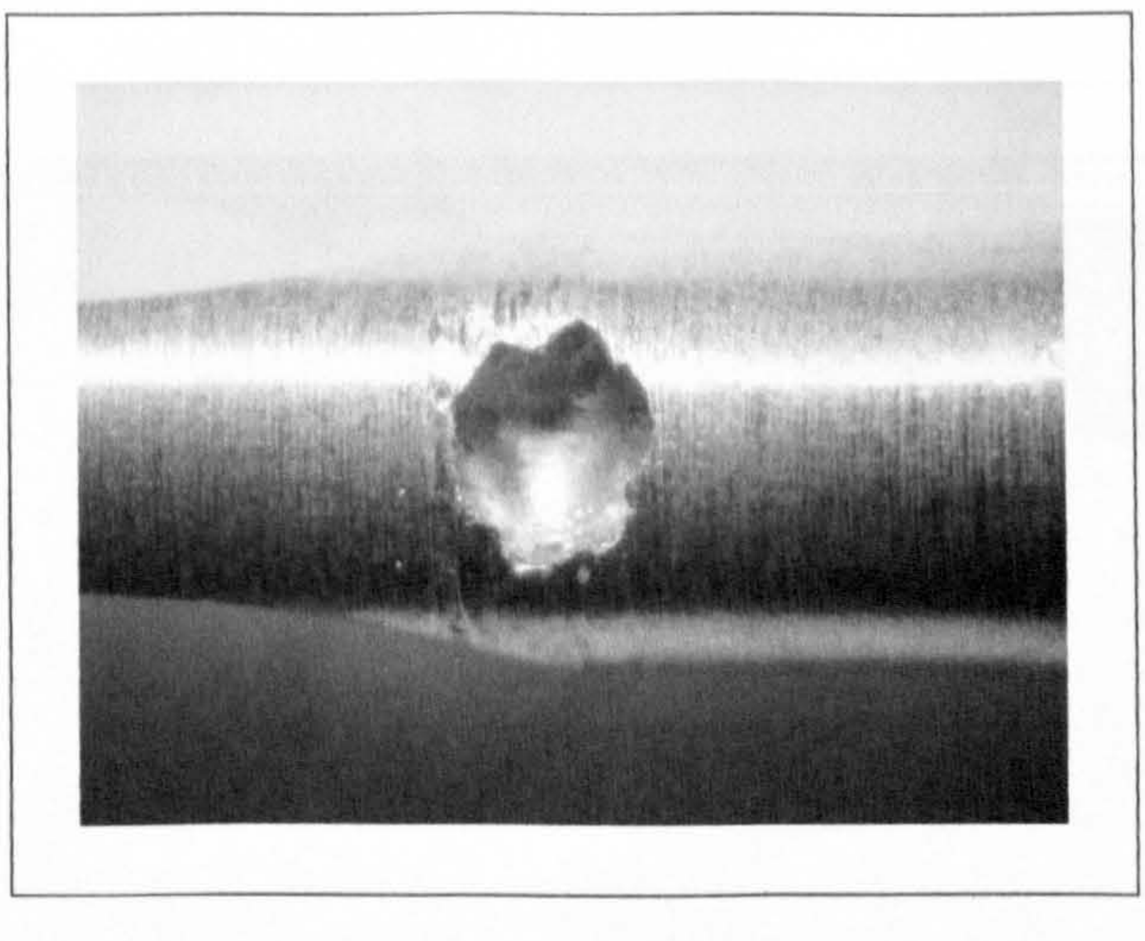

Figure 3.49: Pore within the weld metal of a small crack growth specimen.

3.6.2.2.2 Intermetallic Phases

As fatigue cracks in the MIG LI welds initiated at the weld toe, the effect of any intermetallics on crack initiation would result from those within this region. Therefore the size and distribution of the $FeAl_3$/(Fe,Mn)Al_6 and Mg_2Si intermetallic phases was measured from the 1st pass weld toe, in a straight line, to the 2nd pass weld toe for both sides of each weld pass. The intermetallic phases around the weld toe were as shown in Figure 3.50 and around the intersection of the two weld passes and parent plate in Figure 3.51; the results obtained were as listed in Table 3.16. Values for the maximum size, 269 μm^2 and 98 μm^2 for the $FeAl_3$/(Fe,Mn)Al_6 and Mg_2Si respectively, and mean sizes, 16.4 μm^2 and 15.4 μm^2, were obtained, with the area density being 0.79% for the $FeAl_3$/(Fe,Mn)Al_6 and 0.21% for the Mg_2Si. The weld metal was noted to contain intermetallics, but these were much finer than those found in the parent plate, this may have been due to the AA 5183 filler material, the weld metal would consist of a high proportion of this alloy in contrast to the AA 5383, although it may have been due to the thermal cycle experienced.

Phase	Area examined (mm^2)	No. of particles	Phase size (μm^2)						Area density (%)
			Min	Max	Mean	Median	Std. Dev.	Total area	
$FeAl_3$/(Fe,Mn)Al_6	3.533	1695	1.1	269	16.4	88	20.7	27851	0.79
Mg_2Si		482	1.1	98	15.4	10.8	12.8	7431	0.21

Table 3.16: Size and distribution of Mg_2Si and $FeAl_3$/(Fe,Mn)Al_6 phases in an AA 5383-H321 MIG LI weld.

Figure 3.50: Intermetallic phases at the MIG LI weld toe (weld metal left, parent plate right).

Figure 3.51: Intermetallic phases at the join of the two MIG LI weld runs mid-plate (weld metal left, parent plate right).

3.6.2.3 Mechanical Properties

3.6.2.3.1 Microhardness

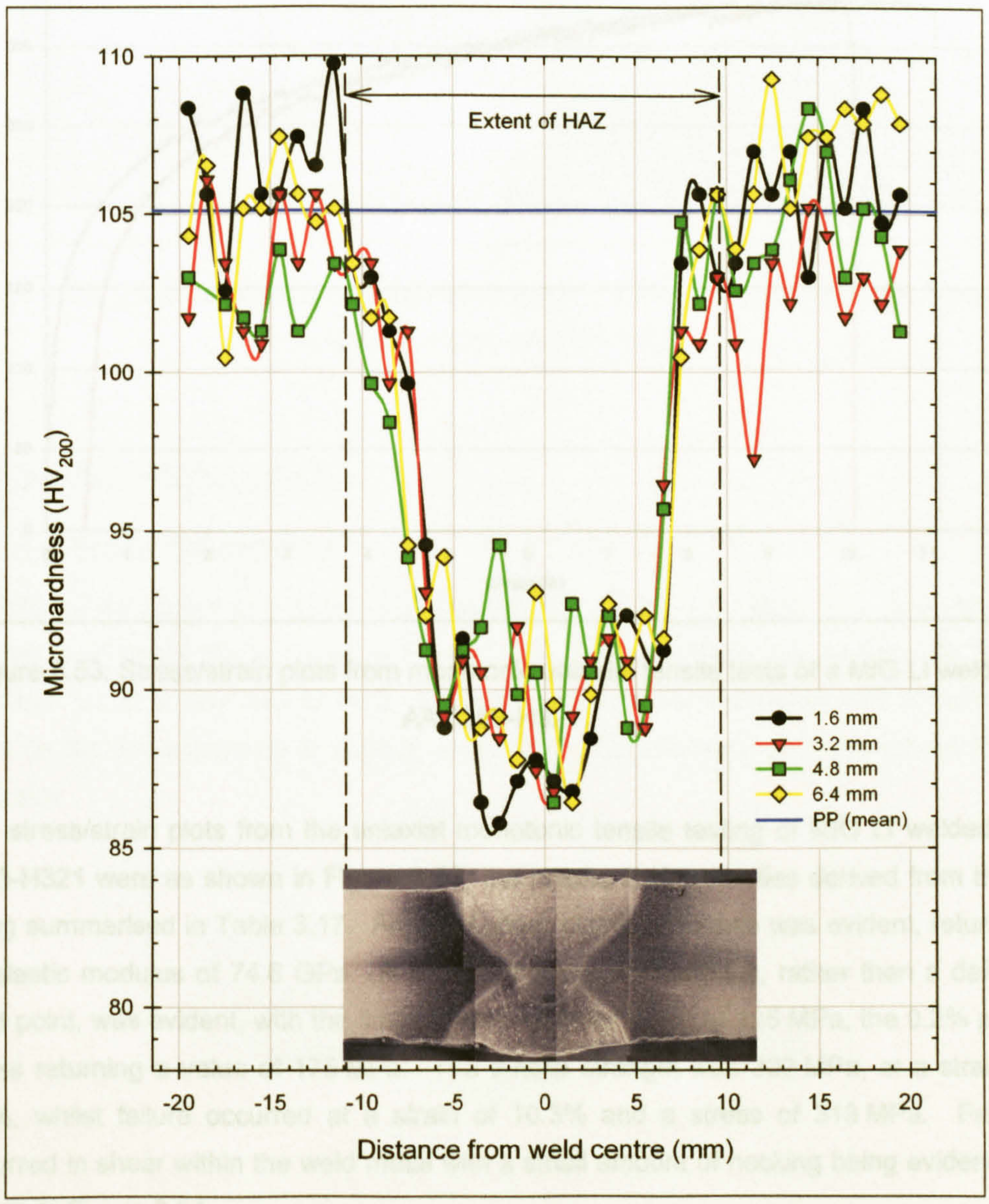

Figure 3.52: Microhardness results for MIG LI butt weld, with respect to the weld position (values in the legend refer to distance from the 2nd pass surface).

The microhardness results for the MIG LI weld, shown in Figure 3.52, exhibited a drop from the parent plate value of 105 HV_{200} to around 90 HV_{200} for the HAZ and weld filler metal. The hardness was reduced for a distance of -11 to +9.5 mm from the centre of the weld, with a rapid transformation between the parent plate and the annealed area. The reduction in hardness compared well with the changes in the grain structure, both indicating that the HAZ extended over a distance of approximately ±11 mm from the centre of the weld.

3.6.2.3.2 Tensile Properties

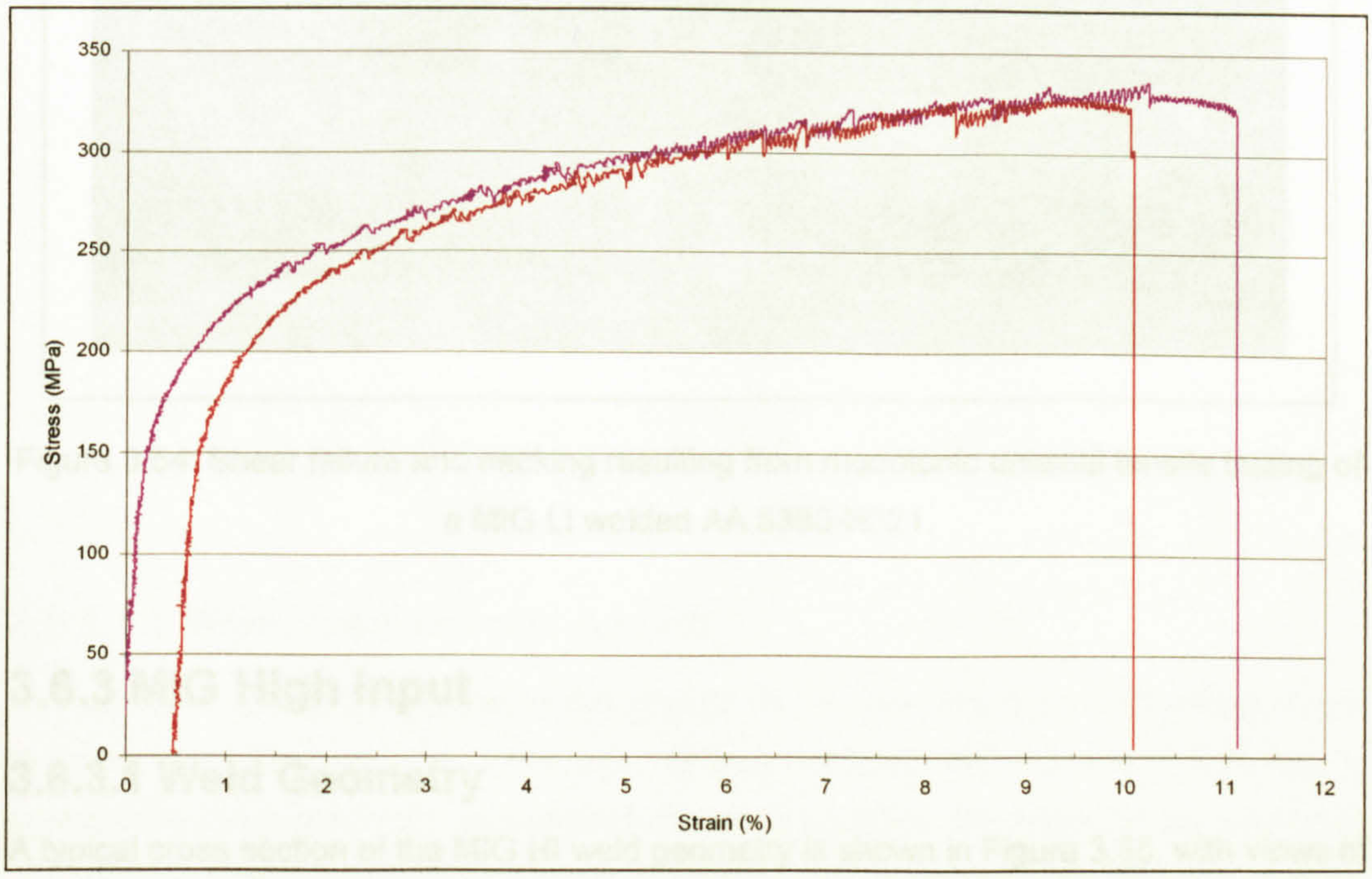

Figure 3.53: Stress/strain plots from monotonic uniaxial tensile tests of a MIG LI welded AA 5383-H321.

The stress/strain plots from the uniaxial monotonic tensile testing of MIG LI welded AA 5383-H321 were as shown in Figure 3.53, the mechanical properties derived from these being summarised in Table 3.17. An initial linear elastic response was evident, returning an elastic modulus of 74.6 GPa. A decreasing tangent modulus, rather than a definite yield point, was evident, with the limit of proportionality being at 125 MPa, the 0.2% proof stress returning a value of 175 MPa. The tensile strength was 332 MPa, at a strain of 9.6%, whilst failure occurred at a strain of 10.3% and a stress of 313 MPa. Failure occurred in shear within the weld metal with a small amount of necking being evident, as shown in Figure 3.54.

Limit of proportionality (MPa)	$\sigma_{0.1\%}$ (MPa)	$\sigma_{0.2\%}$ (MPa)	σ_{TS} (MPa)	ε_{TS} (%)	$\sigma_{failure}$ (MPa)	$\varepsilon_{failure}$ (%)	E (GPa)
125	160	175	332	9.6	313	10.3	74.6

Table 3.17: Mechanical properties of MIG LI welded AA 5383-H321 (mean of two tests).

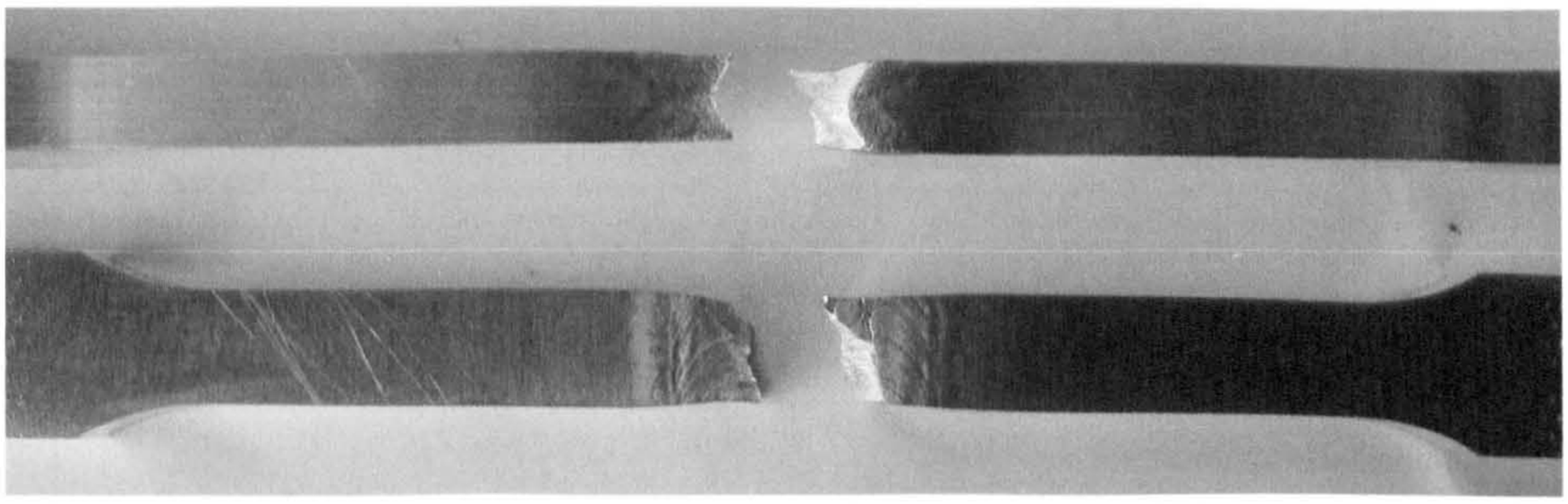

Figure 3.54: Shear failure and necking resulting from monotonic uniaxial tensile testing of a MIG LI welded AA 5383-H321.

3.6.3 MIG High Input

3.6.3.1 Weld Geometry

A typical cross section of the MIG HI weld geometry is shown in Figure 3.55, with views of the two weld beads being shown in Figure 3.56. The weld bead was significantly larger than that found on the MIG LI weld. Distortion between the two plates was evident, the plate on the left appearing at a slight angle from the horizontal when compared to the right side.

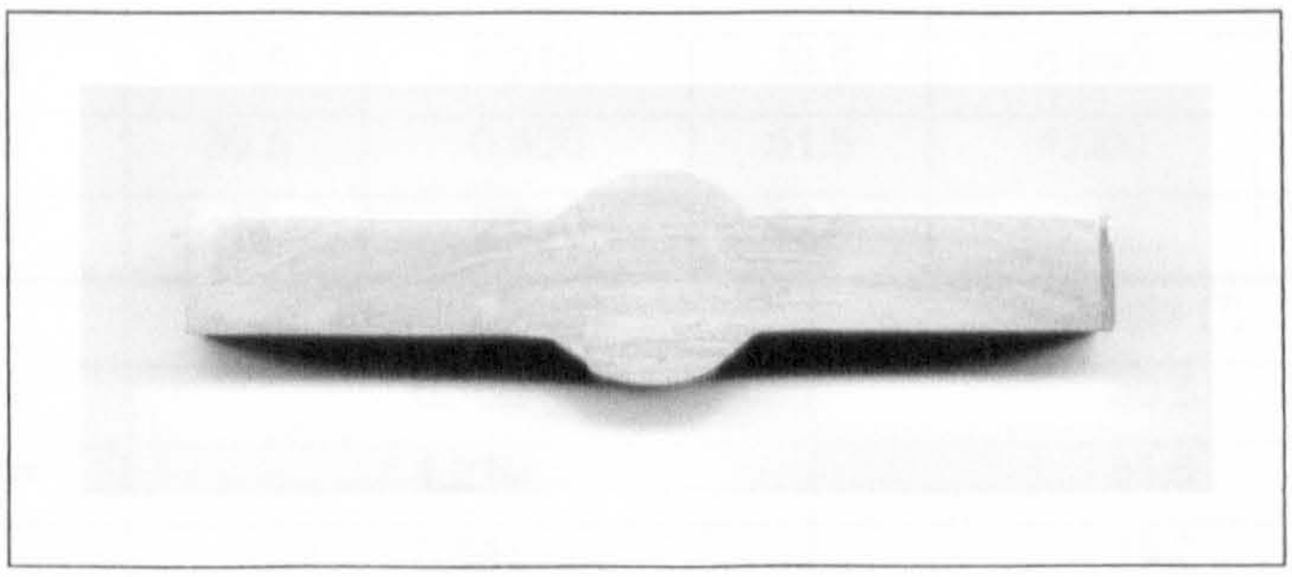

Figure 3.55: MIG HI weld bead geometry, 1st weld pass at the bottom (plate thickness 8 mm).

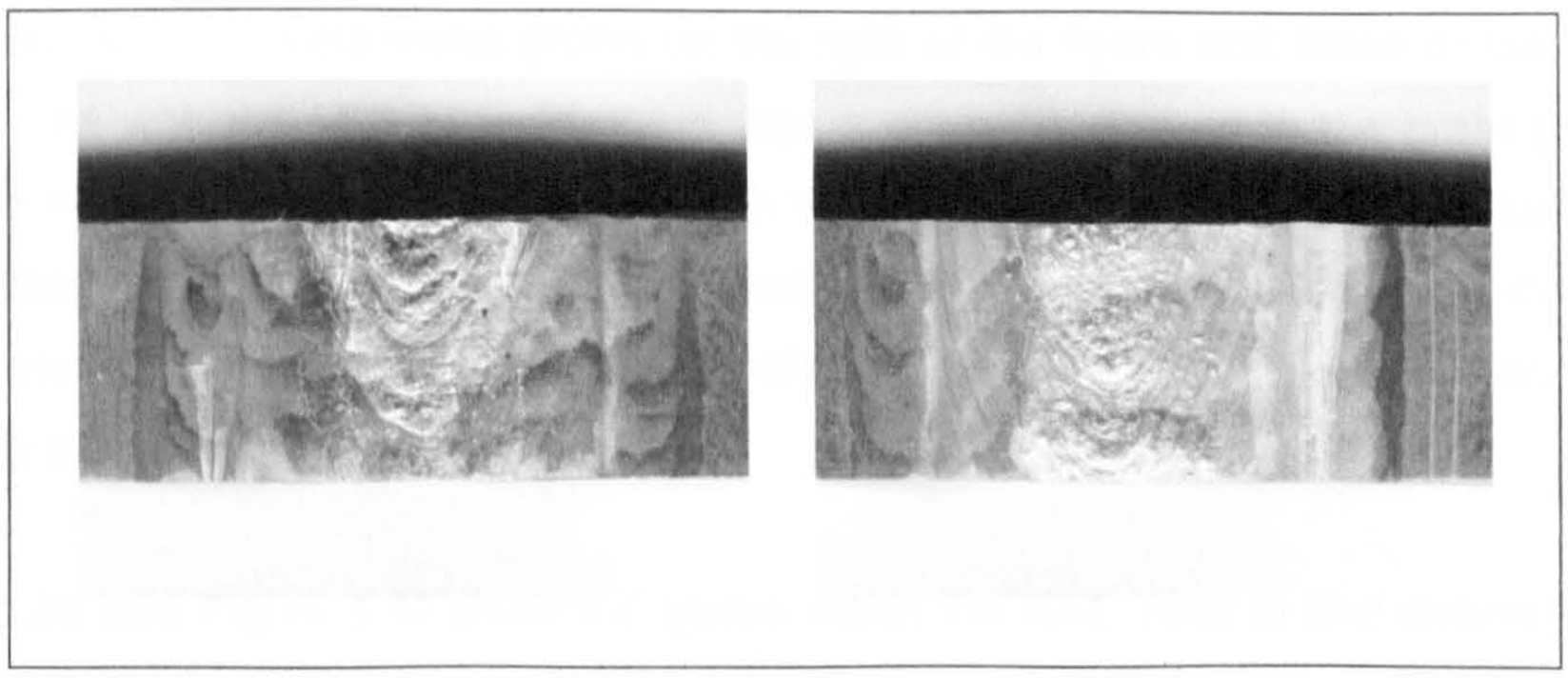

Figure 3.56: MIG HI weld bead, 1st run left, 2nd run right.

3.6.3.1.1 Weld Toe Radii and Angles

The weld toe radii and angles were determined for 14 positions, the results being shown in Table 3.18. The weld toe radius was relatively constant, with a range of 1.05 mm; in contrast the toe angle exhibited a greater degree of variation, the angle having a range of 21°. The comparable values for the median and mean values, for both the angle and the radius, indicate that the values were evenly distributed.

Radius (mm)	Angle (°)	Radius (mm)	Angle (°)	Radius (mm)	Angle (°)
0.240	34	0.330	33	0.160	44
0.900	40	0.980	42	0.600	35
0.550	30.5	1.210	39.5	0.590	43.5
0.250	36.5	0.800	51.5	1.000	41.5
0.560	42	0.810	42.5		

	Radius (mm)	Angle (°)
Minimum	0.160	30.5
Maximum	1.210	51.5
Mean	0.641	39.7
Median	0.595	40.75
Std. dev.	0.322	5.47

Table 3.18: MIG HI weld toe radii and angles.

3.6.3.2 Microstructure

From the macrograph, Figure 3.57, the weld metal, HAZ and variations in grain geometry are evident.

Figure 3.61 depicts the grains in the weld metal, these were typically equiaxed in geometry with an average grain size in the region of 225 μm in diameter (ASTM grain size 1.5G). Figure 3.60 shows the grain structure at the weld toe, the initiation point for

fatigue cracks, with weld metal grains on the right of the figure and those of the HAZ on the left. As with the MIG LI weld, there was a dramatic change in the grain geometry between the weld metal and HAZ, although the transformation was more distinct for the HI process. At, and near to, the plate surface the columnar grains were less developed than in the fusion zone within the plate, as shown by Figure 3.59, Figure 3.64 and Figure 3.65 due to the increased rate of cooling.

Figure 3.63 and Figure 3.62 show the grains within the HAZ, near to and distant from the weld respectively. The grains were more equiaxed nearer to the weld site, due to experiencing a temperature range where recrystallisation and grain growth were possible; further away from the weld, the grains resembled those of the parent metal. Typical grain sizes for the HAZ were 25 μm in width and 50 μm in length, comparable to those found in the MIG LI HAZ, although those near to the weld site had an average diameter of 40 μm (ASTM grain size 6.5G), approximately 10 μm greater than those found near to the MIG LI weld. The HAZ extended to a distance of approximately 8 mm from the weld toe, 15 mm from the weld centreline, although at these distances from the weld only slight changes in the pancake structure of the parent material was evident. At distances of 5 mm from the weld toe, 12 mm from the weld centreline, the changes were more evident, the grains having a near equiaxed geometry, with an average diameter of 40 μm (ASTM grain size 6.5G).

Figure 3.64 and Figure 3.65 depict columnar grains found at the boundary between the weld metal and the parent metal, the columnar grains extending from the second run into the first run exhibited a greater length than those between the weld metal and parent metal, as shown by Figure 3.59. The columnar grains formed where they adjoined the grains of the parent material, exhibited cellular and columnar dendritic structures, represented by (c) and (d) of Figure 3.1 (page 17). The columnar grains of the second weld pass that adjoined those of the first weld (position 1 on Figure 3.57) exhibited planar and cellular growth, (a) and (b) of Figure 3.1, with no dendritic structure being evident. The contrasting dendritic grains of the first pass and planar and cellular grains of the second pass are shown in Figure 3.58. Grains within the weld metal exhibited an equiaxed dendritic structure.

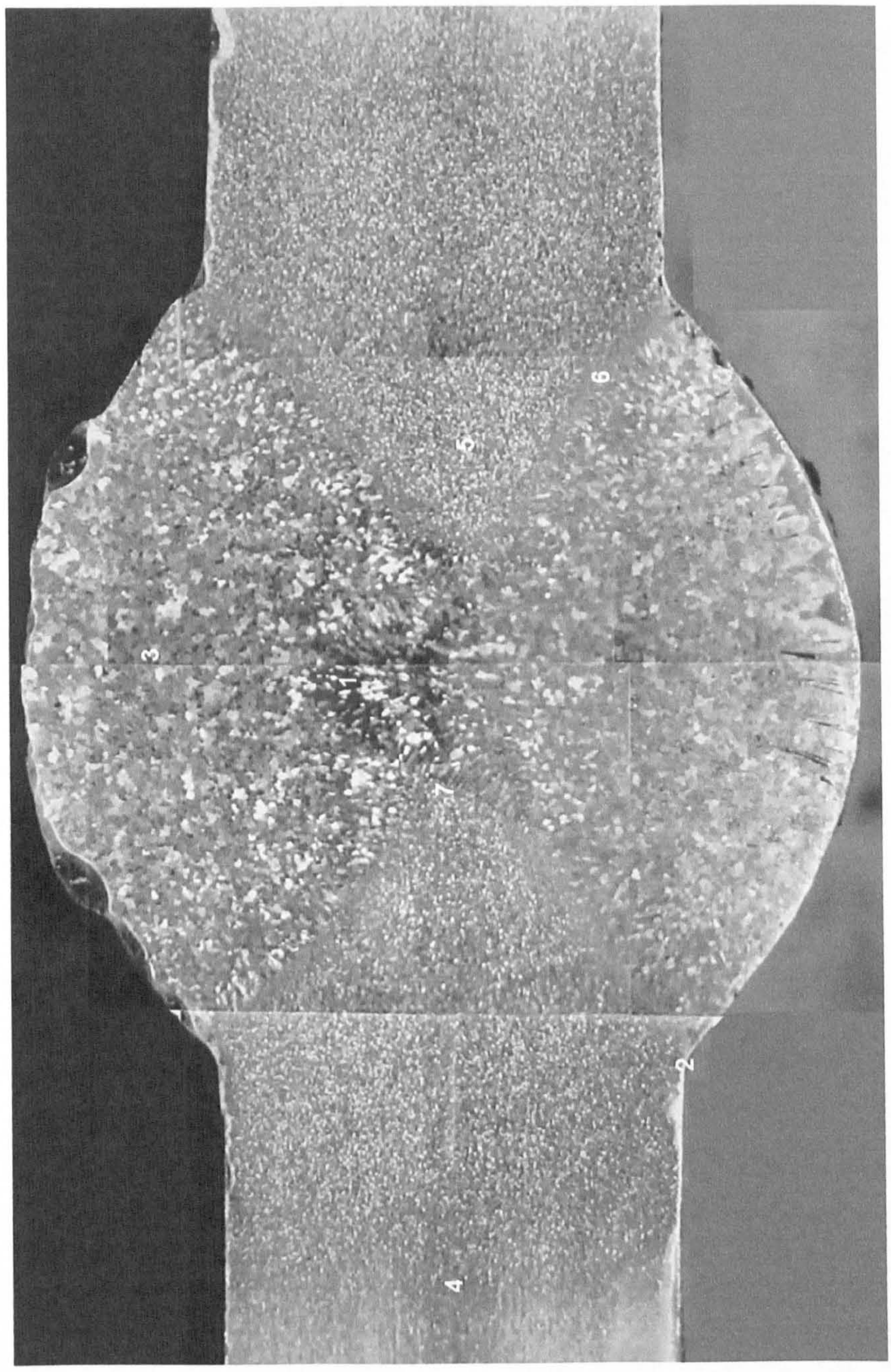

Figure 3.57: Macrograph of AA 5383-H321 MIG HI weld, plate thickness 8 mm, (numbers refer to the positions and orientations of the following micrographs).

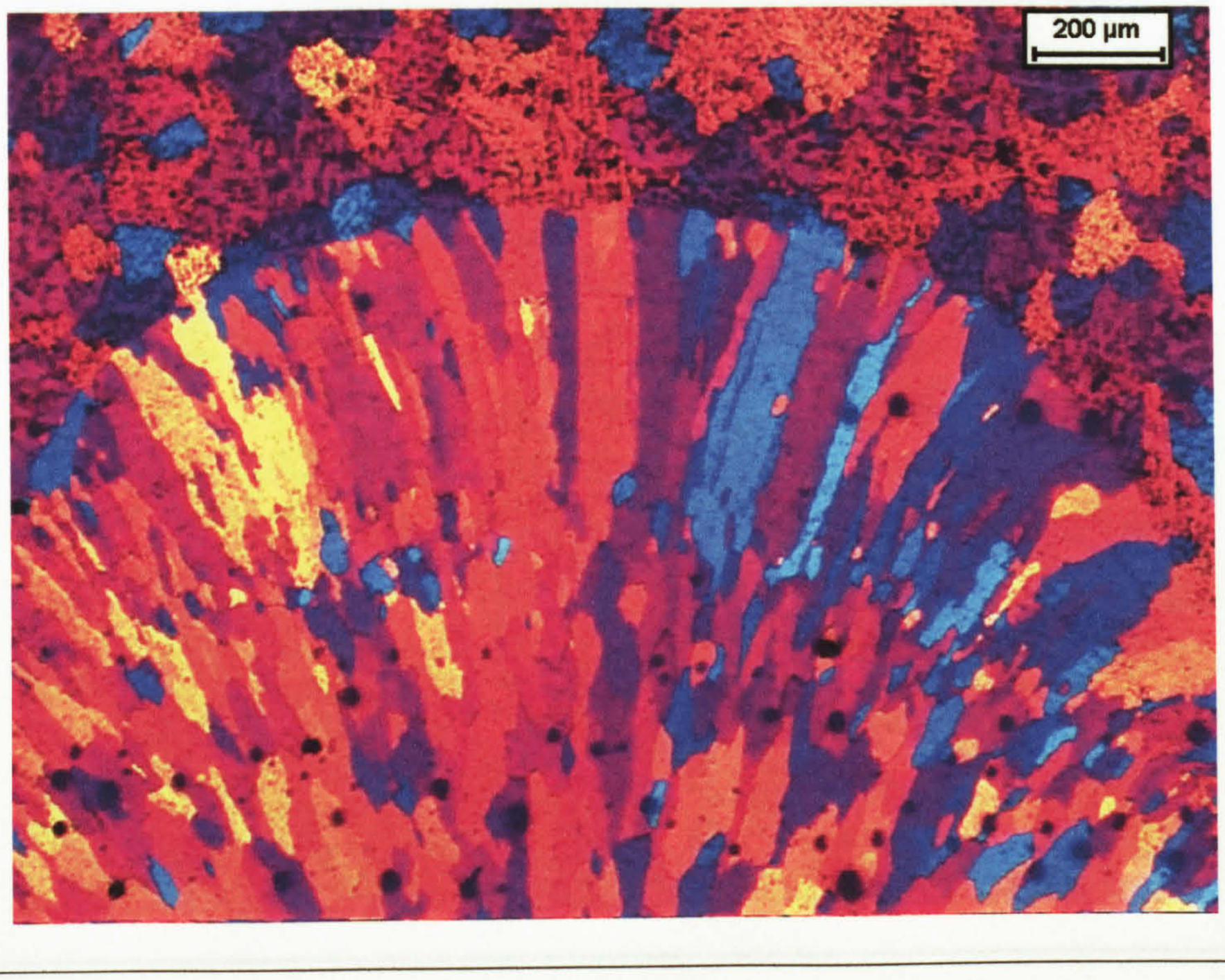

Figure 3.58: MIG HI planar grains of the second weld pass (bottom) adjoining cellular and columnar grains of the first weld pass (top), position 1 in Figure 3.57.

Figure 3.59: MIG HI grains at the weld metal boundaries, the second pass at the bottom, position 1 in Figure 3.57.

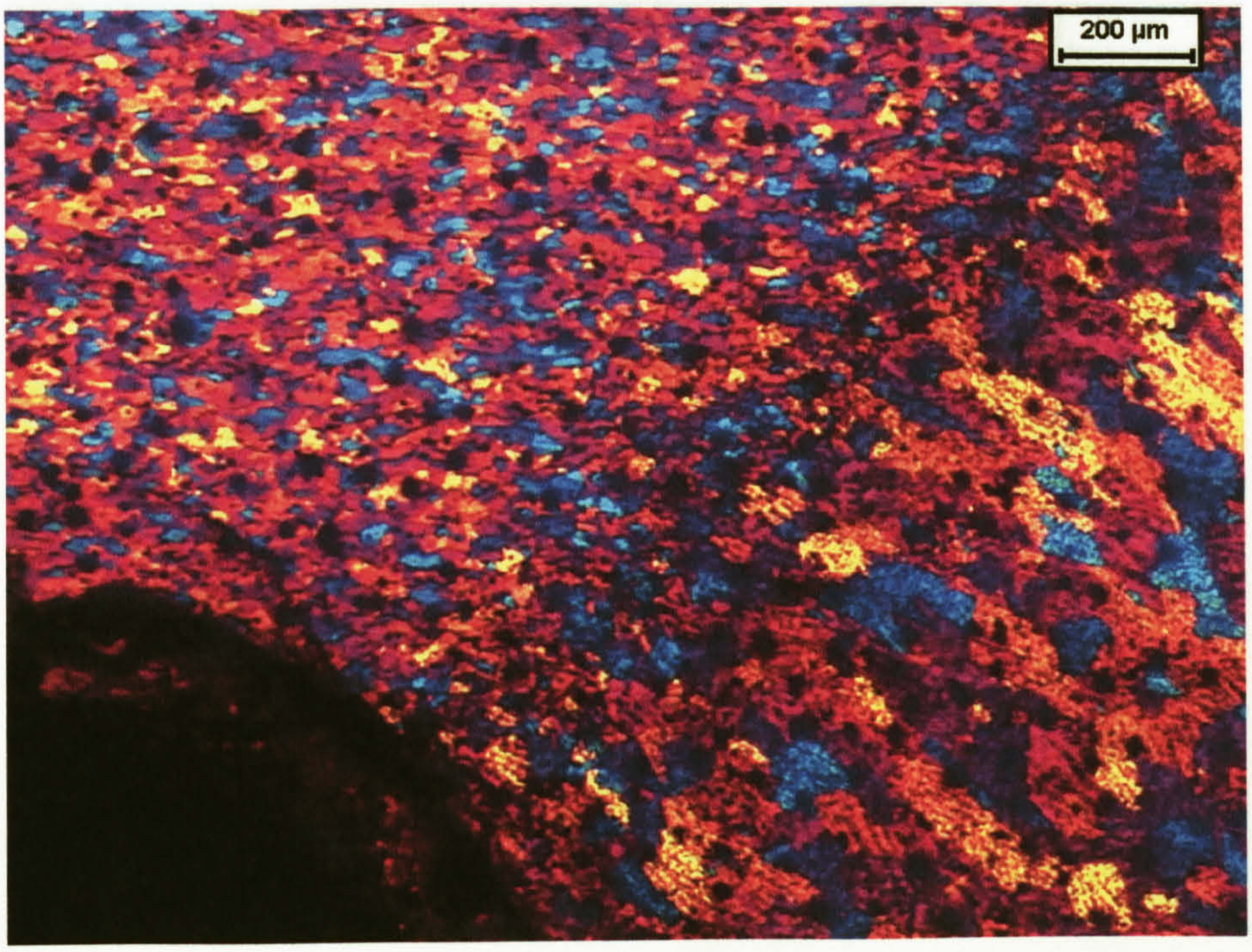

Figure 3.60: MIG HI grains at the HAZ (left) and weld toe (right) boundary, position 2 in Figure 3.57.

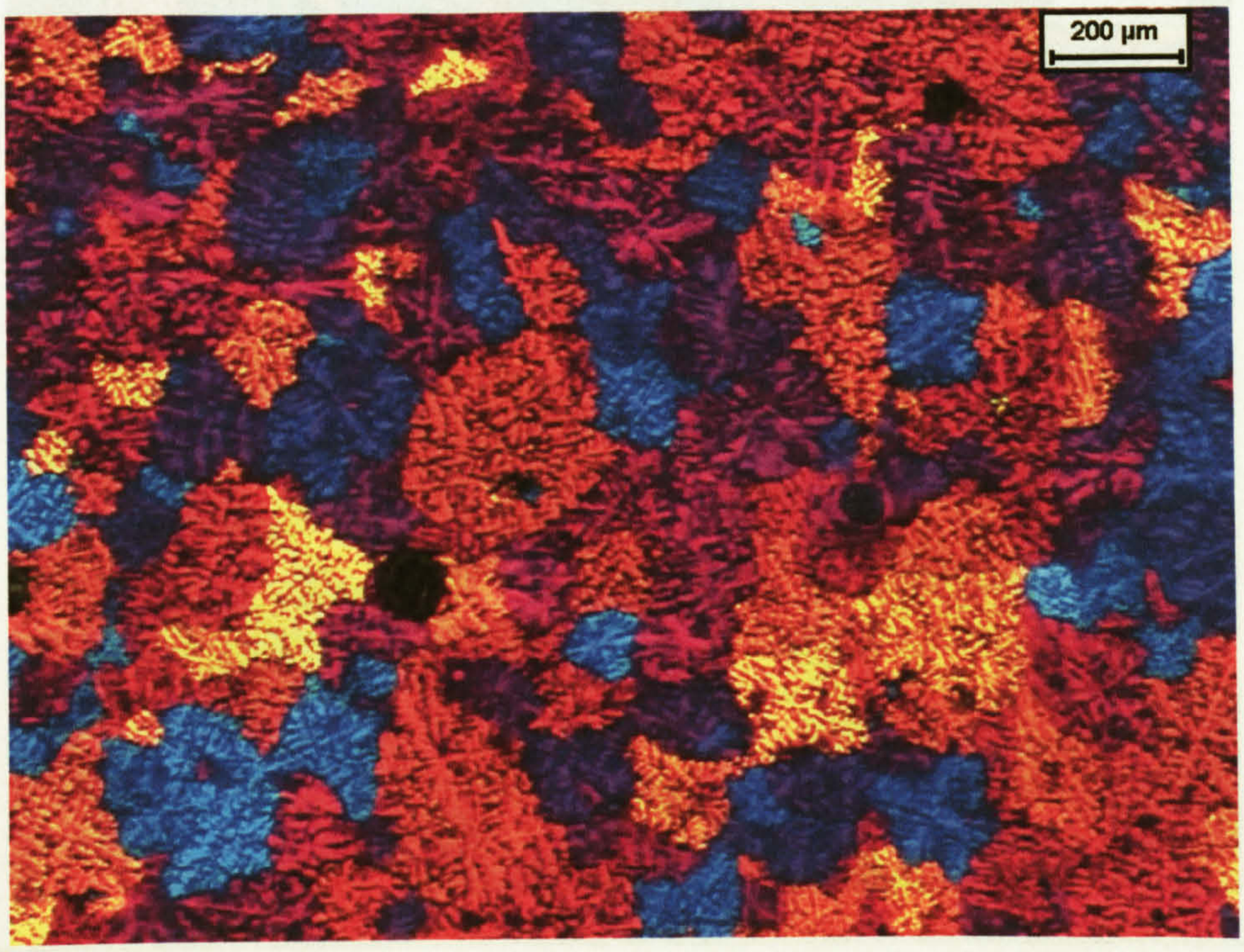

Figure 3.61: MIG HI grains in the weld metal, position 3 in Figure 3.57. Average grain size 225 µm, ASTM 1.5G.

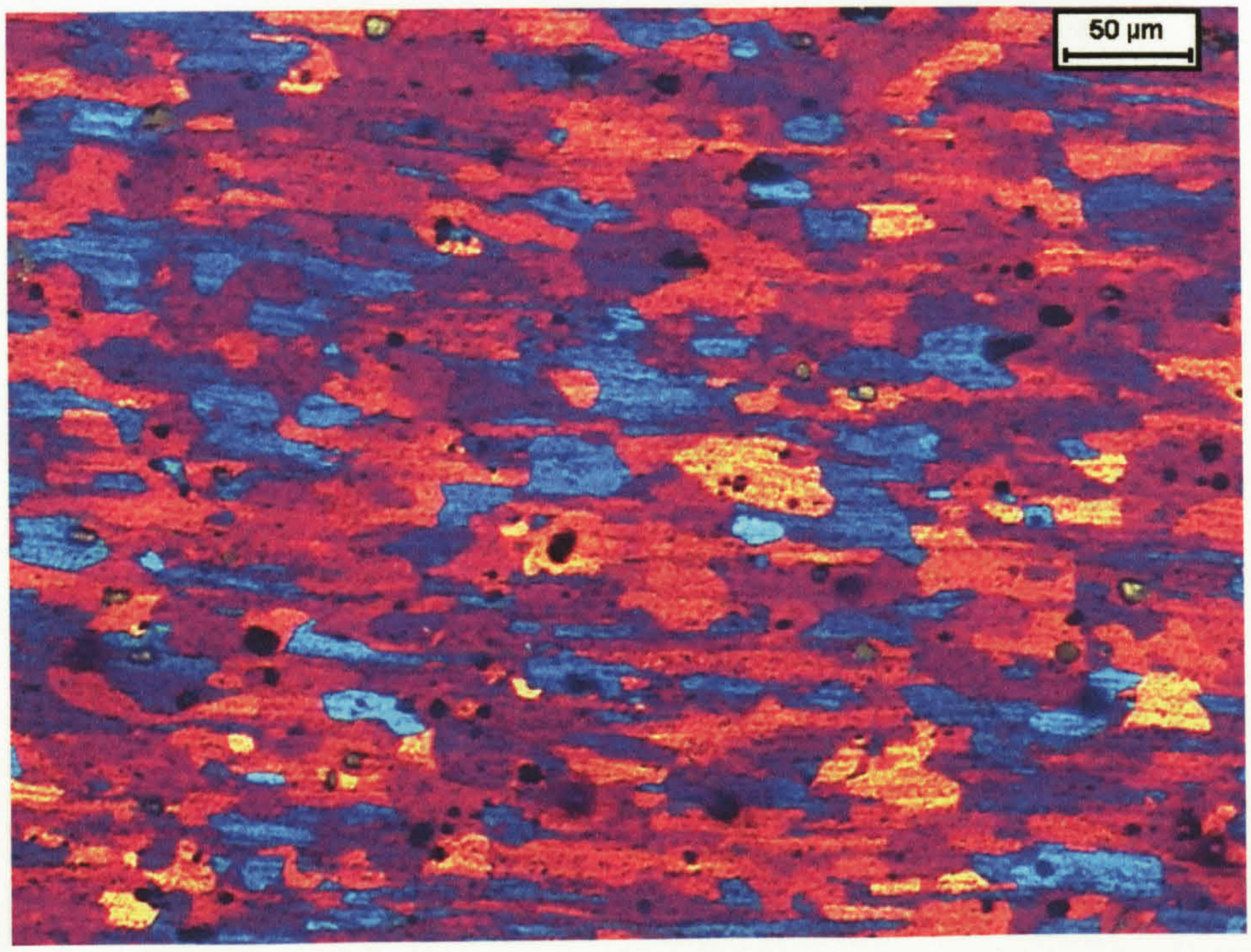

Figure 3.62: MIG HI HAZ grains, position 4 in Figure 3.57.

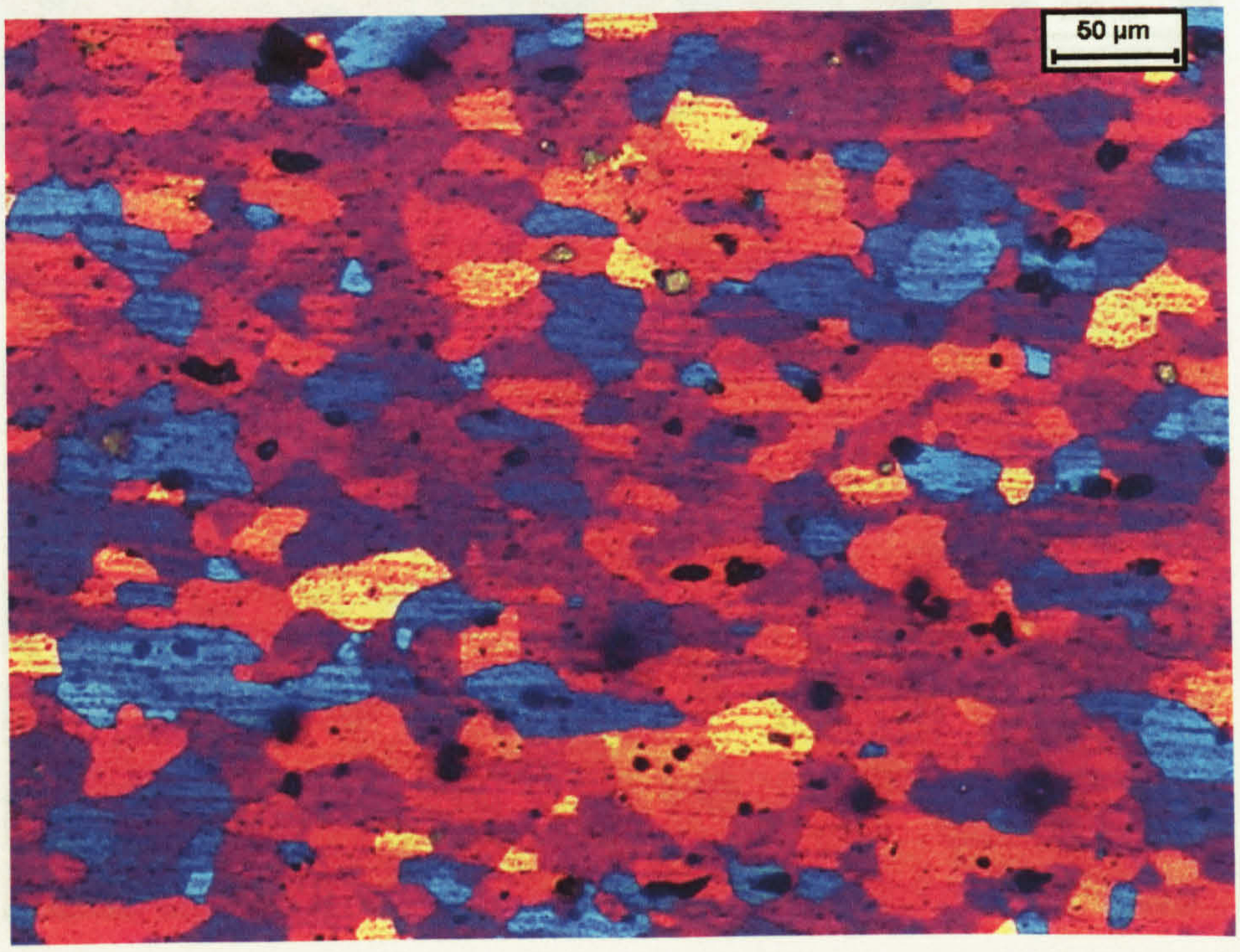

Figure 3.63: MIG HI HAZ grains, position 5 in Figure 3.57. Average grain size 40 µm, ASTM 6.5G.

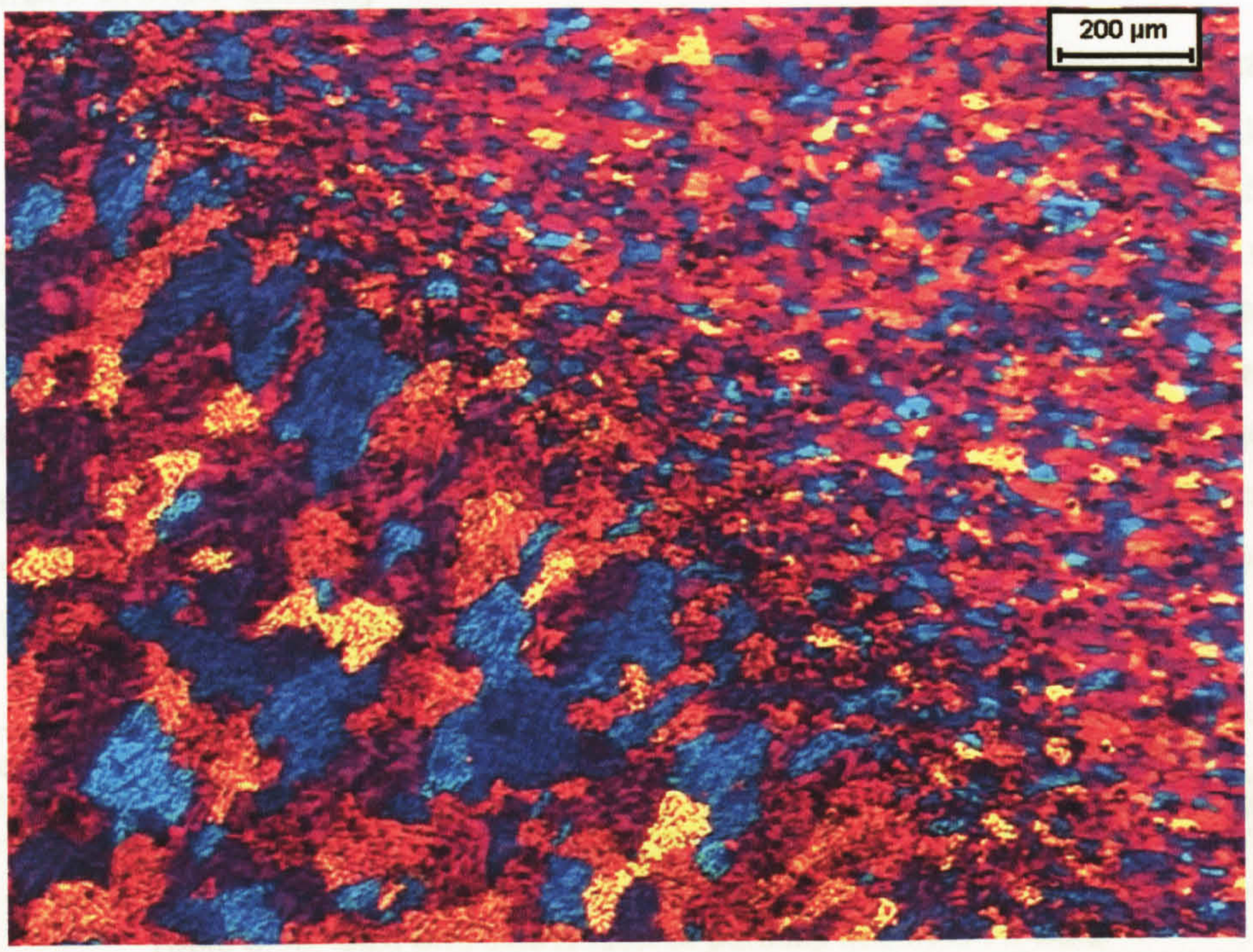

Figure 3.64: MIG HI grains at the HAZ/weld metal boundary, position 6 in Figure 3.57.

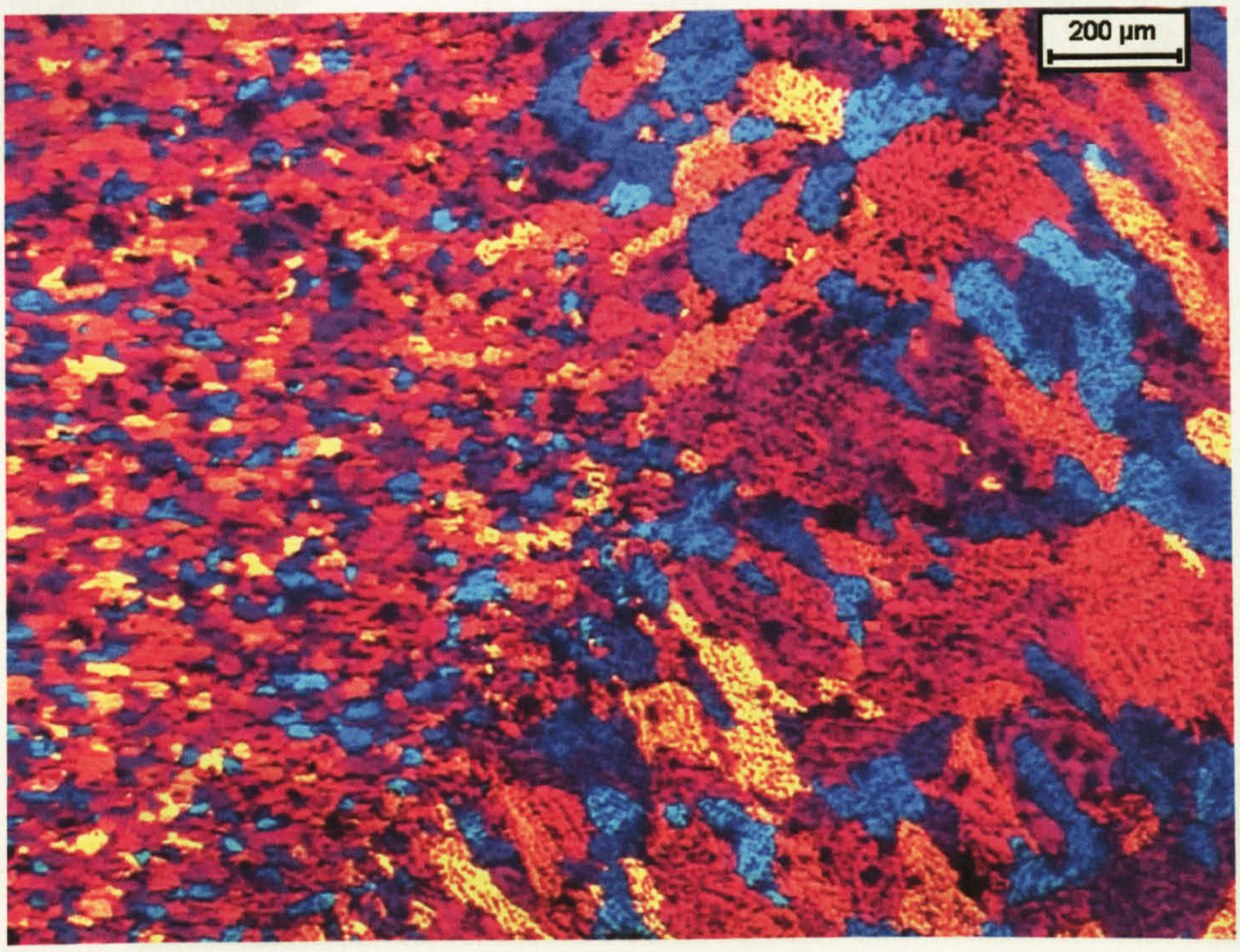

Figure 3.65: MIG HI grains at the boundary of both weld pools and the HAZ, position 7 in Figure 3.57.

3.6.3.2.1 Weld Porosity

A cross-section of the MIG HI weld, as shown in Figure 3.66, was planar ground and polished to reveal the porosity. From the image it can be seen that the majority of pores were in the 2nd pass weld metal, with the largest pores being unevenly distributed throughout this. The 1st pass weld, although having fewer pores than the 2nd pass, tended to have the larger pores located near to the weld bead surface. No pores of a significant size were evident at the weld toe, the site of fatigue crack initiation. The size and distribution of the pores are summarised in Table 3.19. The measured pores ranged in area from 2000 - 17200 μm^2, radius 25 - 74 µm, with a mean value of 5839 μm^2, radius 43 µm. The area density was calculated as the area of total area of pores within the weld metal and returned a value of 0.29%.

No. of Pores	Area (μm^2)				Area density (%)	Radius (µm)		
	Max.	Min.	Mean	Total		Max.	Min.	Mean
67	17200	2000	5839	391200	0.29	74	25	43

Table 3.19: Size and distribution of porosity in a MIG HI weld.

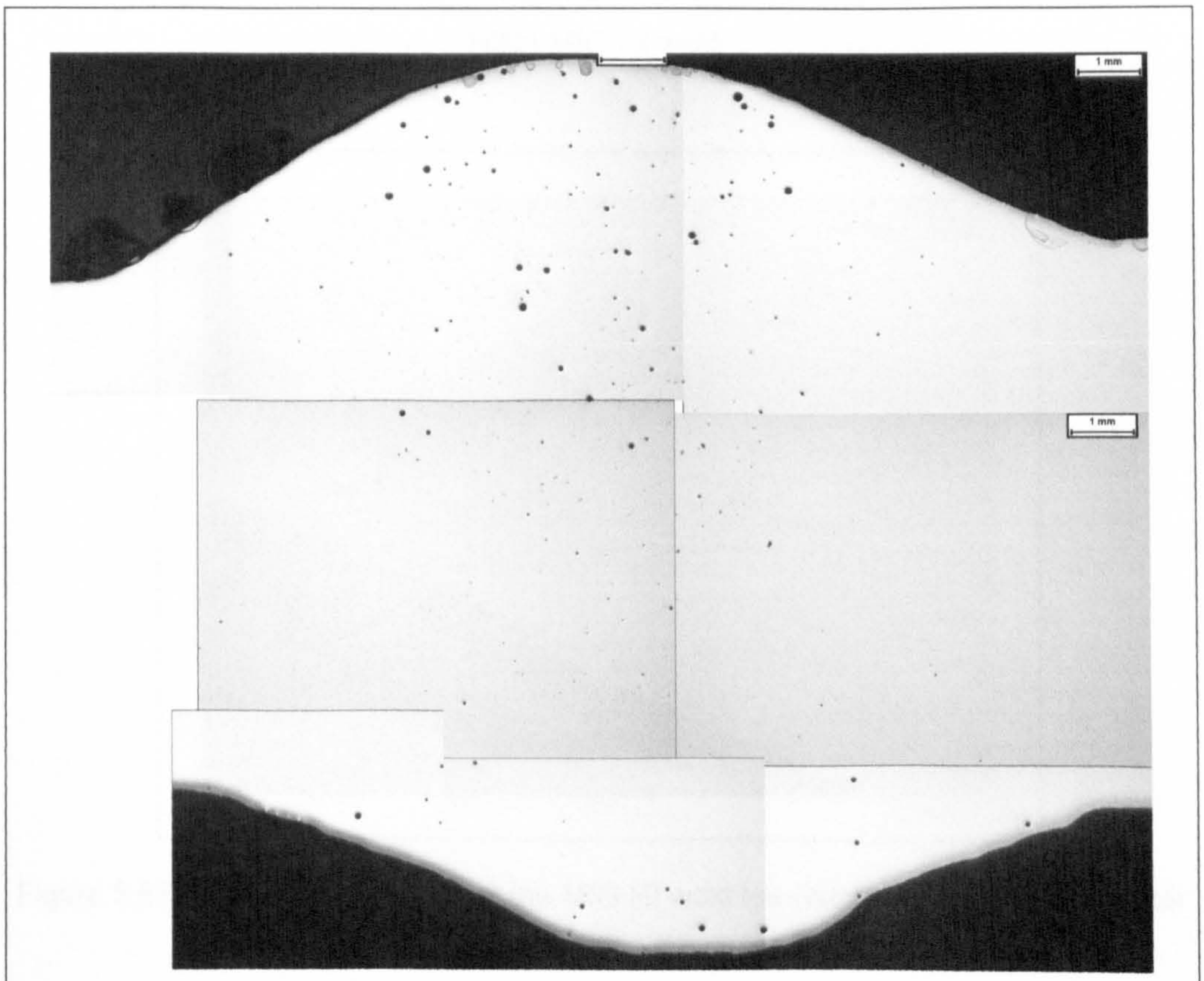

Figure 3.66: Weld porosity in MIG HI weld, second pass uppermost.

3.6.3.2.2 Intermetallic Phases

The size and distribution of the $FeAl_3$/(Fe,Mn)Al_6 and Mg_2Si intermetallic phases were measured from the 1st pass weld toe, in a straight line, to the 2nd pass weld toe, this being the region that fatigue cracks initiated, for both sides of the weld bead. The intermetallic phases are shown around the weld toe in Figure 3.67 and around the intersection of the two weld passes and the parent plate in Figure 3.68, with the results obtained listed in Table 3.20. Values for the maximum size, 265 μm^2 and 96 μm^2 for the $FeAl_3$/(Fe,Mn)Al_6 and Mg_2Si respectively, and mean sizes, 16.2 μm^2 and 13.7 μm^2, were obtained, with the area density being 0.68% for the $FeAl_3$/(Fe,Mn)Al_6 and 0.22% for the Mg_2Si. Intermetallic phases were evident in the weld metal, although these were less coarse than those found in the parent plate adjoining the weld.

Phase	Area examined (mm^2)	No. of particles	Phase size (μm^2)						Area density (%)
			Min	Max	Mean	Median	Std. Dev.	Total area	
$FeAl_3$/(Fe,Mn)Al_6	3.533	1487	1.1	265	16.2	8.6	20.6	24138	0.68
Mg_2Si		556	1.4	96	13.7	10.6	10.4	7621	0.22

Table 3.20: Size and distribution of Mg_2Si and $FeAl_3$/(Fe,Mn)Al_6 phases in an AA 5383-H321 MIG HI weld.

Figure 3.67: Intermetallic phases at the MIG HI weld toe (parent plate left, weld metal right).

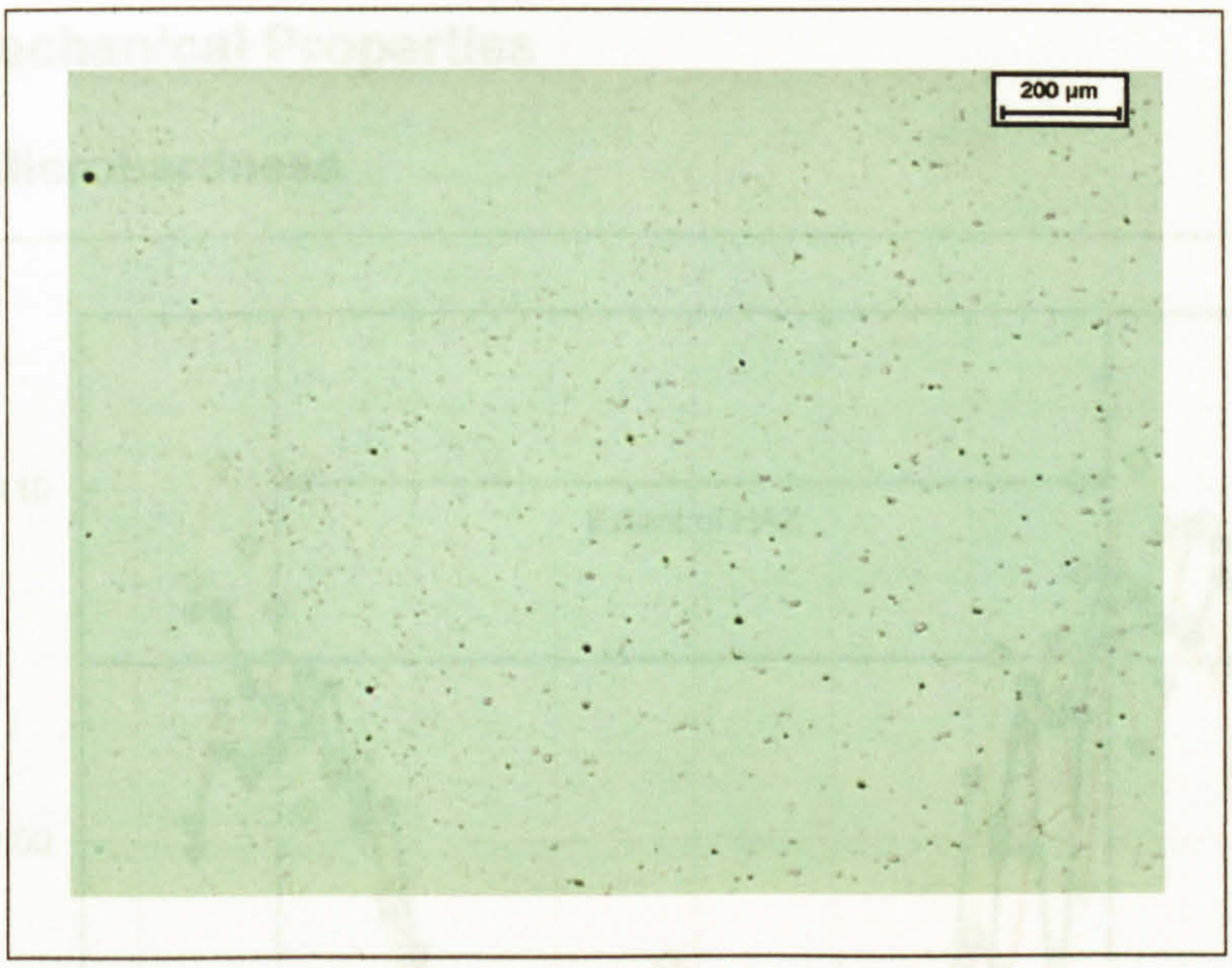

Figure 3.68: Intermetallic phases at the join of the two MIG HI weld runs mid-plate (weld metal left, parent plate right).

3.6.3.3 Mechanical Properties

3.6.3.3.1 Microhardness

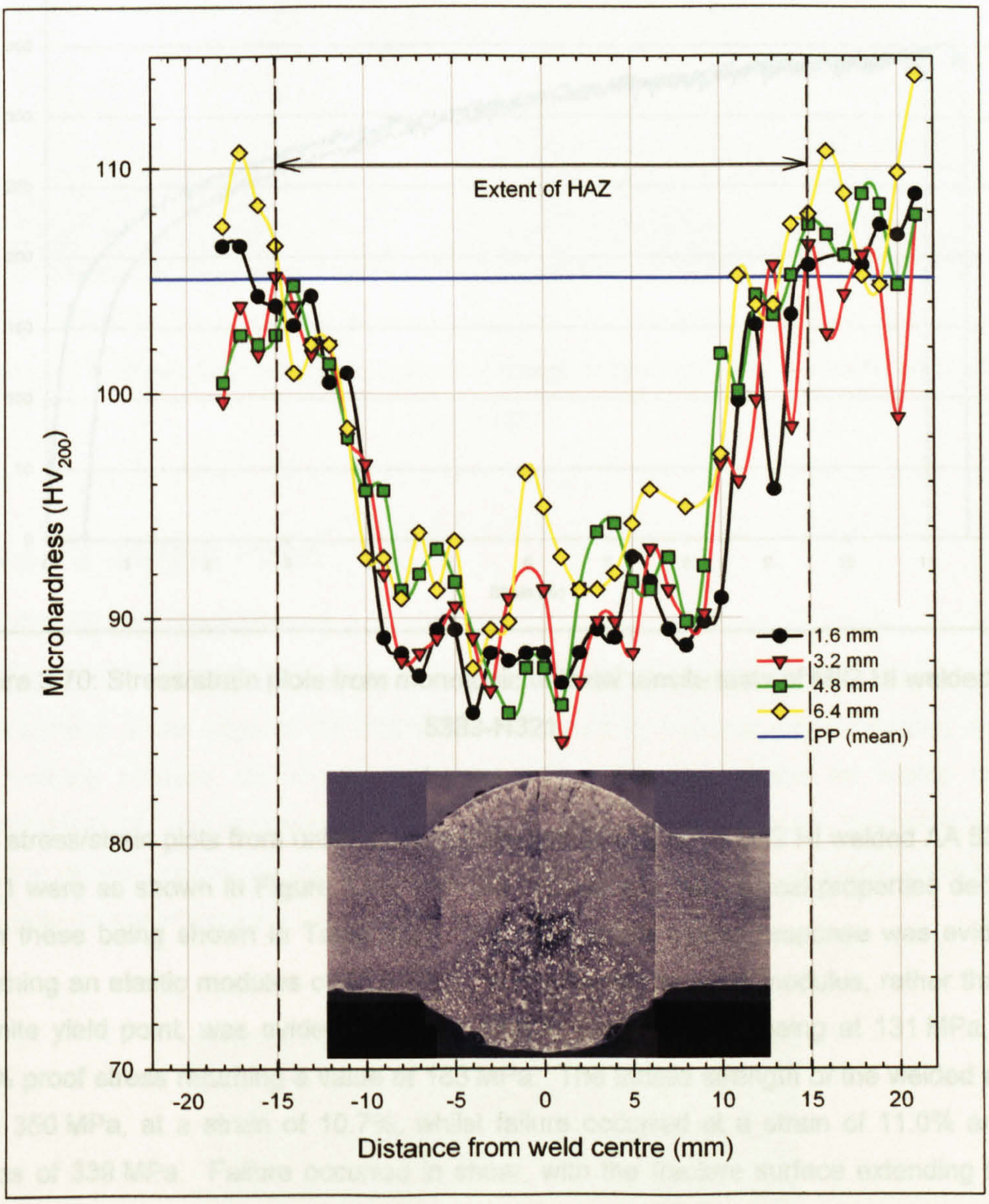

Figure 3.69: Microhardness results for MIG HI butt weld, with respect to the weld position (values in the legend refer to distance from the 2nd pass surface).

Microhardness values for the MIG HI weld, as shown in Figure 3.69, returned a value of 90 HV_{200} for the HAZ and weld filler metal in comparison to the parent plate value of 105 HV_{200}. The transformation between the parent plate and HAZ occurred at distance of ±15 mm from the centre of the weld, this correlating well with the changes observed in the microstructure.

3.6.3.3.2 Tensile Properties

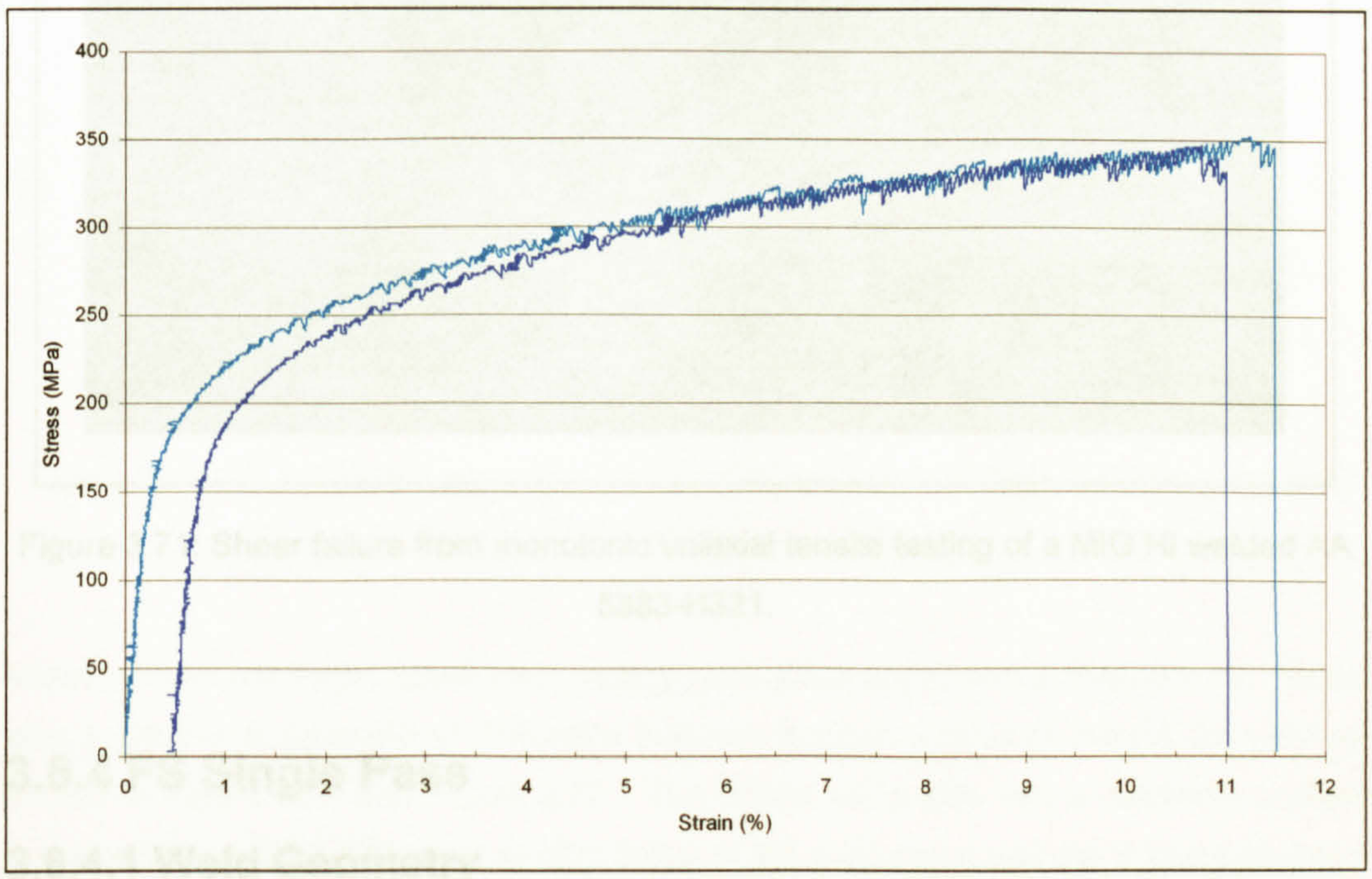

Figure 3.70: Stress/strain plots from monotonic uniaxial tensile tests of MIG HI welded AA 5383-H321.

The stress/strain plots from uniaxial monotonic tensile testing of MIG HI welded AA 5383-H321 were as shown in Figure 3.70, with the subsequent mechanical properties derived from these being shown in Table 3.21. An initial linear elastic response was evident, returning an elastic modulus of 66.9 GPa. A decreasing tangent modulus, rather than a definite yield point, was evident, with the limit of proportionality being at 131 MPa, the 0.2% proof stress returning a value of 183 MPa. The tensile strength of the welded alloy was 350 MPa, at a strain of 10.7%, whilst failure occurred at a strain of 11.0% and a stress of 339 MPa. Failure occurred in shear, with the fracture surface extending from the weld toe into the parent metal, with a small amount of necking being evident, as shown in Figure 3.71.

Limit of proportionality (MPa)	$\sigma_{0.1\%}$ (MPa)	$\sigma_{0.2\%}$ (MPa)	σ_{TS} (MPa)	ε_{TS} (%)	$\sigma_{failure}$ (MPa)	$\varepsilon_{failure}$ (%)	E (GPa)
131	167	183	350	10.7	339	11.0	66.9

Table 3.21: Mechanical properties of MIG HI welded AA 5383-H321 (mean of two tests).

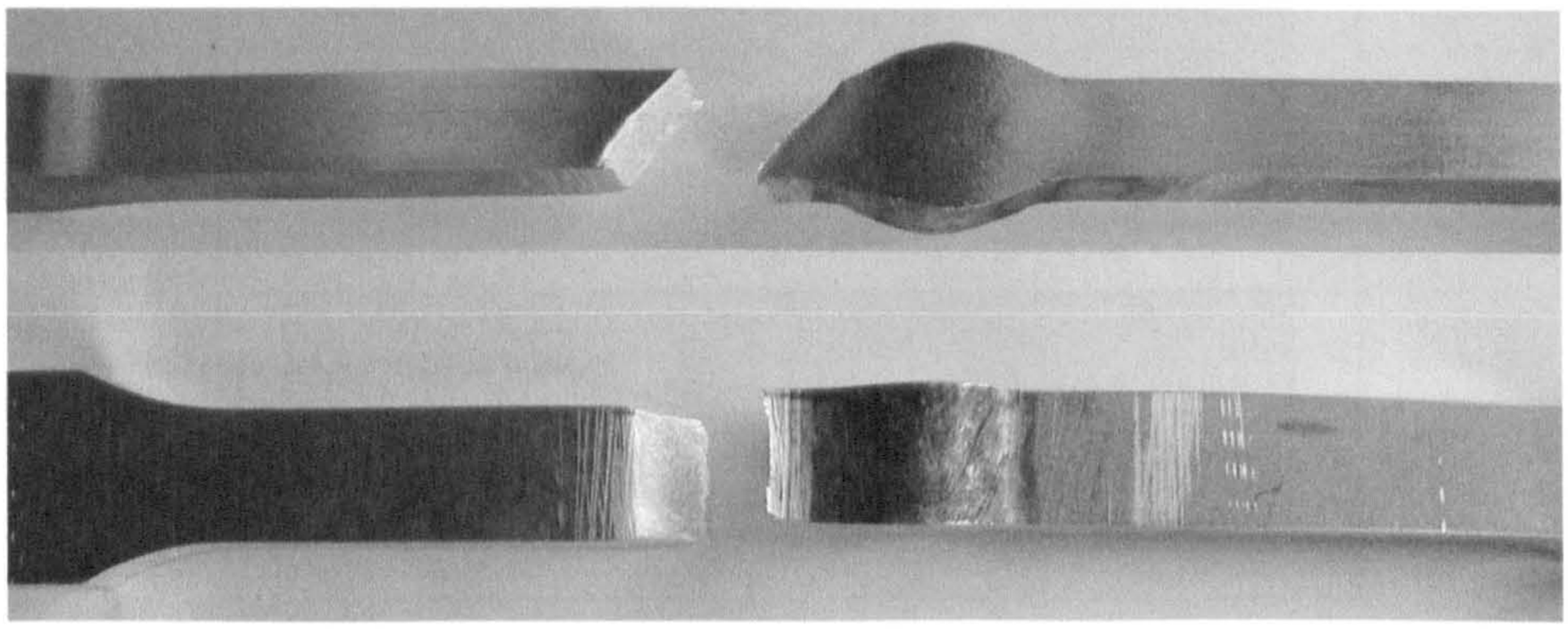

Figure 3.71: Shear failure from monotonic uniaxial tensile testing of a MIG HI welded AA 5383-H321.

3.6.4 FS Single Pass

3.6.4.1 Weld Geometry

The friction stir welding process results in the formation of a small lip that overhangs the plate surface at the edge of the friction band, caused by material being extruded during the welding process, as shown in Figure 3.72. For the friction stir welds under investigation this was removed by the fabricator, using an angle grinder, the result of this was the circular machining marks outside the ridges caused by the extruded material on the upper image of Figure 3.73.

Figure 3.72: Friction stir weld lip and pin exit hole.

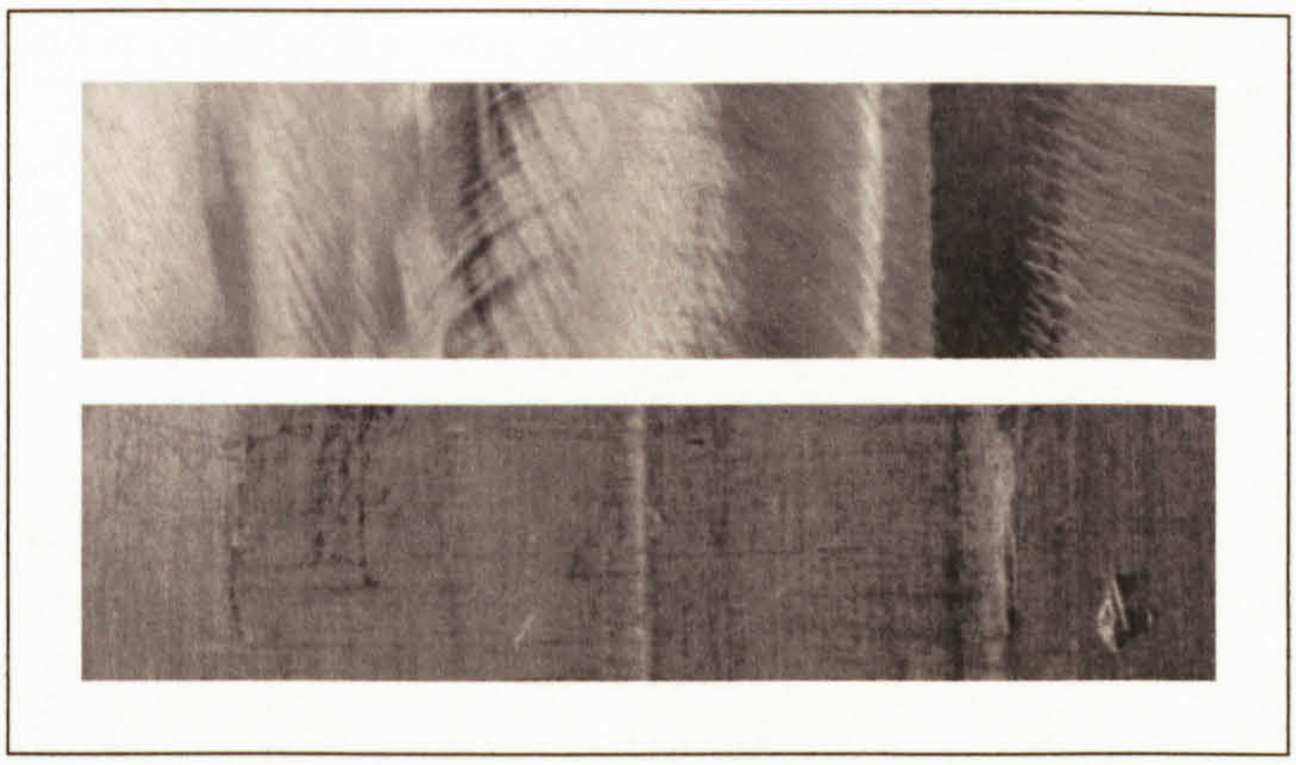

Figure 3.73: FS SP friction band (or tool shoulder) side of weld (top), backing plate side (bottom).

Views of both the friction band and backing plate sides are shown in Figure 3.73. There was a significant geometrical difference between the two profiles of the FS SP weld as shown in Figure 3.74 and Figure 3.77. The friction band side had a markedly profiled cross section, with the thinnest section being at the weld seam and the thickest sections at the edges of the friction band. For the SP weld under investigation the thinnest section was approximately 180 - 350 µm below the parent plate surface. The ridges, the remains of the lip, formed at the edge of the friction band were approximately 100 - 370 µm above the parent material, although the exact sizes of the ridges was dependent on the removal of the lip formed during the welding process. The surface of the friction band consisted of a series of circular grooves resulting from the rotational and transverse movement of the tool, shown in Figure 3.75 and in profile in Figure 3.76, and had a depth of approximately 10 - 35 µm.

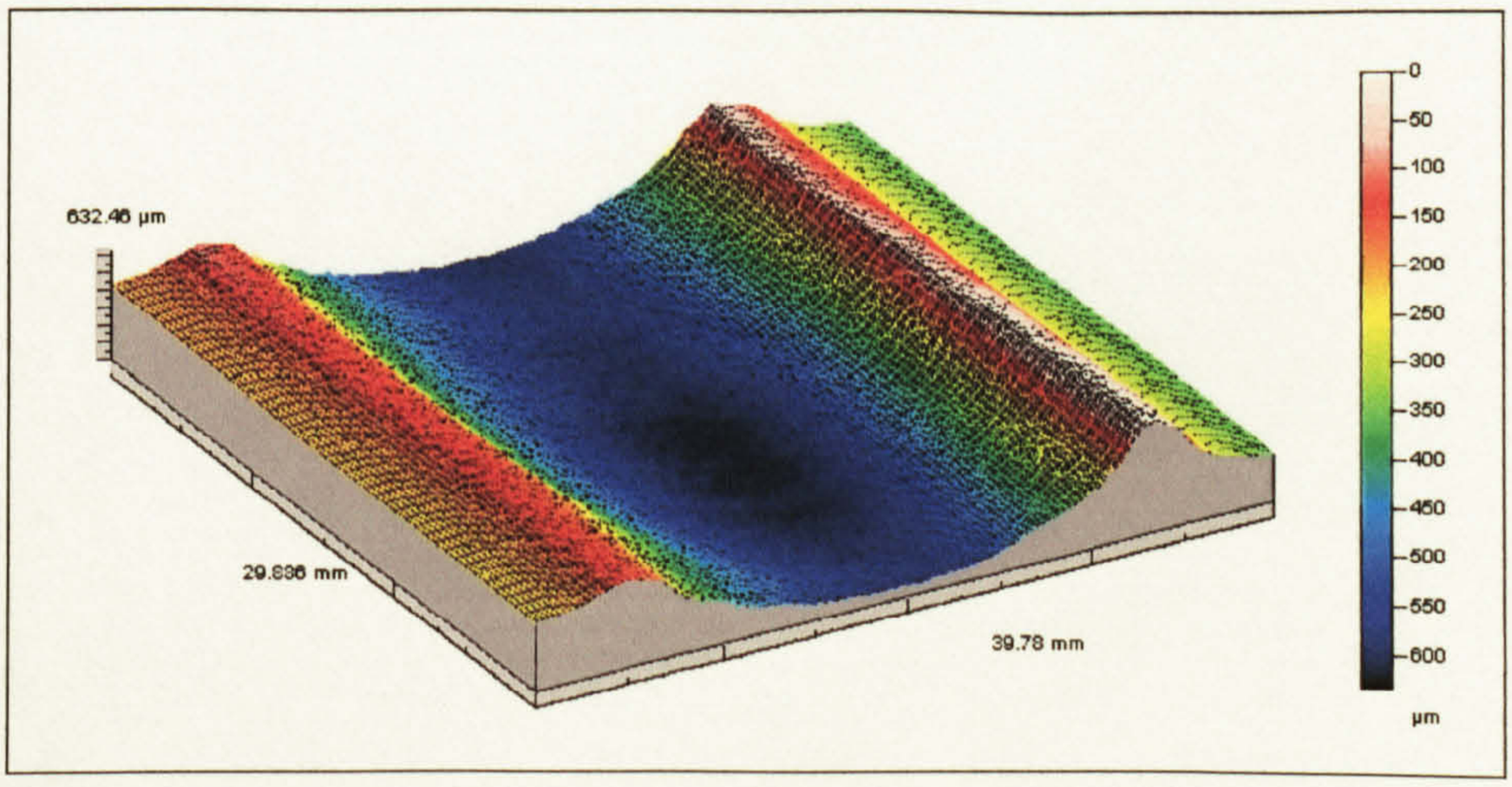

Figure 3.74: Three dimensional representation of the friction band side geometry of the FS SP weld.

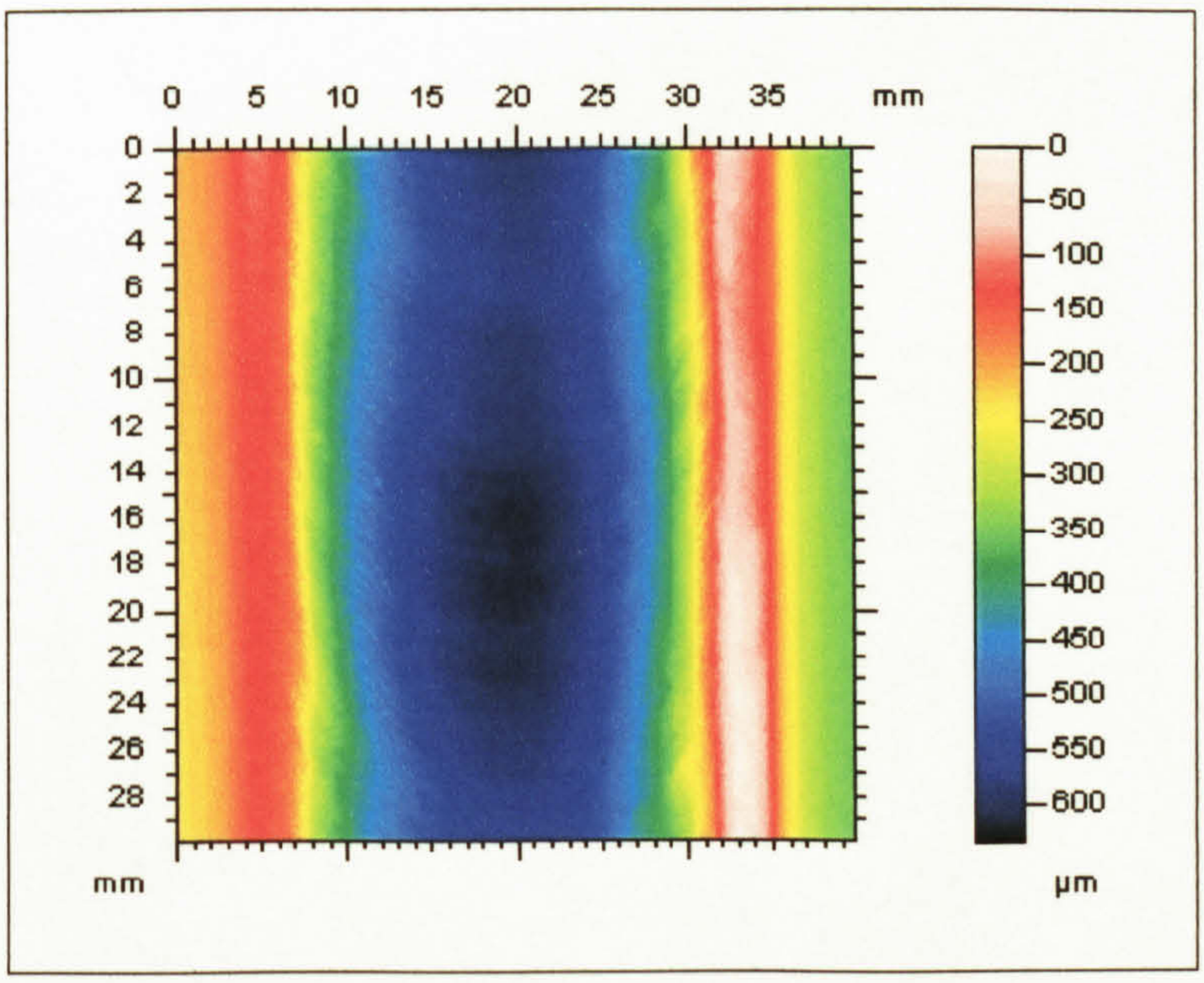

Figure 3.75: Friction band surface of a FS SP weld exhibiting the circular grooves.

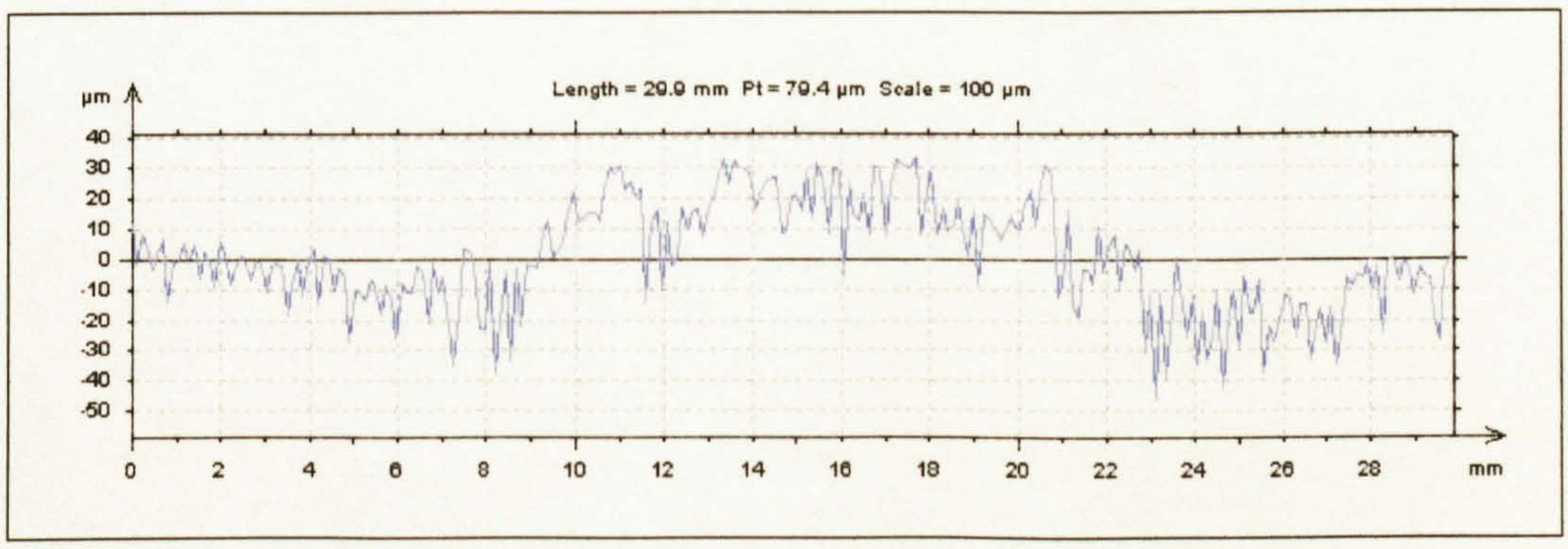

Figure 3.76: Two dimensional profile of the friction band surface of the FS SP weld, measured at the centre of the weld and in the direction of the weld.

The backing plate side of the weld exhibited a raised area that was approximately the width of the tool shoulder diameter. For the weld under investigation this area was raised approximately 120 - 180 µm above the parent material and had a flat profile.

The thinning of the plate on the friction band side was to some extent offset by the thickening on the backing plate side, the result of this being that the overall change in thickness compared to the parent plate was in the range of 0 - 230 µm.

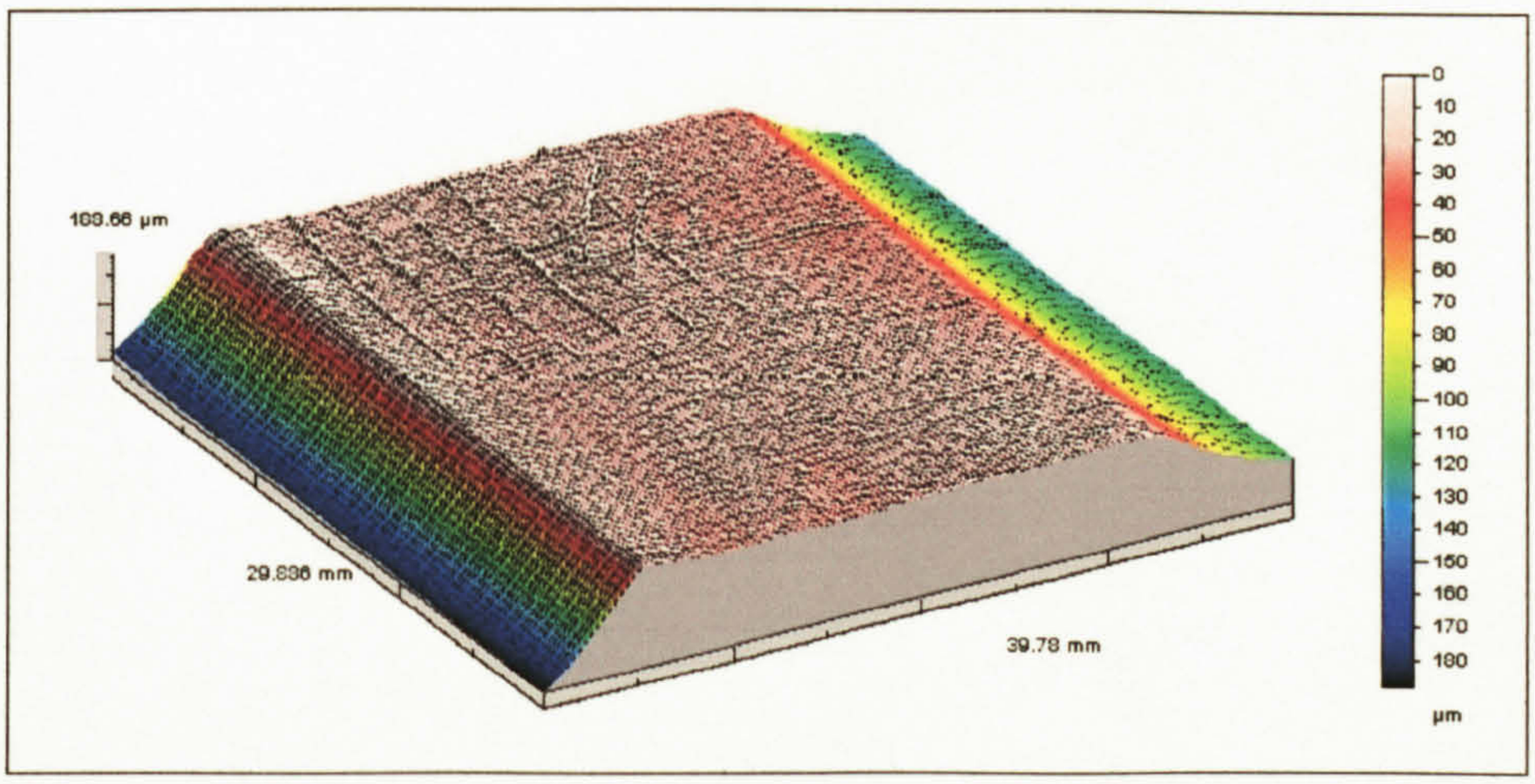

Figure 3.77: Three dimensional representation of the backing plate side geometry of the FS SP weld (the marks in the upper left quadrant are due to abrasions that occurred post weld).

3.6.4.2 Microstructure

From the macrograph, shown in Figure 3.78, both the TMAZ, which consisted of the weld nugget and plastically deformed grains, and part of the HAZ are evident. The concentric rings seen within the nugget are also visible, as is the appendage to the nugget, this extending from the nugget to the surface at the edge of the friction band.

Figure 3.82 shows the small grains within the weld nugget, these were equiaxed in geometry and had an average grain size of 10 µm (ASTM grain size 10.5G). The weld nugget had an elliptical shape with a major axis of approximately 14 mm. The boundary between the grains of the weld nugget and the plastically deformed grains of the TMAZ was as shown in Figure 3.79, although the transition was not always easily defined. Plastic deformation within the TMAZ, the grains rotated by up to ninety degrees[1,2], depicted by the swirl type effect, was as shown in Figure 3.80 and Figure 3.81.

Figure 3.84 depicts a region within the weld nugget where grain growth had occurred[3], this appeared as larger grains surrounded by the smaller grains that were typically seen within the weld nugget. This was only evident in the single pass weld, the larger grains being evident near the top of the weld nugget, the friction band side, the temperature being greater in this area than the backing plate side. The exact cause for the localised grain growth, and its absence in the DP welds, was unclear at the time of writing.

---

[1] Threadgill, P (1997)
[2] Leonard, AJ (2000)
[3] Threadgill, P (2000)

The HAZ was characterised by more equiaxed grains when compared to the parent plate, but no plastic deformation was evident, as shown in Figure 3.83. Grains within the HAZ were typically of width 50 µm, their length being 50 - 100 % greater. The HAZ extended approximately 5 mm beyond the TMAZ.

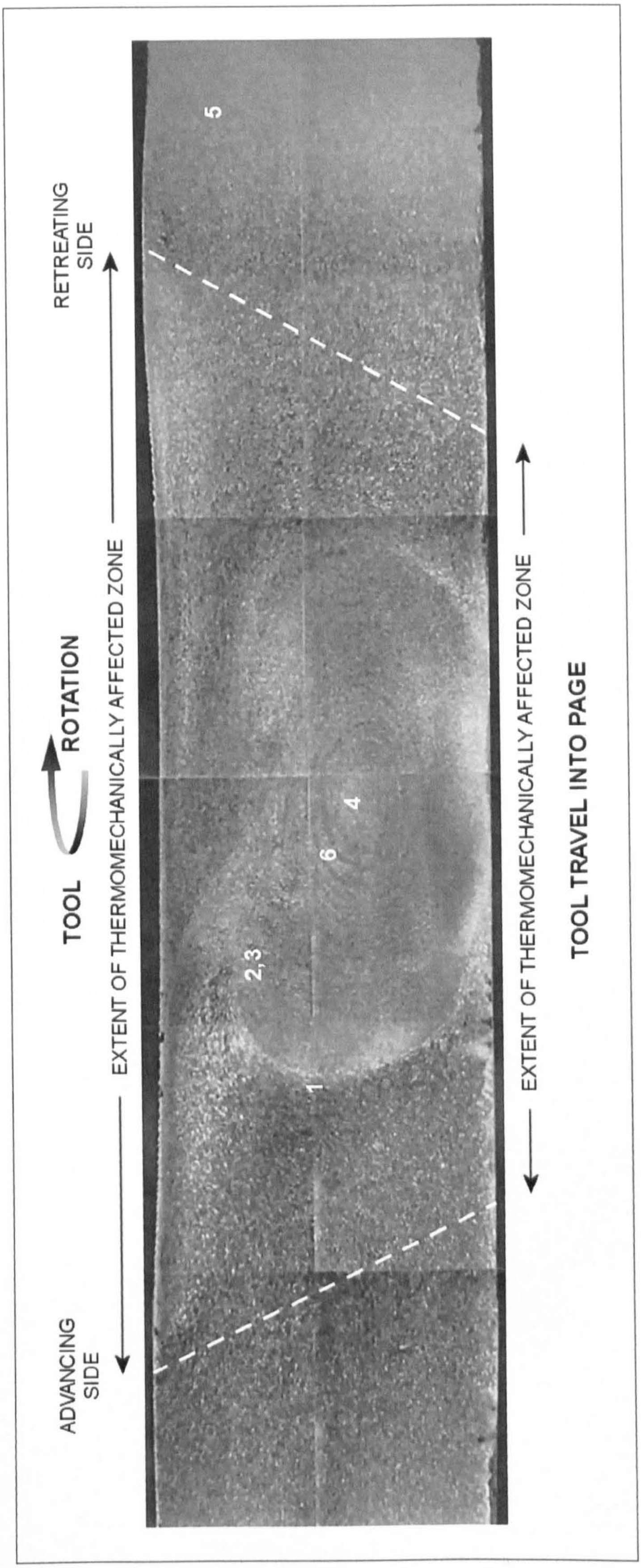

Figure 3.78: Macrograph of AA 5383-H321 FS SP weld, plate thickness 8 mm, friction band side uppermost, clockwise tool rotation when viewed from tool shoulder side, (numbers refer to the positions and orientations of the following micrographs).

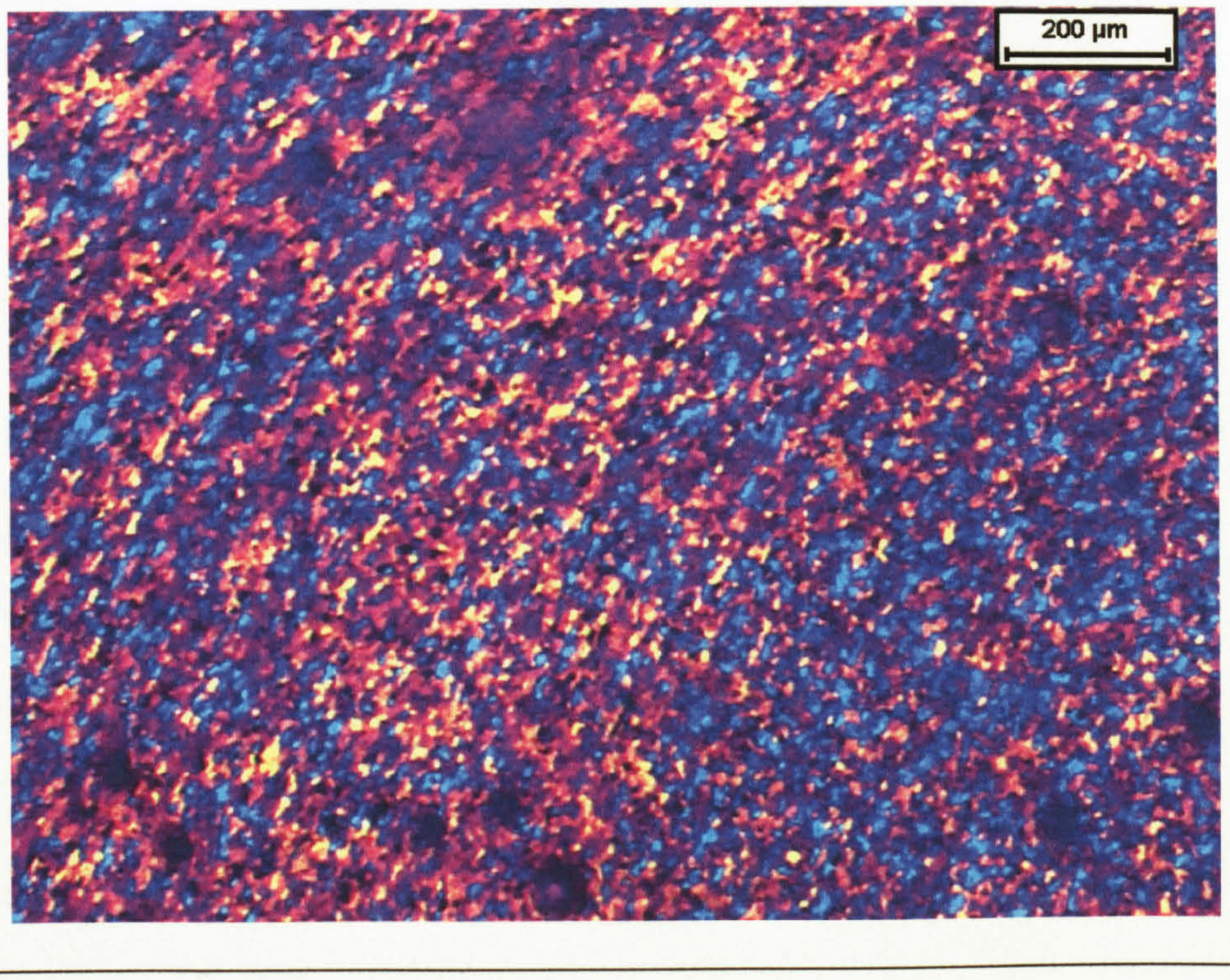

Figure 3.79: FS SP TMAZ. Plastically deformed grains rotated by up to 90° (left) and the smaller grains of the weld nugget (right), position 1 in Figure 3.78.

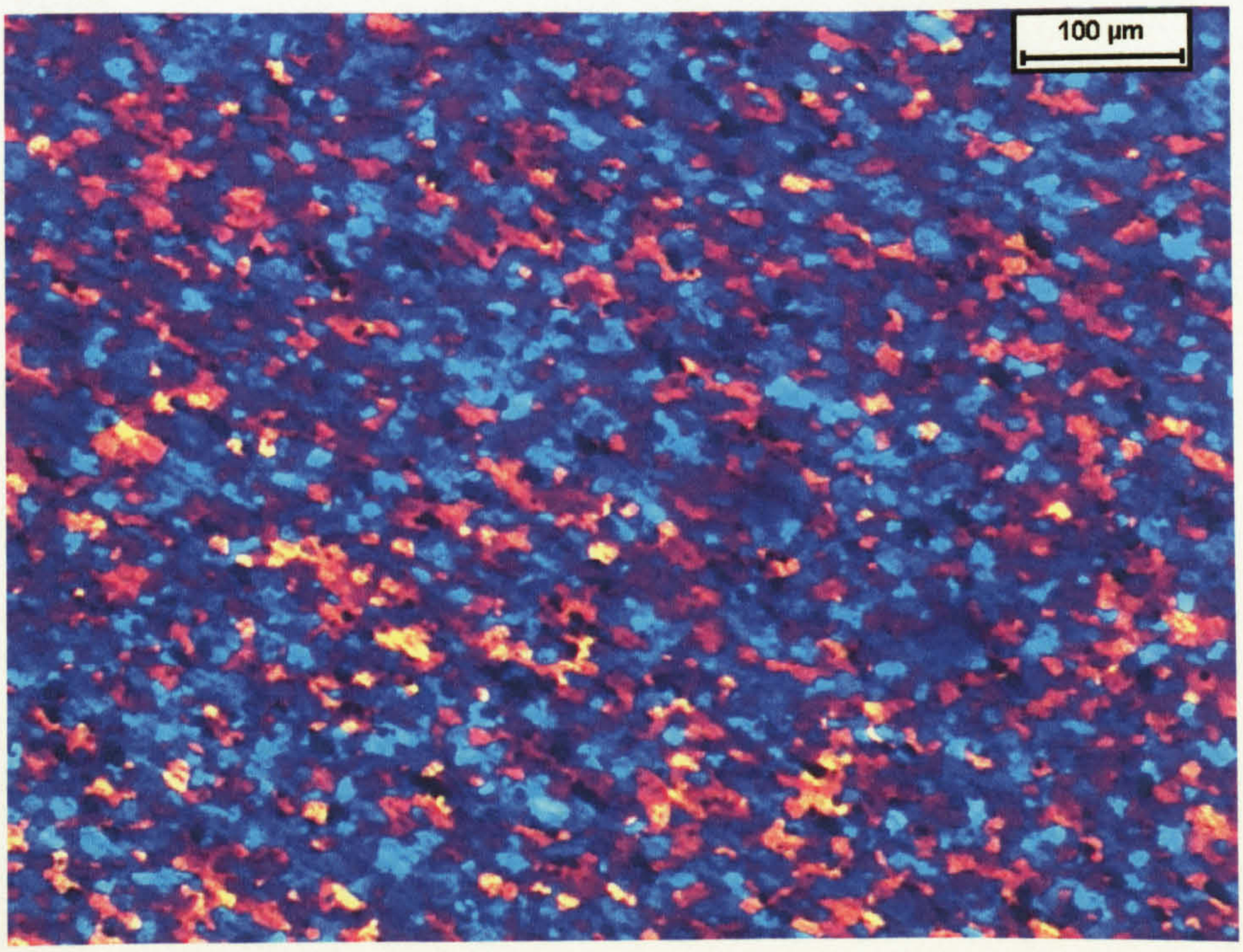

Figure 3.80: FS SP plastic deformation within the TMAZ, position 2 in Figure 3.78.

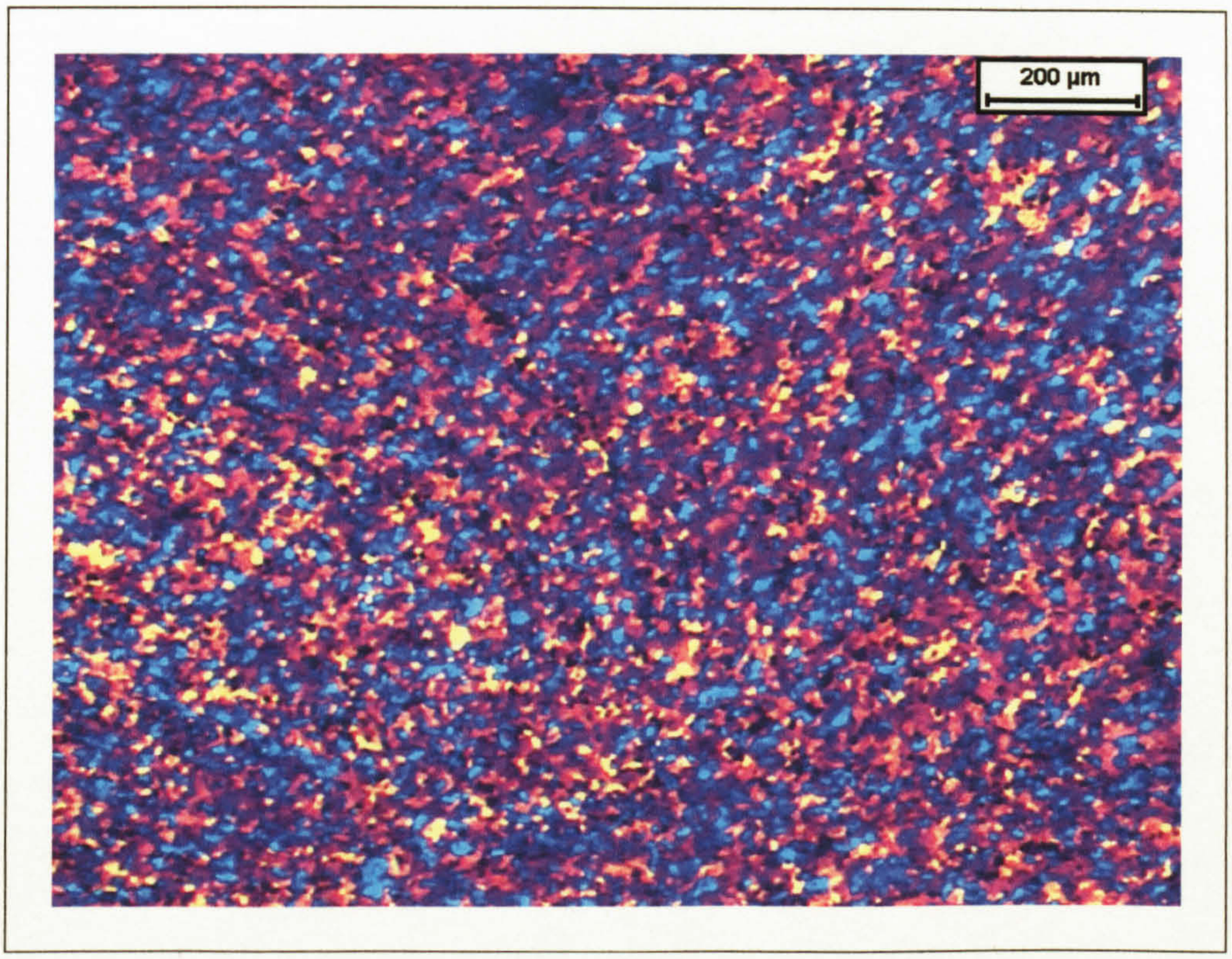

Figure 3.81: FS SP plastic deformation within the TMAZ, position 3 in Figure 3.78.

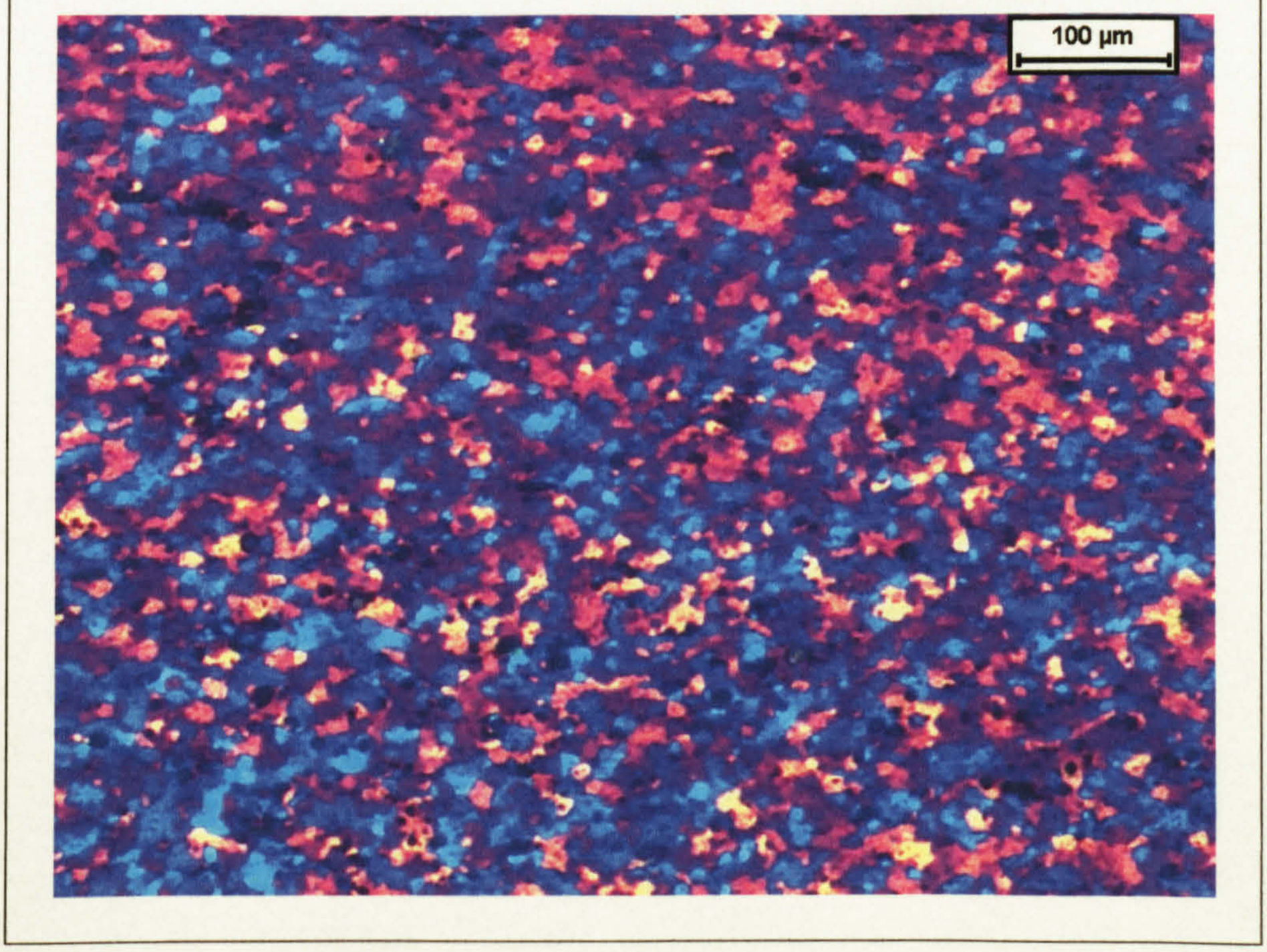

Figure 3.82: FS SP grains in the weld nugget, position 4 in Figure 3.78. Average grain size 10 µm, ASTM 10.5G.

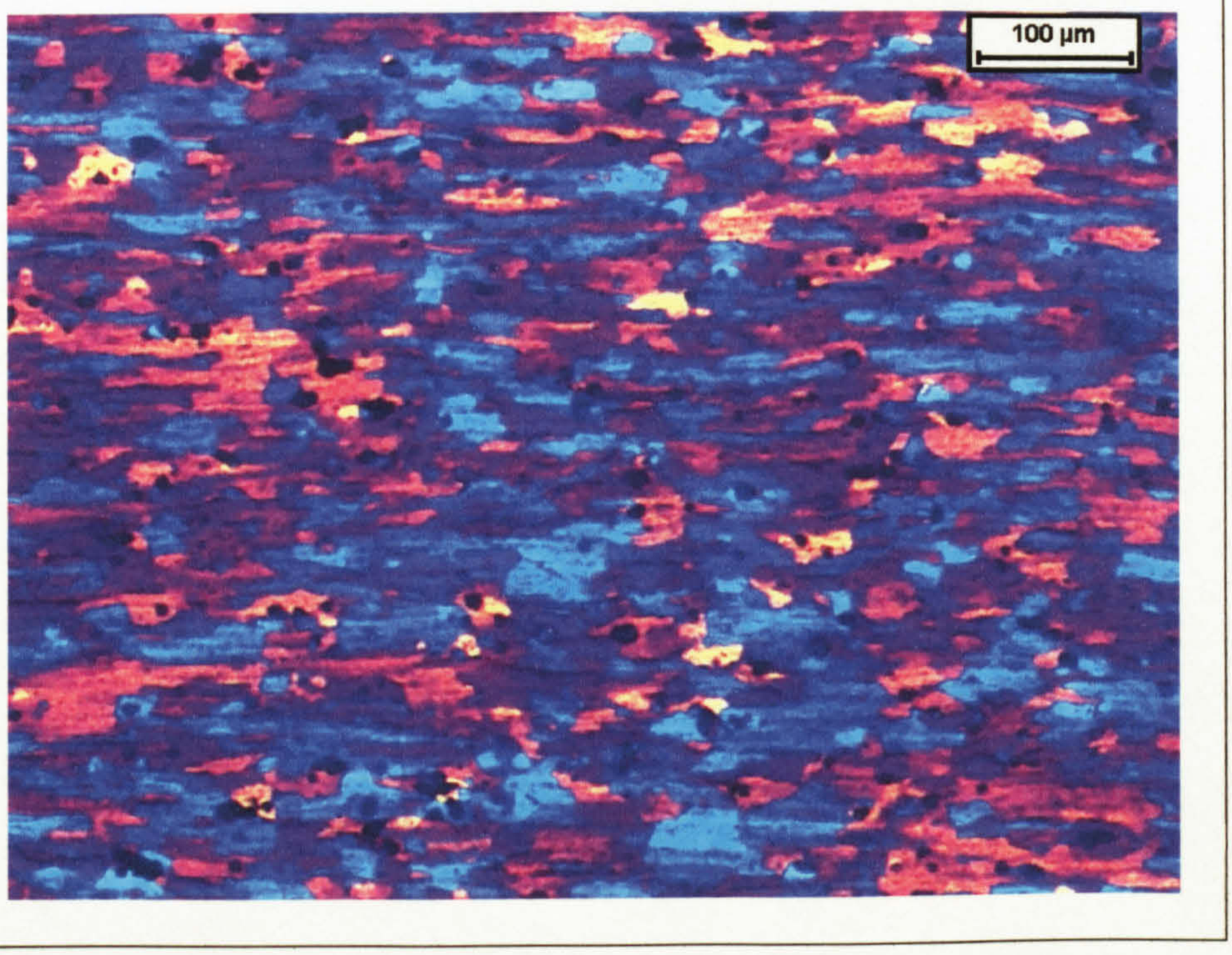

Figure 3.83: FS SP grains within the HAZ, position 5 in Figure 3.78.

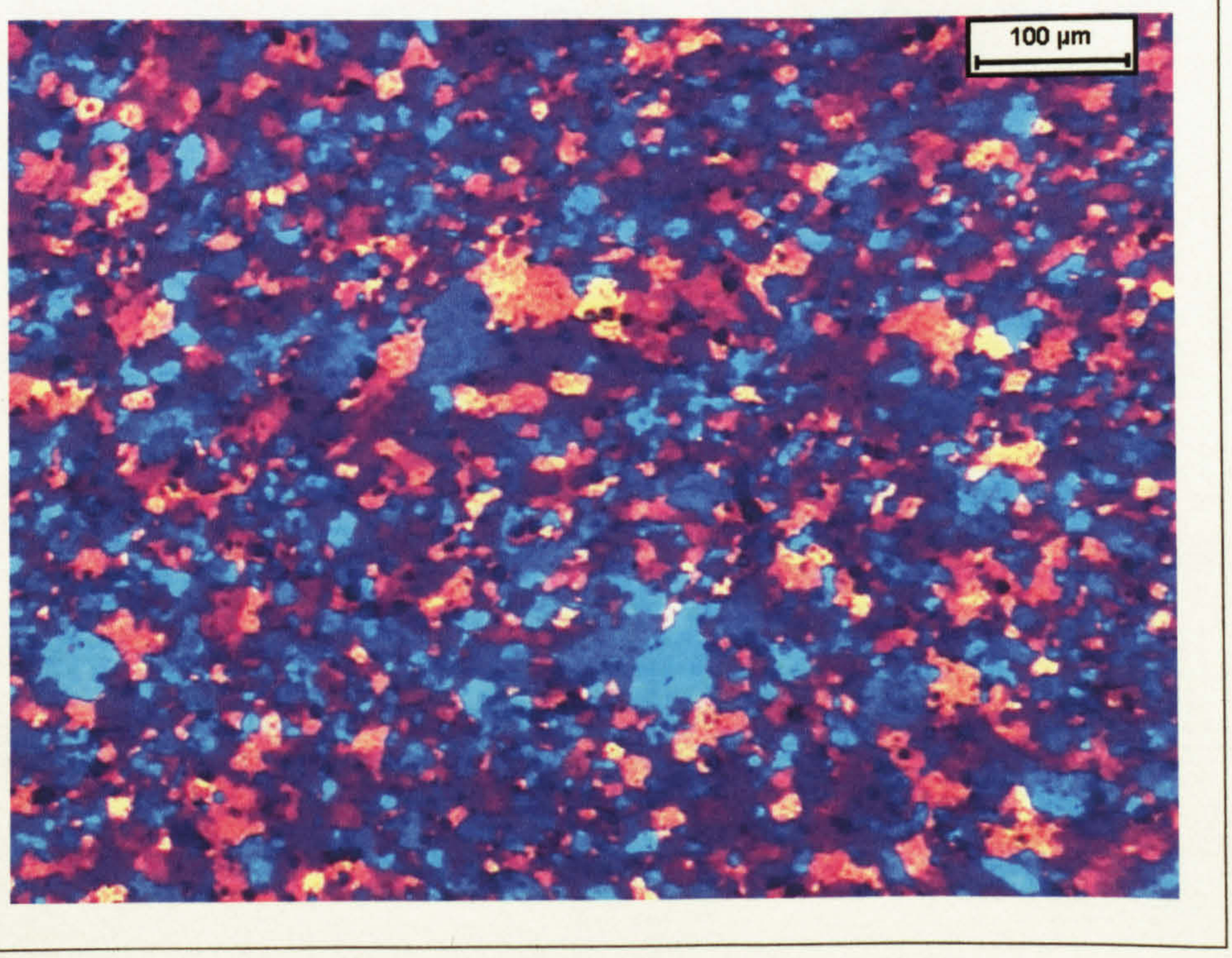

Figure 3.84: Grains within the weld nugget, some of the grains appearing to have experienced grain growth[1], position 6 in Figure 3.78.

[1] Threadgill, P (2000)

3.6.4.2.1 Intermetallic Phases

$FeAl_3$/(Fe,Mn)Al_6 and Mg_2Si intermetallic phases were measured at the centre of the weld from the friction band surface to the backing plate surface, this being the region that fatigue cracks initiated. The intermetallic phases are shown near to the friction band surface and in the weld nugget in Figure 3.85 and Figure 3.86 respectively. The intermetallic phases found in the weld nugget region were less than the typical grain size of 10 µm diameter (for a grain with a circular cross sectional area this would give an area of 79 μm^2), with the maximum area for the $FeAl_3$/(Fe,Mn)Al_6 and Mg_2Si being 93 and 46 μm^2 respectively. Mean sizes were 9.3 μm^2 for the $FeAl_3$/(Fe,Mn)Al_6 phases and 13.9 μm^2 for the Mg_2Si phase. The area densities were 0.71% and 0.13% for the $FeAl_3$/(Fe,Mn)Al_6 and Mg_2Si respectively.

Phase	Area examined (mm^2)	No. of particles	Phase size (μm^2)						Area density (%)
			Min	Max	Mean	Median	Std. Dev.	Total area	
$FeAl_3$/(Fe,Mn)Al_6	1.7667	1343	1.1	93	9.3	6.3	9.5	12542	0.71
Mg_2Si		165	4.6	46	13.9	11.4	8.0	2293	0.13

Table 3.22: Size and distribution of Mg_2Si and $FeAl_3$/(Fe,Mn)Al_6 phases in an AA 5383-H321 FS SP weld.

Figure 3.85: FS SP intermetallic phases near to the friction band surface.

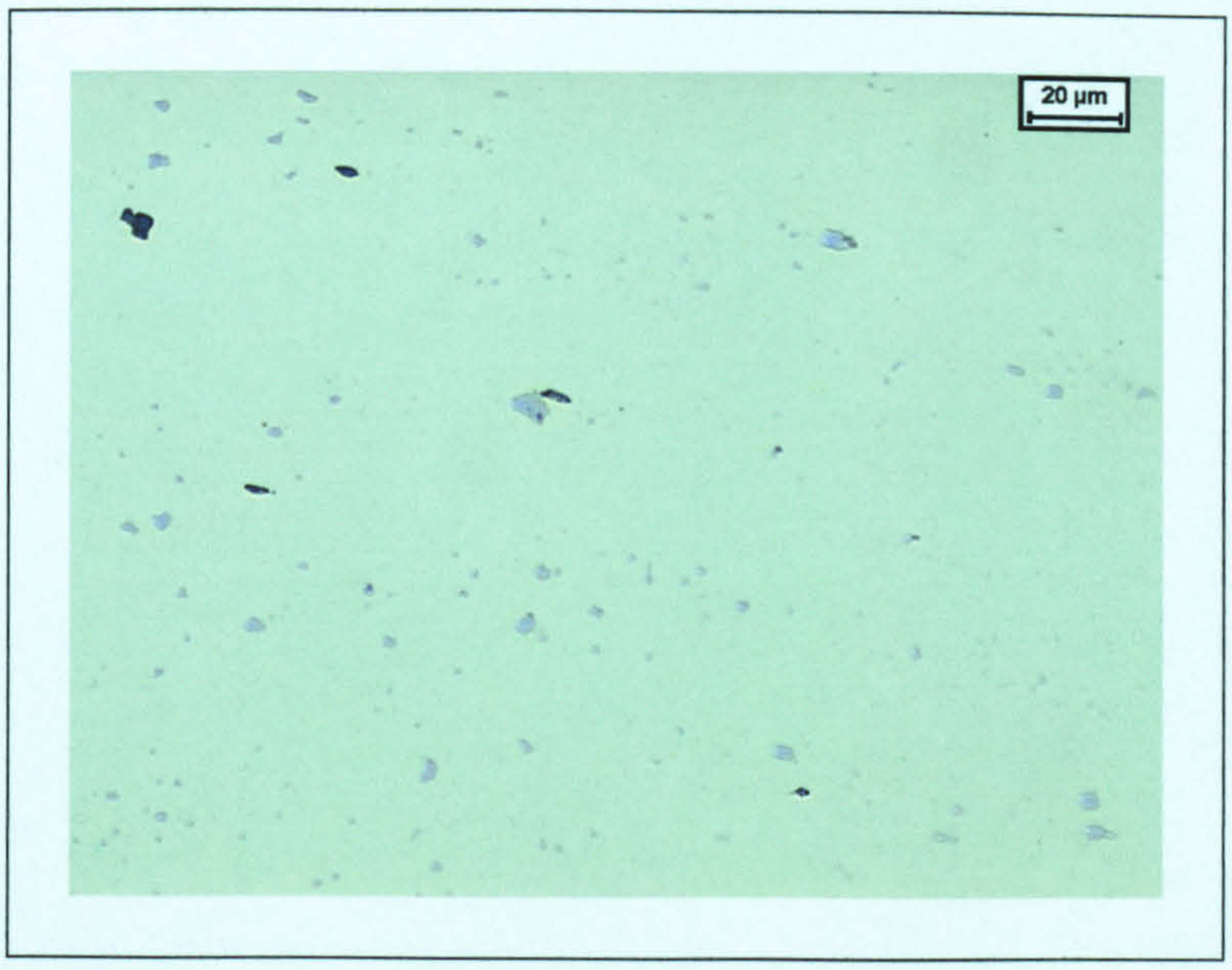

Figure 3.86: FS SP intermetallic phases in the weld nugget.

3.6.4.2.2 Partial Fusion Defects

Due to friction stir welding being a solid state process many of the potential problems associated with MIG welds, such as porosity, do not occur, although what appear to be fusion defects, and were subsequently termed partial fusion defects (PFD), have been observed. These were only observed in the SP welds and were initially noticed on the fracture surfaces of specimens that had undergone fatigue testing and subsequent failure. The defects shown in Figure 3.87 and Figure 3.88 were observed in the weld nugget region of the cross section of the weld, TS plane. Although the welds were radiologically examined post weld, and no defects were observed, they were probably too narrow to be detected with radiological techniques in the unstressed state. Ultrasonic examination may disclose them, although no attempt has been made to confirm this. The one on the left of Figure 3.87 and shown in greater detail in Figure 3.88 is made up of what appears to be four distinct sections, their maximum length being approximately 15 µm.

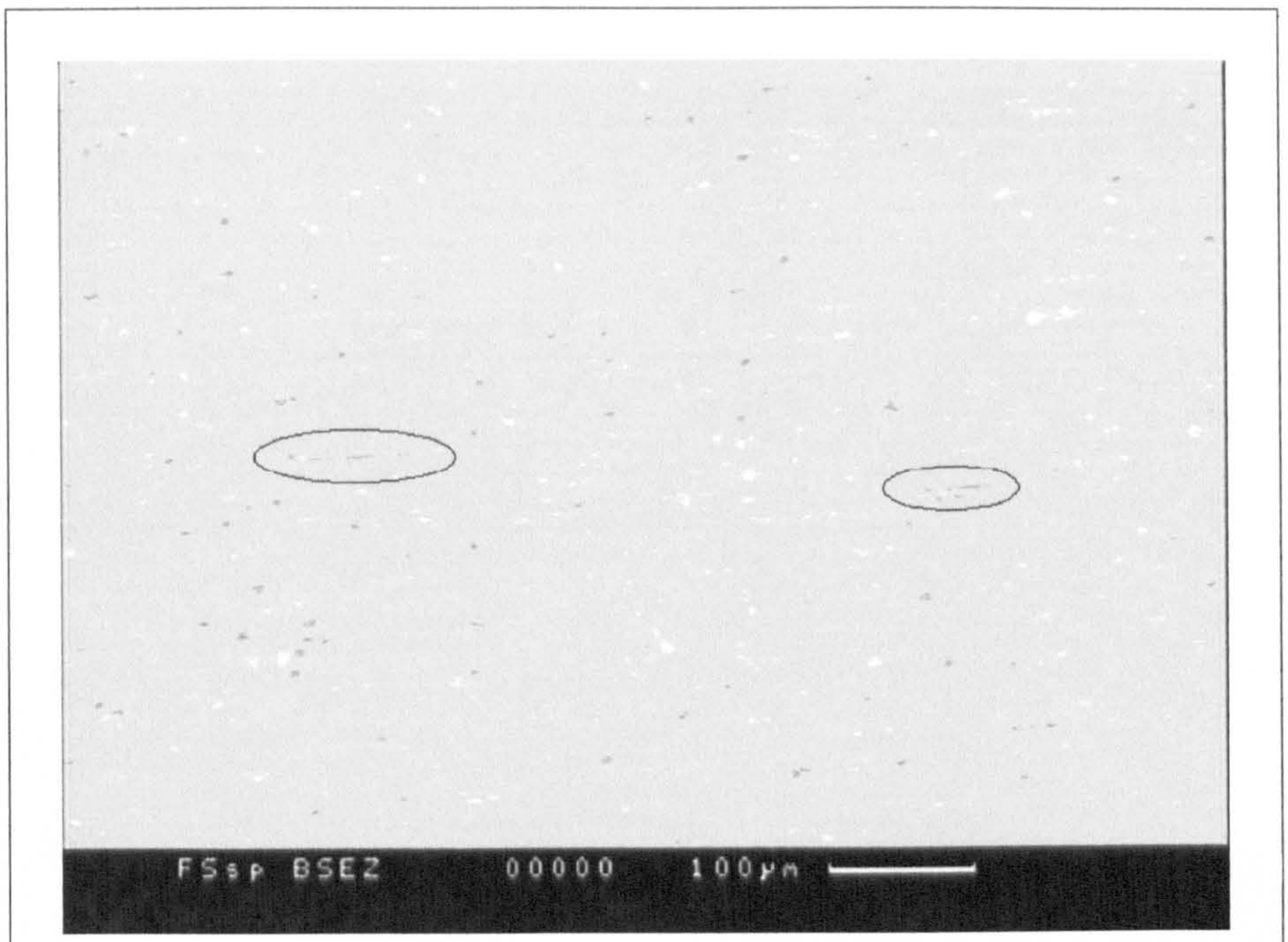

Figure 3.87: Partial fusion defects in the weld nugget, outlined, TS plane.

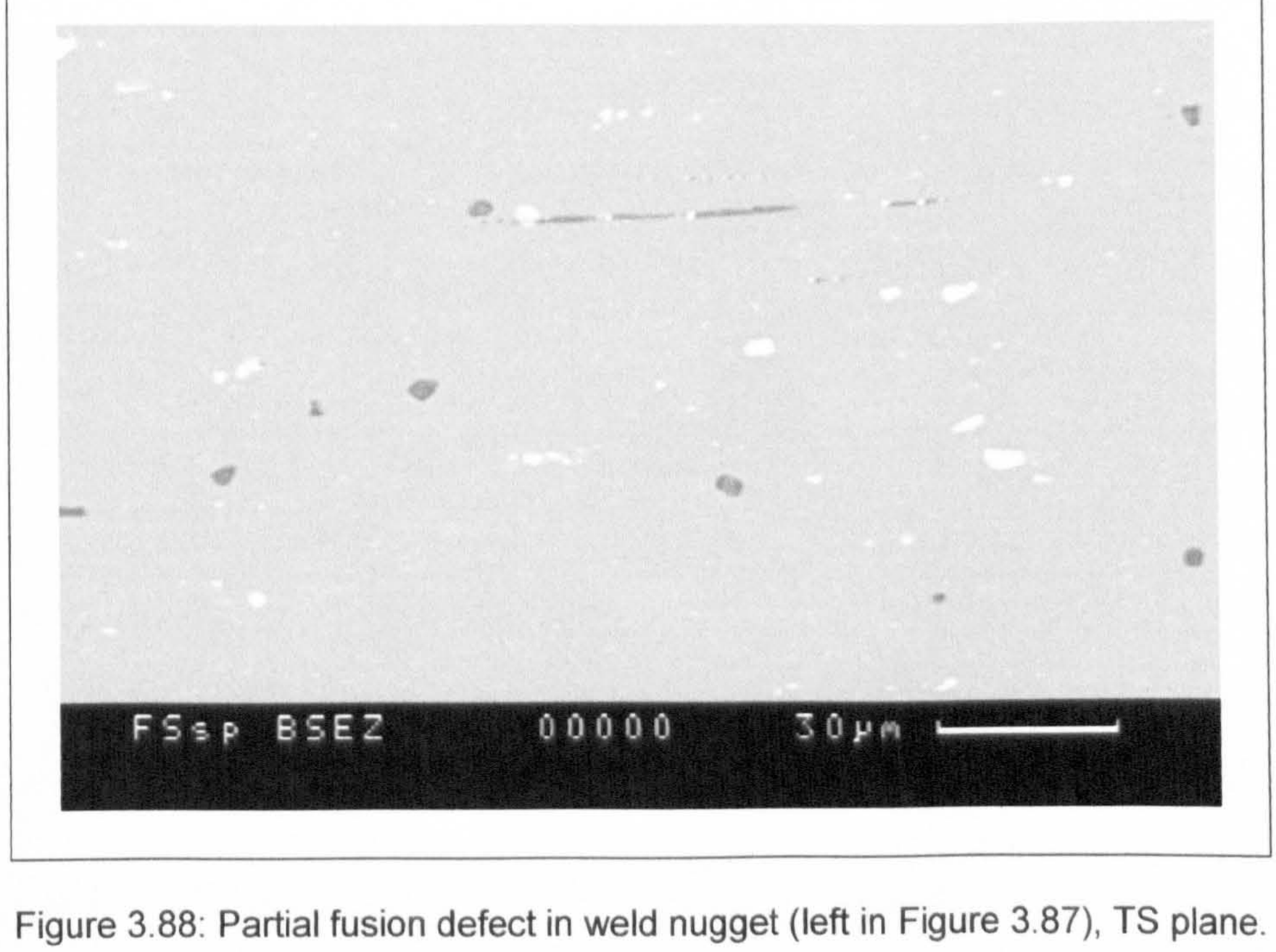

Figure 3.88: Partial fusion defect in weld nugget (left in Figure 3.87), TS plane.

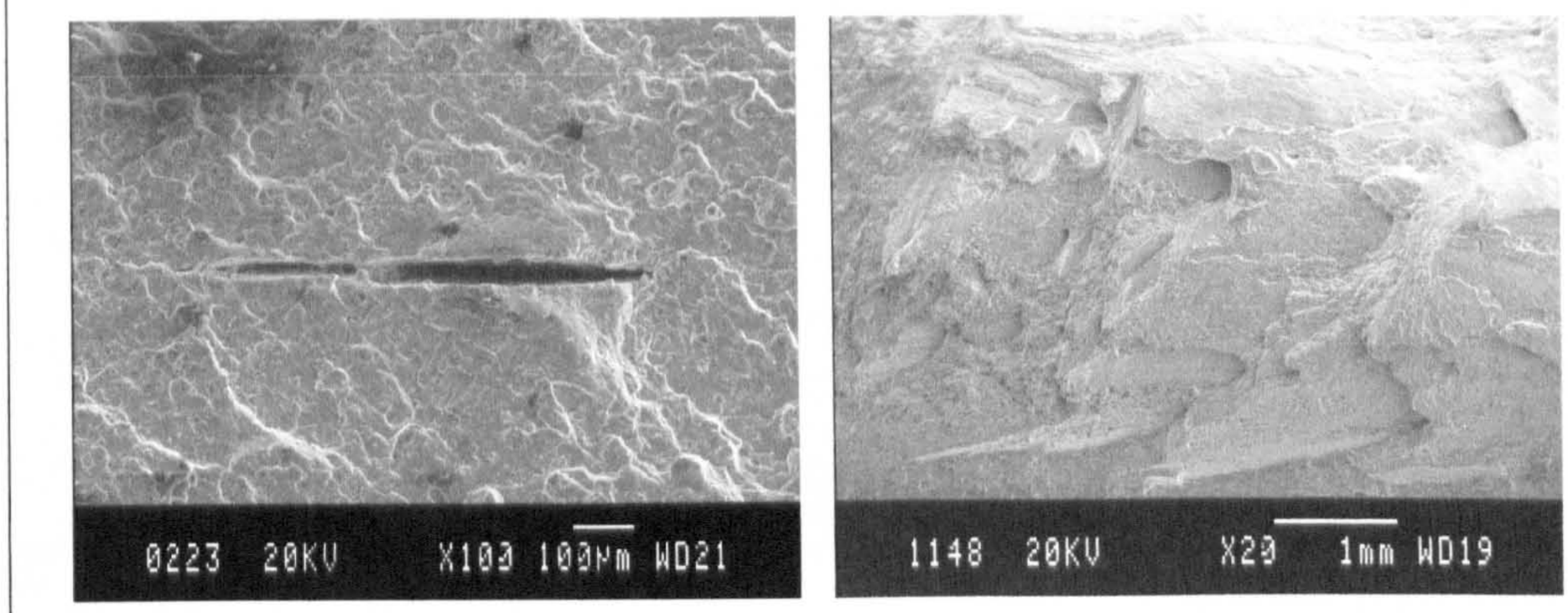

Figure 3.89: Partial fusion defects on FS SP fatigue fracture surfaces, LS plane.

3.6.4.3 Mechanical Properties

3.6.4.3.1 Microhardness

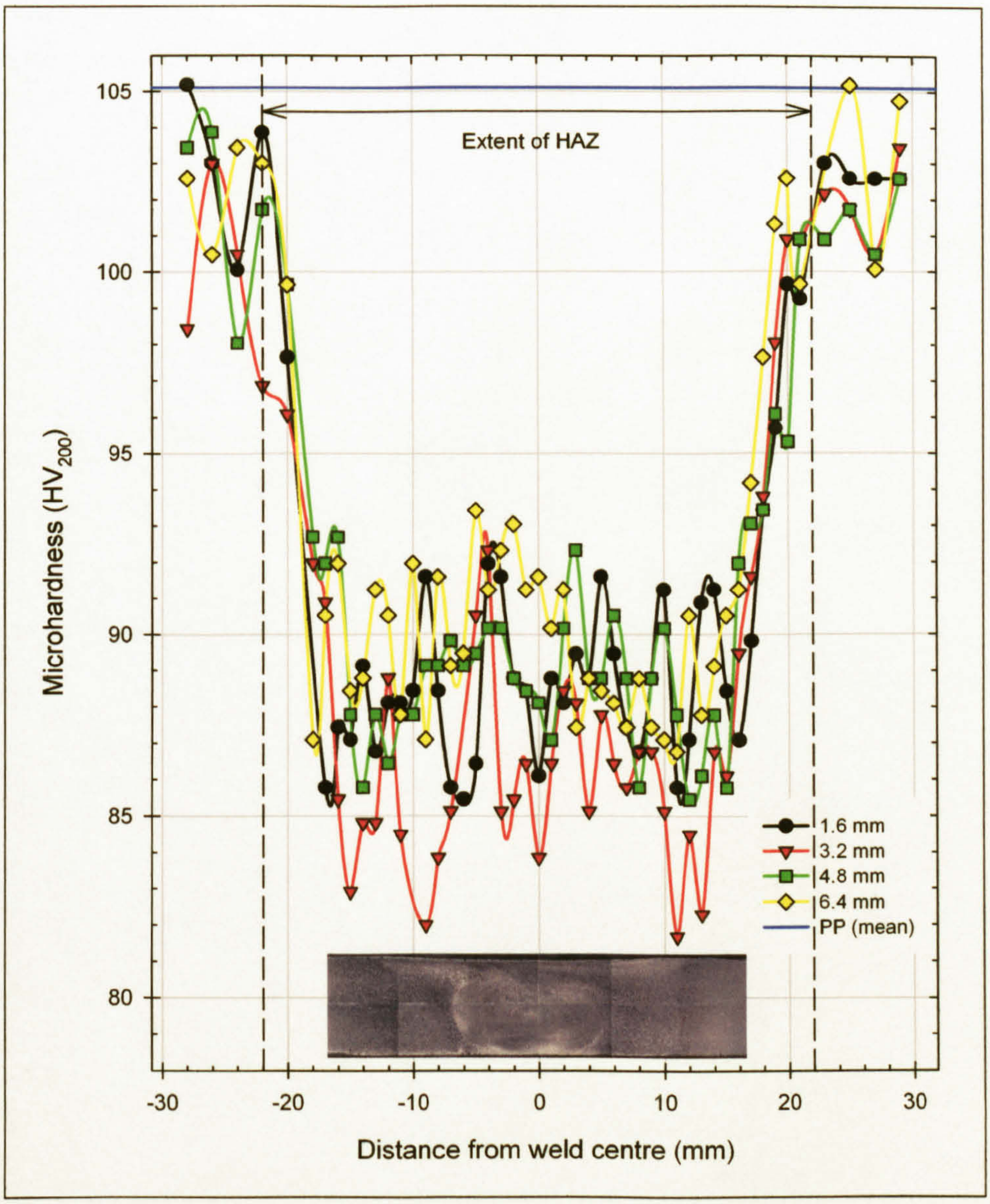

Figure 3.90: Microhardness results for FS SP butt weld, weld with respect to the weld position (values in the legend refer to distance from the friction band surface).

Microhardness values for the FS SP weld, as shown in Figure 3.90, exhibited minimum values of 87 HV_{200} at a distance of approximately ±14 mm from the weld centre, with the value at the centre increasing to 90 HV_{200}. The microhardness was of a relatively constant magnitude throughout the thickness of the weld, although there was some evidence of the HAZ being narrower as the distance from the friction band surface increased. An abrupt change in hardness between the parent plate and HAZ was evident, this occurring at a distance of approximately ±22 mm from the weld centre.

3.6.4.3.2 Tensile Properties

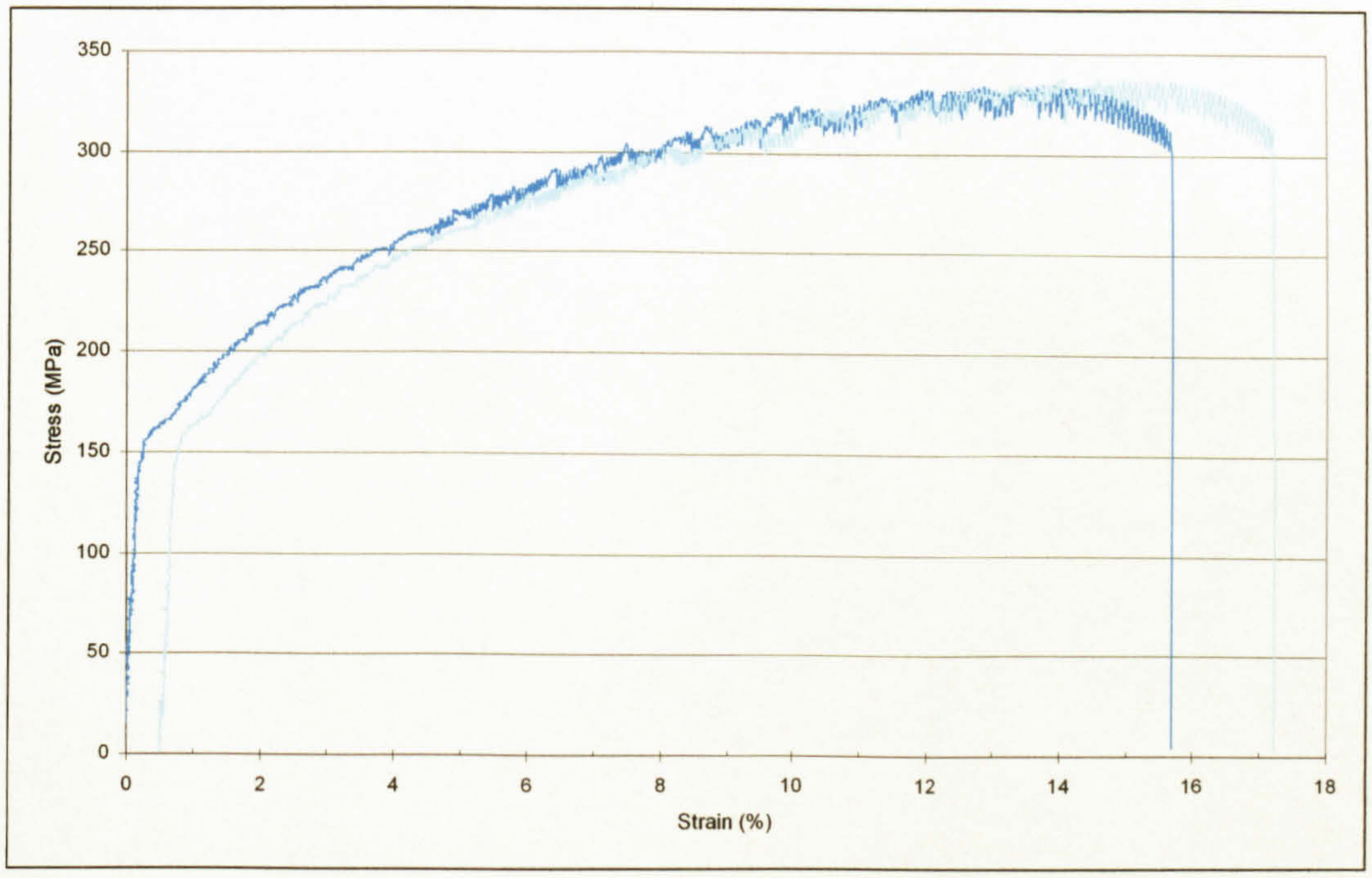

Figure 3.91: Stress/strain plots from monotonic uniaxial tensile tests of FS SP welded AA 5383-H321.

The stress/strain plots from the uniaxial monotonic tensile testing of FS SP welded AA 5383-H321 were as shown in Figure 3.91, with the mechanical properties derived from these shown in Table 3.23. An initial linear elastic response was evident, returning an elastic modulus of 70.4 GPa. A yield point was evident and the limit of proportionality was at 144 MPa, the 0.2% proof stress returning a value of 163 MPa. The tensile strength of the welded alloy was 336 MPa, at a strain of 13.7%, whilst failure occurred at a strain of 16.2% and a stress of 313 MPa. Failure occurred in shear at the centre of the weld with moderate necking being evident, as shown in Figure 3.92.

Specimen	Limit of proportionality (MPa)	$\sigma_{0.1\%}$ (MPa)	$\sigma_{0.2\%}$ (MPa)	σ_{TS} (MPa)	ε_{TS} (%)	$\sigma_{failure}$ (MPa)	$\varepsilon_{failure}$ (%)	E (GPa)
FS SP	144	157	163	336	13.7	313	16.2	70.4

Table 3.23: Mechanical properties of FS SP welded AA 5383-H321 (mean of two tests).

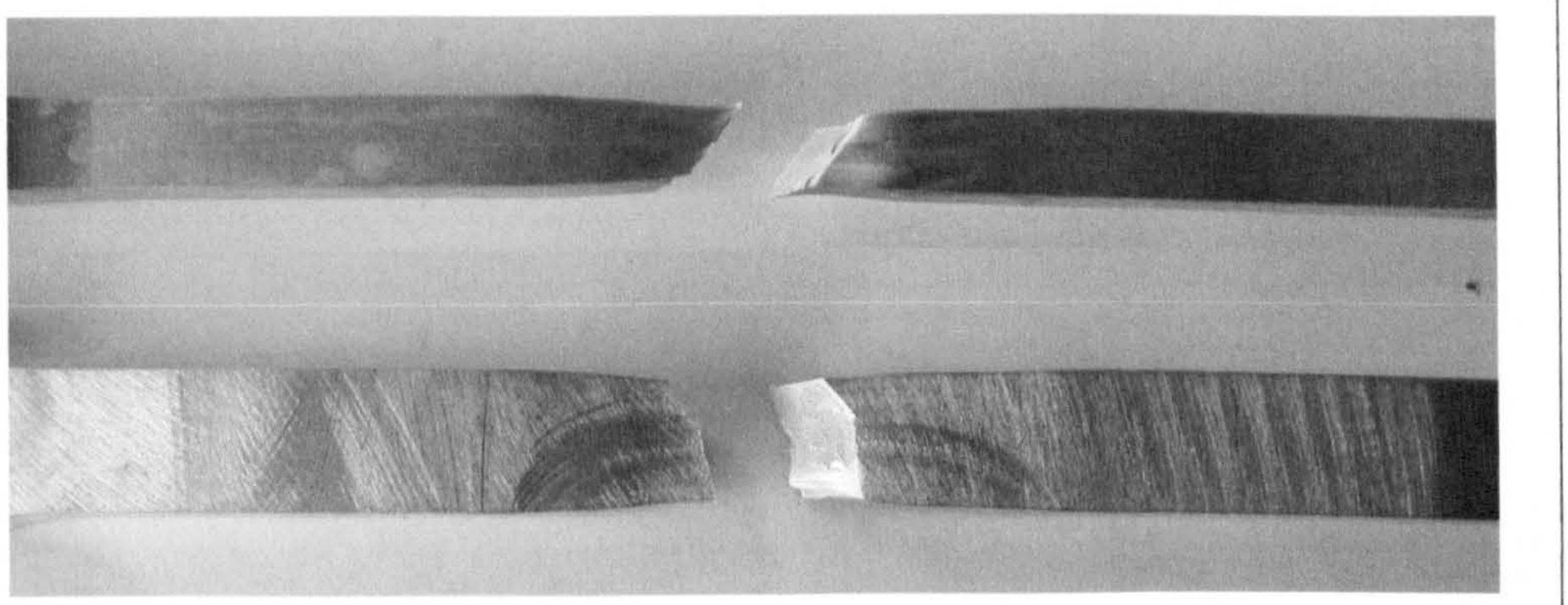

Figure 3.92: Shear failure and necking from monotonic uniaxial tensile testing of a FS SP welded AA 5383-H321.

3.6.5 FS Double Pass Welds

3.6.5.1 Weld Geometry

As with the FS SP weld, the process produced a lip at the edge of the friction band, although with the DP process this occurred on both sides of the joint. These were again removed by the fabricator.

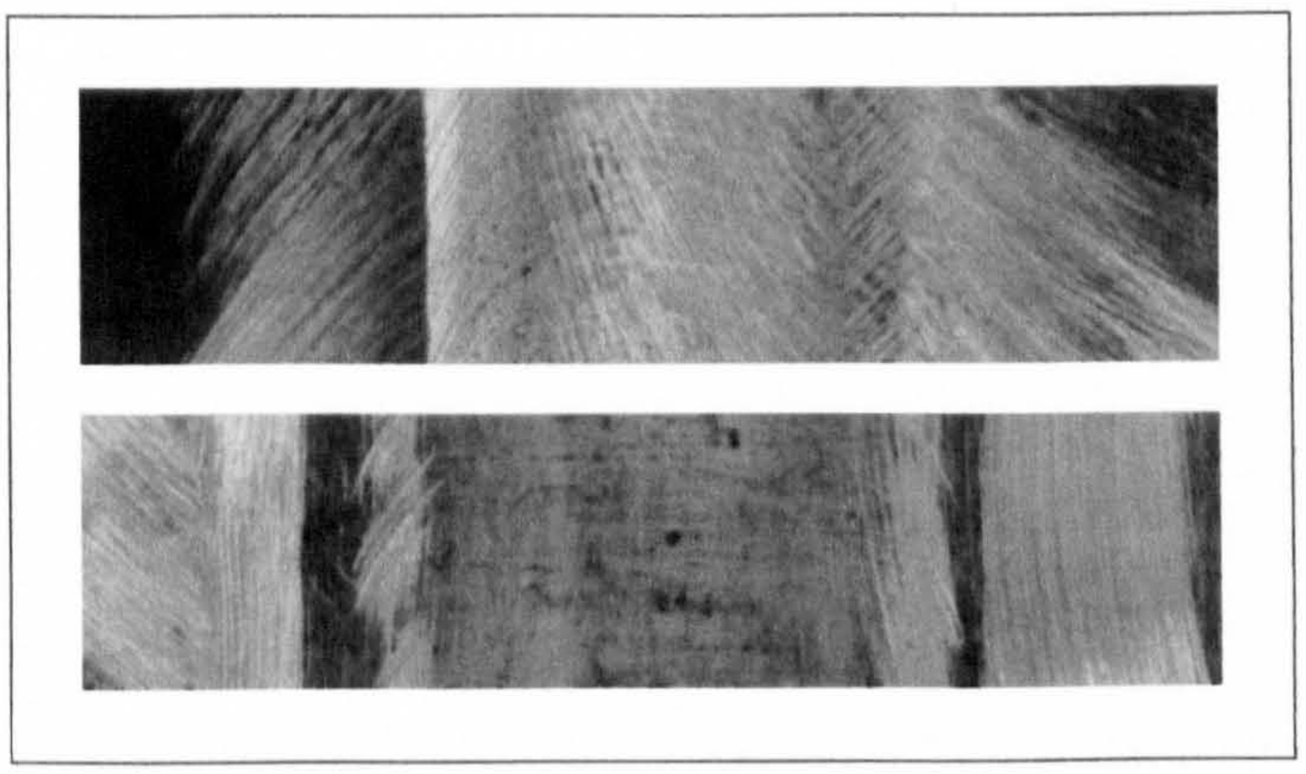

Figure 3.93: FS DP second pass side (top) and initial pass side (bottom).

Typical views of both the 1st and 2nd pass sides of the FS DP weld are shown in Figure 3.93. The 1st pass side, shown in Figure 3.94, appeared as a slightly raised, by approximately 100 - 150 µm, plateau. It was assumed that after the initial pass the surface would exhibit the circular score marks (as seen on the SP friction band and 2nd pass of the DP surfaces), but as an outcome of the pressure and heat from the 2nd pass, the resultant appearance resembled that of the backing plate side of the SP process.

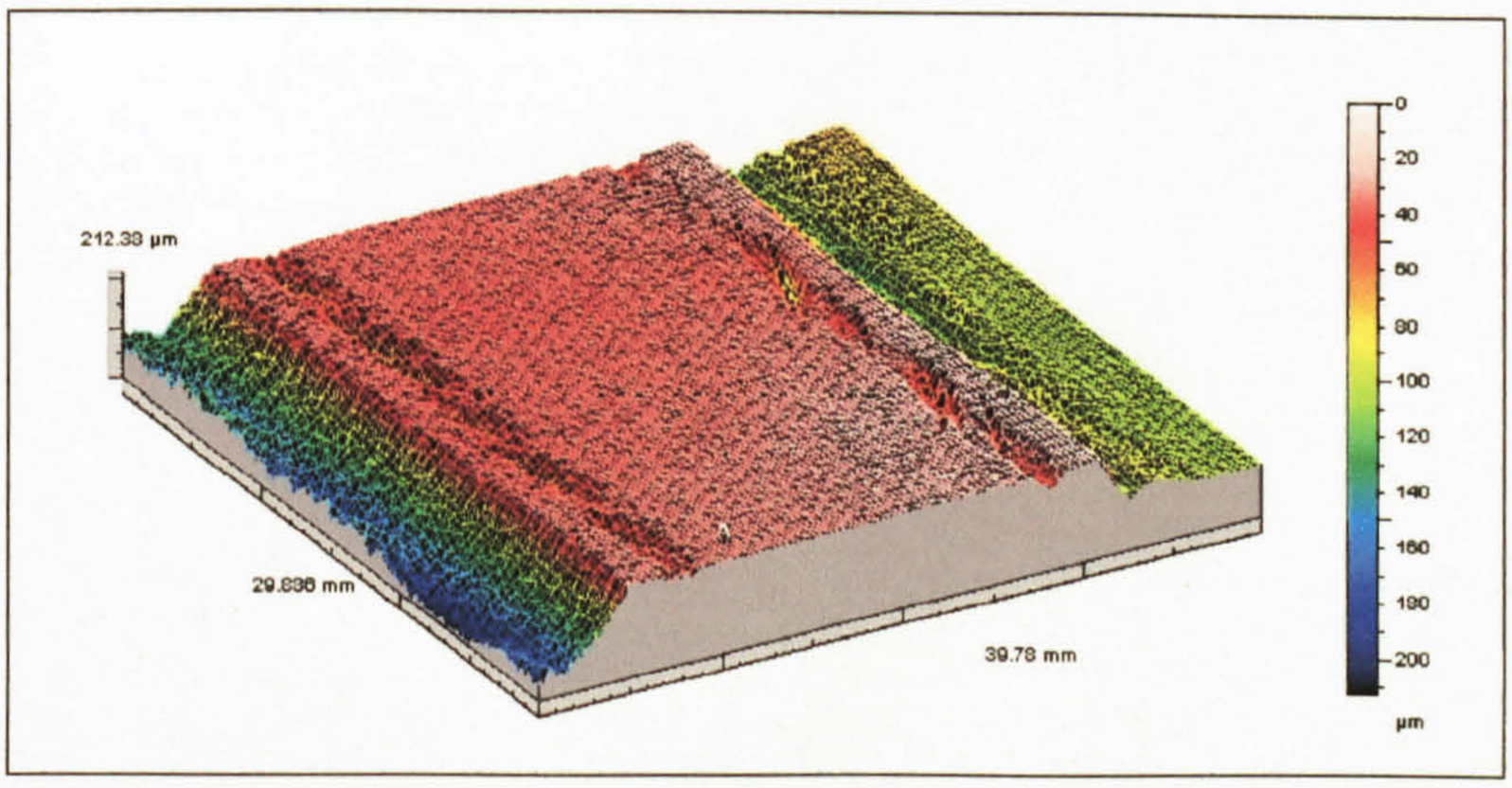

Figure 3.94: Three dimensional representation of the geometry of the 1st pass side of a FS DP weld in AA 5383-H321.

The 2nd pass side, shown in Figure 3.95 and Figure 3.96, exhibited two raised areas, the remnants of the lip, occurring at either edge of the friction band. For the weld under consideration this was typically 50 - 125 µm above the parent plate surface, the exact height being dependent on amount of the lip that was removed. The result of this increase in thickness is an increase in the stress experienced when loaded in bending and fatigue failure of the FS DP welds typically occurred in the areas of these ridges. Between the ridges, at the centre of the weld, a thinner section was evident, for the weld under investigation this was typically 325 µm below the parent material surface. The effect of the raised profile on the 1st pass side and the lowered profile on the 2nd pass side resulted in an overall thinning of the weld area of 175 - 225 µm. The surface beneath the 2nd pass tool shoulder consisted of a series of circular grooves resulting from the rotational and transverse movement of the tool, shown in Figure 3.96 and in profile in Figure 3.97, and had a depth of approximately 10 - 15 µm.

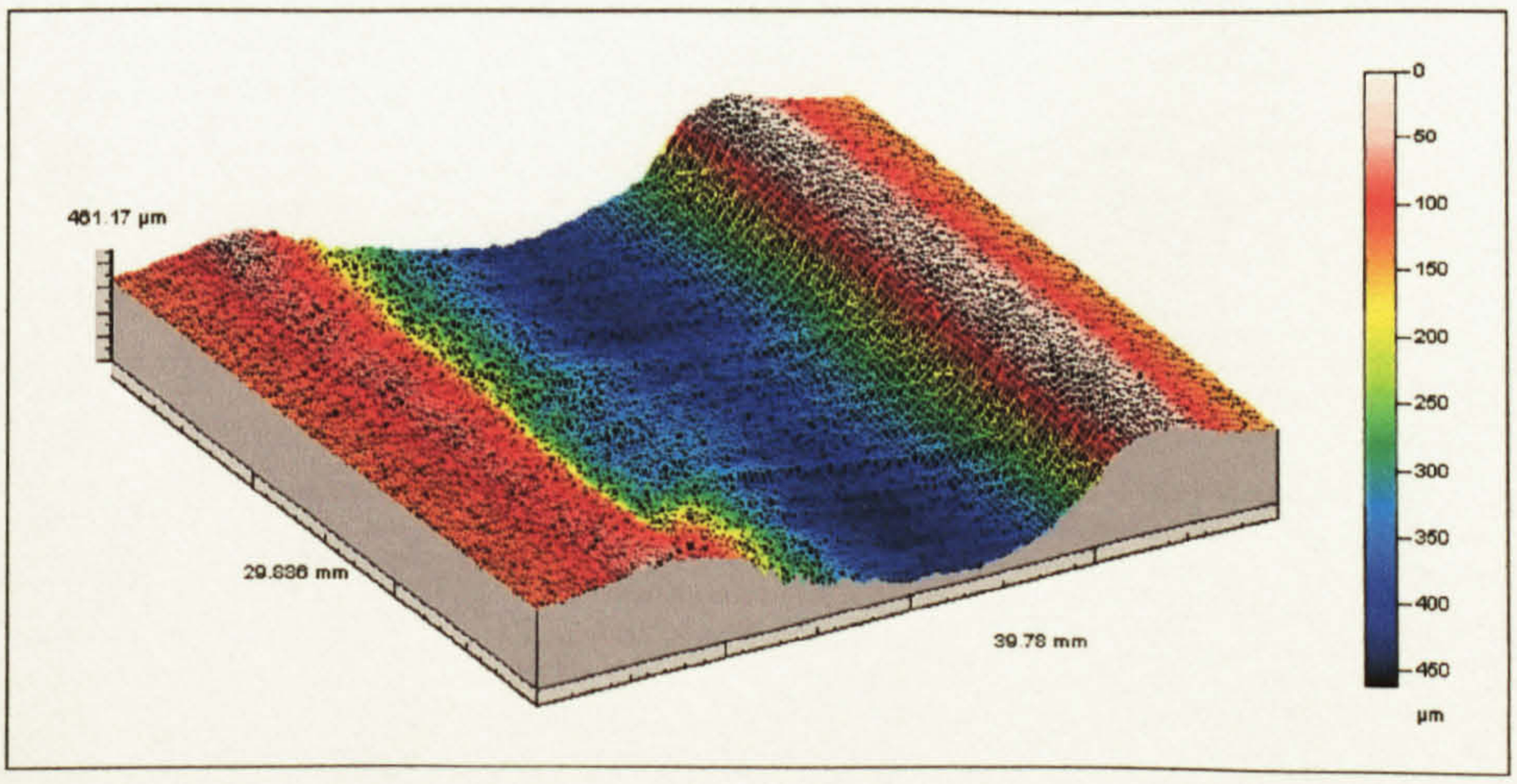

Figure 3.95: Three dimensional representation of the geometry of the 2nd pass side of a FS DP weld in AA 5383-H321.

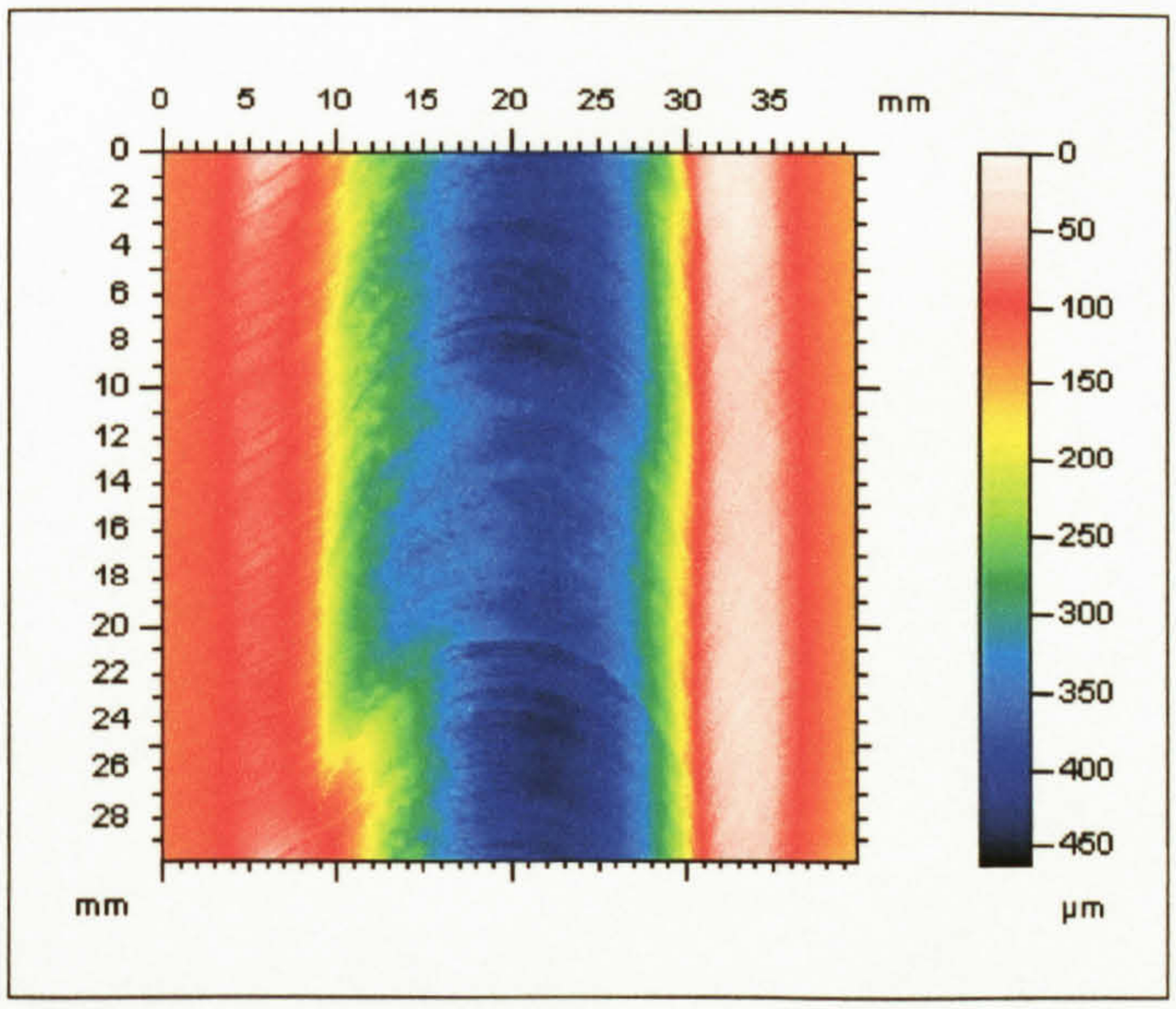

Figure 3.96: Friction band surface, 2nd pass, of a FS DP weld exhibiting the circular grooves.

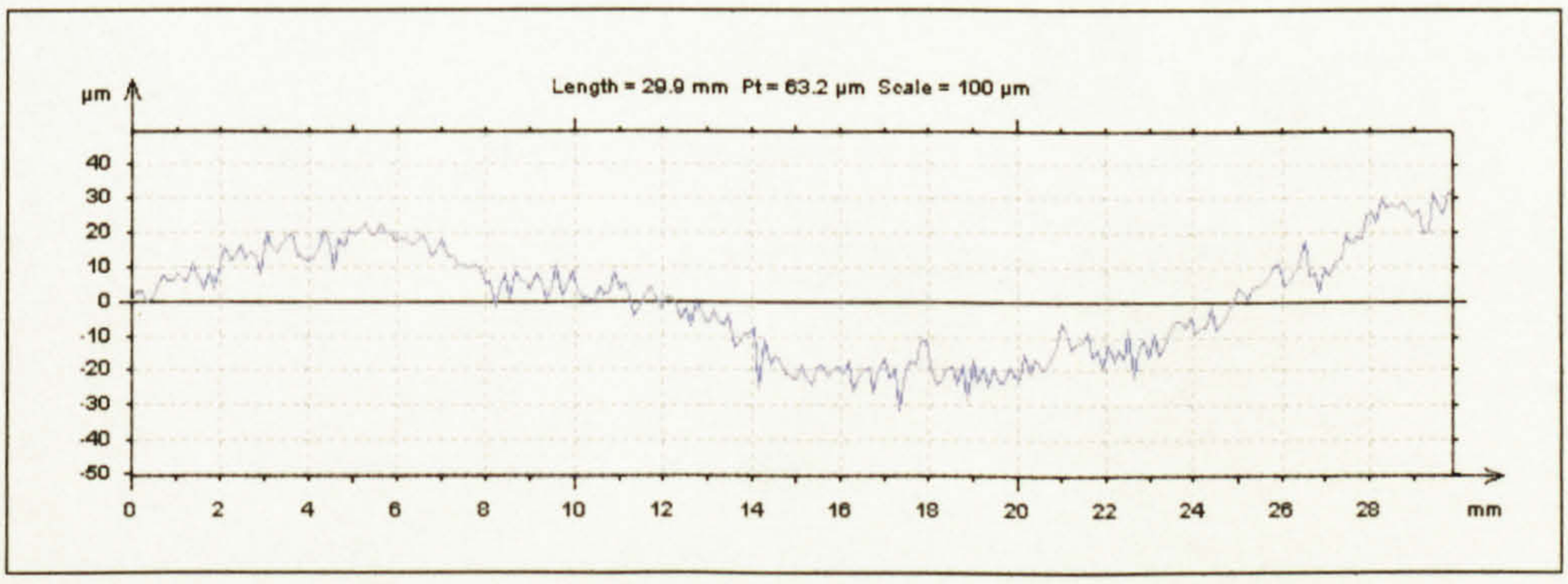

Figure 3.97: Two dimensional profile of the 2nd pass surface of the FS DP weld, measured at the centre of the weld and in the direction of the weld.

3.6.5.2 Microstructure

From the macrograph, Figure 3.98, both the TMAZ, (consisting of the weld nugget and plastically deformed grains), and the HAZ are evident. The concentric rings found in the nugget are also evident, with those produced by the second pass being intact, whilst the remnants of the rings produced by the initial pass are also evident. Due to the two pass process two appendages were present, the clockwise rotation of the tool for both passes resulting in the appendages occurring on opposite sides of the weld seam.

The grains in the weld nugget, shown in Figure 3.100, were equiaxed in geometry with an average size of 10 µm (ASTM grain size 10.5). The concentric rings seen within the weld nuggets, after etching, were as shown in Figure 3.99. Although the rings are evident in many FS welds, it has been claimed that they do not have any effects on the mechanical

properties[1]. The elliptically shaped weld nugget, shown in Figure 3.98, had a major axis of approximately 12 mm at the centre of the weld. The plastically deformed grains of the TMAZ were typically of width 50 µm, with a length around 50 - 100% greater. Although the plastically deformed grains were elongated because of the rolling process, their aspect ratio was lower than that of the parent plate grains.

Plastic deformation was clearly visible in the TMAZ as shown in Figure 3.101 and Figure 3.102. The grains were rotated by up to 90° and swirl effects were evident. Figure 3.101 shows the boundary between the grains of the weld nugget, plastically deformed grains of the TMAZ and those of the HAZ, although this transition was not always easily defined.

The HAZ was characterised by more equiaxed grains when compared to those of the parent plate, but no plastic deformation was evident. The HAZ extended approximately 5 mm beyond the TMAZ boundary, which on the LT surface occurred at the edge of the friction band, as shown in Figure 3.103.

[1] Biallas, G et al (1999)

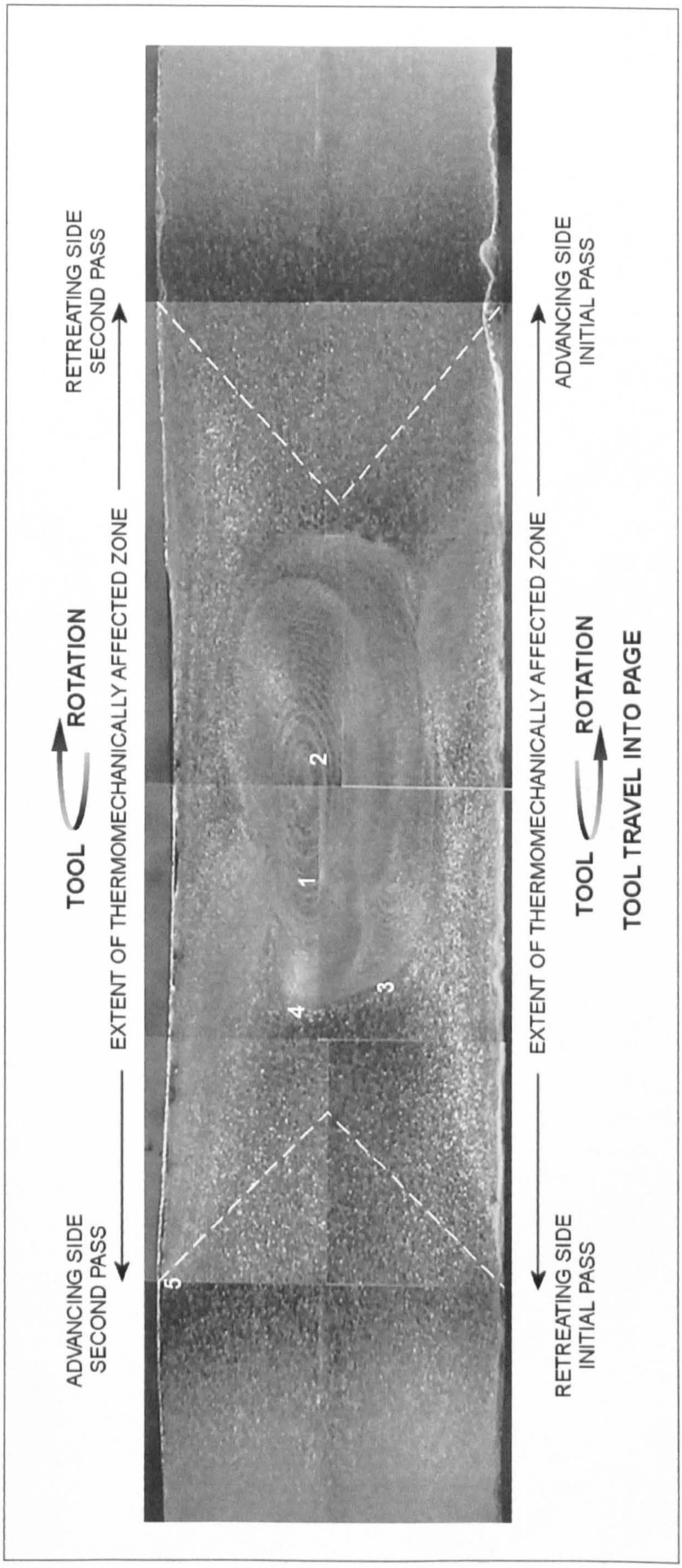

Figure 3.98: Macrograph of AA 5383-H321 FS DP weld, plate thickness 8 mm, 2nd pass friction band side uppermost, clockwise tool rotation when viewed from tool shoulder side, (numbers refer to the positions and orientations of the following micrographs).

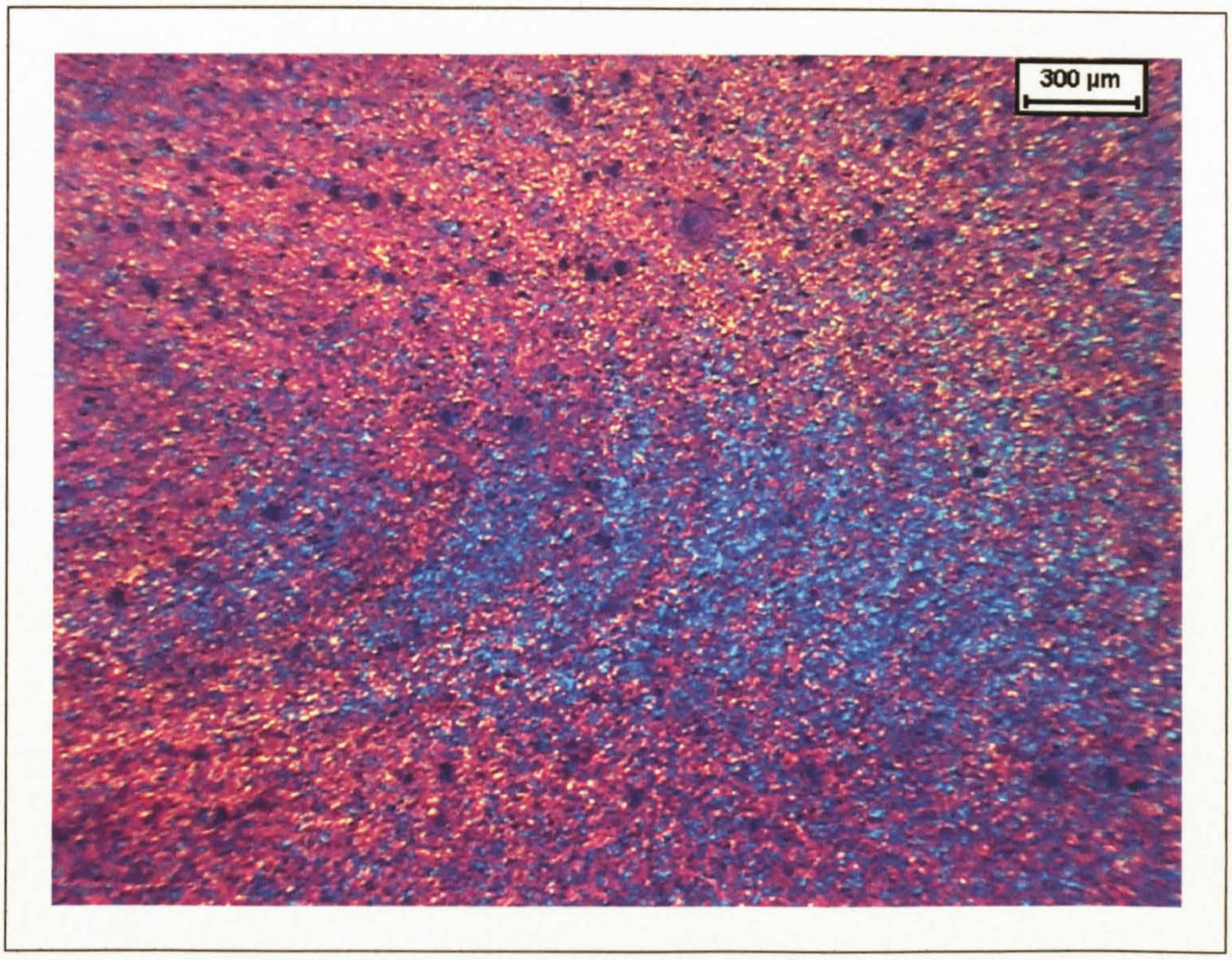

Figure 3.99: FS DP concentric rings evident in the weld nugget, position 1 in Figure 3.98.

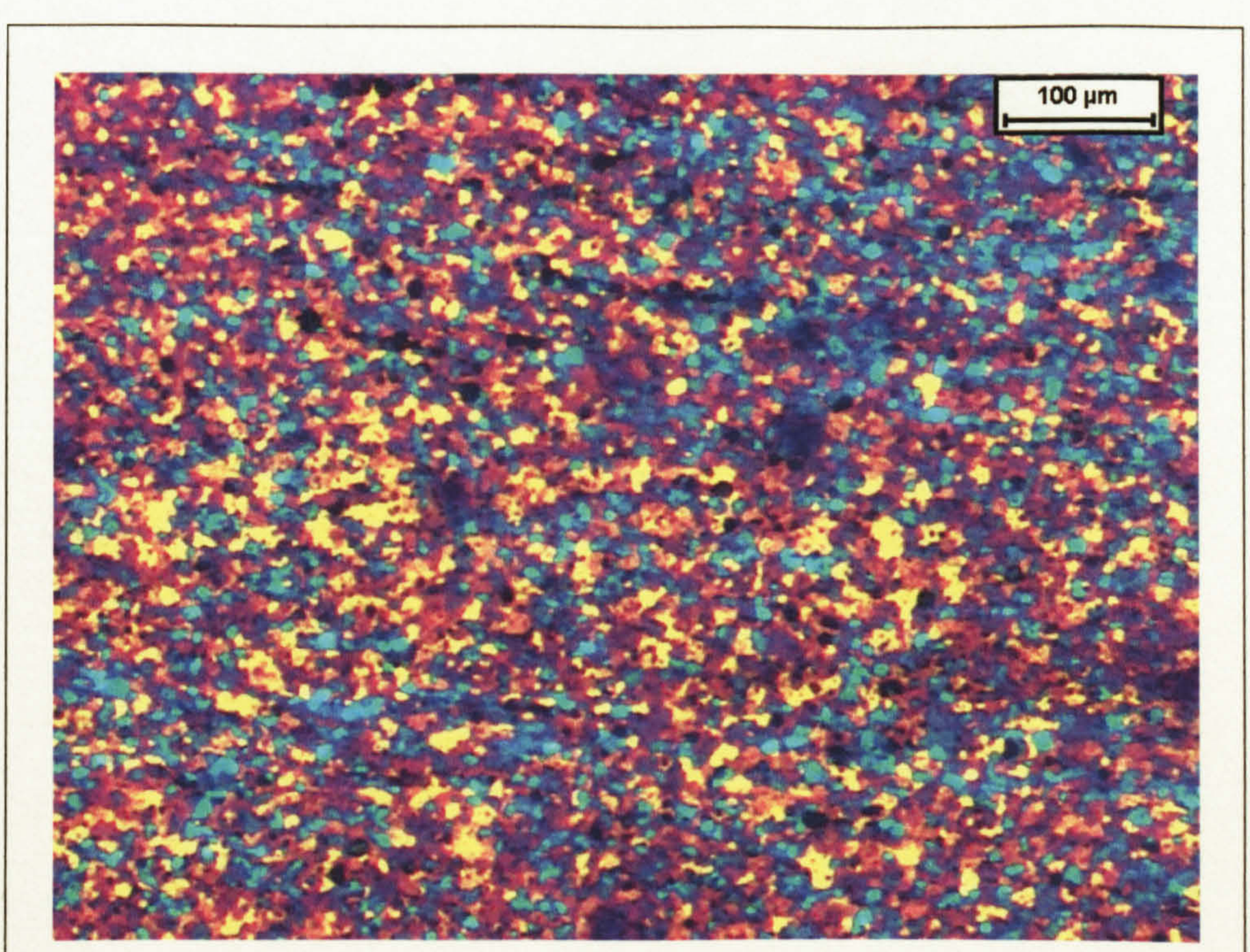

Figure 3.100: FS DP grains in the weld nugget, position 2 in Figure 3.98. Average grain size 10 µm, ASTM 10.5G.

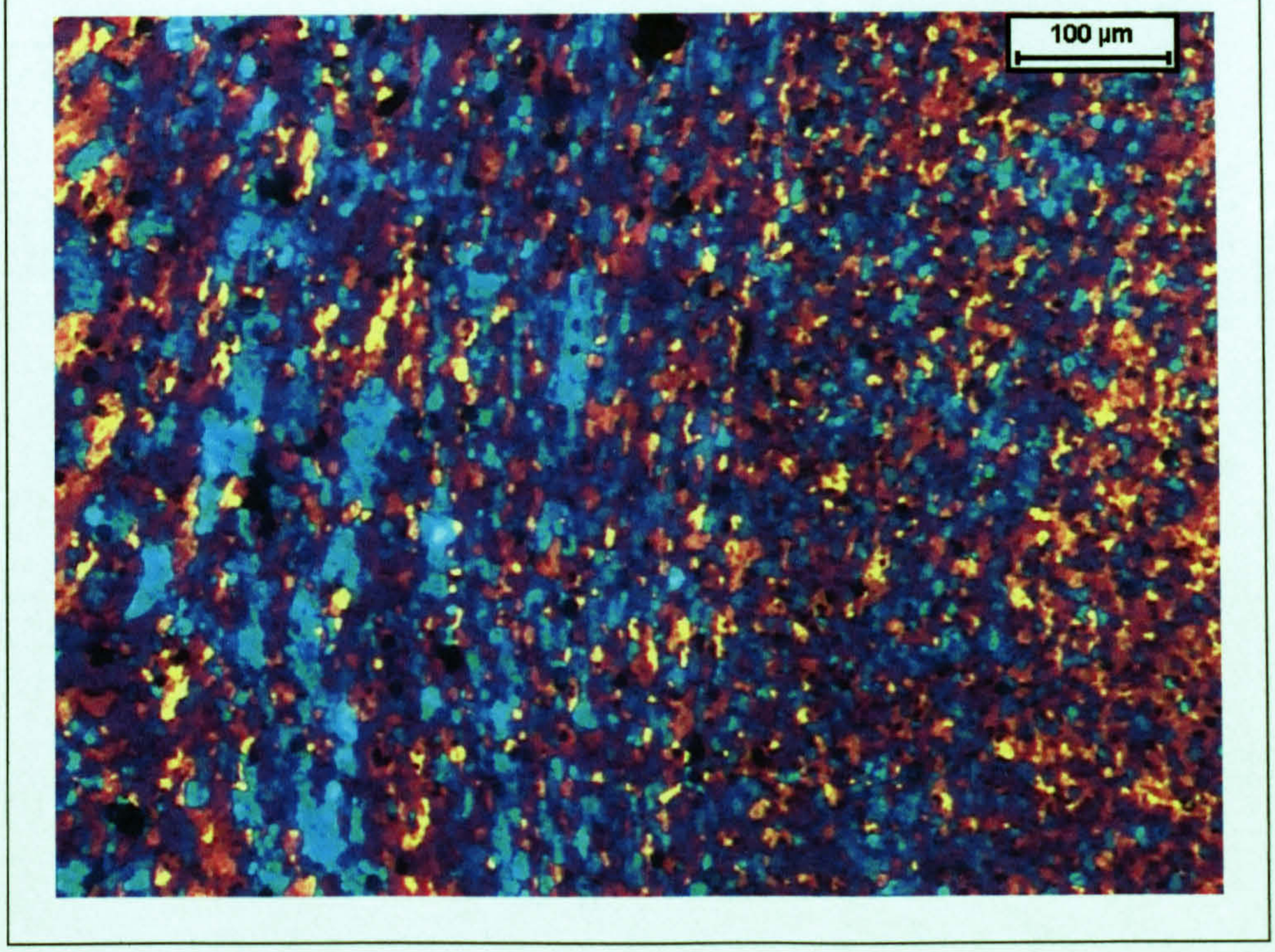

Figure 3.101: FS DP, grains within the weld nugget (right), plastically deformed grains rotated by up to 90° (centre) and grains within the HAZ (upper left), position 4 in Figure 3.98.

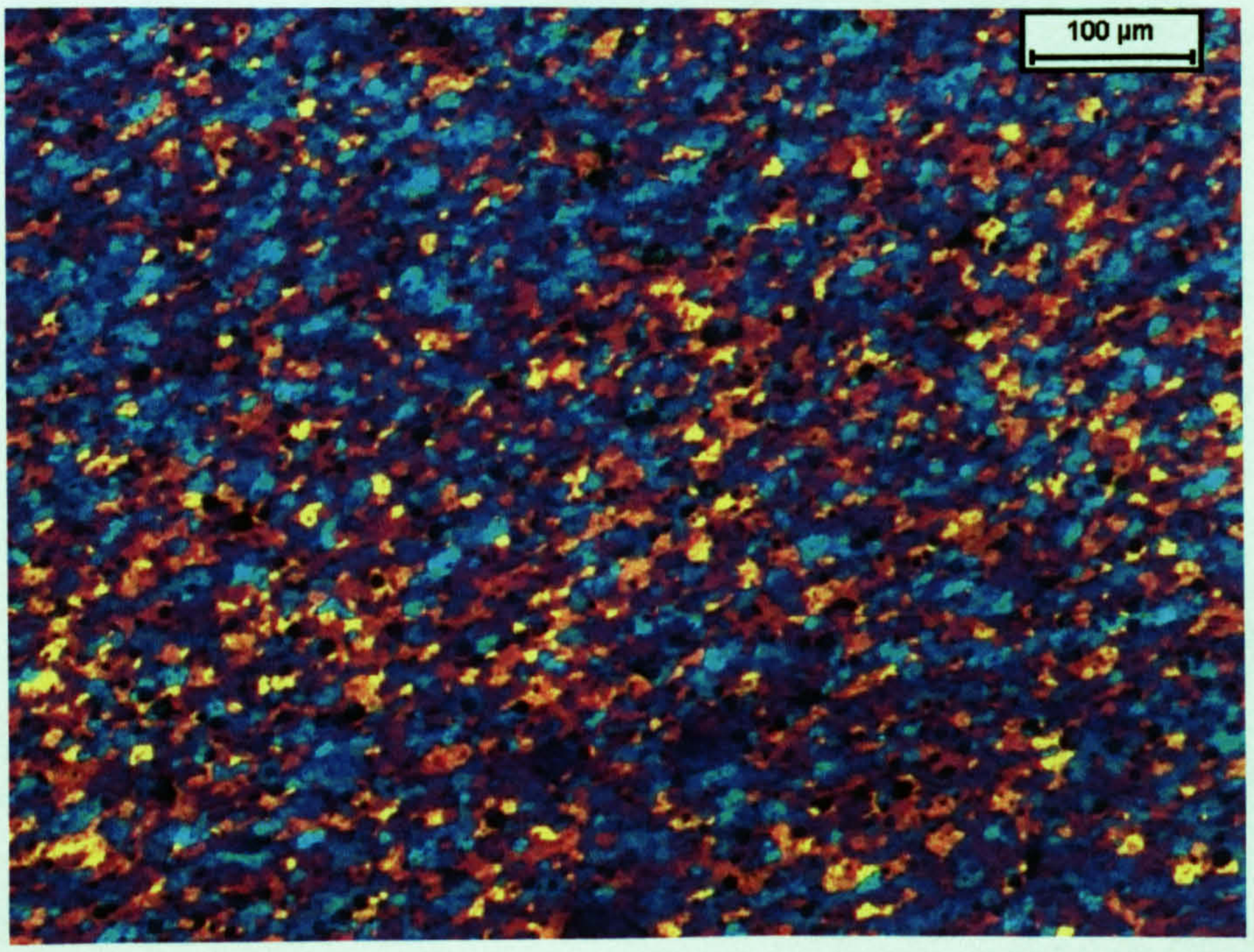

Figure 3.102: FS DP plastically deformed grains within the TMAZ (lower left) and grains within the weld nugget (upper right), position 4 in Figure 3.98.

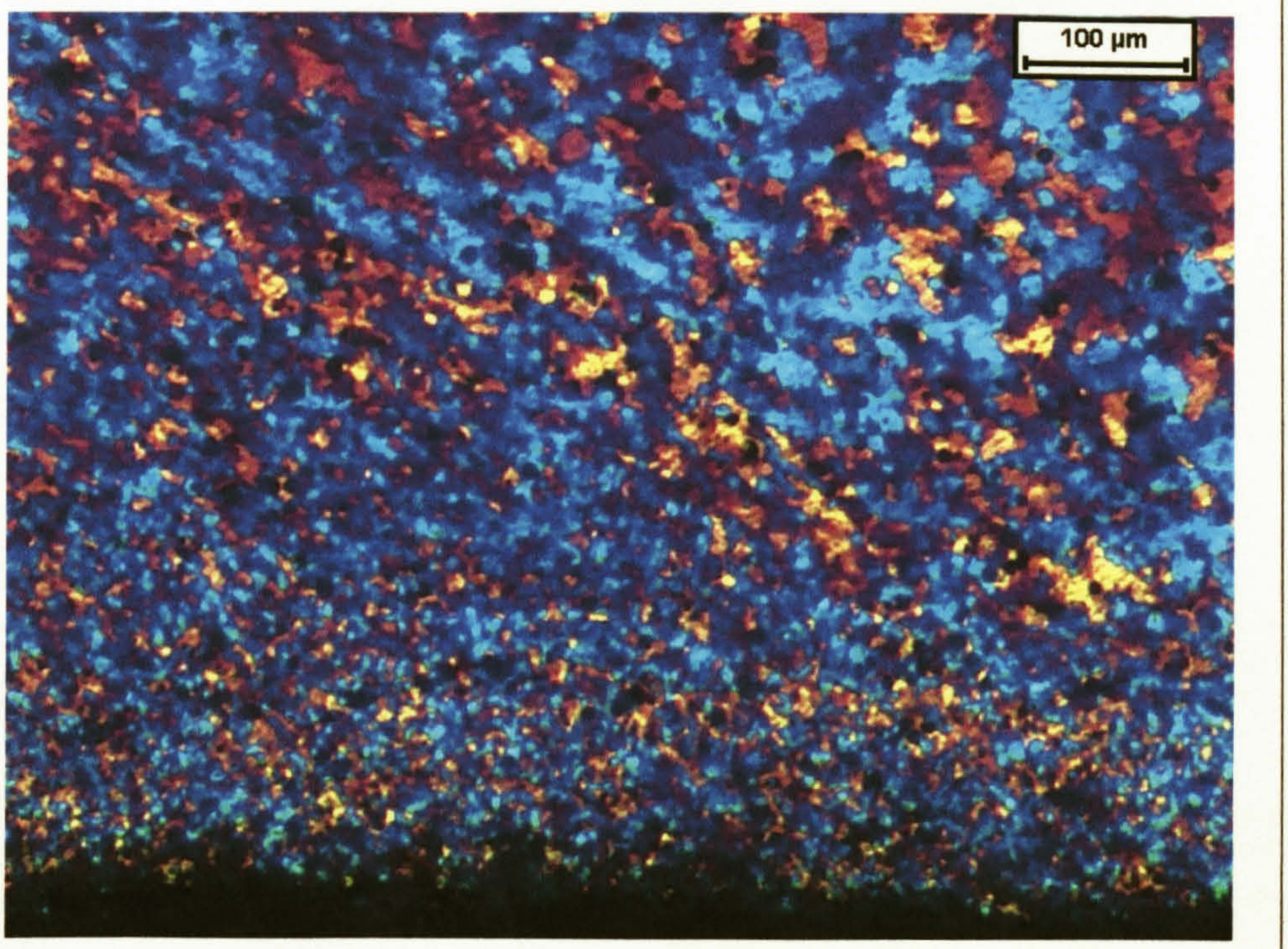

Figure 3.103: FS DP grains within the appendage near to the friction band edge, TMAZ/appendage (left) and HAZ (right), position 5 in Figure 3.98.

3.6.5.2.1 Intermetallic Phases

$FeAl_3$/(Fe,Mn)Al_6 and Mg_2Si intermetallic phases were measured at the edge of the friction band from the 1st pass side to the 2nd pass side, this being the region where fatigue cracks initiated. The intermetallic phases are shown at the edge of the friction band in Figure 3.104 and Figure 3.105. The intermetallic phases found in the weld nugget region were less than the typical grain size of 10 µm diameter, with the maximum area for the $FeAl_3$/(Fe,Mn)Al_6 and Mg_2Si being 196 and 69 μm^2 respectively. Mean sizes were 14.1 μm^2 for the $FeAl_3$/(Fe,Mn)Al_6 phases and 13.2 μm^2 for the Mg_2Si phase. The area densities were 0.70% for the $FeAl_3$/(Fe,Mn)Al_6 and 0.19% for the Mg_2Si.

Phase	Area examined (mm^2)	No. of particles	Phase size (μm^2)						Area density (%)
			Min	Max	Mean	Median	Std. Dev.	Total area	
$FeAl_3$/(Fe,Mn)Al_6	3.533	1747	1.1	196	14.1	7.7	17.8	24594	0.70
Mg_2Si		515	3.7	69	13.2	10.0	9.5	6820	0.19

Table 3.24: Size and distribution of Mg_2Si and $FeAl_3$/(Fe,Mn)Al_6 phases in an AA 5383-H321 FS DP weld.

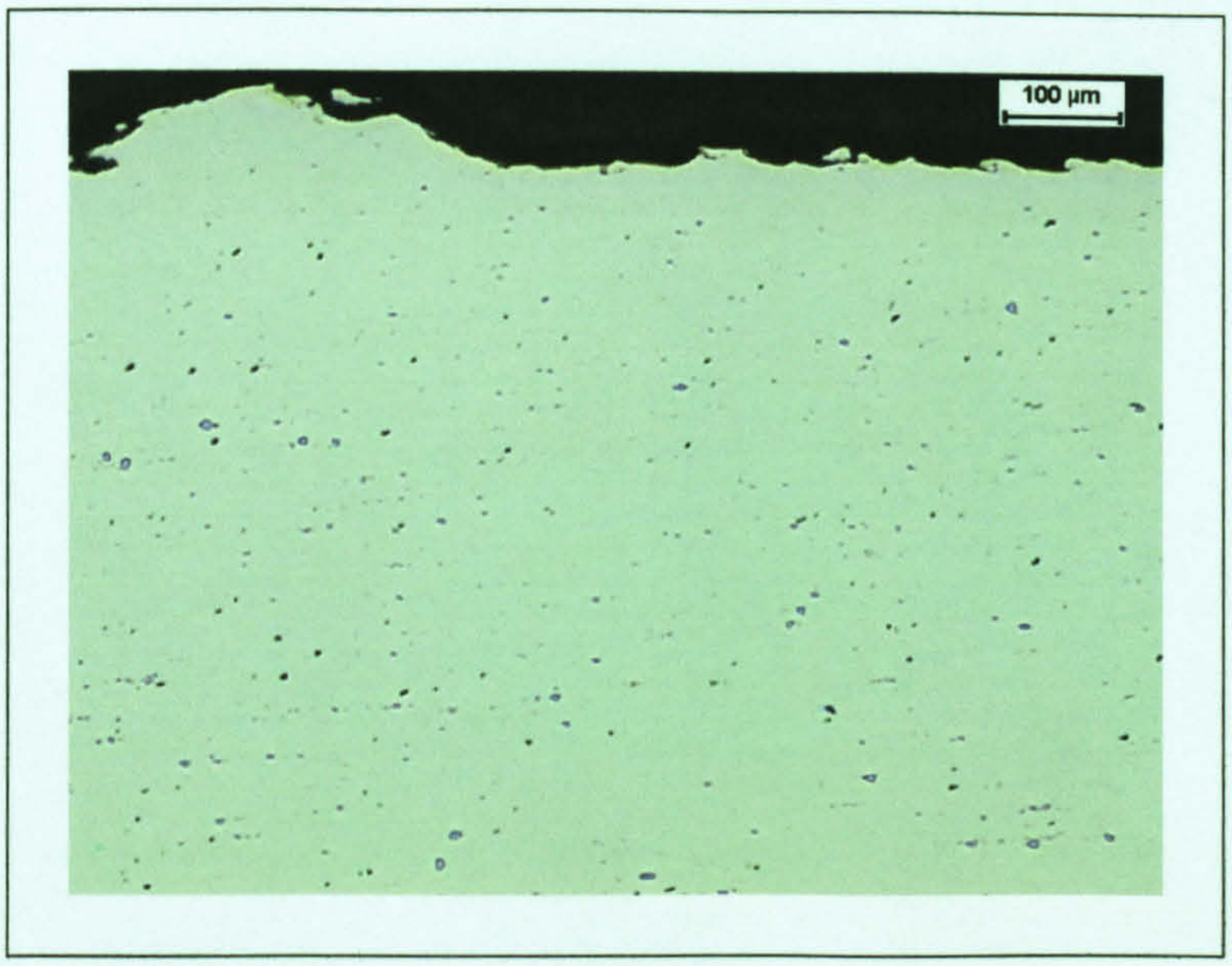

Figure 3.104: FS DP weld intermetallic phases at the edge of the friction band.

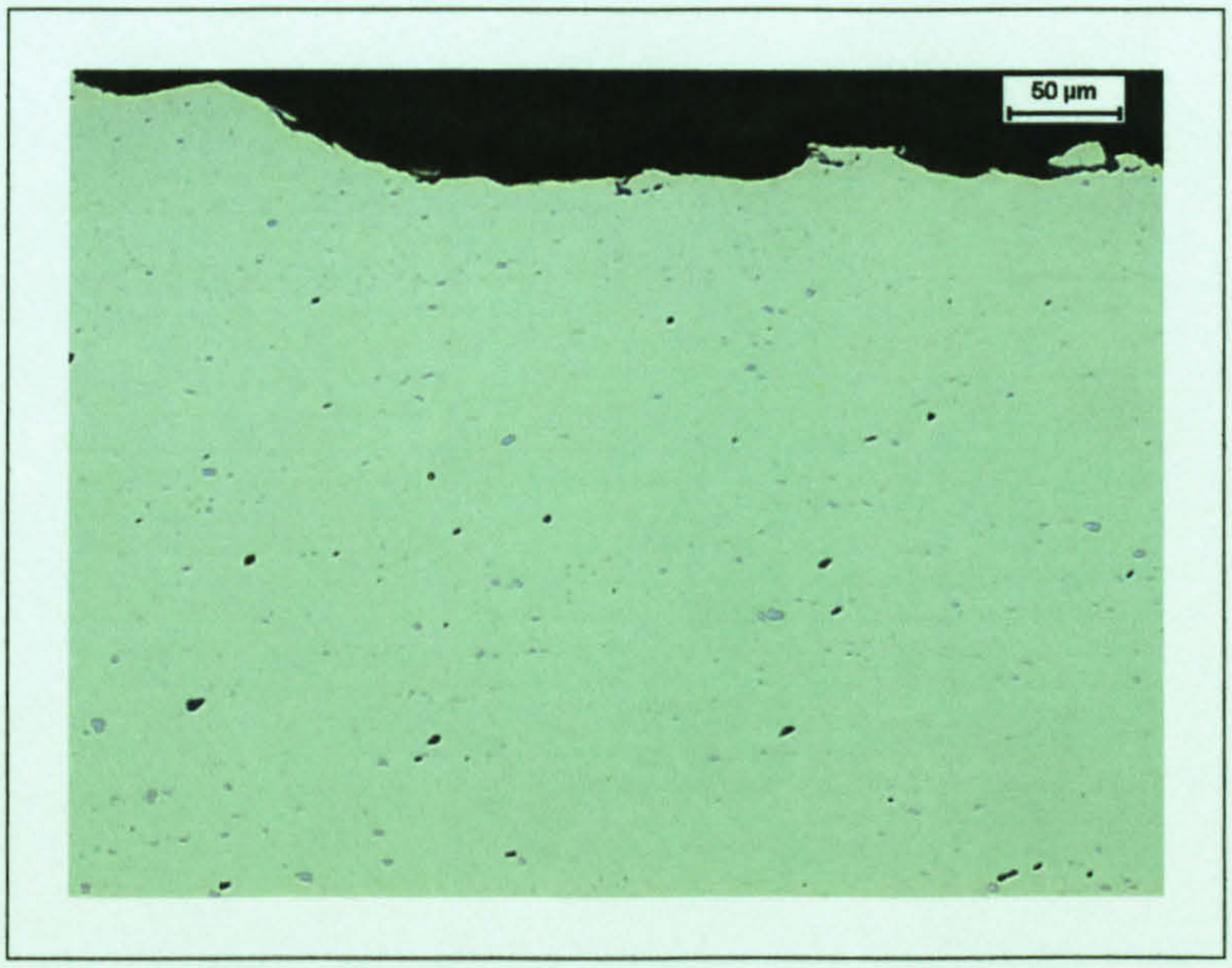

Figure 3.105: Detail of FS DP weld intermetallic phases at the edge of the friction band.

A linear distribution of intermetallics was observed in the weld nugget, as shown in Figure 3.106 and Figure 3.107; the dark colour of the intermetallics suggests that they consisted of the Mg_2Si phase. It was assumed that the distribution was related to the rotational movement of the tool during the welding process. The weld appendage also exhibited an area of increased density of intermetallics as shown in Figure 3.108; the grey and dark colours suggesting that both the $FeAl_3$/$(Fe,Mn)Al_6$ and Mg_2Si phases were present. As with the linear distribution it was assumed that the rotational movement of the pin/tool shoulder was the cause, although the exact reason remained unknown at the time of writing.

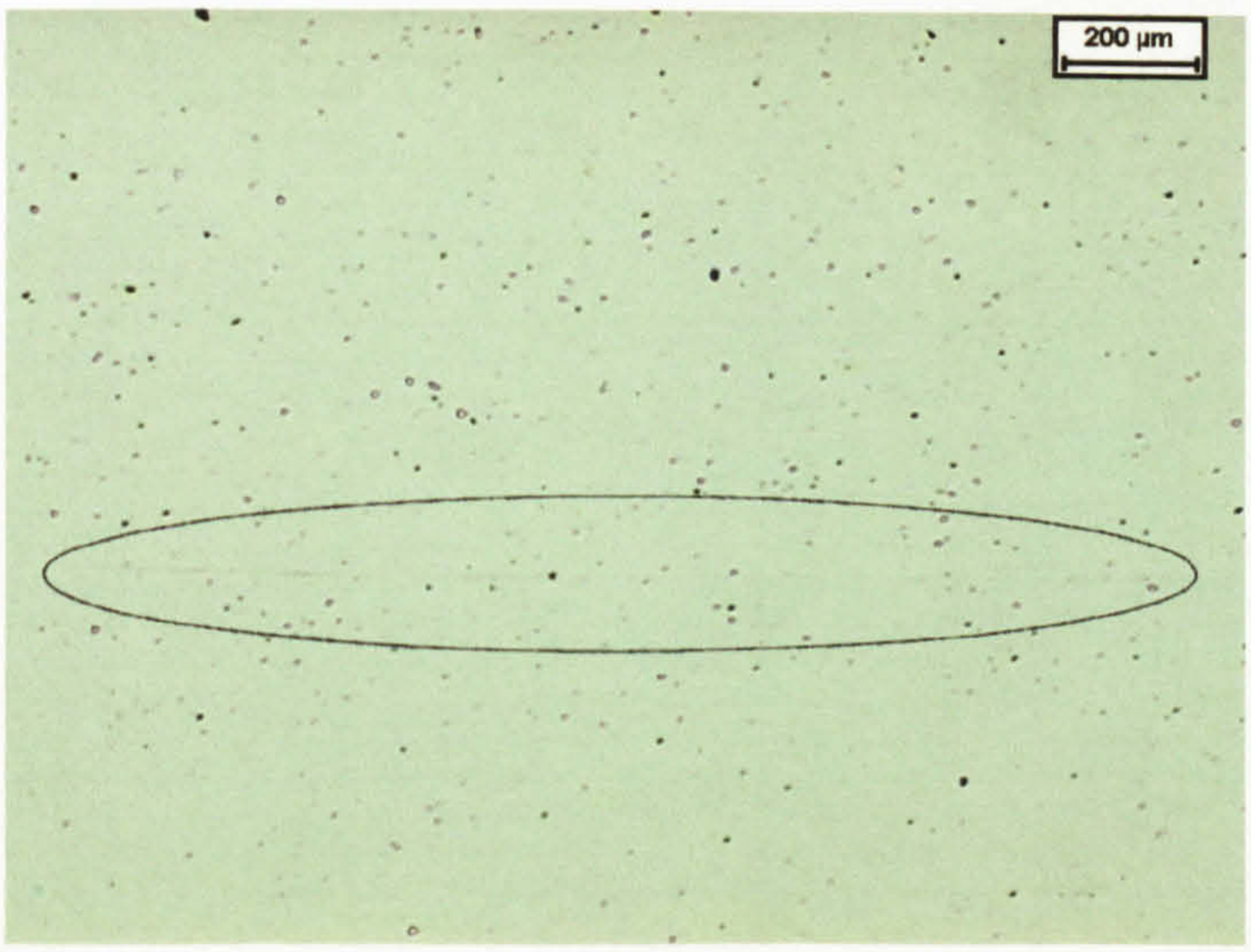

Figure 3.106: Linear distribution of intermetallic phases within the weld nugget (outlined) of FS DP weld.

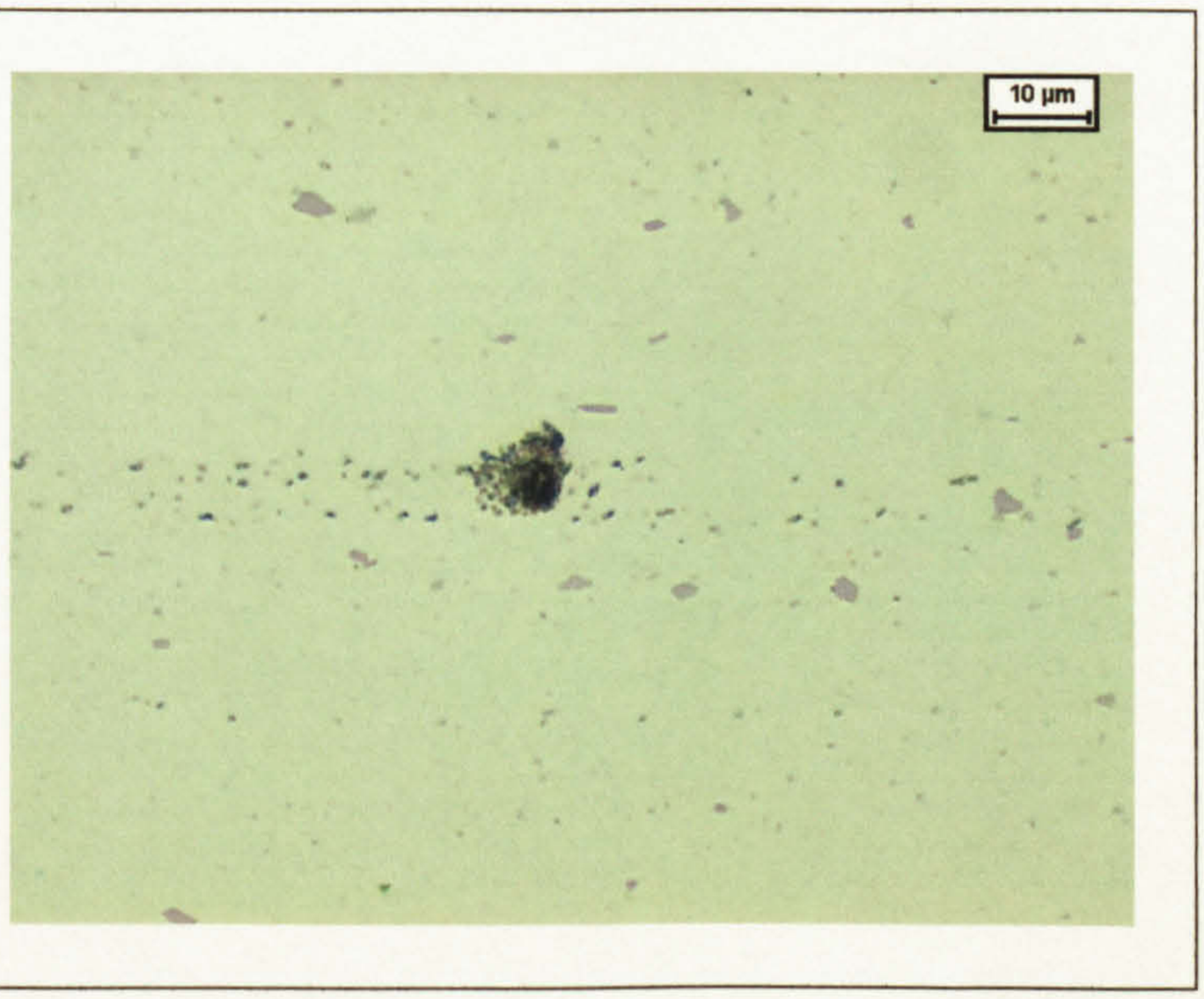

Figure 3.107: Detail of linear distribution of intermetallic phases within the weld nugget of FS DP weld.

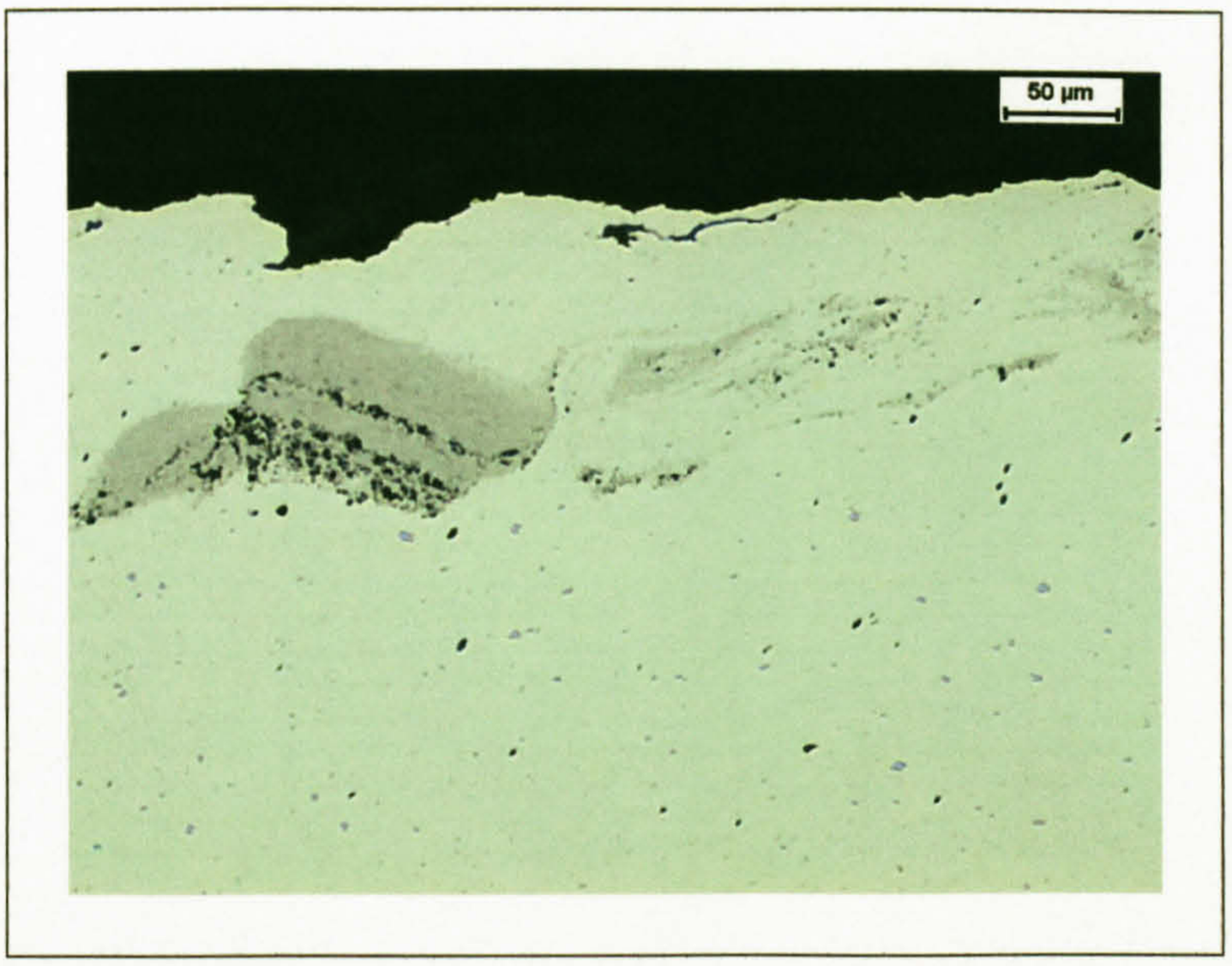

Figure 3.108: Intermetallics in the FS DP weld appendage.

3.6.5.3 Mechanical Properties

3.6.5.3.1 Microhardness

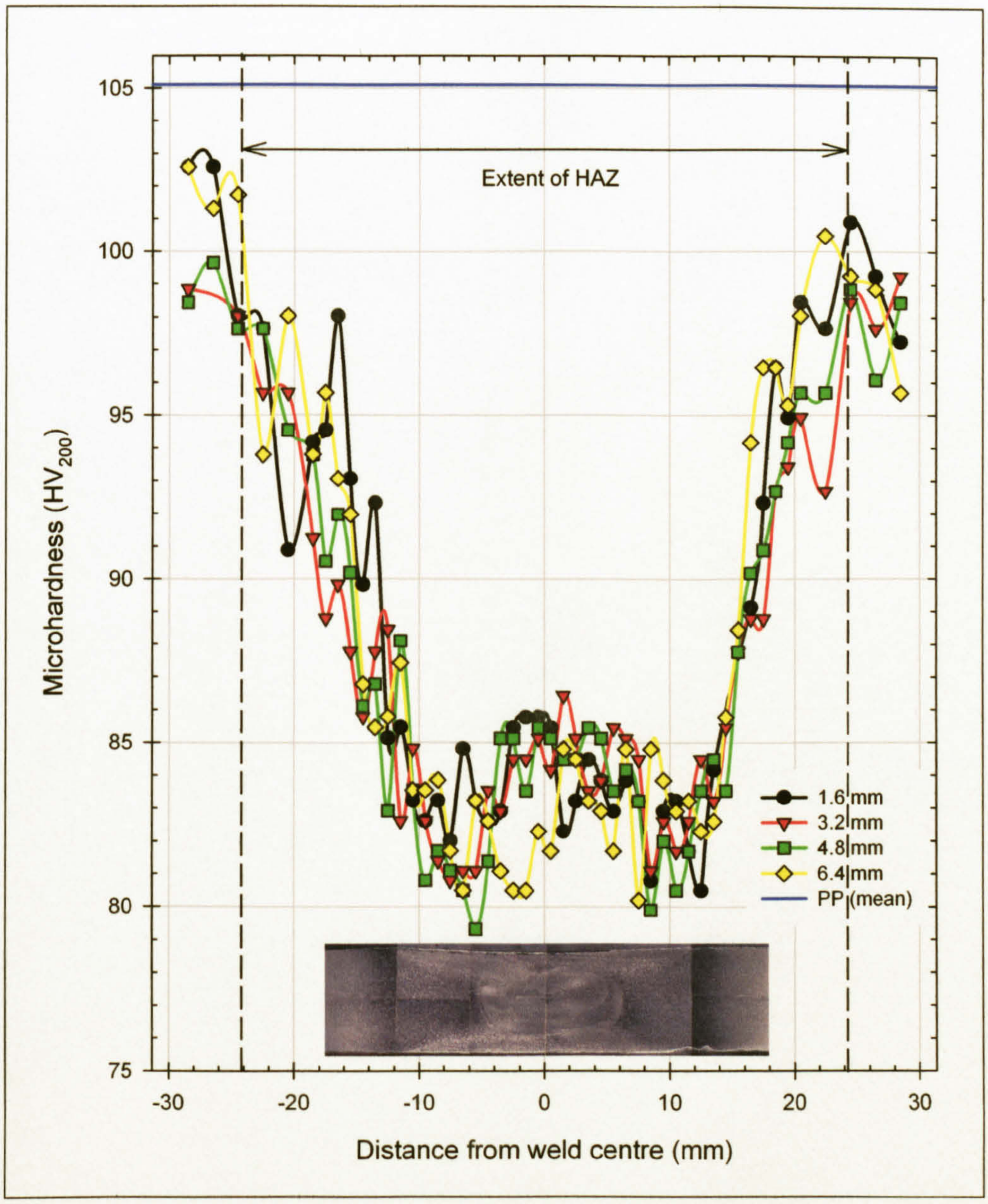

Figure 3.109: Microhardness results for FS DP butt weld, weld with respect to the weld position (values in the legend refer to distance from the 2nd pass surface).

Microhardness measurements for the FS DP weld, as shown in Figure 3.109, returned minimum values of 82.5 HV_{200} at distances of approximately ±10 mm from the centre of the weld. A slight increase, to 85 HV_{200}, was evident at the centre of the weld. A swift change between the parent plate hardness and that of the HAZ was evident, this occurred at a distance of approximately ±24.5 mm from the weld centre. No through thickness variations in the microhardness were evident.

3.6.5.3.2 Tensile Properties

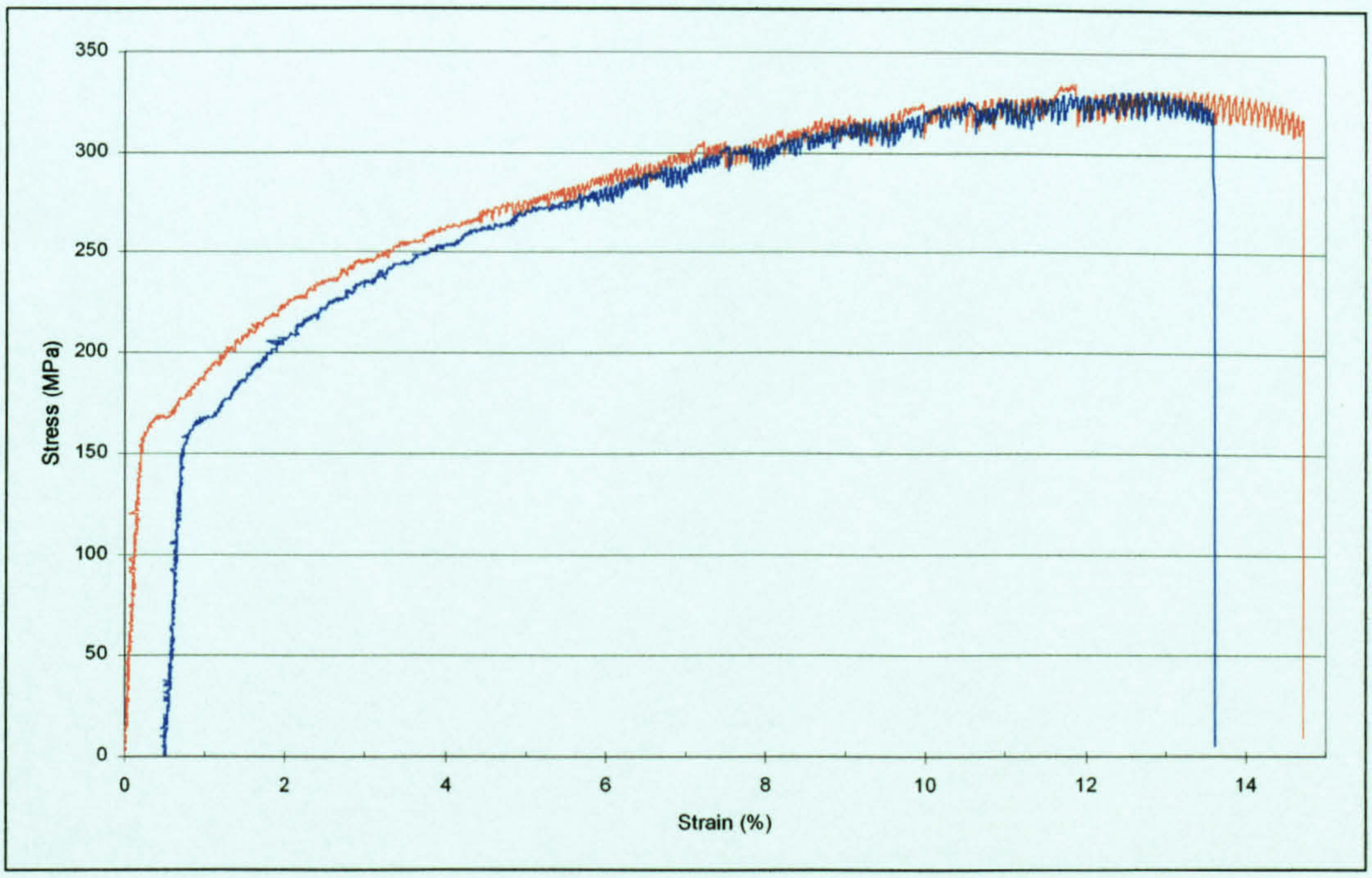

Figure 3.110: Stress/strain plots from monotonic uniaxial tensile tests of FS DP welded AA 5383-H321.

The stress/strain plots from the uniaxial monotonic tensile testing of FS DP welded AA 5383-H321 were as shown in Figure 3.110, with the mechanical properties derived from those shown in Table 3.25. An initial linear elastic response was evident, returning an elastic modulus of 70.3 GPa. A yield point was evident and the limit of proportionality was measured at 156 MPa, the 0.2% proof stress returning a value of 168 MPa. The tensile strength of the welded alloy was 333 MPa, at a strain of 11.9%, whilst failure occurred at a strain of 13.9% and a stress of 319 MPa. Failure occurred in shear near to the edge of the friction band, with the shear surface extending into the TMAZ. Both the specimens tested failed near to the 2nd pass advancing side, although further testing would be required to determine whether there was a preference for either the advancing or retreating sides of the weld. Moderate necking was evident as shown in Figure 3.111.

Limit of proportionality (MPa)	$\sigma_{0.1\%}$ (MPa)	$\sigma_{0.2\%}$ (MPa)	σ_{TS} (MPa)	ε_{TS} (%)	$\sigma_{failure}$ (MPa)	$\varepsilon_{failure}$ (%)	E (GPa)
156	163	168	333	11.9	319	13.9	70.3

Table 3.25: Mechanical properties of FS DP welded AA 5383-H321 (mean of two tests).

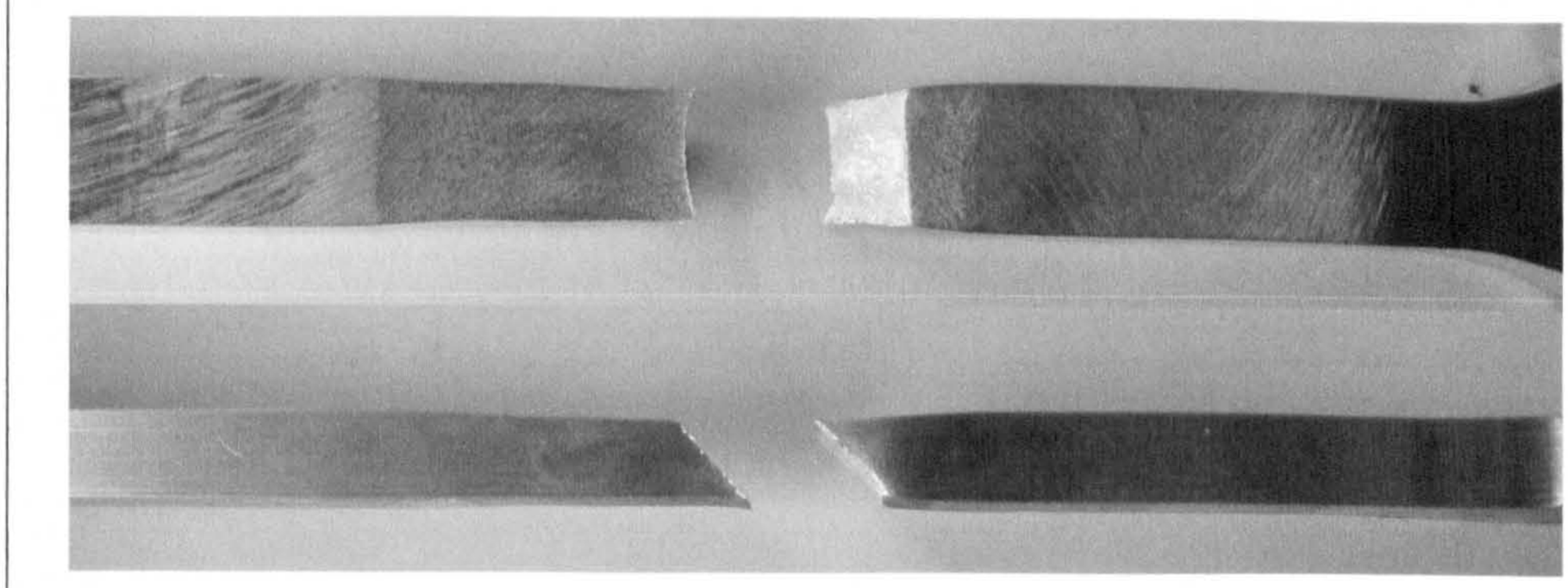

Figure 3.111: Shear failure and necking from monotonic uniaxial tensile testing of a FS DP welded AA 5383-H321.

3.7 Discussion

3.7.1 Weld Geometry

From the examination of the geometry of the MIG and FS welds in AA 5383-H321 it was evident that the two processes resulted in significantly different features; these being due to the fusion process involved in MIG welding and the solid state process involved in FS welding. The variations in the cross section of the MIG and FS welding processes were as shown in Figure 3.112.

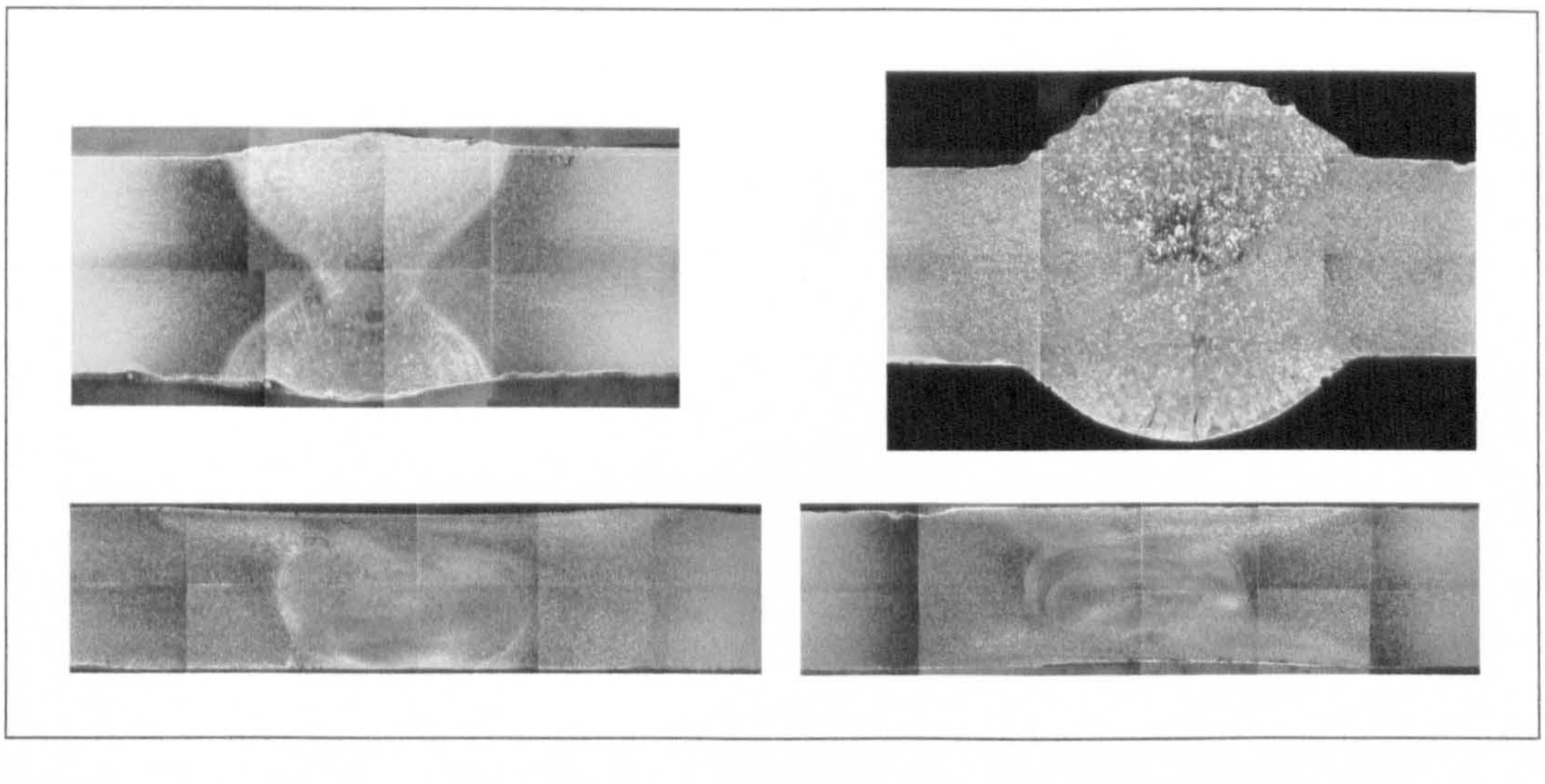

Figure 3.112: Cross sections of MIG LI (upper left), MIG HI (upper right), FS SP (lower left) and FS DP (lower right) (8 mm plate thickness for all welds).

A significant geometric difference was evident between the MIG LI and HI processes; the weld bead produced by the LI method being significantly smaller than that from the HI process. Due to the stress concentration effects of the weld bead it would be expected that the differences in geometry would have an appreciable effect on the fatigue properties of the joint. Several publications, for example[1,2,3,4], have considered the influence of the weld bead angle and radius on the stress concentration and/or fatigue life with varying results. The effects of changes in the weld bead angle and radius on the fatigue strength, as found by Sanders et al[5], are shown in Figure 3.113, and are further commented upon in Section 5.3.1.2, Weld Profile (pages 241 - 250).

---

[1] Aabø, S; Thuestad, JG (1985)
[2] Niu, X; Glinka, G (1987)
[3] Pang, HLJ (1994)
[4] Gurney, TR (1979)
[5] Sanders, WW et al (1965)

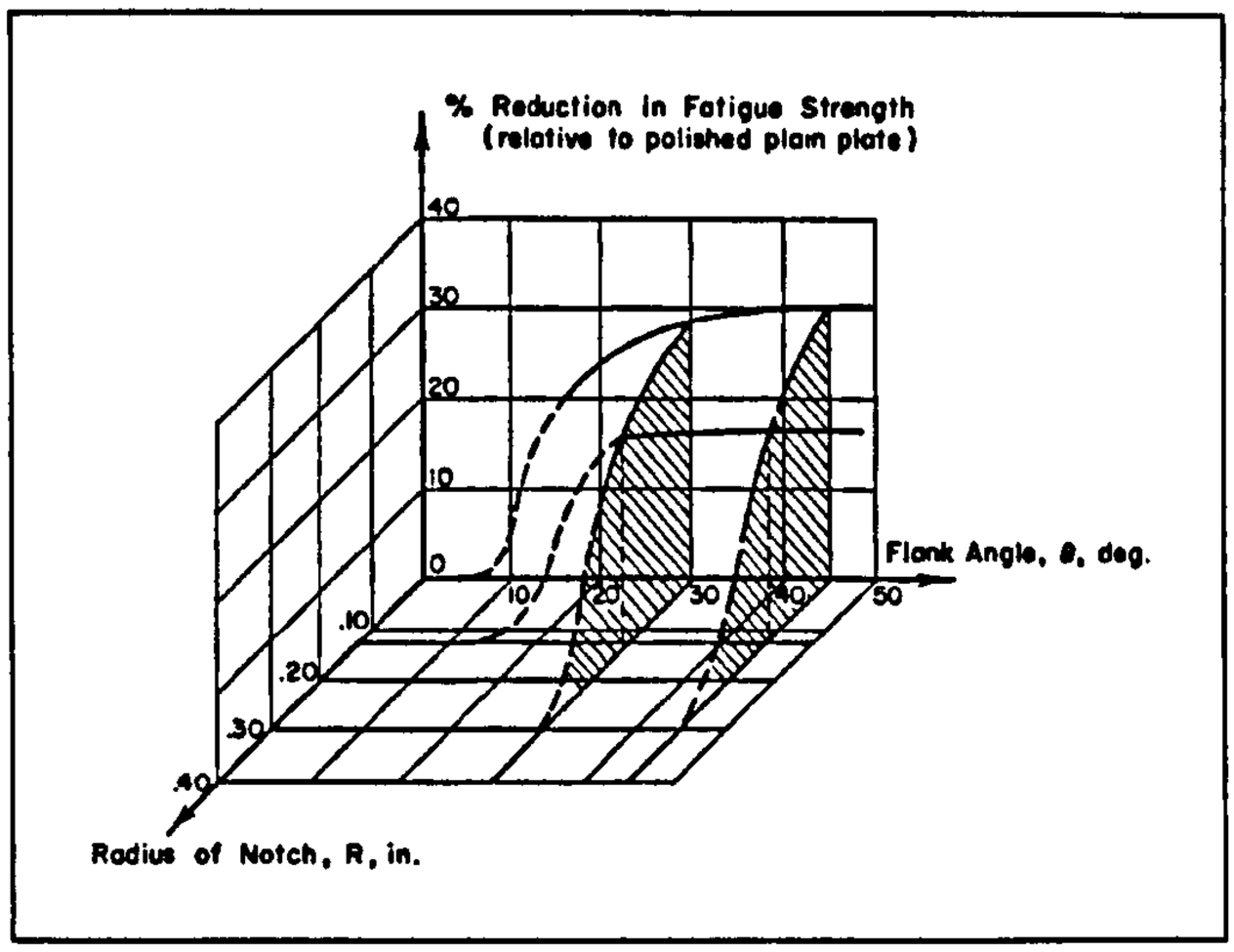

Figure 3.113: The effect of "reinforcement" shape found by Sanders et al[1] in tests on parent metal specimens subjected to R ($\sigma_{min}/\sigma_{max}$) = 0 loading.

There was a significant variation between the weld toe radii and angles for the MIG LI and HI processes, as well as a variation within each process, as shown in Table 3.26, although the values were comparable to those reported by Aabø and Thuestad[2].

	LI		HI	
	Radius (mm)	Angle (°)	Radius (mm)	Angle (°)
Minimum	1.030	6	0.160	30.5
Maximum	4.080	26.5	1.210	51.5
Mean	2.381	13.9	0.641	39.7

Table 3.26: MIG LI and HI weld toe radii and angles.

The general consensus with respect to the weld toe radii and angles is that the smaller the radii and larger the angle the greater the stress concentrating effect. The values obtained for the two processes indicate that the stress concentrating factor will be significantly greater for the HI process and therefore the fatigue strength of this weld will be reduced in contrast to the LI weld. From work undertaken on T-butt welds by Niu and Glinka[3] the weld toe radius has a greater effect on crack initiation and the angle on crack growth. The values obtained for the two processes indicate that both the crack initiation and subsequent crack growth will be greater for the MIG HI process in comparison to the LI one, again resulting in a decrease in its fatigue strength.

[1] Sanders, WW et al (1965)
[2] Aabø, S; Thuestad, JG (1985)
[3] Niu, X; Glinka, G (1987)

In contrast to the MIG welds, the FS welds exhibited similar profiles for both the SP and DP processes. The SP process resulted in a scored surface on the area that had been beneath the tool shoulder and this area exhibited a small reduction in thickness, whilst at the edges of the friction band a raised ridge was evident, the remnants of material extruded during the process and then ground away post weld. The backing plate side was slightly raised above the parent plate and had a flat surface. The reduction in thickness due to the FS SP process ranged from 0 - 230 μm. The 2nd pass side of the DP process exhibited a surface that was comparable to the friction band surface of the SP process, with both the scored surface and raised ridges being evident. The 1st pass side was similar in appearance to the backing plate side of the SP process, although with a slightly more profiled surface as a result of the score marks and ridges from the 1st pass, but these were greatly reduced as a consequence of the pressure and heat from the 2nd pass. The FS DP process resulted in a reduction in thickness at the centre of the weld, in comparison to the parent plate, of 175 - 225 μm. The reduction in thickness across the weld regions will result in an increase in the apparent stress, when loaded uniaxially, when compared to that experienced by the parent material. The scored surface resulting from the tool shoulder will also result in stress concentration, with the outcome of this being an increase in the likelihood of crack initiation and a subsequent reduction in the fatigue strength.

3.7.2 Microstructure

The grains in the parent plate were pancake shaped, due to the rolling process, and had an average length ranging from 30 - 100 μm, the width ranging from 15 - 25 μm for the TS plane. A comparison of grains within the weld beads and weld nuggets, for the MIG and FS processes respectively, is shown in Figure 3.114. Grains within the LI weld metal were equiaxed in geometry and had an average diameter of around 100 μm, whilst those in the HI weld metal were also equiaxed and had an average diameter of around 225 μm. The grains within the weld nuggets of the FS processes were also equiaxed in geometry, although notably smaller than those in the MIG welds, having an average grain size of approximately 10 μm for both the SP and DP processes. The grain sizes found in the weld nuggets of the FS welds compare well with those cited by several authors, for example[1,2,3,4,5], with grain sizes stated as ranging from 2 - 15 μm depending on the alloy and process parameters employed. Li[6] stated that the grain sizes varied from 15 - 5 μm from the top of the weld to the bottom respectively, although this did not appear apparent in the SP and DP welds investigated; some grains within the nugget area of the SP welds

[1] Rhodes, CG et al (1997)
[2] Threadgill, P (1997)
[3] Liu, G et al (1997)
[4] Murr, LE et al (1997)
[5] Karlsson, J et al (1998)
[6] Li, Y et al (1999)

had experienced grain growth and were significantly bigger than the typical 10 µm grain size observed.

Small grain sizes are generally associated with an increase in strength, due to dislocations on intersecting planes interacting with each other and obstructing motion[1]. It would therefore be expected that the FS welds would exhibit a greater strength, within the weld nugget, than the MIG welds, within the weld metal. Several authors, for example[2,3,4,5,6], have reported tensile and yield strengths for FS welds approaching, or equal to, that of the parent material. The reduction in the dislocation density of the weld nugget, reported by Flores et al[7], Liu et al[8] and Murr et al[9], which would be expected to reduce the strength, appears to be less influential. MIG welds are renowned for having tensile strengths significantly lower than that of the parent material due to the annealing effect of the welding process[10].

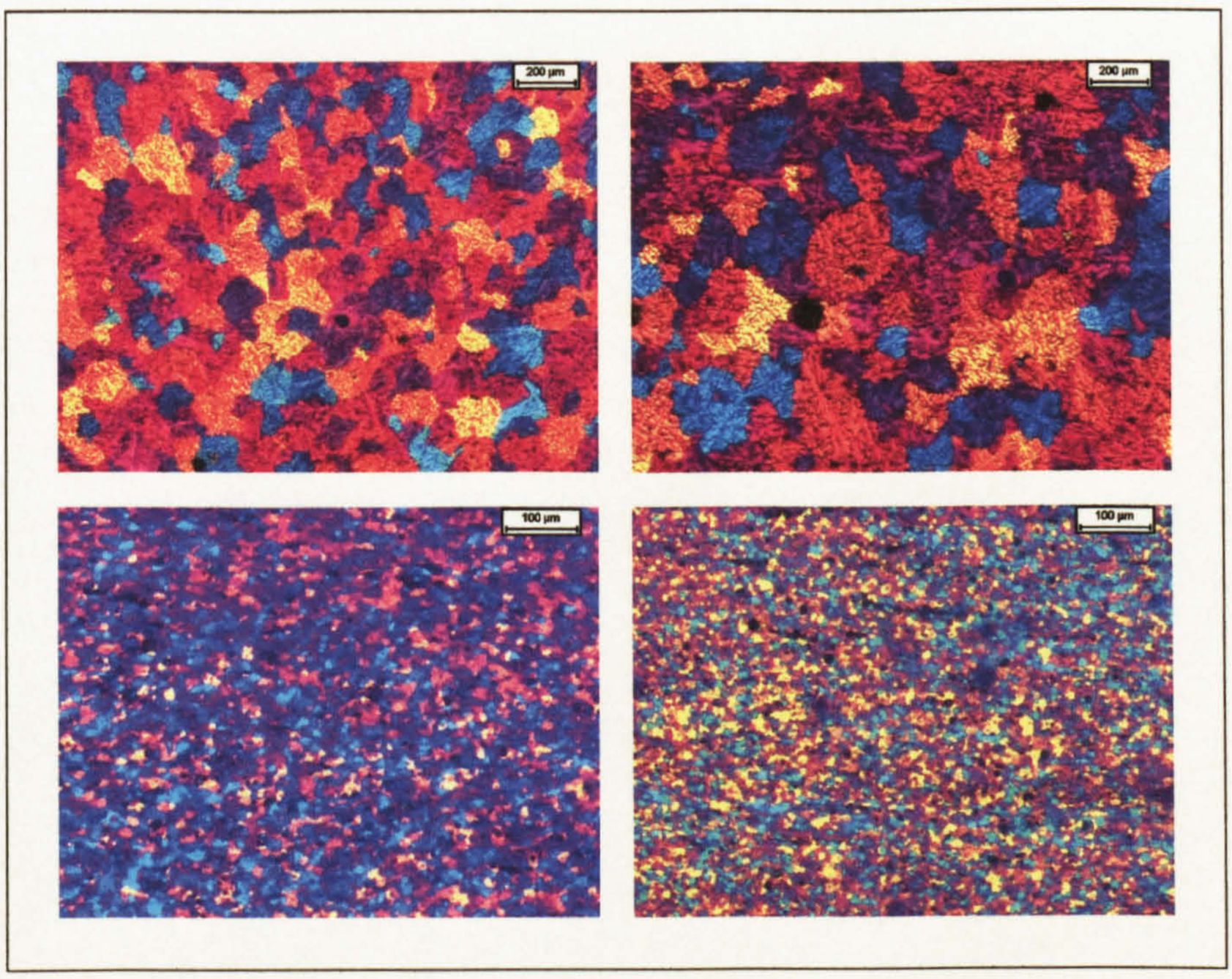

Figure 3.114: Grains within the weld bead, upper left MIG LI (100 µm) and upper right MIG HI (225 µm), and within the weld nugget, lower left FS SP (10 µm) and lower right FS DP 10 µm).

[1] Ashby, MF; Jones, DRH (1980)
[2] Biallas, G et al (1999)
[3] Dalle Donne, C; Biallas, G (1998)
[4] Hashimoto, T et al (1998)
[5] TWI (1999)
[6] Dawes, MG et al (2000)
[7] Flores, DV et al (1998)
[8] Liu, G et al (1997)
[9] Murr, LE et al (1998b)
[10] Lancaster, JF (1999)

Surrounding the weld nugget of the FS welds was an area that had experienced both thermal and mechanical processing. The grains within this region were of a similar size to those within the HAZ, with an average width of approximately 50 µm and length of 75 - 100 µm for the LT plane. The mechanical processing experienced by the grains meant that many had been rotated by up to 90°.

Columnar grains were evident in the MIG welds where fusion had occurred with the parent material, the grains then growing into the weld pool as it cooled. The columnar grains were at their longest where the rate of cooling was the lowest, 300 µm and 200 µm for HI and LI welds respectively, at the center of the weld. Where the cooling rate was rapid, at the surface, the columnar grains were less evident. The grains within both the LI and HI welds generally exhibited a dendritic structure; representing cellular or columnar dendritic growth for the columnar grains in the fusion zone and equiaxed dendritic growth for grains within the weld metal[1]. In the MIG HI weld the columnar grains that existed in the second pass, at the interface with the first pass, were observed to exhibit a planar, rather than dendritic structure. Except for the different energy inputs, which are the cause of the planar structure, the only significant difference between the HI and LI welding processes was that the LI welds were back gouged prior to welding, whilst the HI welds were not. The significance of the planar grains is unknown, although it is unlikely that they would have any influence on the fatigue strength.

The HAZ grain sizes were similar for both the MIG and FS processes; elongated in geometry, although less so than the parent material, and typically 50 x 25 µm in size for the LT plane. Due to the different energy inputs, different sizes of HAZ were observed for the two MIG processes; but for the FS welds, the zones were of a similar size, but not geometry. The MIG HI process resulted in a HAZ that extended approximately 15 mm from the centre of the weld, 8 mm from the weld toe, whilst the HAZ associated with the MIG LI process, extended approximately 10 mm from the weld centreline, 5 mm from the weld toe. For both energy inputs, the changes in the HAZ were more evident nearer to the weld, near equiaxed grains were evident at a distance of 2 mm and 5 mm from the weld toe for the LI and HI respectively. Optical examination of the microstructure of the FS welds suggested that both processes resulted in a HAZ that extended the same distance, 7 mm, beyond the edge of the friction band, this was confirmed by the microhardness results. Figure 3.6 (page 24) suggested that the HAZ extended over different areas with respect to the distance from the tool shoulder surface and microstructural observation confirmed this. The SP process HAZ reduced in size as the through thickness distance from the tool shoulder increased. Similarly, the DP process exhibited a similar trait, but from both sides of the welded plate; the reason for this was

---

[1] Solomon, HD (1993)

that the frictional heat generated by the tool shoulder was greater directly beneath the tool shoulder.

3.7.2.1 Intermetallic Phases

The main intermetallic phases in both the parent and welded material were Mg_2Si and $FeAl_3$/(Fe,Mn)Al_6 (or one of its derivatives). The intermetallic phases are of particular importance because their mechanical properties will differ from those of the matrix, the outcome of this being that they can lead to localised stress concentrations and subsequently crack initiation sites as shown in Figure 3.115.

	AA 5383-H321 Parent Plate					
	LT plane (rolled surface)			LS plane (mid plane)		
	Max. (μm^2)	Mean (μm^2)	Area density (%)	Max. (μm^2)	Mean (μm^2)	Area density (%)
$FeAl_3$/(Fe,Mn)Al_6	543	18.9	1.19	264	16.6	0.98
Mg_2Si	197	27.6	0.30	123	18.6	0.24
	AA 5383-H321 MIG Welds (TS plane)					
	Low input (weld toe)			High input (weld toe)		
	Max. (μm^2)	Mean (μm^2)	Area density (%)	Max. (μm^2)	Mean (μm^2)	Area density (%)
$FeAl_3$/(Fe,Mn)Al_6	269	16.4	0.79	265	16.2	0.68
Mg_2Si	98	15.4	0.21	96	13.7	0.22
	AA 5383-H321 FS Welds (TS plane)					
	Single pass (weld centre)			Double pass (friction band edge)		
	Max. (μm^2)	Mean (μm^2)	Area density (%)	Max. (μm^2)	Mean (μm^2)	Area density (%)
$FeAl_3$/(Fe,Mn)Al_6	93	9.3	0.71	196	14.1	0.70
Mg_2Si	46	13.9	0.13	69	13.2	0.19

Table 3.27: Distribution of intermetallics in AA 5383-H321 parent plate and MIG and FS butt welds.

From Table 3.27 it was evident that the $FeAl_3$/(Fe,Mn)Al_6 intermetallic was more prevalent than the Mg_2Si phase; area densities of 1.0 - 1.2% in the parent plate and 0.7 - 0.8% in the welds for the $FeAl_3$/(Fe,Mn)Al_6 and 0.3% in the parent plate and 0.1 - 0.2% in the welds for the Mg_2Si were observed. The largest intermetallic particles were found on the LT surface of the parent material, in contrast to those found on the LS plane of the parent plate and weld cross sections (TS plane). This was probably related to the rolling process in a similar manner to that in which the pancake shaped grains of the parent plate were formed.

The maximum sizes of both phases were similar for the parent material on the LS plane and the MIG welds, 260 - 270 μm^2 and 100 - 120 μm^2, for the $FeAl_3$/(Fe,Mn)Al_6 and Mg_2Si phases respectively. In contrast to this the FS welds had smaller maximum sized particles, with the values varying for the two welds. The SP weld returned a maximum

$FeAl_3$/(Fe,Mn)Al_6 phase of 93 μm^2 and 46 μm^2 for the Mg_2Si phase, whereas the DP process returned values of 196 μm^2 for the $FeAl_3$/(Fe,Mn)Al_6 and 69 μm^2 for the Mg_2Si. This variation was to some extent related to the SP measurements being undertaken at the centre of the weld and the DP ones at the edge of the friction band, in both cases where fatigue failure was observed. The SP measurements include the weld nugget region, where it was probable that the intermetallic phases would have been broken up by the welding process.

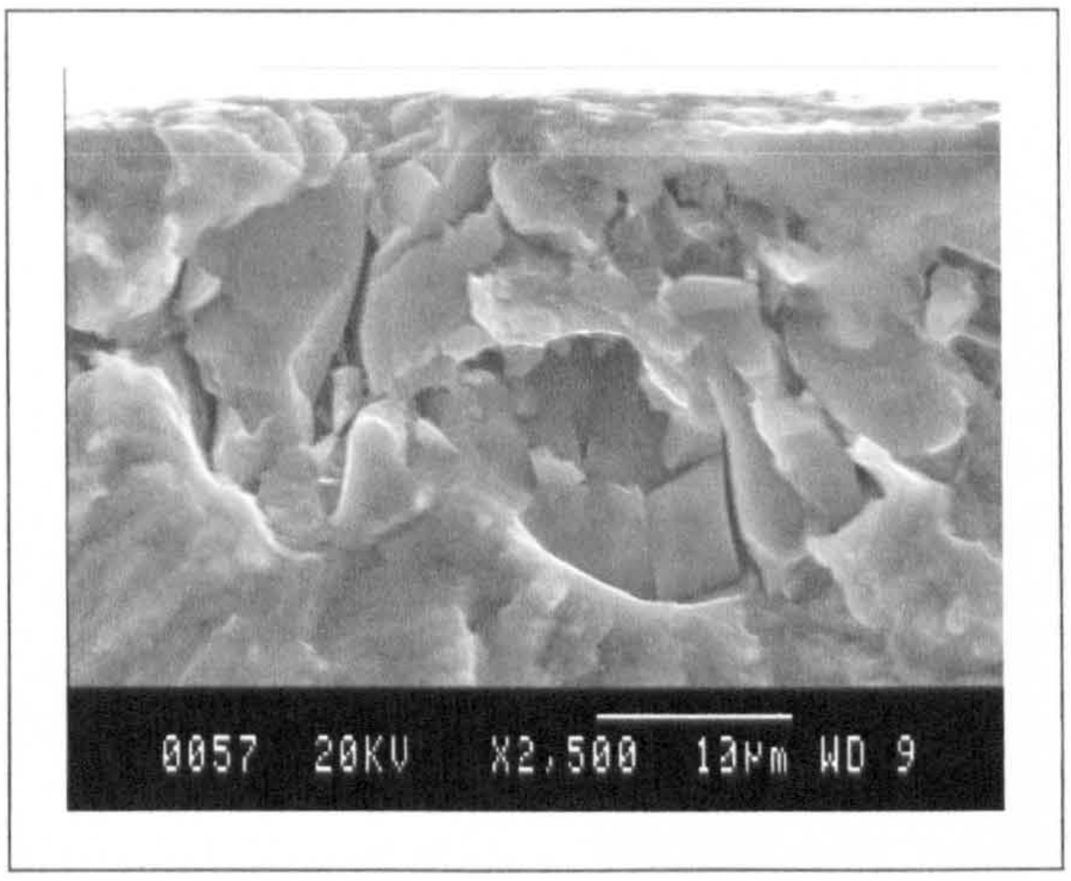

Figure 3.115: Fatigue crack initiated by an intermetallic phase in a MIG LI small crack specimen.

Mean sizes for the intermetallics were similar for the parent plate, LS plane, and both MIG welds for the $FeAl_3$/(Fe,Mn)Al_6 phase, 16.2 - 16.6 μm^2. The Mg_2Si phase in the parent plate had a greater mean value, 18.6 μm^2, in contrast to 15.4 μm^2 and 13.7 μm^2 for the MIG LI and HI welds respectively. The FS welds exhibited mean values that were less than those found in the parent material, for the $FeAl_3$/(Fe,Mn)Al_6, 9.3 μm^2 (SP) and 14.1 μm^2 (DP), and for the Mg_2Si, 13.9 μm^2 (SP) and 13.2 μm^2 (DP). As with the maximum sized particles it was thought that the smaller mean values were related to the breaking up of the intermetallics by the welding process.

Area densities for the parent plate, LS plane, were higher for the $FeAl_3$/(Fe,Mn)Al_6 phase, 1.0%, than both welding processes, 0.7 - 0.8%. The Mg_2Si phase area densities were comparable for the parent plate, LS plane, and the MIG welds and the FS DP weld, 0.19 - 0.24%, but the FS SP weld returned a value of 0.13%. The reduced values of the $FeAl_3$/(Fe,Mn)Al_6 area density suggest that they were broken into particles below the threshold of technique used to measure them, in the case of MIG welds by the thermal cycle and by both the mixing process and thermal cycle of the FS process. The reduced area densities for the Mg_2Si phase found in the FS welds suggest that these particles are less susceptible to the thermal cycle, but more susceptible to the mechanical effects of

the mixing process. This would also explain the lower area density returned by the SP weld as the measurements were undertaken across the weld centreline, including the weld nugget, in contrast to the DP where they were taken at the edge of the friction band.

3.7.2.2 Weld Porosity

Porosity may be considered to constitute a crack like defect, the half crack length being equal to the pore radius, and in a comparable manner to that of the intermetallic phases, it may act as a crack initiation site. Whilst porosity may be considered to be a crack like defect it may not necessarily affect the fatigue strength, the stress concentrating effect of the weld toe generally being considered to be the overriding factor in the fatigue strength of MIG welds. Although a combination of the alloy and large pores or pores present in the weld toe region may influence the fatigue properties, as may pores within the weld metal on welds that have been dressed. Porosity was evident in both the MIG welds as shown in Figure 3.116. The area density was near identical for both the LI and HI processes, 0.30% and 0.29% respectively. The distribution of the pores was notably different between the two processes, with a similar number of pores in both weld passes for the LI process, but significantly more pores in the second pass of the HI weld. Assuming spherical pores, the maximum pore radius measured was 25% less for the HI weld, 74 µm, in contrast to the 101 µm found in the LI weld. Mean pore radii were near identical for both processes, 42 µm and 43 µm, for the LI and HI welds respectively. The porosity was only determined for one surface from each MIG weld type, but the subsequent emergence of a pore in a LI short crack growth specimen, with a pore diameter of 1.45 mm, as shown in Figure 3.49 (page 63), indicated that pores subsequently greater than those determined on the two surfaces existed, even though the welds were radiographically examined.

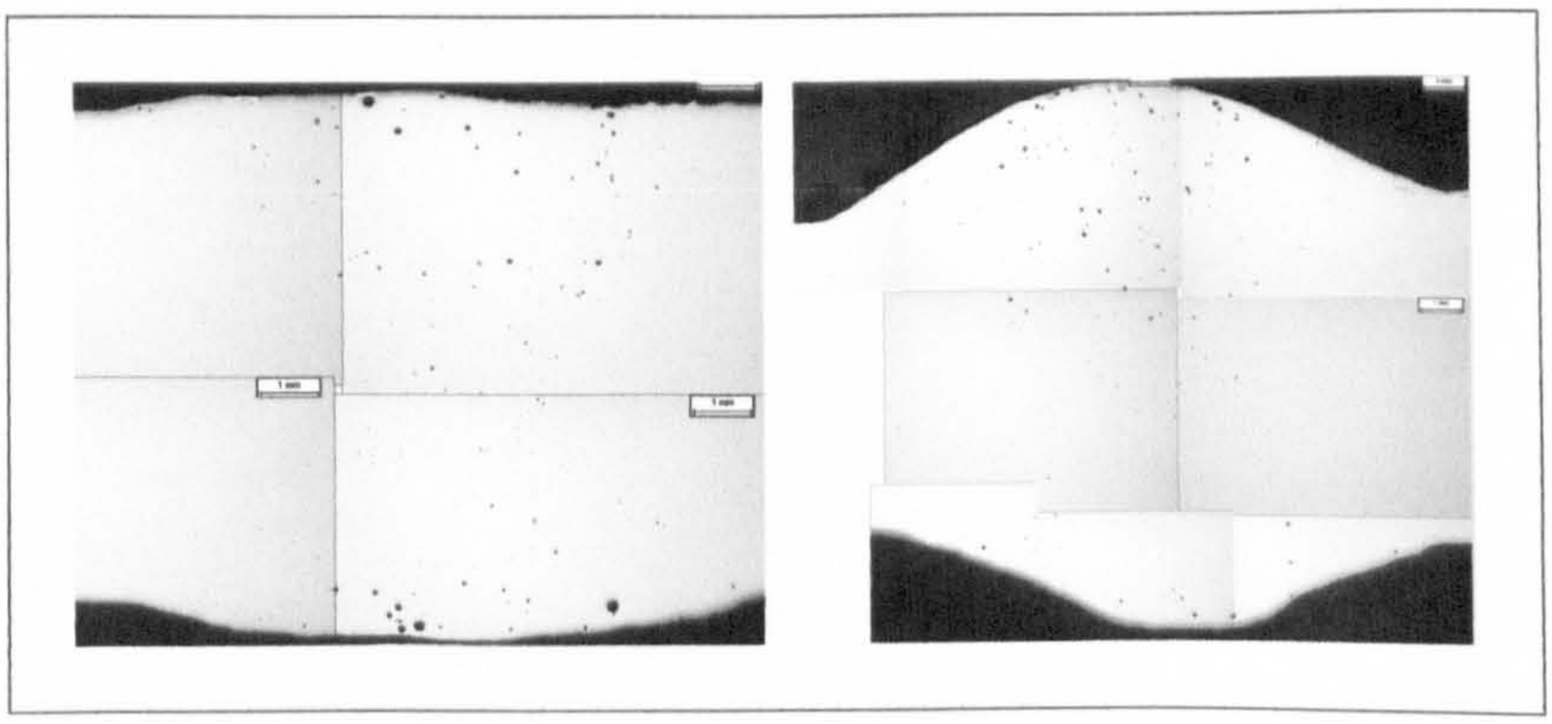

Figure 3.116: Porosity in MIG weld butt joints in AA 5383-H321, (LI input, left; HI, right).

3.7.2.3 Partial Fusion Defects

Although porosity is not a problem in FS welds, what appeared to be PFD were apparent in the SP weld. As with the pores found in the MIG weld the half crack length may be

considered to be equal to half the length of the defect. As with porosity, PFD may not affect the fatigue strength of joint, this depending on which plane they lie and the direction of applied loading, but crack like defects of up to 700 µm length were observed on the fatigue fracture surfaces of FS SP welds, as shown in Figure 3.89 (page 93), although the initial size of these defects was unknown and they were not detected by radiological examination.

3.7.3 Mechanical Properties

3.7.3.1 Microhardness

Mean values for the four microhardness scans for the MIG and FS processes are shown in Figure 3.117. It was evident from the plots that there were significant differences between both the MIG, LI and HI, and the FS, SP and DP, processes, as well as between the MIG and FS processes. The MIG LI and HI showed a similar drop in value from that of the parent plate, 105 to 88 HV_{200}, but the drop occurred over a broader region in the case of the HI weld. The LI process resulted in the reduced microhardness values over a distance of approximately ±11 mm from the weld centre, whilst the HI process resulted in a similar drop, but over a distance of approximately ±15 mm. The reason for this was the increased energy input of the HI process, the thermal cycle causing annealing of the alloy and the increased energy input of the HI process resulted in this occurring over a greater area.

The FS processes also resulted in differing values between the two processes. The SP process had minimum values of 86 HV_{200} recorded at distance of approximately ±14 mm from the weld centre. In contrast, the DP process had minimum values of 82 HV_{200} at distances of approximately ±10 mm from the weld centre. Initially it was thought that this was due to the tool shoulder being narrower for the DP process, but subsequent release of the weld tool specifications by TWI disproved this theory and the cause remained unclear at the time of writing, although the larger pin diameter of the SP weld, 10 mm in contrast to 8 mm for the DP weld, may have been responsible. Both the SP and DP welds exhibited slightly increased values, in comparison to their minimum, at the weld centre, with measurements of 88 and 84 HV_{200} respectively. The position of minimum hardness in the FS welds is of particular importance as Karlsson[2] states that tensile failure of a FS welded AA 6082 occurred at the point of minimum hardness and SN testing of the DP welds undertaken by the author produced similar results.

It was evident from Figure 3.117 that the distance from the weld centre of the reduced (as opposed to the point of minimum hardness) hardness was greater for the FS processes than the MIG ones. The distance for the FS processes being approximately ±22 mm for the SP and ±24.5 mm for the DP, whilst that for the MIG HI was approximately ±15 mm

and ±11 mm for the LI, although the FS welds had still not attained the hardness of the parent plate at distances of ±30 mm from the weld centreline. It was also apparent that the reduced microhardness values for both the MIG processes and the FS SP process were comparable, 86-88 HV_{200}, whilst those for the FS DP process were notably lower, 82 HV_{200}.

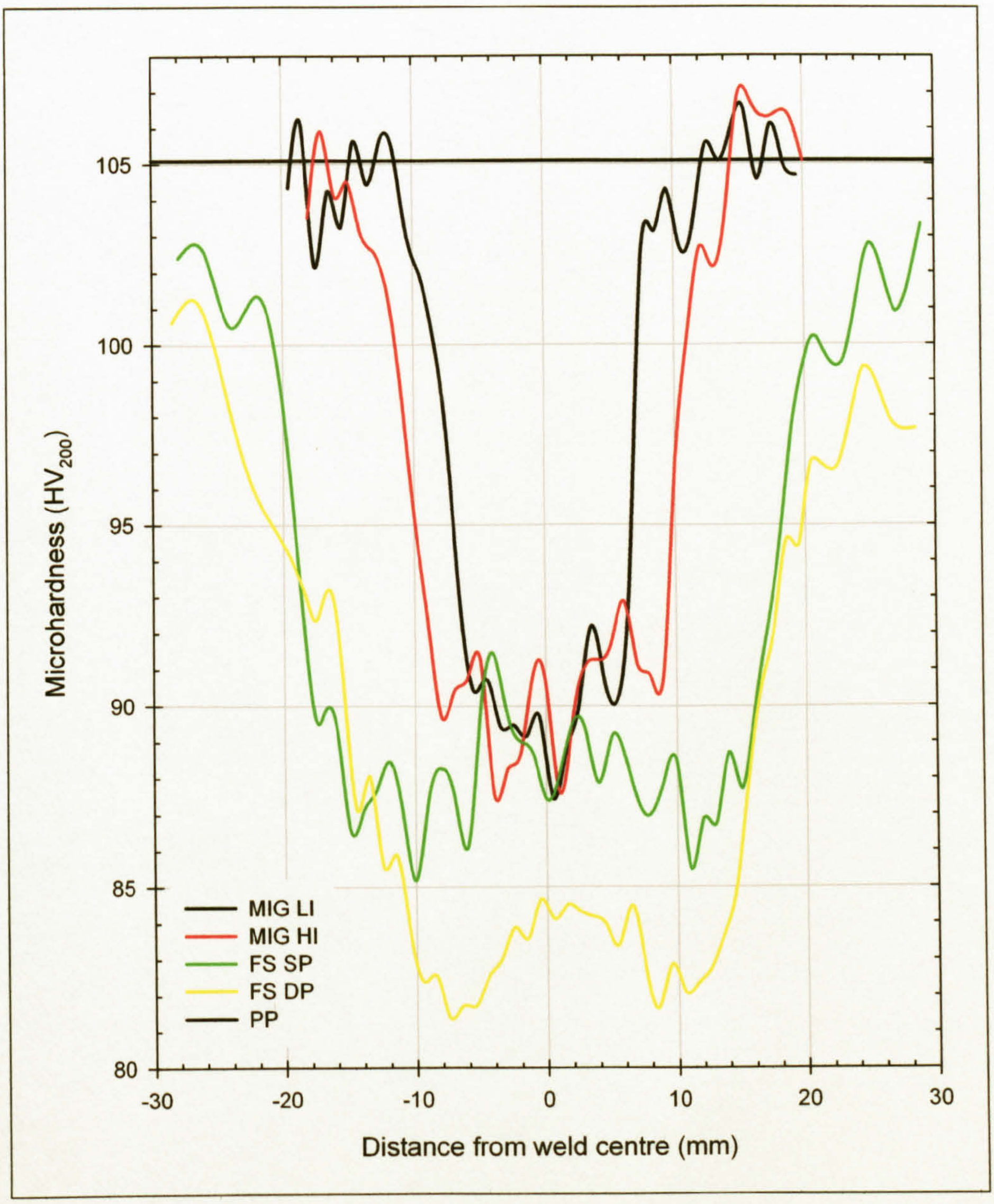

Figure 3.117: Microhardness mean values for AA 5383-H321 parent plate and MIG LI and HI and FS SP and DP butt welds.

3.7.3.2 Tensile Properties

The tensile properties of the of the AA 5083-H321 and AA 5383-H321 8 mm thick plate and the MIG, LI and HI, and FS, SP and DP, butt welds in the 5383 plate were as shown in Table 3.28 and stress/strain plots derived from monotonic uniaxial tensile testing in

Figure 3.118. Both the alloys exhibited directional properties related to the rolling direction of the plate. The properties were typically enhanced for the loading applied // to the rolling direction for values up to the 0.2% proof stress, but the tensile and failure strength were greater when the load was applied |- to the rolling direction. The 5383 alloy was considered to be a similar alloy to the 5083, but with enhanced mechanical properties and this was evident from the results obtained. The butt welded joints showed a reduction in mechanical properties when compared to the AA 5383 plate. A reduction in strength of 53% for the limit of proportionality for the MIG LI weld, and 46% for the FS SP weld was measured, the 0.2% proof stress returning reductions of 36% and 41% for the MIG LI and FS SP respectively. The FS welds had greater limits of proportionality than the MIG welds, but this was reversed for the 0.2% proof stress. The tensile strength of the butt welds was slightly lower than that of the 5383 parent plate, but the applicable strain was greater. The mechanical properties obtained for the FS welded joints compared well with those detailed by Kallee[1] for an AA 5083-H321 and shown in Table 3.29.

Specimen	Limit of proportionality (MPa)	$\sigma_{0.1\%}$ (MPa)	$\sigma_{0.2\%}$ (MPa)	σ_{TS} (MPa)	ε_{TS} (%)	$\sigma_{failure}$ (MPa)	$\varepsilon_{failure}$ (%)	E (GPa)
5383 //	268	272	275	370	9.5	359	13.0	71.1
5383 |-	242	254	263	385	14.8	371	16.4	70.2
5083 //	261	263	264	350	10.2	341	12.0	69.3
5083 |-	205	238	250	348	13.5	338	14.7	65.5
MIG LI	125	160	175	332	9.6	313	10.3	74.6
MIG HI	131	167	183	350	10.7	339	11.0	66.9
FS SP	144	157	163	336	13.7	313	16.2	70.4
FS DP	156	163	168	333	11.9	319	13.9	70.3

Table 3.28: Mechanical properties of AA 5383-H321 and AA 5083-H321 parent plate and MIG and FS welded plate (mean of two tests per specimen).

Poisson's ratio (AA 5383-H321), $\nu = 0.324$

Material	$\sigma_{0.2\%}$ (MPa)	σ_{TS} (MPa)	Elongation (%)
5083-H321 Parent	249	336	16.5
5083-H321 FS Weld	153	305	22.5

Table 3.29: Mechanical properties of AA 5083-H321 parent plate and FS weld[1].

[1] Kallee, S (2000)

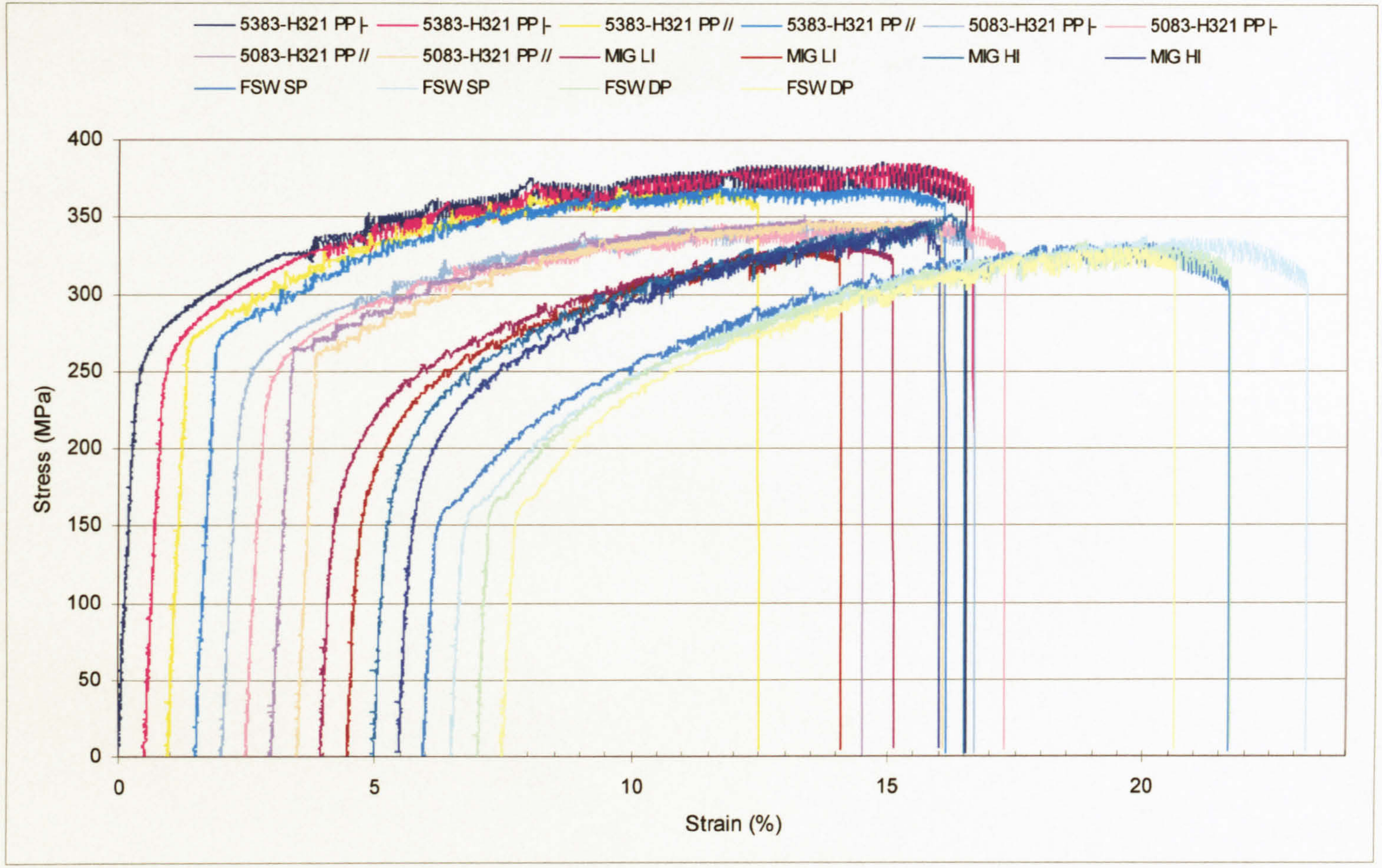

Figure 3.118: Tensile properties of AA 5083-H321 and AA 5383-H321 plate and MIG, LI & HI, and FS, SP & DP, butt welded AA 5383-H321 (all 8 mm thick plate).

4. Residual Stresses and Strains

4.1 Abstract

The following section details the magnitudes and directions of the residual strains and stresses induced by the MIG and FS welding processes. Initial analyses were made using a strain relaxation technique, hole drilling, with measurements being undertaken on the as-welded 1000 x 500 x 8 mm (l x w x t) plates; measurements were undertaken at the weld toe and at incremental distances away from this for the MIG welds and at the edge of the friction band and at incremental distances away from this for the FS welds. Subsequently a more comprehensive analysis of the residual strains was undertaken for the FS welds utilising synchrotron radiation; allowing a comprehensive mapping of the residual strains in 150 x 190 x 8 mm (l x w x t) specimens in both the as-welded and fatigue loaded state.

4.2 Introduction

Residual stresses/strains are defined as stresses/strains that exist in a body in the absence of any externally applied load; this absence means that they are self-balancing. They exist within many materials, although their magnitudes and directions are dependent upon the processes to which they have been subjected. In the case of metallic materials, processes which result in plastic deformation will give rise to their formation; large stresses resulting from processes including welding, rolling and extrusion, whereas drilling and milling result in smaller more localised ones.

Residual stresses induced by the welding process, when considered in conjunction with any other applied loading, can have a substantial effect on fatigue strength, brittle fracture, stress corrosion and structural behaviour. Near surface residual stresses/strains associated with thermal welding processes are of particular importance because they are frequently of yield or greater magnitude in the direction of the weld and fatigue failure of welded structures usually occurs at the weld site, in either the weld metal or at the weld toe. Residual stresses/strains may also approach yield magnitude in the direction transverse to that of the weld. Friction stir welding also involves heating of the parent material due to adiabatic shearing and friction, although the maximum temperature attained is only around 0.8 T_m, hence it may be thought that the residual stresses would be lower when compared to the MIG process. However, the plastic deformation that characterises FS welding will also induce strains into the material and this may negate any benefit derived from the lower temperatures experienced. It is generally accepted that a tensile residual stress field has a deleterious effect on the fatigue strength if subjected to a tensile load.

Relaxation of residual stresses may occur due to plastic flow resulting from the application of a load; although the extent of the relaxation appears to be related to the magnitude and number of applications of the load, the subsequent reduction in the stress field does not appear to be fully predictable at the time of writing.

The techniques employed in the determination of residual stresses/strains have advanced in recent years. Although the hole drilling technique was initially documented in 1934[1] the procedure has been enhanced through the development of strain gauge rosettes and low stress inducing hole forming techniques. The x-ray diffraction technique has also been enhanced through the development of particle accelerators capable of producing synchrotron radiation, hard x-rays, which are capable of greater penetration than the more commonly used soft x-rays.

---

[1] Mathar, J (1934)

4.3 Literature Review

Residual stresses are stresses that exist within a material without the application of an external load or other stress inducing processes, such as a thermal gradient. As there is no external influence, they are self-equilibrating. Macherauch[1] states that they were initially quantified by Neumann[2] in 1841, subsequently numerous publications have detailed their various effects and properties.

4.3.1 Residual Stresses Induced by Welding

Residual stresses are induced by numerous processes; James and Lu[3] detail these under three headings:

- Plastic deformation or forming (rolling, extruding, forging, shot-peening, etc.).
- Manufacturing processes (machining, welding, grinding, coating, etc.).
- Heat or thermochemical treatments (quenching, nitriding, casting, etc.).

Macherauch[1] classifies residual stresses as being of one of three kinds (the first being frequently referred to as macroscopic and the second and third as microscopic residual stresses):

i. Residual stresses that are nearly homogeneous across large areas (several grains in the case of metals) of material and in equilibrium over the bulk of the material. Changes to the equilibrium of forces and moments of volume containing this type of residual stress will result in a change in its dimensions. Many processes generate residual stresses of this kind; machining, forming, joining, heat treatment etc. Any process that causes inhomogeneously elastic or plastic deformations, the result being strain incompatibilities, results in the production of residual stresses of the this type.

ii. Residual stresses that are described as being homogeneous across a microscopic area (one, or a part of one, grain in the case of metals) of material. Equilibrium is attained through a sufficient number of grains; macroscopic changes of dimensions of a volume only occur if distinct disturbances of this equilibrium occur. Processes that result in the formation of this kind of residual stress are uncommon. Homogeneous materials that exhibit a marked anisotropy of the yield strength and strain hardening of the grains display residual grain stresses of different magnitudes after elastic-plastic deformation. Heterogeneous

---

[1] Macherauch, E (1987)
[2] Neumann, FE; (1841) *referenced by Macherauch, E (1987)*
[3] James, MR; Lu, J (1996)

materials may exhibit residual strains of this type; for example, if variations in the thermal coefficients of expansion exist between the phases of an alloy, annealing of the material will result in their formation.

iii. Residual stresses that are described as occurring on an atomic scale (within a grain in the case of metals); they are inhomogeneous across sub-microscopic areas of the material, equilibrium occurring across small parts of a grain. No macroscopic changes of the dimensions of the material occur if the equilibrium is disturbed. Residual stresses of this type are associated with all types of lattice imperfections, occurring within the grains and at grain boundaries. Any processes that result in changes in the density of dislocations, e.g. plastic deformation, will result in a change in the residual stress state.

The residual stress at a point usually consists of a superposition of the three types.

With respect to welding, Gurney[1] states that residual stresses consist of two types, residual and reaction stresses, but that the generic term residual stress is generally used to describe both types. Reaction stresses are described as stresses in a member that are balanced by the reaction of other members, but are not in equilibrium within the member. In contrast, residual stresses are defined as being self-balancing within the member.

Berge and Eide[2] separated residual stresses induced by welding into two types, short and long-range stresses. Short-range stresses are defined as existing only close to the weld and being self-balanced across the member. The stresses are described as being large, typically of yield or above magnitude, and having large through thickness gradients. They are caused by the thermal expansions and contractions that occur during the welding process, but can easily be reduced through heat treatment or by local yielding caused by peak loads. In contrast, long–range stresses are uniform throughout the structure and self-balanced within the structure. The stresses are small, when compared to the yield stress, and are not easily reduced through heat treatment or peak loads. Their origin is from a combination of the welding process and the restraint.

4.3.2 Measurement Techniques

Mathar[3] is credited with devising the method of determining residual stresses by measuring the relaxation of strains around a drilled hole. The claimed benefits of the technique were that it could be used on a wider range of geometries, the method used to

---

[1] Gurney, TR (1979)
[2] Berge, S; Eide, OI (1982)
[3] Mathar, J (1934)

produce the relaxation was the same for various geometries and that the technique was less destructive than the alternatives available at the time. The technique described involved applying an extensometer, in the direction of the stress, to the material under investigation. A hole was then drilled between the gauge points of the extensometer and the change in distance measured as the hole was drilled and the residual strains relaxed. The relationship between the change in extension and the relaxed stress was determined through either calculation or calibration. It was stated that the hole did not have to fully penetrate the test piece, as the material removed at some distance below the surface had no appreciable effect on the deformation at the surface. The author detailed calibration methods for the process and stated that the technique was suitable for measuring stresses up to 40% of the proportionality limit[1].

Since Mathar[1] initiated the hole-drilling technique, the method has been further developed with the use of three element electrical resistance strain gauge rosettes and an ASTM standard, E 837-95[2], has been produced detailing the method, a comparable method is also described by Vishay Measurements Group Tech Note 503-3[3], a manufacturer of the rosettes.

Several shortcomings of the hole drilling technique have also been documented. The main problem has been the residual stresses induced by the drilling of the hole. As this involves plastic deformation of the material this will result in the formation of residual stresses that are additional to those being measured. To minimise the problem several techniques to produce the hole have been developed; these include ultra high-speed drilling, air abrasion, chemical etching, electrical discharge machining (EDM) and laser machining. Flaman[4] compared the stresses induced through hole drilling using both low speed and ultra high-speed drilling techniques. The low speed method involved the use of an end mill and rotational speeds of < 1000 rpm, in comparison to the ultra high-speed technique that used a tungsten carbide, reverse cone profile, dental burr with an air turbine capable of speeds up to 400,000 rpm. The author concluded that the ultra high-speed technique was superior to the low speed end mill method, with smaller chips being produced and a superior hole geometry. The strains induced by the two processes are detailed in Table 4.1.

---

[1] Mathar, J (1934)
[2] ASTM (1995a)
[3] Measurements Group (1988)
[4] Flaman, MT (1982)

	Ultra high-speed drill (με)	Low-speed end mill (με)
Mild steel	-6	-40
Stainless steel	-4	-293
Nickel	+3	-169
Aluminium	-54	-169
Copper	-81	-2843

Table 4.1: Magnitude of total average relief strains (με) as measured by the three gauges of the strain rosette on stress-relieved specimens[1]

Procter[2] stated that residual stresses induced by using the best cutting methods available, although the actual cutting methods were not detailed, resulted in stresses of 40 - 50 MPa being induced in an annealed mild steel.

An alternative method to the ultra high-speed drilling technique, the air abrasion method, has been documented by Procter[2], Schajer et al[3], and Segal and Tait[4]. The technique involves mixing an aluminium oxide cutting powder with compressed air and directing this at the work piece through a nozzle. Although the technique has been developed to produce flat-bottomed holes and any induced stresses are negligible, the equipment required for their production is more complex than that required for the ultra high-speed drilling method. Schajer et al[3] also stated that it is not considered suitable for the incremental drilling of holes, these being preferred where the through thickness residual stresses are non-uniform with respect to depth, as found in weldments.

Plasticity at the hole edge is another problem associated with the hole drilling technique. The stress concentration effects of the hole result in localised plasticity if the stress exceeds $\sigma_y/3$ and $\sigma_y/2$ for uniaxial and equal biaxial fields respectively[3]. The problem is prevalent when employing the hole drilling technique to measure residual stresses near weldments due to the magnitude of the residual stresses. Schajer et al[3] describe an adapted strain gauge rosette containing sequences of three gauges to overcome the problem. They also state that for equal biaxial stresses up to $0.8\sigma_y$ the radius of plasticity around the hole is less than 80% of the gauge radius and therefore the analysis would still be valid, although this would depend on the hole and gauge geometry. Beghini et al[5,6] have analysed the problem using an elastic-perfectly plastic finite element analysis and detail equations suitable for measurement of residual stresses up to $0.9\sigma_y$ to within a few percent.

---

[1] Flaman, MT (1982)
[2] Procter, E (1981)
[3] Schajer, GS et al (1996)
[4] Segal, AM; Tait, RB (1996)
[5] Beghini, M et al (1994)
[6] Beghini, M et al (1995)

A comparison between neutron diffraction, x-ray diffraction, hole drilling and numerical methods (analytical and finite element) of residual stress measurement was undertaken by Roy et al[1], with measurements being made on HY80 and HY100 steel beams. The beams were plastically deformed to a depth greater than 50% of the thickness using four-point loading and then unloaded, thus inducing a compressive residual stress on the convex surface. The results for the HY80 steel are shown in Table 4.2, similar results were obtained for the HY100 steel.

Method	Longitudinal Stress (MPa)		Comments
	Tensile	Compressive	
Neutron diffraction	+250	-210	
X-ray	+156	-153	0.15 mm below the surface.
Analytical analysis	+268	-268	Elastic perfectly plastic response.
FEA	+198	-198	Elastic work hardening response.
Hole drilling	+227/158	-166/-141	Two tests undertaken by different centres. Values extrapolated to the specimen surface.

Table 4.2: Comparison of the residual stresses determined through various techniques in HY80 steel[1].

The authors[1] concluded that the neutron diffraction method was the most suitable for determining all three principal stress components, whereas the x-ray and hole drilling method were suitable for determining surface and subsurface stress gradients. The numerical and experimental methods were considered to generally complement each other.

4.3.3 Formation, Magnitude and Direction of Weld Induced Residual Stresses

The effects of residual stresses may be either detrimental or beneficial to a materials performance. Within the elastic response of a material they may be superimposed as a static load on any other applied loading, whilst once superposition results in plasticity, relaxation of the residual stresses generally occurs due to their redistribution as a result of plastic flow. The residual stress redistribution resulting from fatigue loading is different to that observed in monotonic loading, with cyclically softening materials typically exhibiting redistribution, whilst this may be minimal or non-existent in cyclically hardening materials. Compressive residual stresses may be considered beneficial if the applied loading is tensile and vice versa, superposition resulting in a reduction in the apparent loading. A beneficial compressive residual stress state may be induced in the surface of a weld through shot peening. Conversely, a compressive residual stress may result in

[1] Roy, G et al (1990)

premature buckling if the component is subject to a compressive load. Tensile residual stresses will be detrimental if externally applied loading results in an increase in the tensile stress level that the component experiences, this may have a severe effect on the fatigue and fracture properties of the material, notably crack initiation and propagation.

During a thermal welding process the weld site and immediately surrounding area experience different rates of heating/cooling and thus expansion/contraction, the result being large thermal strains. Due to the localised nature of the heat application, the expansion, due to the thermal strains, is constrained by the cooler material distant to the site of the applied heat.

Figure 4.1 depicts the formation of residual stresses and their typical distribution in a butt-welded plate:

a Shows the weld immediately upon completion, with both the weld site and the region adjacent to this being at the same high temperature and of equal length whilst the remaining plate is at a lower temperature.

b Illustrates the outcome if the three elements were separated and allowed to cool. The plates would remain their original length, whilst the weld would contract on cooling.

c Represents the stress/strain system that would develop on cooling of the plates and weld. The contraction of the weld is resisted by the parent material and thus experiences a tensile stress/strain along its length, while the parent plate, in resisting the contraction of the weld, is subject to a compressive stress/strain.

d,e & f Portray the typical longitudinal residual stress/strain distribution; longitudinal to, transverse to and through the thickness of the weld respectively. The weld bead also contracts across its width and depth resulting in tensile residual stress/strain fields in the near-surface region that are at right angles to the weld direction, whilst below this region these are balanced by compressive stress/strain. The exact distribution is dependent on numerous factors, including the material, geometry, constraint during the process and welding parameters etc.

The magnitude of the residual stresses/strains and their distribution is dependent on numerous factors: type of welding, weld parameters (including the number of passes, energy input etc.), material properties, degree of constraint, weld length etc[1,1]. Material

[1] Parlane, AJA (1981)

that is rigidly constrained will have greater residual stresses/strains than one that is allowed to distort during the process. The physical and chemical properties of the material also change at the weld site and HAZ, both during and after the welding process. These changes may result in differing material properties; yield and tensile strength etc.

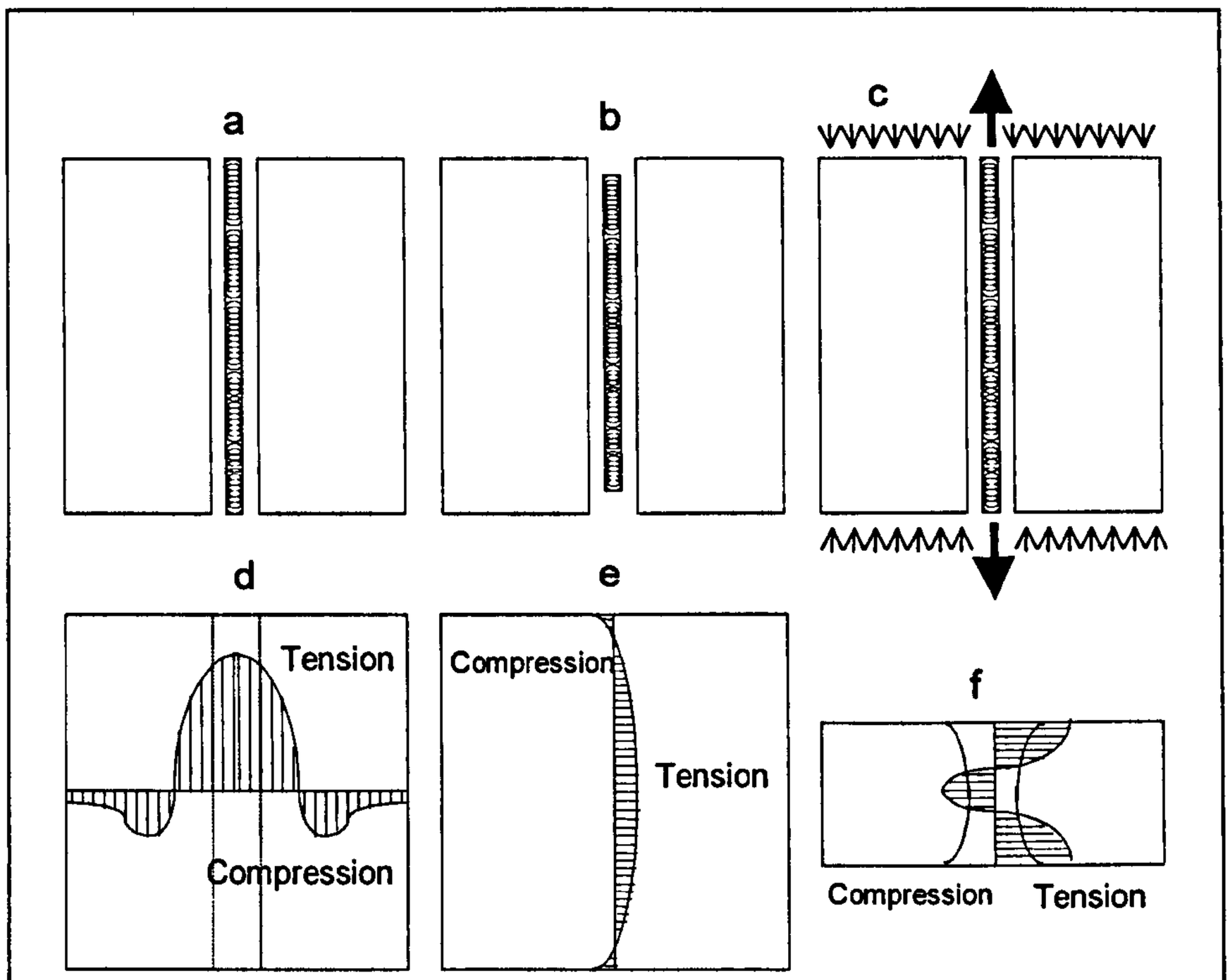

Figure 4.1: The formation of residual stresses around a welded joint[2]

Mathar[3] compared the residual stresses found in butt-welded plates, the electric and gas welding processes being compared. The author concluded that stresses acting in the direction of the seam were near the yield point and of a similar magnitude for both processes. Stresses acting transverse to the weld direction were generally less than those acting parallel when measured at the same point. The stresses running parallel to the weld gradually reduced to zero at the ends of the weld, whereas those measured transverse to the weld direction, but distant to the weld, reduced to zero and then became compressive as the edge of the plates were approached. The area affected by the weld being less for the electric welds. A typical stress distribution for gas welding is shown in Figure 4.2.

---

[1] Wohlfahrt, H (1987)
[2] *After* Gurney, TR (1979) and Parlane, AJA (1981)
[3] Mathar, J (1934)

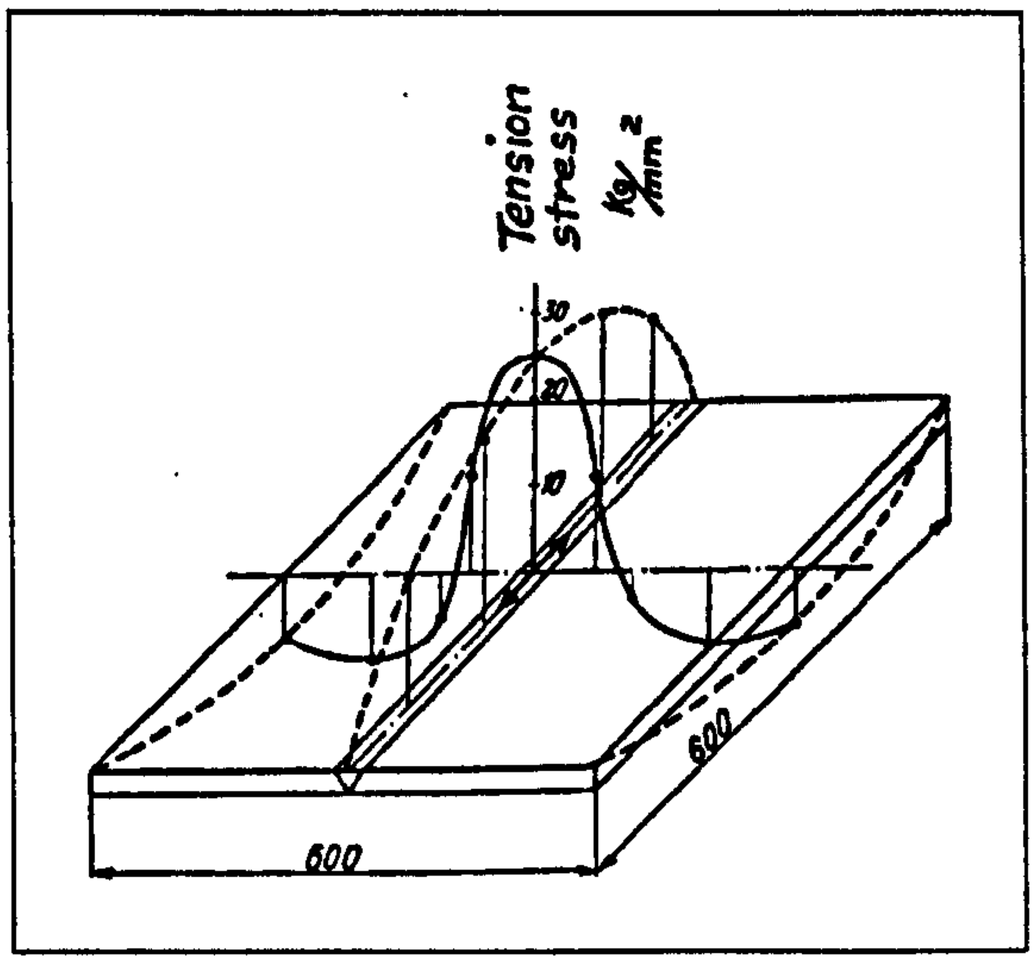

Figure 4.2: Distribution of internal stress in gas-welded seam[1].

Berge and Eide[2] measured the transverse residual stresses in a cruciform welded structural carbon-manganese steel by attaching strain gauges at a distance of 5 mm from the weld toe and then cutting the specimen. An elastic analysis was undertaken, with Poisson's ratio being taken into consideration. The stresses measured were up to $0.7\sigma_y$, which they state as being equivalent to yield magnitude when extrapolated to the weld toe. They also undertook a series of readings at distances up to 36 mm from the weld toe, which showed a rapid diminishing of the stresses over a distance of 10 mm.

Wohlfahrt[3] states that the magnitudes of residual stresses are typically more complex than originally thought; a typical residual stress pattern being indicated in Figure 4.3. The author affirms that residual stresses in steel are associated with shrinkage strains and transformation of the various phases, the transformation from austenite to ferrite, bainite or martensite leading to an increase in volume[3]. He also maintains that the stress fields resulting from multi-pass welds can differ considerably from those resulting from single pass ones. The magnitude of transverse residual stresses measured by x-ray analysis on the surface of a dummy weld in a 10 mm thick fine grained structural steel, German designation St E690, undertaken by Nitschke[4] are detailed, the stresses were measured for three heat inputs, 2.88, 5.82 and 19.80 KJ.cm^{-1}. It is assumed that the dummy weld was equivalent to bead on plate as it is stated that dummy welds can simulate the residual stresses induced by the final or intermediate pass of a multi-pass weld if the depth of the weld pool is less than the sheet thickness[3].

---

[1] Mathar, J (1934)
[2] Berge, S; Eide, OI (1982)
[3] Wohlfahrt, H (1987)
[4] Nitschke, TH (1985) *referenced by Wohlfahrt, H (1987)*

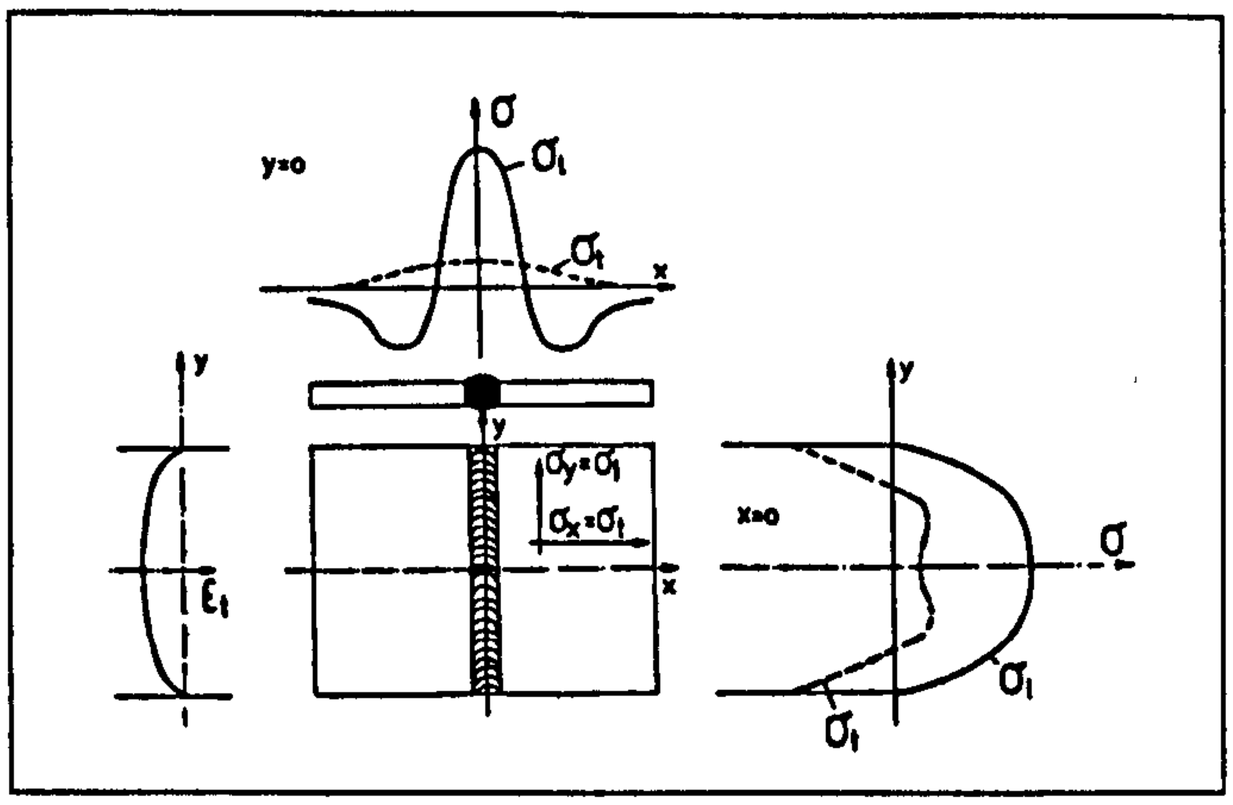

Figure 4.3: Distribution of longitudinal (σ_l) and transverse (σ_t) residual stresses and transverse strains (ε_t) along the y- and x- axis in a single pass welded sheet[1].

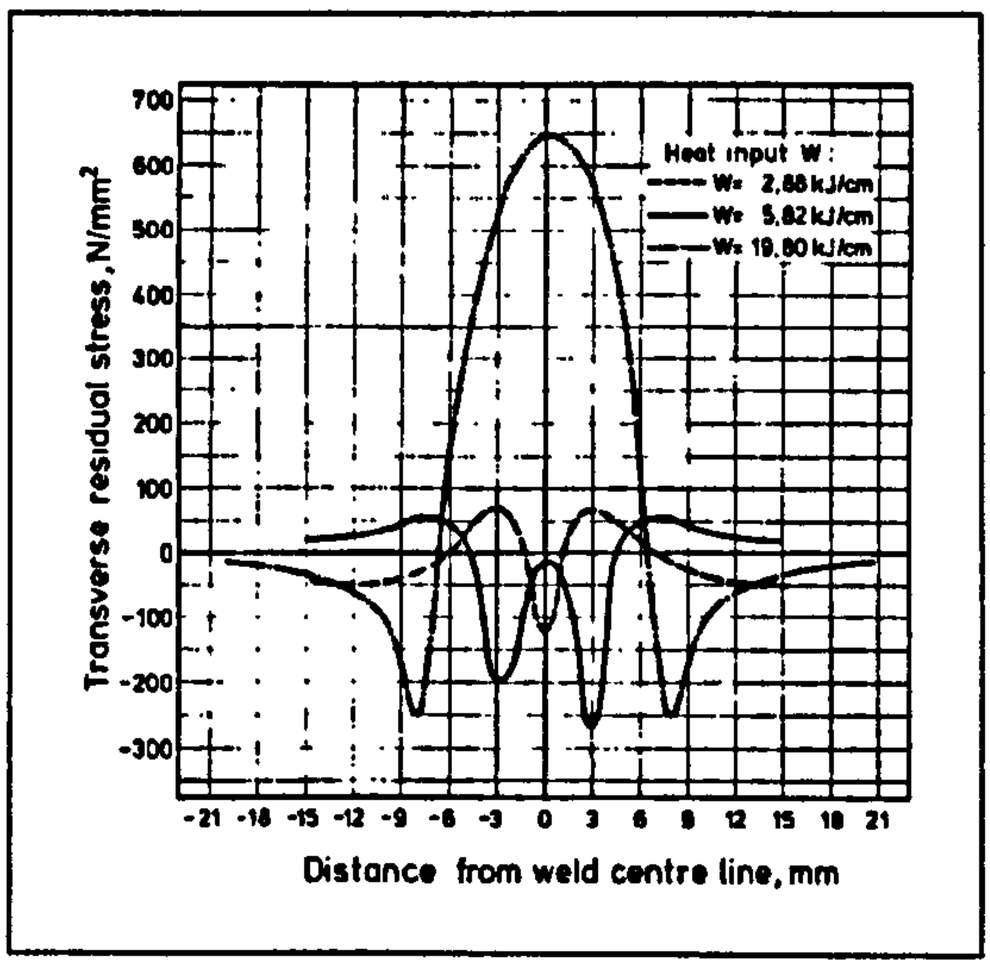

Figure 4.4: Distribution of transverse residual stresses on the surface of a dummy weld[1].

From the results, shown in Figure 4.4, it was evident that the heat inputs affected the surface residual stresses. The low heat input, 2.88 KJ.cm^{-1}, resulted in a peak compressive stress, -100 MPa, at the weld centreline and peak tensile stresses, 70 MPa, at the fusion line, ±3 mm from the weld centreline. At a distance of ±6 mm from the centreline, the stresses again became compressive. The slightly higher input of 5.82 KJ.cm^{-1} resulted in peak compressive stresses at the fusion line of -200 to -260 MPa, whilst at the weld seam a slightly compressive stress of -15 MPa was evident. Peak tensile stresses were recorded at ±7.5 mm from the centreline, the values being slightly less than those for the 2.88 KJ.cm^{-1} weld, at 50 MPa. The 19.80 KJ.cm^{-1} weld resulted in a peak tensile stress at the centre of the weld of 650 MPa, significantly greater than that seen in the other two welds. The peak compressive stresses were recorded at distances of ±8 mm with a value of -250 MPa[1]. The variations in the magnitudes of the transverse

[1] Wohlfahrt, H (1987)

stress fields are described as being associated with the various phase transformations and shrinkage stresses. The phase transformations result in compressive stress formation, in contrast, the shrinkage stresses result in tensile stress formation. The low heat input weld is described as resulting in a higher rate of cooling, thus the major influence at the weld centre is a result of the phase transformation and subsequently a compressive stress. As the weld heat input increased the rate of cooling decreased and the influence of the shrinkage strains increased resulting in tensile stresses at the weld centre[1].

An analysis of the longitudinal stresses, running in the direction of the weld, by Masubuchi[2], stated that they were around yield magnitude and tensile in nature at the weld centreline, but began diminishing at a distance of between 25 - 50 mm from the weld depending on the weld speed, the heat input being constant. At a distance of between 40 - 60 mm a compressive stress was predicted, albeit much lower in magnitude than that at the weld centreline. Kelsey and Nordmark[3] also reported that longitudinal stresses could approach yield strength at the weld surface in their investigation into butt welded AA 5456 with a plate thickness of 51 mm. Transverse stresses varied from 0 - 90 MPa, depending on the number of passes, with a greater number of passes leading to an increase in their magnitude. Gurney[4] also states that the stresses will reach yield magnitude, certainly in the longitudinal and often in the transverse direction. Masubuchi[5] provides a detailed analysis of the residual strains resulting from the welding process, stating that the longitudinal values are typically as high as the yield stress of the weld metal in the case of low-carbon steels. With respect to the transverse values, he states that these are typically of low magnitude and tensile in nature in the middle of the joint and compressive at the ends, as depicted by curve 1 in Figure 4.5. If the lateral contraction is restrained externally during welding, tensile stresses that are approximately uniform along the length are added to the reaction stress, resulting in a stress distribution depicted by curve 2 in Figure 4.5[5].

---

[1] Wohlfahrt, H (1987)
[2] Masubuchi, K (1972)
[3] Kelsey, RA; Nordmark, GE (1979)
[4] Gurney, TR (1979)
[5] Masubuchi, K (1980)

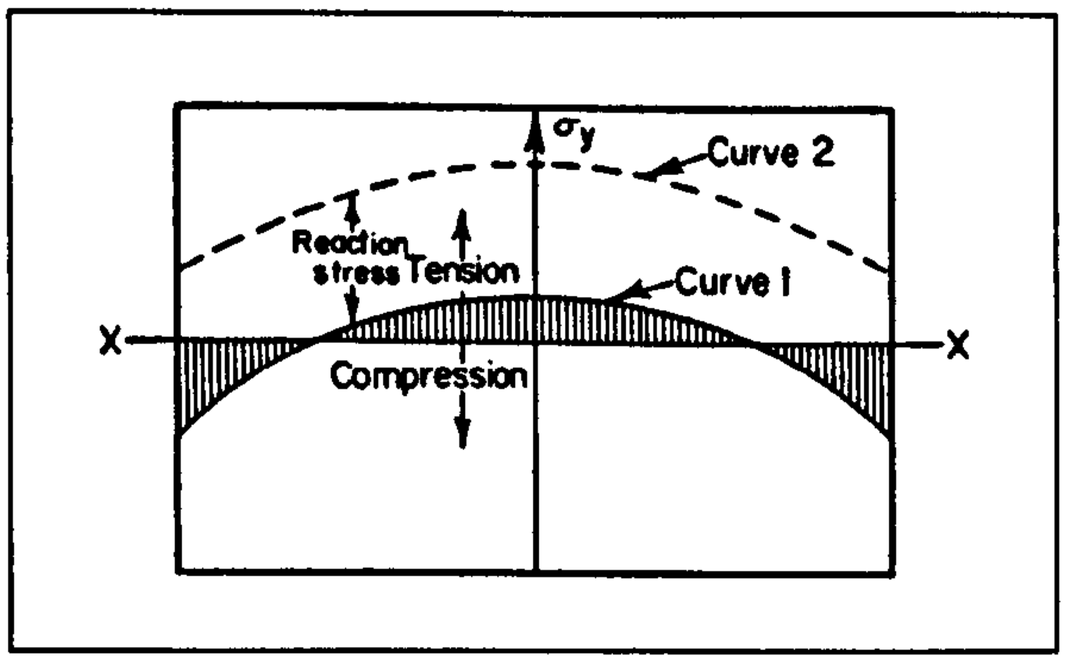

Figure 4.5: Typical distribution of residual stress transverse to the weld direction in a butt weld[1].

Harrison[2] also states that in large as-welded structures residual stresses of yield magnitude will exist parallel to the weld direction and probably transverse to this, an approach taken by Lawrence[3] in his paper on the prediction of the influence of residual stresses on fatigue crack initiation, who assumed that the stresses at the weld toe and running transverse to the weld direction approached yield magnitude. Parlane[4] comments on the transverse field being more complicated than the longitudinal, stating that the latter will be of yield magnitude if the temperature difference is sufficient to induce thermal stresses that exceed the yield strength, the yield strength reducing as the temperature increases. Easterling[5] comments on the longitudinal, transverse and through-thickness stresses, stating that these are frequently of yield magnitude, but does not differentiate between the three types. Kendall et al.[6] also state that residual stresses in a rapidly cooled weld will approach yield magnitude although no indication of direction is given, whilst Schajer et al[7] declare that the residual stresses associated with welding may attain and even exceed the yield point of the material. They also state that the yield point of the HAZ is often much higher than the base metal and that the maximum stresses frequently occur in this zone, although no comments as to specific materials are made.

Mononen and Haagensen[8] measured residual stresses in plasma arc (PA) and FS welded AA 5083-H321 and 6082-T6 by the x-ray diffraction and hole drilling techniques on both large welded plates, 600 x 400 mm, and small fatigue specimens, 30 x 200 mm. In the AA 5083 PA weld peak longitudinal stresses of 100 MPa were measured up to 20 mm from the weld toe, whilst transverse stresses were in the range of 0 to -30 MPa, when measured by x-ray diffraction[8]. The FS weld in the same alloy returned peak longitudinal

---

[1] Masubuchi, K (1980)
[2] Harrison, JD (1981)
[3] Lawrence, FV (1981)
[4] Parlane, AJA (1981)
[5] Easterling, K (1983)
[6] Kendall, JM; et al (1986)
[7] Schajer, GS; et al (1996)
[8] Mononen, J; Haagensen, PJ (1998)

stresses of 130 MPa at distances of ±10 mm from the seam, whilst transverse stresses were in the range of ±25 MPa for the upper surface and ±50 MPa for the longitudinal stresses on the lower surface, with transverse stresses ranging from 0 to -70 MPa[1]. For the PA weld in the 6082 alloy peak stresses were 80 and 20 MPa in the longitudinal and transverse directions respectively. Residual stresses measurements undertaken by the hole drilling method on the same welds resulted in longitudinal stresses of 106, 85 and 168 MPa in the AA 5083 PA, AA 6082 PA and AA 5083 FS welds respectively, the transverse stresses being -59, -11 and -42 MPa respectively[1]. The results from the PA and FS welds measured by x-ray diffraction are shown in Figure 4.6 and Figure 4.7 respectively.

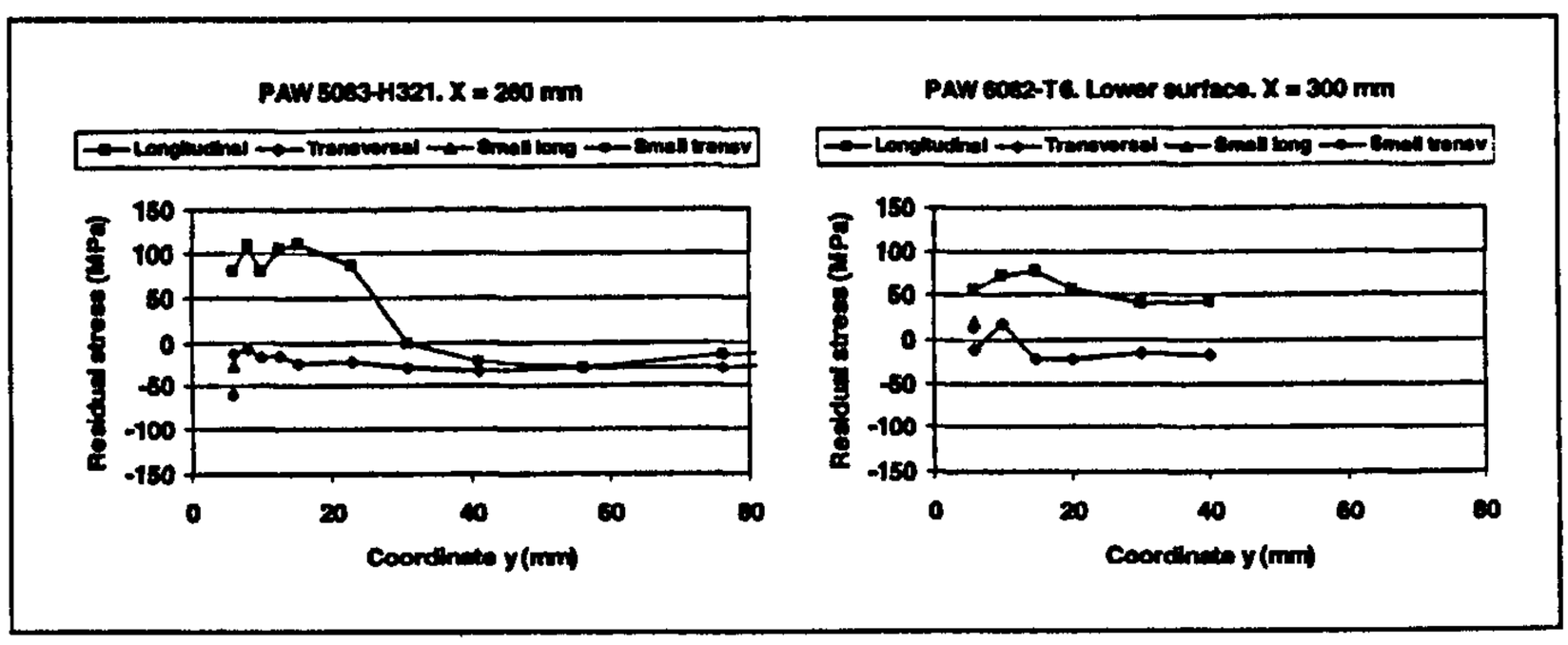

Figure 4.6: Residual stresses measured by x-ray diffraction in plasma arc welded AA 5083-H321 (left) and AA 6082-T6 (right)[1].

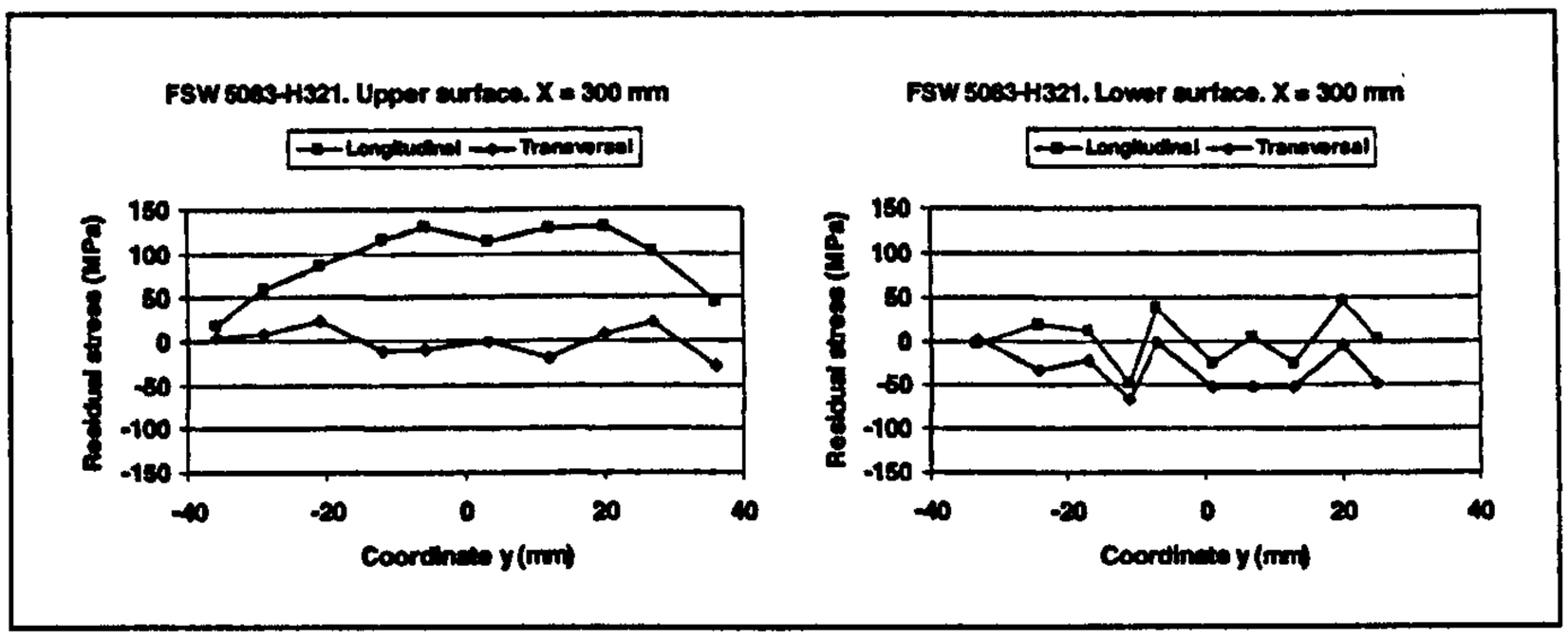

Figure 4.7: Residual stresses measured by x-ray diffraction in friction stir welded AA 5083-H321, upper surface (left) and lower surface (right)[1].

The small fatigue specimens exhibited a diminishing of the residual stress field, with both the longitudinal and transverse stresses ranging from 0 to -25 MPa and -25 to -60 MPa respectively for the AA 5083 PA weld and from -25 to 40 MPa and -20 to 50 MPa for the longitudinal and transverse stresses respectively for the AA 6082 PA weld.

---

[1] Mononen, J; Haagensen, PJ (1998)

James et al[1] measured the surface and near surface residual stresses induced by the FS welding process using the x-ray diffraction $\sin^2\Psi$ method. The accuracy of the process is stated as being approximately ±20 MPa, although measurements in the parent metal resulted in greater scatter due to the larger grain sizes. Measurements on an AA 7075-T7451 FS butt weld, with a plate thickness of 6.35 mm using a 9 mm^2 (3 x 3 mm) beam were undertaken at positions 1, the weld nugget, 2 the HAZ (although their diagram suggests that this was the TMAZ) and 3, parent metal, as indicated in Figure 4.8 (left), on both the advancing (side A) and retreating (side R) sides of both the tool and root faces. Measurements were undertaken at the surface and depths of 25, 50 and 75 µm; electropolishing being utilised for material removal to minimise any residual stresses induced by the removal process. A second set of measurements, as show in Figure 4.8 (right), were made using a smaller beam area, 0.785 mm^2 (1 mm diameter), in an attempt to identify localised stresses that might occur at the transition between the dynamically and partially recrystallised regions. Recordings of both the longitudinal and transverse stresses were made at distances of between 1 and 9 mm from the weld centreline on both the advancing and retreating sides; tests being undertaken on both the tool and root faces, with all the measurements being made at a depth of 75 µm[1].

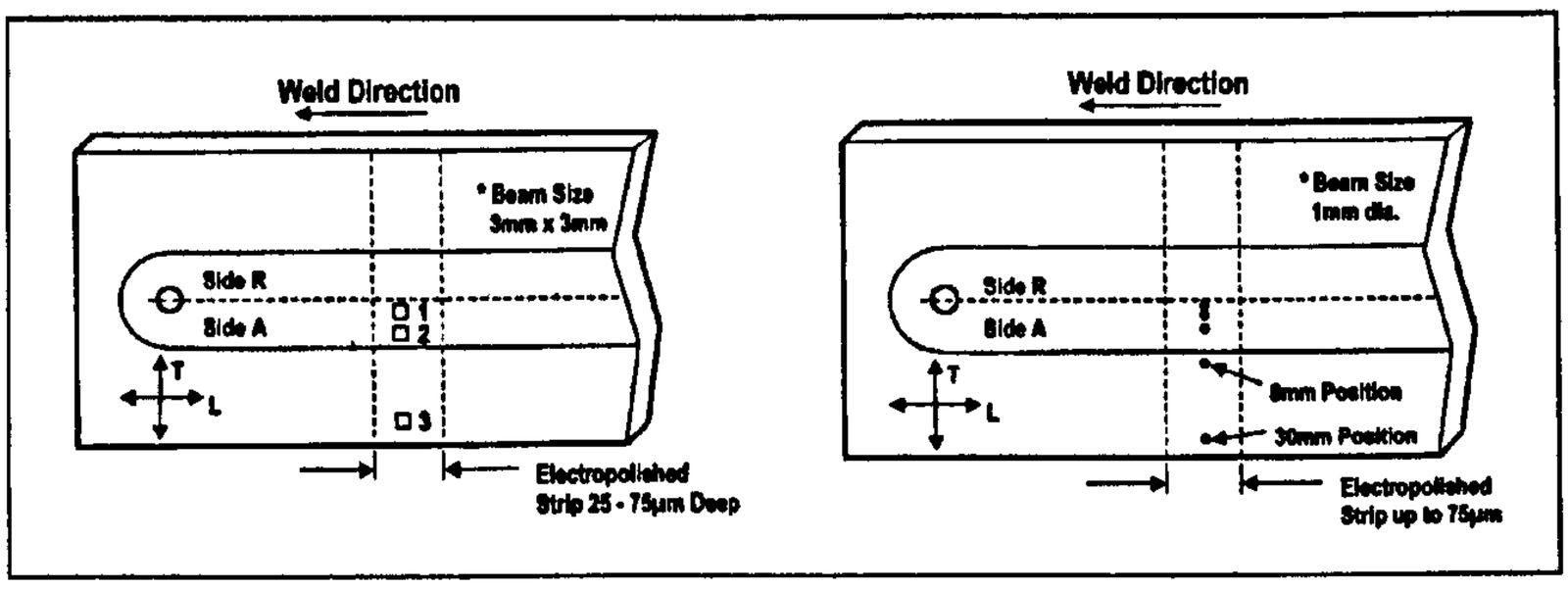

Figure 4.8: Position and nomenclature for large beam (left) and small beam (right) residual stress measurements[1].

Results for the 9 mm^2 beam from the parent material, surface and near surface, returned average values of -62 ±48 MPa. Longitudinal residual stresses for the retreating side of the FS weld, measured at positions 1 and 2 on the tool surface, were small and tensile, ranging from 27 - 30 MPa, whilst transverse stresses were small and compressive, ranging from -40 to -44 MPa. The results are stated as being relatively constant with depth, up to a depth of 75 µm, although analysis of their published data showed that the longitudinal stresses diminished by 49 MPa to -19 MPa at position 1, and by 27 MPa to 0 MPa, at position 2, when the surface and 75 µm depth results were compared. The transverse stresses reduced in magnitude, by approximately 25%, although they remained compressive. The residual stresses measured at position 3, again on the weld

[1] James, M et al (1999)

face, were of a greater magnitude than those at positions 1 and 2, longitudinal stresses ranged from -70 ±83 to -189 ±130 MPa and transverse stresses from 114 ±28 to -14 MPa for the four depths. The values for the advancing side were of a similar magnitude to those returned by the retreating side. The results for the root face exhibited greater scatter than those for the tool face due to the larger grain structure, although they were of a comparable magnitude[1].

Results from the 0.785 mm^2 beam (all undertaken at a depth of 75 µm) exhibited less scatter than the 9 mm^2 beam, the fine grain on the tool face resulted in the errors being generally limited to ±20 MPa, although error values from the root face were greater. Longitudinal residual stresses, for the retreating side of the tool face, ranged from 6 MPa at a distance of 1 mm from the weld centreline to 145 ±48 MPa at a distance of 9 mm, the transverse stresses ranged from -33 MPa at a distance of 2 mm from the weld centreline to -99 MPa at a distance of 8 mm[1]. The results for the advancing side of the tool face exhibited slightly lower values for the longitudinal stresses and similar values for the transverse stresses when compared to those of the retreating side[1]. The transformation, from the fully recrystallised to the partially recrystallised zone, at a distance of between 7 - 8 mm from the weld centreline, was considered evident through an increase in residual stress for three of the four measurements. At the boundary between the two zones, the tensile longitudinal stresses increased in magnitude by 58%, from 48 - 76 MPa. The compressive transverse stresses exhibited greater variation, with those on the retreating side increasing in magnitude by 148%, from -40 to -99 MPa, whilst those on the advancing side decreased by 9%, from -47 to -43 MPa[1]. Residual stresses measured on the root surface returned comparable values to those found on the tool surface, tensile longitudinal and compressive transverse stresses. The authors stated that the transition between the fully and partially recrystallised zones occurred closer to the weld centreline on the root surface due to the smaller volume of recrystallised material. Unlike the tool surface, no noticeable variation in the magnitude of the residual stresses was evident, although the large scatter made complete analysis difficult[1].

Tests were also undertaken on a FS DP butt welded Al-Li alloy, C458. Measurements were performed on both the 1st and 2nd pass surfaces, advancing and retreating sides, at distances between 0 to 9 mm from the weld centreline, although it is not stated at what depth the measurements were made[1]. In contrast to the single pass welded AA 7050-T7451, the longitudinal residual stresses were compressive, varying from -5 to -89 MPa for the advancing side, the 1st pass advancing side having compressive stresses of a greater magnitude than those of the 2nd pass. The longitudinal stresses on the retreating sides were in region of -42 MPa for the 1st pass side, but ranged from -7 to -40 MPa for the 2nd pass side. Transverse stresses were more variable, with values ranging from 47

---

[1] James, M et al (1999)

to -76 MPa on the advancing sides, whilst those on the retreating sides tended to be compressive in the region of -60 MPa. The transition zone, between the fully and partially recrystallised grains, is stated as occurring at a distance of 8 - 9 mm from the weld centreline, although a defining change in the magnitudes of the residual stresses was only evident in one set of results[1].

Measurements of longitudinal residual stresses were made on a friction stir welded AA 2219 at the positions shown in Figure 4.9, these were performed at depths of up to 250 μm for the tool face, but only on the surface for the root face, transverse stresses were not reported. The stresses for both surfaces and the various depths, in the case of the tool surface, returned relatively low values, with the range for all measurements being 31 to -46 MPa. No pattern appeared evident between the results, when the surface, depth and position, were taken into consideration. The transformation between the fully and partially recrystallised grains did not appear to affect the magnitude of the residual stresses[1].

The authors concluded that the residual stresses found in friction stir welds were quite low in comparison to those found in fusion welds, the maximum stresses in FS welds being found at the transition between the fully and partially recrystallised zones[1].

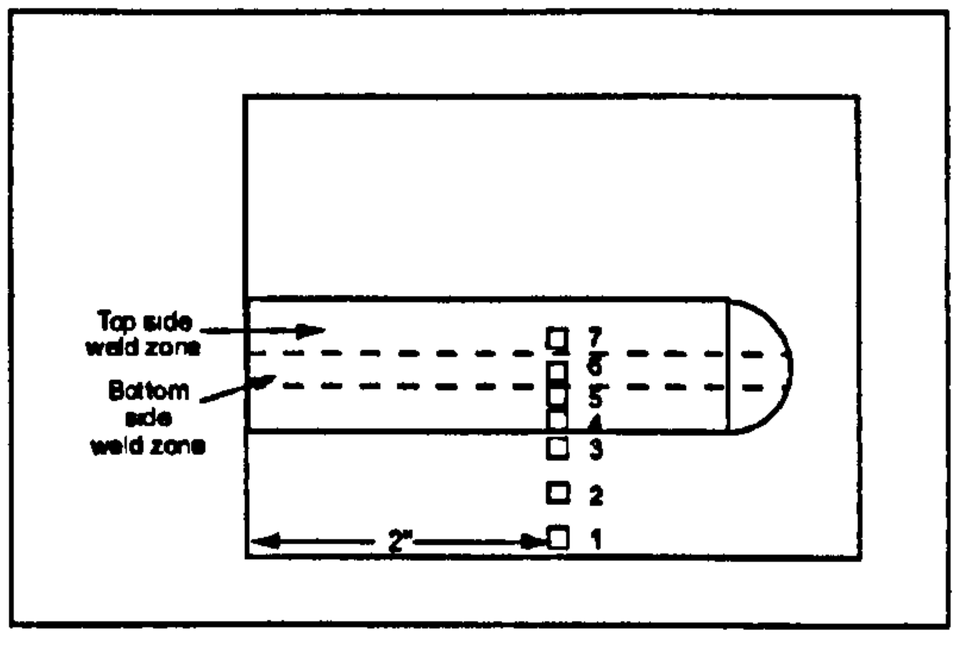

Figure 4.9: Location of residual stress measurements in 2219 aluminium[1].

Webster et al[2] measured the residual stresses in a 6 mm thick AA 7108-T79 FS SP butt weld (the actual weld consisted of two T sections being joined to form an H section) using synchrotron x-ray strain scanning. Synchrotron sources have significantly greater penetration than traditional x-rays, thus allowing measurements to be undertaken through the thickness of the specimen. Although the three-dimensional strain state was not determined due to attenuation, over 600 measurements were made through the thickness of the weld of both the longitudinal and transverse strains. Subsequent stresses were determined assuming all normal stresses at each location were zero[2].

---

[1] James, M et al (1999)
[2] Webster, PJ et al (2001)

The results indicated a complex pattern for the residual strains, as shown in Figure 4.10, and stresses, as shown in Figure 4.11, with a notable asymmetry[1]. Variations for both the advancing, described as flow, and retreating, described as shear, sides of the tool were evident, as were through thickness variations of the longitudinal and transverse stresses. For the longitudinal stresses peak tensile values of around 140 MPa were measured, the maximum compressive values being -60 MPa. The highest tensile stresses were measured at the boundaries of the tool, y = ±3 and ±10 mm for the pin and shoulder respectively, although at different depths. Transverse stresses were described as being much weaker than the longitudinal ones, with peak values in the region of 100 MPa in the region of ±3 to ±9 mm from the weld seam. The authors concluded that fatigue cracks would be likely to initiate on the crown surface, probably on the retreating side, near to the friction band or at the joint line on the root surface, although this would be dependent on the residual stresses having an overriding influence on fatigue crack initiation and growth[1].

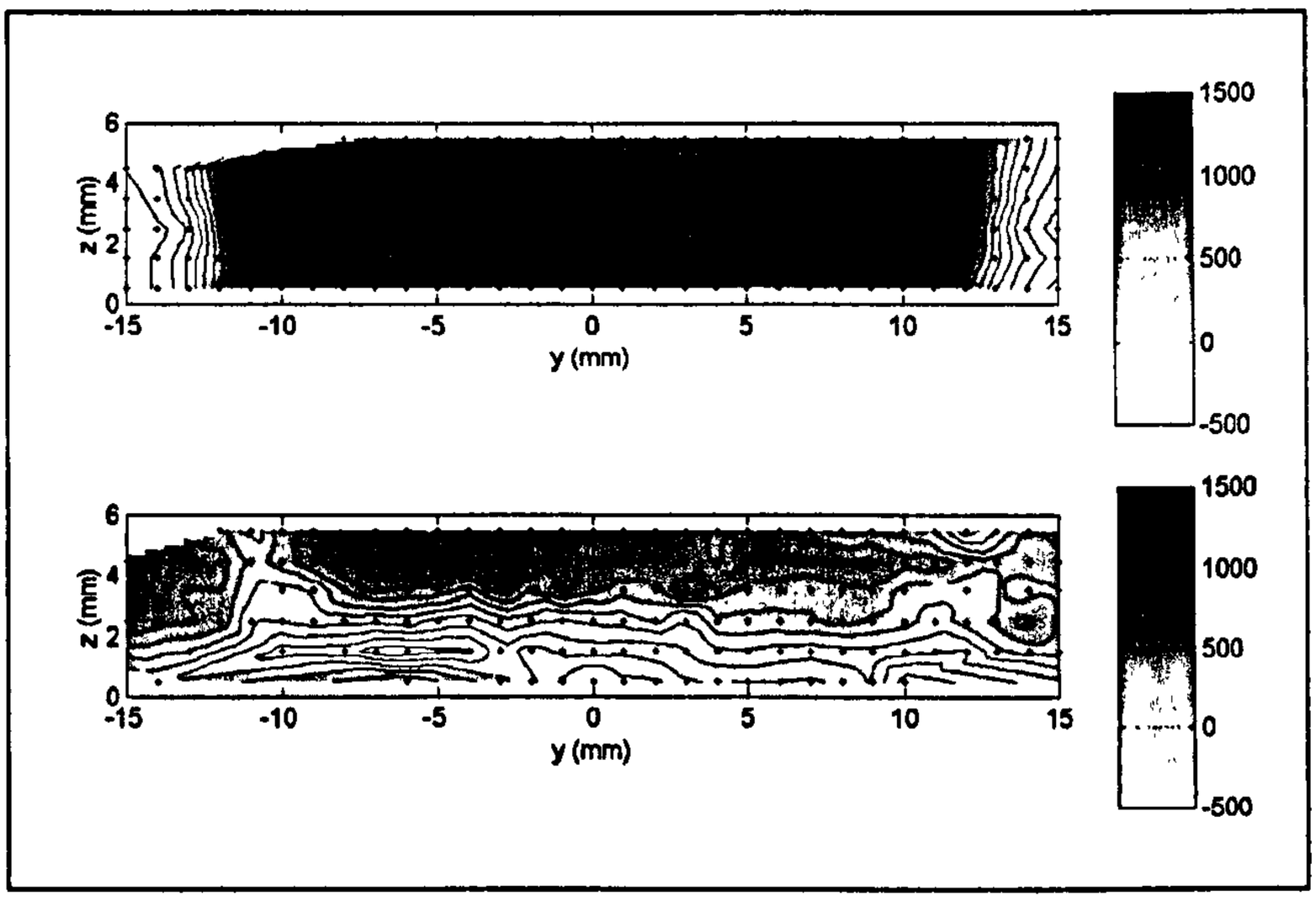

Figure 4.10: Longitudinal (upper) and transverse (lower) residual strain (με) contours for a friction stir welded butt joint in AA 7108-T79; y = 0 relates to the weld seam with the retreating side (left) and advancing side (right), z = 6 tool shoulder surface[1].

[1] Webster, PJ et al (2001)

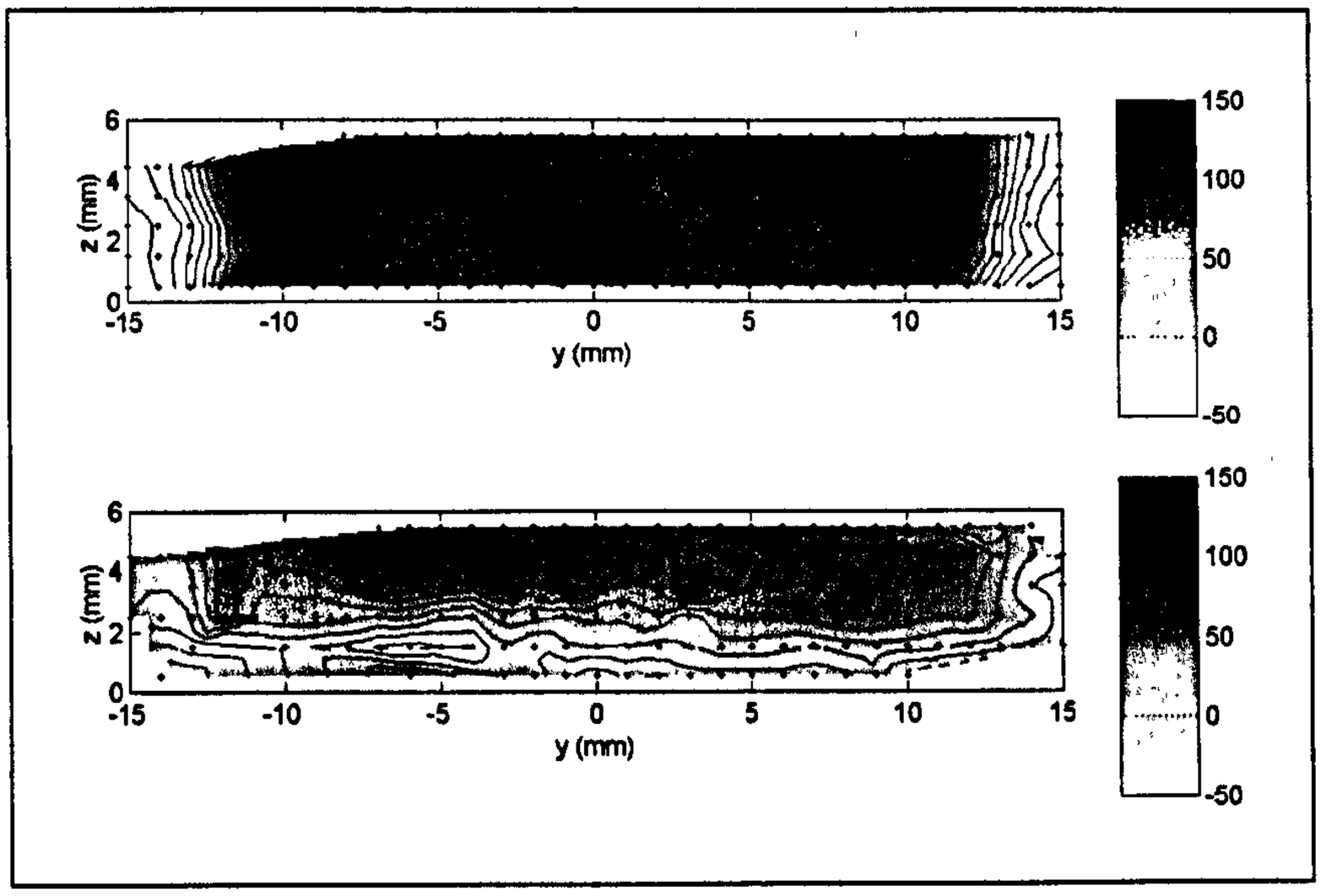

Figure 4.11: Longitudinal (upper) and transverse (lower) residual stress (MPa) contours for a friction stir welded butt joint in AA 7108-T79; y = 0 relates to the weld seam with the retreating side (left) and advancing side (right), z = 6 tool shoulder surface[1].

4.3.4 Relaxation/Redistribution of Residual Stresses

Post-processing treatments have been employed to reduce residual stresses; they may be generally classified under two headings, thermal and mechanical techniques. Thermal techniques generally involve either complete furnace treatments or local treatments, whilst mechanical methods generally involve monotonic overload or vibratory conditioning[2]. Residual stresses induced by the welding process may be reduced by these methods, but their reduction may also occur due to normal in-service loading, although this is a form of mechanical loading its occurrence may be unintentional. Any reduction in tensile residual stresses will generally result in an increase in fracture and fatigue strengths and an increase in the crack initiation period if the applied stresses are of a tensile nature.

James[3] divided the proposed mechanisms for the relaxation of residual stresses through fatigue loading into three cyclic stress amplitude regimes; above the macroscopic yield strength, below the endurance limit and between the previous two. The first regime is stated as resulting in a complete redistribution of residual stresses when gross yielding occurs. The author states that both residual stress reduction and reversal (tensile-tensile loading resulting in compressive residual stresses changing to a tensile residual stresses) have been reported. The second regime has been reported as resulting in residual stress relaxation with stress concentrators and defects or microcracks being suggested as the

[1] Webster, PJ et al (2001)
[2] Saunders, GG (1981)
[3] James, MR (1987)

associated relief mechanism. Residual stress relaxation associated with the third regime is described as being related to the cyclic stress amplitude. It has also been reported that relaxation occurs chiefly within the initial cycles and then decreases in rate with increasing fatigue[1].

Vöhringer[2] states that the reduction in the magnitude of residual stresses, when a load is applied, is due to the movement of dislocations. The reduction increases with increasing stress amplitude and the number of applied cycles, although relaxation does not occur unless the sum of the applied and residual stresses is equal to, or exceeds, the resistance to the onset of plastic deformation, which may be considered to be the yield strength.

Iida and Takanashi[3] studied the relaxation of residual stresses in electron beam bead-on-plate welds. The welds were made on an 11 mm thick JIS SUS316 austenitic stainless steel (σ_y = 255 MPa, σ_{TS} = 586 MPa) and a 9 mm thick high strength steel (σ_y = 415 MPa, σ_{TS} = 535 MPa), JIS SM490A, both were stress annealed prior to welding. Tests were undertaken on waisted specimens, the weld running along the length, with a hole drilled in the centre to restrict the region of fatigue crack initiation. Residual stresses were measured on both faces of the plate, detailed as Surf. A and B in the various figures. The technique involved the use of strain gauges and sectioning, the gauges being positioned parallel and transverse to the weld direction. This technique avoided the problem of hole edge plasticity associated with the hole drilling technique at high stress levels, although it requires the direction of the principal stresses to be known to produce accurate results[3].

The residual stress distributions for the SUS316 and SM490A steels, prior to and after one load cycle (σ_a = 200 MPa, R = -1, for the SUS316 and σ_R = 300 MPa, R = 0, for the SM490A) are shown in Figure 4.12 and Figure 4.13. The initial distribution of stresses for both steels exhibited the patterns typically associated with fusion weld induced residual stresses. The longitudinal stresses being tensile and of yield magnitude at the weld (extrapolation of the data suggests that this would be evident) and the transverse stresses being tensile, but of a lower magnitude than the longitudinal stresses. As the transverse distance from the weld increased the longitudinal stresses became compressive, whilst the transverse stresses tended towards zero[3].

Application of a single load of σ_a = 200 MPa, R = -1, to the SUS316 steel resulted in a reduction in the magnitude of the residual stresses for both the longitudinal and transverse stresses, although the effect was greater for the transverse stresses. The longitudinal stresses, although reduced in magnitude, exhibited a similar pattern to those

---

[1] James, MR; Morris, WL (1981)
[2] Vöhringer, O (1987)
[3] Iida, K; Takanashi, M (1998)

observed in the as-welded specimens as the distance from the weld increased, whilst the transverse ones exhibited a reduction to a constant value before diminishing to zero as the distance from the weld increased, as shown in Figure 4.12 (centre right and far right).

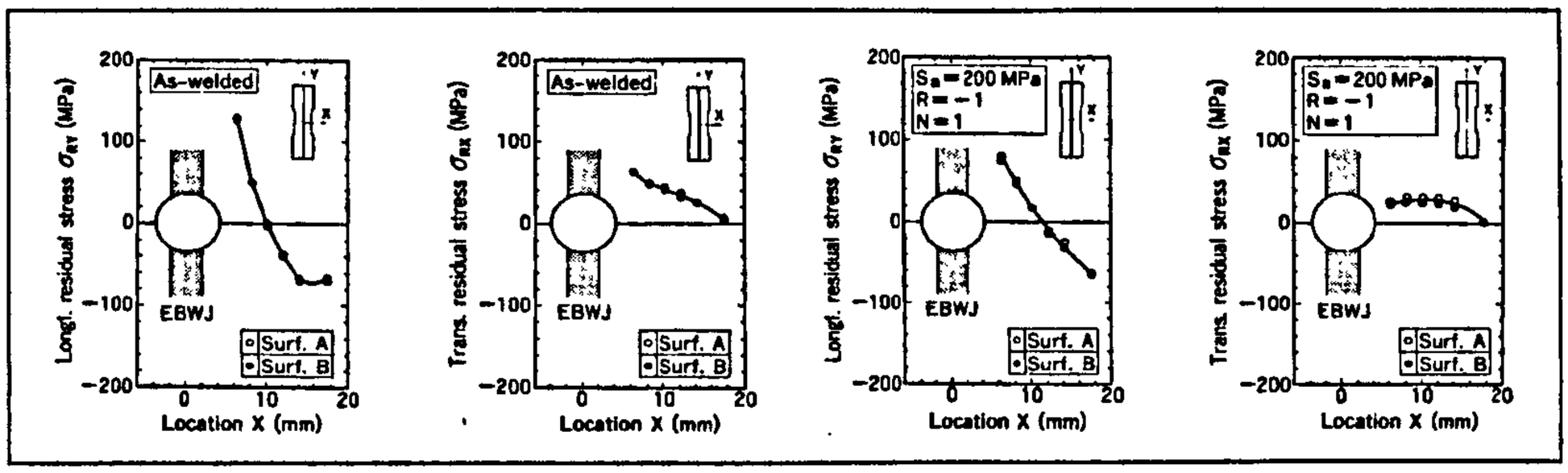

Figure 4.12: Distribution of welding induced residual stresses in SUS316 steel, as welded, longitudinal (far left) and transverse (centre left) and after the application of σ_a = 200 MPa load range, R = -1, longitudinal (centre right) and transverse (far right)[1].

The SM490A steel exhibited a decrease in the magnitude of the residual stresses for both the longitudinal and transverse stresses after the application of a single load σ_R = 300 MPa, R = 0. The longitudinal stresses near to the weld became compressive, increased slightly to become tensile and then decreased to become slightly compressive as the distance from the weld increased. The transverse stresses exhibited a similar response although the change in magnitude was less than that observed for the longitudinal stresses, as shown in Figure 4.13 (centre right and far right)[1].

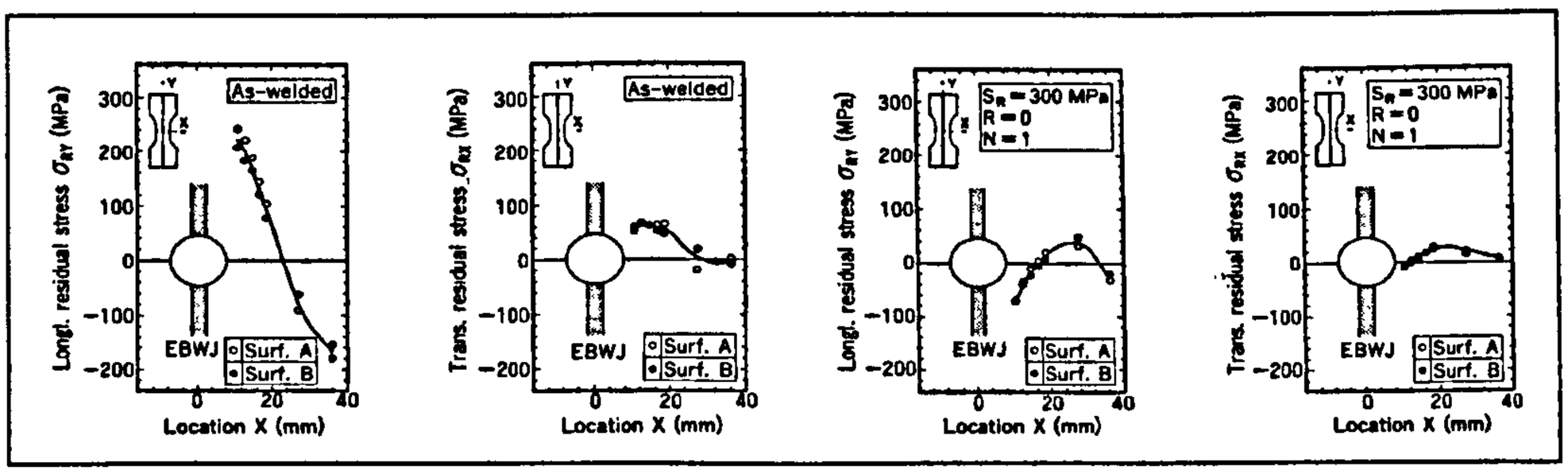

Figure 4.13: Distribution of welding residual stresses in SM490A steel, as welded, longitudinal (far left) and transverse (centre left) and after the application of σ_R = 300 MPa, R = 0, longitudinal (centre right) and transverse (far right)[1].

The magnitude of the residual stresses, transverse and longitudinal, after 0, 1 and 10^x cycles are detailed in Table 4.3 and Figure 4.14; measurements for the SUS316 and SM490A being made at a distances of 6 mm and 10 mm from the weld centreline respectively. From the results, it was clear that the redistribution of the residual stresses,

[1] Iida, K; Takanashi, M (1998)

and hence their reduction, was dependent on stress ratio, R, the stress amplitude/range (S_A and S_R in the figures) and the number of cycles the loading was applied for. The greatest redistribution of residual stresses occurred after the first load cycle, whilst subsequent cycles appeared to redistribute them in a power law type relationship, the two graphs exhibiting a linear reduction after the first cycle when plotted against a logarithmic scale for the number of cycles[1].

Relaxation after a single $\sigma_{max.} = 200$ MPa ($\sigma_a = \sigma_{max.}$) load cycle, R = -1, resulted in residual stresses that were 0.41 of the as-welded value in the transverse direction, but 0.61 of the as-welded value in the longitudinal direction for the SUS316 steel, although if the applied load was reduced to $\sigma_a = 130$ MPa the reduction in magnitude decreased, resulting in stresses of 0.70 and 0.87 of the as-welded values for the transverse and longitudinal stresses respectively. Application of a single $\sigma_{max.} = 200$ MPa ($\sigma_R = \sigma_{max.}$) load cycle, R = 0, resulted in residual stresses that were 0.26 and 0.15 of the as-welded values for the transverse and longitudinal stresses respectively, whilst increasing the load to $\sigma_{max.} = 300$ MPa resulted in compressive residual stresses equal to -0.12 and -0.30 of the as-welded values for the transverse and longitudinal directions. From Figure 4.14 it was evident that if the initial load resulted in a compressive residual stress this typically continued to increase in magnitude, albeit at a significantly reduced rate (the exception to this was the longitudinal residual stresses resulting from the application of load cycles of $\sigma_{max} = 300$ MPa, this remained at a constant, albeit compressive, value), as further load cycles were applied, the effect being evident for both the longitudinal and transverse responses[1].

SUS316 (R = -1)						
$\sigma_{max} = \sigma_a$, (MPa)	Transverse (MPa) ~ (ratio)			Longitudinal (MPa) ~ (ratio)		
	0	1	10^4	0	1	10^4
200	61	25 ~ (0.41)	20 ~ (0.33)	127	78 ~ (0.61)	59 ~ (0.46)
160		33 ~ (0.54)	30 ~ (0.49)		91 ~ (0.72)	75 ~ (0.59)
130		43 ~ (0.70)	37 ~ (0.61)		110 ~ (0.87)	101 ~ (0.80)
SM490A (R = 0)						
$\sigma_{max} = \sigma_R$, (MPa)	Transverse (MPa) ~ (ratio)			Longitudinal (MPa) ~ (ratio)		
	0	1	10^4	0	1	10^4
370	57	-15 ~ (-0.26)	-15 ~ (-0.26)	227	-59 ~ (-026)	-82 ~ (-0.36)
300		-7 ~ (-0.12)	-20 ~ (-0.35)		-69 ~ (-0.30)	-83 ~ (-0.37)
240		3 ~ (0.05)	4 ~ (0.07)		-9 ~ (-0.04)	-13 ~ (-0.06)
200		15 ~ (0.26)	15 ~ (0.26)		34 ~ (0.15)	42 ~ (0.19)

Table 4.3: Residual stress relaxation in SUS316 steel due to reversed, R = -1, cyclic loading at a distance of 6 mm from the weld seam and SM490A steel due to repeated, R = 0, cyclic loading at a distance of 10 mm from the weld seam[1].

[1] Iida, K; Takanashi, M (1998)

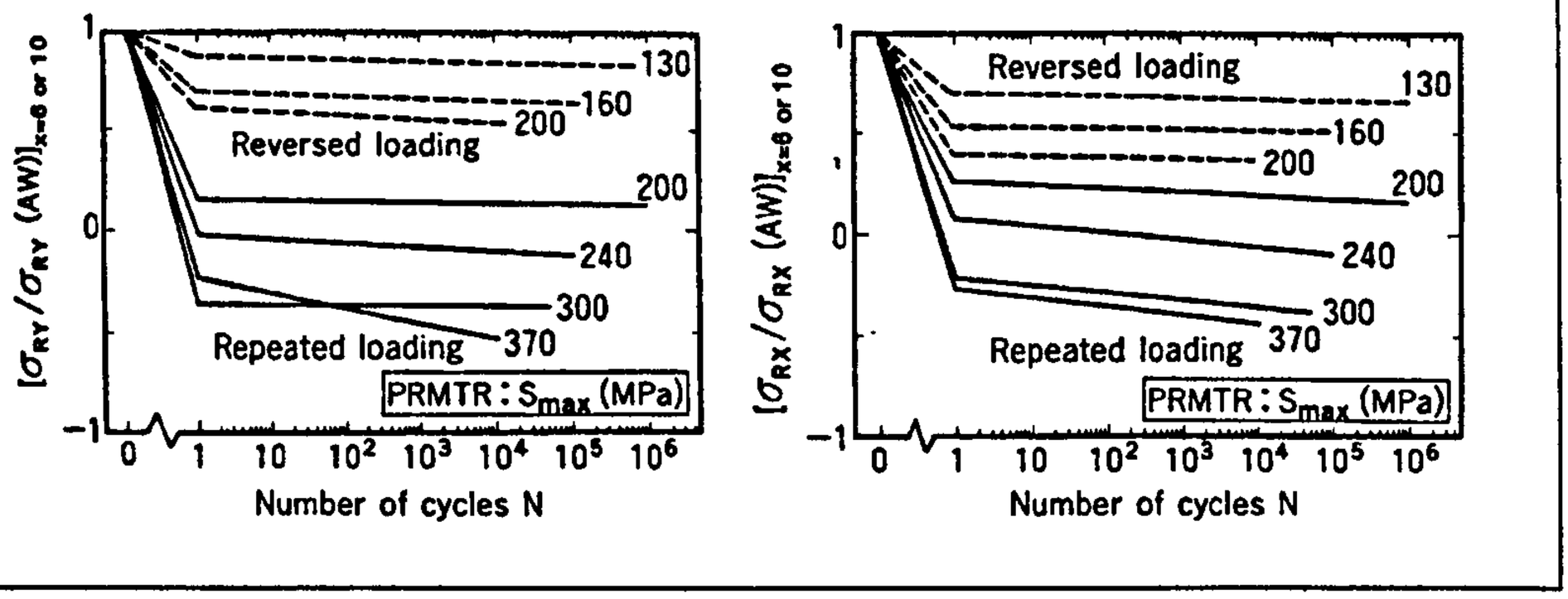

Figure 4.14: Comparison of the relaxation behaviour of peak welding residual stresses under reversed (SUS316), R = -1, and repeated (SM490A), R = 0, loading, longitudinal (left) and transverse (right)[1].

The authors described the resulting compressive stress fields that resulted from loading with R = 0 as being the result of the plastic zone at the notch root[1]. Figure 4.15 depicts the residual stress with a magnitude of σ_R at point A, application of a tensile load increases this to the yield point with subsequent plastic strain resulting in position B being attained for the elastic perfectly plastic analysis shown. The amount of plastic strain, dependent on the notch sharpness and magnitude of the tensile load, determines point B. The unloading process results in the plastic zone close to the notch root being forced into compression by the surrounding elastic stress field due to the release of stored energy. In contrast, reversed loading results in a continuation of the process, the stress being at point D in Figure 4.15 (b) at the load nadir and increasing to $\sigma_{R'}$ after the load cycle has completed[1].

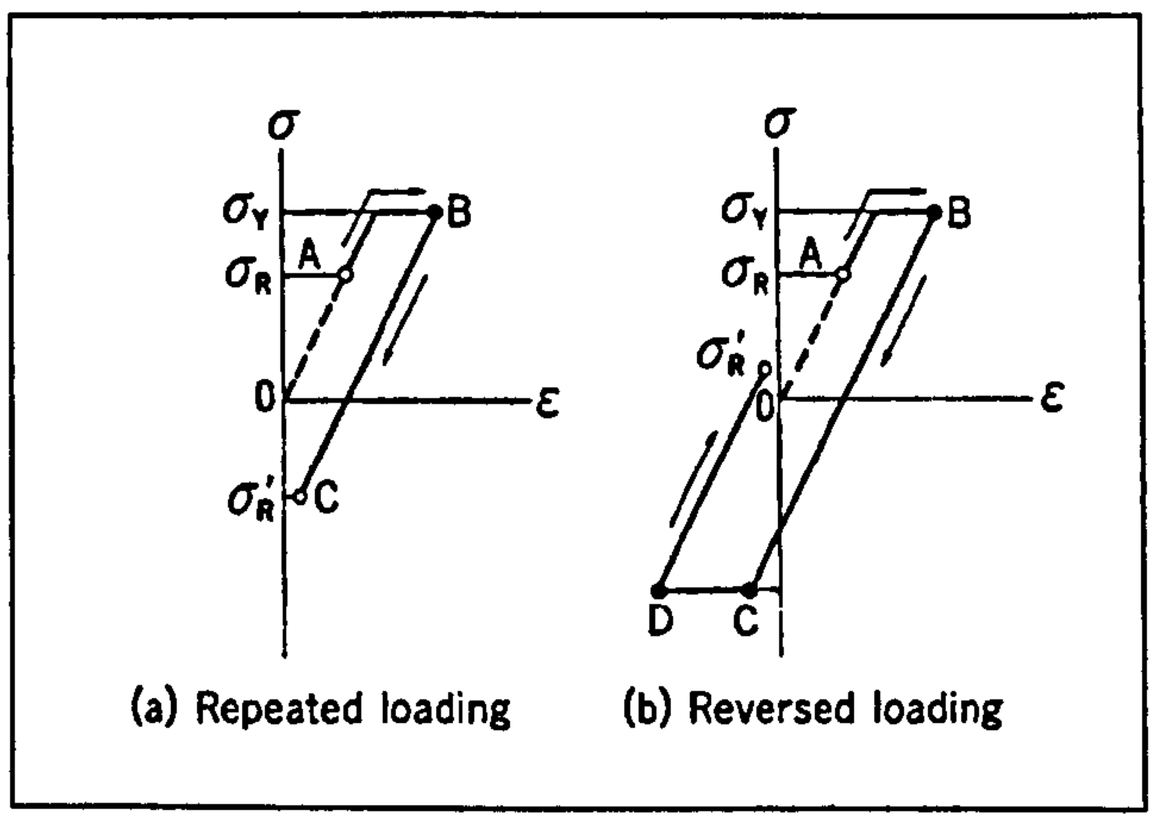

Figure 4.15: Mechanism of residual stress relaxation due to a single cycle loading[1].

[1] Iida, K; Takanashi, M (1998)

The distribution of residual stresses after 10^4, SUS316, and 10^3, SM490A, cycles for various stress amplitudes/ranges are shown in Figure 4.16. It was evident that the greater the maximum applied stress the greater the stress redistribution and hence reduction, although this was less noticeable for the transverse stresses[1].

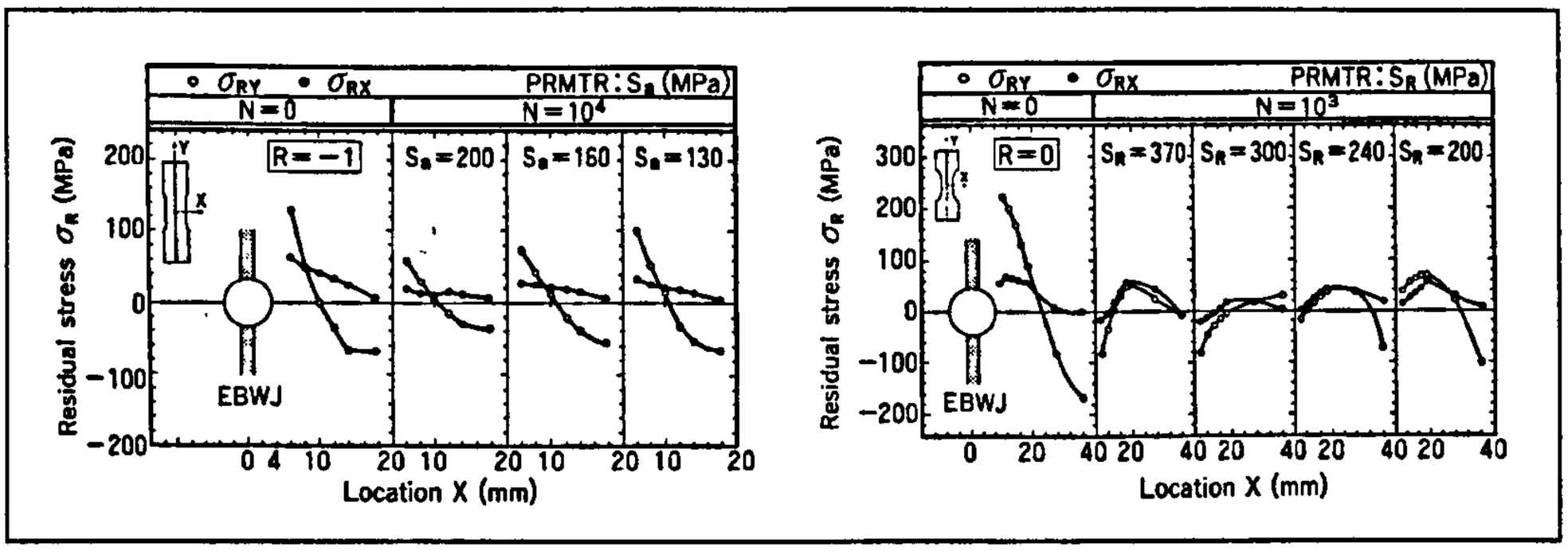

Figure 4.16: Redistribution of the longitudinal and transverse residual stresses in SUS316 steel after 10^4 cycles, R = -1, (left) and in SM490A after 10^3 cycles, R = 0, (right)[1].

Iida and Takanashi concluded that the longitudinal stresses near to the root of the hole were notably reduced after the application of a single load cycle, with the remaining residual stress being inversely proportional to the applied load. Stress relief was greater for cyclic loading, R = 0, than reversed loading, R = -1, with compressive stresses only being observed for cyclic loads, and stress relaxation continued with an increase in the number of applied load cycles[1].

Smith et al[2] studied the relaxation of shot blasting induced compressive residual stresses in round steel bars using a FEA and compared the results to those obtained through x-ray and hole drilling measurements. The FEA consisted of two models, linear kinematic (LK) hardening, which considered the cyclic stress-strain response to be linear elastic-linear plastic, and multilinear kinematic (MK) hardening, which was more representative of the cyclic stress-strain response. The LK model took into consideration the Bauschinger effect, the compressive yield strength reduction found in materials after they have been plastically deformed in tension, whilst the MK model considered the effects of cyclic stress-strain curves with respect to moving yield surfaces. The authors stated that the tension-compression cyclic loading resulted in a more rapid reduction in the residual stresses than the tensile loading[2], which, although predicted by their MK model, did not appear to be corroborated by their results obtained through x-ray analysis, as shown in Figure 4.17, these indicating that the tensile loading had a greater effect, results comparable with those obtained by Iida and Takanashi[1]. The MK model predicted a greater reduction in the residual stresses than the LK model, with a subsequent

[1] Iida, K; Takanashi, M (1998)
[2] Smith, DJ et al (2001)

proportion of the stresses relaxing within the initial cycle and complete relaxation being the final outcome, although the results from x-ray analysis did not conform to this for fully reversed cyclic loading. The LK model, used to predict the relaxation resulting from application of a tensile load, gave better predictions of the tensile relaxation measured by x-ray analysis as shown in Figure 4.17.

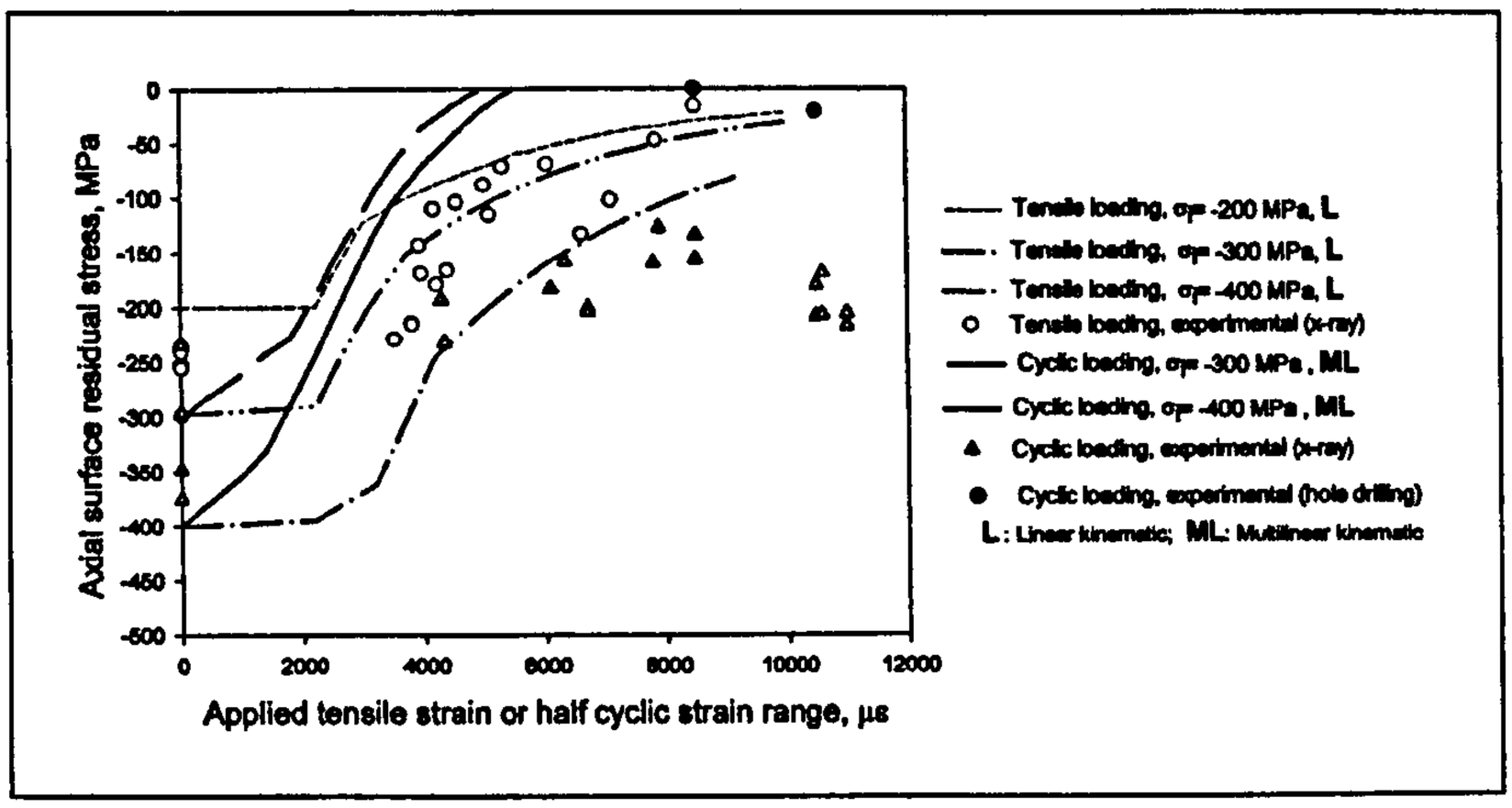

Figure 4.17: Reduction in residual stress due to loading (L = linear kinematic FEA, ML = multilinear kinematic FEA)[1].

Berge and Eide[2] assumed an ideal elastic-plastic behaviour to describe the relaxation of residual stresses following cycling from 10^3 - 10^4 cycles at R = 0:

$$\sigma_{residual} = \sigma_y - \sigma_{max} \text{ for } \sigma_y < \left(\sigma'_{residual} + \sigma_{max}\right) \tag{4.1}$$

$$\sigma_{residual} = \sigma'_{residual} \text{ for } \sigma_y > \left(\sigma'_{residual} + \sigma_{max}\right) \tag{4.2}$$

where: $\sigma_{residual}$ = post cyclic loading residual stress.
$\sigma'_{residual}$ = pre cyclic loading residual stress.
σ_y = yield stress.
σ_{max} = nominal peak applied stress.

The authors state that the interpretation is too simplistic due to the stress concentrating effect of the weld toe and the effect of the heat cycle from the welding process on the yield stress.

[1] Smith, DJ et al (2001)
[2] Berge, S; Eide, OI (1982)

4.3.5 Effects of Residual Stresses on Fatigue

It is generally accepted that residual stresses influence the fatigue properties of a material, although there appears to be some debate regarding the nature of their influence. Compressive residual stresses are frequently considered beneficial due to enhancing crack closure or reducing the likelihood of initiation, whilst tensile residual stresses are considered detrimental due to exacerbating crack opening and initiation.

Masubuchi[1], in 1972, studied the effect of tensile loading on residual stresses, notably longitudinal residual stresses induced by the butt-welding of an aluminium plate. The author concluded that residual welding stresses only affected the performance with respect to phenomena that occurred under low applied stresses, brittle fracture and stress corrosion cracking being stated as examples. The influence of the residual stresses diminishing as the applied stress increased. Their effect on the performance of welded structures being minimal when the applied stresses exceeded the yield stress, although the effect of considering the residual stress as a static load in addition to the applied load is not commented upon.

Kelsey and Nordmark[2] state that one of the problems in determining the effect of residual stresses on the fatigue properties of a weld was that comparisons were frequently made between as-welded and stress relieved/modified specimens. Any stress relief or modification procedure being likely to affect the microstructure and hence the fatigue properties. The authors differentiated between the effects that the residual stresses had on the fatigue properties of a welded joint depending on whether the joint was loaded transversely or longitudinally. For transverse loading, they concluded that the overriding factor in determining the fatigue strength of aluminium (MIG) butt-welds, was the weld profile[2]. They state that in reinforcement intact welds, the residual stresses would have a minimal effect on the fatigue properties due to the stress concentrating effect of the weld toe (see Sections 5.3.1.2 Weld Profile, pages 241 - 250, and 5.4.2 MIG Weld Toe Stress Concentration Factors, pages 254 - 265). It was suggested that peening, which induces compressive residual stresses into the surface and is known to enhance the fatigue properties, probably results in a reduction in the notch severity of the weld, thereby enhancing the fatigue properties[2]. They also stated that the fatigue crack growth enhancing effect of the tensile transverse residual stresses found in the surface region, when the weld reinforcement is removed, was counteracted through the balancing compressive transverse residual stresses found within the structure (see Figure 4.1 f, page 131)[2]. For longitudinal loading, they concluded that the residual stresses were the major factor in affecting the fatigue life, although the weld geometry could have a significant effect when the weld bead was left intact. They stated that as the crack

---

[1] Masubuchi, K (1972)
[2] Kelsey, RA; Nordmark, GE (1979)

propagated into the base metal the residual stresses were relieved and the fatigue crack growth rate approached that of the unwelded metal[1].

Gurney[2] reviewed several publications relating to the effect of residual stresses on the fatigue properties of transverse butt-welds, these dating back to 1939. With the weld reinforcement left intact, the maximum increase in the fatigue strength due to stress relief, for lives of 2×10^6 cycles, was 12.5%, although other publications suggested that stress relief had no beneficial effect. For similar welds, with the reinforcement intact, comparable results were obtained, although the maximum improvement was 17%. Later studies, from around the 1960s, also returned similar results, although the results of a number of Soviet authors at the time declared improvements in the fatigue strength of over 50%.

Iida and Takanashi[3], whilst studying the magnitude of residual stress relaxation due to fatigue loading, measured the effects of welding on the fatigue properties. Reverse stress cycle, R = -1, S-N tests were performed on both the SUS316 parent material and welded plate and repeated stress cycle, R = 0, S-N tests on the SM490A parent material and welded plate. The results for crack initiation, classified as a visible crack of approximate length 0.5 mm emanating from the edge of the centre hole, and fatigue life are shown in Figure 4.18 and Figure 4.19. It was evident from Figure 4.18 that for fully reversed loading, R = -1, the fatigue strength was slightly greater for the welded samples at higher stress amplitudes, with the two curves crossing in the region of 10^5 cycles. This type of response suggests that if the predominant factor in the fatigue behaviour were the residual stresses, their redistribution, which would occur at higher stress amplitudes, resulted in a diminishing of their effect, whilst at lower stress amplitudes they were still influential with respect to the fatigue properties. For repeated loading, R = 0, shown in Figure 4.19, the welded specimens exhibited a fatigue strength that was slightly less than that observed in the parent material with little influence with respect to the magnitude of the stress range except near to the endurance limit. Comparison of the responses from the two types of loading, the reversed loading resulting in an apparent reduction in the influence of the residual stresses, whilst the repeated loading appears to have had minimal effect, even though the peak stresses in both cases were below the yield strength suggests that the Bauschinger effect may have been influential. As the peak stresses were below the yield stress this would only occur if either localised yielding was occurring, due to either local stress concentrations or superposition of the residual stress on the applied stress.

---

[1] Kelsey, RA; Nordmark, GE (1979)
[2] Gurney, TR (1979)
[3] Iida, K; Takanashi, M (1998)

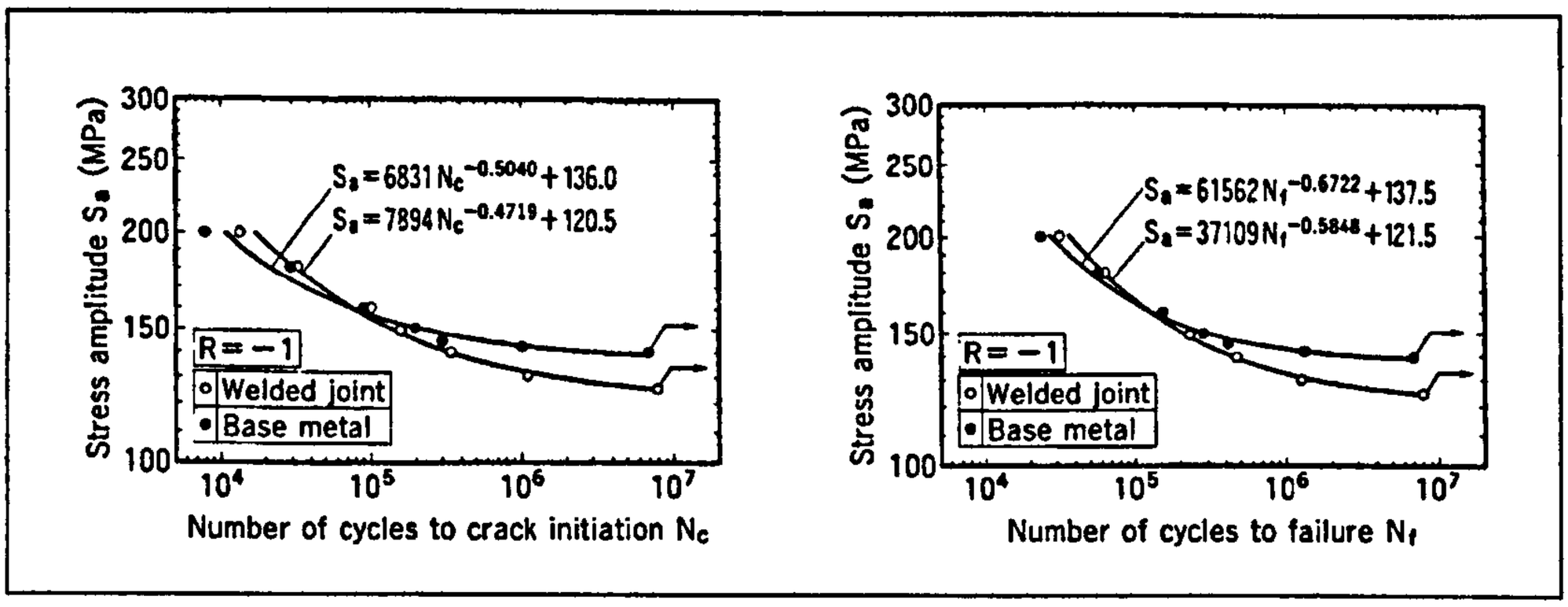

Figure 4.18: S-N curves for SUS316 steel; cycles to crack initiation, crack length ≈ 0.5 mm, (left) and failure (right)[1].

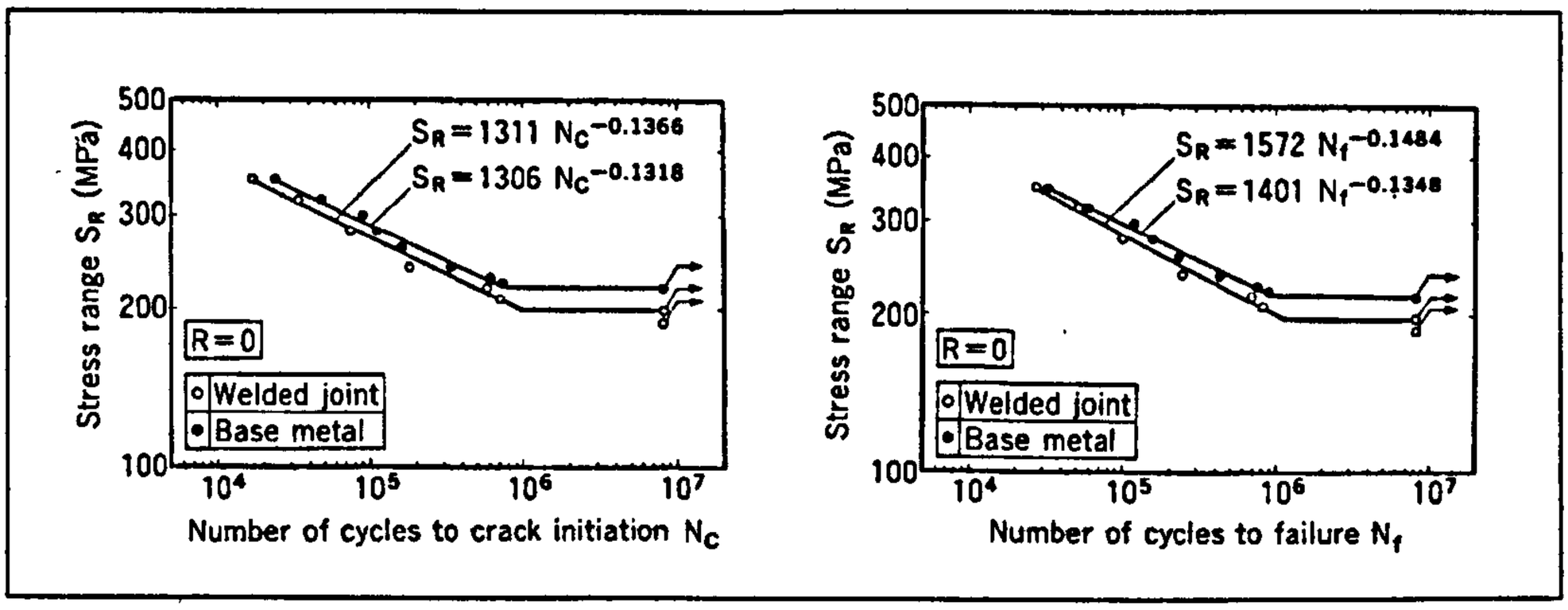

Figure 4.19: S-N curves for SM490A steel; cycles to crack initiation, crack length ≈ 0.5 mm, (left) and failure (right)[1].

Lawrence[2] and Lawrence et al[3] in developing a model which incorporated both the influence of the residual stresses and stress ratio for predicting the fatigue life of welded joints stated that their predictions for AA 5083-O exhibited little dependence on either the residual stress or stress ratio, even though the relaxation of the stabilised mean stress was very slow, due to the high notch root plasticity during the first few cycles before the material cyclically hardened. Their predictions and experimental results, shown in Figure 4.20 and Figure 4.21, suggested that the influence of residual stresses were minimal for fatigue lives < 10^6, although for lives greater than this their effect increased.

[1] Iida, K; Takanashi, M (1998)
[2] Lawrence, FV (1981)
[3] Lawrence FV et al (1982)

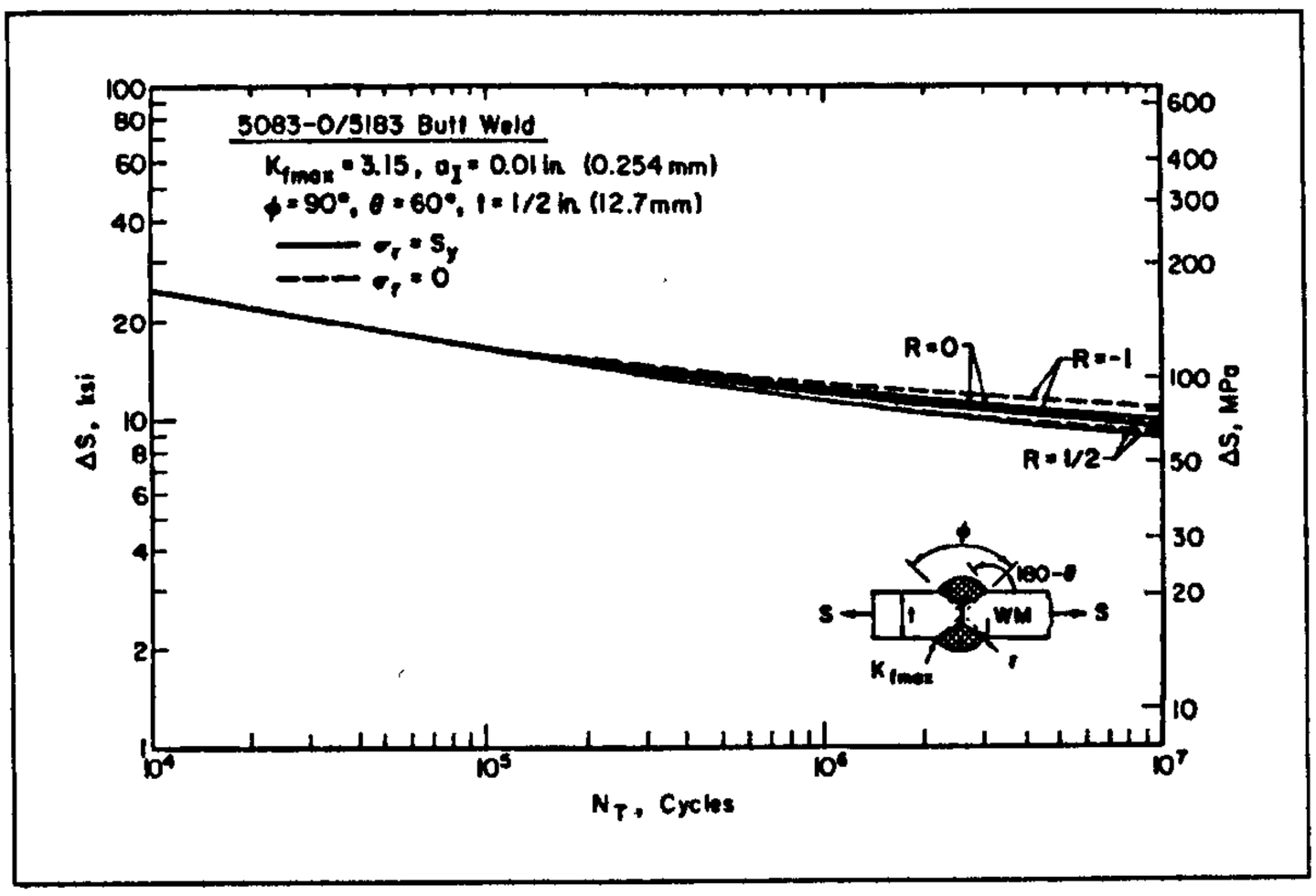

Figure 4.20: Predicted effect of stress relief and stress ratio on butt welded AA 5083-O[1].

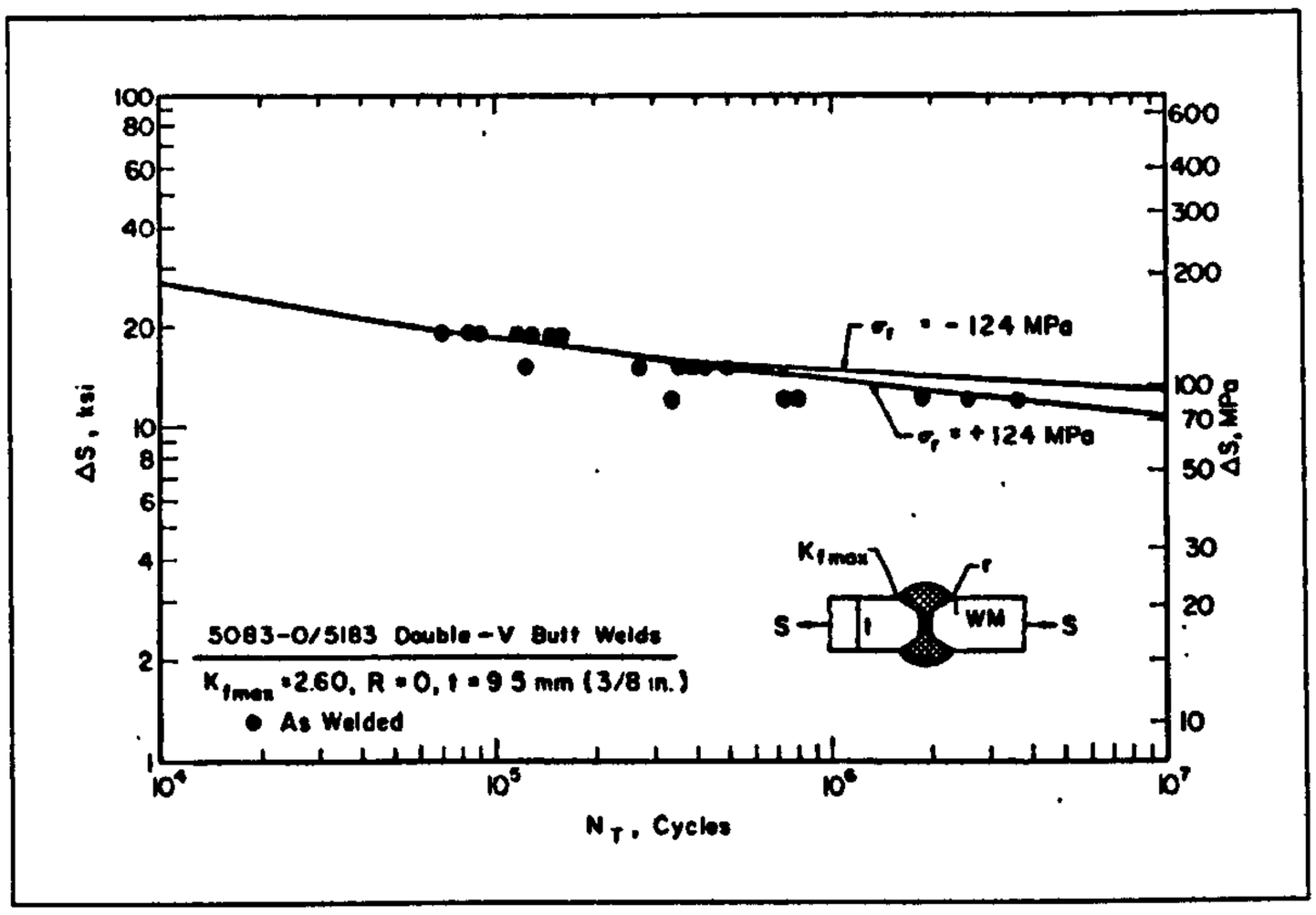

Figure 4.21: Total fatigue life predications and experimental results for butt welded AA 5083-O (σ_r = residual stress)[1].

[1] Lawrence FV et al (1982)

4.4 Measurement of Residual Stresses/strains

Residual strain measurements were undertaken on both the AA 5383-H321 parent plate and both the MIG and FS welds. Hole drilling was undertaken on both the parent material and the welds, with measurements being performed on both the as-welded plates and S-N specimens. Synchrotron radiation strain scanning, an x-ray diffraction technique, was undertaken on the FS welds, with the specimens being of a size between those of the as-welded plates and the S-N specimens; analysis was undertaken for both the as-welded and post fatigue loaded states. Both techniques have advantages and disadvantages.

4.4.1 Distortion due to the MIG and FS Welding Processes

Prior to undertaking the hole drilling residual strain measurements it was evident that the amount of distortion in the welded plates varied depending on the process employed, although the condition of the plates prior to welding was unknown to the author. The distortion manifested itself as a curvature of the welded plates; measurements of the amount of distortion were undertaken by placing a straight edge along the 1 m length and 0.5 m width of the plates and measuring the distance between the arced plate and the straight edge. Longitudinal measurements were made at the centre of the weld in the case of the FS welds and at the weld toe in the case of the MIG. The transverse distortion was also measured at the centre of the plates in the case of the FS welds. Due to the obstruction caused by the weld bead it was not possible to make an accurate measurement for the MIG processes with respect to the transverse distortion, although visual inspection suggested this was greater for the HI weld.

Weld type	Longitudinal distortion (mm)	Transverse distortion (mm)
MIG LI	1	-
MIG HI	12	-
FS SP	7.5	4
FS DP	13	4.5

Table 4.4: Distortion due to fusion welding processess.

The amount of distortion incurred through the welding process is proportional to the magnitude of the strains induced. During the welding procedure the plates were rigidly restrained resulting in unbalanced strains developing within the material. Upon removal of the restraint the strains become self-balancing; this results in distortion of the plate and the further development of the residual stress field. It would be plausible to suggest that the greater the distortion in the plate the greater the redistribution of the residual stresses

and thus the greater the reduction in their magnitude. Thomas[1] states that distortion is almost non-existent in FS welding, although Table 4.4 suggests that for the material and geometry under examination the distortion was as great as that found in MIG welds if the HI and DP processes are compared and worse if the LI and SP welds are compared.

4.4.2 Nomenclature

Throughout this section the subsequent terms, unless otherwise stated, are defined as follows:

Longitudinal relates to the weld direction as viewed from above with the plates in a horizontal plane.

Transverse relates the same horizontal plane as the longitudinal, but at right angles to the weld direction.

Through thickness relates to the plane at right angles to the horizontal plane described above.

Concave side relates to the concave distortion with respect to the longitudinal axis.

Convex side relates to the convex distortion with respect to the longitudinal axis.

Maximum, ε_{Pmax} refers to the maximum principal strain (the strain rosette results provide the magnitude of the principal strains); in the case of the welded plate samples this acted in the longitudinal direction and the transverse direction in the S-N fatigue specimens.

Minimum, ε_{Pmin} refers to the minimum principal strain (principal strains act at right angles to each other); in the case of the welded plate samples this acted in the transverse direction and longitudinally in the S-N fatigue specimens.

[1] Thomas, WM (1998)

4.4.3 Hole Drilling

The hole drilling technique is a semi-destructive technique that involves measuring the relieved strains, using either strain gauges or Moiré gratings, when a small hole is drilled into the material. Typically a strain gauge rosette with three elements, at angles of 0°, 90° and 225° is employed. The rosette is bonded to the material under investigation and then a small hole is drilled at the centre of the rosette. As the local residual strains relax due to the introduction of the hole, the gauges measure the changes in strain at the surface.

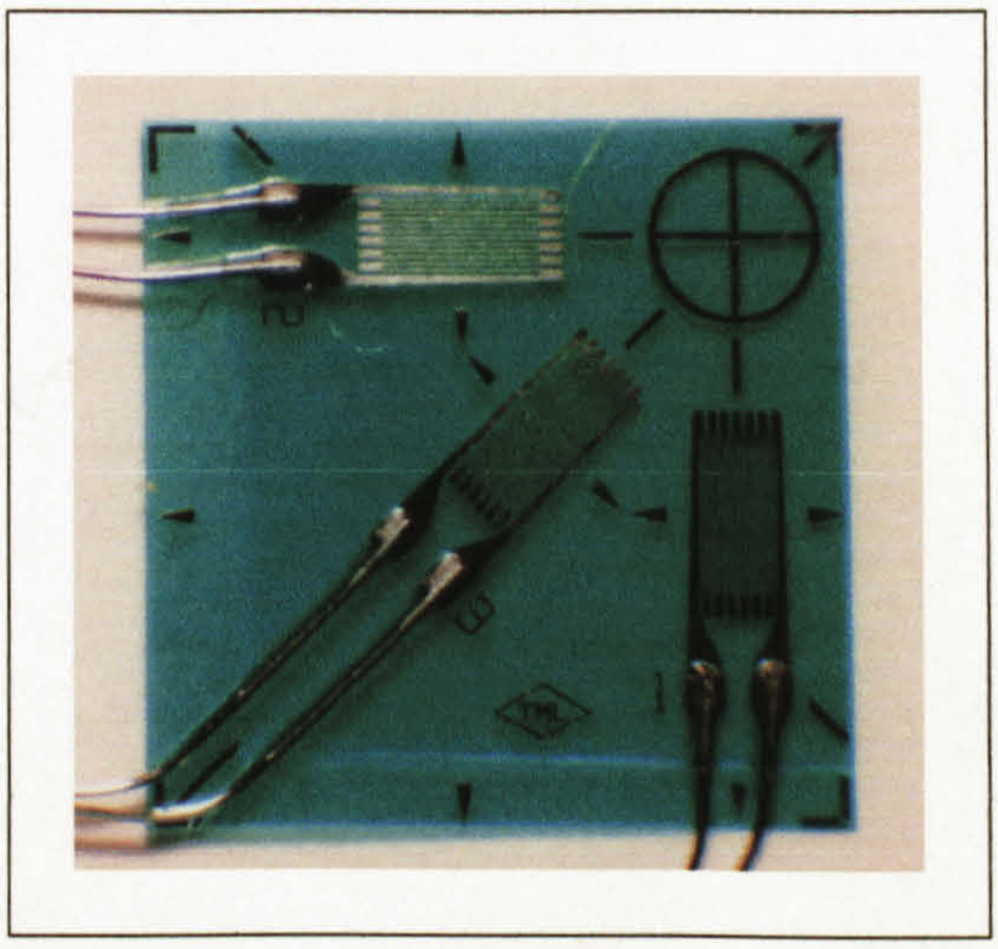

Figure 4.22: TML FRAS-2-23 residual stress rosette.

The rosettes employed were TML type FRAS-2-23, as shown in Figure 4.22, due to the configuration of the three gauges within a 90° angle that allowed the rosette to be positioned in close proximity to the weld toe, in the case of the MIG welds, and edge of the friction band, in the case of the FS welds. Each gauge had a gauge length and width of 2.0 and 1.1 mm respectively, a resistance of 120 Ω and a gauge factor of approximately 2.1. Their gauge centre diameter was 7.0 mm, this being the diameter on which the mid-point of the gauge lengths lie with respect to the hole centre (indicated by the arrowheads at the mid-point of the gauge lengths in Figure 4.22) and they were temperature compensated for use on aluminium[1]. The overall size of the backing material was 9 x 9 mm and the distance between the centre of the hole and the edge was approximately 1.4 mm.

Hole drilling was undertaken using a Measurements Group RS-200 drilling guide and high-speed (300,000 rpm) turbine accessory. Tungsten carbide dental burs of 1.8 mm diameter were used to produce the hole. The analysis relating the measured strains to

[1] Tokyo Sokki Kenkyujo Co., Ltd (undated a).

the residual strains relies on the hole being flat bottomed; this was achieved by employing an inverted cone profiled bur as used by Flaman[1] when developing the technique. The hole was drilled to a depth of 1.2 times the hole diameter, 2.16 mm, as indicated in information supplied with the gauges[2]. For accurate measurement of the relieved strains, ASTM E837-95[3] recommended that the hole diameter for the FRAS-2-23 rosette geometry should be between 2.1 - 3.5 mm diameter, although the maximum sized bur readily available that would produce a flat-bottomed hole and fit the high-speed turbine accessory was of 1.8 mm diameter and as the data sheets supplied with the rosettes suggested that hole diameters of between 1.0 - 3.0 mm were suitable it was decided to proceed with the 1.8 mm diameter bur.

A larger hole could have been made by using an end mill, but the high-speed technique was preferred as the residual strains induced by the process are considerably reduced. Experimental work by Flaman[1] describes how the magnitude of the strains produced by the drilling process in an annealed specimen of 6061 aluminium were more than one third lower using an ultra-high speed drill in comparison to a low-speed end mill. To determine their magnitude in this work, measurements were undertaken on specimens of annealed AA 5383-H321. Annealing was undertaken by heating to either 350 or 375 °C and then slowly cooling to room temperature. Assuming that the annealing process resulted in a fully stress relieved specimen, the minimum magnitude for the residual stresses induced by the high speed hole drilling were < 25 MPa (< 357 με), as indicated in Figure 4.23, although if new burrs were used for each drilling this reduced to < 20 MPa (< 285 με). A tungsten carbide inverted cone bur of 1.5875 mm (1/16") and Measurements Group EA-XX-062RE-120 rosettes were used in the tests. The values obtained compared favourably with those measured by Procter[4] of 40 - 50 MPa in annealed steel specimens.

---

[1] Flaman, MT (1982)
[2] Tokyo Sokki Kenkyujo Co., Ltd. (undated a)
[3] ASTM (1995a)
[4] Proctor, E (1981)

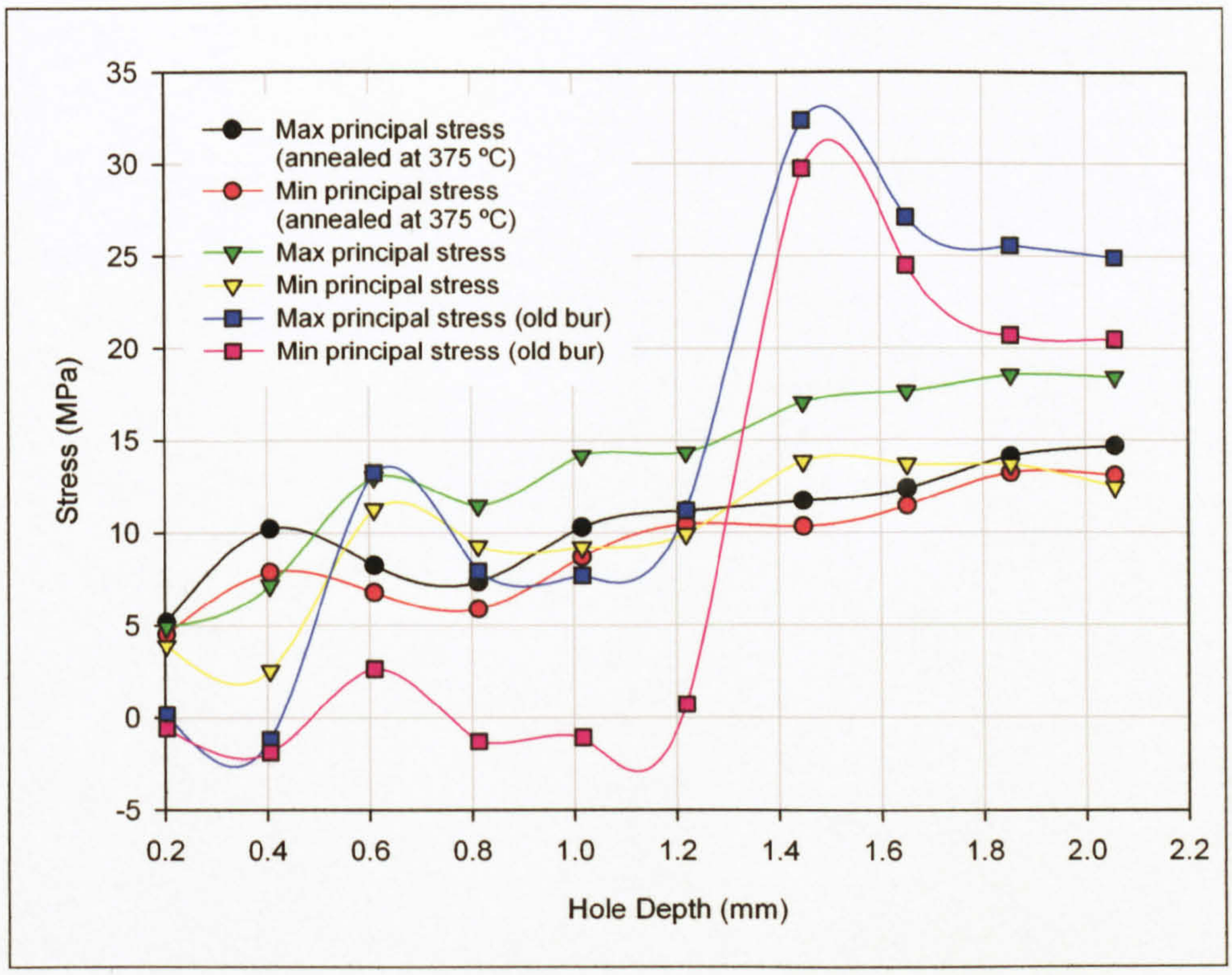

Figure 4.23: Residual stresses induced by high speed hole drilling in annealed (at 350 °C unless stated otherwise) AA 5383.

4.4.3.1 Hole Drilling Experimental Procedure

The following procedure for measuring residual strains using the hole drilling method was employed:

i. The surface was degreased with acetone, then cleaned with Measurements Group M-Prep Conditioner A and finally neutralised with their M-Prep Neutralizer 5A. This process was then repeated to ensure that the process described in ii. resulted in good adhesion.

ii. The rosettes were bonded to the surface with a cyanoacrylate adhesive. Gauge 1 was positioned at right angles to the weld direction, the angle of the maximum principal strain being measured from this gauge. Residual strain rosettes were applied to both sides of the parent and welded plates, as depicted in Figure 4.24 and Figure 4.25. Rosettes were applied at three positions along the length of the weld, at the weld toe in the case of the MIG welds and at the edge of the friction band in the case of the FS welds, shown as rosettes 1(6), 2(7) and 3(8) in Figure 4.25 (the numbers in parenthesis refer to gauges on the opposite surface of the plate). Three or four rosettes were also applied at incremental distances from the weld toe/edge of the friction band by butting the gauges up to each other, allowing measurements to be undertaken at distances of approximately 10.4,

19.4 and 28.4 mm, if four rosettes were employed, from the weld toe/edge of the friction band, shown as rosettes 4(9) and 5(10) in Figure 4.25. The exact layout of the gauges, with respect to the plate and weld geometry, are provided with the results for each of the tests performed.

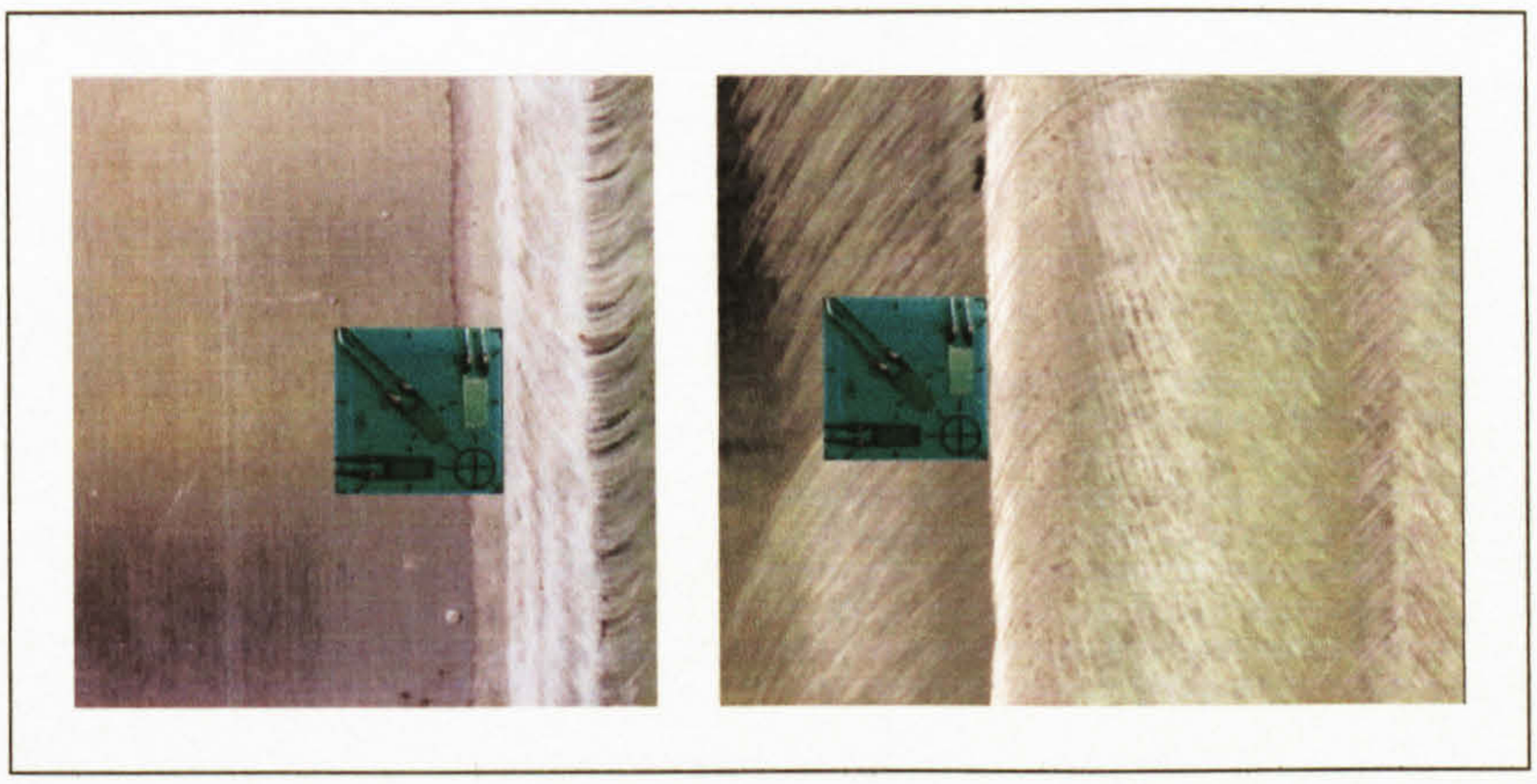

Figure 4.24: Position of residual stress rosettes with respect to the MIG weld toe (left) and the edge of the friction band of the FS welds (right).

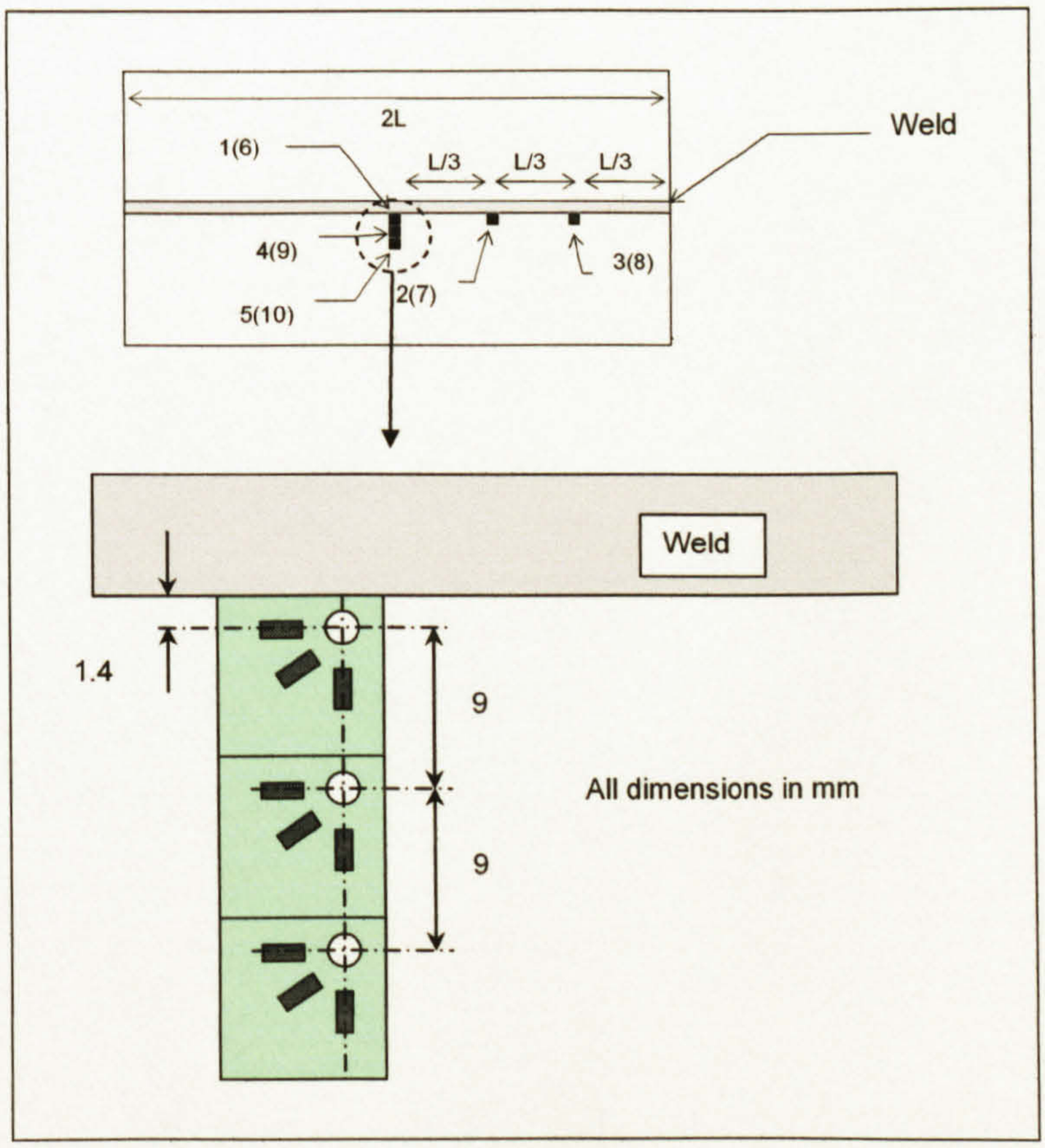

Figure 4.25: Position of residual stress rosettes.

iii. The gauges were connected to a Measurements Group P-3500 strain indicator via a SB-1 switch and balance unit. The three lead, quarter-bridge, method being used for connecting the gauges.

iv. The RS-200 milling guide was placed over the applied rosette and the adjustable feet held in place using double-sided tape. The guide was then levelled with respect to the rosette being utilised. Using the microscope assembly cross-hairs and the adjusting screws the guide was centred over the rosette cross-marks.

v. Prior to drilling the hole an end mill was used to cut through the backing material of the rosette to prevent the bur from becoming choked. The high-speed turbine accessory, as shown in Figure 4.26, rotating at speeds of up to 300,000 rpm when supplied with compressed air at a pressure of 0.276 MPa (40 psi), was then used to drill the hole at a rate of approximately 6.25 - 12.5 $\mu m.s^{-1}$ and measurements of the relieved strains recorded at depth intervals of 0.216 mm to a final depth of 2.16 mm. A micrometer housed within the drilling guide was used to measure the vertical displacement. Prior to stopping the turbine to record the strains the bur was raised slightly from the hole bottom to allow it to decelerate, and accelerate when drilling was recommenced, without cutting into the aluminium. Each bur was used a maximum of two times to minimise the amount of plastic deformation induced by the drilling of the hole.

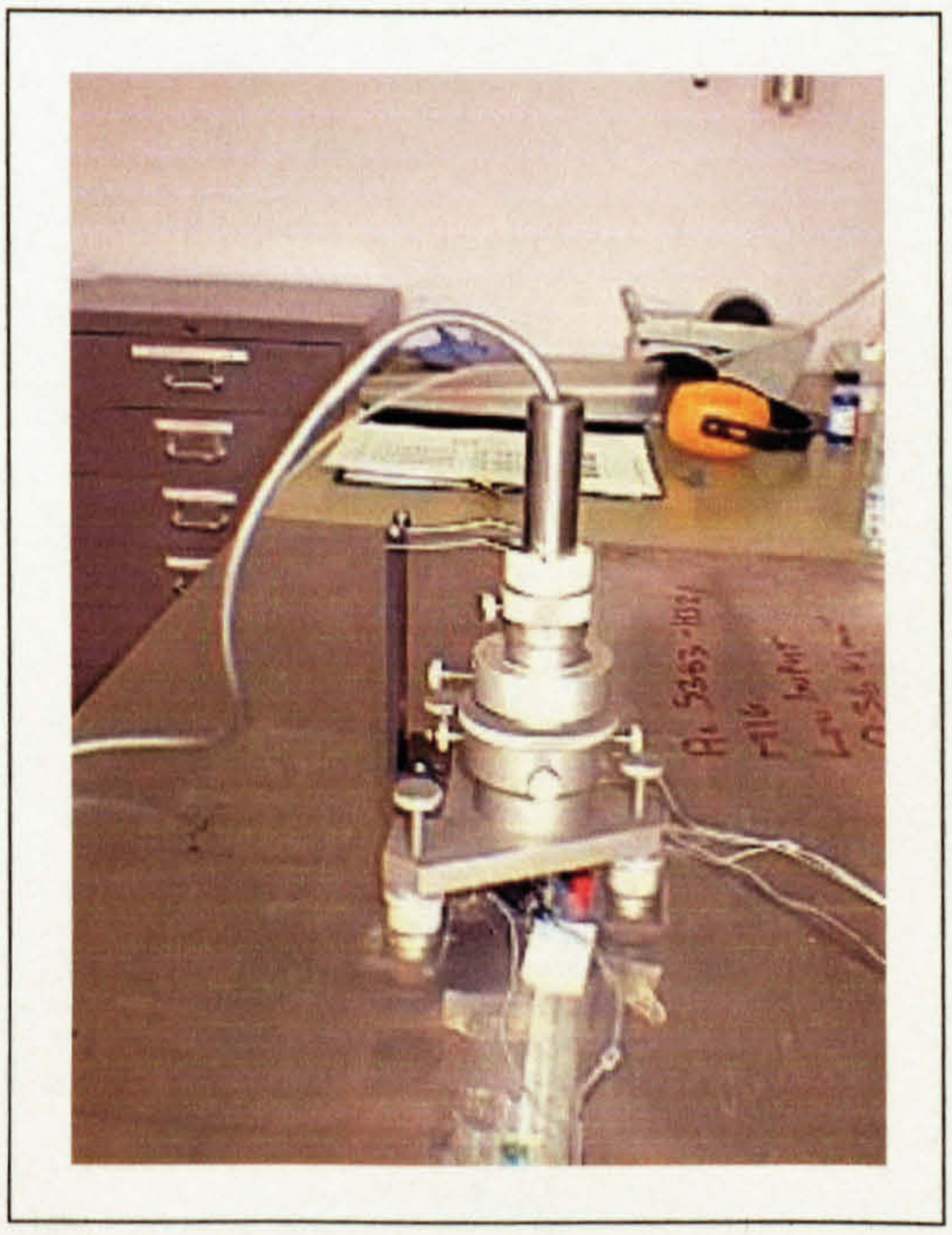

Figure 4.26: Measurement of residual strains using the RS-200 milling guide and high speed air turbine drill.

4.4.4 Determination of Residual Stresses/strains

Due to the magnitude of the longitudinal residual stresses in the near vicinity of the weld the values obtained for residual stresses were converted to strains, with the assumption being made that $\sigma_z = 0$ (σ_z = through thickness stress). Residual stresses were then determined with reference to the appropriate stress-strain responses, as shown in Figure 3.118 (page 121). The following equations and properties were used to determine the residual strains:

$$\sigma_{min} = \left[\frac{\varepsilon_3 + \varepsilon_1}{4\bar{A}} + \frac{\sqrt{(\varepsilon_3 - \varepsilon_1)^2 + (\varepsilon_3 + \varepsilon_1 - 2\varepsilon_2)^2}}{4\bar{B}} \right] \quad (4.3)^1$$

$$\sigma_{max} = \left[\frac{\varepsilon_3 + \varepsilon_1}{4\bar{A}} - \frac{\sqrt{(\varepsilon_3 - \varepsilon_1)^2 + (\varepsilon_3 + \varepsilon_1 - 2\varepsilon_2)^2}}{4\bar{B}} \right] \quad (4.4)^1$$

$$\theta = \frac{1}{2} \arctan \left[\frac{\varepsilon_3 + \varepsilon_1 - 2\varepsilon_2}{\varepsilon_3 - \varepsilon_1} \right] \quad (4.5)^1$$

$$\varepsilon_{min} = \frac{\sigma_{min}}{E} - \frac{\nu.\sigma_{max}}{E} \quad (4.6)$$

$$\varepsilon_{max} = \frac{\sigma_{max}}{E} - \frac{\nu.\sigma_{min}}{E} \quad (4.7)$$

where: σ_{min} = minimum principal stress.

σ_{max} = maximum principal stress.

ε_1, ε_2 & ε_3 = the measured strains from rosette gauges 1, 2 & 3 respectively.

θ = angle from gauge 1 of the rosette (in a clockwise (CW) direction) to σ_{max}.

ε_{min} = minimum principal strain (assuming plane stress, $\sigma_{thickness} = 0$).

ε_{max} = maximum principal strain (assuming plane stress, $\sigma_{thickness} = 0$).

$4\bar{A}$ and $4\bar{B}$ = calibration constants.

$$4\bar{A} = -\frac{(1+\nu)d^2}{2ER^2} = -2.501 \times 10^{-12} \quad (4.8)^2$$

$$4\bar{B} = -\frac{2d^2}{ER^2} + \frac{3(1+\nu)d^4}{8ER^4} = -7.061 \times 10^{-12} \quad (4.9)^2$$

where: ν = Poisson's ratio, 0.324*.

d = diameter of hole, 1.8×10^{-3} m.

E = elastic modulus, 70 GPa*.

---

[1] ASTM (1995a)
[2] Tokyo Sokki Kenkyujo Co., Ltd. (undated b)
* Determined from uniaxial tensile test.

R = Radius of lateral grid centreline, 3.5×10^{-3} m (the radial distance from the centre of the drilled hole and the centre of the gauges).

For the values of the residual stresses, calculated through equations (4.3) and (4.4), to be valid the analysis must be elastic. Invalid results will be obtained if the residual stresses exceed $\sigma_y/3$ or $\sigma_y/2$, for uniaxial or equal biaxial stress states respectively, due to plastic deformation at the hole perimeter resulting from its stress concentrating nature. This deformation invalidates the relationship between the measured surface strains and the calculated residual strains-stresses, although Schajer[1] states that studies have been undertaken that show that the simple analysis for a biaxial stress state of 0.8 σ_y still provides accurate stress data. Due to the values obtained for the residual strains the appropriate stresses, enclosed in parenthesis after the strain values in Table 4.6 to Table 4.17, were determined with reference to the appropriate stress-strain responses, as shown in Figure 3.118 (page 121), for magnitudes that were greater than the yield strain of the weld, as shown in Table 4.5; if their magnitude was below the yield strain the values determined with respect to Hooke's law.

The above comments suggest that the results from the welded plates should be treated with discretion. It would be prudent to consider the results as qualitative rather than quantitative especially those that are greater in magnitude than $\sigma_y/2$.

Specimen	σ_y(MPa)	ε_y (με)	E (GPa)	ν
5383 |-	244	3486	70*	0.324
5383 //	267	3814		
MIG LI	135	1929		
MIG HI	135	1929		
FS SP	140	2000		
FS DP	158	2257		

Table 4.5: Yield stress and strain of AA 5383-H321 PP and MIG and FS butt welds.

Details of the results returned by the individual rosettes are detailed in Section 11, Appendix A ~ Determination of Residual Strains and Stresses by the Hole Drilling Technique ~ Individual Rosette Results (pages 489 - 498).

---

[1] Schajer, GS (1996)

* A constant value of 70 GPa was employed for the elastic modulus as measurements were made in the HAZ of the weld and it may be considered reasonable to assume that the modulus in this region would be comparable to that of the parent material rather than those measured across the weld during uniaxial tensile testing.

4.4.4.1 Parent Plate

TML FRAS-2-23 rosettes were placed as indicated in Figure 4.27, the plates being 1000 x 250 x 8 mm (length x width x thickness).

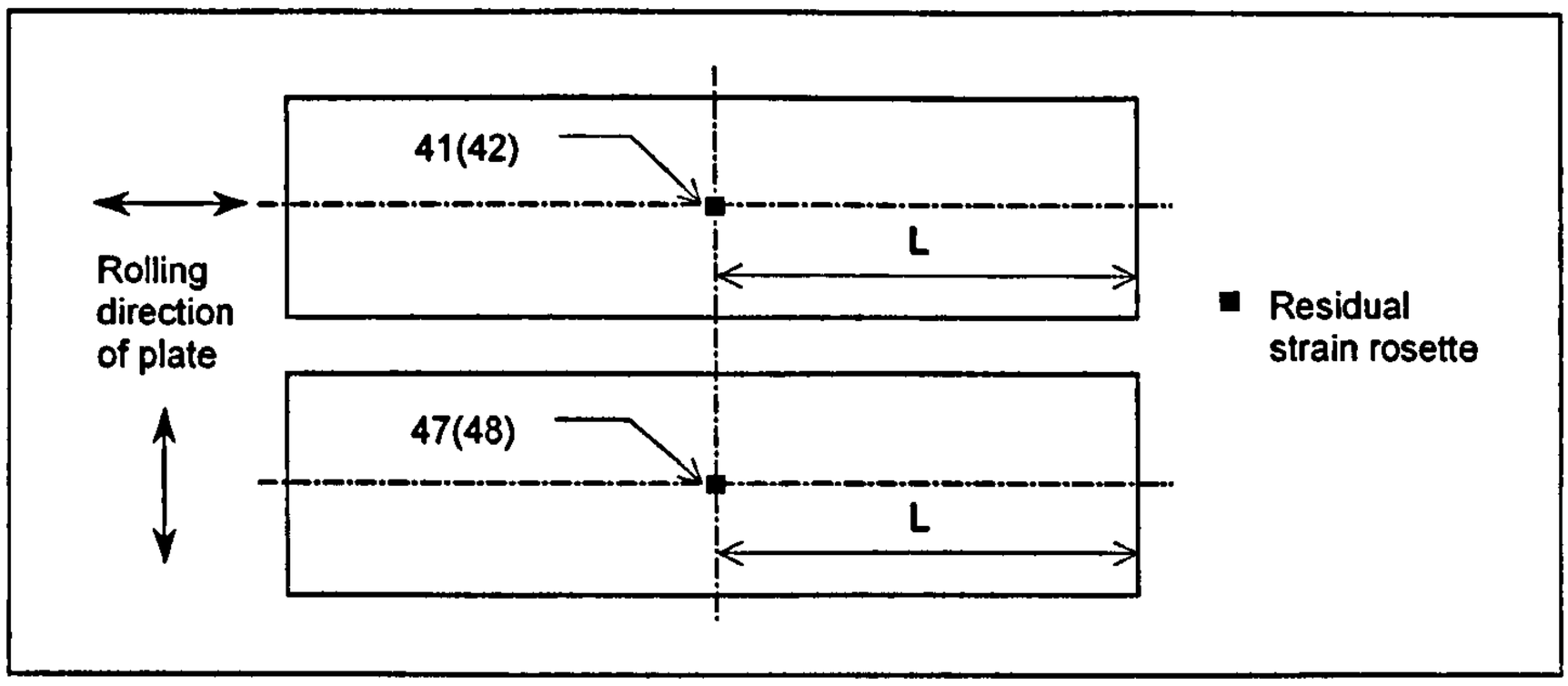

Figure 4.27: Position of residual strain gauge rosettes with respect to the rolling direction of the plate.

Rolling direction along length of plate			
Rosette Number	Residual strain, plane stress, equations (4.6) & (4.7)		Angle of ε_{Pmax} from the rolling direction, CW, equation (4.5)
	ε_{Pmax} (με) (σ_{Pmax}) (MPa)	ε_{Pmin} (με) (σ_{Pmin}) (MPa)	
41	788 (55)	-46 (-3)	-14°
42	604 (42)	-967 (-68)	-59°

Table 4.6: Residual strains in AA 5383-H321 parent plate.

Rolling direction along width of plate			
Rosette Number	Residual strain, plane stress, equations (4.6) & (4.7)		Angle of ε_{Pmax} from the rolling direction, CW, equation (4.5)
	ε_{Pmax} (με) (σ_{Pmax}) (MPa)	ε_{Pmin} (με) (σ_{Pmin}) (MPa)	
47	265 (19)	75 (5)	66°
48	411 (29)	207 (15)	-42°

Table 4.7: Residual strains in AA 5383-H321 parent plate.

The plate with the rolling direction along the length (identical to the rolling direction of the welded plates) returned values for the peak residual strain of 788 με (55 MPa) and a nadir of -46 με (-3 MPa). The opposite side resulted in values of 604 με (42 MPa) and -967 με (-68 MPa) for the peak and nadir values respectively. The angles of -14° and -59° for the direction of the maximum strain from the rolling direction suggested that the rolling process did not fully influence the direction of the residual strains.

The residual strains measured in the plate with the rolling direction along the width resulted in ranges of 265 με (19 MPa) and 75 με (5 MPa) for the peak and nadir values

respectively for one side. The values for the reverse side were 411 με (29 MPa) and 207 με (15 MPa) for the peak and nadir values respectively. The angle of the maximum residual strains, 66° and -42° from the rolling direction, again suggested that the rolling process did not overly influence their direction.

It was evident that although the rolling process did not fully influence the direction of the residual strains, the plate with the rolling direction along the length returned greater values for the residual strains than that with the rolling direction across the width of the plate. This suggested that cutting the plate into smaller sections resulted in a redistribution of the strains and a subsequent diminishing in their magnitude.

4.4.4.2 MIG Low Input

TML FRAS-2-23 rosettes were positioned as indicated in Figure 4.28.

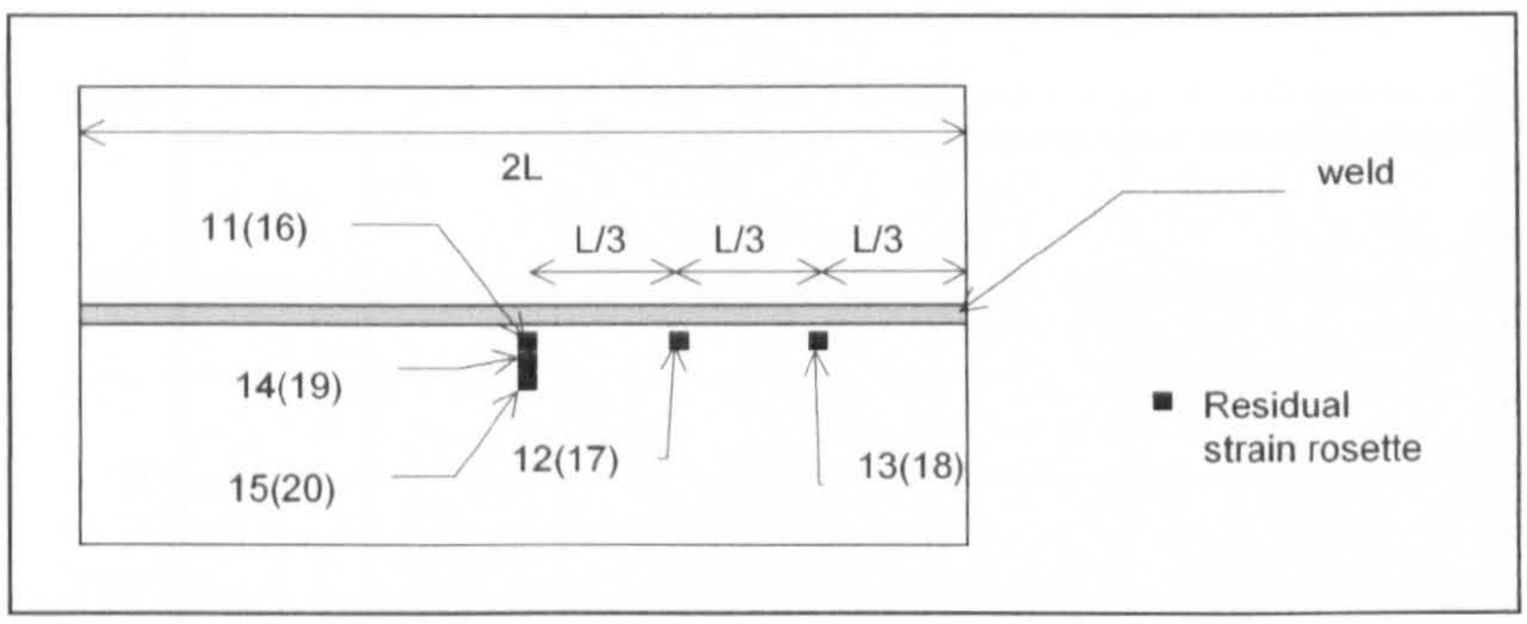

Figure 4.28: Position of residual strain gauge rosettes in relation to the MIG LI weld.

Convex side					
Rosette Number	**Residual strain, plane stress, equations (4.6) & (4.7)**				**Angle of ε_{Pmax} from the weld, CW, equation (4.5)**
	ε_{Pmax} (με) (σ_{Pmax}) (MPa)		**ε_{Pmin} (με) (σ_{Pmin}) (MPa)**		
11	4974 (188)	Mean 5016 (188)	-1306 (-91)	Mean -1497 (-105)	-7°
12	5464 (192)		-1456 (-102)		-9°
13	4610 (185)		-1730 (-123)		-6°
14	4254 (181)		-238 (-17)		2°
15	1178 (82)		188 (13)		14°

Table 4.8: Residual strains in the region of the MIG LI weld (convex side).

Concave side					
Rosette Number	**Residual strain, plane stress, equations (4.6) & (4.7)**				**Angle of ε_{Pmax} from the weld, CW, equation (4.5)**
	ε_{Pmax} (με) (σ_{Pmax}) (MPa)		**ε_{Pmin} (με) (σ_{Pmin}) (MPa)**		
16	4635 (185)	Mean 4453 (183)	-1469 (-103)	Mean -981 (-69)	-5°
17	4488 (184)		-859 (-60)		-8°
18	4237 (181)		-615 (-43)		-6°
19	3490 (173)		-432 (-30)		0°
20	865 (61)		61 (4)		0°

Table 4.9: Residual strains in the region of the MIG LI weld (concave side).

Table 4.8 and Table 4.9 detail the magnitudes of the residual strains returned by the MIG LI weld, with Figure 4.29 representing those at the weld toe and Figure 4.30 representing those at a distance perpendicular to the weld direction. The maximum principal strains at the weld toe were within -5° to -9° of the weld direction, with the minimum principal strains acting at right angles to these, approximately transverse to the weld direction.

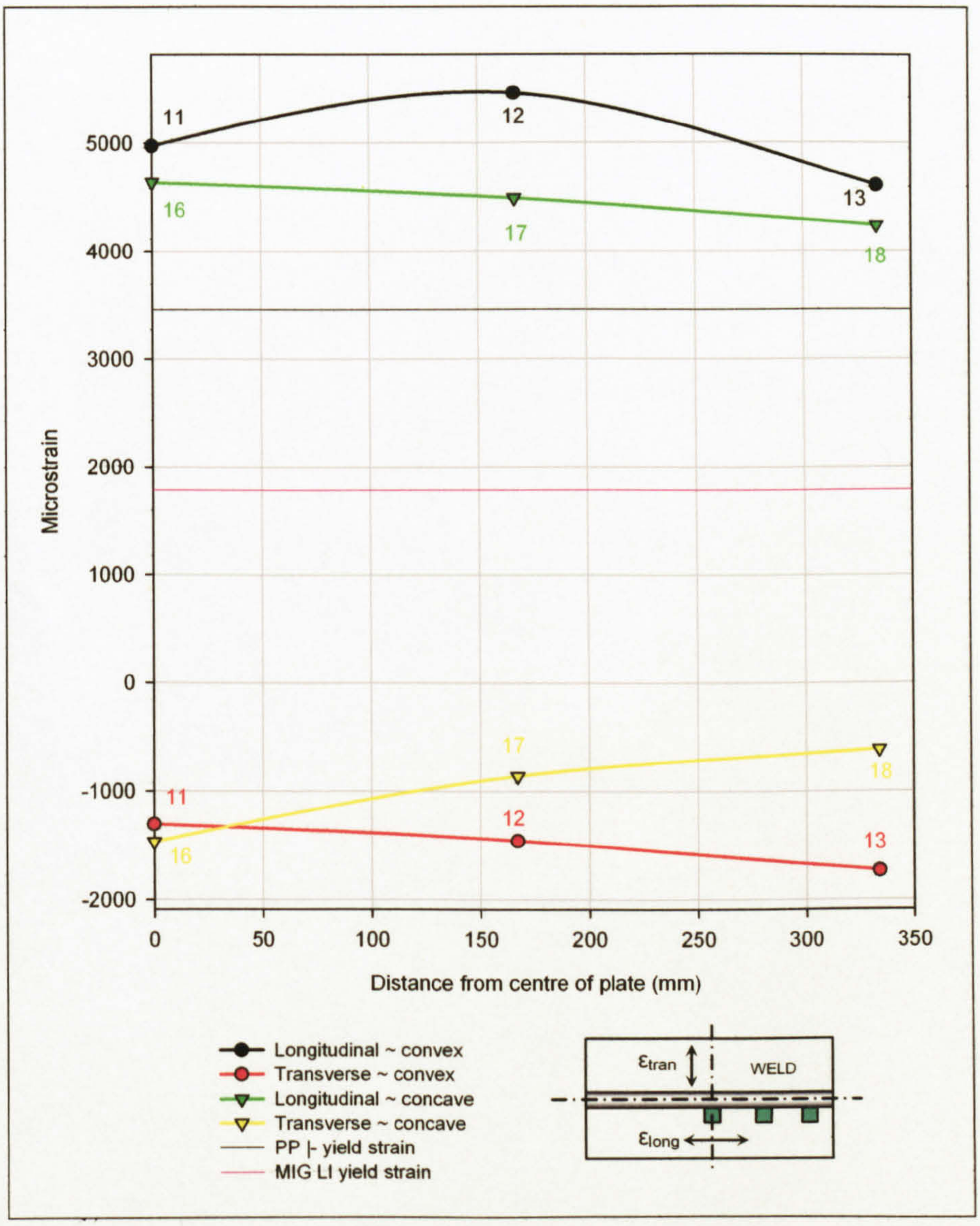

Figure 4.29: Residual strains at the MIG LI weld toe, measured at various points along the length of the plate (numbers refer to rosettes, see Figure 4.28).

The longitudinal residual strains measured at the weld toe (ε_{Pmax}, running in the direction of the weld), on both the concave and convex sides exhibited values greater than the yield strain of the PP |-, with those on the convex side typically returning slightly greater values than those on the concave side, as shown in Figure 4.29 The magnitude of the strains on the concave side remained relatively constant, ranging from 4237 - 4365 με (181 - 185 MPa) with a mean value of 4453 με (183 MPa), whilst the convex side of the

plate exhibited greater variability, with the strains ranging from 4610 - 5464 με (185 - 192 MPa) with a mean value of 5016 με (188 MPa).

The transverse residual strains measured at the weld toe (ε_{Pmin}, running transverse to the direction of the weld) returned values that were compressive, as shown in Figure 4.29. The values for both the convex and concave sides were relatively constant in magnitude up to a distance of 167 mm from centre of the plate, with greater disparity exhibited at a distance of 334 mm. The convex side returned values that ranged from -1730 to -1306 (-123 to -91 MPa) and a mean value of -1497 με (-105 MPa), while the transverse residual strains on the concave side returned values ranging from -1469 to -615 με (-103 to -43 MPa) with a mean value of -981 με (-69 MPa).

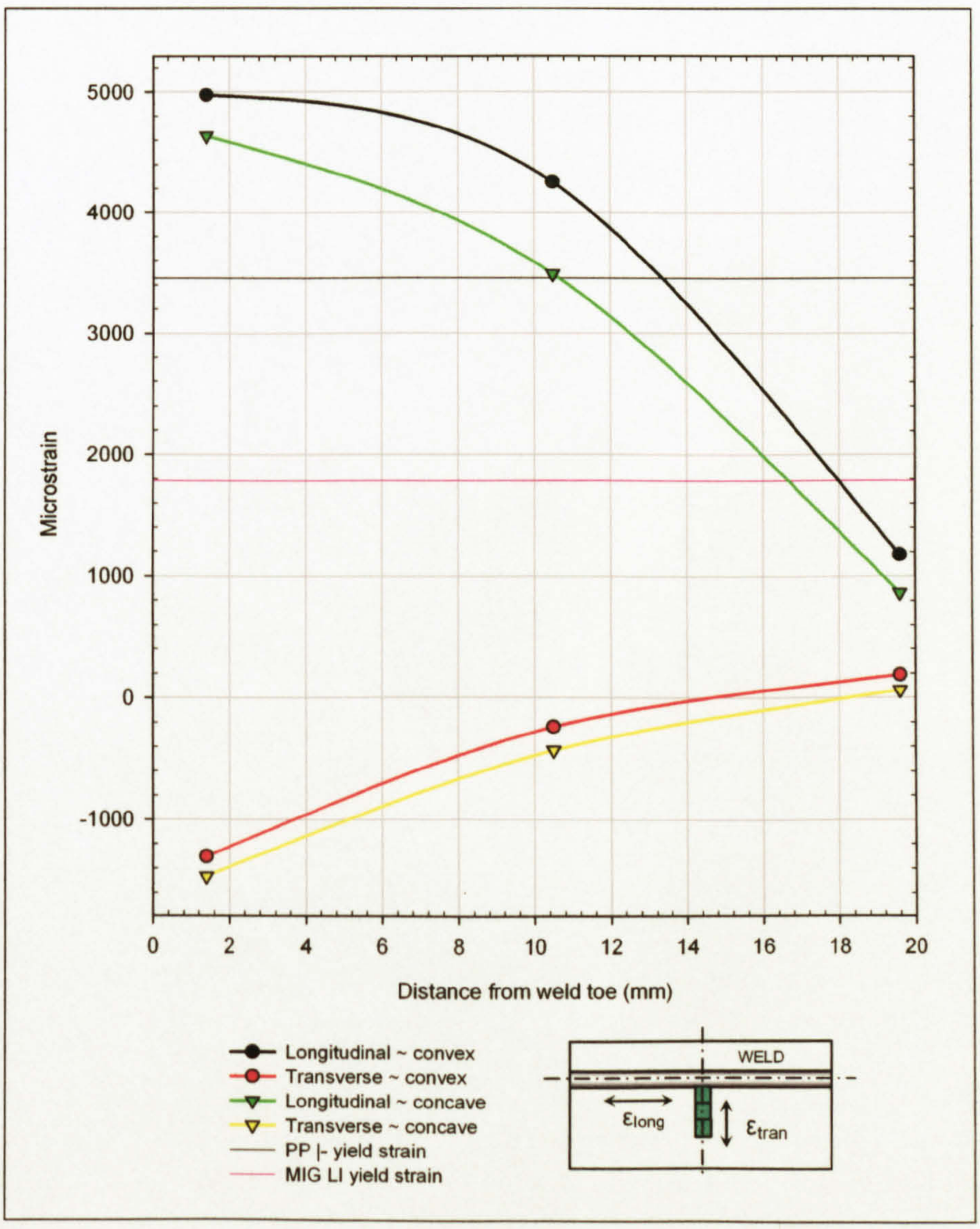

Figure 4.30: Residual strains at the MIG LI weld toe and HAZ, measured at the centre of the length, (numbers refer to rosettes, see Figure 4.28).

The longitudinal residual strains (ε_{Pmax}, running in the direction of the weld) remained above the magnitude of the PP |- yield strain up to a distance of 10 mm from the weld toe for both the convex and concave sides, but these reduced to a value less than that of the MIG LI yield strain at a distance of 19 mm, as shown in Figure 4.30. Peak values for both sides were recorded at the weld toe, with the range of the strains measured in the longitudinal direction being 1178 - 4974 με (82 - 188 MPa) and 865 - 4635 με (61 - 185 MPa) for the convex and concave sides respectively.

The transverse residual strains (ε_{Pmin}, running transverse to the direction of the weld) were compressive in nature at a distance of 10 mm from the weld toe for both the convex and concave sides of the plate, as shown in Figure 4.30. The most compressive values were measured at the weld toe, although this gradually diminished up to a distance of 19 mm from the toe where both sides of the plate returned small tensile values. The transverse residual strains ranged in value from -1306 to 188 με (-91 to 13 MPa) and -1469 to 61 με (-103 to 4 MPa) for the convex and concave sides respectively.

4.4.4.3 MIG High Input

TML FRAS-2-23 rosettes were placed as indicated in Figure 4.31.

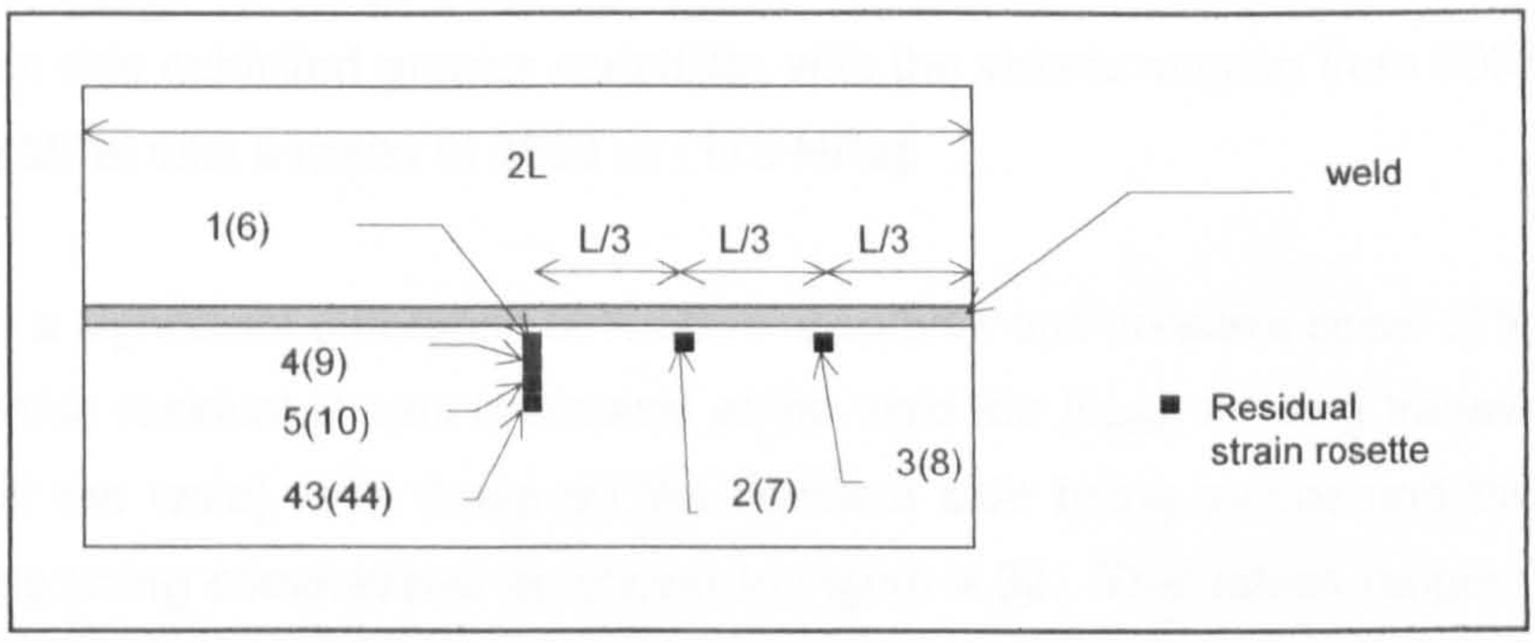

Figure 4.31: Position of residual strain gauge rosettes in relation to the MIG HI weld.

Convex side					
Rosette Number	**Residual strain, plane stress, equations (4.6) & (4.7)**				**Angle of ε_{Pmax} from the weld, CW, equation (4.5)**
	ε_{Pmax} (με) (σ_{Pmax}) (MPa)		**ε_{Pmin} (με) (σ_{Pmin}) (MPa)**		
1	4347 (180)	Mean 3830 (173)	-2092 (-136)	Mean -1091 (-76)	-6°
2	3003 (160)		-254 (-18)		-3°
3	4140 (177)		-928 (-65)		0°
4	5089 (189)		-2016 (-133)		-2°
5	3526 (169)		-971 (-68)		1°
43	1785 (125)		-928 (-65)		-2°

Table 4.10: Residual strains in the region of the MIG HI weld (convex side).

Concave side					
Rosette Number	Residual strain, plane stress, equations (4.6) & (4.7)				Angle of ε_{Pmax} from the weld, CW, equation (4.5)
	ε_{Pmax} (με) (σ_{Pmax}) (MPa)		ε_{Pmin} (με) (σ_{Pmin}) (MPa)		
6	3280 (165)	Mean 3246 (164)	751 (53)	Mean 564 (40)	1°
7	3371 (166)		452 (32)		2°
8	3087 (162)		488 (34)		-3°
9	4595 (183)		-224 (-16)		-2°
10	3518 (169)		512 (36)		2°
44	1104 (77)		710 (50)		38°

Table 4.11: Residual strains in the region of the MIG HI weld (concave side).

Table 4.10 and Table 4.11 detail the magnitudes of the residual strains returned by the MIG HI weld, with Figure 4.32 representing those at the weld toe and Figure 4.33 representing those at a distance perpendicular to the weld direction. The maximum principal strains at the weld toe acted within -6° to 2° of the weld direction, with the minimum principal strains acting at right angles to these, transverse to the weld direction.

The longitudinal residual strains measured at the weld toe (ε_{Pmax}, running in the direction of the weld), on both the concave and convex sides exhibited values that were in the region of, or greater than, the yield strain of the PP |-, as shown in Figure 4.32. The magnitude of the strains measured on the concave side remained relatively constant, ranging from 3087 - 3371 με (162 - 166 MPa) with a mean value of 3246 με (164 MPa). The convex side exhibited greater variability, with the values ranging from 3003 - 4347 με (160 - 180 MPa) with a mean of 3830 με (173 MPa).

There was a significant difference between the convex and concave sides of the plate for the transverse residual strains measured at the weld toe (ε_{Pmin}, running transverse to the direction of the weld), with those on the concave side being tensile and those on the convex side being compressive as shown in Figure 4.32. The values ranged from 452 - 751 με (32 - 53 MPa) with a mean value of 564 με (40 MPa) for the concave side with the convex side returning a mean value of -1091 με (-76 MPa) from a range of -2092 to -254 με (-136 to -18 MPa).

For both the longitudinal and transverse strains measured at the weld toe it was evident that the convex side, in contrast to the concave side, exhibited greater variability in their magnitudes.

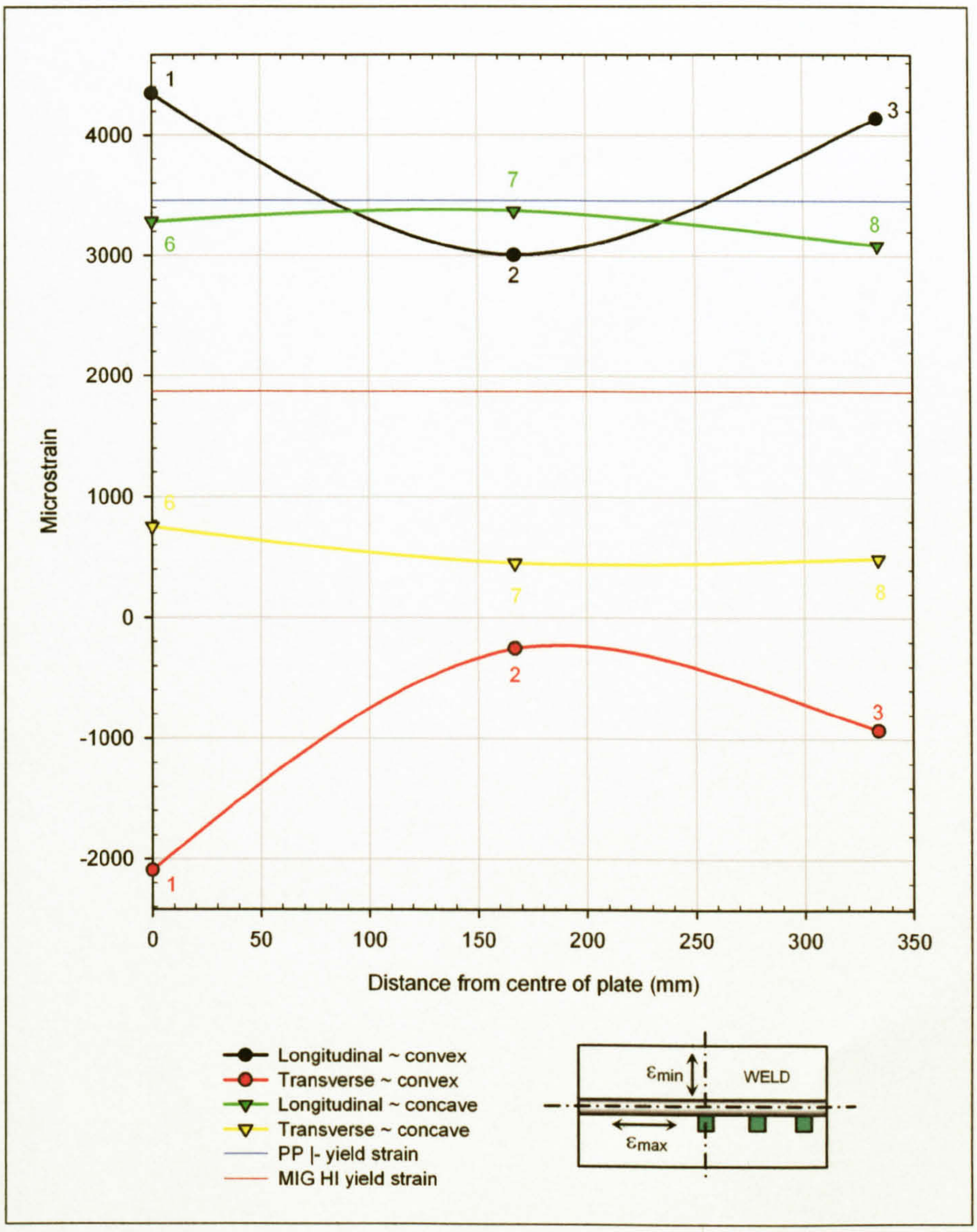

Figure 4.32: Residual strains at the MIG HI weld toe, measured at various points along the length of the plate (numbers refer to rosettes, see Figure 4.31).

The longitudinal residual strains (ε_{Pmax}, running in the direction of the weld), on both the concave and convex sides of the plate typically remained above the magnitude of the PP |- yield strain up to a distance of 19 mm from the weld toe, although they rapidly reduced to below the magnitude of the MIG HI weld yield strain at a distance of 28 mm, as shown in Figure 4.33. Peak values were observed at a distance 10 mm from the weld toe. The range of the strains acting in the longitudinal direction was 1785 - 5089 με (125 - 189 MPa) and 1104 - 4595 με (77 - 183 MPa) for the convex and concave sides respectively.

The transverse residual strains (ε_{Pmin}, running transverse to the direction of the weld) were compressive for the convex side, but were predominantly tensile for the concave side, as shown in Figure 4.33. The magnitudes of the residual strains ranged from -2092

to -928 με (-136 to -65 MPa) and -224 to 751 με (-16 to 53 MPa) for the convex and concave sides respectively.

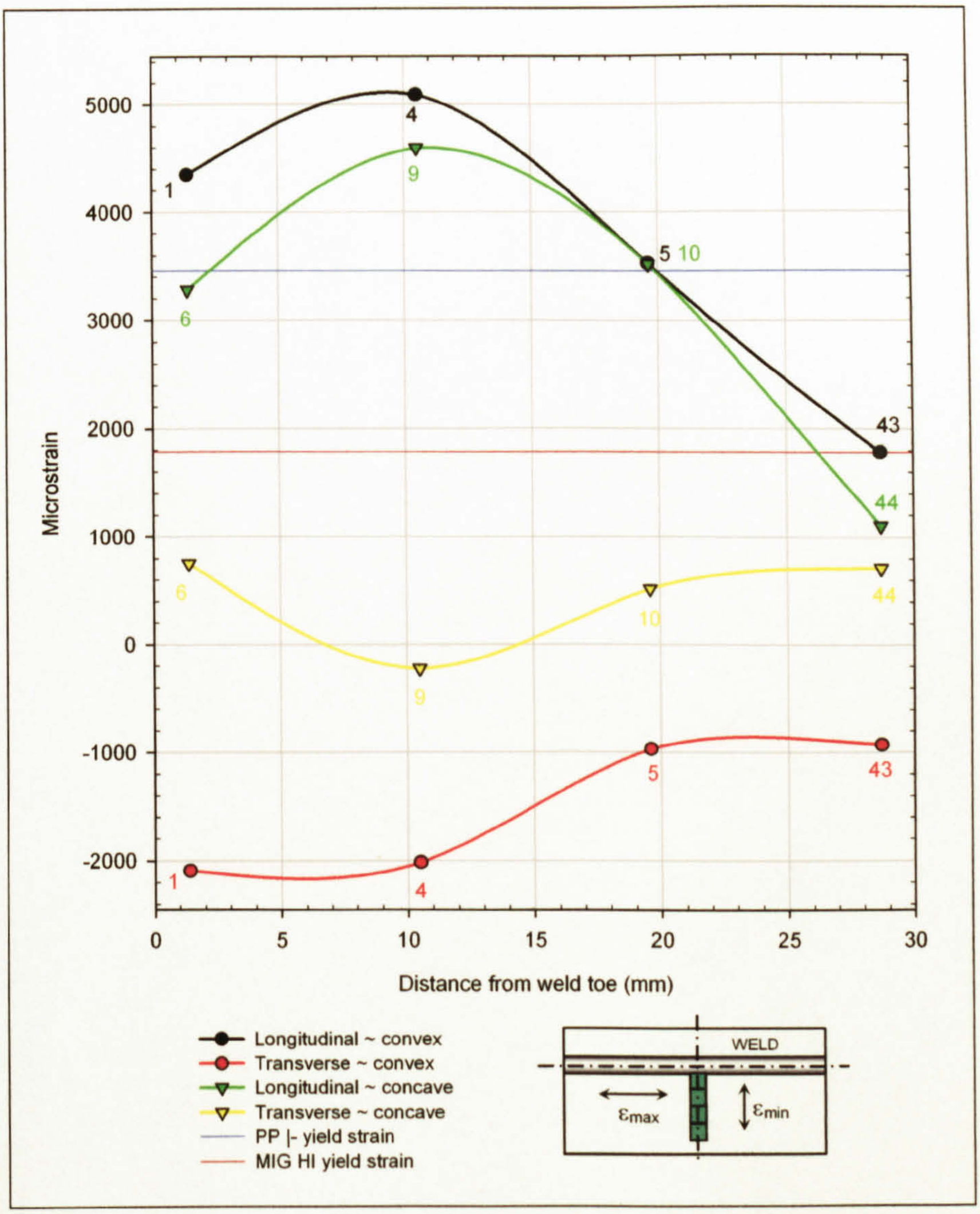

Figure 4.33: Residual strains at the MIG HI weld toe and HAZ, measured at the centre of the length, (numbers refer to rosettes, see Figure 4.31).

4.4.4.4 FS Single Pass

TML FRAS-2-23 rosettes were placed as indicated in Figure 4.34.

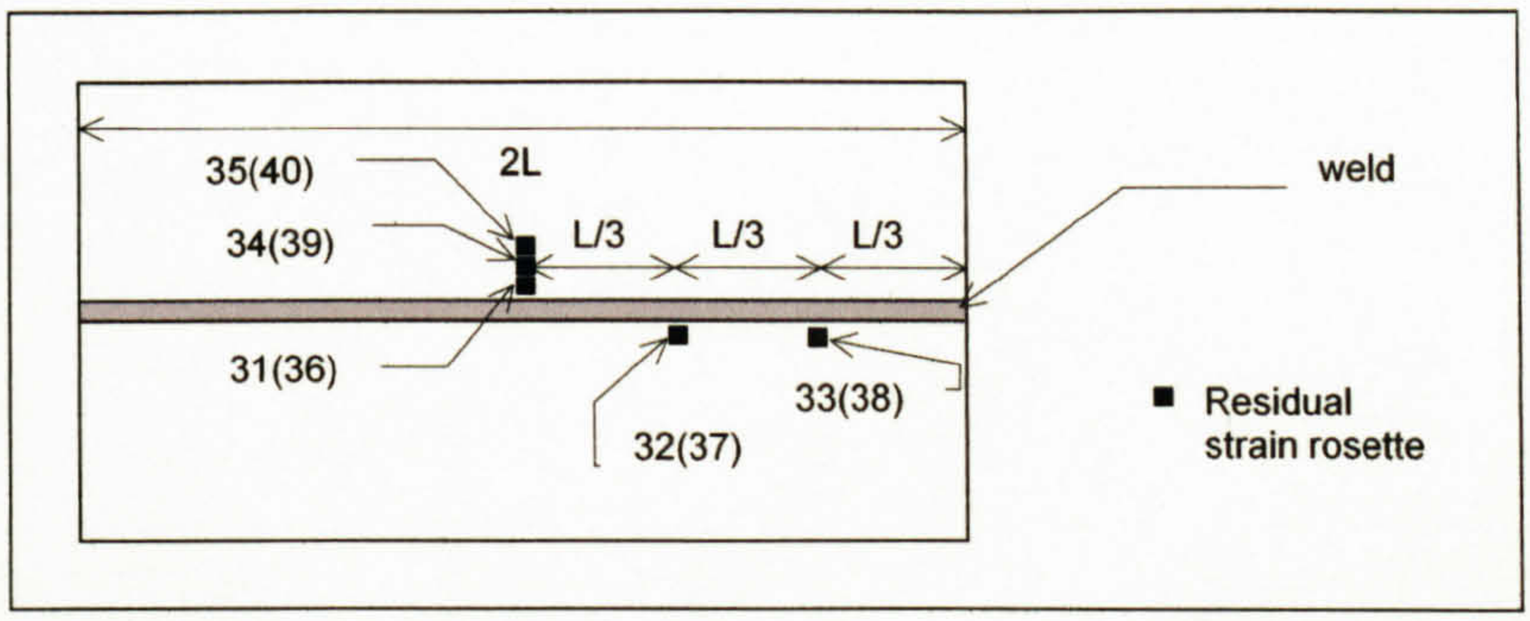

Figure 4.34: Position of residual strain gauge rosettes in relation to FS SP weld.

Friction band side					
Rosette Number*	Residual strain, plane stress, equations (4.6) & (4.7)				Angle of ε_{Pmax} from the weld, CW, equation (4.5)
	ε_{Pmax} (με) (σ_{Pmax}) (MPa)		ε_{Pmin} (με) (σ_{Pmin}) (MPa)		
31(R)	1901 (133)	Mean 2589 (153)	-1060 (-74)	Mean -800 (-56)	-5°
32(A)	3143 (157)		-834 (-58)		3°
33(A)	2722 (155)		-506 (-35)		-2°
34(R)	2235 (149)		-730 (-51)		-1°
35(R)	1641 (115)		-567 (-40)		-2°

Table 4.12: Residual strains in the region of the FS SP weld (friction band side).

Weld seam side					
Rosette Number*	Residual strain, plane stress, equations (4.6) & (4.7)				Angle of ε_{Pmax} from the weld, CW, equation (4.5)
	ε_{Pmax} (με) (σ_{Pmax}) (MPa)		ε_{Pmin} (με) (σ_{Pmin}) (MPa)		
36(R)	1485 (104)	Mean 1711 (120)	306 (21)	Mean 607 (43)	1°
37(A)	1771 (124)		483 (34)		2°
38(A)	1878 (131)		1033 (72)		5°
39(R)	1839 (129)		555 (39)		13°
40(R)	1305 (91)		517 (36)		6°

Table 4.13: Residual strains in the region of the FS SP weld (weld seam side).

Table 4.12 and Table 4.13 detail the residual strains for the FS SP weld, with Figure 4.35 detailing the strains at the edge of the friction band and Figure 4.36 detailing those at a distance perpendicular to the weld direction. The maximum principal strains measured at the edge of the friction band acted within ±5° of the direction of the weld, with the minimum principal strains acting at right angles to these, transverse to the weld direction.

* Letter in parenthesis refers to advancing side (A) and retreating side (R).

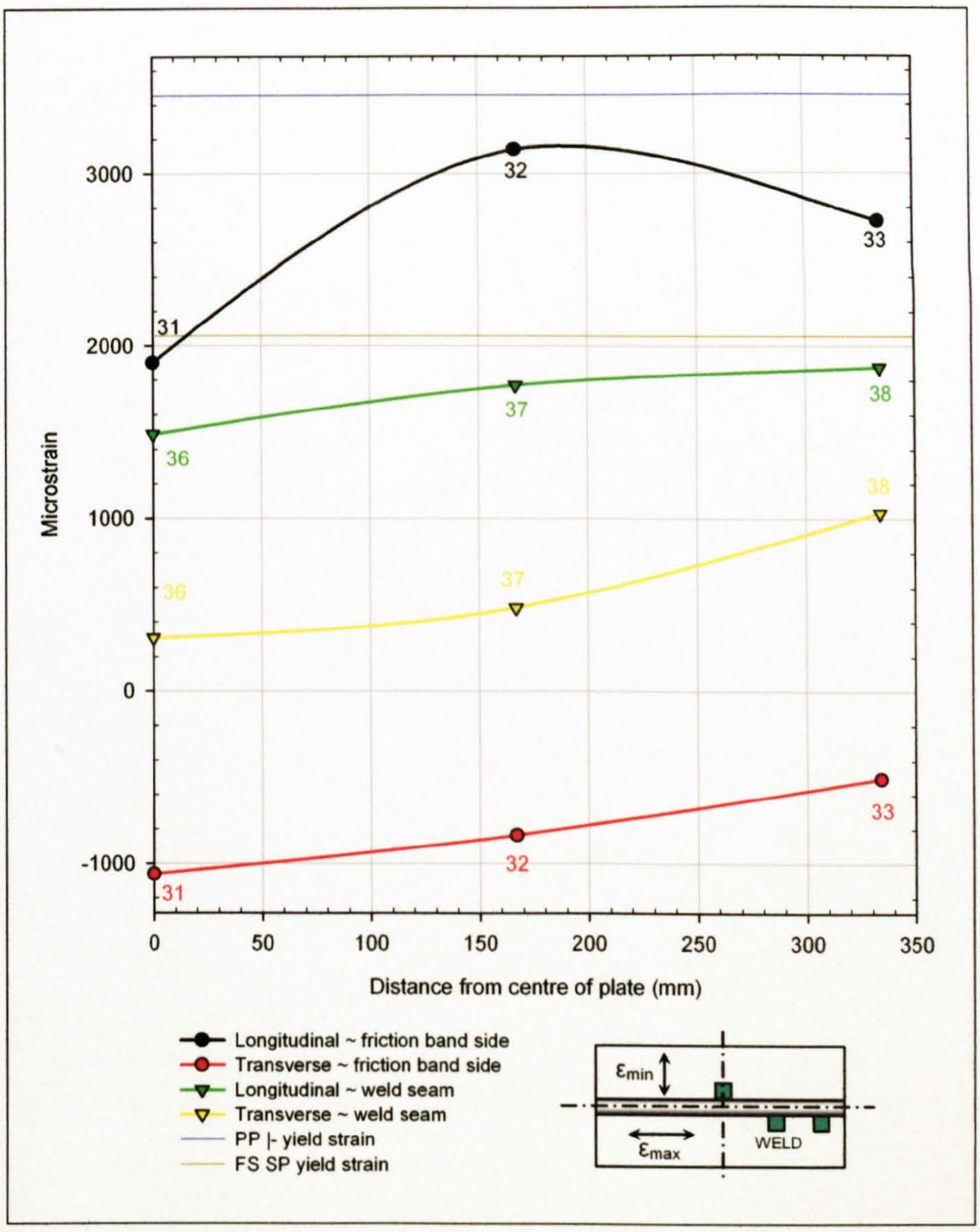

Figure 4.35: Residual strains at the edge of the friction band of the FS SP weld, measured at various points along the length of the plate (numbers refer to rosettes, see Figure 4.34).

The longitudinal residual strains measured at the edge of the friction band (ε_{Pmax}, running in the direction of the weld), on both the friction band and weld seam sides, exhibited values that were less than the yield strain of the FS SP weld at the centre of the plate length. As the distance from the centre of the plate increased the magnitudes of the residual strains increased, with those on the friction band side reaching a peak at a distance of 167 mm from the centre, whilst those on the weld seam side continued to increase, as shown in Figure 4.35. The values measured on the friction band side ranged from 1901 - 3143 με (133 - 157 MPa) with a mean value of 2589 με (153 MPa), whilst those on the weld seam side ranged from 1485 - 1878 με (104 - 131 MPa) with a mean value of 1711 με (120 MPa).

The transverse residual strains measured at the edge of the friction band (ε_{Pmin}, running transverse to the direction of the weld) increased in magnitude as the distance from the centre of the plate increased. The strains on the weld seam side were observed to be tensile in nature, whilst those on the friction band side were compressive, as shown in Figure 4.35. The stresses measured on the friction band side ranged from -1060 to -506 με (-74 to -35 MPa) with a mean value of -800 με (-56 MPa), whilst those on the weld seam side ranged from 306 - 1033 με (21 - 72 MPa) with a mean of 607 με (42 MPa).

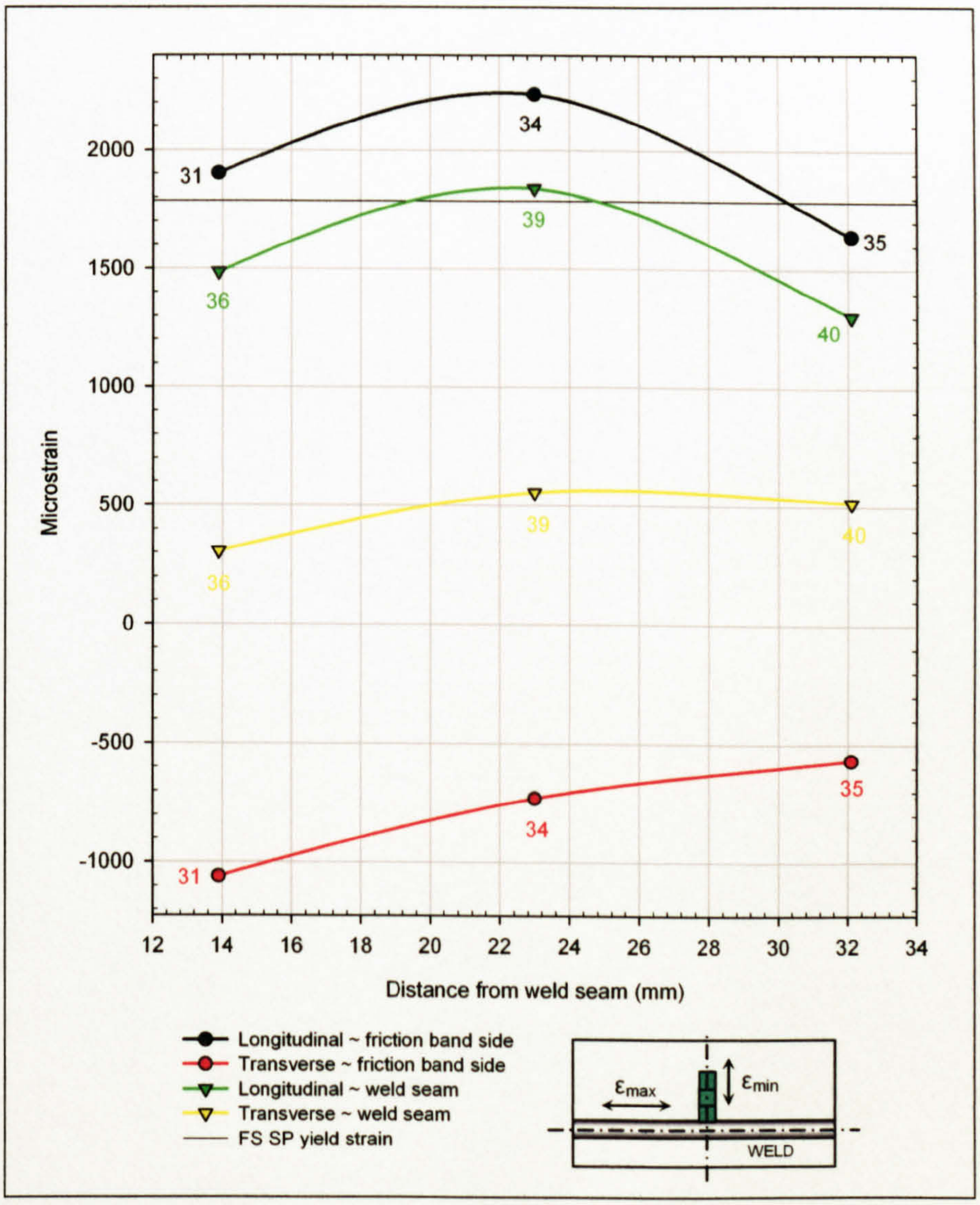

Figure 4.36: Residual strains in the region of the FS SP weld and HAZ, measured at the centre of the length, (numbers refer to rosettes, see Figure 4.34).

The longitudinal residual strains (ε_{Pmax}, running in the direction of the weld) were greater for the friction band side of the plate than the weld seam side as shown in Figure 4.36, although both sides exhibited peak values at distances of 23 mm from the weld seam. At a distance of 23 mm from the weld seam both sides returned values below that of the FS

SP yield strain. The residual strains ranged from 1641 - 2235 με (115 - 149 MPa) and 1305 - 1809 με (91 - 129 MPa) for the friction band and weld seam and sides respectively.

The transverse residual strains (ε_{Pmin}, running transverse to the direction of the weld) were compressive on the friction band side and tensile on the weld seam side, as shown in Figure 4.36. The strains on the friction band side ranged from -1060 to -567 με (-74 to -40 MPa), whilst the tensile strains on the weld seam side ranged from 306 - 555 με (21 - 39 MPa).

4.4.4.5 FS Double Pass

TML FRAS-2-23 rosettes were positioned as indicated in Figure 4.37.

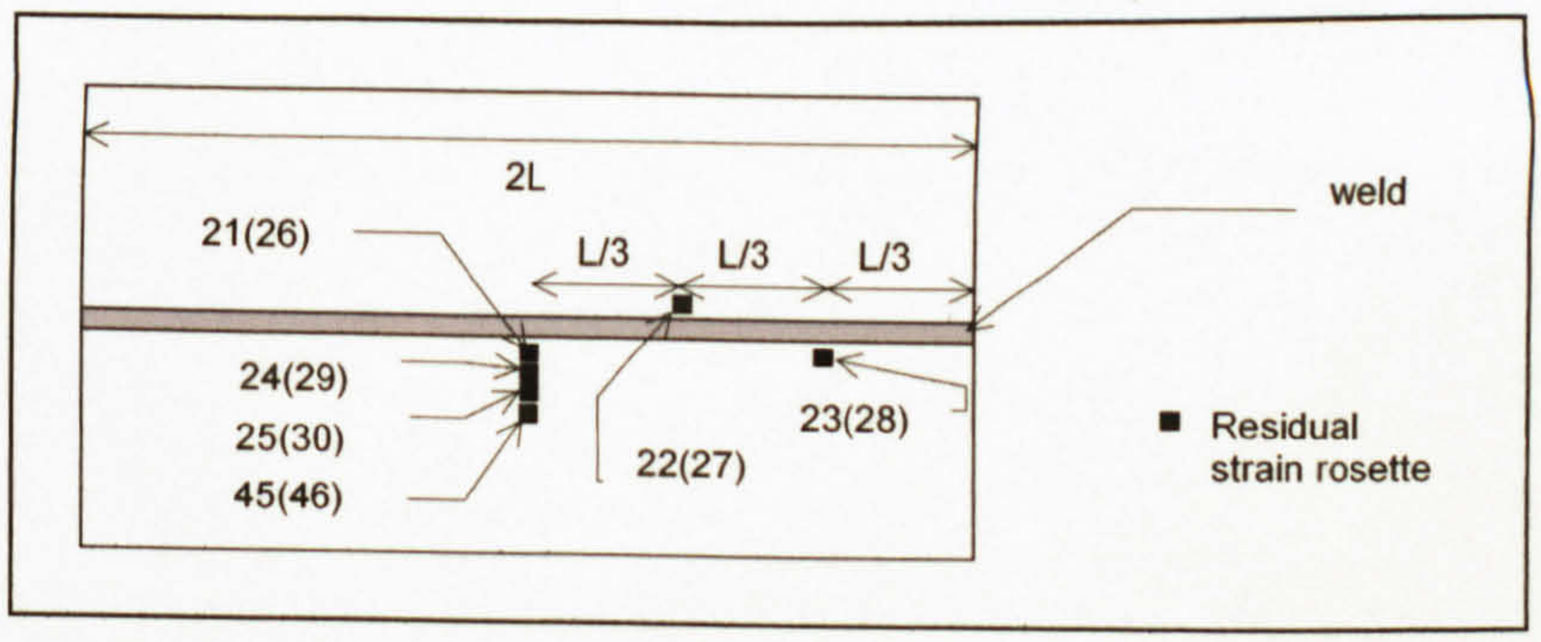

Figure 4.37: Position of residual strain gauge rosettes in relation to FS DP weld.

2nd pass side					
Rosette Number*	Residual strain, plane stress, equations (4.6) & (4.7)				Angle of ε_{Pmax} from the weld, CW, equation (4.5)
	ε_{Pmax} (με) (σ_{Pmax}) (MPa)		ε_{Pmin} (με) (σ_{Pmin}) (MPa)		
21(R)	3,015 (164)	Mean 3135 (165)	-1,879 (-132)	Mean -1330 (-93)	-1°
22(A)	3,393 (166)		-1,501 (-105)		-2°
23(R)	2,996 (164)		-610 (-43)		6°
24(R)	4,028 (167)		-1,425 (-100)		1°
25(R)	3,510 (166)		-1,162 (-81)		-4°
45(R)	2,561 (159)		-1,086 (-76)		-2°

Table 4.14: Residual strains in the region of the FS DP weld (2nd pass side).

1st pass side					
Rosette Number*	Residual strain, plane stress, equations (4.6) & (4.7)				Angle of ε_{Pmax} from the weld, CW, equation (4.5)
	ε_{Pmax} (με) (σ_{Pmax}) (MPa)		ε_{Pmin} (με) (σ_{Pmin}) (MPa)		
26(A)	2,097 (147)	Mean 2379 (156)	405 (28)	Mean 669 (47)	13°
27(R)	2,689 (161)		693 (49)		-3°
28(A)	2,351 (155)		908 (64)		3°
29(A)	2,756 (162)		711 (50)		14°
30(A)	2,229 (152)		945 (66)		20°
46(A)	1,506 (105)		780 (55)		29°

Table 4.15: Residual strains in the region of the FS DP weld (1st pass side).

* Letter in parenthesis refers to advancing side (A) and retreating side (R) of their respective sides.

Table 4.14 and Table 4.15 detail the residual strains measured in the FS DP welds, with Figure 4.38 detailing those at the edge of the friction band and Figure 4.39 those at a distance perpendicular to the weld. The maximum principal strains acted within -3° to 13° of the direction of the weld, with the minimum principal strains acting transverse to these, at right angles to the direction of the weld.

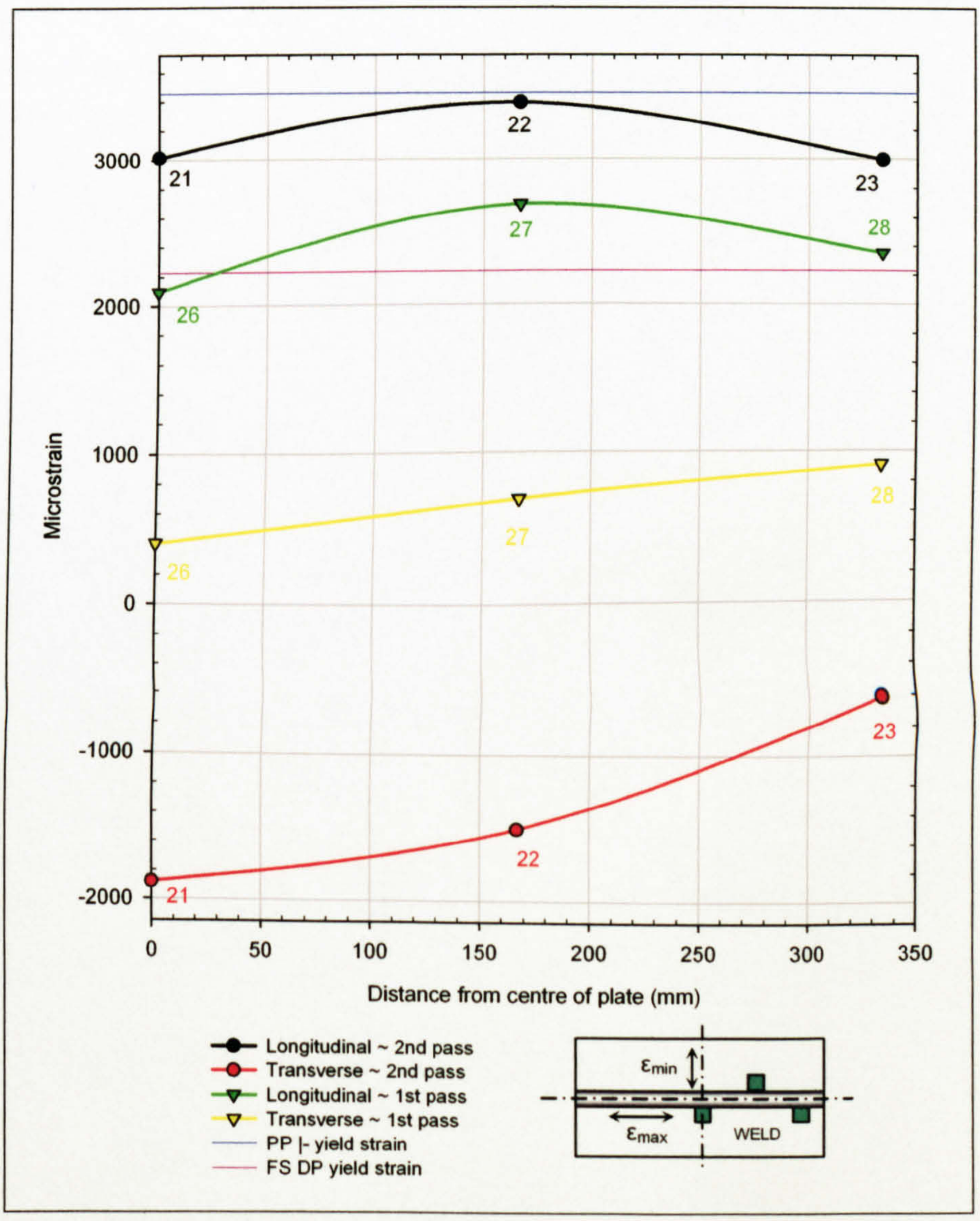

Figure 4.38: Residual strains at the edge of the friction band of the FS DP weld, measured at various points along the length of the plate (numbers refer to rosettes, see Figure 4.37).

The longitudinal residual strains measured at the edge of the friction band (ε_{Pmax}, running in the direction of the weld), on both the tool and weld seam sides exhibited values that were greater than, or in the region of, the FS DP yield strain, but less than the PP |- yield strain, as shown in Figure 4.38. The magnitude of the strains on the 2nd pass side were greater than those on the 1st pass side, although both exhibited peak values at a distance

of 167 mm from the centre of the plate. Values for the 1st pass side ranged from 2097 - 2689 με (147 - 161 MPa) with a mean of 2379 με (156 MPa) and from 2996 - 3393 με (164 - 166 MPa) with a mean of 3135 με (165 MPa) for the 2nd pass side.

The transverse residual strains measured at the edge of the friction band (ε_{Pmin}, running transverse to the direction of the weld) were observed to be tensile on the 1st pass side and compressive on the 2nd pass, although both increased in magnitude (became more tensile) as the distance from the centre of the plate increased, as shown in Figure 4.38. Strains on the 1st pass side ranged from 405 - 908 με (28 - 64 MPa), whilst those on the 2nd pass side ranged from -1879 to -610 με (-132 to -43 MPa), with mean values of 669 με (47 MPa) and -1330 με (-93 MPa) for the 1st and 2nd pass sides respectively.

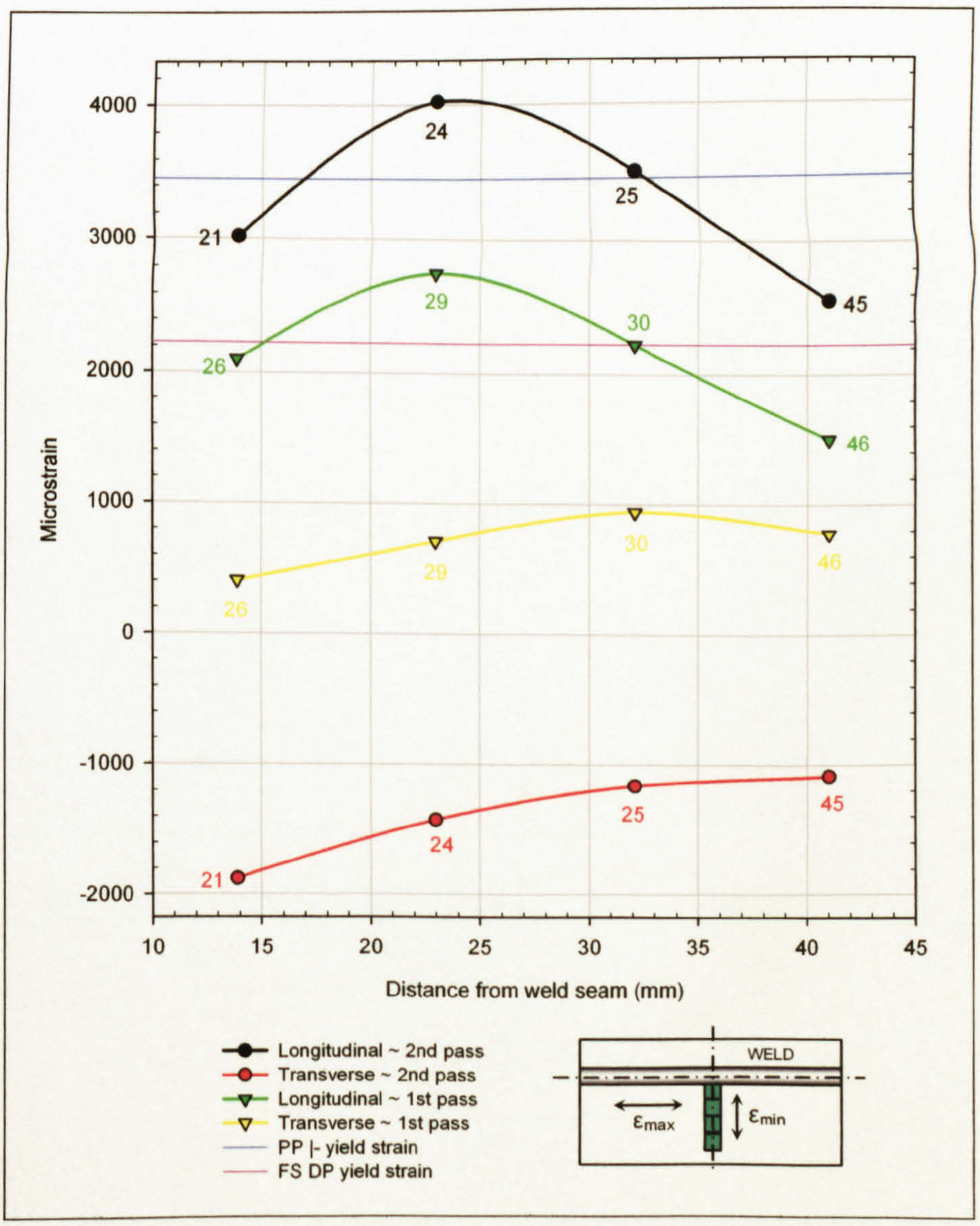

Figure 4.39: Residual strains in the region of the FS DP weld and HAZ, measured at the centre of the length, (numbers refer to rosettes, see Figure 4.37).

The longitudinal residual strains (ε_{Pmax}, running in the direction of the weld) were of a greater magnitude on the 2nd pass side of the plate, although the responses were comparable for both sides, as shown in Figure 4.39. Peak values were observed at a distance of 23 mm from the weld seam, with the 2nd pass side returning a value greater than the PP |- yield strain, whilst the 1st pass side returned a value between this and the FS DP yield strain. The 2nd pass side strains ranged from 2561 - 4028 με (159 - 167 MPa), whilst those on the 1st pass side ranged from 1506 - 2759 με (105 - 162 MPa).

The transverse residual strains (ε_{Pmin}, running transverse to the direction of the weld) were observed to be compressive on the 2nd pass side and tensile on the 1st pass side, although the two responses were similar for both sides, as shown in Figure 4.39. The lowest values were observed at a distance of 14 mm from the weld seam, the edge of the friction band, with the maximum values being returned at a distance of 32 mm and 41 mm for the 1st and 2nd pass sides respectively. The values for the 1st pass side ranged from 405 - 945 με (28 - 66 MPa), with the range for the 2nd pass side being -1879 to -1086 με (-132 to -76 MPa).

4.4.4.6 S-N Test Specimens

S-N testing of the as-welded specimens was undertaken utilising four point loading, the specimens having the geometry shown in Figure 4.40, their thickness being that of the supplied plate, 8 mm. To determine the effect on the residual strains that cutting the plates would have measurements were made at the middle of the specimens, at the weld toe in the case of the MIG welds and at the edge of the friction band in the case of the FS welds. The measurements were made on both sides, with respect to the thickness, the gauges being applied directly above one another.

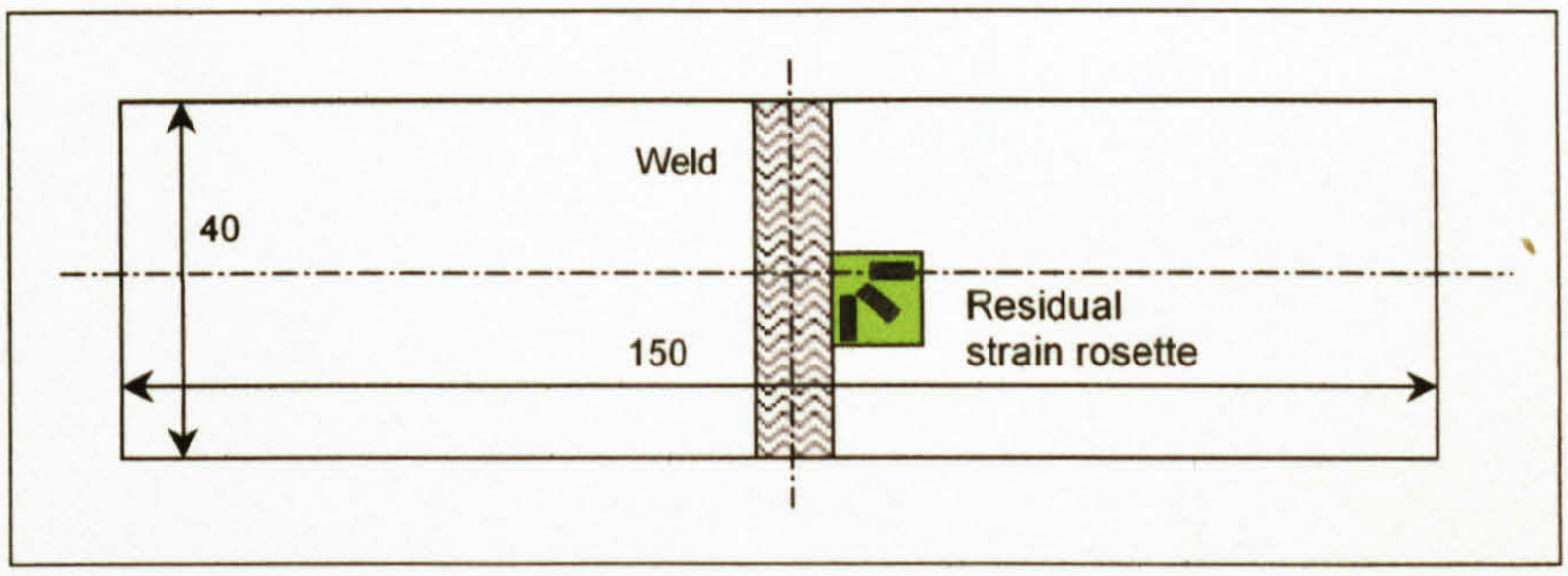

Figure 4.40: Position of residual strain rosette on S-N fatigue specimen

The S-N specimens were cut from separate welded plates to those used for the initial residual strain measurements, although it is reasonable to assume that the residual strains and distortion in the plates would be of a similar magnitude as the welding processes, fabricator and material were identical.

4.4.4.6.1 MIG Low Input and High Input

From the results shown in Table 4.16 and Figure 4.41 it was evident that a redistribution of the residual strains had occurred in the MIG welded S-N specimens when compared to the results returned by the 1000 x 500 x 8 mm (length x width x thickness) as-welded plates. The direction of the principal strains in the S-N specimens was at right angles to those observed in the as-welded plates, the maximum principal strain acting approximately transverse to the weld direction.

Weld	Rosette Number	Residual strain, plane stress, equations (4.6) & (4.7)				Angle of ε_{Pmax} from the weld, CW, equation (4.5)
		ε_{Pmax} (με) (σ_{Pmax}) (MPa)		ε_{Pmin} (με) (σ_{Pmin}) (MPa)		
MIG LI	53	1040 (73)	Mean 875 (61)	-283	Mean -160 (-11)	-79°
	54	709 (50)		-37		-70°
MIG HI	49	1117 (78)	Mean 1033 (72)	-515	Mean -458 (-32)	-82°
	50	949 (66)		-401		86°

Table 4.16: Residual strains measured in MIG LI and HI S-N specimens at the weld toe.

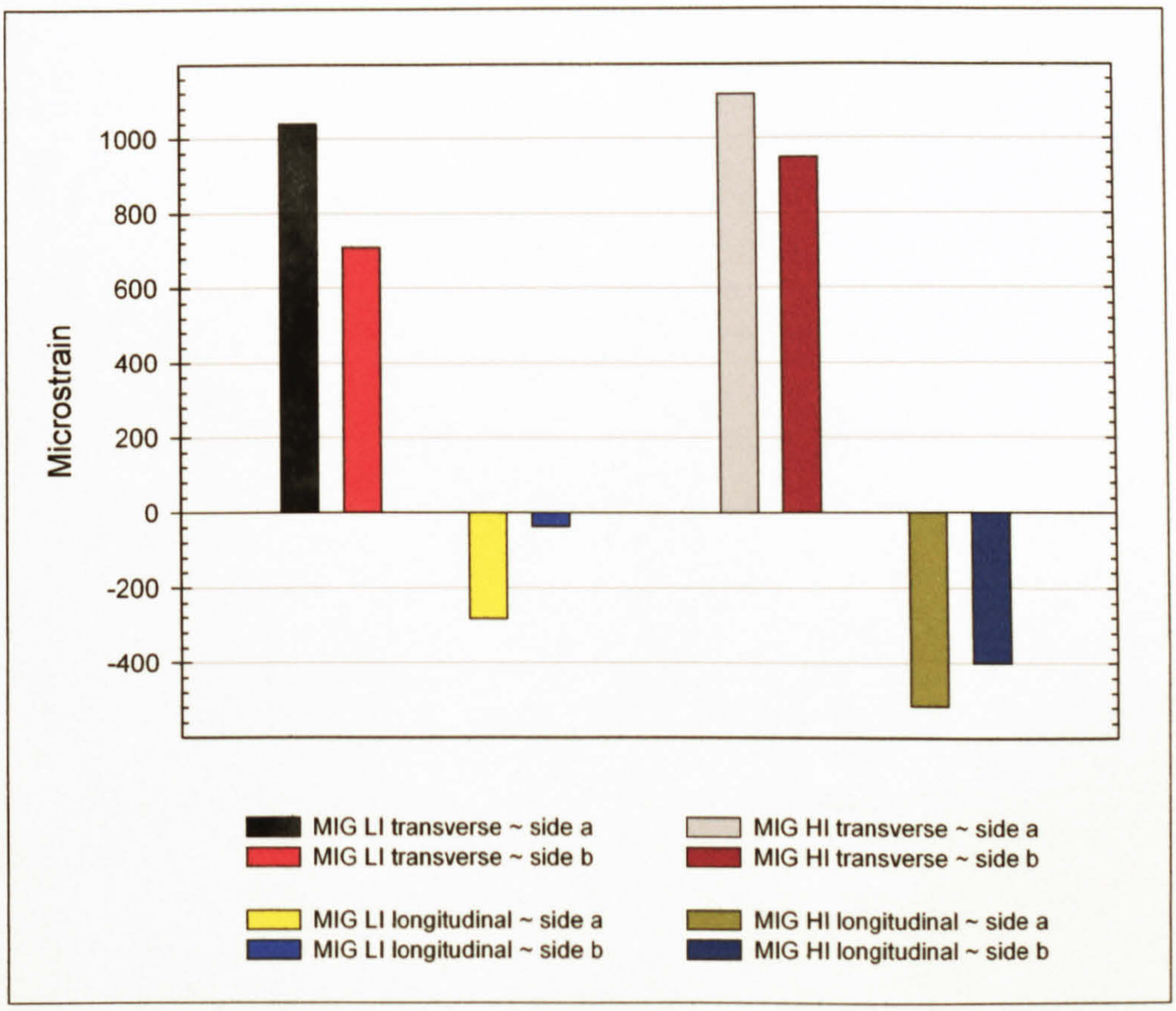

Figure 4.41: MIG LI and HI butt weld S-N specimen residual strains.

The mean value for the strains acting transverse to the weld in the LI S-N specimen was 875 με (61 MPa), in contrast to this the mean value measured at the centre of the LI welded plates was -1388 με (-97 MPa). The mean value for longitudinal strains, acting in the direction of the weld, in the LI S-N specimen was -160 με (-11 MPa), in contrast to the mean value recorded at the centre of the welded plate of 4805 με (186 MPa).

The mean value for the strains acting transverse to the weld in the HI S-N specimen was 1033 με (72 MPa), in contrast to this the mean value measured at the centre of the HI welded plates which was -671 με (-47 MPa). The mean value for strains acting in the direction of the weld in the HI S-N specimen was -458 με (-32 MPa), whilst the mean value measured at the centre of the HI welded plates was 3814 με (173 MPa).

4.4.4.6.2 FS Single Pass and Double Pass

Weld	Rosette Number	Residual strain, plane stress, equations (4.6) & (4.7)				Angle of ε_{Pmax} from the weld, CW, equation (4.5)
		ε_{Pmax} (με) (σ_{Pmax}) (MPa)		ε_{Pmin} (με) (σ_{Pmin}) (MPa)		
FS SP	63 (tool side)	563 (39)	Mean 428 (30)	-123 (-9)	Mean -80 (-6)	-87°
	64 (weld seam side)	292 (20)		-37 (-3)		-87°
FS DP	58 (2nd pass side)	262 (18)	Mean 367 (26)	-316 (-22)	Mean -170 (-12)	-87°
	59 (1st pass side)	471 (33)		-23 (-2)		-78°

Table 4.17: FS SP and DP butt weld S-N specimen residual strains.

As with the MIG welded S-N specimens, the residual strains in the FS welded S-N specimens exhibited a redistribution of the residual strains when compared to the as-welded plates. The residual strains acting transverse to the weld having a greater magnitude than those acting in the direction of the weld, as shown in Table 4.17 and Figure 4.42.

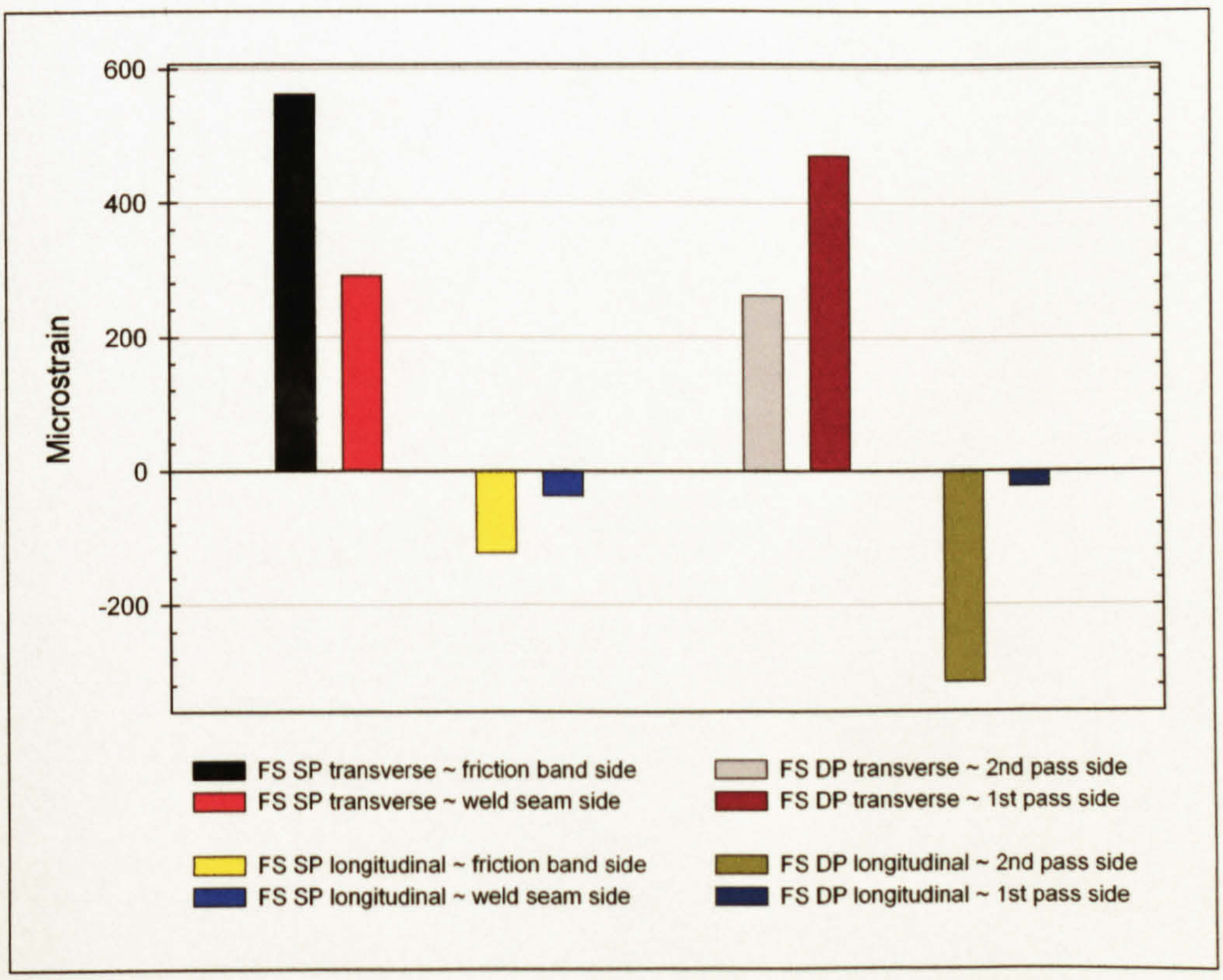

Figure 4.42: FS SP and DP butt weld S-N specimen residual strains.

The strains acting transverse to the weld of the SP S-N specimen were 563 με (39 MPa) and 292 με (20 MPa) for the friction band and weld seam sides respectively, whilst those

measured at the centre of the as-welded plates were -1060 με and 306 με for the friction band and weld seam sides respectively. The values of the longitudinal residual strains, acting parallel to the weld, were comparable for both sides of the SP S-N specimen returning values of -123 με (-9 MPa) for the friction band side and -37 με (-3 MPa) for the weld seam side, these being significantly less than the values of 1901 με (133 MPa) and 1485 με (104 MPa) returned by the friction band and seam sides respectively of the as-welded plates.

The residual strains acting transverse to the weld direction in the FS DP S-N specimens returned mean values of 262 με (18 MPa) and 471 με (33 MPa) for the 2nd and 1st pass sides respectively, in contrast to the values of -1879 με (-132 MPa) and 405 με (28 MPa) for the welded plates. The longitudinal residual strains in the DP S-N specimens were -316 με (-22 MPa) and -23 (-2 MPa) for the 2nd and 1st pass sides respectively, significantly lower than the 3015 με (164 MPa) and 2097 με (147 MPa) returned by the 2nd and 1st pass sides of the welded plates.

4.4.5 Synchrotron Radiation Strain Scanning

Electromagnetic radiation with wavelengths in the region of 10^{-8} - 10^{-11} m are termed x-rays, with the longer wavelengths often being designated as soft and the shorter wavelengths as hard. Synchrotron radiation, or hard x-rays, with respect to the soft x-rays typically used in the determination of residual strains, have a greater penetrating power which allows the determination of residual strains to a much greater depth. Typically soft x-rays are capable of measuring residual strains in metallic materials to a depth in the region of 10 μm[1], whereas the ESRF produces hard x-rays capable of through thickness analysis of the 8 mm thick aluminium alloy under consideration.

X-ray determination of residual strains is based on diffraction, where the atoms in a crystalline structure act like the centres of concentric waves resulting in a small amount of the radiation being scattered. Diffracted rays are the result of parallel planes of atoms reflecting the rays and these then interfering in an additive manner according to Bragg's law, equation (4.10), and shown schematically in Figure 4.43:

$$2d_{h,k,l}.\sin\theta = n\lambda \qquad (4.10)$$

where: d = lattice spacing (the distance between two planes of atoms).

h,k,l = relevant diffraction plane, 311.

θ = the angle of incidence.

n = integer.

λ = wavelength of the radiation.

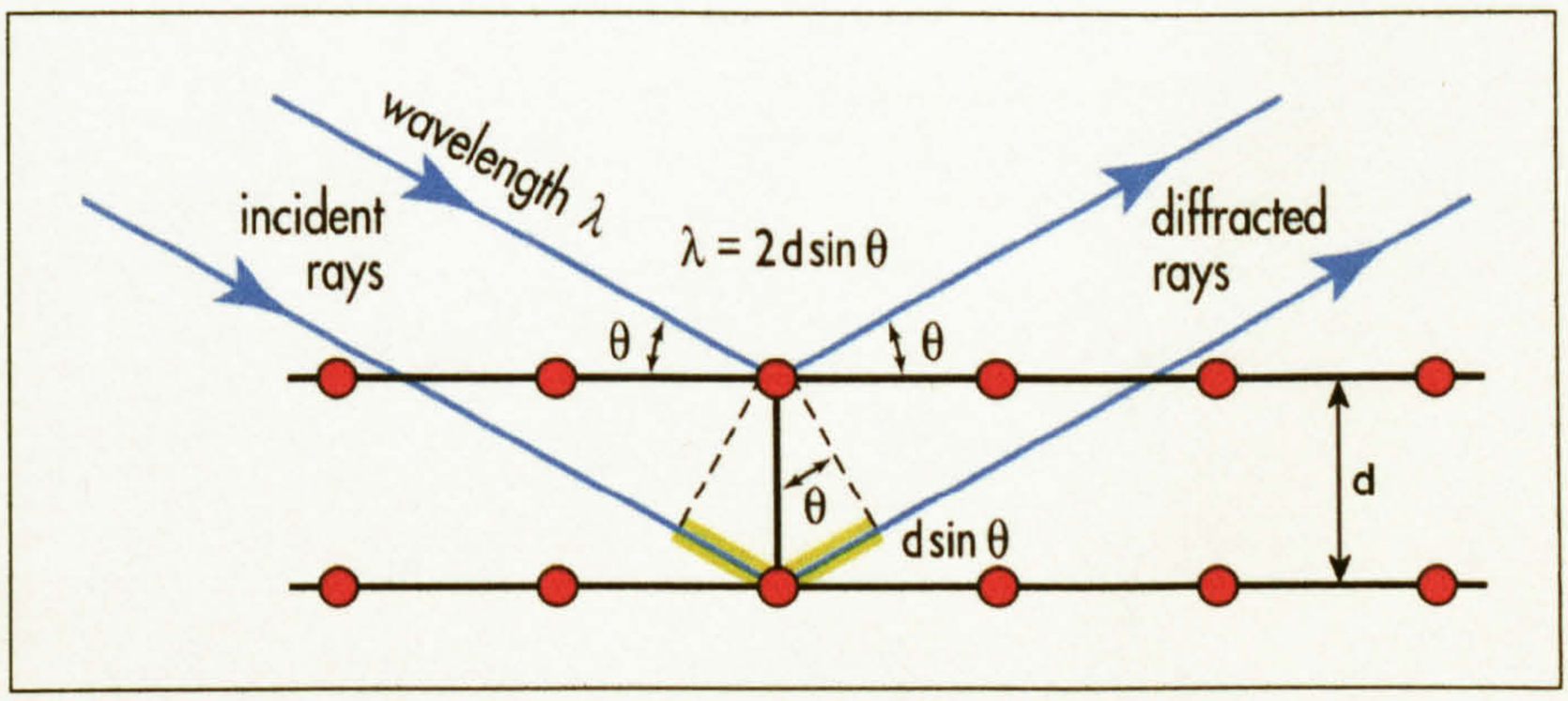

Figure 4.43: X-ray diffraction[2].

Residual strains result in a distortion in the lattice spacing, d; compressive and tensile strains resulting in a decrease and increase in d respectively. For diffraction to occur in

---

[1] Webster PJ et al (2001)
[2] ESRF (undated)

an additive manner the distance d.sin θ must remain constant (or change by a complete wavelength), therefore as the lattice spacing changes, sin θ, and consequently θ, must change in an inverse manner, as indicated by equation (4.10) and Figure 4.43. Thus, the application of a tensile strain to a crystalline material results in an increase in the lattice spacing, d, therefore, for additive diffraction to occur the angle of the incident/diffracted x-ray beam, θ, reduces. The residual strains induced from a process such as welding may then be determined from:

$$\varepsilon = \frac{d - d_0}{d_0} \tag{4.11}$$

$$\therefore \varepsilon = \frac{\sin 2\theta_0}{\sin 2\theta} - 1 \tag{4.12}$$

where: d = measured lattice spacing

d_0 = strain free lattice spacing

$2\theta_0$ = strain free diffraction angle

2θ = measured diffraction angle

The FS welds utilised for the synchrotron residual strain analysis were produced from the same 8 mm thick AA 5383-H321 plate, but the rolling direction was transverse to the weld, the opposite direction to the FS welds subjected to the hole drilling technique, due to limitations on the amount of plate available. The fabricator was again TWI, and the weld parameters were identical to those of the initial welds studied, although the welded sections were produced from plates of 250 x 500 x 8 mm (w x l x t), producing welded plates of 500 x 500 x 8 mm (w x l x t). The reduction in the length of the welds, the original welds were one metre in length, was due to distortion in the plates supplied to the fabricator resulting in them having to be cut in half to allow satisfactory butting and clamping of the two pieces when undertaking the welds, a process liable to have had a significant influence on the resulting residual strain distribution.

The dimensions of the specimens used to determine the magnitude of the residual strains were as shown in Figure 4.44. Measurements of the residual strains were made at the positions indicated in Figure 4.46 for both the transverse, at right angles to the weld, and longitudinal, parallel to the weld, strains. Typical analyses consisted of measurements being made at 1 mm increments to a distance of 40 mm from the weld centreline, 2 mm increments for distances of 42 - 60 mm and 4 mm increments for distances of 64 - 92 mm. Measurements were made at depths, with respect to the plate thickness, of 1, 4 and 7 mm in the case of the three line analyses and 0 - 8 mm in 1 mm increments in the case of the nine line analyses. Quadrant analyses consisted of a nine line analysis at the centre of the plate followed by subsequent three line analyses at distances of 25, 45, 60, 68 and 73 mm from the plate centreline. Complete examination of both sides of the weld was

achieved by repeating the analyses for the opposite side of the weld centreline. The coordinate system utilised for each FS weld type was as detailed in Figure 4.45.

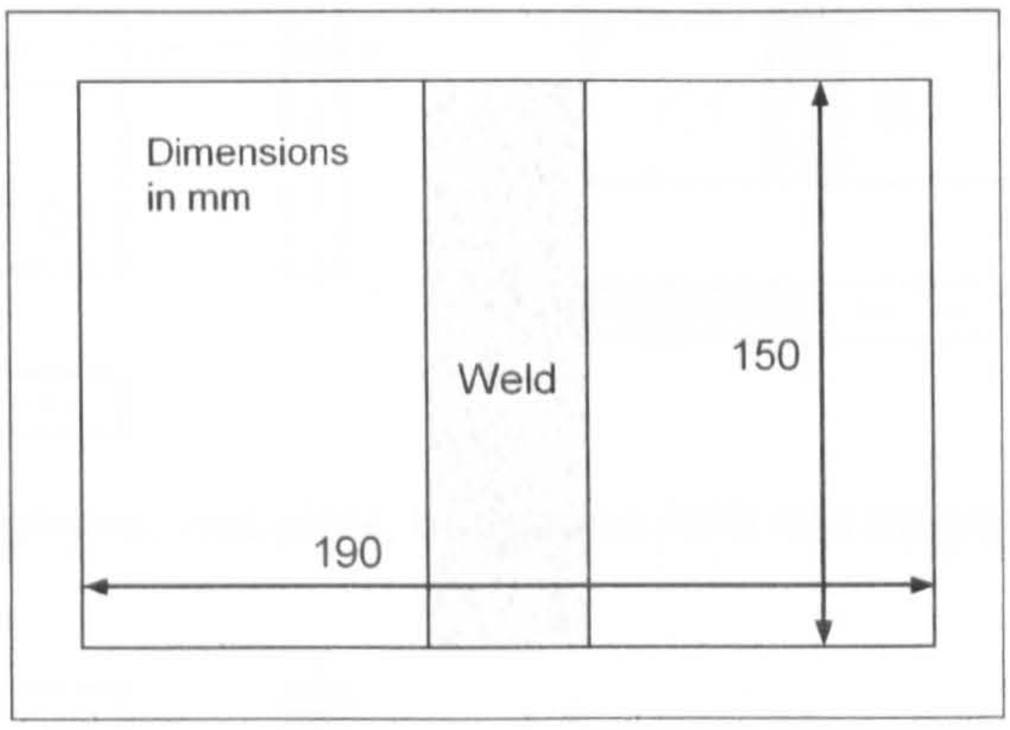

Figure 4.44: Dimensions of the FS welded specimens utilised for synchrotron radiation strain scanning analysis of the residual strain field.

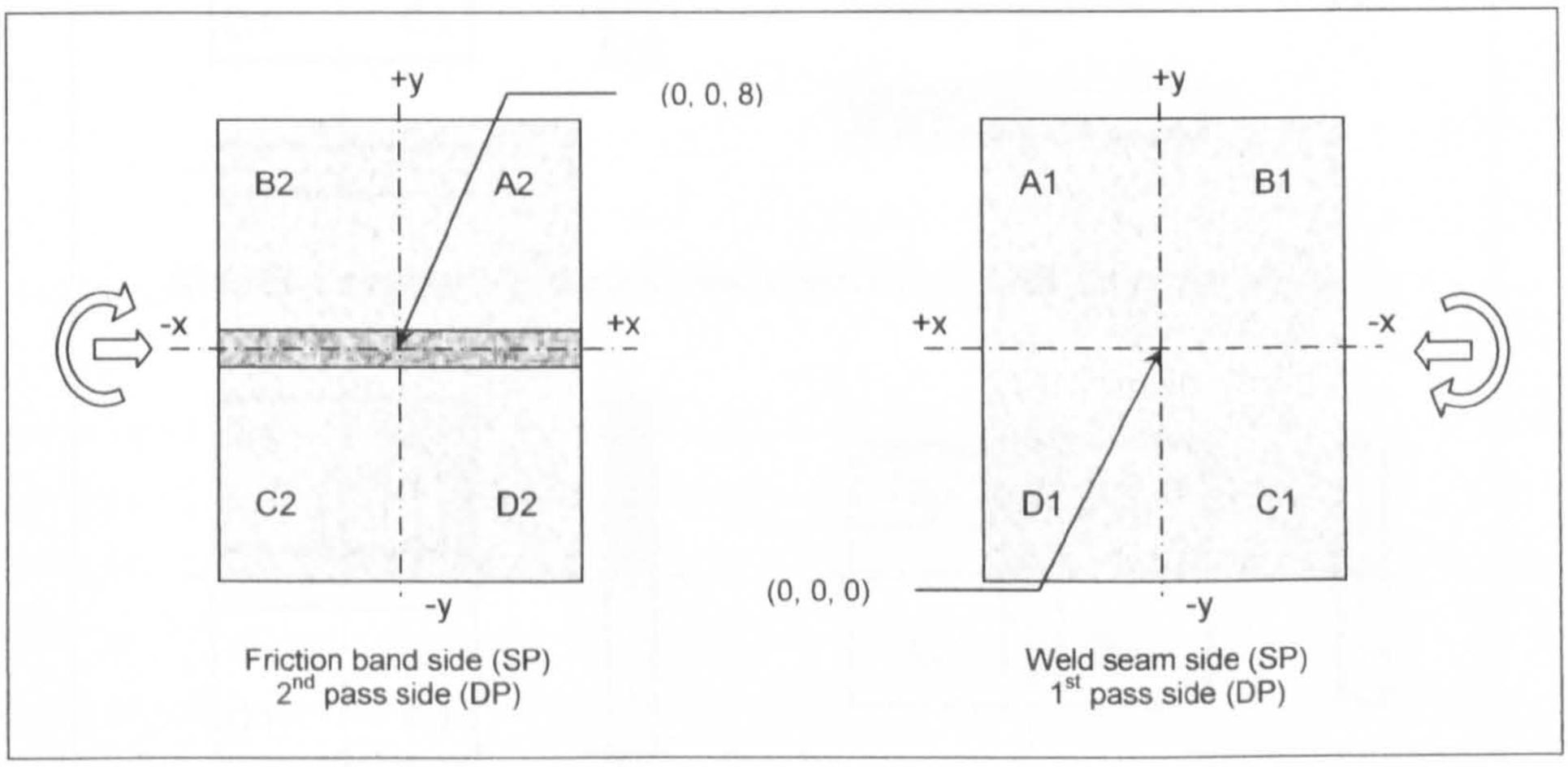

Figure 4.45: Coordinate system utilised for the FS welded plates synchrotron analysis (distance from the specimen centreline = ±x, distance from the weld centreline = ±y, distance from weld seam (SP)/1st pass (DP) side (through thickness) = z).

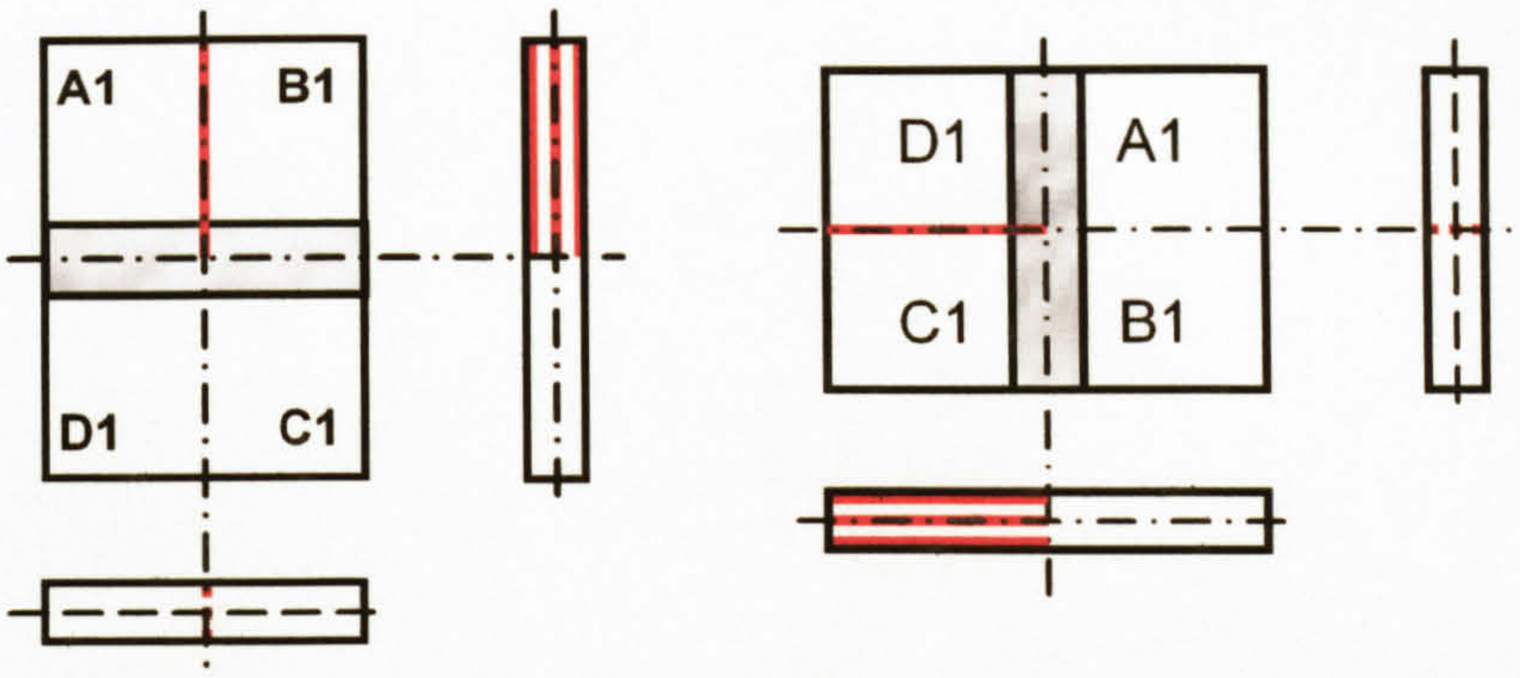

Three line analysis, mid-plate, transverse (left) and longitudinal (right).

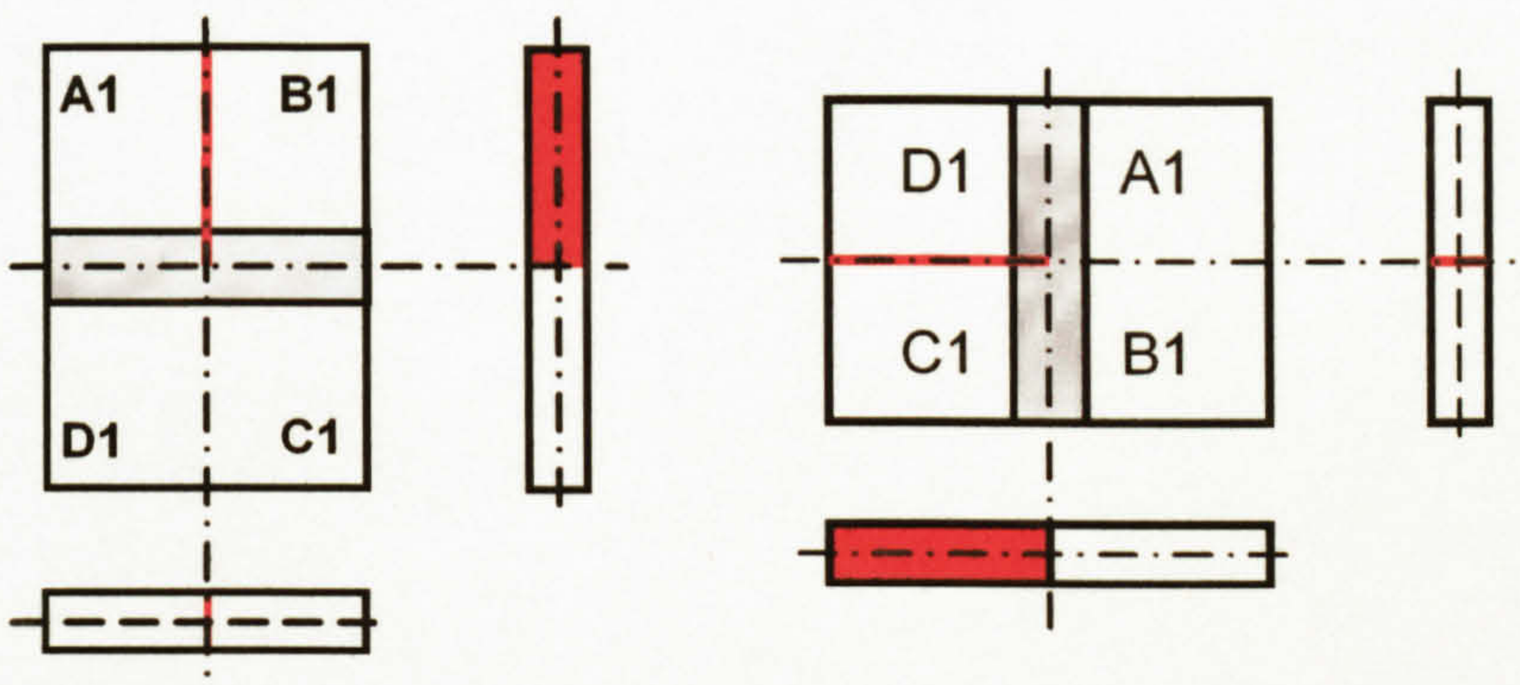

Nine line analysis, mid-plate, transverse (left) and longitudinal (right).

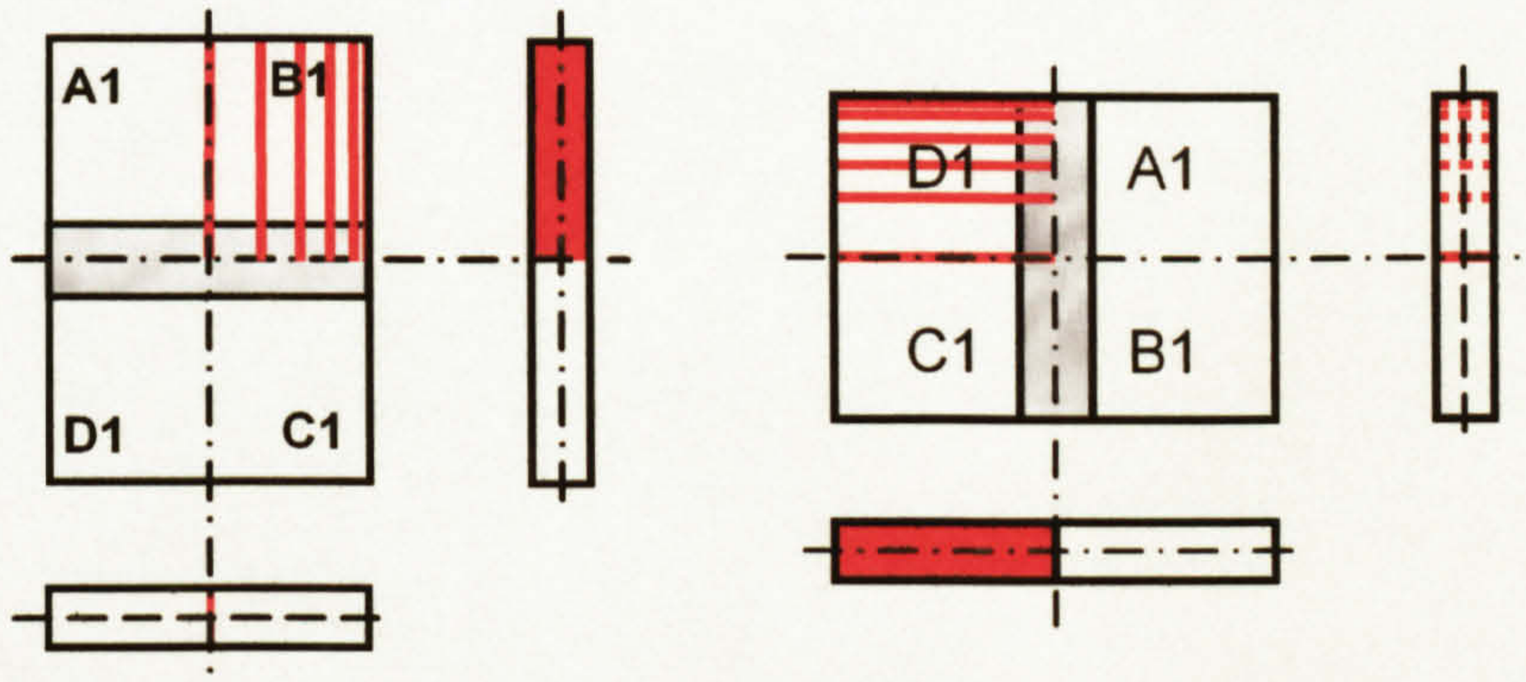

Quadrant analysis (nine line analysis, mid-plate, subsequent three line analyses), transverse (left) and longitudinal (right).

Figure 4.46: Schematic representation of the positions transverse and longitudinal residual strain analyses were undertaken.

The synchrotron radiation had a wavelength of 0.3100639 Å and energy of 39.987 KeV. The detector slit height was 0.3 mm and the incident slit height and width were typically 0.3 and 1.0 mm respectively (for initial analyses the values for both the incident slit height and width ranged from 0.3 - 1.0 mm), giving a trapezoidal shaped gauge volume of 0.72 mm^2. The 311 diffraction plane was utilised, with diffraction angles in the region of 14.5° being obtained. The peak diffraction angles were determined through computational

numerical analysis of the Gaussian distribution with the peak centre error also being determined. Although errors are not included in the results they were typically in the region of the 0.0002° - 0.001°, equating to 15 - 100 με, with the greater errors being more prevalent in the larger grained microstructure of the parent material.

Smoothing of the data to produce the 3d meshes shown in Figure 4.47 to Figure 4.72 was undertaken utilising an inverse square technique, where the average values at neighbouring points was calculated using the Cauchy density function, with a sampling proportion of 0.05 - 0.25, typically with 8 intervals in the x and z directions and 92 in the y direction (x, y and z as depicted in Figure 4.45). The advancing side of the 2nd pass side of the DP weld and the advancing side of the SP weld are represented by the positive values of the distance from the weld centreline. Measurements at y = ±94 mm were omitted as they were affected by the residual strains induced when the specimens were cut from the welded plates and any other points that were considered to be the result of non-weld criteria were also omitted.

Typical plots of the variation in 2θ with respect to the longitudinal and transverse residual strains are detailed for a FS SP weld in Figure 4.47 and Figure 4.48 and for a FS DP weld in Figure 4.49 and Figure 4.50; the measurements corresponding to the quadrant analysis shown in Figure 4.46.

From Figure 4.47 to Figure 4.50 it was evident that the variation in 2θ was comparable for both weld types and that features were common for both the longitudinal and transverse variations. The smallest values of 2θ were observed in the region of the weld, with either a "W" or "U" shaped response being evident in the weld region, 0 to ±16 mm from the centre of the weld, this type of response being typical for both welds types and directions. As the distance from the weld increased the value of 2θ increased, the longitudinal values of 2θ, shown in Figure 4.48 and Figure 4.50, exhibited a greater rate of increase with respect to the distance from the weld centreline than the transverse measurements, peak values were observed at a distance in the region of 20 - 30 mm from the weld centreline followed by a gradual reduction as the edges of the specimens were approached. In contrast, the transverse values of 2θ increased at a lesser rate than the longitudinal ones, although the values continued to increase up to the edge of the specimens.

A degree of symmetry about the weld seam was evident in both welds and for both the transverse and longitudinal analyses. For the transverse measurements in the SP weld the two minimum values of 2θ were observed at distances of ±16 mm from the weld centreline, although the advancing side returned the smallest values, 2θ = 14.5066°, minimal through thickness variation was evident. For the SP longitudinal measurements minimum values of 2θ were evident at distances of ±12.5 mm from the weld centreline for

the weld seam surface region, although the friction band surface exhibited a "U" shaped trough with the nadir being slightly offset from the weld centreline by 5 mm towards the advancing side. The DP weld transverse measurements exhibited a "W" shaped response in the region of the weld, with minimum values being observed at distances comparable to the tool shoulder width, ±12.5 mm. The minimum values were of a near identical magnitude in the region of the 2nd pass surface, $2\theta = 14.5034°$, whilst the 1st pass side exhibited a variation between the two nadirs, with the 1st pass retreating side exhibiting the lowest value. The DP longitudinal measurements returned a more "U" shaped response, although minimum values were observed at distance of ±12.5 mm from the weld centreline for the 1st pass side region, whilst the 2nd pass side exhibited a nadir at the centreline.

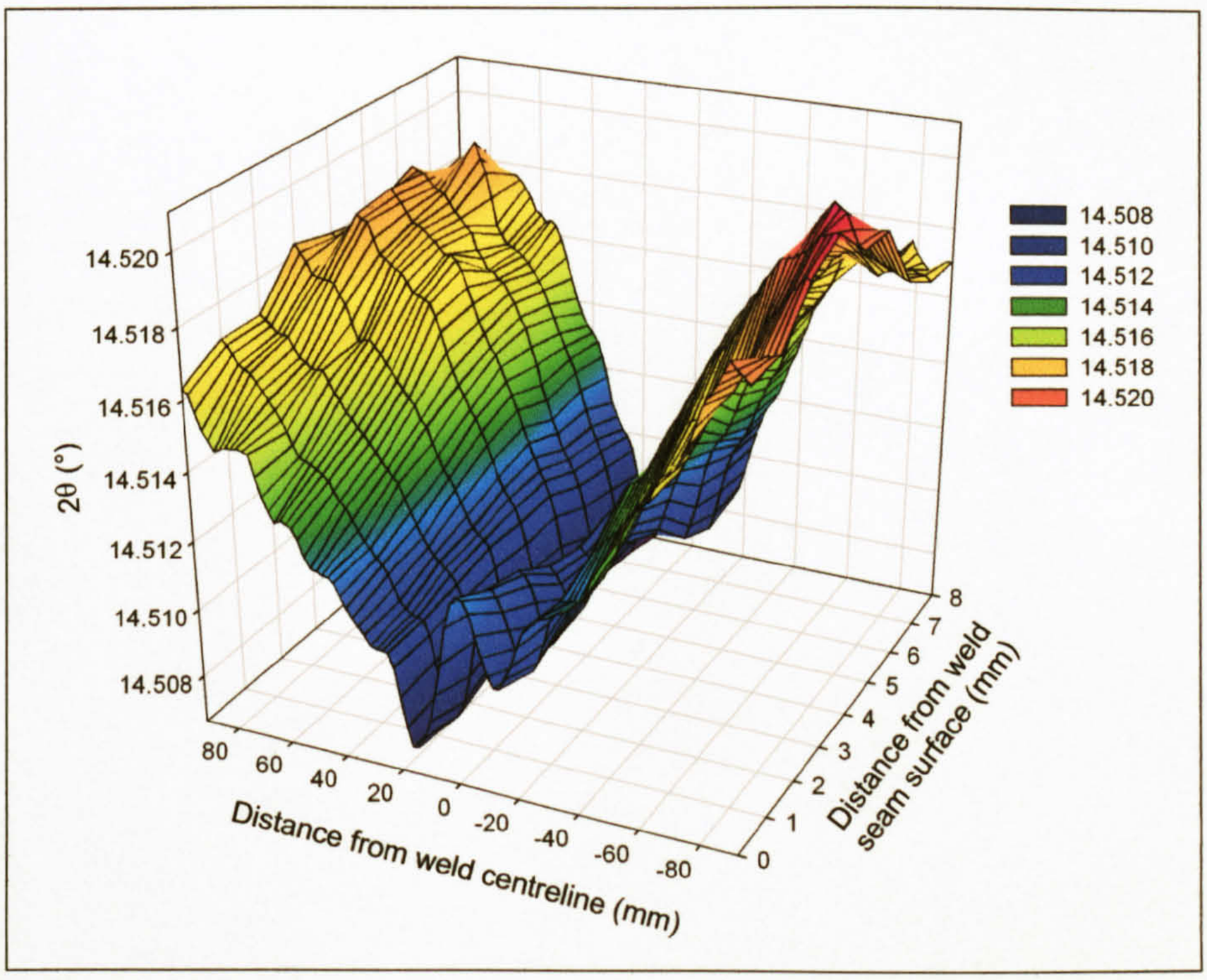

Figure 4.47: Variation of the diffraction angle, 2θ, in a direction transverse to the weld with respect to the distance from the weld centreline and thickness at the centre of a FS SP weld specimen.

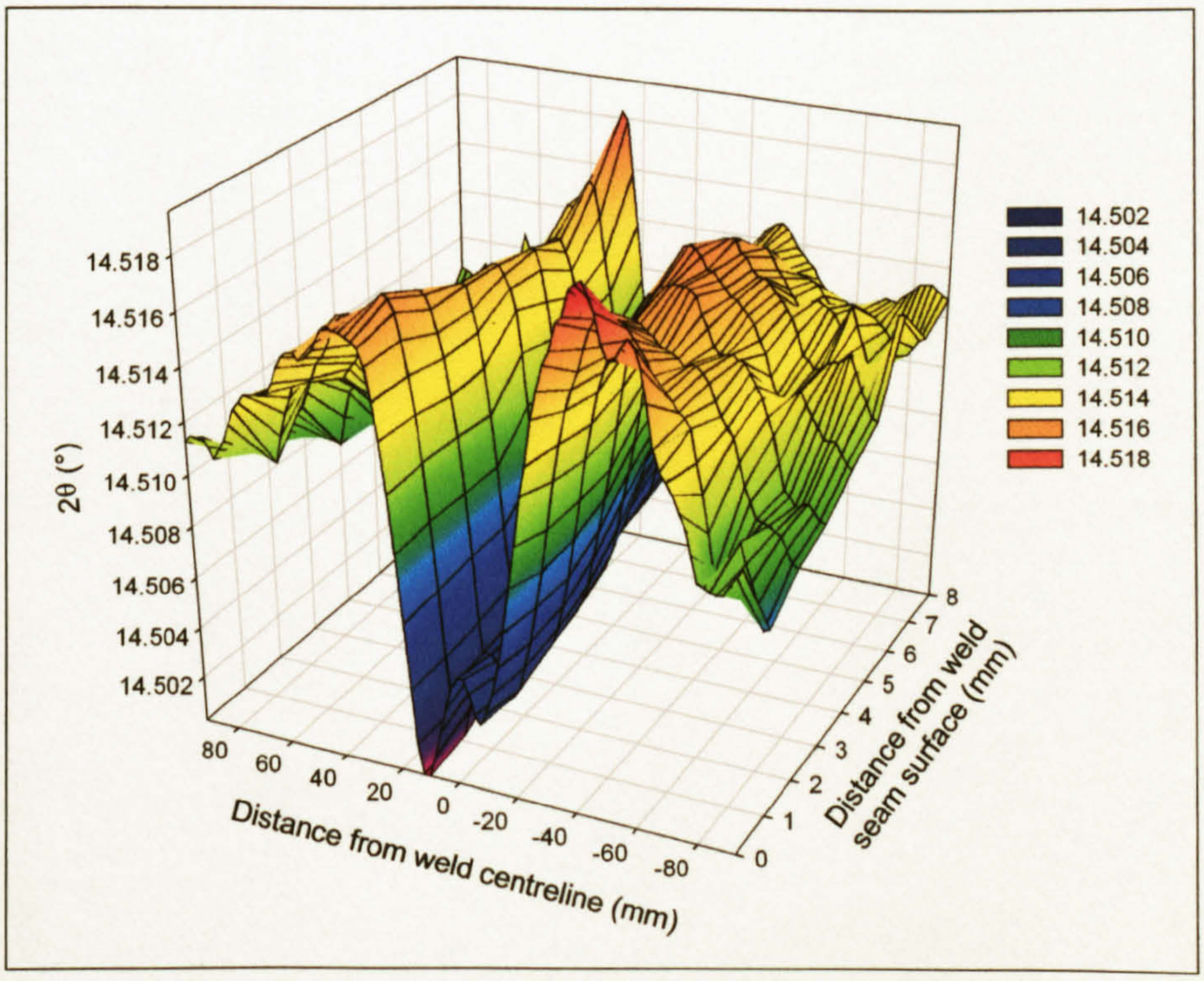

Figure 4.48: Variation of the diffraction angle, 2θ, in a direction parallel to the weld with respect to the distance from the weld centreline and thickness at the centre of a FS SP weld specimen.

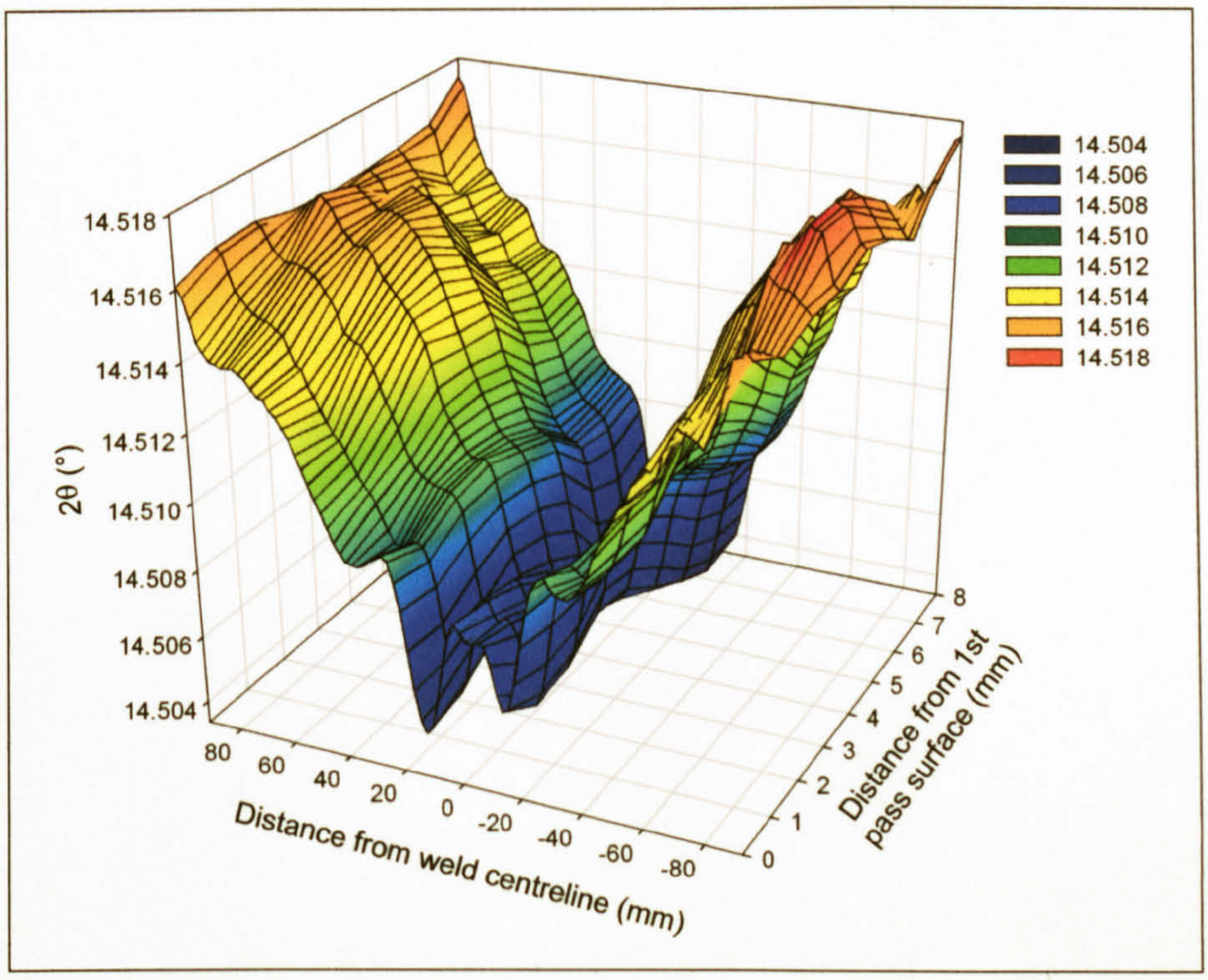

Figure 4.49: Variation of the diffraction angle, 2θ, in a direction transverse to the weld with respect to the distance from the weld centreline and thickness at the centre of a FS DP weld specimen.

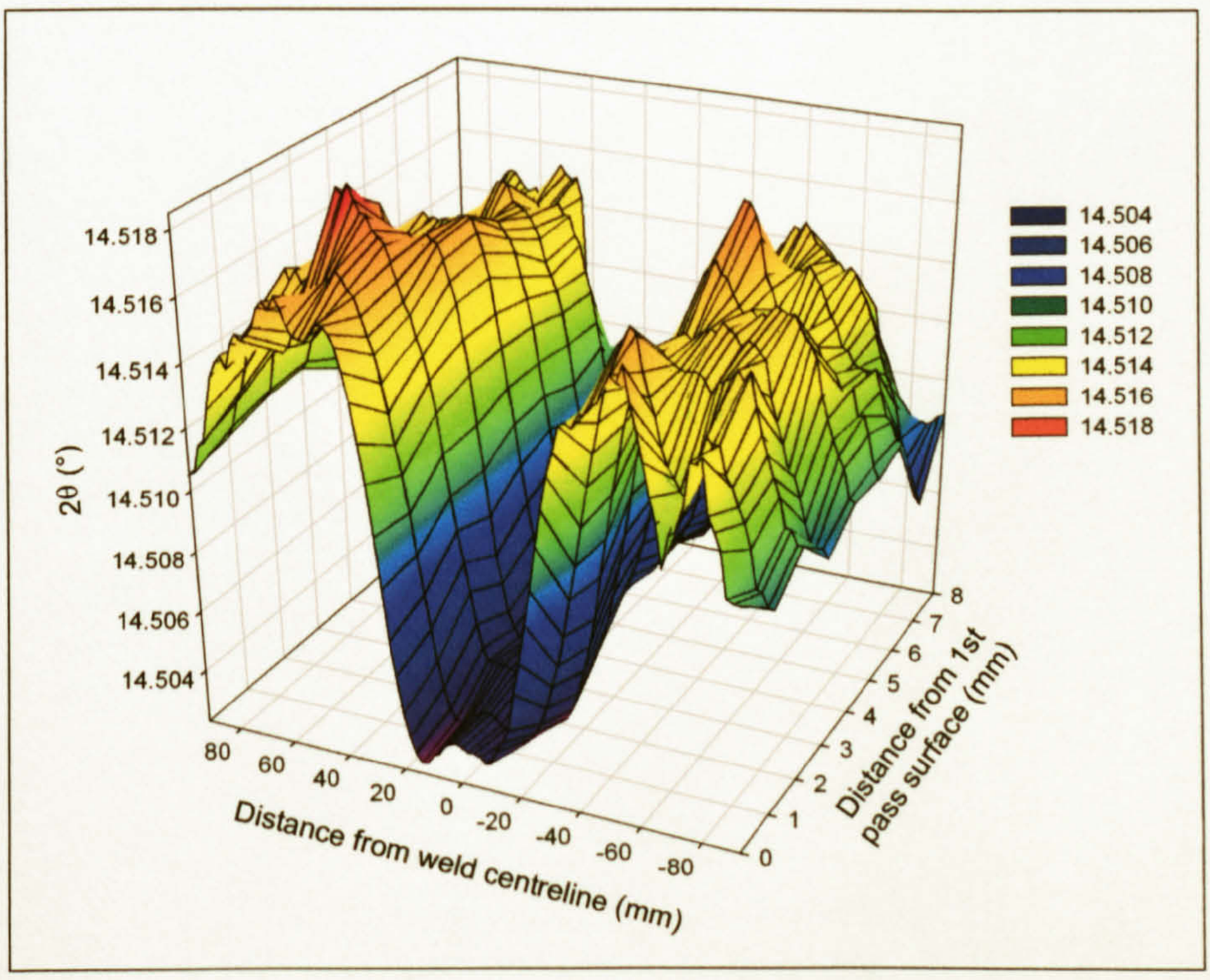

Figure 4.50: Variation of the diffraction angle, 2θ, in a direction parallel to the weld with respect to the distance from the weld centreline and thickness at the centre of a FS DP weld specimen.

4.4.6 Determination of the Strain Free Lattice Angle ($2\theta_0$) and Spacing (d_0)

The results from the synchrotron analyses undertaken were presented as a series of global coordinates and an angle for the peak diffraction, from which the residual strains and stresses may be determined. One of the problems associated with x-ray analysis of residual strains is determining the strain free lattice spacing, d_0. For the parent material d_0 can be determined through x-ray diffraction of an unstressed specimen, but in the case of material affected by the welding process, the weld nugget, TMAZ and HAZ in the case of the FS welds under investigation, the value of d_0 is considered to be process/ microstructure dependent. Annealing is not suitable for relieving the residual strains to allow the unstressed lattice spacing to be determined because the process results in a change in the microstructure. Grinding the material into a powder and hence relieving the strains is one technique that is employed, in the case of a FS weld this would require several volumes to be analysed to give an accurate assessment of the strain free lattice spacing across and through the thickness of the weld. Another technique, and the one initially employed, is to cut teeth into the area under investigation, as shown in Figure 4.51. The teeth were produced through EDM, the aim being that any residual strains resulting from the process would be confined to the near surface region. The theory behind the technique is that the majority of the weld induced residual strains would dissipate due to the small sections and that if measurements are made near to the teeth surfaces any remaining residual strains will be negligible, it not being possible to have a strain acting in a direction normal to a surface.

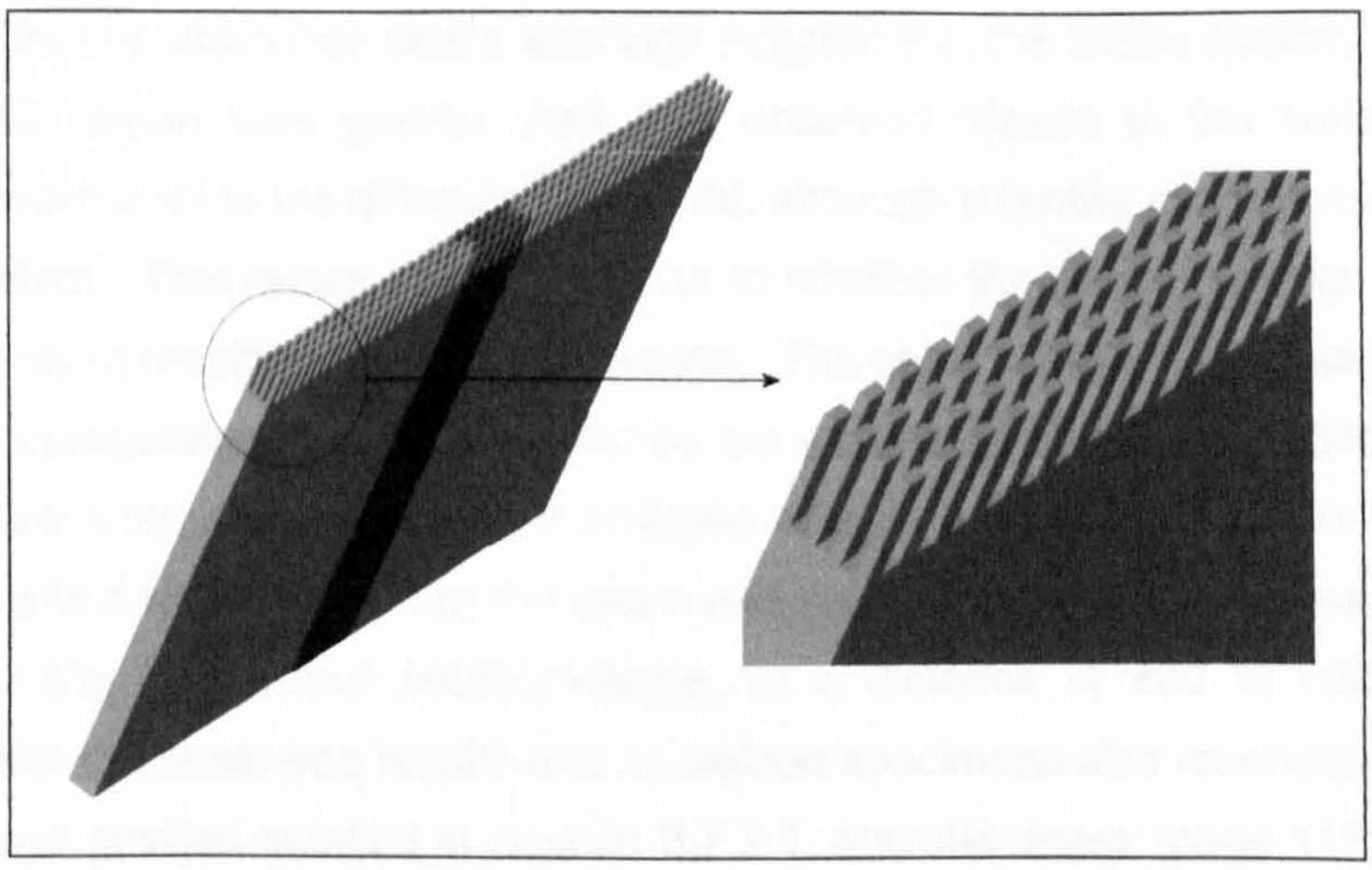

Figure 4.51: Schematic representation of the teeth cut into the FS DP welded specimen used to determine d_0 at various positions across the weld.

Two specimens were produced with the teeth having slightly different geometries. The first specimen had teeth that were 10 x 2 x 2 mm (l x w x t) with a 1 mm spacing between

each tooth and three teeth across the thickness. A second specimen (detailed as original as it was produced from the original welds, with the rolling direction of the plate being parallel to the weld direction) had teeth that were 10 x 5 x 1.8 (l x w x t) with a narrow notch between each tooth and four teeth across the thickness; the section containing the teeth was also removed from the main specimen, approximately 5 mm below the length of the teeth.

Figure 4.52 depicts the transverse and Figure 4.53 the longitudinal values of $2\theta_0°$ obtained for measurements made at the ends of the teeth and at various positions through the thickness in the FS SP weld, comparable results being returned by the DP weld, with Table 4.18 summarising all the measurements undertaken.

For the strain free lattice spacing measurements made in the weld nugget/TMAZ region, with the spacing being determined in a direction transverse to the weld, mean values of $2\theta_0$ ranging from 14.49376°-14.49583° were returned by a SP specimen, whilst values distant to the weld returned a range of 14.50136°-14.50585°. Measurements of $2\theta_0$, in a direction parallel to the SP weld, returned a mean value of 14.49453° for the weld nugget/TMAZ region and a range of 14.49283°-14.51374° for measurements made distant to the weld. The DP specimen $2\theta_0$, measured transverse to the weld, resulted in mean values ranging from 14.49332°-14.49668° for the weld nugget/TMAZ region and 14.50059°-14.50476° distant to the weld. The values for $2\theta_0$ parallel to the weld returned a mean value of 14.49115° in the region distant to the weld, no results were obtained for the weld nugget/TMAZ region.

The results for the strain free lattice spacings suggest that the lattice spacing in the weld nugget/TMAZ region was greater than that observed distant to the weld, d_0 being inversely proportional to the diffraction angle 2θ, although a tensile strain would also have the same effect. This raises the question as to whether the measurements undertaken on the teeth were resulting in strain free results. The general pattern exhibited by the $2\theta_0$ results was comparable to those returned by the as-welded plates, as detailed in Figure 4.47 to Figure 4.50, notably the small increase at the weld seam, minimum values at a distance of ±12.5 to ±16 mm from the seam and an increase to the maximum values, in the case of the longitudinal measurements, at a distance of ±20 to ±30 mm. The response from the strain free results and as-welded specimens also resembled that of the microhardness profiles detailed in Section 3.7.3.1, Microhardness (page 118). Accurate analysis of the results depends heavily on the value of $2\theta_0$ as determination of the strains is dependent solely on the ratio of $2\theta_0$ to 2θ, as indicated in equation (4.12); an increase in the value of $2\theta_0$, underestimating the strain free lattice spacing, by 0.01% can result in an overestimate of the strain by 17% at values of $2\theta = 14.50305°$ and $2\theta_0 = 14.49456°$. There was evidence of a through thickness variation in the lattice spacing with

measurements undertaken near to the rolled surfaces, z = 1 and 7 mm, returning lower values for $2\theta_0$ in the parent material, the effect was less evident in the weld nugget region. Later experiments undertaken on the AA 5383-H321 MIG welds returned mean values of $2\theta_0$ of 14.5054° and 14.5135° for the transverse and longitudinal values, both being undertaken at distances of 17 - 26 mm from the weld[1].

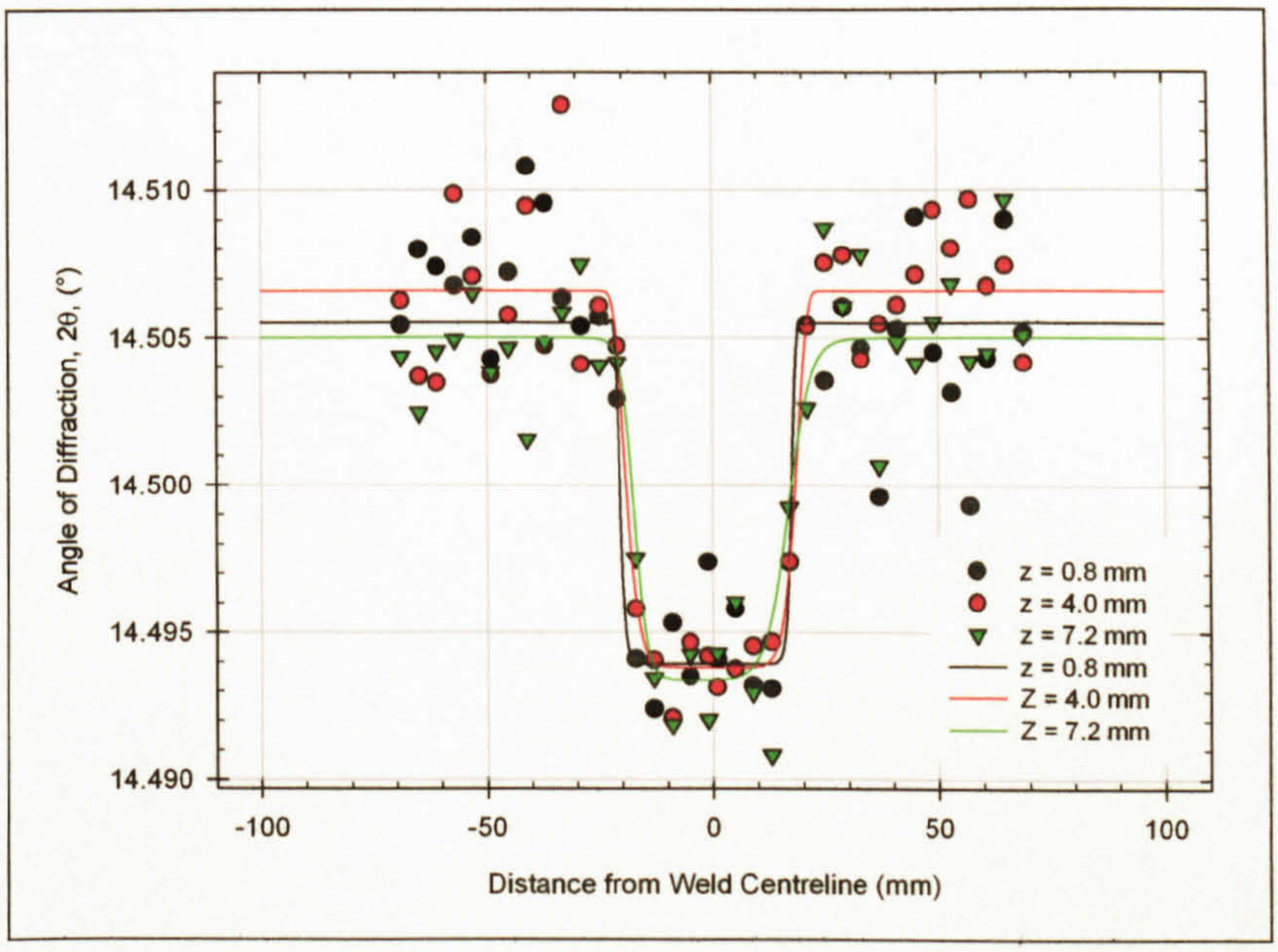

Figure 4.52: Determination of transverse lattice spacing, d_0, in a FS SP weld at depths, z, of 0.8, 4.0 and 7.2 mm.

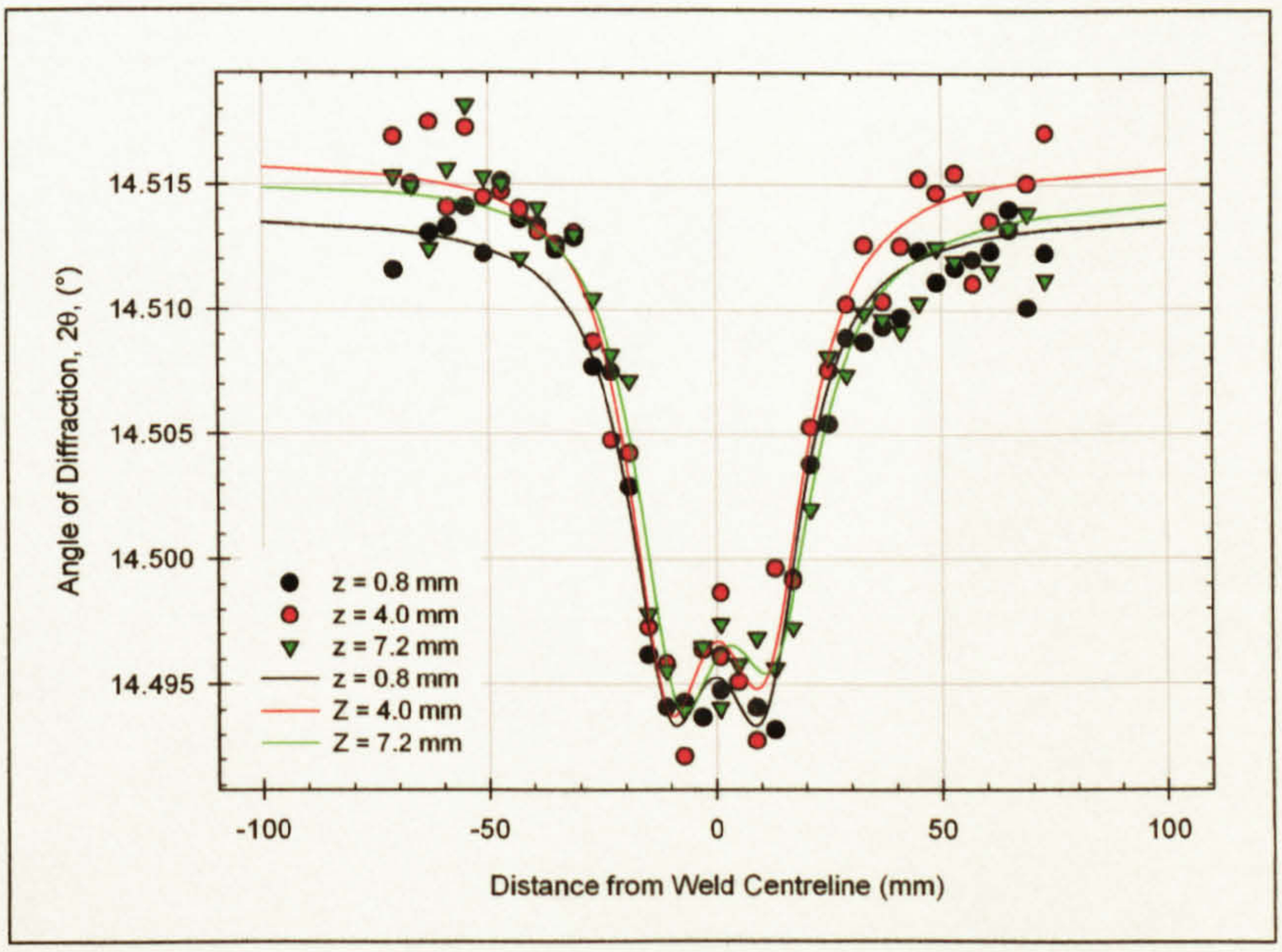

Figure 4.53: Determination of longitudinal lattice spacing, d_0, in a FS SP weld at depths, z, of 0.8, 4.0 and 7.2 mm.

[1] Hughes, DJ (2001)

FS weld type	Specimen	Direction of strain	Depth from weld seam (SP)/1st pass (DP) side(mm)	$2\theta_0$ (°) Distance from weld seam (mm)	
				0-12.5	30-70
SP	SP (original weld)	Longitudinal (// to rolling direction)	0.8	14.49390	14.51265
			4.0	14.49484	14.51485
			7.2	14.49484	14.51372
			Mean	*14.49453*	*14.51374*
		Transverse (|- to the rolling direction)	0.8	14.49762	14.50494
			4.0	14.49518	14.50778
			7.2	14.49469	14.50340
			Mean	*14.49583*	*14.50537*
			0.8	14.49431	14.50582
			4.0	14.49384	14.50645
			7.2	14.49314	14.50529
			Mean	*14.49376*	*14.50585*
	1SP	Transverse (// to rolling direction)	7.0	14.49154	14.49745
			1.0	14.49511	14.50235
			3.0	14.49448	14.50173
			5.0	14.49320	14.50050
			7.0	14.49393	14.50085
			Mean	*14.49418*	*14.50136*
		Longitudinal (|- to the rolling direction)	3.0	-	14.49241
			5.0	-	14.49313
			7.0	-	14.49296
			Mean	-	*14.49283*
DP	DP (original weld)	Transverse (|- to the rolling direction)	0.8	14.49658	14.50550
			7.2	14.49678	-
			Mean	*14.49668*	-
			0.8	14.49458	14.50343
			4.0	14.49610	14.50742
			7.2	14.49546	14.50343
			Mean	*14.49538*	*14.50476*
	1DP	Transverse (// to rolling direction)	1.0	14.49376	14.50022
			3.0	14.49277	14.50081
			5.0	14.49341	14.50039
			7.0	14.49332	14.50092
			Mean	*14.49332*	*14.50059*
		Longitudinal (|- to the rolling direction)	1.0	-	14.49167
			3.0	-	14.49276
			5.0	-	14.48789
			7.0	-	14.49227
			Mean	-	*14.49115*

Table 4.18: Summary of $2\theta_0$ measurements on FS SP and DP welds.

On the basis of the results obtained for the strain free diffraction angle, $2\theta_0$, the values initially utilised in calculating the residual strains were as indicated in Table 4.19. As the weld nugget region is generally considered to be fully recrystallised the strain free lattice spacing was considered to be identical for both the transverse and longitudinal directions, it was also assumed that the strain free spacing was identical in the remainder of the TMAZ where full recrystallisation does not occur. The values in the parent material, outwith the HAZ, were considered to be identical for both the SP and DP welds as both welds were produced from the same AA 5383-H321 plate. A simple linear transition was utilised between the two values, i.e. for $-12.5 > y > -30$ mm and $12.5 < y < 30$ mm.

$2\theta_0$ (°)					
		Transverse		Longitudinal	
	Distance from weld centreline (mm)				
	-12.5 ≤ y ≤ 12.5	-12.5 > y > -30 & 12.5 < y < 30	-30 ≥ y ≥ 30	-12.5 > y > -30 & 12.5 < y < 30	-30 ≥ x ≥ 30
FS SP	14.49433	$(704.571 \times 10^{-6}.\bar{Y}) + 14.485523$	14.50666	$(644.571 \times 10^{-6}.\bar{Y}) + 14.486273$	14.50561
FS DP	14.49475	$(680.571 \times 10^{-6}.\bar{Y}) + 14.486243$		$(620.571 \times 10^{-6}.\bar{Y}) + 14.486993$	

Table 4.19: FS SP and DP strain free diffraction angles, $2\theta_0$.

Utilisation of the strain free diffraction angles shown in Table 4.19 resulted in residual strain patterns that were wholly in compression as shown in Figure 4.54 and Figure 4.55 for the transverse strains in a FS SP welded specimen, comparable results were observed for the longitudinal strains with analogous results also being returned by the FS DP weld. The results were clearly invalid as the residual strains within a body are self-balancing and therefore compressive strains must be balanced by tensile ones.

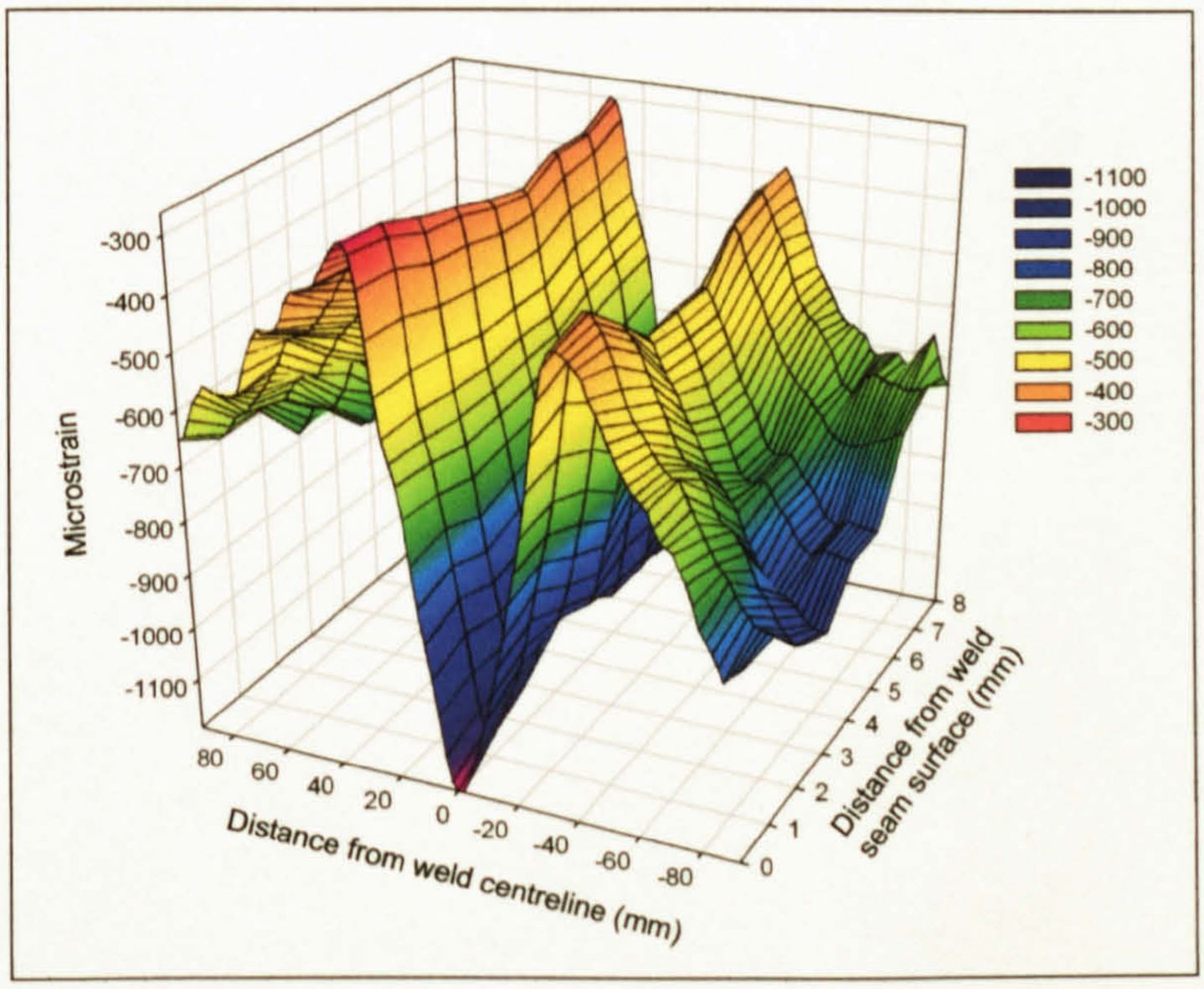

Figure 4.54: Variation of the transverse residual strains, when determined through utilisation of the values for $2\theta_0$ detailed in Table 4.19, with respect to the distance from the weld centreline and thickness at the centre of a FS SP welded specimen (1SP).

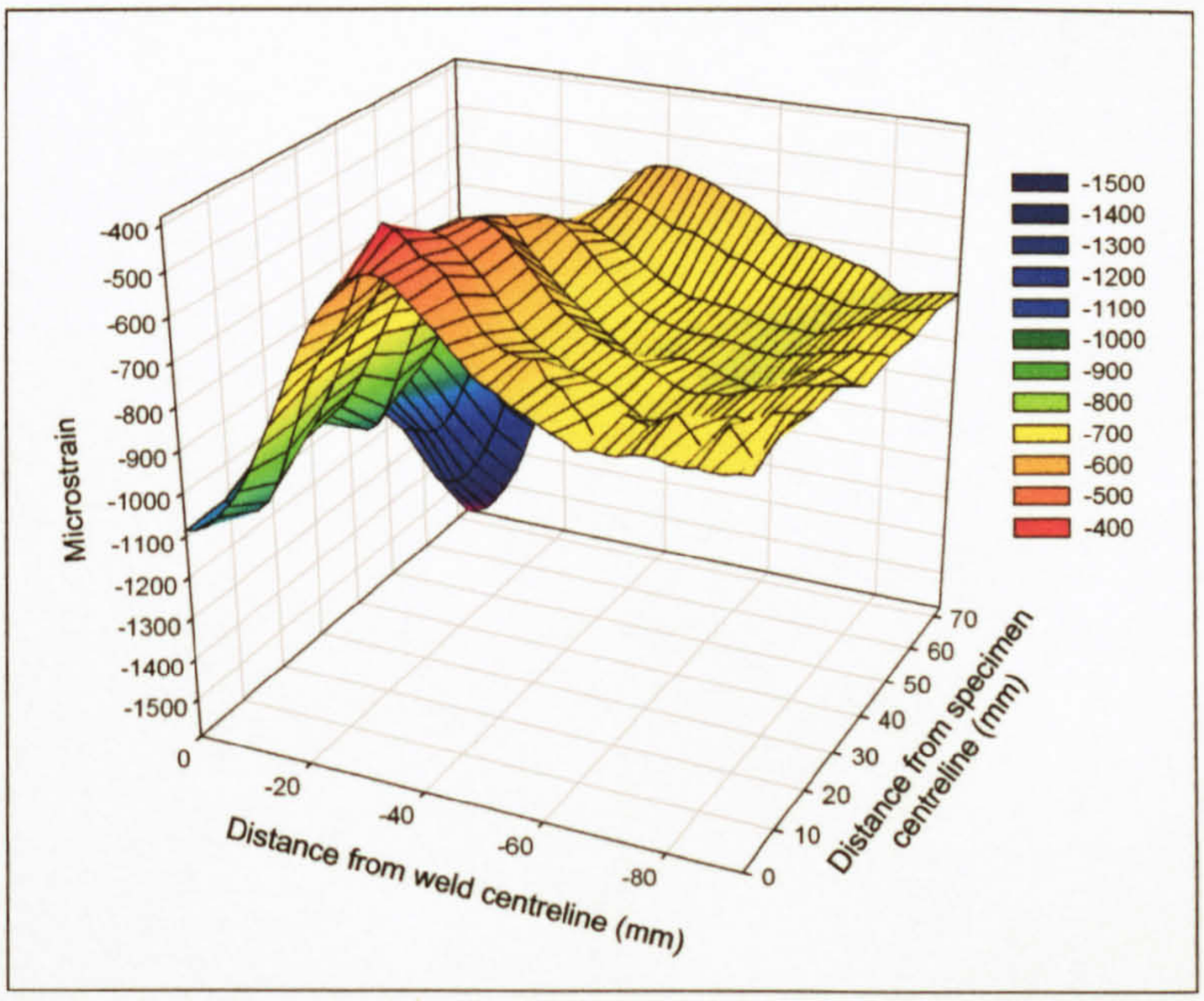

Figure 4.55: Variation of the transverse residual strains, when determined through utilisation of the values for $2\theta_0$ detailed in Table 4.19, in a FS SP weld (1SP) with respect to the distance from the weld and specimen centrelines at a depth of 1 mm below the friction band surface.

To overcome the imbalance of the residual strains when determined through utilisation of the experimentally determined values of $2\theta_0$ a force and moment equilibrium approach was instigated for each specimen. All the strains were considered to be elastic resulting in the forces being directly proportional to the measured strains. As the approach utilised a strain balance along a line, rather than throughout the volume of the specimen as would occur in reality, a single line of best fit was determined, taking into consideration all the measured positions with respect to the thickness (z = 1, 4, 7 mm or 0 - 8 mm in 1 mm steps depending on the analysis undertaken), thereby giving an "area" analysis and thus a more realistic determination of $2\theta_0$. Values of $2\theta_0$ were determined for the weld region, approximately ±12.5 mm from the weld centreline, and the region outside of the HAZ, distances greater than 30 mm from the weld centreline, with a linear transition being employed between to two regions. Although the approach returned what were considered to be appropriate results for the transverse strains, below the yield strain of the welded specimens in the region of the weld, the longitudinal strains returned values that were greater than the yield strain of the parent material. To overcome this a force balance with the strains at the edge of the plate tending towards zero was implemented for the longitudinal residual strains, this frequently being reported as their typical distribution in butt welded joints, as show in Figure 4.2 (page 132) and Figure 4.3 (page 133) for example. The outcome of this approach resulted in what were considered to be appropriate values, the maximum strains typically being no greater than the yield strain of the weld. The typical strain distribution for the transverse and longitudinal strains in a DP

weld were as shown in Figure 4.56, with the SP weld returning comparable results. Details of the values employed for $2\theta_0$ were as indicated in Table 4.20.

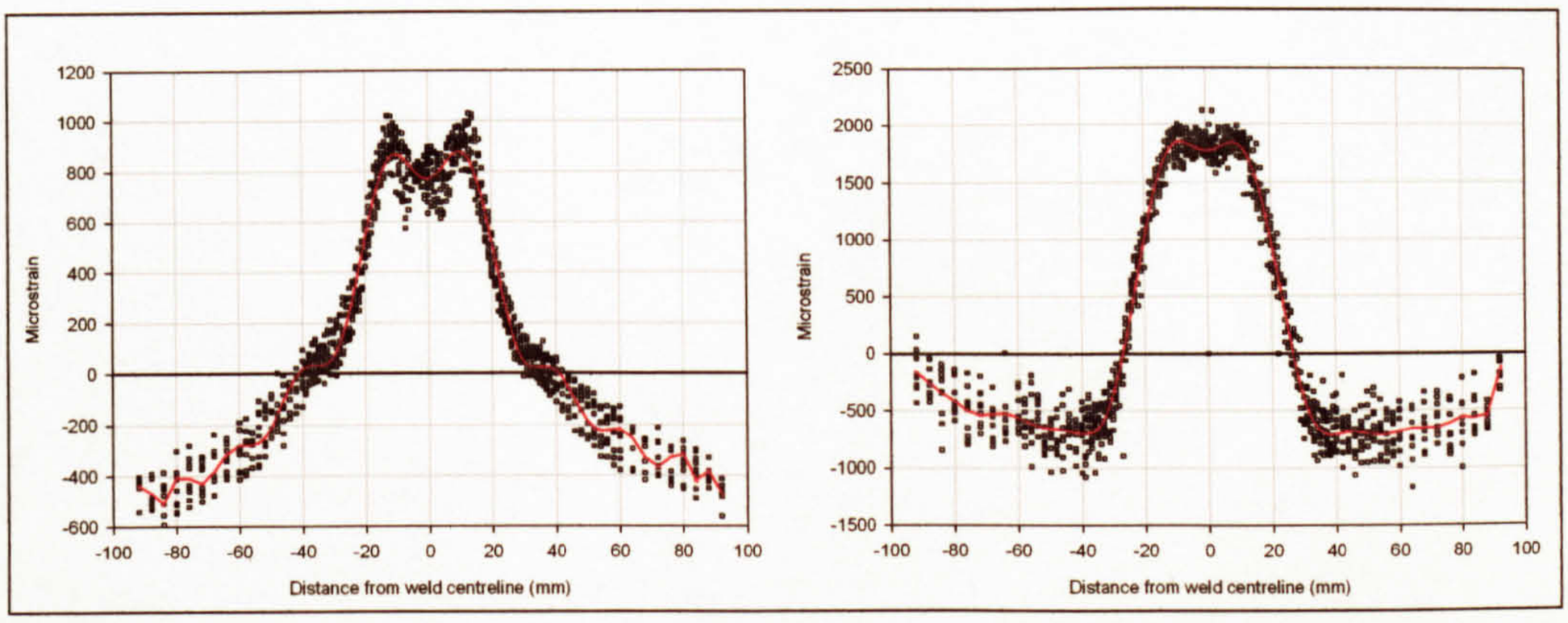

Figure 4.56: Microstrains resulting from the determination of $2\theta_0$ in a direction transverse (left), through a force and moment balance, and longitudinal (right) through a force balance with the strains tending towards zero at the edge of the specimen, in a FS DP weld.

		FS SP		FS DP	
		As-welded $2\theta_0$ (°)			
Distance from weld centreline		-12.5 ≤ y ≤ 12.5	-30 ≥ y ≥ 30	-12.5 ≤ y ≤ 12.5	-30 ≥ y ≥ 30
Transverse		14.52252	14.5125	14.518	14.51
Longitudinal		14.52175	14.508	14.53	14.50538
		Fatigue loaded $2\theta_0$ (°)			
Distance from weld centreline		-12.5 ≤ y ≤ 12.5	-30 ≥ y ≥ 30	-12.5 ≤ y ≤ 12.5	-30 ≥ y ≥ 30
Longitudinal	Minimum			14.5047	14.4900
	Maximum			14.5092	14.5035
	Mean			14.5063	14.4945
	Standard deviation			0.002516	0.007794

Table 4.20: Theoretical transverse and longitudinal values of $2\theta_0$.

4.4.6.1 FS Single Pass

Figure 4.57 depicts the variation in the transverse residual strains in a FS SP weld with respect to the weld centreline and plate thickness. Peak values were observed at distances in the region of ±12.5 mm from the weld seam with values of 1050 με and 950 με being observed for the advancing and retreating sides respectively on the friction band surface and 60 - 100 με lower on the weld seam surface. A decrease in the magnitude of the residual strains was observed at the centre of the weld, with values in the region of 800 με being returned by the friction band side and in the region of 100 με lower for the weld seam surface. From the peak values a constant reduction in the magnitudes of the residual strains was observed up to a distance of ±30 mm from the weld seam. A slight reduction in the rate of decrease was then observed with the advancing side returning values in the region of -350 με and the retreating side values of -350 to -470 με, for the friction band and weld seam surfaces respectively, at the edge of the specimen.

The longitudinal residual strains, shown in Figure 4.58, returned peak values for the weld seam surface of the specimen in the region of ±12.5 mm from the weld seam, with the advancing and retreating sides returning values of 1500 με and 1400 με respectively. The friction band surface of the weld exhibited a peak value of 1250 με at the centre of the weld, with a gradual transition being observed between the two surfaces. From the peak values a constant decrease in the magnitude of the strains was observed up to distances of ±30 mm from the weld centreline, with typical values of -500 to -600 με being observed, the lower value being returned by the advancing side on the friction band surface. From ±30 mm from the weld centreline to the edge of the specimen a gradual increase in the magnitude of the residual strains was observed with these approaching zero at the edge of the specimen.

The transverse and longitudinal residual stresses, as shown in Figure 4.59 and Figure 4.60 respectively, exhibited comparable responses to those observed for the residual strains. The transverse stresses returned peak values on the friction band surface in the region of 115 MPa and 100 MPa for the advancing and retreating sides respectively at distances of ±12.5 mm from the weld centreline. The minimum transverse stresses were observed at the edge of the plate, with values ranging from -30 to -50 MPa. The longitudinal residual stresses returned peak values in the region of 140 MPa and 120 MPa for the advancing and retreating sides on the weld seam surface at distances of ±12.5 mm, whilst the friction band side returned a value of 100 MPa at the weld seam. Nadir values were recorded at distances of ±35 mm from the centreline with values ranging from -40 to -60 MPa, as the edges of the specimens were approached the stresses tended towards zero.

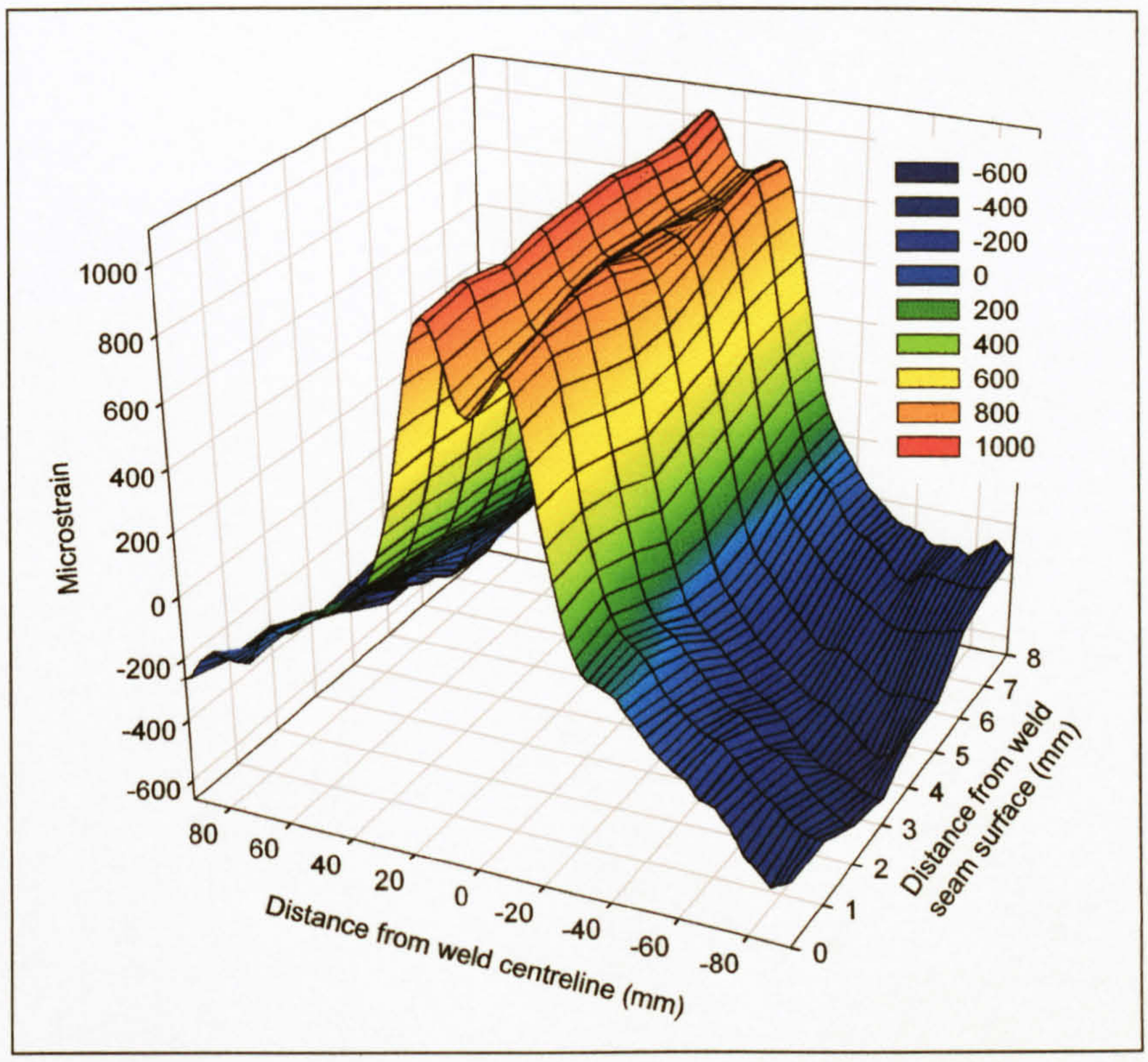

Figure 4.57: Variation of the transverse residual strains with respect to the distance from the weld centreline and thickness at the centre of a FS SP welded plate (1SP).

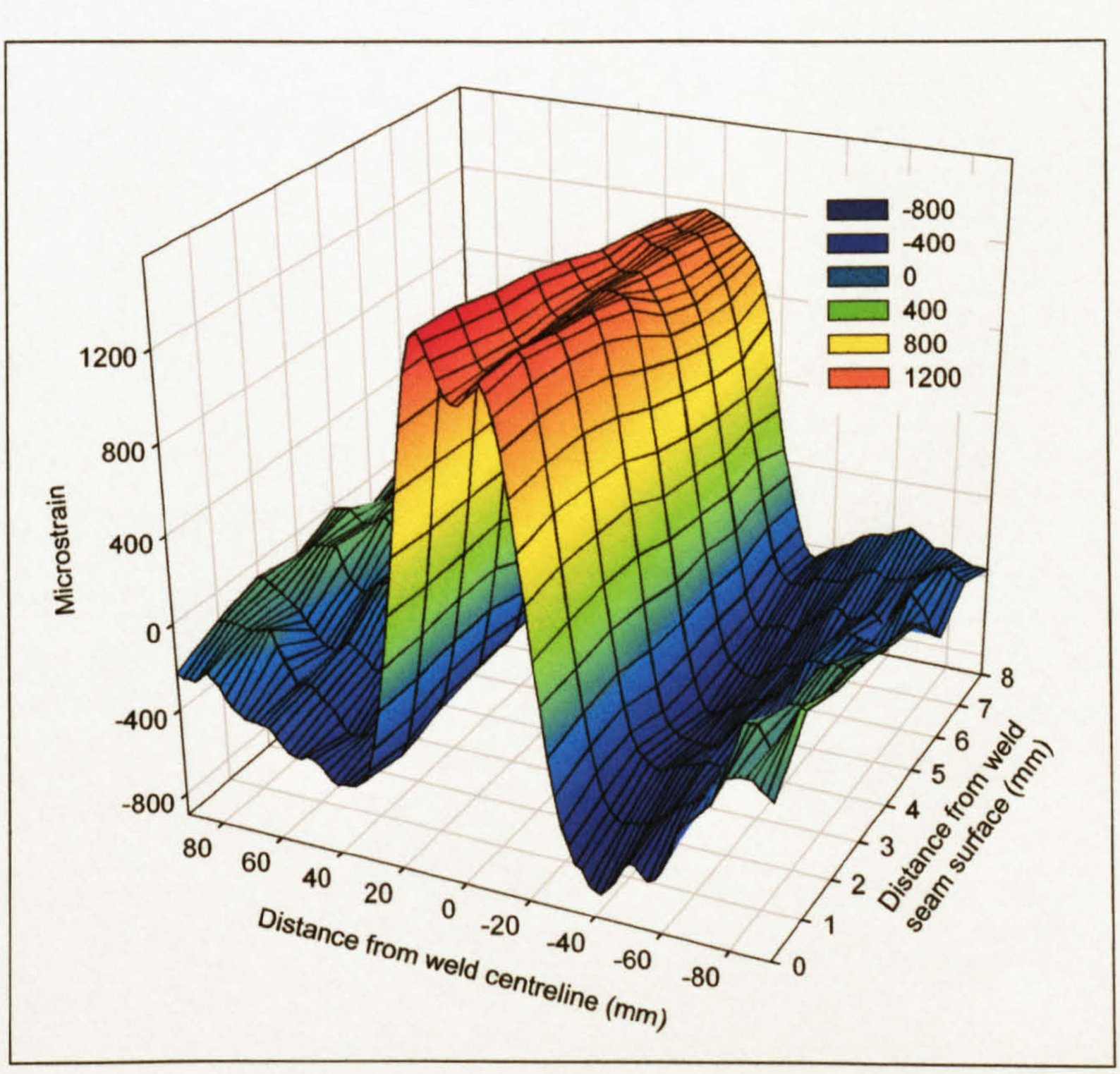

Figure 4.58: Variation of the longitudinal residual strains with respect to the distance from the weld centreline and thickness at the centre of a FS SP welded plate (1SP).

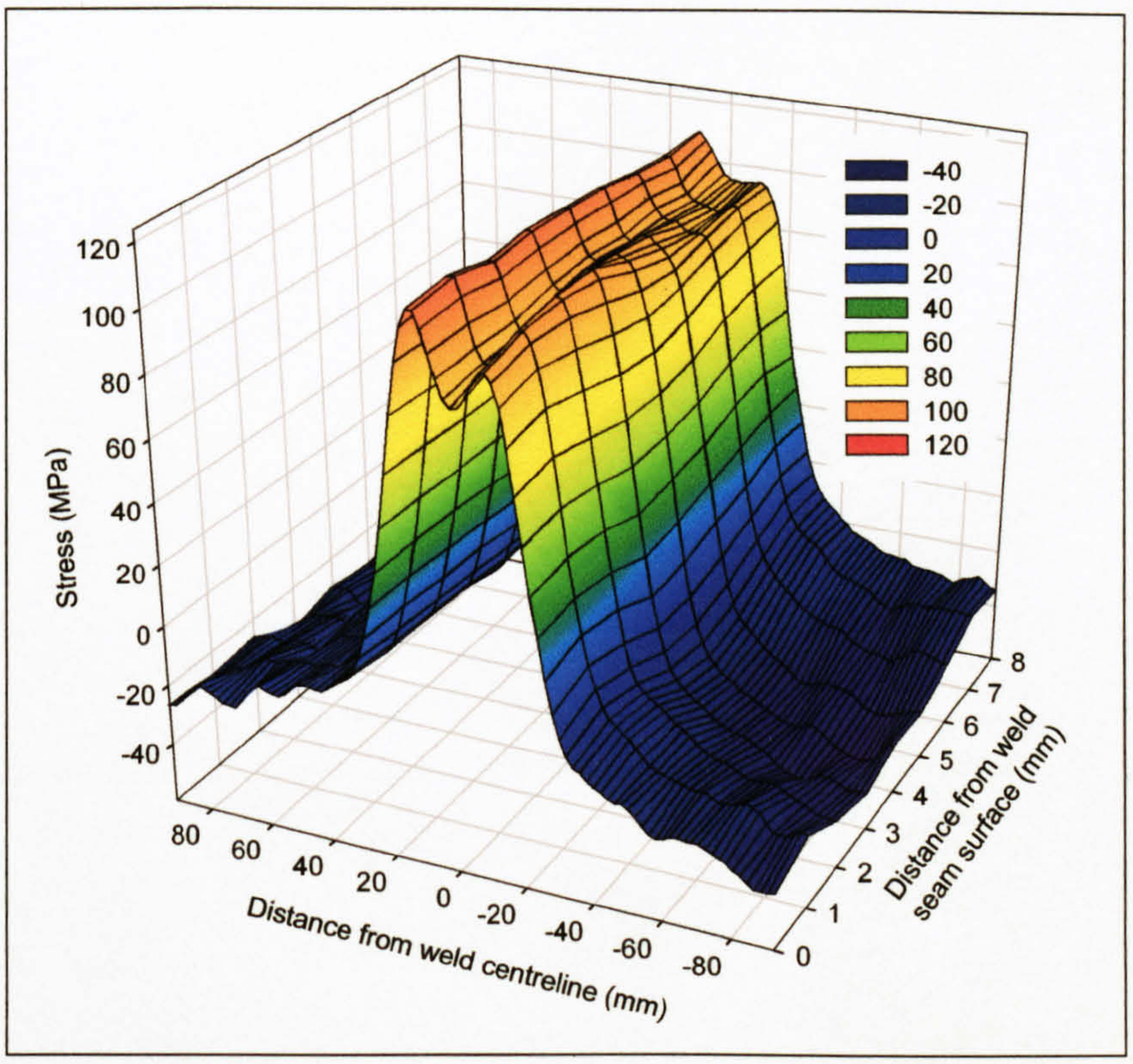

Figure 4.59: Variation of the transverse residual stress with respect to the distance from the weld centreline and thickness at the centre of a FS SP welded plate (1SP).

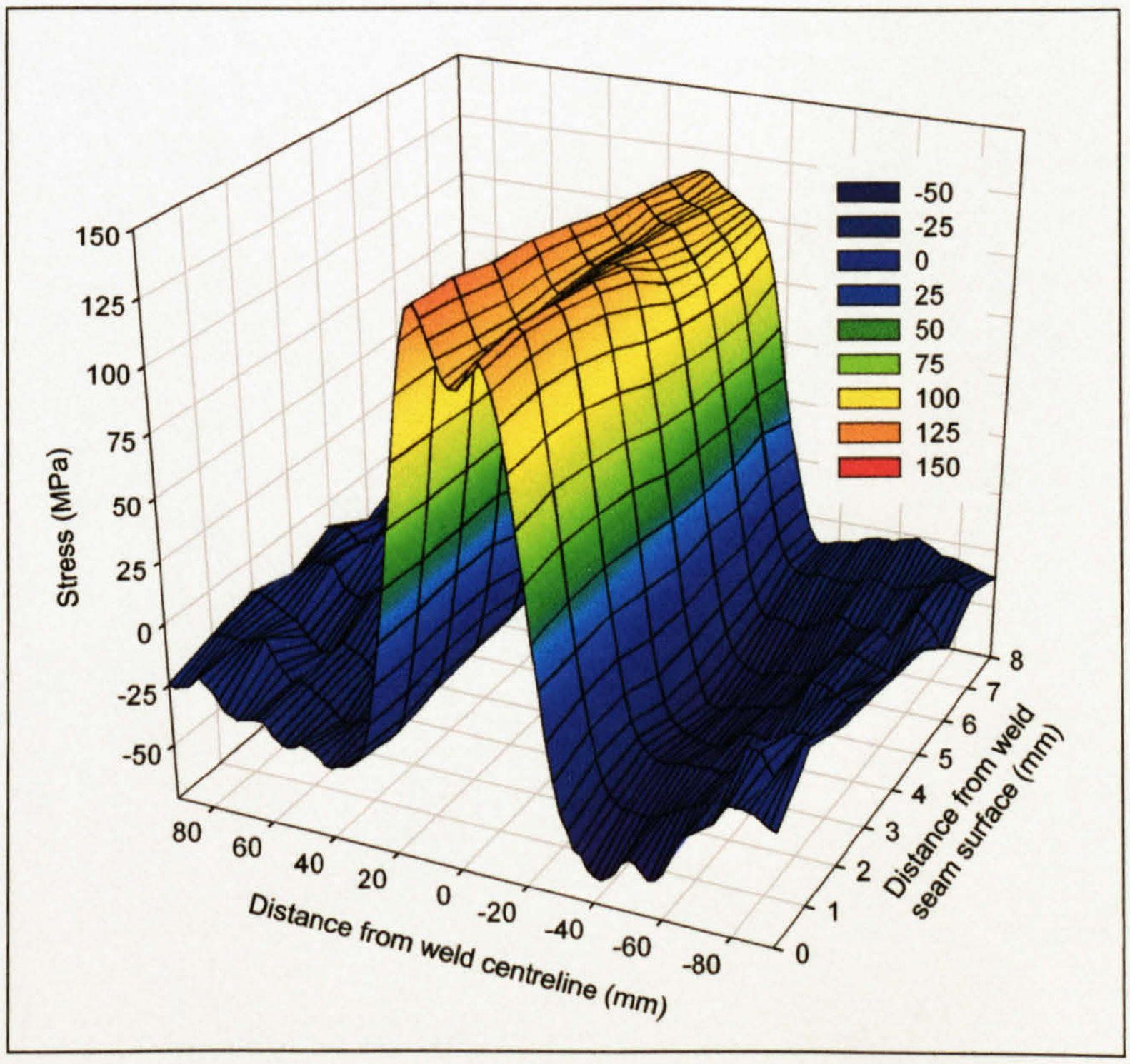

Figure 4.60: Variation of the longitudinal residual stress with respect to the distance from the weld centreline and thickness at the centre of a FS SP welded plate (1SP).

The variation in the transverse residual strains with respect to the distance from the weld and specimen centrelines was as shown in Figure 4.61. The magnitude of the strains at the edge of the specimen to 60 mm from the weld centreline ($-92 \leq y \leq -60$ mm) remained relatively constant with respect to the distance from the specimen centreline ($0 \leq x \leq 73$ mm) with a magnitude in the region of -300 με. At a distance of 12.5 mm from the weld centreline ($y = -12.5$ mm) peak values in the region of 800 - 900 με were observed up to a distance of 50 mm from the specimen centreline ($0 \leq x \leq 50$ mm), with a reduction to 100 με being evident at the centreline of the weld. At the centreline of the weld and edge of the plate ($x = 73$ mm, $y = 0$ mm) a reduction to 300 με was observed with the magnitudes of the surrounding strains exhibiting a gradual transition towards this.

The variation in the longitudinal residual strains at the edge of the specimen with respect to the weld centreline ($y = -92$ mm) remained relatively constant at -200 με for the length of the plate with respect to the plate centreline ($0 \leq x \leq 73$ mm) as depicted in Figure 4.62. The strains reduced in magnitude in a constant manner up to a distance of 40 mm from the weld centreline ($y = -40$ mm) with nadir values of -400 to -500 με being observed. As the centreline of the weld was approached the strains gradually increased up to a magnitude of 1100 με at the centre of the specimen ($x = 0$ mm, $y = 0$ mm) and 700 με at the edge of the specimen ($x = 0$ mm, $y = 73$ mm).

The transverse and longitudinal residual stresses, shown in Figure 4.63 and Figure 4.64, observed in the FS SP weld with respect to the weld and specimen centrelines exhibited comparable responses to those returned by the residual strains. The transverse stresses remained relatively constant in value, -30 to -35 MPa, for distances from the edge of the specimen to -60 mm from the weld centreline, with little variation with respect to the distance from the specimen centreline being evident. At distances of 12.5 mm from the weld centreline peak values in the region of 95 MPa were observed at the centre of the specimen, with this reducing to 40 MPa at the edge of the specimen. Longitudinal stresses remained relatively constant, in the region of -30 MPa, with respect to the distance from the plate centreline and for distances of 30 to 92 mm from the weld centreline. At distances greater than 30 mm from the weld centreline an increase in the magnitude of the residual stresses was evident, with peak values being evident at the weld centreline, returning values up to 115 MPa at the centre of the specimen ($x = 0$ mm) and 60 MPa at the edge of the plate ($x = 73$ mm).

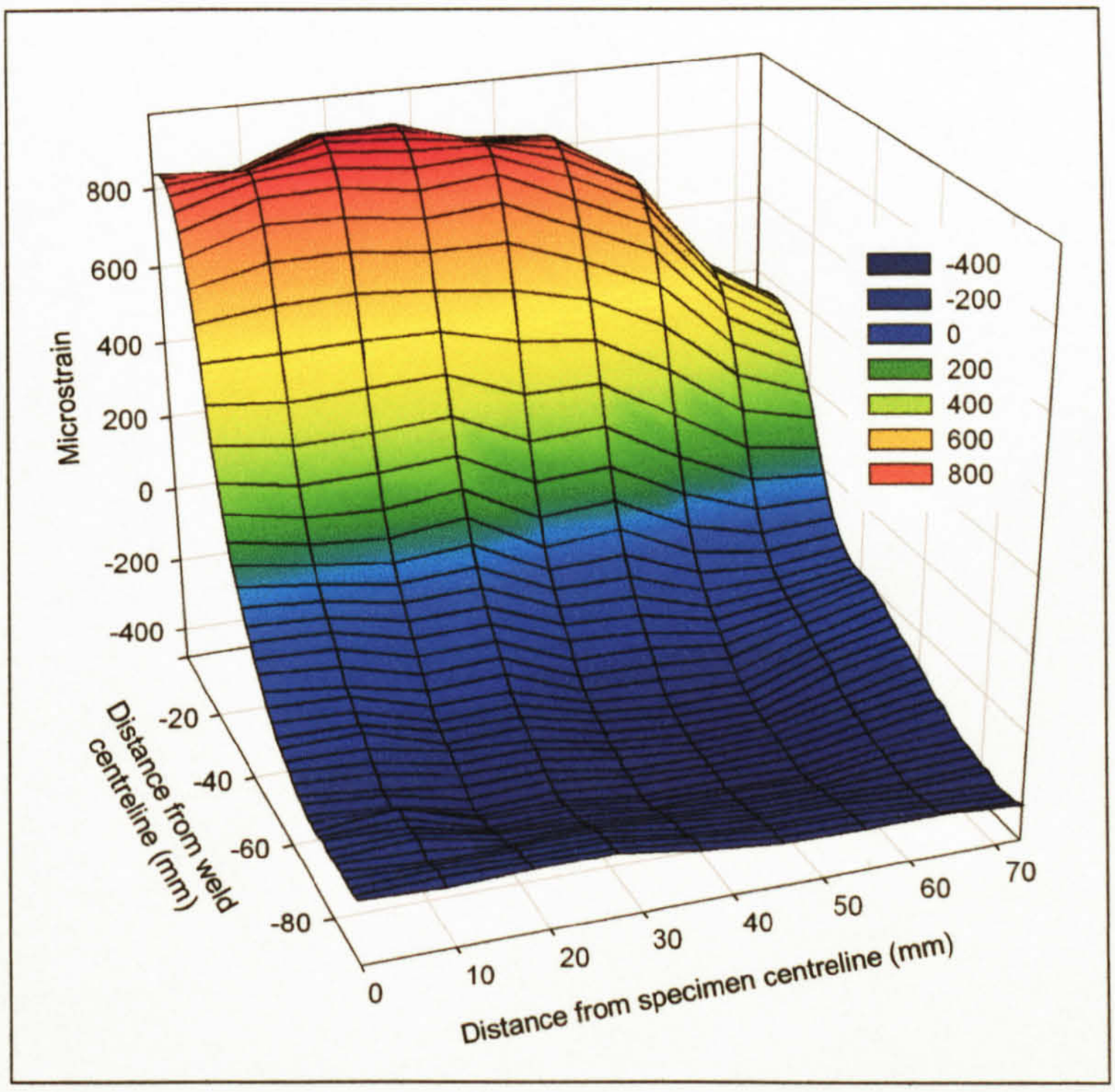

Figure 4.61: Variation of the transverse residual strains in a FS SP weld (1SP) with respect to the distance from the weld and specimen centrelines at a depth of 1 mm below the tool surface.

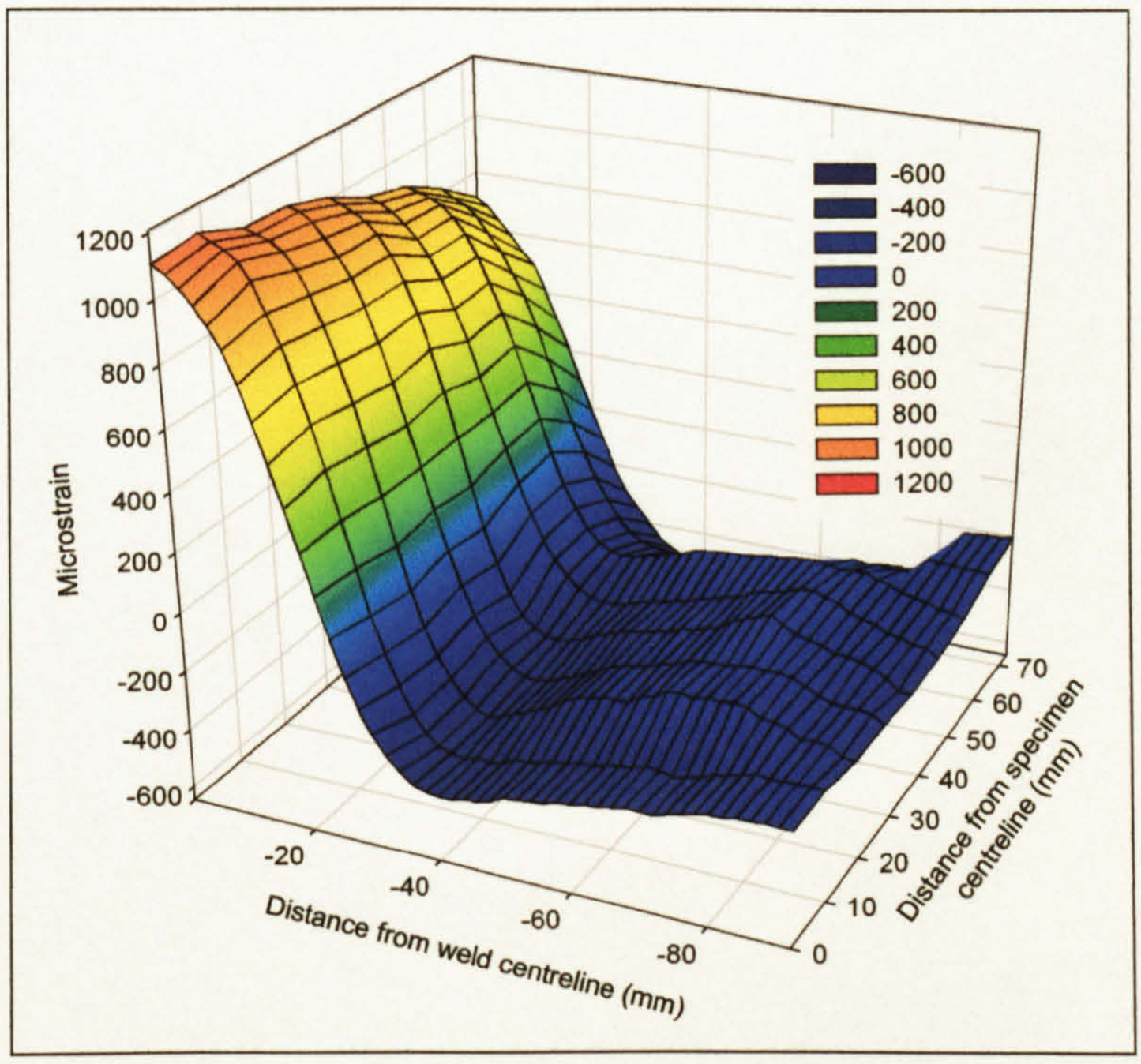

Figure 4.62: Variation of the longitudinal residual strains in a FS SP weld (1SP) with respect to the distance from the weld and specimen centrelines at a depth of 1 mm below the tool surface.

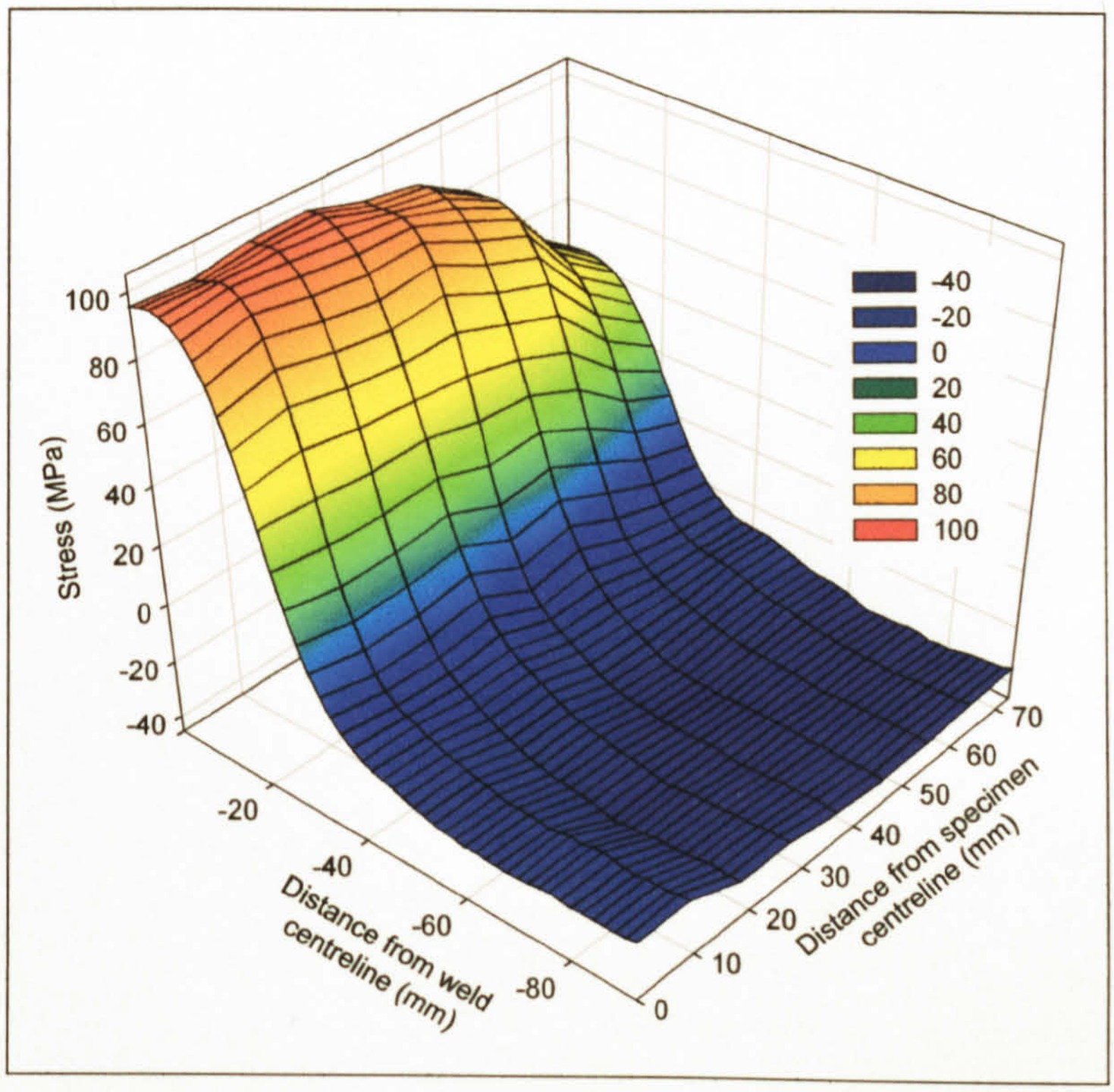

Figure 4.63: Variation of the transverse residual stresses in a FS SP weld (1SP) with respect to the distance from the weld and specimen centrelines at a depth of 1 mm below the tool surface.

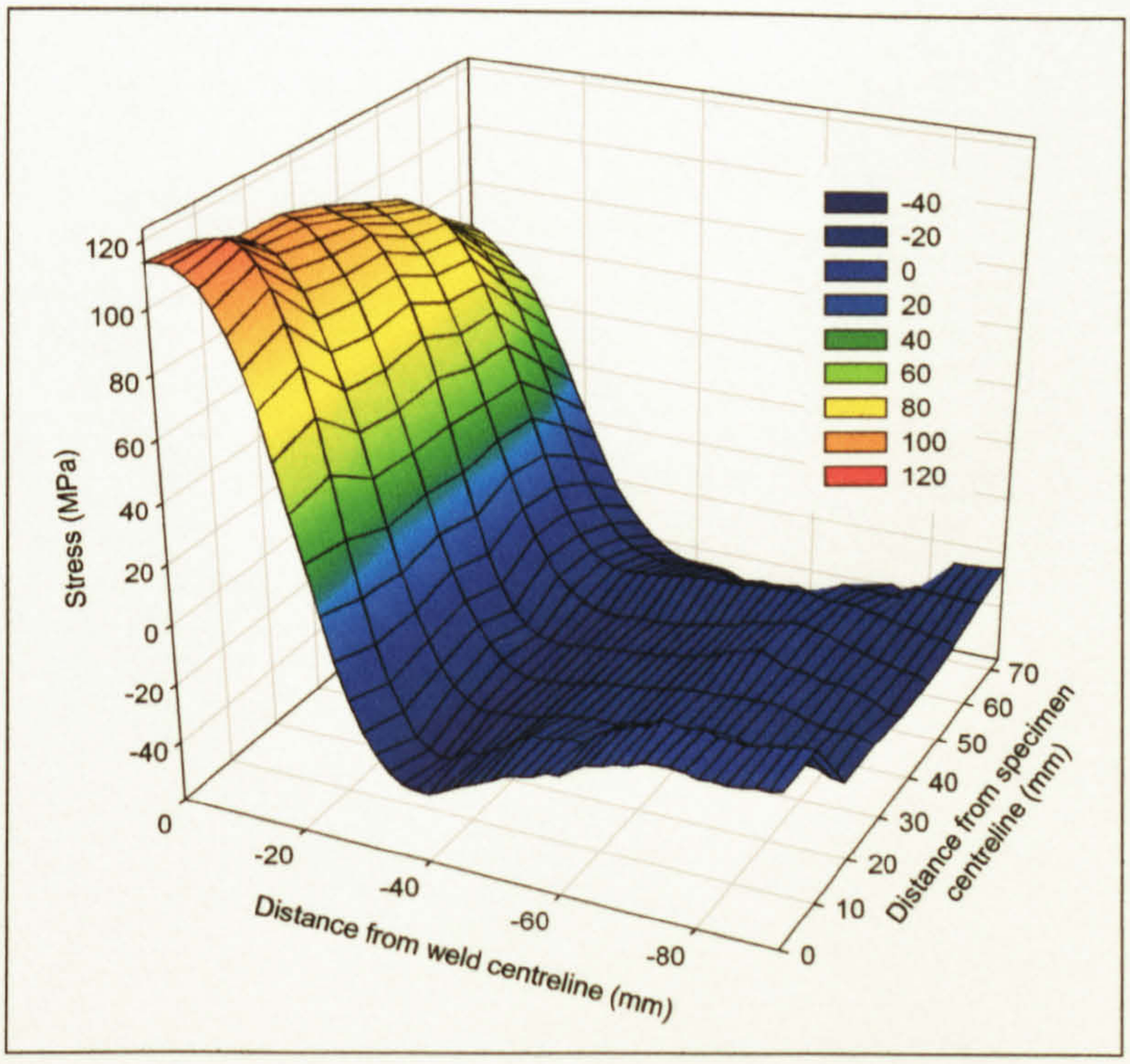

Figure 4.64: Variation of the longitudinal residual stresses in a FS SP weld (1SP) with respect to the distance from the weld and specimen centrelines at a depth of 1 mm below the tool surface.

4.4.6.2 FS Double Pass

Peak values for the transverse residual strains, shown in Figure 4.65, were observed at distances of ±12.5 mm from the centre of the weld, returning values in the region of 1000 με in the vicinity of the 2nd pass surface, the 1st pass surface returning values that were approximately 100 με lower. At the centre of the weld values in region of 200 με lower than the peak values were returned. From the position of the peak values to the edges of the specimen a gradual reduction in the magnitude of the strains to -400 με was observed, negligible variation between the advancing and retreating sides of the specimen was apparent.

The longitudinal residual strains, shown in Figure 4.66, returned peak values in the region of ±12.5 mm from the weld centreline with values in the region of 2000 με. Unlike the transverse strains the area did not exhibit a significant reduction at the centre of the weld. From the plateau containing the peak residual strains a reduction to the nadir values of -800 to -900 με at distances of ±40 to ±45 mm was observed. From the nadir values a gradual increase towards zero was observed as the edge of the specimen was approached.

The residual stresses acting in a direction transverse to the weld were as shown in Figure 4.67, with their general appearance being comparable to those returned by the residual strains. Peak values in the region of 120 MPa for the 2nd pass surface and up to 20 MPa less for the 1st pass surface were observed at distances of ±12.5 mm from the weld centreline. A slight reduction of 10 - 20 MPa was observed at the centre of the weld. From the position of the peak stress to the edge of the specimen a gradual reduction to -40 MPa was observed, with any variation between the advancing and retreating sides being negligible. The longitudinal residual stresses, as depicted in Figure 4.68, exhibited a comparable response to that observed for the residual strains, with peak values of 170 MPa being observed in a plateau extending from ±12.5 mm from the weld centreline. From the area containing the peak values a reduction to nadir values of -60 MPa, at a distance of ±55 mm from the weld centreline was observed, with the values tending towards zero as the edge of the specimen was approached.

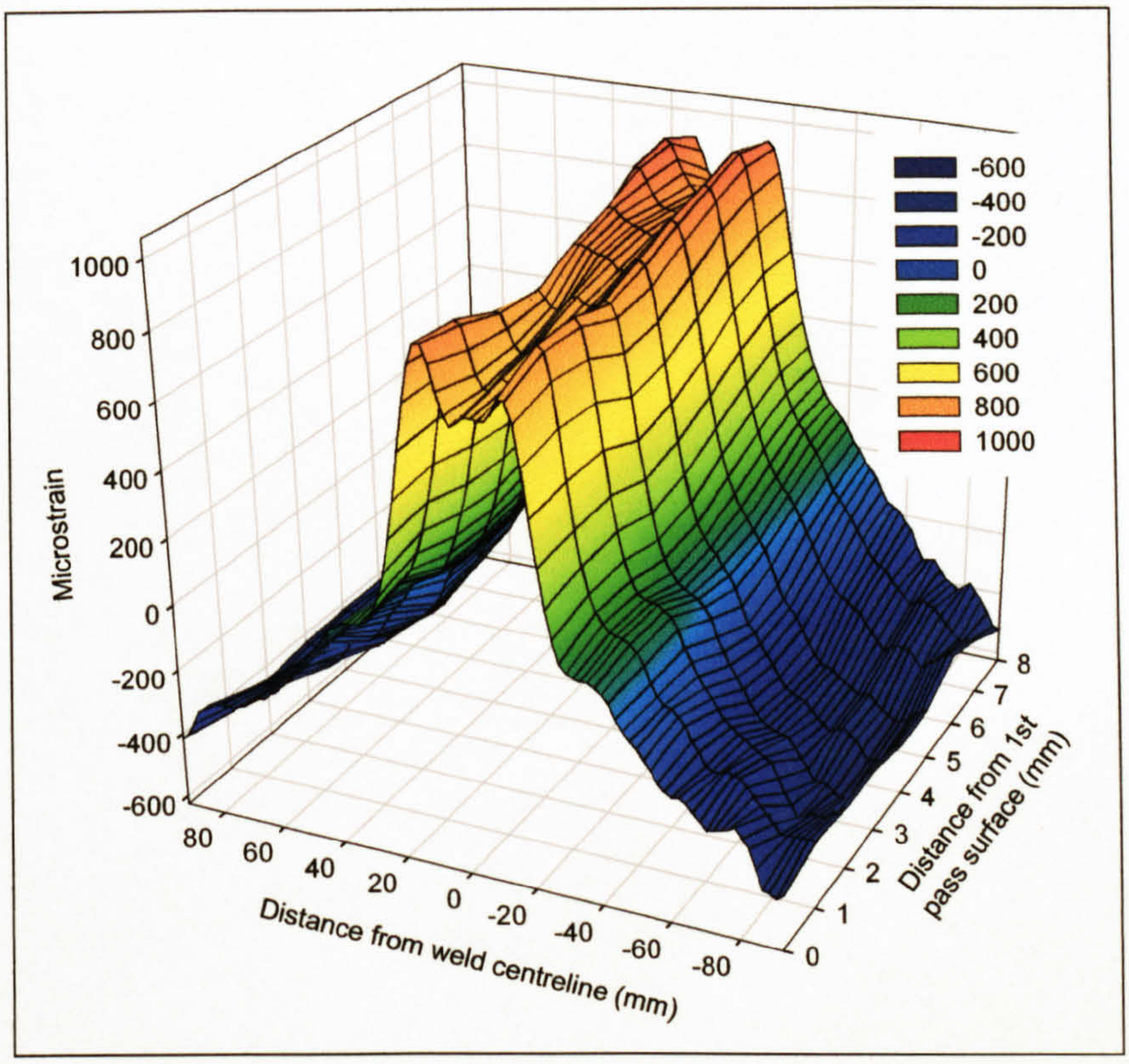

Figure 4.65: Variation of the transverse residual strains with respect to the distance from the weld centreline and thickness at the centre of a FS DP welded specimen (1DP).

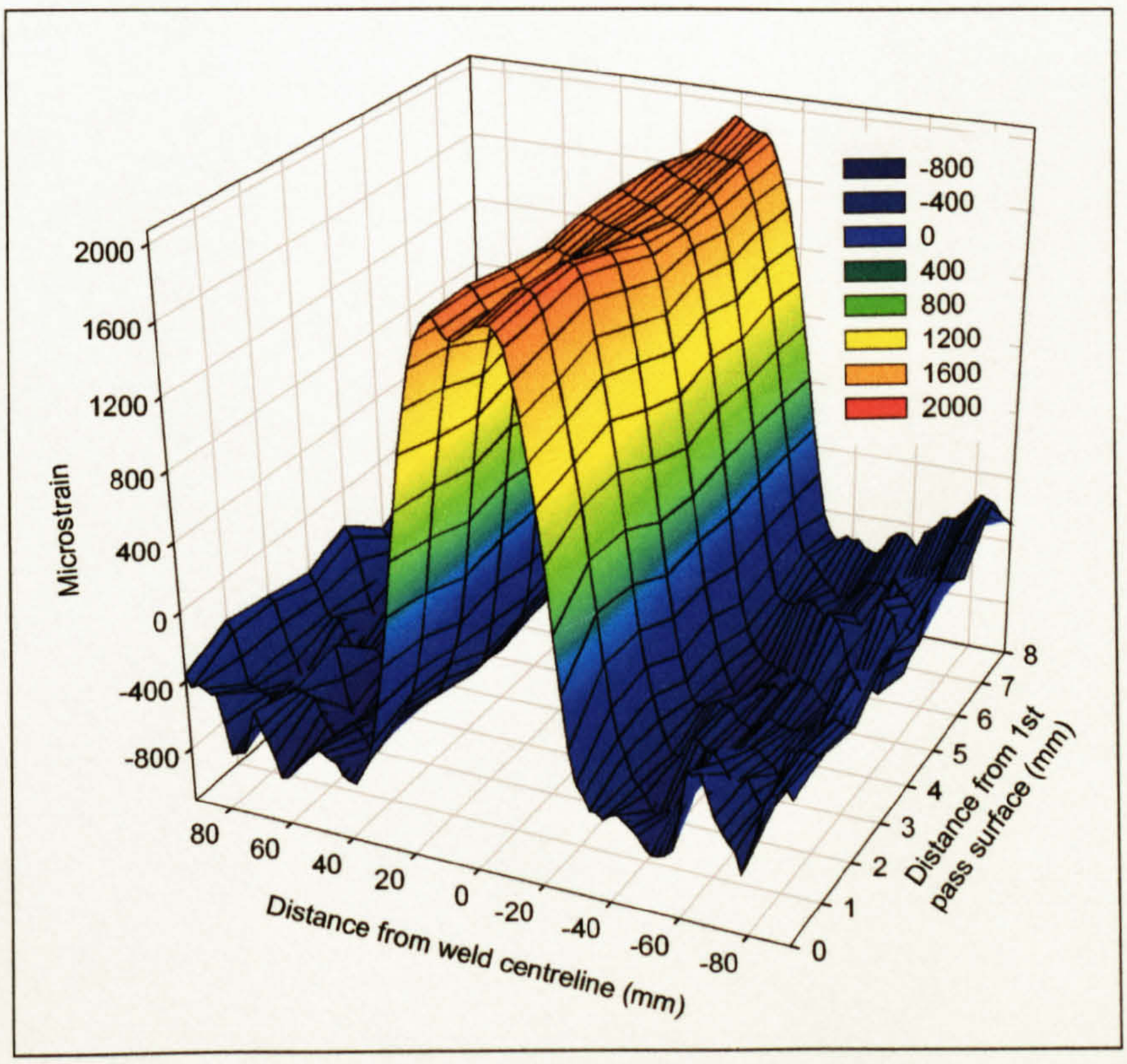

Figure 4.66: Variation of the longitudinal residual strains with respect to the distance from the weld centreline and thickness at the centre of a FS DP welded specimen (1DP).

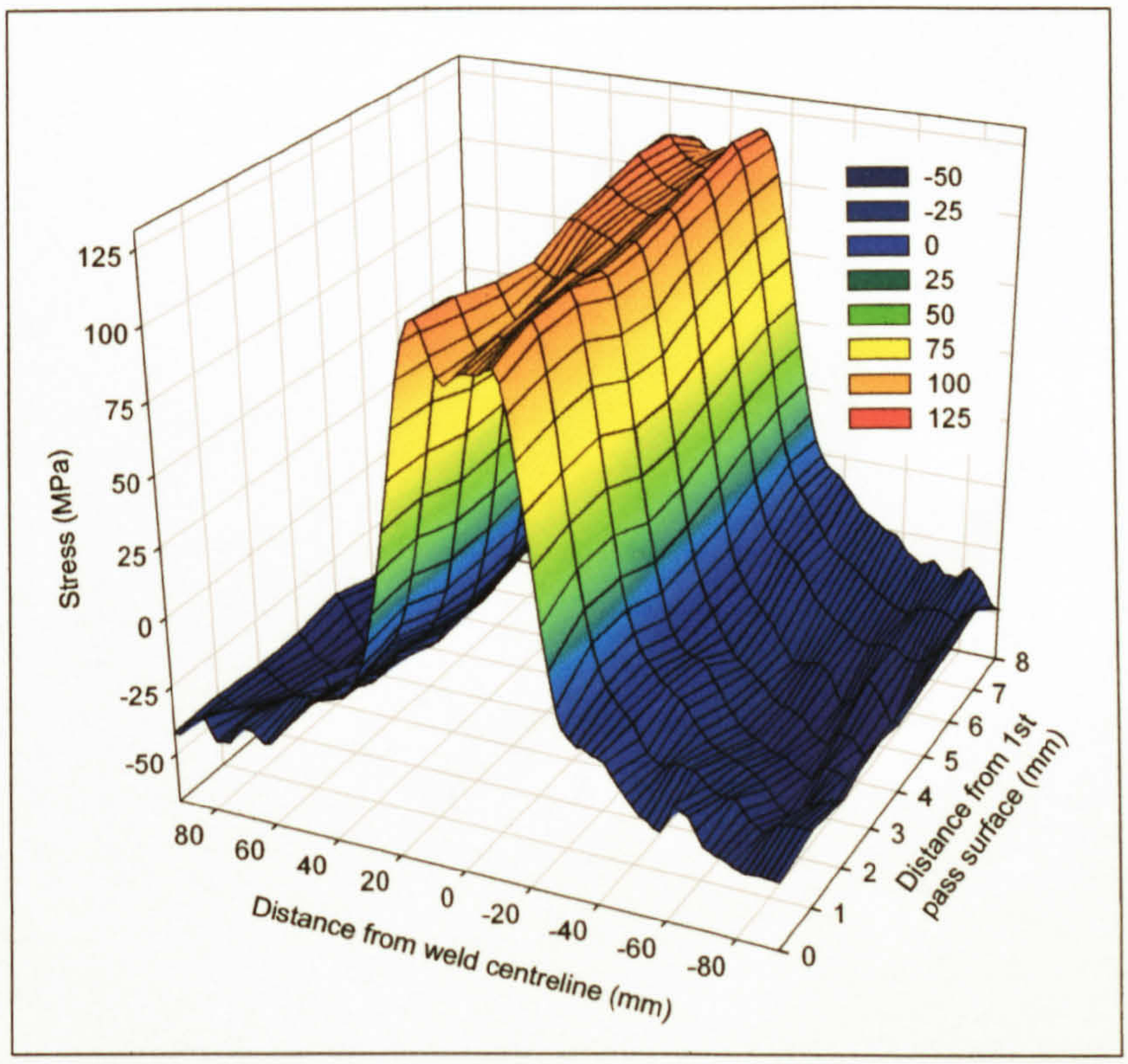

Figure 4.67: Variation of the transverse residual stresses with respect to the distance from the weld centreline and thickness at the centre of a FS DP welded specimen (1DP).

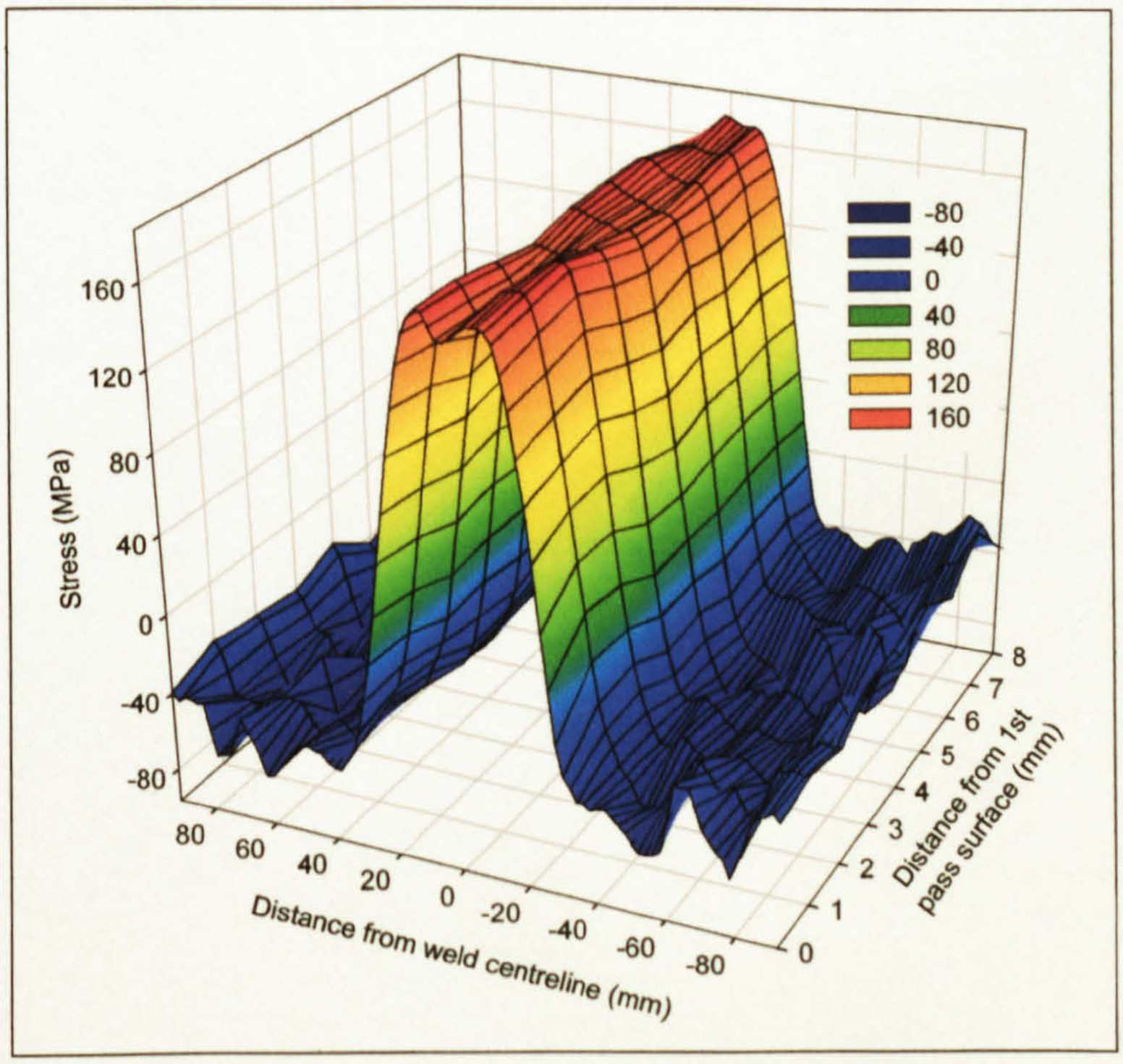

Figure 4.68: Variation of the longitudinal residual stresses with respect to the distance from the weld centreline and thickness at the centre of a FS DP welded specimen (1DP).

The variation in the magnitude of the transverse residual strains with respect to the distance from the weld and specimen centrelines were as shown in Figure 4.69. At the edge of the specimen (y = -92 mm) the strains remained relatively constant across the width of the specimen ($0 \leq x \leq 73$ mm) returning a value of -400 με. From the edge of the specimen and at distances of 0 - 30 mm from the specimen centreline, (x = 0 - 30, y = -92 mm) the residual strains gradually increased up to a distance of 12.5 mm (y = -12.5 mm) from the weld centreline, where peak values of 900 με were observed. As the distance from the specimen centreline increased above 30 mm ($30 \leq x \leq 60$, y = -12.5 mm) a reduction in the magnitude of the strains was observed, with values of 200 με being observed at a distance of 60 mm.

The longitudinal residual strains, with respect to the distance from the weld and specimen centrelines, varied as shown in Figure 4.70. At the weld centreline the strains reduced from 2000 to 1500 με as the distance from the centre of the specimen increased from 0 - 73 mm. As the distance from the weld centreline increased the magnitude of the strains decreased with negligible variation with respect to the distance from the specimen centreline, at distances of -40 to -55 mm from the weld centreline minimum values in the region of -600 to -700 με were returned. From the minimum values a gradual increase in the magnitude of the strains towards zero was observed as the edge of the specimen, with respect to the distance from the weld centreline, was approached.

The residual stresses acting in both the transverse and longitudinal directions returned responses comparable to the residual strain fields observed, as shown in Figure 4.71 and Figure 4.72 respectively. The transverse stresses at the weld centreline ranged from 115 MPa at the centre of the specimen (x = 0, y = 0 mm) to 60 MPa at the edge of the specimen, (x = 73, y = 0 mm). A slight increase in the magnitude of the stresses, in the region of 5 MPa, was observed at a distance of 12.5 mm from weld centreline at distances of 0 - 35 mm from the centreline of the specimen, with these then reducing as the edge of the specimen with respect to the specimen centreline was approached. At the edge of the specimen with respect to weld centreline values of -40 MPa were observed, these being constant from the centre of the specimen to the edge. Peak stresses acting in the longitudinal direction ranged from 160 - 120 MPa and were observed at the weld centreline, with the values decreasing as the distance from the centre of the specimen increased. Nadir values of -40 MPa were observed at distances ranging from -40 to -45 mm from the weld centreline with these then approaching zero at the edge of the plate, with minimal variation with respect to the distance from the specimen centreline being observed.

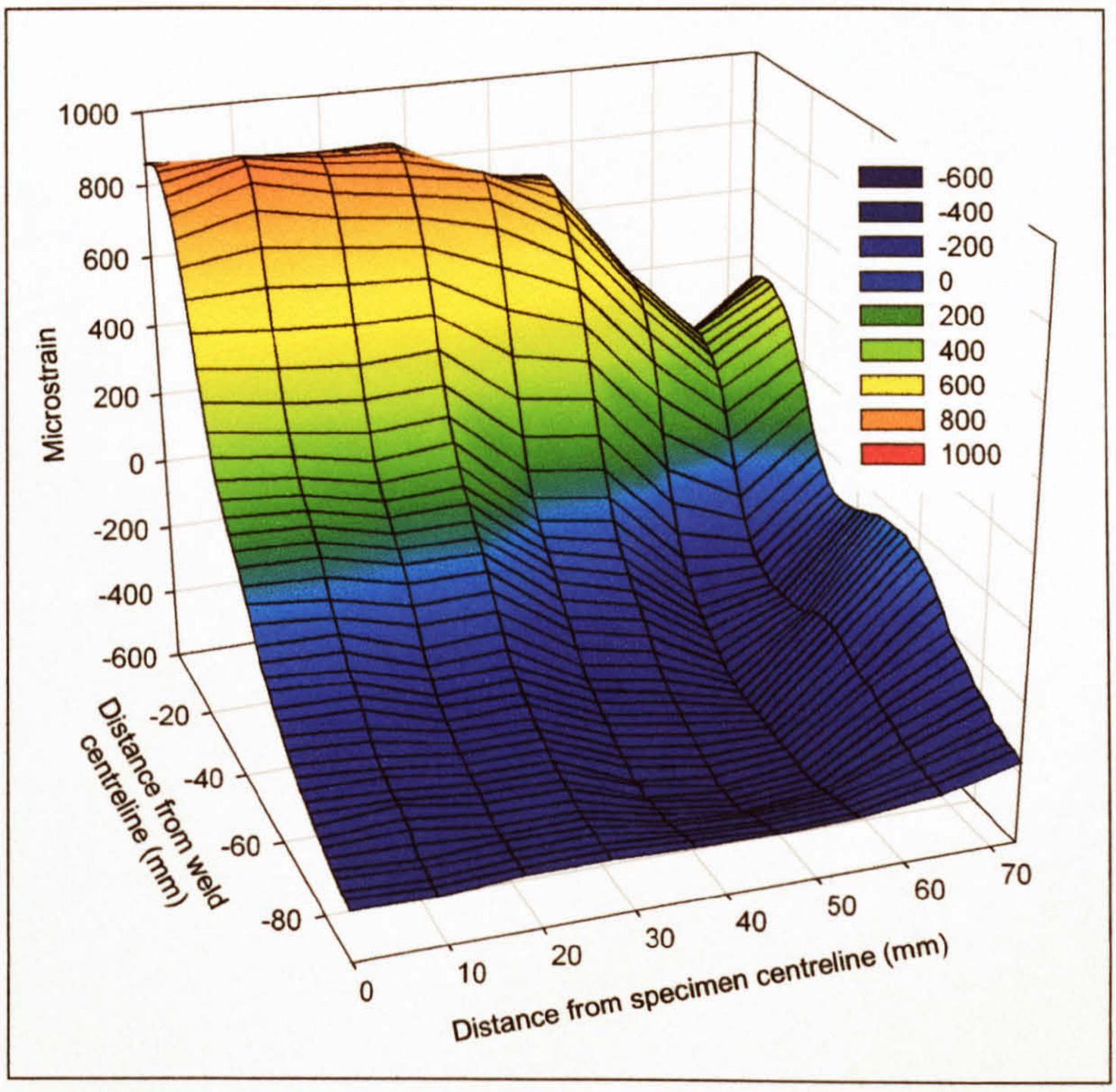

Figure 4.69: Variation of the transverse residual strains in a FS DP weld (1DP) with respect to the distance from the weld and specimen centrelines at a depth of 1 mm below the 2nd pass surface.

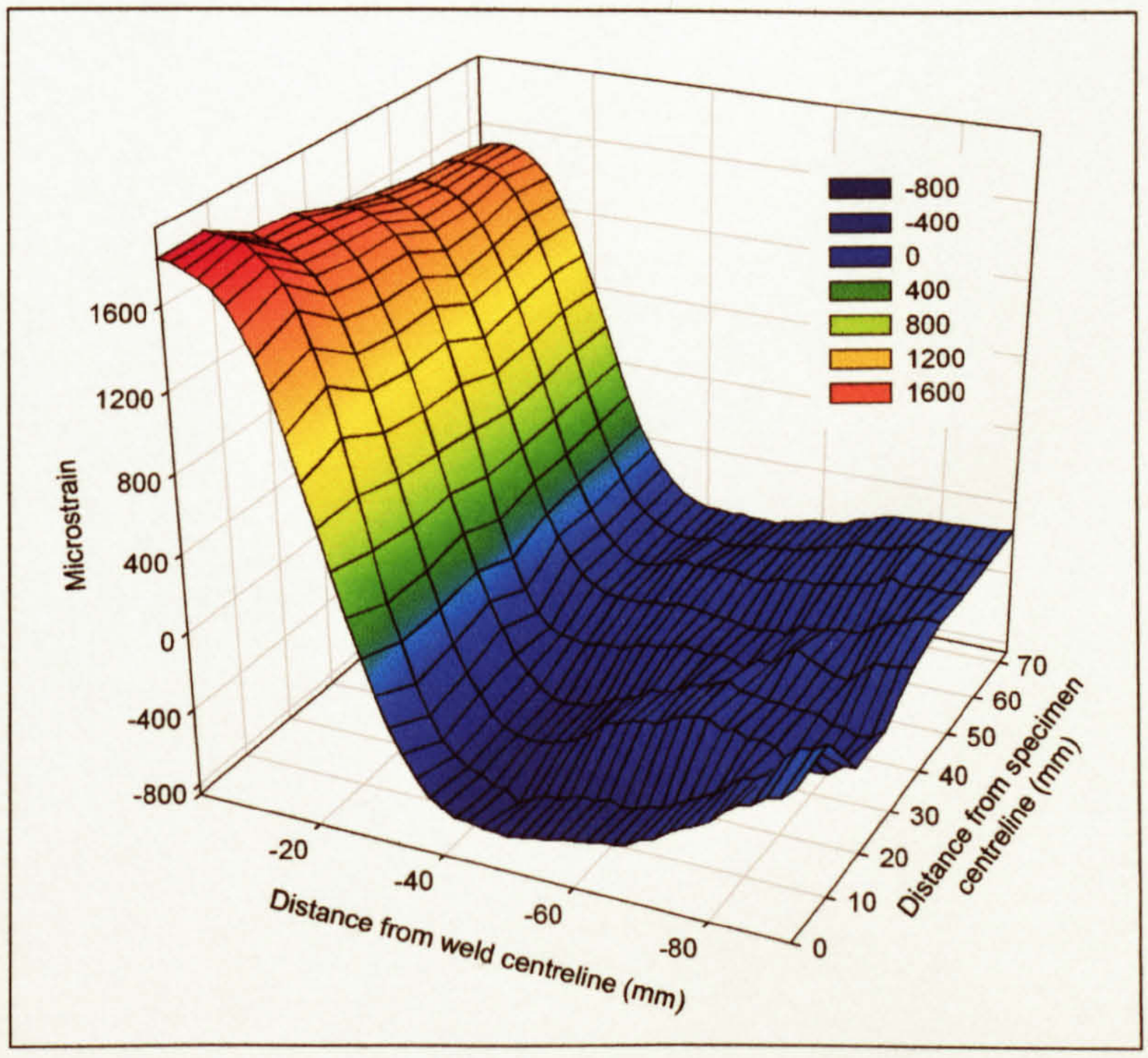

Figure 4.70: Variation of the longitudinal residual strains in a FS DP weld (1DP) with respect to the distance from the weld and specimen centrelines at a depth of 1 mm below the 2nd pass surface.

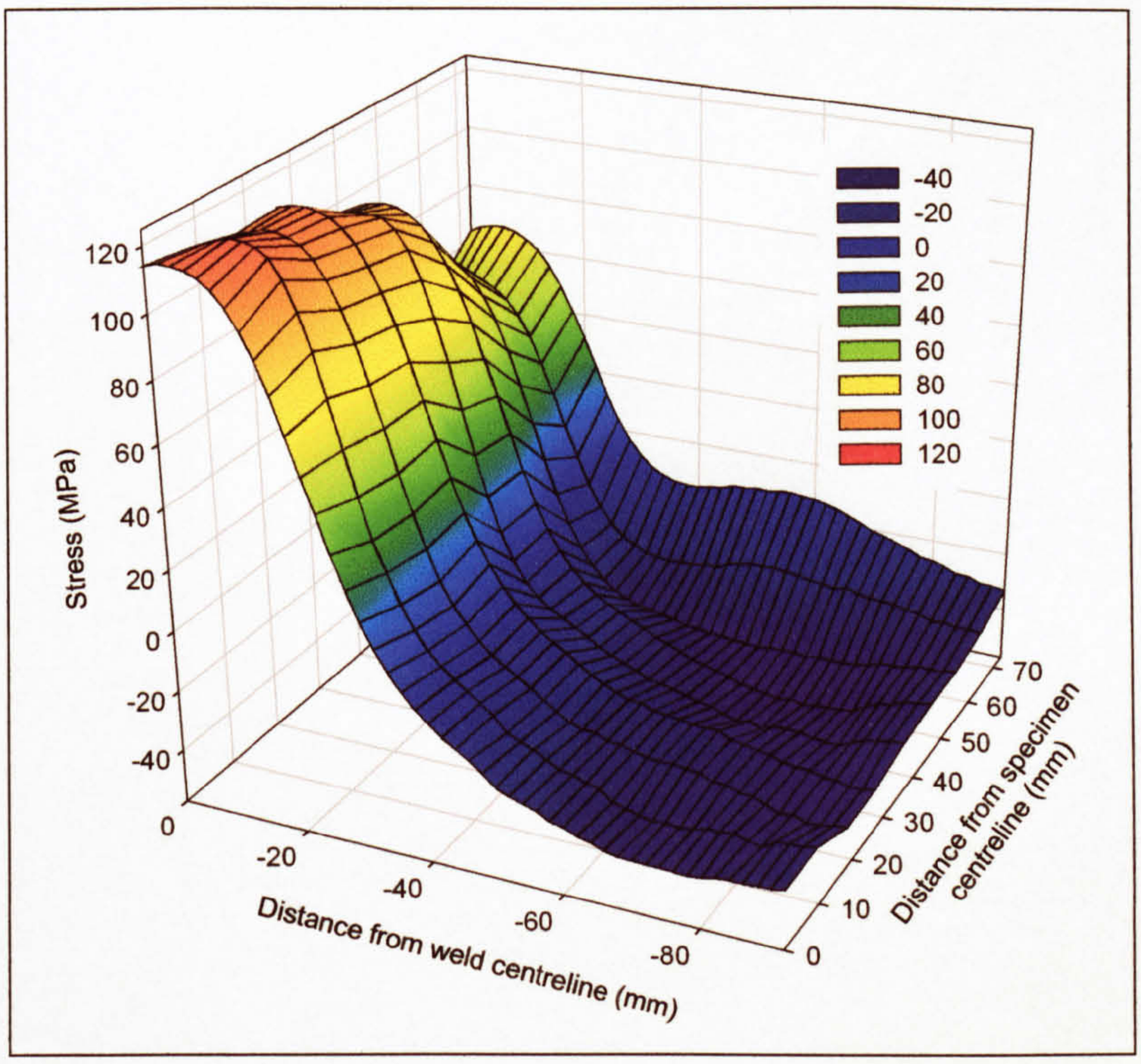

Figure 4.71: Variation of the transverse residual stresses in a FS DP weld (1DP) with respect to the distance from the weld and specimen centrelines at a depth of 1 mm below the 2nd pass surface.

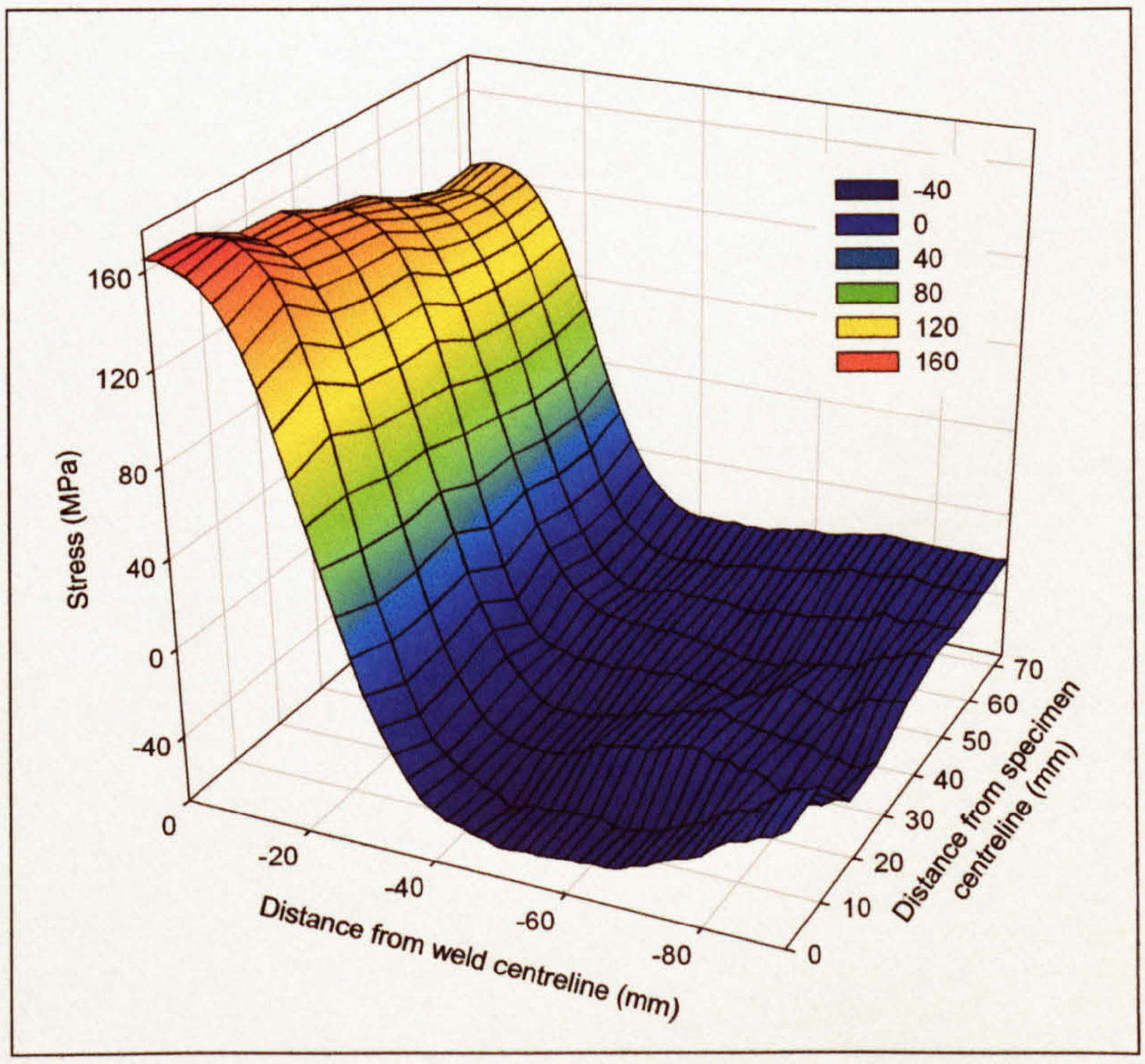

Figure 4.72: Variation of the longitudinal residual stresses in a FS DP weld (1DP) with respect to the distance from the weld and specimen centrelines at a depth of 1 mm below the 2nd pass surface.

4.4.7 Redistribution of the Longitudinal Residual Strains due to Fatigue Loading

Specimen	Maximum tensile load, σ_{max}, outer fibre/1 mm below surface (MPa)	Load cycles	R ($\sigma_{min}/\sigma_{max}$)	Direction of residual strains measured
2DP	150/112.5	1	0	Longitudinal
5DP	150/112.5	100	0.1	
8DP	200/150	1	0	

Table 4.21: Summary of the fatigue loading applied to the FS welds prior to synchrotron radiation analysis of their residual strain distribution.

In an attempt to determine the effect of fatigue loading on the residual strain distribution three specimens were analysed using synchrotron radiation after having fatigue loading applied as indicated in Table 4.21; the strain distribution was then compared to that observed in the as-welded state. Four point loading was utilised, resulting in pure bending, with the tensile loading being applied transverse to the weld direction and to the 2nd pass surface of the DP weld. All stresses, unless otherwise indicated, are detailed as the tensile load applied to the outer fibre of the plate surface, although synchrotron measurements were typically made 1 mm below the surface, z = 7 mm. No consideration was given to the slight variation in the external geometry of the weld region.

Figure 4.73 depicts the distribution of the longitudinal residual strains in both an as-welded FS DP weld and after the application of a single cycle of a peak stress of 150 MPa. The post loading results depicted a similar pattern to those observed in the as-welded specimens, but with an apparent reduction of 800 με in magnitude in the region of the weld. At distances of ±35 mm from the weld centreline a slight increase, in the region of 200 με, in the magnitude of the residual strains was evident. Although the tensile load was applied to the 2nd pass surface (z = 8 mm) no significant through thickness effect was evident.

The effect of the number of fatigue cycles and the magnitude of the load at 1 mm below the 2nd pass surface (z = 7 mm), that the tensile loading was applied to, is shown in Figure 4.74. The residual strain redistribution appeared to be independent of both the number of load cycles and their magnitude in the region of the weld, ±12.5 mm from the weld centreline, with a drop in magnitude in the region of 800 με being observed. At distances of ±40 mm from the weld centreline an increase in the amount of scatter in the distribution was evident, the 200 MPa peak load cycle appeared to exhibit little redistribution when compared to that of the as-welded plate, with the single and multiple 150 MPa peak loads exhibiting similar reductions in magnitude in the region of 200 με.

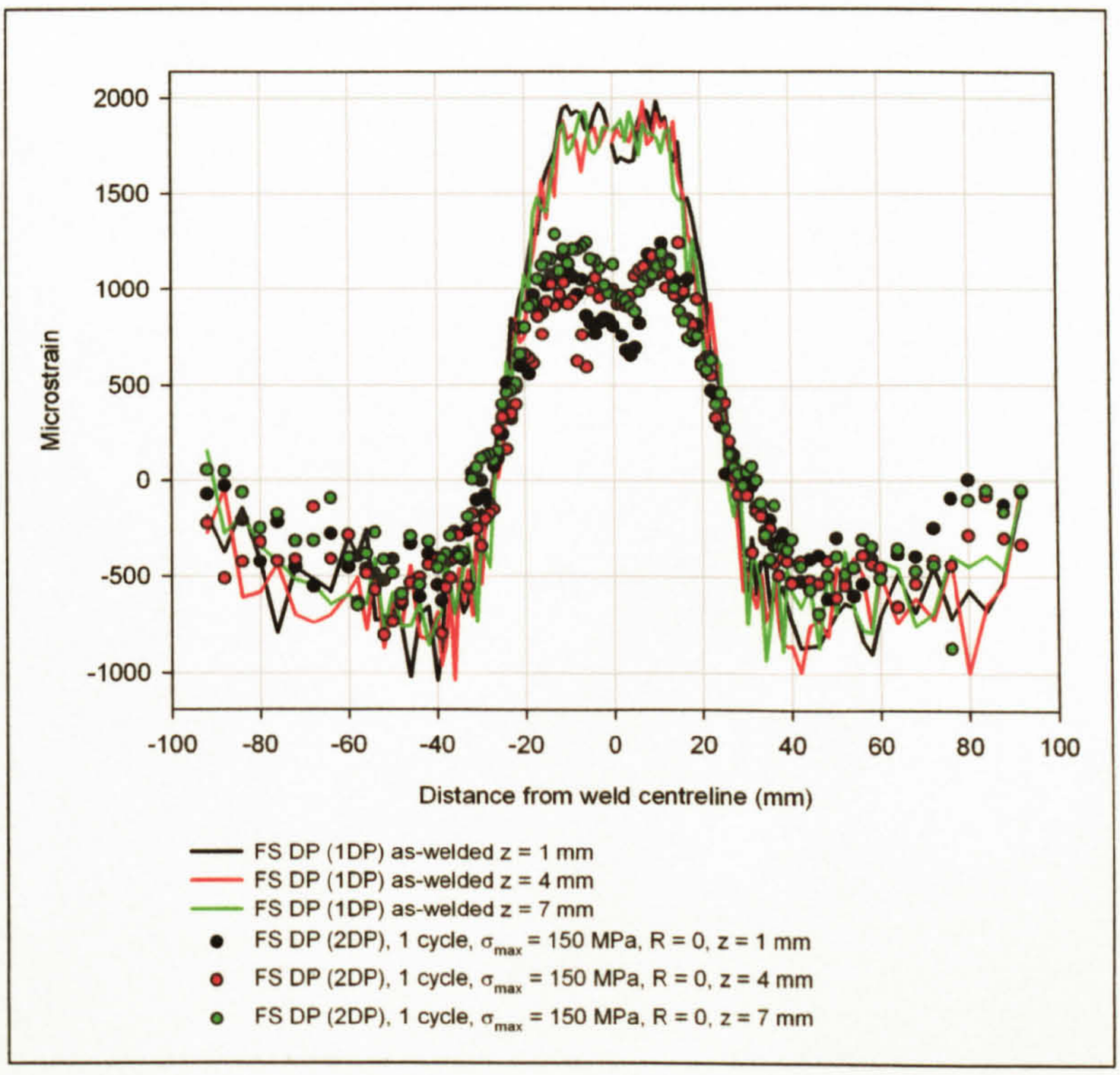

Figure 4.73: Longitudinal residual strains as-welded and after fatigue loading (1 cycle, σ_{max} = 150 MPa, R = 0) in a FS DP weld (2DP) with respect to the weld centreline (y) and plate thickness (z) (measurements made at the centre of the specimen, x = 0 mm).

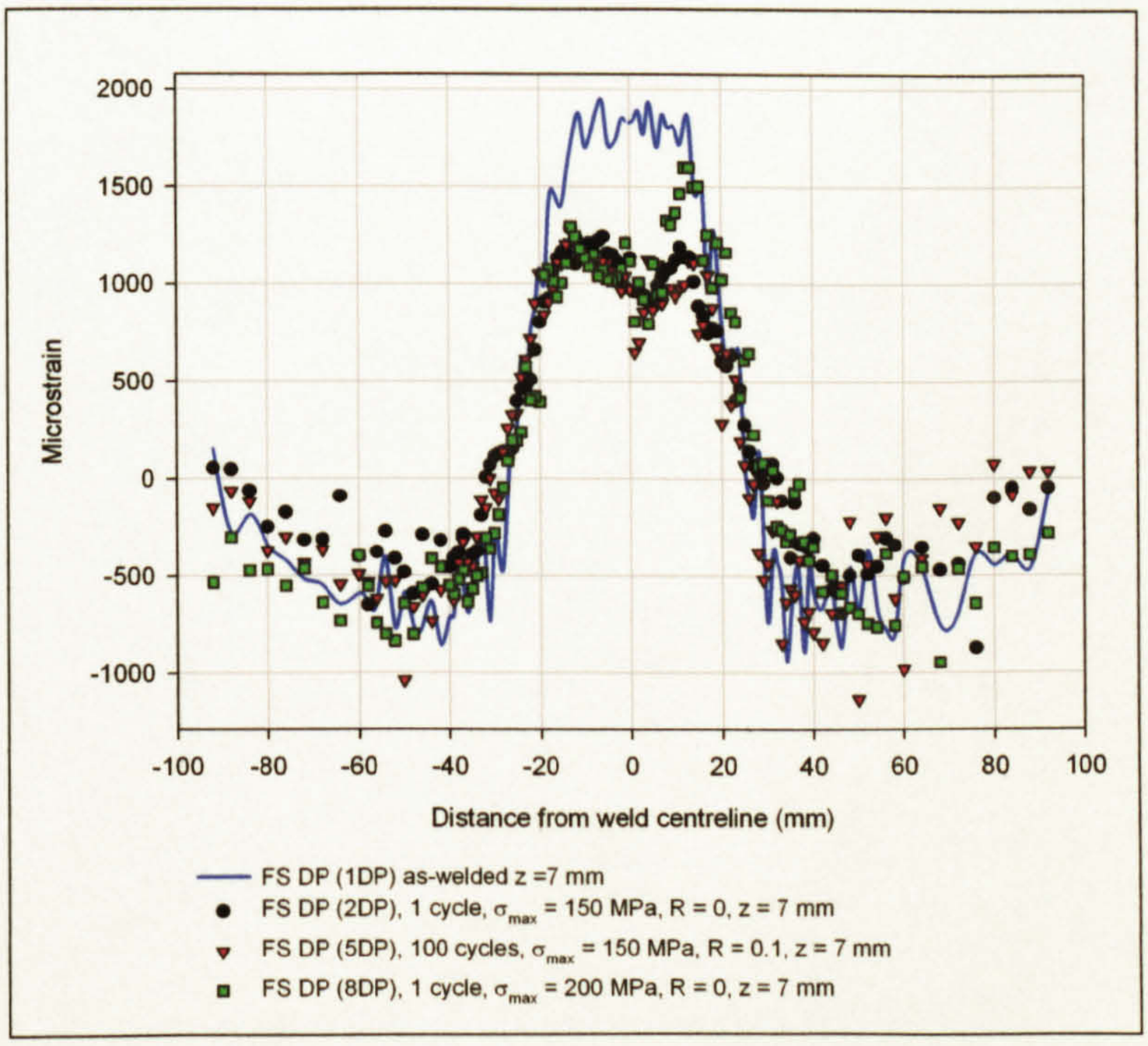

Figure 4.74: The effect of the number and magnitude of load cycles on the distribution of the longitudinal residual strains in a FS DP weld (1 mm below the 2nd pass surface, z = 7 mm, measurements made at the centre of the specimen, x = 0 mm).

4.5 Discussion

From the results obtained for the magnitudes of the residual stresses/strains induced by both the MIG and FS welding processes it was evident that these were dependent on the specimen type, as-welded plates, S-N specimens and synchrotron radiation specimens, the measurement techniques employed, hole drilling and synchrotron radiation and the load history of the specimens, as-welded and fatigue loaded. Some of the variation in the results may be considered to be due to experimental error and/or analysis, whilst redistribution of the strains due to the cutting of the welded plates may be considered to be influential with respect to the disparity between the as-welded plates and the smaller specimens analysed.

4.5.1 Residual Strains Determined by the Hole Drilling Technique

The hole drilling technique is not ideally suited to the measurement of weld induced residual stresses due to their magnitude, the analysis relying on the response being not only elastic with respect to the strains being relaxed, but also elastic when the stress concentrating effect of the drilled hole is taken into consideration. The result of this is that the accuracy diminishes in uniaxial stress fields greater than $0.3\sigma_y$ and equal biaxial fields greater than $0.5\sigma_y$, values which were considerably exceeded according the values obtained for the as-welded plates. Of the two techniques utilised the hole drilling technique of the as-welded plates returned the greatest magnitudes as summarised in Table 4.22 and shown in Figure 4.75 to Figure 4.78, whilst the S-N specimens analysed using the same technique exhibited a redistribution of the residual strains.

Weld Type	Gauge Position	Residual strains acting transverse to the weld (με)		Residual strains acting parallel to the weld (με)	
		Convex side	Concave side	Convex side	Concave side
MIG LI	Centre of plate length at the weld toe.	-1306	-1469	4974	4635
	167 mm from centre of the plate at the weld toe.	-1456	-859	5464	4488
	333 mm from the centre of the plate at the weld toe.	-1730	-615	4610	4237
	Centre of plate length, 10.4 mm from the weld toe.	-238	-432	4254	3490
	Centre of plate length, 19.5 mm from weld toe.	188	61	1178	865
	S-N specimen (mean values of 2 sides)	875		-160	
MIG HI	Centre of plate length at the weld toe.	-2092	751	4347	3280
	167 mm from centre of the plate at the weld toe.	-254	452	3003	3371
	333 mm from the centre of the plate at the weld toe.	-928	488	4140	3087
	Centre of plate length, 10.4 mm from the weld toe.	-2016	-224	5089	4595
	Centre of plate length, 19.5 mm from weld toe.	-971	512	3526	3518
	Centre of plate length, 28.6 mm from weld toe.	-928	710	1785	1104
	S-N specimen (mean values of 2 sides)	1033		-458	
	Gauge Position	**Friction band/2nd pass side (convex)**	**Weld seam/1st pass side (concave)**	**Friction band/2nd pass side (convex)**	**Weld seam/1st pass side (concave)**
FS SP	Centre of plate length at the edge of the friction band.	-1060	306	1901	1485
	167 mm from centre of the plate at the edge of the friction band.	-834	483	3143	1771
	333 mm from the centre of the plate at the edge of the friction band.	-506	1033	2722	1878
	Centre of plate length, 23 mm from the weld seam.	-730	555	2235	1839
	Centre of plate length, 32 mm from the weld seam.	-567	517	1641	1305
	S-N specimen	563	292	-123	-37
FS DP	Centre of plate length at the edge of the friction band.	-1879	405	3015	2097
	167 mm from centre of the plate at the edge of the friction band.	-1501	693	3393	2689
	333 mm from the centre of the plate at the edge of the friction band.	-610	908	2996	2351
	Centre of plate length, 23 mm from the weld seam.	-1425	711	2756	2756
	Centre of plate length, 32 mm from the weld seam.	-1162	945	3510	2229
	Centre of plate length, 41 mm from the weld seam.	-1086	780	2561	1506
	S-N specimen	262	471	-316	-23

Table 4.22 : Summary of the residual strains induced by the MIG LI and HI and FS SP and DP welding processes and measured by the hole drilling technique.

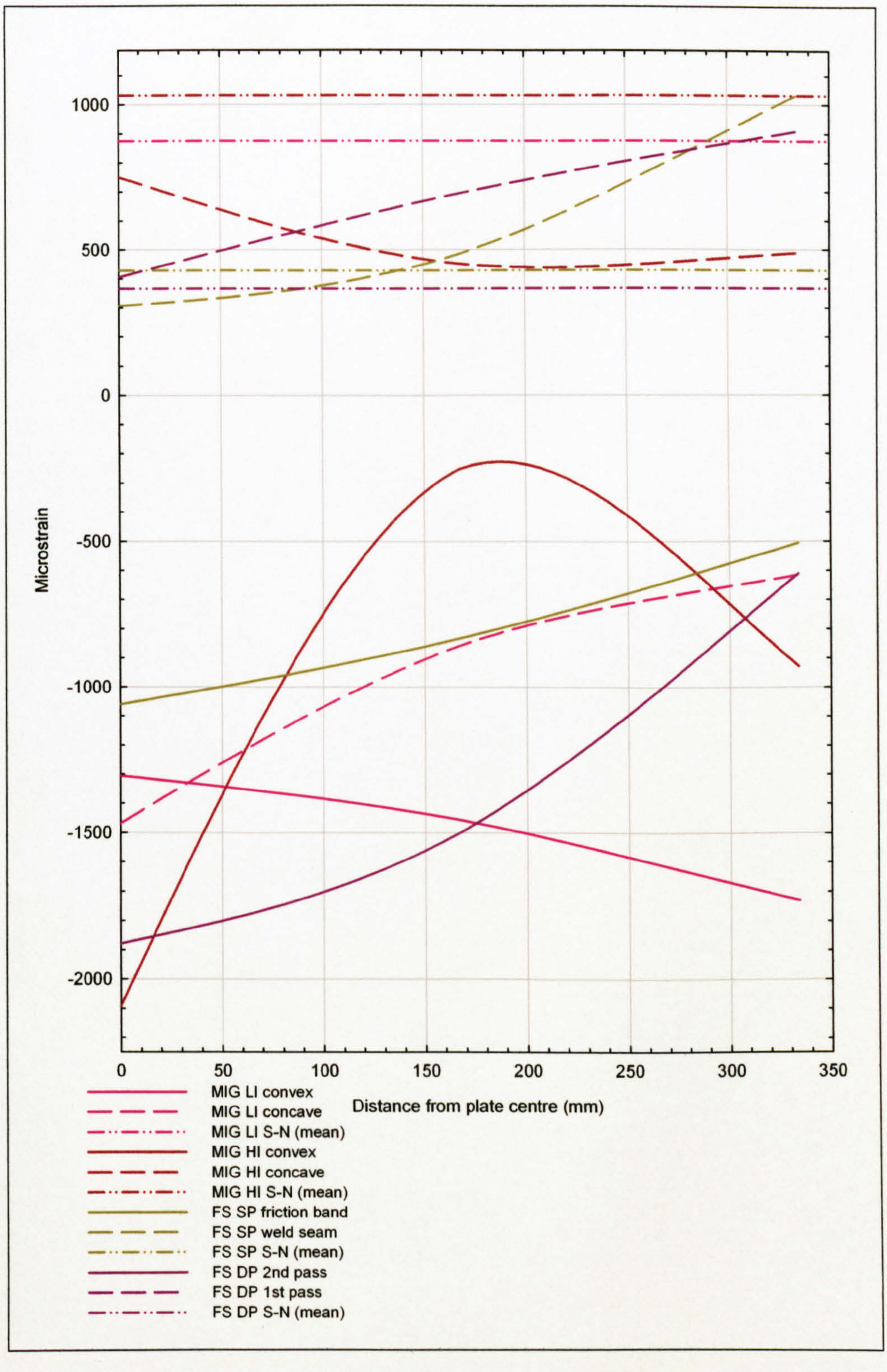

Figure 4.75: Residual strains measured by the hole drilling technique and acting transverse to the weld direction measured at the MIG weld toe and edge of the friction band in the FS welds.

From Figure 4.75 it was evident that there was considerable variability between the magnitudes of the residual strains measured by the hole drilling method at the weld

toe/edge of the friction band and acting in a direction transverse to the weld, with the variability being evident not only when comparing the different weld processes, but also between the two sides, convex and concave, of the as-welded plate. The concave sides of the MIG welds and weld seam, of the SP, and 1st pass side, of the DP, (these were also concave with respect to the as-welded plate geometry) FS welds exhibited the greater magnitudes of the two sides; excluding the LI weld the transverse residual strains were tensile on the concave side and compressive of the convex. Values for the concave sides were typically within 300 - 1000 με, whilst those on the convex side exhibited greater variability and a range of -2000 to -500 με. At the centre of the plate their magnitudes ranged from -1469 με, for the MIG LI concave side, to 751 με for the MIG HI concave side, with the FS welds returning values in the region of 300 - 400 με. All increased in magnitude, except for the MIG HI which reduced slightly, as the distance from the centre of the plate increased. At a distance of 167 mm from the centre of the plate the MIG HI and FS welds returned comparable magnitudes for the weld toe/edge of the friction band ranging from 452 - 693 με, although the value returned by the MIG LI weld was considerably lower at -859 με. At a distance of 333 mm from the centre of the plate the LI value had increased to -615 με, the HI weld returned a value of 488 με whilst the FS welds returned values in the region of 900 - 1000 με. With respect to the convex sides, at the centre of the plate length the values ranged from -1306 to -2092 με for the MIG welds and -1060 to -1879 for the FS welds. The magnitudes of the strains observed in the FS welds increased as the end of the plate was approached, at a distance of 333 mm from the centre the values were in the region of -500 to -600 με, whilst those of the LI weld had decreased in magnitude to -1730 με. The HI weld increased in magnitude at a distance of 167 mm from the centre to -254 με and then reduced to -928 με at a distance of 333 mm from the centre, although the overall change was an increase in the magnitude from that recorded at the centre of the plate.

It was also apparent that the variation between the two sides of the as-welded plates was proportional to the amount of longitudinal distortion, the HI and DP welds exhibiting the greatest disparity in values and also the greatest distortion (detailed in Table 4.4, page 152), in contrast to this the LI weld exhibited minimal distortion and returned the smallest disparity, both sides returning compressive transverse residual strains. The SP weld exhibited values for both the strain disparity and the distortion that fell between those of the LI and HI/DP welds.

The S-N specimens returned mean values that were tensile and comparable for each process; the MIG welds returning mean values of 875 με and 1033 με for the LI and HI process respectively, whilst the FS welds returned mean values of 428 με and 367 με for the SP and DP processes respectively. In the case of the MIG welds the values returned by the S-N specimens were slightly greater than those observed at the centre of the

concave side of the HI as-welded plate and significantly greater than those observed in the LI plate. The values exhibited by the FS S-N specimens were comparable to those observed at the centre on the as-welded plates for the concave sides, although slightly less than the values observed near to the edge of the as-welded plates.

The magnitudes of the transverse strains measured at the centre, with respect to the length, of the as-welded plates and at increasing distances from the weld toe, in the case of the MIG welds, and seam, in the case of the FS welds, were as shown in Figure 4.76. Both the concave and convex sides of both the MIG and FS as-welded plates returned comparable residual strain responses, although the magnitudes were notably different for the two sides except for the MIG LI weld, which returned similar magnitudes for both sides. The LI weld returned values ranging from -1469 to -1306 με at the weld toe, but this increased to 61 - 188 με at a distance of 19.5 mm from the weld toe. In contrast to the LI weld the other welds returned greater magnitudes of residual strains for the concave sides, with the HI and DP welds exhibiting the greatest discrepancy between the two sides. The HI weld exhibited a decrease in magnitude up to a distance of 10 mm from the weld toe followed by an increase at a distance of 20 mm to an apparently more constant value in the region of -900 με and 700 με for the convex and concave sides respectively. In contrast to the HI response the DP weld exhibited a gradual increase in magnitude up to a distance of 32 mm from the weld seam with a apparent levelling off of the values being attained at 41 mm from the weld seam with values in the region of -1100 με and 800 με being returned by the convex and concave sides respectively. The SP weld exhibited a similar response to that observed in the DP weld, although a levelling off of the magnitudes was apparent at a distance of 32 mm from the weld seam, values of -600 με being exhibited by the convex side and 500 με by the concave side. As with the transverse strains measured at the weld toe/edge of the friction band the magnitude of the disparity between the two sides was proportional to the amount of longitudinal distortion in the as-welded plates.

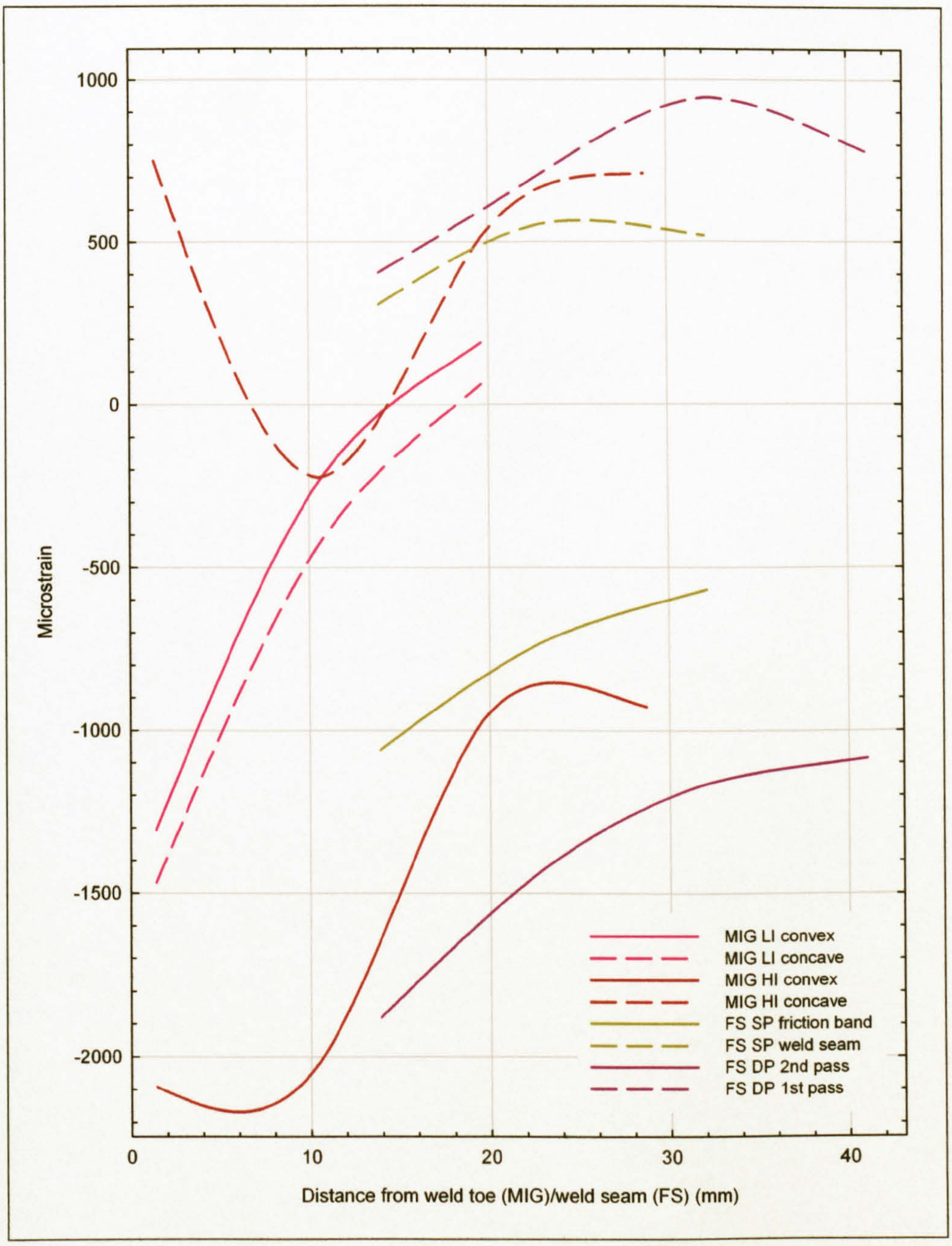

Figure 4.76: Residual strains measured by the hole drilling technique and acting transverse to the weld direction measured at the centre of the plate.

The longitudinal residual strains, acting parallel to the direction of the weld, measured at the weld toe/edge of the friction band at various positions along the length of the weld are shown in Figure 4.77. Similar characteristics to those observed for the transverse strains were evident, notably the variation in their magnitudes between the two sides of the as-welded plate, although in contrast to the transverse strains both sides exhibited tensile strains, with the convex sides returning the greater values. Excluding the response of the HI weld the overall responses were similar, with the convex sides increasing slightly in magnitude at a distance of 167 mm from the centre of the plate and then decreasing

slightly as the distance increased to 333 mm. The response of the convex side of the HI weld was opposite to that observed in the other welds, with the magnitude decreasing slightly at a distance of 167 mm from the centre and then increasing as the distance increased to 333 mm. The LI weld exhibited the greatest magnitudes, with values in the range of 4600 - 5000 με at the centre and a distance of 333 mm from the centre and a peak value of 5464 με at a distance of 167 mm. In contrast to the LI weld the SP weld returned the smallest magnitudes for the strains, with a value of 1901 με at the centre of the plates and values in the region of 1800 - 1900 με at distances of 167 and 333 mm from the centre. If the results from the HI weld are disregarded the concave sides of the as-welded plates returned values that were less than those observed for the convex sides. The deformed geometry of the as-welded plates would suggest that the concave side would return lower values for the longitudinal strains, although the observation that the values remained tensile suggests that in the case of the MIG and FS DP welds the residual strains from the initial weld run were influential in the overall magnitudes observed, although this does not explain the tensile strains observed in the SP weld. The magnitudes of the strains on the concave sides exhibited less variability than those on the convex side, typically values were contained within a range of less than 400 με at the various positions that measurements were undertaken. As with the convex side the greatest magnitudes were observed in the LI weld, values ranging from 4237 - 4635 με, and the smallest values, ranging from 1485 - 1878 με, in the SP weld. Variations between the magnitudes observed on the two sides were typically less at the centre and 333 mm from the centre of the as-welded plates, values typically being in the region of 400 - 600 με, whilst greater disparities were observed at distances of 167 mm from the centre with values in the region of 1000 - 1500 με being measured. It was also apparent that both the concave and convex sides of the MIG welds and the 2nd pass side (convex) of the FS DP weld returned values that were greater than, or in the region of, the yield strain of the parent material, whilst the remaining observations returned values that were less. Unlike the transverse strains no relationship between the degree of distortion in the as-welded plates and the disparity between the strain measurements for the two sides of the plate was evident.

The mean values for the longitudinal residual strains returned by the S-N specimens were notably less than those observed in the as-welded plates, with the measurements all returning compressive values. The values observed in the S-N specimens fell within a narrow range of -80 με to -170 με for the both the FS and MIG LI welds, whilst the MIG HI weld returned a value of -458 με.

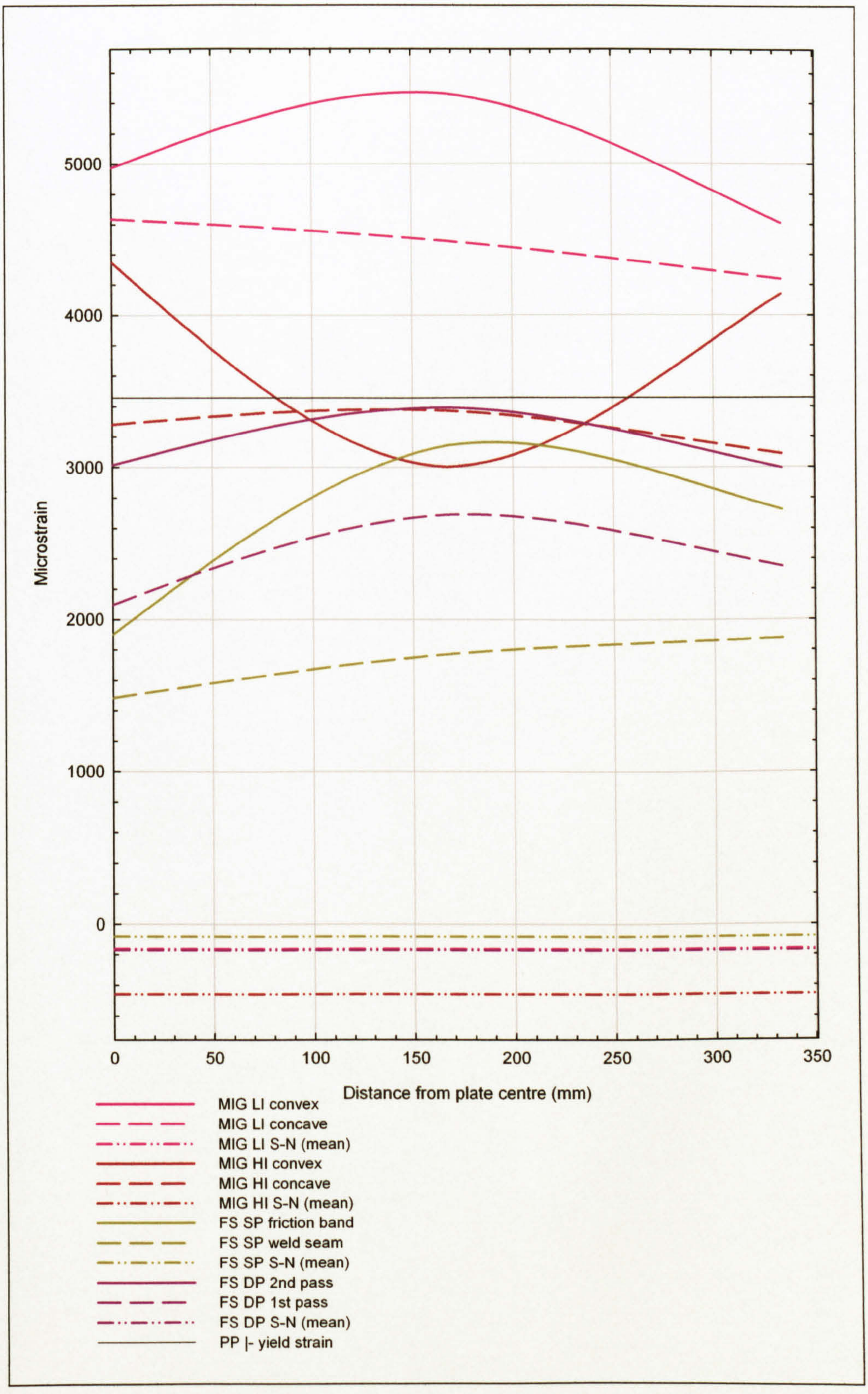

Figure 4.77: Residual strains acting in the direction of the weld at the MIG weld toe and edge of the friction band of the FS weld.

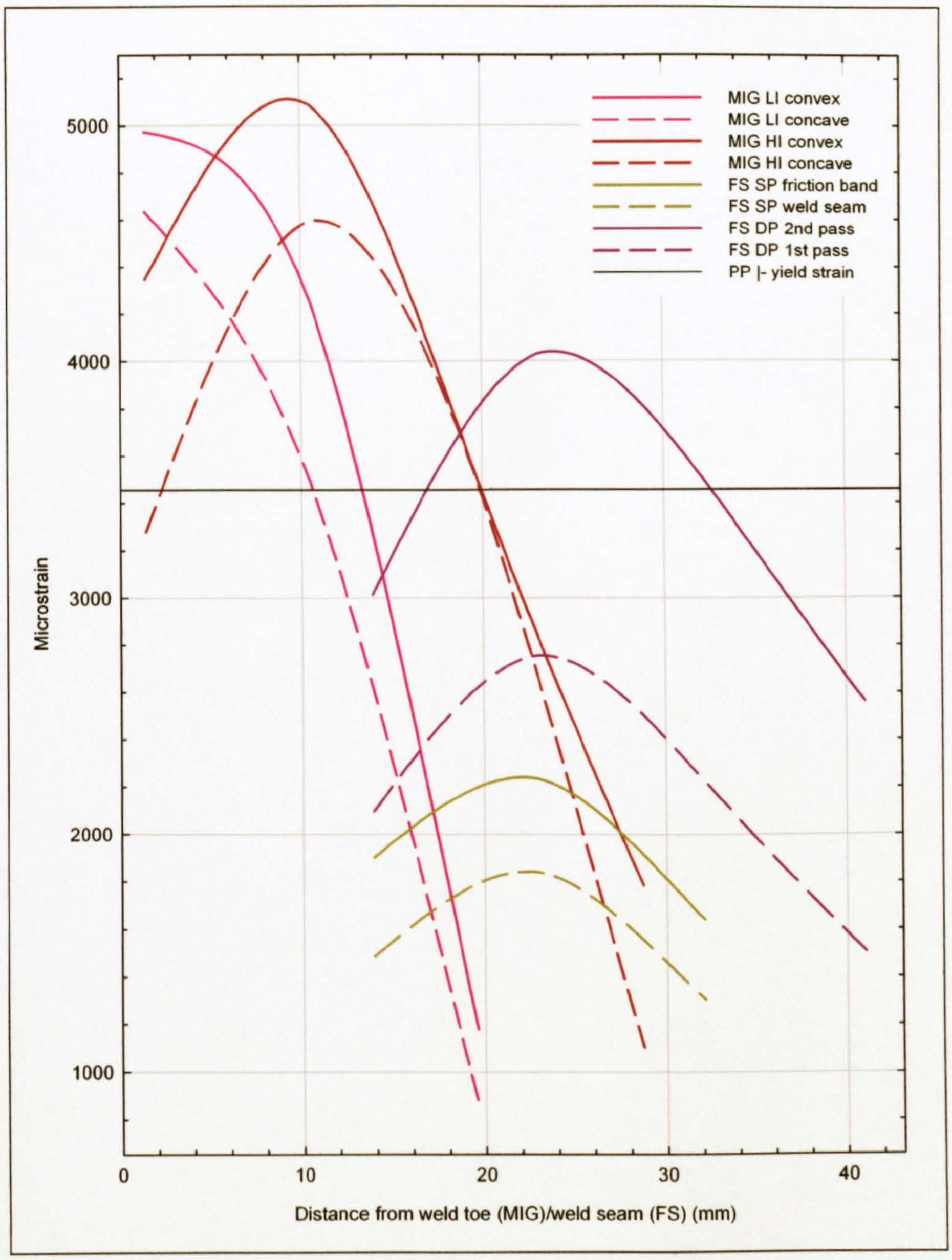

Figure 4.78: Residual strains acting parallel to the weld direction measured at centre of the plate.

The longitudinal residual strains measured at the centre of the as-welded plates, with respect to the length, but at incremental distances away from the weld toe and weld seam in the case of the MIG and FS welds respectively, were as shown in Figure 4.78. All the welds exhibited comparable responses, albeit with differing magnitudes. The typical response consisted of a slight increase in the magnitude of the strains, observed for both the convex and concave sides of the plate, as the distance from the weld toe/seam increased followed by a reduction in their magnitude as the distance increased. The MIG welds returned the greatest values, for both the convex and concave sides, with peak

magnitudes being in the region of 4600 - 5000 με at a distance of 1 mm and 10 mm from the weld toe for the LI and HI weld respectively, although at distances of 20 mm and 29 mm these values had reduced to below 1800 με. In contrast to the MIG welds that exhibited peak values greater than the yield strain of the parent plate, the FS welds typically returned peak values below 2800 με, although the DP 2nd pass side (convex) returned a peak value of 4000 με, with the maximum values being observed at a distance of 32 mm from the weld seam, 20 mm from the edge of the friction band. The disparity between the concave and convex sides was evident in the MIG welds from the weld toe to the distance where the peak values were measured, with the HI weld exhibiting a greater discrepancy, in the range of 500 - 1000 με compared to that 400 με observed in the LI weld, as the distance from the position of the peak values increased the discrepancy between the two sides began to diminish. The disparity between the values measured for the two sides of the FS welds remained relatively constant for the range of measurements, with values of 500 με and 1000 με being returned by the SP and DP welds respectively.

The overall transverse and longitudinal residual strain pattern depicted by the hole drilling technique exhibited a comparable response to that typically suggested for welded joints, shown in Figure 4.1 (page 131). The discrepancies between the two sides of the as-welded plates may be to some extent explained by anticlastic bending; longitudinal tensile strains on the convex surface resulting in compressive strains acting in the transverse direction on the same surface, as shown in Figure 4.75 and Figure 4.76. The concave surface would typically be expected to exhibit a compressive longitudinal strain, but it would be plausible to assume that the localised expansion and plastic flow resulting from the initial weld run, resulting in tensile longitudinal residual strains, would only be partially offset by the expansion and plastic flow resulting from the second pass. The transverse strains resulting from the concave surface again exhibiting an anticlastic bending response and being tensile in nature. Comparison of the residual strains measured in the S-N specimens suggested that the reduction in size resulted in a considerable redistribution of the residual strain fields; the longitudinal strains diminishing, or becoming compressive in the case of the HI weld, at the weld toe/edge of the friction band, whilst the transverse strains, the reduction in size being significantly less for the length of the S-N specimens, returned mean values for the two sides that were comparable to tensile values observed for the concave side of the as-welded plates.

4.5.2 Residual Strains Determined by Synchrotron Radiation Strain Scanning

Determination of the residual strain fields through the synchrotron radiation strain scanning technique presented other problems, notably the determination of the strain free lattice spacings. The values utilised for the strain free lattice angle, $2\theta_0$, (detailed in Section 4.4.6, Determination of the Strain Free Lattice Angle (2θ0) and Spacing (d0, pages 188 - 194) had a significant effect on the accuracy of the results obtained, with a slight underestimate of the strain free diffraction angle resulting in a significant reduction in the apparent strains. An underestimate of $2\theta_0$ would result from the supposedly strain free lattice spacing being subjected to a tensile strain and the use of teeth to determine the value rather than a powder was more likely to result in this scenario occurring. The overall pattern of the strain free lattice spacing measurements, as shown in Figure 4.52 and Figure 4.53 (page 190) exhibited a comparable response to that observed in the as-welded specimens that underwent synchrotron analysis, suggesting that the teeth may still have contained significant residual strains. From the analyses undertaken utilising the values of $2\theta_0$ obtained from the teeth, the as-welded specimens returned strain fields that were compressive throughout the whole volume of the plate, although, by their nature, residual strains must be self-balancing.

To overcome the problems that resulted from the experimentally determined values for $2\theta_0$ their values were determined by instigating a force and moment balance at the centre of the plates, but taking into consideration any through thickness variation. The transverse strains returned $2\theta_0$ values that resulted in residual strains that were typically less than the yield strain of the weld and therefore considered acceptable. The values that resulted from the longitudinal strains returned residual strain values that were greater than the yield strain of the parent material, it was therefore decided to determine their value of $2\theta_0$ through a force balance with the resulting strains approaching zero at the edge of the specimen. This approach resulted in strains that were typically less than the yield strain of the weld and were therefore considered acceptable. The typical results returned by the two approaches are shown in Figure 4.56 (page 194).

The values of $2\theta_0$ determined experimentally and through the force and moment balances are depicted in Table 4.23. In the as-welded specimen it was evident that the values returned by the experimental approach were 0.028° lower than those determined through the force and moment balance approach for $2\theta_0$ in the weld region of the SP weld, whilst those in the DP weld were 0.023° and 0.035° lower for the transverse and longitudinal angles respectively. The values returned by the experimental approach in the parent material, greater than 30 mm from the weld centreline, were more comparable to those returned by the force and balance approach, with the difference in the case of the SP

weld being -0.002° and -0.006° for the longitudinal and transverse directions respectively. The force and moment balance approach for the parent material of the DP weld returned values that were 0.003° greater for the transverse angle and 0.0002° for the longitudinal angle.

Comparison of the values for $2\theta_0$, in the longitudinal direction, returned by the force and balance approach for the as-welded and fatigue loaded specimens resulted in mean values that were 0.024° and 0.011° lower for the weld and parent regions respectively in the fatigue loaded specimens.

		FS SP		FS DP	
		As-welded $2\theta_0$ (°)			
Distance from weld centreline		-12.5 ≤ y ≤ 12.5	-30 ≥ y ≥ 30	-12.5 ≤ y ≤ 12.5	-30 ≥ y ≥ 30
Transverse		14.52252	14.5125	14.518	14.51
Longitudinal		14.52175	14.508	14.53	14.50538
		Fatigue loaded $2\theta_0$ (°)			
Distance from weld centreline		-12.5 ≤ y ≤ 12.5	-30 ≥ y ≥ 30	-12.5 ≤ y ≤ 12.5	-30 ≥ y ≥ 30
Longitudinal	Minimum	-	-	14.5047	14.4900
	Maximum	-	-	14.5092	14.5035
	Mean	-	-	14.5063	14.4945
	Standard deviation	-	-	0.002516	0.007794
		Experimental $2\theta_0$ (°) (Table 4.19)			
Distance from weld centreline		-12.5 ≤ y ≤ 12.5	-30 ≥ y ≥ 30	-12.5 ≤ y ≤ 12.5	-30 ≥ y ≥ 30
Transverse		14.4943	14.5067	14.4948	14.5067
Longitudinal			14.5056		14.5056

Table 4.23: Transverse and longitudinal theoretical and experimental values of $2\theta_0$.

The exact cause of the variation in the values of $2\theta_0$ was unknown, although tensile strains in the teeth may have resulted in the underestimate returned by the experimental approach. Another cause may have been due to the experimental values of $2\theta_0$ being determined when the fatigue loaded specimens were being analysed; the as-welded and fatigue loaded measurements were undertaken in two separate allocations of beam time. A slight variation in the calibration of the equipment between the two measuring periods may have been the cause of the as-welded specimens displaying wholly compressive residual strain fields, whilst the fatigue loaded ones were predominantly tensile. It was notable that the variation in the values of $2\theta_0$ was greater for the measurements undertaken in the region of the weld, in contrast to those measured in the parent material, giving credence to the theory that the production of the teeth had not resulted in a complete redistribution of the residual strains. This would also suggest that the residual

strain in the vicinity of the weld acted over relatively short distances. The variation between the force and moment balance approach between the as-welded and fatigue loaded specimens may have been the result of a change in the lattice spacing due to the fatigue loading. The exact causes of the variations in the values for $2\theta_0$ warrant further investigation.

4.5.2.1 Variation of the Residual Strains with Respect to the Friction Stir Welding Process

The two friction stir welding processes, SP and DP, returned comparable residual strain distributions when the transverse strains were compared, as shown in Figure 4.79. In contrast to the transverse strains the DP longitudinal strains returned values that were in the region of 800 με greater than those of the SP weld in the region of the weld, and in the region of 200 με lower in the material outwith the HAZ, ±40 mm from the weld centreline. This may have been the result of the double pass weld experiencing two thermal/mechanical cycles, with the strains resulting from the 2nd pass being superimposed to on those from the 1st pass, although this would not fully explain why the transverse strain profiles were near identical for the SP and DP welds.

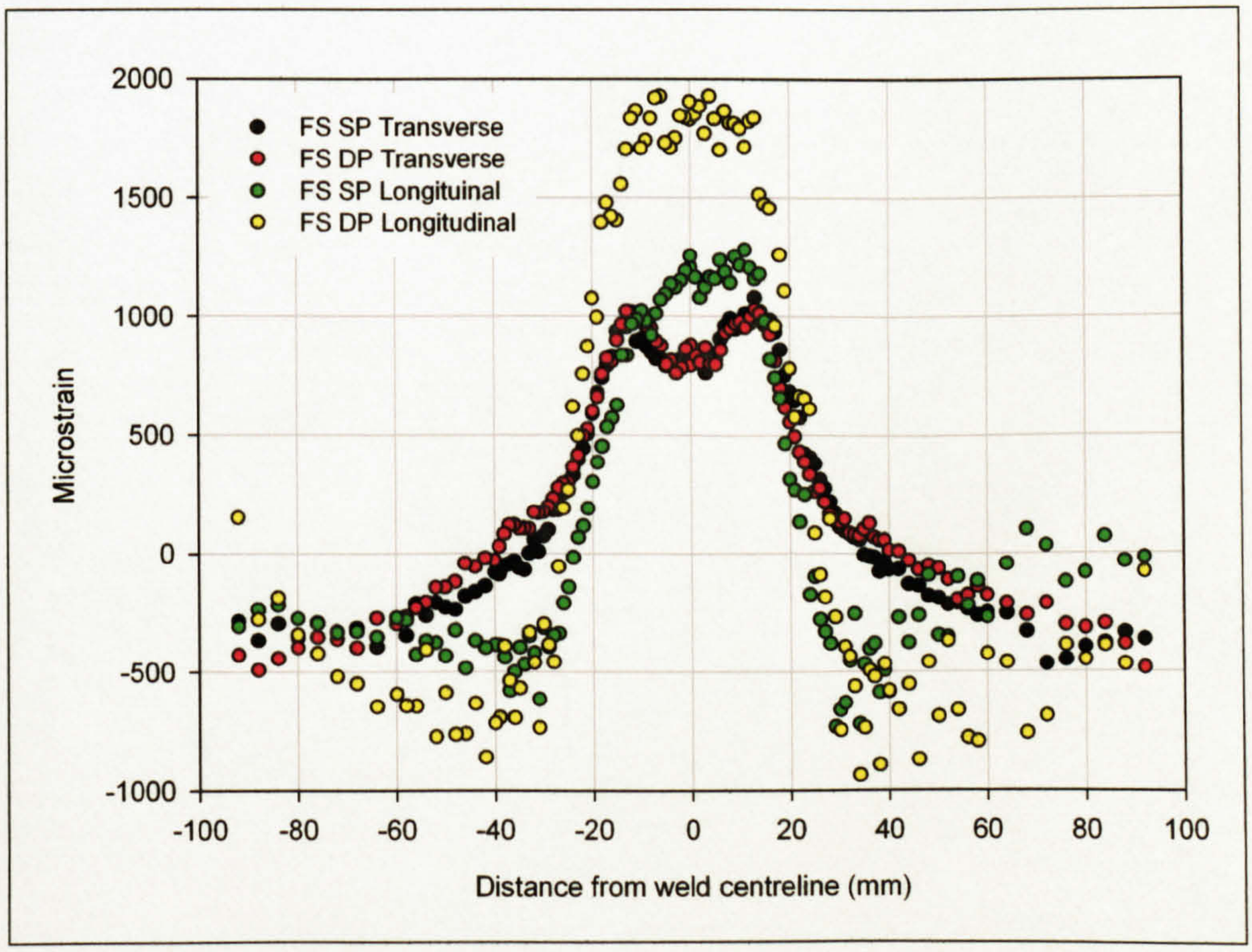

Figure 4.79: Comparison of the transverse and longitudinal residual strains in FS SP and DP as-welded specimens with respect to the weld centreline (1 mm below the friction band (SP) and 2nd pass (DP) surfaces and at the centre of the specimen, x = 0 mm).

4.5.3 Comparison of the Hole Drilling and Synchrotron Radiation Techniques

Due to the variation in the magnitudes of the residual strains observed between the as-welded plates and the as-welded S-N specimens when analysed using the hole drilling technique, both sets of results were compared with those from those synchrotron strain scanning. The two techniques returned the values detailed in Table 4.24 and shown in Figure 4.80 and Figure 4.81 for the as-welded S-N specimens and plates respectively.

The hole drilling method, with respect to the as-welded S-N specimens, returned transverse strains that were tensile and in the range of 262 - 563 με, whilst the longitudinal strains were compressive and in the range of -23 με to -316 με. These values contrasted with those returned by the synchrotron radiation analysis that returned values in the range of 950 - 1100 με and 975 - 1800 με for the transverse and longitudinal strains respectively. The disparity between the two techniques was noted to be less for the transverse strains, although this still resulted in the strains measured by the synchrotron technique being in the region of 2 - 4 times greater than those returned by the hole drilling method. The disparity between the longitudinal strains may be partially explained by the S-N specimens being nearly one quarter the width of the synchrotron specimens.

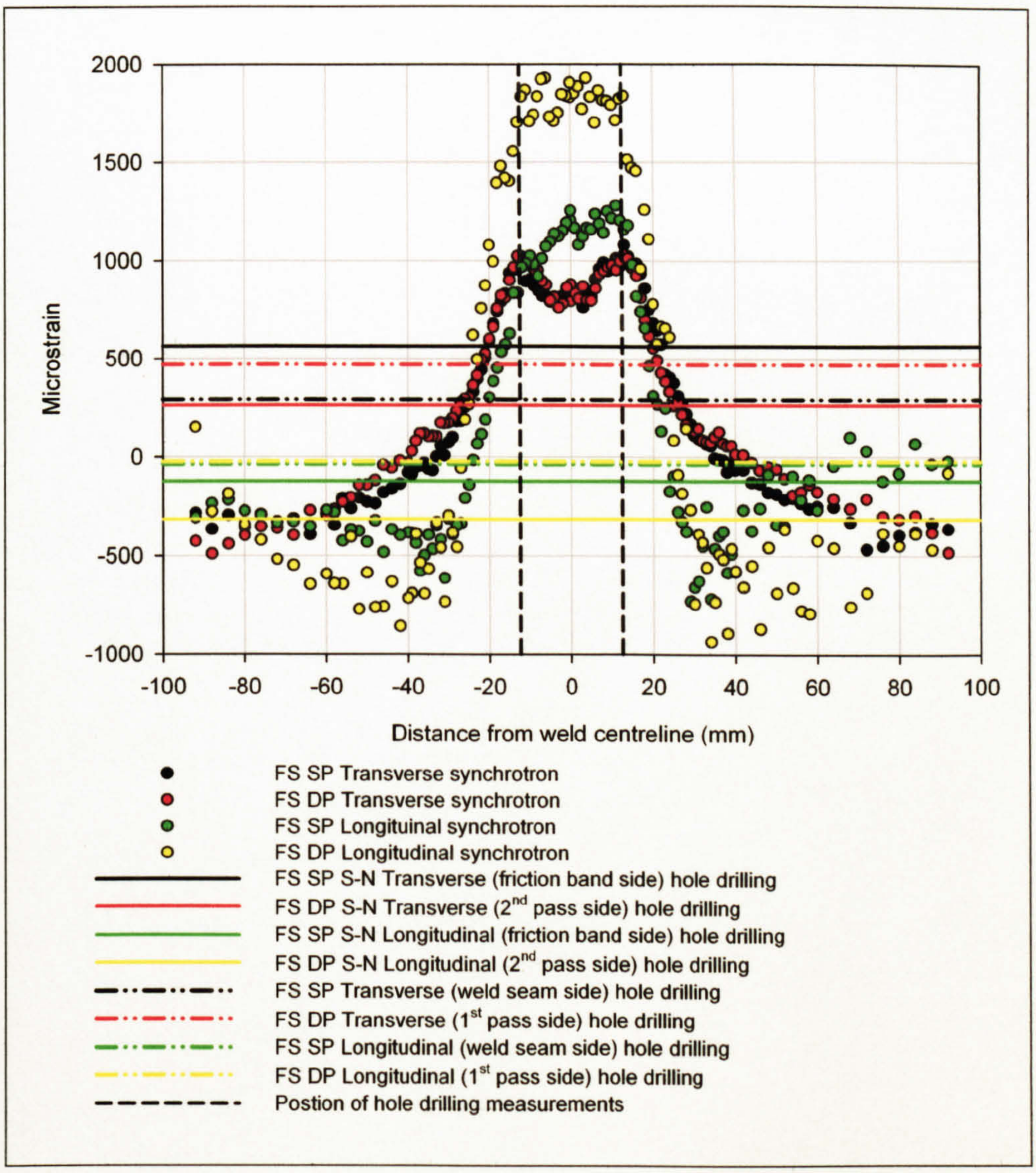

Figure 4.80: Comparison of the transverse and longitudinal residual stresses in FS welds measured by synchrotron radiation (150 mm wide specimens, z = 7 mm) and hole drilling (40 mm wide S-N specimens).

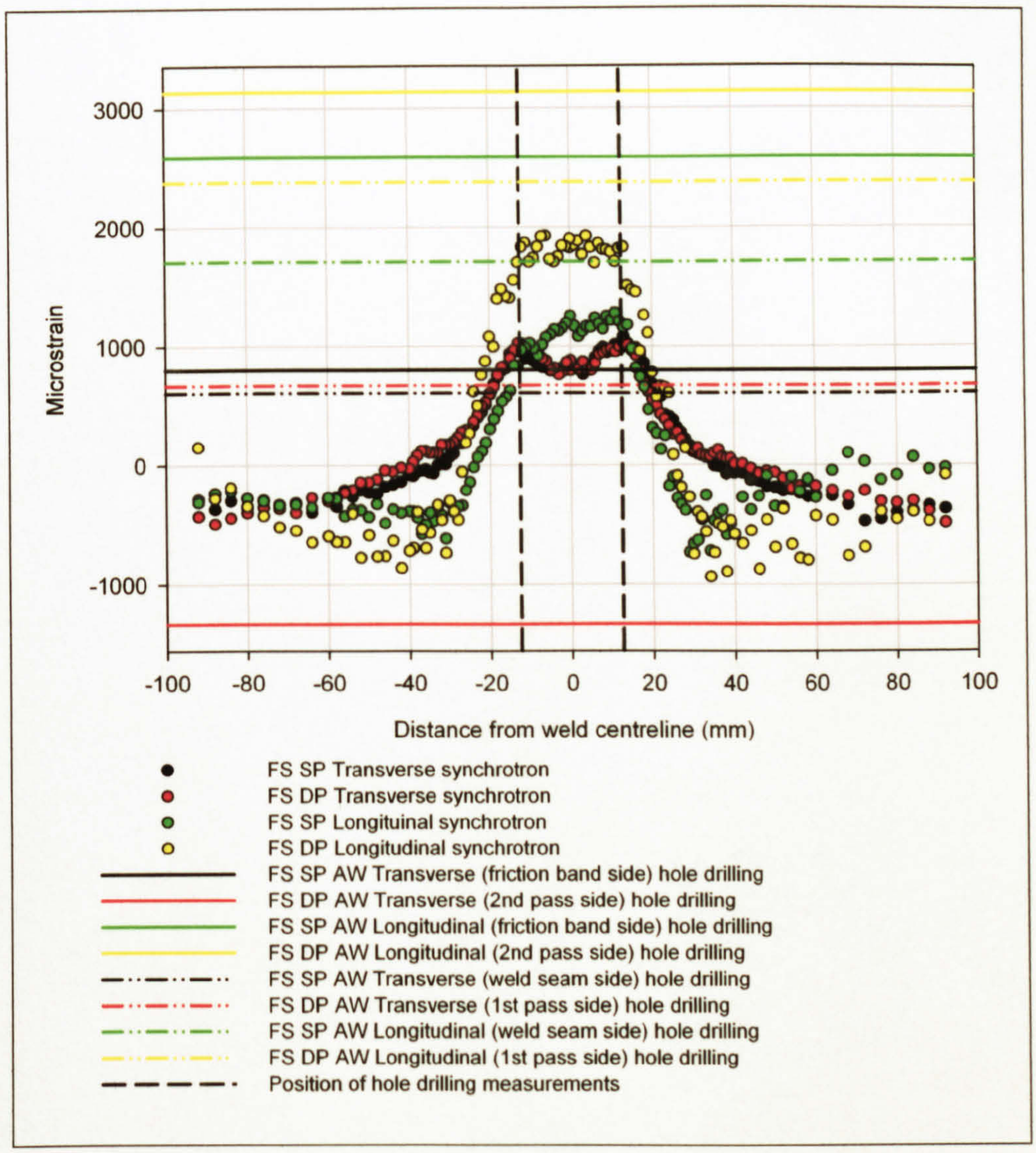

Figure 4.81: Comparison of the transverse and longitudinal residual stresses in FS welds measured by synchrotron radiation (150 mm wide specimens, z = 7 mm,) and hole drilling (1000 mm wide as-welded plates)*.

The hole drilling method, with respect to the as-welded plates, returned transverse strains for both sides of the SP weld and the 1st pass side of the DP weld that were comparable to those returned by the synchrotron technique. The other measurements that resulted from the hole drilling approach overestimated values when compared to those returned by the synchrotron method, the overestimate being in the region of 400 - 1200 με, although the DP transverse strains were underestimated by 2250 με. As with the S-N specimens some of the variation may be considered to be the result of the dissimilarity in the sizes of the specimens, the as-welded plates were distorted both across their length and width, whereas the synchrotron specimens were near flat.

---

* Mean of three measurements undertaken at the different positions along the length of the weld.

				Residual strains (με)		
				Friction band/2nd pass side	Weld seam/1st pass side	Mean
SP	Transverse	Hole drilling	S-N	563	292	428
			AW*	800	607	704
		Synchrotron		950 - 1100		
	Longitudinal	Hole drilling	S-N	-123	-37	-80
			AW*	2589	1711	2150
		Synchrotron		975 - 1200		
DP	Transverse	Hole drilling	S-N	262	471	367
			AW*	-1330	669	-331
		Synchrotron		1025		
	Longitudinal	Hole drilling	S-N	-316	-23	-170
			AW*	3135	2379	2757
		Synchrotron		1700 - 1800		

Table 4.24: Residual strains measured by the hole drilling method in FS S-N (S-N) specimens and as-welded (AW) plates at the edge of the friction band and subsequent values determined through a synchrotron radiation strain scanning analysis.

4.5.4 Redistribution of Residual Strains due to Fatigue Loading

Residual strains are generally considered to act in an additive manner with respect to any applied load, for an applied tensile load a tensile residual strain will result in an apparent increase in the magnitude of the load, whilst a compressive residual strain would result in an apparent reduction in the load and vice versa for an applied compressive load. The expected outcome of the four point loading, R = 0 and 0.1, applied to the FS welded specimens would be a redistribution of the residual strain field due to plastic flow if the applied strain was of a magnitude that, when combined with that of the residual strain field, exceeded the yield strain. Assuming that the synchrotron radiation analysis of the residual strain distribution was accurate and that the applied loading was of a great enough magnitude it would be expected that the friction band and 2nd pass sides, of the SP and DP welds respectively, subjected to a tensile load, would exhibit a redistribution of the residual strain field, with the resultant distribution exhibiting a diminishing of the magnitude or a compressive field. The effect of the loading on the weld seam and 1st pass sides, of the SP and DP welds respectively, would be more dependent on the magnitude of the applied loading, if the loading was of an insufficient magnitude, it would be expected that the compressive residual strain field would negate any effect of the applied tensile loading. A load of sufficient magnitude to exceed both the residual strain

* Mean of three measurements undertaken at the different positions along the length of the weld.

field and yield strain would result in a similar response to that expected to occur on the weld seam and 1st pass sides, a redistribution of the residual strains with the outcome being a diminishing of their influence. In contrast to the two surfaces of the welded specimen the neutral axis, at the mid-thickness of the specimen, would be expected to exhibit minimal change in its residual strain field.

The synchrotron measurements undertaken on the FS DP welds exhibited a reduction of 800 με in longitudinal residual strains in the region of the weld when the 2nd pass surface was subjected to a 150 MPa transverse load, with no noticeable through thickness effects being evident, as shown in Figure 4.73 (page 208). The compressive strains in the material distant to the weld exhibited an increase in their magnitude in the region of 200 με. A similar reduction in the longitudinal residual strains, as shown in Figure 4.74 (page 208), was also observed when the load was applied for 100 cycles and a single load of 200 MPa was applied. It would generally be expected that the greater load would have resulted in a greater redistribution of the residual strain field in a similar manner to that observed by Iida and Takanashi[1]. The minimal variation resulting from the application of multiple loads and the increased load may partially be explained by the fact that the loading was applied in the direction transverse to the weld direction, therefore it's influence on the longitudinal residual strains would be less than that experienced by the transverse ones. The measurements were also undertaken 1 mm below the surface, the effect of this would also be to diminish the redistribution observed.

[1] Iida, K; Takanashi, M (1998)

5. Stress Range/Cycles to Failure (S-N) Testing

5.1 Abstract

The following section details four point loading stress range/life, S-N, testing of AA 5383-H321 plate and MIG, LI and HI, and FS, SP and DP, butt welds in the same material, with supplementary information detailed in Section 12, Appendix B ~ S-N Test Specimen Results (pages 499 - 505). Both the experimental procedure and results are detailed, including the method employed to determine the elastic-plastic SCF resulting from the MIG weld toe geometry and the curve fitting technique utilised for production of S-N curves. The types of failure observed are detailed, with both optical and scanning electron microscopy (SEM) fractographs of the fatigue crack initiation sites and fracture paths and surfaces.

5.2 Introduction

Fatigue properties are typically expressed as S-N curves, the number of cycles to failure for a given stress range and/or crack growth rate, (da/dN) or (dc/dN)-ΔK curves, these allow engineers to determine a safe life for a given number of load cycles. The fatigue properties of various metallic materials vary considerably, with high strength steels and titanium alloys typically having high fatigue strengths whilst aluminium and magnesium alloys have lower values. As well as the fatigue strength of different materials varying, the type of fabrication utilised also affects the fatigue properties and as the majority of structures are fabricated, the fatigue strength of the appropriate fabrication is as relevant, if not more so, than that of the parent material. The fatigue strengths of various methods of fabrication are included in design codes that allow relatively simple determination of their respective fatigue strengths. Due to the proliferation of steel structures the codes have typically related to these, but the increase in the use of aluminium structures has resulted in the need for dedicated design codes. The codes for aluminium structures have generally been factored from steel codes, although the significant crack initiation period observed in welded aluminium joints advocates codes in which factors such as this are taken into consideration.

S-N testing of large fabricated structures is generally difficult to undertake, but smaller specimens can be utilised to provide a relevant analysis, although with respect to welded structures the parameters associated with any changes in the fatigue response must be representative of those in the fabricated structure. With weld specimens this means that the residual stress fields, the microstructure, weld geometry, HAZ, loading, defect and porosity distribution etc. must be comparable and this is generally attained through scaled models of the original. To determine the effect of each parameter it is necessary to reduce to the number of variables through either negating their influence or understanding their effect. In the case of MIG welds this means that the influence of the stress concentrating effect of the weld toe requires determining as this will affect not only the local stresses at the weld toe, but also the effect of the residual stress field as this may be redistributed due to plastic flow. It is also important to understand the extent of fatigue crack initiation and the factors that are influential in this. Crack initiation represents a significant proportion of the fatigue life, particularly in high cycle fatigue, although in aluminium alloys the initiation period may often be considered to consist of short crack growth. Advances in the understanding these factors may result in techniques leading to the enhancement of the fatigue life.

5.3 Literature Review

One of the aims of the present research is to advance the understanding of the fatigue properties and hence life prediction of both MIG and FS butt welded joints in aluminium. It is intended that this will enable further development of the fatigue design codes for this type of joint in aluminium alloys. During the early 1980s it was decided that the recommendations for aluminium structures should be adapted from steel structures to guarantee a ready accessibility to engineers in practice[1]. This was due to the limited volume of data available for aluminium structures in comparison to those manufactured in steel and this process has continued with aluminium design codes, such as BS 118, NS 3471 and DVS 1608, being factored from steel codes[2]. In more recent times, the technique of factoring the steel design codes has been considered by authors such as Kuitunen and Rahka[2] who undertook experiments on both small welded specimens and welded components. They concluded that the fatigue design codes were conservative in the case of BS 118, whereas the International Institute of Welding (IIW) recommended design data for steel structures, BS/PD 6493, when reduced by a factor of three for aluminium alloys, resulted in values that were conservative at low stresses, but too optimistic for higher stresses that resulted in a low number of cycles to failure ($N < 10^5$)[2].

Maddox[3] proposed that as the factors, in many respects, that influenced the fatigue strengths of welded joints in steel and aluminium were the same, the rules for steel structures could be adapted for aluminium simply by factoring the stresses. This assumption relied on the welding processes being comparable and therefore problems arise when friction stir welds are under consideration. Although it is possible to friction stir weld steels, the fact that the FS welding process is a relatively new technique, at the time of writing, means that the amount of fatigue data available is limited, although the majority of the data relates to aluminium alloys as the technique has been particularly suited to joining these. For Maddox's[3] hypothesis to be relevant, for comparable processes, several assumptions that had to be made are detailed. One conjecture is that the fatigue strength for an aluminium joint is one third that for the same joint in steel. This hypothesis is based on numerous assumptions; that the rate of fatigue crack propagation in steels and aluminium alloys are similar when expressed in terms of $\Delta K/E$ and that the fatigue lives of most welded joints consist entirely of crack propagation, the crack initiation phase being negligible; although the author does state that initiation may be more significant in higher fatigue strength joints, such as butt welds[3]. The minimal crack initiation period may be considered appropriate for steel welds, where weld toe defects are more common[4], but aluminium welds do not generally exhibit such defects, although

---

[1] Kosteas, D; Sanders Jr, WW (1987)
[2] Kuitunen, R; Rahka, K (1991)
[3] Maddox, SJ (1982)
[4] Gurney, TR (1979)

porosity is more common, and crack initiation is considered an appreciable part of the fatigue life.

Other factors require consideration if the factoring of steel design rules are to accurately reflect the behaviour of aluminium alloys, one of note being the size of the HAZ. Welded joints in both heat treatable and strain hardenable aluminium alloys exhibit a much larger HAZ, due to the increased thermal conductivity, and softening, due to annealing, when compared to welded joints in steel.

Gurney[4] lists eight factors that are considered to influence the fatigue strength of butt welds, excluding the type of loading, applied stress ratio and any defects, and it is intended that the research being undertaken will address factors i, iv and vi:

i. Composition and mechanical properties of the parent material.
ii. Specimen width and thickness.
iii. Type and method of welding preparation.
iv. Welding process and type of electrode.
v. Welding position.
vi. Weld shape.
vii. Post-weld machining.
viii. Post-weld heat treatment.

5.3.1 General Fatigue Properties

Fatigue data is frequently presented as either fatigue crack growth rate curves, $(da/dn)/\Delta K$, and/or stress life curves, stress range (or stress amplitude or peak stress) against the number of cycles to failure, $\Delta\sigma/N$. The fatigue strength of a structure is known to depend on several factors; with regards to loading both the stress range, or peak load, and the ratio of the minimum to maximum stress, $R = \sigma_{min}/\sigma_{max}$, are known to significantly affect the fatigue strength. With respect to the material, both the macrostructure and microstructure are known to have an influence on the fatigue characteristics. In the case of MIG welds the stress concentrating effect of the weld toe, which is typically the point of crack initiation for full penetration butt welds, has a significant affect on the fatigue strength. In the case of FS welds the score marks from the rotational and transverse movement of the tool shoulder are capable of causing cracking initiation and influencing the subsequent crack growth. The microstructure of a material can also effect crack growth and the resulting change in microstructure due to both MIG and FS welding is considerable, as detailed in Section 3, Geometry, Microstructure and Mechanical Properties (pages 13 - 121). For instance, short cracks, typically described as growing at rates significantly greater than those for long cracks subject to the same crack driving

force, ΔK, are known to be influenced by the microstructure, as are long cracks exhibiting unstable crack growth in regime C[1].

5.3.1.1 Fatigue Strength of Butt Welded Aluminium Structures

5.3.1.1.1 MIG Welded Joints

S-N curves for MIG butt welded aluminium joints are included in "Eurocode 9 Ontwerp en berekening van aluminiumconstructies – Deel 2: Constructies gevoelig voor vermoeiing"[2], "Static and fatigue strength of butt welded joints in aluminium alloys"[3] and "European recommendations for aluminium alloy structures fatigue design"[4].

Eurocode 9[2] considers AA 5083 plate as detail category 86-7 and 69-7, for loading parallel and normal to the rolling direction respectively. Two pass butt welds, with the weld bead intact and loading normal the weld axis, are detailed as 35-4 and 39-4, with the relevant fatigue strengths taking into consideration the effect of the weld toe geometry through acceptance level criteria for production welds. The respective fatigue strengths, quoted as two standard deviations below the mean, of the parent plate and weld joints are detailed in Table 5.1.

	Detail category ($N = 2 \times 10^6$)		$N = 10^5$	$N_D = 5 \times 10^6$	$N_L = 10^8$
	$\Delta\sigma_c$ (MPa)	m_1	$\Delta\sigma$ (MPa)	$\Delta\sigma_D$ (MPa)	$\Delta\sigma_L$ (MPa)
Parent material //	86	7	131.9	74.4	54.1
Parent material |-	69	7	105.9	60.5	43.4
Butt weld	35	4	74.0	27.8	16.8
Butt weld (high quality)	39	4	82.5	31.0	18.8

Table 5.1: Fatigue strength of AA 5083 parent plate and two pass butt welds[2].

where: $\Delta\sigma_c$ = reference fatigue strength at 2 million cycles.

m_1 = value of m for $N \leq 5 \times 10^6$ cycles (inverse slope constant of a log $\Delta\sigma$/log N fatigue strength curve).

$\Delta\sigma$ = nominal stress range.

$\Delta\sigma_D$ = constant amplitude fatigue limit.

$\Delta\sigma_L$ = cut-off limit.

The ESDU International[3] publication details typical fatigue data for several butt welded configurations for AA 5083, O and H113 temper, as detailed in Table 5.2. S-N curves for the O temper parent material and both welded and post-weld treated joints are shown in

[1] Ritchie, RO (1999)
[2] Nederlands Normalisatie-instiuut (1998)
[3] ESDU International (1991)
[4] ECCS Technical Committee 2 (1992)

Figure 5.1. Observation of the results indicates that the fatigue strength for the as-welded joint was 35% of that returned by the parent material for a life of 10^6 cycles, whereas the bead removed joint had a fatigue strength of 73% of that for the parent plate.

Alloy and temper designation	Loading type	No. of weld passes	t (mm)	R	Test conditions	Mean fatigue strength ($2\sigma_a$) (MPa)	
						10^6 cycles	10^7 cycles
5083-O	Axial	2	4	0	*(parent metal)*	147	-
5083-O	Axial	2	4	0	welded, bead removed	108	-
5083-O	Axial	2	4	0	welded, toe ground	78	70
5083-O	Axial	2	4	0	as-welded	52	45
5083-O	Axial	2	4	0	welded, stress relieved	60	-
5083-O	Axial	2	4	0	toe peened	102	83
5083-O	Axial	2	4	0	as-welded, arc = 23V	82	70
5083-O	Axial	2	4	0	as-welded, arc = 21V	65	55
5083-O	Axial	2	20	0	as-welded	65	55
5083-O	Axial	2	20	0.6-0.82	as-welded, $\sigma_{max} = \sigma_y$	50	33
5083-O	Axial	2	12	0	*(parent metal)*	138	-
5083-O	Axial	2	12	0	as-welded	83	-
5083-H113	Axial	1	9.5	0	as-welded	92	80
5083-H113	Axial	1	9.5	0	bead removed	127	10
5083-H113	Axial	1	9.5	0	as-welded	73	58
5083-H113	Axial	1	9.5	0	bead removed	120	95
5083-H113	Bending	1	9.5	-1	as-welded	160	112
5083-H113	Bending	1	9.5	-1	bead removed	218	-

Table 5.2: Fatigue strength of butt welded AA 5083[1].

Figure 5.2 details the fatigue response of butt welds in the H113 temper subjected to both bending and axial loading; for a fatigue life of 2×10^6 cycles the axially loaded samples had a fatigue strength of 47% of that returned by the specimens loaded in bending, whilst for the bead off specimens the value increased to 57%. It is not clear from the publication though whether both the axially loaded and bending specimens were subjected to the same stress ratio, the S-N diagram, Figure 5.2, suggesting that all specimens underwent testing at R = -1, whilst the chart, Table 5.2, suggests that the axial specimens were tested at a stress ratio of 0. Although it would be expected that the specimens subject to bending would have a greater fatigue strength due to only the outer fibres being subjected to the full tensile load, greater reversed plasticity and crack closure effects from the fully reversed loading would exacerbate the difference between the loading methods.

[1] ESDU International (1991)

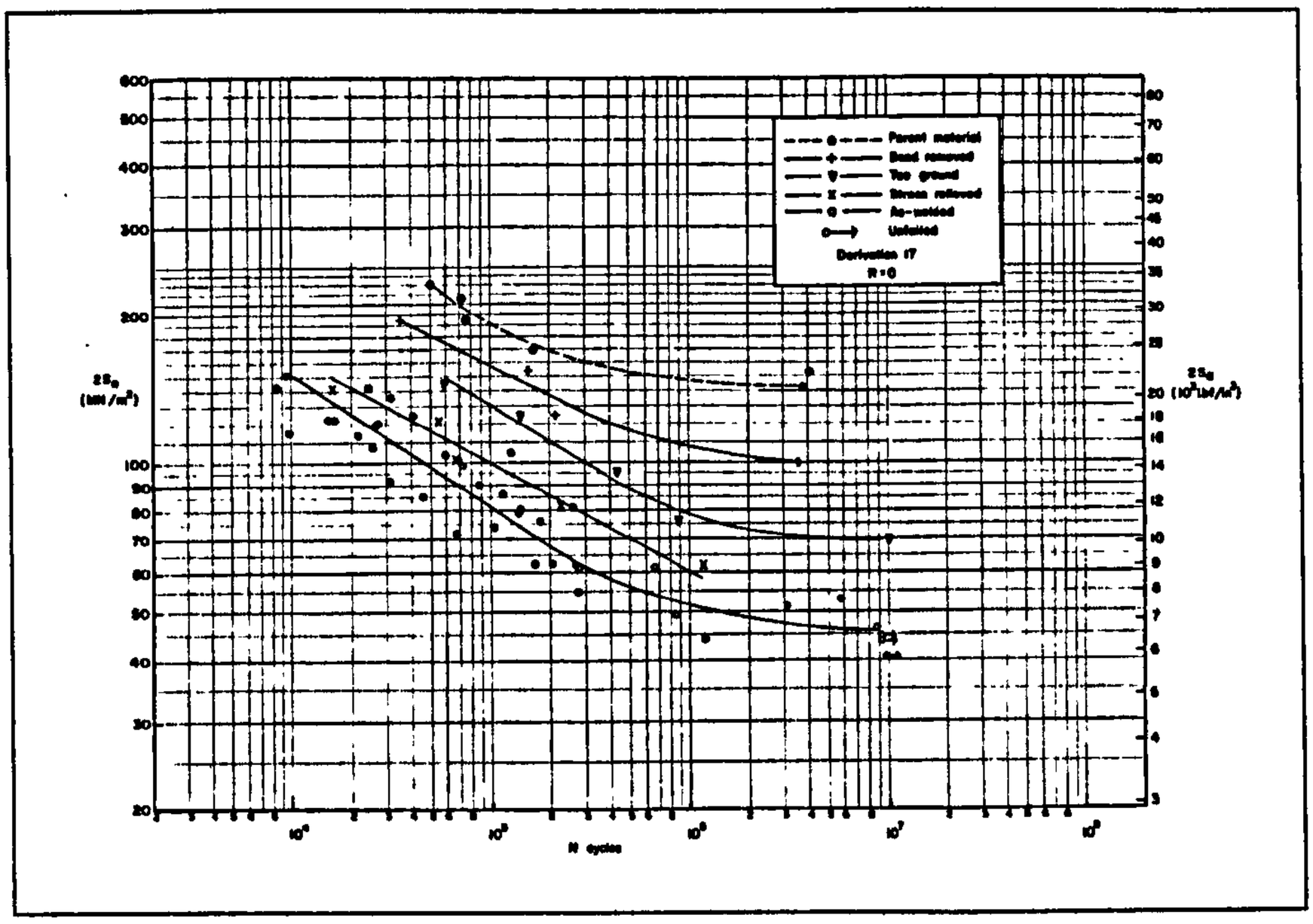

Figure 5.1: S-N curves for AA 5083-O parent material, butt welds and butt welds with post-weld treatments[1].

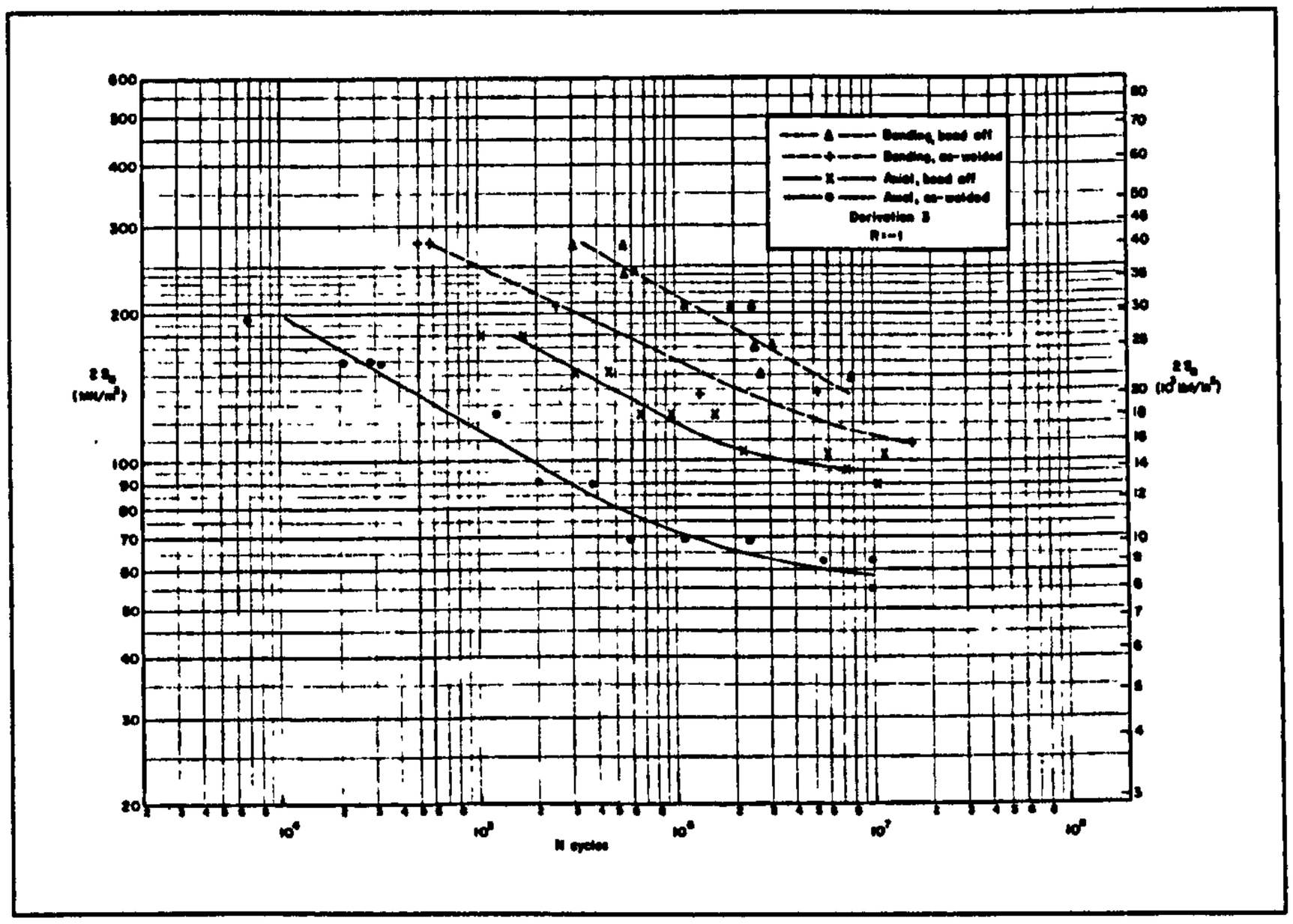

Figure 5.2: S-N curves for AA 5083-H113 butt welded joints under axial and bending loads[1].

The effect of the mean stress on the fatigue strength of butt welded NP 5/6 M (equivalent to AA 5083-F) is shown in Figure 5.3 As would be expected the fatigue strength decreased as the mean stress increased due to the crack being open for a greater

[1] ESDU International (1991)

proportion of the load cycle, thereby allowing greater crack propagation. For a fatigue life of 2×10^6 cycles the fatigue strength decreased by 25, 39, 41 and 46% for increases in the mean stress from 0 to 23, 46, 77 and 108 MPa respectively; indicating that the influence of the mean stress diminished as the mean stress increased. For a fatigue life of $< 10^6$ cycles the fatigue strength was noted to be greater for a mean stress 108 MPa, rather than for the mean stress of 77 MPa.

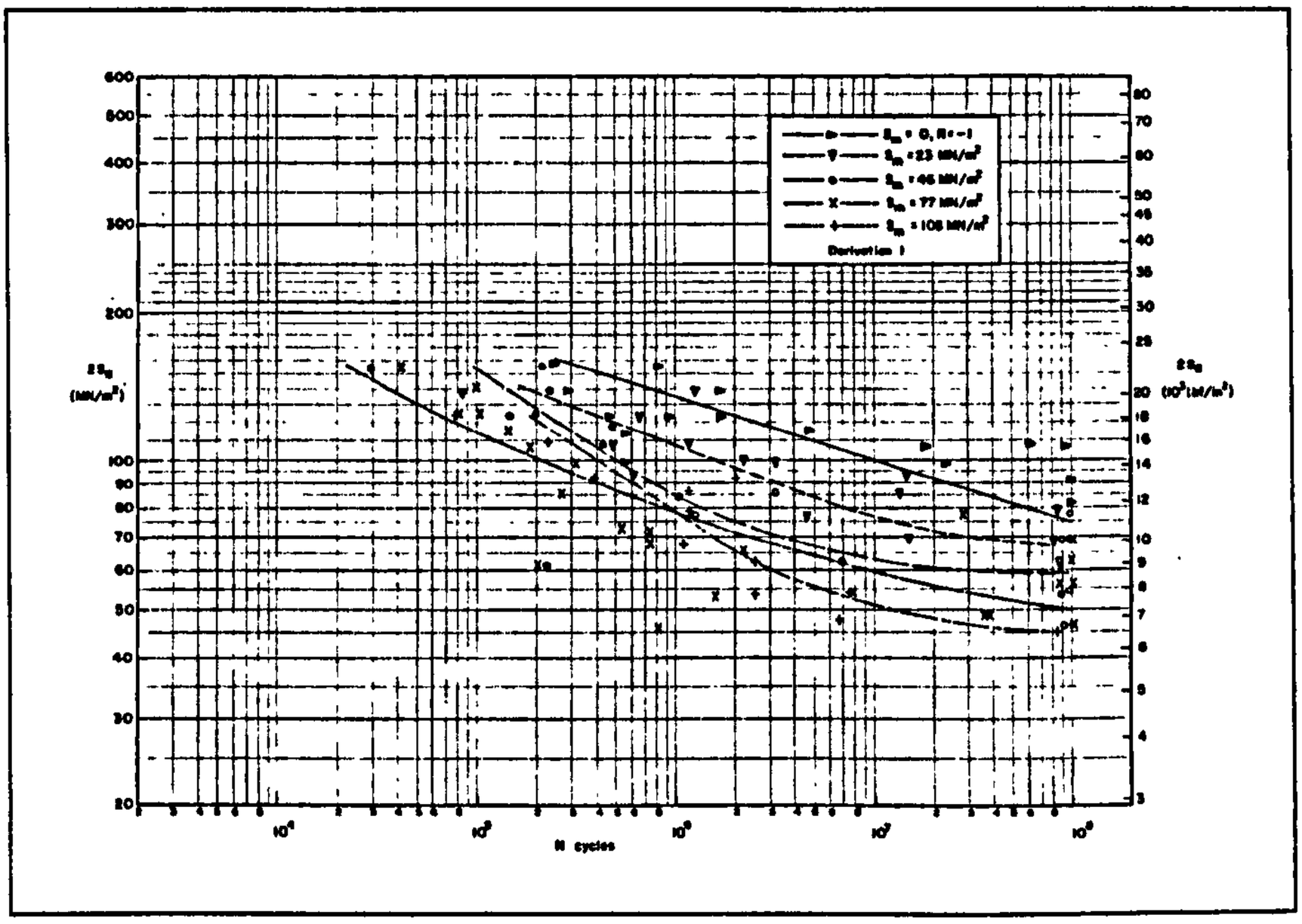

Figure 5.3: Effect of mean stress on the fatigue strength of butt welded joints in NP 5/6 M (comparable to AA 5083 F)[1].

	Structural detail	m_1	Cycles			
			10^4	10^5	2×10^6	10^8
			$\Delta\sigma_R$ (MPa)			
Base metal	A3	7	202.5	145.7	95.0	95.0
Butt weld, $\theta > 150°$	B2	4.32	170.5	100	50.0	40.4
Butt weld, $130° < \theta < 150°$	B3	4.32	153.4	90	45.0	36.4

Table 5.3: Fatigue design strengths of AA 5XXX alloy parent plate and two pass butt welds[2].

Table 5.3 details the fatigue strengths for a 5XXX series aluminium alloy for both the parent material and two, bead intact, butt welded joints. For a butt welded joint with a weld toe angle, θ, of greater than 150° the fatigue strength is 53% that of the parent material, whilst for a weld bead angle between 130° - 150° the fatigue strength reduces to 47%, for a life of 2×10^6 cycles at R = 0.5.

---

[1] ESDU International (1991)
[2] ECCS Technical Committee 2 (1992)

Fatigue strength design codes tend to be conservative in nature, generally the upper bound load is compared with the lower bound S-N curve. The ECCS[1] curves are based on two standard deviations below the mean value, with Eurocode 9[2] utilising the same policy. A comparison of the fatigue strength at 2×10^6 cycles for AA 5083 parent plate and as-welded butt welds, from the three publications, is shown in Table 5.4. It is clearly evident that the published values vary considerably, the fatigue strength for the parent material ranging from 69 - 144 MPa and 35 - 70 MPa for the welded joints; as the ESDU[3] publication details the mean values this returned the greater magnitudes.

	Fatigue strength for $N = 2 \times 10^6$					
	Eurocode 9[2]		ESDU[3]		ECCS[1]	
	$\Delta\sigma_R$ (MPa)	Observations	$\Delta\sigma_R$ (MPa)	Observations	$\Delta\sigma_R$ (MPa)	Observations
Parent plate	86/69	Parallel/normal to rolling direction. For EN AW 5083, S-N curves are 2 std. dev. below the mean line.	144/131	4/12 mm thickness. R = 0. AA 5083-O Mean fatigue strength.	95	R = 0.5. For AA 5XXX series. S-N curves are 2 std. dev. below the mean line.
Butt weld	35/39	Normal/high quality. For EN AW 5083, S-N curves are 2 std. dev. below the mean line.	47/70	4/12 mm thickness. R = 0. AA 5083-O Mean fatigue strength.	45/50	$130 < \theta < 150°/\theta > 150°$ R = 0.5. S-N curves are 2 std. dev. below the mean line.

Table 5.4: Summary of published fatigue strengths of the parent plate and as-welded butt welds for an AA 5083.

Calcraft et al[4] undertook uniaxial fatigue testing of 10 mm thick AA 5383 (the temper is not detailed) parent material and MIG welded butt joints with a stress ratio of 0.1, the results being shown in Figure 5.4. The tests returned $\Delta\sigma_R$ values of 155 MPa (σ_a = 77.5 MPa) for the parent material and values of 90 MPa and 123 MPa for the as-welded and dressed welds respectively for lives of 2×10^6 cycles. The values for the parent material and welded joints were 18% and 29% greater respectively than the highest comparable values for AA 5083 shown in Table 5.4.

---

[1] ECCS Technical Committee 2 (1992)
[2] Nederlands Normalisatie-instiuut (1998)
[3] ESDU International (1991)
[4] Calcraft, RC et al (1999)

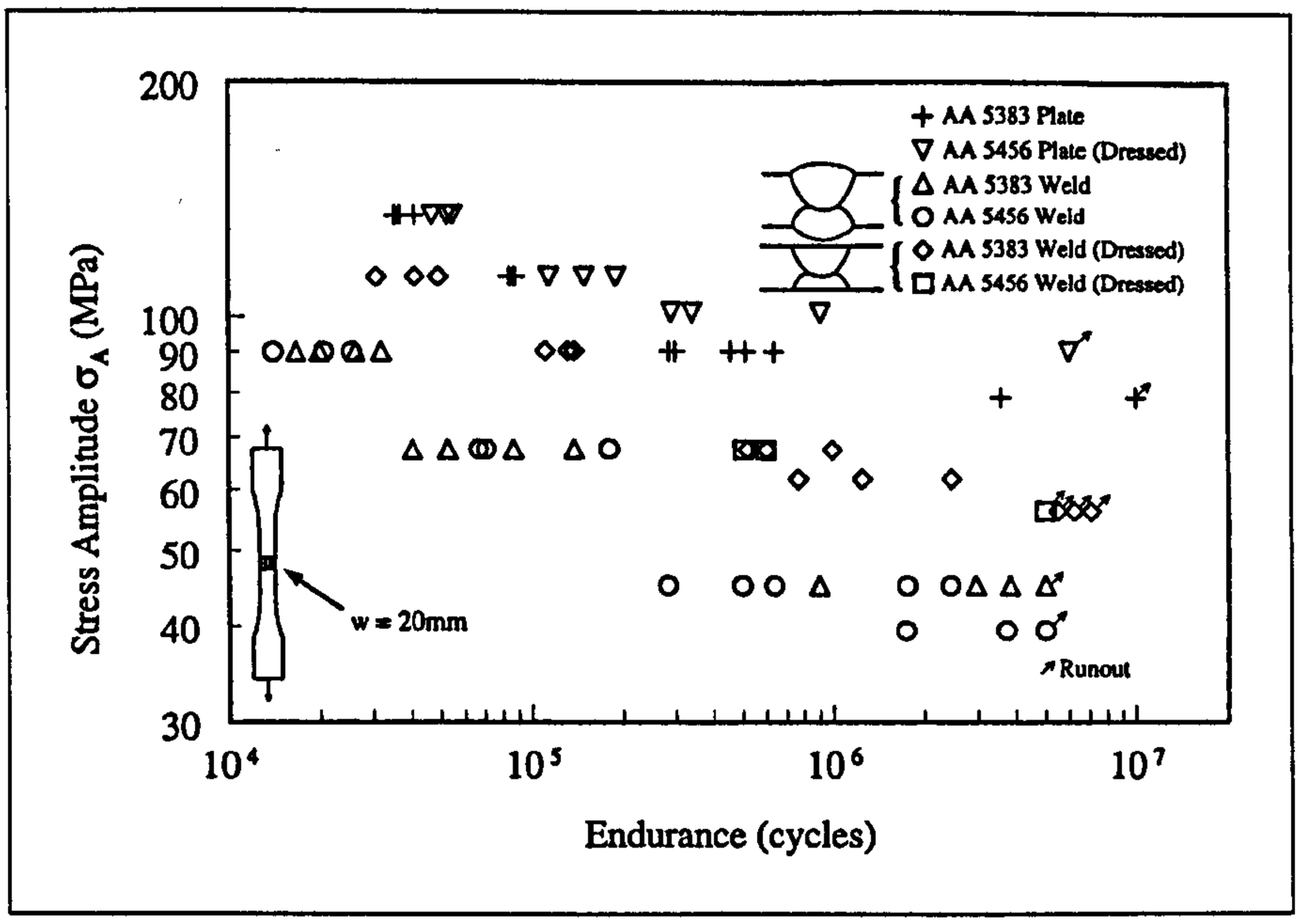

Figure 5.4: Fatigue test results for AA 5383 and 5456 base materials and MIG weldments, R = 0.1[1].

5.3.1.1.2 FS Welded Joints

At the time of writing FS welding may be considered a relatively new process and as far as the author was aware no design codes detailing the fatigue strength of their respective joints had been published, although several research publications detailing the fatigue strength of various aluminium alloys were available.

Magnusson and Källman[2] detailed the fatigue properties of 2 mm thick AA 2024-T3 and AA 7475-T76 sheet and 1.6 mm thick AA 6013-T6 as shown in Figure 5.5. The sheet rolling direction was transverse to the weld direction, parallel to the applied loading, and a stress ratio of 0.1 was employed. The results at a life of 2×10^6 cycles are summarised in Table 5.5. The range of 72 - 81% of the parent material fatigue strength is significantly greater than those returned by MIG welds, typically 30 - 50% of the parent material, as shown in Table 5.4; although thin sections tend to return values that are optimistic for the prediction of fatigue life due to lower residual stresses and reduced crack growth rates from defects of the same size[3].

---

[1] Calcraft, RC et al (1999)
[2] Magnusson, L; Källman, L (2000)
[3] ESDU International (1991)

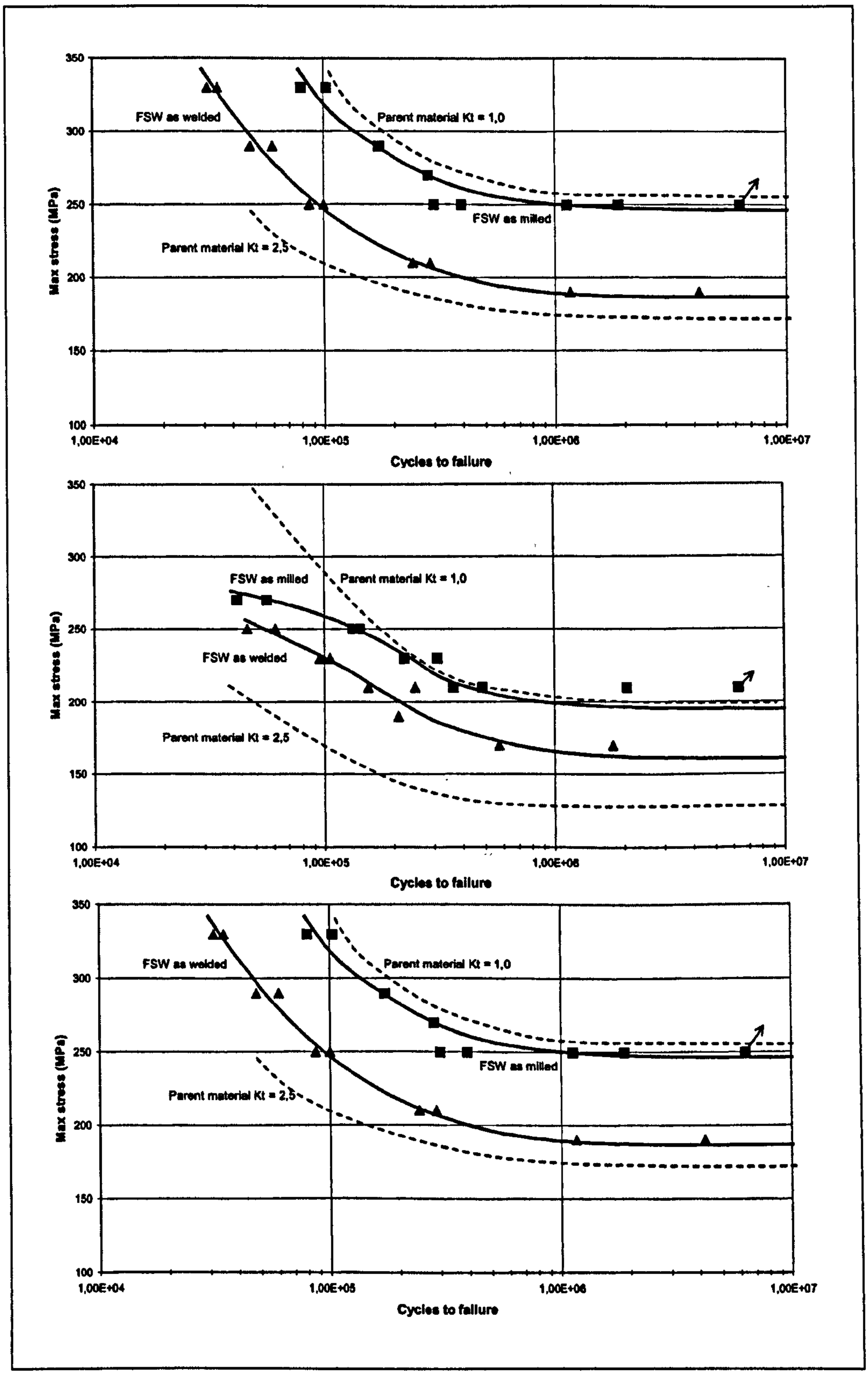

Figure 5.5: Fatigue properties of the parent plate and FS welded joints in 2024-T3 (upper), 6013-T6 (middle) and 7475-T76 (lower) aluminium alloys[1].

[1] Magnusson, L; Källman, L (2000)

	2024-T3		6013-T6		7475-T76	
	$\Delta\sigma_R$ (MPa)	% of parent material	$\Delta\sigma_R$ (MPa)	% of parent material	$\Delta\sigma_R$ (MPa)	% of parent material
Parent material	254	100	180	100	229	100
FS welded	184	72	146	81	167	73
FS welded milled finish	230	91	178	99	223	97

Table 5.5: Fatigue strength of AA 2024-T3, 6013-T6 and 7475-T76 for lives of 2×10^6 cycles[1].

S-N testing of 6.35 mm thick AA 2024-T351 was undertaken by Bussu and Irving[2], their results being shown in Figure 5.6. They obtained results of 177 MPa for $\Delta\sigma_R$ for the parent material at 2×10^6 cycles and 92 MPa for the FS weld, a reduction of 48%, whilst skimmed welds returned a fatigue strength that was 88% of the parent material. Dawes and Thomas[3] undertook axial testing at R = 0.1 of butt welds in both AA 5083 and 2014 as shown in Figure 5.7. From Figure 5.7 fatigue strengths for 2×10^6 cycles of 118 MPa for the FS welded AA 5083, 140 MPa for the parent material, and in the region of 106 MPa for the FS welded AA 2014-T6, 169 MPa for the parent material, may be deduced.

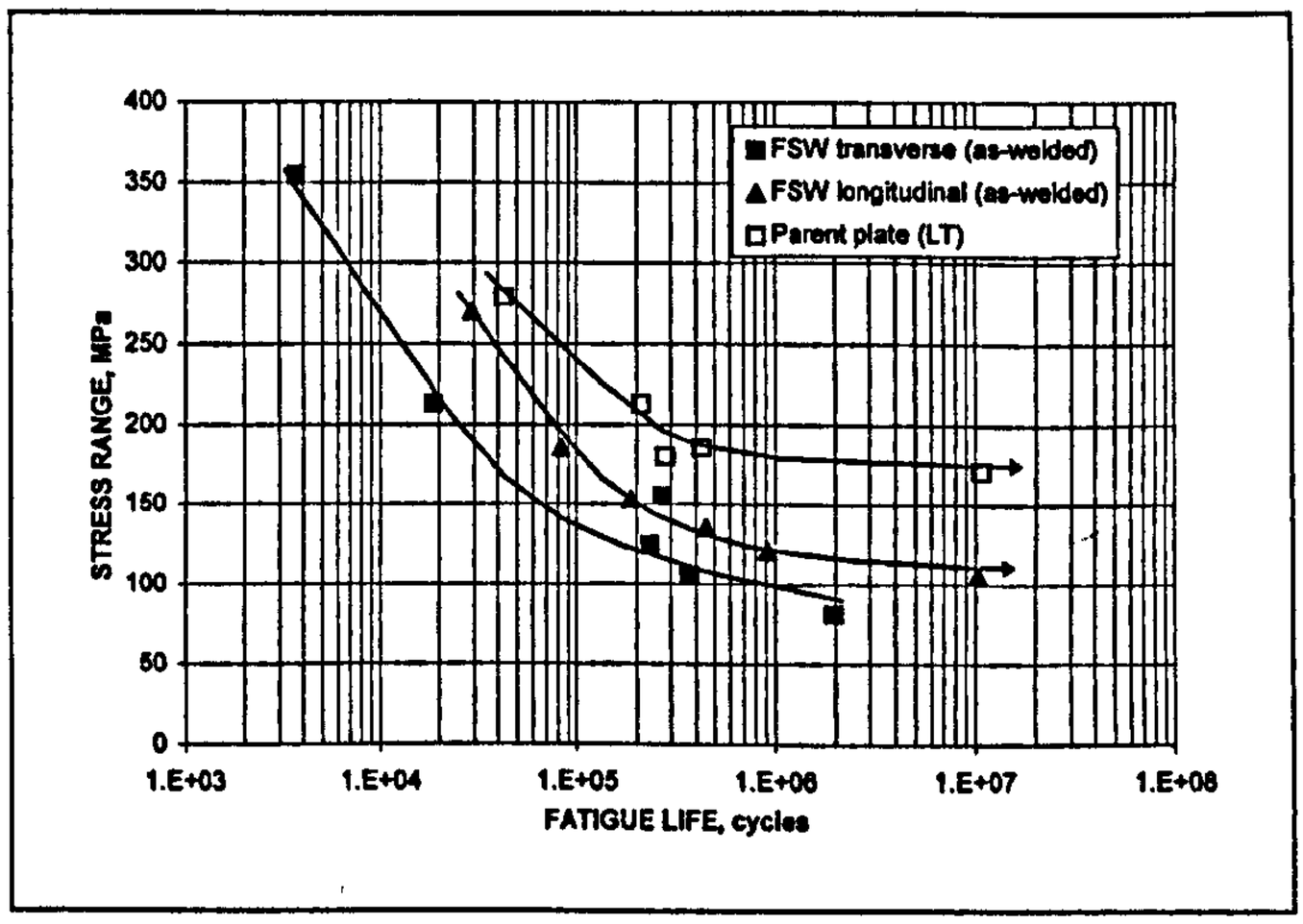

Figure 5.6: Fatigue properties of AA 2024-T351[2].

[1] Magnusson, L; Källman, L (2000)
[2] Bussu, G; Irving, PE (1999)
[3] Dawes, C; Thomas W (1995)

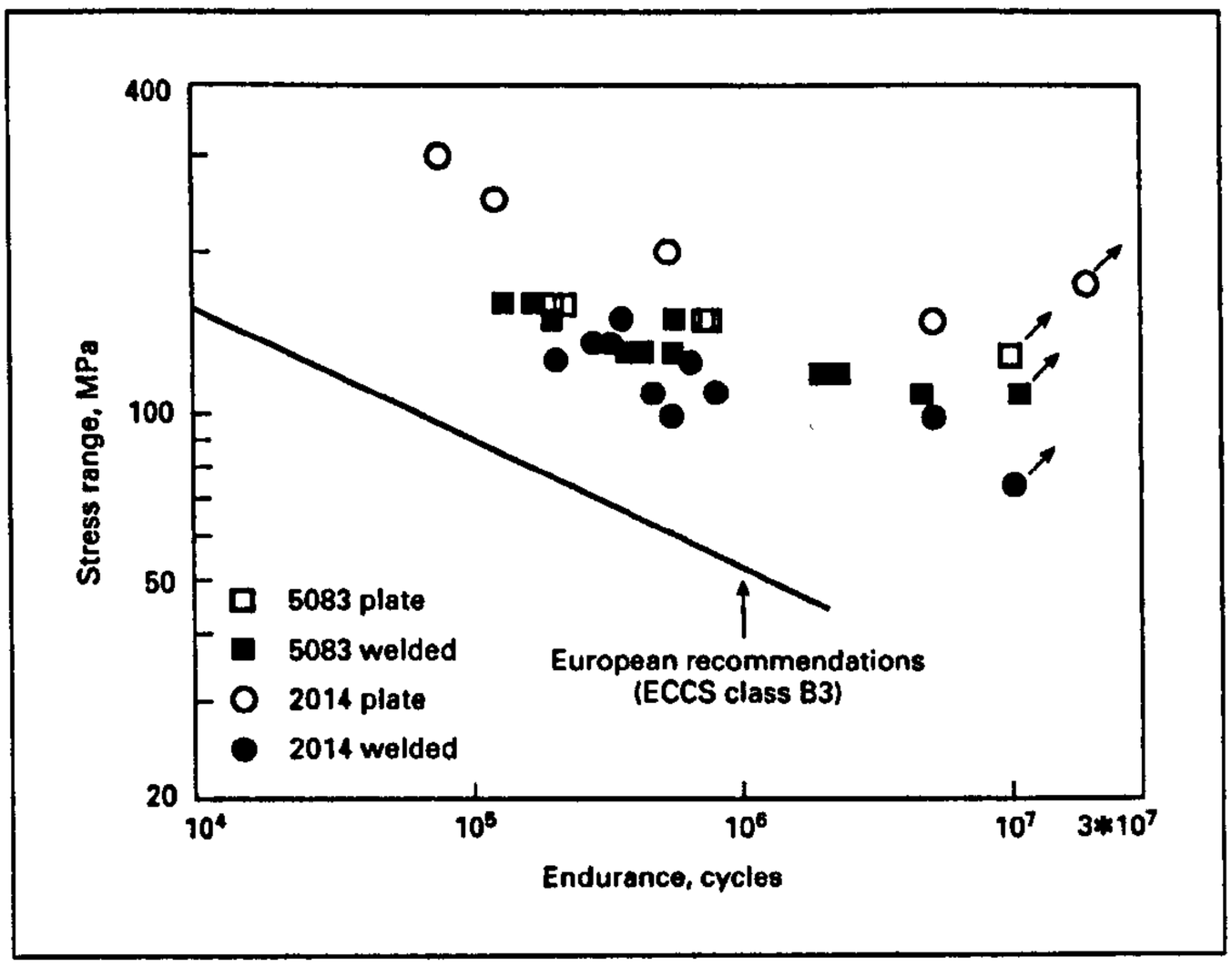

Figure 5.7: AA 5083-O and AA 2014-T6 S-N data[1].

From the literature reviewed it was apparent that the fatigue strength of the FS welded joints, when compared to that of their parent material, was greater than that of MIG welds, as shown in Table 5.6. The MIG welded joints returned fatigue strengths at 2×10^6 cycles of 33 - 55% of the parent material for as-welded joints, with this increasing to 60 - 70% for dressed joints, whilst the FS welds returned values of 52 - 84% for as-welded joints and 88 - 99% for dressed joints.

Publication	AA designation and temper	Fatigue strength at 2×10^6 cycles ~ MPa (% parent plate)			Comments
		Parent plate	MIG	FS	
ESDU[2]	5083-O	144/131	47/70 (33/53)		4/12 mm thick plate.
	5086-H116	242	144 (60)		Bead removed, bending.
Calcraft et al[3]	5383	175	96/123 (55/70)		As-welded/dressed
Dawes & Thomas[1]	5083	140		118 (84)	
	2014-T6	169		106 (63)	
Magnusson & Källman[4]	2024-T3	254		184/230 (72/91)	As-welded/milled finish
	6013-T6	180		146/178 (81/99)	
	7475-T76	229		167/223 (73/97)	
Bussu & Irving[5]	2024-T351	177		92/156 (52/88)	As-welded/skimmed

Table 5.6: Fatigue strengths at 2×10^6 cycles for various aluminium alloys and butt welds.

[1] Dawes, C; Thomas W (1995)
[2] ESDU International (1991)
[3] Calcraft, RC et al (1999)
[4] Magnusson, L; Källman, L (2000)
[5] Bussu, G; Irving, PE (1999)

5.3.1.2 Weld Profile

The profile of the weld is known to have a significant influence on its fatigue properties. The weld bead of a MIG weld acts as a stress concentrator, similarly the scored surface that results from the rotational and transverse motion of the tool shoulder during the FS process will have a analogous effect. Kelsey and Nordmark[1], in their study into the effects of residual stresses on the fatigue properties of aluminium butt welds, state that the most significant factor affecting the fatigue strength of transversely loaded welds is the profile of the weld bead. The authors stated that the removal of the reinforcement of a weld in a thin section results in a significant increase in the fatigue strength, although the effect is less evident in thicker section welds due to higher tensile residual stresses at the surface[1]. Unfortunately one of the problems in determining the effect of the weld bead is that it is difficult to measure weld toe angles and radii, with this being further compounded by the fact that the values vary considerably within the same weld run.

Sanders et al[2] undertook studies into the effects of the weld bead profile on the fatigue properties of the joint using both simulated, the profile being machined from the base material, and as-welded specimens. The authors concluded that relative to the parent material a reduction in fatigue strength of up to 45 - 50% could occur. An increase in the angle, θ (as shown in Figure 5.8 and Figure 5.9), of the weld bead resulted in a decrease in the fatigue strength, conversely, an increase in the radius at the weld toe resulted in an increase in the fatigue strength[2]. The reductions in fatigue strength for the simulated welds are shown in Figure 5.8 and for the as-welded specimens in Figure 5.9. The interaction between the flank angle and radius of the notch for the simulated welds are shown in Figure 5.10.

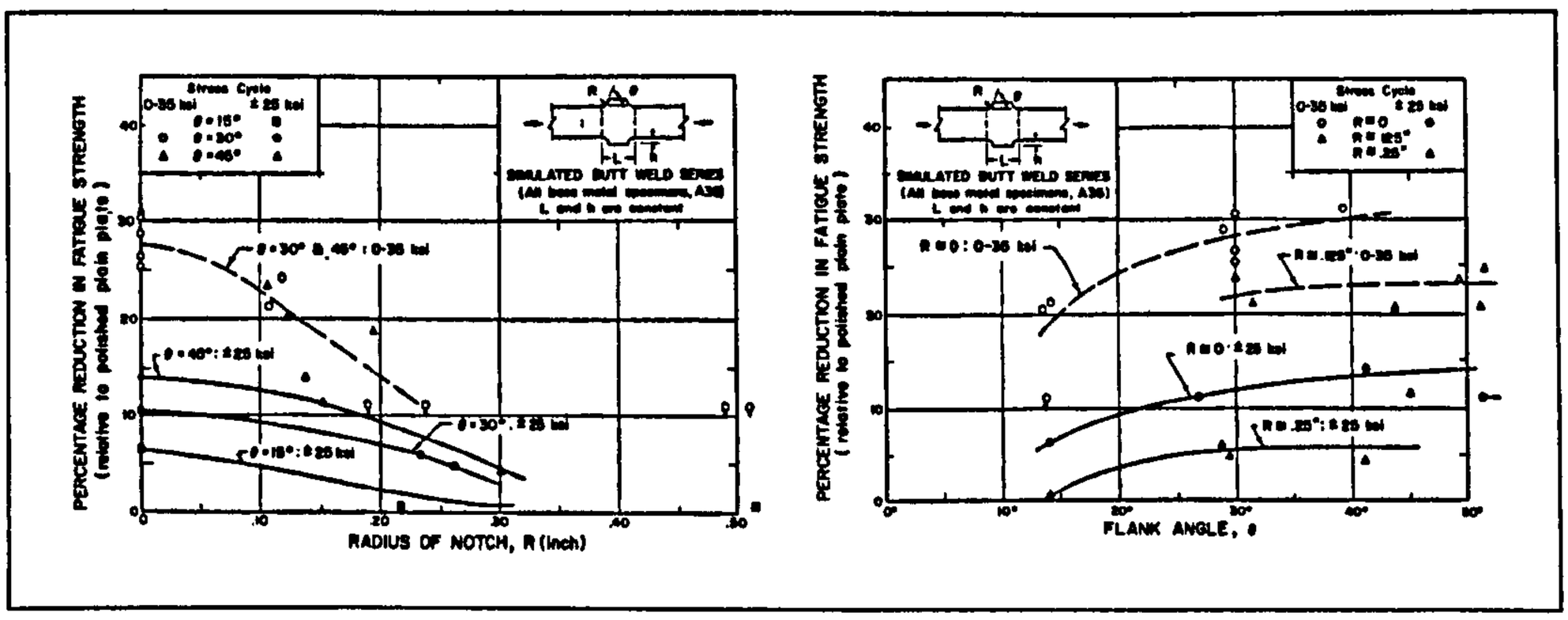

Figure 5.8: Variation of the reduction in fatigue strength with radius of notch, R (left) and flank angle, θ, (right) for simulated butt welds[2].

[1] Kelsey, RA; Nordmark, GE (1979)
[2] Sanders, WW et al (1965)

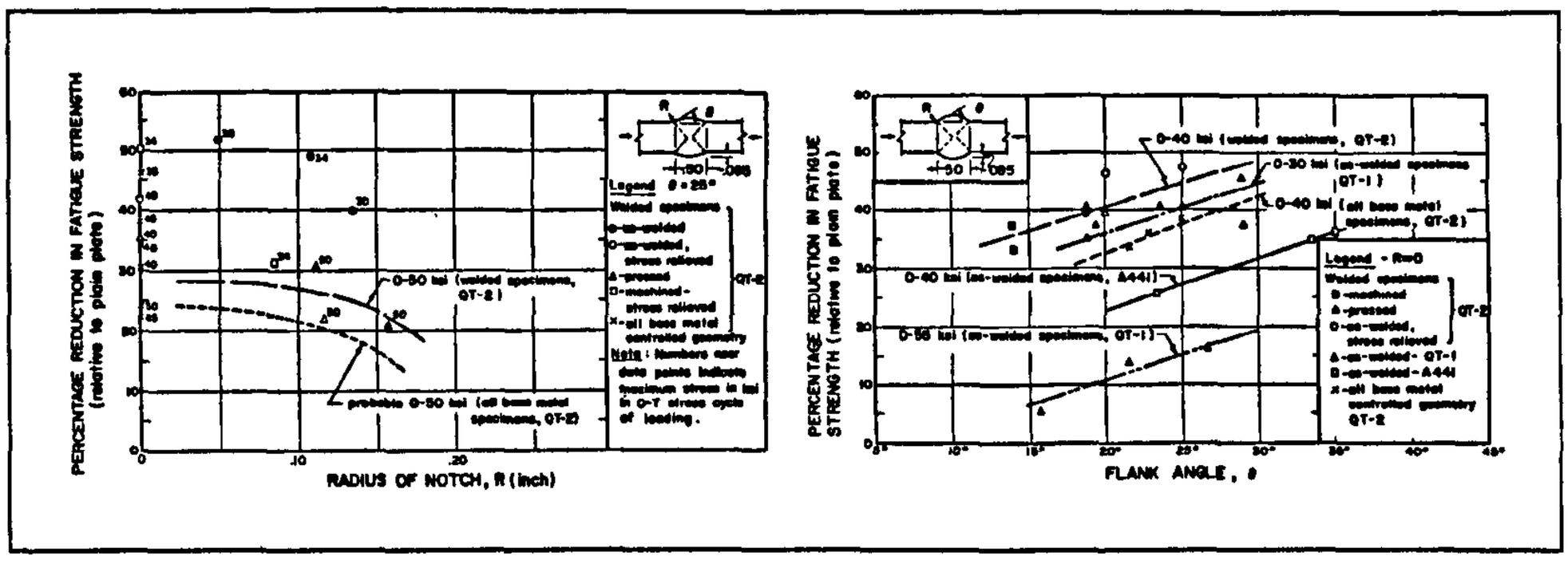

Figure 5.9: Variation of the reduction in fatigue strength with radius of notch, R (left) and flank angle, θ, (right) for as-welded welds[1].

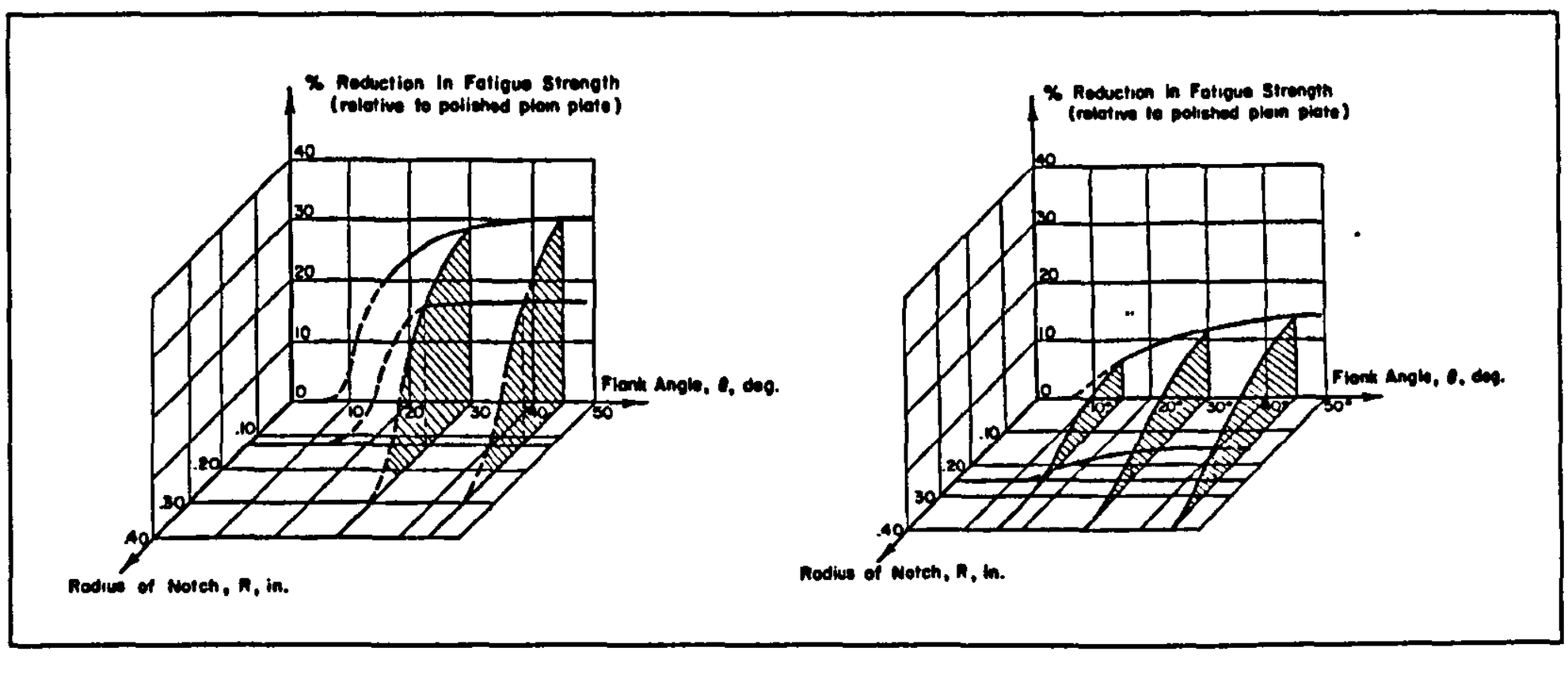

Figure 5.10: Interacting effect between the notch radius, R, and flank angle, θ, on the reduction in fatigue strength for simulated butt welds, R = 0 (left), R = -1 (right)[1].

Yung and Lawrence[2] presented a model for determining the fatigue behaviour of weldments which used a fatigue notch factor, K_f, to quantify the severity of the weld bead discontinuity. Although they state that it is difficult to determine K_f for defects such as the weld toe because the notch root radii are generally unknown, difficult to measure and highly variable. K_f is calculated using the following formula:

$$K_f = 1 + \frac{(K_t - 1)}{\left(1 + \frac{a}{r}\right)} \qquad (5.1)$$

where: K_t = elastic SCF.

a = Peterson's material parameter* (mm), detailed as being approximated by $1.807 \times 10^5 . S_u^{-2} \lim_{x \to \infty}$ for steel,

---

[1] Sanders, WW et al (1965)
[2] Yung, J-Y; Lawrence, FV (1985)
* Brandt, U et al (2001) state that Peterson's material parameter is determined experimentally.

S_u = ultimate strength of the notch-root material.

r = notch root radius (equivalent to the weld toe radius) (mm).

The elastic SCF, K_t, was calculated from the following equation:

$$K_t = \beta\left[1+\alpha\left(t/r\right)^{\lambda}\right] \qquad (5.2)$$

where: α, β and λ are material constants whose values are determined by the weld geometry and nature of the remote stresses; for a butt weld transversely loaded in bending:

$\alpha = 0.165.(\tan\theta)^{0.167}$.

θ = weld bead angle as show in Figure 5.11 (left).

β = 1

λ = 0.5

t = plate thickness (mm).

r = notch root radius (equivalent to the weld toe radius) (mm).

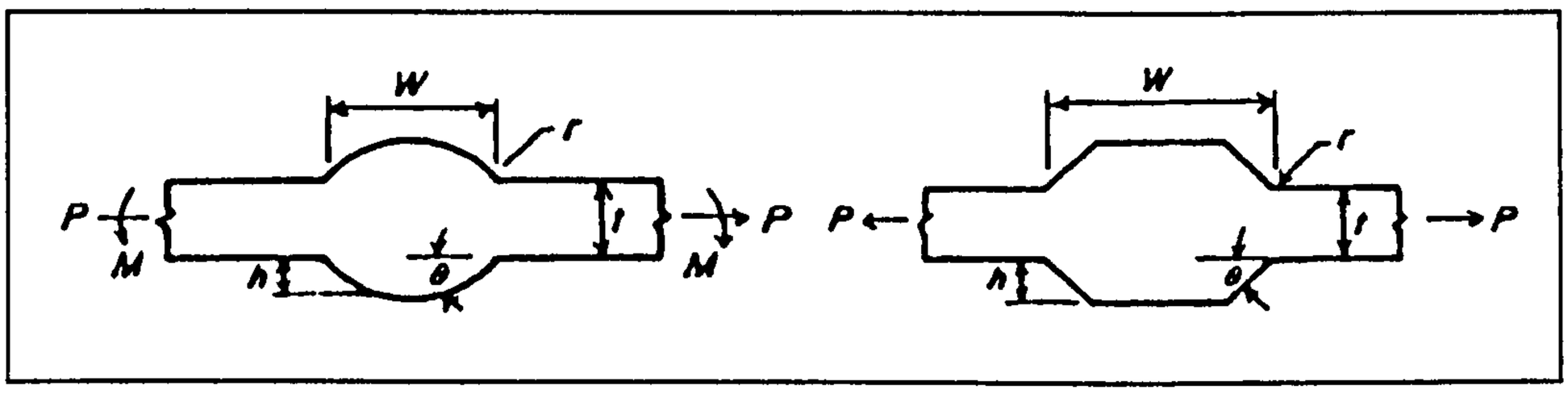

Figure 5.11: Weld geometry for calculation of SCF[1].

The authors[1] claim that Peterson's equation, (5.1), correctly interrelates the fatigue notch and elastic SCF.

The SCF may also be calculated by treating the weld bead as a trapezoidal protuberance on a tension member[2], as shown in Figure 5.11 (right), although the associated equation[1] and graphs[2], shown in Figure 5.12 and Figure 5.13, only relate to uniaxial tensile loading, rather than pure bending.

[1] Yung, J-Y; Lawrence, FV (1985)
[2] Pilkey, WD (1997)

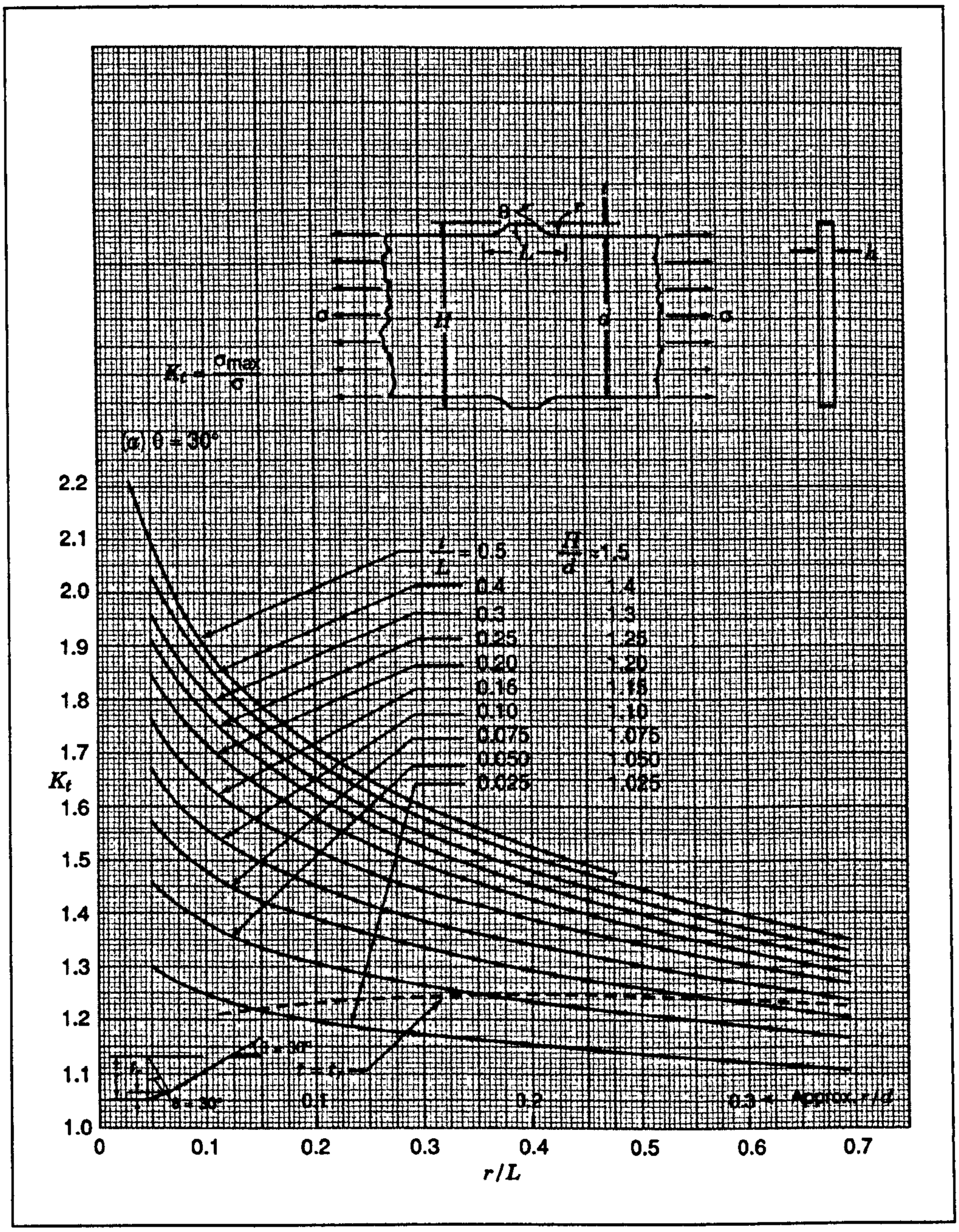

Figure 5.12: SCF, K_t, for a trapezoidal protuberance on a tension member L/(d/2) = 1.05 (Derecho and Munse 1968). θ = 30°[1].

[1] Pilkey, WD (1997)

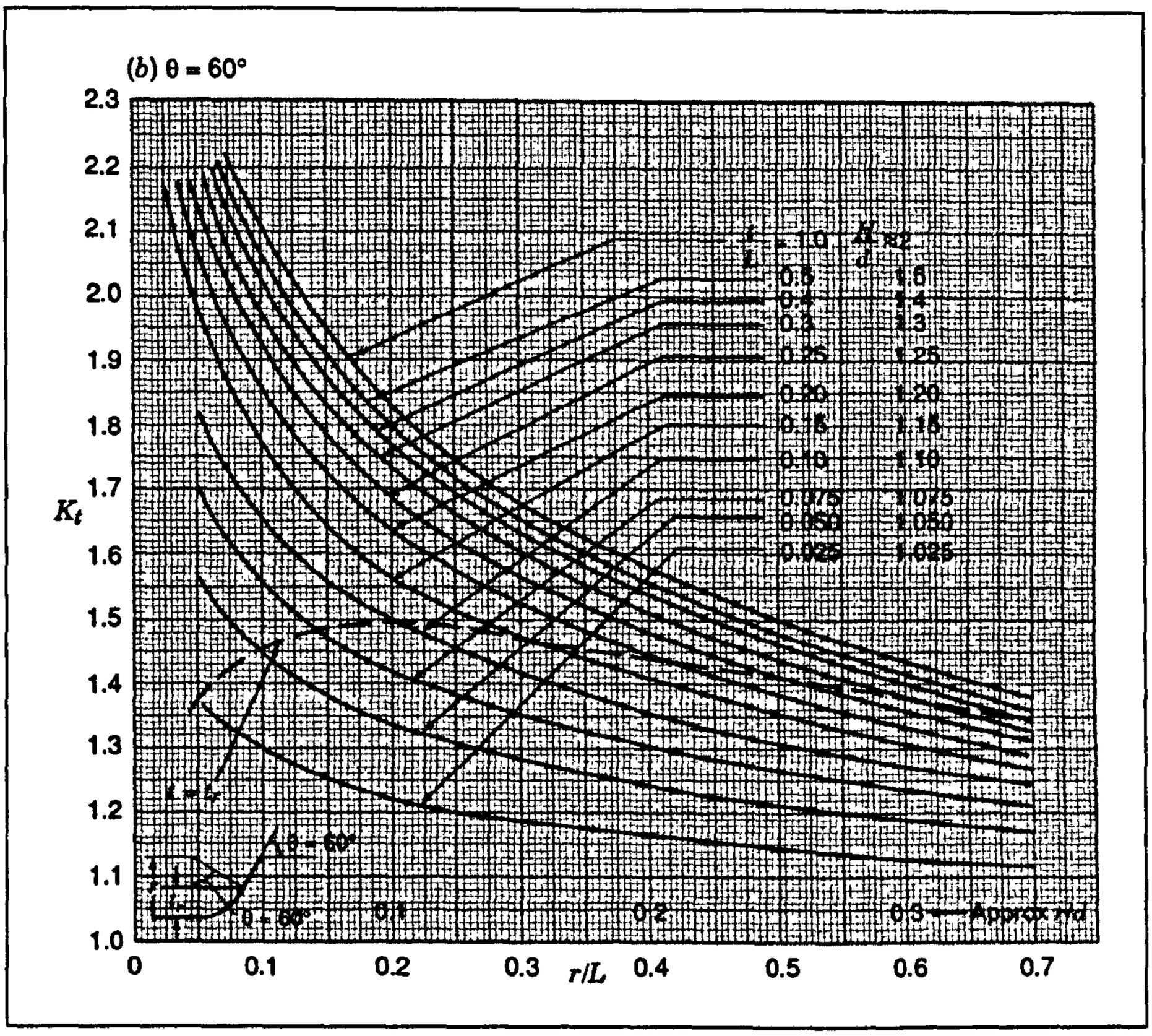

Figure 5.13: SCF, K_t, for a trapezoidal protuberance on a tension member L/(d/2) = 1.05 (Derecho and Munse 1968). θ = 60°[1].

Weld toe radii, 95% of which were in the range of 0.35 - 0.65 mm, were measured by Bertini et al[2], for GMAW butt welds in AA 6063. The mean toe radius was 0.5 mm and a FEA of the weld toe returned a SCF, K_t, of 1.8, with the 95% range being within ±5.6% of this. As no weld toe angles were commented upon in the paper, it may be assumed that the radius of the weld bead was considered constant and that the weld toe radius intersected this at a tangent. The range of SCF for the various weld toe radii are shown in Figure 5.14.

[1] Pilkey, WD (1997)
[2] Bertini, L et al (1998)

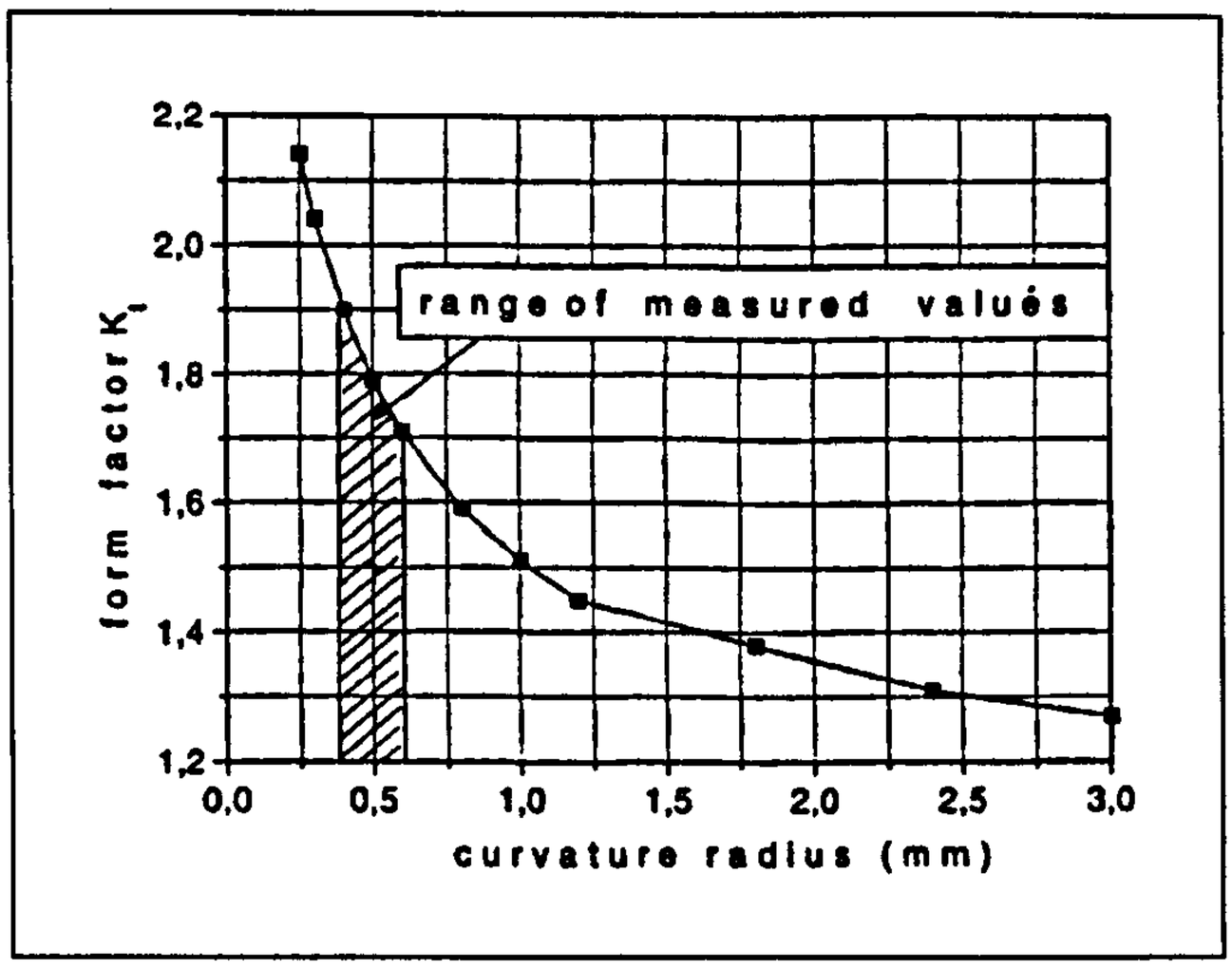

Figure 5.14: FEA analysis results for the SCF for various weld toe radii.

The weld toe angles and radii for a fillet weld in a high strength structural steel, shown in Table 5.7, were measured by Bignonnet et al[1]. Weld toe radii, ρ, ranged from 0.4 - 2.0 mm and 0.5 - 3.0 mm for the conventional and improved processes respectively, whilst the weld toe angles, θ, ranged for 40° - 90° for the conventional weld and 17° - 69° for the improved process.

Procedure		Mean	Std. Dev.	Min/max
Improved welding procedure	ρ (mm)	1.7	0.6	0.5/3.2
	θ (°)	36	8	17/69
Conventional	ρ (mm)	0.9	0.4	0.4/2
	θ (°)	60	12	40/90

Table 5.7: Weld toe radii and angles detailed by Bignonnet et al[1].

Dinsdale and Young[2] showed that the fatigue strength of an NP 5/6 alloy (equivalent to BS 5083-F except for Cr content[3]) reduced from 16 to 6.5 ksi (110 to 45 MPa) as the weld toe became sharper, the angle decreasing from 180° - 110° (weld angle, θ, as shown in Figure 5.11 increasing from 0° - 70°) as shown in Figure 5.15.

[1] Bignonnet, A et al (1986)
[2] Dinsdale, WO; Young, JG (1964) *referenced by Masubuchi, K (1980)*
[3] ESDU International (1991)

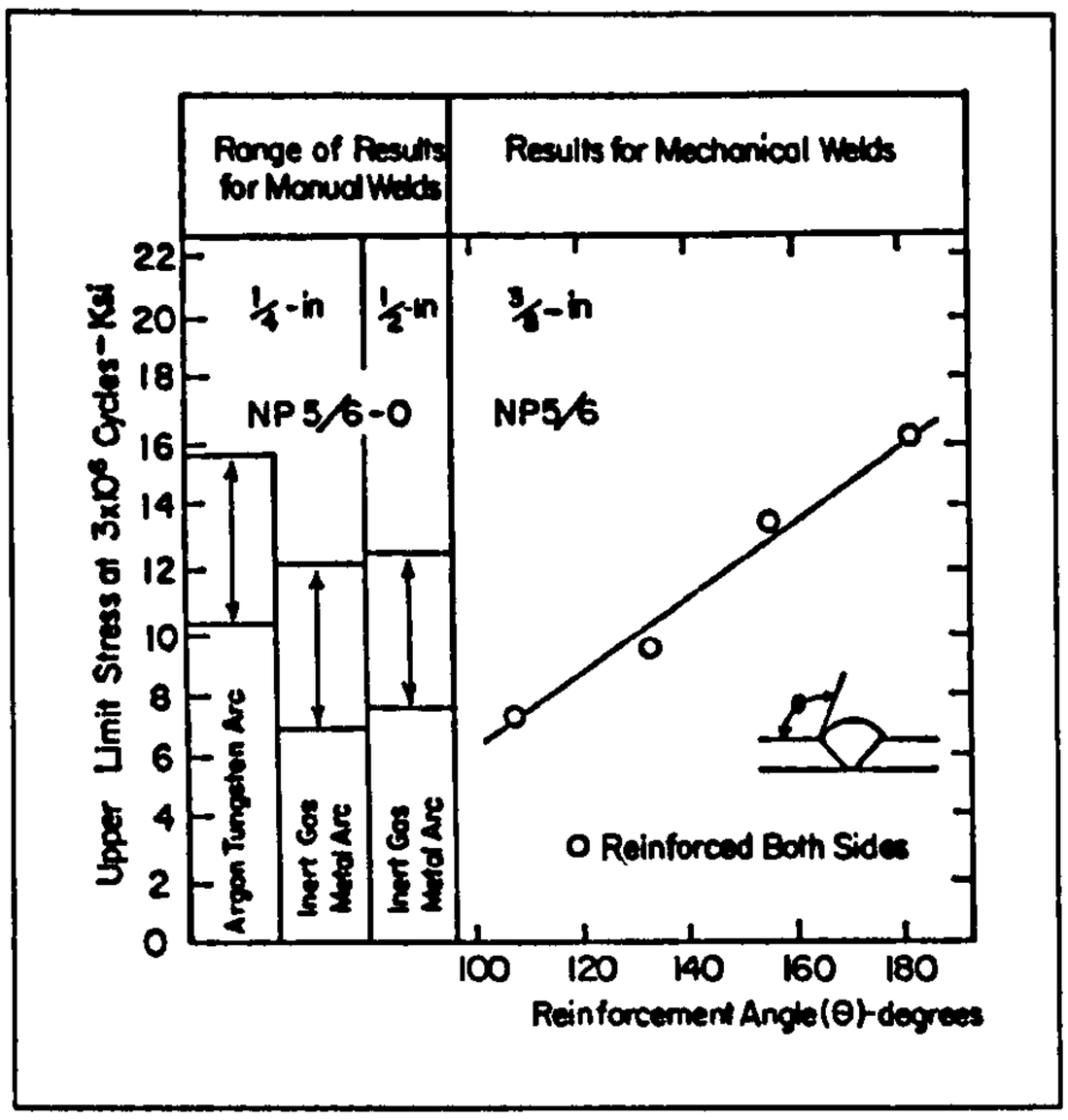

Figure 5.15: Effects of reinforcement angle on fatigue strength[1].

Mindlin[2] showed a significant increase in the fatigue strength of butt welded AA 5083-H113, tested in axial tension at R = 0, when the weld bead was removed, as shown in Figure 5.16. There was also a marked increase in the fatigue strength for a single sided weld in contrast to a two pass process, Masubuchi[3] suggesting that this type of response was due to the notch effects of the double reinforcement.

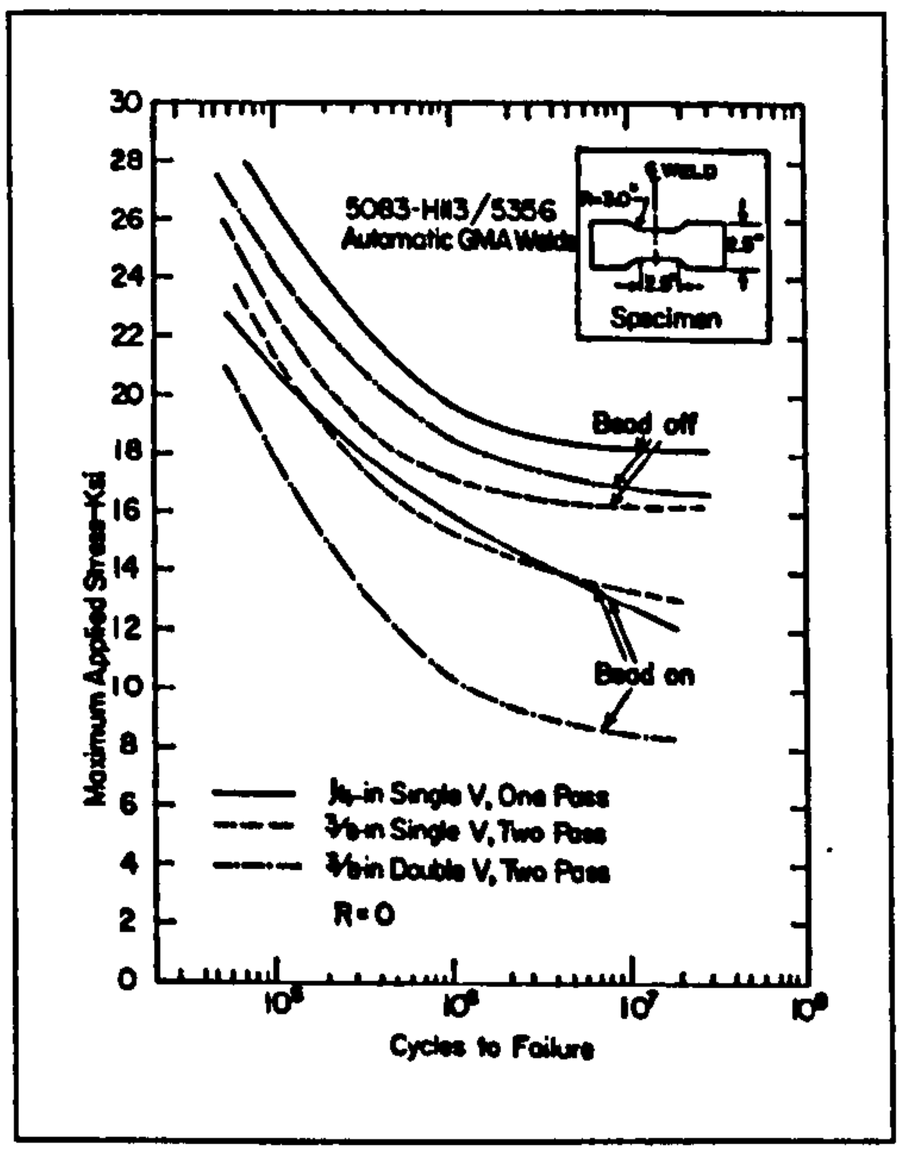

Figure 5.16: Effects of the weld bead on the fatigue strength of butt welded AA 5083-H113[2].

[1] Dinsdale, WO; Young, JG (1964) *referenced by Masubuchi, K (1980)*
[2] Mindlin, A (1963) *referenced by Masubuchi, K (1980)*
[3] Masubuchi, K (1980)

5.3.1.2.1 Weld Toe Profile Modification

Due to the influence that the weld bead exerts on the fatigue strength a considerable amount of research has been undertaken into improving the fatigue properties through the modification of the weld toe profile.

Modification of the weld toe profile in steel welds has two objectives, a reduction in the SCF and the removal of the intrusions at the weld toe[1]. The absence of weld toe defects in aluminium welds means that the process is employed solely to reduce the SCF, although the increased porosity found in aluminium welds can result in the process exposing pores with a resultant decrease in the fatigue strength being observed. Modification of the weld toe profile can be undertaken by a number of techniques, heavy disc, toe burr and full burr grinding[2] and TIG dressing[3,4,5,6] (peening[5] can also result in modification of the weld toe profile, although this is generally considered a secondary effect to the compressive residual stresses that it induces in the region treated).

Pang[7] states that weld toe grinding is the most common technique employed to increase the fatigue strength, although the technique tends to be both time consuming and expensive and is therefore frequently limited to critical welds. Weld toe grinding, involving the removal of between 0.8 - 1.0 mm of material from the weld toe, resulted in a reduction in the SCF as well as the removal of any crack like flaws and inclusions (these also being more typical in steel welds than aluminium ones). The SCF determined by the finite element method for a fillet weld, $\theta = 45°$, ranged from 3.309 for a weld toe radius, ρ, = 0.5 mm to 1.948 for $\rho = 5.0$ mm, leading to predicted improvements in the fatigue life of up to 53% for uniaxial tensile loading with $R = 0$. Woodley[2] declares that increases of 50%, 40% and 80% in the allowable design stress of a Class F detail ($N = 2 \times 10^6$ cycles) for heavy disc, toe burr and full burr grinding respectively can be obtained, although it is not indicated whether this relates only to steel welds.

TIG dressing involves the re-melting of the weld toe region to a shallow depth without the addition of filler material[6], the aim of the process being to increase the radius and reduce the angle of the weld toe. Improvements in the fatigue strength equivalent to an upgrading of two design classes, in BS 5400, at 2×10^6 cycles were quoted by Haagensen[6] for TIG dressing. Improvements in the fatigue lives of 3 - 5 times for fillet welded[8] and 2 - 3 times for butt welded[9] joints in AA 5083-H321 that had been TIG

---

[1] Booth GS (1983)
[2] Woodley, CC (1983)
[3] Polmear, IJ (1982)
[4] Polmear, IJ (1985)
[5] Wohlfahrt, H et al (1996)
[6] Haagensen, PJ (1982)
[7] Pang, HLJ (1994)
[8] Polmear, IJ (1985)
[9] Polmear, IJ (1982)

dressed have been reported by Polmear. Wohlfahrt et al[1] detail improvements in the fatigue life of 5 times for butt welded aluminium at 2×10^6 cycles, although there was no benefit at higher stresses.

Chapetti and Otegui[2] investigated the effect of controlling the waviness of the weld toe in automatic bead on plate welds on SAE 1010 low carbon steel. Fatigue testing was undertaken using three point loading with R = 0.2. The waviness was caused by rotating the arc, the degree of this being dependent on the rotational frequency, values of 0.5 to 2 Hz being stated. The typical geometry of a weld toe with induced waviness is shown in Figure 5.17.

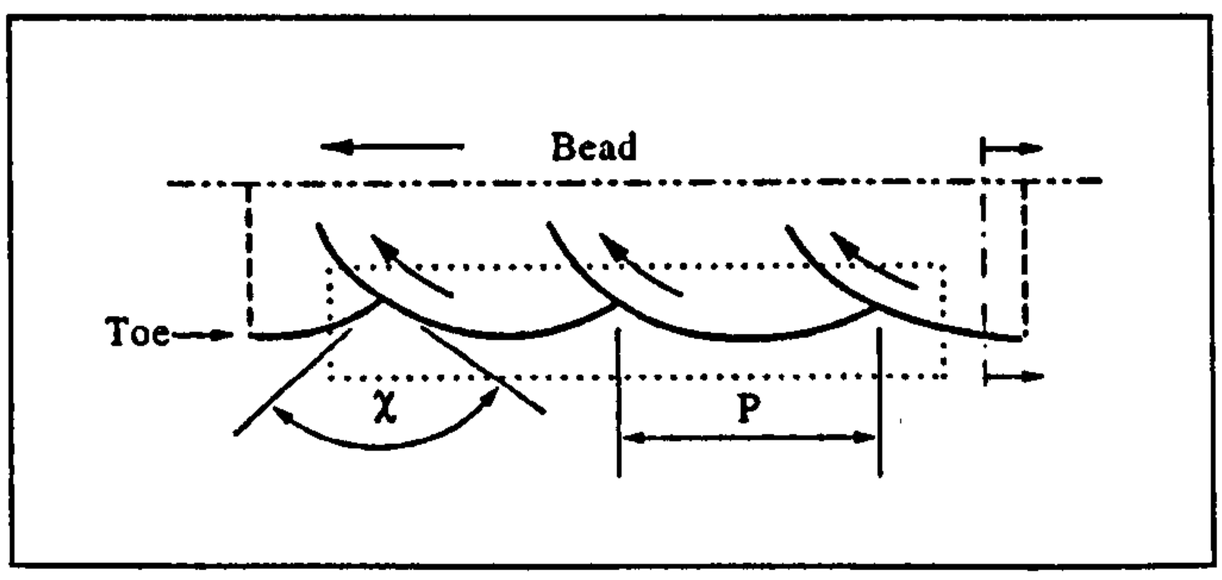

Figure 5.17: Weld toe macro geometry[2].

Propagation lives were shown to increase as the wave period, distance P in Figure 5.17, increased, although the subsequent reduction in χ (χ decreases as P increases) was stated as the basis for the increase in the propagation life[2]. For an optimal propagation life the authors stated that P should be kept to a minimum and χ at 100°. The authors hypothesise, with respect to crack propagation, that as χ reduces, the internal regions of the toe are able to act as crack anchors, delaying coalescence. Increases of 100% in the propagation lives are quoted for two stress amplitudes and P = 12 mm when compared to a straight weld toe profile[2]. All cracks were noted to propagate along the weld toe, although at small values of χ, the crack would bridge the adjacent toes near to the cusp region. Increases in crack initiation lives of up to 70% were observed, with the initiation sites being the external toe zones where the toe angles were lower and the radii greater than those for a straight toe. The maximum toe angles and minimum radii, where crack imitation would generally be considered to occur, were found at the internal points, where the two toes merged. The authors claimed that the cause of the non-initiation at the internal points was due to the angle, χ in Figure 5.17, between the merging toes, this varying from 90° to 180°. It was stated that cracks could not easily propagate along the toe because the direction of crack growth did not correlate with the maximum applied

---

[1] Wohlfahrt, H et al (1996)
[2] Chapetti, MD; Otegui, JL (1997)

stress[1]. Although not mentioned by the authors, the toe waviness would result in the internal points being shielded from the applied stress to some extent, resulting in a lower overall stress concentration. Details of the measured toe angles, χ, are not provided, so it is not possible to compare the initiation periods for given angles. The authors concluded that the weld toe radius and angle were only appropriate parameters, with respect to crack initiation, at the external points of the toe wave profile. From the experiments undertaken overall improvements in the total fatigue lives ranged from 127 - 192%[1]. Increasing the waviness of the weld toe will result in a larger weld bead and thus HAZ, although the authors do not comment on the effects that this may have on the fatigue properties.

Improving the profile of MIG welds can result in a quintupling of the fatigue strength, although the cost and time involved in the processes generally results in only the most critical of welds being treated. Weld improvement techniques that do not involve modification of the weld profile also exist, including ageing, to homogenise the microstructure, and peening, to modify the residual stress field[2], although due to the overriding influence of the weld profile on the fatigue strength these are frequently considered secondary processes. Due to the profile of FS welds, as detailed in Section 3.6, Geometry, Microstructure and Mechanical Properties (pages 47 - 109), they may be considered to evade many of the problems associated with MIG welds, although the scored surface that results from the rotational and transverse movement of the tool shoulder and the flash extruded at the edges of the tool shoulder can result in initiation sites due to localised stress concentrations. The effect of these can be seen in the fatigue strengths detailed in Table 5.6 for the as-welded and milled FS welds.

Further details with respect to the geometry of the weld profile are given in Section 3.2.1.2, Effects of the Weld Profile (pages 19 - 21).

---

[1] Chapetti, MD; Otegui, JL (1997)
[2] Bertini, L et al (1998)

5.4 S-N Testing

S-N specimens for four point loading, pure bending, were manufactured as shown in Figure 5.18. Specimens were produced from the parent plate, with the rolling direction running parallel to the 150 mm length of the specimen, PP //, and transverse to the length of the plate (as the welded specimens), PP |-. For the specimens produced from the welded plates the weld was positioned in the centre, with respect to 150 mm length. The weld profile, the weld bead in the case of the MIG welds and friction band surface in the case of the FS welds, was left intact. If any difference was apparent between the two sides of the MIG welds, ascertained through visual inspection, the tensile loading was applied to the side that it was expected would result in the lowest fatigue strength. In a similar manner tensile loading was applied to the friction band side of the SP weld and the 2nd pass side of the DP weld. This method of loading for the FS welds was intended to produce a "worst case scenario" that would be more applicable to industrial results rather than laboratory ones.

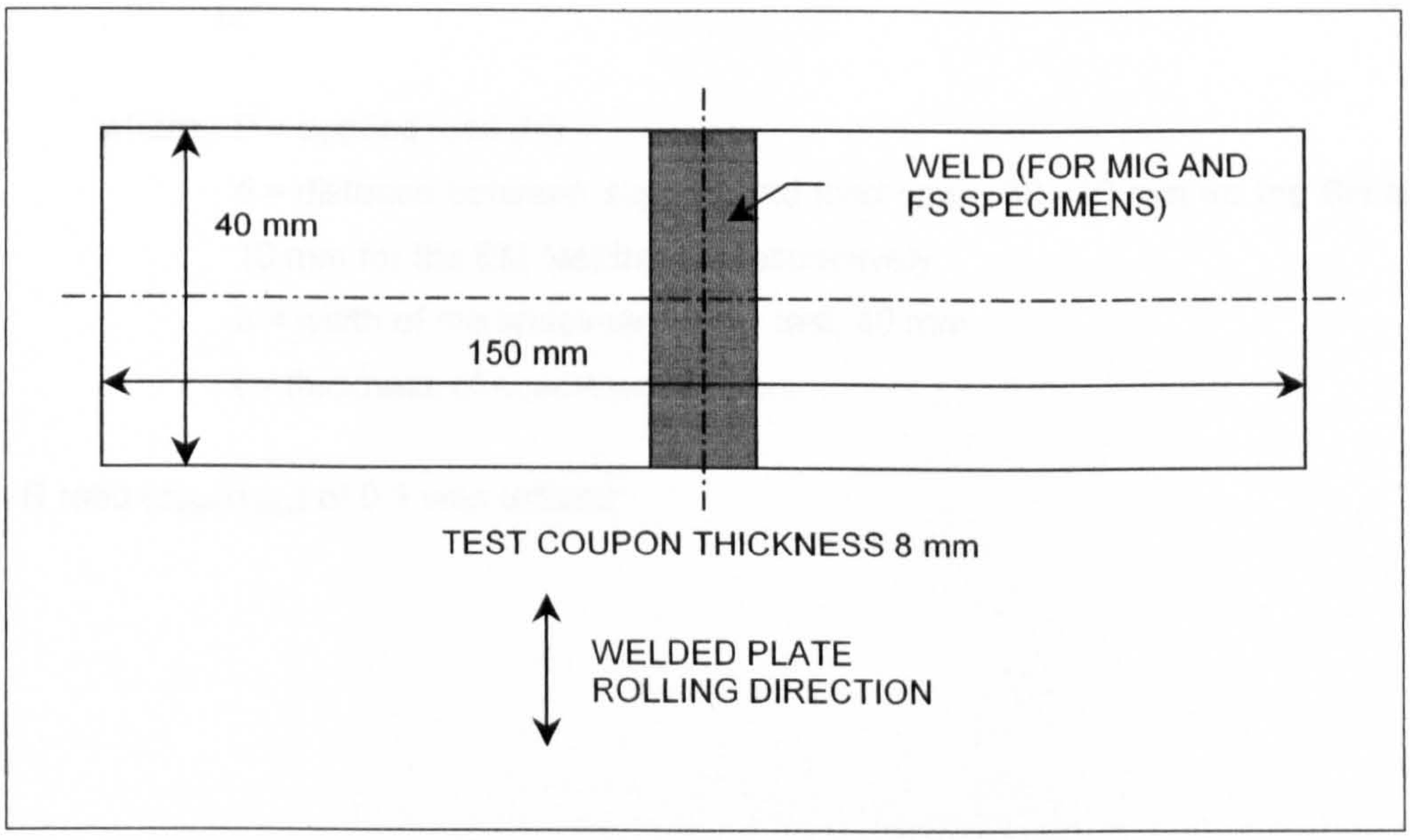

Figure 5.18: Four point load S-N test specimen.

5.4.1 Four Point Load Testing

Four point constant load amplitude S-N testing, for $N \leq 2 \times 10^6$, was undertaken on an Instron 8501 servo-hydraulic (SH) test frame, shown in Figure 5.20, utilising either an Instron 8500 or 8800 controller. For loads that resulted in lives between 10^6 - 10^7 cycles an Instron 1603 electro-magnetic resonance (EM) test frame was employed, shown in Figure 5.21. A ±10 KN load cell was employed in the SH frame and a ±20 KN load cell in the EM frame. The cyclic frequency was 25 Hz and 118 - 124 Hz for the SH and EM

frames respectively, both utilising a sinusoidal loading response, testing was undertaken at room temperature and in laboratory air.

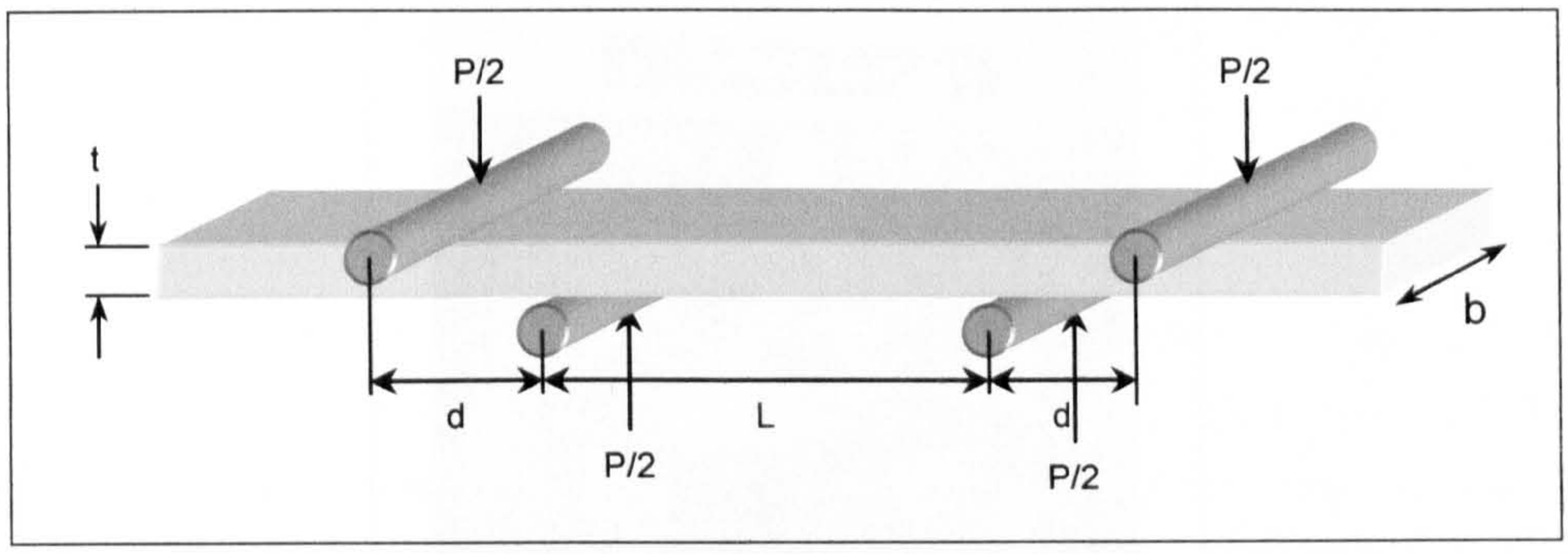

Figure 5.19: Four point loading geometry.

The maximum tensile stress, in the outer fibre, was determined from:

$$\sigma_{max} = \frac{3Pd}{bt^2} \tag{5.3}$$

where: P = applied load (N)

d = distance between support and load span, 30 - 40 mm for the SH and 10 mm for the EM test frames respectively.

b = width of the specimen under test, 40 mm.

t = thickness of specimen, ~ 8 mm

An R ratio ($\sigma_{min}/\sigma_{max}$) of 0.1 was utilised.

Figure 5.20: Instron 8501 servo-hydraulic test frame with four point bend apparatus in position.

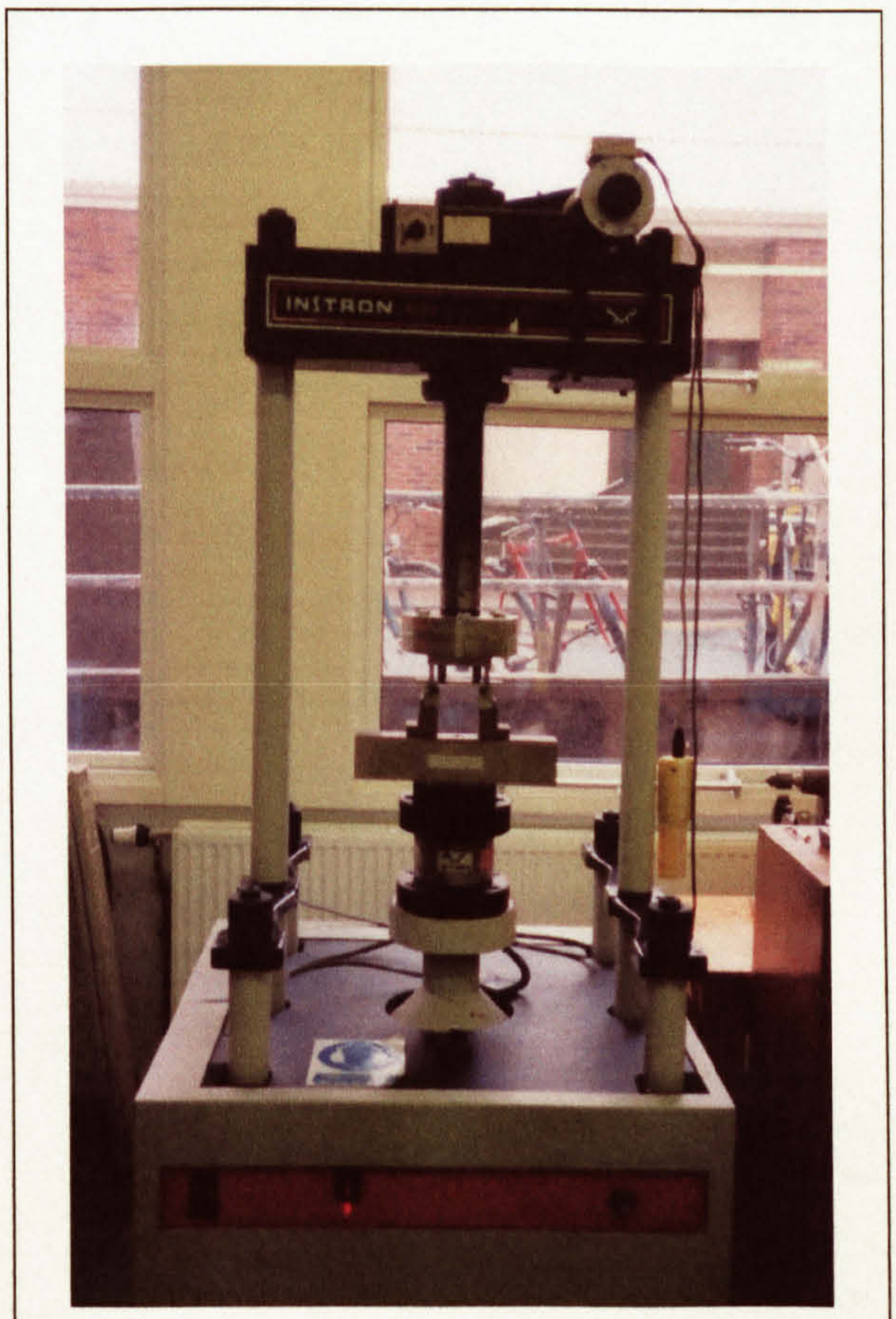

Figure 5.21: Instron 1603 electro-magnetic resonance test frame with four point bend apparatus in position.

Due to the low R ratio employed, 0.1, and the consequent low minimum load, it was found that the slight distortion in the welded specimens resulted in the specimen moving between the rollers during testing. To overcome the problem a small jig was constructed, shown in Figure 5.22, to prevent lateral movement of the specimen. With the specimen in position on the lower rollers the four bolts were moved to allow a minimal amount of lateral movement of the specimen, these were then held in place using locking nuts. The bolts were not tightened against the specimen as it was thought that excessive friction between the bolt and specimen surface may have resulted in failure initiating from this point or failure of the bolt. It may be argued that the loading should take into consideration the distortion of the specimen, although this was not considered a requirement for the research being undertaken.

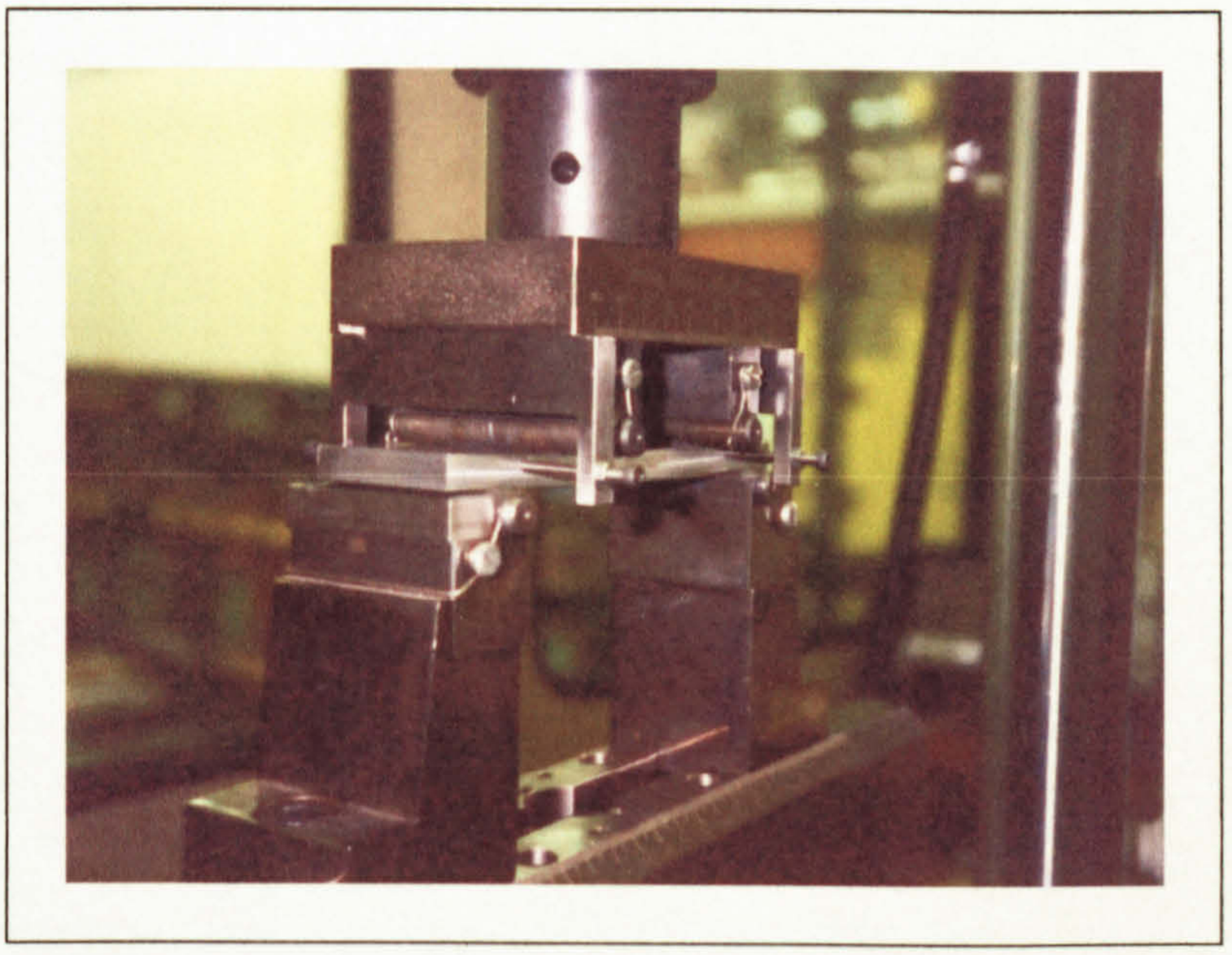

Figure 5.22: Jig to align S-N specimens.

5.4.2 MIG Weld Toe Stress Concentration Factors

To determine the stress concentrating effect of the MIG weld toe finite element analysis (FEA) was undertaken with the results being compared to those returned by an equation detailed by Yung and Lawrence[1] and published values[2,3,4]. FEA was undertaken using Ansys 5.61 software.

---

[1] Yung, J-Y; Lawrence, FV (1985)
[2] Brandt, U et al (2001)
[3] Bertini, L et al (1998)
[4] Niu, X; Glinka, G (1987)

The geometry of the weld toes was determined from the measurements detailed in Section 3.6, Geometry, Microstructure and Mechanical Properties (pages 56 and 69) and summarised in Table 5.8.

	LI		HI	
	Radius (μm)	**Angle (°)**	**Radius (μm)**	**Angle (°)**
Minimum	1030	6	160	30.5
Maximum	4080	26.5	1210	51.5
Mean	2381	13.9	641	39.7

Table 5.8: MIG weld toe radii and angles.

The elastic SCF, K_t, for the toe of a butt weld subject to bending was calculated by means of equation (5.4)[1] and are given in Table 5.9:

$$K_t = \beta\left[1+\alpha\left(t/r\right)^{\lambda}\right] \qquad (5.4)$$

where: α, β and λ are material constants, for a butt weld transversely loaded in bending:

$\alpha = 0.165(\tan\theta)^{0.167}$

θ = weld bead angle (as shown in Figure 5.24)

$\beta = 1$

$\lambda = 0.5$

t = plate thickness, 8 mm

r = notch root radius (mm)

Due to the difficulty in measuring the weld toe radii and angles and the variability of these it has been assumed that all scenarios, with respect to the measurements, may exist and that best, mean and worst case scenarios would exist through combining the appropriate values. With respect to the K_t values shown in Table 5.9, the theoretical values relate to the worst case that could exist, this resulting from the smallest weld toe radii measured in combination with the largest angle measured, although these may not have been measured at the same point. Whereas the actual values were calculated from the radius and angle that were measured at a particular point, therefore $K_{t\ actual} \leq K_{t\ theoretical}$ for the worst case scenario and vice versa for the best case scenario.

[1] Yung, J-Y; Lawrence, FV (1985)

Scenario	LI			HI		
	Radius (μm)	Angle (°)	K_t theoretical (actual)	Radius (μm)	Angle (°)	K_t theoretical (actual)
Best	4080	6	1.159 (1.159)	1210	30.5	1.388 (1.411)
Mean	2381	13.9	1.239 (1.256)	641	39.7	1.565 (1.637)
Worst	1030	26.5	1.409 (1.369)	160	51.5	2.212 (2.160)

Table 5.9: Assumed scenarios due to variations in the MIG weld toe radii and angles.

Assuming a worst case scenario resulted in the value of K_t being 2.9% greater than the actual worst case measured for the LI process ($r = 1030$ μm, $\theta = 15°$) and 2.4% greater for the HI process ($r = 160$ μm, $\theta = 44°$).

For both the LI and HI processes two FEA models were made for each of the best, mean and worst case scenarios. Both analyses were undertaken utilising a twenty point elastic-plastic stress/strain response based on that shown in Figure 5.23 and detailed in Table 5.10; due to the stress-strain responses for both the LI and HI welds being near identical, as shown in Section 3.7.3.2, Tensile Properties (page 119), it was decided that one response would suffice for both models. Analyses were undertaken for loads ranging from 1.0 - 9.0 KN, giving a stress in the outer fibre of plate (8 mm thickness) remote to the weld of 35 - 233 MPa.

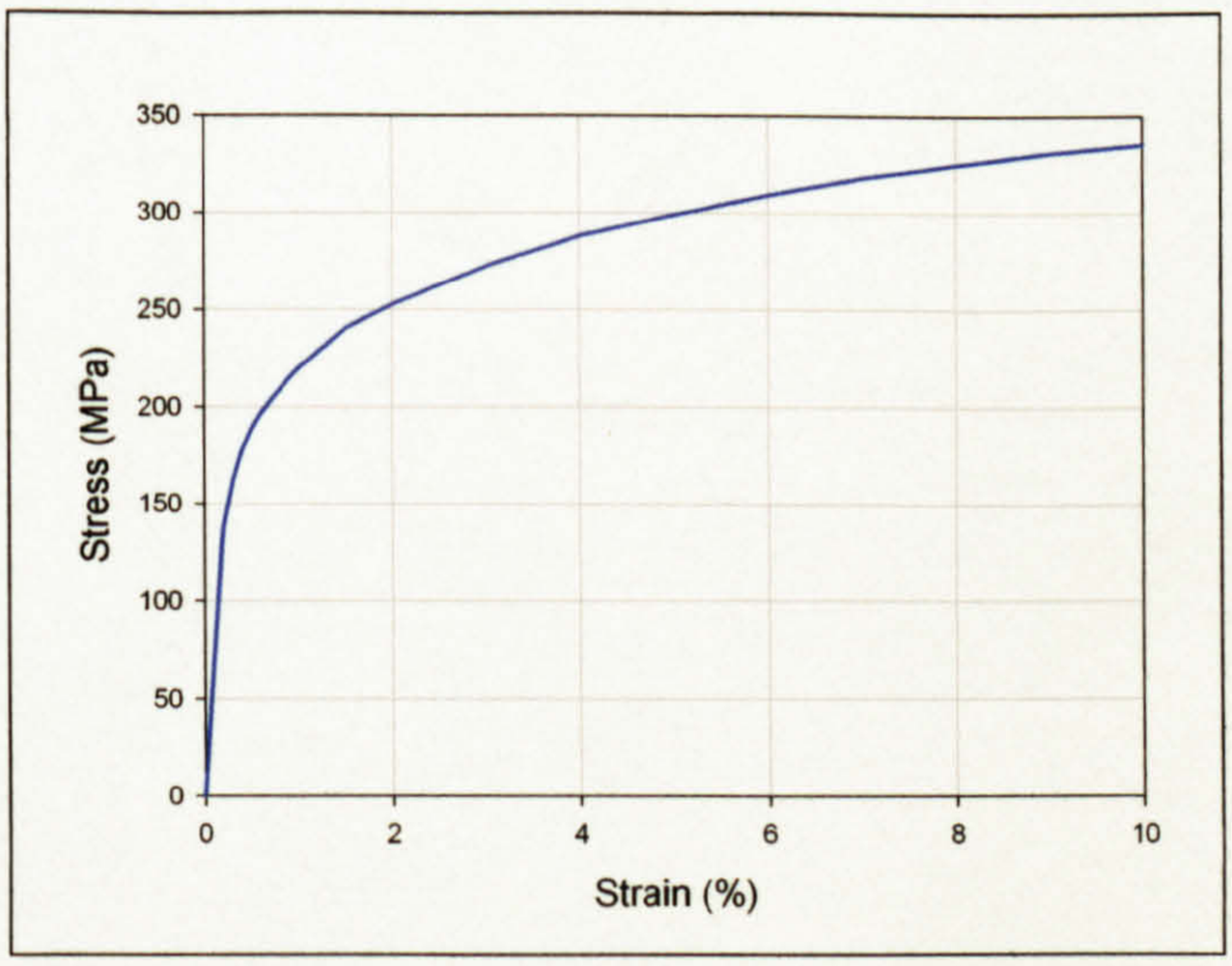

Figure 5.23: Elastic-plastic stress-strain response for MIG welds.

E = 70 GPa, σ_Y = 128 MPa							
ε (%)	σ (MPa)	ε (%)	σ (MPa)	ε (%)	σ (MPa)	ε (%)	σ (MPa)
0.183	128.1	0.6	196.8	1.5	240.2	6.0	309.0
0.2	138.0	0.7	203.1	2.0	252.6	7.0	317.7
0.3	161.4	0.8	208.8	3.0	272.2	8.0	324.6
0.4	177.8	0.9	214.4	4.0	287.9	9.0	330.5
0.5	188.9	1.0	219.7	5.0	298.8	10.0	334.7

Table 5.10: Elastic-plastic stress/strain response for MIG welds.

The initial technique utilised the weld toe angle and radius to produce a trapezoidal protuberance on a member subjected to pure bending, as shown schematically in Figure 5.24. FEA models showing the deformed weld and weld toe detail are shown in Figure 5.25 and Figure 5.26. The FEA models were meshed with PLANE2 elements (2-d, 6-node, triangular structural solid with 2 degrees of freedom at each node), the number of elements ranging from 1448 - 1460 elements per model and the number of nodes from 3095 - 3117.

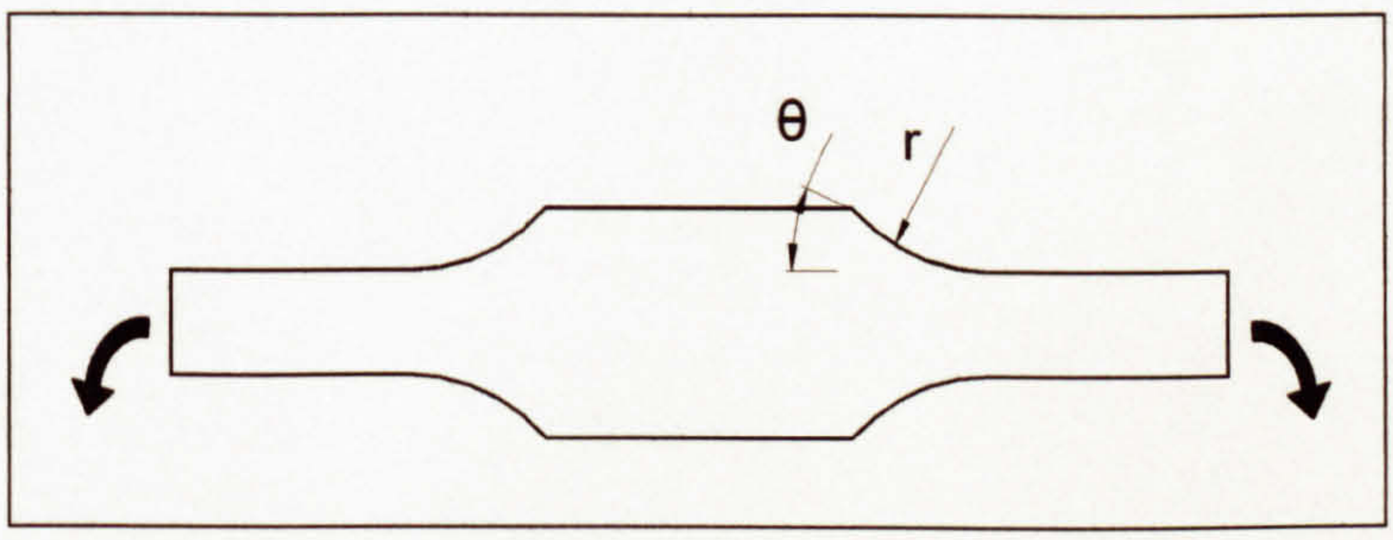

Figure 5.24: Schematic representation of a weld toe angle and radius subject to bending.

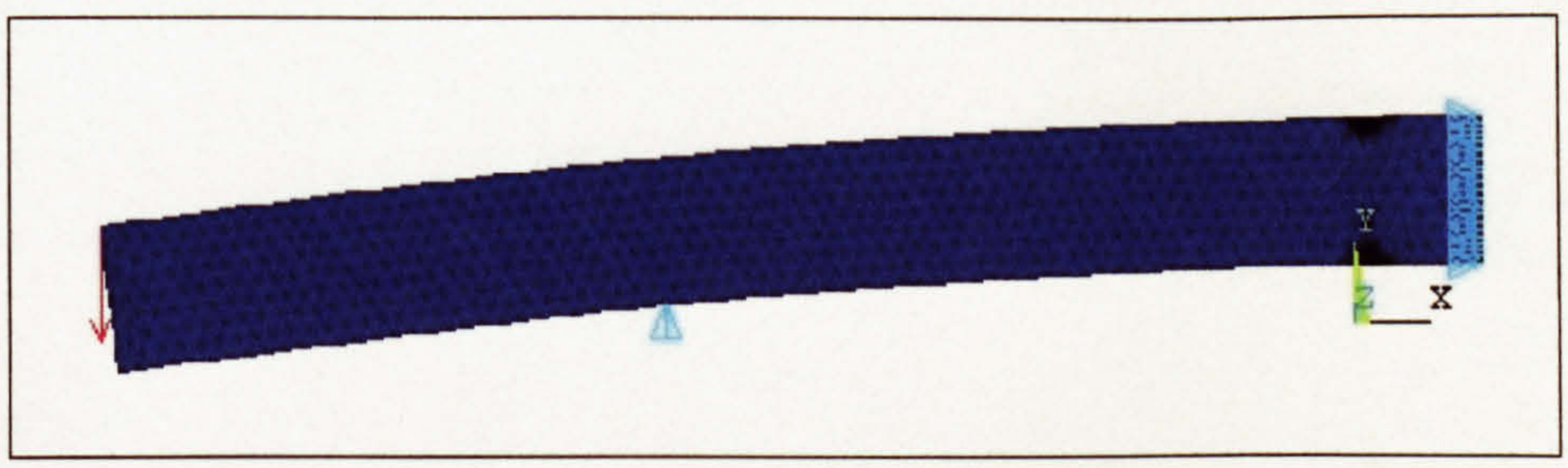

Figure 5.25: FEA model, utilising both weld toe angle and radius, used to determine K_t at the weld toe of a MIG HI (worst case scenario) subjected to pure bending.

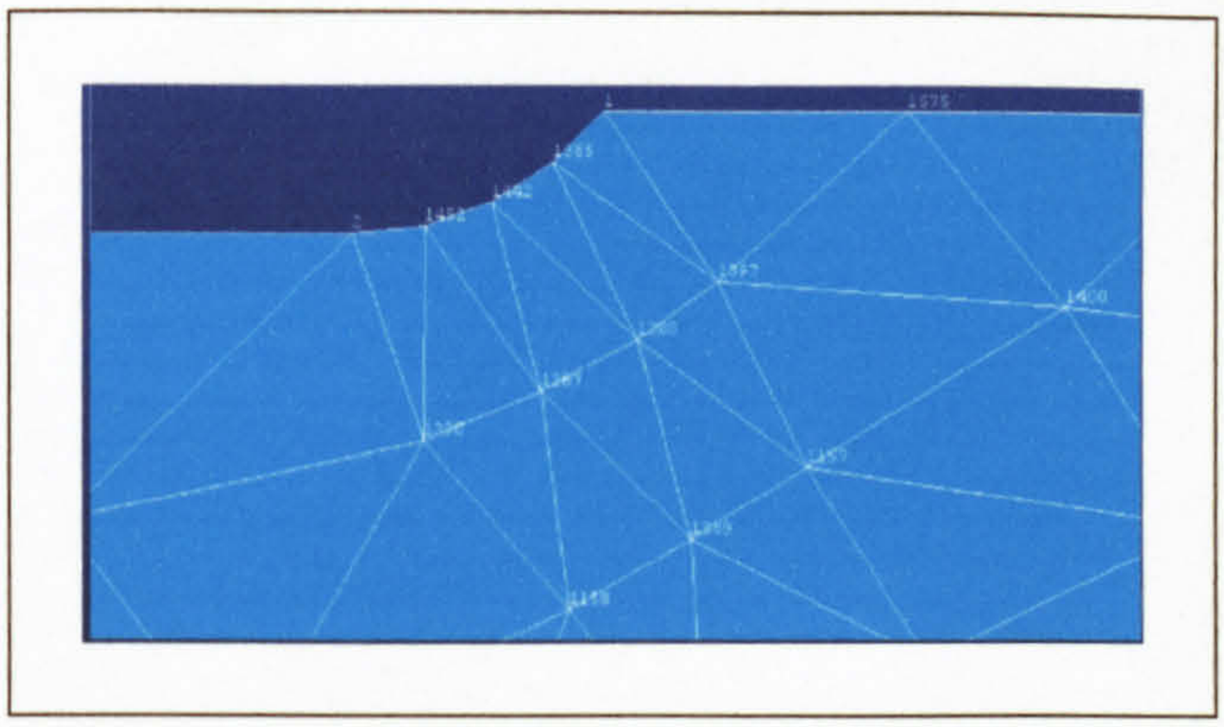

Figure 5.26: FEA model weld toe detail, utilising both the toe angle and radius, used to determine K_t at the weld toe of a MIG HI (worst case scenario) subjected to pure bending.

Scenario	SCF (K_t)					
	LI			HI		
	FEA	Equation (5.4)	FEA/Equation (5.4) (%)	FEA	Equation (5.4)	FEA/Equation (5.4) (%)
Best	1.074	1.159	92.7	1.257	1.388	90.6
Mean	1.155	1.239	93.2	1.331	1.565	85.1
Worst	1.273	1.409	90.4	1.354	2.212	61.2

Table 5.11: MIG weld toe elastic SCF, determined by FEA utilising both the weld toe angle and radius and through equation (5.4).

The elastic K_t values obtained from the FEA and those from the equation (5.4), $K_t = \beta[1 + \alpha(t/r)^{\lambda}]$, both utilising the same weld toe angle and radius, are shown in Table 5.11, with the elastic-plastic responses from the FEA being shown in Figure 5.27. From the elastic results it was evident that the values from the FEA were 7.3 - 9.6% lower than the values calculated by equation (5.4) for the LI weld and 9.4 - 38.8% lower for the HI weld.

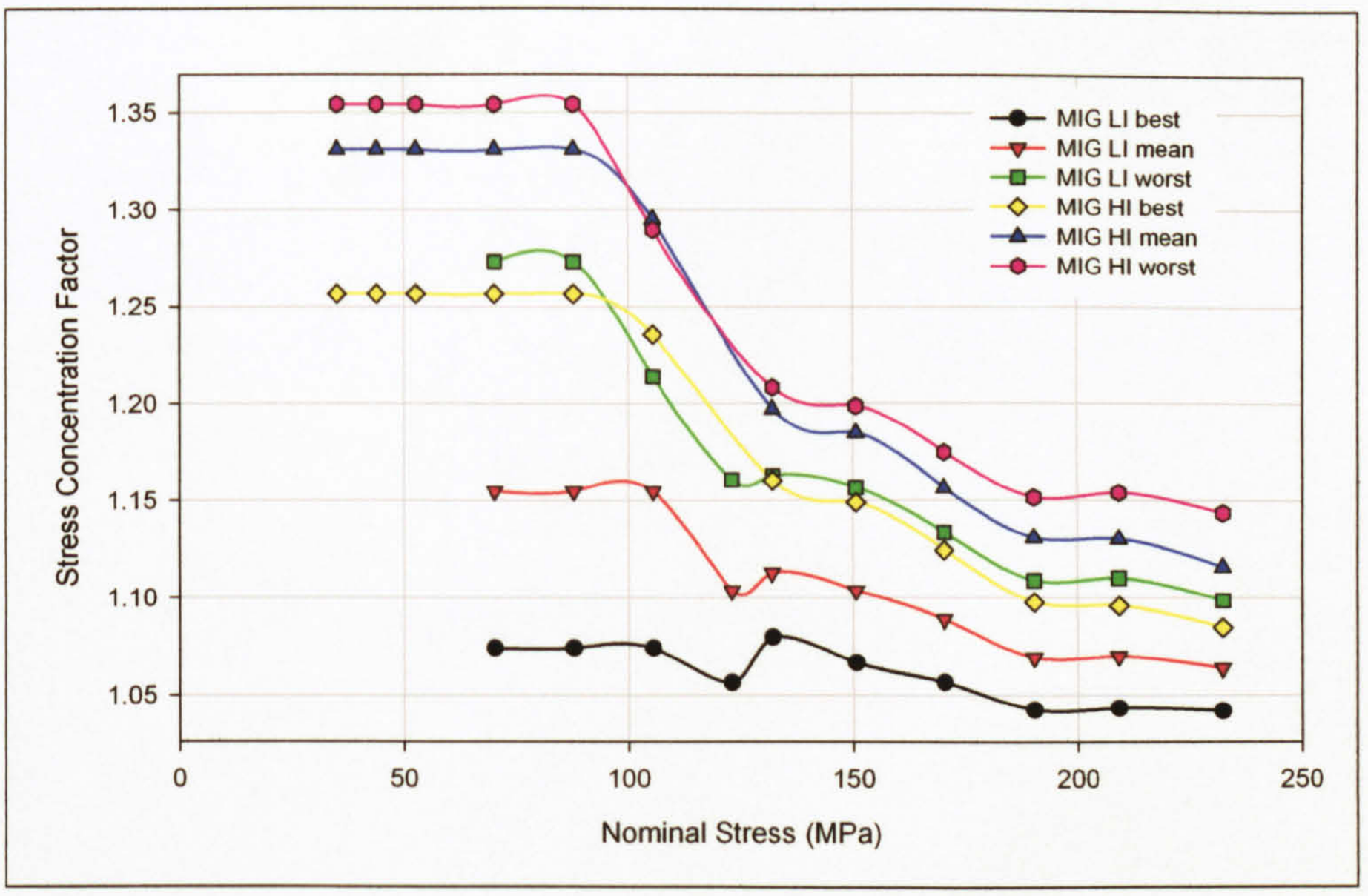

Figure 5.27: Weld toe elastic-plastic SCF for FEA of weld geometry utilising the weld toe radius and angle to produce a trapezoidal protuberance subject to pure bending.

Although the elastic K_t values for the LI weld compared favourably with those from equation (5.4) the HI values compared less favourably, notably for the worst case scenario. In an attempt to enhance the K_t results the FEA models were refined using geometry based on the weld toe angle and weld bead. The weld toe radius is considered to have a greater effect on crack initiation than the toe angle, the toe angle being considered to have a greater effect on crack growth[1]. The models were based on weld bead outlines determined in a similar manner to those used for determining the weld toe angles and radii, as detailed in Section 3.5.2, Surface Topography and Weld Geometry (page 37). The LI geometry, shown in Figure 5.28, was considered to have a weld bead of fixed radius of 15 mm, the radius centre being ±10.25 mm from the plate centreline. The weld toe radius, varying for the three scenarios, was then assumed to intersect both the weld bead and parent plate tangentially, the deformed FEA model being shown in Figure 5.29. The HI geometry consisted of a weld bead of fixed radius of 7.5 mm and a centre at the mid section of the plate, as shown in Figure 5.30. The weld toe radius, varying for the three scenarios, was again assumed to intersect both the weld bead and plate tangentially, the deformed FEA geometry shown in Figure 5.31. This technique results in the weld toe angle being dependent on the weld bead geometry and weld toe radius, therefore the angle for the FEA is represented by θ', rather than the angle measured at the same point as the radius, θ. For the geometries utilised for the three scenarios for each weld process the FEA weld toe angles, θ', fell within a small range, from 16.1° - 17.6° for the LI process and 52.0° - 55.8° for the HI process. The FEA

[1] Niu, X; Glinka, G (1987)

models were again meshed with PLANE2 elements (2-d, 6-node, triangular structural solid with 2 degrees of freedom at each node), the number of elements ranging from 1234 - 1396 elements per model and the number of nodes from 2633 - 2963.

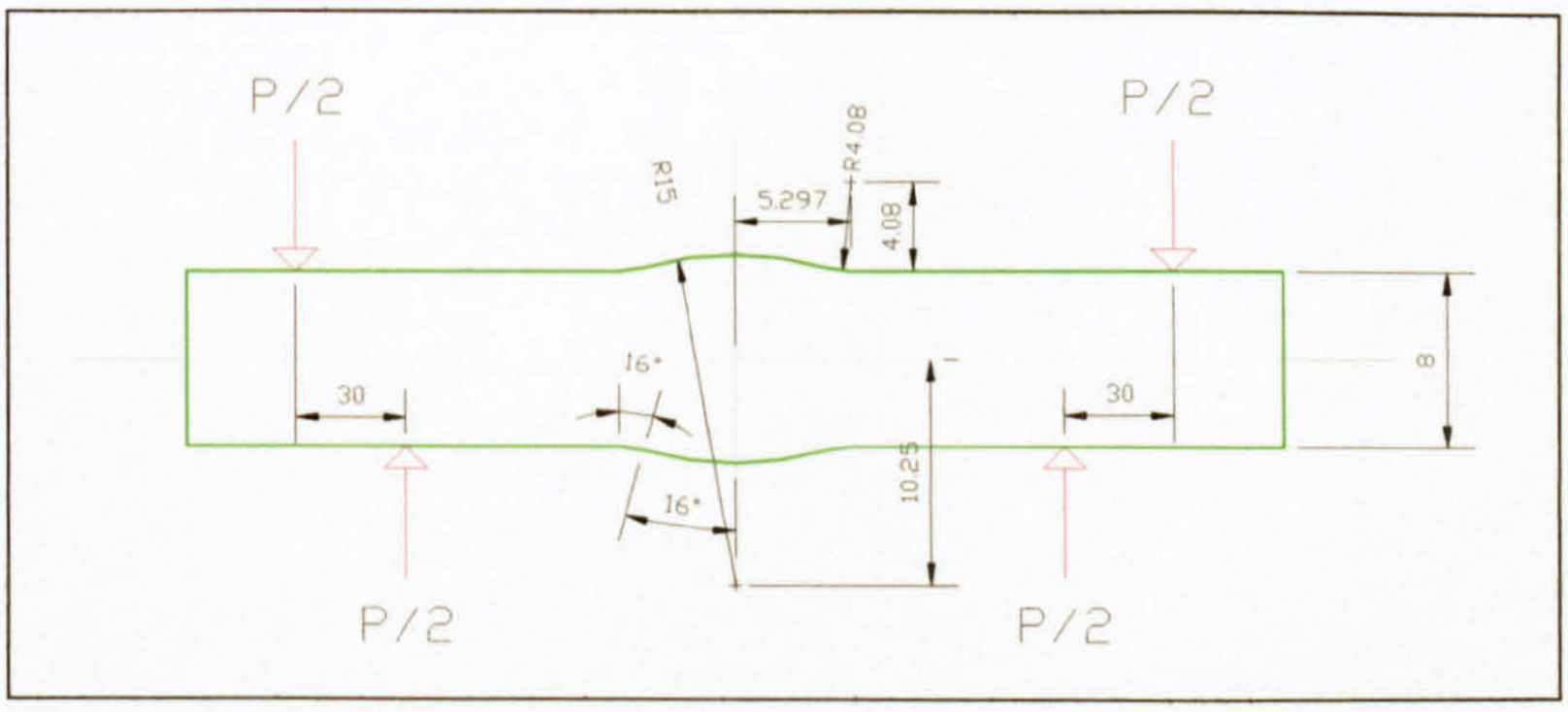

Figure 5.28: MIG LI (best case scenario, r = 4.08 mm) weld geometry utilising constant weld bead geometry and tangentially intersecting weld toe radius, θ' = 16°.

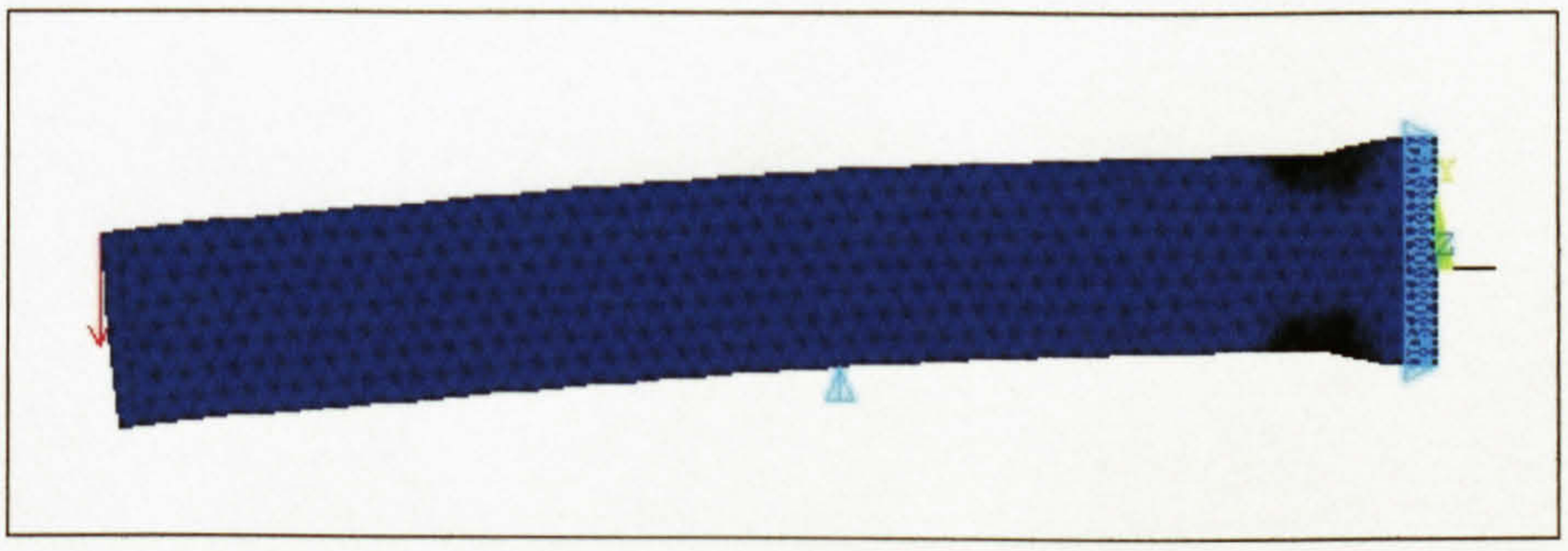

Figure 5.29: FEA model utilising constant weld bead geometry and tangentially intersecting weld toe radius used to determine K_t at the weld toe of a MIG LI (worst case scenario) subjected to pure bending.

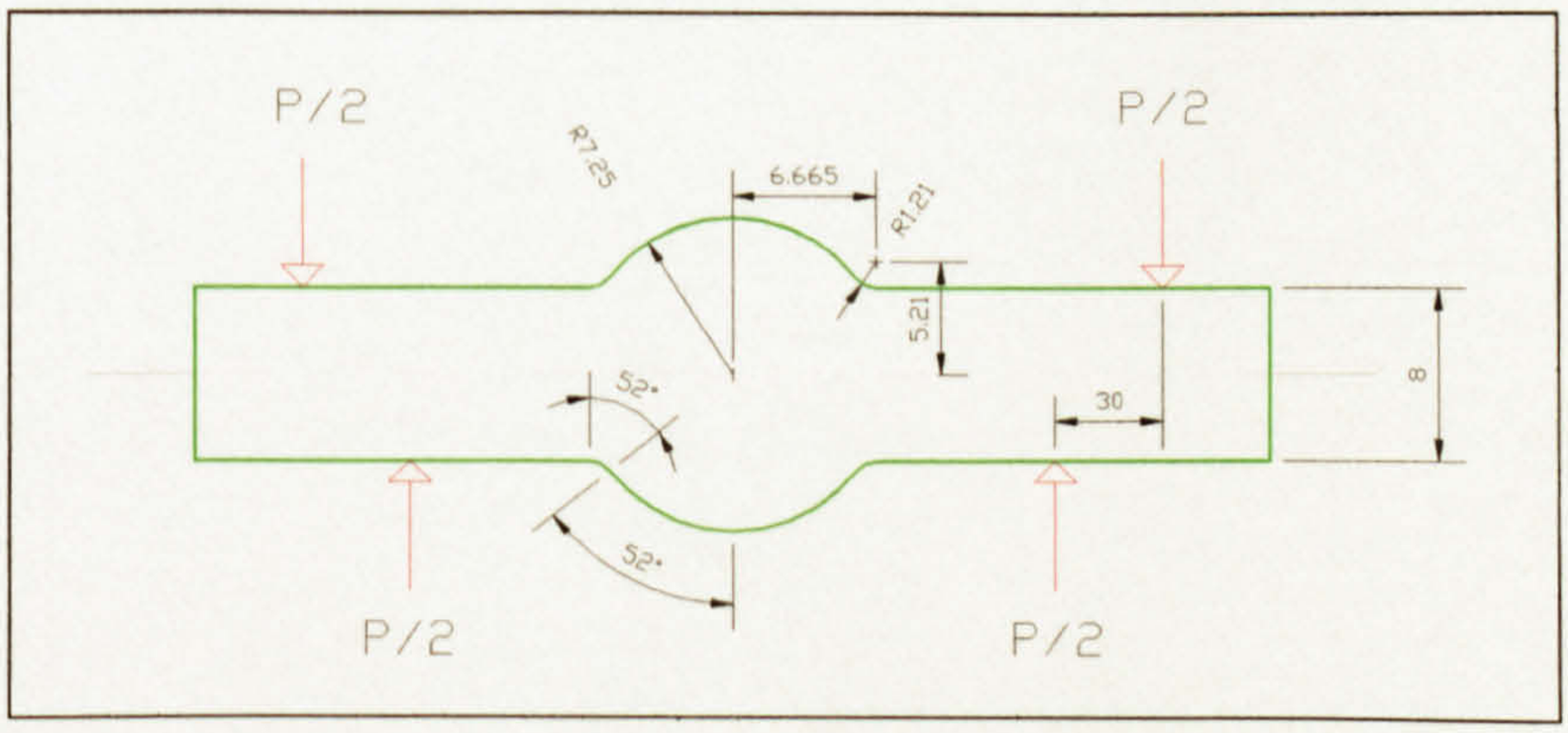

Figure 5.30: MIG HI (best case scenario, r = 1.21 mm) weld geometry utilising constant weld bead geometry and tangentially intersecting weld toe radius, θ' = 52°.

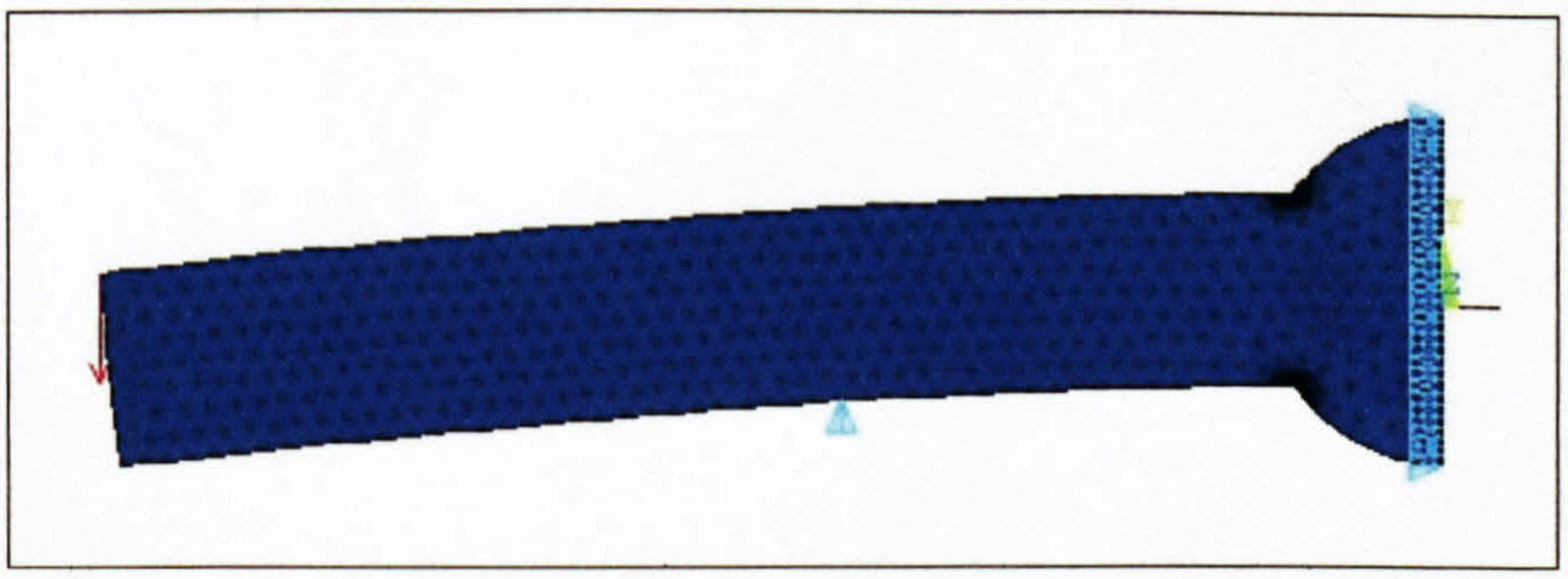

Figure 5.31: FEA model utilising constant weld bead geometry and tangentially intersecting weld toe radius used to determine K_t at the weld toe of a MIG HI (worst case scenario) subjected to pure bending.

The values for the elastic K_t determined through FEA for the refined model are shown in Table 5.12, the equivalent elastic-plastic values being shown in Figure 5.32. The values determined through FEA for the LI weld were slightly greater, 2.6 - 5.0%, than those determined through equation (5.4), although if θ is considered to be the toe angle in equation (5.4) the disparity between the values increased slightly to 2.8 - 5.2% greater. For the HI weld the FEA values were 10.1 - 25.2% greater, although these increased slightly to 16.9 - 27.1% when θ was employed in equation (5.4).

Scenario	SCF (K_t)					
	LI			HI		
	FEA	Equation (5.4) θ' (θ)	FEA/Equation (5.4) (%) θ' (θ)	FEA	Equation (5.4) θ' (θ)	FEA/Equation (5.4) (%) θ' (θ)
Best	1.219	1.188 (1.159)	102.6 (105.2)	1.587	1.442 (1.358)	110.1 (116.9)
Mean	1.296	1.248 (1.239)	103.9 (104.6)	1.860	1.615 (1.565)	115.2 (118.9)
Worst	1.449	1.380 (1.409)	105.0 (102.8)	2.811	2.245 (2.212)	125.2 (127.1)

Table 5.12: MIG weld toe elastic SCF, due to bending, determined by FEA utilising a tangential intersect between the weld toe radius and weld bead/parent plate and equation (5.4).

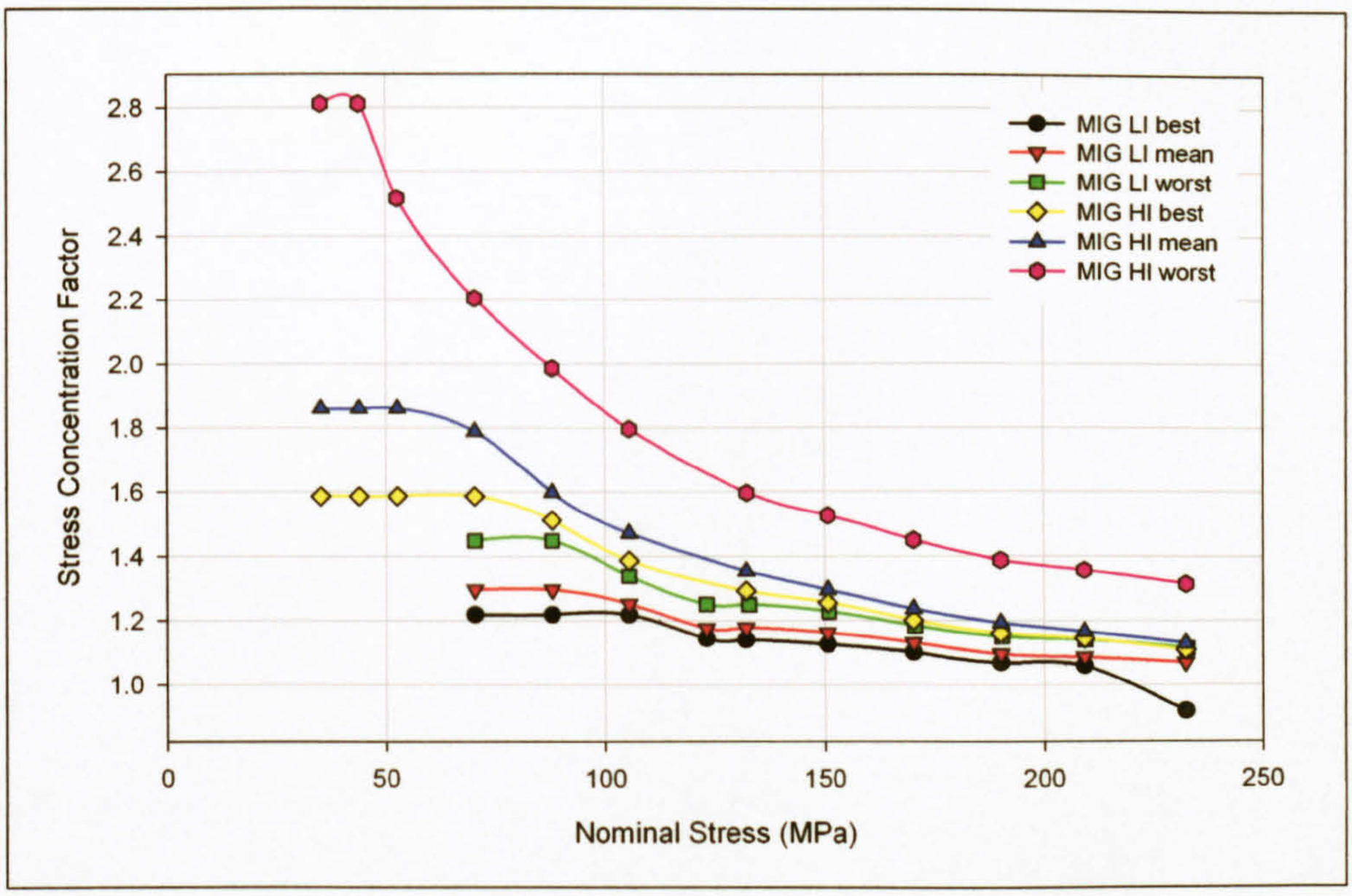

Figure 5.32: Weld toe elastic-plastic SCF/applied stress for FEA utilising a tangential intersect between the weld toe radius and weld bead/parent plate.

The results for both the FEA models and values obtained through utilisation of equation (5.4) are summarised in Table 5.13:

Scenario	LI				HI			
	FEA		Equation (5.4)		FEA		Equation (5.4)	
	Radius & angle	Toe & bead radii	θ	θ'	Radius & angle	Toe & bead radii	θ	θ'
Best	1.074	1.219	1.159	1.188	1.257	1.587	1.358	1.442
Mean	1.155	1.296	1.239	1.248	1.331	1.860	1.565	1.615
Worst	1.273	1.449	1.409	1.380	1.354	2.811	2.212	2.245

Table 5.13: Summary of MIG weld toe elastic SCF, due to bending, determined through FEA and equation (5.4).

From Table 5.13 it was evident that the magnitude of K_t obtained from the FEA utilising both the weld toe angle, θ, and radius was less than the values obtained from equation (5.4), this being particularly evident for the mean and worst case scenarios for both the LI and HI welds. The values obtained from the FEA utilising the weld bead and toe radii returned values that were greater than those obtained from equation (5.4); although the values were more comparable than those obtained from the FEA utilising the weld toe radius and angle.

In an attempt to clarify the variation in the values obtained for K_t between the FEA results and equation (5.4) a uniaxial tensile load FEA was undertaken for both model types and

this was compared to equation (5.4) with the material constant, $\alpha = 0.27(\tan\theta)^{0.25}$ (for bending $\alpha = 0.165(\tan\theta)^{0.167}$)[1]. The results from tensile analyses are detailed in Table 5.14.

Scenario	LI					
	Weld toe radius & angle, θ			Weld toe & bead radii (θ')		
	FEA	Equation (5.4)	FEA/Equation (5.4) (%)	FEA	Equation (5.4)	FEA/Equation (5.4) (%)
Best	1.07	1.22	87.7	1.32	1.28	103.1
Mean	1.15	1.35	85.2	1.41	1.37	102.9
Worst	1.27	1.63	77.9	1.59	1.57	101.3
Scenario	**HI**					
	Weld toe radius & angle, θ			Weld toe & bead radii (θ')		
Best	1.28	1.61	79.5	1.93	1.74	110.9
Mean	1.36	1.91	71.2	2.28	2.03	112.3
Worst	1.42	3.02	47.0	2.74	3.10	88.4

Table 5.14: Summary of MIG weld toe elastic SCF, due to uniaxial tensile loading, determined through FEA and equation (5.4).

From the uniaxial tensile analyses results detailed in Table 5.14 it was evident that the FEA utilising the weld toe radius and angle, θ, returned SCF results that were lower than those returned by equation (5.4), with the reduction ranging from 12.3 - 22.1% for the LI weld and 20.5 - 53.0% for the HI weld. The analyses employing the weld bead and toe radii returned values that were slightly greater than those from equation (5.4) for the LI process, 1.3 - 3.3%. The HI process returned values that were 10.9 - 12.3% greater for the best and mean case scenarios, whilst the worst case scenario returned a value that was 11.6% less than that returned by equation (5.4). From the uniaxial tensile FEA results it was apparent that the FEA model utilising the weld toe and bead geometry returned K_t values that were more comparable to those attained from equation (5.4) than those returned by the FEA model employing the weld toe radius and angle.

On the basis of the FEA results for both the bend and uniaxial tension tests and SCF detailed by Brandt et al[2] ($K_t = 1.4$), Bertini et al[3] ($K_t = 1.7 - 1.9$) and Niu and Glinka[4] (K_t = 2.6 - 3.3 for a fillet weld) it was decided to proceed with the FEA model based on a fixed geometry for the weld bead and variable weld toe radius utilising the values obtained for the worst case scenario. The worst case scenario was chosen as it was considered that the weld toe geometry would consist of the complete range of weld toe angles and radii measured and therefore the worst case scenario would be more likely to include the site where crack initiation would commence. It could be eloquently argued that the mean

[1] Yung, J-Y; Lawrence, FV (1985)
[2] Brandt, U et al (2001)
[3] Bertini, L et al (1998)
[4] Niu, X; Glinka, G (1987)

case scenario should be utilised, as subsequent curve fitting through the S-N data results in a curve of best fit, and this, by its nature, is representative of a mean response. As further weld toe geometry data becomes available the model will be able to be further enhanced, possibly encompassing a complete range of scenarios for a given weld. The FEA analysis based on the weld bead and toe radii was chosen for subsequent analyses on the basis that it returned conservative results with respect to the fatigue analysis, compared to the initial analysis utilising the weld toe radius and angle and because the results obtained were also of a more comparable magnitude to those returned by equation (5.4). Figure 5.33 and Table 6.3 detail the SCF for both MIG weld toes for both the elastic and plastic state, the equations for the plastic response being determined through TableCurve 2D V5.00 software.

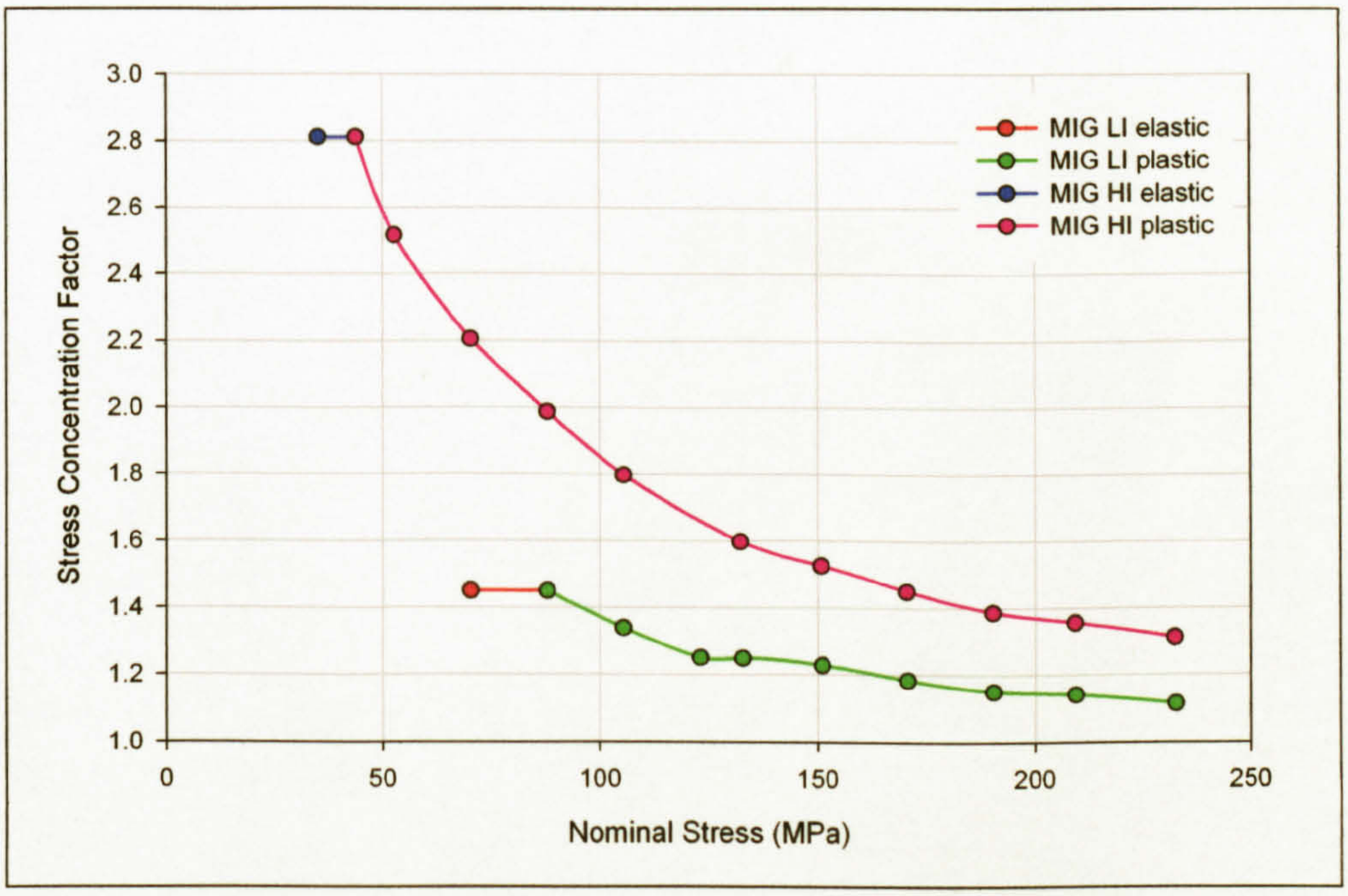

Figure 5.33: FEA elastic/plastic SCF, worst case scenario, for MIG weld toe.

Weld process	Elastic SCF		Plastic SCF	
	Nominal stress (MPa)	SCF	Nominal stress (MPa)	SCF (σ = nominal stress)
LI	≤ 87.26	$K_t = 1.449$	> 87.26	$K_t = \left(1.014 + \frac{-28.278}{\sigma}\right)^{-1}$
HI	≤ 43.77	$K_t = 2.811$	> 43.77	$K_t = 0.733 + \left(24.067 \times \left(\frac{\ln\sigma}{\sigma}\right)\right)$

Table 5.15: Elastic and plastic SCF for MIG welds.

To determine the stress at the toe of the MIG welds the nominal stress, that found in the outer fibre of the 8 mm thick specimens, was multiplied by the appropriate value for K_t as shown in Figure 5.33 and Table 5.15. The stress concentrating effect of the weld toe has

been considered to be constant throughout the life of the crack, although in reality it would, with respect to crack growth, have varied as the crack propagated. Although analyses taking this effect into consideration may be undertaken, it was considered to be outwith the scope of the current research.

5.5 S-N Test Results

The results from S-N tests of the parent material and as-welded specimens were as shown in Figure 5.34, in the case of the parent plate and Figure 5.44 and Figure 5.58 for the MIG and FS welds respectively, with the individual specimen results being given in Table 12.1 - Table 12.6 of Section 12, Appendix B ~ S-N Test Specimen Results (pages 500 - 505). Fractographs detailing various aspects of the fracture surfaces are shown as Figure 5.35 - Figure 5.79.

The curves fitted through the data were all based on a three parameter power law curve, $y = a + bx^c$ (where y = stress range and x = number of cycles to failure and a, b and c were constants), with the parameters being determined through the use of TableCurve 2D, V5.00 software. Curve fitting was achieved using data points from all the specimens that failed and runouts that had undergone 10^7 cycles. Where more than one runout occurred at 10^7 cycles, the point relating to the highest stress range was employed. The three parameter power law curve was chosen on the basis that it was frequently one of the two most accurate fits, with respect to the r^2 value, of the "simple" curve fitting equations analysed. The utilisation of a single format for the equation would also enhance comparison between the models for the various welds. The parameters for the various curve fittings and subsequent r^2 values are detailed in Table 5.16.

Aluminium is generally considered not to have a fatigue limit, although if the S-N curve in the lower stress ranges analysed, exhibited a trend that was near parallel to the abscissa the term endurance limit has been employed.

Material	Power law curve parameters			r^2
	a	b	c	
PP |-	186.0464785	15250.87589	-0.44566294	0.6745942426
PP //	197.2274330	4.19266e+06	-0.93101764	0.7699385877
MIG LI (weld toe*)	183.1164548	1.14021e+06	-0.81009682	0.7357479613
MIG LI (nominal†)	151.6856860	1.29035e+06	-0.81626820	0.7292519707
MIG HI (weld toe*)	-74.7533513	1003.575928	-0.09374319	0.9136324205
MIG HI (nominal†)	-121.359481	1190.166088	-0.11625964	0.9130859515
FS SP	82.05495550	5028.974901	-0.29027393	0.8302778868
FS DP	102.1679903	20700.29327	-0.41343496	0.8007265503

Table 5.16: S-N data curve fitting parameters.

* Weld toe refers to the stress range experienced at the weld toe, determined through multiplication of the nominal stress by the appropriate elastic-plastic value for K_t detailed in Table 5.15.
† Nominal refers to the stress in the outer fibre of the 8 mm thickness specimen, the stress concentrating effect of the weld bead geometry not being taken into consideration.

5.5.1 Parent Plate

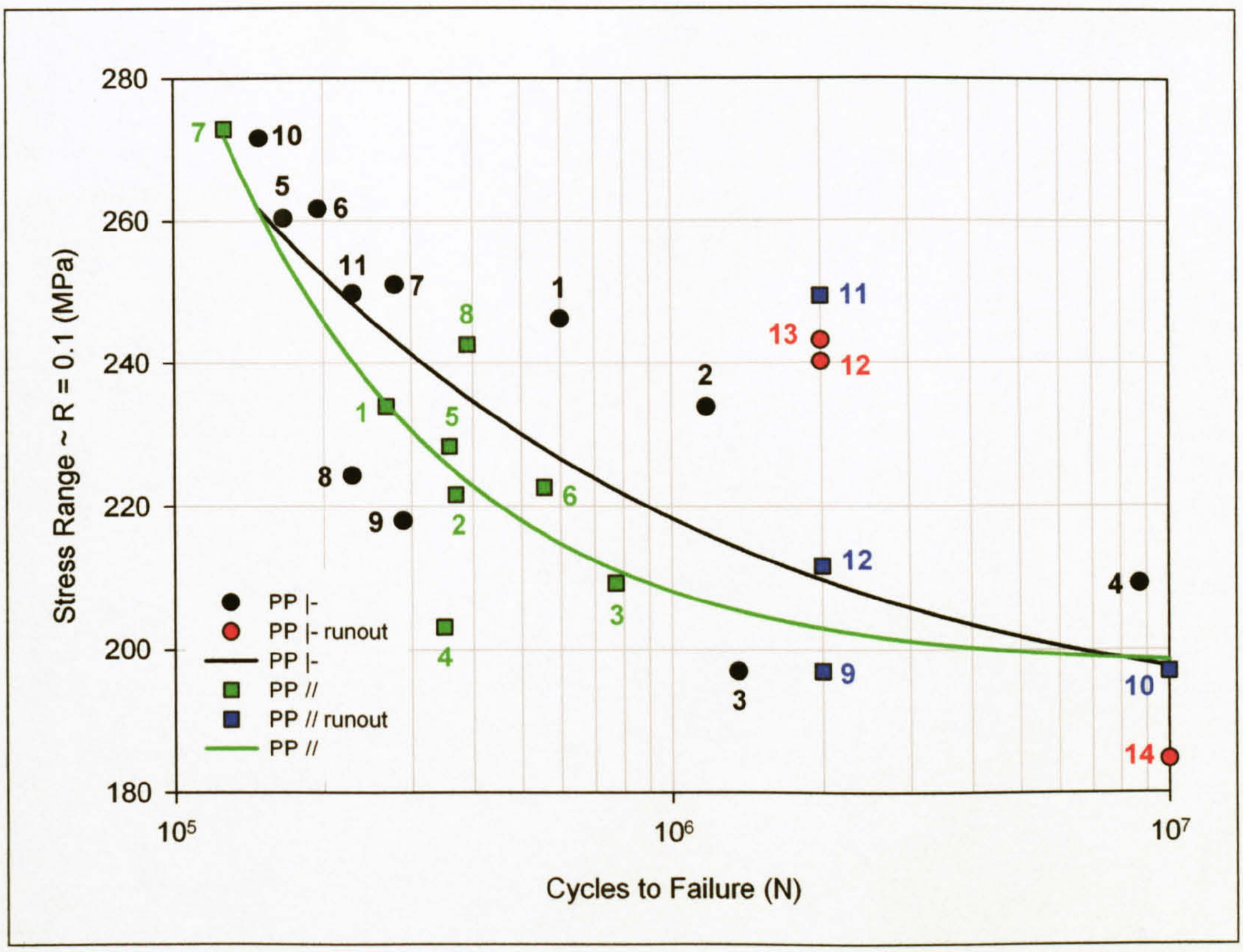

Figure 5.34: AA 5383-H321 parent plate S-N data (numbers refer to specimens in Table 12.1 and Table 12.2).

From the four point loading S-N test results obtained, shown in Figure 5.34, it was evident that there was a significant amount of scatter in the data, this was also apparent in the r^2 values, 0.67 for the PP |- and 0.77 for the PP //, returned by the three parameter power law curve fitting employed. The curve fitting technique returned a greater fatigue strength for the |- specimens when compared to the // specimens for lives of $0.15 - 8 \times 10^6$ cycles, with a maximum increase of 5 - 6% in the region of $5 - 6 \times 10^5$ cycles. Although extrapolation of the curves would advocate that outside of this lifespan range the // specimens had the greater fatigue strength. The shape of the two curves suggest that the // material was approaching the endurance limit at a stress range of 198 MPa, whilst the limit was below this value for the |- material. To increase the accuracy of the curve fitting it would be prudent to undertake further tests, although at the time of writing material and time constraints prohibited this.

Due to contact stresses between the rollers and the parent plate specimens several of these, typically at the higher stress ranges, failed beneath the roller and have been omitted from both the subsequent S-N graphs and when calculating the parameters for the power law curves.

Material	Fatigue Strength ~ Δσ (MPa)				
	Number of Cycles				
	2×10^5	10^6	2×10^6	5×10^6	10^7
PP |-	252	218	210	202	198
PP //	246	208	203	200	199

Table 5.17: Parent plate fatigue strengths (R = 0.1).

Both specimen types exhibited multiple crack initiation sites, these being more prevalent at higher stresses, followed by subsequent coalescence of the cracks. Crack initiation was typically intermetallic induced in the |- specimens, as shown in Figure 5.36, although the // specimens tended to be more susceptible to edge initiation, as shown in Figure 5.42. Both specimens showed evidence of secondary cracking on the exposed fatigue crack faces, evident in Figure 5.38, and microvoid coalescence on the fast fracture surfaces, evident in Figure 5.39.

5.5.1.1 Fractography ~ Parent Plate |-

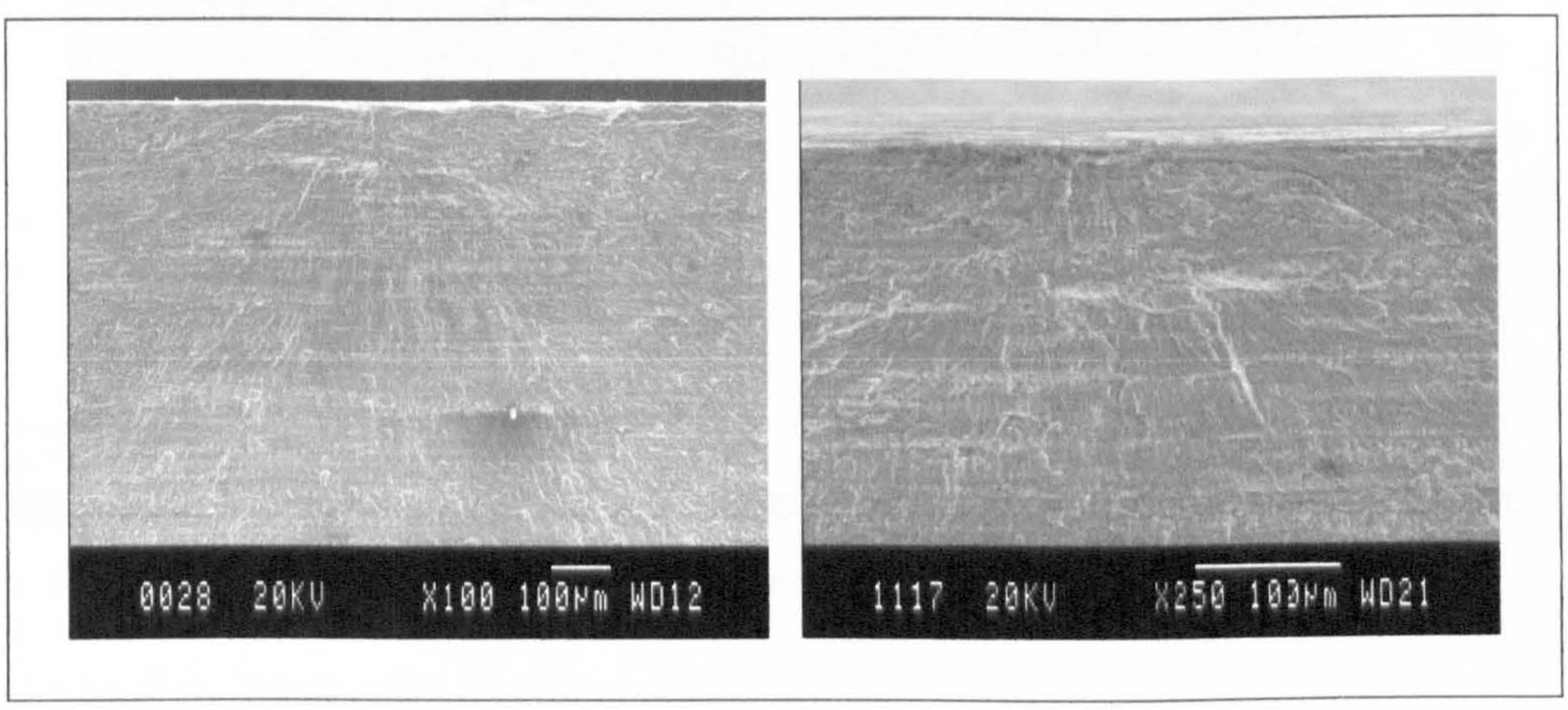

Figure 5.35: Crack initiation site (left), secondary (right) cracking (PP |- 1).

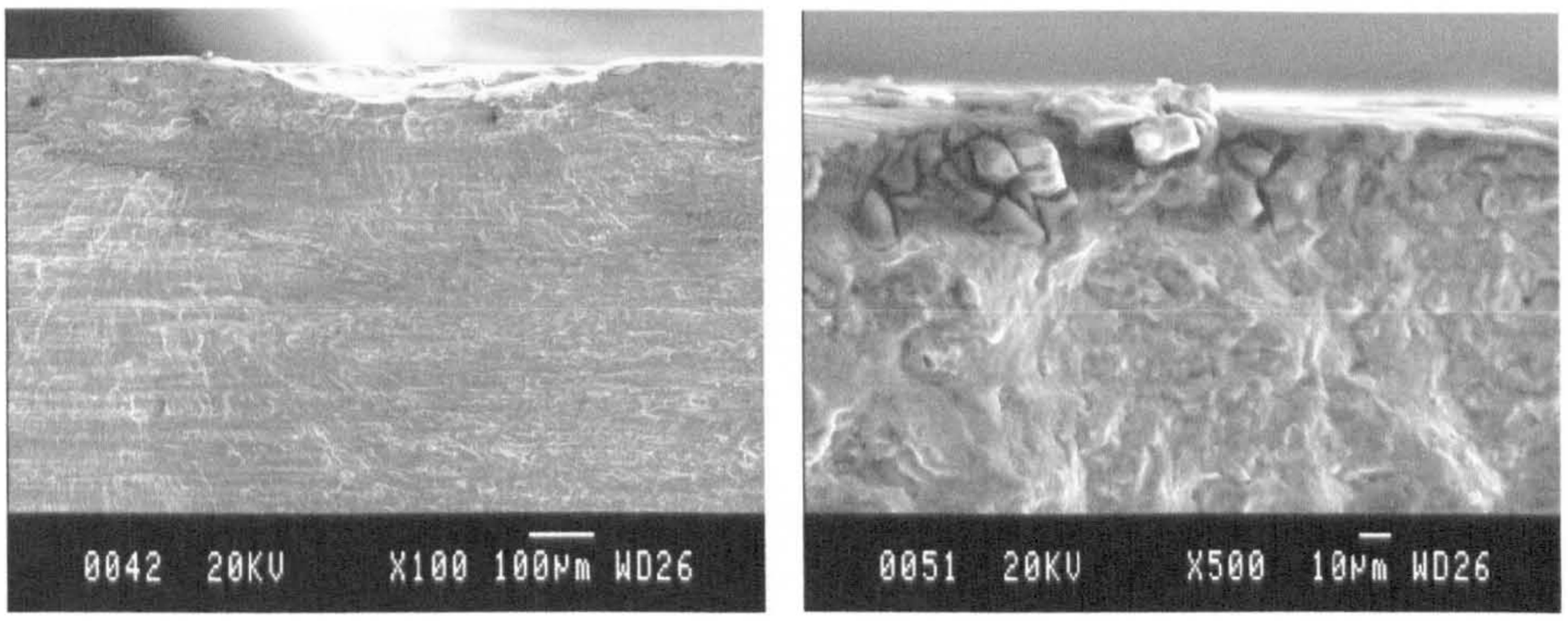

Figure 5.36: Crack initiation sites, main crack from surface defect (left), secondary crack from intermetallic (right) (PP |- 2).

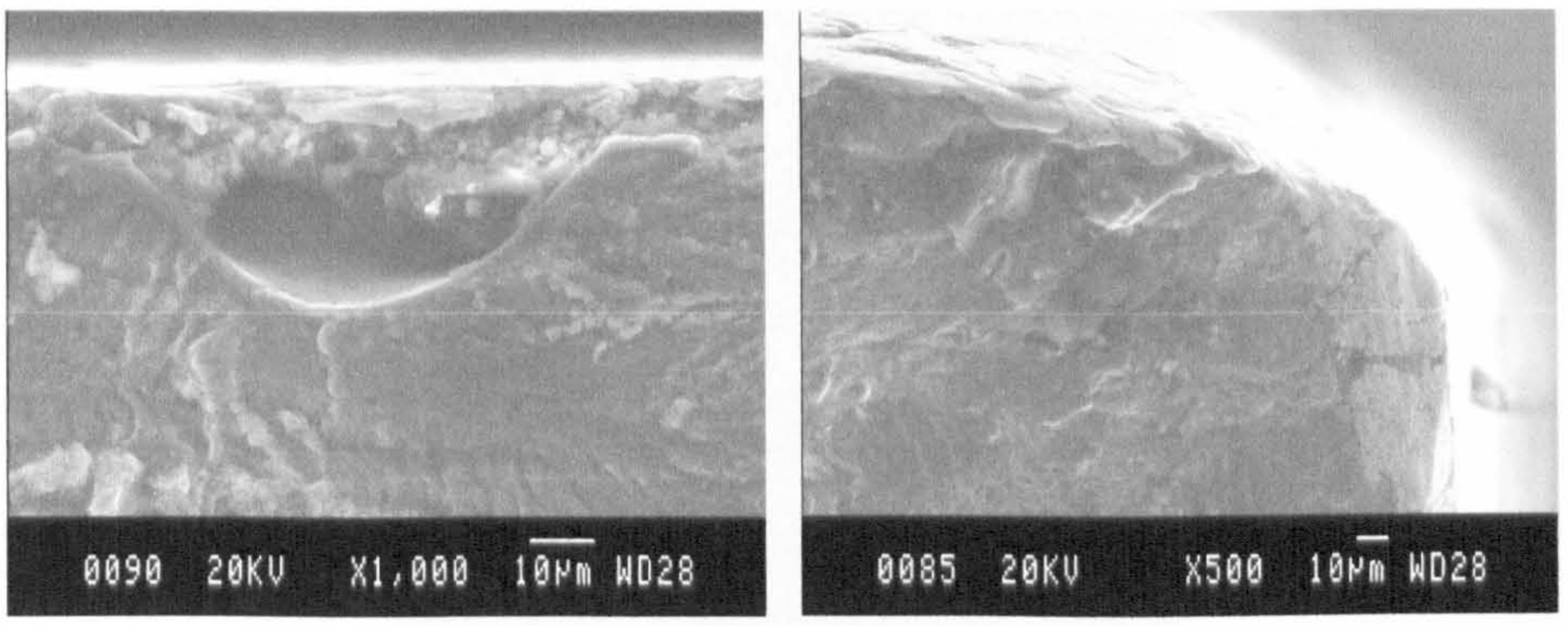

Figure 5.37: Crack initiation sites, intermetallic or sub-surface defect (left), intermetallic near the specimen edge (right) (PP |- 4).

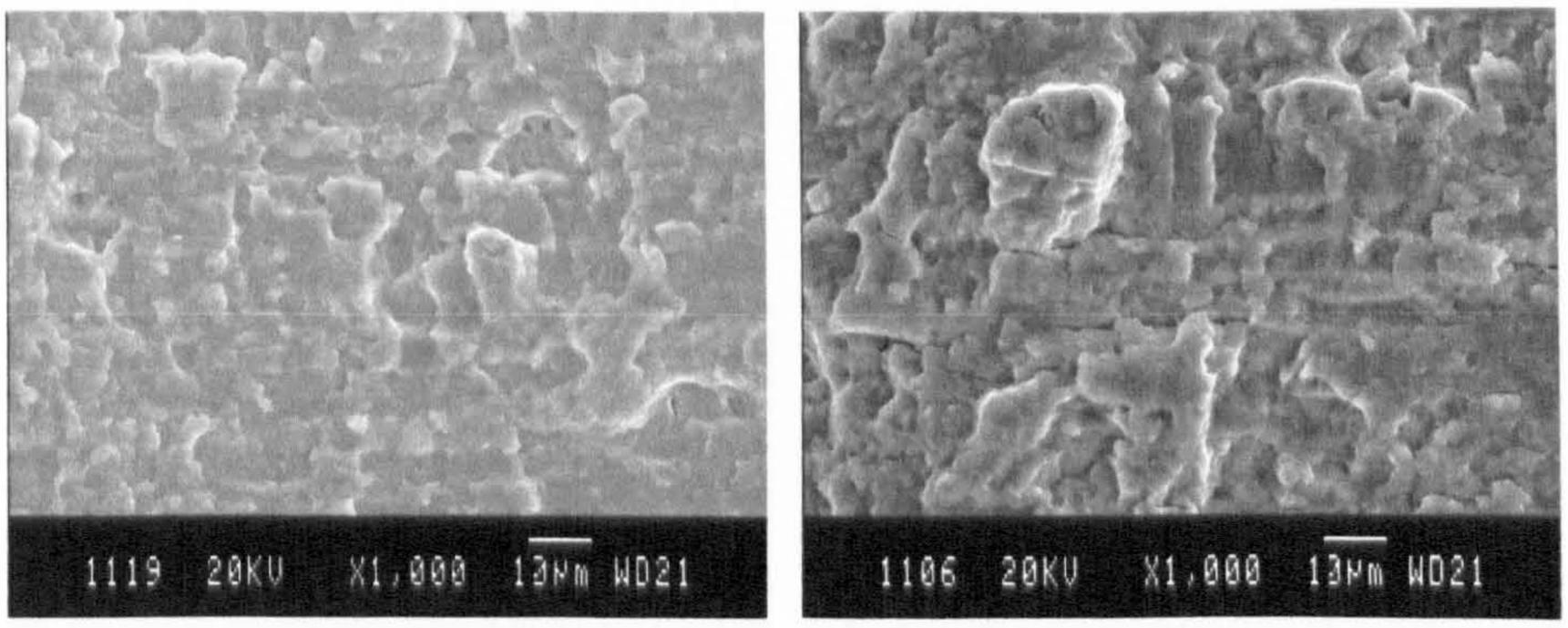

Figure 5.38: Secondary cracking low cycle, PP |- 1, (left), high cycle PP |- 4 (right).

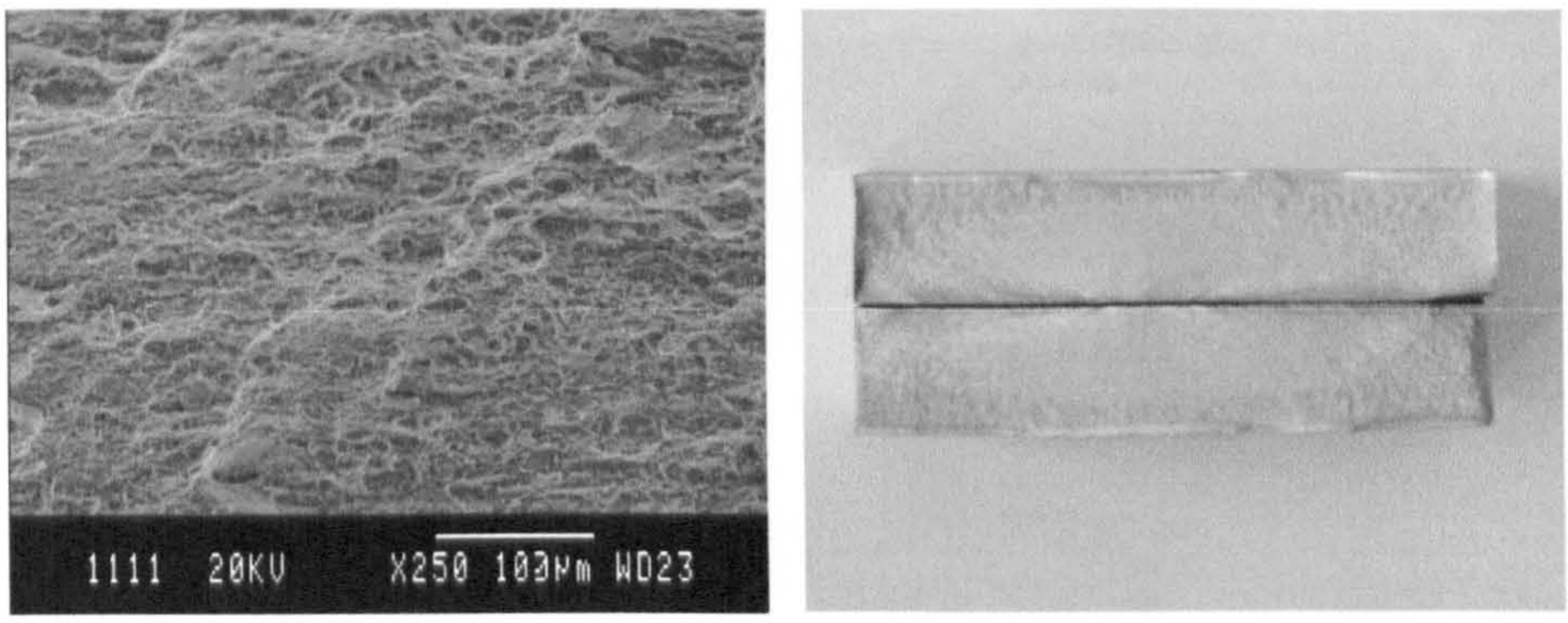

Figure 5.39: Typical fast fracture surface exhibiting microvoid coalescence (left), complete fracture surface (right).

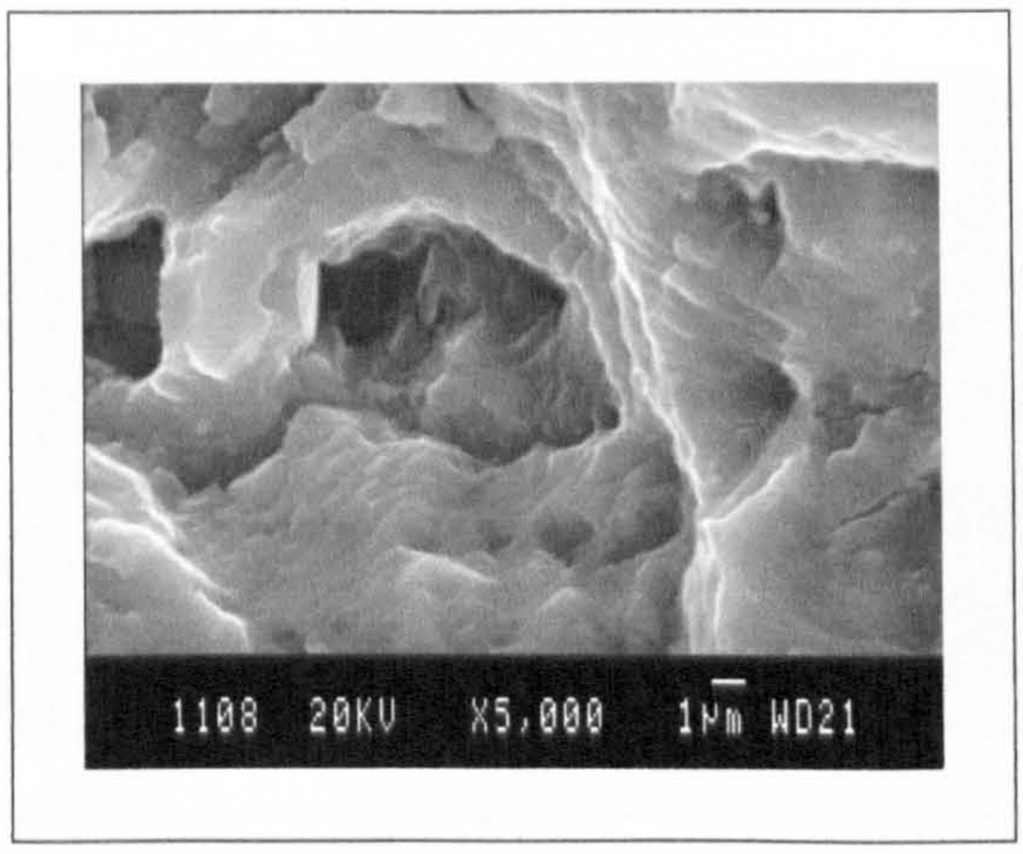

Figure 5.40: Fatigue striations near to fast fracture surface (PP |- 4).

5.5.1.2 Fractography ~ Parent Plate //

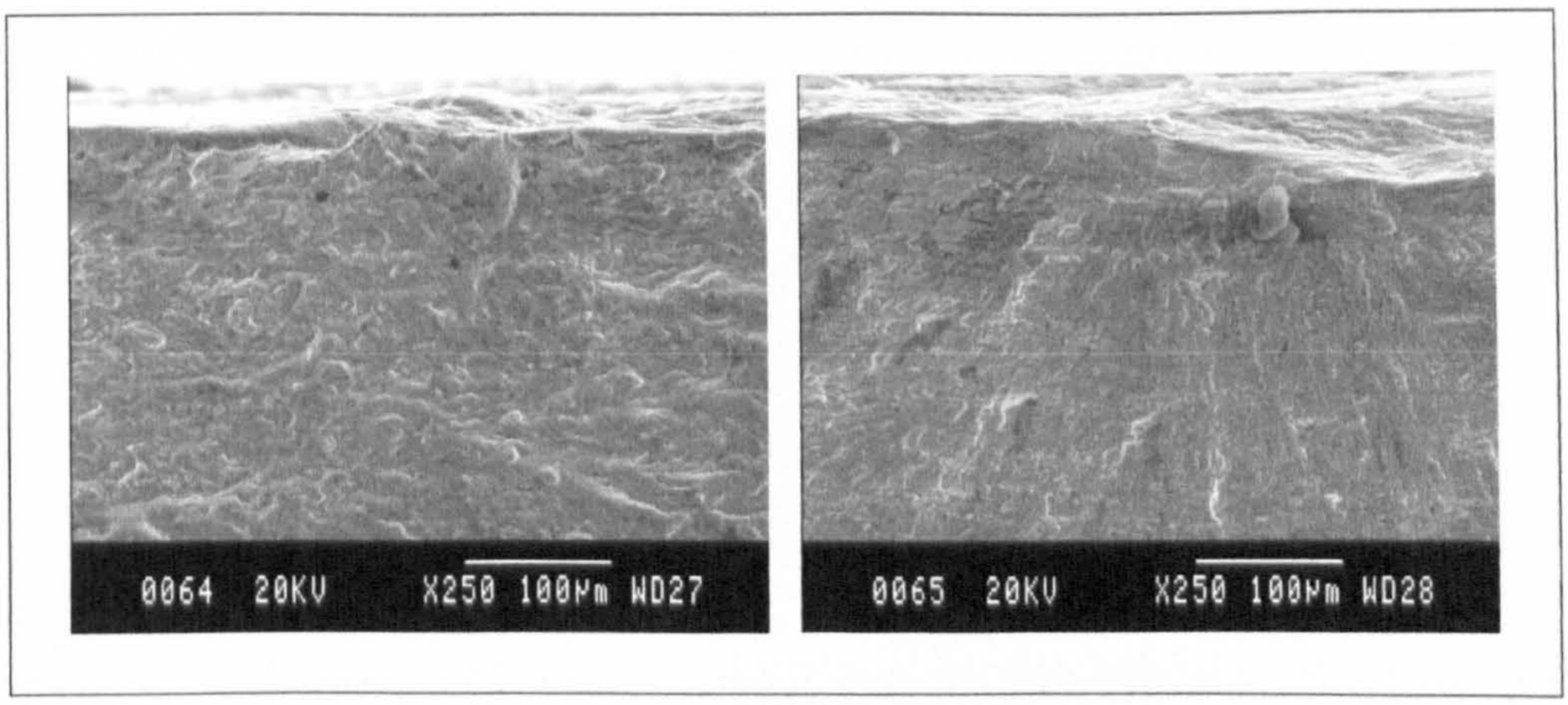

Figure 5.41: Crack initiation sites (PP // 1).

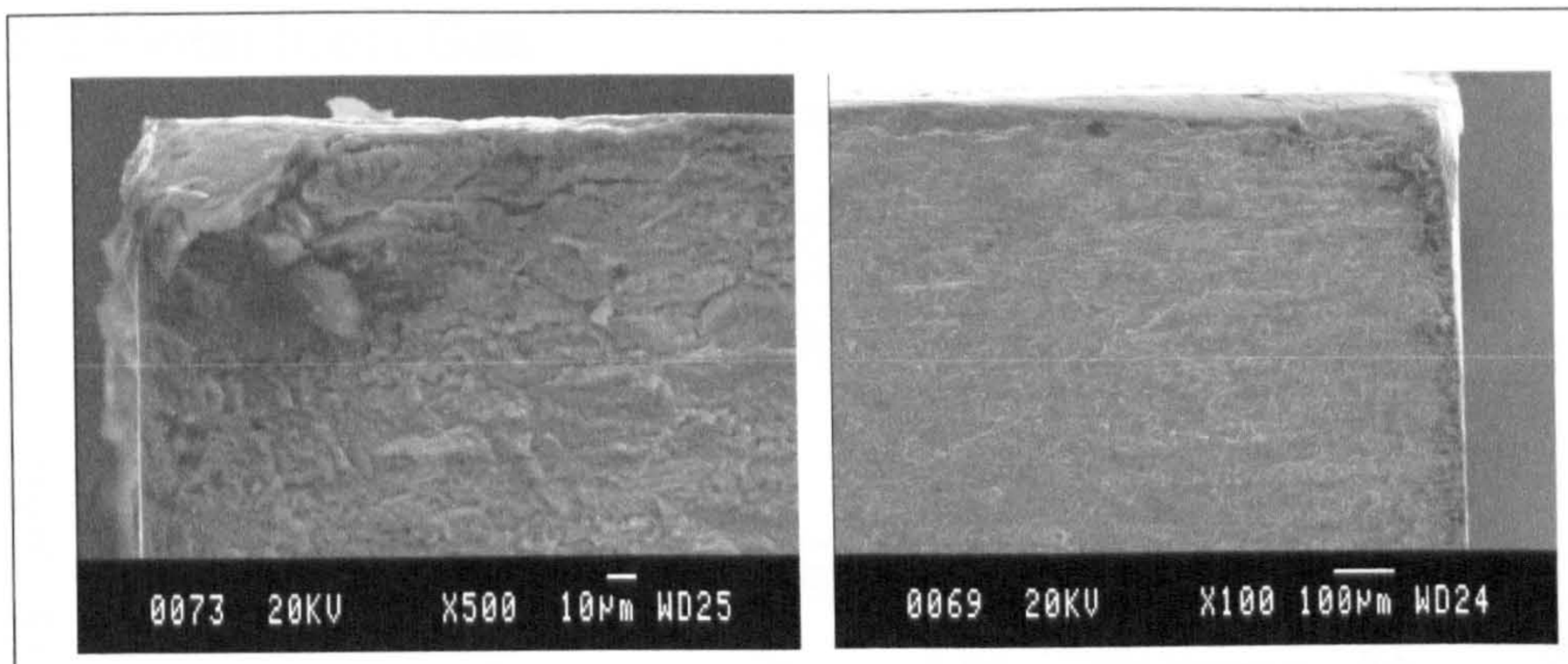

Figure 5.42: Smaller of two main cracks crack initiated through intermetallic inclusion near to edge (left), edge initiated main crack (right) (PP // 2).

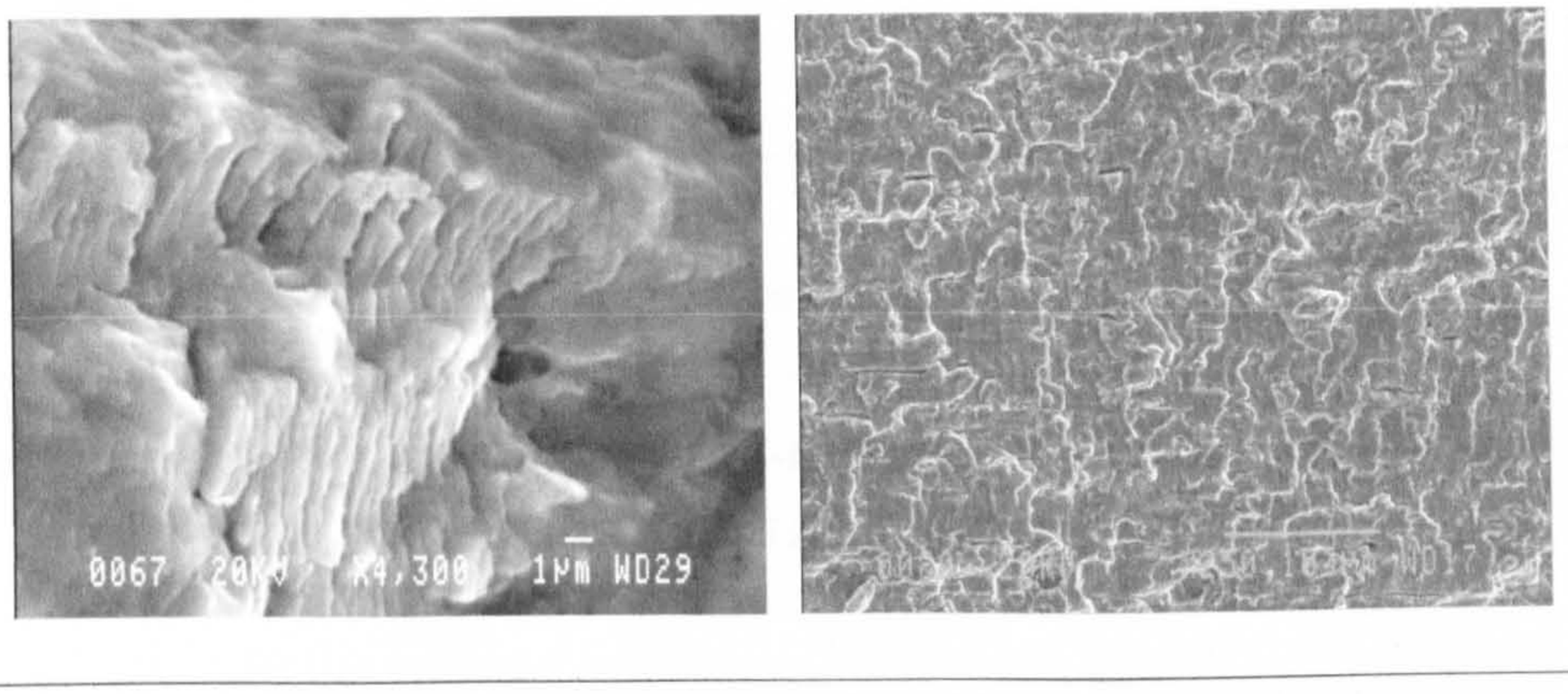

Figure 5.43: Fatigue striations (left), secondary cracking (right) (PP // 3).

5.5.2 Metal Inert Gas

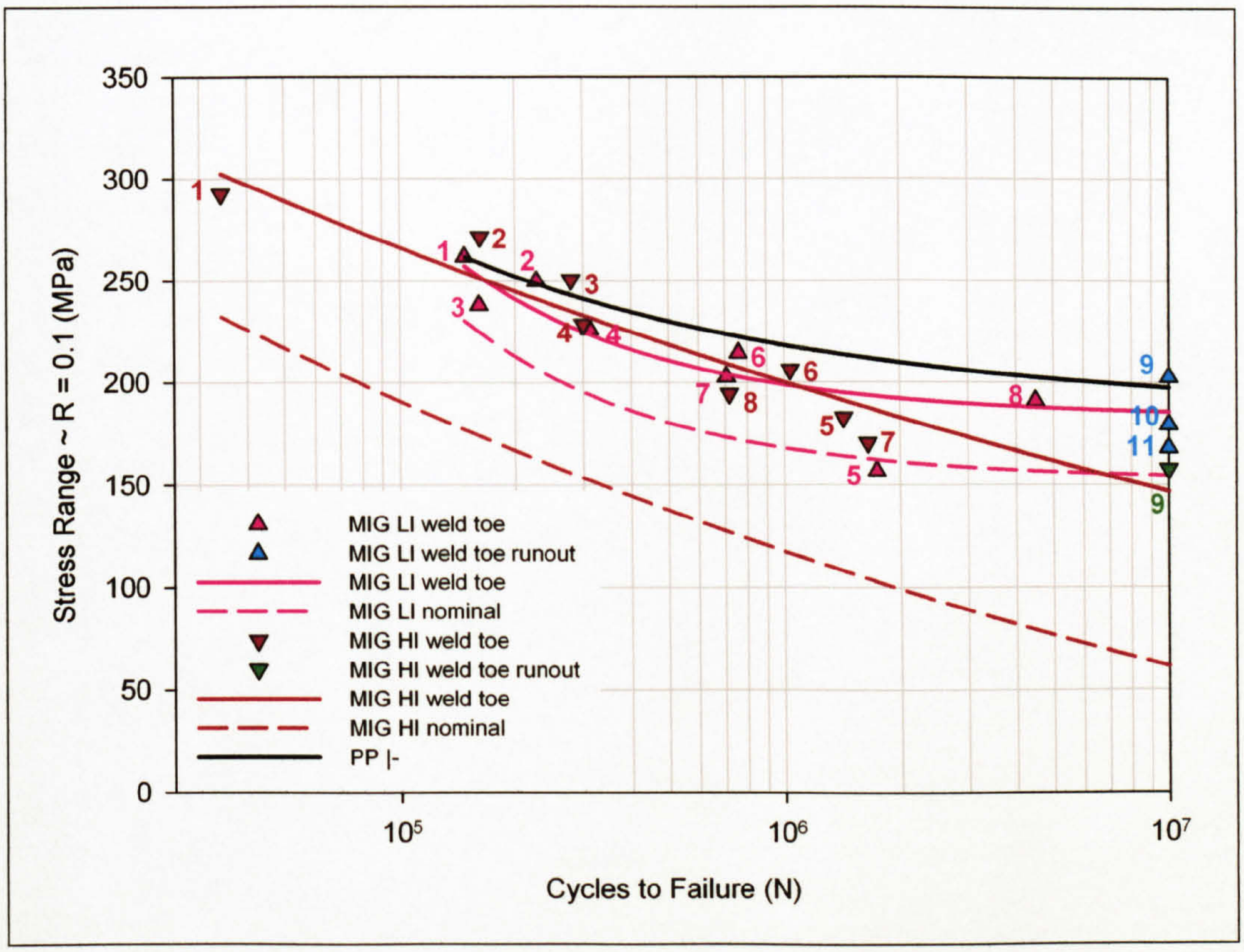

Figure 5.44: AA 5383-H321 MIG butt weld S-N data (numbers refer to specimens in Table 12.3 and Table 12.4).

Both the MIG LI and HI welds S-N test results fell within narrow scatter bands as shown in Figure 5.44, r^2 values for the curve fittings returned values of 0.73 and 0.92 for the LI and HI welds respectively (the value for the LI weld increased to 0.87 if the result from the MIG LI 5 specimen was excluded).

Weld	Fatigue Strength ~ Δσ (MPa) (weld toe/nominal)				
	Number of Cycles				
	2×10^5	10^6	2×10^6	5×10^6	10^7
MIG LI	241/212	199/168	192/161	187/156	186/154
MIG HI	245/167	200/117	183/99	162/77	147/61

Table 5.18: MIG weld fatigue strengths, R = 0.1.

From the results, shown in Figure 5.44 and Table 5.18, it was evident that the two MIG processes had comparable fatigue strengths for lives of 2×10^5 - 10^6 cycles when the stress concentrating effect of the weld toe was taken into consideration. At lives greater than 10^6 cycles the fatigue strength of the LI weld was greater than that of the HI, with the

disparity between the two increasing as the cycles to failure increased, at 10^7 cycles the strength being 21% lower. The curve fitting technique employed suggested that the LI weld was approaching the endurance limit at a weld toe stress range of 186 MPa. In contrast to this the HI weld exhibited a near linear response for the 150-300 MPa weld toe stress range considered, with no evidence of an endurance limit being approached.

All the specimens exhibited multiple crack initiation sites and subsequent crack coalescence, the path of the crack following that of the weld toe as shown in Figure 5.51 and Figure 5.57. Crack initiation of all the specimens occurred in the weld toe region, due to its stress concentrating effects, although initiation sites were typically associated with porosity in this region, evident in Figure 5.47 and Figure 5.56. LI specimens also displayed initiation sites due to a blow hole, shown in Figure 5.45, weld toe geometry, shown in Figure 5.47, and weld spatter, shown in Figure 5.49. Secondary cracking was visible on the fatigue crack surfaces as was microvoid coalescence on the fast fracture surfaces as shown in Figure 5.47.

5.5.2.1 Fractography ~ MIG Low Input

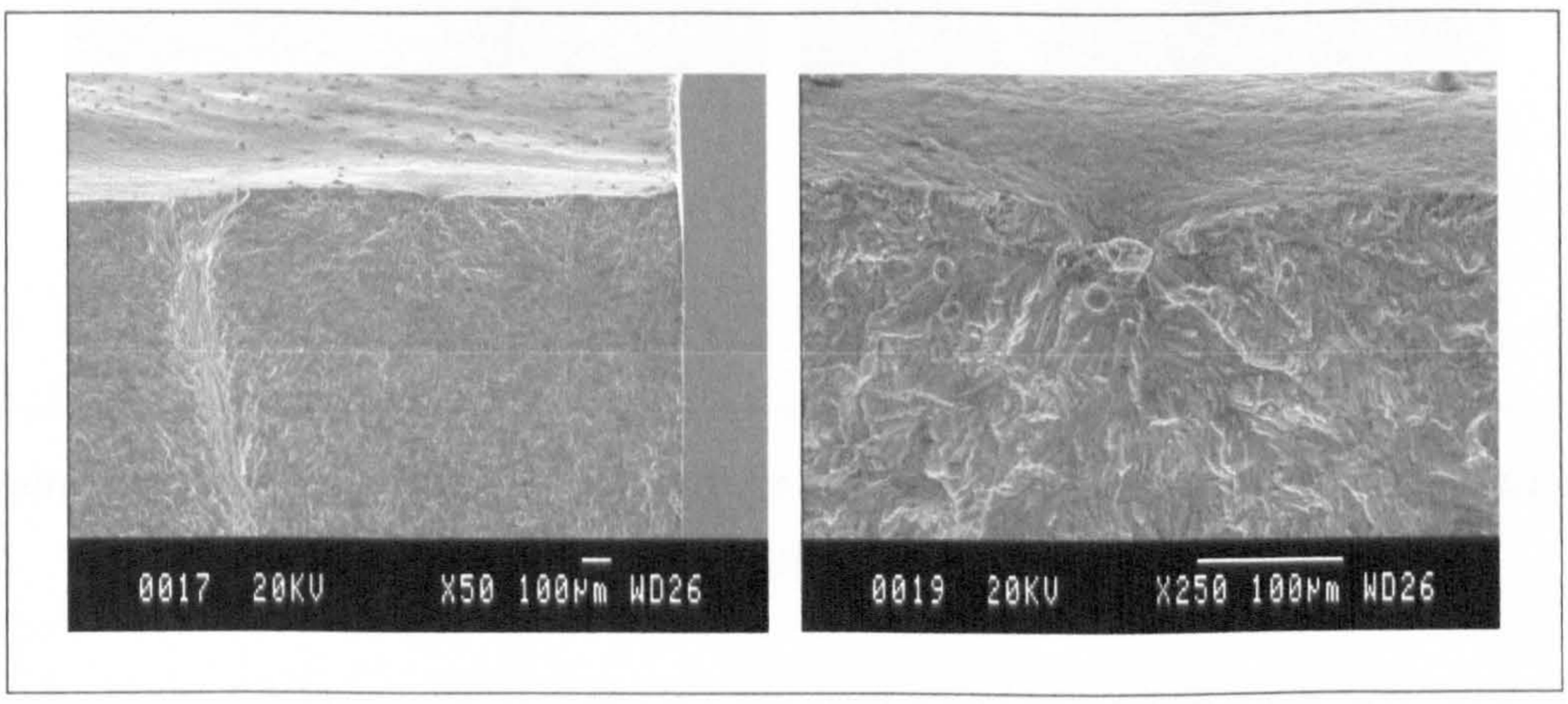

Figure 5.45: Blow hole induced crack initiation and porosity (left & right) (MIG LI 1).

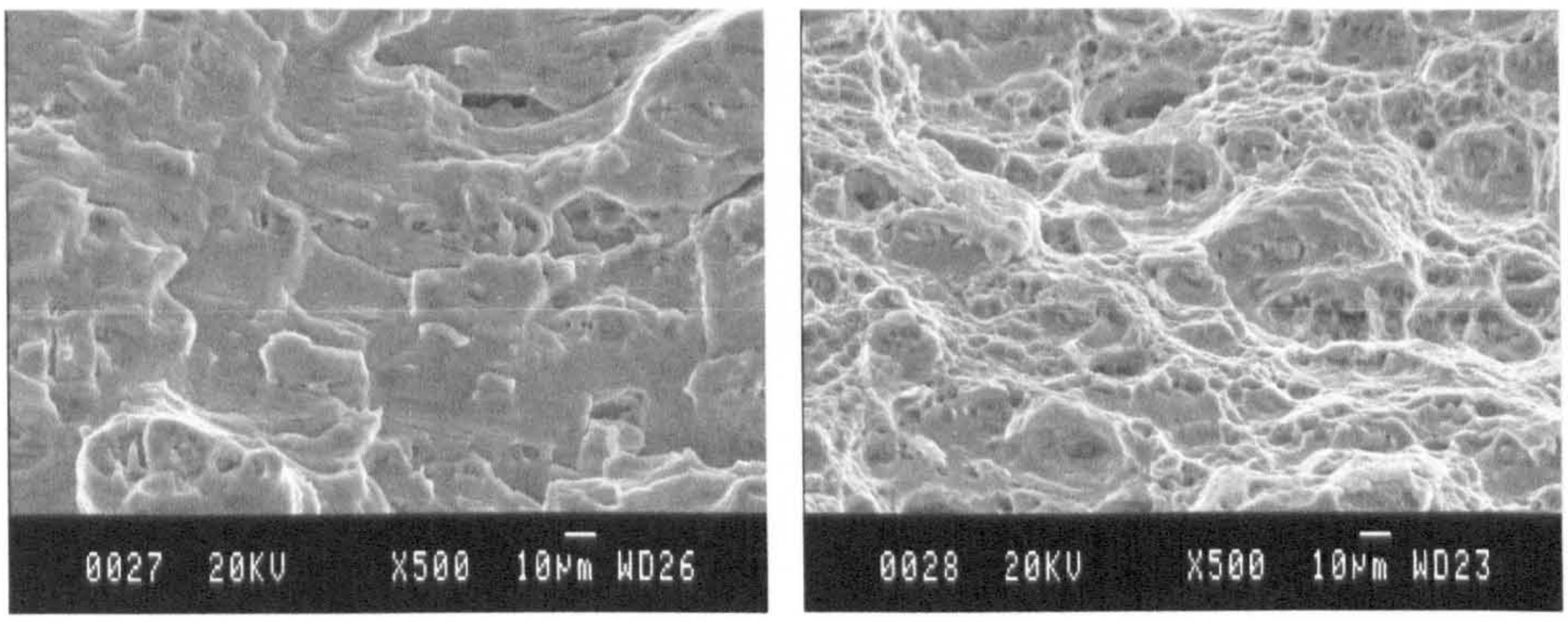

Figure 5.46: Fatigue fracture surface showing striations and secondary cracking (left), microvoid coalescence on the fast fracture surface (right) (MIG LI 1).

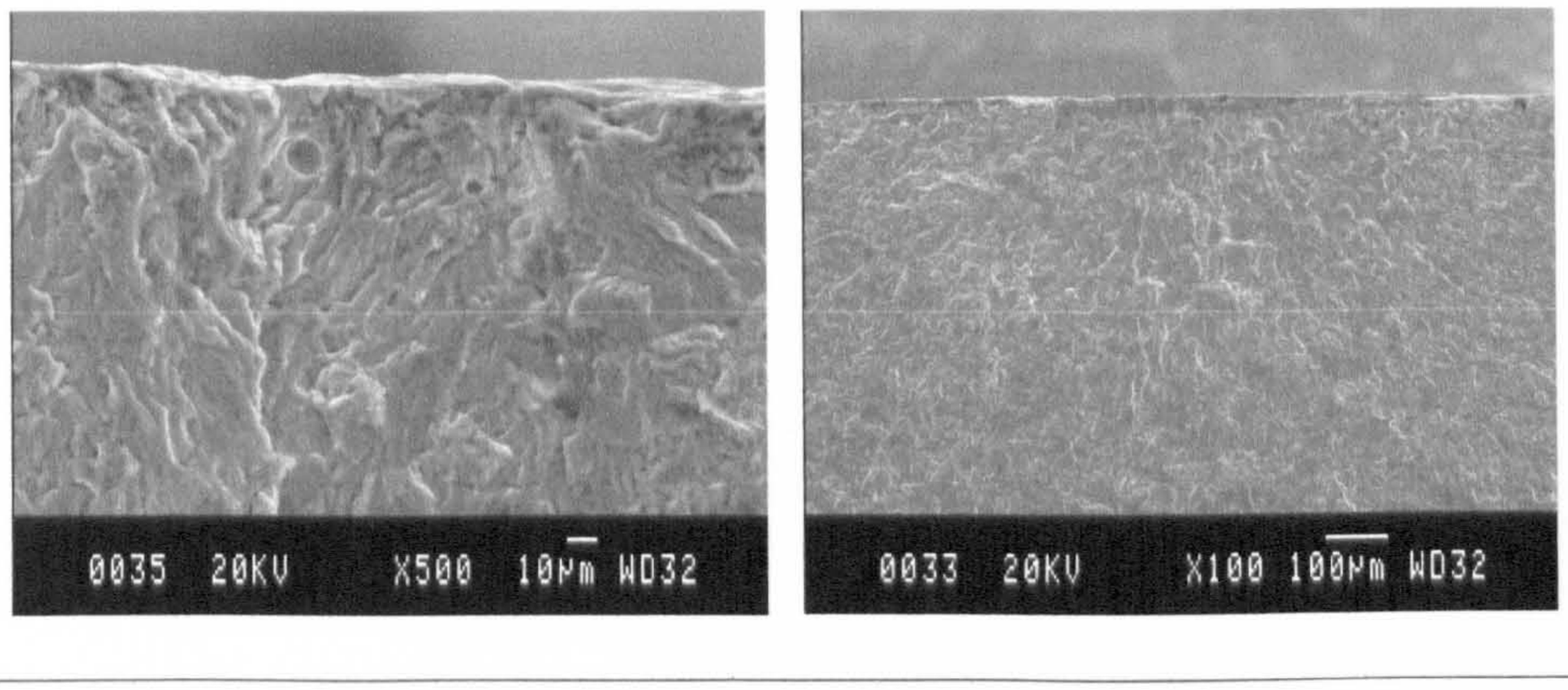

Figure 5.47: Porosity induced crack initiation (left), possible stress concentration induced crack initiation (right) (MIG LI 2).

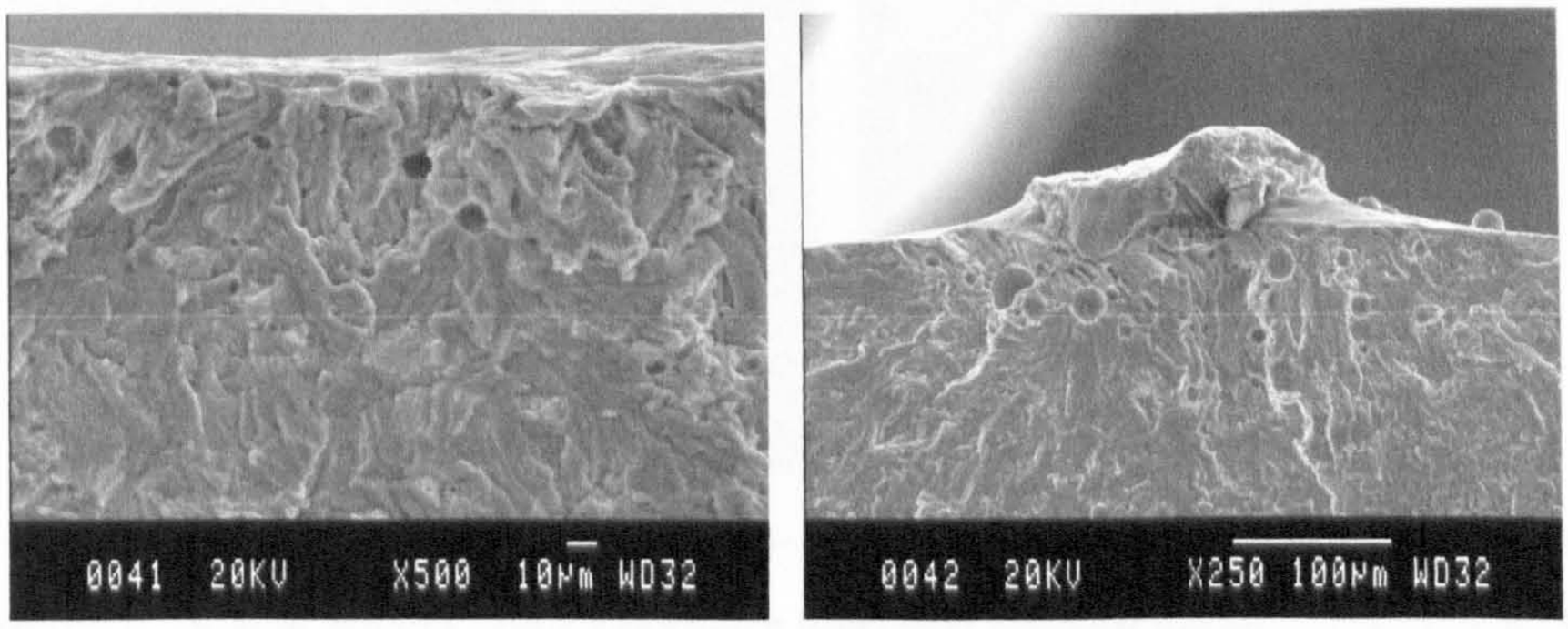

Figure 5.48: Porosity induced crack initiation (left), porosity and stress concentrator crack initiation (right) (MIG LI 3).

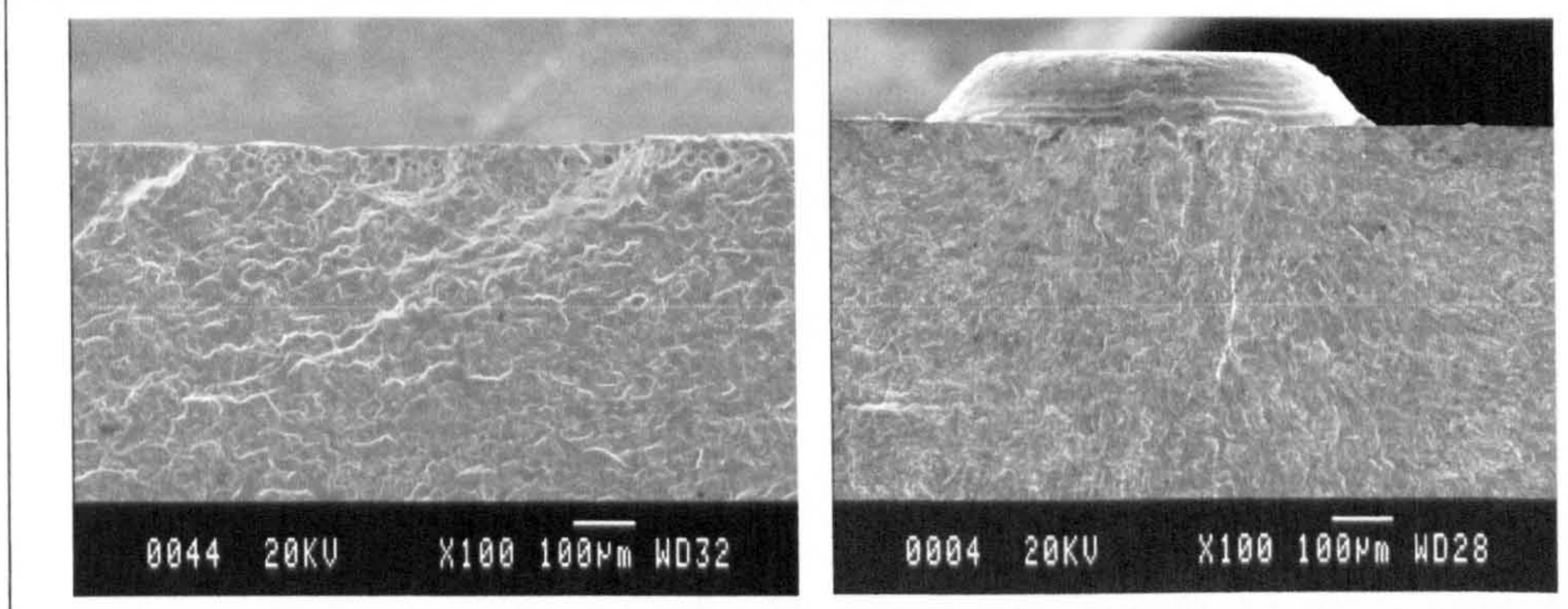

Figure 5.49: Crack initiation and coalescence due to line of pores (left) (MIG LI 4), initiation due to weld spatter (right) (MIG LI 7).

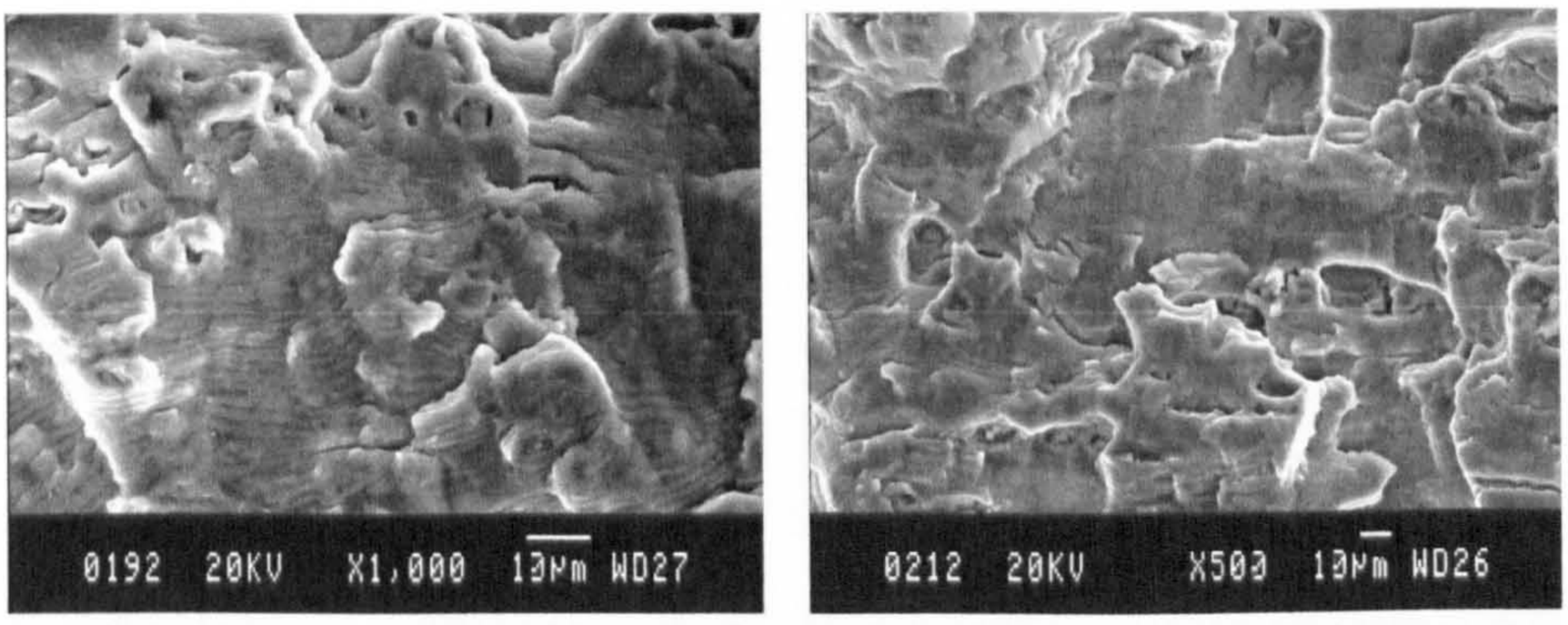

Figure 5.50: Fatigue striations high cycle, left, (MIG LI 8) and low cycle, right, (MIG LI 1).

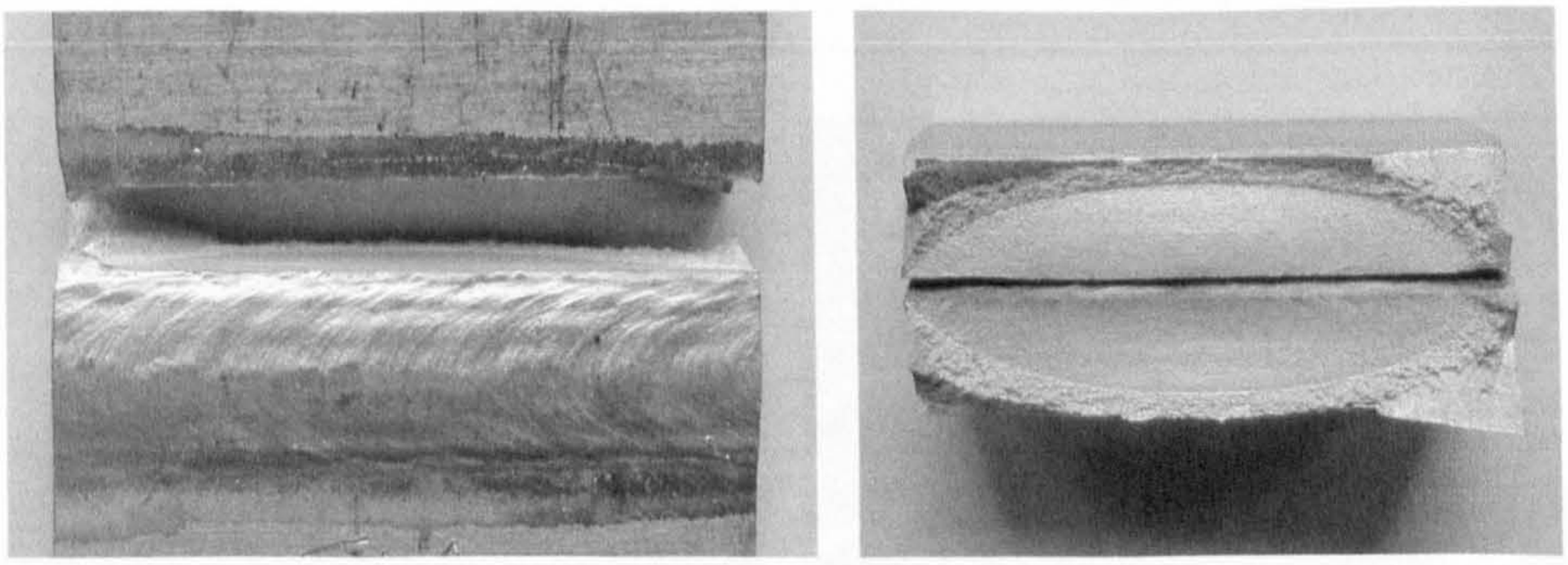

Figure 5.51: Typical MIG LI crack geometry (left) and fracture surface (right) (MIG LI 8).

5.5.2.2 Fractography ~ MIG High Input

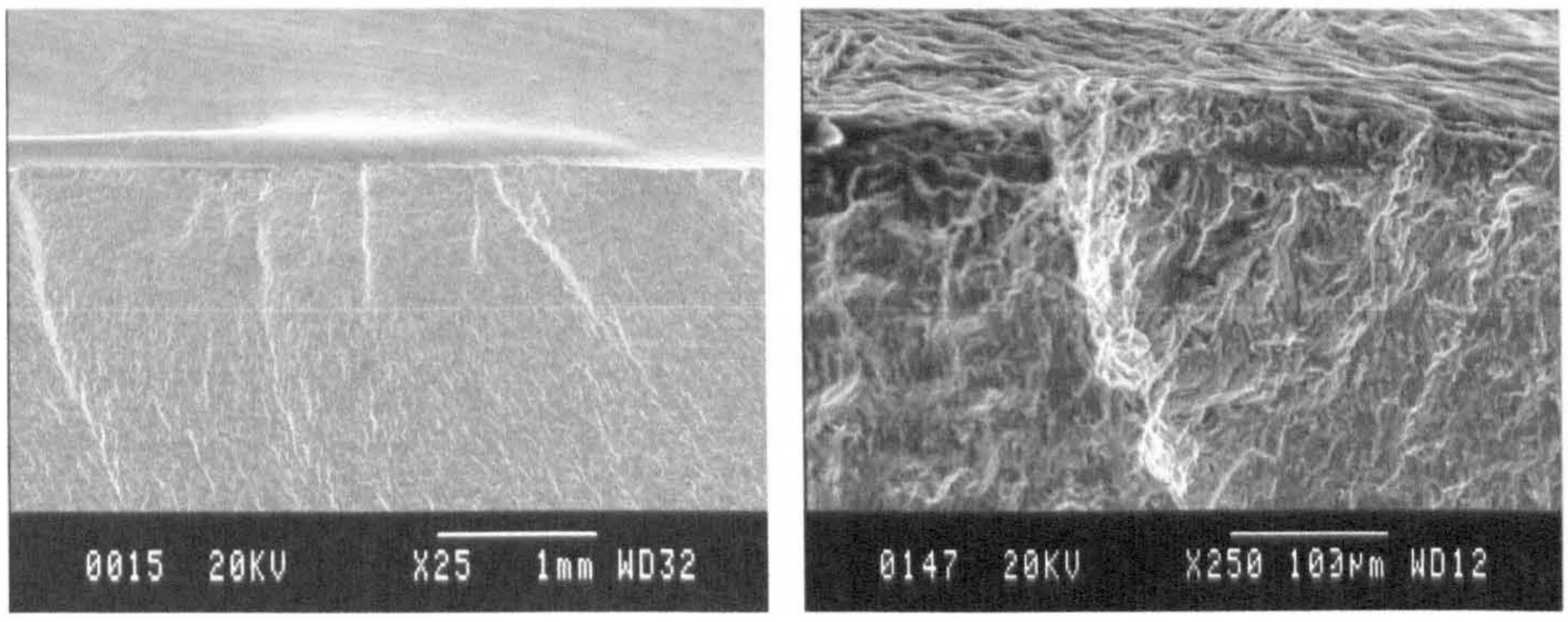

Figure 5.52: Fatigue crack initiation sites and coalescence (left & right) (MIG HI 2).

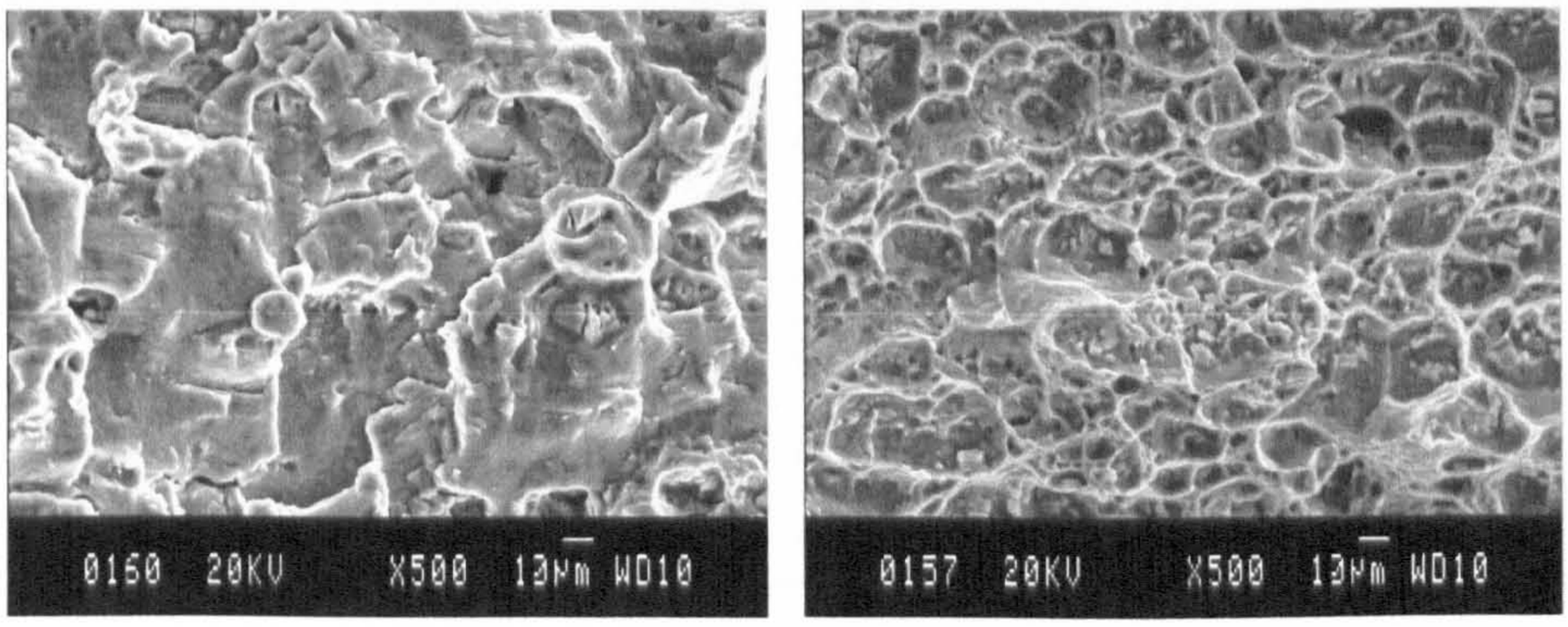

Figure 5.53: Fatigue crack fracture surface (left), fast fracture surface exhibiting microvoid coalescence (right) (MIG HI 2).

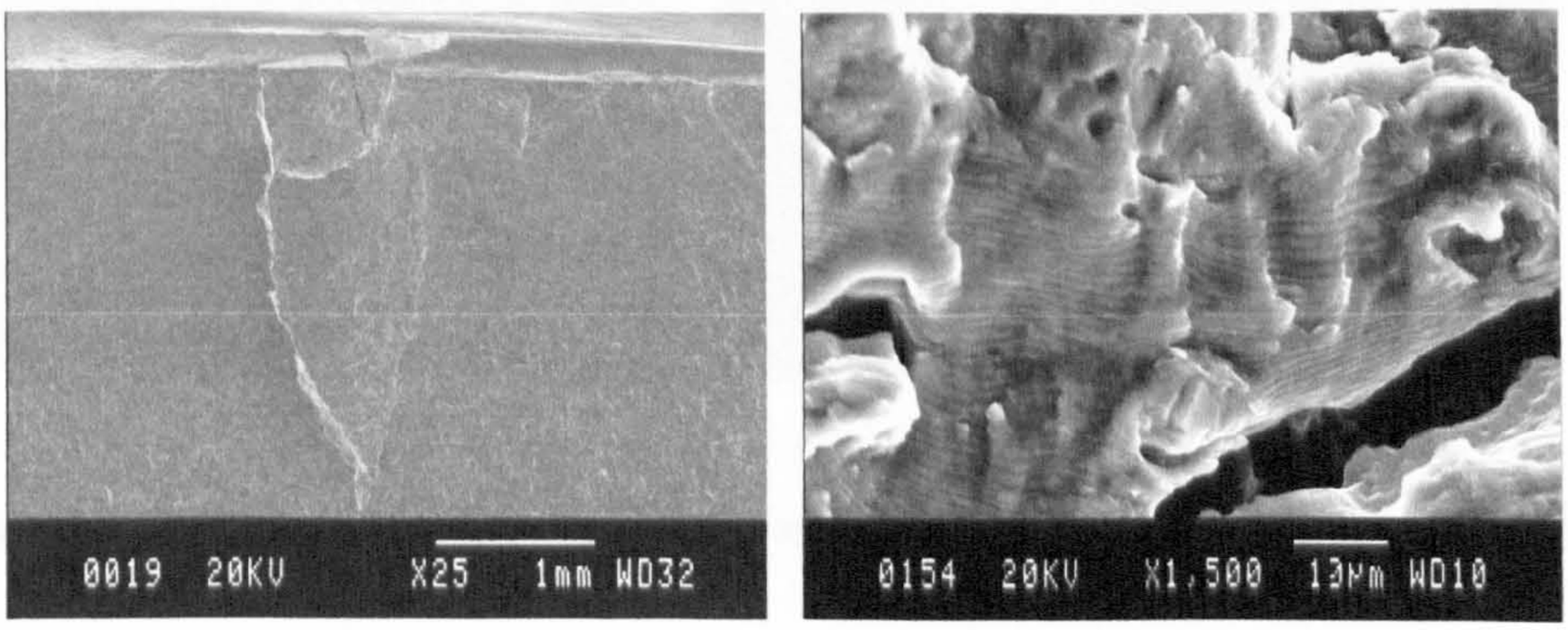

Figure 5.54: Fatigue crack initiation and coalescence (left), fatigue striations and secondary cracking (right), (MIG HI 2).

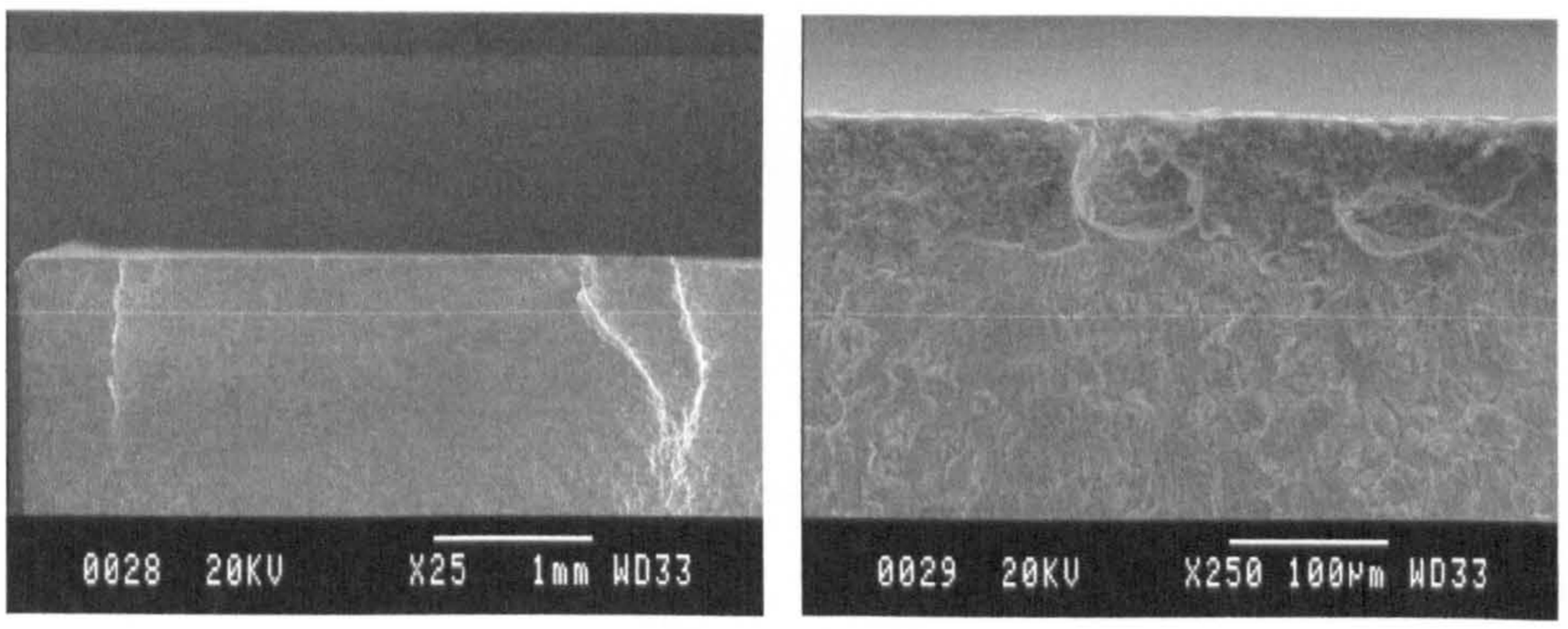

Figure 5.55: Porosity induced crack initiation sites (left & right) (MIG HI 4).

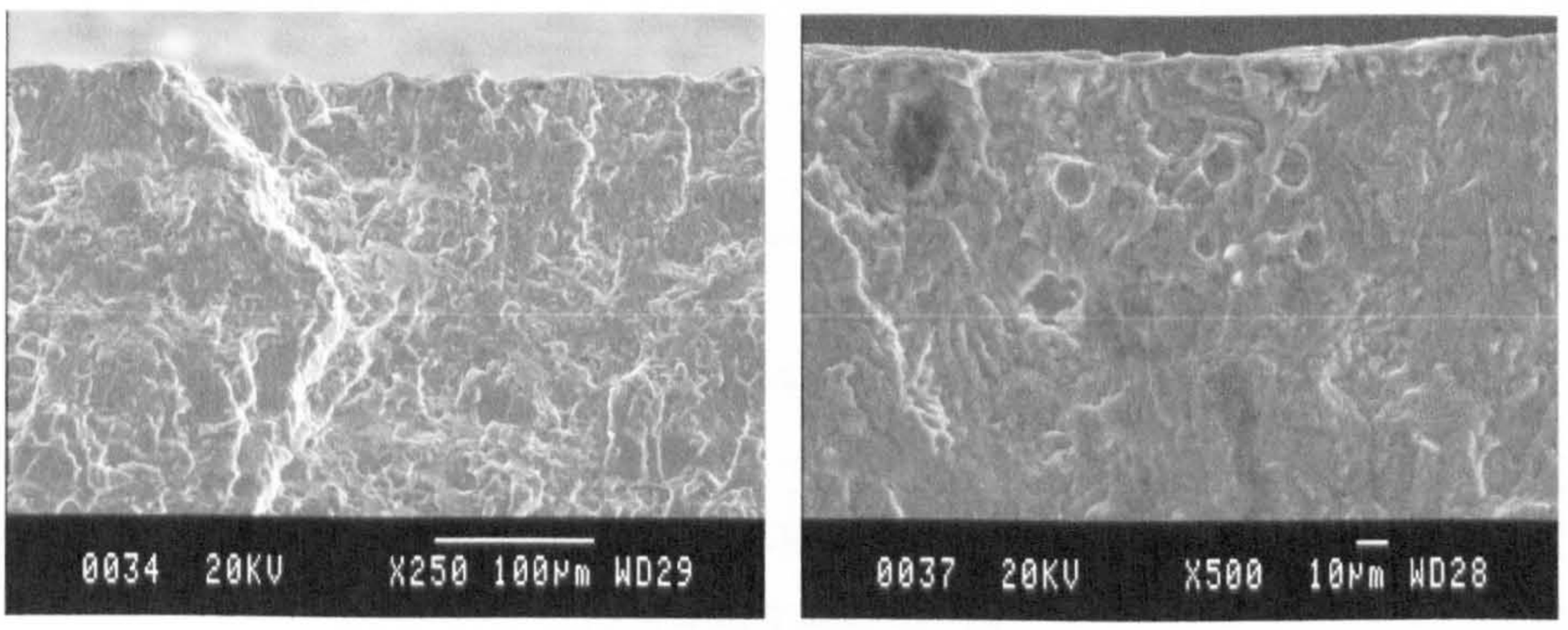

Figure 5.56: Porosity induced crack initiation (left & right) (MIG HI 5).

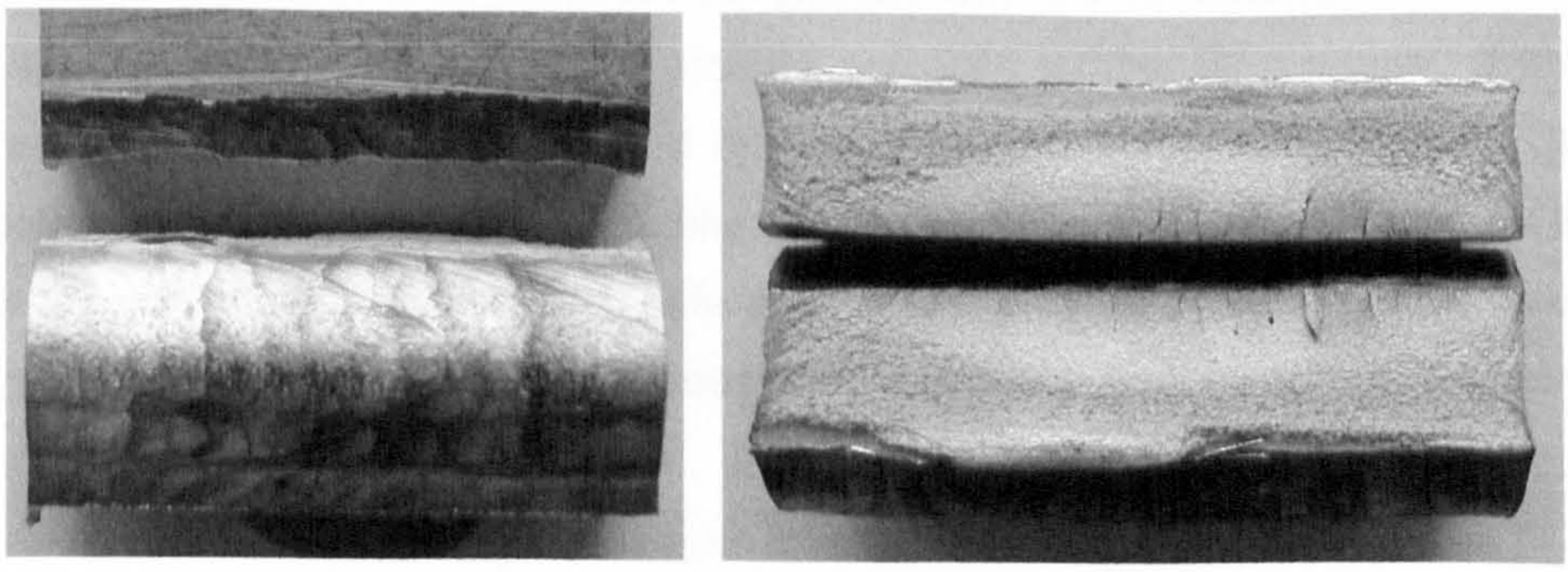

Figure 5.57: Typical MIG HI fracture path (left) and fracture surface (right) (MIG HI 2).

5.5.3 Friction Stir

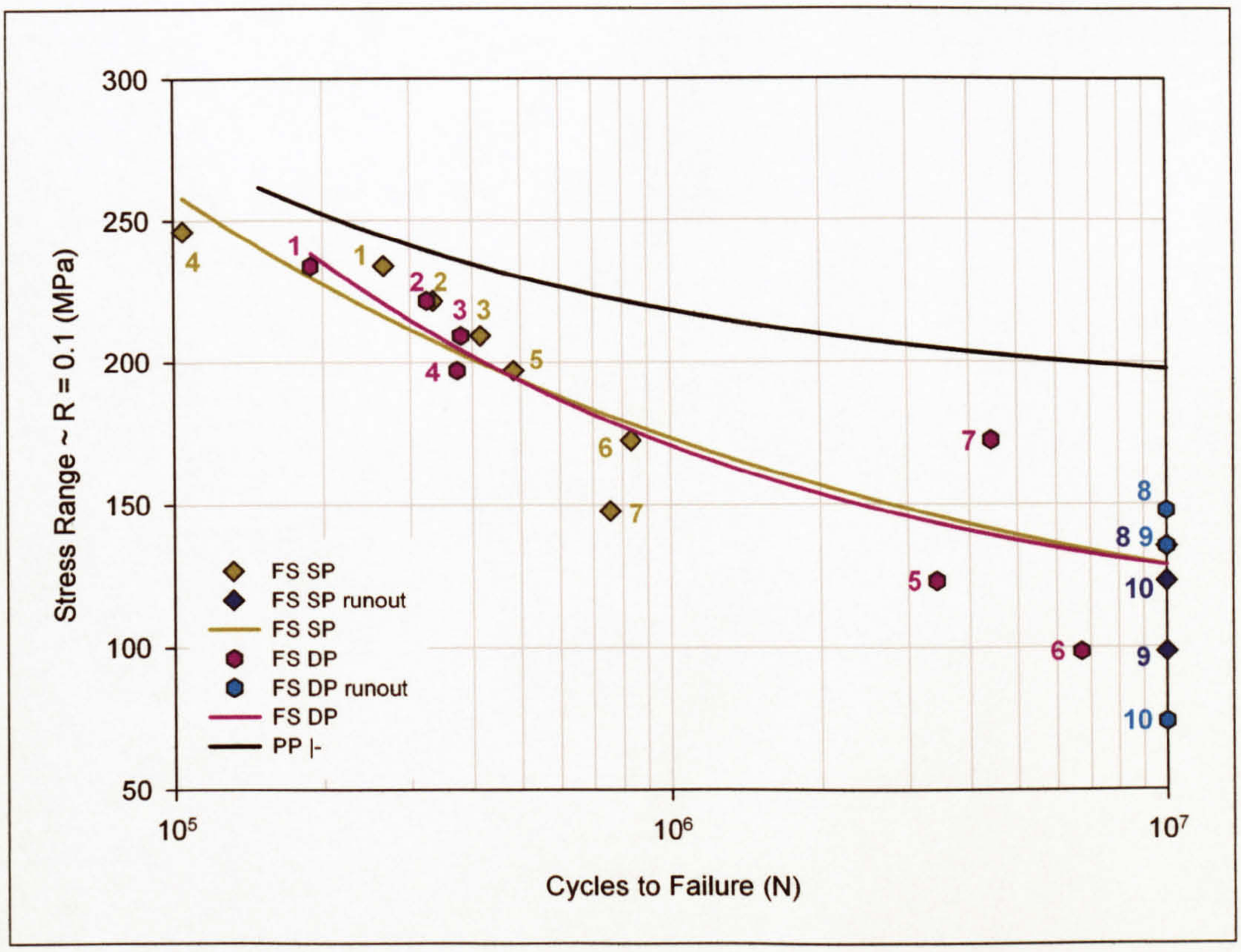

Figure 5.58: AA 5383-H321 FS butt weld S-N data (numbers refer to specimens in Table 12.5 and Table 12.6).

From Figure 5.58 it was evident that at lives below 10^6 cycles the S-N results from both the SP and DP welds fell within a narrow scatter band, although a notable increase in scatter was evident in the DP data at lives greater than 3×10^6 cycles. The curve fitting returned r^2 values of 0.83 for the SP process and 0.80 for the DP process. It was also apparent from the test results obtained and the three parameter power law curve fitting technique employed that the resulting difference between the fatigue strengths for the two processes was minimal; the greatest difference between the two processes, at around 2×10^5 cycles, resulted in a difference of less than 3% in the respective fatigue strengths.

Weld	Fatigue Strength ~ Δσ (MPa) Number of Cycles				
	2×10^5	10^6	2×10^6	5×10^6	10^7
FS SP	228	173	157	139	129
FS DP	235	171	154	137	129

Table 5.19: Summary of fatigue strengths, R = 0.1.

The SP process typically resulted in failure occurring in the region of the weld nugget, as shown in Figure 5.61 and Figure 5.68. The welds exhibited multiple initiation sites, evident in Figure 5.68, with subsequent coalescence of the resulting cracks leading to the development of a predominant crack, further growth resulting in failure. Crack initiation sites observed mid-specimen, with respect to the width, were generally related to the circular score marks that resulted from the rotational and transverse movement of the tool shoulder, shown in Figure 5.59, Figure 5.61 and Figure 5.62. Cracks were also noted to have followed the grinding marks that resulted from removal of the weld material extruded at the edge of the tool shoulder, although whether the marks had also caused initiation was unclear. The effect of the circular marks was notably influential in that as well as causing crack initiation; they resulted in crack growth occurring along their path. The outcome of this being that the initial crack growth occurred in a similar direction to that of the applied load, observable in Figure 5.59, rather than transverse to the load as would typically be observed.

Partial fusion defects (PFD) were observed on both the fatigue and fast fracture surfaces of four of the seven SP specimens that failed, shown in Figure 5.60, Figure 5.63 - Figure 5.65 and Figure 5.70. Although the effect of PFD at the time of writing is unknown, it was thought that they may have resulted in initiation of the predominant crack in two of the specimens, FS SP 3 and FS SP 6; although neither specimen returned a fatigue life significantly lower than expected.

Secondary cracking was evident on the fatigue crack fracture surfaces, as shown in Figure 5.66, and microvoid coalescence on the fast fracture surfaces, shown in Figure 5.60.

The DP process typically resulted in failure occurring at or near the ridges that occurred at the edge of the tool shoulder during the welding process, evident in Figure 5.71 and Figure 5.77; no preference for either the advancing or retreating side of the weld was noted, the advancing side being evident in four of the seven specimens tested to failure. The raised ridges may enhance initiation under four point loading as they result in an increased applied stress at this point, although it is probable that the cause was a combination of this and the minimum hardness occurring in this region. FS DP 5 and 6 failed in the HAZ, although near to the advancing side ridge. Multiple crack initiation sites were again observed, although the predominant cracks tended to be edge initiated. Figure 5.71 depicts multiple crack initiation with the initial crack growth following the score marks on the surface, these score marks being the result of the grinding used post weld to remove the extruded material at the edge of the tool shoulder.

Secondary cracking was again evident on the fatigue fracture surface, evident in Figure 5.78, and microvoid coalescence on the fast fracture surface, depicted in Figure 5.73.

5.5.3.1 Fractography ~ FS Single Pass

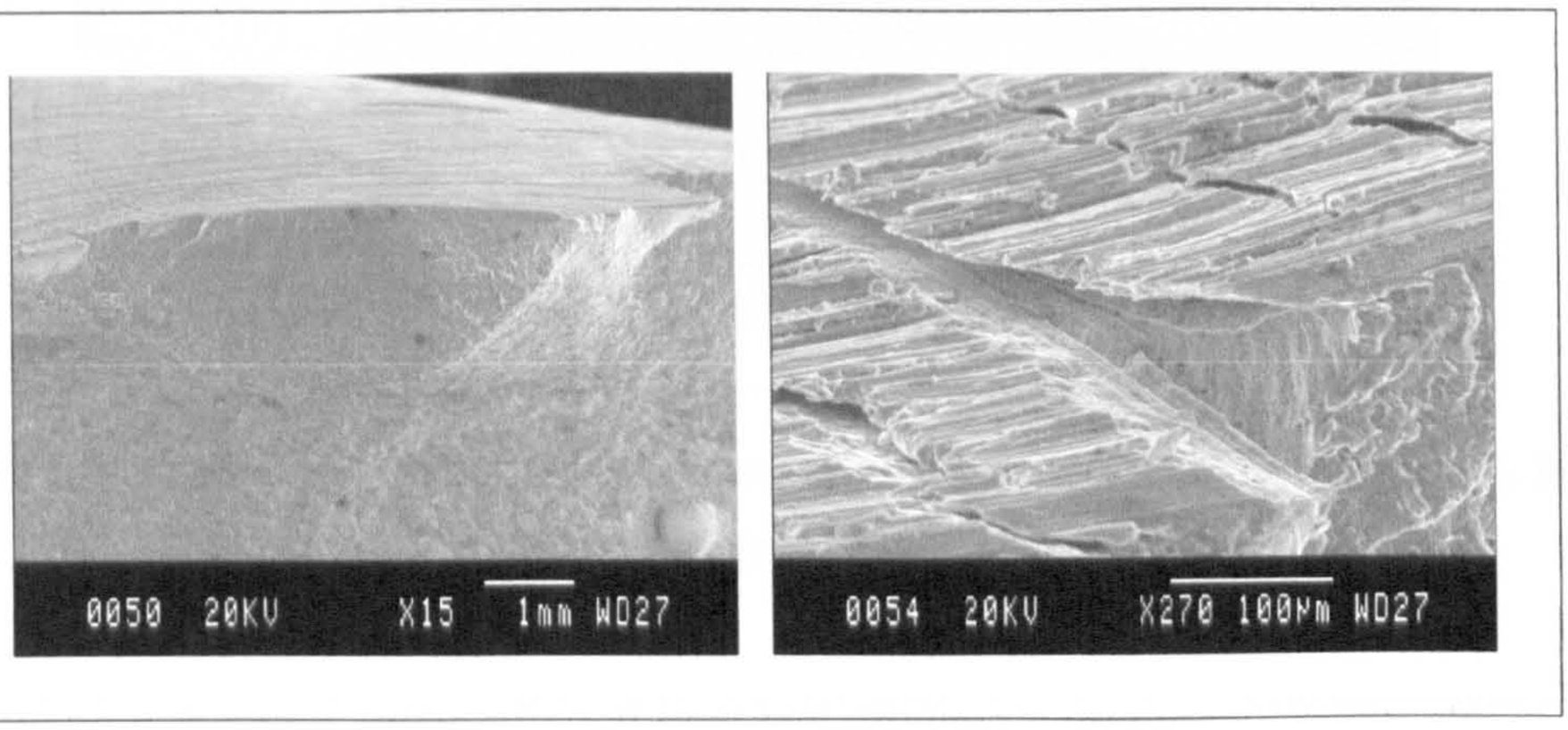

Figure 5.59: Secondary crack initiation site (left), multiple initiation sites from tool shoulder surface marks (right), (FS SP 1).

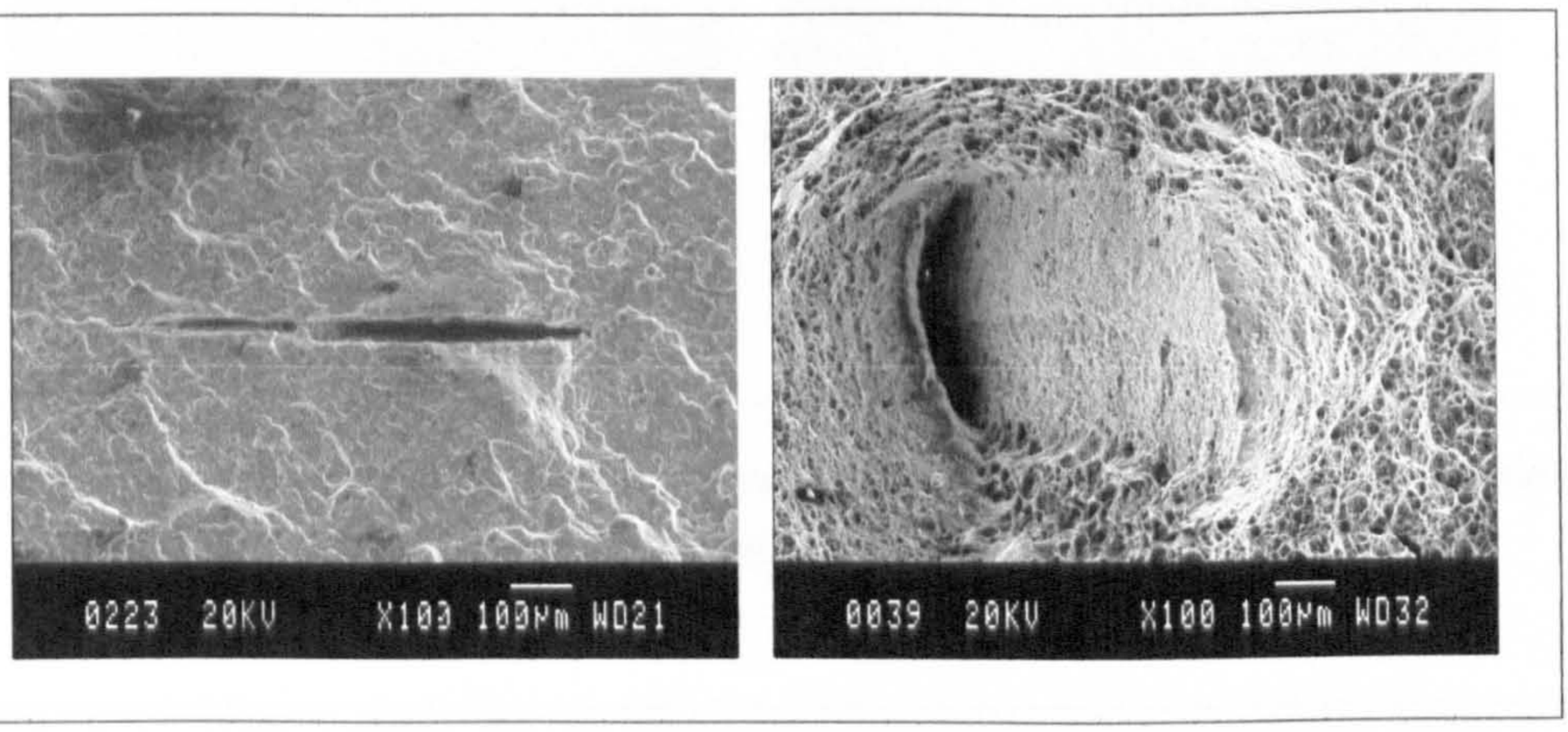

Figure 5.60: PFD, fatigue fracture surface (left), fast fracture surface (right), (FS SP 1).

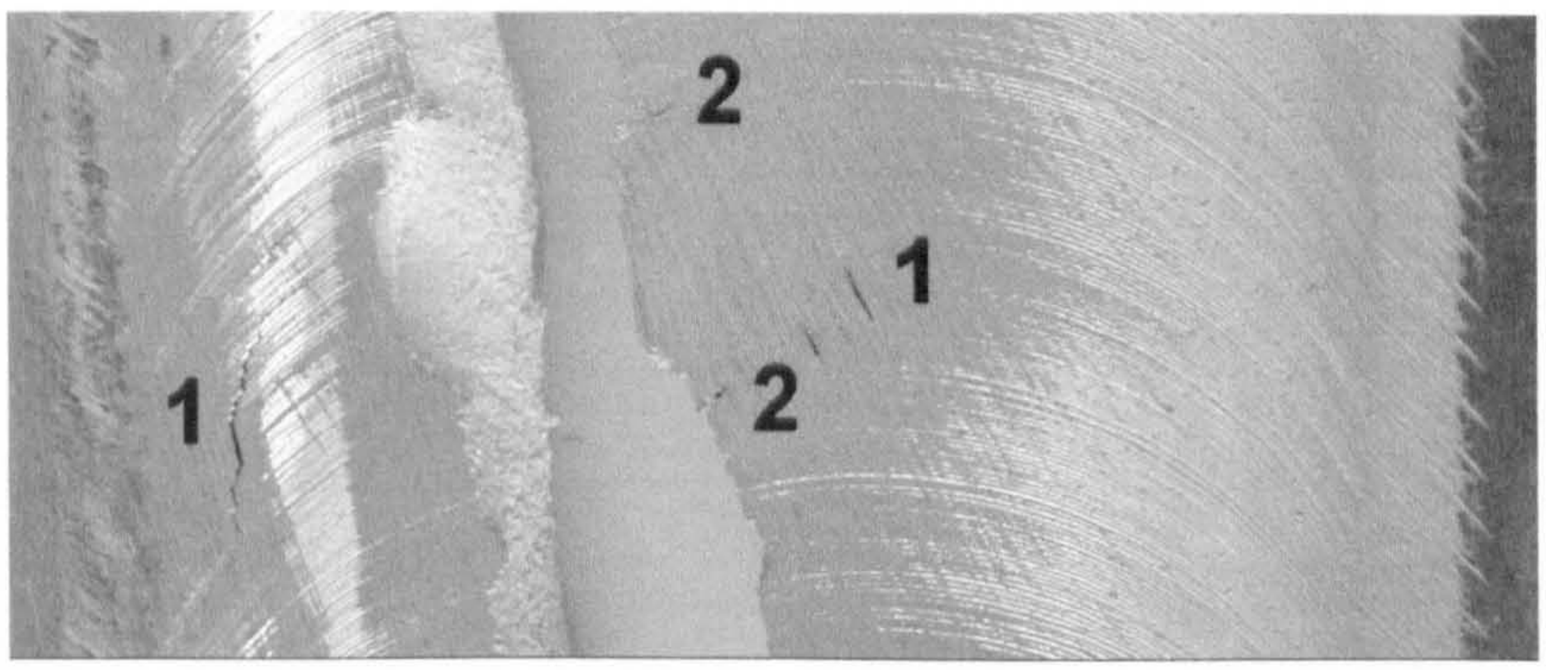

Figure 5.61: Secondary initiation sites; removal of weld flash machining marks (1), tool shoulder marks (2) (FS SP 1).

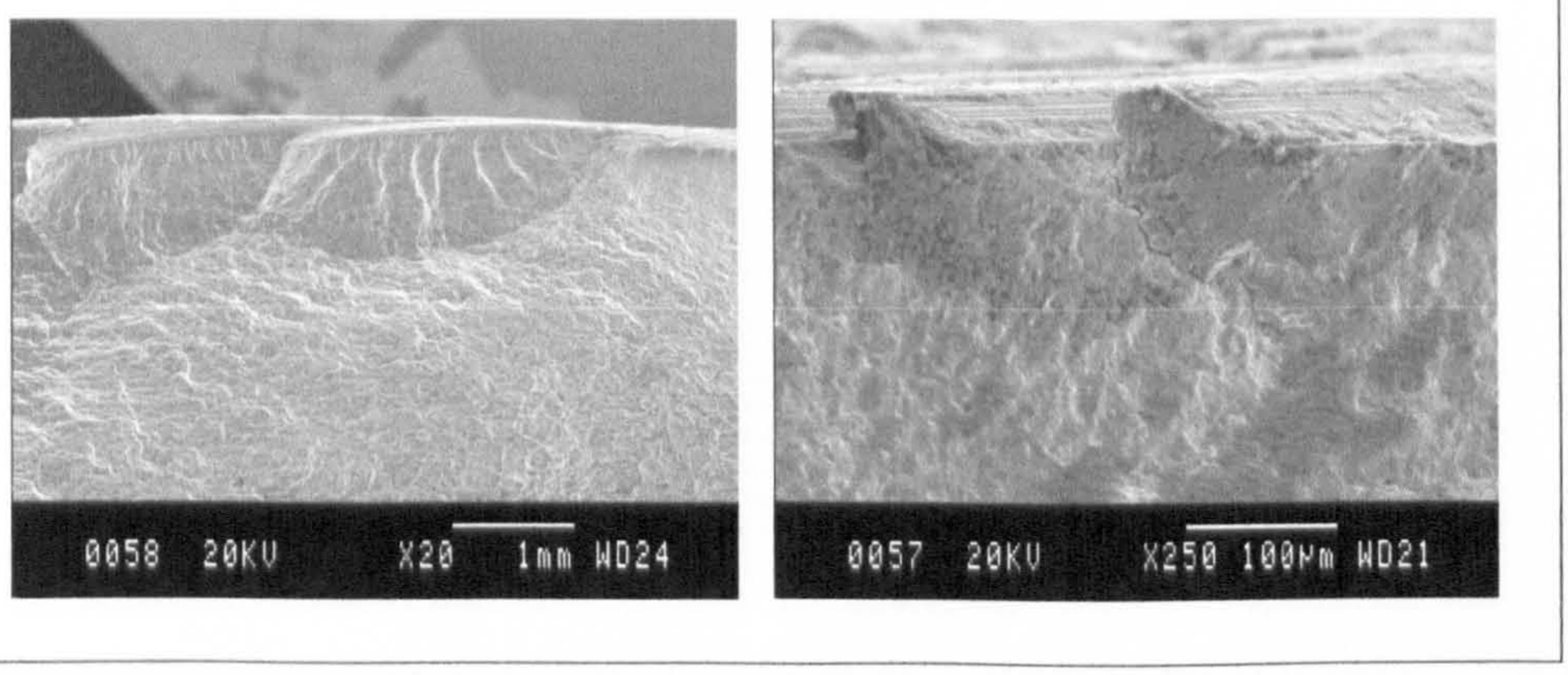

Figure 5.62: Fatigue crack initiation at circular score marks on weld surface (left & right) (FS SP 2).

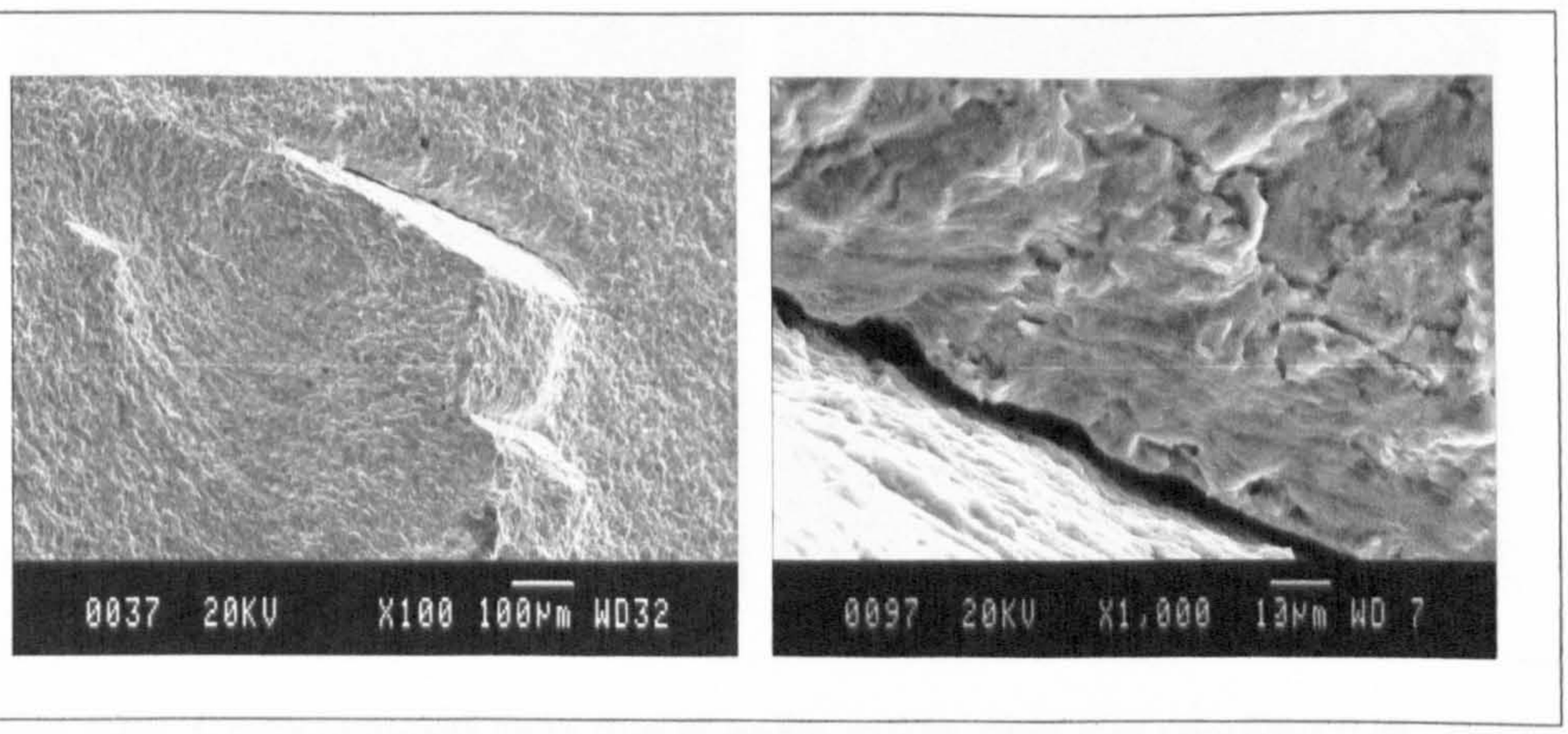

Figure 5.63: PFD on fatigue fracture surface (left & right), possible initiation site for main crack, (FS SP 3).

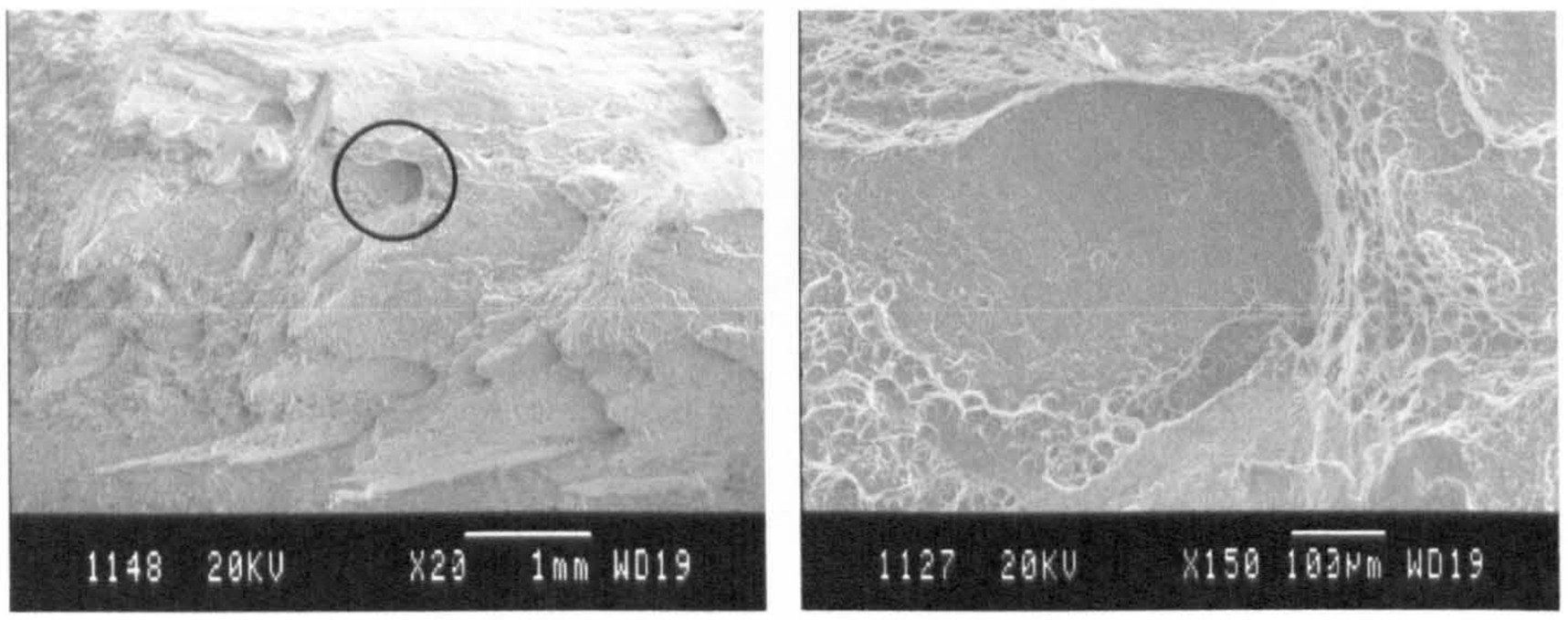

Figure 5.64: Weld nugget PFD on the fast fracture surface (left) and higher magnification view of highlighted area (right), (FS SP 3).

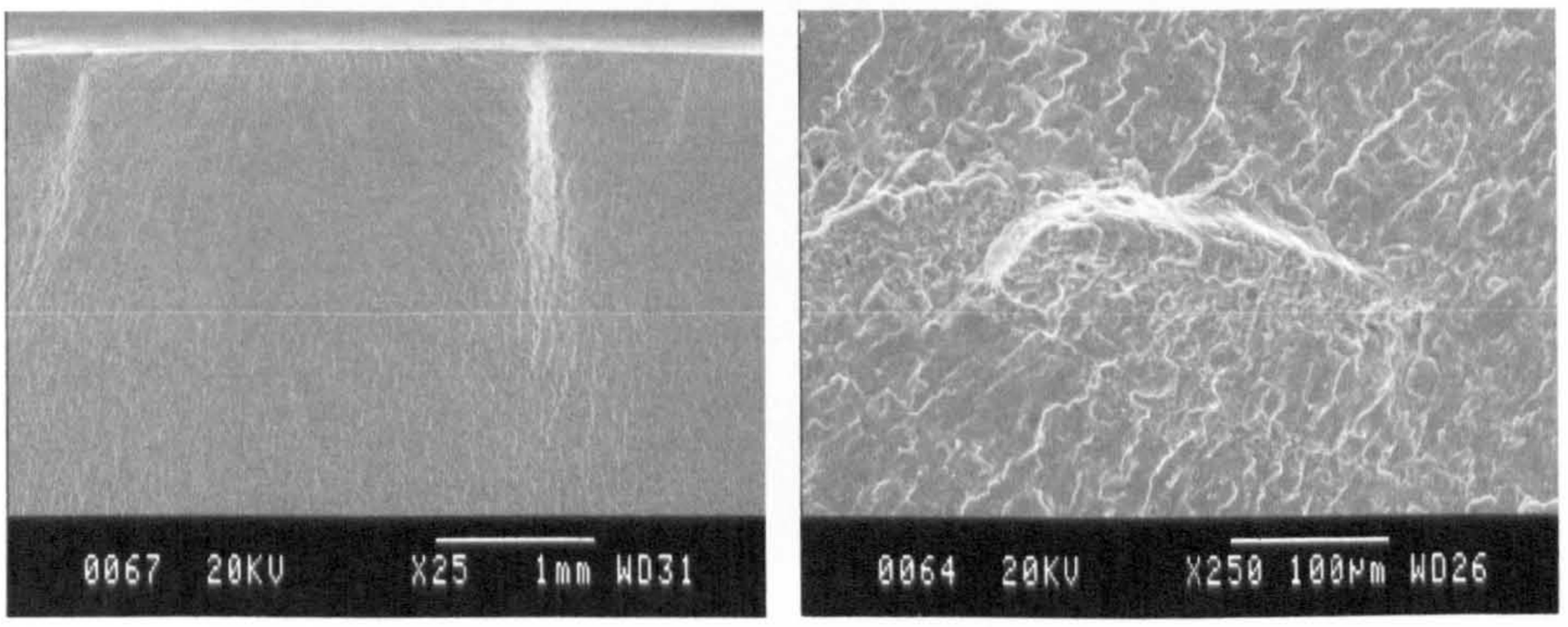

Figure 5.65: Line initiation (left), PFD on fatigue fracture surface (right), (FS SP 4).

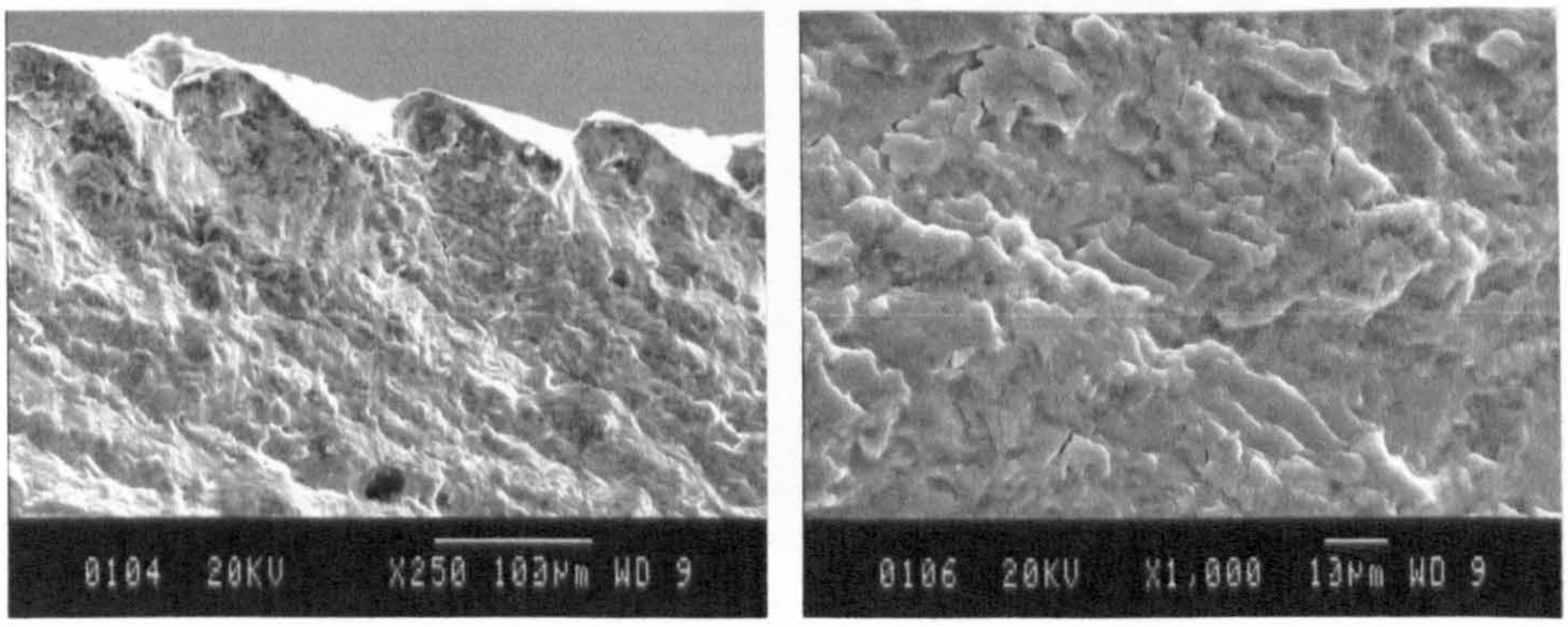

Figure 5.66: Crack initiation sites due to score marks from tool shoulder (left), fatigue crack surface with secondary cracking evident (right), (FS SP 6).

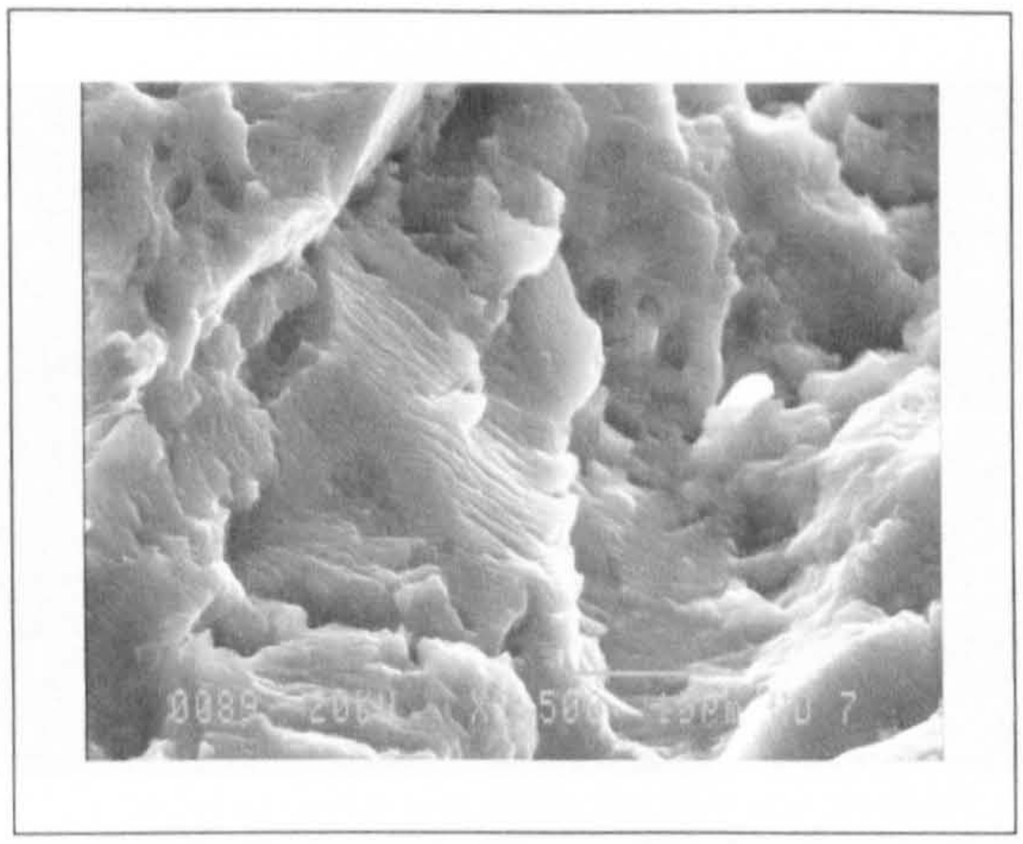

Figure 5.67: Fatigue striations (FS SP 3).

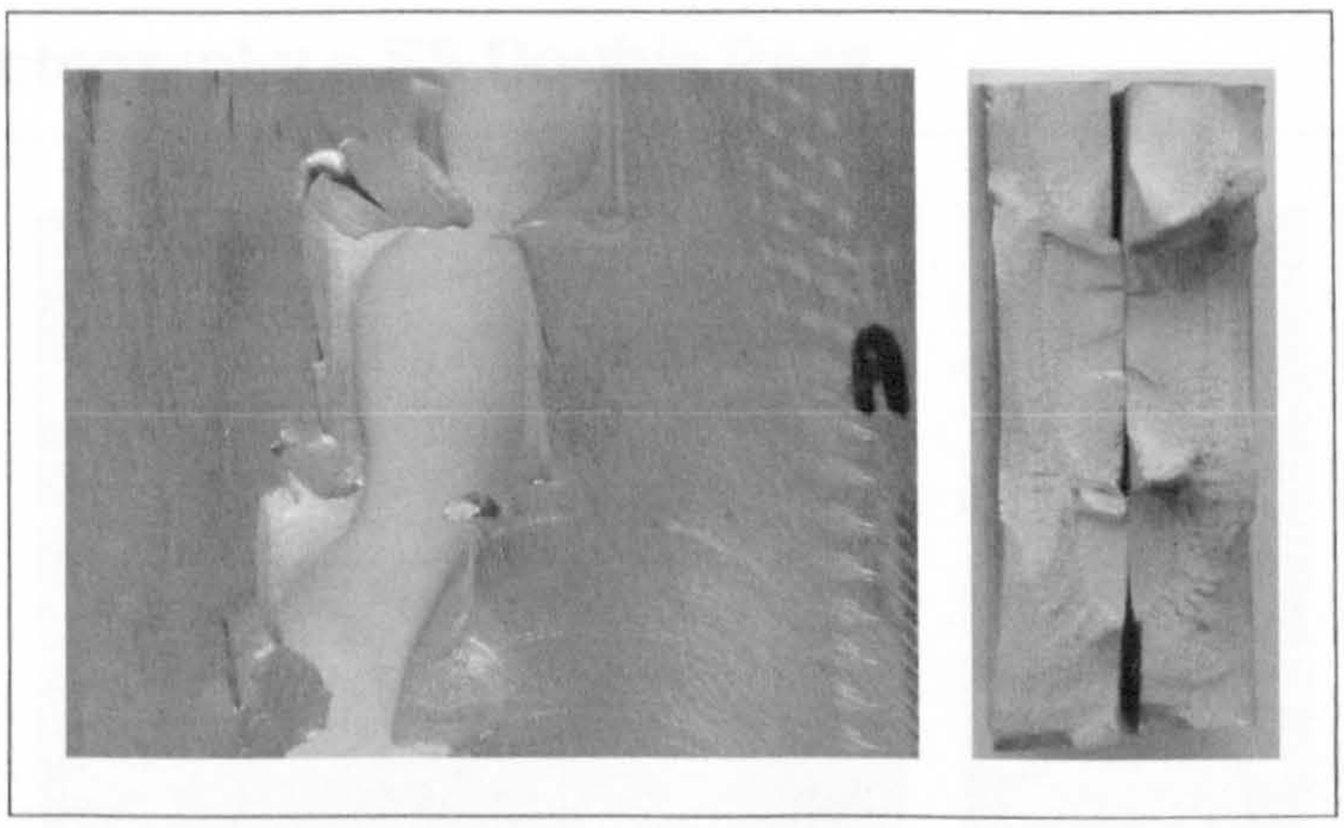

Figure 5.68: Multiple initiation crack sites (left) and fracture surfaces (right), (FS SP 4).

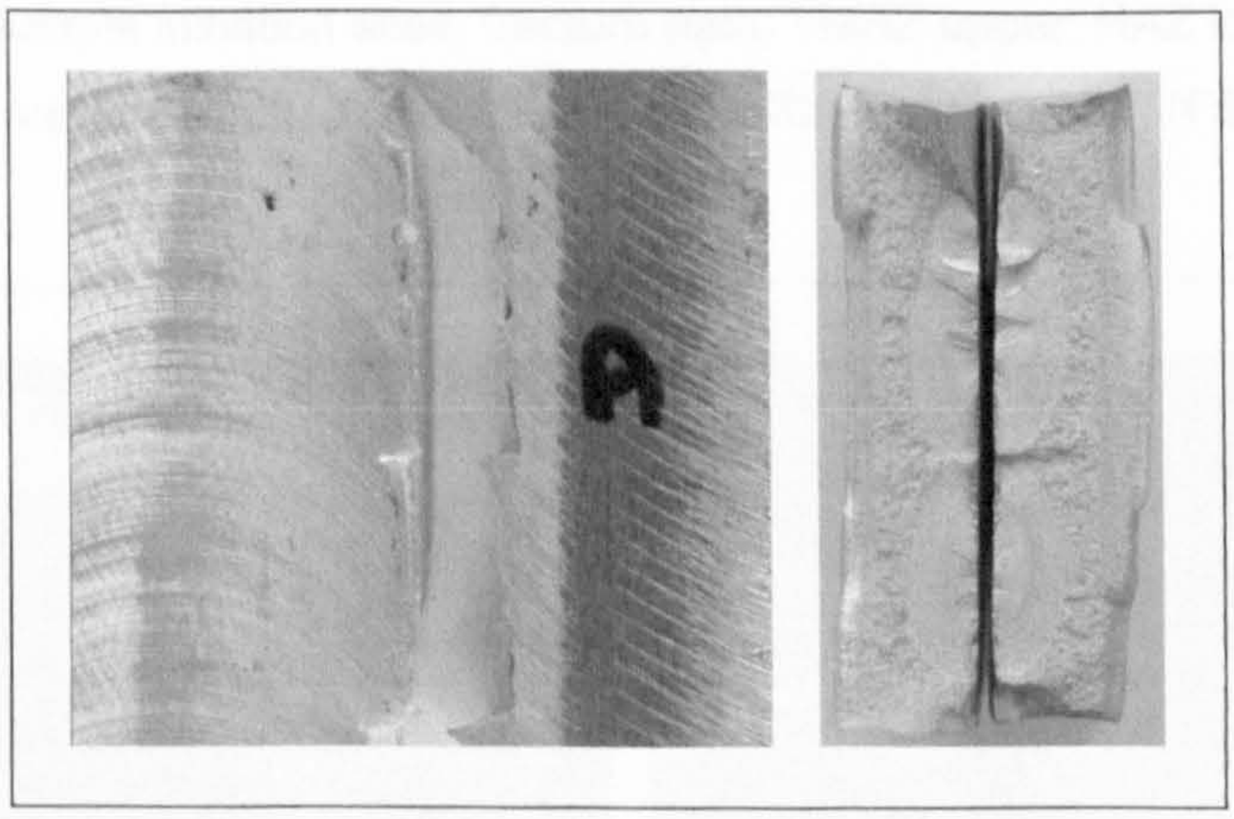

Figure 5.69: Fracture path near to advancing side tool shoulder edge (left) and fracture surfaces (right), (FS SP 5).

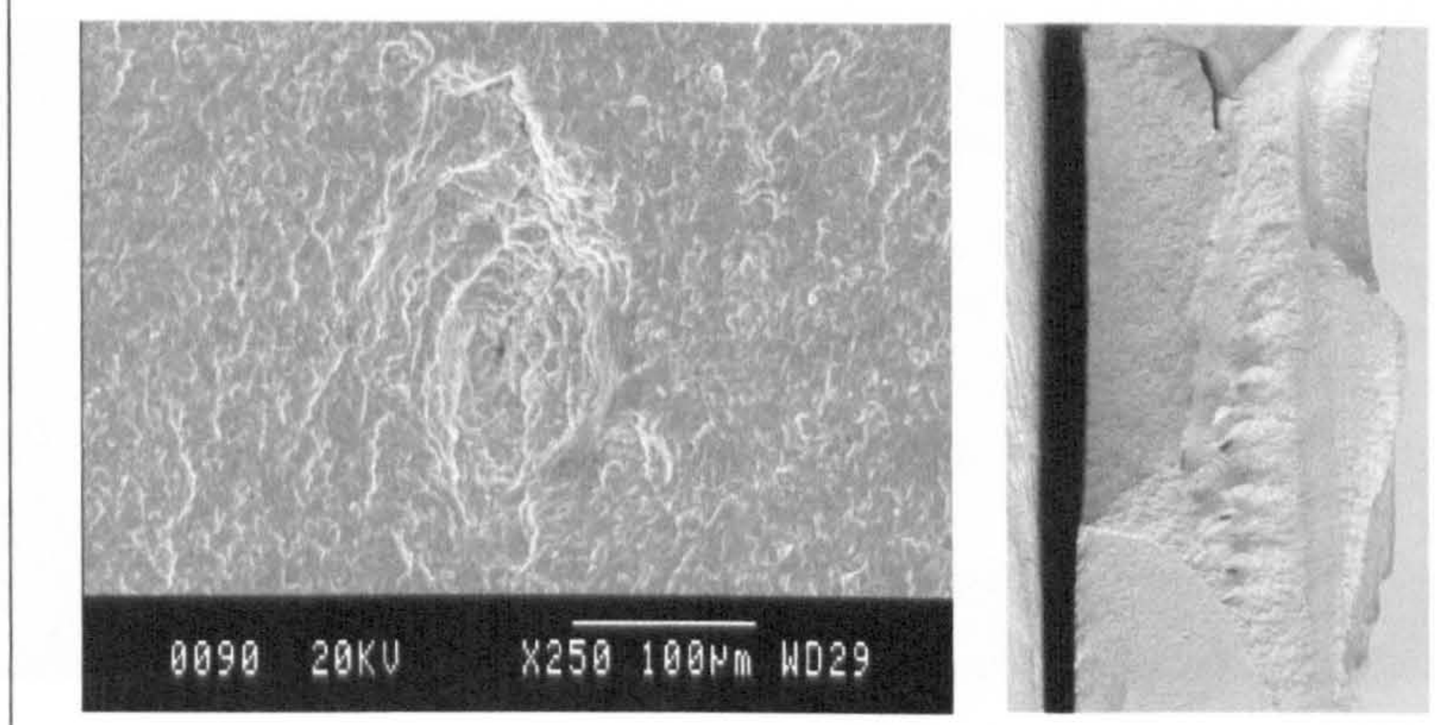

Figure 5.70: PFD on fatigue (left) and fast fracture (right) surfaces, (FS SP 7).

5.5.3.2 Fractography ~ FS Double Pass

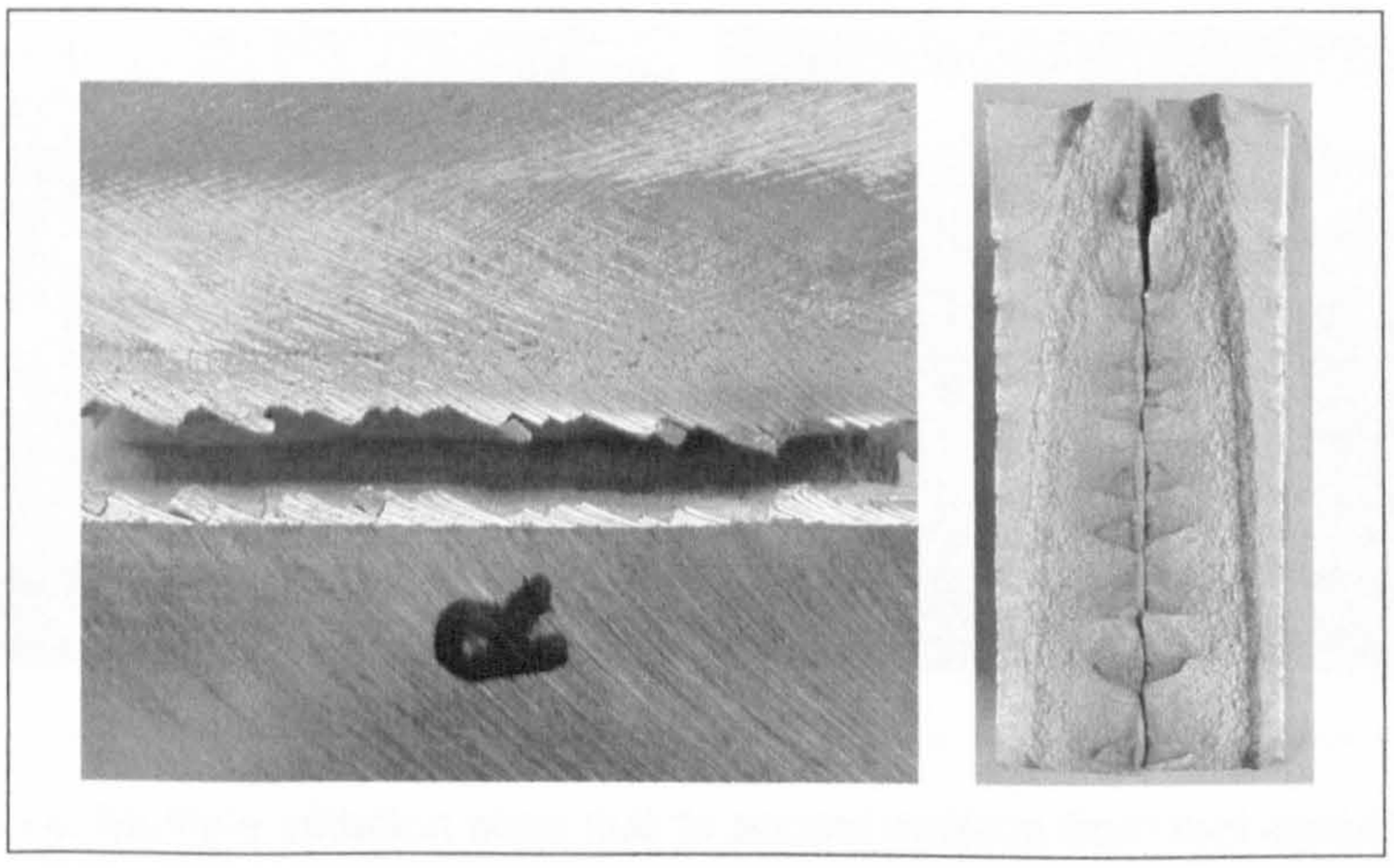

Figure 5.71: Multiple initiation sites, fracture path, TMAZ upper, HAZ lower, (left) and fatigue surface (right) at retreating side of the tool shoulder, (FS DP 1).

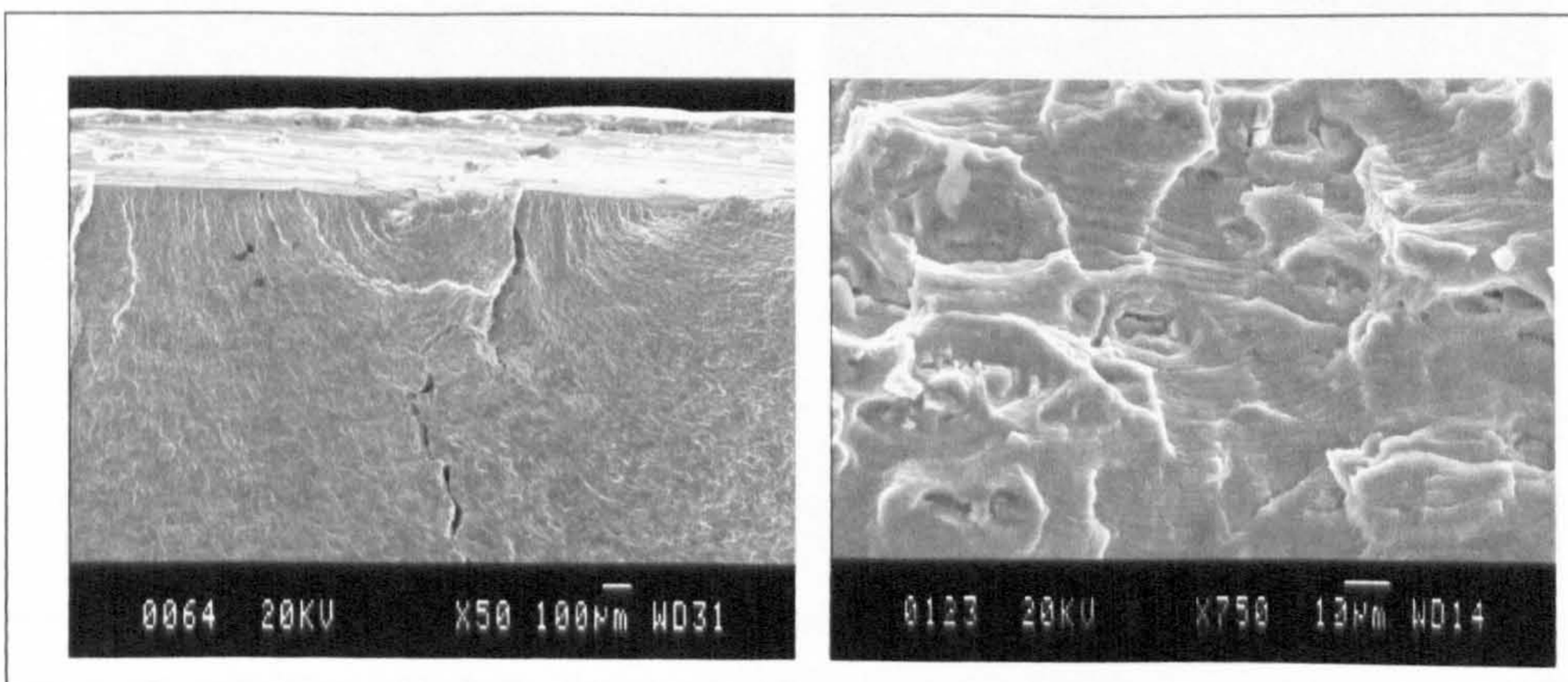

Figure 5.72: Initiation sites (left), fatigue striations (right), (FS DP 1).

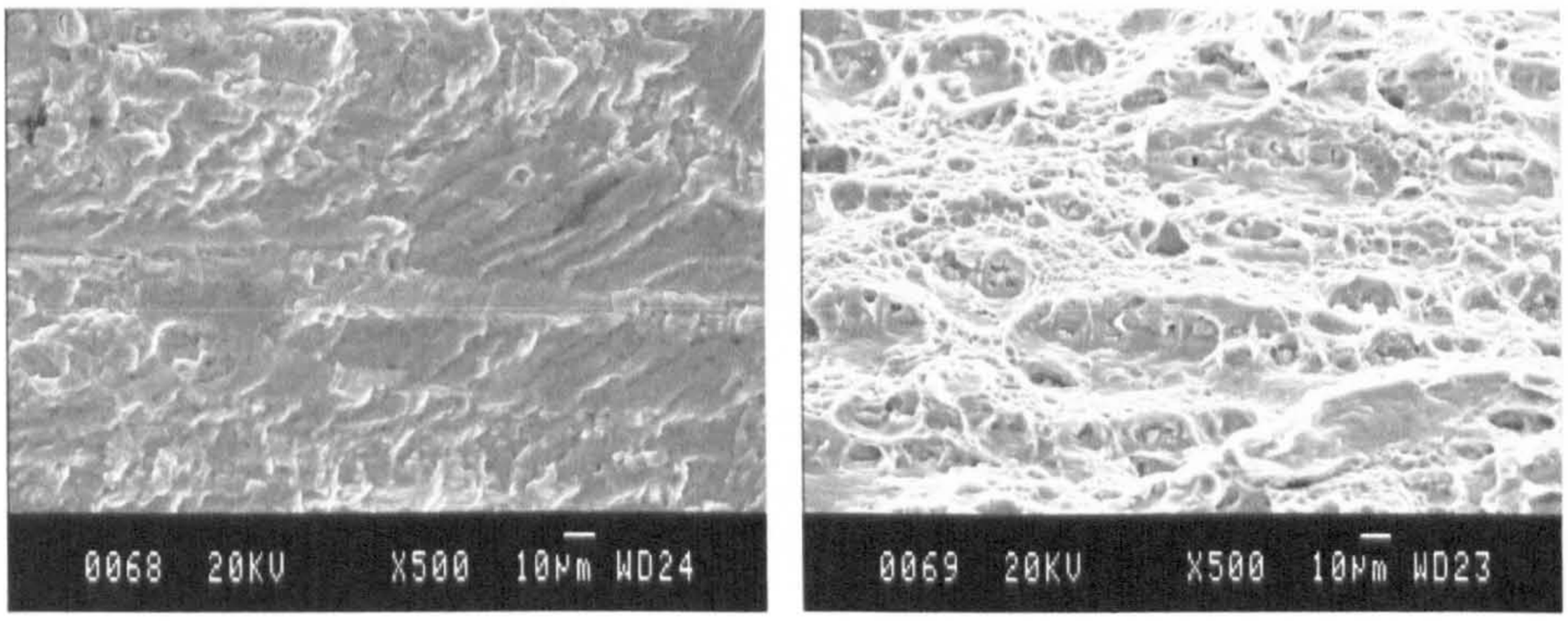

Figure 5.73: Fatigue fracture surface (left), microvoid coalescence on the fast fracture surface (right), (FS DP 2).

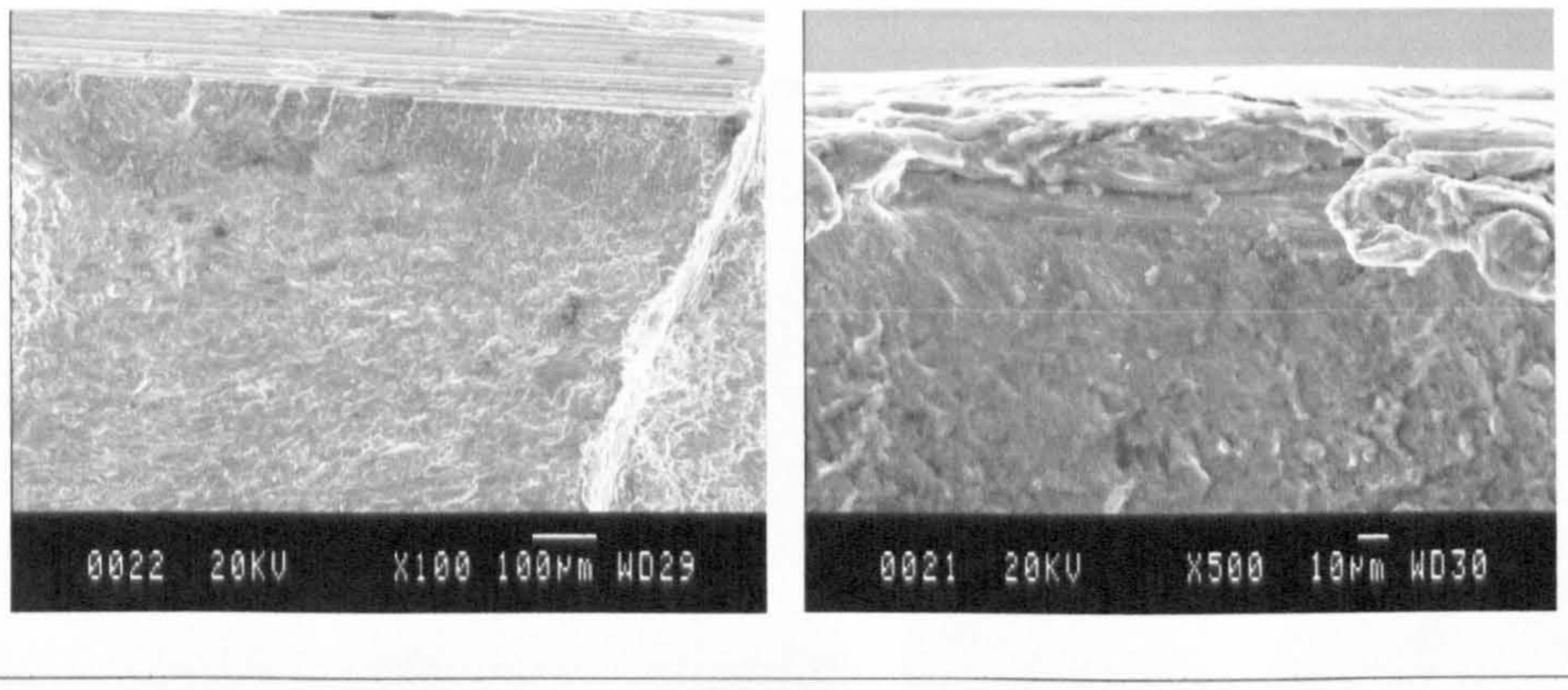

Figure 5.74: Multiple initiation sites due to scored surface from tool shoulder (left), possible initiation sites from weld flash (right), (FS DP 4).

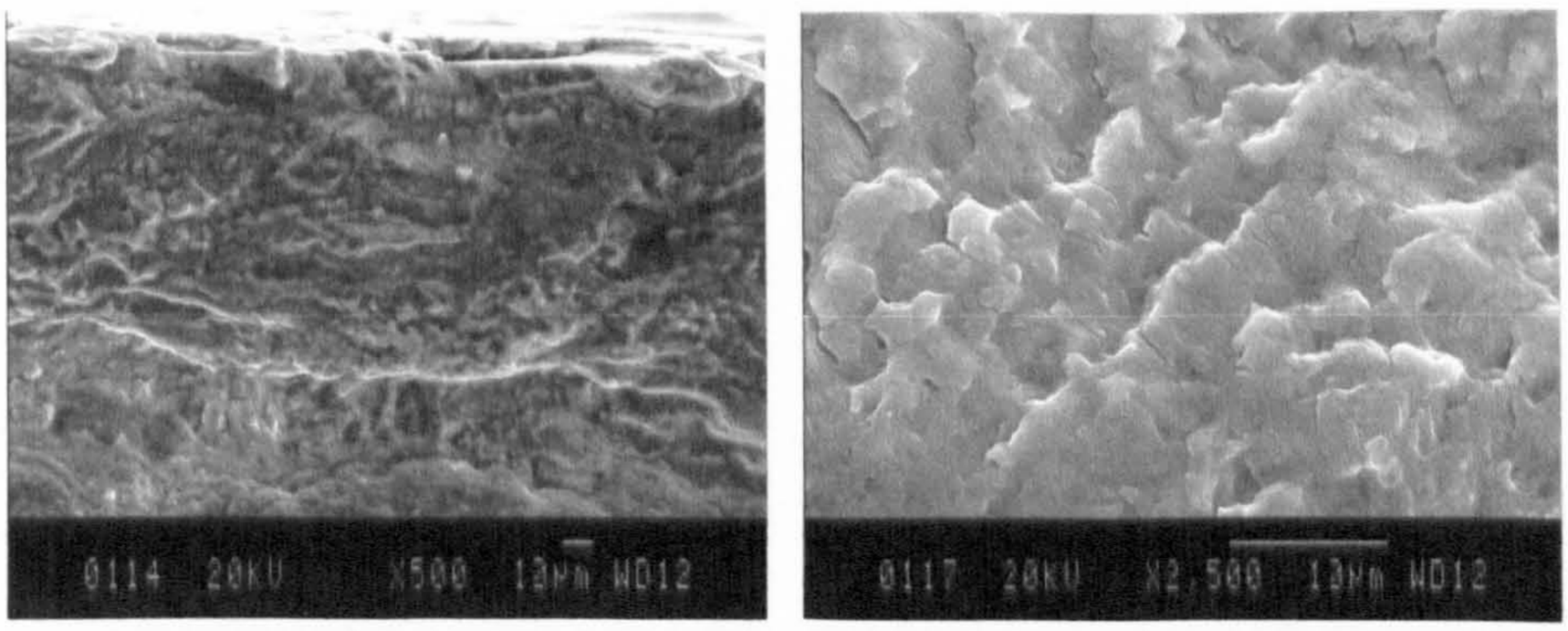

Figure 5.75: Initiation site (left), fatigue fracture surface (right), within the HAZ, (FS DP 6).

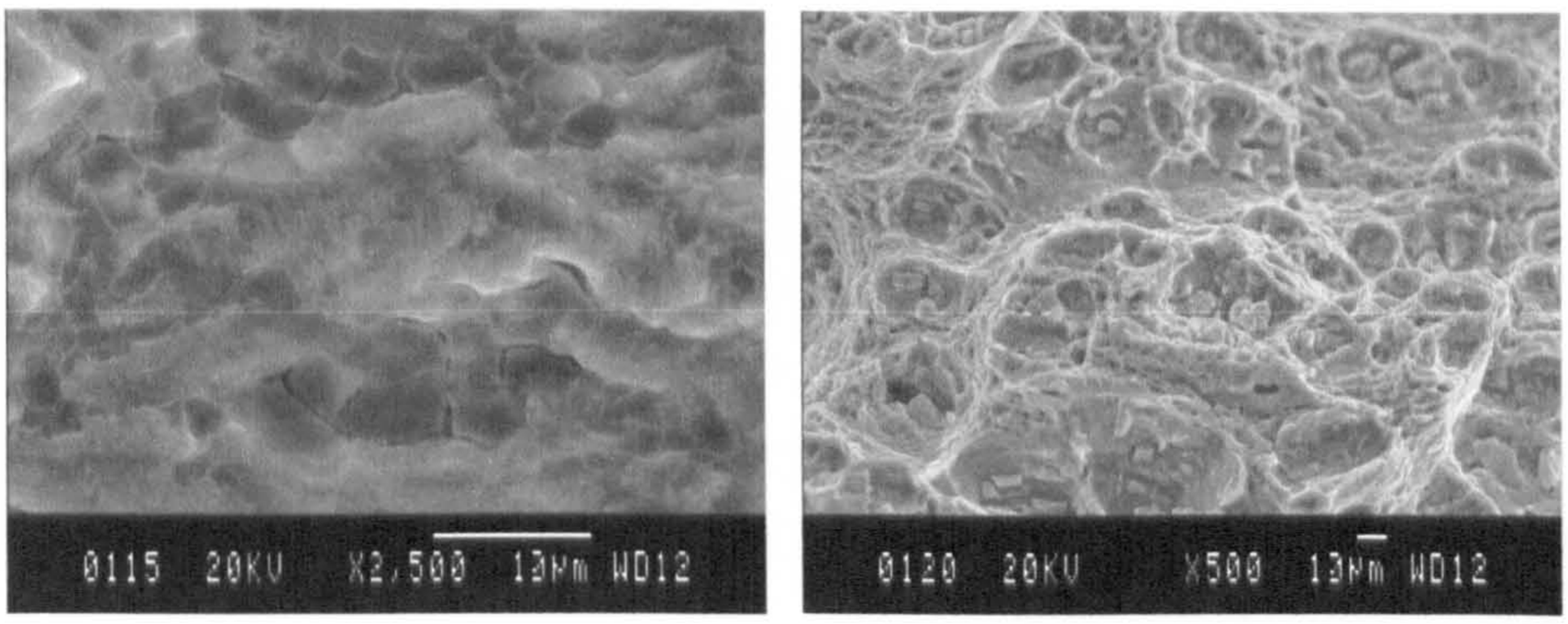

Figure 5.76: Fatigue fracture surface within the HAZ containing intermetallics (left), intermetallics and microvoid coalescence observed on the fast fracture surface within the HAZ (right), (FS DP 6).

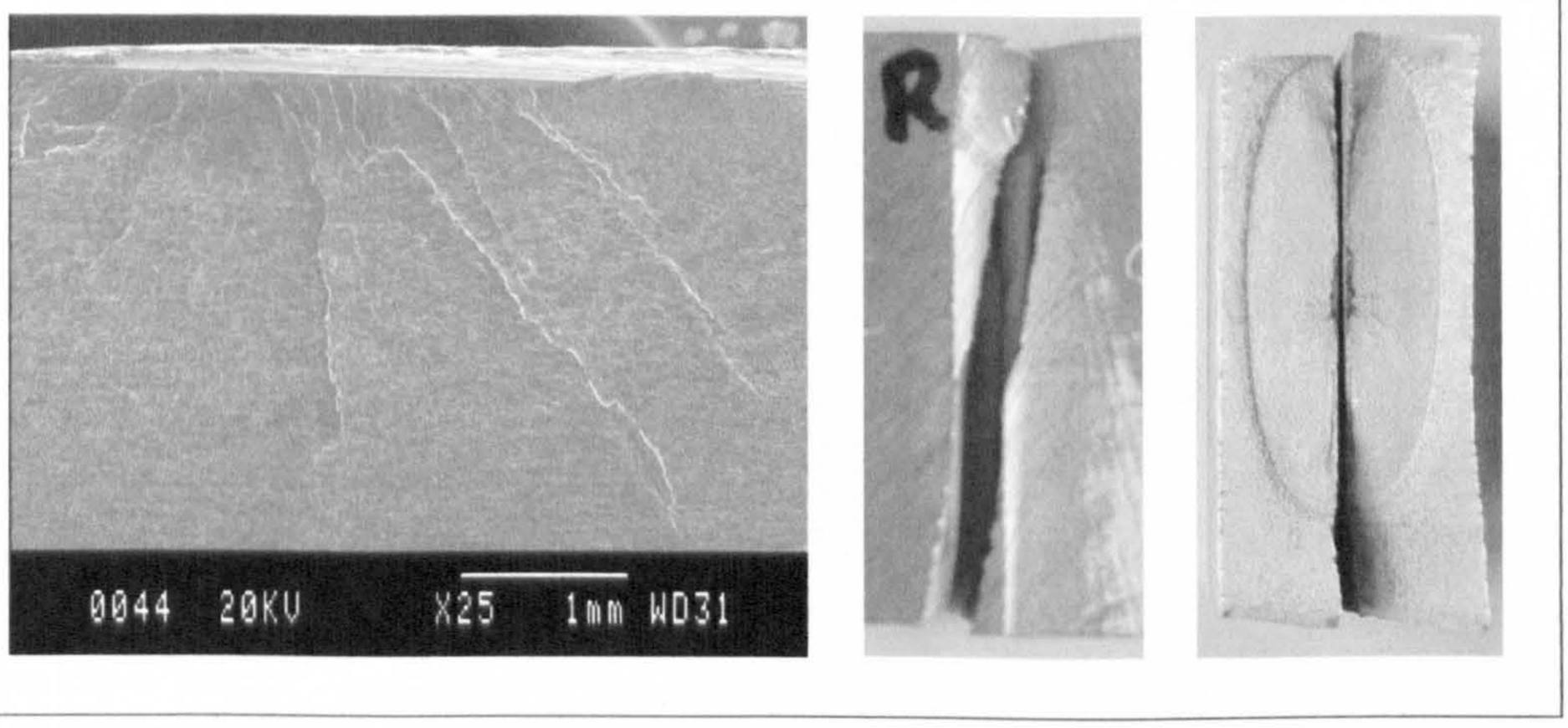

Figure 5.77: Multiple initiation sites (left), fracture path (centre), fracture surface (right), (FS DP 7).

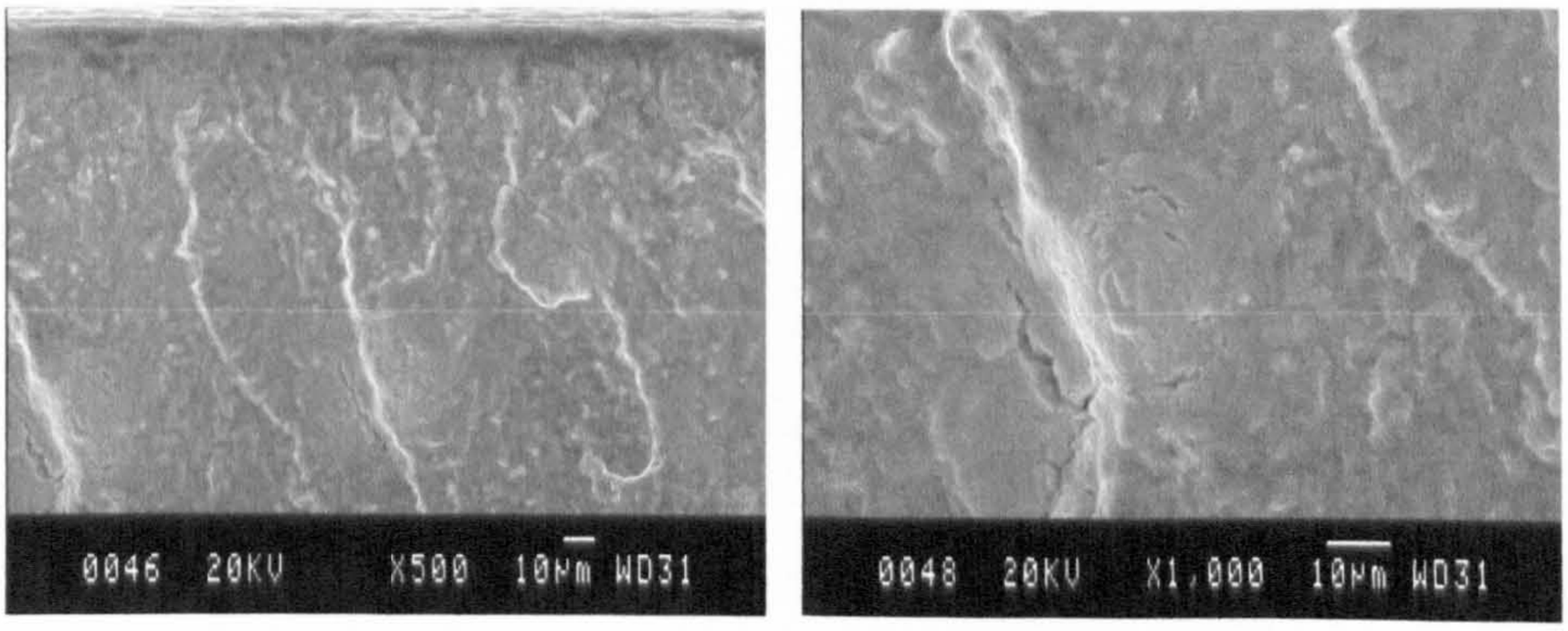

Figure 5.78: Secondary cracking on fatigue surface (left and right), (FS DP 7).

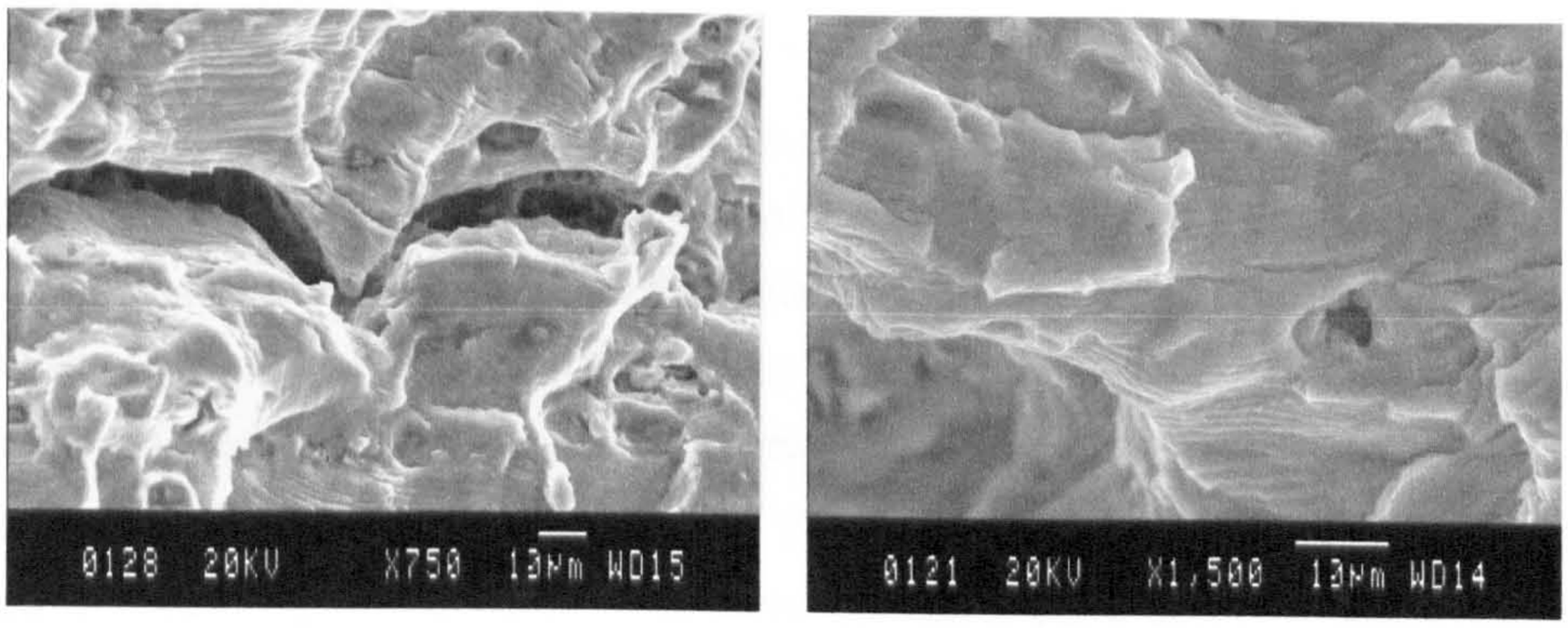

Figure 5.79: Fatigue striations and secondary cracking, left, and striations, right, (FS DP 1).

5.6 Discussion

Presentation of the S-N fatigue data for the AA 5383-H321 parent material and welded specimens involved two variables that had a significant effect on the results; these being the method used for curve fitting and the determination of the SCF at the weld toe of the MIG welds, both affecting the way the results are perceived. S-N data frequently exhibits significant scatter, but the process of fitting curves through the data, rather than presenting only the data points, enhances the lucidity of the results and simplifies the process of modelling of the data. It is therefore essential that when assessing fatigue data presented as S-N curves that significant variation may result not only from the test results, but also from the curve fitting technique employed. The three parameter power law, $\sigma_R = a + bN^c$, employed for the fatigue data presented within this dissertation has been utilised on the basis that it provided a satisfactory fit through the experimental data points, although significant scatter in the results was evident through the values returned for r^2. The use of a single equation to describe the results will ultimately simplify the modelling process. It would be hoped that as more S-N data becomes available the curve fitting technique employed will not only be viable, but also enhanced in its in accuracy.

The SCF for determining the stress at the weld toe of the MIG welds was also subjective due to both the variability of the weld geometry, notably the toe radius, angle and weld bead radius, and the difficulty in accurately measuring them. Measurements for the MIG welds under investigation are detailed in Table 3.26, these resulted in elastic SCF ranging from 1.159 - 1.449 for the LI weld and 1.388 - 2.811 for the HI weld depending on the technique utilised.

	LI		HI	
	Radius (mm)	**Angle (°)**	**Radius (mm)**	**Angle (°)**
Minimum	1.030	6	0.160	30.5
Maximum	4.080	26.5	1.210	51.5
Mean	2.381	13.9	0.641	39.7

Table 5.20: MIG LI and HI weld toe radii and angles.

The method employed considered the weld bead to be of a fixed radius with the weld toe radius intersecting both the parent material and bead tangentially, the weld toe angle being determined by the two radii. The SCF was then determined by utilising an elastic-plastic, based on the tensile properties of the MIG welded material, finite element analysis. Due to the variability of the weld toe radii this technique results in a range of values for the SCF and the worst case scenario was employed on the basis that all the specimens would contain a toe radius equivalent to the smallest measured, 1.030 and

0.160 mm for the LI and HI welds respectively. The SCF applied ranged from 1.119 - 1.275 for the LI weld and 1.320 - 2.135 for the HI weld, the SCF reducing at higher applied stresses due to plastic deformation.

5.6.1 S-N Test Results

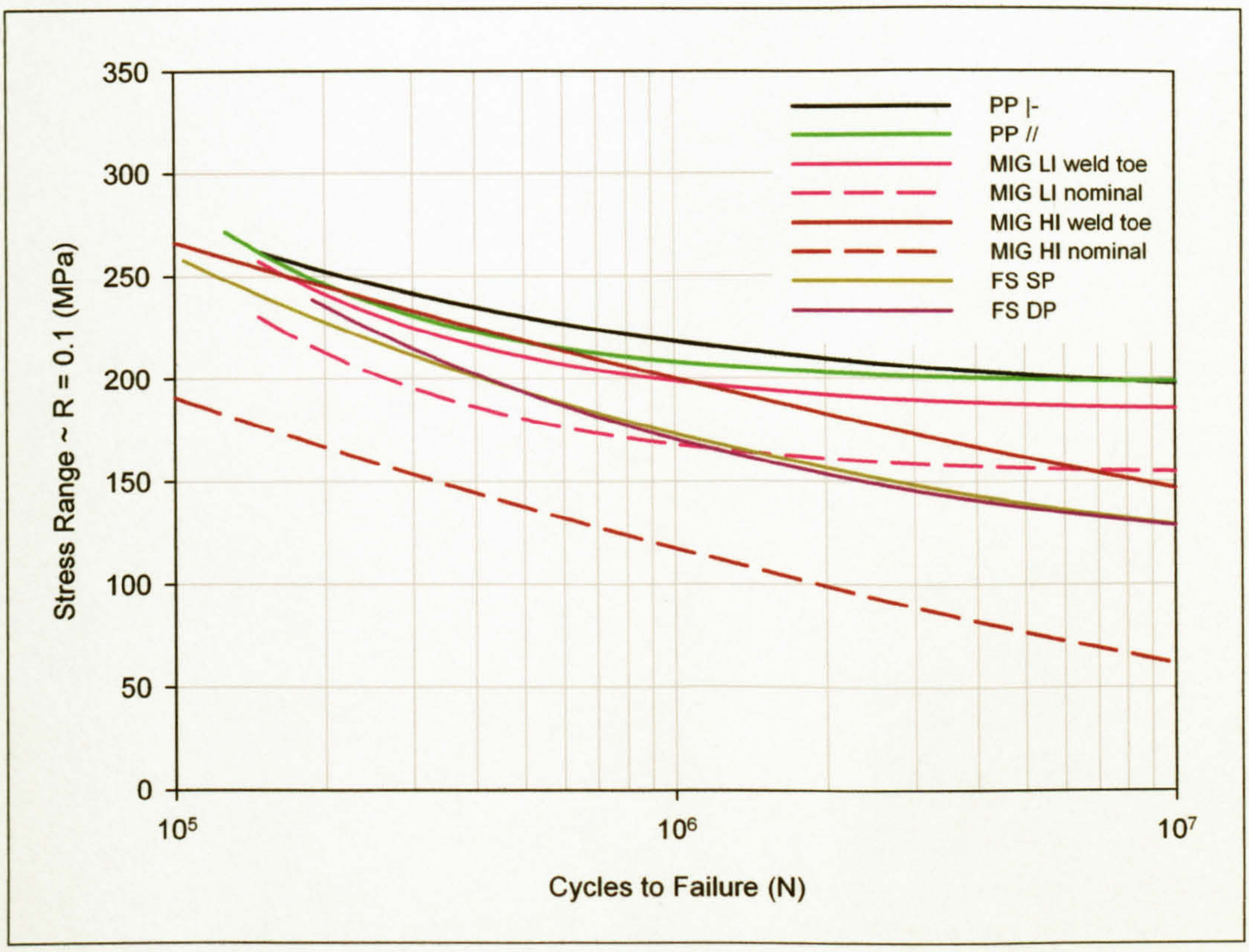

Figure 5.80: Four point loading S-N fatigue curves for AA 5383-H321 parent plate, MIG LI and HI and FS SP and DP welds.

From the four point loading S-N test results obtained, shown in Figure 5.80 and Table 5.21, it was evident that over the cycles to failure range for which results were obtained, typically 10^5 - 10^7 cycles, the PP |- specimens had the greatest fatigue strength, although at both extremities of the range, extrapolation of the curves would suggest that the PP // specimens had the greater strength. Due to the considerable scatter observed in the data for the parent material it would be prudent to undertake further tests to enhance curve fitting and to develop confidence limits if the results were to be considered for design purposes, although for the purposes of this work the results were considered satisfactory. An attempt to enhance the accuracy in the lower cycle regime, for lives less than 2×10^5 cycles, of both the |- and // specimens was attempted, but this was hampered through specimens failing due to the contact stresses imposed by the loading rollers, thereby making these results invalid.

When the stress concentrating effect of the weld toe was taken into consideration the two MIG processes returned fatigue strengths that were 0.96 - 0.97 of that returned by the PP |- for a life of 2×10^5 cycles and 0.91 - 0.92 for a life of 10^6 cycles, resulting in them having the greatest strength of the welds under test. In contrast to these results, if the stress concentrating effect of the weld was ignored the MIG HI weld had the lowest fatigue strength for all the welds tested. The LI weld, although having a greater fatigue strength than the HI, had an inferior fatigue strength to that returned by the FS welds for lives up to $1 - 2 \times 10^6$ cycles, although for lives greater than this the LI weld had a superior fatigue strength. It should be noted that for a true comparison of the fatigue strength of a welded structure the nominal stresses should be compared; for a MIG weld the nominal and local stresses would only be comparable if the stress concentrating effects of the weld geometry had been removed through appropriate weld bead modification.

The friction stir welds both returned comparable fatigue strengths for the two processes, with values ranging from 0.65 - 0.93 of the values observed for the PP |-, the increase in the disparity occurring as the stress range decreased. For lives below 3×10^5 cycles the DP process started to exhibit an increase in fatigue strength when compared to the SP weld, amounting to an increase of 5.7% over the SP process.

Comparison of the two welding processes showed that the MIG LI weld had a greater fatigue strength than the FS welds for lives greater than 2×10^6 cycles when the nominal stresses were compared, at 10^7 cycles the LI weld having a fatigue strength 19% greater than that observed for the FS welds. For lives below 10^6 cycles the FS welds had a greater fatigue strength; at a life of 2×10^5 cycles the LI weld was between 7 - 10% weaker than the FS welds. The HI weld was observed to have the lowest fatigue strength of all the welds under consideration, with a strength 27 - 29% lower at 2×10^5 cycles and 53% lower at 10^7 cycles.

Material/ Weld	Fatigue Strength									
	Number of Cycles									
	2×10^6		10^6		2×10^6		5×10^6		10^7	
	Δσ (MPa)	Specific w.r.t. PP |-	Δσ (MPa)	Specific w.r.t. PP |-	Δσ (MPa)	Specific w.r.t. PP |-	Δσ (MPa)	Specific w.r.t. PP |-	Δσ (MPa)	Specific w.r.t. PP |-
PP |-	252	1.00	218	1.00	210	1.00	202	1.00	198	1.00
PP //	246	0.98	208	0.95	203	0.97	200	0.99	199	1.01
MIG LI toe/ nominal	241/ 212	0.96/ 0.84	199/ 168	0.91/ 0.77	192/ 161	0.91/ 0.77	187/ 156	0.93/ 0.77	186/ 154	0.94/ 0.78
MIG HI toe/ nominal	245/ 167	0.97/ 0.66	200/ 117	0.92/ 0.54	183/ 99	0.87/ 0.47	162/ 77	0.80/ 0.38	147/ 61	0.74/ 0.31
FS SP	228	0.90	173	0.79	157	0.75	139	0.69	129	0.65
FS DP	235	0.93	171	0.78	154	0.73	137	0.68	129	0.65

Table 5.21: Summary of fatigue strengths for AA 5383-H321, R = 0.1.

The values obtained for the fatigue strength of the AA 5383-H321 parent material and MIG welds, detailed in Table 5.21, exceeded those contained within three published design codes, detailed in Table 5.22. Although when comparing the design curves with the experimental results obtained the following points must be considered:

i. The design curves are not specific to the AA 5383-H321 alloy under consideration.
ii. It was assumed that the values utilised in the design curves were developed from uniaxial tensile tests and would therefore tend to be conservative with respect to four point loading results.
iii. In the case of both Eurocode 9[1] and ECCS[2] the design curves were two standard deviations below the mean.

[1] Nederlands Normalisatie-instiuut (1998)
[2] ECCS Technical Committee 2 (1992)

Material/ Weld	Fatigue Strength at N = 2 x 10^6 cycles, Δσ (MPa)					
	Test Results		Design Codes			Calcraft[1]
	Δσ	Two std. dev. below curve	Eurocode 9[1]	ESDU[2]	ECCS[2]	
PP ⊦-	210	180	86	144	95	175
PP //	203	183	69			
MIG LI (weld toe/nominal)	192/161	162/128	39	70	50	96
MIG HI (weld toe/nominal)	183/99	159/70			45	
FS SP	157	126				
FS DP	154	113				

Table 5.22: Comparison of parent material and MIG and FS butt welded joint fatigue strengths at 2 x 10^6 cycles.

The test results obtained compared favourably with those obtained by Calcraft[1] who undertook testing of AA 5383, returning values of 175 MPa and 96 MPa at lives of 2 x 10^6 cycles for the parent plate and MIG welded butt joint respectively. Calcraft's[1] results were determined through uniaxial tensile loading which may partially explain the lower values obtained.

Published fatigue data on friction stir welds is limited due to the process being relatively new at the time of writing, although Magnusson and Källman[3] obtained values of 72 - 83% of the parent material fatigue strength at 2 x 10^6 for 2024, 6013 and 7475 alloys as shown in Table 5.23. The values obtained for the AA 5383-H321 alloy compared well with these, returning values of 73 - 75% of the parent material strength. Similar results were obtained by Dawes and Thomas[4], with values of 84% of the parent material for a single pass 5083-O alloy under tensile loading with a stress ratio of 0.1 and a slightly lower value for a 2014-T6 weld.

---

[1] Calcraft, RC (1999)
[2] ESDU International (1991)
[3] Magnusson, L; Källman, L (2000)
[4] Dawes, C; Thomas W (1995)

	Fatigue Strength at N = 2 x 10^6 cycles									
	Aluminium alloy									
	5383-H321 (Test results)		2024-T3[1]		6013-T6[1]		7475-T76[1]		5083-O[2]	
	$\Delta\sigma_R$ (MPa)	% of parent material	$\Delta\sigma_R$ (MPa)	% of parent material	$\Delta\sigma_R$ (MPa)	% of parent material	$\Delta\sigma_R$ (MPa)	% of parent material	$\Delta\sigma_R$ (MPa)	% of parent material
Parent material	210	100	254	100	180	100	229	100	140	100
FS welded	154-157	73-75	184	72	146	81	167	73	118	84

Table 5.23: Comparison of parent material and friction stir butt welded fatigue strengths at 2 x 10^6 cycles with published data.

5.6.2 Crack Initiation and Fatigue Fracture Surfaces

There was a notable difference between the crack initiation observed in the parent material, MIG welds and FS welds. All the specimens exhibited multiple initiation sites, with these being more abundant at higher stress ranges; typically coalescence of the cracks resulting from the initiation sites then occurred as crack growth progressed.

Cracks in the parent material generally initiated at surface intermetallics as shown in Figure 5.81. There would be an increase in the likelihood of both surface and sub-surface intermetallic induced crack initiation if uniaxial testing was performed due to the complete plane being subjected to the same stress rather than only the outer fibres as initially occurs in four point loading, although the surface would still be the favoured site for initiation due to the plastic constraint being minimised at the surface.

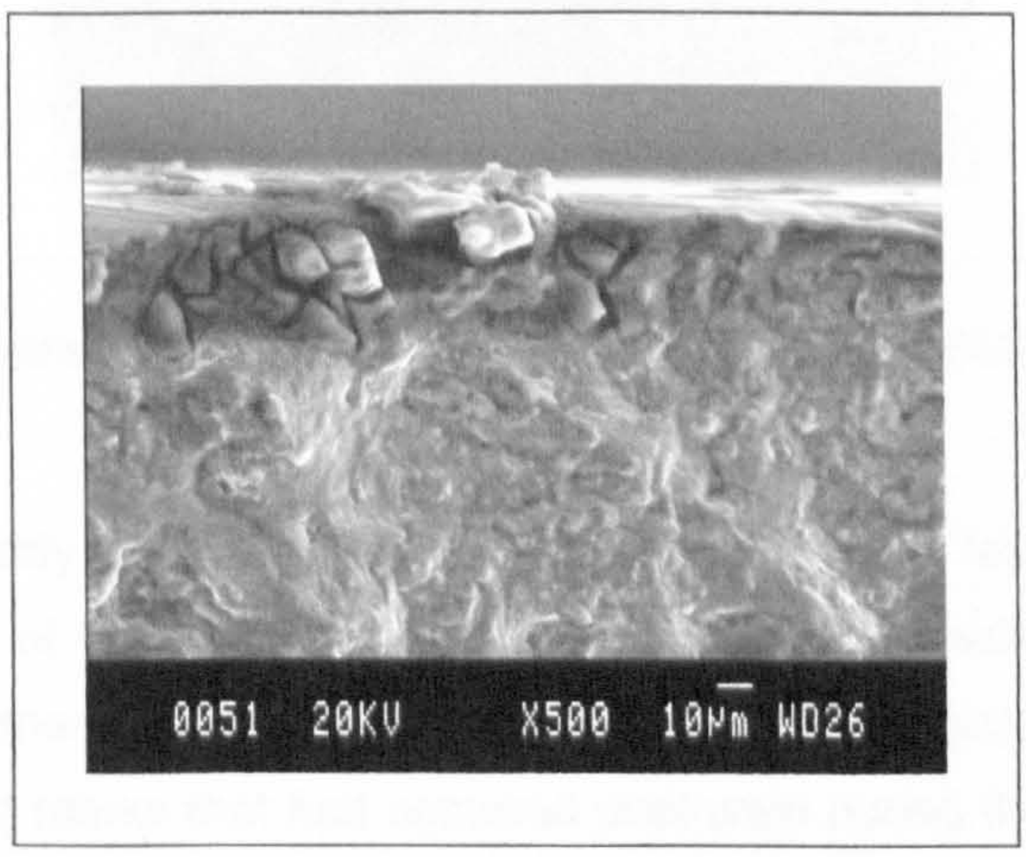

Figure 5.81: Intermetallic induced crack initiation site in AA 5383-H321 parent plate.

[1] Magnusson, L; Källman, L (2000)
[2] Dawes, C; Thomas W (1995)

Crack initiation in the MIG welds occurred at the weld toe, with the exact initiation sites generally being associated with clusters of porosity. A typically MIG weld crack initiation site is shown in Figure 5.82, similar initiation sites being observed by Masuda[1] in his study of butt welded AA 5083-O, shown in Figure 5.83. The LI weld also exhibited initiation sites due to the stress concentrating effects of weld spatter, a blow hole and the weld geometry.

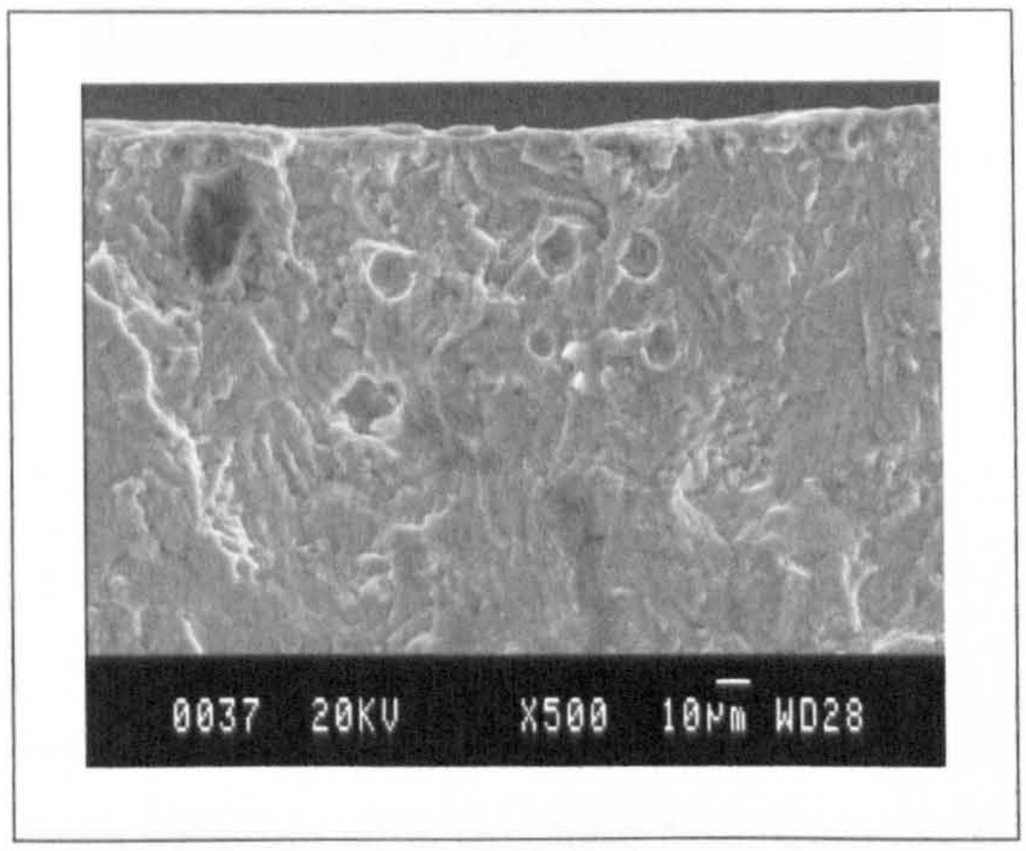

Figure 5.82: Porosity induced crack initiation site in MIG butt welded AA 5383-H321.

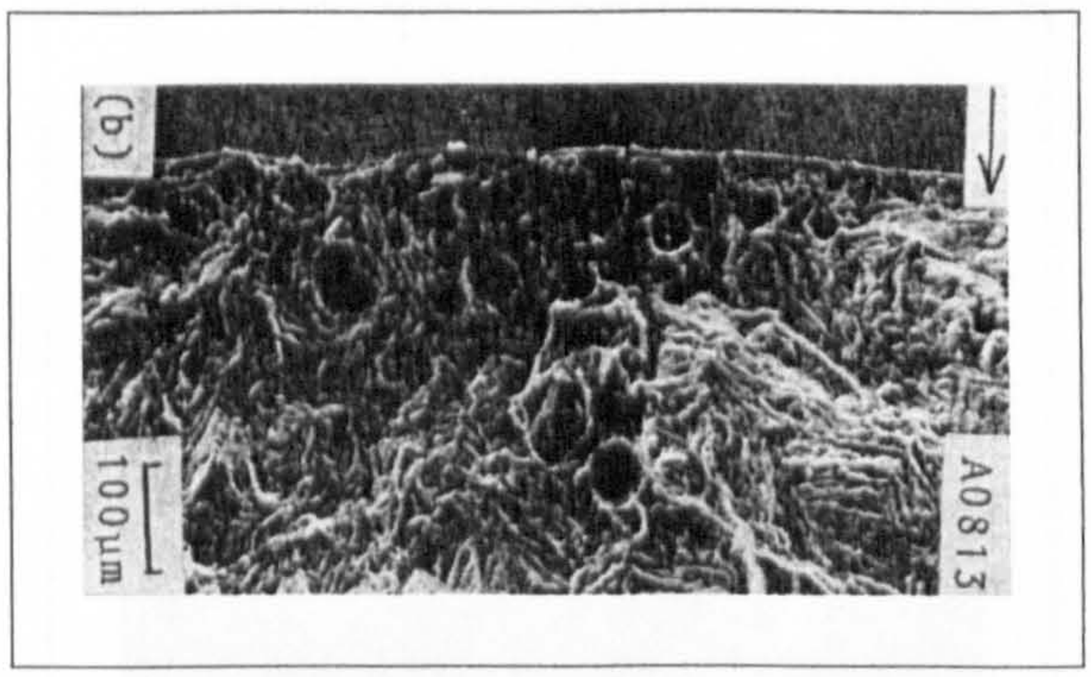

Figure 5.83: Porosity induced crack initiation sites in AA 5083-O weld metal[1].

FS SP welds frequently exhibited multiple initiation sites that resulted from the stress concentration effects of the score marks that predominantly resulted from the rotational and transverse movements of the tool shoulder, as shown in Figure 5.84, although some resulted from grinding marks that had occurred post weld during the removal of extruded material, with failure occurring within the TMAZ. FS DP welds generally failed in the region of the ridges formed at the edge of the tool shoulder, this area being the point of minimum hardness, but also subjected to a slight increase in the applied stress, when subjected to four point loading, due to the increase in thickness. No preference was observed for either the advancing or retreating side, although two specimens were

[1] Masuda, C et al (1983)

observed to fail in the HAZ adjacent to the advancing side, albeit in close proximity to the ridge. In a similar manner to the SP welds the cracks appeared to initiate at score marks on the surface, although the marks were the result of post weld grinding that had been used to remove the material extruded at the edge of the tool shoulder, shown in Figure 5.85.

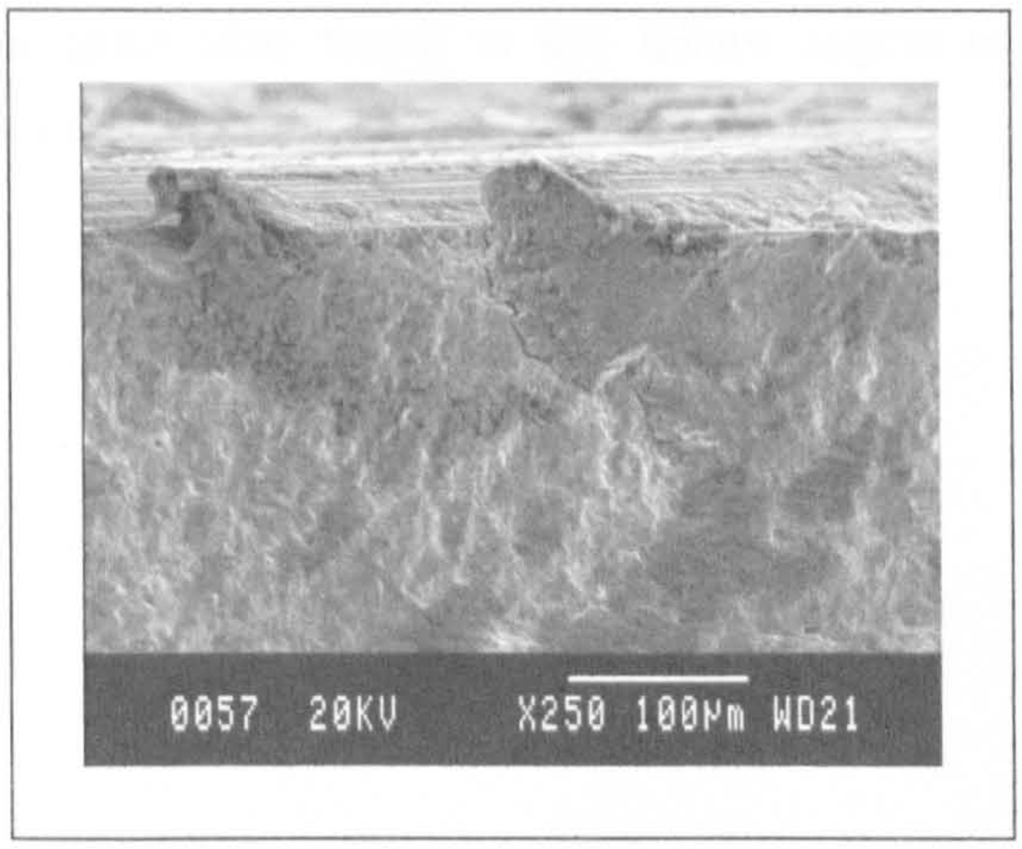

Figure 5.84: FS SP crack initiation sites resulting from tool shoulder induced the score marks.

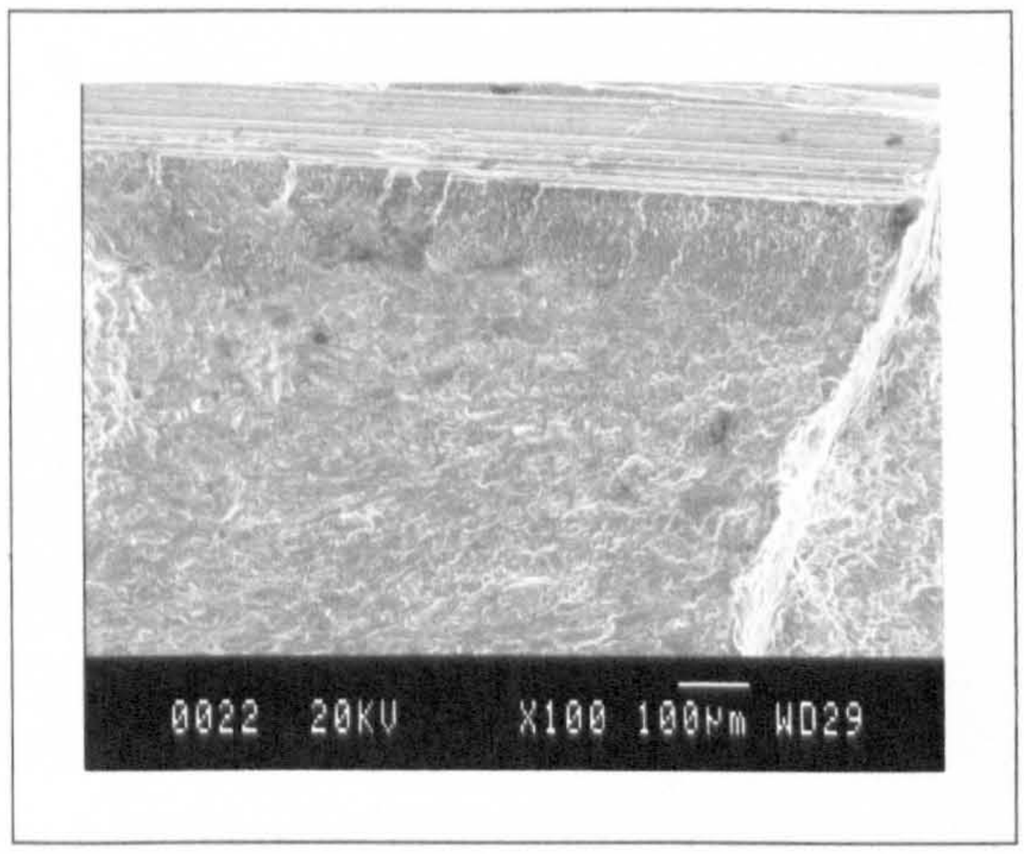

Figure 5.85: FS DP crack initiation sites resulting from score marks induced from the grinding process used to remove the flash that occurs at the edge of the tool shoulder.

The fatigue crack fracture surfaces, shown in Figure 5.86, all exhibited secondary cracking, although the cracks tended to be larger in the MIG welds, with the smallest being observed in the FS welds. The fatigue fracture surface of the FS welds was observed to have a surface consisting of small undulations, whilst the overall surface was relatively flat, in contrast to this the overall surface of the parent plate and MIG welds was more uneven, although flat planes within the surface were visible. It was assumed that this phenomenon was related to the grain size at the point of fracture.

The fast fracture surfaces all displayed microvoid coalescence with secondary intermetallics frequently evident in the dimples, as shown in Figure 5.87. The dimples appeared elongated on the parent plate fractographs, this probably being an artefact of the rolling process. The welded specimens exhibited more equiaxed dimples, although the FS welds revealed a more complex pattern with a proclivity for smaller dimples, this being particularly evident in the SP welds; it was assumed that the phenomenon was related to the smaller grain size found in the failure region of the FS welds when compared to the same region in the MIG welds.

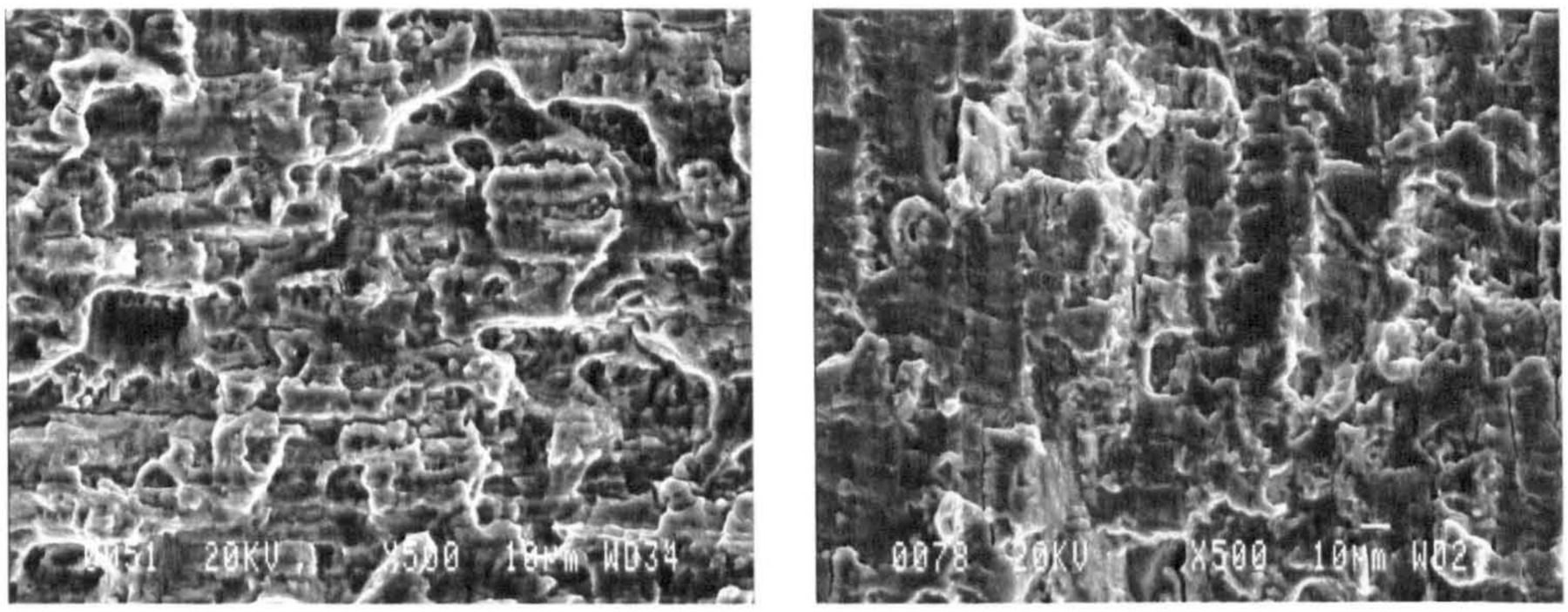

Figure 5.86: SEM fractographs of the fatigue crack fracture surface at 500x magnification: PP |- 2 (upper left), PP // 4 (upper right), MIG LI 1 (middle left), MIG HI 3 (middle right), FS SP 3 (bottom left) & FS DP 6 (bottom right).

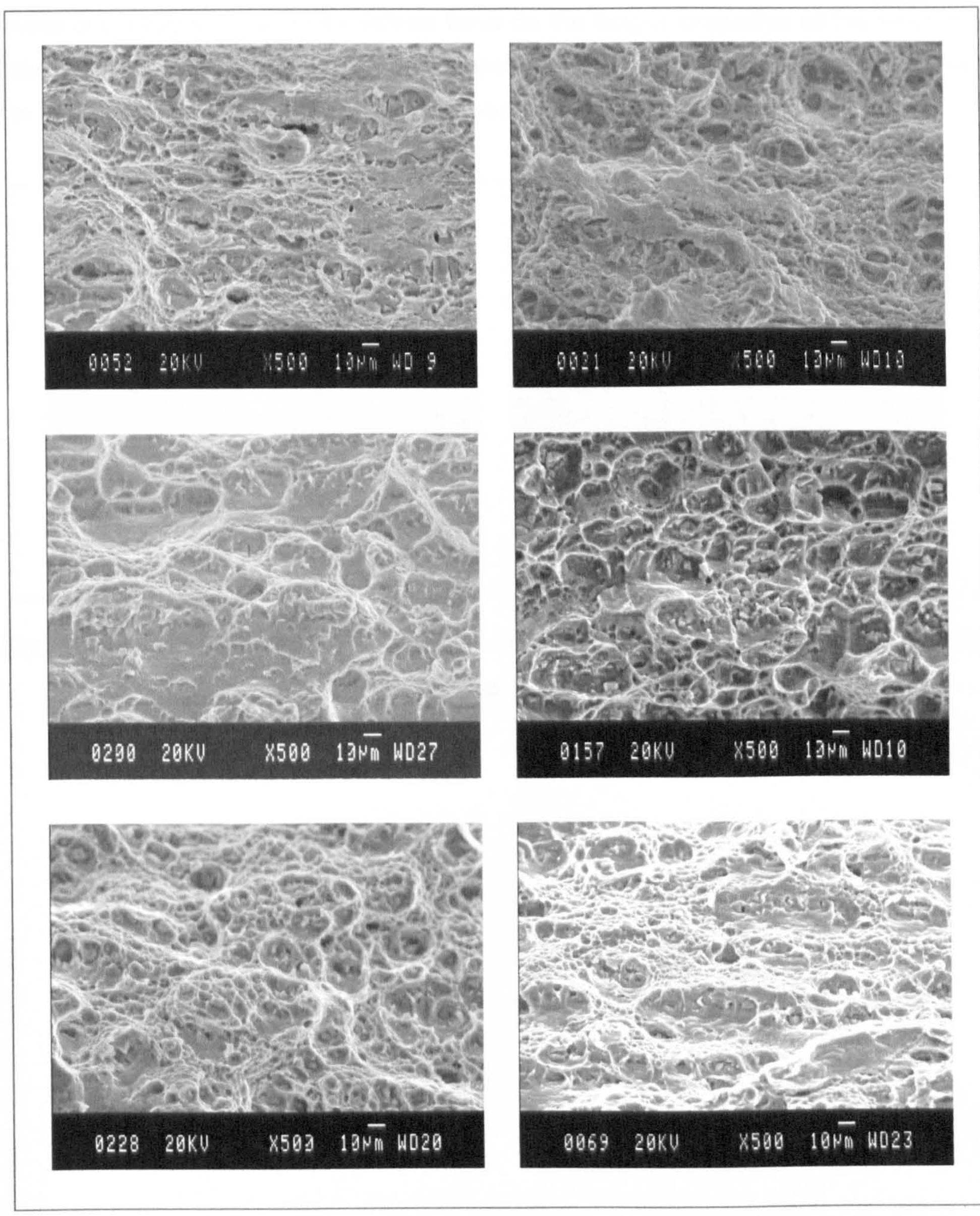

Figure 5.87: SEM fractographs of the fast fracture surface at 500x magnification: PP |-SCG* 23 (upper left), PP // SCG* 11 (upper right), MIG LI 8 (middle left), MIG HI 1 (middle right), FS SP 1 (bottom left) & FS DP 2 (bottom right).

PFD were observed on both the fatigue and fast fracture surfaces of some of the FS SP welds, shown in Figure 5.88, none were observed on any of the DP fracture surfaces. The exact cause of the defects was, at the time of writing, unclear, although it was likely that they were related to the welding parameters. The defects did not appear to have any significant effect on the fatigue strength, although two of the specimens tested may have failed from cracks initiating at a PFD. Uniaxial fatigue testing would be more likely to

---

* AA 5383-H321 parent plate SEM fractographs of the fast fracture surface were taken from small crack growth (SCG) fatigue specimens that had failed in axial tension rather than four point loading.

reveal any influence that these defects have on the fatigue properties of the weld, four point loading being more predisposed to result in a surface or near surface defect giving rise to crack initiation due to the nature of the resultant stress field.

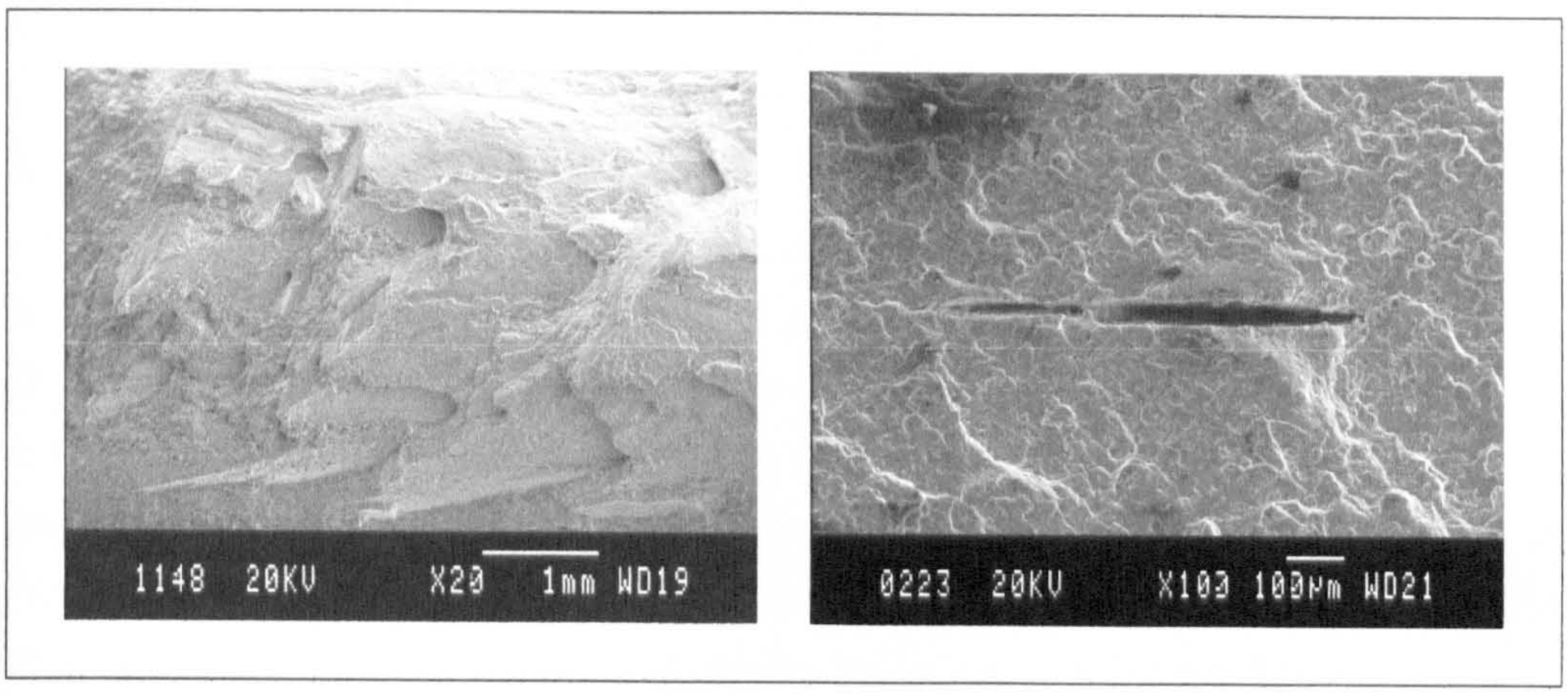

Figure 5.88: PFD observed in FS SP welds, fast fracture surface (left) and fatigue fracture surface (right).

6. Fatigue Crack Growth

6.1 Abstract

The following section details the short and long crack growth rates measured in AA 5383-H321 8 mm thick plate and MIG and FS butt welded joints in the same alloy (the MIG LI long crack measurements were made in a comparable alloy, AA 5083-H321), with supplementary data included in Section 13, Appendix C ~ Crack Growth (pages 506 - 537). Long crack growth rates were determined using compact tension (CT) specimens and a travelling microscope, with the growth rate being plotted with respect to the stress intensity factor range, ΔK; the linear regime growth rate (regime B in Figure 6.1, page 302) being represented as a power law function of ΔK. Short crack growth rates were determined through surface replication utilising an optical microscope and are plotted against the number of cycles to failure, crack length and stress intensity factor range. A comparison of the long and short crack growth rates with respect to the stress intensity factor range is detailed, and factors influencing the crack growth rates are discussed.

6.2 Introduction

Fatigue crack growth is typically divided into three regions as depicted in Figure 6.1. Regime A exhibits a threshold stress intensity factor value, ΔK_{th}, below which cracks are generally considered not to propagate. As the stress intensity factor increases above the threshold level the rate of crack growth increases relatively rapidly until a linear response, when observed on a log-log scale, is exhibited. This linear response, regime B, is frequently termed the Paris law regime. Further increases in ΔK lead to regime C, where the crack growth rate again increases rapidly resulting in unstable crack growth and eventually catastrophic failure at $K = K_c$, the critical stress intensity factor being equal to the fracture toughness[1].

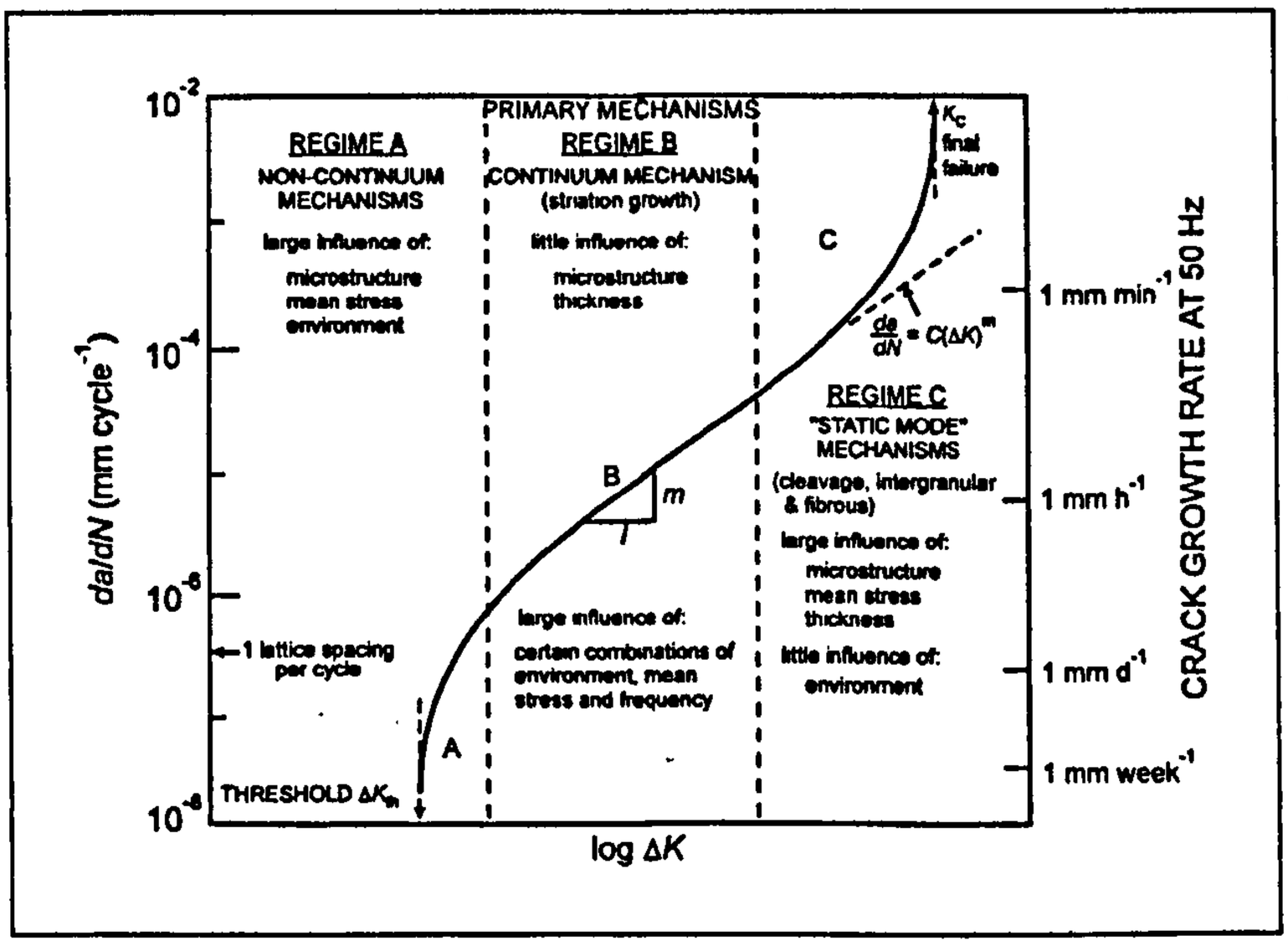

Figure 6.1: Schematic illustration of the typical variation in fatigue crack growth rates as a function of the applied stress intensity factor range in metallic materials[2].

Regime B, the Paris regime, is generally of most interest to engineers, the propagation rate being expressed in terms of LEFM and conforming to the similitude concept; that two cracks experiencing small scale yielding and subject to the same stress intensity factor, in the same material, microstructure and environment, will have the equally sized plastic zones and crack extension. The similitude concept breaks down when unstable crack growth occurs, regime C, prior to catastrophic failure and in the threshold region, regime A, often considered to consist of either crack initiation or arrest. Although the microstructure is generally considered to have little effect on the crack propagation rate in regime B, this is generally not true with regards to the mean stress, with an increase in

---

[1] Ewalds, HL; Wanhill, RJH (1984)
[2] Ritchie, RO (1999)

the magnitude of the mean stress resulting in an increase in the growth rate. In welded structures, where both tensile and compressive residual stresses of up to yield magnitude may be found, the effect on the mean stress, and therefore the fatigue strength, may be considerable.

With the increasing use of defect-tolerant design criteria for fatigue critical components in recent years, considerable interest has been shown in the behaviour of short cracks. These are typically described as being of a length comparable to one of the following; the plastic zone size, the local microstructure, or less than 0.5 - 2.0 mm. Short cracks typically grow at rates in excess of those observed in long cracks for the same stress intensity factor, a breakdown of the similitude concept, and also exhibit growth below the threshold stress intensity factor, where long crack growth is considered to have arrested. The outcome of these features may be an overestimation of the fatigue life when defect-tolerant criteria are employed. Short crack growth (SCG) rates in welded joints are of particular interest as they are known to be influenced by the local microstructure and stress ratio, both of which are affected by the welding process, the HAZ affecting the microstructure and the weld induced residual stress distribution affecting the mean stress and hence the stress ratio.

6.3 Literature Review

6.3.1 Long Fatigue Cracks

The long crack growth (LCG) of concern in the present study, as shown in Figure 6.1, is that occurring in regime A, the threshold regime where LCG arrest is observed, and regime B, where the rate of growth is commonly represented by a power law equation.

The fracture mechanics approach to fatigue crack growth involves the determination of a crack driving force, the stress intensity factor range, ΔK. The stress intensity factor is a function of the crack length, a, remotely applied stress, σ^{∞}, and geometry of the crack. For an edge cracked fatigue specimen:

$$\Delta K = Y.\Delta\sigma^{\infty}.\sqrt{\pi a} \qquad (6.1)$$

where: ΔK = stress intensity factor range.
Y = geometric factor relating to the crack length and specimen width.
$\Delta\sigma^{\infty}$ = remotely applied stress range, $\sigma^{\infty}_{max} - \sigma^{\infty}_{min}$.
a = crack length.

For regime B, the Paris law regime, crack growth is then described by:

$$\frac{da}{dN} = C(\Delta K)^m \qquad (6.2)$$

where: da/dN = crack growth increment per cycle.
C and m are scaling constants.

The scaling constants, C and m, of the Paris law are often considered to be material, microstructural, environmental and load ratio, R, based constants, although Davidson and Lankford[1] conclude that no plausible relationship between the parameters has been demonstrated. The constant m is typically between 2 - 4 for ductile metallic alloys[2].

6.3.1.1 Near Threshold Fatigue Crack Growth ~ Regime A

Near threshold fatigue crack growth is primarily a non-continuum process where the average crack extension has a growth rate less than 10^{-9} m.cycle^{-1}. The threshold stress intensity factor is generally considered to occur when growth rates do not exceed 10^{-11} m.cycle^{-1}, although ductile alloys may still undergo discontinuous crack growth but at levels that are undetectable by the typical measuring systems deployed. Threshold

---

[1] Davidson, DL; Lankford, J (1992)
[2] Ritchie, R (1999)

stress intensities are also influenced by the load ratio, R, the magnitude of the threshold decreasing with increasing R. The effect is more noticeable at lower values of R and may also be observed in both different alloy systems as well as different microstructures of the same alloy. Figure 6.2 shows how the threshold stress intensity factor range, ΔK_0, decreases as R increases until a minimum value, ΔK_{th}, is attained at $R \geq R_{cr}$. Therefore, for values of R greater than the critical value, R_{cr}, ΔK_0, is independent of R and equal to ΔK_{th}, whereas, below R_{cr}, ΔK_0 is dependent on the value of R. The opposite effect is observed when the threshold is categorised in terms of the maximum stress intensity factor, $K_{max,0}$, with $K_{max,0}$ being a constant value for $R < R_{cr}$. For $R \geq R_{cr}$, $K_{max,0}$ increases with R, ΔK_0 remaining constant and equal to $K_{max,0}.(1 - R)^1$. Zhao et al[2] concluded that in the near-threshold regime the reduction in crack deflection and crack closure were the overriding reasons for the increase in crack growth rates and threshold level with increasing stress ratio in the high strength aluminium alloy they investigated.

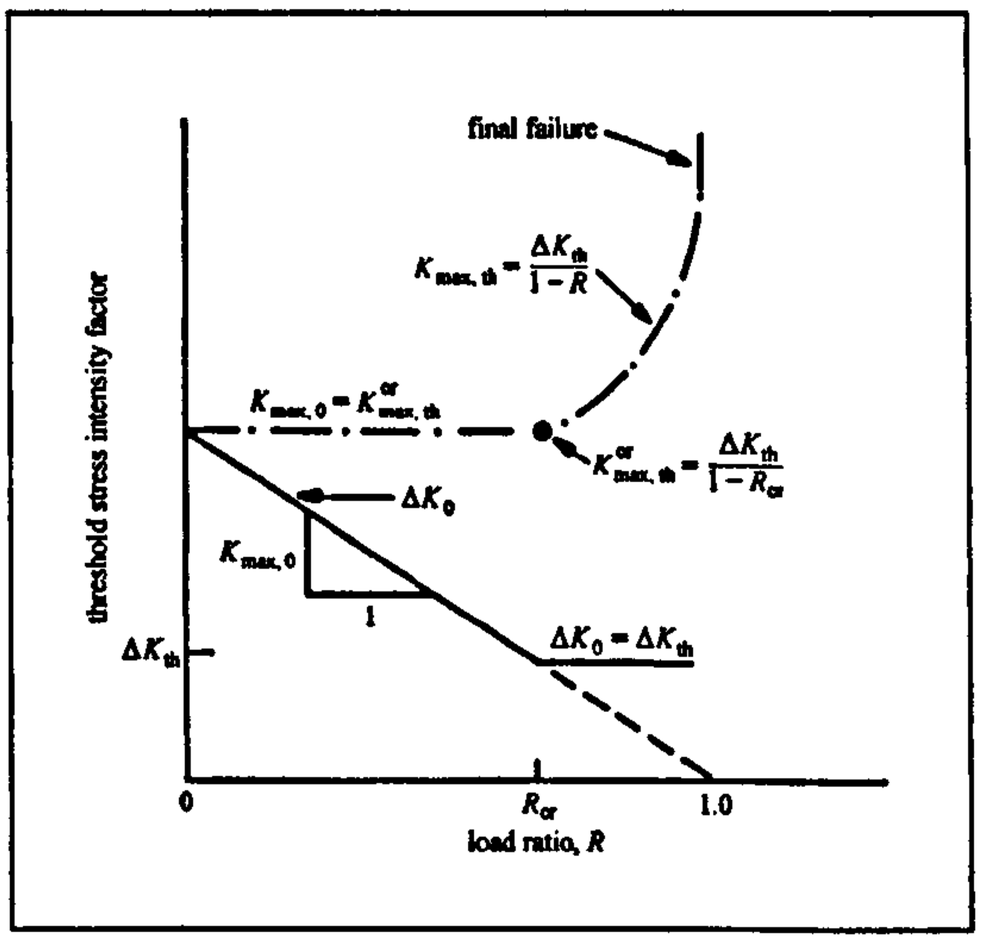

Figure 6.2: Effect of the stress ratio of the stress intensity factor, range or peak value, on the fatigue crack threshold[1].

The microstructure is also known to influence crack growth in the near threshold regime. The transition from regime A to B occurring as the cyclic plastic zone size, r_c, attains the magnitude of the characteristic microstructural dimension, l^*, of the alloy system[1]. l^* varies depending on the alloy under consideration but has been detailed as the Widmanstätten packet size for titanium alloys, and the ferrite grain size for low carbon steels[1]. Karjalainen[3] concluded that in AA 5056-O, a fine grained structure, grain size 0.03 mm, had a greater fatigue life than a coarse grained structure, grain size 1 - 2 mm, at constant plastic strain amplitudes, due to better tensile ductility and subsequently a longer

---

[1] Suresh, S (1998)
[2] Zhao, W et al (1986)
[3] Karjalainen, LP (1973)

initiation phase. Turnbull and Rios[1], in investigating the effect of the grain size on crack growth rates in an AA 5754 found that coarsening of the grain size, up to a certain limit, reduced that fatigue strength, although the effect on crack growth was most significant when the cracks were the size of the microstructure. Long cracks propagated faster in the coarser grained alloy due to the greater plastic zone at the crack tip, this being due to the lower cyclic yield strength[1].

6.3.1.2 Intermediate Fatigue Crack Growth ~ Regime B

As the stress intensity factor increases the plastic zone surrounding the crack tip extends over several grains and growth involves flow along two slip systems. In many ductile alloys this process results in the formation of ripples on the fracture surface, termed striations, as shown in Figure 6.3. The spacing of the striations has been found to correspond to the measured crack growth rate per cycle[2], although Davidson and Lankford[3] suggest that striation spacing only relates to the growth rate per cycle for growth rates in excess of 10^{-6} m.cycle^{-1} and at lower growth rates the striation spacing is greater than the growth rate. Striations are thought to result from the blunting, under a tensile load, and re-sharpening, under a compressive load (or tensile loads if crack closure has occurred, see Section 6.3.1.4, Fatigue Crack Closure, page 307) of the crack tip as the load cycle alternates.

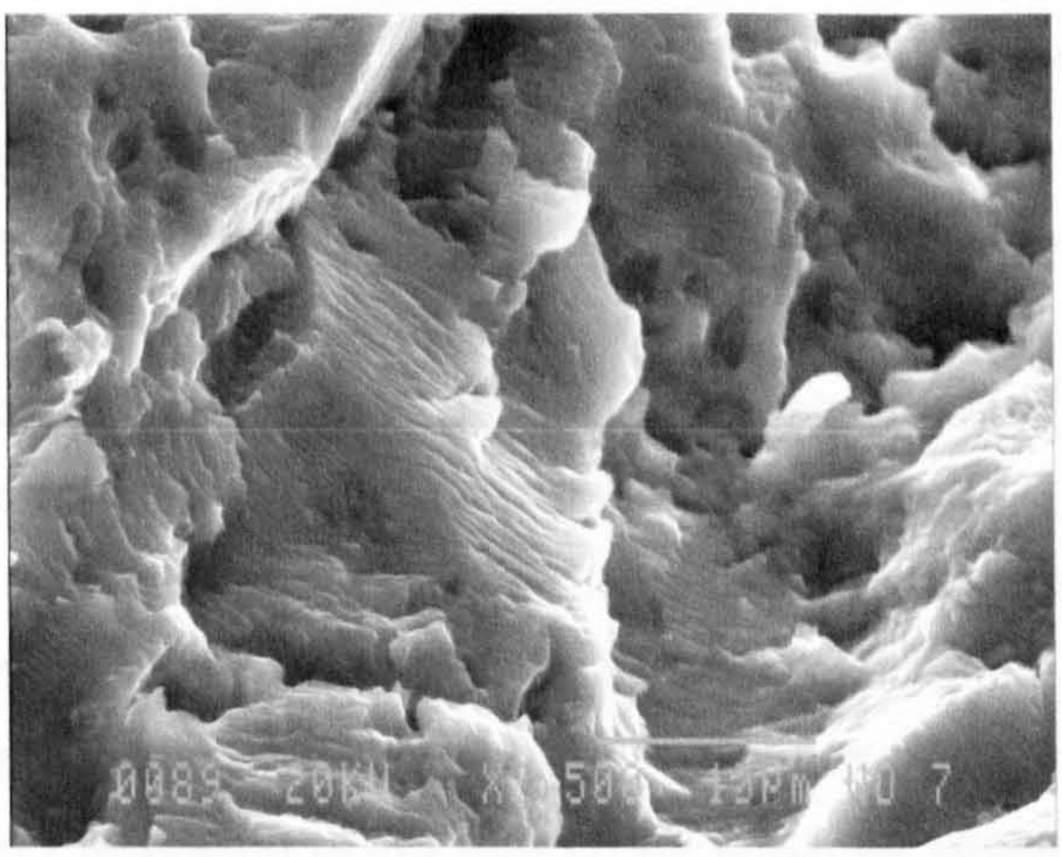

Figure 6.3: Fatigue crack growth surface striations in a friction stir weld.

6.3.1.3 High Fatigue Crack Growth ~ Regime C

The high stress intensities experienced in regime C result in the crack growth rate increasing rapidly, with the growth rate being influenced by the microstructure, load ratio

---

[1] Turnbull, A; Rios, ER de los (1995)
[2] Suresh, S (1998)
[3] Davidson, DL; Lankford, J (1992)

and stress state (plane strain or plane stress). The influence of the load ratio results from K_{max} increasing as R increases for the same magnitude of ΔK, with failure resulting when $K_{max} \rightarrow K_{Ic}$. Crack growth at high ΔK levels may exhibit striations, but as the fracture toughness is approached static fracture modes, cleavage, intergranular separation and fibrous failure are observed, with the static modes being influenced by the microstructure[1]. The influence of the stress state on the fracture toughness results in the fatigue crack growth in regime C being susceptible to constraint along the crack front when subjected to a state of predominantly plane stress, the result of this is an apparent increase in the fracture toughness and therefore ΔK[1].

6.3.1.4 Fatigue Crack Closure

Premature crack closure, defined as fracture surface contact which occurs under a non-zero tensile loading, was initially observed by Elber[2], who concluded that this was the result of permanent tensile plastic deformations in the wake of the crack. Several reasons, including plasticity induced closure, are now considered to result in crack closure, with the overall result being a reduction in the stress intensity factor as propagation is generally thought to occur only when the crack is open[3]:

i. Plasticity induced closure - elastic material surrounding the plastic wake (the remnants of the crack tip plastic zone as the crack advances) adjacent to the crack surfaces has a constraining effect, McEvily[3] considering this to be predominantly a plane strain effect.
ii. Roughness induced closure - contact occurs due to the mismatch of fracture surface asperities that result from combined mode I and II/III propagation.
iii. Crack filling closure - corrosion deposits, oxides, fretting debris and liquids prevent closure of the fracture surfaces.
iv. Transitional closure (arising from i, ii and iii) – occurs due to a reduction in the ΔK or R level and results in crack retardation.
v. Transformation induced closure – a phase transformation may occur in some metastable alloys due to the crack tip stress field, if the result of this is an increase in volume, then closure can develop until the region is penetrated by the advancing crack.
vi. Grain boundary closure – the presence of a stiffer grain ahead of the crack tip, possibly due to its orientation, results in retardation until penetration of the grain occurs.

A schematic representation of crack closure induced by i-iii and v is shown in Figure 6.4:

---

[1] Suresh, S (1998)
[2] Elber, W (1970)
[3] McEvily, AJ (1988)

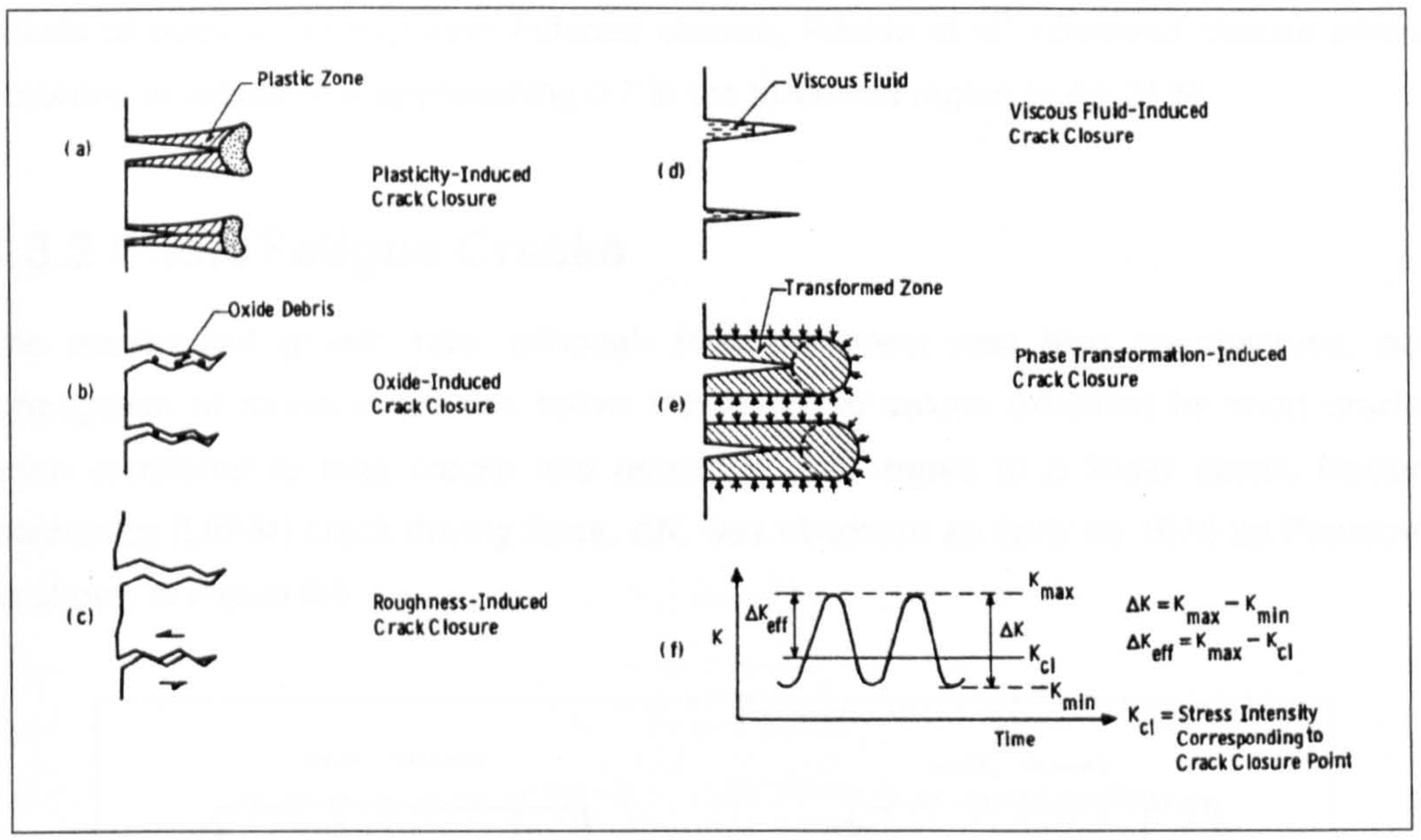

Figure 6.4: Mechanisms of fatigue crack closure[1].

The reduction in the stress intensity factor due to crack closure has lead to the development of an effective stress intensity factor range, ΔK_{eff}:

For a non-closing crack:

$$\Delta K_{eff} = K_{max} - K_{min} = \Delta K \tag{6.3}$$

For a crack exhibiting closure:

$$\Delta K_{eff} = K_{max} - K_{cl} \leq \Delta K \tag{6.4}$$

where: K_{cl} stress intensity factor at which closure occurs.

Crack closure mechanisms, except for plasticity induced closure, generally increase as the growth rate approaches the threshold[2]. At low R ratios, < 0.5, an increase in yield strength results in a decrease in K_0, although for values of R > 0.5, where crack closure is less influential, the yield strength has little effect on crack growth in the threshold region[2]. Increasing the grain size of the material generally results in an increase in K_0 for low values of R, whilst the effect diminishes as crack closure reduces with increasing R, Liaw considering this to be related to roughness induced closure[2]. As R increases in value crack closure is generally considered to lessen, this being related to the diminishing

[1] Suresh, S; Ritchie, RO (1984) *referenced by Liaw, PK (1988)*
[2] Liaw, PK (1988)

effects of oxide and roughness induced closure, Ritchie et al[1] observed closure effects occurring at values of R approaching 0.7 in the threshold region in AA 2124.

6.3.2 Short Fatigue Cracks

The accelerated growth rate, although frequent arrest may also be observed, and propagation at stress intensities below the threshold values exhibited by short cracks, when compared to long cracks and assessed with regard to a linear elastic fracture mechanics (LEFM) crack driving force, ΔK, was observed as early as 1975 by Pearson[2], as shown in Figure 6.5.

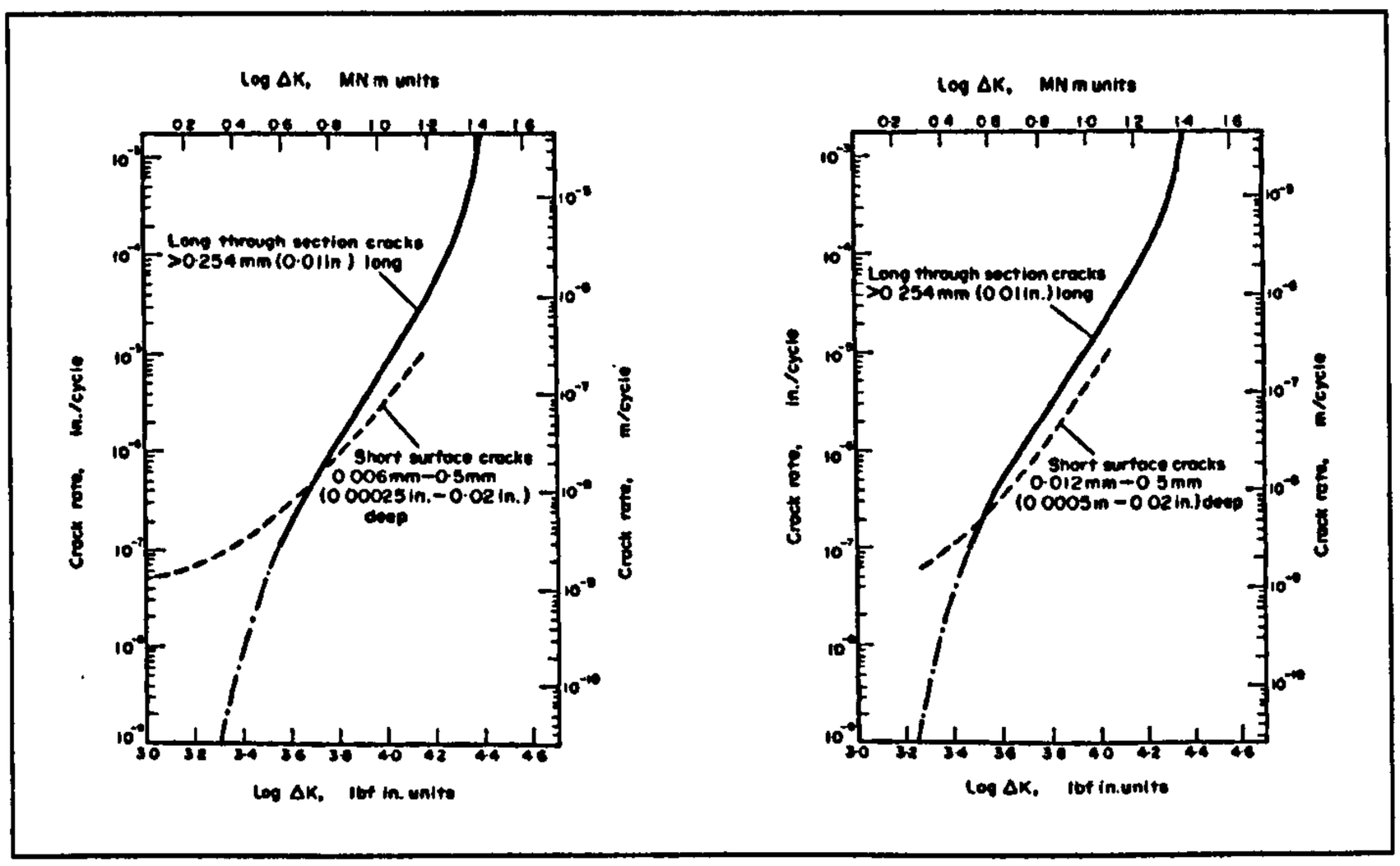

Figure 6.5: Comparison of long and short crack propagation observed in AA BS L65 (left) and AA DTD 5050 (right)[2].

In a review of published material on short cracks by Suresh and Ritchie[3] and the comprehensive account of fatigue by Suresh[4] short cracks are grouped into the following categories (throughout this dissertation no distinction is made between small, short or micro cracks):

i. Microstructurally small (MSSC) ~ the crack size is comparable to a characteristic of the microstructure, e.g. the grain size.
ii. Mechanically small (MCSC) ~ the near tip plasticity is comparable to the crack size or the crack is engulfed in the plastic strain of a notch.

---

[1] Ritchie, RO et al (1988)
[2] Pearson, S (1975)
[3] Suresh, S; Ritchie, RO (1984)
[4] Suresh, S (1998)

iii. Physically small (PSC) ~ fatigue flaws that are typically larger than the microstructure and plastic zone size, but are physically small, typically less than 0.5 - 2.0 mm.

iv. Chemically small (CSC) ~ cracks that would normally exhibit a LEFM response, but display apparent anomalies below a certain crack size as a consequence of environmental stress corrosion fatigue effects on crack dimensions*.

Short cracks present their own problems for the engineer as they do not conform to the similitude concept; that two cracks of different sizes, experiencing small scale yielding, in a given material, microstructure and environment, when subjected to the same stress intensity factor will have equally sized plastic zones and crack extension. Suresh and Ritchie[1] state a number of circumstances, i - vi below, where the similitude concept is no longer valid:

i. Crack sizes approach the local microstructural dimensions.
ii. Crack sizes are comparable with the extent of local plasticity for non-stationary flaws.
iii. Through thickness, out of plane stresses (which are independent of K_I) are different.
iv. Crack extension mechanisms are different.
v. Extensive fatigue crack closure is observed.
vi. External environments significantly influence crack growth.

The breakdown of the similitude concept has been used to explain the increase in propagation observed in short cracks when subject to the same stress intensity factor as a long crack and also their ability to exhibit growth below the long crack threshold, ΔK_{th}, at which crack arrest is normally observed. The accelerated crack growth is generally associated with the diminishing crack closure experienced by short cracks, although the use of ΔK_{eff}, which takes into account crack closure occurring under a positive load, does not fully explain the propagation patterns observed in short cracks when characterised utilising a LEFM approach.

MSSC have a size comparable to that of the local microstructure, this typically being the grain size in metals. Tokaji and Ogawa[2] studied the effect of microstructure on the growth of MSSC in several metals including AA 7075-T6 that had pancake shaped grains and they considered the microstructural unit size to be the average grain size in the

---

* CSC are outwith the scope of this dissertation, further details may be found in Suresh, S; Ritchie, RO (1984) & Suresh, S (1998).
[1] Suresh, S; Ritchie, RO (1984)
[2] Tokaji, K; Ogawa, T (1992)

normal direction because the grain boundaries in that direction were found to have the greatest influence on surface crack growth rates. Their results showed that crack propagation for MSSC, though greater than that for long cracks, arrested for many cycles at obstacles such as ferrite grain boundaries and triple points of grain boundaries in a low carbon steel, as shown in Figure 6.6, with arrested growth being more prevalent in the finer grained material. For crack lengths ≥ 200 μm and ≥ 250 μm, for the fine (24 μm microstructural unit size) and coarse (84 μm microstructural unit size) grained materials respectively, growth rates increased monotonically with increasing crack length, these being 3 - 8 times greater than the microstructural unit size[1]. A similar outcome was observed in a high tensile steel and comparable responses were also observed in a low alloy steel, where arrests were also evident at austenite grain boundaries and martensite packet boundaries[1]. A medium carbon steel (ferrite/pearlite) and dual phase stainless steel (ferrite/austenite) exhibited growth retardation at the boundaries between hard and soft phases, when crack extension was from the soft to hard phase[1].

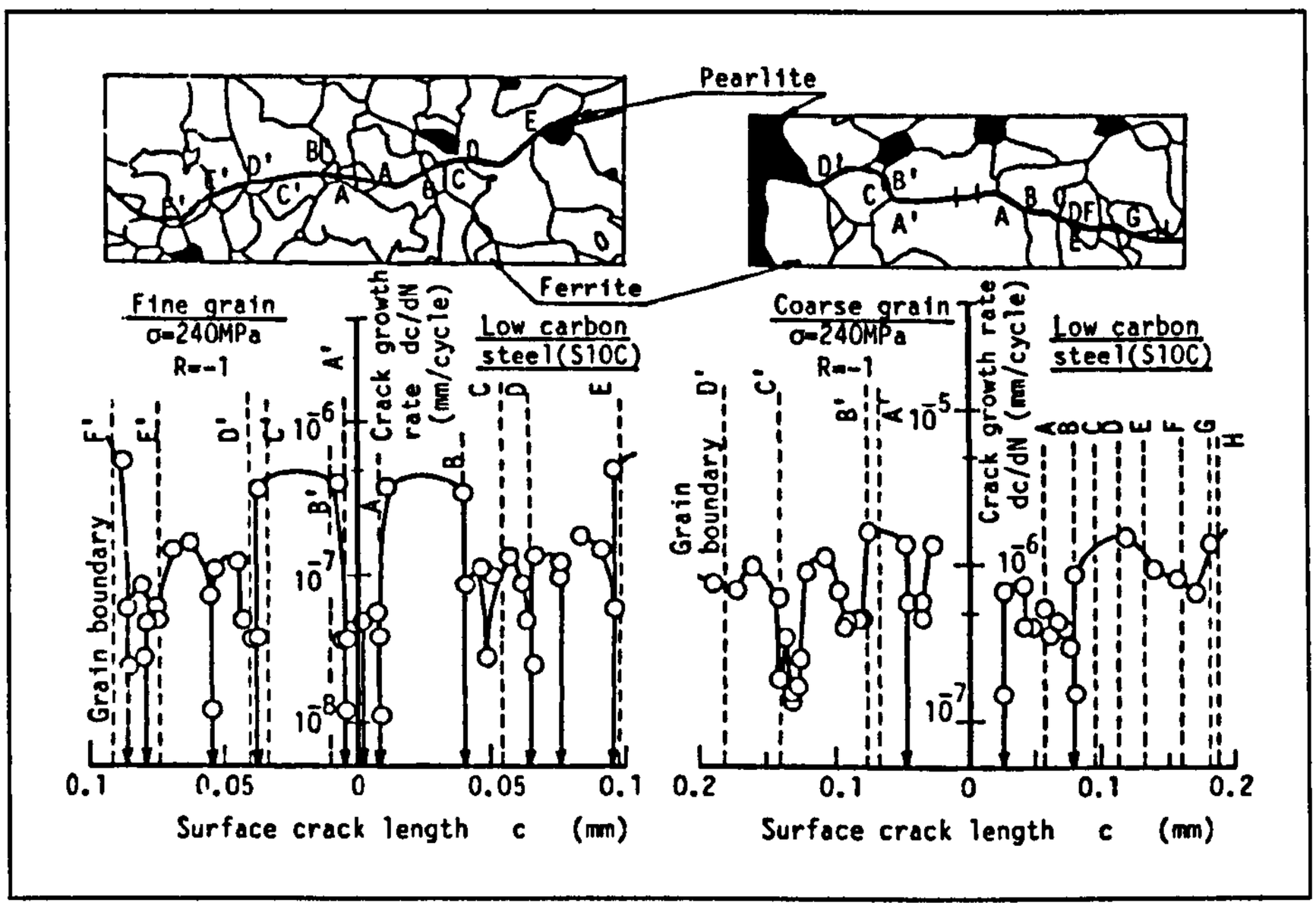

Figure 6.6: Growth behaviour of MSSC for fine (left) and coarse (right) grained materials in low carbon steel[1].

MSSC were studied in an AA 7075-T6 at stress ratios of 0 and -1 with the microstructure having no effect at R = 0, but with crack arrest being evident at R = -1, as shown in Figure 6.7, suggesting that MSSC growth is stress ratio dependent[1]. In both a fine and coarse grained titanium alloy the crack path was noted to be extremely tortuous, with the tortuousity increasing with increasing grain size. In the fine grained alloy arrests in crack growth were observed more frequently, but the arrests extended to a greater crack length

[1] Tokaji, K; Ogawa, T (1992)

in the coarser material indicating that decreases in growth rate were related to both grain boundaries and crack deflection[1].

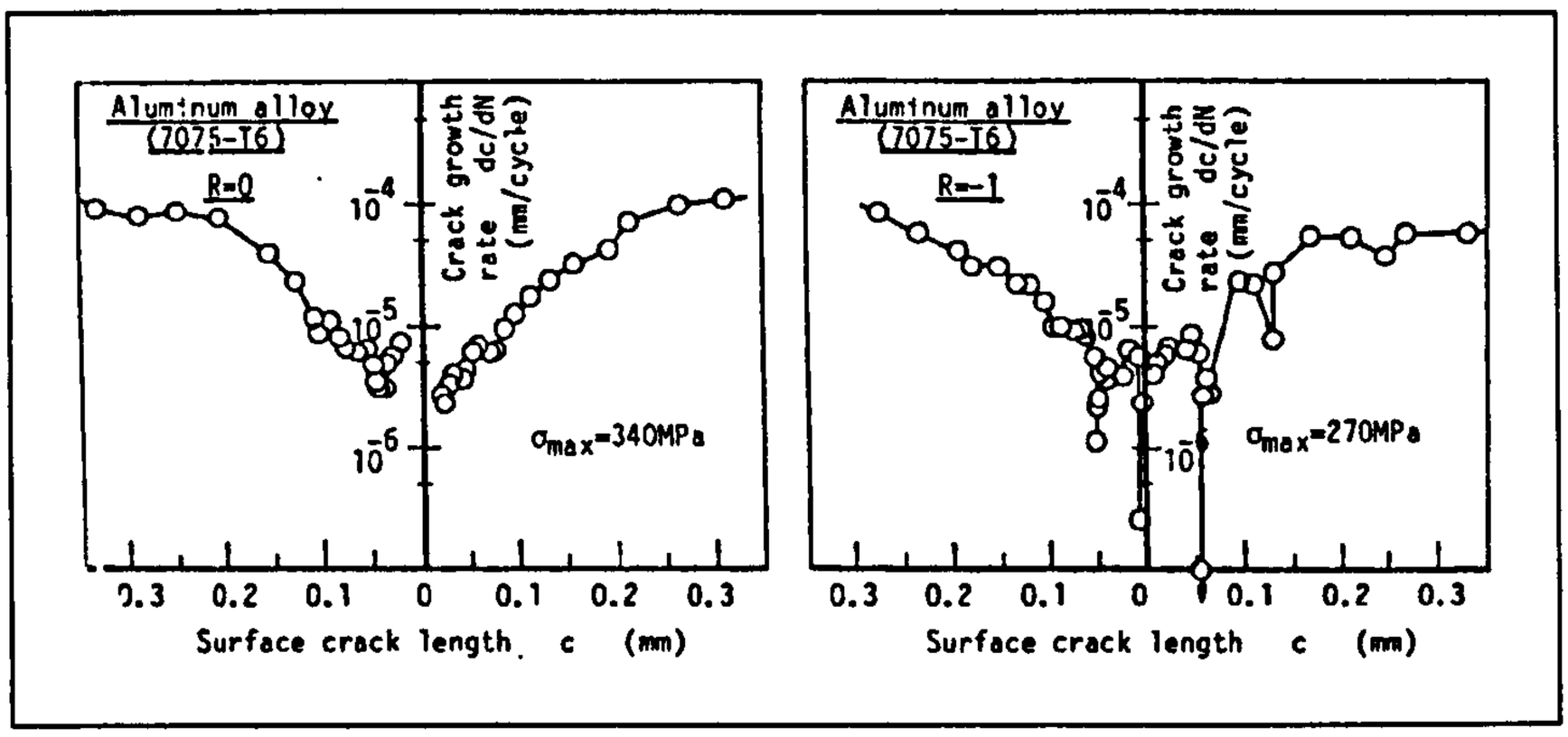

Figure 6.7: Growth behaviour of MSSC at R = 0 (left) and R = -1 (right) in AA 7075-T6[1].

The authors suggested that misorientation between the grain containing the crack and the following grain, this being encountered at the grain boundary, were the main cause of arrest. This would result in an increase in the fatigue strength, with respect to MSSC, in finer grained materials as the blocking effect of grain boundaries would be encountered more frequently[1]. Results corroborating the grain size observations have been reported by Caton et al[2,3] in a W319-T7 casting aluminium alloy when the MSSC growth rate is plotted with respect to the stress intensity factor and similarly by Lankford[4] in AA 7075-T6 as shown in Figure 6.8. Tokaji and Ogawa[1] conclude that propagation arrest of MSSC was evident up to crack lengths of $2c = 8d$, where c was the crack length and d the microstructural unit, for $R = -1$, although they state that MSSC growth was heavily dependent on the stress ratio.

---

[1] Tokaji, K; Ogawa, T (1992)
[2] Caton, MJ et al (1999a)
[3] Caton, MJ et al (1999b)
[4] Lankford, J (1983) *Referenced by Suresh, S; Ritchie, RO (1984)*

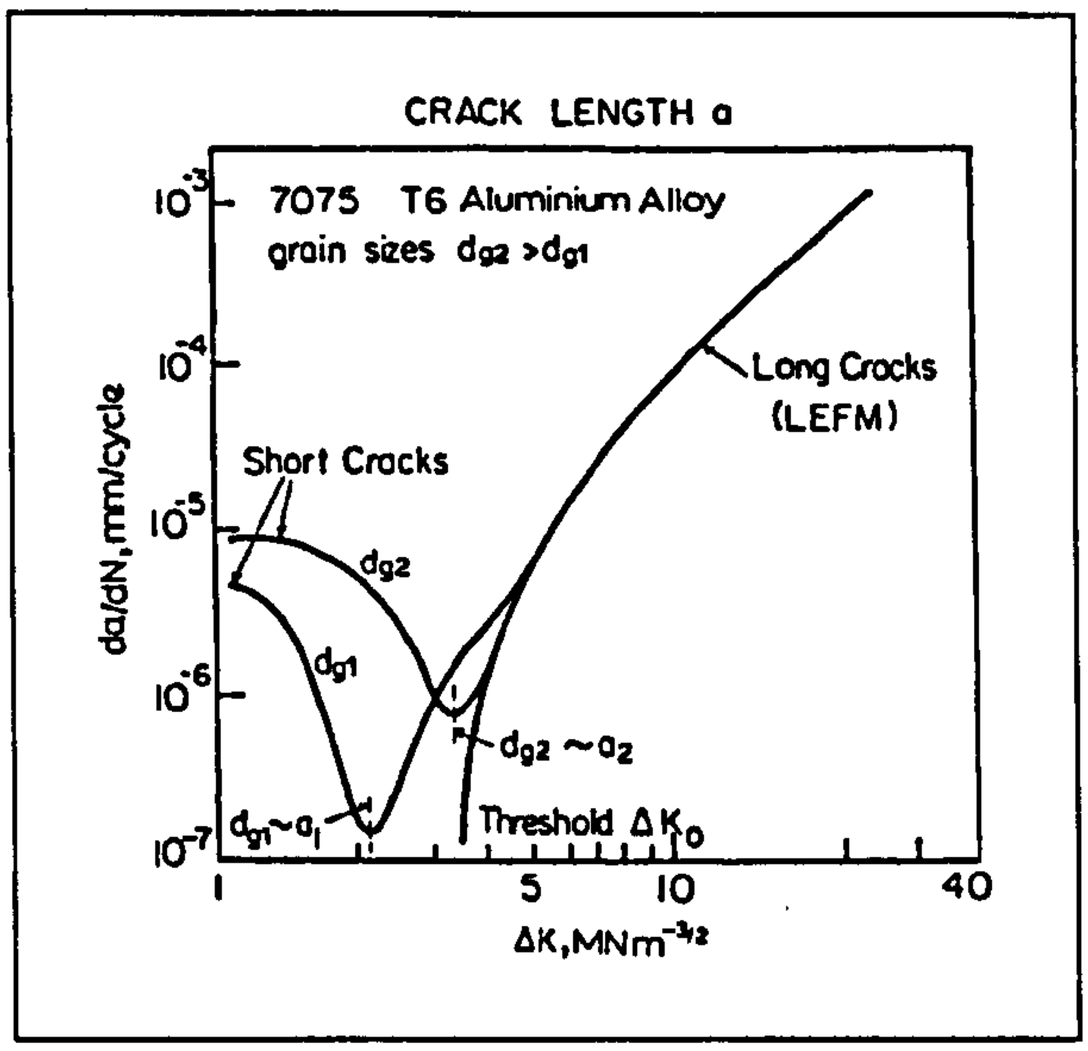

Figure 6.8: Effect of grain size on the propagation of long and short fatigue cracks in AA 7075-T6[1].

Suresh and Ritchie[2] also considered the arrest of propagation observed in MSSC to be due to interactions with microstructural features, i.e. grain boundaries, but also considered crack closure and the degree of microplasticity to be influential. It has been hypothesised by Suresh[3] that on reaching a grain boundary a short crack will reorientate itself in a new crystallographic direction, this being that of the most favourable slip system, with the outcome of this being crack deflection. The result of the reorientation is a reduction in the stress intensity factor which has been considered to be influential in SCG deceleration or arrest. A diagrammatic representation of the deflection and subsequent reduction in the stress intensity factor immediately after the deflection are shown in Figure 6.9.

---

[1] Lankford, J (1983) *Referenced by Suresh, S; Ritchie, RO (1984)*
[2] Suresh, S; Ritchie, RO (1984)
[3] Suresh, S (1983)

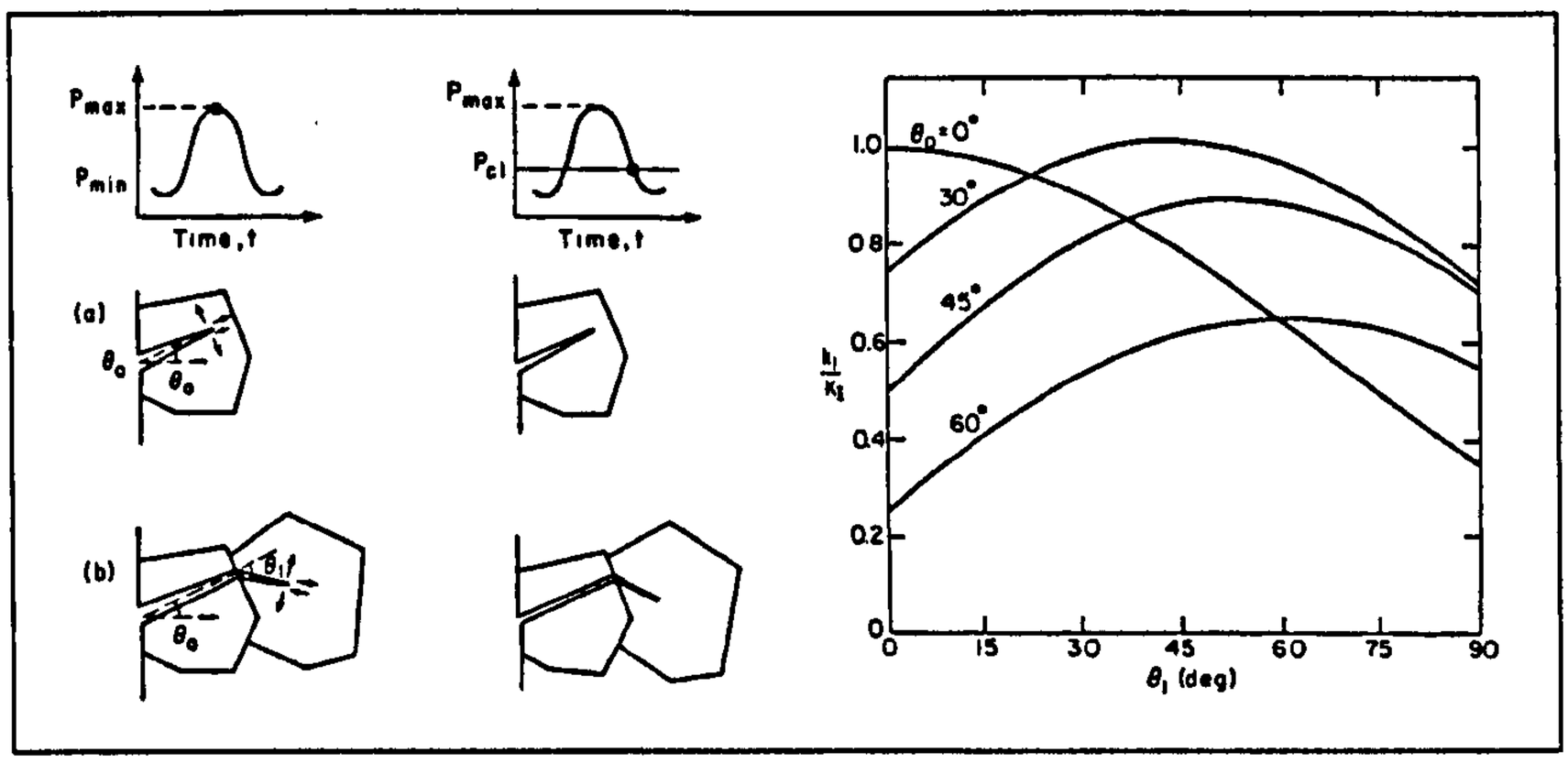

Figure 6.9: Schematic representation of the growth and deflection of MSSC and the resultant crack tip displacements and closure (left) and the predicted variation in the normalised mode I stress intensity factor (right)[1].

Tanaka et al[2] developed the blocked slip band (BSB) model to determine the threshold stress for short cracks. The model was based on the theory that the mobility of the slip band at the crack tip is impaired at a grain boundary and hence crack propagation or arrest is observed. The BSB model confers that the threshold for short cracks decreases with decreasing crack size and that the driving force is stress dependent rather than stress intensity factor dependent as is the case with long cracks. The deceleration of short crack growth has also been considered to be a result of the mobility of the plastic zone engulfing the crack tip being blocked by the grain boundary, with non-propagation occurring until the plastic zone in the following grain develops[3].

MCSC are defined as cracks whose size is comparable to the local plasticity, this may be the crack tip plastic zone, near tip plasticity, or as a result of the plasticity induced by a notch, notch field plasticity[4], as shown in Figure 6.10. In both cases it might be expected that crack growth retardation would be the outcome, the scenario being comparable to that observed in long cracks due to the plastic wake. Panasyuk et al[5] state that MCSC propagate at higher growth rates than long cracks at the same stress intensity factor, but that their rate of propagation decreases due to plastic closure and then increases because of the increase in the total stresses in the process zone, with these effects leading to a reduction in the rate of propagation or arrest. Morris[6,7] observed a change in the crack closure characteristics of short cracks as they grew from MSSC to MCSC, with the closure mechanism changing from the contact of opposing fracture surfaces at a

---

[1] Suresh, S (1983)
[2] Tanaka, K et al (1981)
[3] James, MR; Morris, WL (1983) *referenced by Suresh, S (1998)*
[4] Suresh, S; Ritchie, RO (1984)
[5] Panasyuk, VV et al (2001)
[6] Morris, WL (1979)
[7] Morris, WL (1980)

positive tensile stress for the MSSC to closure occurring due to a residual tensile strain in the plastic zone for the MCSC.

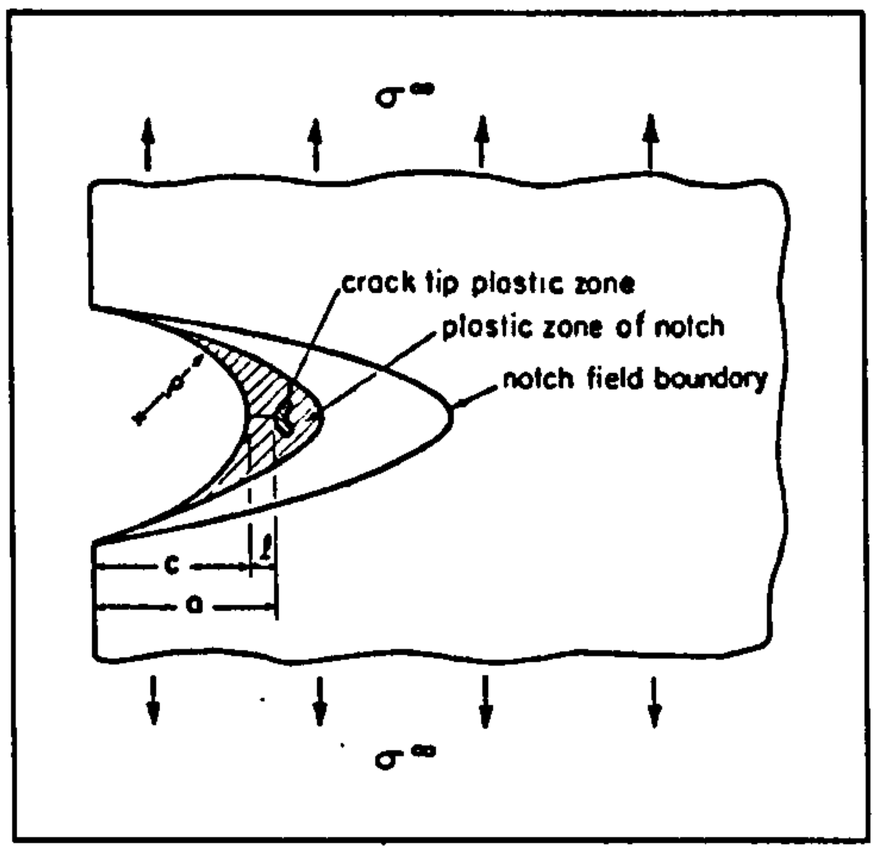

Figure 6.10: Schematic representation of crack tip and notch tip plastic strain fields associated with short crack growth[1].

Due to the breakdown of the similitude concept for short cracks the J integral has been employed to describe the propagation of MCSC[2], although Suresh[3] states that the use of this to characterise rapidly growing short cracks remains open to debate. The J integral has also been employed in an attempt to explain the behaviour of short cracks in the plastic zone of a notch, as have intrinsic crack lengths and constant plastic zone sizes[3]. Short cracks growing within the plastic zone of a notch exhibit propagation rates greater than their long crack counterparts and below the long crack threshold when analysed with respect to LEFM, although they may also exhibit growth arrest[1]. Typical responses of SCG propagation from notches, depending on the local stress state, with respect to the stress intensity factor, are shown in Figure 6.11[4].

It may be expected that PSC, typically considered to be less than 0.5-2.0 mm in length, would conform to LEFM and the similitude concept on the basis that they are typically larger than the local microstructure, MSSC, and local plasticity, MCSC, although several publications have reported crack growth rates greater than those observed in long cracks for the same stress intensity factor[1,3,5,6]. This increase in propagation has been attributed to the effects of crack closure (see Section 6.3.1.4, Fatigue Crack Closure, page 307) with PSC being less susceptible to this phenomenon.

---

[1] Suresh, S; Ritchie, RO (1984)
[2] Dowling, NE (1977) *referenced by Suresh, S (1998)*
[3] Suresh, S (1998)
[4] Ewalds, HL; Wanhill, RJH (1984)
[5] Suresh, S (1983)
[6] Schijve, J (1988)

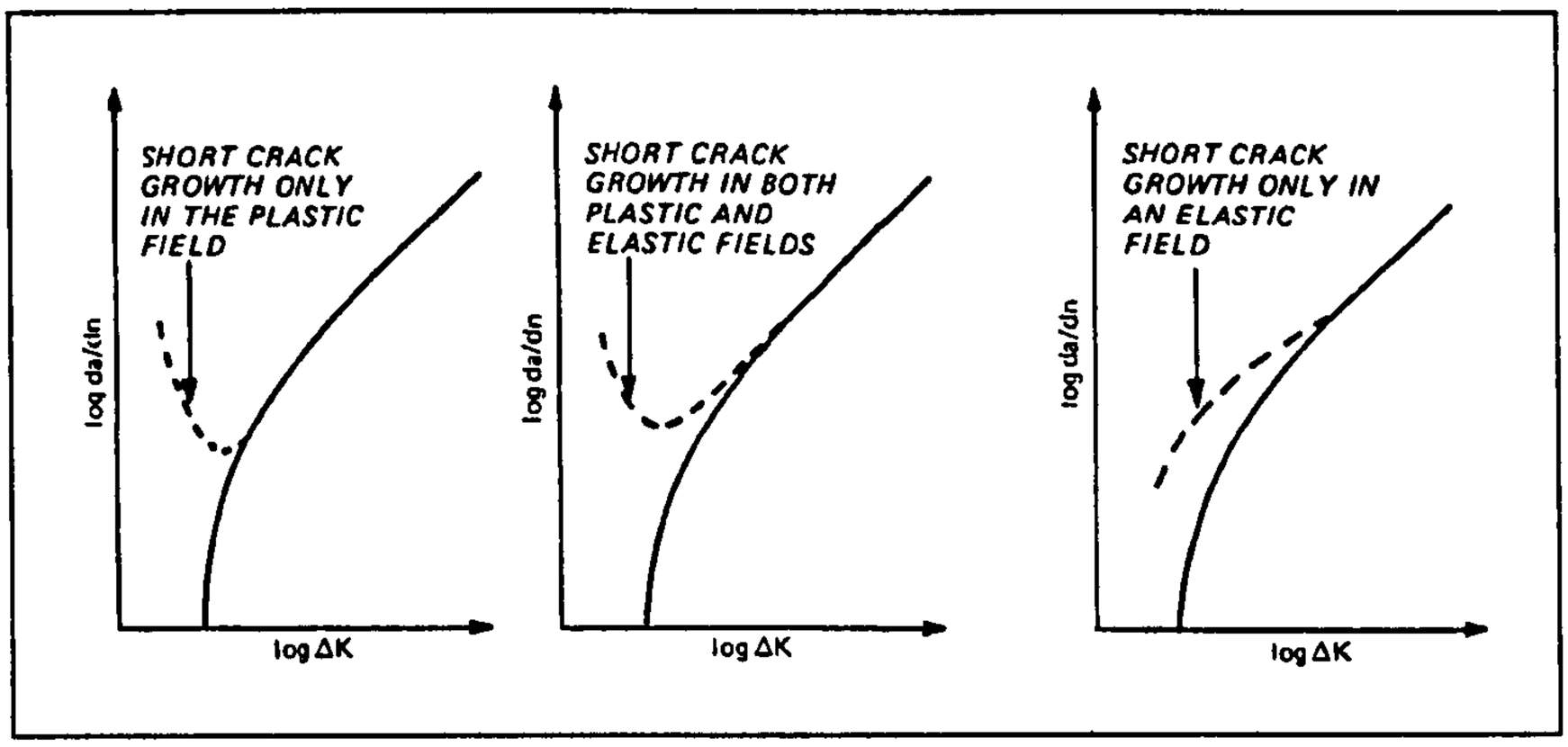

Figure 6.11: Schematic representation of SCG from notches, depending on the local stress state, with respect to the stress intensity factor[1].

6.3.2.1 Measurement of Short Cracks

Short cracks also present their own difficulties with respect to accurately measuring the crack length and subsequent growth. One technique commonly utilised is the replication technique where a reproduction of the surface is obtained, usually using either cellulose acetate film that is softened by soaking in acetone, described by Swain[2], or with a hardening silicone rubber[3]. When the replication material has set it is mounted on a suitable medium and viewed through either an optical or scanning electron microscope. Although the technique is relatively simple and inexpensive it is notoriously tedious and difficulties can arise when attempting to view the mounted replicas due to problems associated with the area under inspection having several focal depths if an optical microscope is used. It also has the disadvantage that the test has to be periodically interrupted to obtain a replica and Newman et al[4] state that the acetone used in the cellulose acetate replication method resulted in an increase in the fatigue life of an AA 7075-T6 by a magnitude of 2-4 times.

Electron microscopy has also been employed, with either the specimen being transferred to the SEM chamber or in situ testing being undertaken, although both require regular interruptions of the test to allow crack measurements to be recorded. Other techniques that have been successfully employed include the alternating current and direct current[5] potential drop (ACPD and DCPD) methods where electrodes are attached to the specimen and the drop in voltage monitored as the crack advances, giving a continuous in-situ monitoring of crack growth. The AC technique, having a greater skin effect, is claimed to have a greater resolution than the DC technique making it more suitable for

---

[1] Ewalds, HL; Wanhill, RJH (1984)
[2] Swain, MH (1992)
[3] Slatcher, S; Knott, JF (1981)
[4] Newman, JC et al (2000)
[5] Gangloff RP et al (1992)

the measurement of short cracks, although if multiple cracks exist between the two electrodes the techniques will only measure the sum of the crack growth rather than that of individual cracks. Other techniques that have been employed are photomicroscopy[1] and a strain gauge technique[2] described as suitable for measuring cracks as small as 0.2 mm deep at weld toes.

6.3.3 Fatigue Crack Growth in Weldments

Nosair and Jolley[3] measured the fatigue crack growth rates in a 9 mm thick MIG welded Al4.5Mg plate as shown in Figure 6.12, measurements were made both in the parent material, HAZ and weld metal in a direction transverse to the weld (left) and in the weld metal (right), with R = 0.1. For both the parent plate and welded specimens, and also for subsequent tests undertaken at R = 0.27, the long crack threshold was constant at 400 $N.mm^{-3/2}$ (12.6 $MPa.m^{0.5}$)[3], these being considerably greater than the 3.5 $MPa.m^{0.5}$ reported by Costa et al[4] in an AA 5083 plate with R = 0.05. The weld metal specimens were observed to have a higher resistance to crack growth, with this being most notable at the onset of plane stress. The increase in the resistance of the weld metal to crack growth was considered to be influenced by the large β phase intermetallics evident in the weld metal, the residual stresses due to the welding procedure were not considered in the analysis. The authors also noted that the stress ratio had a marked influence on the crack growth of the parent plate, but this was much less notable in the welded specimens[3].

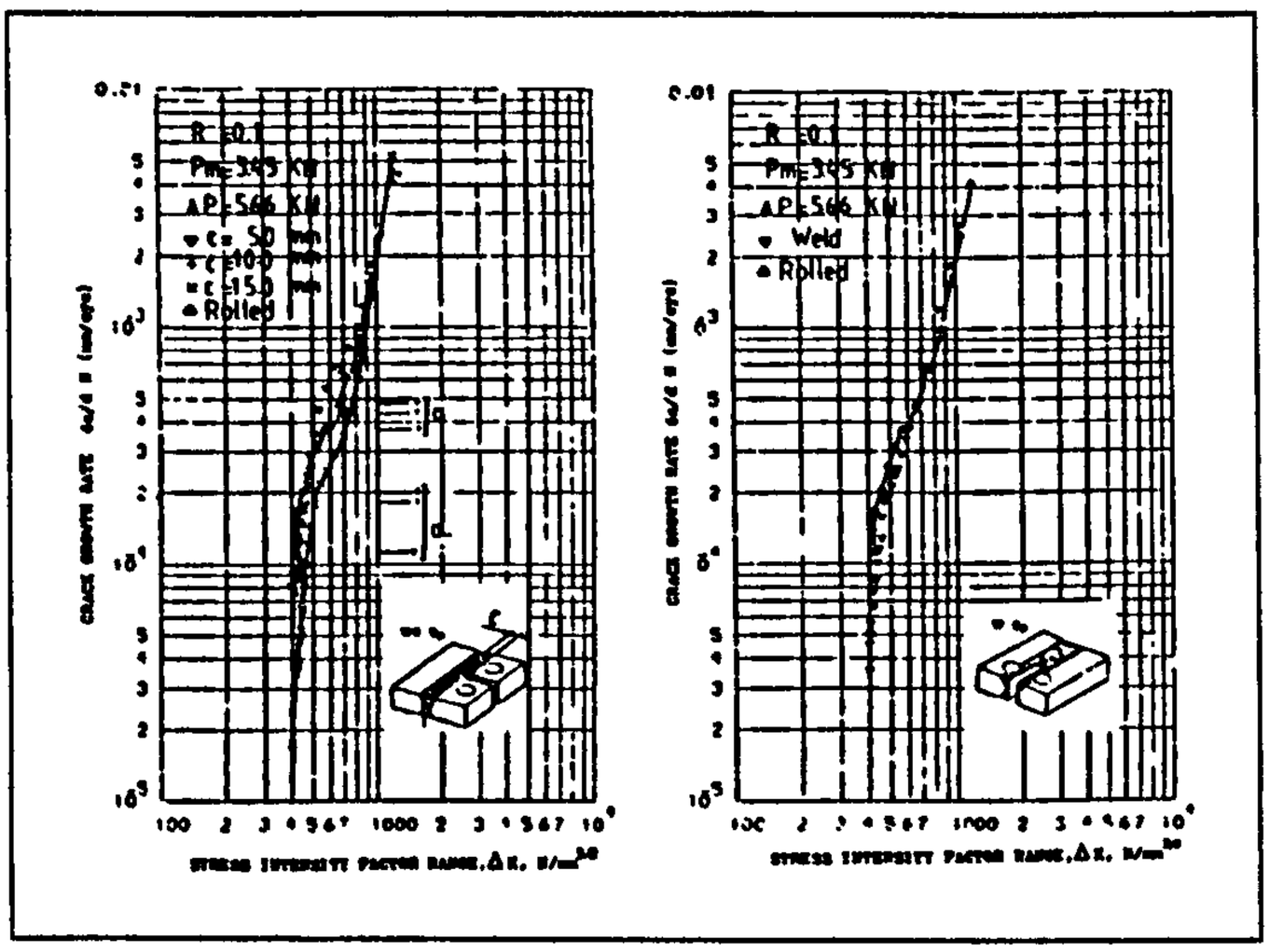

Figure 6.12: Fatigue crack growth rates in MIG butt welded Al-Mg plate[3].

[1] Larsen, JM et al (1992)
[2] Otegui, JL et al (1991)
[3] Nosair, S; Jolley, G (1985)
[4] Costa, JD et al (1997)

The increase in magnitude of the stress intensity factor thresholds returned by the MIG welds in contrast to values returned by the base material has also been observed by Link[1]. The author reporting $\Delta K_0 = 3.6 - 5.0$ MPa.m$^{0.5}$ for AA 5456-H116 parent plate with R = 0.1, whilst for the MIG weld metal, values of 11.2 - 12.8 MPa.m$^{0.5}$ and 6.4 MPa.m$^{0.5}$ were recorded for R = 0.1 and 0.5 respectively. Link[1] states that the increase in the threshold values, and also the reduction in crack growth rates, was due to the production of the notch in the CT specimen, the consequence of this being that a redistribution of the residual stress field in the region of the weld results in a compressive residual stress at the crack tip. This results in crack closure, and subsequently no crack growth, for a significant part of the applied load or stress intensity factor range, with values up to 80% of the load being considered, as shown in Figure 6.13. The crack growth rates obtained for the weldments and corrected for crack closure were as shown in Figure 6.14.

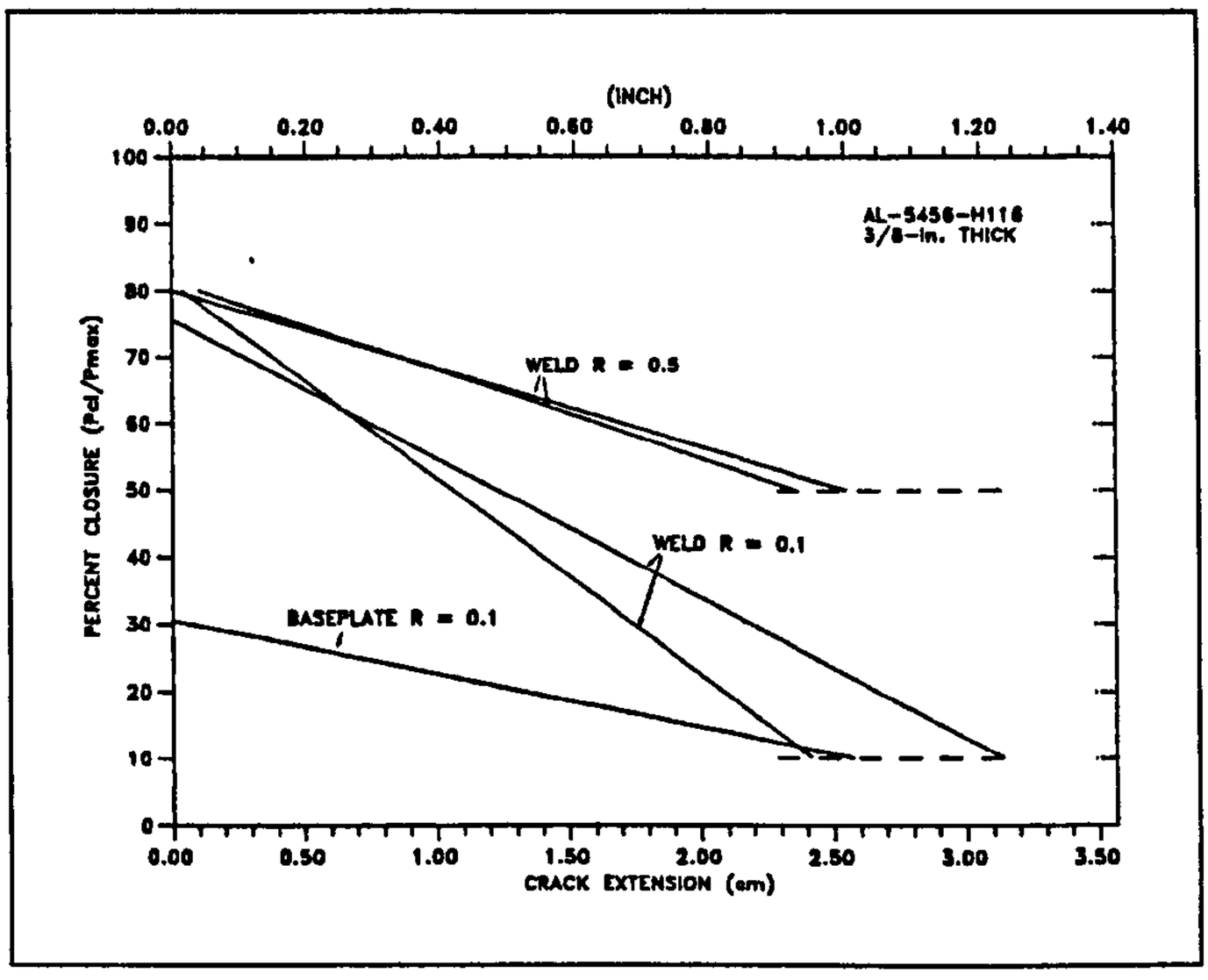

Figure 6.13: Crack closure with respect to crack length for AA 5456-H116 weld and parent material[1].

[1] Link, LR (1990)

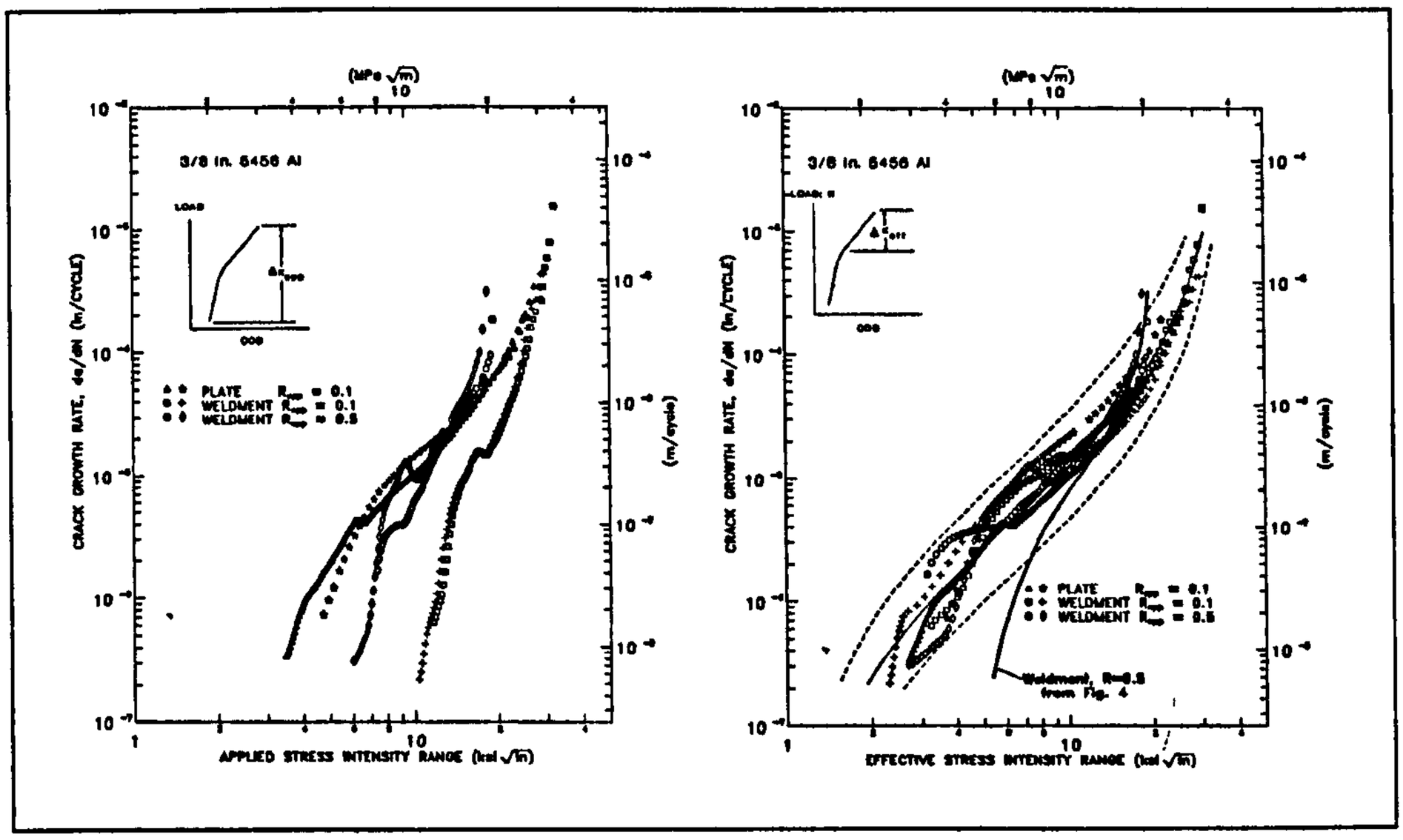

Figure 6.14: Crack growth rates in AA 5456-H116 parent plate and weld metal, applied (left) and effective (right) stress intensity factor[1].

Crack closure has also been studied by Nordmark et al[2] in high deposition rate butt welds in 51 mm thick AA 5456-H117 plate. Measurements were undertaken in the HAZ, weld metal and parent plate, as shown in Figure 6.15 and Figure 6.16, with the CT specimens being produced at the surface and mid-thickness. The greatest resistance to crack growth was observed in the HAZ, with the lowest being in the AA 5556 weld metal, when growth rates were measured with respect to ΔK, although when measured with respect to ΔK_{eff} the results were equivalent, as shown in Figure 6.16. The authors concluded that the variation between the growth rates, when determined with respect to ΔK, was the result of crack closure due to the weld induced residual stresses[2].

[1] Link, LR (1990)
[2] Nordmark, GE et al (1982)

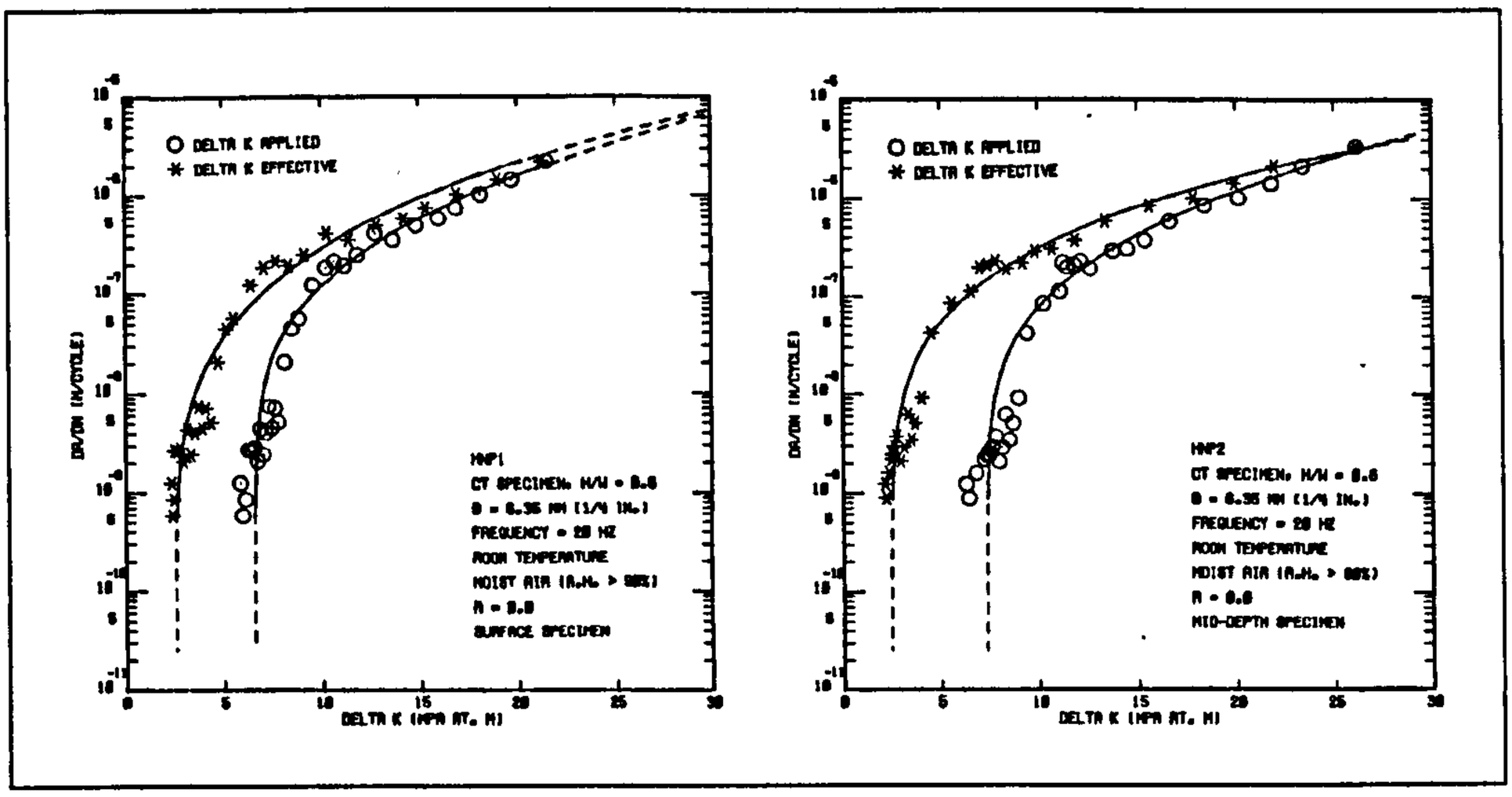

Figure 6.15: Crack growth rates, R = 0, with respect to ΔK and ΔK_{eff} at the weld toe (left) and mid-plate HAZ (right) in butt welded AA 5456[1].

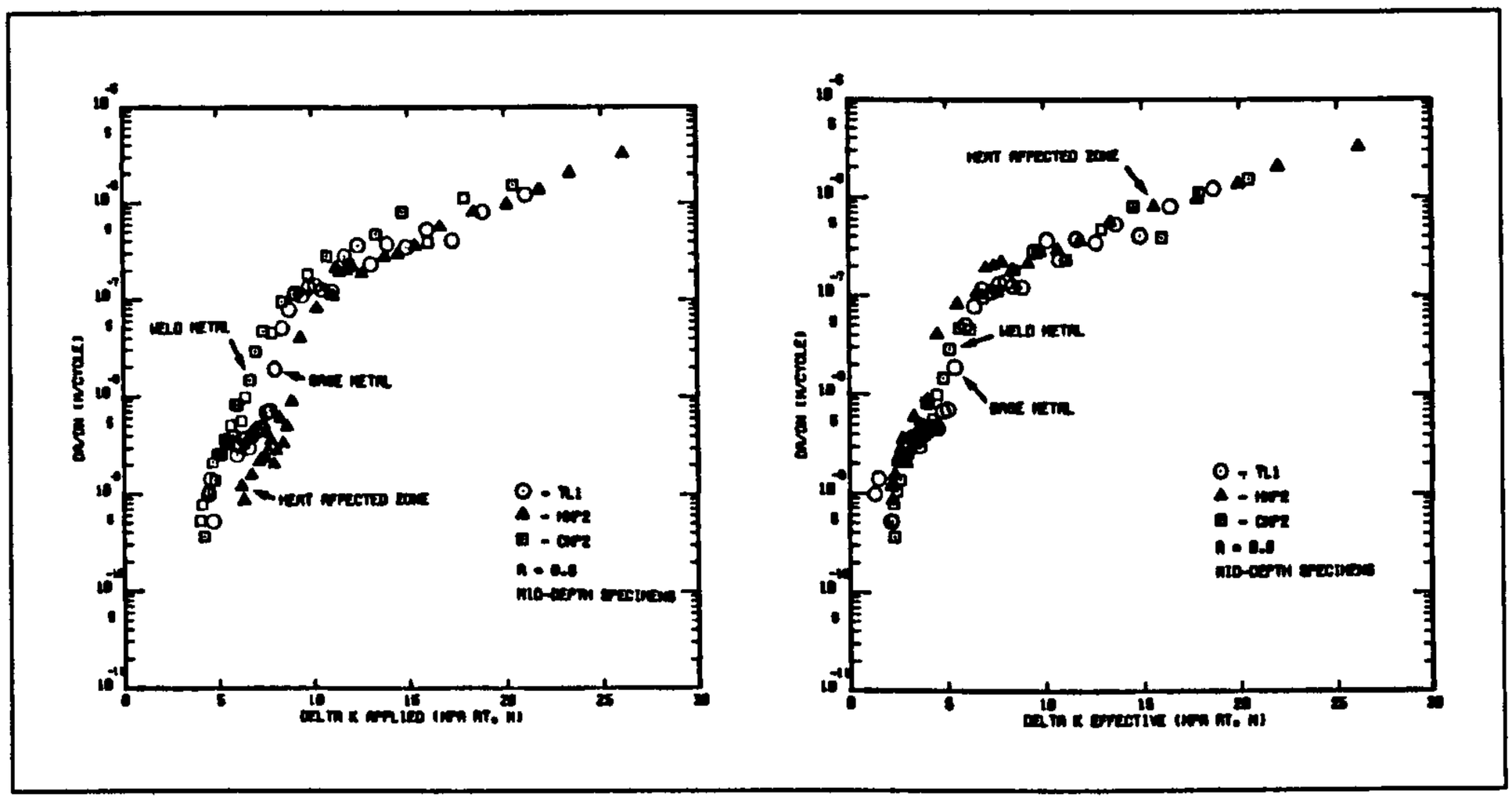

Figure 6.16: Crack growth rates in butt welded AA 5456, R = 0; parent plate (TL1), mid-plate HAZ (HNP2) and mid-plate weld metal (CNP2) with respect to ΔK (left) and ΔK_{eff} (right)[1].

Dalle Donne et al[2] also considered the effect of the residual stress distribution in both friction stir welded CT (compact tension) and MT (middle tension) specimens as shown in Figure 6.17. It was evident from the two specimen types that the crack tip of the CT specimen was subjected to a compressive residual stress, this would be expected to increase crack closure and therefore reduce ΔK, the expected outcome being an increase in the fatigue threshold and resistance to crack propagation. In contrast to this

[1] Nordmark, GE et al (1982)
[2] Dalle Donne, C et al (2000)

the crack tip of the MT specimen was subject to a tensile residual stress, this would be expected to decrease crack closure and therefore increase ΔK, the outcome being a decrease in the crack threshold and an increase in the growth rate.

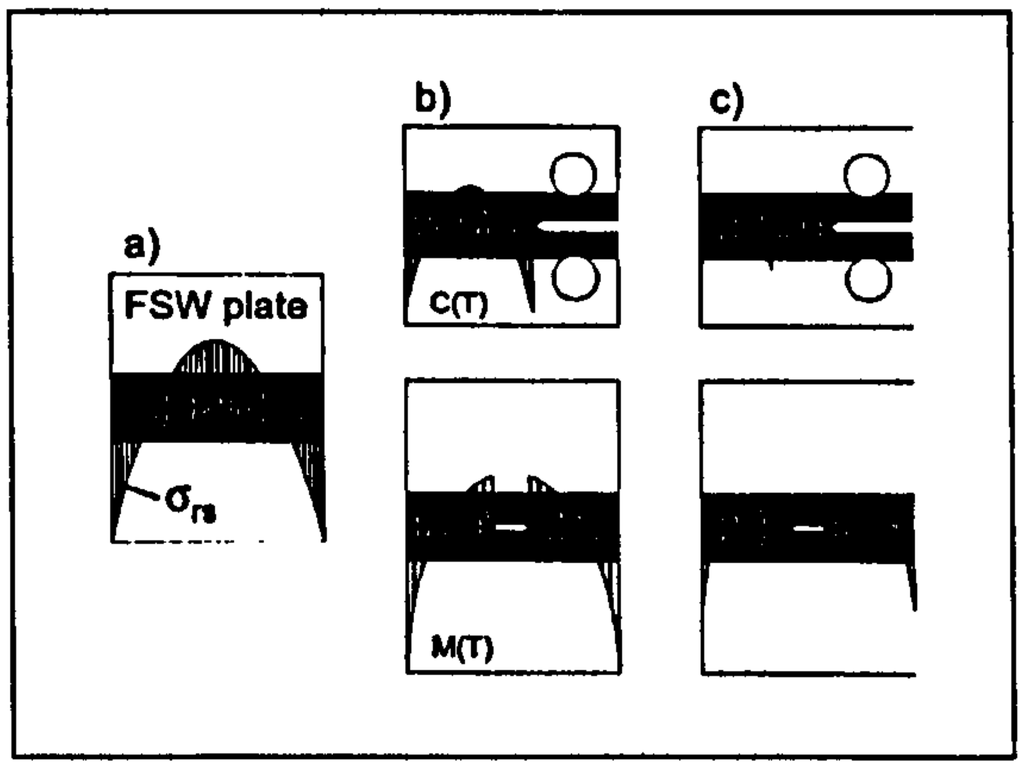

Figure 6.17: Schematic representation of the distribution of residual stresses in a friction stir welded CT (upper) and MT (lower) specimen[1].

The effect of the residual stresses on a FS welded AA 6013-T6 material are shown in Figure 6.18, the crack growth being measured at the centre and in the direction of the weld. From Figure 6.18 it was evident that the application of ΔK_{eff} resulted in the values for both the CT and MT specimens and various stress ratios falling within a narrow scatter band[1].

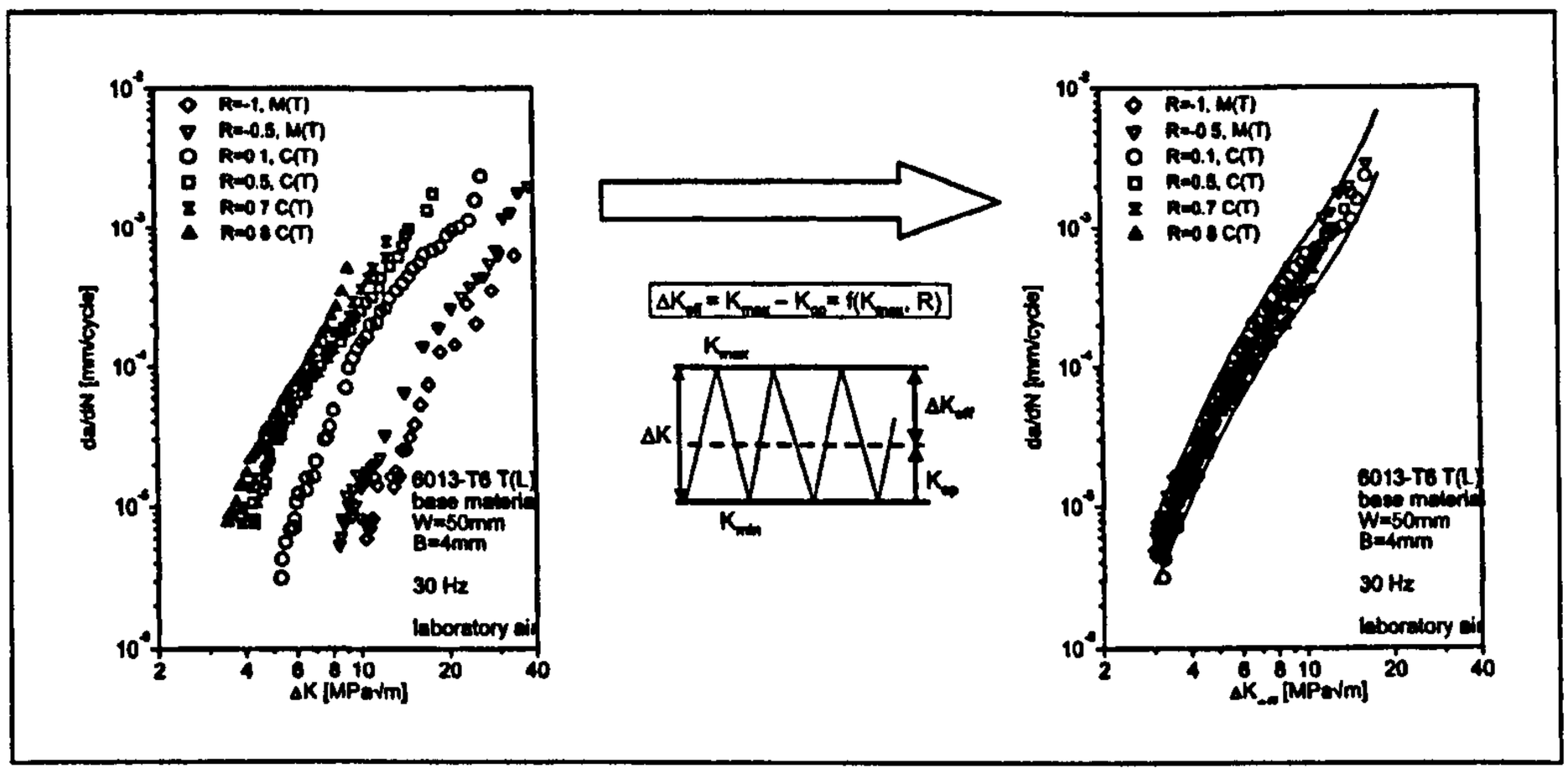

Figure 6.18: Effect of residual stress on the fatigue crack propagation in a friction stir welded AA 6013-T6[1].

The fatigue crack propagation rates in FS welded AA 2024-T3 and 6013-T6 utilising a basic tool (A), that resulted in joints containing pores, and a more advanced tool (B), that

---

[1] Dalle Donne, C et al (2000)

resulted in "defect free" joints, was also undertaken[1], the results being shown in Figure 6.19. In the AA 2024-T3 welds at R = 0.1 the crack growth rates were comparable for both tools at $\Delta K > 13$ MPa.m$^{0.5}$, below this value the tool A joints exhibited a slight increase in the propagation rates. The growth rates were comparable to those of the base material for $\Delta K > 17$ MPa.m$^{0.5}$, but the welds had a greater resistance to crack growth below this value. For the R = 0.7 tests the growth rates were comparable for $\Delta K <$ 7 MPa.m$^{0.5}$, with a slight increase in the tool A growth rates for values greater than this, both welds exhibited comparable results to the base material tested at the same stress ratio[1]. This type of response is in agreement with residual stress induced crack closure of a CT specimen; the welded material having a greater resistance to crack propagation until the stress intensity factor range increased above 17 MPa.m$^{0.5}$, when plastic flow would result in a redistribution of the residual stress field with a subsequent reduction in its influence. At R = 0.7 the significant increase in K_{max} that would be associated with a comparable stress intensity factor range to that observed for R = 0.1 would result in a redistribution of the residual stress at a much lower stress intensity factor range, hence the comparable growth rates observed for both the base and welded material.

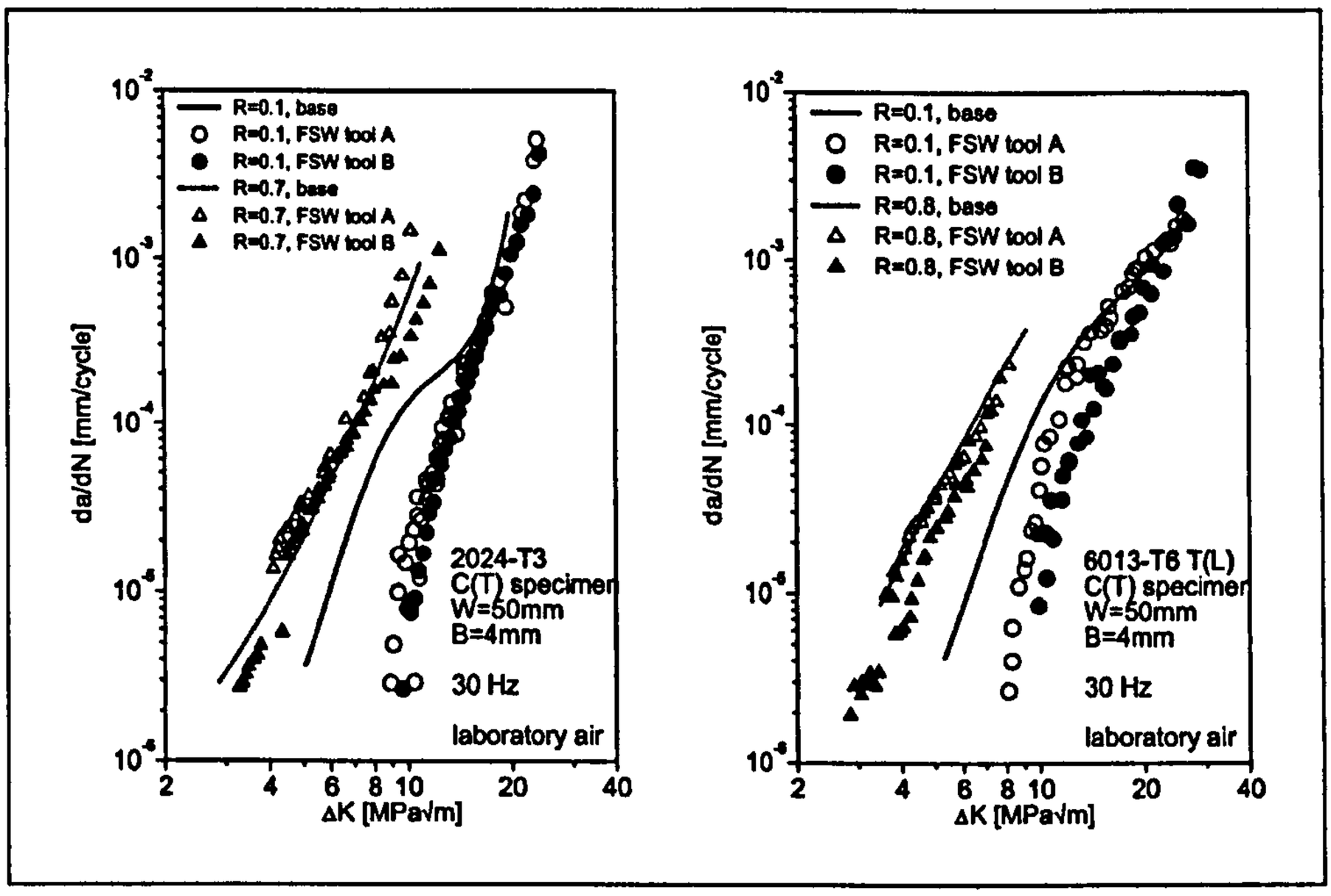

Figure 6.19: Comparison of the fatigue crack propagation in friction stir welded AA 2024-T3 (left) and 6013-T6 (right) joints using a basic tool (A) and a more advanced tool (B)[1].

The results from the AA 6013-T6 material exhibited a greater tool effect, with the tool B joints having a greater resistance to crack propagation than the tool A joints for $\Delta K < 25$ MPa.m$^{0.5}$ for R = 0.1 and $\Delta K < 7$ MPa.m$^{0.5}$ for R = 0.8. In comparison to the growth rates observed in the base material, the tests undertaken at R = 0.8 resulted in the tool A welds

[1] Dalle Donne, C et al (2000)

having a comparable growth rate, whilst the tool B joint had a slightly greater resistance to crack propagation. For R = 0.1 the tool A joints had a greater resistance to crack propagation for $\Delta K < 13$ MPa.m$^{0.5}$, whilst for the tool B joints this was evident for $\Delta K < 20$ MPa.m$^{0.5}$ when compared to that of the base material[1]. This again suggested that the results were predominantly influenced by the weld induced residual stresses, with the effect of this reducing as plastic flow occurred due to the increase in K_{max}. The effect of the weld induced residual stresses are confirmed by plotting the crack growth rate against ΔK_{eff}, with the values falling within a narrow scatter band as shown in Figure 6.20[1].

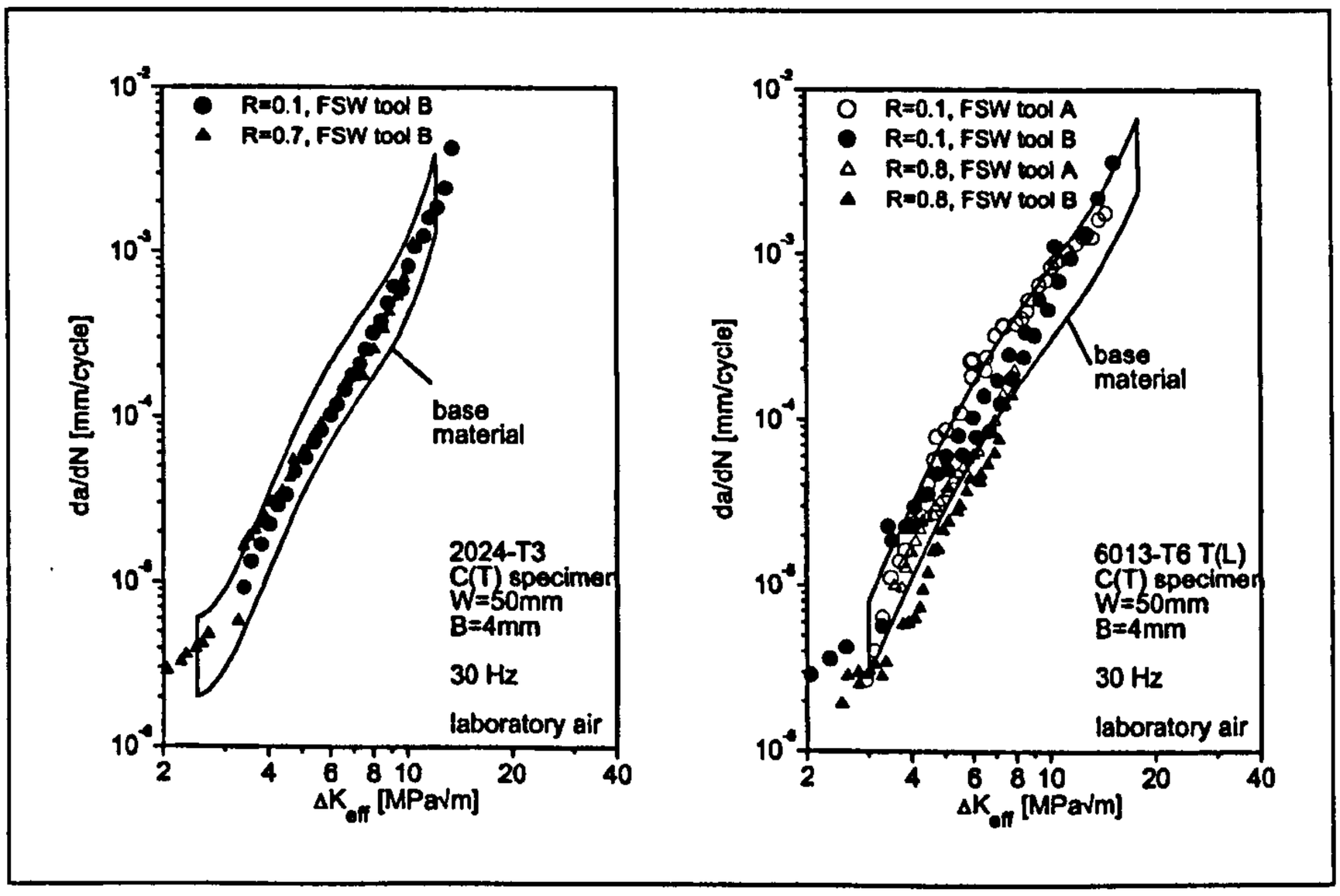

Figure 6.20: Effective crack propagation rates for friction stir welded AA 2024-T3 and 6013-T6 friction stir welded joints and base material[1].

Brandt et al[2] measured the fatigue crack propagation rates utilising centre cracked specimens in AA 5083, measurements being undertaken in both the parent material and the weld metal of GMAW joints utilising an AA 5183 filler, as shown in Figure 6.21. ΔK_0 values of 200 MPa.mm$^{0.5}$ (6.3 MPa.m$^{0.5}$) and 300 MPa.mm$^{0.5}$ (9.5 MPa.m$^{0.5}$) for the base metal at R = -1 and 0 respectively were reported, whist the weld metal returned values of 170 MPa.mm$^{0.5}$ (5.4 MPa.m$^{0.5}$) for R = -1 and 200 MPa.mm$^{0.5}$ (6.3 MPa.m$^{0.5}$) for R = 0. Except for the increased threshold value for the base metal at R = -1 the crack growth rates were comparable for the base and weld metal for the two stress ratios, with no evidence of the effect of tensile residual stresses increasing the growth rate and threshold value of the GMAW.

---

[1] Dalle Donne, C et al (2000)
[2] Brandt, U et al (2001)

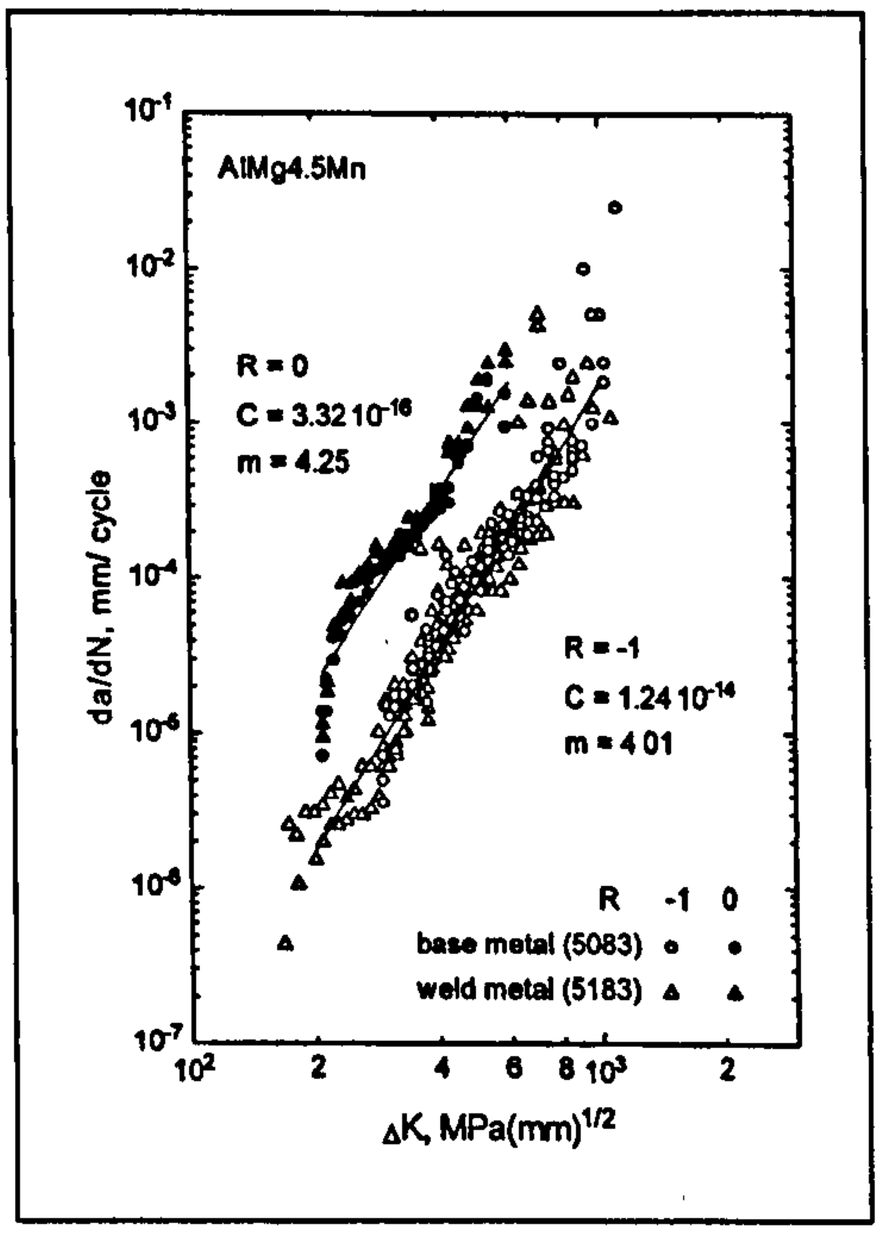

Figure 6.21: Crack propagation rates of AA 5083 base metal and AA 5183 weld metal[1].

Comparable results to those obtained by Brandt et al[1] were also obtained by Sonsino et al[2], but utilising the same material, AA 5083, for both the parent plate and filler metal. Crack growth measurements were again undertaken on a centre cracked specimen at the weld toe and in the parent material as shown in Figure 6.22.

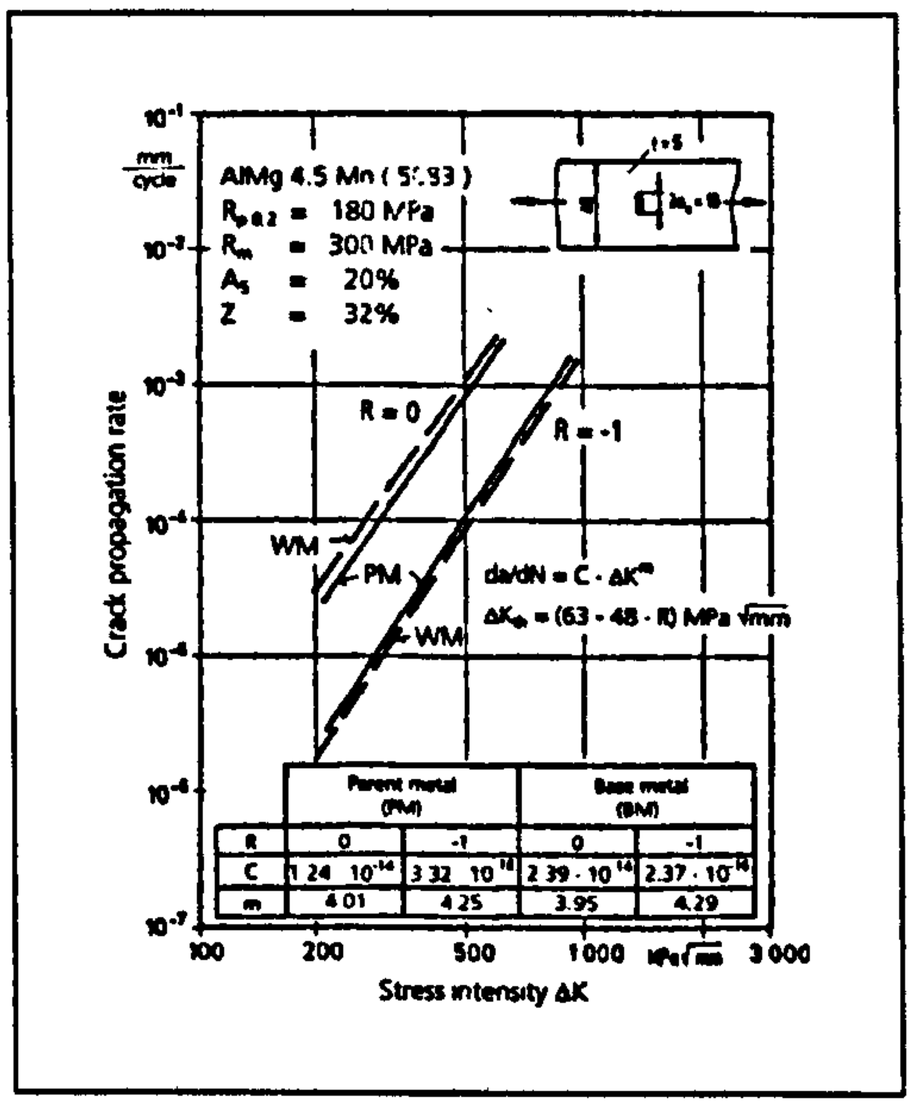

Figure 6.22: Crack propagation rates in AA 5083 parent plate and at the weld toe of a MIG weld in the same material[2].

[1] Brandt, U et al (2001)
[2] Sonsino, CM et al (1999)

Haagensen et al[1] constructed the crack propagation curves shown in Figure 6.23, showing crack growth rates at various points in the profile of a friction stir weld. The authors concluded that the growth rates were lower in the weld and HAZ than those in the base material and assumed that this was due to the smaller grain size in these regions. As the data for the curves was taken from other publications it was not apparent what material the curves related to, although it was assumed that it was a 6XXX aluminium alloy.

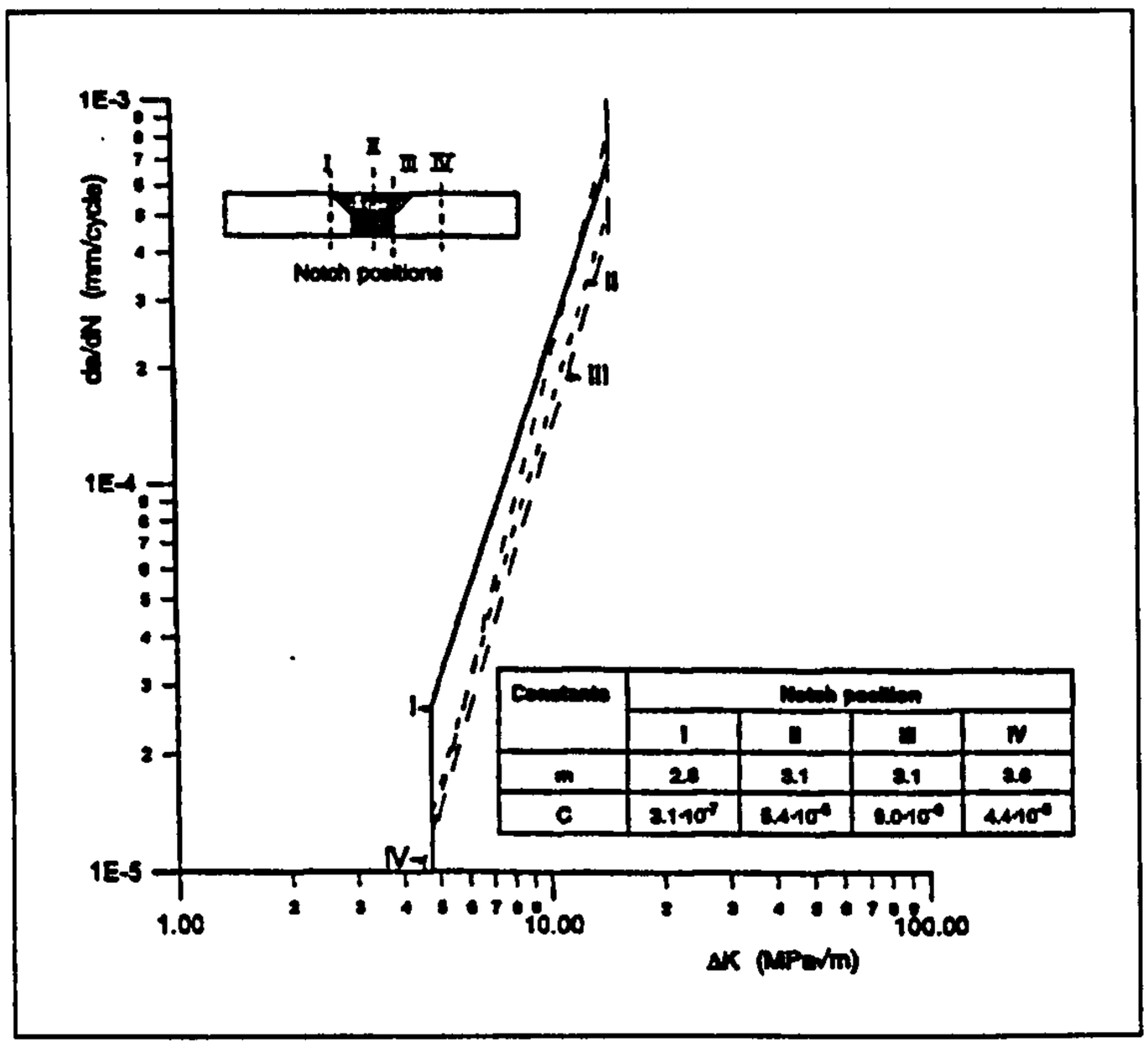

Figure 6.23: Crack propagation in a friction stir weld[1].

Wanhill et al[2] studied the crack propagation rates for both long and short cracks in an AA 2024-T3, as shown in Figure 6.24, at R = 0 (left) and 0.5 (right). A small crack effect was evident for R = 0, with growth rates below the fatigue threshold for long cracks and at rates greater than those observed in long cracks for $\Delta K \leq 5\ MPa.m^{0.5}$. The effect was less evident for R = 0.5, although short cracks continued to propagate below the long crack threshold, for $\Delta K \geq 2\ MPa.m^{0.5}$ the propagation rates were comparable to those observed for the long cracks. This response would suggest that the small crack effect for the 2024-T3 alloy under consideration was predominantly related to crack closure due to the stress ratio, R, effect.

[1] Haagensen, PJ et al (1995)
[2] Wanhill, RJH et al (1999)

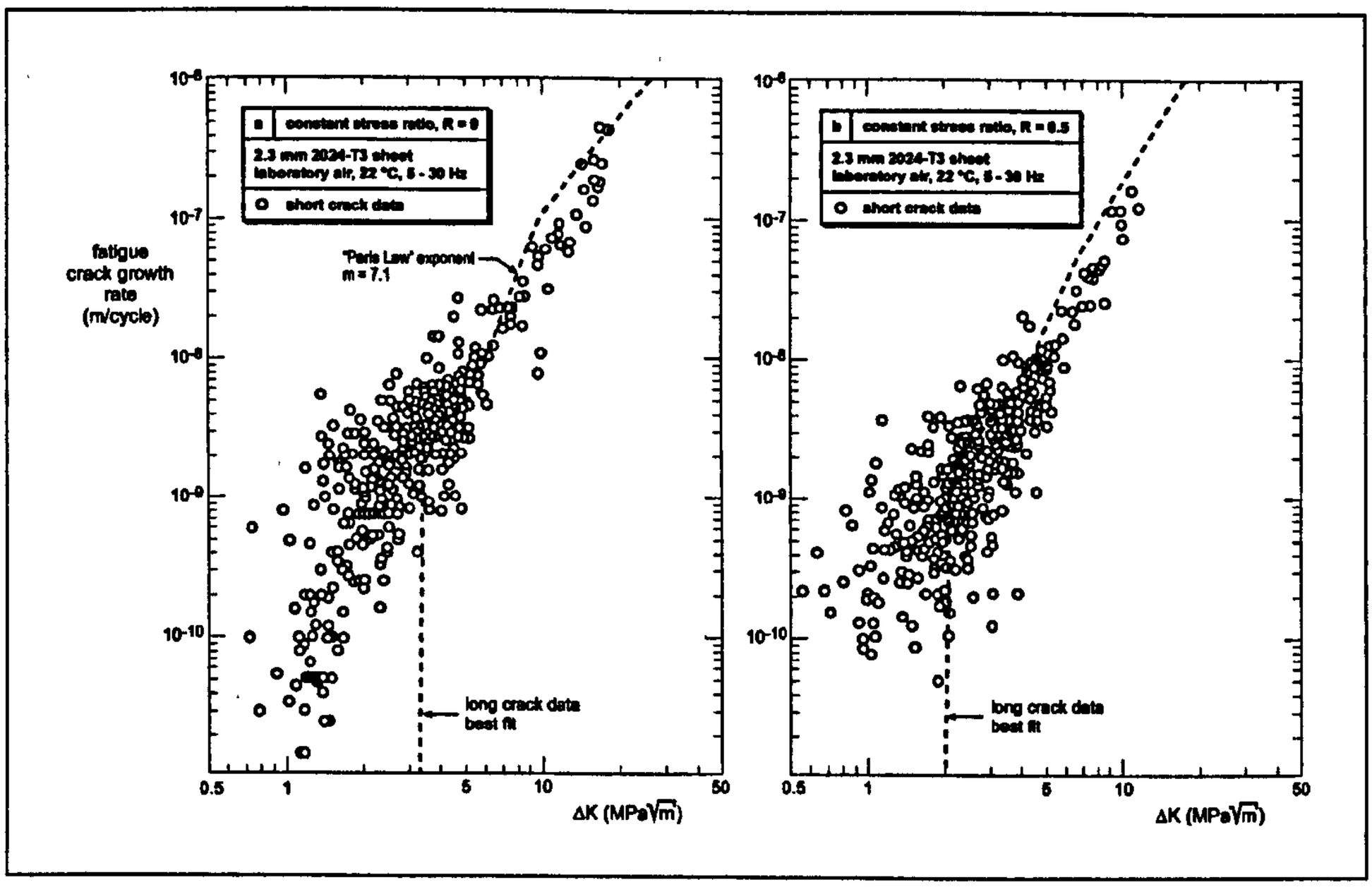

Figure 6.24: Comparison of long a short fatigue crack growth rates for AA 2024-T3 sheet loaded parallel to the rolling direction[1].

[1] Wanhill, RJH et al (1999)

6.4 Fatigue Crack Growth Rate Measurements

SCG, utilising notched cylindrical specimens, and LCG, utilising CT specimens, rates were measured to enable metallurgical evaluation of the fatigue properties to be determined; integration of the resulting crack growth rates enabling metallurgical S-N curves to be developed. The S-N curves should be comparable to those from the four point loading specimens when the effects of the SCF, resulting from the weld geometry, and residual stresses are taken into consideration.

SCG rate measurements were made for short cracks typically ranging from 10 - 30 μm to 0.5 - 1 mm. It was intended to measure SCG rates for lives of 10^5 and 10^6 cycles to determine whether there was any variation in the slope of the curves for the two lives. In order to determine the loads required to result in failure at 10^5 and 10^6 cycles a series of S-N curves were developed from tests undertaken on SCG specimens identical to those used for the SCG rate measurements. LCG rates were determined for stress intensities ranging from the threshold to approaching the fracture toughness, regimes A to C inclusive.

6.4.1 Short Crack Growth Specimens

The geometry of the specimens utilised for determining the rate of SCG were as shown in Figure 6.25 and Figure 6.26. The specimens were based on one detailed by Caton et al[1]; the aim of the design being that cracks initiate in the centre of the two notches, the area of maximum stress, thereby simplifying the surface replication and subsequent crack measurement processes.

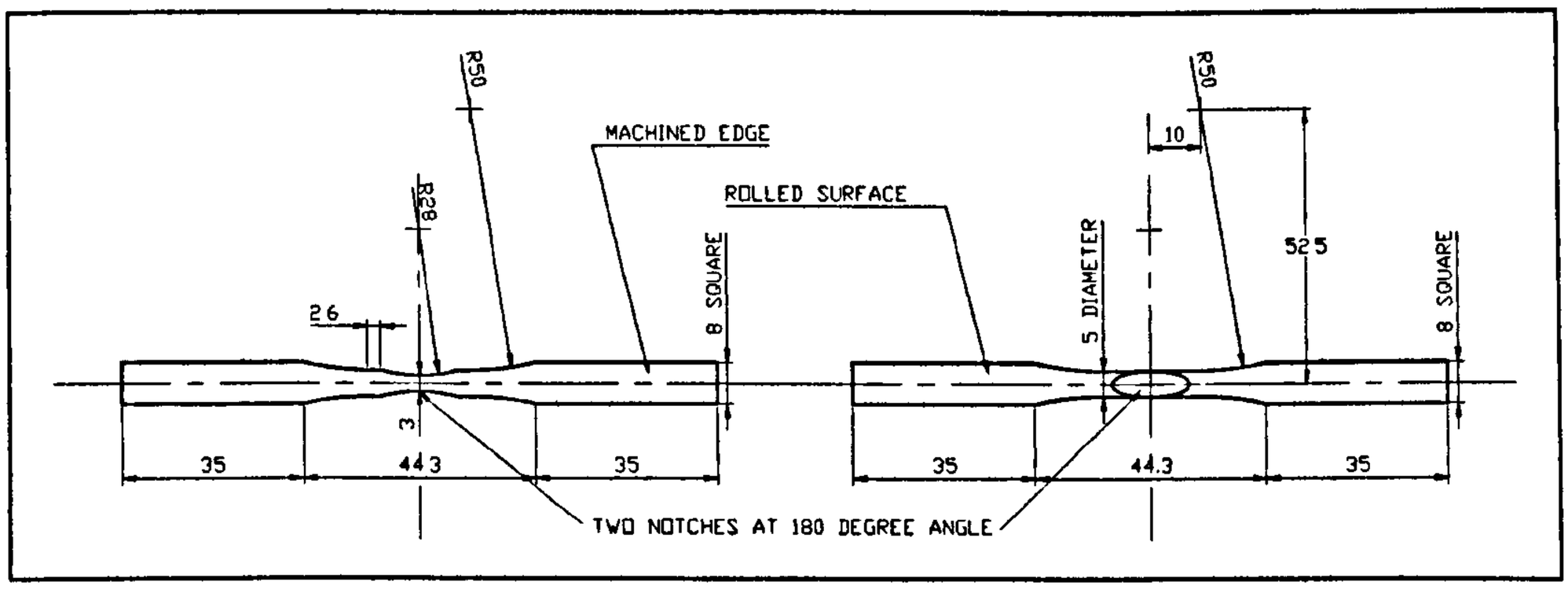

Figure 6.25: Short crack growth fatigue specimen.

[1] Caton, MJ et al (1999b)

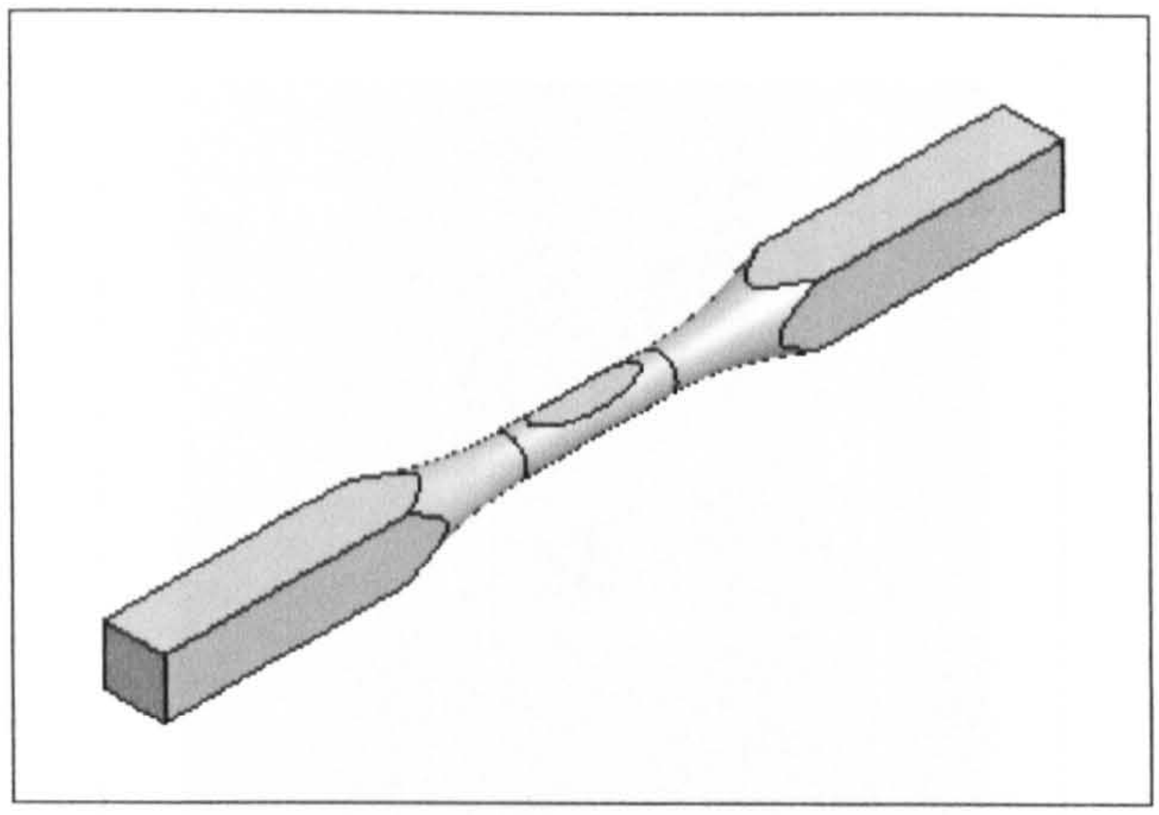

Figure 6.26: Short crack growth fatigue specimen.

The specimens were orientated, with respect to the original welded plate, to allow SCG measurements to be undertaken in the region where fatigue crack initiation occurred in the four point loading specimens:

i. Two parent plate specimens were produced with the rolling direction of the plate both transverse, |-, and parallel, //, to the loading direction.
ii. For the MIG welds the weld toe was at the centre of the notches.
iii. For the FS SP the weld seam was at the centre of the notches.
iv. Two specimens were produced for the FS DP weld, with the centre of the notches being at the tool shoulder edge for both the advancing, FS DPA, and retreating, FS DPR, sides (with respect to the 2nd pass).

The positions of the SCG specimen notches with respect to the various welds are shown in Figure 6.27 and Figure 6.28.

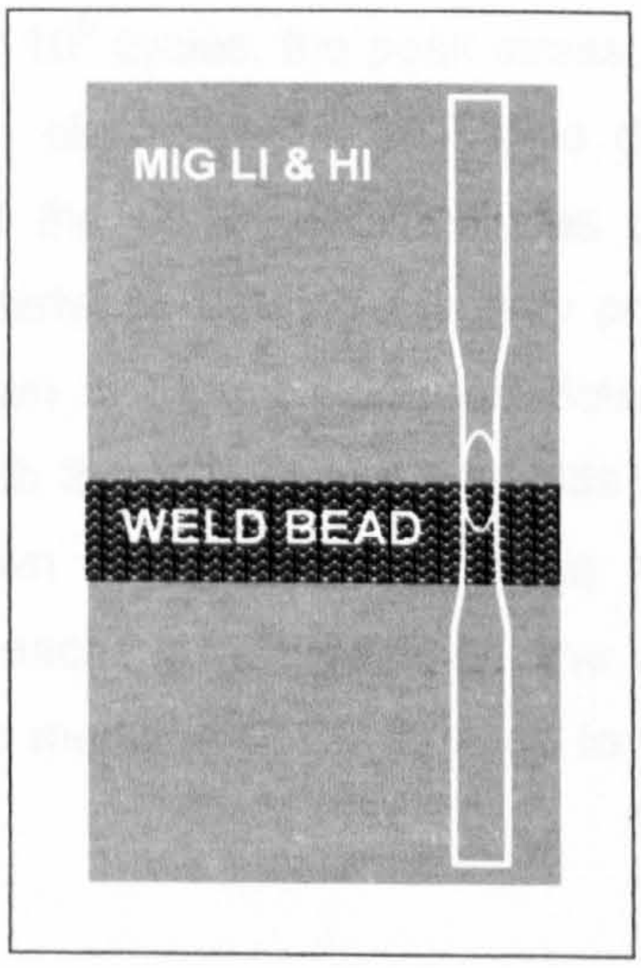

Figure 6.27: Position of SCG specimen notch with respect to the MIG welds (not to scale).

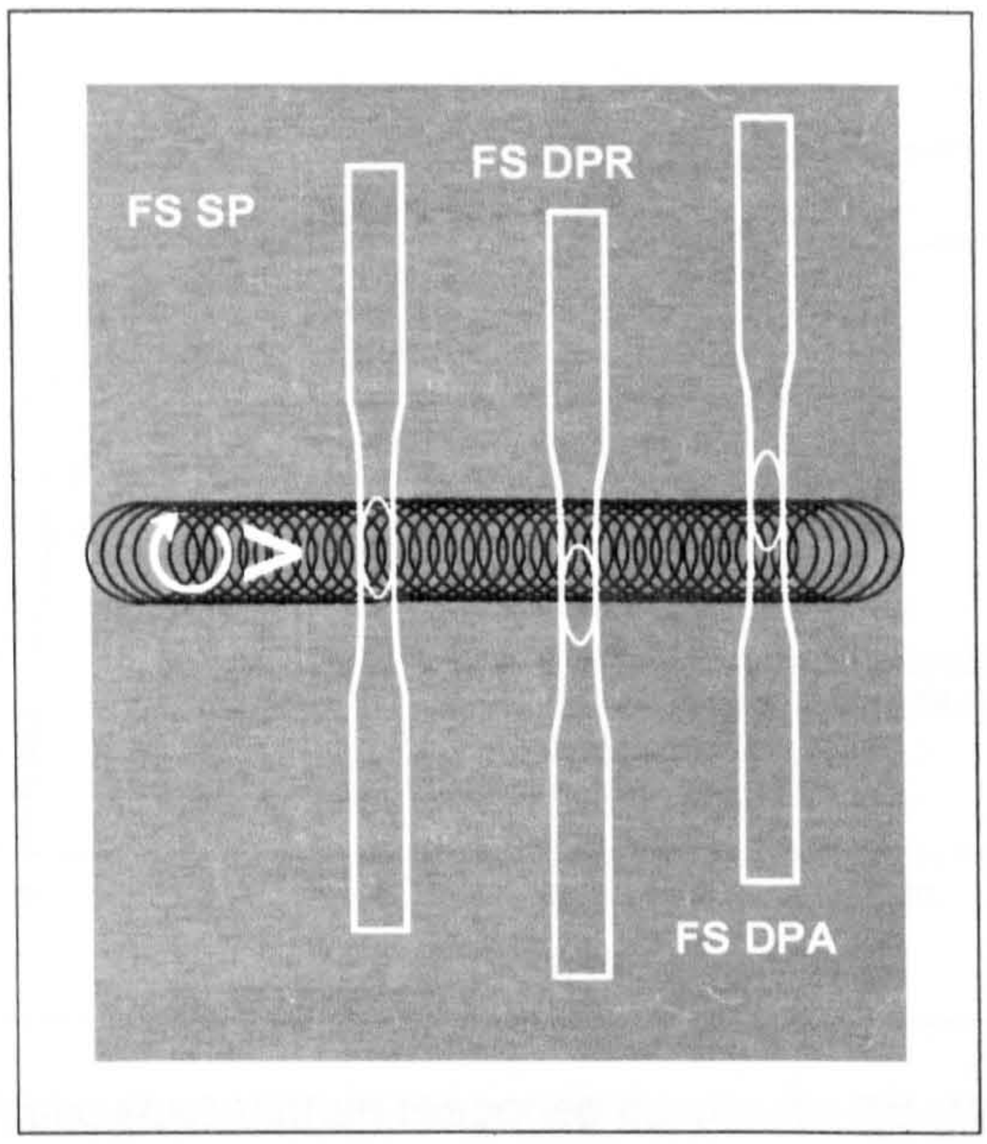

Figure 6.28: Position of the SCG specimen notch with respect to the FS welds (not to scale).

Due to a high proportion of the MIG LI SCG specimens failing in the weld metal, rather than at the weld toe (the centre of the notch), the design was modified for the specimens used for the SCG replication in an attempt to force failure to occur at the centre of the notch. This was achieved by reducing the radius of the notch from 28 mm to 15 mm, although the minimum thickness was maintained at 3 mm, and therefore the cross-sectional area, thereby increasing the stress concentration at the centre of the notch.

6.4.1.1 Stress Concentration Factors

Caton et al[1], on whose model the short crack specimen was based, used an elastic SCF, approximated from Peterson's handbook[2], of 1.04. As it was intended to determine the SCG rates for lives of 10^5 and 10^6 cycles, the peak stress, for R = 0.1, resulted in plastic deformation and therefore an elastic-plastic SCF was determined. To establish the elastic-plastic SCF a FEA of the SCG specimen was undertaken using Ansys 5.61 software. Analyses were undertaken utilising a twenty point elastic-plastic stress/strain response based on that shown in Figure 6.29 and detailed in Table 6.1; due to the stress/strain responses for both the MIG LI and HI welds and the FS SP and DP welds being near identical, as shown in Figure 3.118, page 121, it was decided that one response would suffice for each weld type. All the stress/strain responses were considered to have an elastic modulus of 70 GPa up to yield and a Poisson's ratio of 0.324.

---

[1] Caton, MJ et al (1999b)
[2] Pilkey, WD (1997)

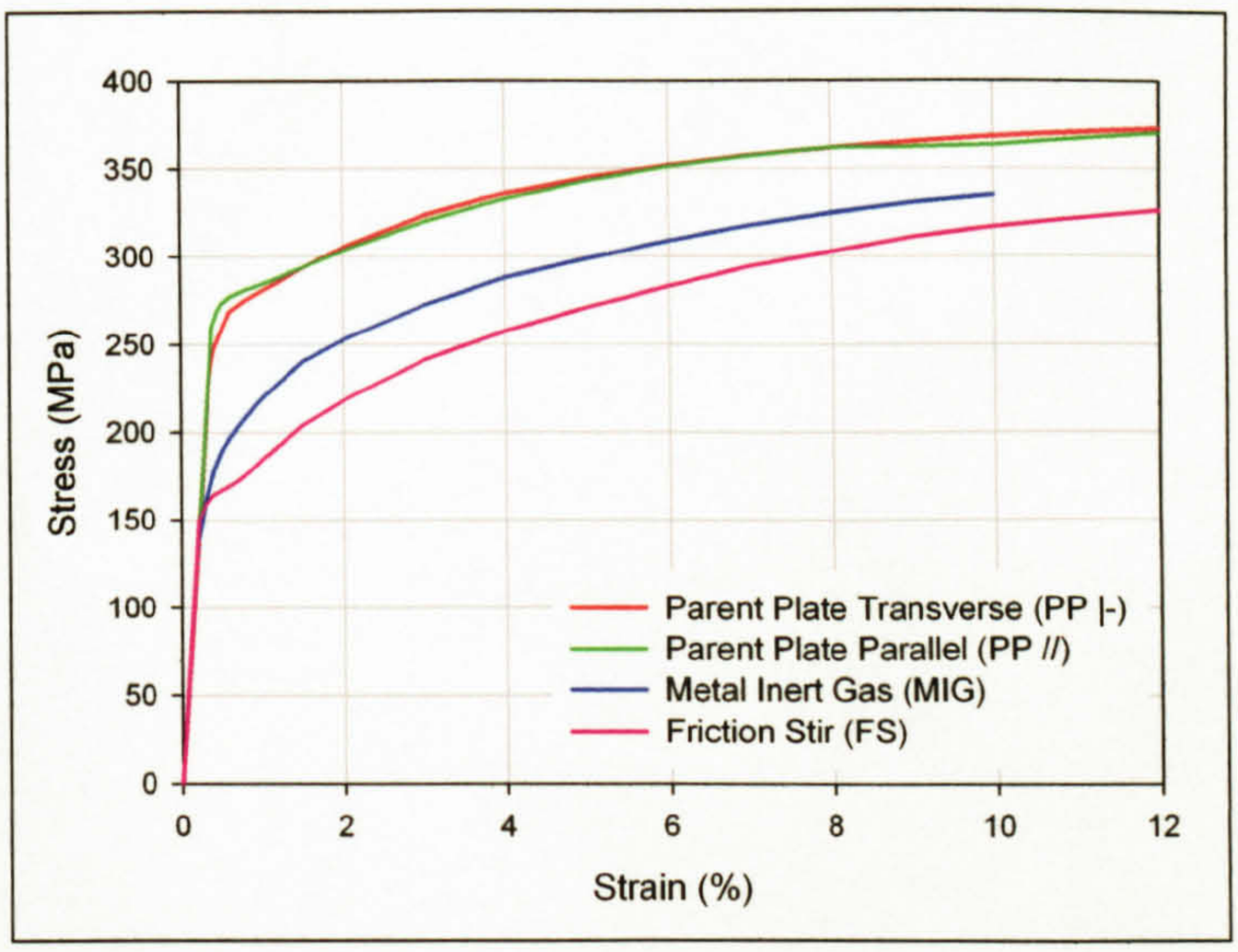

Figure 6.29: Elastic-plastic stress/strain response curves for the determination of the SCF of the SCG specimens.

Parent Plate Transverse (PP |-)		**Parent Plate Parallel (PP //)**		**Metal Inert Gas (MIG)**		**Friction Stir (FS)**	
E = 70 GPa, ν = 0.324							
σ_Y = 237 MPa		σ_Y = 259 MPa		σ_Y = 128 MPa		σ_Y = 150 MPa	
ε (%)	**σ (MPa)**	**ε (%)**	**σ (MPa)**	**ε (%)**	**σ (MPa)**	**ε (%)**	**σ (MPa)**
0	0	0	0	0	0	0	0
0.36	237.1	0.38	258.8	0.183	128.1	0.214	149.8
0.38	242.4	0.39	260.6	0.2	138.0	0.3	159.3
0.4	247.0	0.40	262.2	0.3	161.4	0.4	164.2
0.6	268.4	0.45	268.4	0.4	177.8	0.5	166.8
0.8	275.2	0.5	272.5	0.5	188.9	0.6	169.3
1.0	280.4	0.6	276.9	0.6	196.8	0.7	172.4
1.25	286.8	0.8	281.0	0.7	203.1	0.8	176.1
1.5	293.2	1.0	284.2	0.8	208.8	0.9	180.4
1.75	299.4	1.25	288.7	0.9	214.4	1.0	184.8
2.0	305.0	1.5	293.5	1.0	219.7	1.5	203.9
3.0	323.3	1.75	298.5	1.5	240.2	2.0	218.0
4.0	336.0	2.0	303.2	2.0	252.6	3.0	241.2
5.0	345.1	3.0	319.7	3.0	272.2	4.0	257.5
6.0	352.0	4.0	332.7	4.0	287.9	5.0	270.9
7.0	357.4	5.0	343.4	5.0	298.8	6.0	283.1
8.0	361.6	6.0	351.3	6.0	309.0	7.0	294.5
9.0	365.1	7.0	357.1	7.0	317.7	8.0	302.7
10.0	368.0	8.0	361.7	8.0	324.6	9.0	311.1
12.0	372.5	9.0	362.0	9.0	330.5	10.0	316.7
		10.0	363.1	10.0	334.7	12.0	326.0
		12.0	370.0			14.0	325.2

Table 6.1: Elastic-plastic stress/strain responses for determination of the SCF of the SCG specimens.

The FEA models were based on a quarter section with two axes of symmetry as shown in Figure 6.30. The models were analysed using SOLID92 (3-d, 10-node, corner and mid-element nodes, tetrahedral structural solid,) elements with the 28 mm notch radius model consisting of 455 elements and 1029 nodes and the 15 mm notch radius model consisting of 413 elements and 933 nodes, a typical stress response is shown in Figure 6.31. Analyses were undertaken for loads ranging from 1.5 - 5.0 KN, as shown in Table 6.2, giving a nominal stress at the centre of the notch of 107 - 356 MPa.

Load (KN)									
PP |-	3.0	3.25	3.5	3.75	4.0	4.25	4.5	5.0	
PP //	3.0	3.25	3.5	3.75	4.0	4.25	4.5	5.0	
MIG	1.5	1.75	2.0	2.5	3.0	3.5	4.0	4.5	5.0
FS	1.5	1.75	2.0	2.5	3.0	3.5	4.0	4.5	5.0

Table 6.2: SCG specimen SCF determination loads.

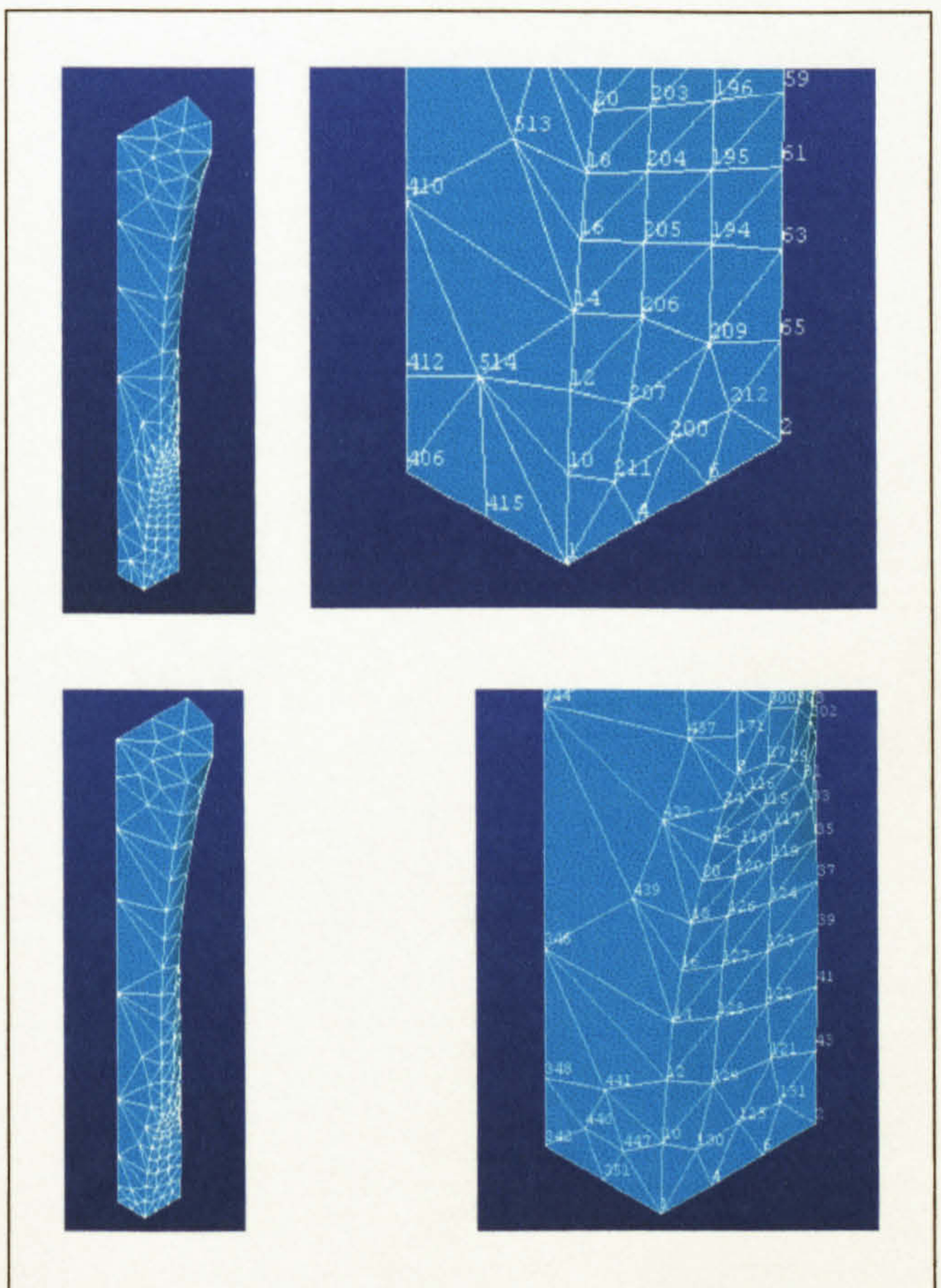

Figure 6.30: FEA models of 28 mm notch radius (upper) and 15 mm notch radius (lower) SCG specimens used for the determination of the notch SCF.

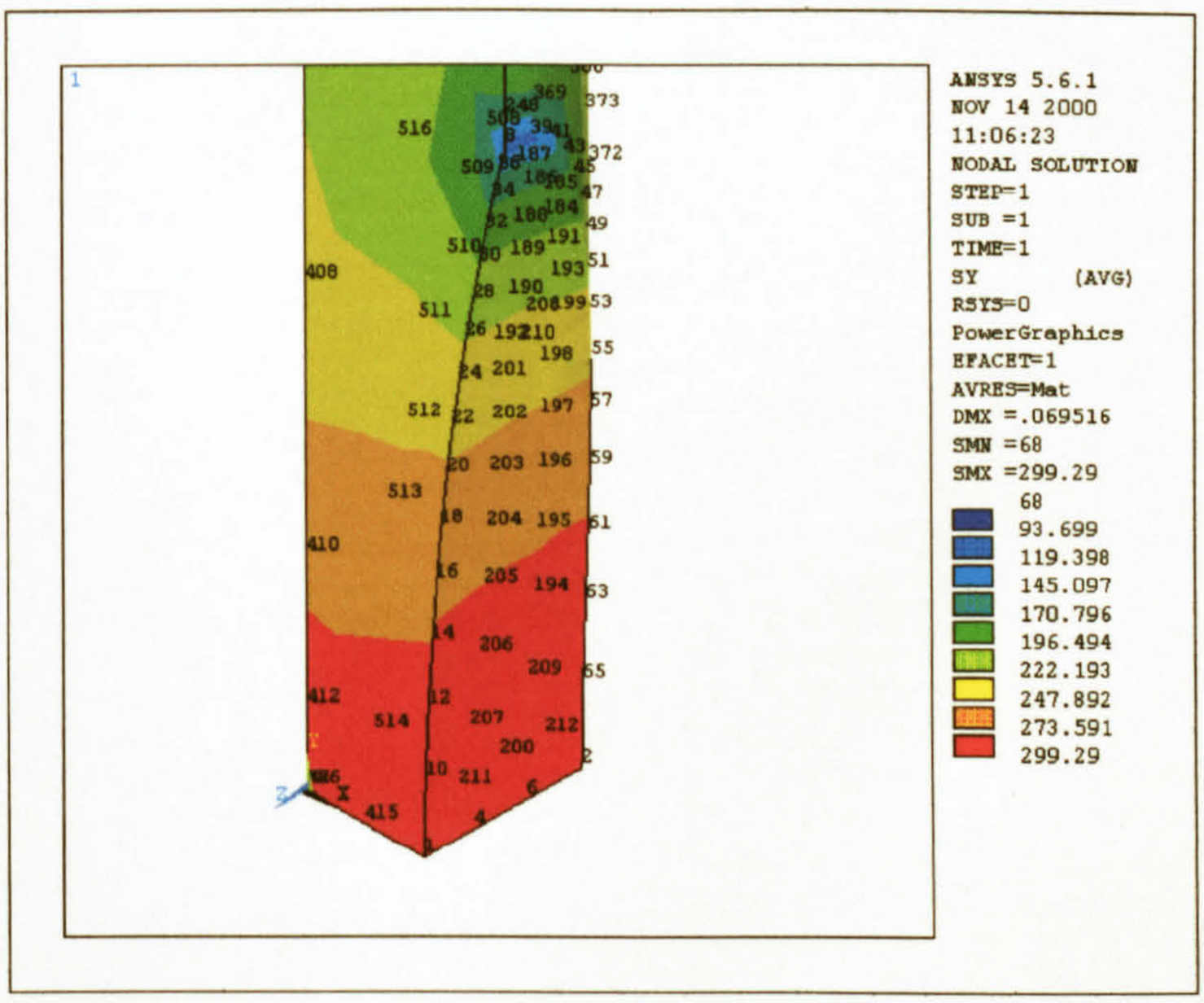

Figure 6.31: Typical FEA stress response of a SCG specimen.

All SCF values were determined by comparing the magnitude of the stress at node 1, located at the mid point of the notch surface, with the nominal stress expected at the centre of the notch. Although subsequent observation of the failed SCG specimens suggested that the cracks initiated at the surface, the FEA, typically within the plastic region, suggested that the highest stresses were found at internal nodes; this may have been due to increasing triaxial constraint below the surface or may have been an anomaly of the analysis process. The elastic and plastic SCF are detailed in Table 6.3 and Figure 6.32, the equations for the plastic SCF being determined through curve fitting using TableCurve 2D V5.00 software.

Weld process	Elastic SCF		Plastic SCF	
	Nominal stress (MPa)	SCF	Nominal stress (MPa)	SCF (σ = nominal stress)
PP |-	≤ 224.44	K_t = 1.05	> 224.44	$K_t = 0.983 + \left(1031.647 \times \exp\left(-\sigma/23.296\right)\right)$
PP //	≤ 248.14		> 248.14	$K_t = 0.980 + \left(6.757e6 \times \exp\left(-\sigma/13.501\right)\right)$
MIG LI (15 mm radius notch)	≤ 109.54	K_t = 1.10	> 109.54	$K_t = \left(1.032 + \left(-1430.904/\sigma^2\right)\right)^{-1}$
MIG (LI & HI)	≤ 118.60	K_t = 1.05	> 118.60	$K_t = 0.992 + \left(9.255 \times \sigma^{-4.436}\right)$
FS (SP & DP)	≤ 142.31		> 142.31	$K_t = 0.997 + \left(27877.124 \times \exp\left(-\sigma/10.806\right)\right)$

Table 6.3: Elastic-plastic SCF for SCG specimens.

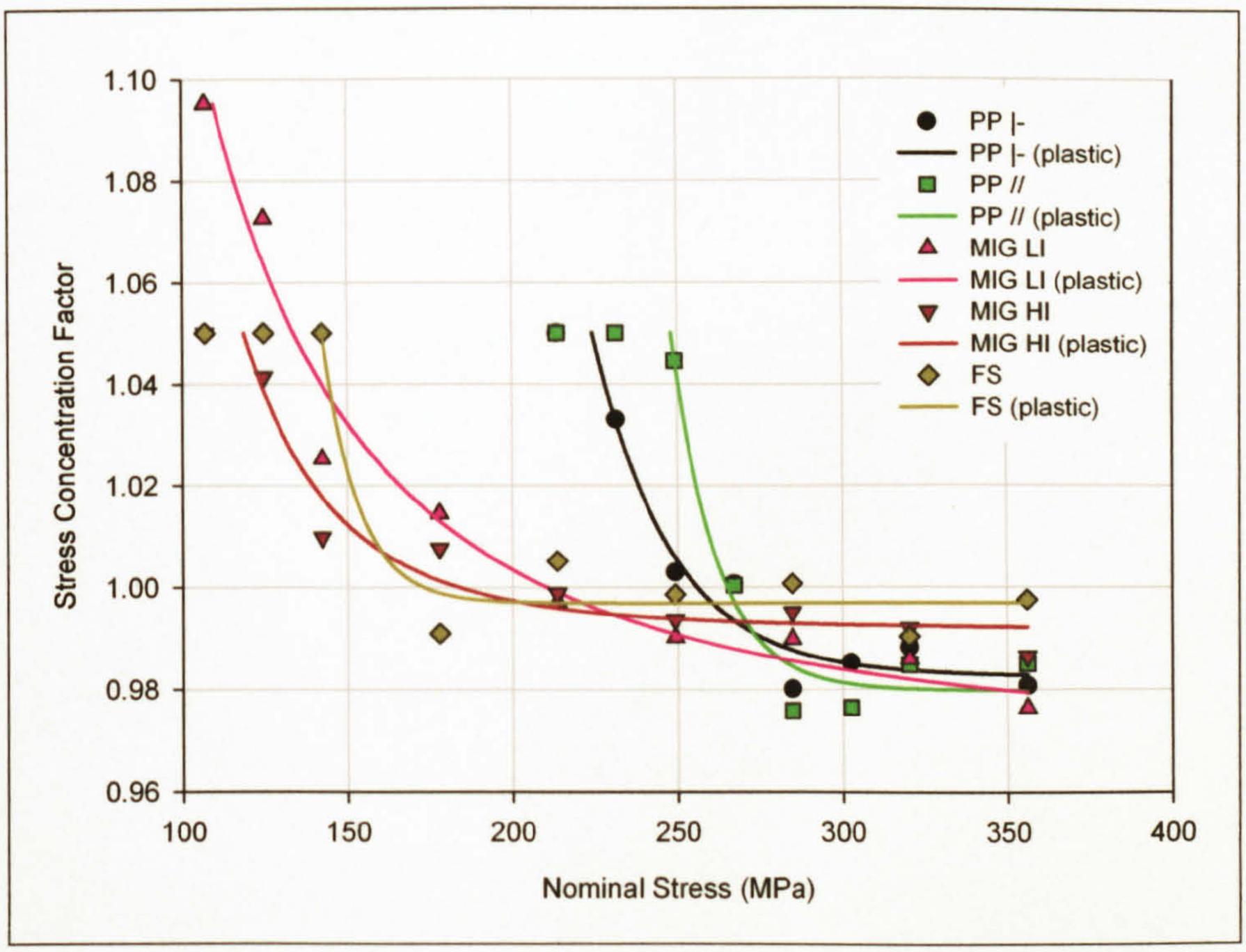

Figure 6.32: FEA results for an elastic-plastic SCF for short crack specimen.

6.4.1.2 Stress Intensity Factor Range

Although SCG cannot typically be modelled with respect to LEFM, ΔK_I was calculated for the short cracks to enable the responses for the SCG and LCG to be compared. ΔK_I was calculated utilising equation (6.5)[1], this considered the cracks to be semi-elliptical surface flaws in tension, as depicted in Figure 6.33. The crack aspect ratios, a/c, were determined by measuring the width and depth, by means of an optical microscope, of the exposed fatigue fracture surfaces, the mean values, shown in Table 6.4, being employed for the determination of ΔK_I.

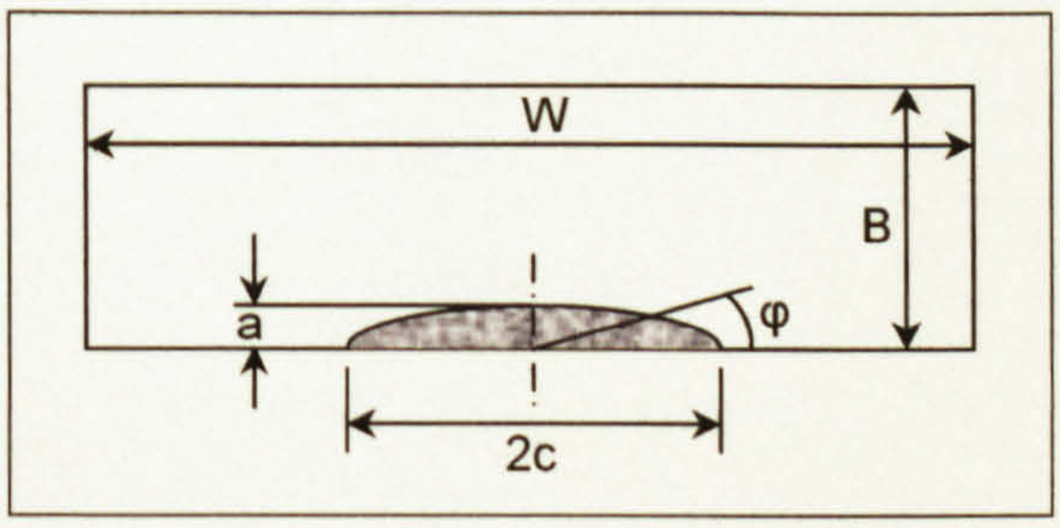

Figure 6.33: Schematic diagram of a semi-elliptical surface flaw.

[1] Newman Jr, JC; Raju, IS (1981)

Material	Crack aspect ratio (a/c)	Material	Crack aspect ratio (a/c)
PP |-	0.929	PP //	0.777
MIG LI	0.908	MIG HI	0.833
FS SP	0.871	FS DPA	0.855
FS DPR	0.929		

Table 6.4: Crack aspect ratios used for determining ΔK_I.

$$K_I = C\sigma\frac{\sqrt{\pi a}}{\varphi} \tag{6.5}$$

$$C = f\left(\frac{a}{B},\frac{a}{c},\frac{c}{W},\varphi\right) \tag{6.6}$$

$$C = \left[C_1 + C_2\left(\frac{a}{B}\right)^2 + C_3\left(\frac{a}{B}\right)^4\right]C_4 g(\varphi)g(w) \tag{6.7}$$

$$C_1 = 1.13 - 0.09\left(\frac{a}{c}\right) \tag{6.8}$$

$$C_2 = -0.54 + \frac{0.89}{0.2 + \left(\frac{a}{c}\right)} \tag{6.9}$$

$$C_3 = 0.5 - \frac{1.0}{0.65 + \left(\frac{a}{c}\right)} + 14\left(1.0 - \frac{a}{c}\right)^{24} \tag{6.10}$$

$$C_4 = 1 + \left[0.1 + 0.35\left(\frac{a}{B}\right)^2\right](1 - \sin\varphi)^2 \tag{6.11}$$

$$g(\varphi) = \left[\sin^2\varphi + \left(\frac{a}{c}\right)^2\cos^2\varphi\right]^{0.25} \tag{6.12}$$

$$g(W) = \left[\sec\frac{\pi c}{W}\sqrt{\frac{a}{B}}\right]^{0.5} \tag{6.13}$$

for: $0 < \frac{a}{c} < 1, \quad 0 < \frac{a}{B} \le 1, \quad 0 < \frac{c}{B} < 0.5, \quad 0 < \varphi < \pi$

where: a, B, c, W and φ are as shown in Figure 6.33.

Both the notches of the specimens and surrounding area, typically bounded by the circumferential lines in Figure 6.26, were hand ground, the final grinding being undertaken with a 2500 grit SiC paper. The specimens were then manually polished, with the final polishing consisting of a 0.25 µm diamond paste. The grinding and polishing were undertaken to reduce the likelihood of crack initiation occurring outwith the notches due to the surface finish that resulted from their manufacture. Due to the process being undertaken manually and the time involved in the process some marks from the coarser diamond pastes, 15, 6 and 1 µm, were evident on the specimens that were tested when viewed under an optical microscope. All the initial machining marks were removed and any remaining marks ran parallel to the applied loading thereby minimising their influence on fatigue crack initiation and growth.

6.4.2 Short Crack Growth Specimen S-N Testing

In order to determine the loads required to cause failure of the SCG specimens at 10^5 and 10^6 cycles S-N testing of the SCG specimens was undertaken. An Instron 8501 servo-hydraulic test frame, utilising an Instron 8800 controller and a ±10 KN load cell was employed for the tests. Constant load amplitude, with a sinusoidal loading response, uniaxial testing was undertaken at a frequency of 40 Hz and R = 0.1. The specimens were clamped in hydraulic grips, with a load protection device being employed to prevent the specimens being preloaded as the clamps were engaged. Testing was undertaken in a laboratory atmosphere at room temperature. The SCG S-N plots are shown as Figure 6.42, Figure 6.59 and Figure 6.76 with the results returned by the individual specimens being detailed in Section 13, Appendix C ~ Crack Growth Results (pages 506 - 537).

6.4.3 Short Crack Growth Tests

The SCG tests were undertaken utilising the same equipment, specimens and procedures detailed for the SCG S-N tests detailed above. The cyclic loading was stopped at regular intervals, at the mean load to maintain crack opening, and replicas of the crack taken with reference to a technique described by Swain[1]. A thin strip of cellulose acetate of 35 µm thickness was dipped into acetone and then applied to each of the polished notch surfaces, when the acetone had evaporated the cellulose acetate was peeled off and mounted on a microscope slide using double sided tape. Observation of the mounted cellulose acetate replica through an optical microscope revealed details of the surface of the notches including any cracks, as shown in Figure 6.34. The polishing of the notches aided the replication technique by both enhancing determination of the position of the crack tip and also allowing the replica to be more easily removed from the polished surface.

---

[1] Swain, MH (1992)

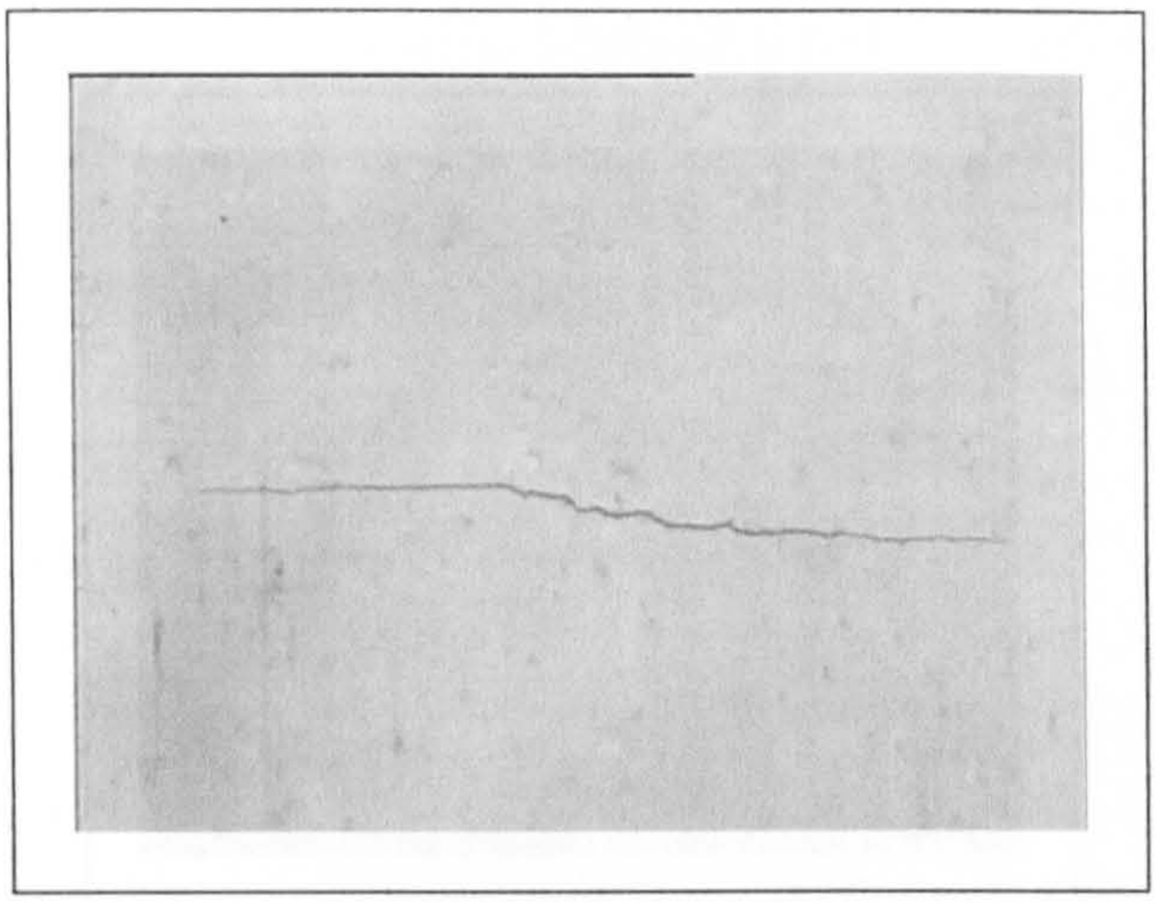

Figure 6.34: Optical micrograph of a short crack, length (2c) 537.6 µm, plastic replica.

Short crack measurements, obtained from the plastic replicas, were done in reverse order utilising an Olympus BX60M optical microscope; images were captured directly to a personal computer using a video camera and the crack length was determined using Image Tool software*. Typically the crack that resulted in the final failure and two or three other main cracks were measured. The length of the crack, c, was determined through measurements of the complete path, rather than in a straight line from tip to tip, with c being calculated as half of this length (the length of the crack, c, with respect to the SCG measurements refers to half the distance from one tip to the other, following the outline of the crack, unless stated otherwise.).

An attempt was made to determine the position and growth rate of the crack with respect the grain structure, to see if this had any influence on the SCG rate, by electroetching the surfaces of the notches utilising the same technique that was used to reveal the microstructure (described in Section 3.5.1, Planar Grinding, Polishing and Electro-etching, page 36). Unfortunately two problems became apparent which resulted in the attempt being abandoned and the notch surfaces being left in their polished state. The anodising of the surface that occurred during the etching process exhibited multiple cracking, due to its brittle nature, when fatigue loaded, as shown in Figure 6.35 and Figure 6.36. The cracks in the anodised surface appeared to influence the path taken by the crack that subsequently developed in the alloy, this phenomenon being evident in Figure 6.36. The other problem was that the roughened surface that occurred due to the etching resulted in difficulty in maintaining the integrity of the replica when attempting to remove it from the specimen. The combination of these problems made accurate determination of the crack length and subsequent growth more difficult, hence the abandonment of the attempt.

---

* Image Tool Software 2.00 developed at the University of Texas Health Science Centre at San Antonio, Texas and available from the internet by anonymous ftp from ftp://maxrad6.uthscsa.edu

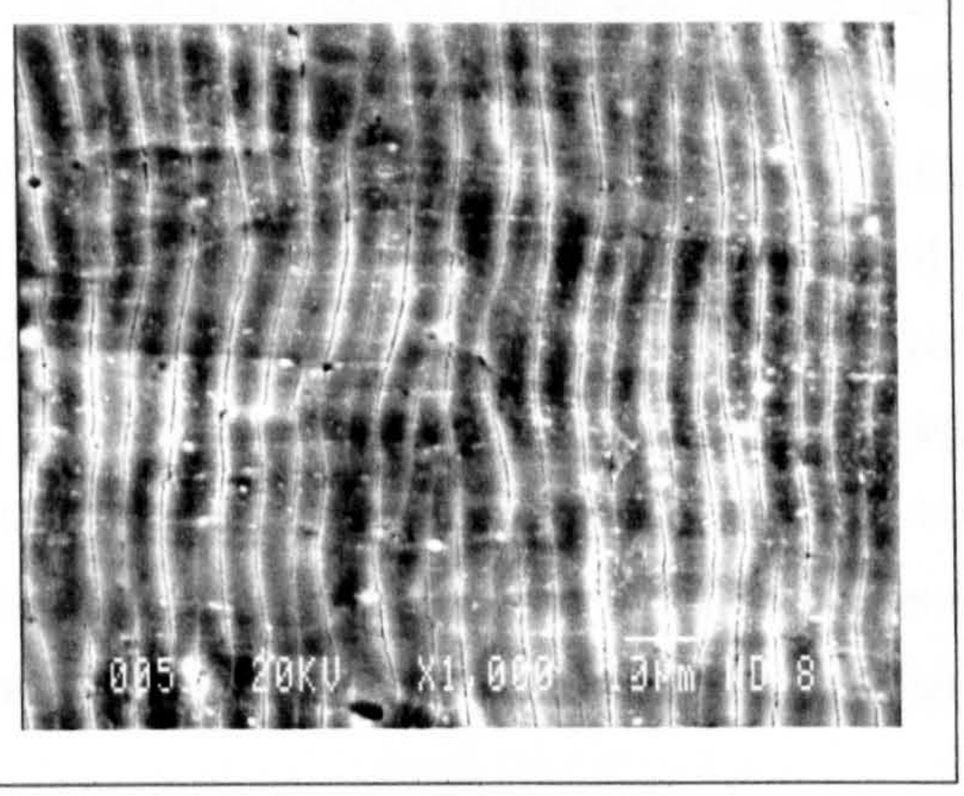

Figure 6.35: Scanning electron micrograph of the multiple cracking of the oxide surface that occurred after fatigue loading of a SCG specimen that had undergone electroetching of the notch surfaces prior to loading.

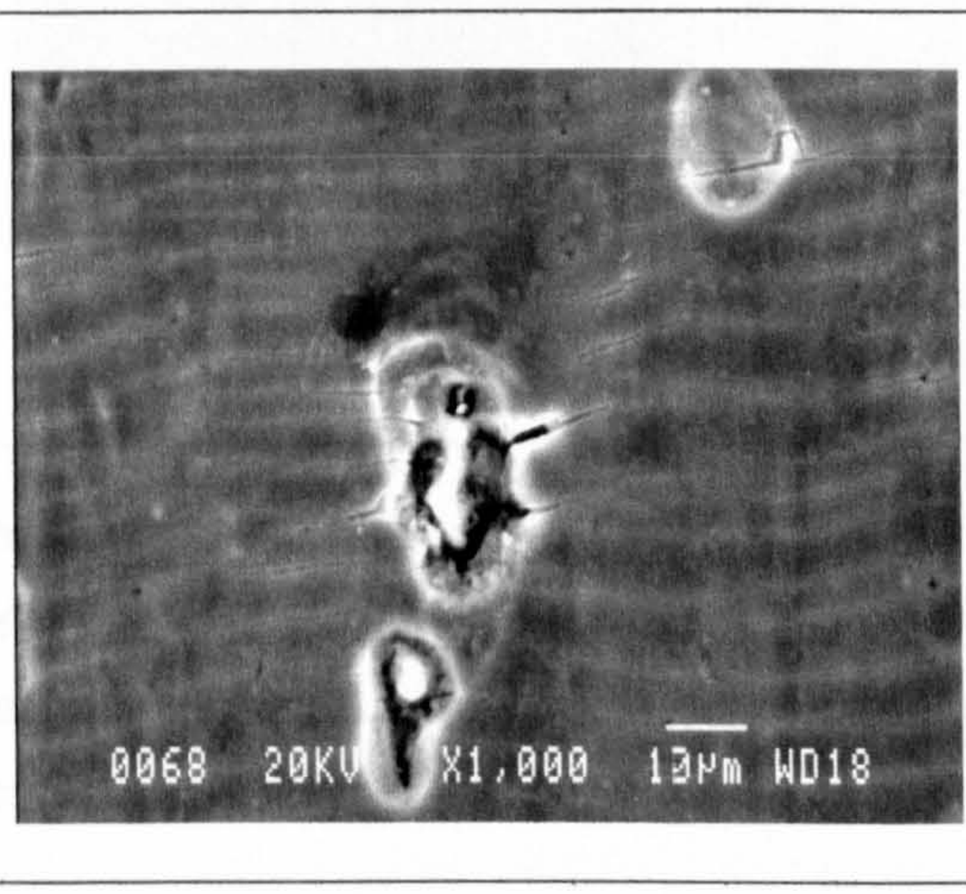

Figure 6.36: Crack initiation site and SCG occurring along the cracks in the anodised surface of the etched notch surface of a SCG specimen.

Several problems were encountered with the measurement process that were related to the crack replication technique, observable in Figure 6.37. Due to the stress fields around the crack tips crack interaction frequently occurred, typically prior to coalescence. As the cracks grew and began to interact the crack tips tended to rotate towards each other; determining when coalescence between the two cracks had occurred was complicated due to the fact the slip bands between the two cracks became visible and therefore the exact point of coalescence was difficult to determine. Coalescence of the cracks did not generally occur tip to tip, resulting in the overall length of the coalesced crack being less than that of the two cracks involved.

Other difficulties that were encountered involved bubbles forming between the SCG specimen surface and the plastic replica; this was more noticeable, although not exclusively, on larger cracks. If bubbles were evident on the replica at the time it was taken further attempts were made to produce a replica with no bubbles, although this was not always possible, the cause of the bubbles not being known. If bubbles on the replica obscured the path of the crack the length was considered to be from the point the bubble obscured the crack in a straight line to where it became visible again, any tortuousity of the path beneath the bubble being ignored. If the path of the crack was only partially obscured by the bubble and could be readily determined beneath the bubble any tortuousity was measured. If the crack tip was obscured the replica was ignored.

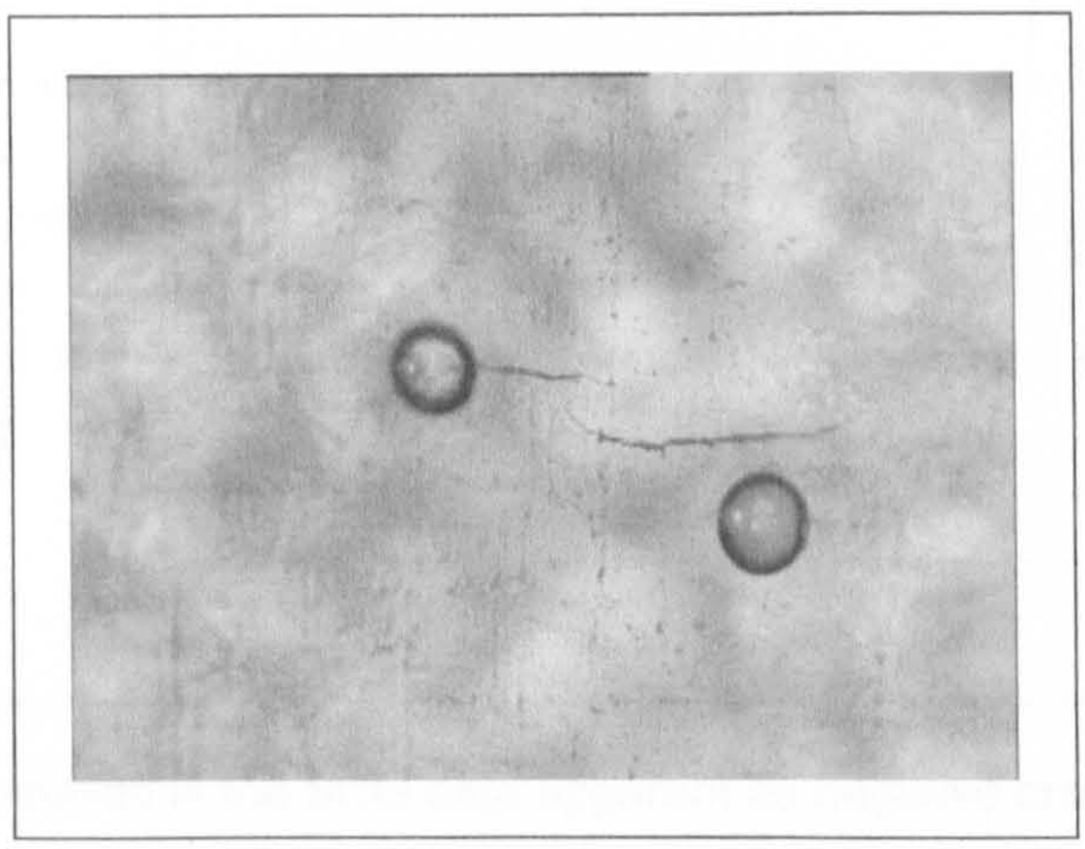

Figure 6.37: Optical micrograph of a short crack plastic replica, crack lengths, c, 190 µm (upper left) and 239 µm (lower right), detailing some of the problems associated with the plastic replication technique; path curvature due to crack tip stress field interaction, bubbles obscuring the path and variable focal depth across the image.

Due to the curved surface of the notches, the replica of the crack, when viewed under an optical microscope, tended to be only partially in focus. This resulted in several measurements having to be made, to readily determined points, e.g. a change in direction of the crack, to determine the overall length of the crack. The smallest cracks measurable were typically of the order of 10 - 30 µm in length, cracks smaller than this generally required high magnification that resulted in the majority of the replica being out of focus.

It was initially intended that the short crack growth would be determined for fatigue lives of 10^5 and 10^6 cycles to determine whether there was any variation in the slope of the curves, the loads for the appropriate lives being determined from Figure 6.42, Figure 6.59 and Figure 6.76. Although it was possible to obtain fatigue lives of 10^5 ±20% cycles, attempts to obtain lives of 10^6 cycles proved impractical, with specimens either failing at $2\text{-}3 \times 10^5$ cycles or not failing after attaining 2×10^6 cycles. Due to the time involved in

obtaining replicas it was eventually decided to abandon the attempt to obtain SCG data for lives of 10^6 cycles.

Due to these difficulties in measuring the cracks using the replication technique the results obtained typically exhibited some values that suggested that the crack had reduced, rather than increased, in length, as shown in Figure 6.38. Any measured values that resulted in negative crack growth were considered to be erroneous measurements and were subsequently omitted from the SCG analyses.

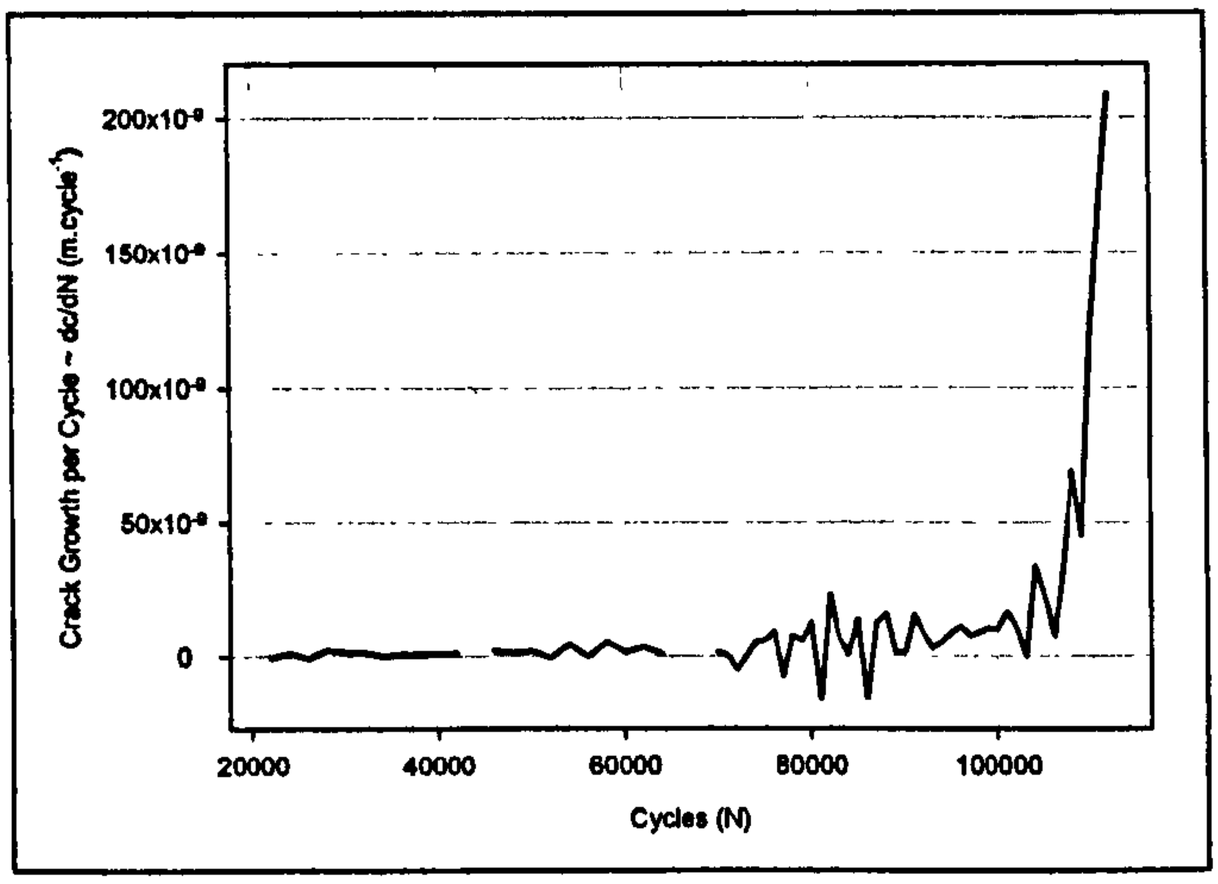

Figure 6.38: Anomalies in the SCG data apparent as negative crack growth due to difficulties in accurately measuring the crack length using the plastic replication technique.

Details of the various SCG rates with respect to the number of cycles and the crack length are detailed in the following sections. Although SCG cannot typically be modelled with respect to the stress intensity factor range, ΔK, plots of both the LCG and SCG propagation rates with respect to the stress intensity factor range are shown in Figure 6.100 to Figure 6.106, with the technique utilised to determine the stress intensity factor range being detailed in Section 6.4.1.2, Stress Intensity Factor Range (pages 333 - 334).

6.4.4 Long Crack Growth Specimens

LCG rates are generally determined using either CT or MT specimens as detailed in ASTM E 647[1]; the specimen employed being based on the CT specimen, the exact geometry being shown in Figure 6.39. The notch was cut with a 60° tip angle and 0.125" width due to this being the only suitable cutter available at the time of production, ASTM E 647[1] recommending a 30° tip angle. The specimens were 5 mm thick to allow any distortion in the welded specimens to be accounted for in the production of flat and

[1] ASTM (1995b)

parallel sided specimens, therefore approximately 1.5 mm was removed from each side of the parent and as-welded material. Initial specimens were ground to an 800 SiC grit finish, but difficulties in determining the exact position of the crack tip during the initial stages of the tests resulted in subsequent specimens being ground to a 2500 SiC grit finish and then polished, eventually to a 1 μm diamond paste finish. This resulted in a finish where nearly all the marks from the machining process had been removed, making subsequent determination of the crack tip more accurate.

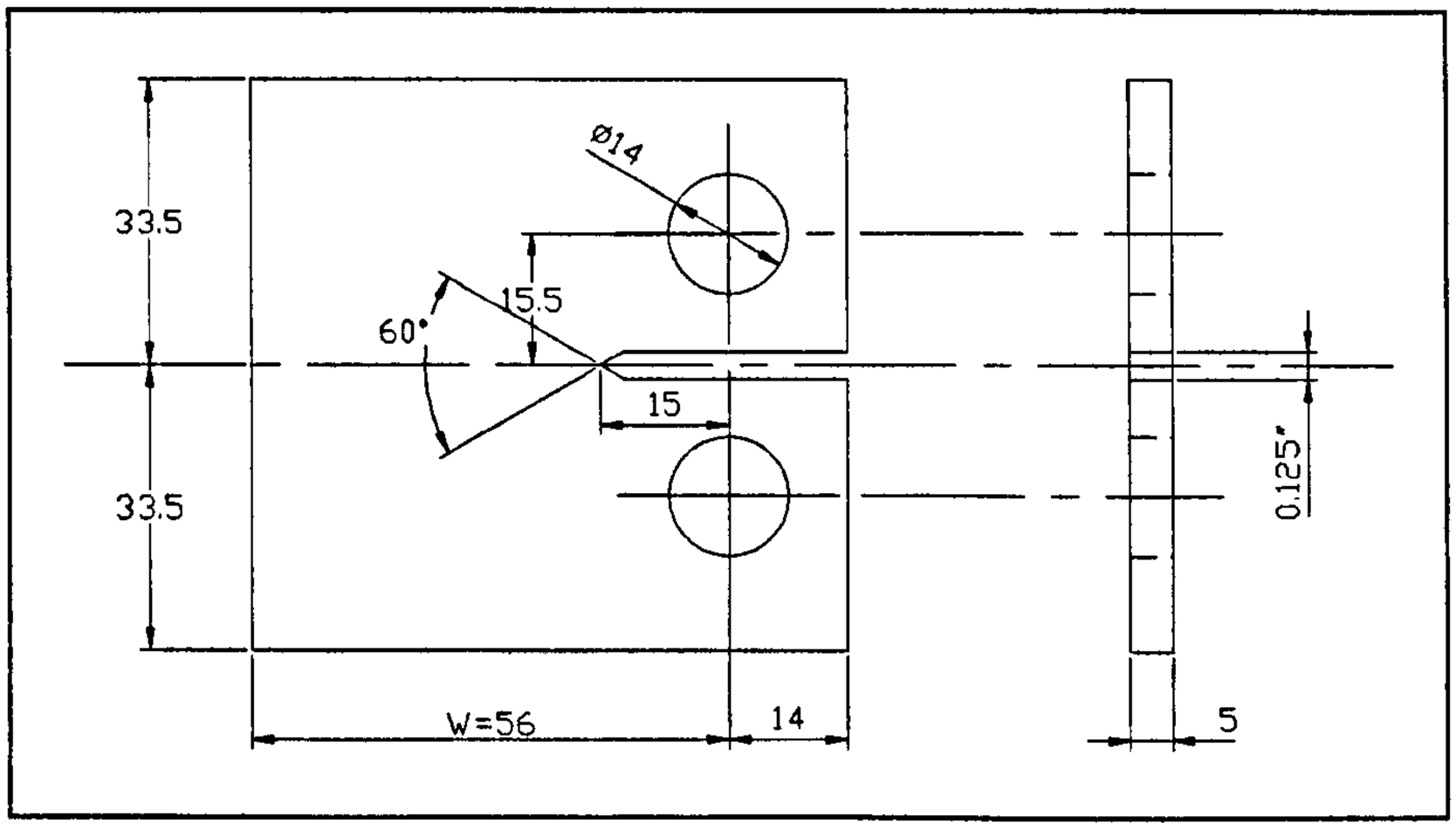

Figure 6.39: Compact tension specimen (all dimensions in mm, except for the notch width, inches, and angle, degrees).

Seven types of CT specimen were produced, enabling LCG rates to be determined in a comparable manner to those employed for the SCG measurements. The AA 5383-H321 parent plate specimens were manufactured with the direction of the notch being parallel (|-) and transverse (//) to the rolling direction (the |- and // relate to the rolling direction with respect to the applied loading to aid continuity throughout this dissertation). The specimens produced from the butt welds were designed to reproduce crack growth rates that would be representative of those for the appropriate welded structure, the notch being positioned where crack growth occurred in the four point load S-N tests (detailed in Section 5.5, S-N Test Results, page 266). MIG weld CT specimens, both LI and HI, were produced with the notch at the weld toe and running in the direction of the weld as shown in Figure 6.40 (the MIG LI specimens were from a comparable weld in AA 5083-H321 due to limitations on the amount of AA 5383-H321 material available). The centre of the notch was in alignment with the weld toe at the surface, before the plate was reduced in thickness to 5 mm, as the crack typically grew from the weld toe through the HAZ (i.e. perpendicular to the applied loading, rather than following the tapered shape of the weld metal). The FS welds also had the notch running in the direction of the weld, but it was positioned at the centre of the weld in the case of the SP specimens, whilst the DP specimens were produced with the notch at the edge of the friction band on both the

advancing (FS DPA) and retreating (FS DPR) sides (with respect to the 2nd pass), as shown in Figure 6.41.

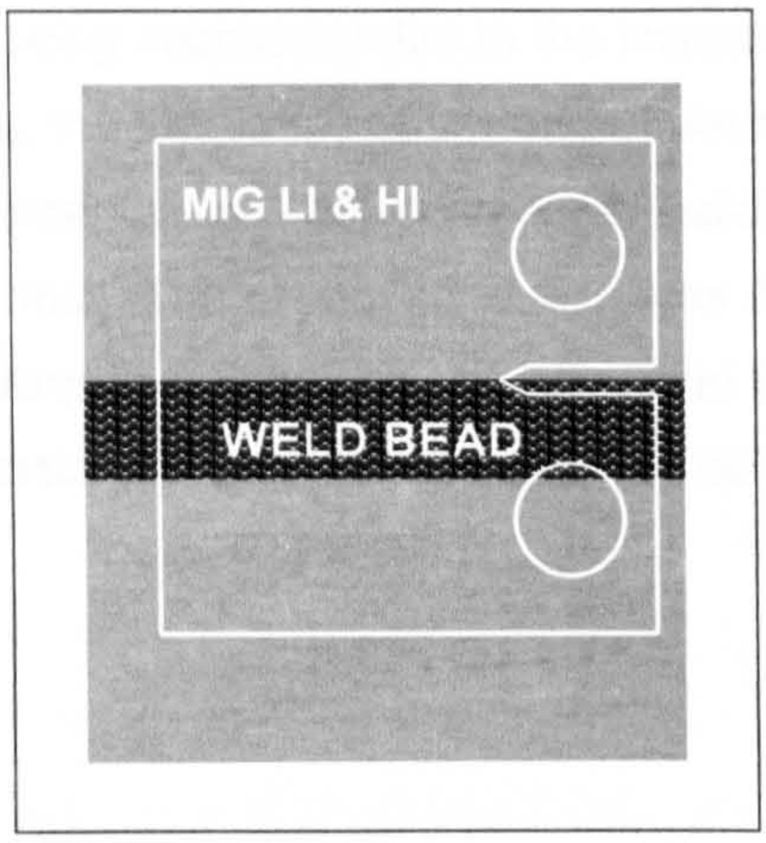

Figure 6.40: Position of CT specimens in relation to the MIG welds.

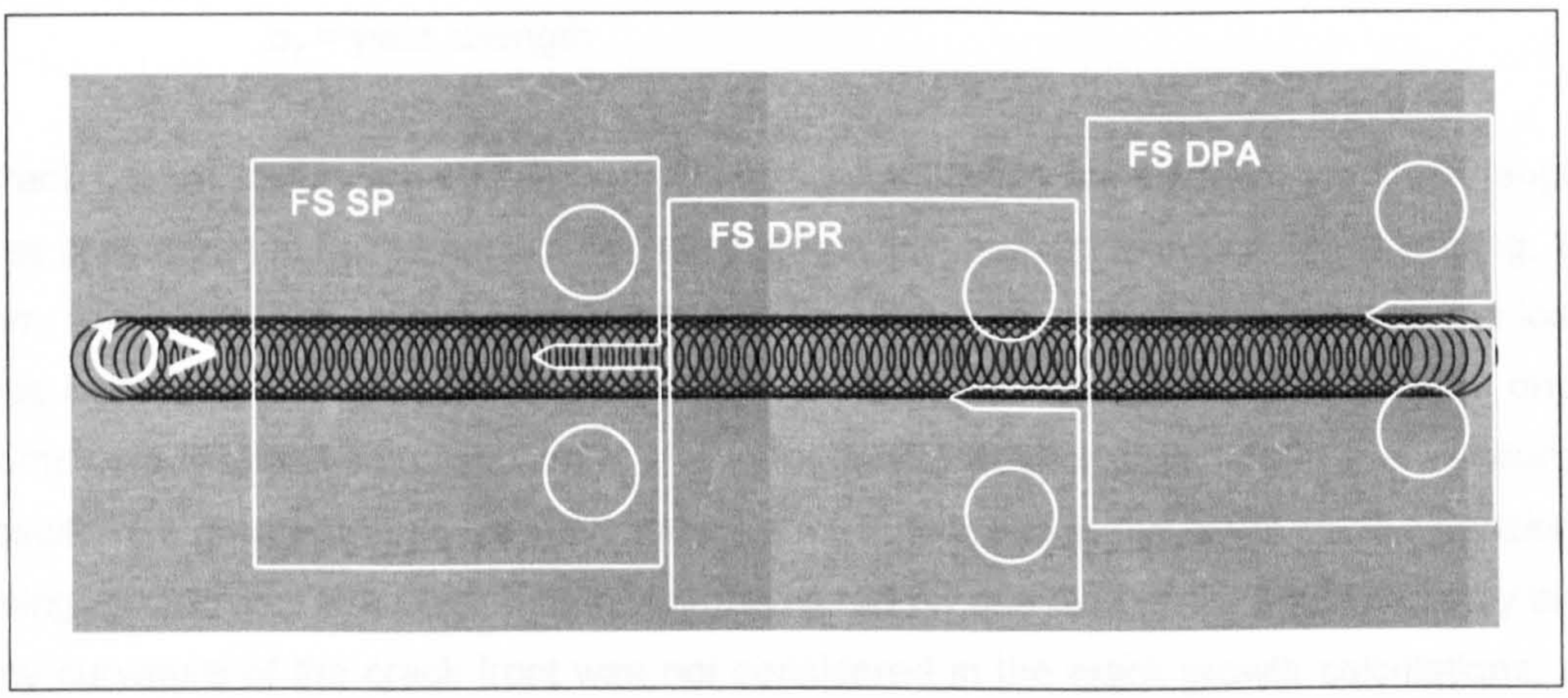

Figure 6.41: Position of CT specimens in relation to FS welds (friction band side for the single pass and second pass side for the double pass weld uppermost).

6.4.5 Long Crack Growth Tests

LCG rate measurements were made with reference to ASTM E 647[1]. Constant amplitude loading, with a sinusoidal loading response and R = 0.1, was undertaken on an Instron 8501 servo-hydraulic test frame, utilising an Instron 8800 controller and a ±10 KN load cell, the CT specimens being clamped as described in ASTM E 647. The tests were undertaken at room temperature and in laboratory air.

All specimens were pre-loaded with a compressive load equal in magnitude to the initial peak tensile load to aid crack initiation, subsequent pre-cracking was then undertaken

[1] ASTM (1995b)

with the load gradually being reduced until the desired initial value of ΔK had been attained. Testing was initially commenced at a frequency of 40 - 50Hz. This was gradually reduced throughout the test to ensure that the constant load amplitude was accurately maintained, this being necessary due to the increase in displacement resulting from the growth of the crack, the frequency at the end of each test typically being 10 - 15 Hz. Crack growth measurements were not considered valid until the plastic zone from prior loads had been breached. The plastic zone size was determined using Dugdale's equation[1], (6.14), this resulting in a greater zone size, and hence a more conservative value with respect to the tests being undertaken, than that determined through Irwin's equation[1].

$$\Delta a_n = 0.393\left(K_I/\sigma_y\right)^2 \tag{6.14}$$

where: Δa_n = plastic zone size

K_I = mode I stress intensity factor

σ_y = yield strength

Crack growth measurements were made using a travelling microscope, the crack length was considered to be the sum of the notch length with respect to the centre of loading, 15 mm, and any subsequent crack extension. To aid identification of the crack tip the load was increased to slightly below the peak load whilst the measurement was made, once completed the load was reduced to the mean load. Scatter observed in the measured results was greater at the commencement of each test due to the small crack extensions being measured. The crack length was measured on one side of the specimen only and any curvature of the crack front was not considered in the crack growth calculations, all the cracks followed a path that was within ±10° of the plane of symmetry. Two or three tests were undertaken with different initial values of ΔK, resulting in the crack growth rates overlapping, to enable the full crack growth rate spectrum to be determined.

ΔK was determined as described in ASTM E 647[1], it was assumed that the 60° notch tip would have minimal influence on the result:

$$\Delta K = \frac{\Delta P}{B\sqrt{W}}\frac{(2+\alpha)}{(1-\alpha)^{1.5}}\left(0.886+4.64\alpha-13.32\alpha^2+14.72\alpha^3-5.6\alpha^4\right) \tag{6.15}$$

where: $\Delta P = P_{max} - P_{min}$ for $R > 0$ ($\Delta P = P_{max}$ for $R \le 0$)

B = specimen thickness, 5 mm

$\alpha = a/W$ (valid for $a/W \ge 0.2$)

---

[1] Ewalds, HL; Wanhill, RJH (1984)

W = distance from load centreline to specimen edge, 56 mm (see Figure 6.39)

a = distance from load centreline to crack tip

For the (da/dN)/ΔK graphs the value for ΔK was calculated for the mid-crack length for the period of cycles, $(a_{i+1} + a_i)/2$, and the crack growth was determined utilising a simple secant method.

The Paris law regime, regime B, of the (da/dN)-ΔK graphs exhibited a point of inflexion, typically in the stress intensity factor range region of 8.5 - 10.0 MPa.$m^{0.5}$, a subsequent reduction in the growth rate was also evident after the point of inflexion. It was assumed that this was the result of the stress condition changing from predominantly plane strain to plane stress. As the measurements of the crack length were undertaken on the visible surface of the CT specimen, the curvature of the crack front not being considered in the crack growth-ΔK calculations, the crack growth may be considered to be the result of a plane stress condition, although during the initial growth period, typically ΔK < 10 MPa.$m^{0.5}$, the plane stress condition of the surface would be constrained to some extent by the predominantly plain strain condition within the specimen, hence the point of inflexion observed in the crack growth curves. Ewalds and Wanhill[1] state that primarily plane strain behaviour may be expected when the calculated size of the plane stress plastic zone diameter, according to Irwin's analysis, is less than 1/10 of the specimen thickness, as calculated by equation (6.17).

$$r_y = \frac{1}{2\pi}\left(K_I / \sigma_y\right)^2 \qquad (6.16)$$

$$K_{I_{Plane\ strain}} < \sigma_y \left(\pi t / 10\right)^{0.5} \qquad (6.17)$$

where: r_y = plastic zone radius.

K_I = mode 1 stress intensity factor.

σ_y = yield stress.

t = specimen thickness.

Power law crack growth rate curves were determined through a combination of visual inspection of the (da/dN)/ΔK data and computational analysis utilising TableCurve 2D V5.00 software. Details of the individual LCG specimen results are contained in Section 13, Appendix C ~ Crack Growth Results (pages 506 - 537).

---

[1] Ewalds, HL; Wanhill, RJH (1984)

6.4.6 Parent Plate

6.4.6.1 SCG S-N Testing

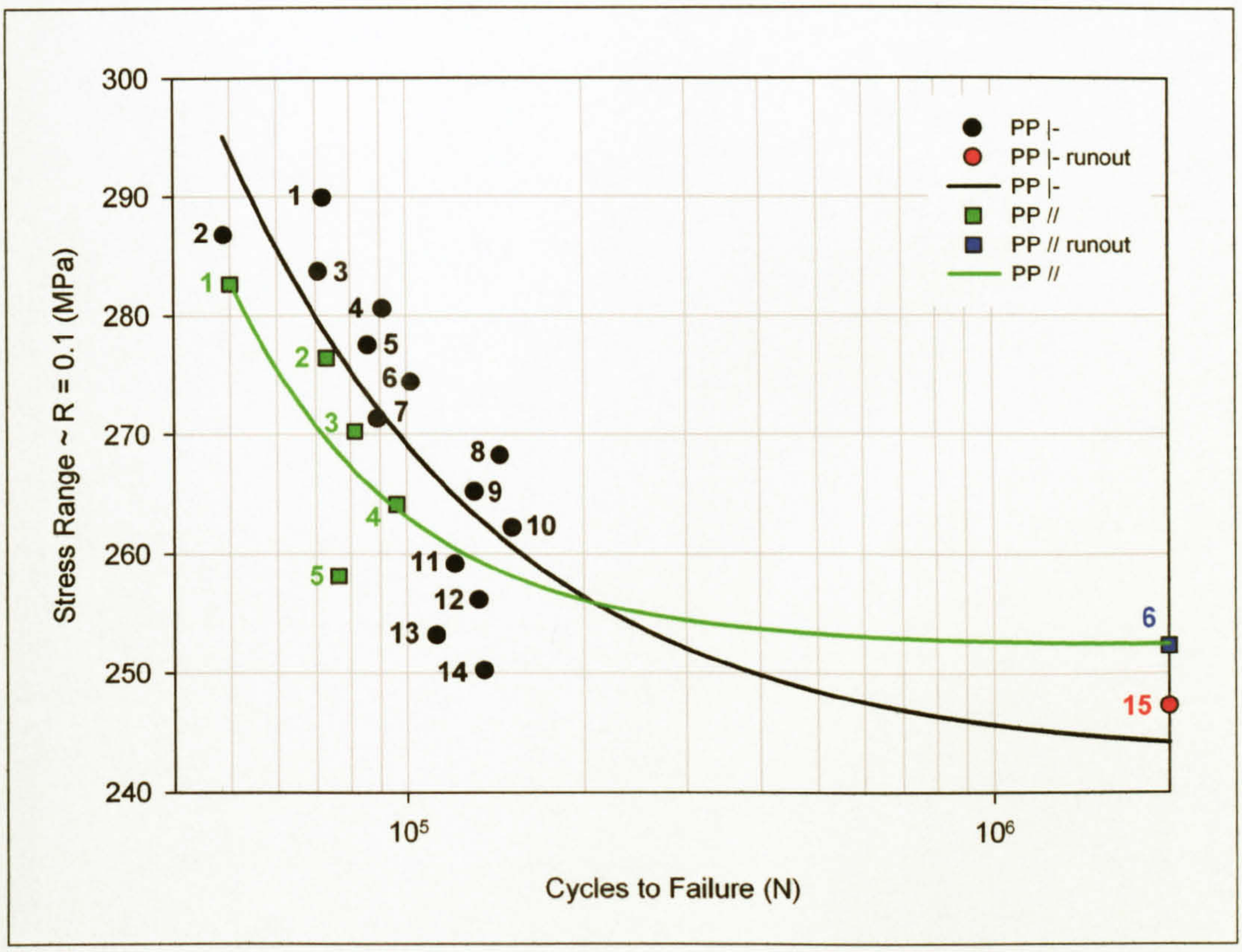

Figure 6.42: AA 5383-H321 parent plate SCG specimen S-N data (numbers refer to specimens detailed in Table 13.1, page 507, and Table 13.9, page 511).

Material	Fatigue Strength ~ Δσ (MPa)			
	Number of Cycles			
	10^5	2×10^5	10^6	2×10^6
PP |-	269.2	256.4	245.7	244.3
PP //	263.1	256.1	252.7	252.4

Table 6.5: Parent plate SCG specimen fatigue strengths (R = 0.1).

The S-N test results for AA 5383-H321 parent plate SCG specimens are shown in Figure 6.42 and Table 6.5, with the stress range representing that at the centre of the notch. The results show that the PP |- specimens had a greater fatigue strength than the PP // specimens for stress ranges above 256 MPa, although below this value the scenario is reversed. When comparing the results the relatively small number of specimens tested should be taken into consideration, although as the tests were specifically undertaken to determine suitable loads for producing short crack data up to a specific lifespan they were considered satisfactory.

6.4.6.1.1 SCG S-N Specimen Fractography

Crack initiation in the parent plate SCG specimens was typically associated with intermetallic phases as shown in Figure 6.43 to Figure 6.45. Due to the relatively homogenous nature of the microstructure of the parent material, with respect to thickness, it would be expected that any variations in initiation would be related to the applied stress field. The maximum stress is only experienced by the outer fibre when subjected to four point loading, whereas uniaxial tensile loading subjects the complete plane to the applied stress and subsequently internal initiation sites, as depicted in Figure 6.44 (right), are likely to be more prevalent.

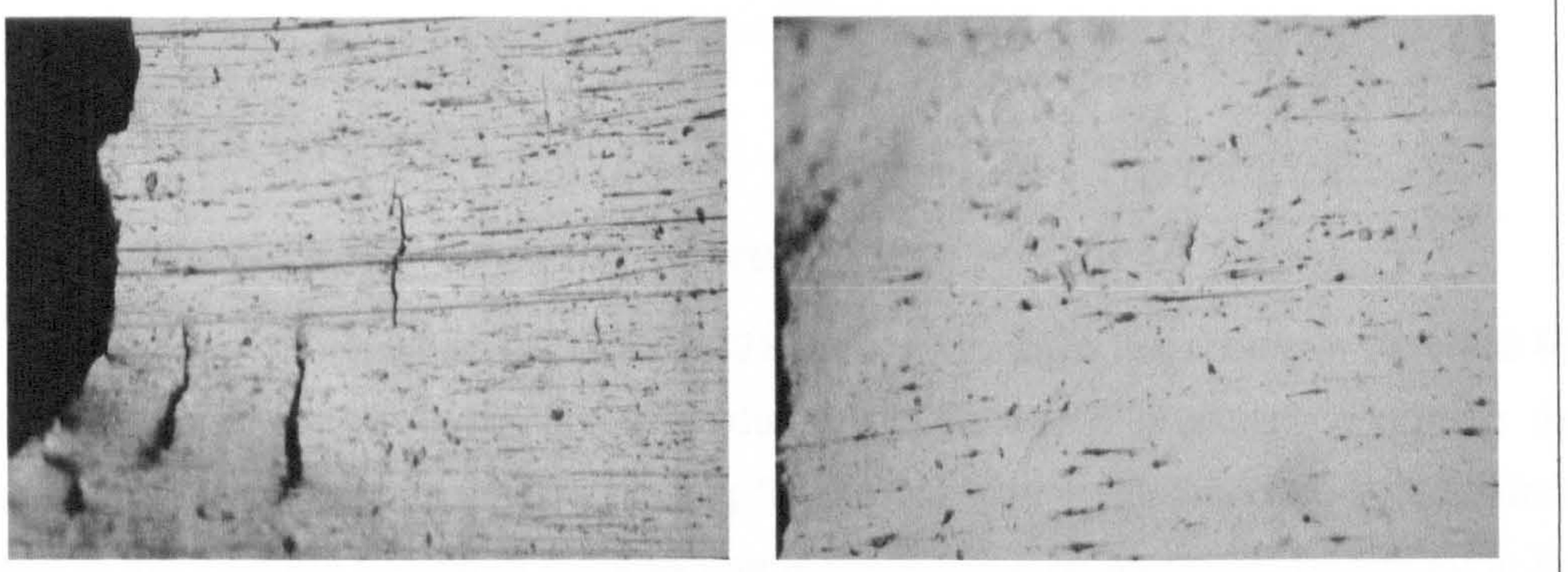

Figure 6.43: PP |- SCG 2 (left) and PP |- SCG 10 (right) fatigue cracks typically emanating from intermetallics.

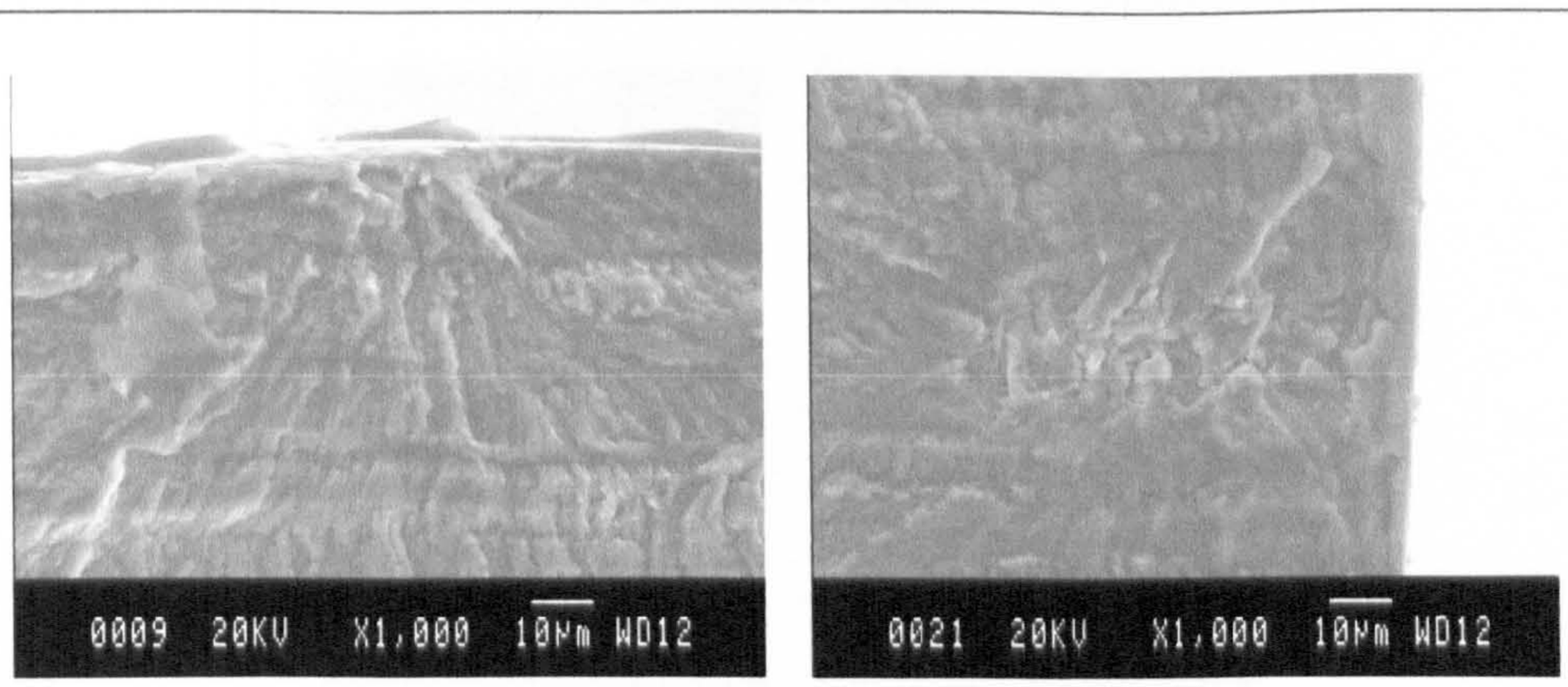

Figure 6.44: PP |- SCG 2 intermetallic induced crack initiation sites, notch surface (left) and subsurface initiated secondary edge crack (right).

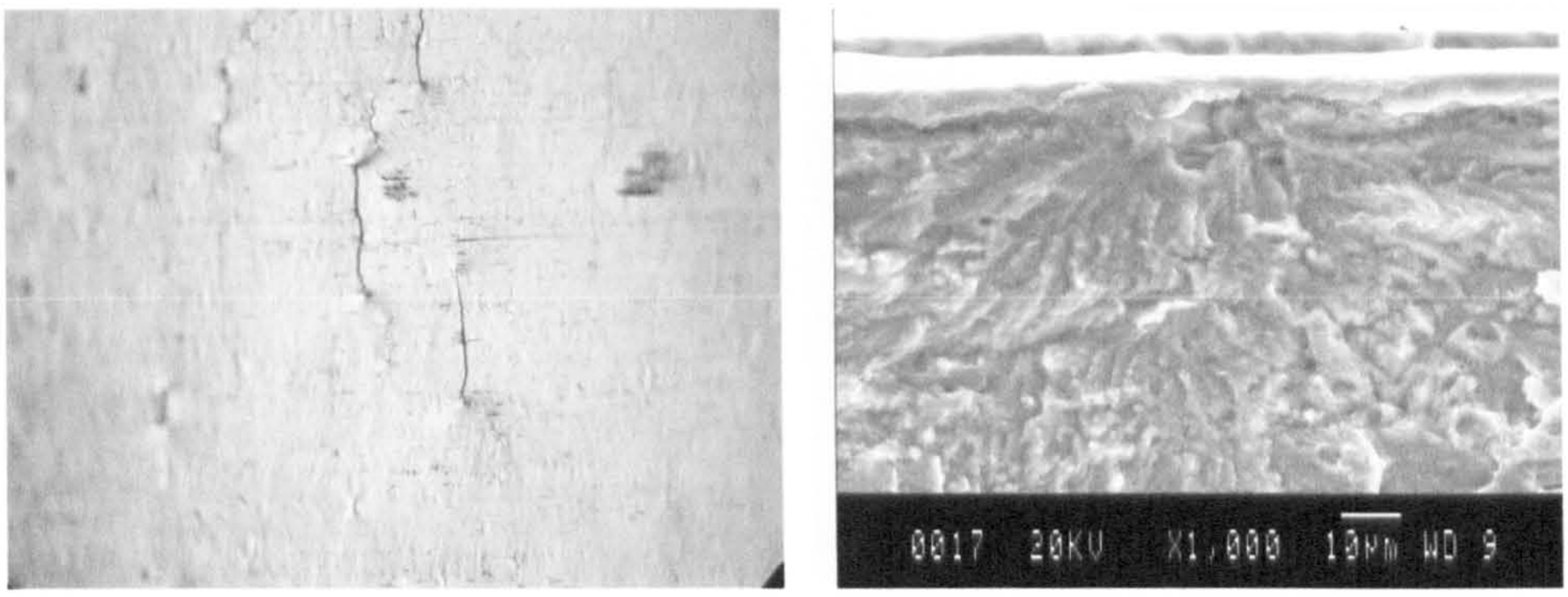

Figure 6.45: PP // SCG 1 intermetallic induced crack initiation sites.

6.4.6.2 Crack Growth

6.4.6.2.1 Short Crack Growth ~ Parent Plate |-

Crack initiation in the polished AA 5383-H321 PP |- specimens, as shown in Figure 6.46, Figure 6.47 and Figure 6.48, occurred due to intermetallic phases, confirming the observations seen in the four point loading S-N tests. Crack coalescence was evident, but due to the inherent design of the specimens crack initiation tended to be limited to the centre of the notch and therefore the number of initiation sites was reduced. Crack tortuousity, as shown in Figure 6.49, was more apparent at smaller crack lengths, typically below 50 µm.

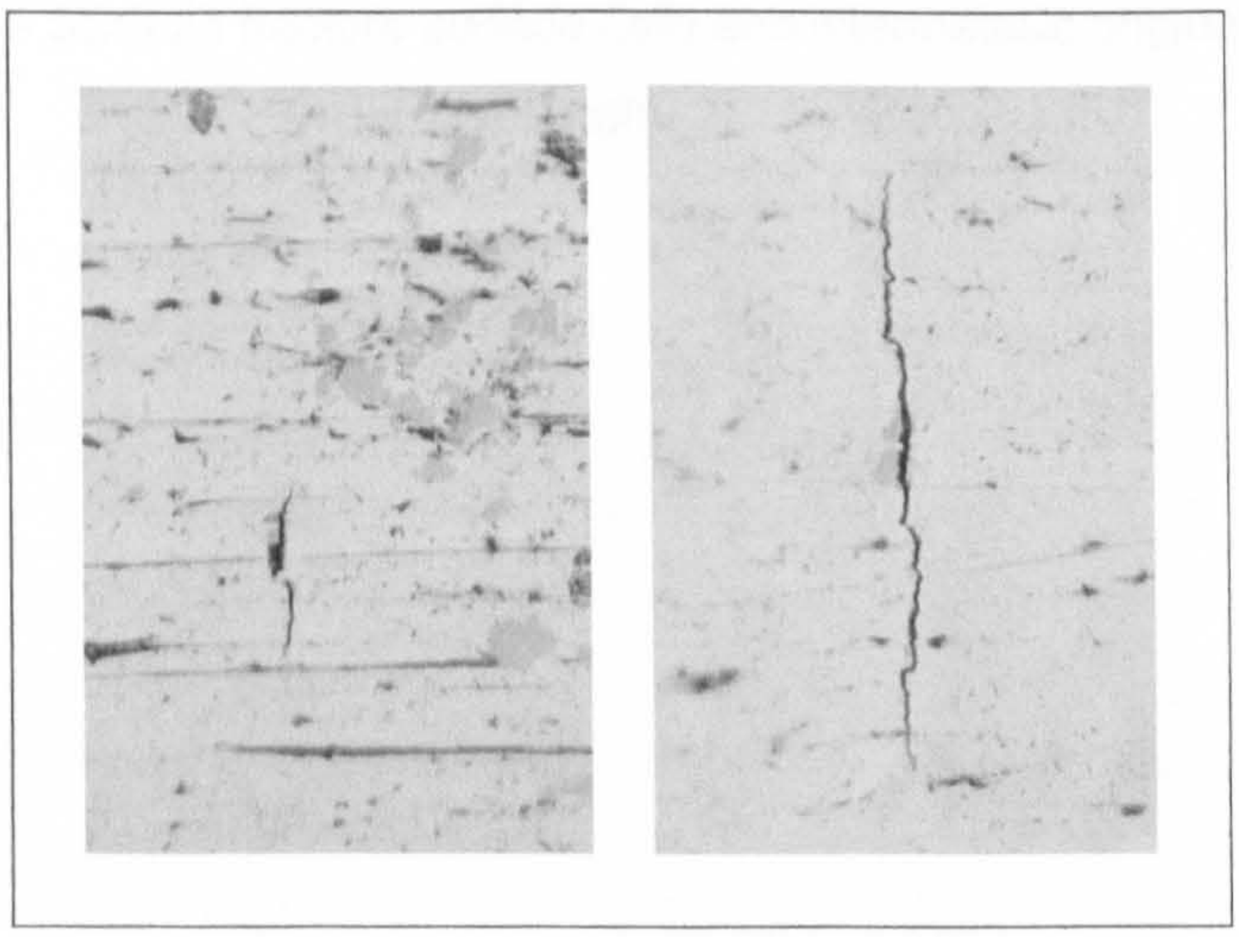

Figure 6.46: Optical micrographs of crack initiation from intermetallics PP |- SCG 21 (left) and PP |- SCG 23 (right).

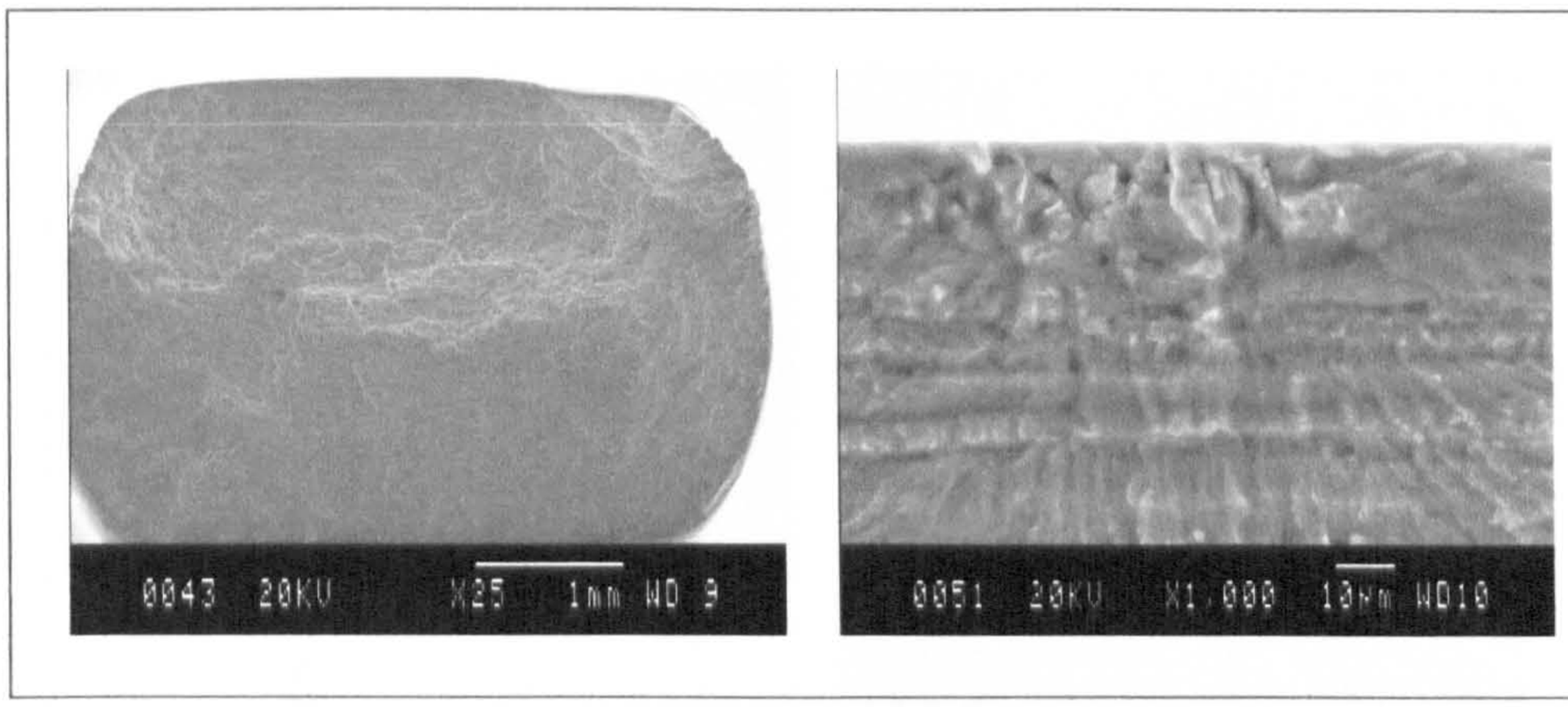

Figure 6.47: PP |- SCG 21 fracture surface (left) and intermetallic originated initiation site (right).

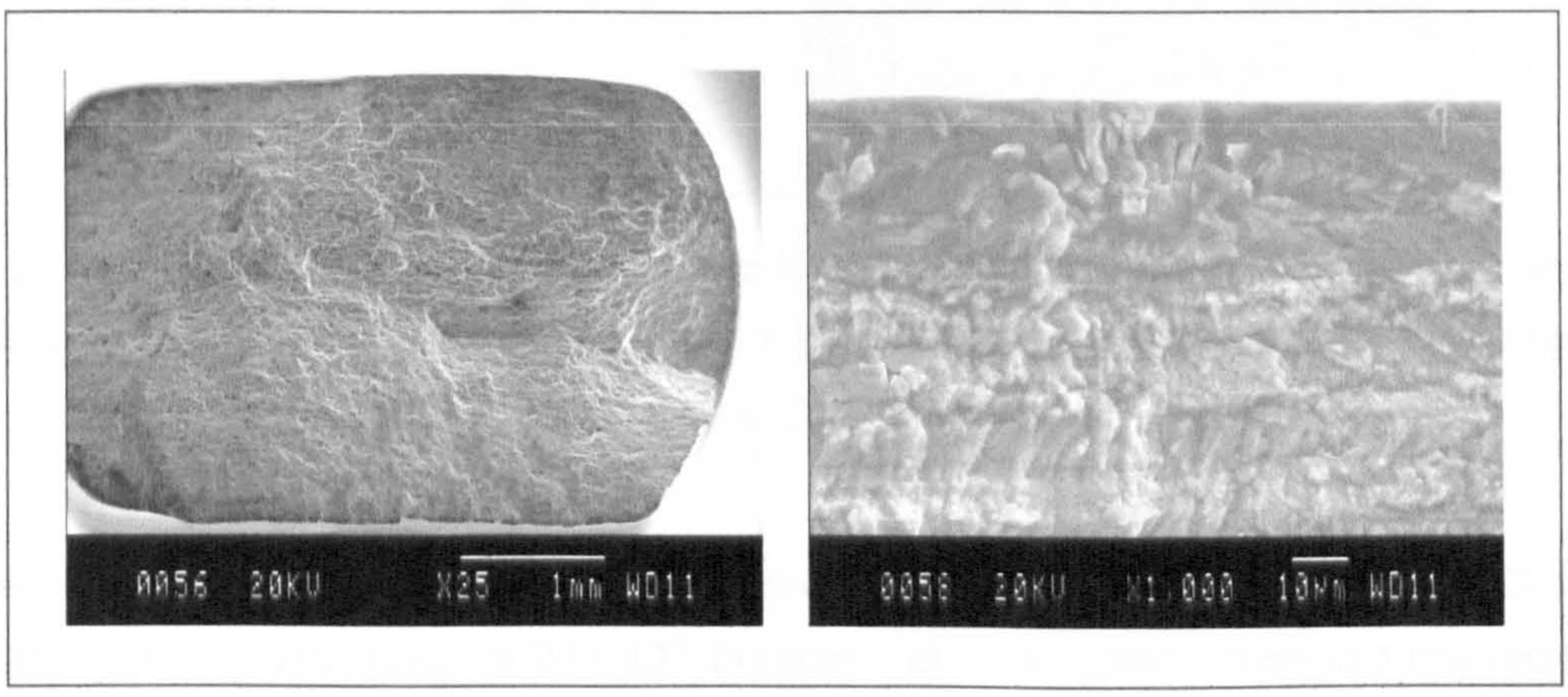

Figure 6.48: PP |- SCG 23 fracture surface (left) and intermetallic originated initiation site (right).

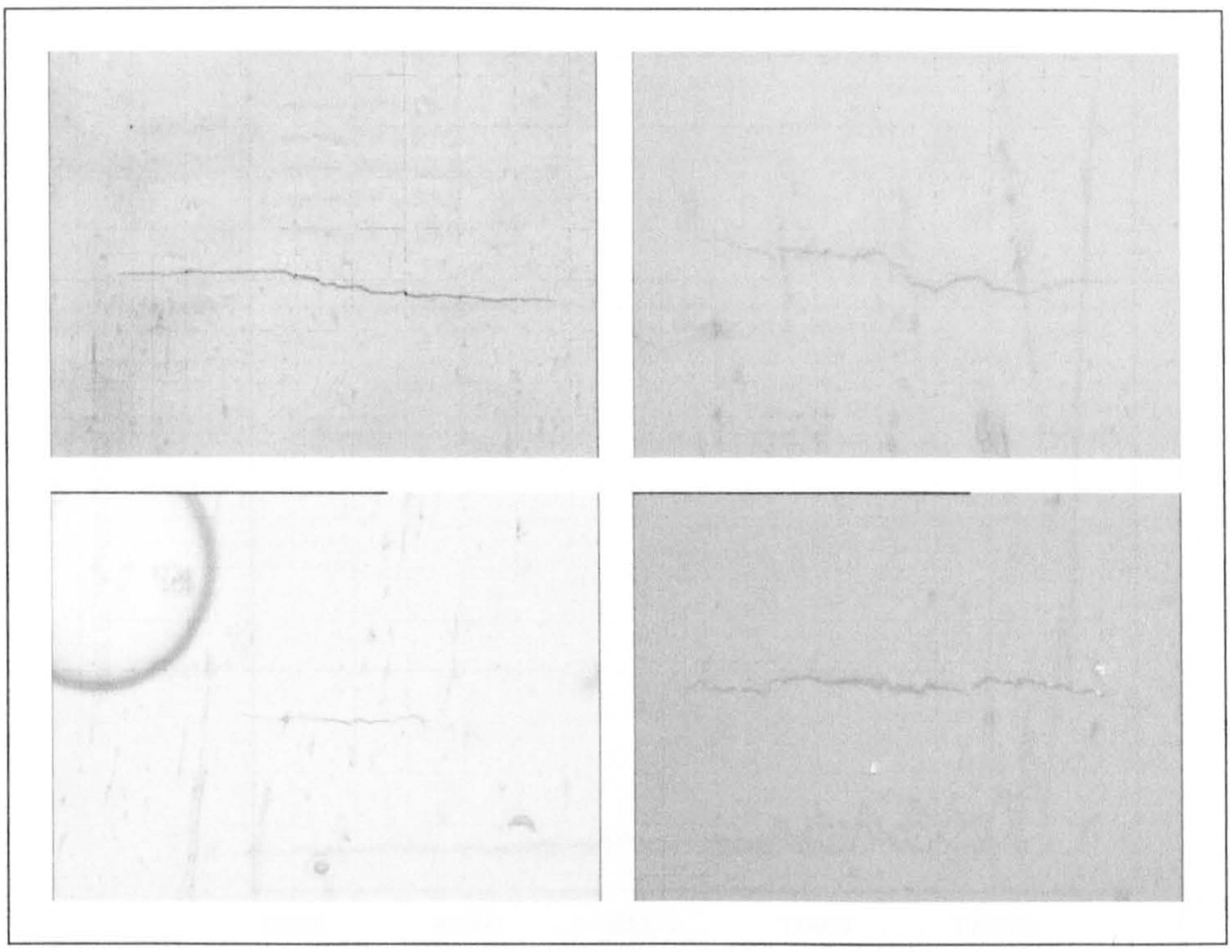

Figure 6.49: PP |- SCG replicas of 21.1 at 95000 cycles, 2c = 538 µm, (upper left) and 34000 cycles, 2c = 114 µm, (upper right), 23.1 at 48000 cycles, 2c = 144 µm, (lower right) and 23.2 at 99000 cycles, 2c = 123 µm, (lower right).

The variability in the crack growth rate evident in Figure 6.50 suggested that SCG was evident up to growth rates of 25×10^{-9} m.cycle^{-1}, at rates greater than this macrocrack growth was observed as the specimen approached failure. Reference to Figure 6.51 suggested this growth rate would be observed in short cracks with lengths, c, in the region of 300 - 400 µm, equating to 3 - 8 grains. The corresponding crack depth, a, for a crack of 300 - 400 µm length was 279 - 372 µm, utilising an aspect ratio of 0.929, this equated to 11 - 25 grains. From Figure 6.51 it was evident that there was a lot of variation in the SCG rates with respect to the crack length in the PP |- material, minimum rates of less than 10^{-10} m.cycle^{-1} being recorded at crack lengths below 100 µm, although the rates were typically within the range of a factor of ten. On the log-log scale shown in Figure 6.51 a linear relationship appeared evident for crack lengths of 90 - 400 µm, whereas the data shows more scatter below this level and appears to be approaching an asymptotic mean value of 10^{-9} m.cycle^{-1}.

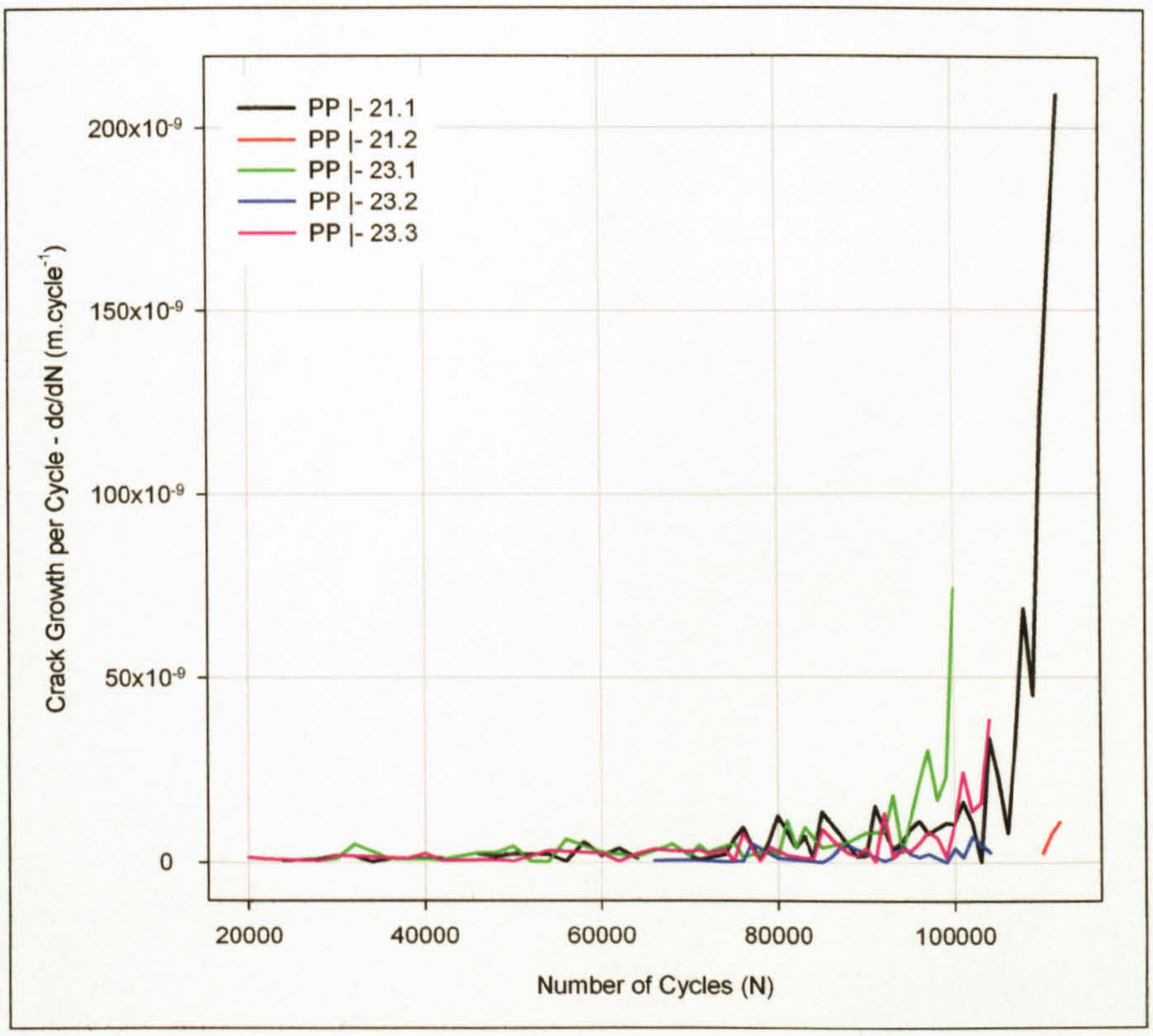

Figure 6.50: PP |- SCG data, crack growth per cycle/number of cycles.

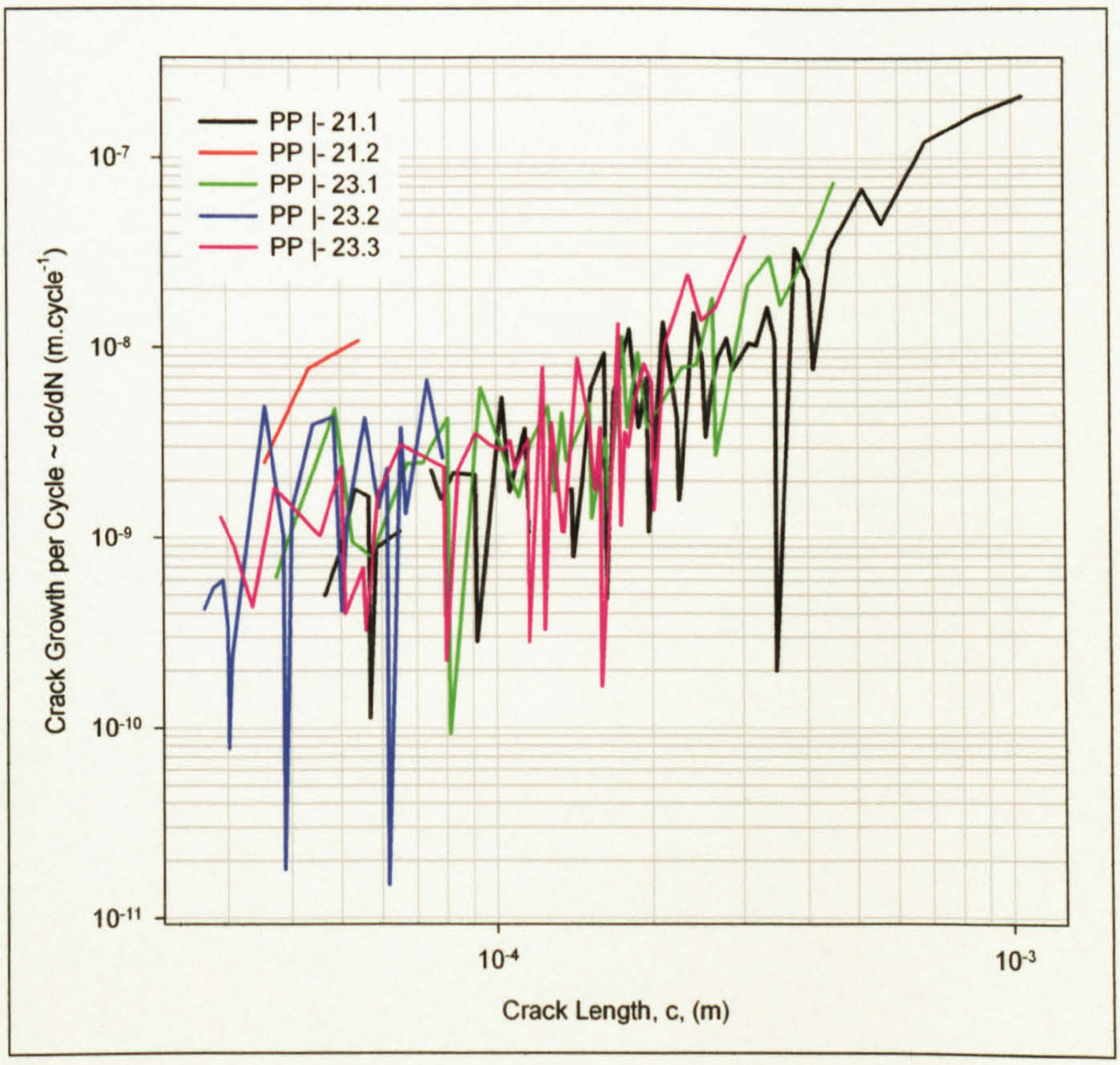

Figure 6.51: PP |- SCG data, crack growth per cycle/crack length.

6.4.6.2.2 Long Crack Growth ~ Parent Plate |-

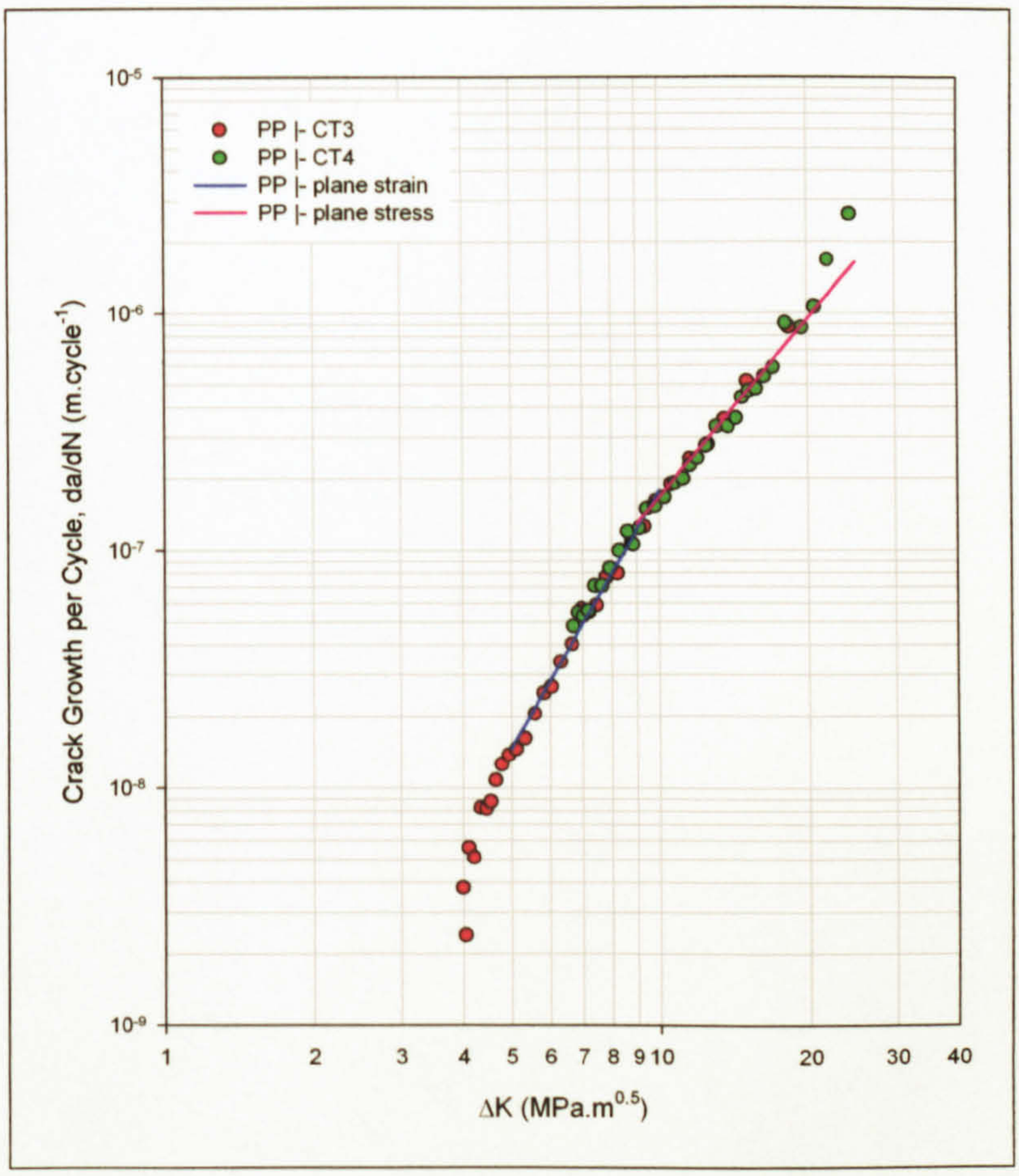

Figure 6.52: Fatigue crack growth rate (R = 0.1) ~ AA 5383-H321 parent plate loading transverse to the rolling direction.

ΔK_0 ($K_{max,0}$) (MPa.m$^{0.5}$)	Paris Equation $da/dN = C(\Delta K_{R=0.1})^m$				
	Plane strain $\Delta K \leq 9.5$		Calculated K_{max} for plane strain (6.17)	Plane stress $9.5 < \Delta K$	
	C	m		C	m
4.0 (4.4)	44.24×10^{-12}	3.604	9.6	541.80×10^{-12}	2.489

Table 6.6: Paris equation constants for fatigue crack growth in AA 5383-H321 parent plate with the rolling direction transverse to the applied load, PP|-.

From the results shown in Figure 6.52 it was evident that the crack growth diminished in the region of $\Delta K < 4.0$ MPa.m$^{0.5}$ ($K_{max,0} = 4.4$ MPa.m$^{0.5}$). A point of inflexion in the Paris law regime of crack growth was evident in the region of $\Delta K = 8.5 - 9.5$ MPa.m$^{0.5}$ resulting from the change in the stress state from predominantly plane strain to plane stress as the crack driving force increased. The observed value for the change in the stress state compared well to that calculated by equation (6.17), $\Delta K = 8.63$ MPa.m$^{0.5}$, and was accompanied by a small decrease in the propagation rate as plane stress predominated.

The Paris equations for the plane strain, (6.18), and plane stress, (6.19), regions of the regime B crack growth were as shown below.

$$\left(da/dN\right)_{\text{plane strain}} = 44.24 \times 10^{-12} \times (\Delta K)^{3.604} \quad (6.18)$$

$$\left(da/dN\right)_{\text{plane stress}} = 541.80 \times 10^{-12} \times (\Delta K)^{2.489} \quad (6.19)$$

6.4.6.2.3 Short Crack Growth ~ Parent Plate //

As with the PP |- SCG specimens the PP // specimens exhibited crack initiation from intermetallic phases as shown in Figure 6.53. Coalescence of cracks was more apparent than on the PP |- specimens, although crack tortuousity appeared less so, except that related to the local crack tip stress field prior to coalescence, as shown in Figure 6.55 and Figure 6.55.

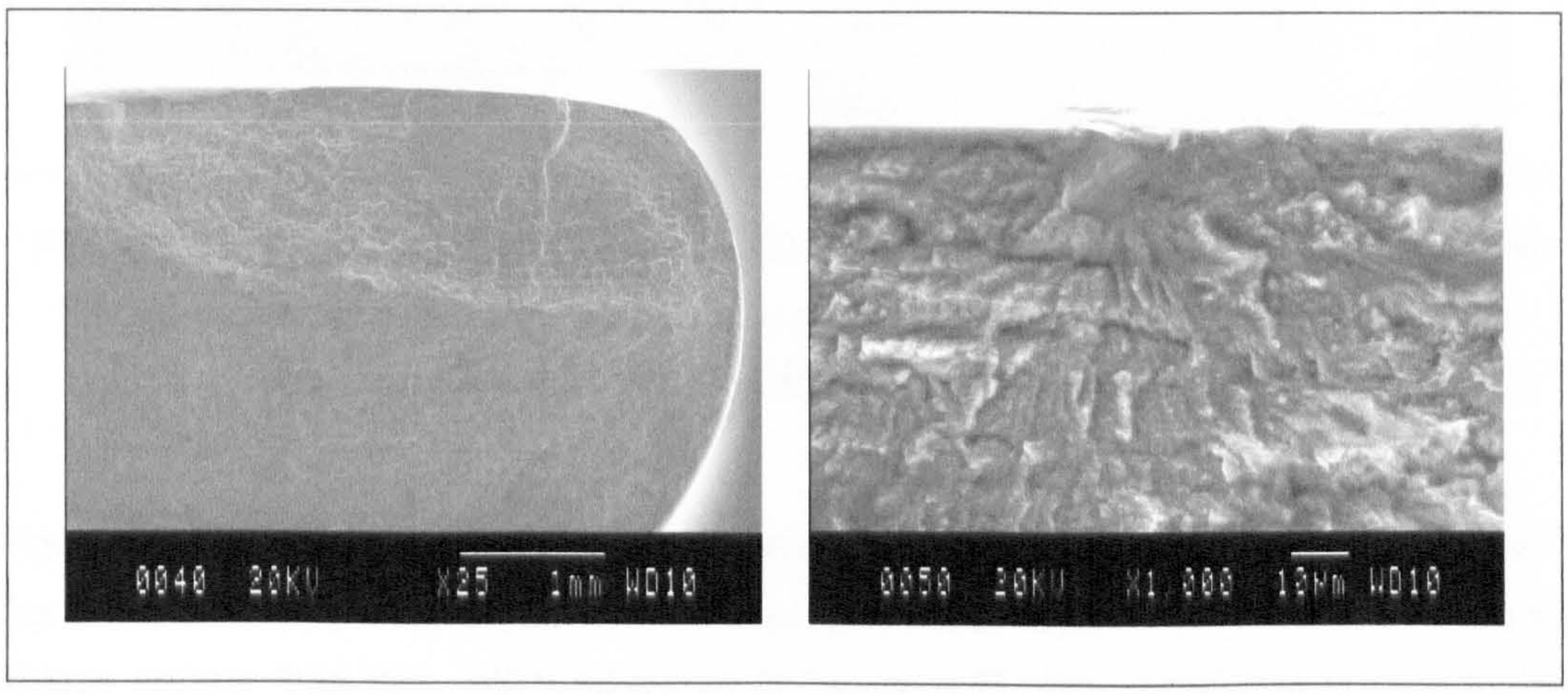

Figure 6.53: PP // SCG 8 fracture surface (left) and intermetallic originated initiation site (right).

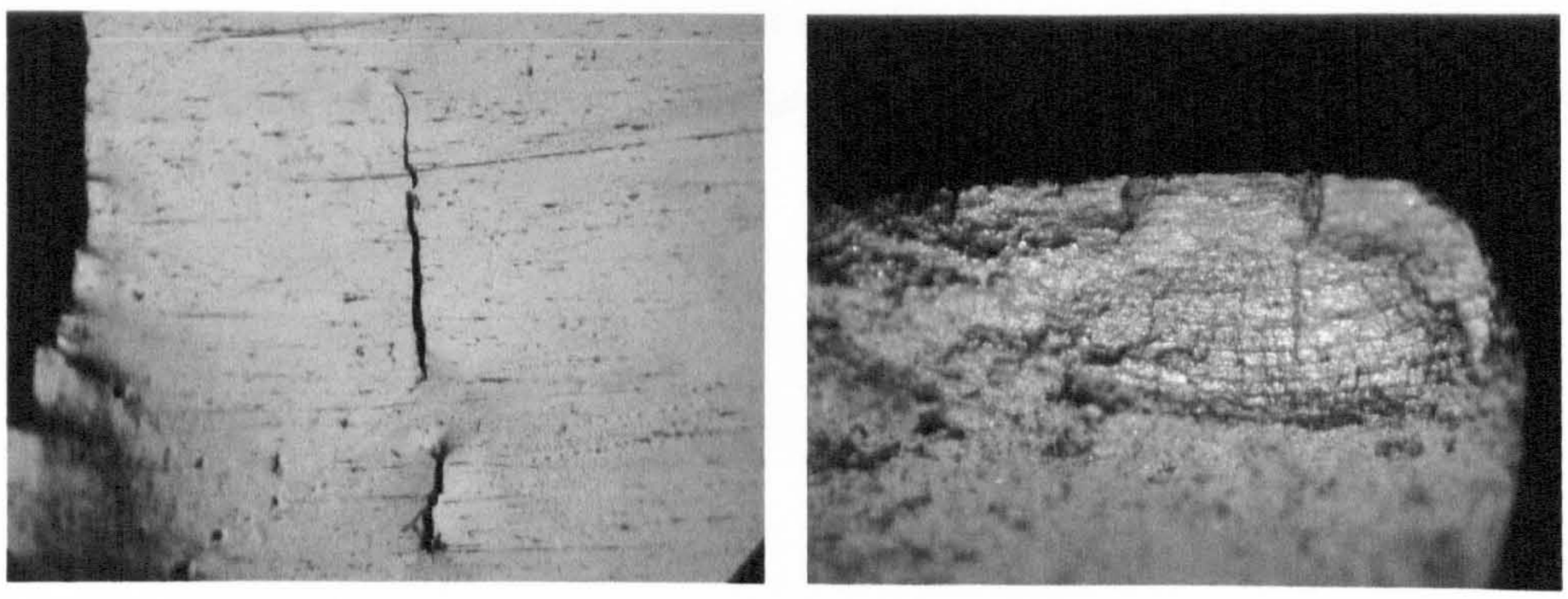

Figure 6.54: PP // SCG 8 optical micrographs of secondary cracks and the fracture surface of the main crack.

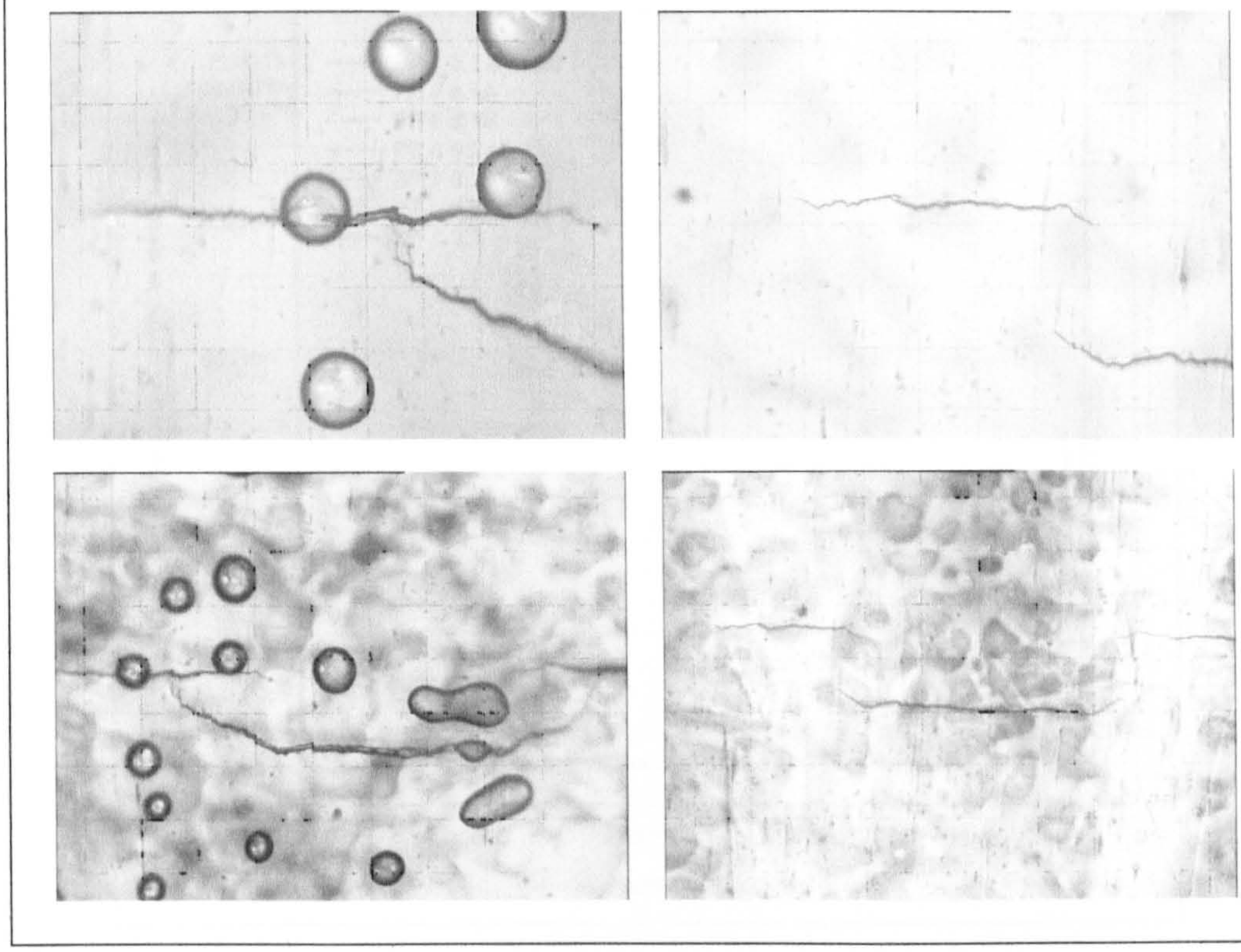

Figure 6.55: PP // SCG 8.2 replicas at 112000 cycles, 2c = 602 µm, (upper left) and at 108000 cycles, 2c = 391 µm, (upper right) and 8.3 at 112000 cycles, 2c = 1096 µm, (lower left) and at 108000 cycles, 2c = 716 µm, (lower right).

Figure 6.56 suggested that SCG occurred at crack growth rates below 15×10^{-9} m.cycle^{-1}, the onset of a rapid rise in growth rate, leading to catastrophic failure, being evident for values greater than this. With reference to Figure 6.57, this magnitude of growth rate would represent a crack length, c, in the region of 300 µm, approximately 5 - 10 grains. The corresponding crack depth, a, was 233 µm, 9 - 16 grains, when an aspect ratio of 0.777 was employed. Figure 6.57 exhibited significant variability in the growth rate when plotted against the crack length, the range typically being within a factor of ten, although on the log-log scale employed the general trend suggested a linear relationship for a crack length range of 50 - 300 µm. For crack lengths in the region of 10 - 50 µm a reduction in this slope was apparent.

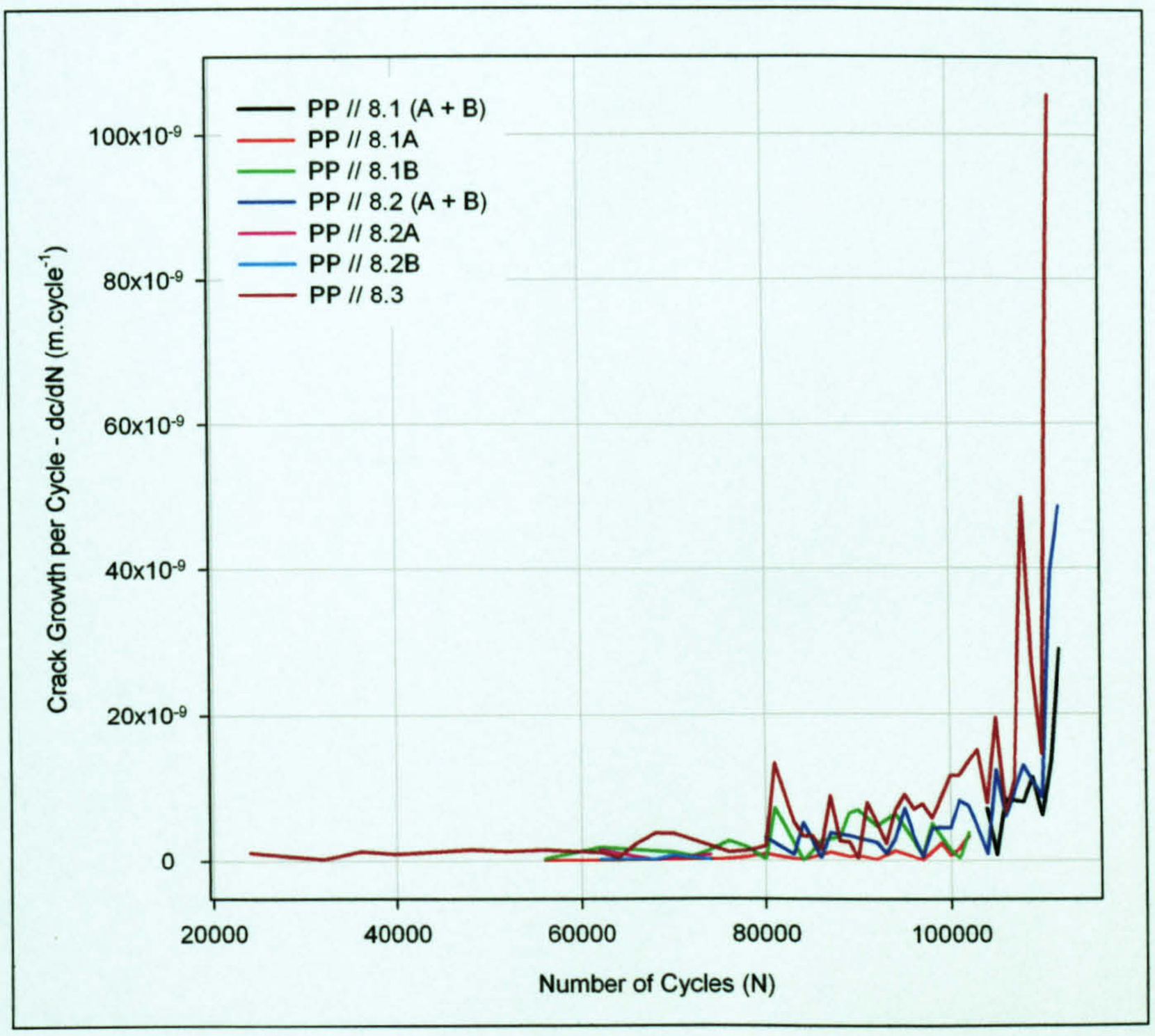

Figure 6.56: PP // SCG data, crack growth per cycle/number of cycles.

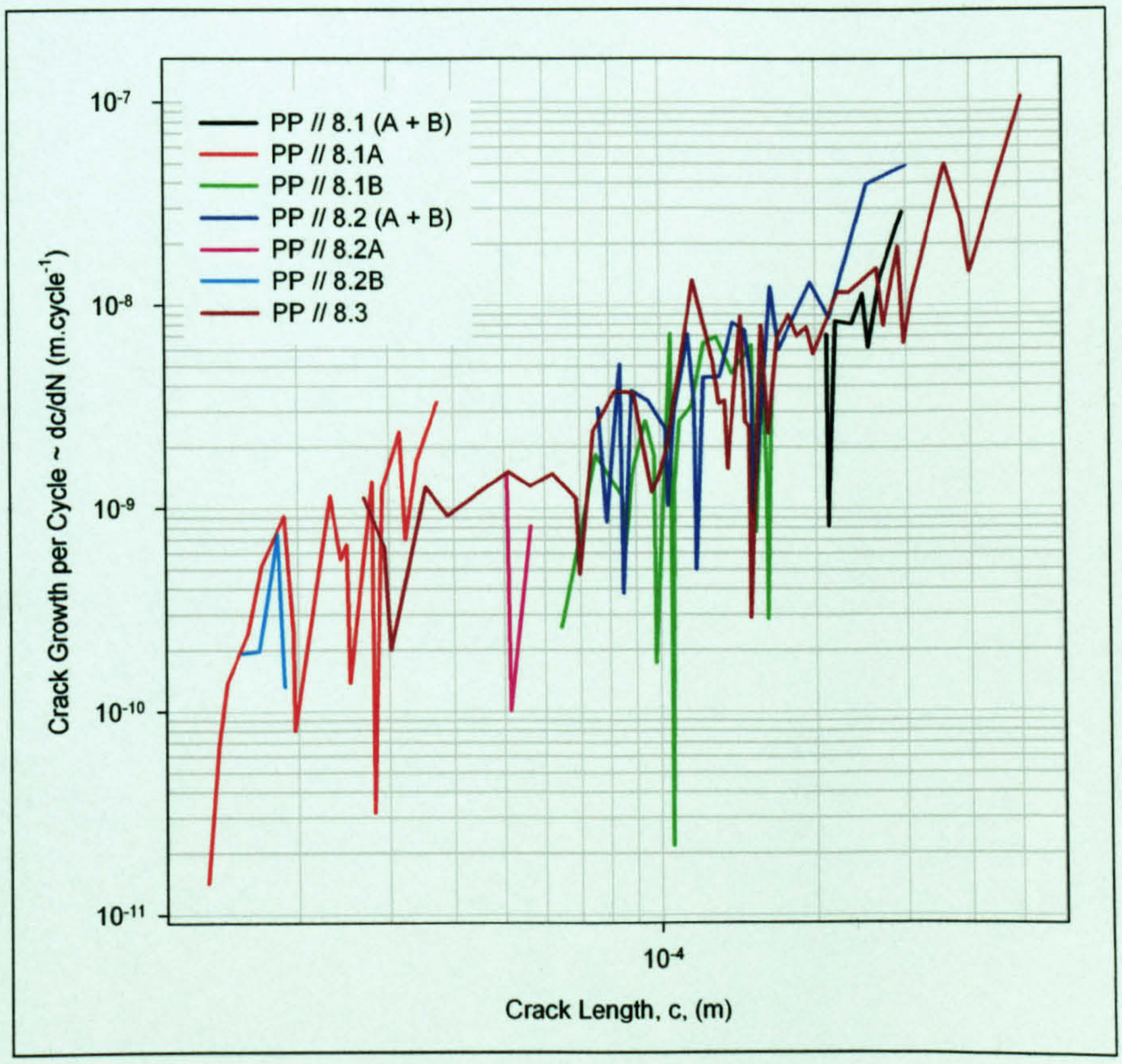

Figure 6.57: PP // SCG data, crack growth per cycle/crack length.

6.4.6.2.4 Long Crack Growth ~ Parent Plate //

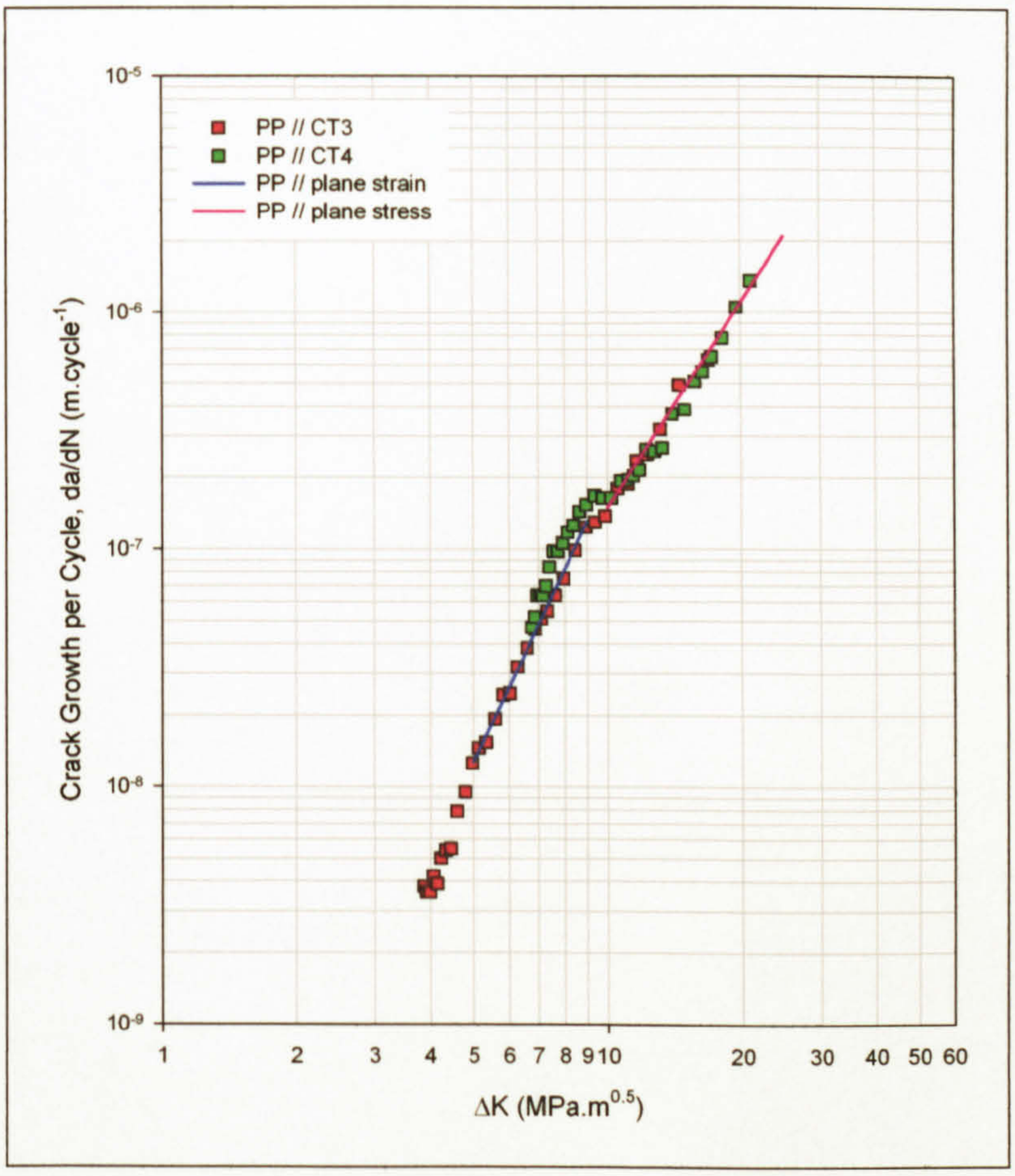

Figure 6.58: Fatigue crack growth rate (R = 0.1) ~ AA 5383-H321 parent plate loading parallel to the rolling direction.

ΔK_0 ($K_{max,0}$) (MPa.m$^{0.5}$)	Paris Equation $da/dN = C(\Delta K_{R=0.1})^m$				
	Plane strain $\Delta K \leq 9.5$		Calculated K_{max} for plane strain (6.17)	Plane stress $9.5 < \Delta K$	
	C	m		C	m
3.9 (4.3)	21.41 x 10^{-12}	3.968	10.6	198.72 x 10^{-12}	2.877

Table 6.7: Paris equation constants for fatigue crack growth in AA 5383-H321 parent plate with the rolling direction parallel to the applied load, PP //.

In contrast to the results obtained for PP |- the threshold stress intensity factor was more difficult to ascertain for the PP // specimens, with crack growth frequently arresting whilst the crack driving force was being reduced during pre-cracking. The minimum stress intensity factor range that crack growth was observed at was 3.9 MPa.m$^{0.5}$, as shown in Figure 6.58. A reduction in the crack growth rate was observed as the change from predominantly plane strain to plane stress occurred, this was evident as a point of inflexion in the Paris law region of crack growth at $\Delta K = 9 - 10$ MPa.m$^{0.5}$, comparing well

to the value returned by equation (6.17), $\Delta K = 9.54$ MPa.m$^{0.5}$. The Paris law constants for the plane strain, (6.20), and those for the plane stress, (6.21), regimes are shown below.

$$\left(da/dN\right)_{\text{plane strain}} = 21.41\times10^{-12}\times(\Delta K)^{3.968} \tag{6.20}$$

$$\left(da/dN\right)_{\text{plane stress}} = 198.72\times10^{-12}\times(\Delta K)^{2.877} \tag{6.21}$$

6.4.7 Metal Inert Gas Welds

6.4.7.1 SCG S-N Testing

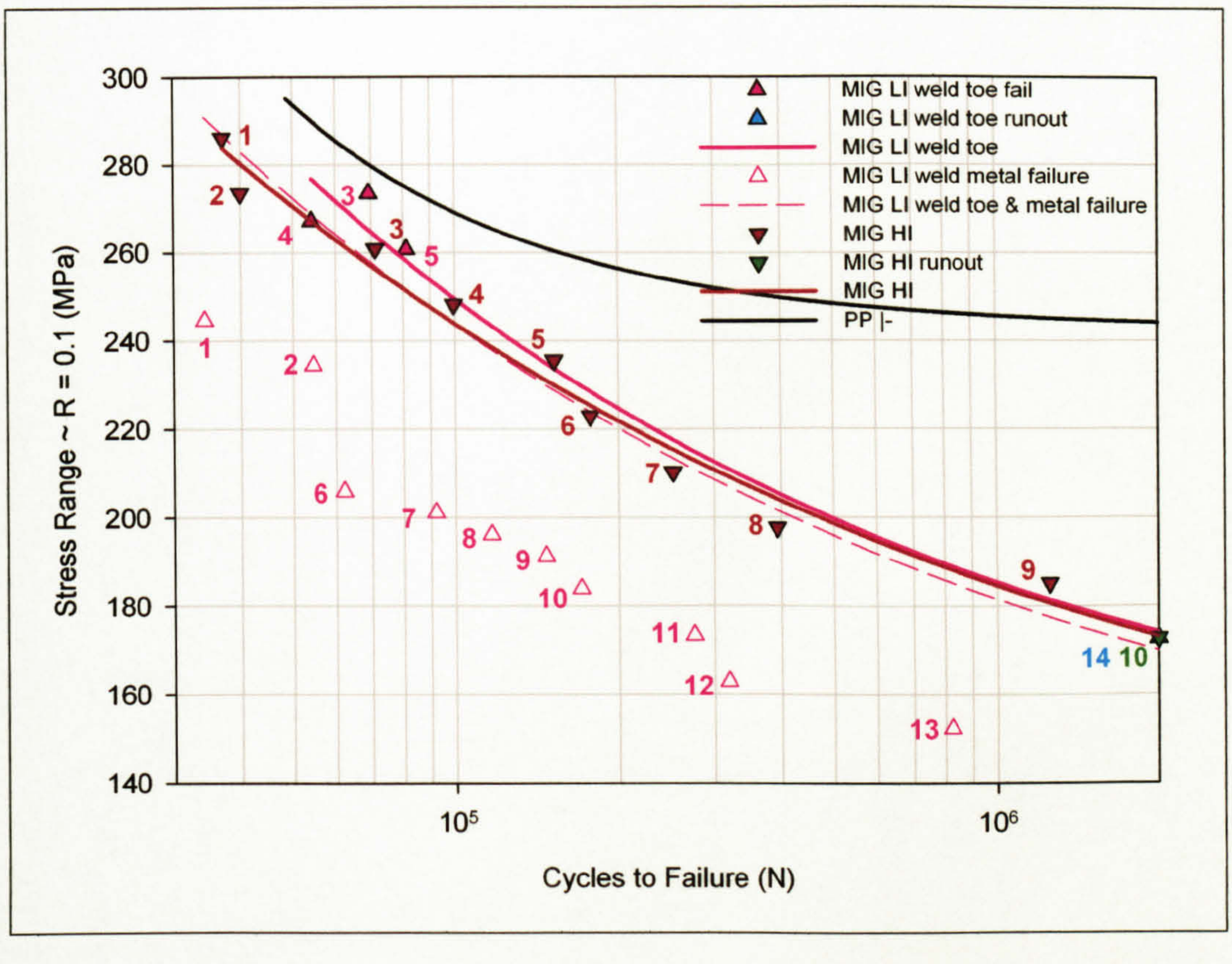

Figure 6.59: MIG SCG specimen S-N data (numbers refer to specimens in Table 13.19, page 515, and Table 13.31, page 520).

Material	Fatigue Strength ~ Δσ (MPa)			
	Number of Cycles			
	10^5	2×10^5	10^6	2×10^6
MIG LI (weld toe failure)	249.4	224.7	185.4	174.2
MIG LI (weld toe and metal failure)	243.5	220.1	181.6	169.9
MIG HI	243.8	221.8	184.7	173.2
PP |-	269.2	256.4	245.7	244.3

Table 6.8: MIG LI and HI SCG specimen fatigue strengths (R = 0.1).

Figure 6.59 details the S-N test results for the MIG welds, with the weld toe being positioned at the centre of the notch. The stress range represents the stress at the centre of the notch for all the MIG HI specimens and for MIG LI specimens 3, 4, 5 and 14. For the MIG LI specimens that failed in the weld metal the stress range is considered to be that applied to the parallel sided cylindrical section of the specimen that adjoined the notch. The MIG LI weld toe & metal failure, represented by the dashed line in Figure

6.59, signifies the stress range experienced at the centre of the notch for all the LI specimens that failed in the weld metal and the LI runout specimen.

Due to the high proportion of the LI specimens that failed in the weld metal, rather than the at the weld toe, the S-N curve representing the weld toe failures was constructed from only four points. If the stress experienced at the weld toe for the specimens that failed in the weld metal was considered then it would be expected that this would lie slightly below the curve representing the fatigue strength for the weld toe failures as the stress at the centre of the notch was obviously not great enough to cause failure and this was apparent from the results shown in Figure 6.59 and Table 6.8. It was also apparent from the results that the LI and HI weld SCG specimens had similar fatigue strengths for $\Delta\sigma <$ 200 MPa, whilst for stress ranges greater than this the LI weld had a superior fatigue lifespan, with this increasing as $\Delta\sigma$ increased; for $N = 10^5$ cycles the LI weld exhibited a 2% increase in fatigue strength over the HI weld.

6.4.7.1.1 SCG S-N Specimen Fractography

The MIG LI and HI SCG specimens that failed at the weld toe, the centre of the notch, exhibited intermetallic induced crack initiation as shown in Figure 6.60 and Figure 6.63. This was in contrast to four point loading welded specimens that typically exhibited crack initiation at the weld toe, but the cause was generally associated with porosity or analogous welding flaws. The change in the cause of initiation was probably the result of the notch surface being situated within the HAZ, rather than at the weld toe, due to the machining of the SCG specimens, subsequently the centre of the notch would be free of porosity or other welding artefacts. The LI specimens frequently failed in the weld metal due to porosity as shown in Figure 6.61 and Figure 6.62, this phenomenon tended to be more prevalent at lower stress ranges, this also being noticed in specimens that were used for SCG replication.

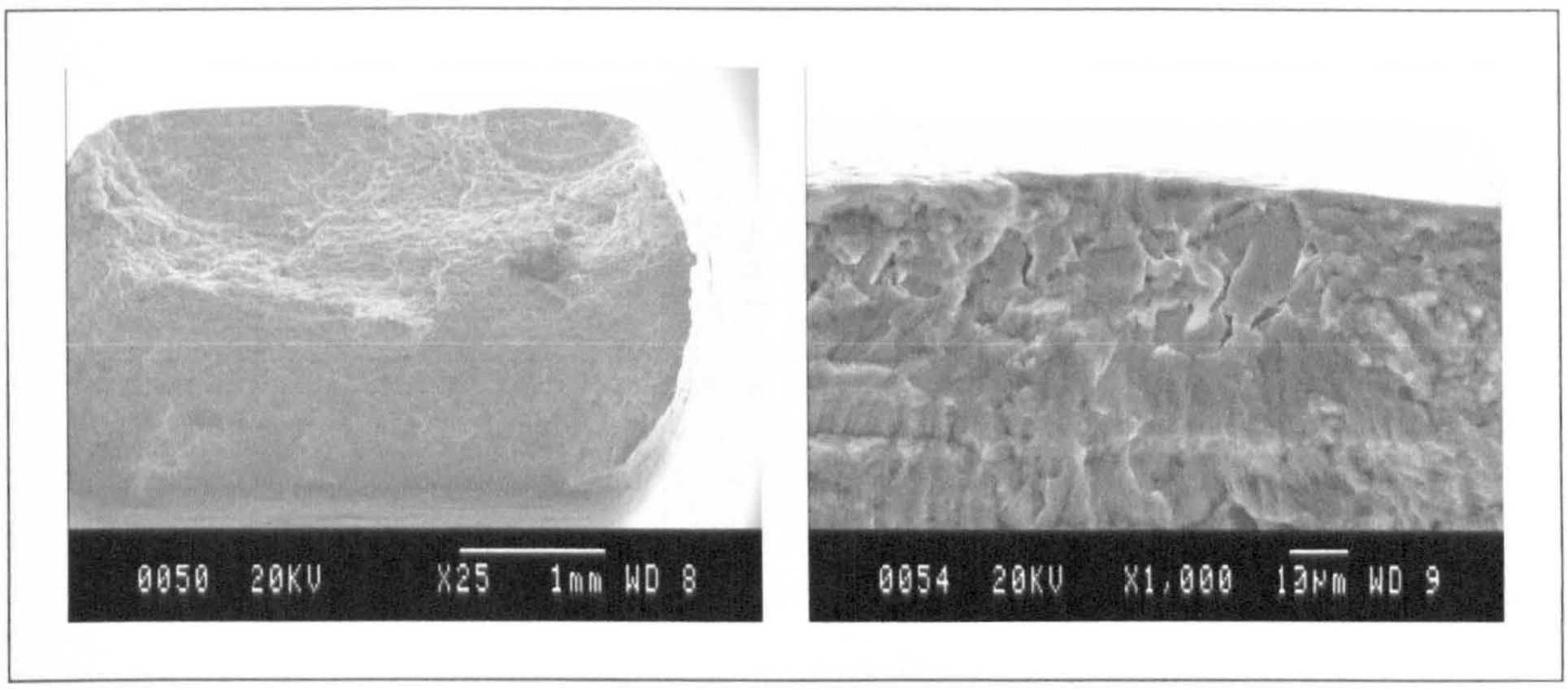

Figure 6.60: MIG LI SCG 4 weld toe fatigue crack fracture surfaces (left) and intermetallic induced initiation site (right).

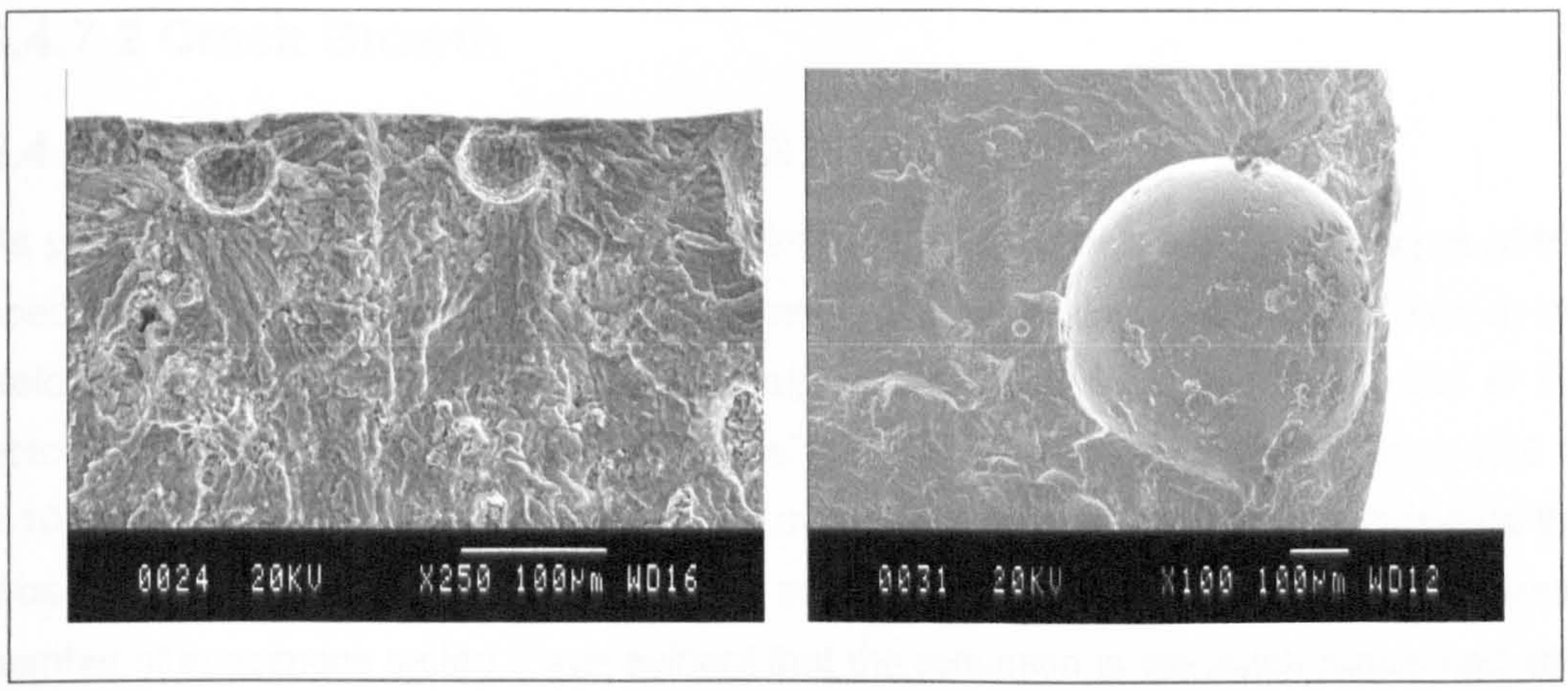

Figure 6.61: MIG LI SCG 1 (left) and 16 (right) porosity initiated weld metal fatigue cracks.

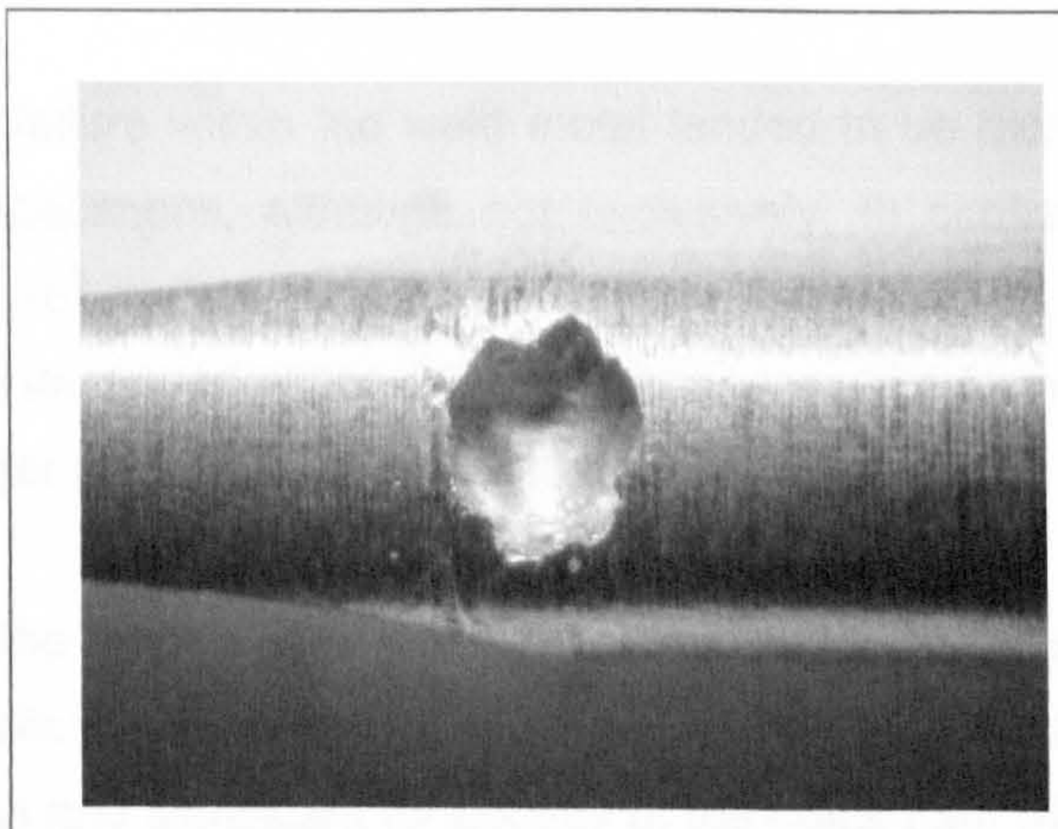

Figure 6.62: Porosity in a MIG LI SCG specimen, the notch is to the left of the pore.

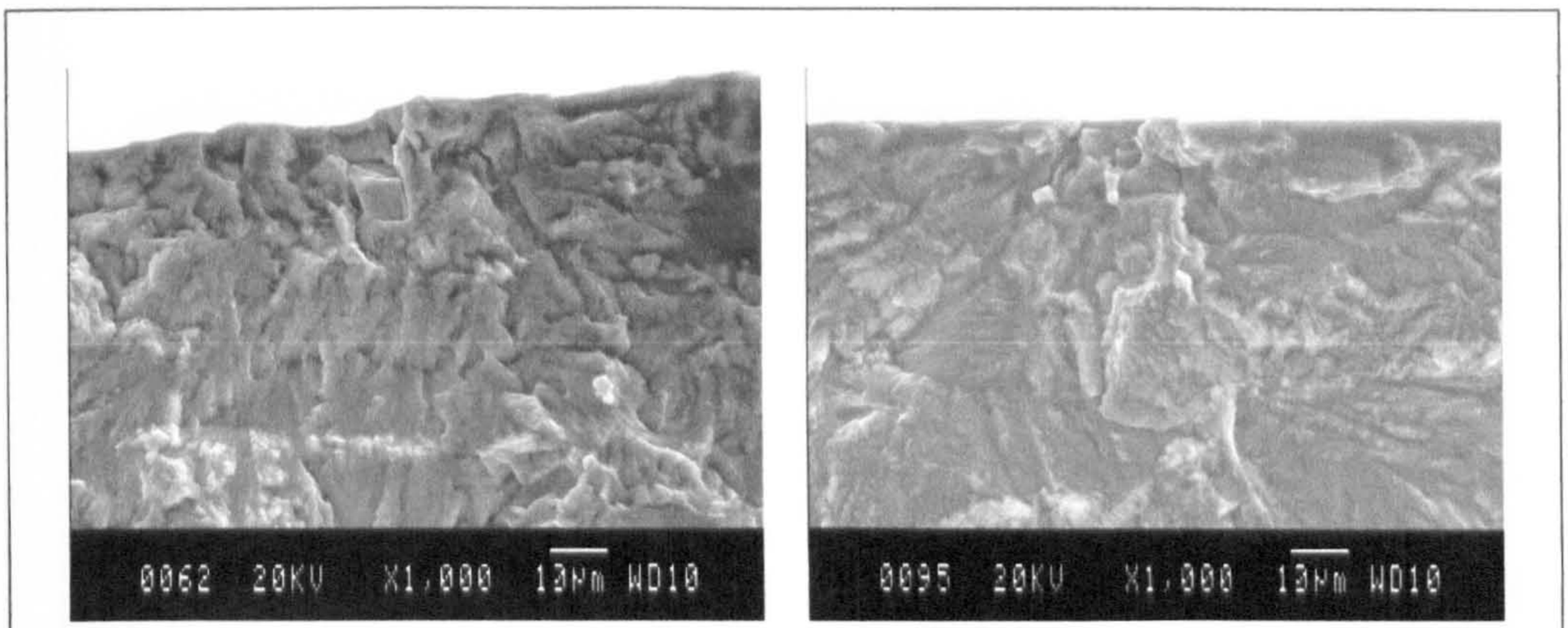

Figure 6.63: MIG HI SCG 1 (left) and 9 (right) intermetallic induced fatigue crack initiation sites.

6.4.7.2 Crack Growth

6.4.7.2.1 Short Crack Growth ~ MIG Low Input

As previously stated S-N testing of the MIG LI SCG specimens resulted in failure of the specimens in the weld metal, the 5 mm diameter parallel sided section, rather than at the weld toe, the centre of the notch. In attempt to resolve the problem the radius of the notch was decreased thereby increasing the SCF at the centre of the notch from 1.05 to 1.10 for the elastic response; although the minimum thickness, 3 mm, and therefore the cross-sectional area remained identical to the other SCG specimens. From the small number of specimens tested it was evident that the reduction in the notch radius had little effect on the point of failure, although a specimen that had been surface replicated with a notch radius of 15 mm failed at the centre of the notch, thereby providing SCG data for a fatigue life of ~10^5 cycles.

It was evident that failure within the weld metal tended to be more prevalent in the low stress/high cycle specimens, although not exclusively, in contrast to specimens with fatigue lives below 10^5 cycles. The cause for this was unknown, although it may have been related to the increased stress intensity factor resulting from the lower yield stress associated with larger grain sizes in the weld metal failures.

Crack initiation in the MIG LI SCG specimen that plastic replicas were analysed from exhibited intermetallic based crack initiation as shown in Figure 6.64. Coalescence of cracks was common and significant tortuousity of the crack path was evident as shown in Figure 6.65 and Figure 6.66. Plastic deformation in the weld metal revealed both the grain structure, evident as the undulating topography in Figure 6.65 (right), and also slip bands within the grains.

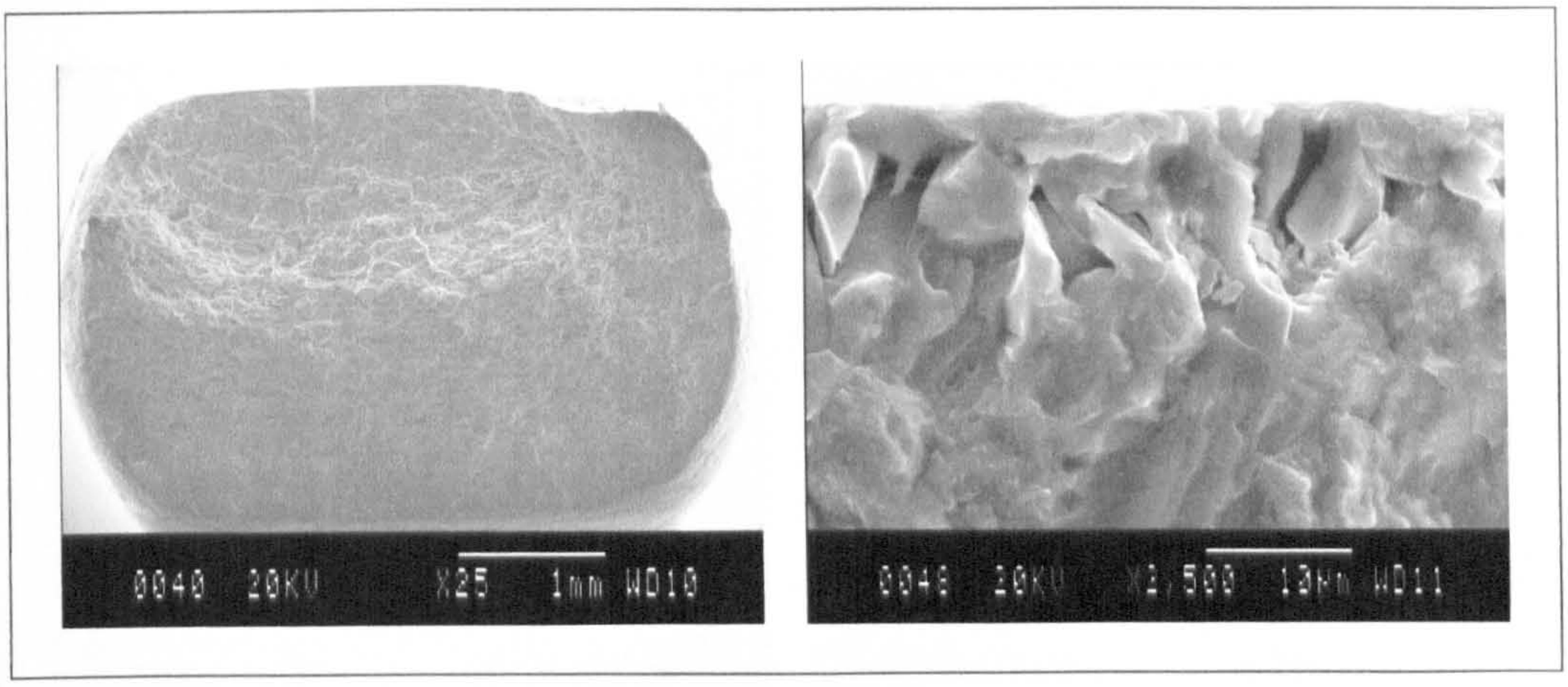

Figure 6.64: MIG LI SCG fracture surface (left) and intermetallic induced crack initiation site (right).

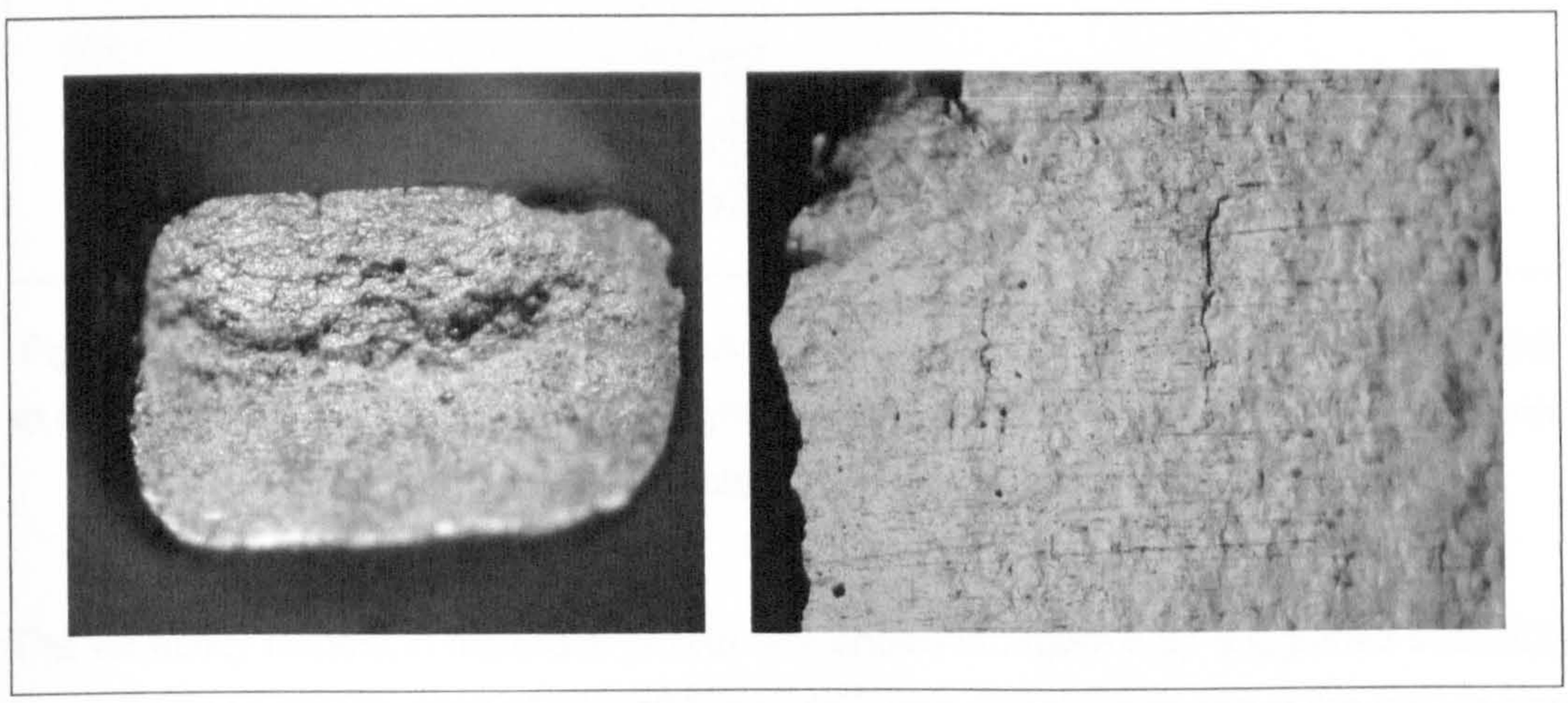

Figure 6.65: MIG LI SCG fracture surface (left) and path of secondary cracks (right).

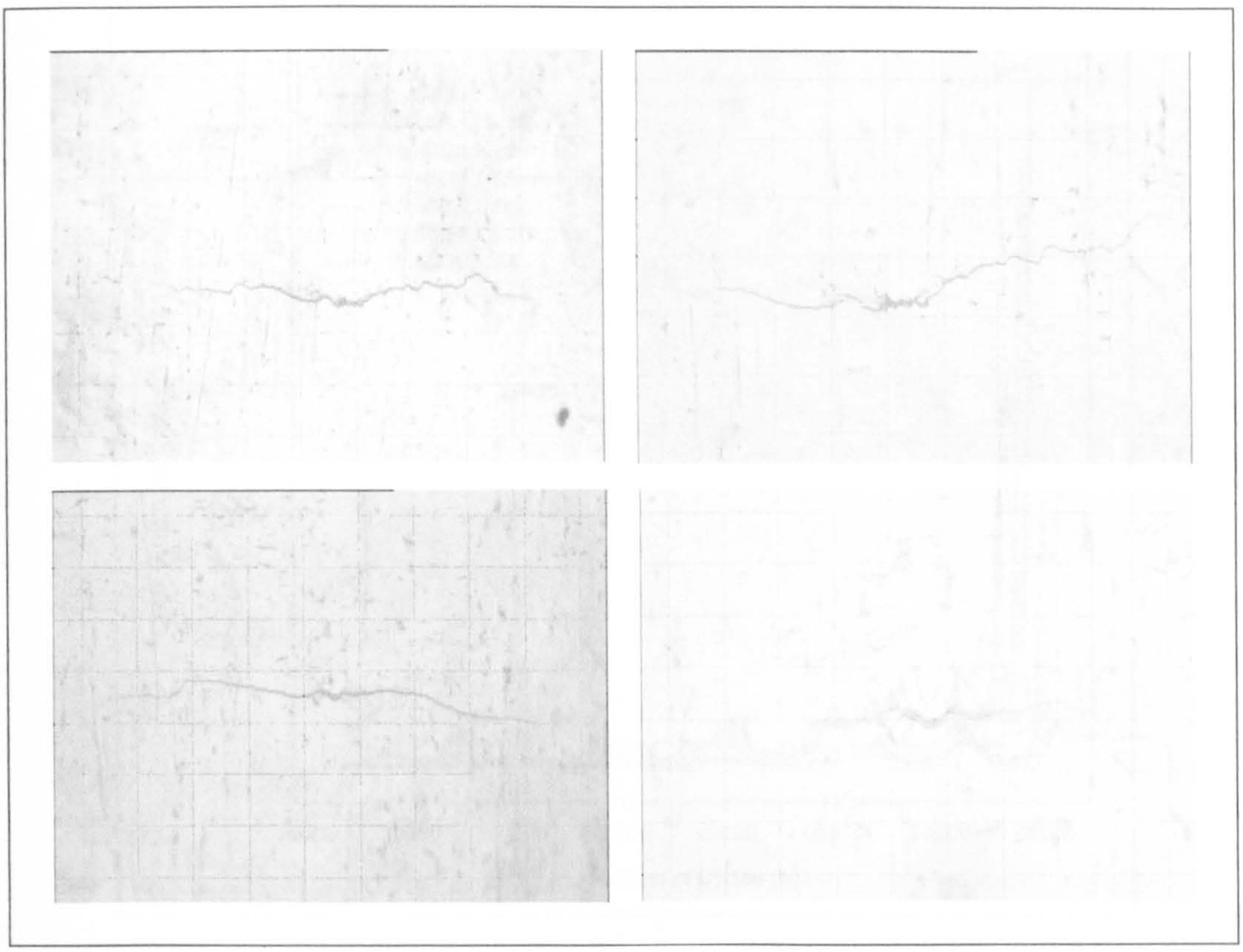

Figure 6.66: MIG LI SCG replicas of 3.1A at 72000 cycles, 2c = 498 µm, (upper left) and at 62000 cycles, 2c = 332 µm, (upper right) and 3.2 at 70000 cycles, 2c = 284 µm, (lower left) and at 32000 cycles, 2c = 74 µm, (lower right).

The variability evident in the crack growth rate shown in Figure 6.67 suggested that SCG occurred up to growth rates of 20×10^{-9} m.cycle^{-1}, with a rapid increase in the growth rate being evident after this and subsequent catastrophic failure. From Figure 6.68 this value of growth rate corresponded to a crack length, c, of ~300 µm, equating to approximately 9 - 10 grains in the LI HAZ. Although the (dc/dN)/c data exhibited significant variability, this tended to be more significant as c decreased; the log-log plot exhibited a linear trend for crack lengths ranging from 100 - 300 µm and a similar linear response, but with a lesser gradient, from 20 - 100 µm. Minimum growth rates of 2×10^{-11} m.cycle^{-1} were measured, although the typical range was $0.2\text{-}20 \times 10^{-9}$ m.cycle^{-1}.

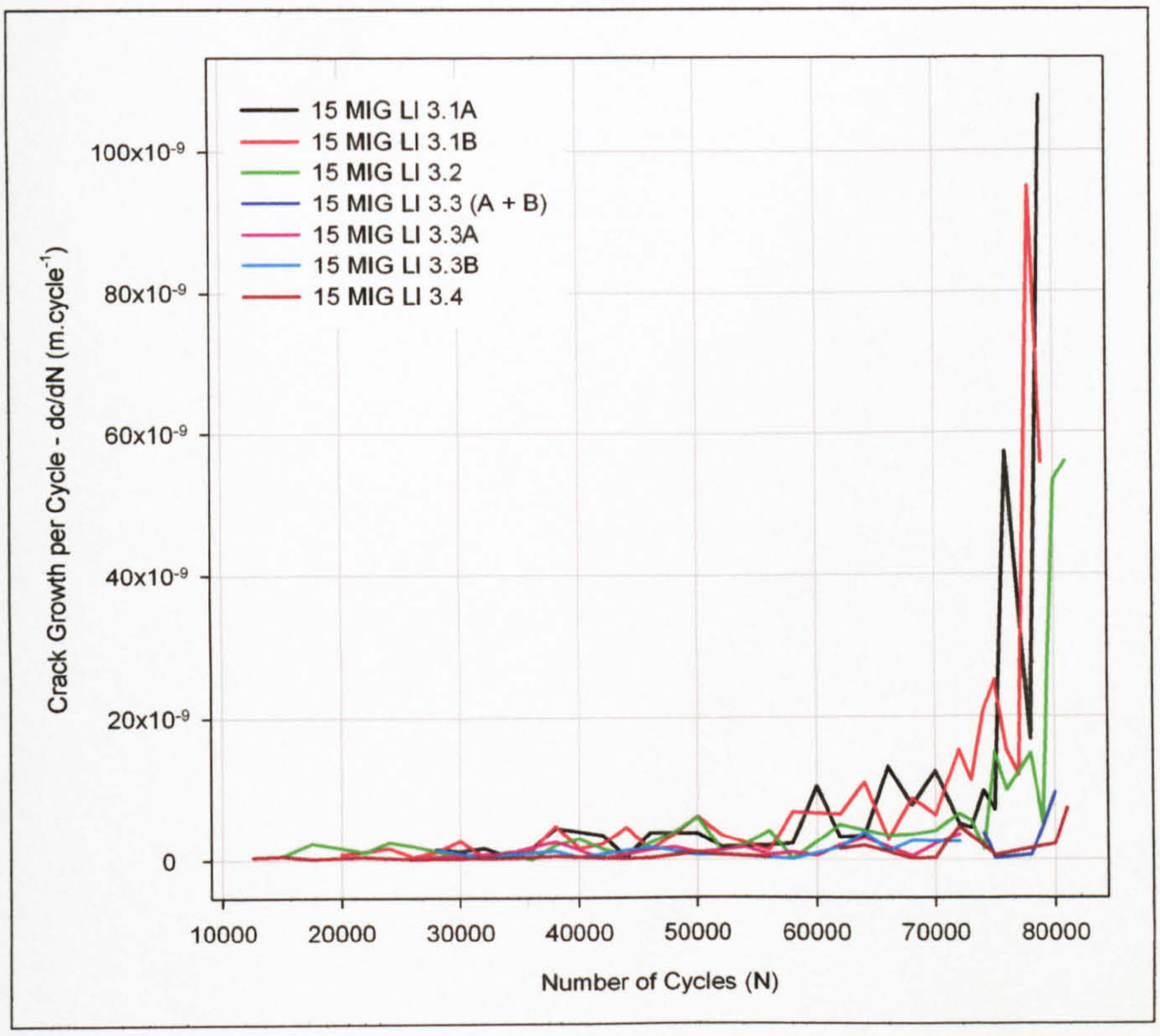

Figure 6.67: MIG LI SCG data, crack growth per cycle/number of cycles.

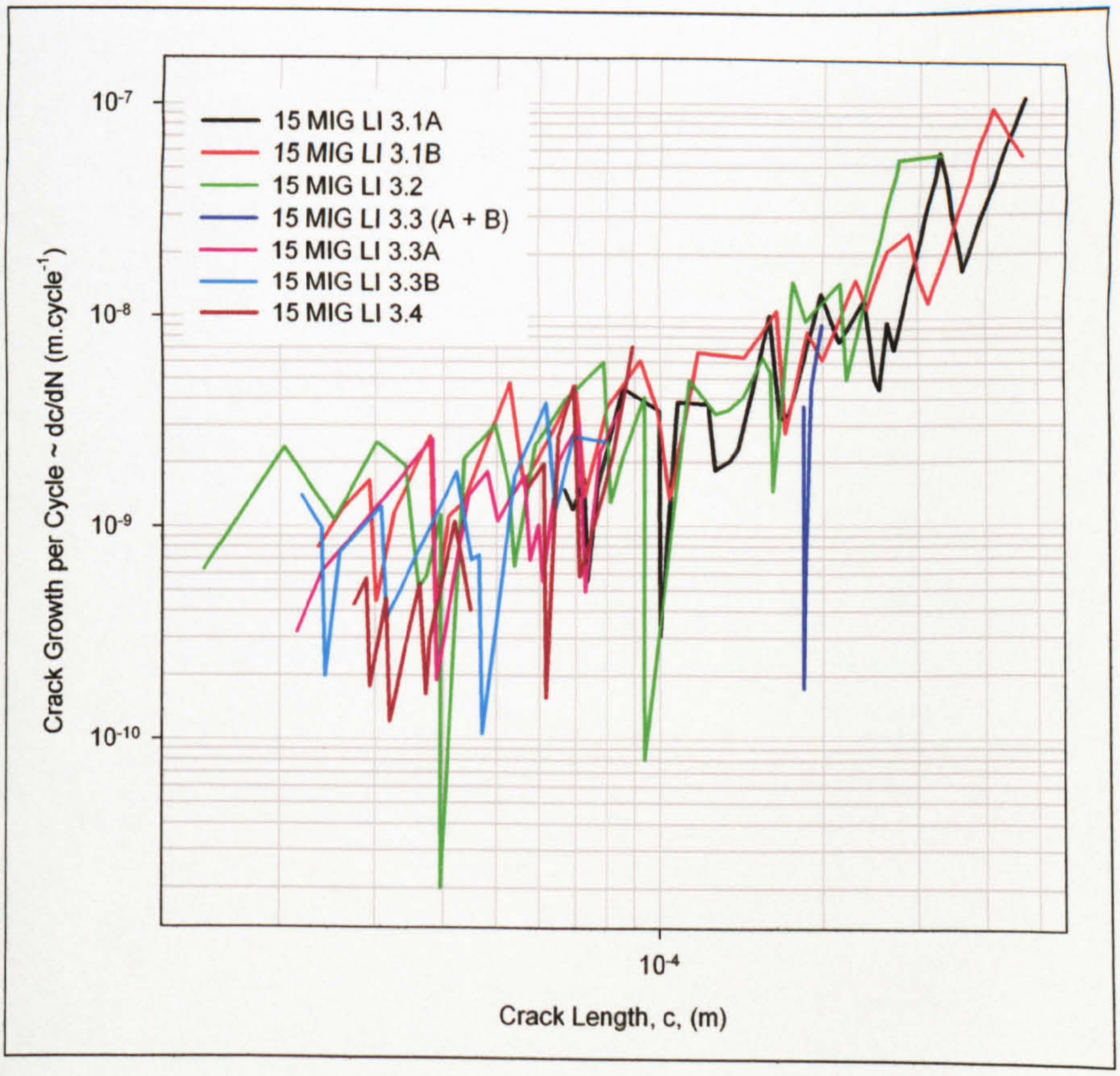

Figure 6.68: MIG LI SCG data, crack growth per cycle/crack length.

6.4.7.2.2 Long Crack Growth ~ MIG LI

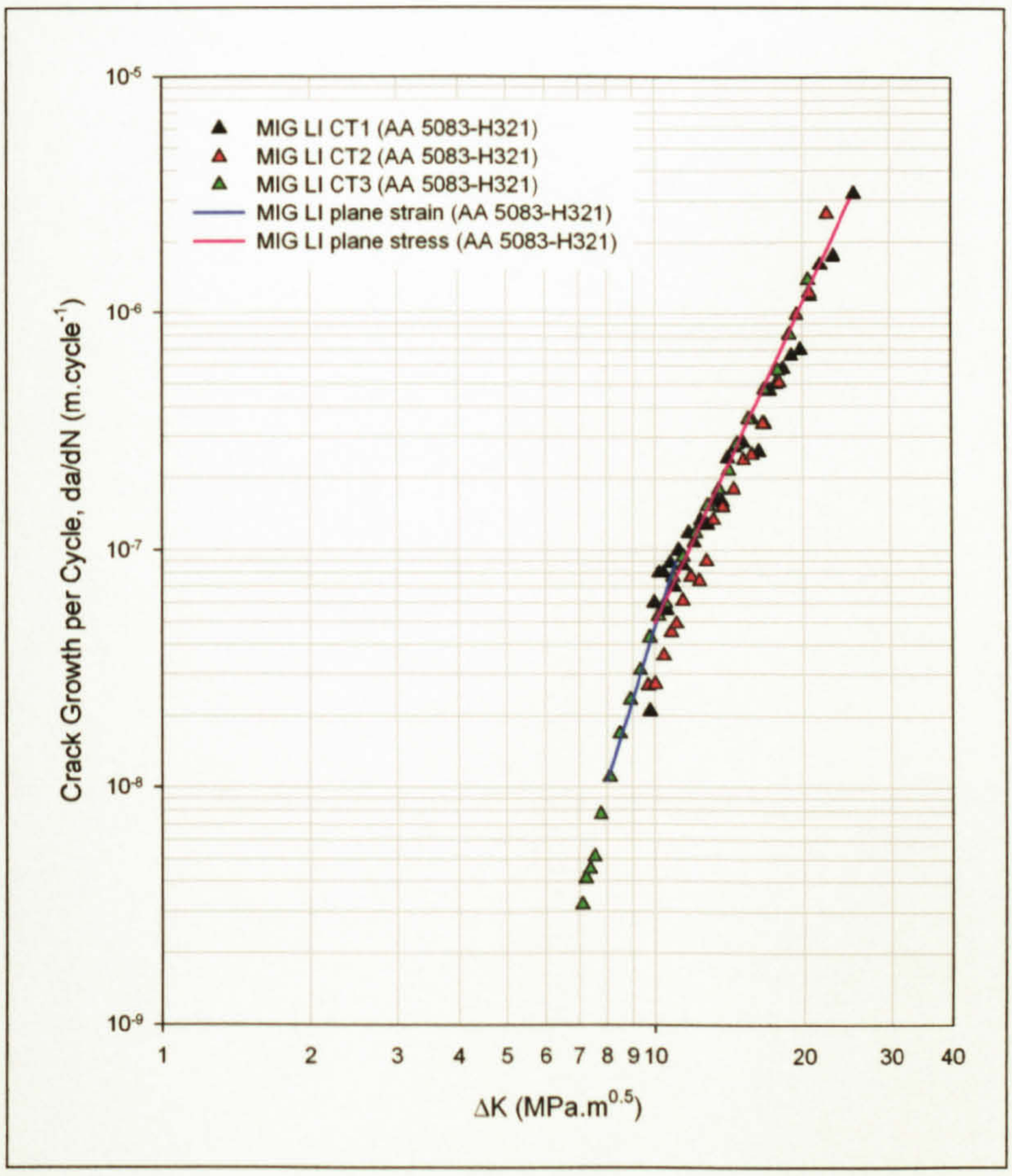

Figure 6.69: Fatigue crack growth rate (R = 0.1) ~ AA 5083-H321 MIG LI butt weld.

ΔK_0 ($K_{max,0}$) (MPa.$m^{0.5}$)	Paris Equation $da/dN = C(\Delta K_{R=0.1})^m$				
	Plane strain $\Delta K \leq 10$		Calculated K_{max} for plane strain (6.17)	Plane stress $10 < \Delta K$	
	C	m		C	m
7.1 (7.8)	9.42×10^{-15}	6.701	5.0	1.61×10^{-12}	4.488

Table 6.9: Paris equation constants for fatigue crack growth in AA 5383-H321 MIG LI butt weld.

The threshold stress intensity factor was difficult to determine for the MIG LI crack growth rates, with frequent crack arrest being noted during the pre-cracking period. Crack arrest was noted at values as high as $\Delta K = 8.6$ MPa.$m^{0.5}$, although this was under the influence of the plastic zone resulting from the previous pre-cracking load history. The lowest stress intensity factor range value that crack growth could be attained, with no influence from the prior plastic zone, was 7.0 MPa.$m^{0.5}$. The calculated value, utilising equation (6.17), for the change in stress state from plane strain to plane stress returned a value of $\Delta K = 4.50$ MPa.$m^{0.5}$, due to the low yield strength, 125 MPa, of the MIG LI weld. Visual

observation of Figure 6.69 suggested that the change occurred at around 10 MPa.m$^{0.5}$ with a slight decrease in the crack growth rate being evident as plane stress predominated. The Paris equations for the predominantly plane strain and plane stress regimes are shown as equations (6.22) and (6.23).

$$\left(da/dN\right)_{\text{plane strain}} = 9.42\times10^{-15}\times(\Delta K)^{6.701} \tag{6.22}$$

$$\left(da/dN\right)_{\text{plane stress}} = 1.61\times10^{-12}\times(\Delta K)^{4.488} \tag{6.23}$$

6.4.7.2.3 Short Crack Growth ~ MIG High Input

Crack initiation in the MIG HI SCG specimens was the result of intermetallic inclusions as shown in Figure 6.70 and Figure 6.71. Crack paths were again convoluted and coalescence common, as shown in Figure 6.71 and Figure 6.72, although slightly less so than that observed in the MIG LI SCG specimen.

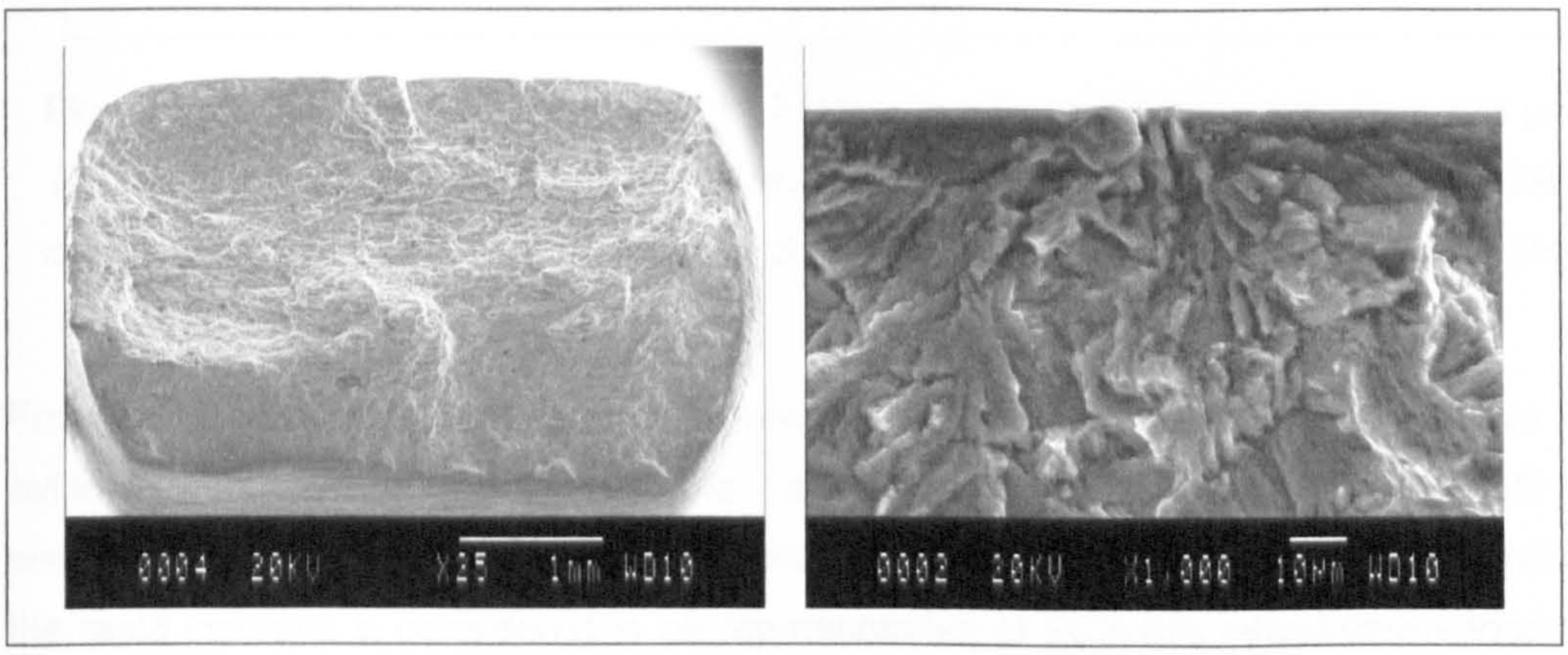

Figure 6.70: MIG HI SCG fracture surface (left) and intermetallic induced crack initiation site (right).

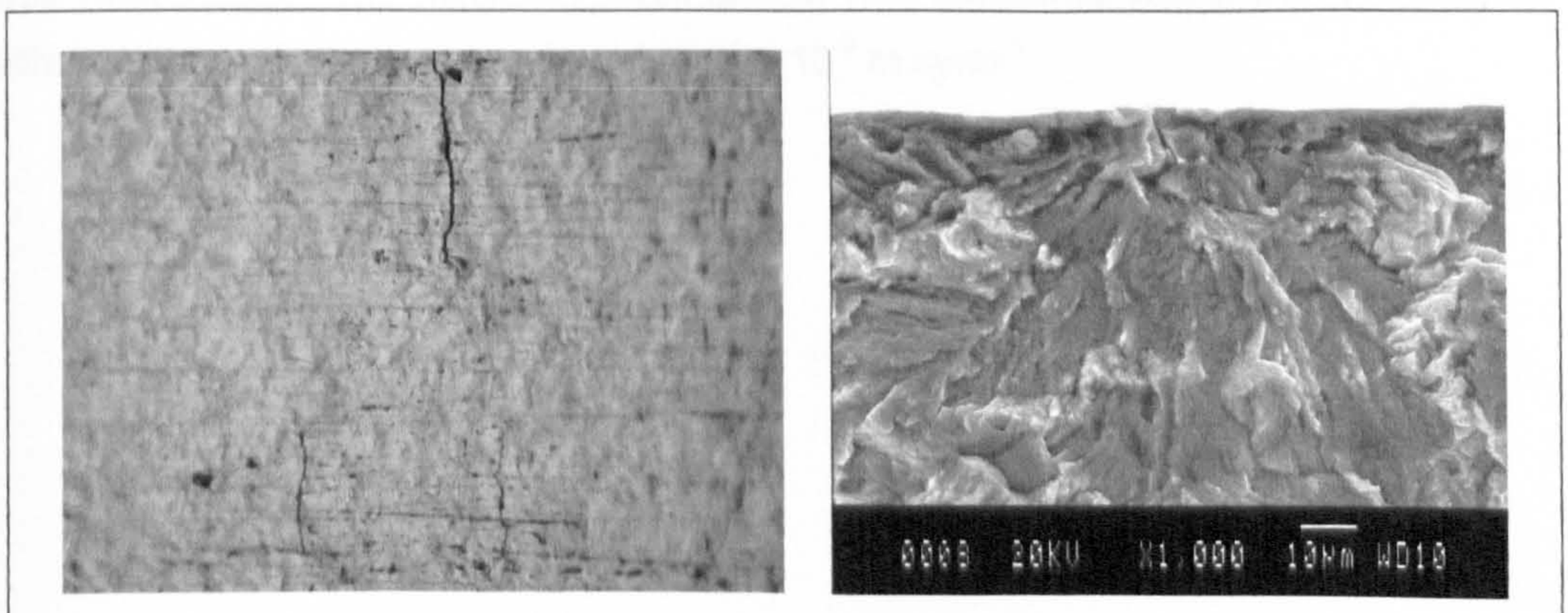

Figure 6.71: MIG HI SCG crack path (left) and intermetallic induced crack initiation site (right).

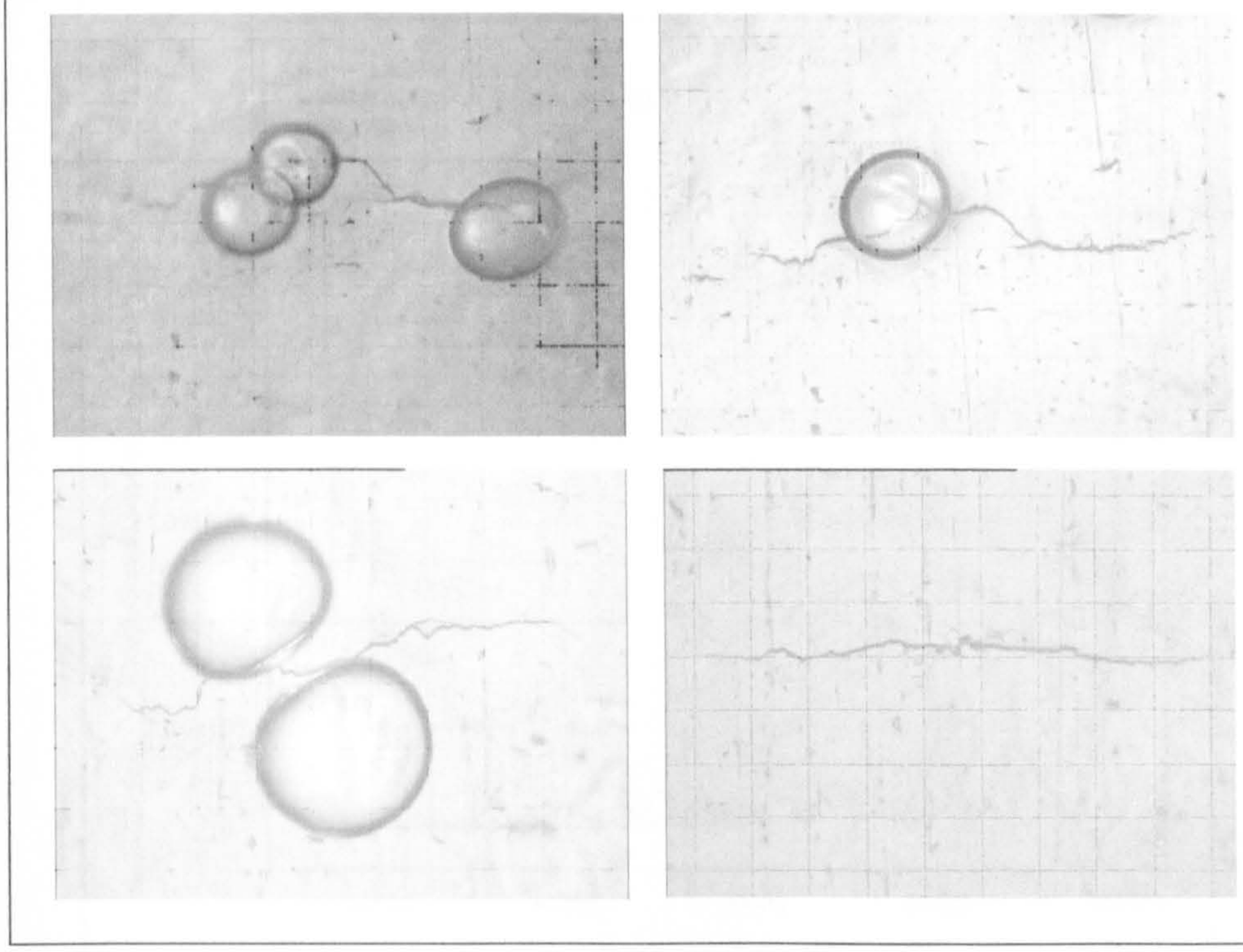

Figure 6.72: MIG HI SCG replicas of 11.2 ((A + B) + C) at 96000 cycles, 2c = 723 μm, (upper left), 11.2 (A + B) at 91000 cycles, 2c = 593 μm, (upper right), 11.2A at 84000 cycles, 2c = 312 μm, (lower left) and 11.3 at 88000 cycles, 2c = 323 μm, (lower right).

From the (dc/dN)/N graph shown in Figure 6.73 variability in the crack growth rate was evident up to a rate of 15×10^{-9} m.cycle^{-1}, after which a rapid increase in the growth rate was evident, with this being followed by failure. If the variability of the growth rate prior to the rapid increase is considered to be representative of SCG this would correspond to a crack length, c, of ~250 μm according to Figure 6.74, in the region of 5 - 6 grains of the HI HAZ. Although the log-log plot of the (dc/dN)/c graph, shown in Figure 6.74, exhibited considerable unevenness, the general trend was again linear, suggesting a power law type relationship. The minimum crack growth rate measured was $2\text{-}3 \times 10^{-12}$ m.cycle^{-1}, although the typical range was from $0.2\text{-}20 \times 10^{-9}$ m.cycle^{-1}.

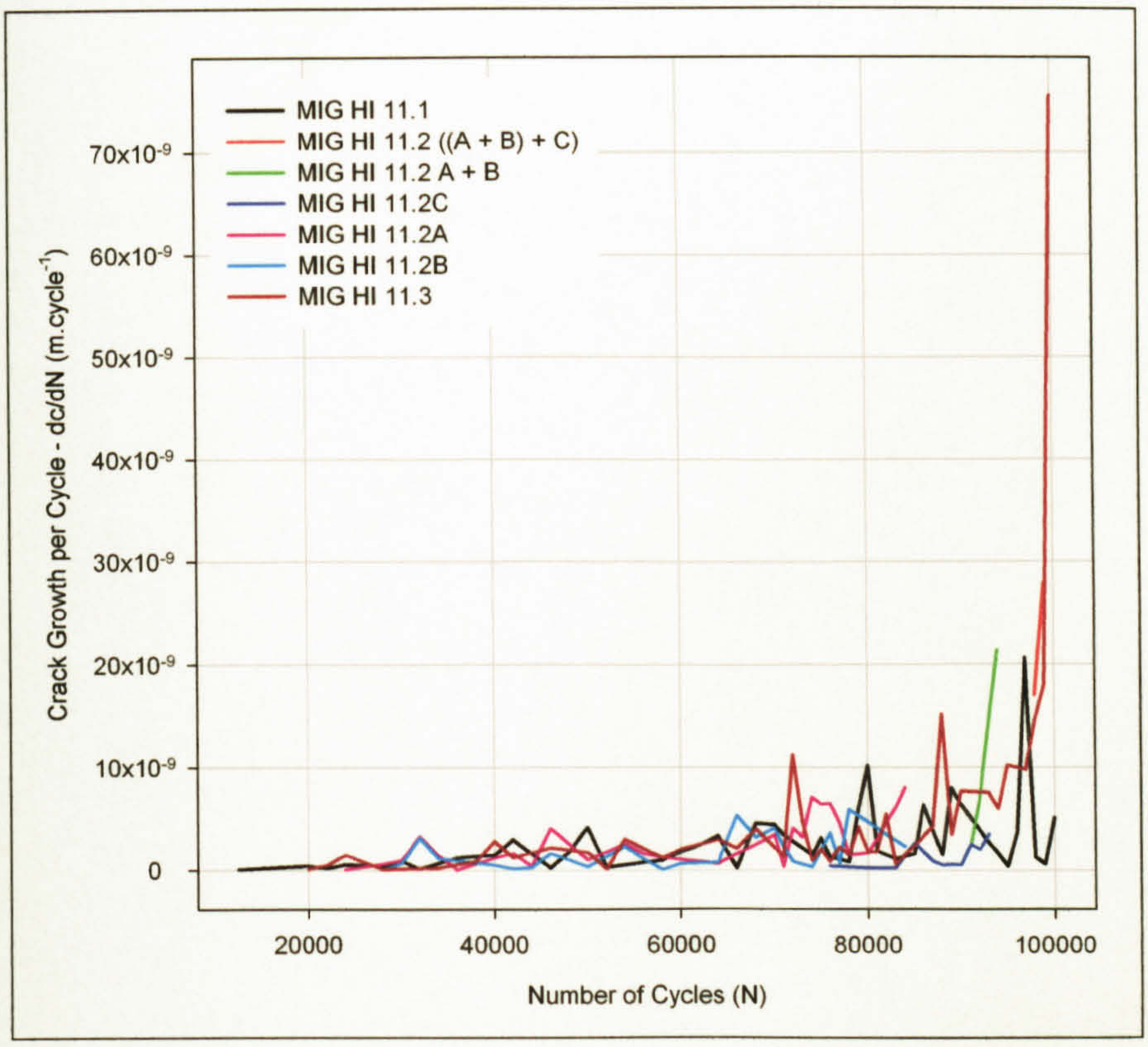

Figure 6.73: MIG HI SCG data, crack growth per cycle/number of cycles.

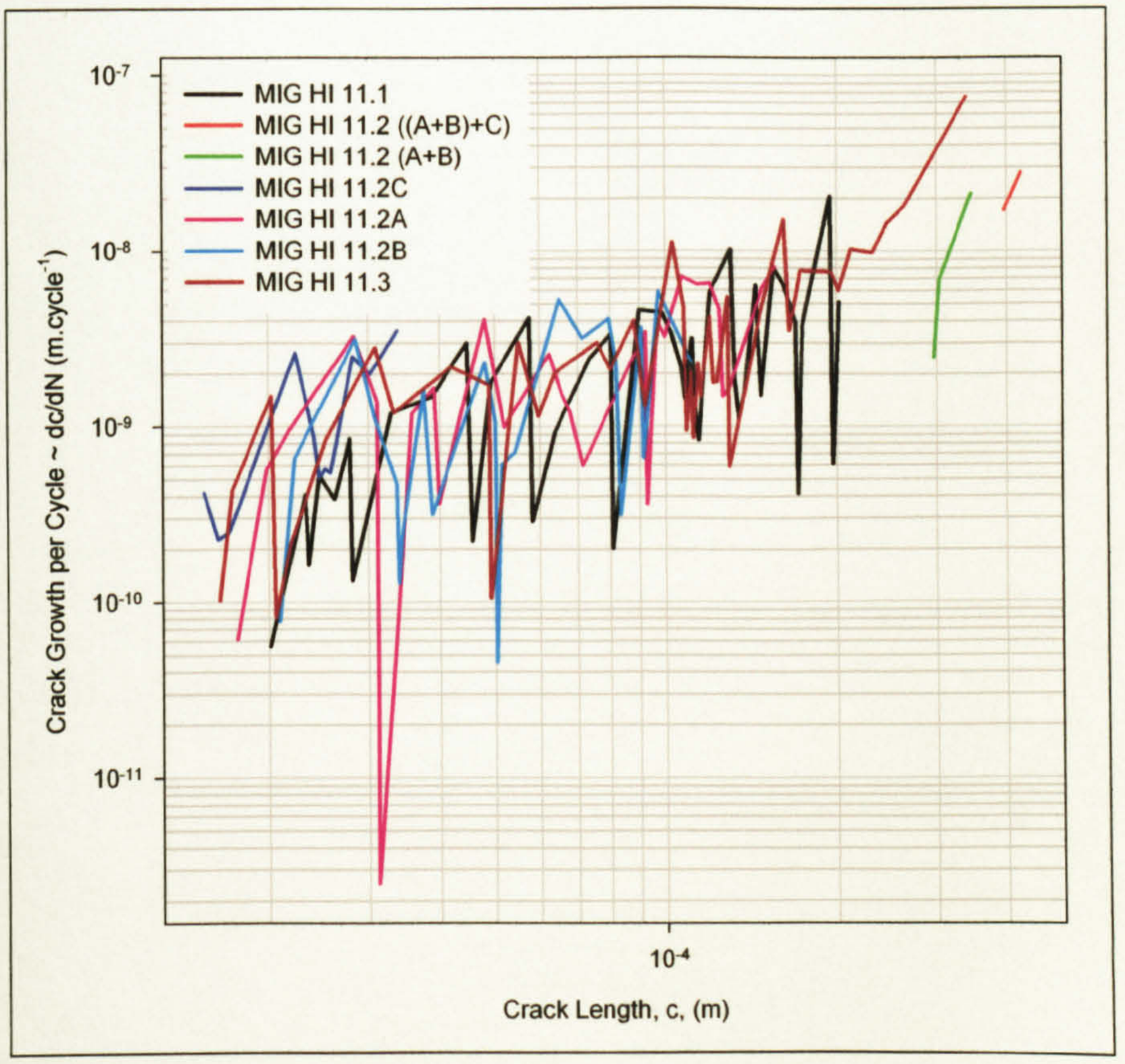

Figure 6.74: MIG HI SCG data, crack growth per cycle/crack length.

6.4.7.2.4 Long Crack Growth ~ MIG High Input

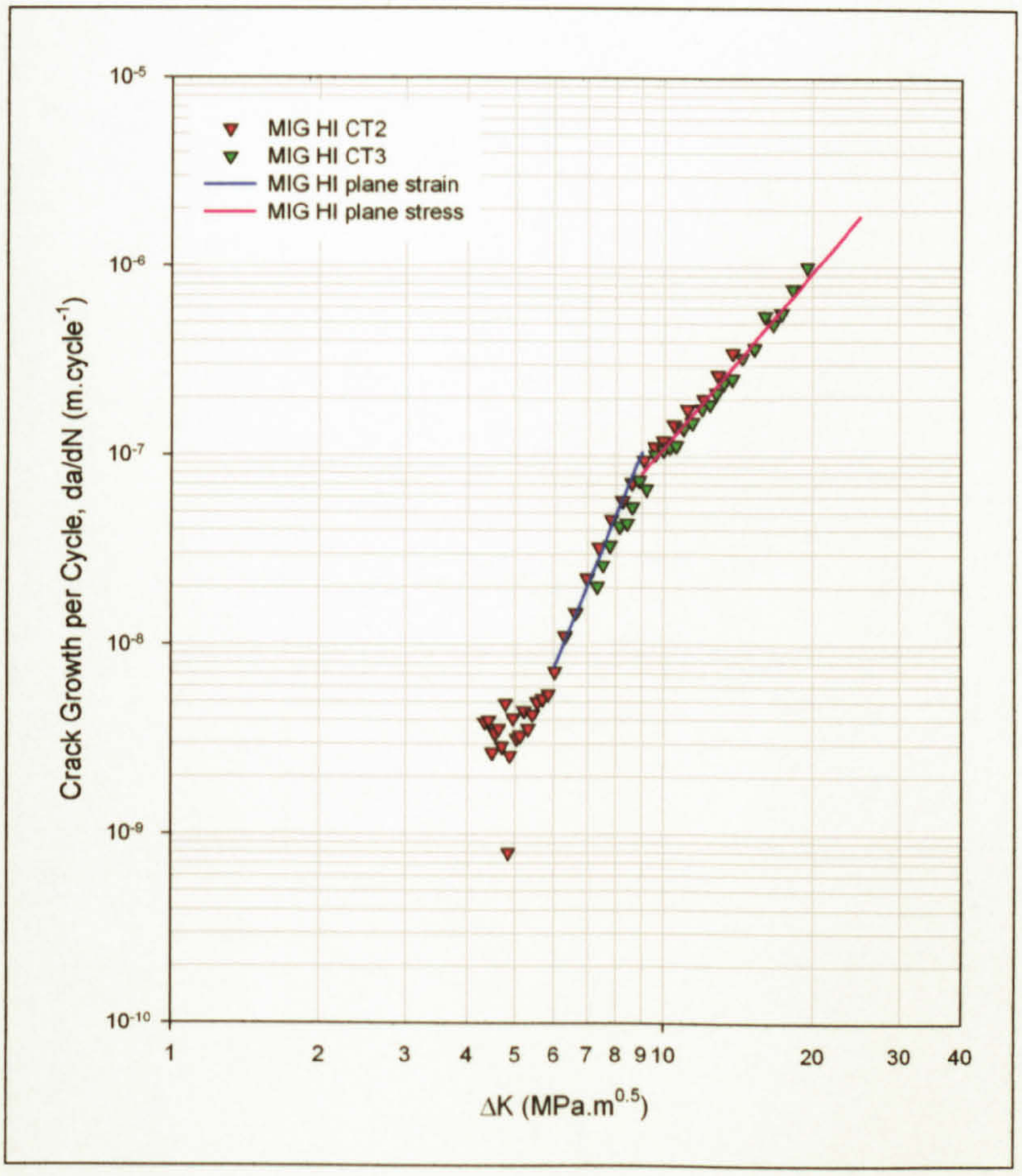

Figure 6.75: Fatigue crack growth rate (R = 0.1) ~ AA 5383-H321 MIG HI butt weld.

ΔK_0 ($K_{max,0}$) (MPa.m$^{0.5}$)	Paris Equation $da/dN = C(\Delta K_{R=0.1})^m$				
	Plane strain $\Delta K \leq 9.5$		Calculated K_{max} for plane strain (6.17)	Plane stress $9.5 < \Delta K$	
	C	m		C	m
4.3 (4.8)	68.87×10^{-15}	6.476	5.2	93.30×10^{-12}	3.072

Table 6.10: Paris equation constants for fatigue crack growth in AA 5383-H321 MIG HI butt weld.

From Figure 6.75 the threshold for long crack growth was observed to occur in the region of $\Delta K = 4.5$ MPa.m$^{0.5}$. The change from plane strain to plane stress occurred at $\Delta K = 9.5$ MPa.m$^{0.5}$, significantly greater than the calculated value of $\Delta K = 4.68$ MPa.m$^{0.5}$, with a decrease in the propagation rate being evident as plane stress predominated. The Paris equations, accounting for the change in stress state from plane strain, equation (6.24), and plane stress, equation (6.25), are shown below, the change resulting in a decrease in the crack growth rate.

$$\left(da/dN\right)_{\text{plane strain}} = 68.87 \times 10^{-15} \times (\Delta K)^{6.476} \tag{6.24}$$

$$\left(da/dN\right)_{\text{plane stress}} = 93.297 \times 10^{-12} \times (\Delta K)^{3.072} \tag{6.25}$$

6.4.8 Friction Stir Welds

6.4.8.1 SCG S-N Testing

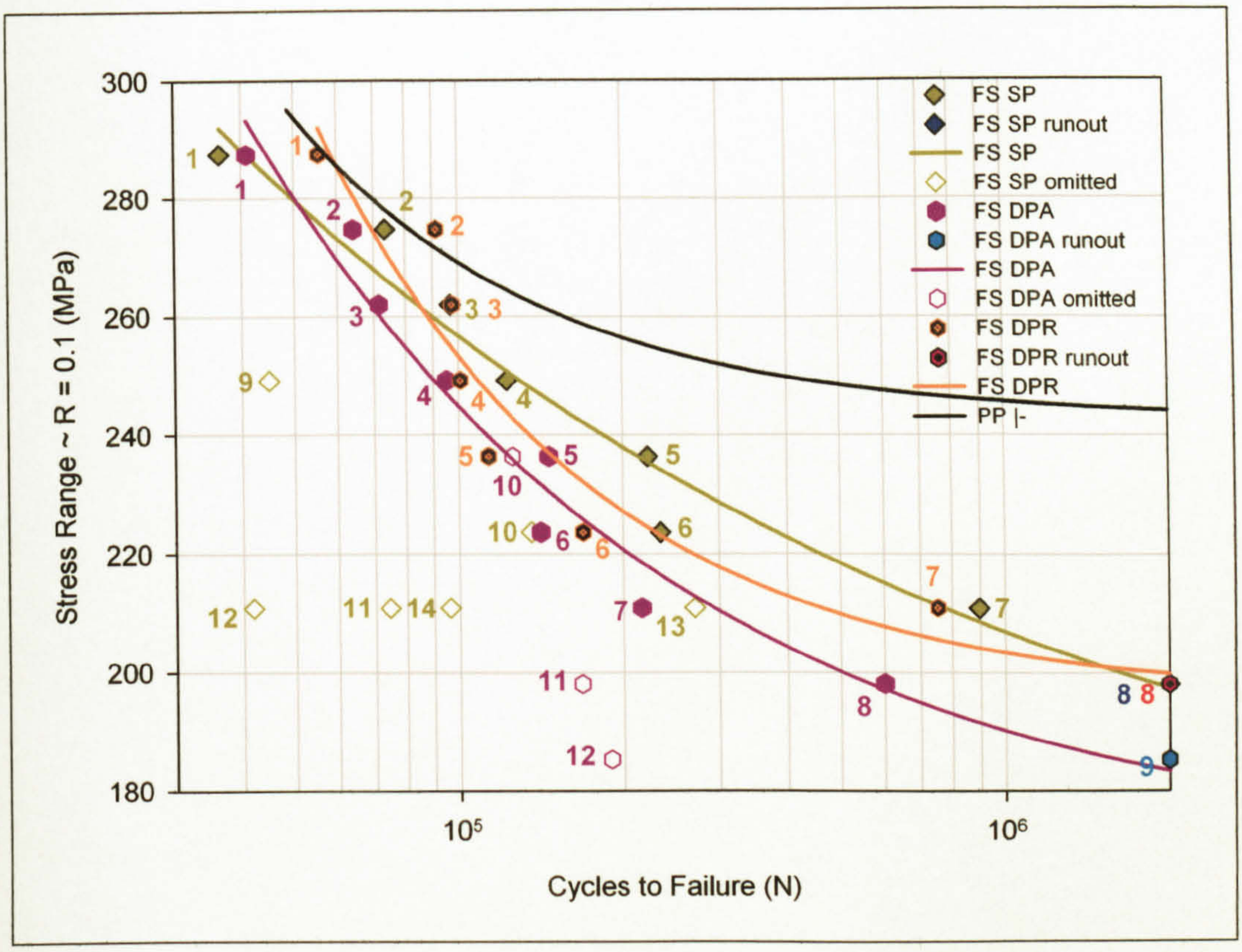

Figure 6.76: FS butt welded short crack growth specimen S-N data (numbers refer to specimens in Table 13.41 (page 524), Table 13.48 (page 528) and Table 13.59 (page 533).

Material	Fatigue Strength ~ Δσ (MPa)			
	Number of Cycles			
	10^5	2×10^5	10^6	2×10^6
FS SP	256.7	237.9	206.8	197.4
FS DPA	244.8	220.7	190.2	183.4
FS DPR	253.3	227.1	203.3	199.8
PP |-	269.2	256.4	245.7	244.3

Table 6.11: FS SP and DP advancing (DPA) and retreating (DPR) SCG specimen fatigue strengths (R = 0.1).

The FS SP SCG specimens, with the centre of the notch positioned at the weld seam, exhibited numerous specimens that failed either due to PFD or cracks that initiated at the edge of the notch, these were subsequently omitted from the S-N curves. Some FS SP specimens that were included in the S-N curves also exhibited PFD, but if they were

considered to fall within a satisfactory scatter envelope they were considered suitable for the development of the curve on the basis that the curves were only to be used for determining load ranges for the subsequent SCG measurements and due to material and time constraints. Three FS DPA specimens were also omitted from the S-N curves due to failure occurring outside the notch. The FS SP SCG specimens exhibited the greater fatigue strength for stress ranges of 200 - 260 MPa. For stress ranges greater than this the FS DPR SCG specimens returned the greater fatigue strength and for a stress ranges greater than 280 MPa the FS DPA SCG specimens also exhibited superior fatigue strength than the FS SP ones. Of the two FS DP SCG specimens those machined from the retreating side had the greater fatigue strength, with the increase ranging from 3 - 9%.

6.4.8.1.1 SCG S-N Specimen Fractography

The FS SP SCG specimens exhibited numerous PFD failures that resulted in crack initiation and subsequent growth as shown in Figure 6.77. The PFD surface tended to be featureless, as shown in Figure 6.78, in comparison to both the typical fatigue crack surface, that exhibited both beach marks and ratchet lines, and the dimple marked appearance fast fracture surface. The source of initiation in specimens that did not appear to be related to PFD was difficult to determine, although intermetallics of around 10 µm diameter appeared to be the main instigators in some cases, as shown in Figure 6.79. The FS DP specimens, both from the advancing and retreating sides, typically exhibited intermetallic induced crack initiation as shown in Figure 6.80 and Figure 6.81.

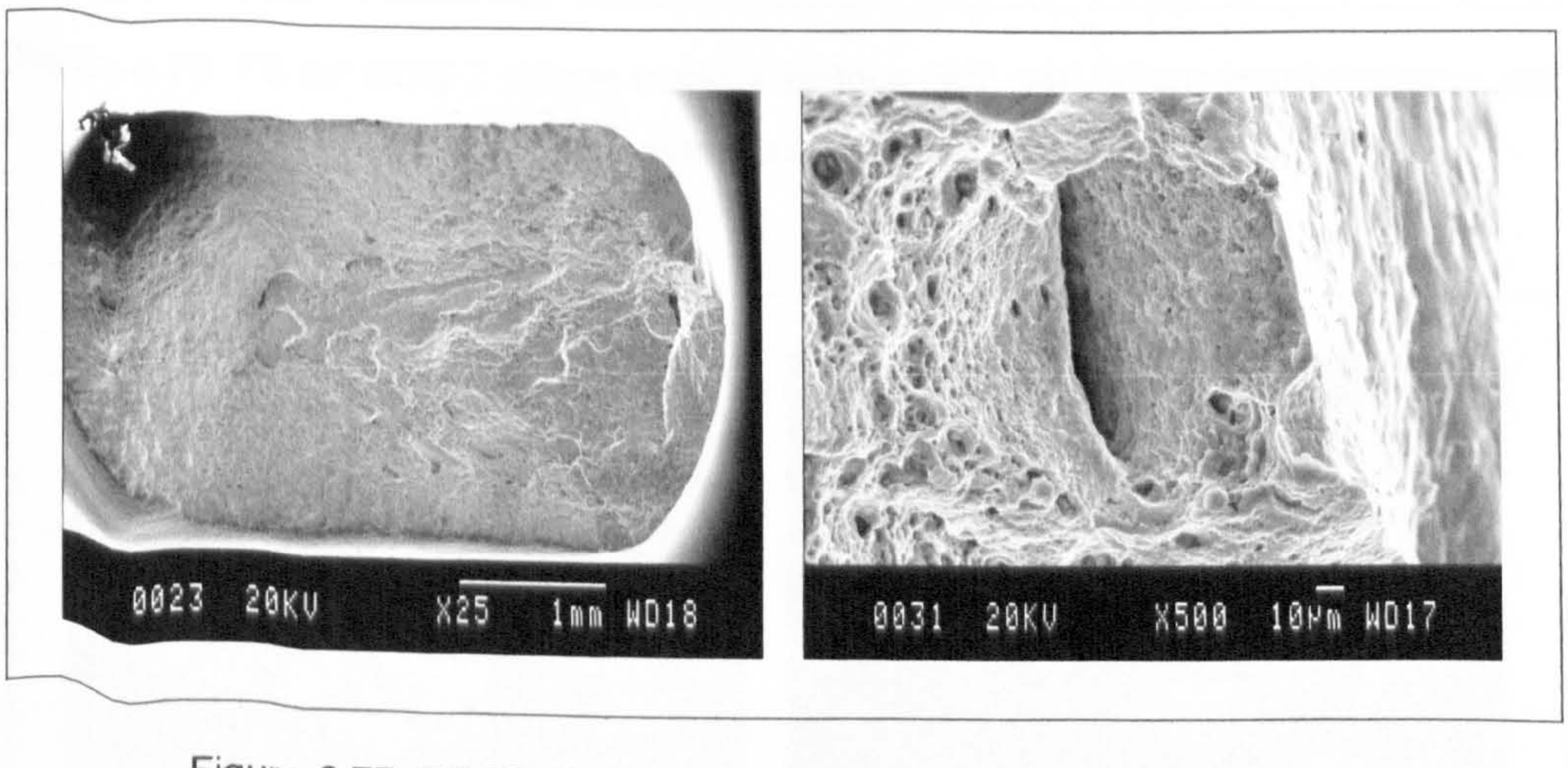

Figure 6.77: FS SP SCG 1 exhibiting PFD on the fracture surface.

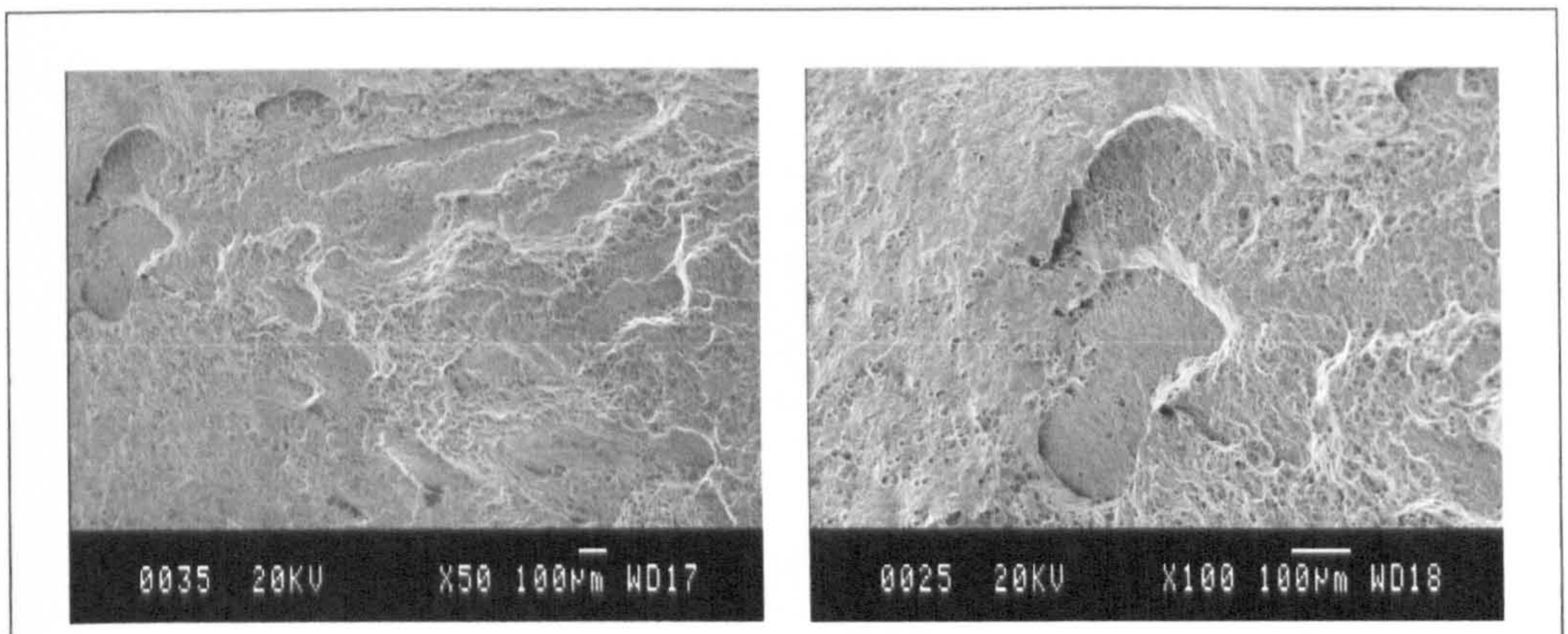

Figure 6.78: FS SP SCG 1 PFD surface.

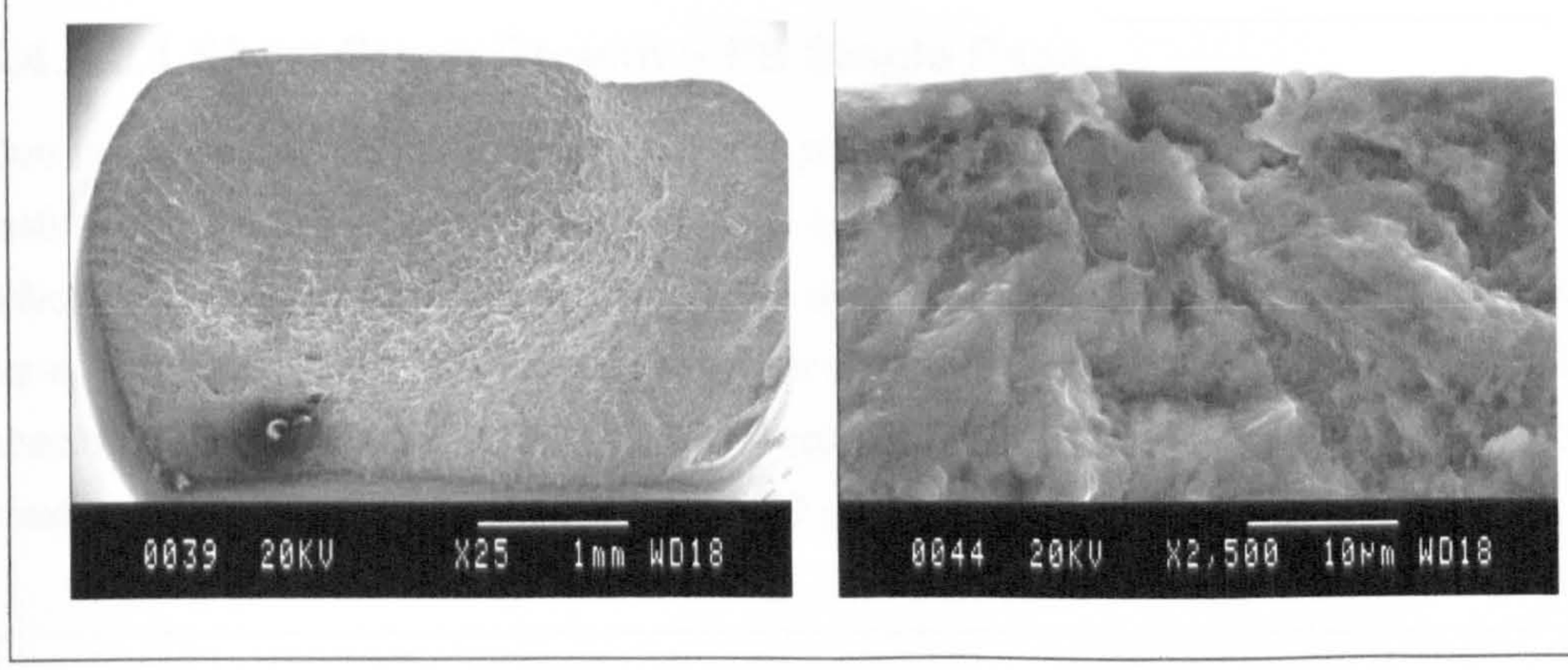

Figure 6.79: FS SP SCG 7 fatigue fracture surface (left) and fatigue crack initiation site possibly intermetallic induced (right).

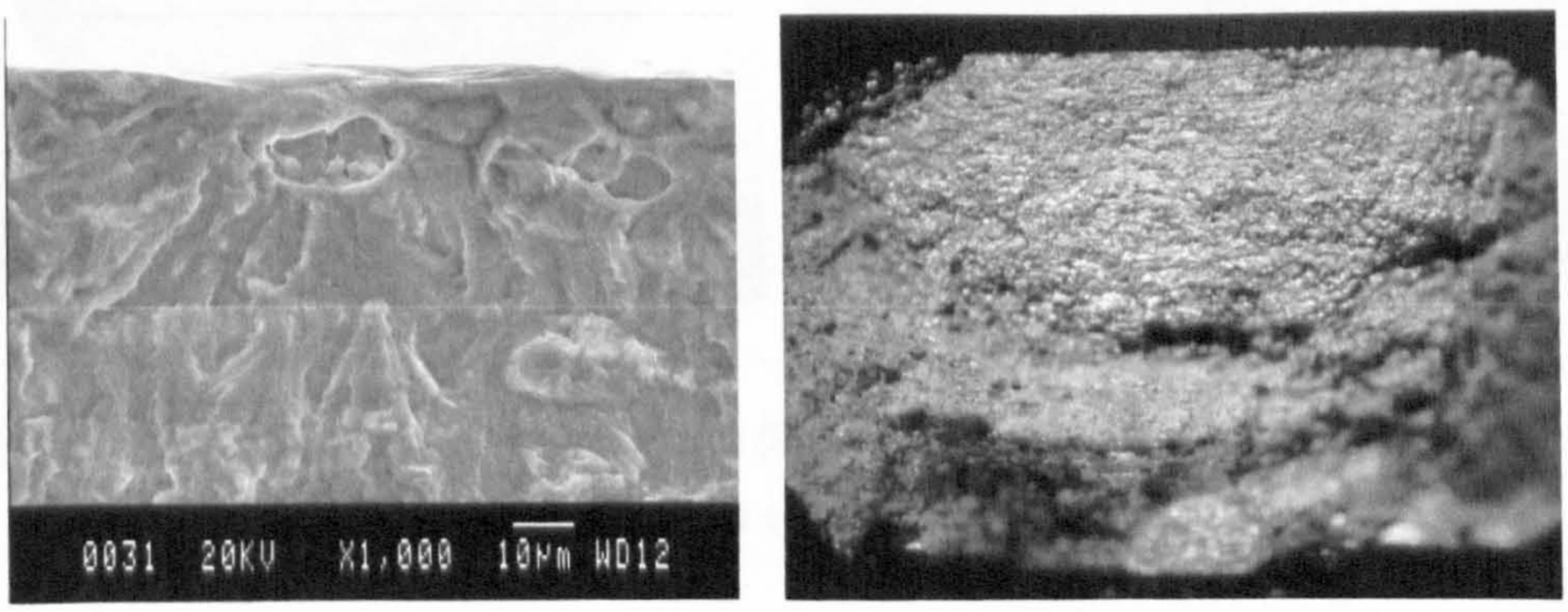

Figure 6.80: FS DPA SCG 1 intermetallic induced fatigue crack initiation site (left) and FS DPA SCG 8 fracture surface, cause of initiation unknown (right).

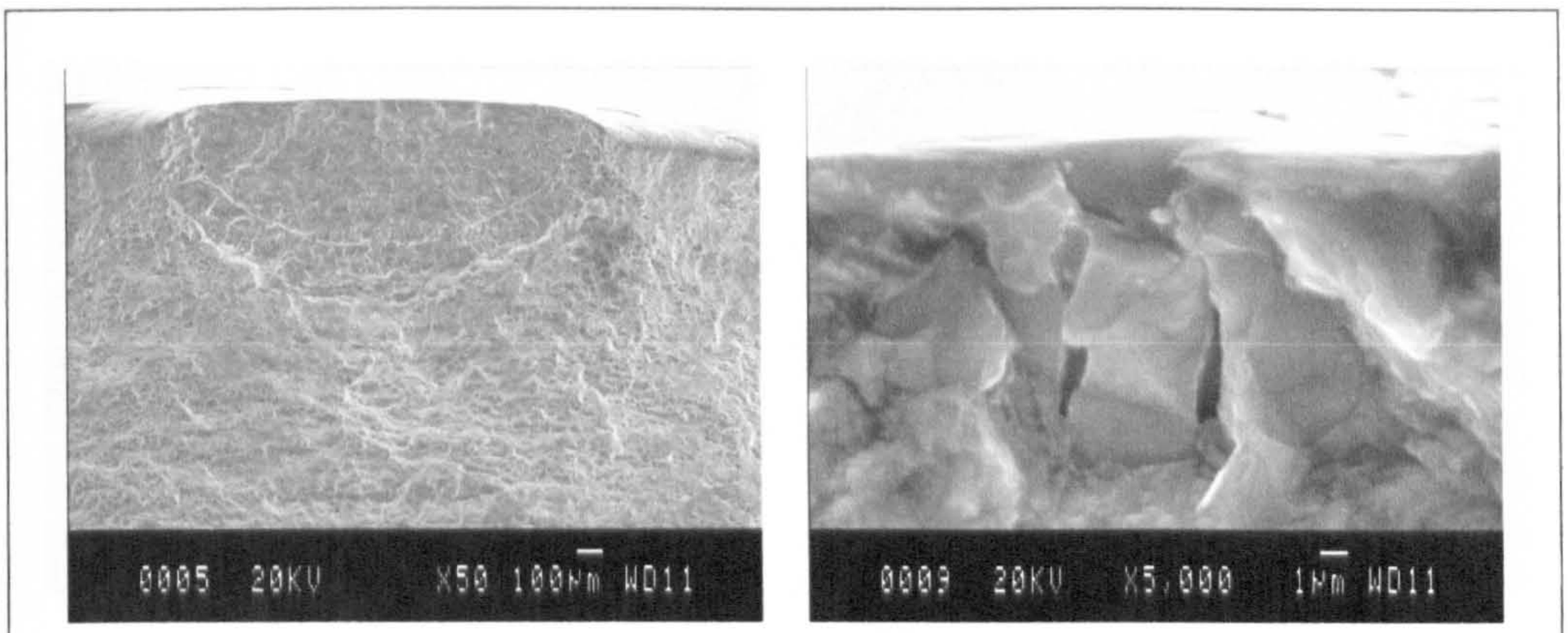

Figure 6.81: FS DPR SCG 1 fatigue crack surface and intermetallic induced initiation site.

6.4.8.2 Crack Growth

6.4.8.2.1 Short Crack Growth ~ FS Single Pass

Due to the partial fusion defects (PFD) that presented themselves whilst undertaking S-N testing of the FS SP SCG specimens (also evident in the four point loading specimens), difficulties arose in obtaining a fatigue life of ~10^5 cycles and hence the SCG replicas were obtained from a specimen where the principal crack initiated on the side of the specimen. This resulted in the crack that resulted in failure not being analysed and the maximum crack length measured, being 169 µm.

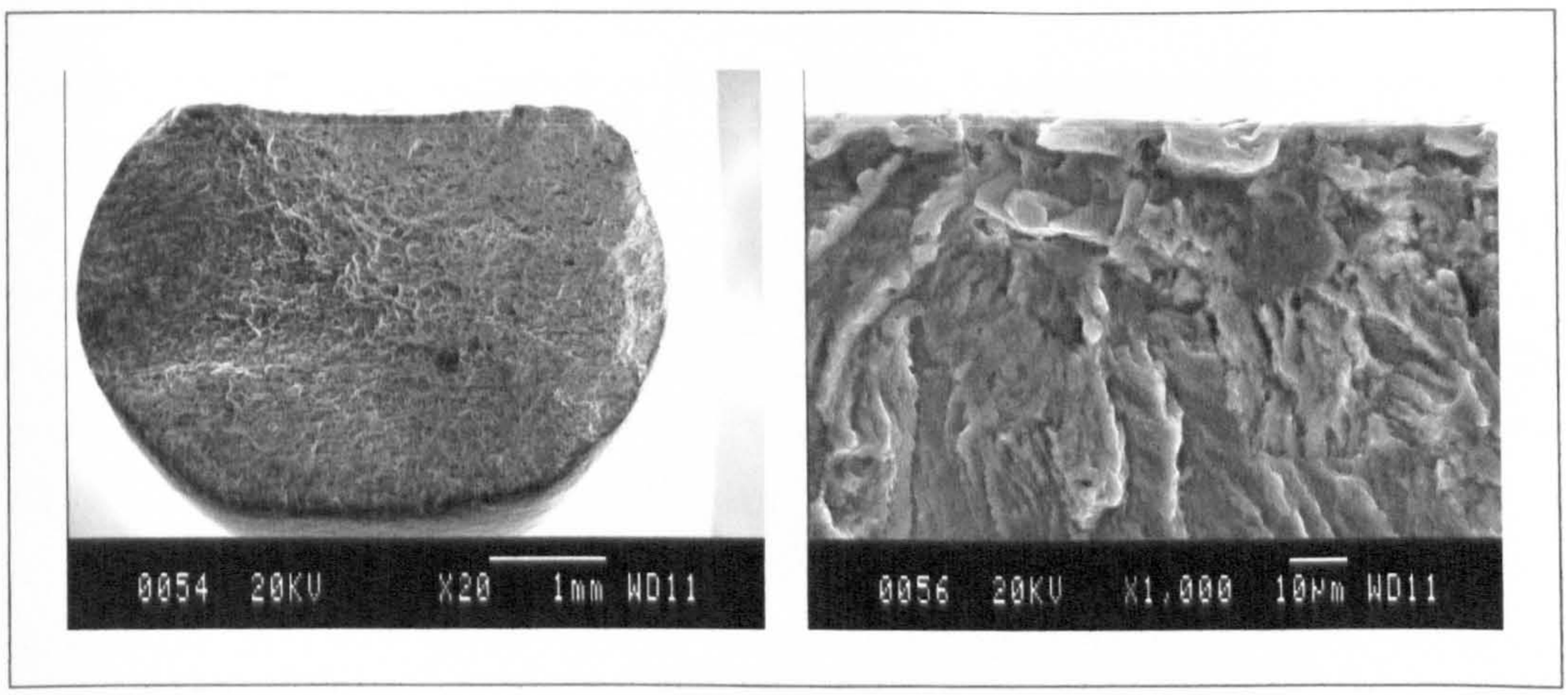

Figure 6.82: FS SP SCG fracture surface (left) and intermetallic induced crack initiation site (right).

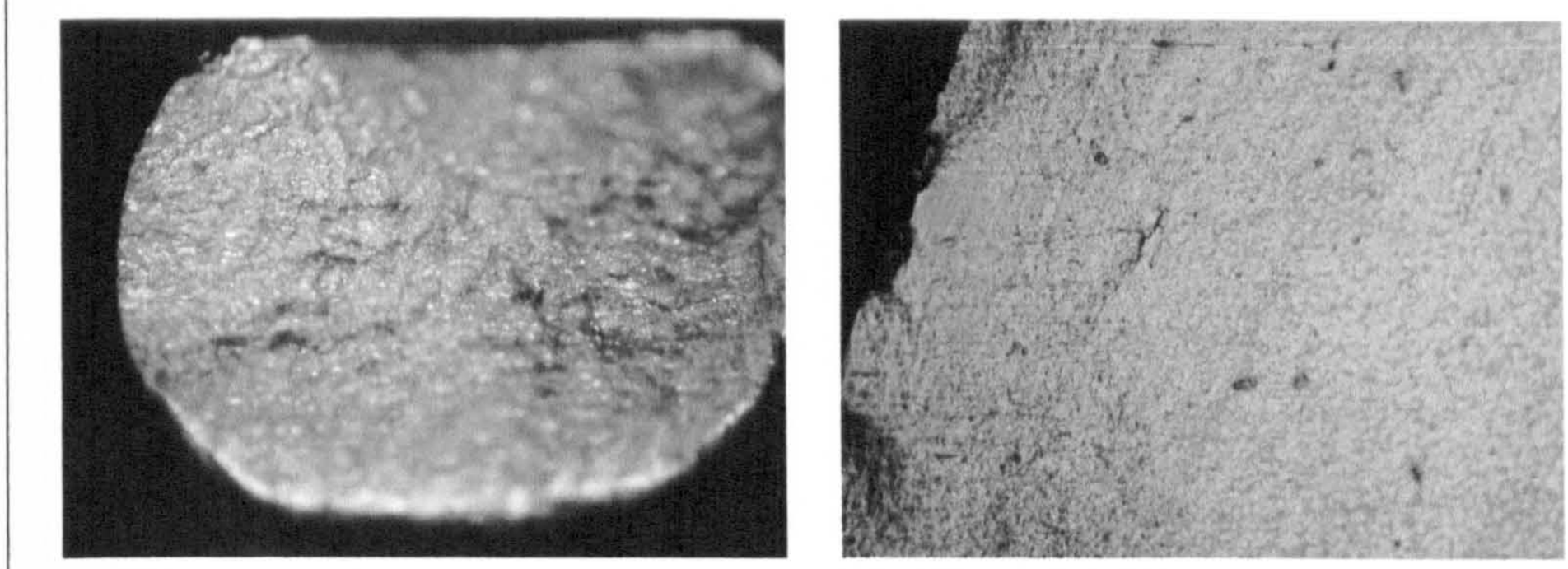

Figure 6.83: FS SP SCG 19 fracture surface (left) and FS SP SCG 21 notch surface.

From Figure 6.82 (left) and Figure 6.83 (left) the principal crack that resulted in failure can be seen to have initiated from the edge of the specimen. Figure 6.82 (right) suggested that the cause of initiation was an intermetallic inclusion of diameter ~10 μm, comparable to the grain size of the weld nugget. The grain structure of the weld nugget region was evident in Figure 6.83 (right) as the finely dimpled surface. Crack coalescence was infrequent, only being observed in one crack; this may have been the result of the maximum crack size measured being less than those measured in the other SCG specimens, subsequently there would be less time for interaction to occur between crack tip stress fields. Crack tortuousity was evident in smaller cracks, as shown in Figure 6.84, becoming less discernable as crack growth occurred.

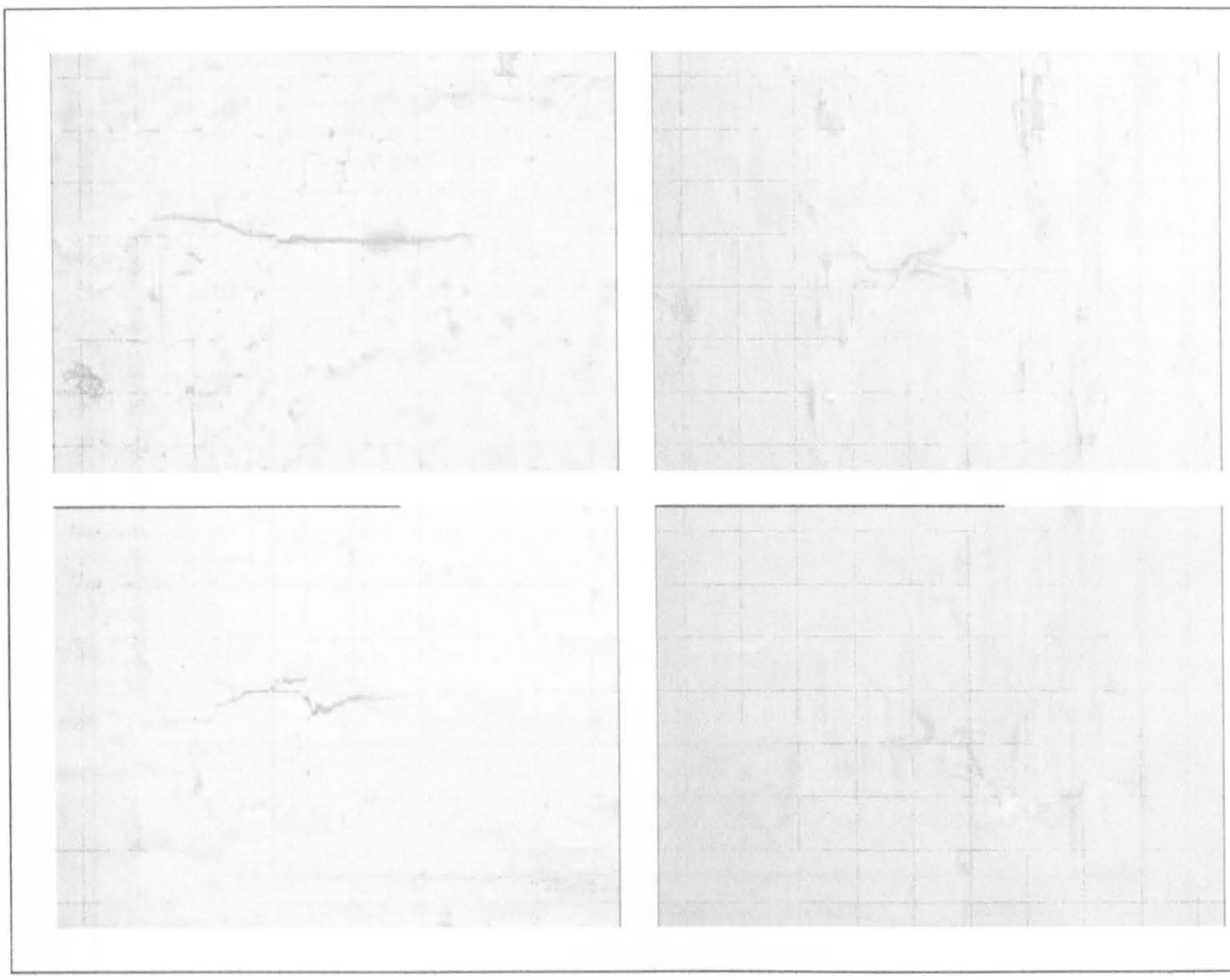

Figure 6.84: FS SP SCG replicas of 18.1 at 112000 cycles, 2c = 192 μm, (upper left) and at 77000 cycles, 2c = 65 μm, (upper right) and 18.3 at 93000 cycles, 2c = 205 μm, (lower left) and at 15000 cycles, 2c = 72 μm, (lower right).

Variability in the crack growth rate was evident throughout the range of measurements as depicted in Figure 6.85. As the other SCG specimens exhibited considerable variability in the propagation rate in the SCG regime, Figure 6.86 suggested that SCG occurred up to the maximum crack length measured, 169 μm, equivalent to approximately 17 grains in the SP weld nugget. The (dc/dN)/c data displayed in Figure 6.86 exhibited scatter greater than that observed in the other SCG specimens, this may be partly explained by the smaller range over which the cracks were measured, scatter generally being more pronounced in the earlier stages of crack growth in all the specimens. Although the scatter was more prominent, the log-log scale still exhibited a linear trend representing a decrease in the crack growth rate as the crack size decreased. The minimum crack growth rate measured was 10^{-11} m.cycle^{-1}, but the typical range extended from 0.1-10 x 10^{-9} m.cycle^{-1}.

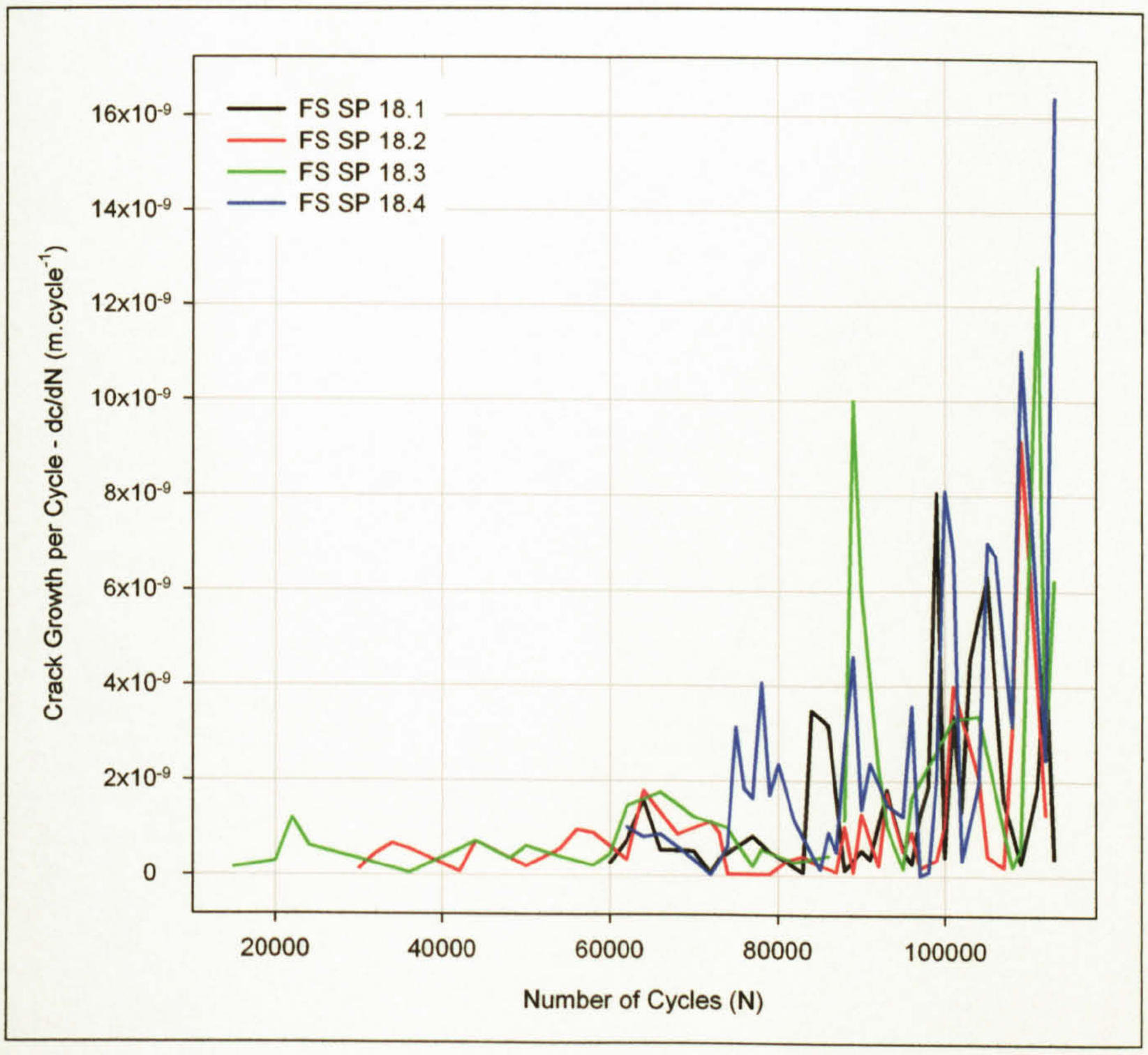

Figure 6.85: FS SP SCG data, crack growth per cycle/number of cycles.

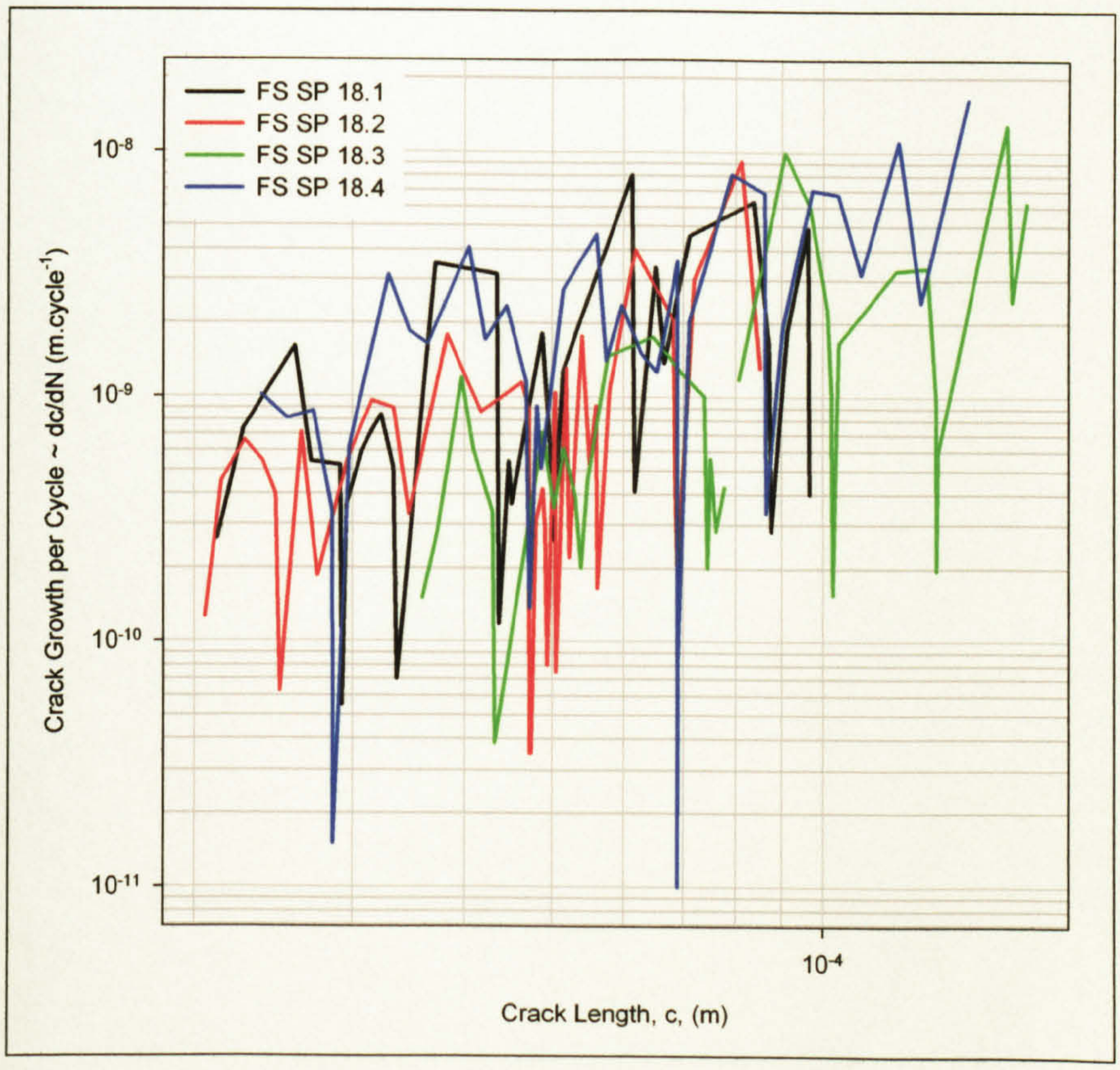

Figure 6.86: FS SP SCG data, crack growth per cycle/crack length.

6.4.8.2.2 Long Crack Growth ~ FS Single Pass

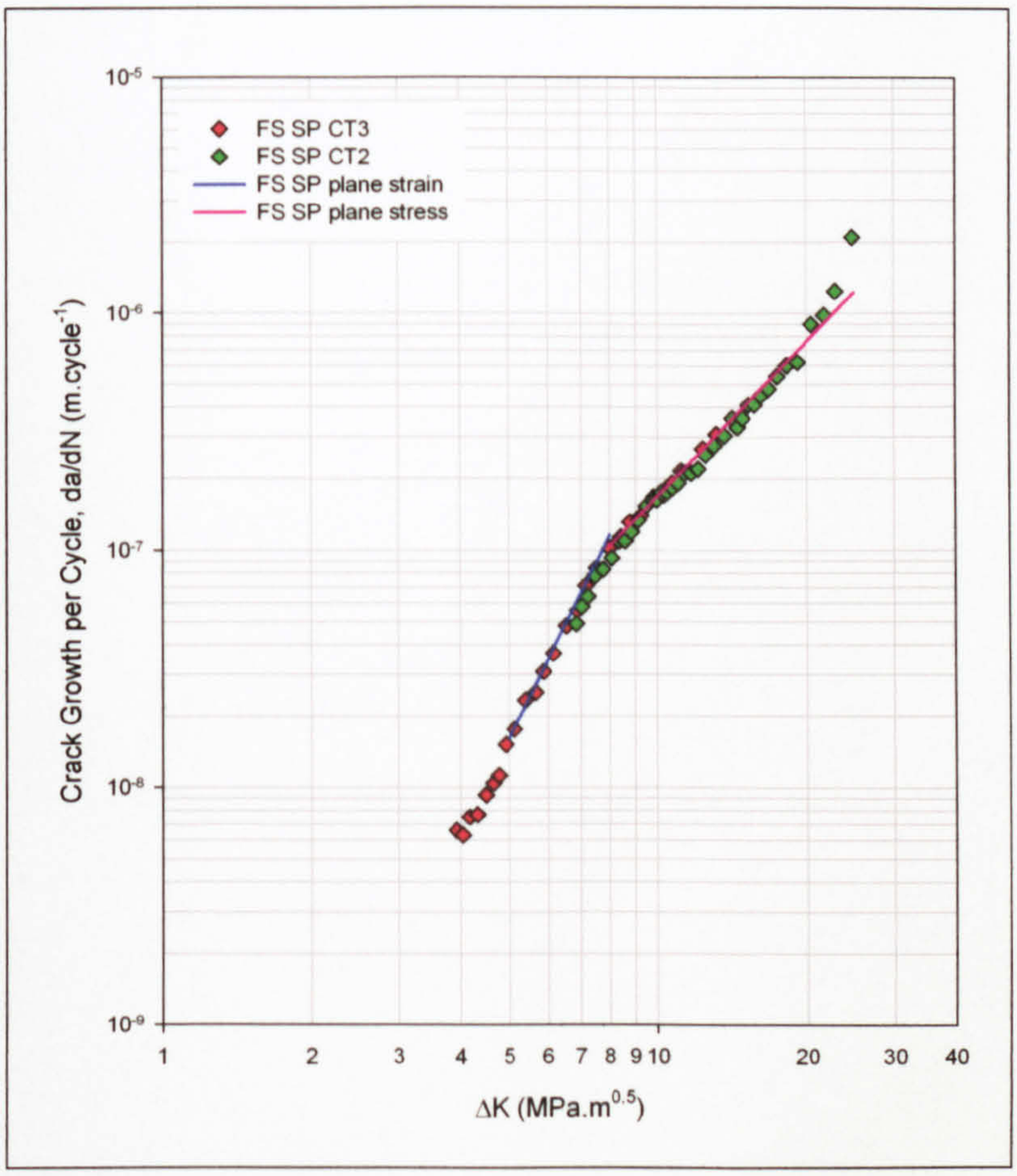

Figure 6.87: Fatigue crack growth rate (R = 0.1) ~ AA 5383-H321 FS SP butt weld.

ΔK_0 ($K_{max,0}$) (MPa.m$^{0.5}$)	Paris Equation $da/dN = C(\Delta K_{R=0.1})^m$				
	Plane strain $\Delta K \leq 9.0$		Calculated K_{max} for plane strain (6.17)	Plane stress $9.0 < \Delta K$	
	C	m		C	m
3.9 (4.3)	17.99×10^{-12}	4.219	5.7	1.18×10^{-9}	2.159

Table 6.12: Paris equation constants for fatigue crack growth in AA 5383-H321 FS SP butt weld.

The long crack threshold for the friction stir single pass weld, as shown in Figure 6.87, was in the region of 4.0 MPa.m$^{0.5}$. The change between predominantly plane strain and plane stress occurred between 8.5 - 9.5 MPa.m$^{0.5}$, a value greater than that returned by equation (6.17), $\Delta K = 5.13$ MPa.m$^{0.5}$, this being accompanied by a decrease in the crack propagation rate. The Paris equation constants are shown as equations (6.26) and (6.27) for the predominantly plane strain and plane stress regimes respectively.

$$\left(da/dN\right)_{\text{plane strain}} = 17.99\times10^{-12}\times(\Delta K)^{4.219} \tag{6.26}$$

$$\left(da/dN\right)_{\text{plane stress}} = 1.176\times10^{-9}\times(\Delta K)^{2.159} \tag{6.27}$$

6.4.8.2.3 Short Crack Growth ~ FS Double Pass Advancing

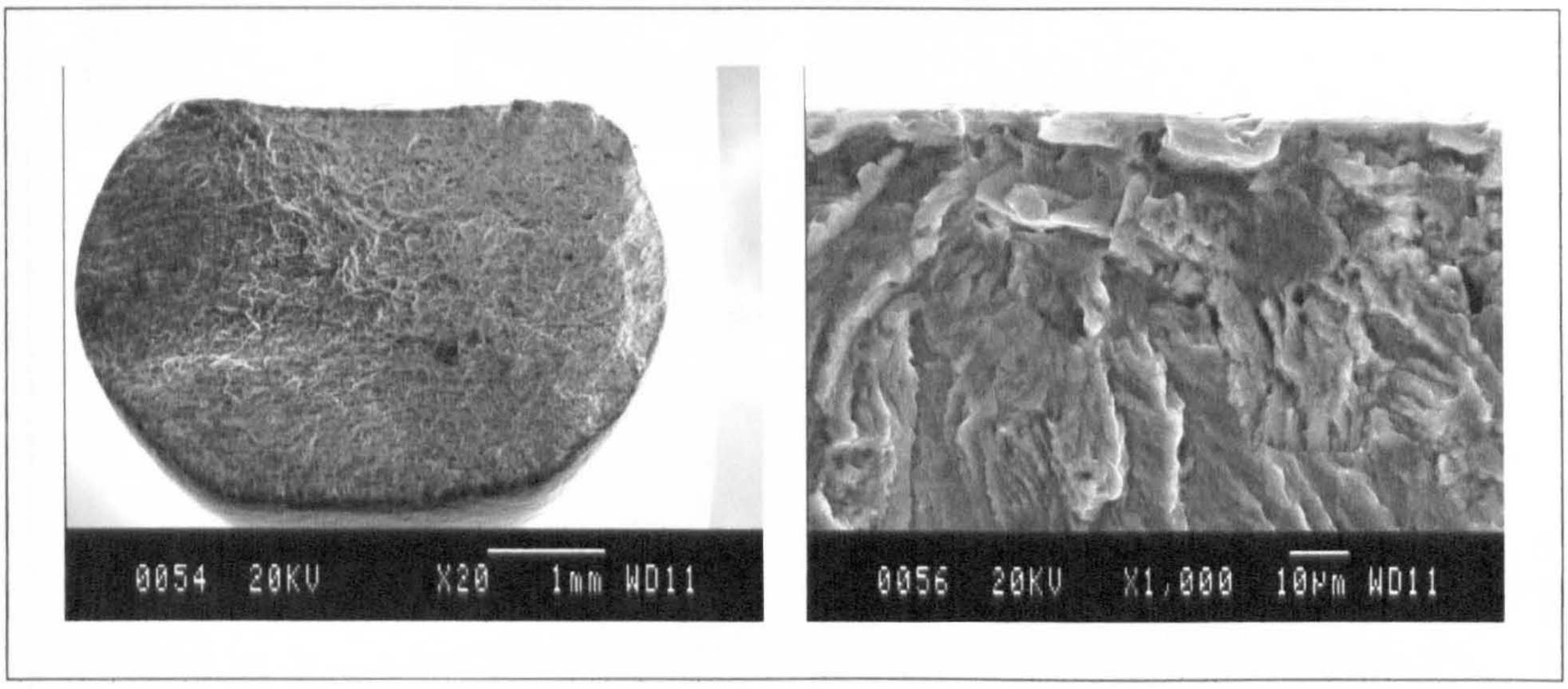

Figure 6.88: FS DPA SCG fracture surface (left) and initiation site (right).

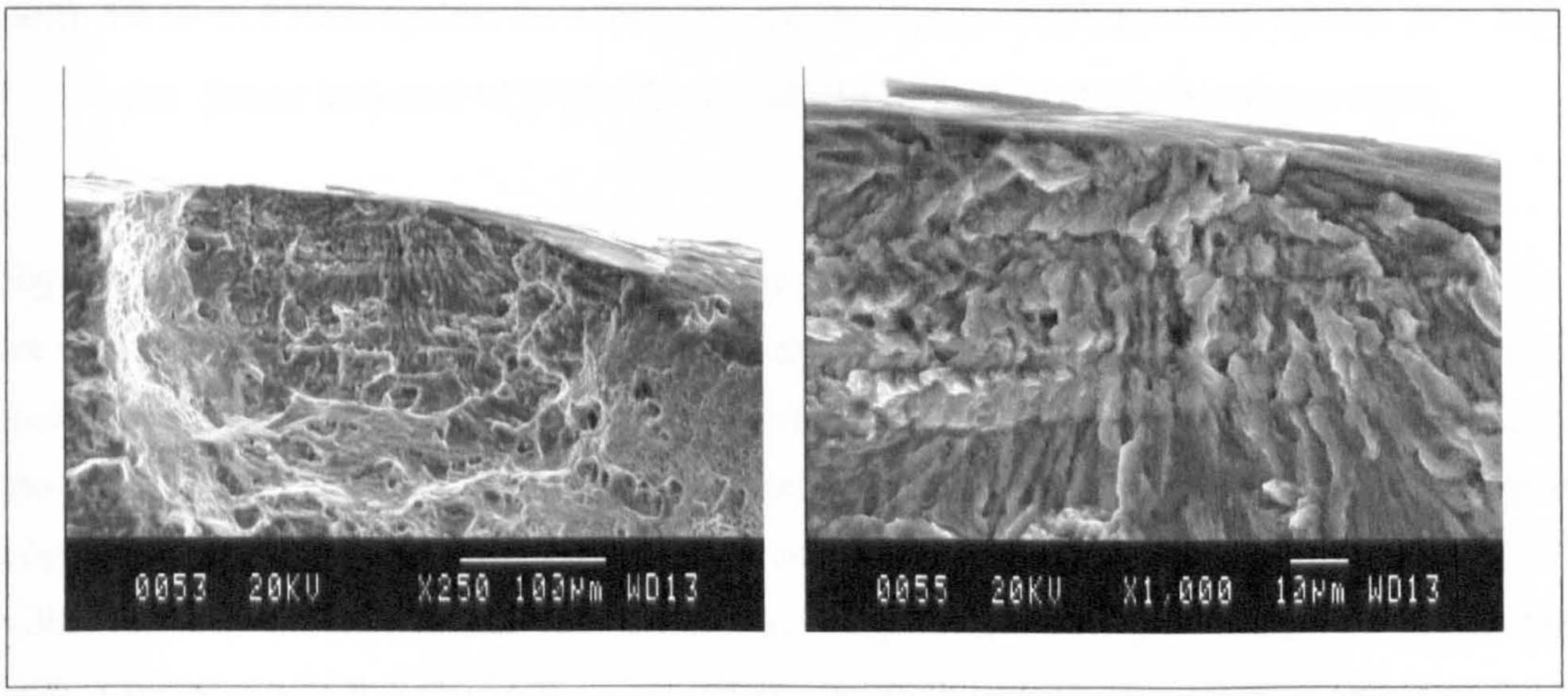

Figure 6.89: FS DPA SCG secondary crack fracture surface (left) and initiation site (right).

Failure of the specimen revealed multiple cracks on the exposed fracture surface, as shown in Figure 6.88 (left); the main crack being evident in the middle of the upper surface and secondary cracks being evident, upper right (Figure 6.89 (left)) and lower middle. Crack initiation of both the main crack, Figure 6.88 (right) and a secondary crack, Figure 6.89 (right), were the result of intermetallic inclusions. Crack coalescence was observed in all the cracks analysed and path tortuousity was also prevalent, evident in Figure 6.90.

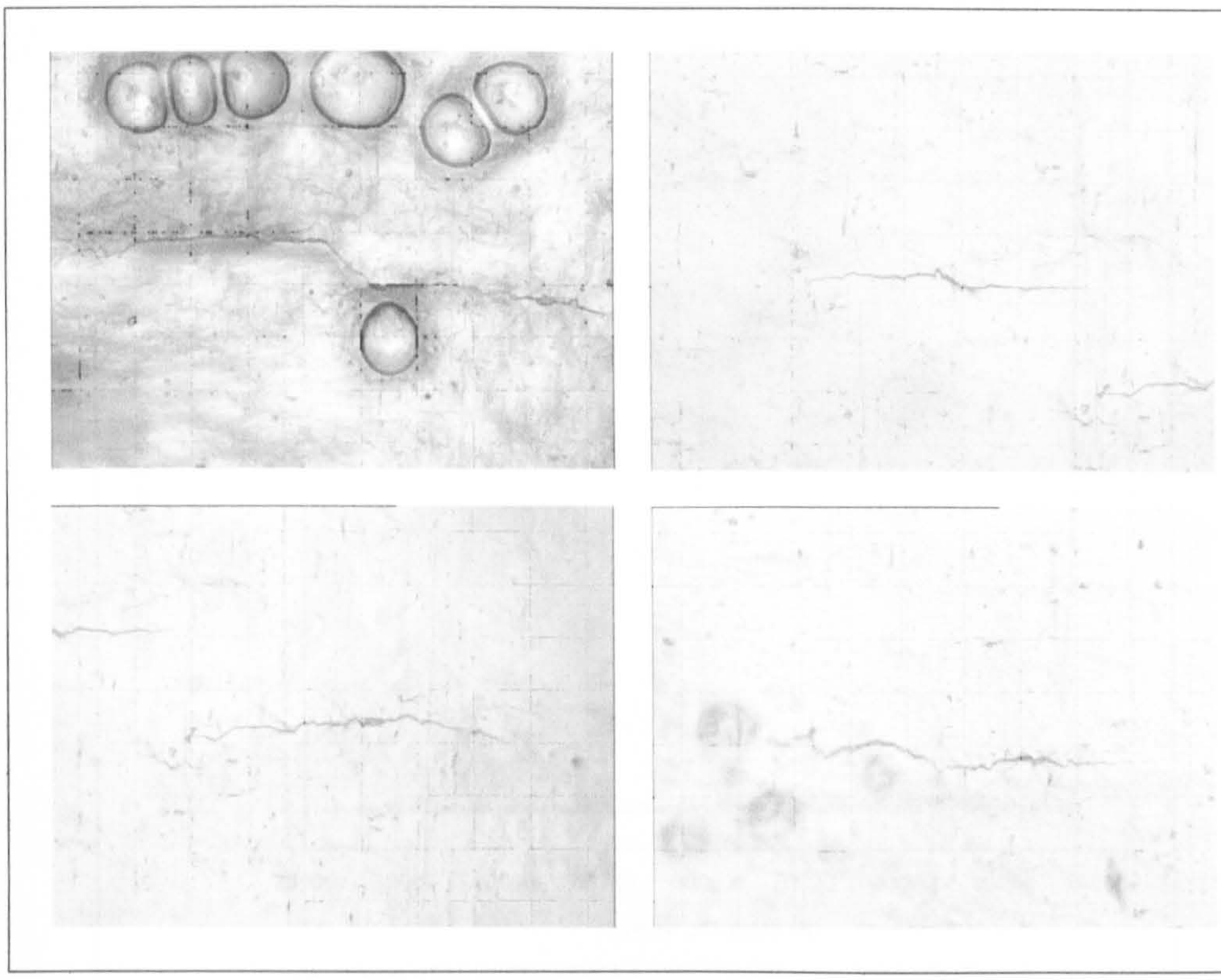

Figure 6.90: FS DPA SCG replicas of 13.1 (A + B) at 95000 cycles, 2c = 1457 µm, (upper left), 13.1A at 81000 cycles, 2c = 343 µm, (upper right), 13.1B at 81000 cycles, 2c = 382 µm, (lower left) and 13.2 (A + B) at 99000 cycles, 2c = 528 µm, (lower right).

Significant variation in the crack growth rates was evident in the FS DPA SCG specimen, as shown in Figure 6.91, up to 20 x 10^{-9} m.cycle^{-1}. Reference to Figure 6.92 suggested that this would equate to a crack length, c, of 250 - 300 µm, approximately 5 - 6 grains in the HAZ of the DP weld. Visual examination of the (dc/dN)/c plots in Figure 6.92 again suggested a linear relationship, when observed on a log-log scale, for crack lengths of 70 - 300 µm, with a similar linear relationship existing for crack lengths from 30 - 70 µm, but with a decrease in the gradient. The minimum crack growth rate determined was 2-3 x 10^{-11} m.cycle^{-1}, although the characteristic range was 0.2-20 x 10^{-9} m.cycle^{-1}.

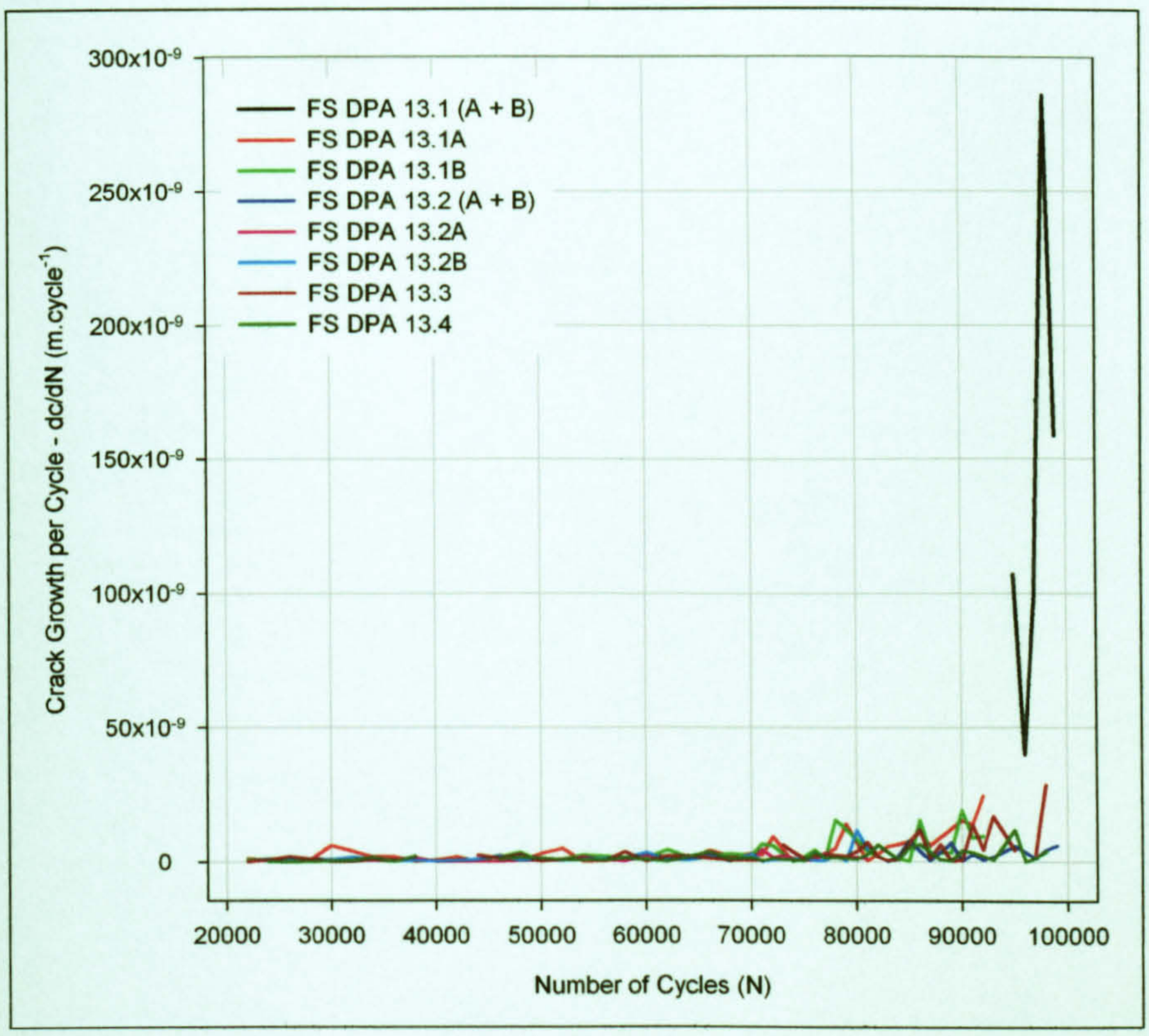

Figure 6.91: FS DPA SCG data, crack growth per cycle/number of cycles.

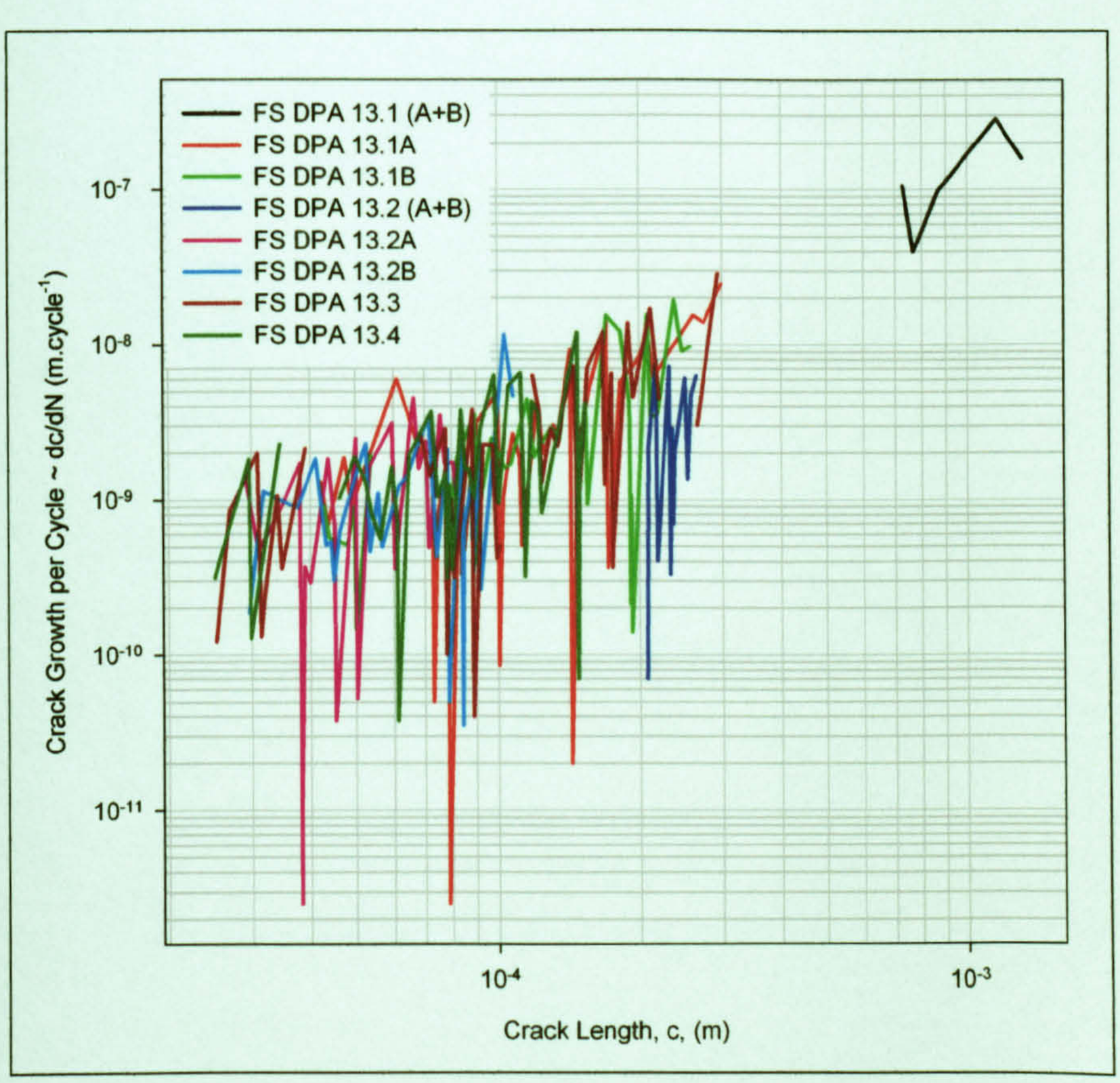

Figure 6.92: FS DPA SCG data, crack growth per cycle/crack length.

6.4.8.2.4 Long Crack Growth ~ FS Double Pass Advancing

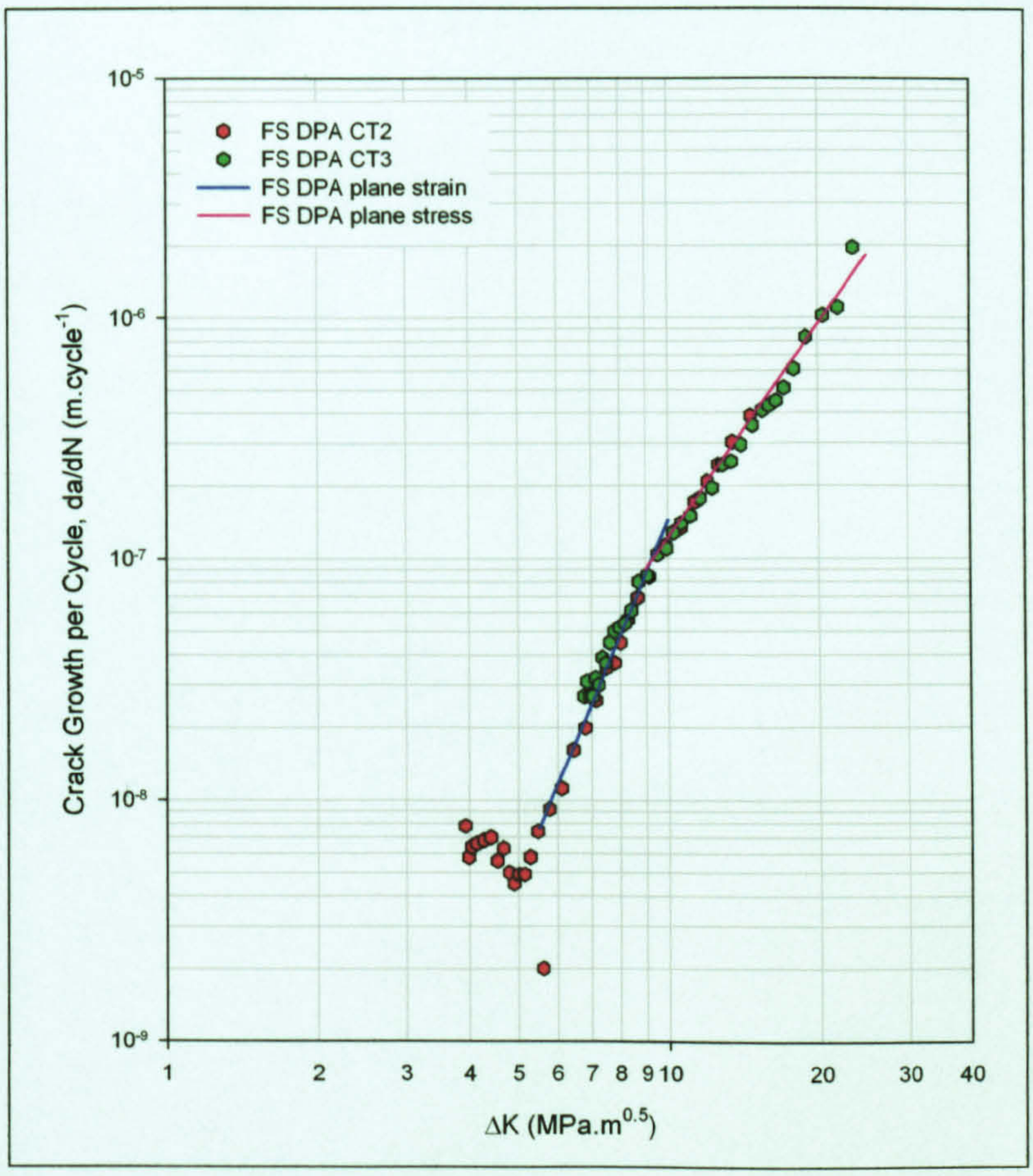

Figure 6.93: Fatigue crack growth rate (R = 0.1) ~ AA 5383-H321 FS DPA butt weld.

ΔK_0 ($K_{max,0}$) (MPa.m$^{0.5}$)	Paris Equation $da/dN = C(\Delta K_{R=0.1})^m$				
	Plane strain $\Delta K \leq 9.0$		Calculated K_{max} for plane strain (6.17)	Plane stress $9.0 < \Delta K$	
	C	m		C	m
3.9 (4.3)	1.77×10^{-12}	4.908	6.2	138.38×10^{-12}	2.946

Table 6.13: Paris equation constants for fatigue crack growth in AA 5383-H321 FS DPA butt weld.

The Paris equations are detailed as equation (6.28), for plane strain, and equation (6.29), for plane stress; the transition between the two occurring in the region of $\Delta K = 9 - 10$ MPa.m$^{0.5}$, the calculated value for the change in the stress state, $\Delta K = 5.58$ MPa.m$^{0.5}$, being considerably less than the experimental value. The change in the stress state resulted in a reduction in the propagation rate as plane stress prevailed. The long crack fatigue threshold was difficult to determine with some growth being evident below 4 MPa.m$^{0.5}$, although further crack growth arrest occurred between 4 - 5 MPa.m$^{0.5}$.

$$\left(da/dN\right)_{\text{plane strain}} = 1.77 \times 10^{-12} \times (\Delta K)^{4.908} \tag{6.28}$$

$$\left(da/dN\right)_{\text{plane stress}} = 138.38 \times 10^{-12} \times (\Delta K)^{2.946} \tag{6.29}$$

6.4.8.2.5 Short Crack Growth ~ FS Double Pass Retreating

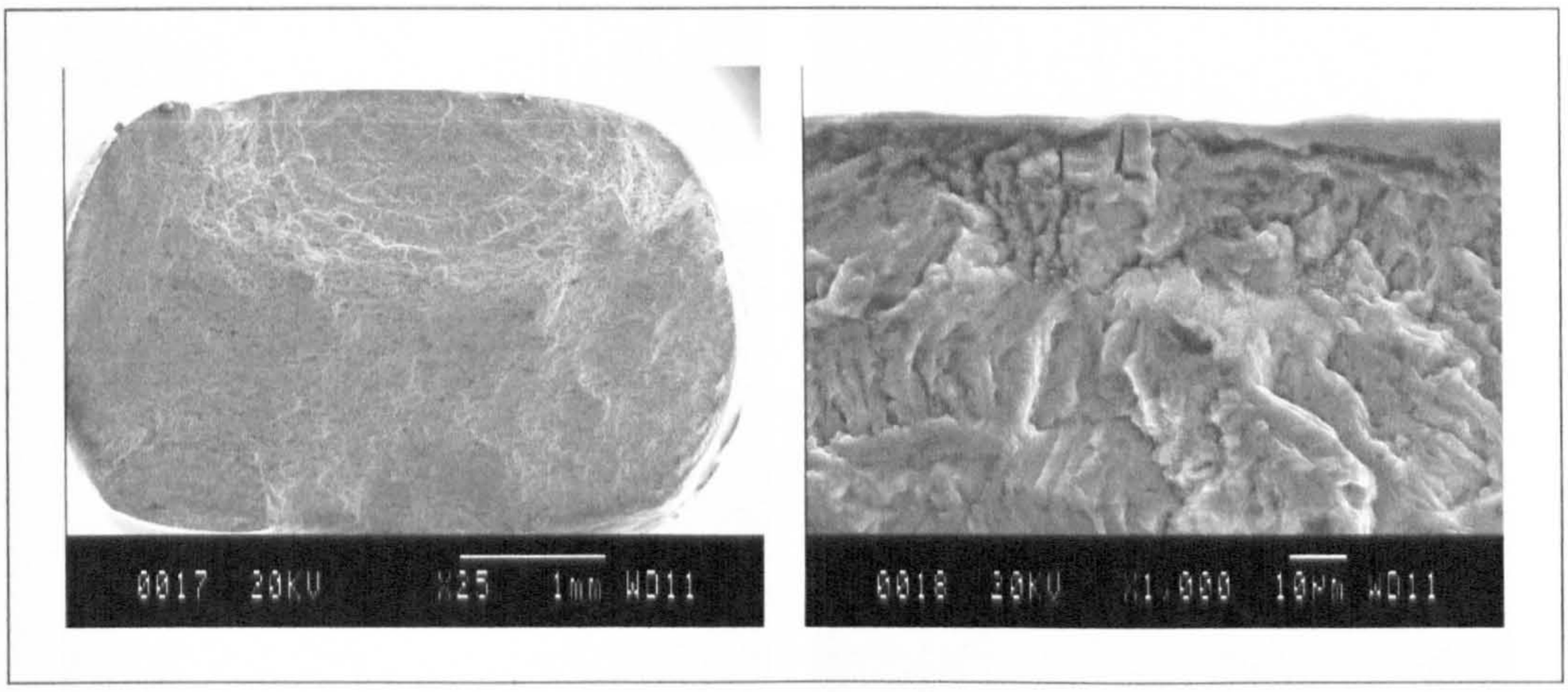

Figure 6.94: FS DPR SCG specimen fracture surface (left) and principal crack initiation site (right).

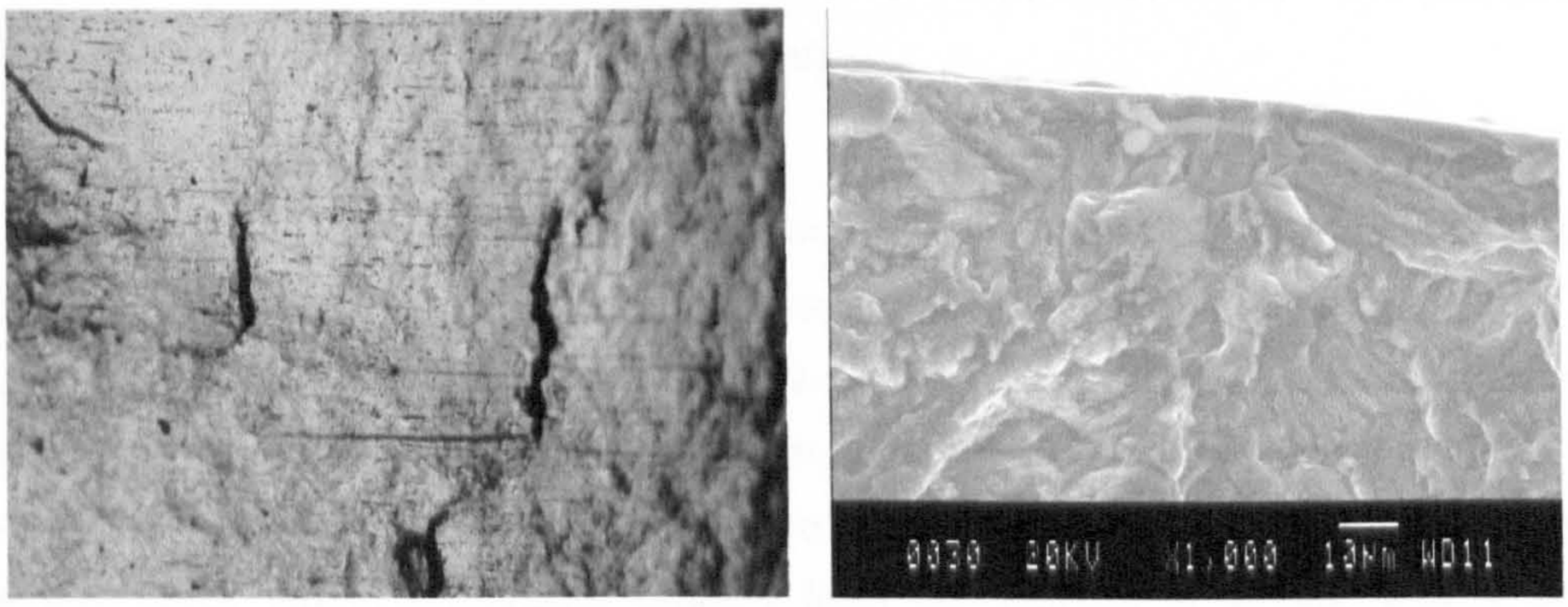

Figure 6.95: FS DPR SCG crack paths (left) and intermetallic induced initiation site of a secondary crack (right).

Crack initiation in the FS DPR SCG specimen was intermetallic induced, as evident in Figure 6.94 (right) and Figure 6.95 (right). The exposed fracture surface, shown in Figure 6.94 (left), shows both the principal and two other significant cracks. Crack coalescence was observed in half of the four cracks analysed, with crack tortuousity increasing in those cracks exhibiting coalescence, as shown in Figure 6.95 (left) and Figure 6.96.

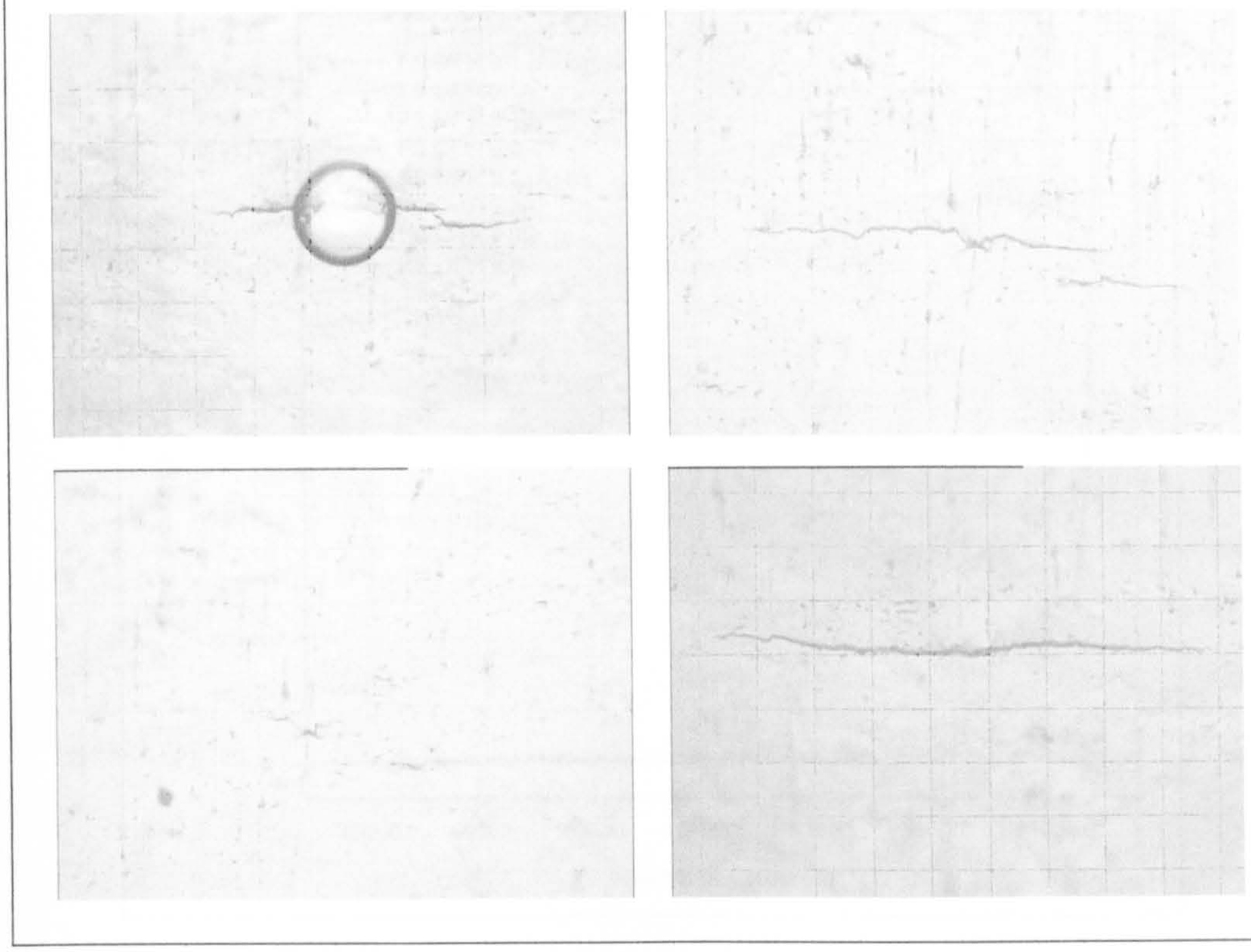

Figure 6.96: FS DPR SCG plastic replicas of 9.1 (A + B) at 91000 cycles, 2c = 384 µm, (upper left), 9.1A & 9.1B at 82000 cycles, 2c = 221 & 84 µm respectively, (upper right), 9.1A 26000 cycles, 2c = 60 µm, (lower left) and 9.2 at 87000 cycles, 2c = 289 µm, (lower right).

As with the other SCG specimens that surface replicas were obtained from, significant variability was evident in the data up to crack growth rates of 20×10^{-9} m.cycle^{-1}, as shown in Figure 6.97 and Figure 6.98. This growth rate would suggest that SCG was occurring up to crack sizes of ~225 µm, in the region of 4 - 5 grains of the DP HAZ. The log-log plot depicted in Figure 6.98 exhibited a linear response between the crack growth rate and crack length for cracks ranging from 50 - 225 µm in length, with a linear response, albeit with a slightly lesser gradient, for cracks of 10 - 50 µm in length. The typical range of crack growth rates was from $0.2\text{-}20 \times 10^{-9}$ m.cycle^{-1}, whilst the lowest recorded was ~6×10^{-12} m.cycle^{-1}.

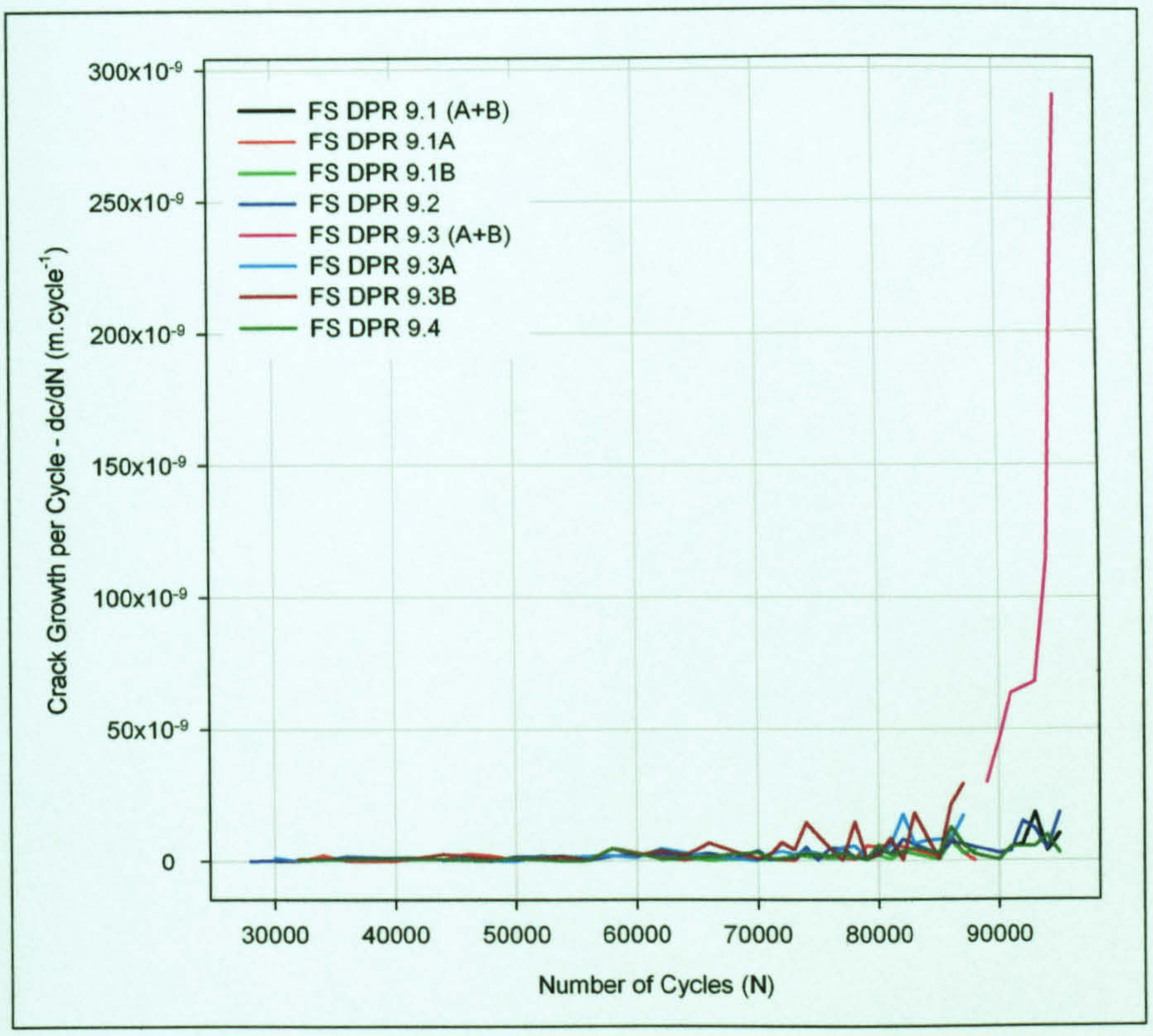

Figure 6.97: FS DPR SCG data, crack growth per cycle/number of cycles.

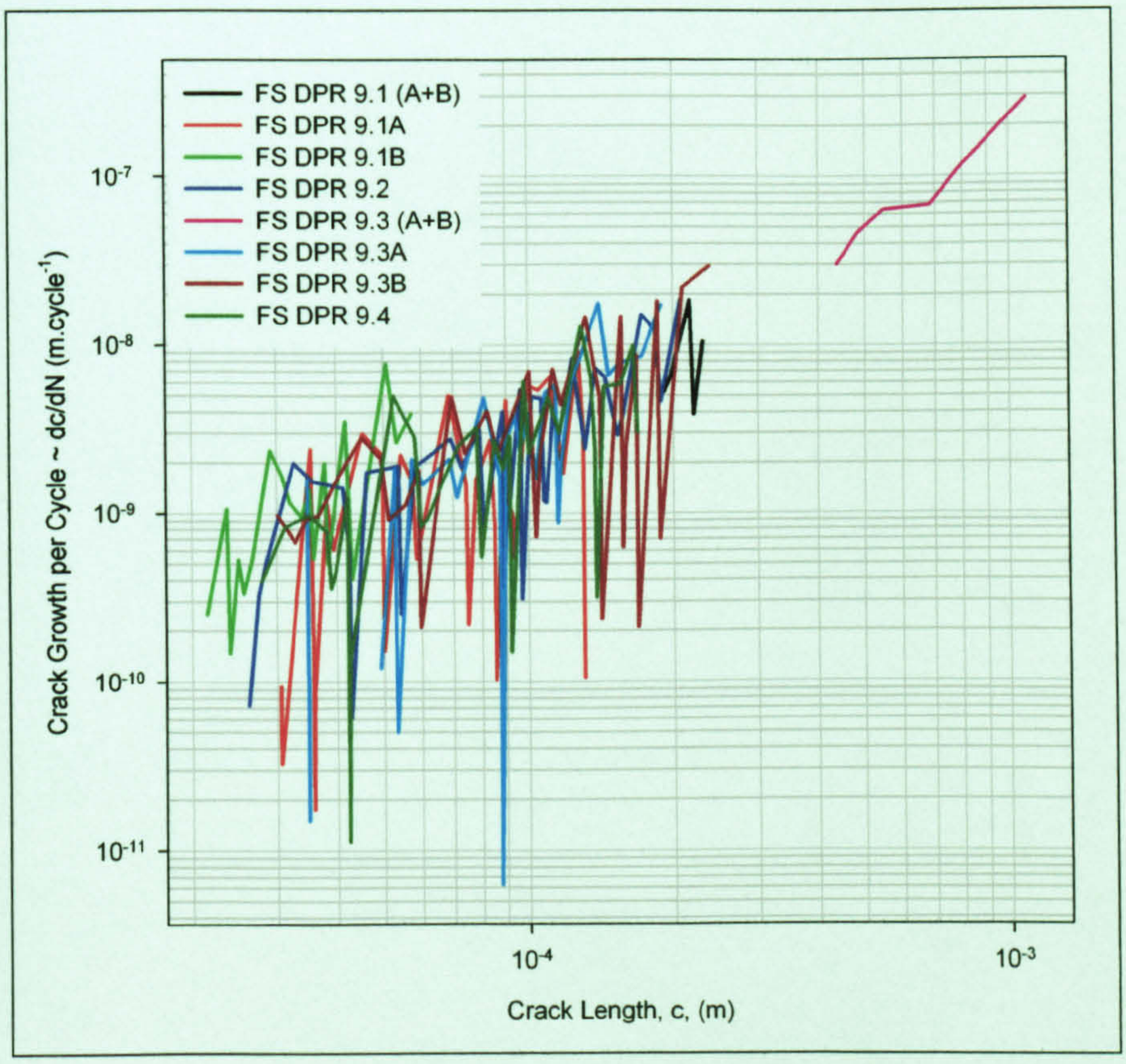

Figure 6.98: FS DPR SCG data, crack growth per cycle/crack length.

6.4.8.2.6 Long Crack Growth ~ FS Double Pass Retreating

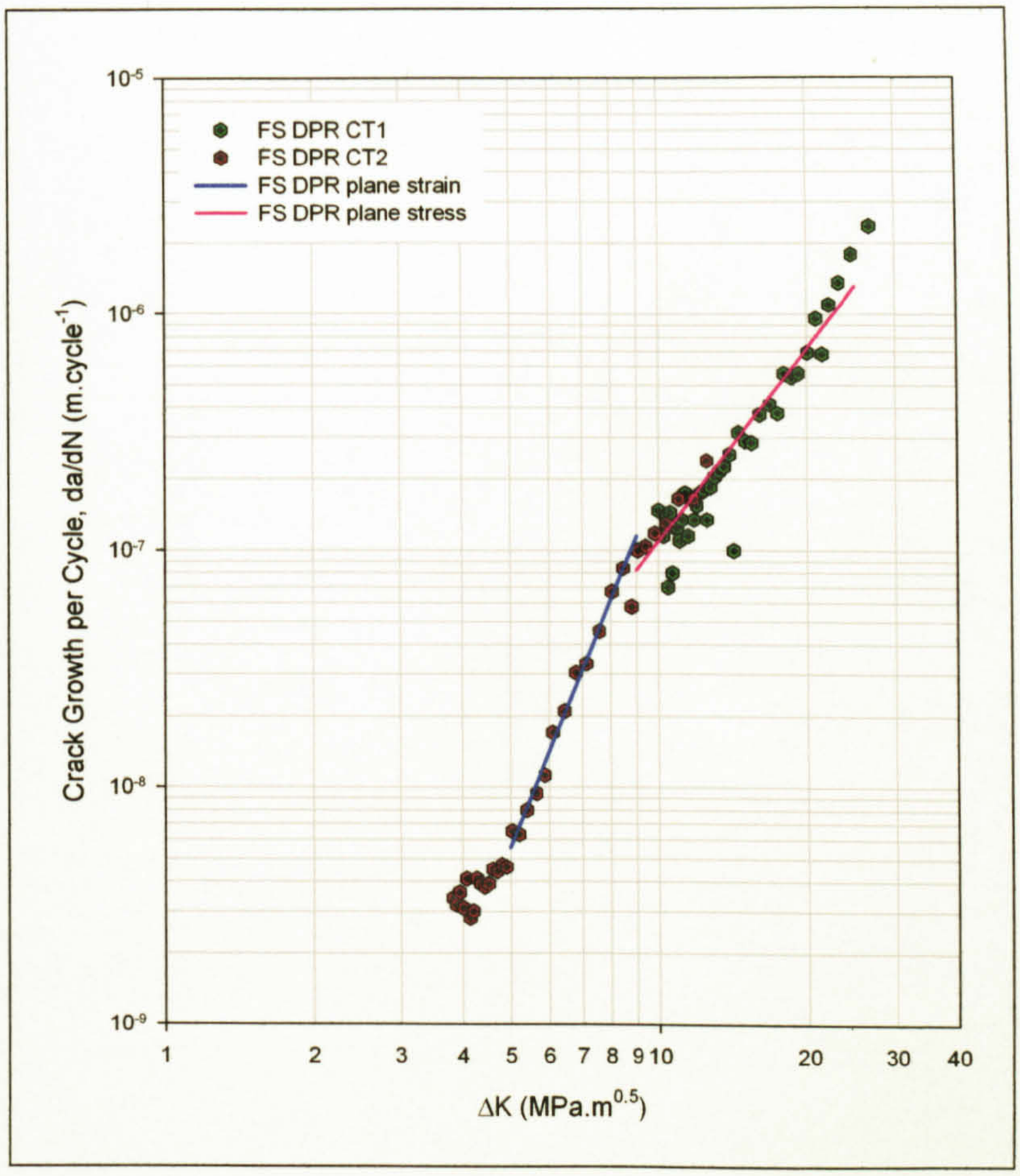

Figure 6.99: Fatigue crack growth rate (R = 0.1) ~ AA 5383-H321 FS DPR butt weld.

ΔK_0 ($K_{max,0}$) (MPa.$m^{0.5}$)	Paris Equation $da/dN = C(\Delta K_{R=0.1})^m$				
	Plane strain $\Delta K \leq 9.0$		Calculated K_{max} for plane strain (6.17)	Plane stress $9.0 < \Delta K$	
	C	m		C	m
3.8 (4.2)	1.40×10^{-12}	5.147	6.2	211.62×10^{-12}	2.713

Table 6.14: Paris equation constants for fatigue crack growth in AA 5383-H321 FS DPR butt weld.

A decrease in the crack propagation rate was evident as the stress state changed from primarily plane strain to plane stress, the change being observed at 9 MPa.$m^{0.5}$, notably greater than the value returned by equation (6.17), $\Delta K = 5.58$ MPa.$m^{0.5}$. The fatigue threshold occurred around $\Delta K = 4.0$ MPa.$m^{0.5}$. The Paris equations are depicted as equations (6.30) and (6.31) for plane strain and stress respectively.

$$\left(da/dN\right)_{\text{plane strain}} = 1.40 \times 10^{-12} \times (\Delta K)^{5.147} \tag{6.30}$$

$$\left(da/dN\right)_{\text{plane stress}} = 211.62 \times 10^{-12} \times (\Delta K)^{2.713} \tag{6.31}$$

6.5 Discussion

6.5.1 Short Crack Growth

One of the problems associated with the analysis of short crack growth rates has been the difficulty in assigning a crack driving force parameter. Long cracks in the regime B growth region frequently exhibit a power law relationship between the growth rate and the crack driving force ΔK, but short cracks do not conform to the same relationship. Figure 6.100 to Figure 6.106 (the line plots on the right of the figures have been smoothed using a bisquare weighting with a sampling proportion of 0.2 and a single degree polynomial) depict both the short and long crack growth rates for the parent material and welds against the crack driving force. In regime B, when plotted on a log-log plot, a linear relationship was clearly apparent between the growth rate and crack driving force for the long cracks (the slight deviation in this considered to be due to the change in stress state from being predominantly plane strain to plane stress), but this relationship was only observed in the SCG specimen results when the short crack had grown to a length that resulted in it exhibiting long crack behaviour, evident in Figure 6.100 to Figure 6.106. For values of ΔK below the long crack growth threshold short cracks continued to exhibit growth and this was frequently at values greater than that observed for the long cracks in the threshold region.

The SCG results obtained from both the PP |- and // specimens exhibited propagation below the long crack threshold stress intensity factor and at rates greater than those returned by the long cracks for $\Delta K < \Delta K_0$, as shown in Figure 6.100 and Figure 6.101. The PP |- SCG data, Figure 6.100, appeared to be merging with that of the corresponding LCG data for $\Delta K \geq 10\ MPa.m^{0.5}$ although the response appeared comparable to that depicted in Figure 6.11 (page 316) for a short crack propagating in a notch subjected to an elastic stress field. The PP // SCG data, Figure 6.101, exhibited a comparable response to that observed in the PP |- specimen, although there was less evidence of the short and long crack growth data merging, this may have been due to the short cracks only being subjected to a maximum stress intensity factor of $5\ MPa.m^{0.5}$, half that experienced by the PP |-. It was assumed that the reason for the disparity between the SCG and LCG results, with respect to the stress intensity factor, was a consequence of the typical anomalies observed for short cracks; with microstructural effects and coalescence being responsible for the variability observed in the growth rate for c < 100 - 500 μm for the PP |- (50 - 100 μm structural unit size) and c < 60 - 300 μm for the PP // (30 - 60 μm structural unit size). The increased growth rates observed, when compared to the long crack data, were considered to be a consequence of reduced crack closure in the short cracks.

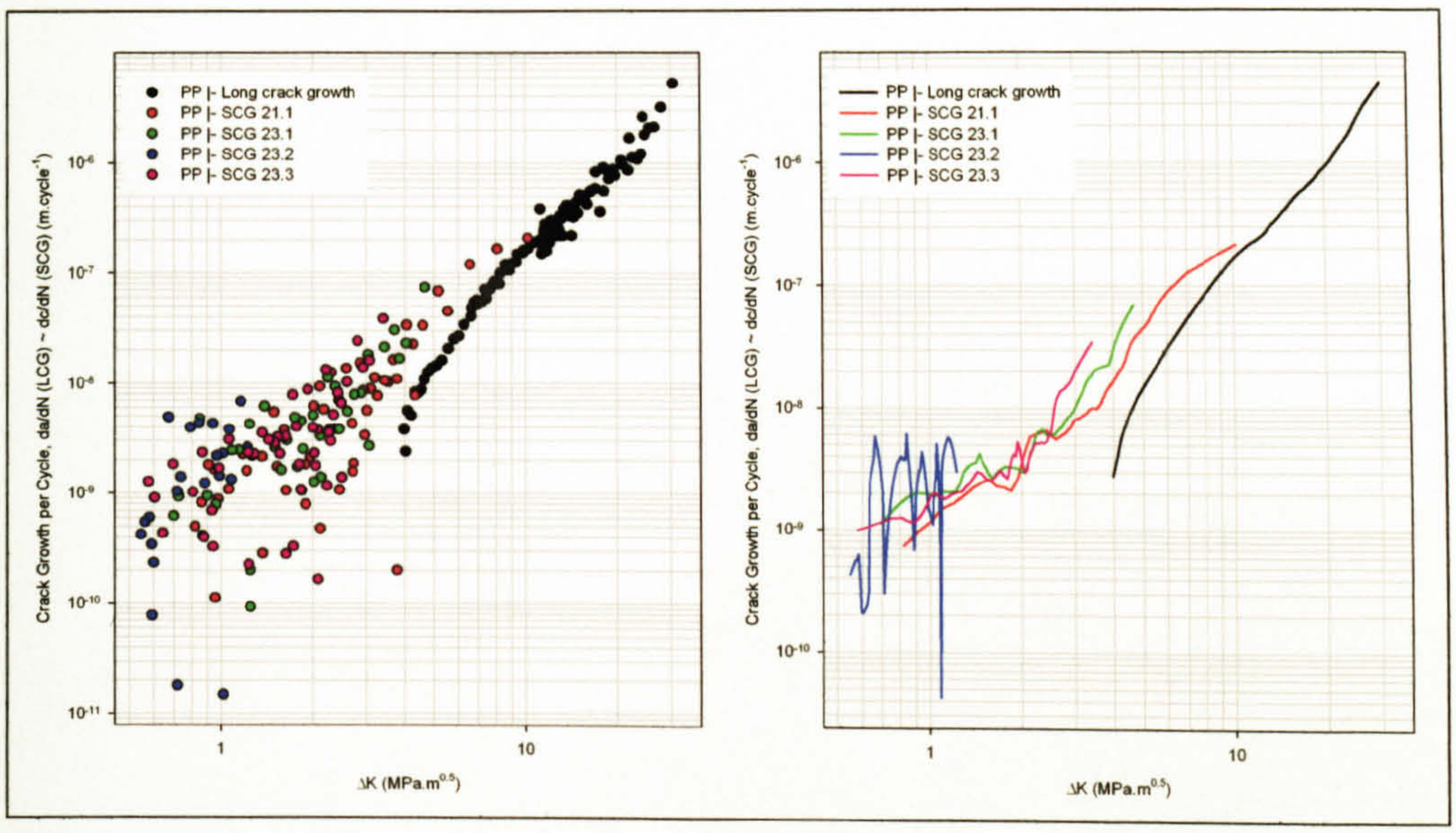

Figure 6.100: AA 5383-H321 parent plate |- long and short crack growth rates with respect to ΔK.

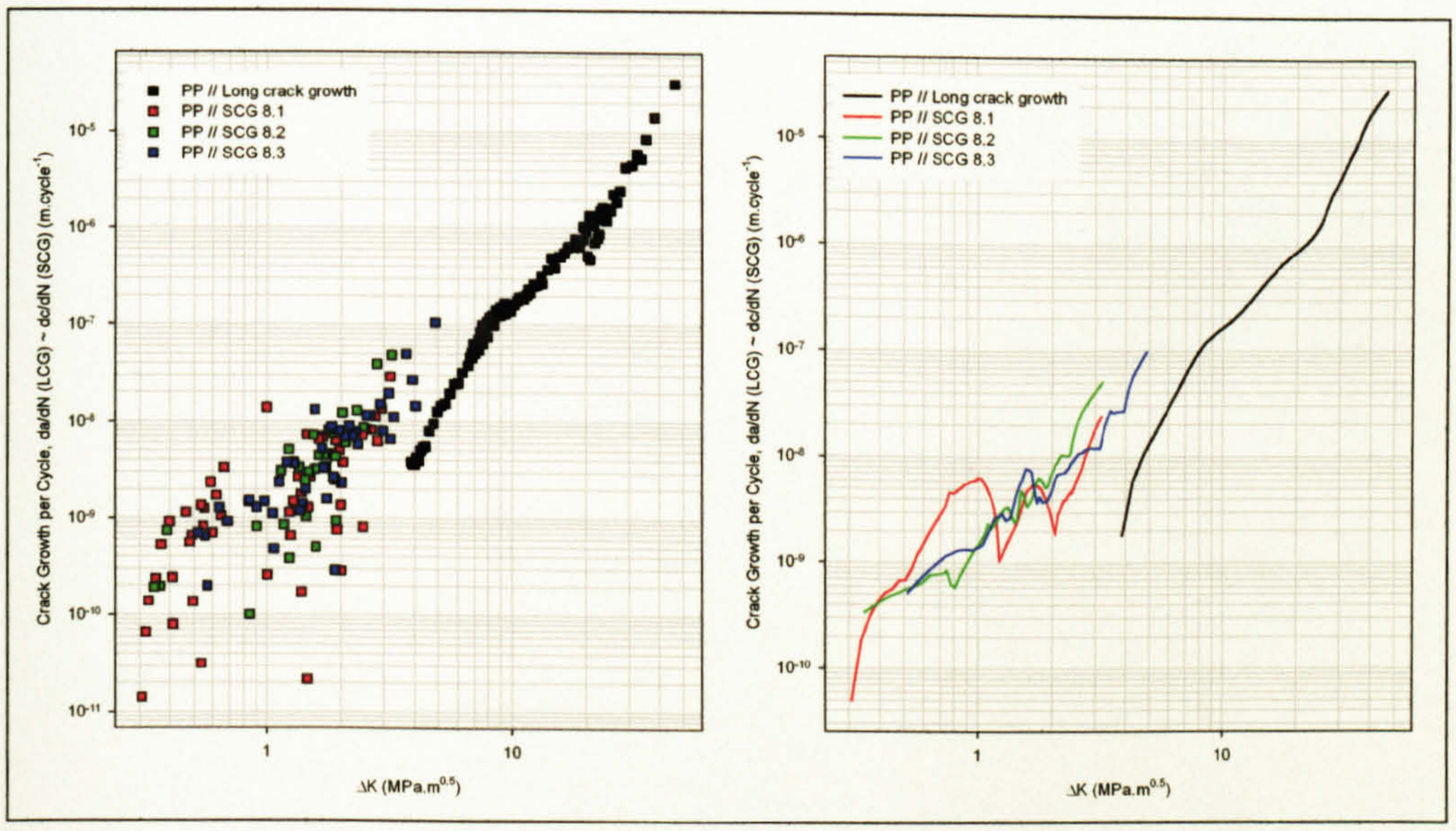

Figure 6.101: AA 5383-H321 parent plate // long and short crack growth rates with respect to ΔK.

The SCG observed in the MIG welded specimens exhibited crack growth both below the long crack threshold and at greater rates when analysed with respect to the stress intensity factor, as shown in Figure 6.102 and Figure 6.103. For $\Delta K > 2 - 3$ MPa.m$^{0.5}$ the growth rate was observed to be increasing in a manner comparable to that observed in the LCG data, although it was displaced by -5 to -6 and -3 to -4 MPa.m$^{0.5}$ for the LI and HI welds respectively. Weld induced residual stress closure was probably the main instigator of this difference in propagation rates as the residual stress field in the SCG specimens would generally be considered to be reduced due to the small specimen size

in contrast to the CT specimens utilised for the LCG data. Figure 6.17 (page 321) suggested that the compressive residual stress field found in the vicinity of the crack tip in CT specimens, and resisting crack propagation, would be tensile in the SCG specimens, their geometry being more comparable to that of a MT specimen, and therefore any influence would be considered to result in enhanced propagation rates.

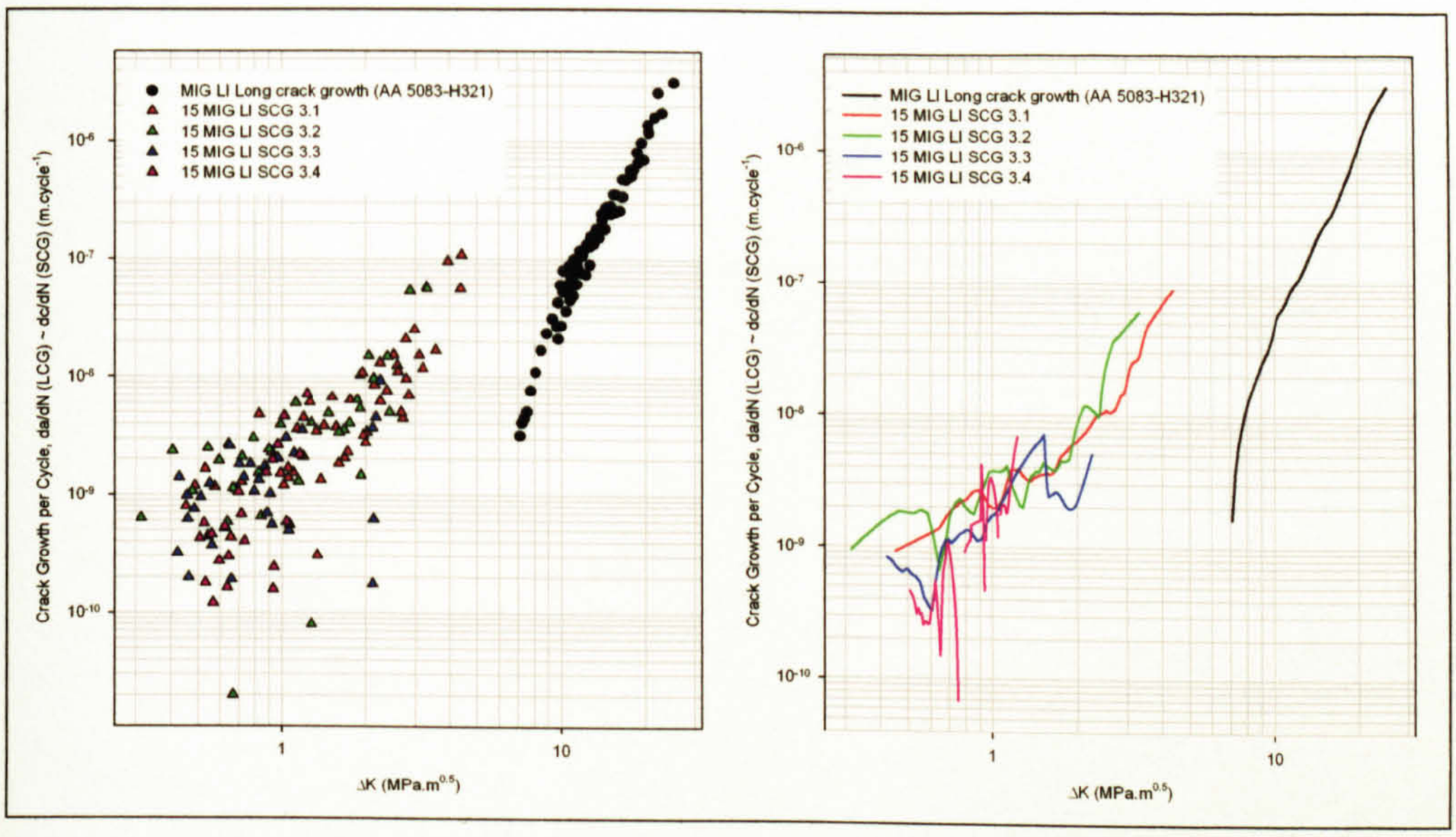

Figure 6.102: MIG LI butt weld long (AA 5083-H321) and short (AA 5383-H321) crack growth rates with respect to ΔK.

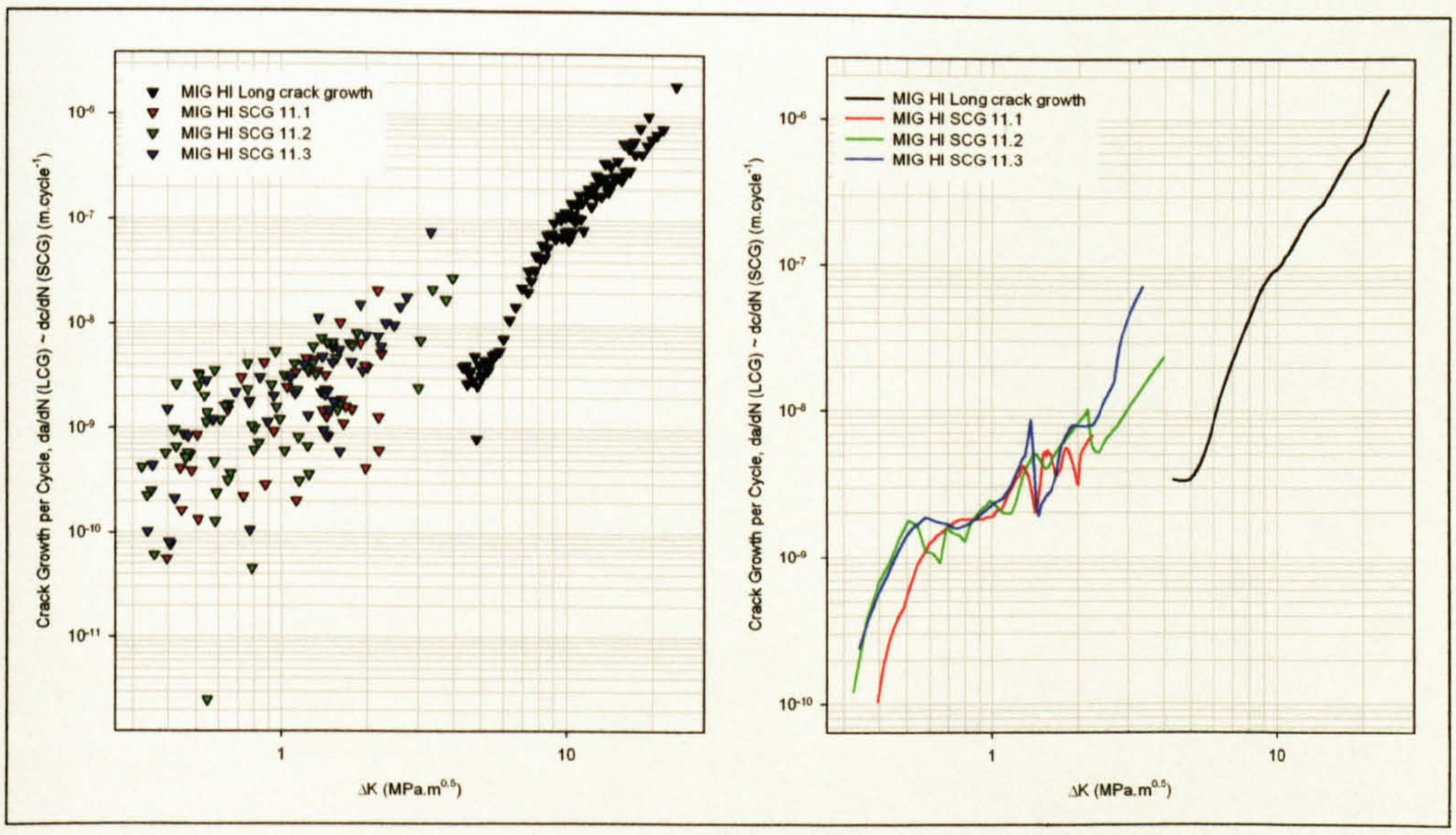

Figure 6.103: AA 5383-H321 MIG HI butt weld long and short crack growth rates with respect to ΔK.

For $\Delta K < 2 - 3$ MPa.m$^{0.5}$ the propagation rates exhibited greater variability, suggesting that microstructural influences and coalescence were reducing the propagation rate,

although this would be counteracted by reduced crack closure, the result being growth rates comparable to those observed in the long cracks near to their threshold limit and below this.

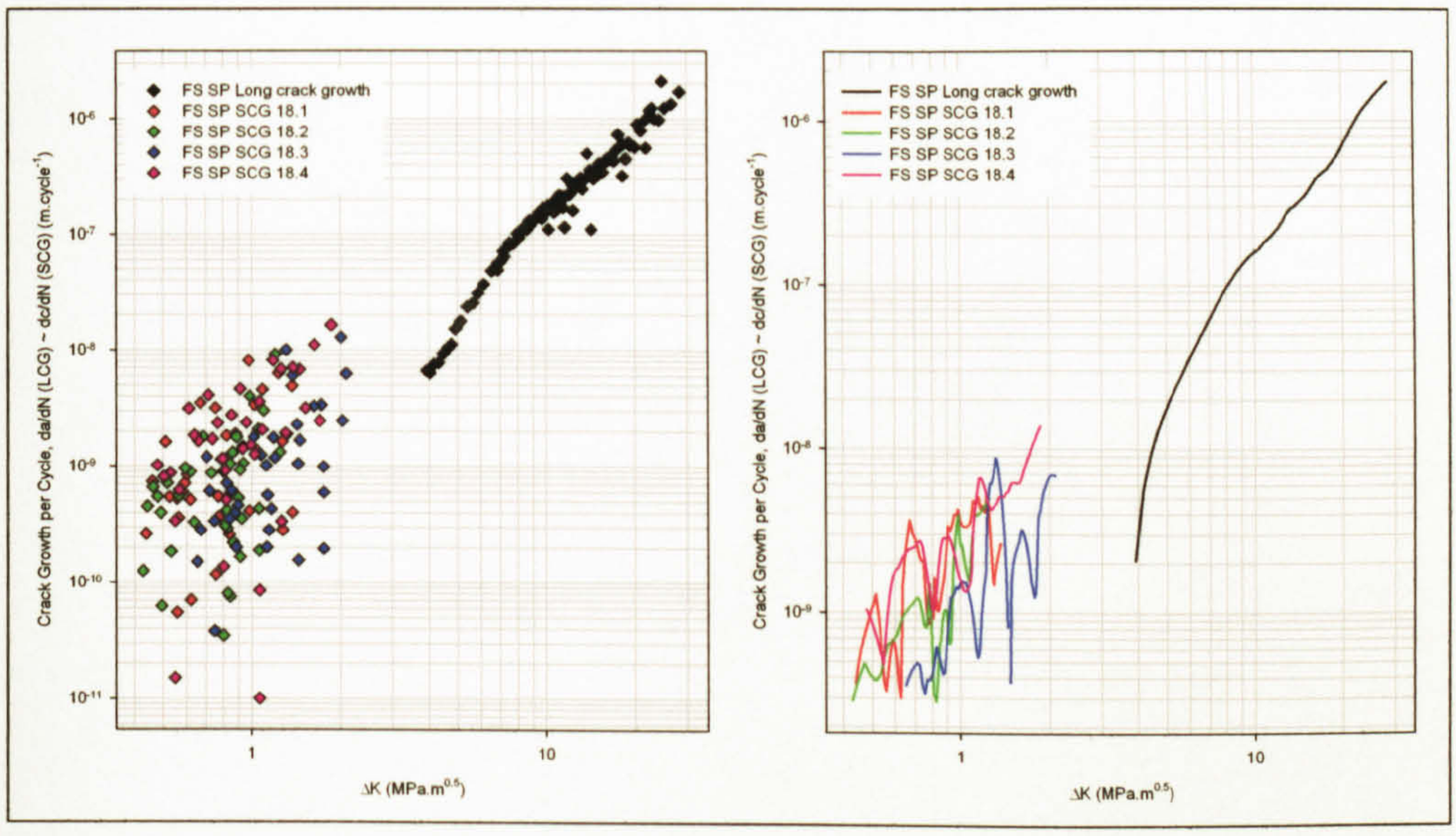

Figure 6.104: AA 5383-H321 FS SP butt weld long and short crack growth rates with respect to ΔK.

Due to PFD failures being prevalent in the FS SP specimens, growth rates were typically below 10^{-8} m.cycle^{-1} and stress intensities below 2 MPa.m$^{0.5}$, as shown in Figure 6.104. The transition between short and long cracks was not evident from the SCG specimen results. Crack propagation was evident below the long crack threshold stress intensity factor and at growth rates in excess of those observed in the LCG data. Significant variability was evident in the SCG rates even when data smoothing was applied and it is probable that this was related to the small grain size within the weld nugget, 10 μm, resulting in both crack deflection and retardation due to the propensity for grain boundary interactions. As with the MIG SCG specimens it would be expected that they would be influenced by the residual stress field enveloping the crack tip and that this would be tensile, in contrast to the compressive one in the vicinity of the (long) crack tip in the CT specimens. The tensile residual stress field would be expected to increase the crack propagation rates and also reduced crack closure in the SCG specimens, going someway to explaining the difference in the observed growth rates.

SCG rates observed in the FS DP weld, for both the advancing and retreating sides are shown in Figure 6.105 and Figure 6.106. For both sides of the weld crack propagation was observed at stress intensities below the long crack threshold and at growth rates greater than those observed in the long cracks. For both short and long cracks subjected to the same stress intensity factor range, ΔK = 4 - 10 MPa.m$^{0.5}$ the disparity between the

growth rates decreased as the stress intensity factor increased, with a subsequent near convergence of propagation rates being evident in the DPA results, Figure 6.105, for $\Delta K > 12$ MPa.m$^{0.5}$, although a similar convergence was not evident in the DPR results. The disparity between long and short crack growth rates at stress intensities and crack lengths greater than those typically associated solely with SCG was again considered to be associated with the weld induced residual stress field surrounding the crack tip region, with this causing increased crack closure in the CT specimens, and reduced crack closure in the SCG specimens.

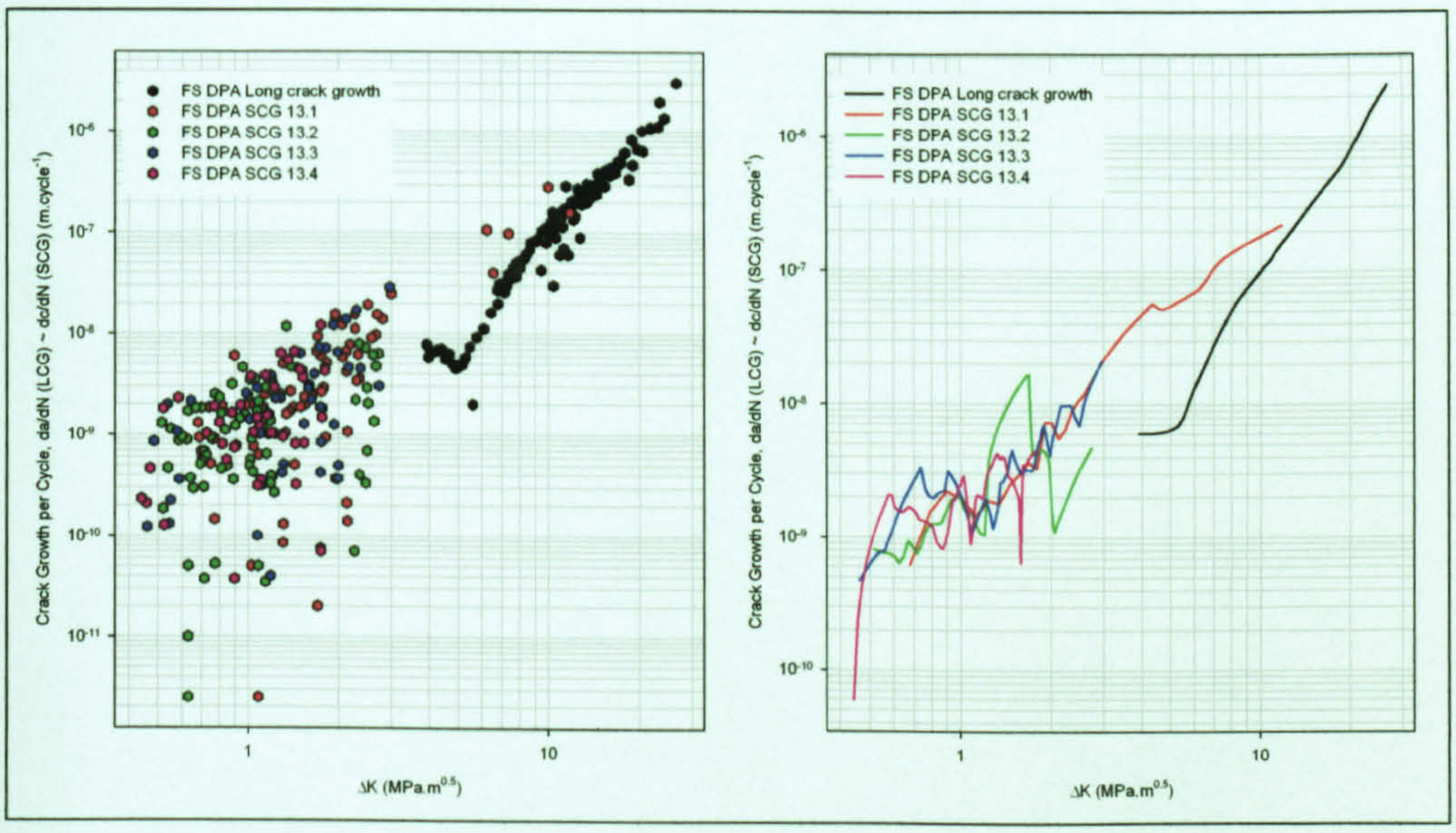

Figure 6.105: AA 5383-H321 FS DP butt weld, advancing side, long and short crack growth rates with respect to ΔK.

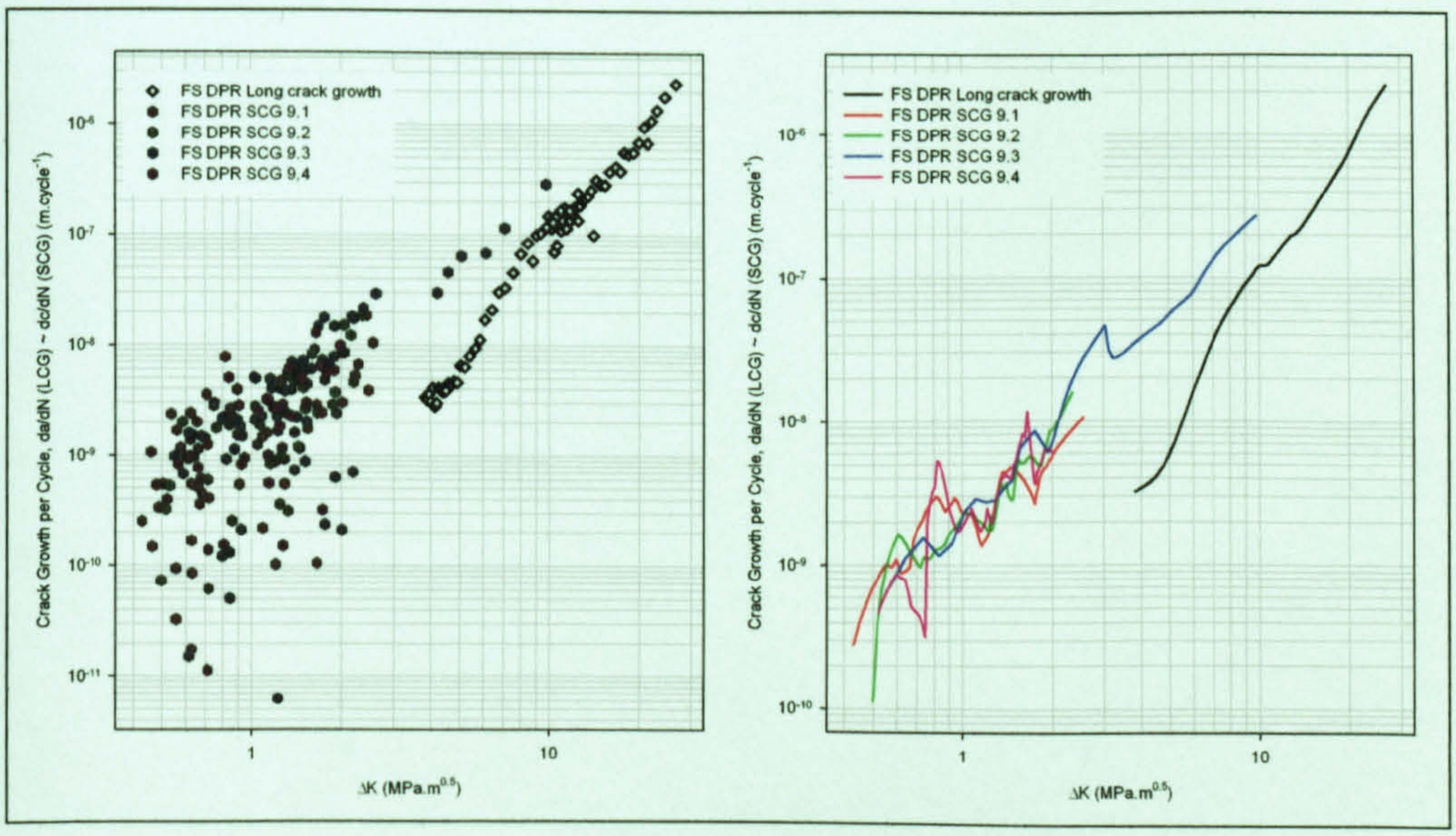

Figure 6.106: AA 5383-H321 FS DP butt weld, retreating side, long and short crack growth rates with respect to ΔK.

Growth rates below the long crack threshold exhibited considerable variability, although this was not as prolific as observed in the SP SCG, again presumed to be due to grain boundary interactions and crack coalescence.

Figure 6.107 and Figure 6.108 depict various short crack propagation rates for the AA 5383-H321 parent plate and MIG and FS welds (bisquare smoothing with a 0.2 sampling ratio and single degree polynomial has been applied to the data). The various plots were included on the basis of them covering a significant stress intensity factor range and/or crack length. The variability in the measured growth rates was evident in both figures, although this tended to be more prevalent in the welded specimens. The two parent plate samples exhibited the greatest resistance to crack growth in Figure 6.107, although the FS SP weld appeared to exhibit the greater resistance in Figure 6.108, excluding the FS SP results the MIG and FS welded specimens returned values within comparable scatter bands.

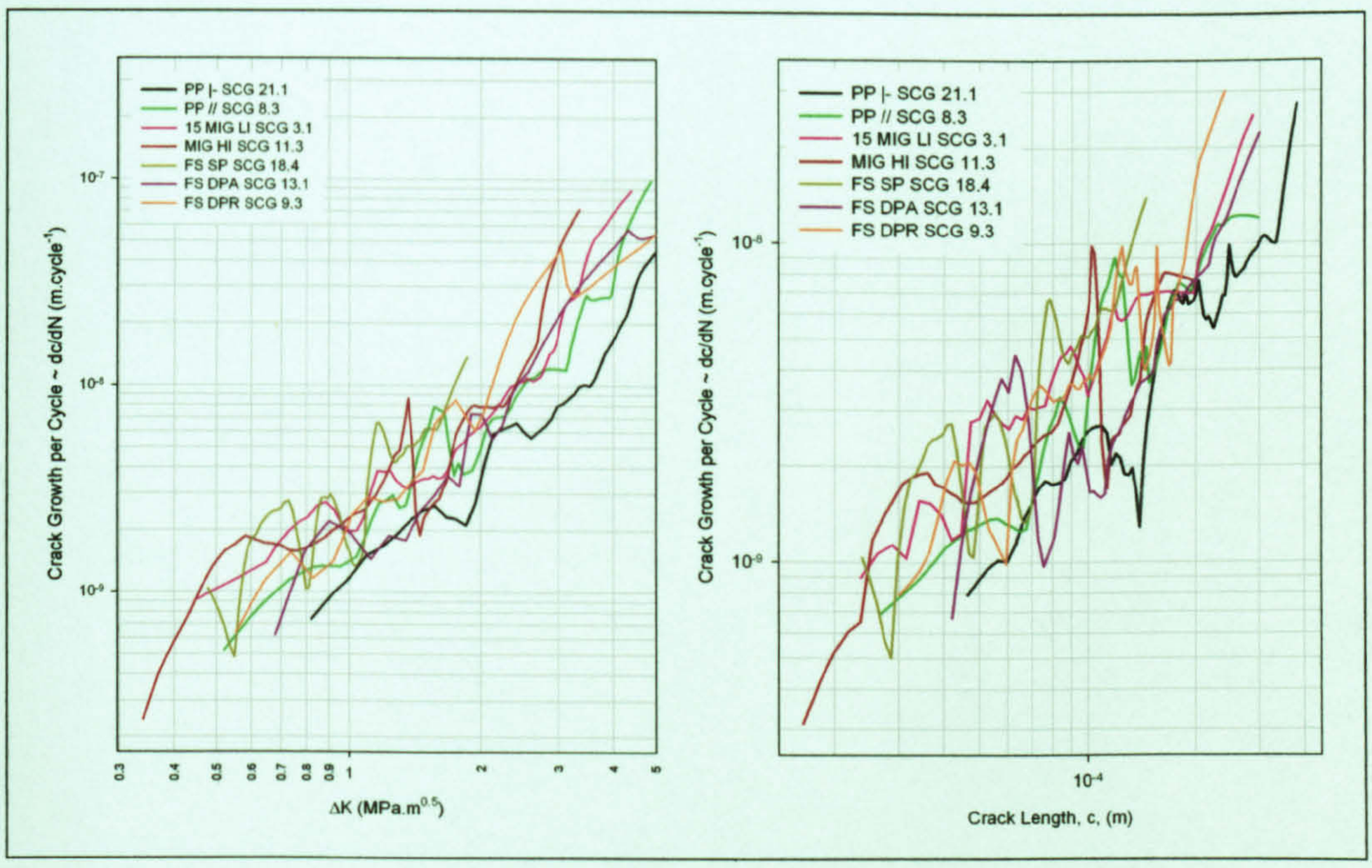

Figure 6.107: Comparison of short crack propagation rates with respect to the stress intensity factor range (left) and crack length (right).

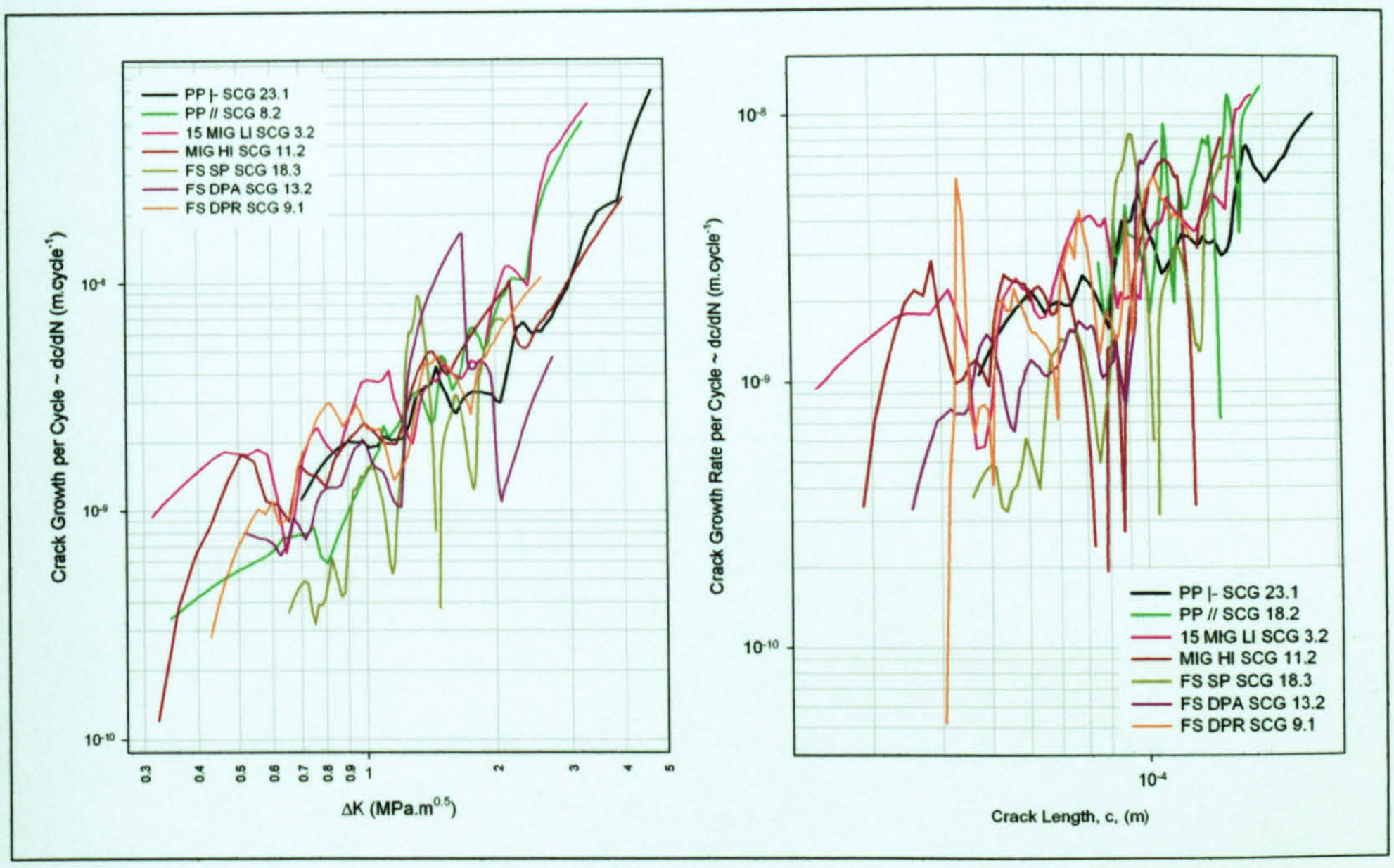

Figure 6.108: Comparison of short crack propagation rates with respect to the stress intensity factor range (left) and crack length (right).

The maximum length of crack measured, that was considered to be exhibiting SCG behaviour, and the average numbers of grains entailed are shown in Table 6.15, the values, excluding that for the FS SP weld, being comparable to the 3 - 8 grains observed by Tokaji and Ogawa[1] in AA 7075-T6.

Specimen	Grain size in the SCG region (μm)	Maximum sized crack exhibiting SCG behaviour, c, (μm)	No. of grains
PP |-	50 - 100	300 - 400	3 - 8
PP //	30 - 60	~300	5 - 10
MIG LI	30	~300	9 - 10
MIG HI	40	~250	5 - 6
FS SP	10	*169 (maximum crack size measured)*	*17*
FS DPA	50	~250 - 300	5 - 6
FS DPR	50	~225	4 - 5

Table 6.15: Maximum SCG crack sizes and microstructural unit size.

[1] Tokaji, K; Ogawa, T (1992)

6.5.2 Long Crack Growth

Material	ΔK_0 ($K_{max,0}$) (MPa.m$^{0.5}$)	Crack growth rate (ηm.cycle^{-1})		Paris Equation $da/dN = C(\Delta K_{R=0.1})^m$			
				Plane strain		Plane stress	
		Plane strain (ΔK = 7.5 MPa.m$^{0.5}$)	Plane stress (ΔK = 15 MPa.m$^{0.5}$)	C_ε (x10^{-12})	m_ε	C_σ (x10^{-12})	m_σ
PP |-	4.0 (4.4)	63.06	463.61	44.24	3.604	541.80	2.489
PP //	3.9 (4.3)	63.48	480.94	21.41	3.968	198.72	2.877
MIG LI*	7.1 (7.8)	≈ 6.89	305.88	0.01	6.701	1.610	4.489
MIG HI	4.3 (4.8)	32.00	382.98	0.07	6.476	93.30	3.072
FS SP	3.9 (4.3)	88.51	406.95	17.99	4.219	1175.84	2.159
FS DPA	3.9 (4.3)	34.95	403.61	1.77	4.908	138.38	2.946
FS DPR	3.8 (4.2)	44.77	328.50	1.40	5.147	211.62	2.713

Table 6.16: Fatigue threshold, crack growth rates and Paris equation constants.

6.5.2.1 Fatigue Threshold

As can be seen from Table 6.16 the long crack fatigue threshold, ΔK_0, was in the region of 3.8 - 4.0 MPa.m$^{0.5}$ for the AA 5383-H321 parent material and for both the SP and DP friction stir welds. The MIG* welds returned values for ΔK_0 greater than those for the parent material and FS welds with values of 7.1 MPa.m$^{0.5}$ and 4.3 MPa.m$^{0.5}$ for the LI* and HI welds respectively. The thresholds for the parent material and FS welds were comparable to the 4 - 5 MPa.m$^{0.5}$ detailed by Nordmark et al[1] for AA 5456 parent plate, with R = 0, but slightly greater in magnitude than the 3.5 MPa.m$^{0.5}$ for AA 5083 plate published by Costa et al[2] with R = 0.05. The values of $\Delta K_0 \approx 400$ N.mm$^{-3/2}$ (12.6 MPa.m$^{0.5}$) obtained by Nosair and Jolley[3], for R = 0.1 and 0.27, for crack growth in both Al4.5Mg plate and weld metal were significantly greater than those measured.

The increase in magnitude of the stress intensity factor thresholds returned by the MIG welds in contrast to values returned by the base material has also been considered by Link[4], Nordmark et al[1] and Dalle Donne et al[5]. Link reported values of ΔK_0 = 3.6 - 5.0 MPa.m$^{0.5}$ for AA 5456 parent plate with R = 0.1, whilst for the MIG weld metal values of 11.2 - 12.8 MPa.m$^{0.5}$ and 6.4 MPa.m$^{0.5}$ were recorded for R = 0.1 and 0.5 respectively. The author stated that the increase in the threshold values, and also observed reduction in crack growth rates, was due to the production of the notch in the CT specimen[4]. This resulted in a redistribution of the weld induced residual stress field in the region of the weld, the outcome being a compressive residual stress at the crack tip. The result of this was that crack closure occurred for a significant part of the applied tensile loading

---

* The parent material of the MIG LI CT specimens was AA 5083-H321.
[1] Nordmark, GE et al (1982)
[2] Costa, JD et al (1997)
[3] Nosair, S; Jolley, G (1985)
[4] Link, LR (1990)
[5] Dalle Donne, C et al (2000)

reducing the effective stress intensity factor and thereby increasing the apparent magnitude of the threshold. Nordmark et al[1] reported threshold values of ~6 MPa.m$^{0.5}$ for the HAZ of a high deposition rate weld in AA 5456 with R = 0, comparable to the 4.3 - 7.1 returned by the HI and LI welds respectively, although the values of 8 - 10 MPa.m$^{0.5}$ detailed by Dalle Donne et al[2] in both AA 6013 and AA 2024 FS welds were slightly greater than those measured.

6.5.2.2 Crack Propagation Rates

From Table 6.16 and Figure 6.109 it was evident that the long crack propagation rates for the AA 5383-H321 base material were equal for both the |- and // rolling directions in the plane strain region, crack growth rates of 63 x 10^{-9} m.cycle^{-1} were returned for both rolling directions for $\Delta K = 7.5$ MPa.m$^{0.5}$. An increase in the PP // rate was evident in the predominantly plane stress region as the stress intensity factor range exceeded 15 MPa.m$^{0.5}$, crack growth rates of 464 x 10^{-9} and 481 x 10^{-9} m.cycle^{-1} were returned for the |- and // rolling directions respectively for $\Delta K = 15$ MPa.m$^{0.5}$.

The MIG welds exhibited lower propagation rates than the PP |- material for the region predominated by plane strain, with the LI* weld exhibiting the greatest resistance to propagation. For $\Delta K = 7.5$ MPa.m$^{0.5}$ the HI weld returned a growth rate of 32 x 10^{-9} m.cycle^{-1}, whilst extrapolation of the LI* weld data predicted a value of 7 x 10^{-9} m.cycle^{-1}, although in the tests undertaken the growth rate exhibited by the LI* weld was considered to be in regime A and not characterised by the Paris equation. The growth rates were 11 and 51%, for the LI* and HI respectively, of the values returned by the PP |-. In the region predominated by plane stress the crack growth rates returned by the MIG welds were lower than those returned by the PP |- for $\Delta K < 19 - 21$ MPa.m$^{0.5}$, at magnitudes greater than this the roles were reversed. For $\Delta K = 15$ MPa.m$^{0.5}$ the LI* weld returned a growth rate of 306 x 10^{-9} m.cycle^{-1}, 66% of that returned by the PP |-, whilst the HI weld returned a rate of 383 x 10^{-9} m.cycle^{-1}, 83% of that returned by the PP |-. As with the increase in the threshold observed in the MIG welds, the reduction in the propagation rates observed for both stress states was considered to be primarily due to crack closure resulting from the effects of the weld induced residual stress field. The increased crack propagation, in contrast to that of the PP |-, for $\Delta K > 19 - 21$ MPa.m$^{0.5}$, was considered to be a combination of plastic flow reducing the effect of the residual stress field and therefore reducing crack closure and a general lower resistance to propagation in contrast to that of the PP |-.

---

[1] Nordmark, GE et al (1982)
[2] Dalle Donne, C et al (2000)
* The parent material of the MIG LI CT specimens was AA 5083-H321.

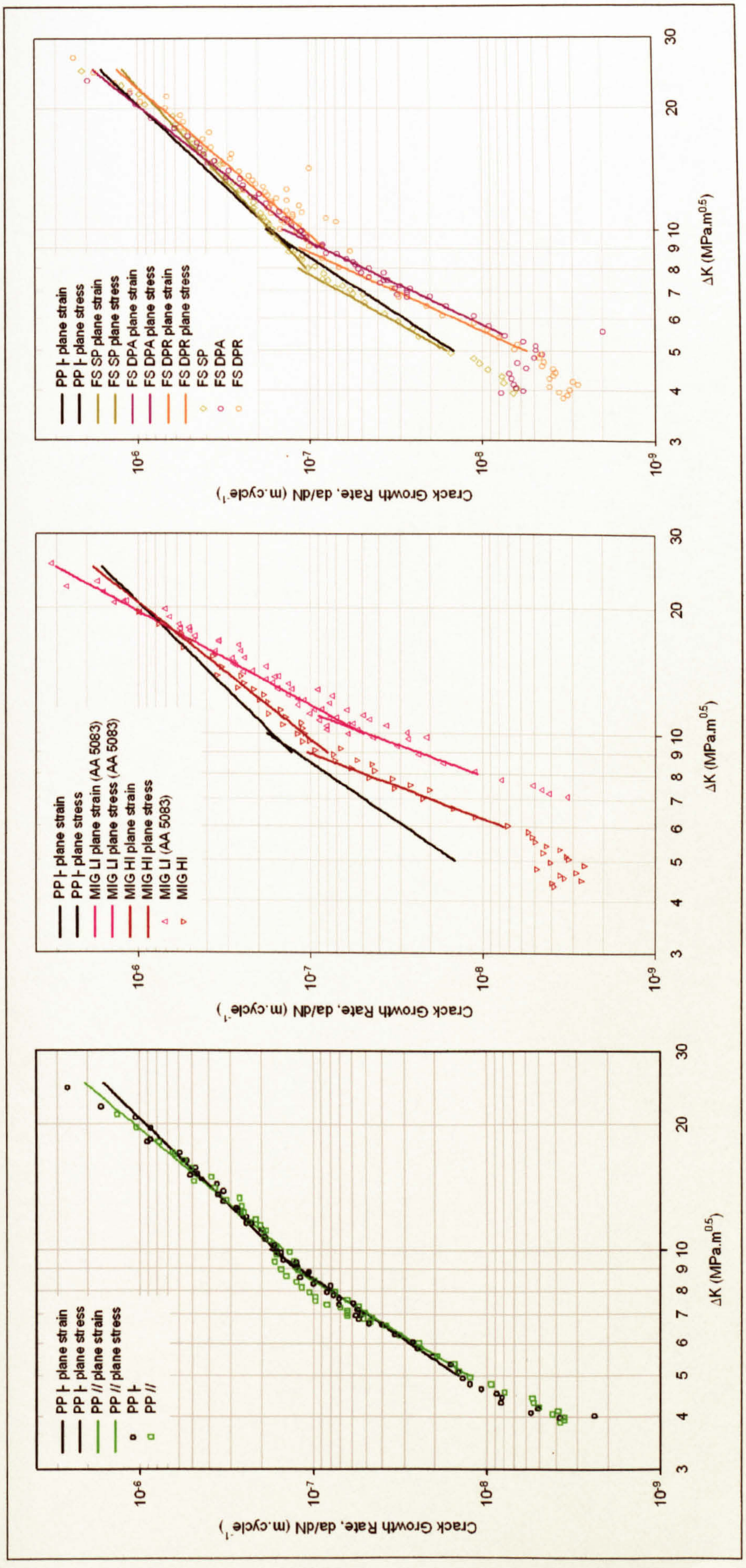

Figure 6.109: Long crack growth in AA 5383-H321 PP |- and PP // (left), MIG LI and HI (centre) and FS SP, DPA and DPR (right)

In the predominantly plane strain regime the crack growth rates returned by the FS DP, both the advancing and retreating sides, were less than those returned by the PP |-; for $\Delta K = 7.5$ MPa.m$^{0.5}$ values of 35×10^{-9} and 45×10^{-9} m.cycle^{-1} were recorded for the advancing and retreating sides respectively, 55 and 71% of the 63×10^{-9} m.cycle^{-1} observed in the PP |-. In contrast to this the FS SP weld had a greater propagation rate, for $\Delta K = 7.5$ MPa.m$^{0.5}$ a value of 89×10^{-9} m.cycle^{-1} was returned, 40% greater than that of the PP |-. The lower propagation rates for the DPA and DPR specimens, in contrast to that observed in the PP |-, were again considered to be predominantly the result of the weld induced residual stress field prevalent at the edge of the friction band of the FS welds under investigation (as detailed in Section 4.4, Measurement of Residual Stresses/strains, page 152 onwards). The geometry of the CT specimens resulting in a compressive stress in the region of the crack tip in a comparable manner to that observed in the MIG welds, the outcome of this being increased crack closure. In contrast to the DP weld the SP weld exhibited a propagation rate that was greater than that returned by the PP |- in the predominantly plane strain region. Although a slight decrease in the magnitude of the residual stress field has been observed at the centre of FS welds it is not considered to be of a great enough magnitude to significantly reduce crack closure in the CT specimens employed. It was therefore assumed that the small grain size, ~10 μm, and reduction in hardness, found within the weld nugget region (as detailed in Section 3.6.4.3.1, Microhardness, page 94) was responsible for the increased propagation rates observed. Although small grain sizes are frequently associated with an increase in the strength of metallic materials long crack growth tends to be less susceptible to microstructural influences. Assuming that the reduced dislocation density observed in the weld nugget in AA 1100[1] and 6061[2,3] occurs in AA 5383-H321 this would also partially offset the influence of the small grain size. PFD were not considered to be the cause of the increased growth rates observed as it was considered that these would result in sudden rapid increases in the growth rate, but that this would only occur for a short period until the defect was breached by the crack tip, the change in the propagation rate then returning to that previously observed. This type of response was not observed and if PFD were considered to be having an effect on the growth rate they would also be expected to have a similar effect in the predominantly plane stress region as well. Within the principally plane stress region the FS DPR specimen had the lowest propagation rate, whilst the DPA had a lower rate than the SP for $\Delta K < 16$ MPa.m$^{0.5}$, their positions being reversed for values greater than this. For $\Delta K = 15$ MPa.m$^{0.5}$ the DP specimens returned propagation rates of 404×10^{-9} and 329×10^{-9} m.cycle^{-1} for the DPA and DPR respectively, 87% and 71% of the values returned by the PP |-, whilst the SP specimens returned a value of 407×10^{-9} m.cycle^{-1}, 88% of the PP |- magnitude. The reduced propagation rates for the DP specimens were again presumed to be chiefly the result of

---

[1] Flores, OV et al (1998)
[2] Liu, G et al (1997)
[3] Murr, LE et al (1998b)

the residual stress field, although the reason for the decreasing growth rate observed in the SP remains unknown.

From Figure 6.110 it was evident that MIG LI weld had the greatest, whilst the FS SP weld had the least, resistance to crack propagation in the plane strain region. The parent plate had a growth rate slightly less than that observed in the FS SP weld, whilst the FS DP specimens and the MIG HI weld returned values between that observed in the MIG LI and FS SP specimens. In the plane stress region the parent material, FS and MIG HI welded specimens had values that fell within a narrow band, typically bounded by the PP // and FS DPR results, although the FS SP propagation rates changed from being the highest of the group to the lowest within the plane stress region covered. The MIG LI results lay outwith the narrow band, although the growth rate increased from the lowest of all the specimens tested to the highest as ΔK increased from 16 - 20 $MPa.m^{0.5}$.

From Table 6.16 it was evident that the values for the Paris law constant m ranged from 3.6 - 6.7 and 2.2 - 4.5 for the plane strain and stress regions respectively. m is typically considered to lie within 2 - 4 for metallic materials[1] and this was observed for the parent material in the plane strain region and all the specimens, excluding the MIG LI, in the plane stress region, it was therefore assumed that the residual stresses were the main instigator in the increased values typically observed in the plane strain region.

[1] Ritchie, RO (1999)

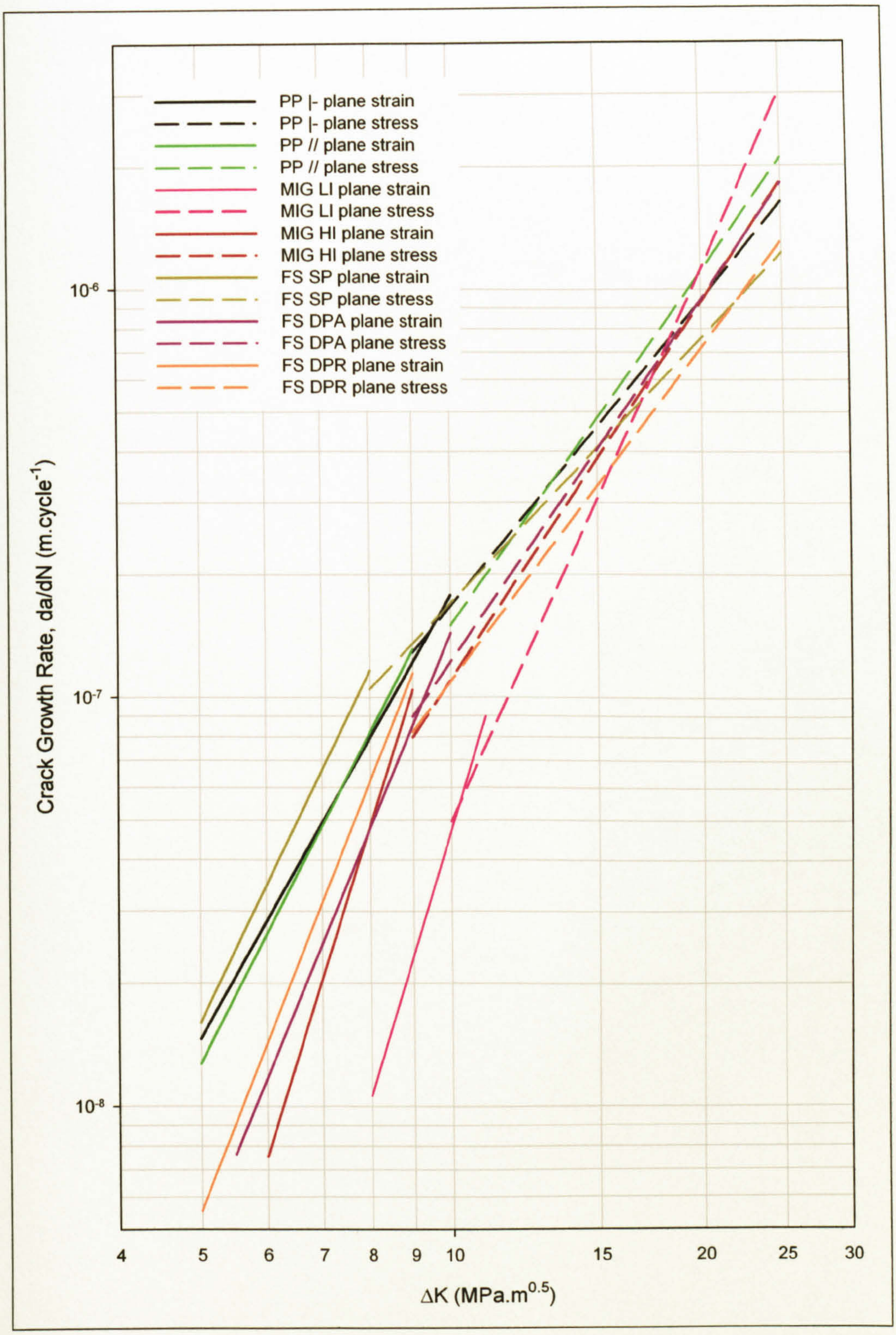

Figure 6.110: Fatigue crack growth rates of AA 5383-H321 parent plate and butt welds (MIG LI AA 5083-H321).

7. Modelling of the Fatigue Properties of Metal Inert Gas and Friction Stir Welded Butt Joints

7.1 Abstract

The following section details the application of a simple defect-tolerant based model and its accuracy in predicting the fatigue life of AA 5383-H321 parent material and MIG and FS butt welds through unification of the short and long crack growth regimes.

7.2 Introduction

Since Pearson[1] identified the non-continuum behaviour of short cracks in 1975 numerous investigators have striven to develop a unified model to determine the overall fatigue life. Integration of the Paris equation, $dc/dN = C(\Delta K)^m$, will typically provide accurate assessment of fatigue life when this consists of predominantly LCG, but due to the accelerated growth frequently observed in SC this approach returns non-conservative values and, if the fatigue life consists predominantly of SCG, this underestimate may be considerable.

Several models have involved various adaptations to the stress intensity factor range, ΔK. Such techniques have included the application of an effective stress intensity factor, which takes into account the reduction in crack closure considered influential in the accelerated growth of SC, or the adaptation of the crack length, through the assimilation of the plastic zone size. These techniques tend to be empirical based and are often complex in nature. A relatively simple approach has been proposed by Nisitani et al[2,3] and subsequently employed by Caton et al[4,5] which considers the SCG to be a function of the stress amplitude, yield or tensile stress and crack length. Although Caton et al[4] have successfully applied the approach to a cast aluminium alloy the following section considers its application to MIG and FS welded butt joints in AA 5383-H321.

---

[1] Pearson, S (1975)
[2] Nisitani, H; Goto, M (1986)
[3] Nisitani, H et al (1992)
[4] Caton, MJ et al (1999a)
[5] Caton, MJ et al (1999b)

7.3 Literature Review

Several approaches have been proposed that result in an amendment of the stress intensity factor range to model the accelerated growth of SC. In one of the first of such approaches El Haddad et al[1] applied a modification to the apparent crack length as shown in equation (7.1):

$$\Delta K = \Delta\sigma Y\sqrt{\pi(a + a_0)} \tag{7.1}$$

where: a_0 = material constant that is a function of the plastic zone size.

Philips and Newman[2] and Kaynak et al[3] utilised a SCG and LCG Paris law approach as depicted in equations (7.2) and (7.3) and Figure 7.1:

$$\left(\frac{dc}{dN}\right)_{scg} = C_{scg}(\Delta K)^{m_{scg}} \tag{7.2}$$

$$\left(\frac{dc}{dN}\right)_{lcg} = C_{lcg}(\Delta K)^{m_{lcg}} \tag{7.3}$$

$$N_T = N_{scg} + N_{lcg} \tag{7.4}$$

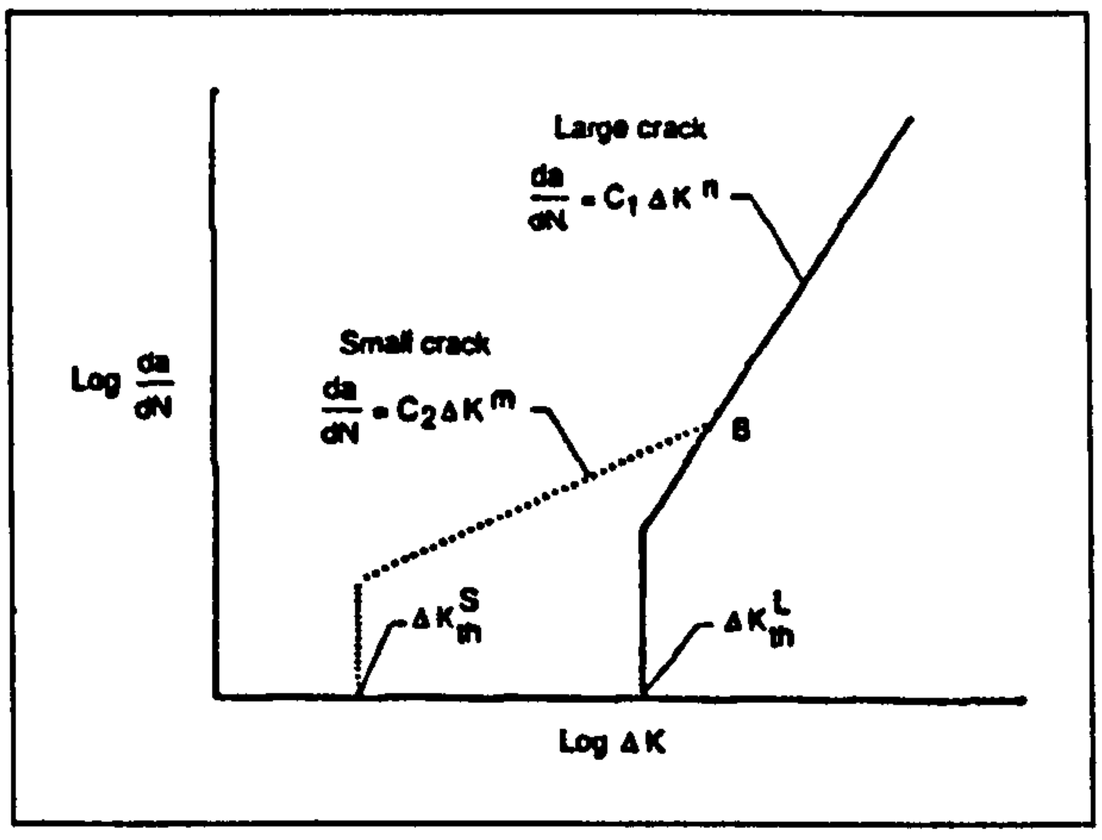

Figure 7.1: Analytical representation of the growth rate data for small and large cracks[2].

For initial crack or defect sizes > 300 µm in length, in the AA 2024-T3 studied by Philips and Newman[2], the implementation of N_{scg} was found to have a negligible effect on the overall fatigue life, although for initial crack or defect sizes in the region of 10 µm their results tended to be conservative, as shown in Figure 7.2. This suggests that the transition from SCG to LCG occurred in the region of c = 300 µm, although the approach

---

[1] El Haddad, MH et al (1981)
[2] Philips, EP; Newman Jr, JC (1989)
[3] Kaynak, C et al (1996)

of utilising a SCG Paris law approach was not suitable for the material under consideration. Another shortcoming of the approach was the variation of the SCG Paris law constants with the maximum stress, unlike the LCG Paris constants that are generally considered constant for a range of applied stresses. Kaynak et al[1] reported minimal influence of SCG on the prediction of the fatigue life for initial crack or defect lengths > 1 mm in an En7A steel, although for initial crack or defect sizes in the range of 40 - 100 μm they reported good correlation between predicted and experimental values, as shown in Figure 7.3.

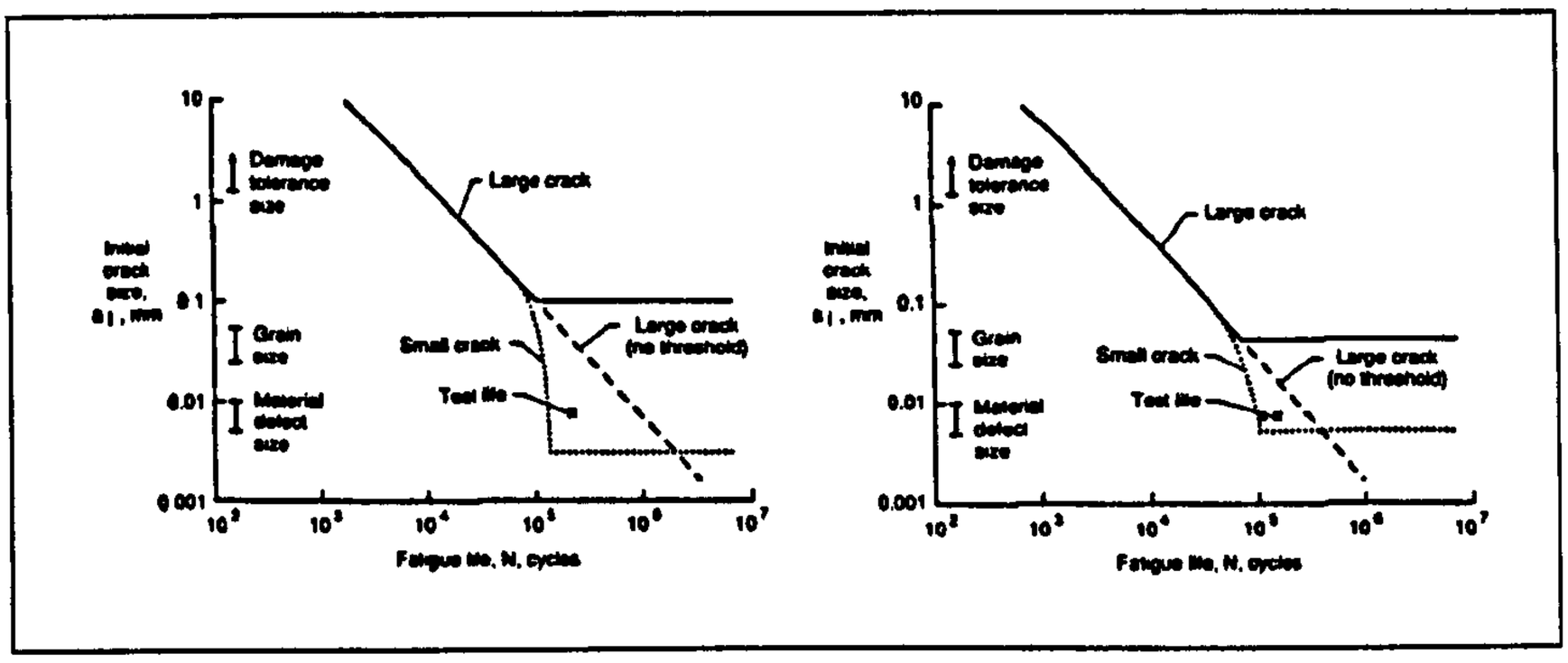

Figure 7.2: Calculated crack growth lives for R = -1, σ_{max} = 80 MPa (left) and R = 0, σ_{max} = 120 MPa (right)[2].

[1] Kaynak, C et al (1996)
[2] Philips, EP; Newman Jr, JC (1989)

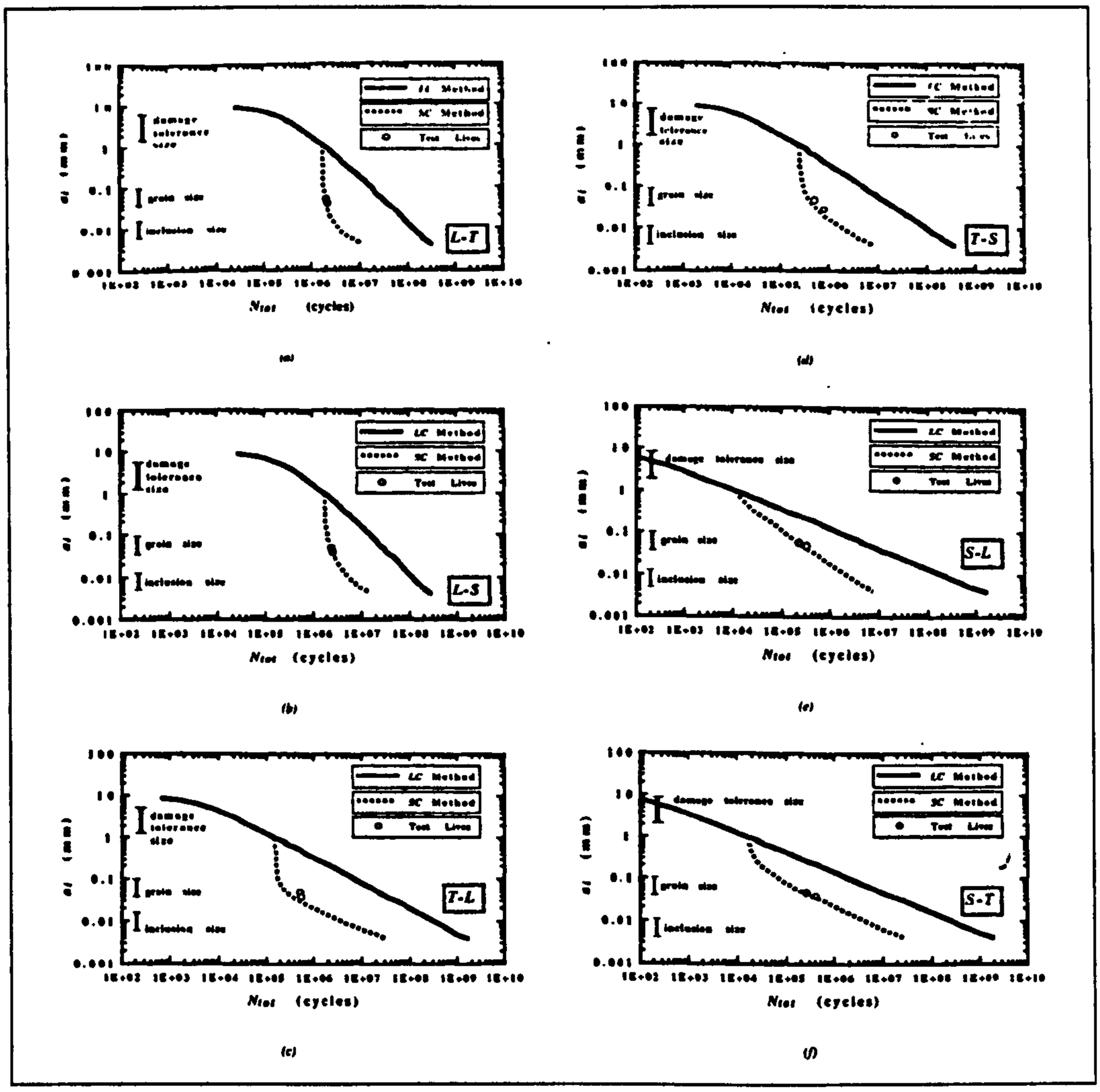

Figure 7.3: Comparison of the test lives with the calculated crack growth lives of the long crack and short crack methods[1].

Newman[2] attained good correlation between experimental and theoretical results for both aluminium, as shown in Figure 7.4, and steel utilising an effective stress intensity factor range, ΔK_{eff}, with the initial crack size being considered equal to that of inclusion particles. This type of approach taking into consideration the reduction in plasticity induced crack closure, considered to be one of the causes of the accelerated growth observed in SC:

$$\Delta K_{eff} = \left(\sigma_{max} - \sigma_{op}\right) Y \sqrt{\pi a} \qquad (7.5)$$

where: ΔK_{eff} = effective stress intensity factor.

σ_{max} = maximum applied stress.

σ_{op} = crack opening stress.

---

[1] Kaynak, C et al (1996)
[2] Newman Jr, JC (1999)

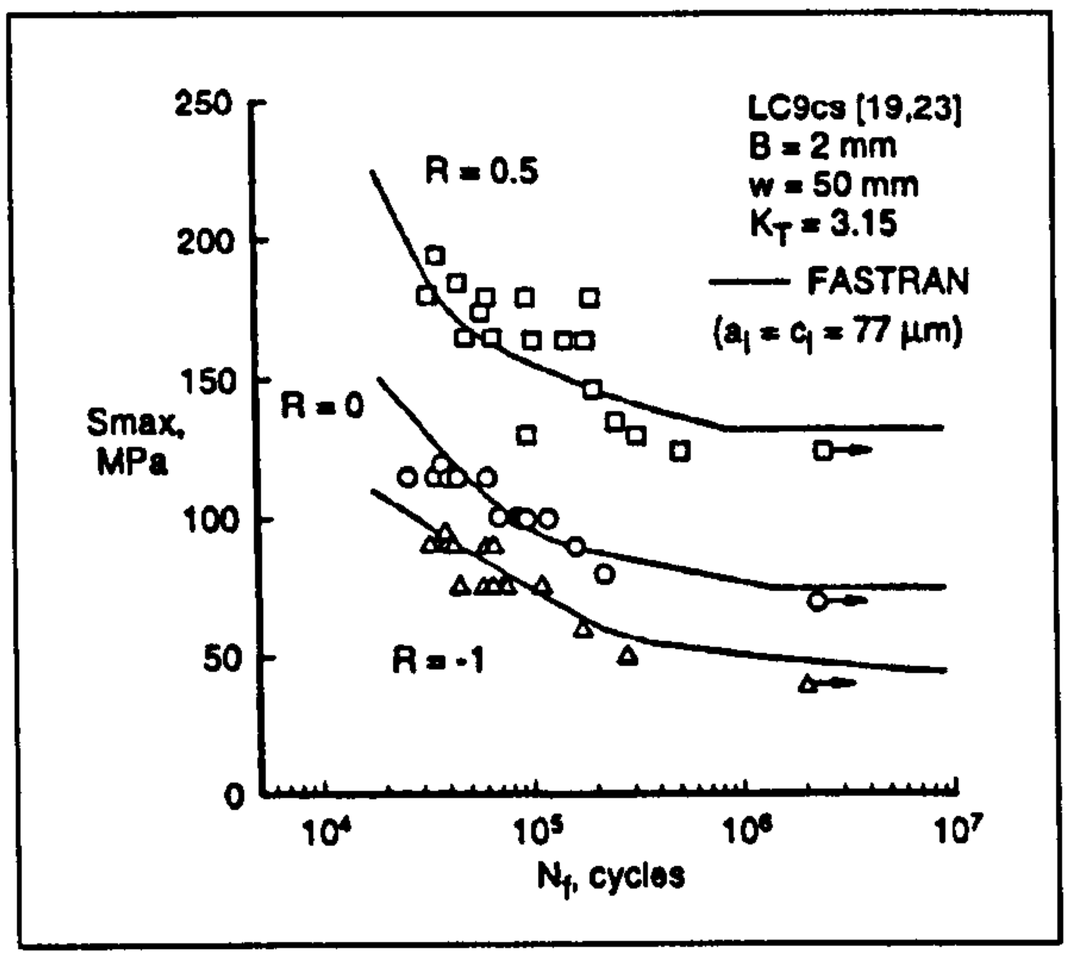

Figure 7.4: Measured and predicted fatigue lives for LC9cs aluminium alloy[1].

Nakai and Ohji[2] utilised a comparable approach to that by Newman[1], although they state that the approach was more suited to mechanically short, but microstructurally long, short cracks (see Section 6.3.2, Short Fatigue Cracks, page 309, for a definition of the applicable SC terminology) where crack closure is considered to be more influential due to the diminishing influence of grain boundary interactions:

$$\left(\frac{dc}{dN}\right)_{lcg} = C\left(\Delta K^{m} - \Delta K^{m}_{th,\infty}\right) \tag{7.6}$$

or

$$\left(\frac{dc}{dN}\right)_{lcg} = C'\left(\Delta K^{m'} - \Delta K^{m'}_{eff,th,\infty}\right) \tag{7.7}$$

$$\left(\frac{dc}{dN}\right)_{scg} = C'\left(\Delta K^{m'}_{eff} - \Delta K^{m'}_{eff,th}\right) \tag{7.8}$$

where: $\Delta K_{th,\infty}$ = threshold stress intensity factor range of long cracks.

$\Delta K_{eff,th,\infty}$ = effective component of threshold stress intensity factor range of long cracks.

ΔK_{eff} = effective stress intensity factor range.

$\Delta K_{eff,th}$ = effective component of threshold stress intensity factor range of short cracks.

[1] Newman Jr, JC (1999)
[2] Nakai, Y; Ohji, K (1992)

Nisitani et al[1,2] proposed that large and short cracks in ductile materials could be represented by equation (7.9), the Paris equation, and equation (7.10) respectively.

$$\left(\frac{dc}{dN}\right)_{lcg} = C(\Delta K)^m \qquad (7.9)$$

$$\left(\frac{dc}{dN}\right)_{scg} = B.\sigma_a^n.c \qquad (7.10)$$

where: B and n = scaling constants.

σ_a = stress amplitude.

c = crack length.

The Paris equation was considered representative of crack growth under low nominal stresses where small scale yielding is present, typical of the scenario observed for large cracks, whilst equation (7.10) was considered representative of crack growth under high nominal stresses found in the region of short cracks. The authors claimed that the two equations were valid if the crack growth rate, dc/dN, was proportional to the reversible plastic zone size, r_{pr}:

$$\left.\begin{array}{l} U \propto \Delta K \\ \therefore \Delta K_{eff} = U\Delta K \propto \Delta K^2 \\ \text{Assuming } {}^{dc}/_{dN} \propto r_{pr} \end{array}\right\} \frac{dc}{dN} = C\Delta K^4 \qquad \text{Long cracks}$$

$$\left.\begin{array}{l} U \cong \text{constant} \\ \therefore r_{pr} \propto c \ (\sigma_a : \text{constant}) \\ r_{pr} \propto \sigma_a^n \ (\text{c:constant}) \\ \text{Assuming } {}^{dc}/_{dN} \propto r_{pr} \end{array}\right\} \frac{dc}{dN} = B\sigma_a^n c \qquad \text{Short cracks}$$

where: $U = \Delta K_{eff}/\Delta K$

The authors[1,2] reported good correlation between theoretical and experimental results through the application of equation (7.10), for $\sigma_a > \frac{1}{2}\sigma_y$ and $N < 10^6$ cycles, for the analysis of a 0.45% C steel and Fe-3% Si alloy. They stated that the method was not suitable for the comparison of different materials, although in an attempt to overcome this limitation they adapted the equation to take into consideration material properties, in the form of the yield or tensile strength, as depicted in equation (7.11):

---

[1] Nisitani, H; Goto, M (1986)
[2] Nisitani, H et al (1992)

$$\frac{dc}{dN} = B\left(\frac{\sigma_a}{\sigma_{y\ or\ TS}}\right)^n .c \qquad (7.11)$$

where: B and n = scaling constants, with n typically in the region of 7 - 9.

Figure 7.5 depicts the relationship between the short crack growth rate in annealed and heat treated steels and the stress amplitude/yield stress and the corresponding values for the constant n.

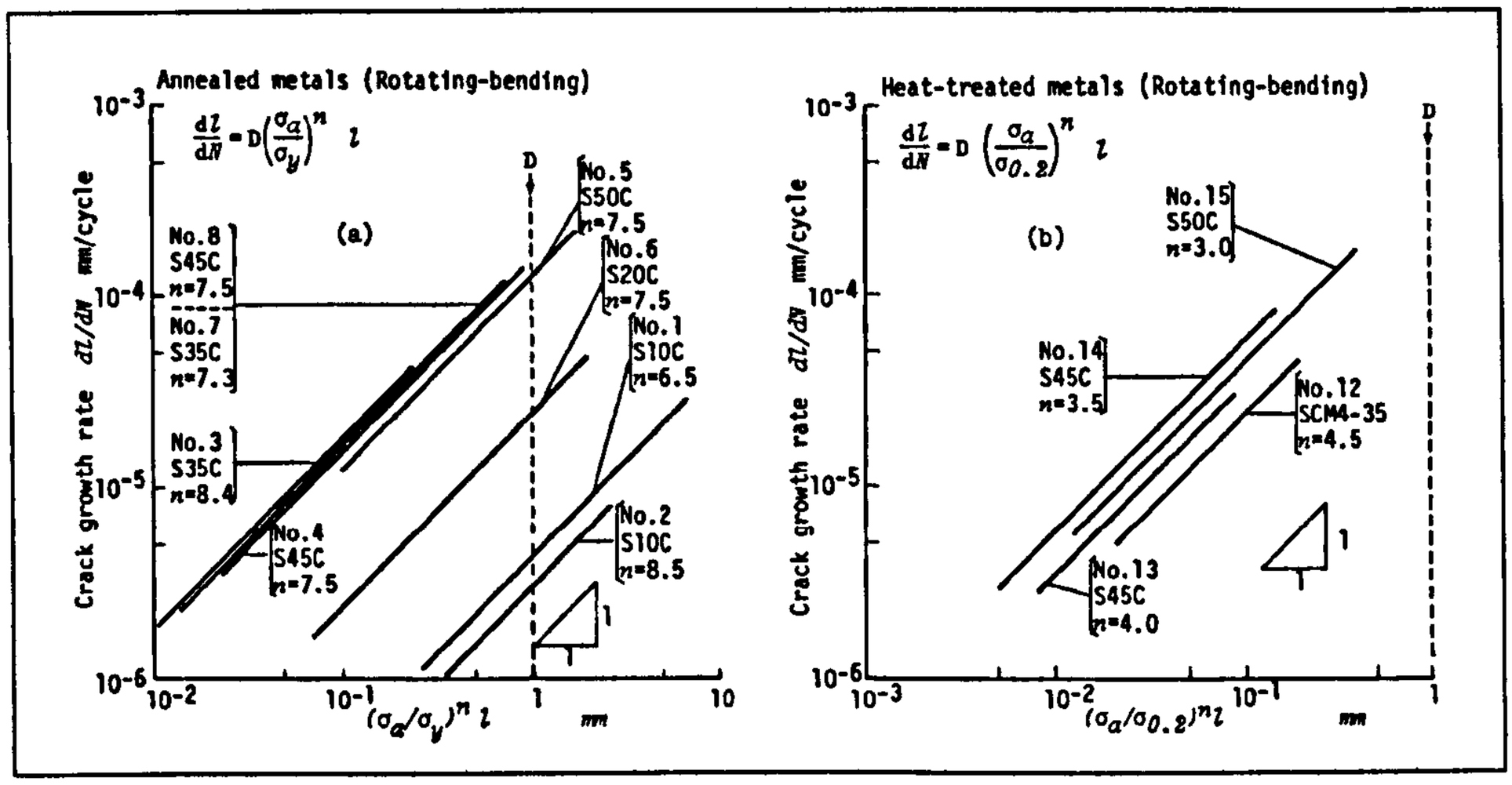

Figure 7.5: Short crack growth relationships for annealed carbon steels (left) and heat treated carbon steels (right)[1].

A further application of the approach by Nisitani et al[1,2] has been undertaken by Caton et al[3,4] in a cast AA 319, with SCG data attained at values of $\sigma_{max}/\sigma_y = 0.49$ and 0.69 in a fine microstructure and 0.65 and 0.91 in a coarse microstructure. Utilisation of equation (7.11) and n = 7 was found to normalise the data with respect to the crack growth rate for both microstructures and stress levels, as shown in Figure 7.6. The authors[3,4] also suggested modifying the equation to take into consideration the maximum strain to account for the different elastic-plastic responses of the fine and coarse grained specimens, as shown in equation (7.12), although the application of the maximum strain, with n = 2.5, had the effect of introducing greater variability into the results, as shown in Figure 7.7, when compared to those determined through equation (7.11):

$$\frac{dc}{dN} = B\left(\frac{\sigma_a}{\sigma_{y\ or\ TS}}\varepsilon_{max}\right)^n .c \qquad (7.12)$$

[1] Nisitani, H; Goto, M (1986)
[2] Nisitani, H et al (1992)
[3] Caton, MJ et al (1999a)
[4] Caton, MJ et al (1999b)

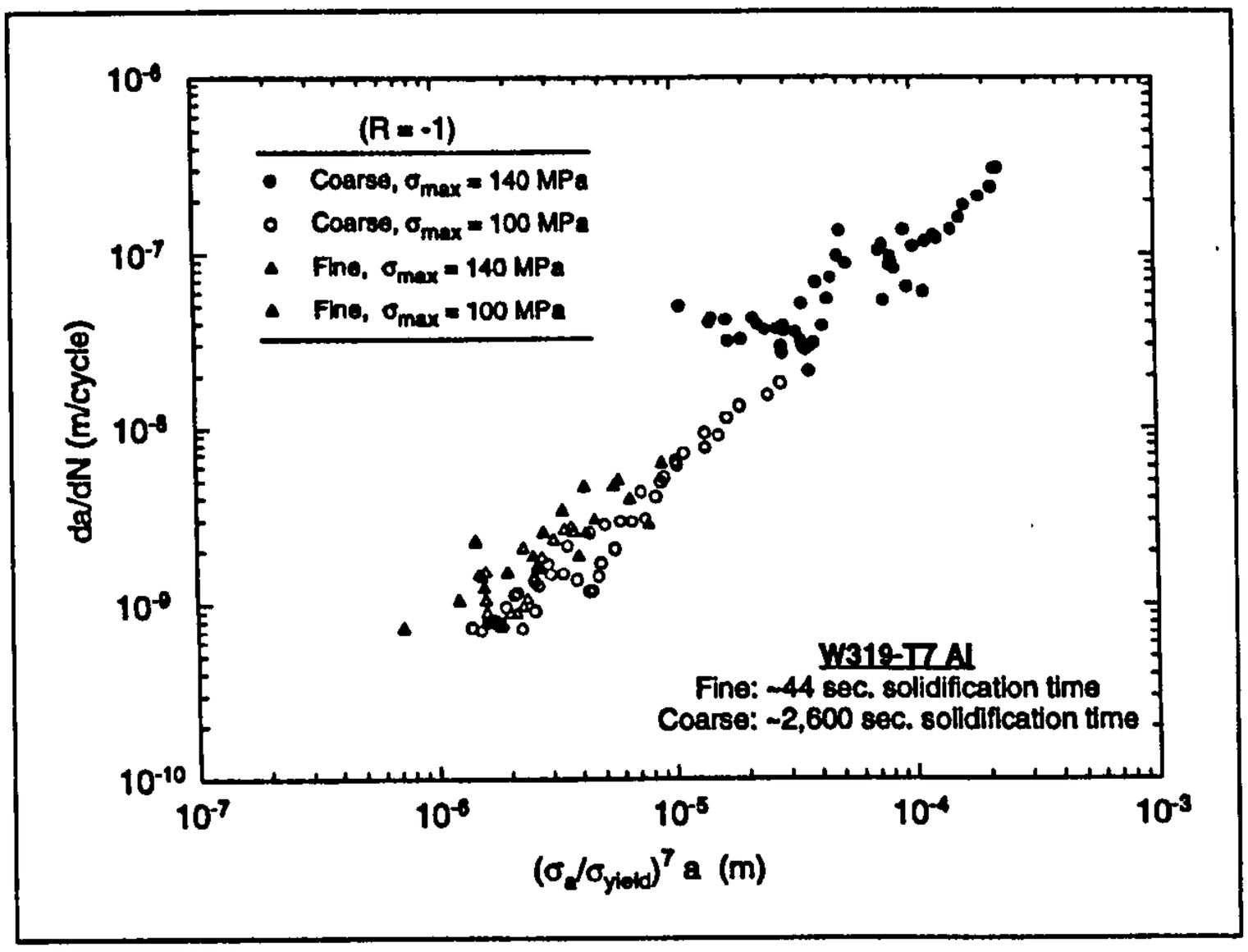

Figure 7.6: Short crack growth rates with respect to the stress amplitude and yield stress in both a fine and coarse structured cast 319 type aluminium alloy[1].

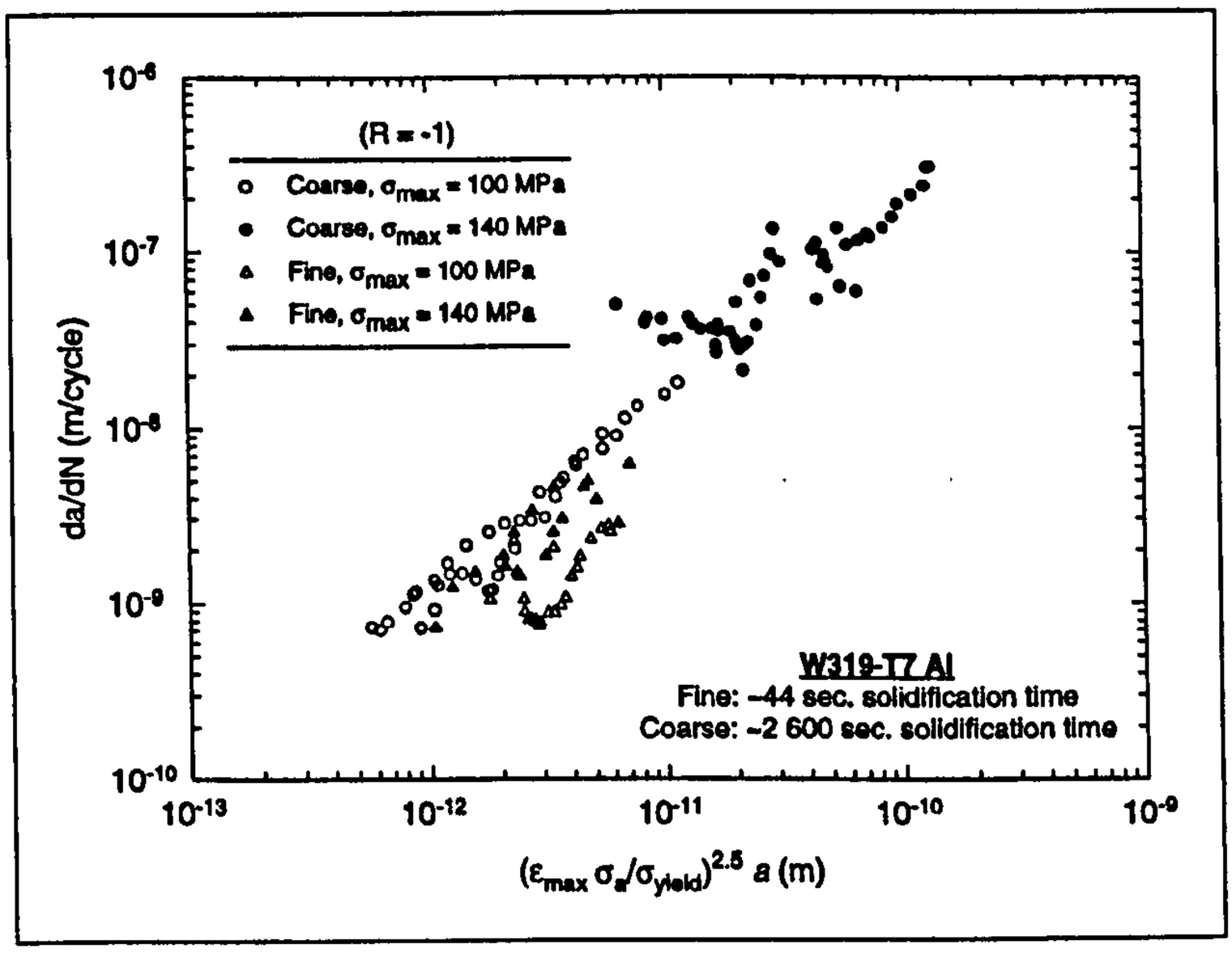

Figure 7.7: Short crack growth rates with respect to the stress amplitude, yield stress and maximum strain in both a fine and coarse structured cast 319 type aluminium alloy[1].

A limitation of the approach by Nisitani et al[2,3] and Caton et al[4,1] results from the integration of equations (7.11) or (7.12), to determine the number of cycles for a crack to grow from an initial crack size, c_i, to the SCG to LCG transition size, c_t, for a specific

---

[1] Caton, MJ et al (1999b)
[2] Nisitani, H; Goto, M (1986)
[3] Nisitani, H et al (1992)
[4] Caton, MJ et al (1999a)

stress amplitude, as shown in equations (7.13) and (7.14) respectively. The integration results in a two parameter power law equation of the form $y = ax^b$. When viewed on a S-N log-log plot this type of equation returns a linear response and this tends to limit the accuracy, when using the technique to predict S-N curves, to the high stress-low life linear region of the plot. A typical S-N curve often exhibits exponential decay, or in the case of the ones developed for the AA 5383-H321 parent plate and welded specimens, detailed in Section 5.5, S-N Test Results (page 266), the curves were described by a three parameter power law, $y = a + bx^c$, therefore limiting the range over which the approach can be employed.

$$N_{c_i \to c_t} = \frac{1}{B}\left(\frac{\sigma_{y \text{ or } TS}}{\sigma_a}\right)^n \ln\frac{c_t}{c_i} \tag{7.13}$$

$$N_{c_i \to c_t} = \frac{1}{B}\left(\left(\frac{\sigma_{y \text{ or } TS}}{\sigma_a}\right).\frac{1}{\varepsilon_{max}}\right)^n \ln\frac{c_t}{c_i} \tag{7.14}$$

7.4 Modelling

7.4.1 Crack Initiation

In the modelling performed in this research, any crack initiation period has been considered negligible; the smallest cracks measured, typically in the region of c = 10 - 20 μm, were observed after approximately 15,000 - 20,000 cycles and it has therefore been assumed that the size of the crack initiator, as shown in Table 7.1, was equivalent to a crack of the same length prior to fatigue loading. This type of approach being utilised by Newman[1]. Therefore the lower bound crack size for the purposes of modelling was represented by the typical crack initiator in the parent or as-welded specimens; intermetallics in the case of the parent material, porosity in the case of the MIG welds and surface marks in the case of the FS welds.

	PP |-	PP //	MIG LI	MIG HI	FS SP	FS DP
Crack Initiator	I	I	P/I	P/I	SM/PFD/I	SM/I
Typical crack initiator size, $2c_i$, (μm)	26	26	42/35	43/30	-/?/15	-/20
Typical crack initiator half size, c_i, (μm)	13	13	21/17.5	21.5/15	20/?/7.5	20/10

Table 7.1: Values considered representative of crack initiation sizes.

where: I = intermetallic.
P = porosity.
SM = surface mark.
PFD = partial fusion defect.

7.4.2 Short Crack Growth

A significant short crack effect was evident in both the AA 5383-H321 parent plate and welded joints, as shown in Section 6.5.1, Short Crack Growth (page 386), when the SCG and LCG rates were compared with respect to the stress intensity factor range, ΔK.

Utilising the approach by Nisitani et al[2,3] and Caton et al[4,5], considering the short crack growth rate to be a function of the crack length when the stress amplitude, yield or tensile strength and maximum applied strain, equation (7.15), were taken into consideration resulted in equations (7.16) to (7.19):

---

[1] Newman Jr, JC (1999)
[2] Nisitani, H; Goto, M (1986)
[3] Nisitani, H et al (1992)
[4] Caton, MJ et al (1999a)
[5] Caton, MJ et al (1999b)

$$\left(\frac{dc}{dN}\right)_{scg} = f\left(\sigma_a, \sigma_y, \sigma_{TS}, \varepsilon_{max}, c\right) \tag{7.15}$$

$$\left(\frac{dc}{dN}\right)_{scg} = \left[\left(\sigma_a / \sigma_y\right).c\right] \tag{7.16}$$

$$\left(\frac{dc}{dN}\right)_{scg} = \left[\left(\sigma_a / \sigma_{TS}\right).c\right] \tag{7.17}$$

$$\left(\frac{dc}{dN}\right)_{scg} = \left[\varepsilon_{max}\left(\sigma_a / \sigma_y\right).c\right] \tag{7.18}$$

$$\left(\frac{dc}{dN}\right)_{scg} = \left[\varepsilon_{max}\left(\sigma_a / \sigma_{TS}\right).c\right] \tag{7.19}$$

where: dc/dN = crack growth rate (surface half-crack length)

σ_a = stress amplitude

σ_y = yield stress ($\approx \sigma_{0.1\%PS}$)

σ_{TS} = tensile strength

ε_{max} = maximum applied strain

c = crack length (surface half-crack length)

Figure 7.8 to Figure 7.14 depict the experimental short crack growth rates, with respect to crack length, as shown in Section 6.4, Fatigue Crack Growth Rate Measurements (page 327), as a function of equations (7.16) to (7.19) for the parent plate and welded specimens; regression curves were determined using TableCurve 2D V 5.00 software, with the curve equations and constants shown in Table 7.3 to Table 7.9. Values for the stress amplitude, peak stress, yield strength (0.1% proof stress was considered to be equivalent to the yield stress), tensile strength and maximum applied strain were as shown in Table 7.2. Values for the stress amplitude and peak stress were those employed in the determination of the SCG rate measurements, as detailed in Section 13, Appendix C ~ Crack Growth Results (page 506), whilst values for the peak strain were determined from monotonic uniaxial stress/strain plots as shown in Figure 3.118 (page 121), as were the yield and tensile strengths. From the values for the peak stress it was evident that the 0.1% proof stress was exceeded, suggesting that a redistribution of any remaining residual stresses in the SCG specimens would result, and therefore their influence would diminish.

	PP |-	PP //	MIG LI	MIG HI	FS SP	FS DPA	FS DPR
Stress amplitude, σ_a, (MPa)	134.3	133.8	123.4	124.2	131.0	121.6	129.7
Stress max, σ_{max}, (MPa)	298.4	297.3	274.2	276.0	291.1	270.2	288.2
0.1% Proof stress, σ_y, (MPa)	254	272	160	167	157	163	
Tensile Strength, σ_{TS}, (MPa)	385	370	332	350	336	333	
σ_a/σ_y	*0.529*	*0.492*	*0.771*	*0.744*	*0.834*	*0.746*	*0.796*
σ_a/σ_{TS}	*0.349*	*0.362*	*0.372*	*0.355*	*0.390*	*0.365*	*0.375*
Peak strain, ε_{max}, (%)	1.652	1.782	3.249	3.169	6.843	4.606	5.328
$\varepsilon_{max}.\sigma_a/\sigma_y$ $(x10^{-3})$	*8.74*	*8.77*	*25.05*	*23.58*	*57.07*	*34.36*	*42.41*
$\varepsilon_{max}.\sigma_a/\sigma_{TS}$ $(x10^{-3})$	*5.77*	*6.45*	*12.05*	*11.25*	*26.69*	*16.81*	*19.98*

Table 7.2: Values used for determination of equation (7.15) with respect to parent material rolling direction and weld type.

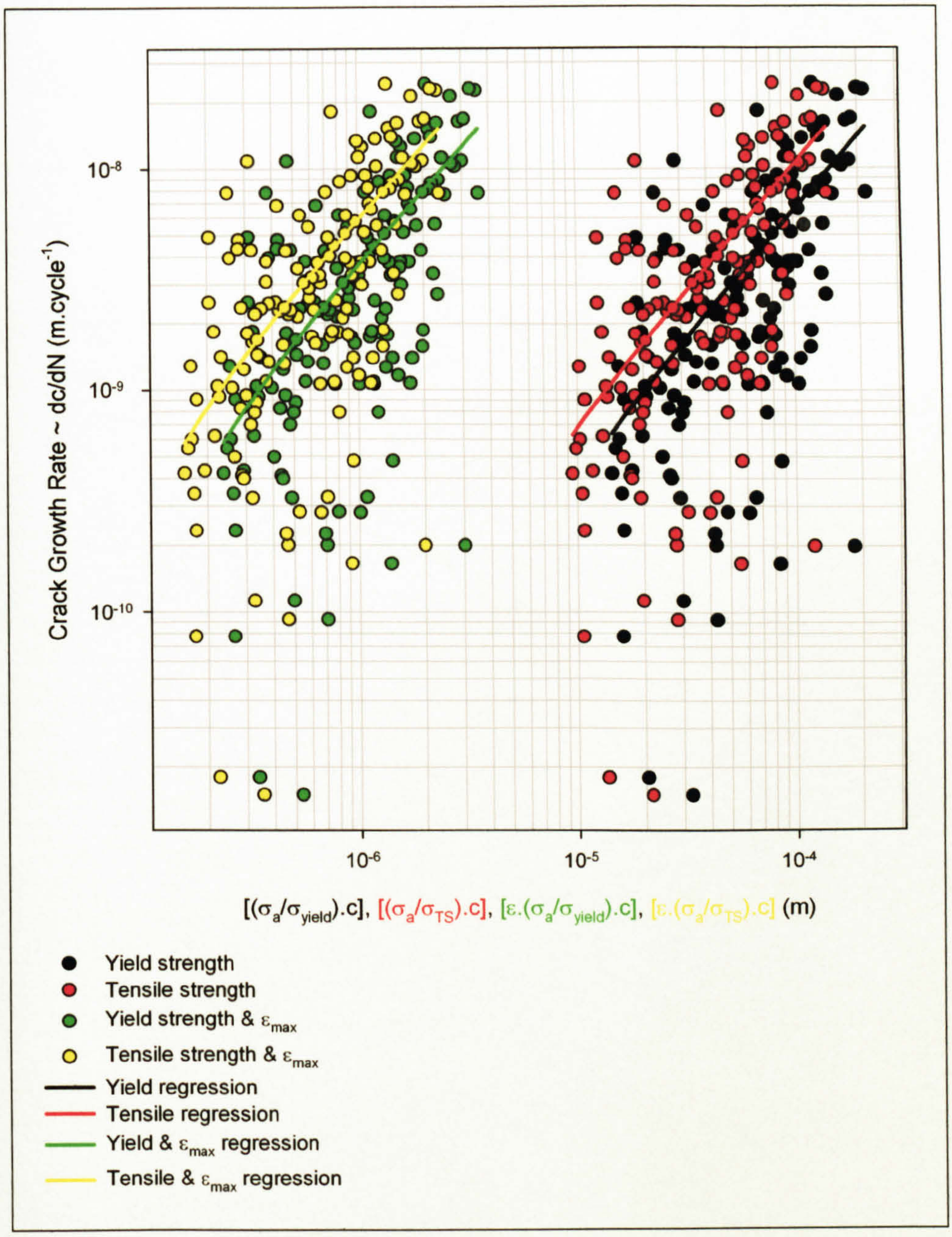

Figure 7.8: PP |- experimentally determined crack growth rates (see Figure 6.50 and Figure 6.51, page 349) as a function of equations (7.16) to (7.19).

Analysis	Equation	a	b	r^2
Yield strength	$y = a + bx/\ln x$	1.3436×10^{-1}	-0.00026096	0.45
Tensile strength		-1.5117×10^{-1}	-0.00041481	
Yield strength & ε_{max}		-2.5736×10^{-1}	-0.02339140	
Tensile strength & ε_{max}		-2.66×10^{-1}	-0.03662330	

Table 7.3: Regression analysis equation and constants for PP |- SCG data.

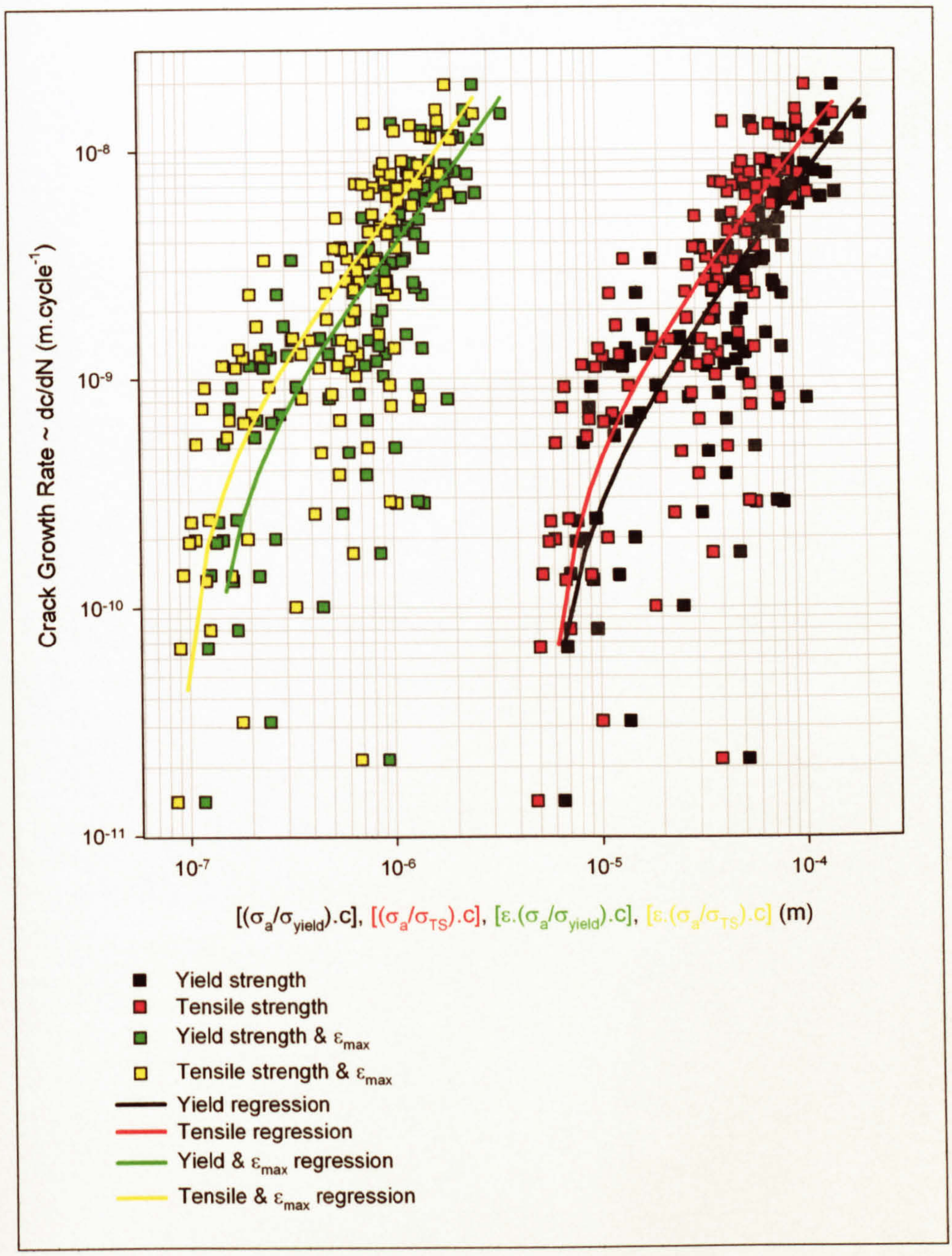

Figure 7.9: PP // experimentally determined crack growth rates (see Figure 6.56 and Figure 6.57, page 353) as a function of equations (7.16) to (7.19).

Analysis	Equation	a	b	c	r^2
Yield strength	$y = a + bx^c$	-2.4358×10^{-1}	0.000384716	1.175799836	0.62
Tensile strength		-4.3167×10^{-1}	0.000314247	1.113751978	
Yield strength & ε_{max}	$y = a + b.\exp(-x/c)$	-2.6834×10^{-8}	2.63689×10^{-8}	-6.8953×10^{-6}	
Tensile strength & ε_{max}				-5.069×10^{-6}	

Table 7.4: Regression analysis equations and constants for PP // SCG data.

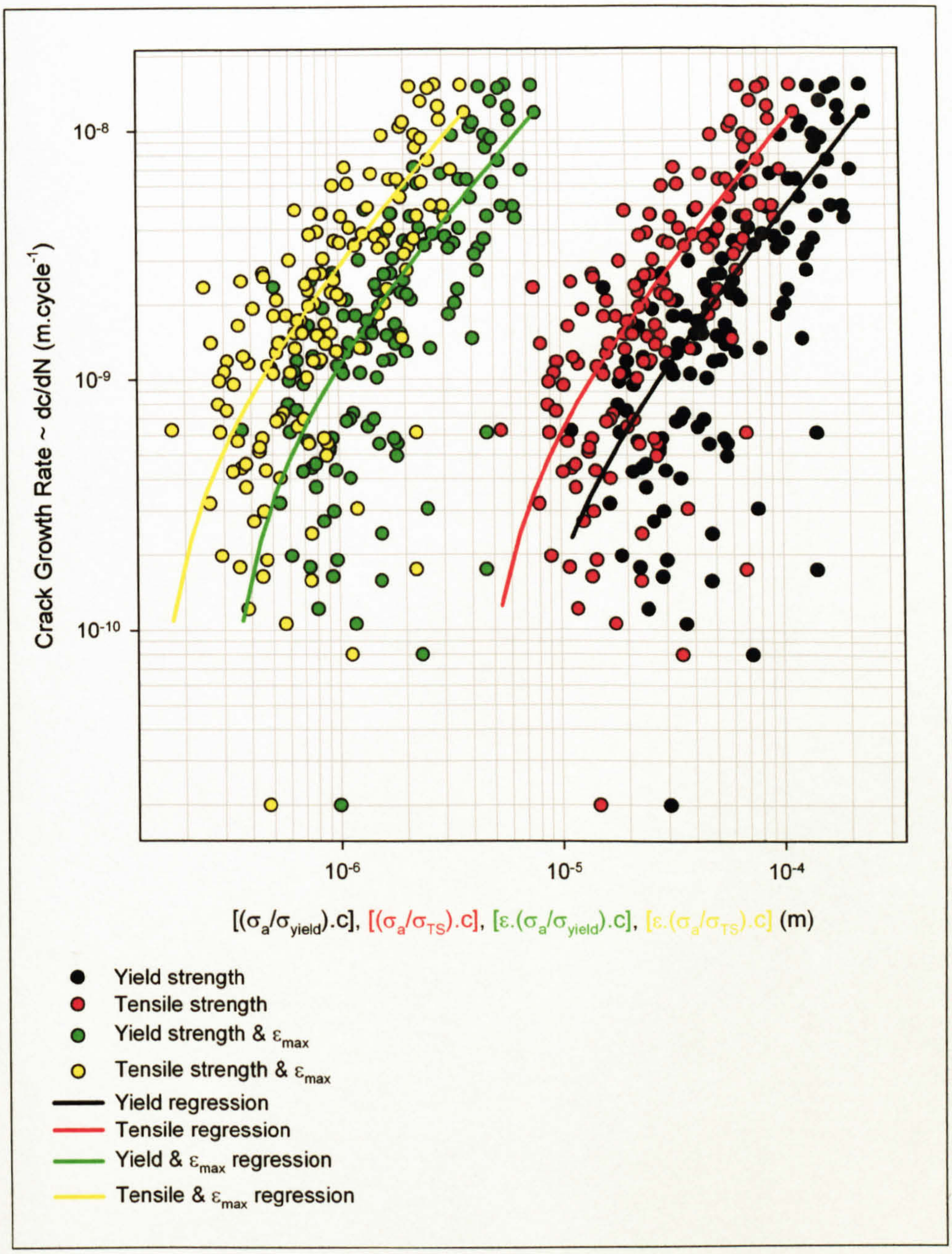

Figure 7.10: MIG LI experimentally determined crack growth rates (see Figure 6.67 and Figure 6.68, page 362) as a function of equations (7.16) to (7.19).

Analysis	Equation	a	b	c	r^2
Yield strength	$y = a + bx^c$	-2.262×10^{-1}	9.21937×10^{-5}	1.070799003	0.58
Tensile strength		-4.3229×10^{-1}	0.000113677	1.007852236	
Yield strength & ε_{max}	$y = a + bx$	-4.6308×10^{-1}	0.001572564		
Tensile strength & ε_{max}			0.003263070		

Table 7.5: Regression analysis equations and constants for MIG LI SCG data.

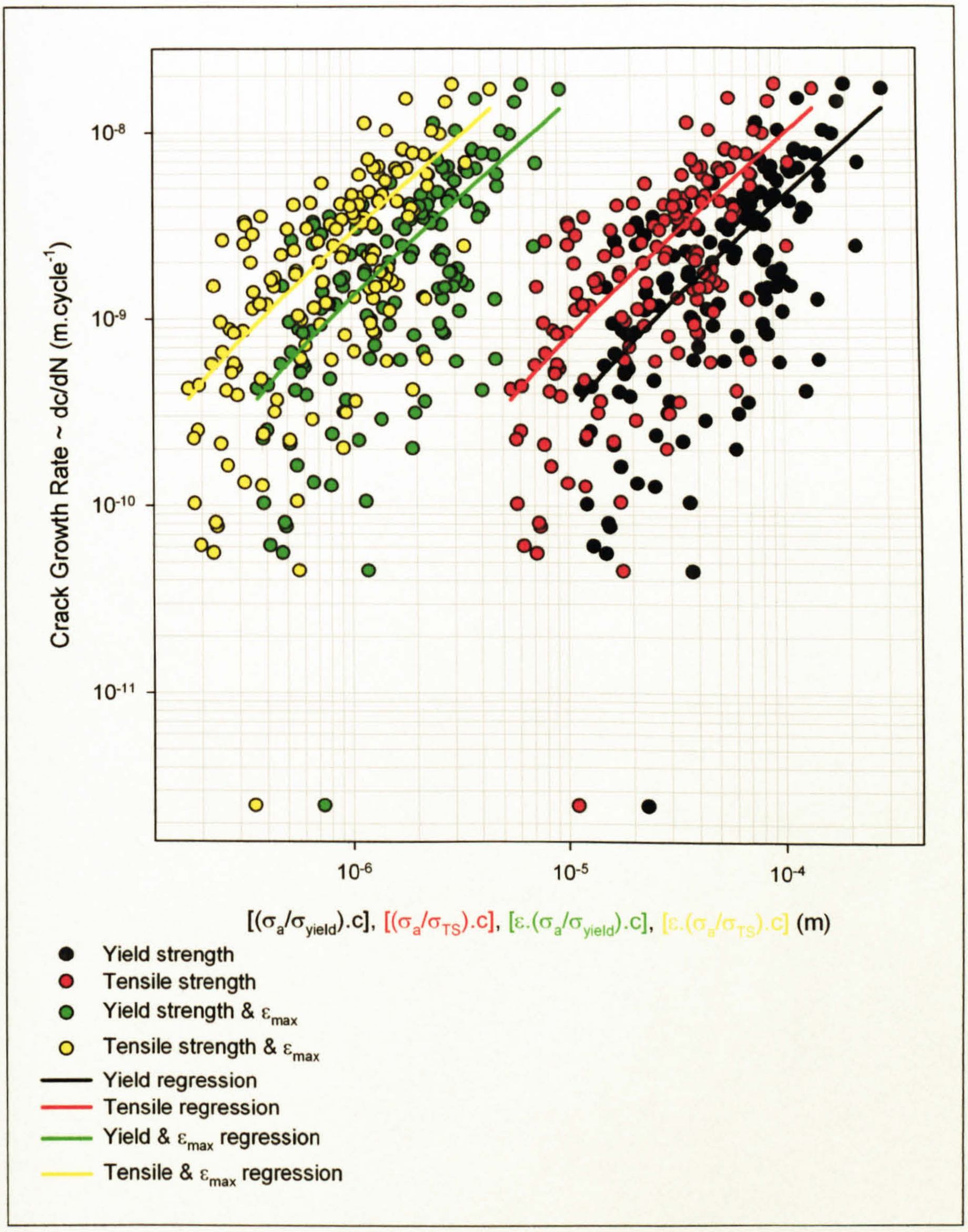

Figure 7.11: MIG HI experimentally determined crack growth rates (see Figure 6.73 and Figure 6.74, page 366) as a function of equations (7.16) to (7.19).

Analysis	Equation	a	b	r^2
Yield strength	$y = a + bx$	-1.5422×10^{-1}	4.58763×10^{-5}	0.47
Tensile strength			9.61479×10^{-5}	
Yield strength & ε_{max}			0.001447658	
Tensile strength & ε_{max}			0.003034015	

Table 7.6: Regression analysis equation and constants for MIG HI SCG data.

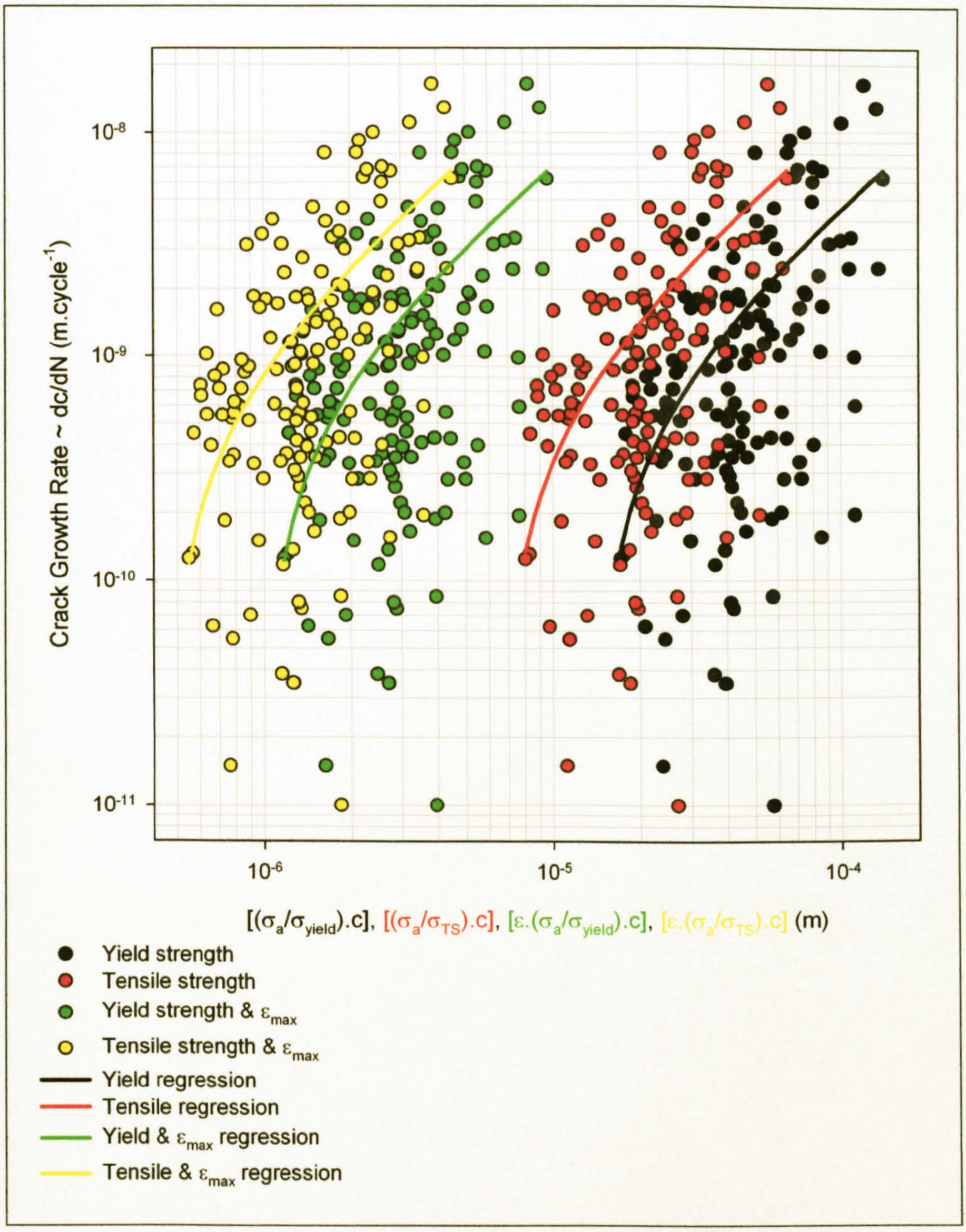

Figure 7.12: FS SP experimentally determined crack growth rates (see Figure 6.85 and Figure 6.86, page 375) as a function of equations (7.16) to (7.19).

Analysis	Equation	a	b	r^2
Yield strength	$y = a + bx/\ln x$	-5.8086×10^{-1}	-0.00020054	0.28
Tensile strength		-5.9814×10^{-1}	-0.00046610	
Yield strength & ε_{max}		-6.3293×10^{-1}	-0.00381984	
Tensile strength & ε_{max}		-6.4407×10^{-1}	-0.00871545	

Table 7.7: Regression analysis equation and constants for FS SP SCG data.

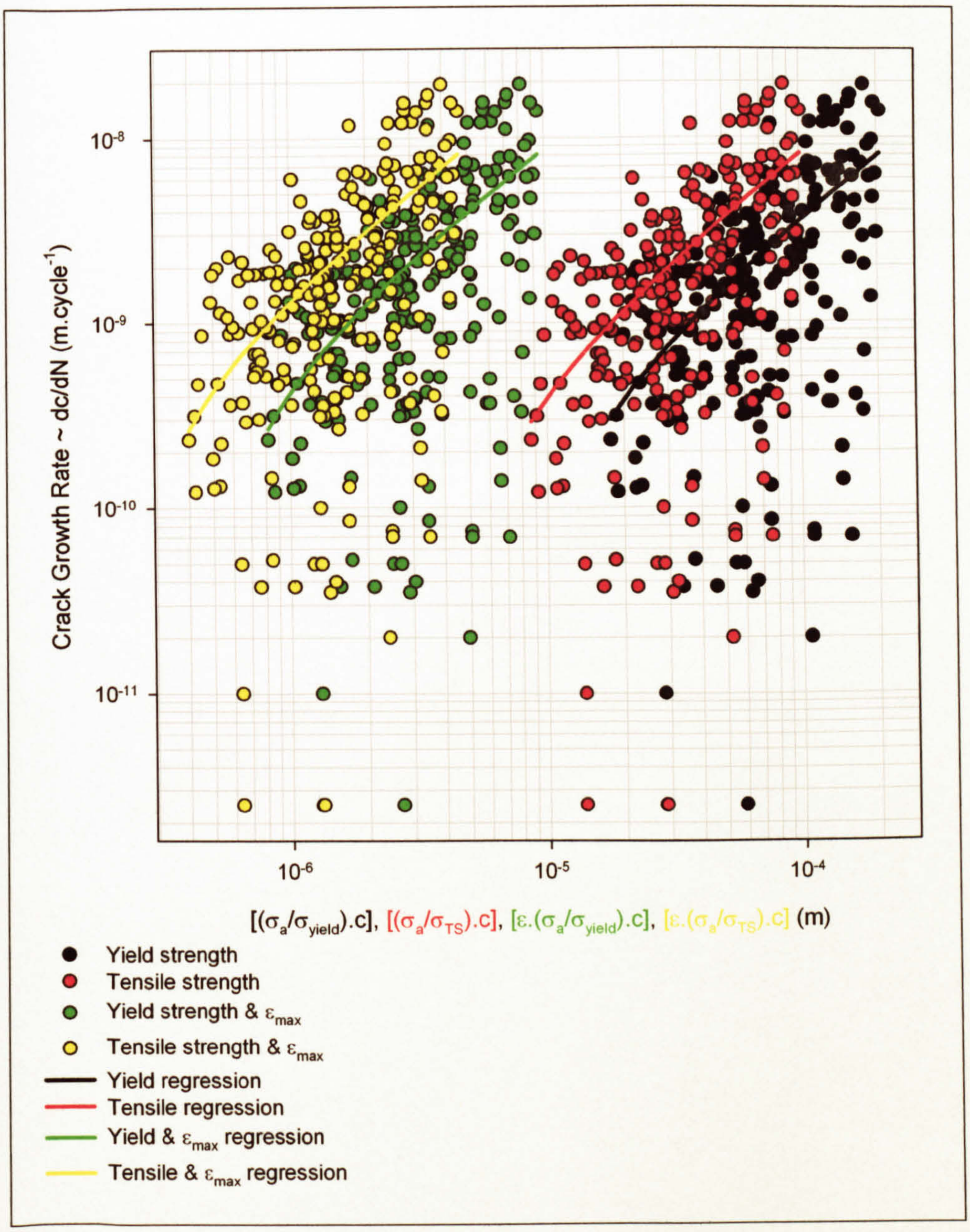

Figure 7.13: FS DPA experimentally determined crack growth rates (see Figure 6.91 and Figure 6.92, page 379) as a function of equations (7.16) to (7.19).

Analysis	Equation	a	b	r^2
Yield strength	$y = a + bx/\ln x$	-2.6331×10^{-1}	-0.00015081	0.31
Tensile strength		-2.8312×10^{-1}	-0.00033419	
Yield strength & ε_{max}		-3.3344×10^{-1}	-0.00446970	
Tensile strength & ε_{max}		-3.453×10^{-1}	-0.00969883	

Table 7.8: Regression analysis equation and constants for FS DPA SCG data.

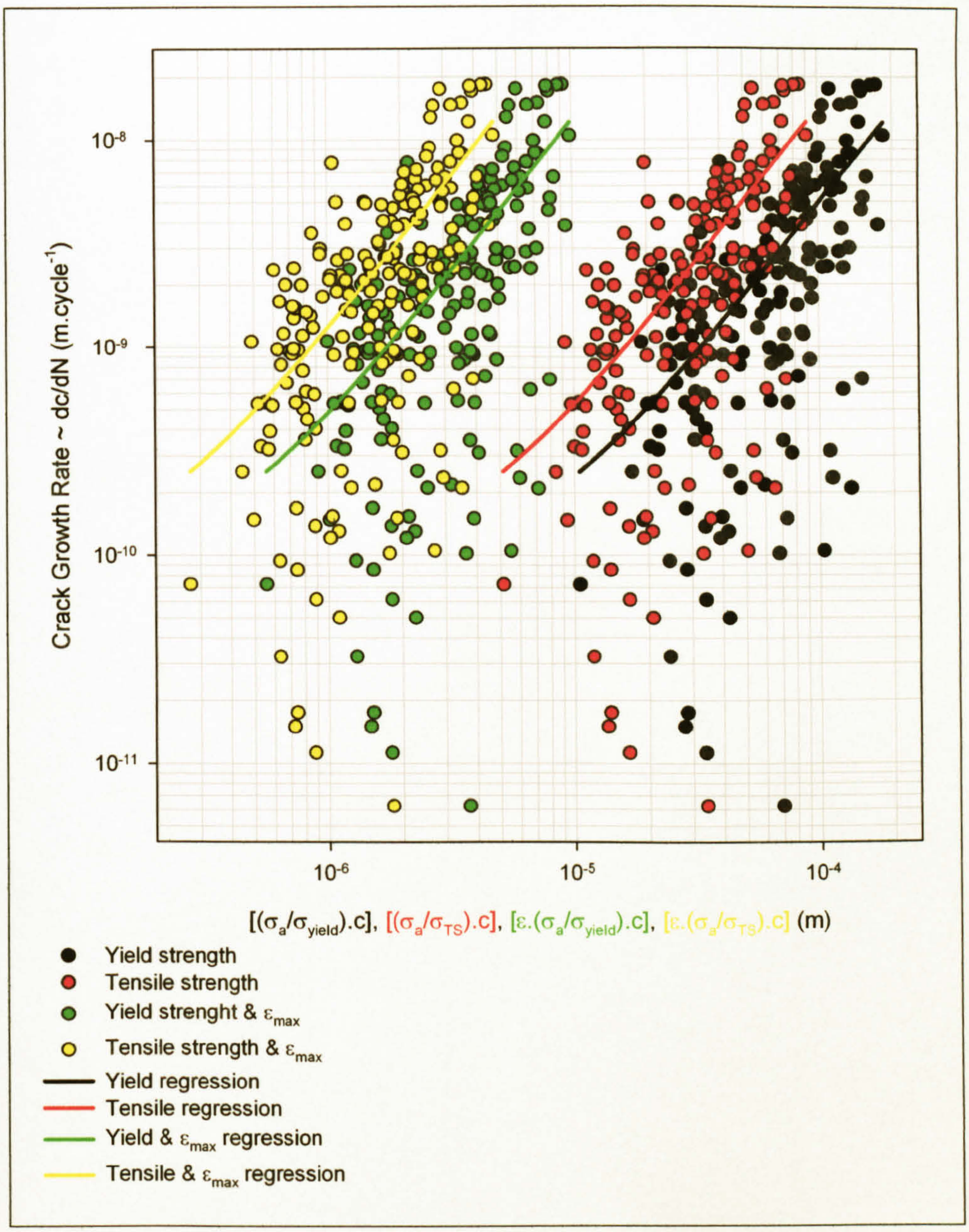

Figure 7.14: FS DPR experimentally determined crack growth rates (see Figure 6.97 and Figure 6.98, page 383) as a function of equations (7.16) to (7.19).

Analysis	Equation	a	b	c	r^2
Yield strength	$y = a + bx^c$	8.85024×10^{-11}	0.004817725	1.5	0.44
Tensile strength			0.014067825		
Yield strength & ε_{max}			0.391737998		
Tensile strength & ε_{max}			1.143880465		

Table 7.9: Regression analysis equation and constants for FS DPR SCG data.

Regression analysis on the experimental SCG crack growth rate/crack length data, as shown in Figure 7.8 to Figure 7.14, resulted in the curves shown in Figure 7.15 to Figure 7.18. The analysis was undertaken on crack lengths and growth rates considered to be representative of SCG, as shown in Table 7.10; such growth rates were considered to be $\leq 2 \times 10^{-8}$ m.cycle^{-1} (excluding the PP |- where the rate was considered to be $\leq 3 \times 10^{-8}$ m.cycle^{-1}) and crack lengths, c, $\leq$ 225 - 350 µm (excluding the FS SP where the SC region was considered to be $\leq$ 169 µm as this was the maximum SC length measured). Regression curves were determined through the analysis of all the SC data for each specimen type rather than for each individual crack, therefore giving a representation of the typical growth rates that would be observed; although this method precludes any specific interaction between individual cracks it means that they are incorporated into the overall analysis. 100 point regression curves, determined using TableCurve 2D V 5.00 software, were as shown in Table 7.11.

	PP |-	PP //	MIG LI	MIG HI	FS SP	FS DPA	FS DPR
Minimum short crack length*, c_i, (µm)	13	13	21	21.5	20	10	10
SCG → LCG transition length, c_t, (µm)	350	300	300	250	?169	250	225
Maximum SCG rate (m.cycle^{-1})	3×10^{-8}	2×10^{-8}	2×10^{-8}	2×10^{-8}		2×10^{-8}	2×10^{-8}
Grain size (µm)	50 - 100	30 - 60	30	40	10	50	50
Max. SC (grains)	3 - 8	5 - 10	9 - 10	5 - 6	~17	5	4 - 5

Table 7.10: Crack lengths and growth rates considered to be representative of SCG.

Analysis	Equation	a	b	c	r^2
PP |-	$y = a + bx/\ln x$	-0.10574	-0.00012769		0.45
PP //	$y = a + bx^c$	-0.21169	0.000182420	1.186760505	0.62
MIG LI		-0.16555	8.21394×10^{-5}	1.090834968	0.58
MIG HI	$y = a + bx.\ln x$	-0.50341	-9.6503×10^{-6}		0.46
FS SP	$y = a + bx/\ln x$	-0.57637	-0.00016390		0.28
FS DPA	$y = a + bx/\ln x$	-0.25435	-0.00010860		0.31
FS DPR	$y = a + bx^{1.5}$	8.85024×10^{-11}	0.003419563		0.44

Table 7.11: Summary of the regression analysis resulting from the experimental SCG data, dc/dN-c.

Utilising the crack lengths determined through the regression analysis of the SCG experimental data, as shown in Table 7.10 and Table 7.11, analysis was undertaken employing equations (7.16) to (7.19) (page 411), as shown in Figure 7.15 to Figure 7.18. Application of the stress amplitude, σ_a, and tensile strength, σ_{TS}, as shown in Figure 7.15,

* Crack Initiator size, see 7.4.1Crack Initiation, page 410.

resulted in the parent plate and weld SCG data all falling within a narrow range, whilst utilisation of the yield strength, as shown in Figure 7.16, resulted in the welded specimens and parent plate specimens falling within their own narrow bands. Employment of the peak strain in combination with either the tensile or yield strengths, shown in Figure 7.17 and Figure 7.18, resulted in greater variability in the results for the welded specimens, values ranging in magnitude by up to a factor of 10, although the values returned by the parent plate specimens, exhibited a smaller range and were near-identical for the maximum strain and yield stress combination. The results from the experimental analyses were also noted to fall within a relatively narrow range and the change in the crack growth rates with respect to the crack length, the slope of the curves, were also comparable for both the parent material and welded specimens.

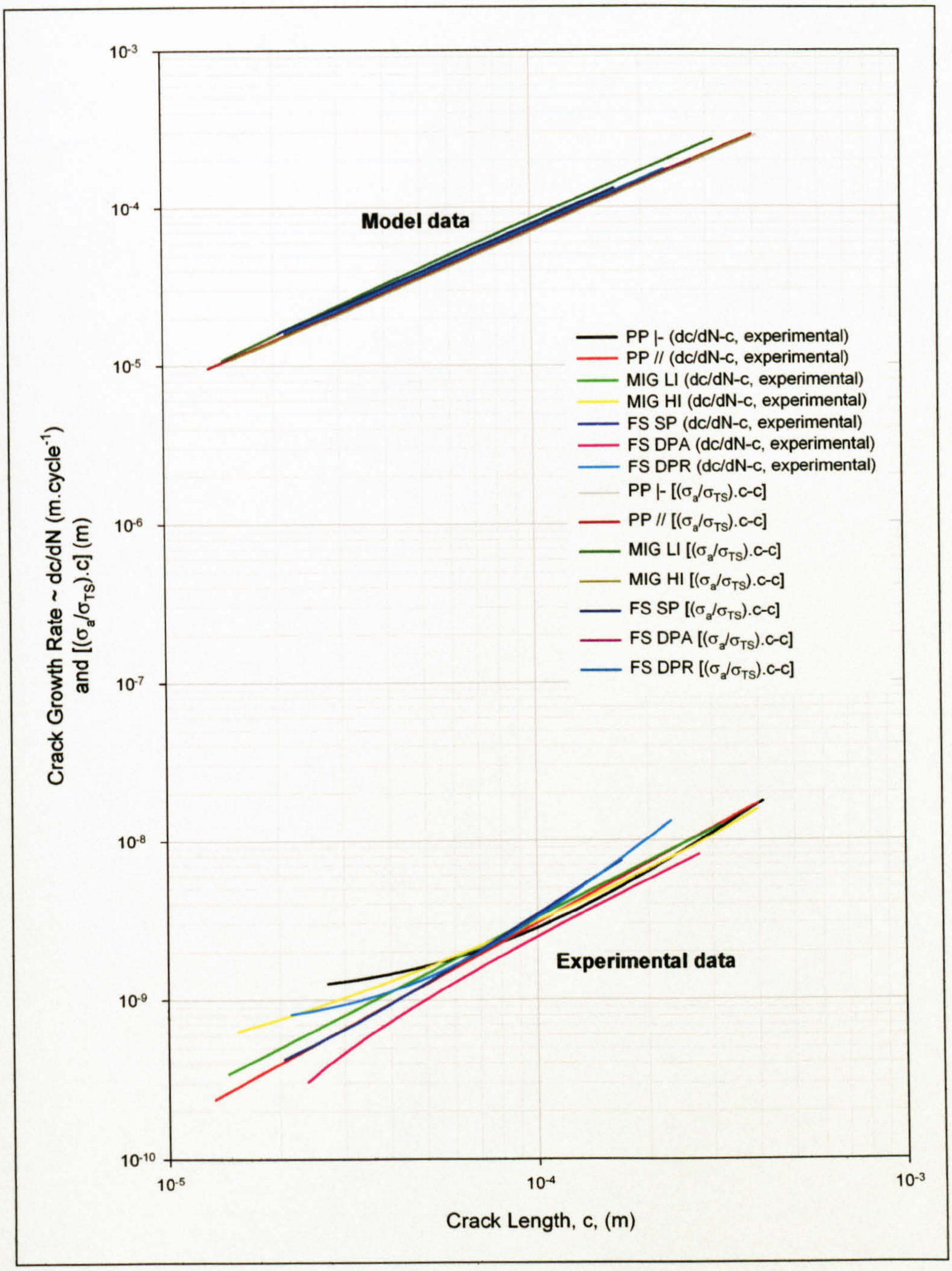

Figure 7.15: Experimentally determined crack growth rate, (dc/dN)/c, regression curves, compared with the growth rate model curves, predicted by $[(\sigma_a/\sigma_{TS}).c]/c$.

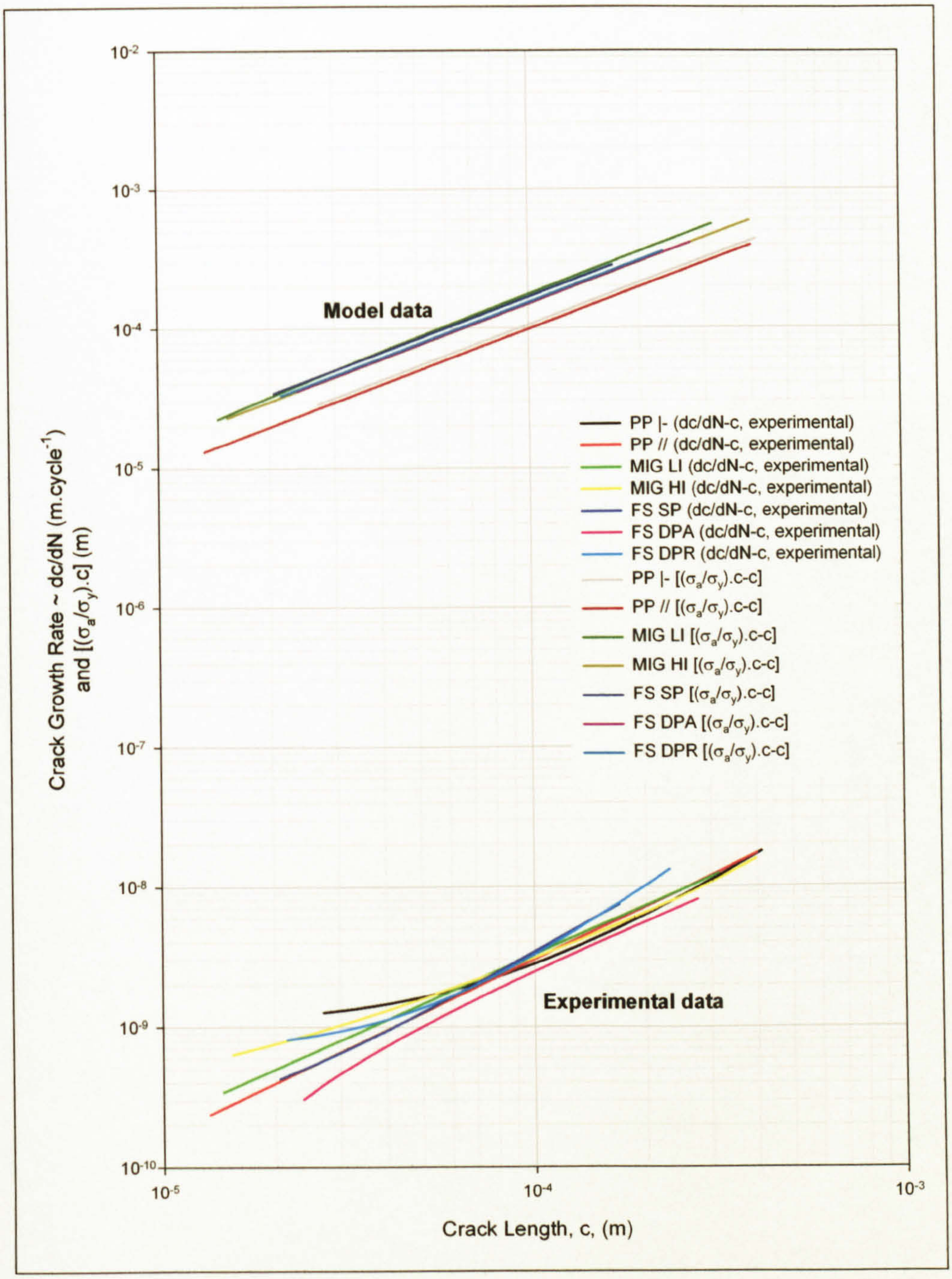

Figure 7.16: Experimentally determined crack growth rate, (dc/dN)/c, regression curves, compared with the growth rate model curves, predicted by $[(\sigma_a/\sigma_y).c]/c$.

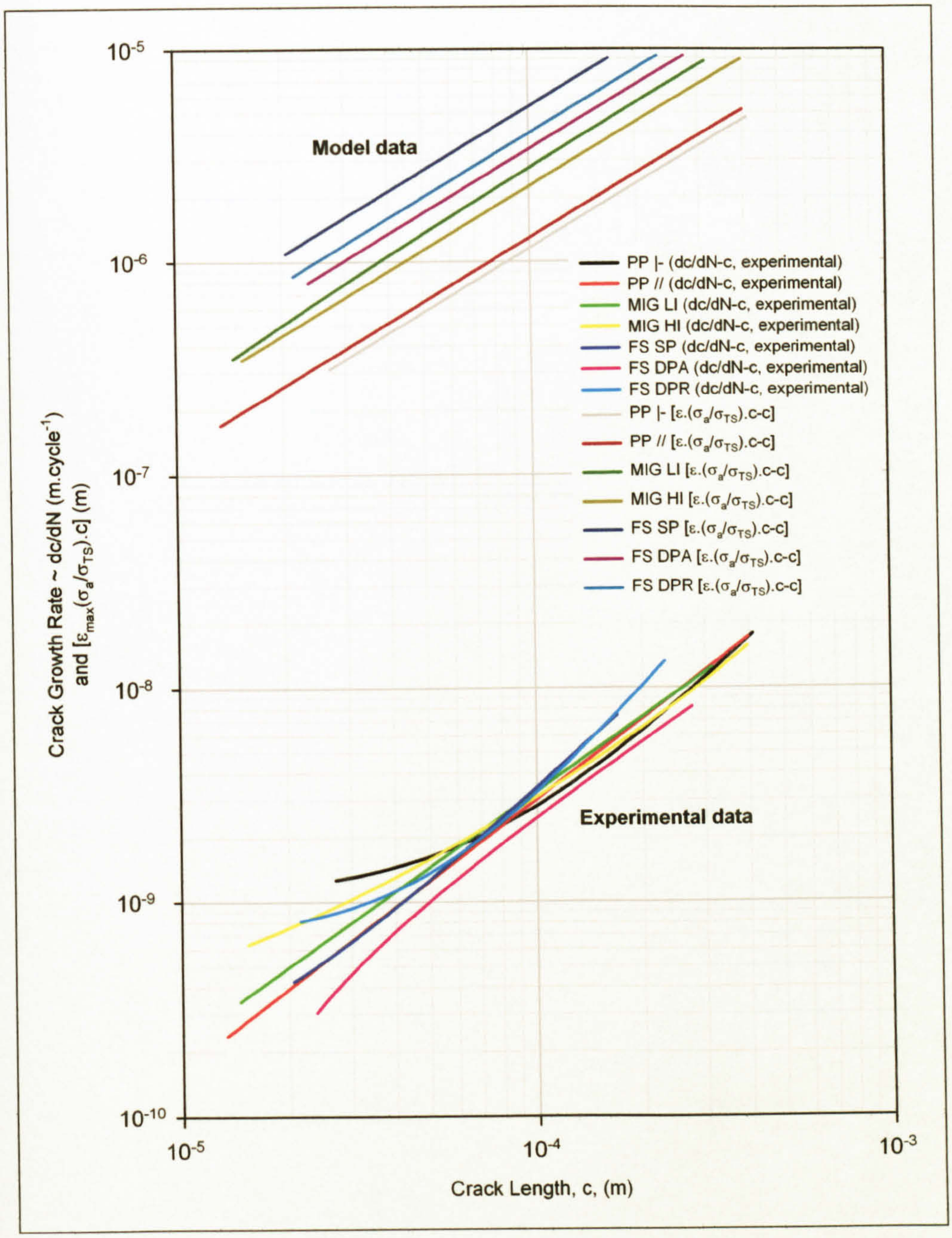

Figure 7.17: Experimentally determined crack growth rate, (dc/dN)/c, regression curves, compared with the growth rate model curves, predicted by $[\varepsilon_{max}.(\sigma_a/\sigma_{TS}).c]/c$.

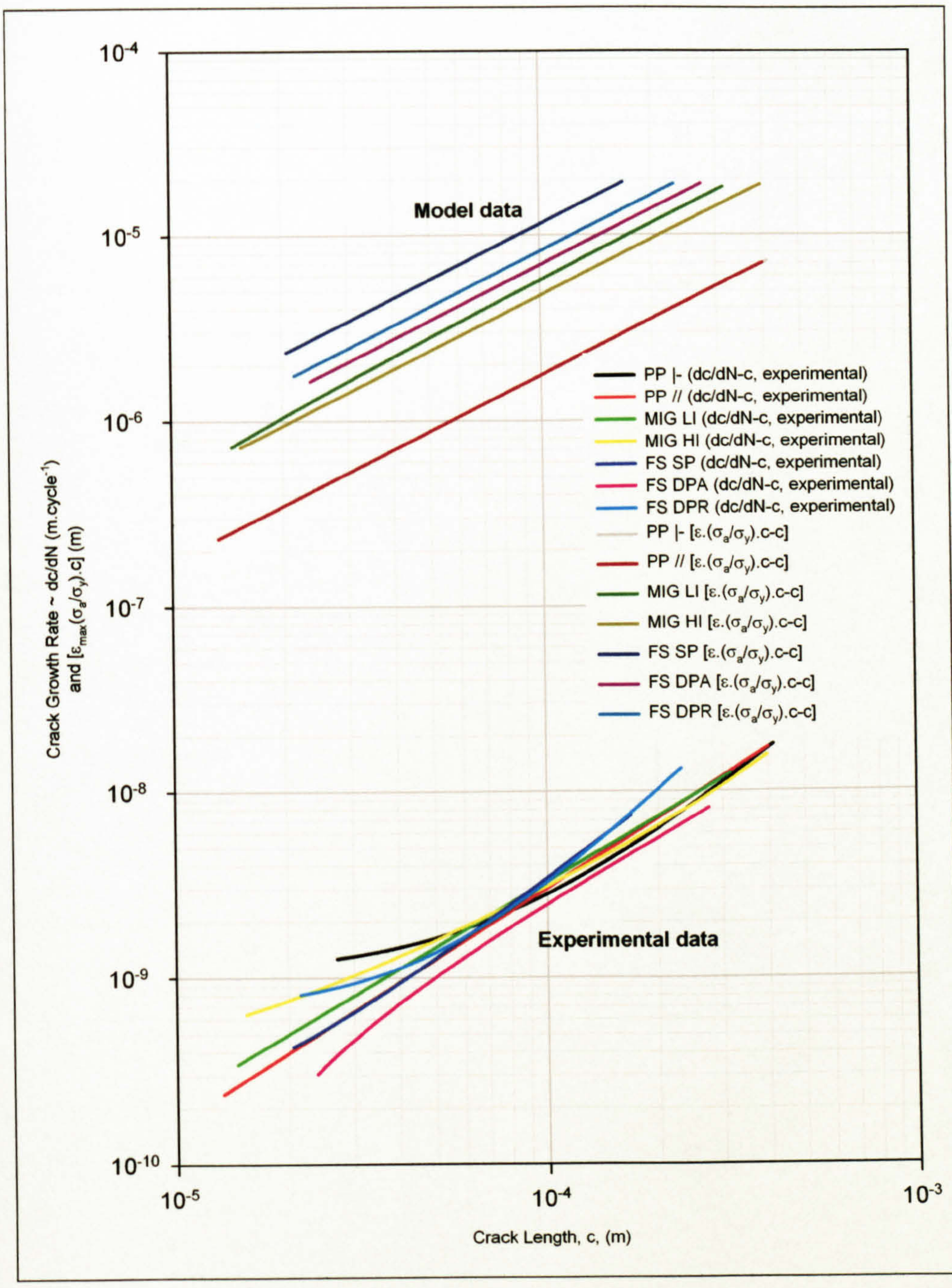

Figure 7.18: Experimentally determined crack growth rate, (dc/dN)/c, regression curves, compared with the growth rate model curves, predicted by $[\varepsilon_{max}.(\sigma_a/\sigma_y).c]/c$.

Nisitani et al[1,2] and Caton et al[3] determined the values of the scaling constants, B and n of equation (7.20), for SCG through the analysis of the growth rates at a number of stress levels; the values being used to normalise the SCG rate with respect to the stress amplitude, yield or tensile strength and crack length.

$$\left(\frac{dc}{dN}\right)_{scg} = B.\sigma_a^n.c \qquad (7.20)$$

Due to problems in attaining a second series of results for a SCG specimen fatigue life of 10^6 cycles this option was not available to the author. The values for the constants were therefore determined through trial and error, fitting the equations to SCG S-N curves. These were attained through subtraction of the S-N curves that resulted from the integration of the LCG Paris equations, as detailed in Section 6.5.2, Long Crack Growth (page 393), from the overall S-N curves obtained from the 40 mm wide parent material and as-welded specimens, as detailed in Section 5.5, S-N Test Results (page 266), the technique being represented by equation (7.21).

$$N_{scg} = N_T - N_{lcg} \qquad (7.21)$$

where: N_{scg} = number of cycles under which short crack growth was considered to occur.
N_T = total number of cycles to failure or a predetermined crack length.
N_{lcg} = number of cycles under which long crack growth was considered to occur.

It has been assumed that the difference between the crack growth rates resulting from the pure bending applied to the 40 mm wide specimens and uniaxial loading applied to the SCG specimens would be minimal and was therefore not considered in the approach:

Determination of the number of cycles for a crack to grow from the crack initiator length to the SCG to LCG transition length was determined through integration of equation (7.22), without taking the maximum applied strain into consideration, or equation (7.25), taking the maximum applied strain into consideration, resulting in equations (7.24) and (7.27) respectively.

---

[1] Nisitani, H; Goto, M (1986)
[2] Nisitani, H et al (1992)
[3] Caton, MJ et al (1999b)

$$\frac{dc}{dN} = B.\left(\frac{\sigma_a}{\sigma_{y\ or\ TS}}\right)^n .c \tag{7.22}$$

$$N_{c_i \to c_t} = \frac{1}{B}\left(\frac{\sigma_{y\ or\ TS}}{\sigma_a}\right)^n \int_{c_i}^{c_t} \frac{1}{c} \tag{7.23}$$

$$N_{c_i \to c_t} = \frac{1}{B}\left(\frac{\sigma_{y\ or\ TS}}{\sigma_a}\right)^n \ln\frac{c_t}{c_i} \tag{7.24}$$

$$\frac{dc}{dN} = B.\left(\frac{\sigma_a}{\sigma_{y\ or\ TS}}.\varepsilon_{max}\right)^n .c \tag{7.25}$$

$$N_{c_i \to c_t} = \frac{1}{B}\left(\frac{\sigma_{y\ or\ TS}}{\sigma_a}\frac{1}{\varepsilon_{max}}\right)^n \int_{c_i}^{c_t} \frac{1}{c} \tag{7.26}$$

$$N_{c_i \to c_t} = \frac{1}{B}\left(\left(\frac{\sigma_{y\ or\ TS}}{\sigma_a}\right).\frac{1}{\varepsilon_{max}}\right)^n \ln\frac{c_t}{c_i} \tag{7.27}$$

where: c_i = initial crack size.

c_t = transition (between SCG and LCG) crack size.

7.4.3 Long Crack Growth

An estimate of the total fatigue life of a specimen can be made through integration of the power law used to describe the Paris regime, although this is made more complex in fabricated structures due to presence of residual stresses and stress concentrating effects. In an uncracked specimen account of the crack initiation and/or SCG period also needs to be taken into consideration.

From Section 6.5.2, Long Crack Growth (page 393) the Paris law equations were integrated for each specimen type as shown in equations (7.28) to (7.30).

$$\frac{dc}{dN} = C(Y\Delta\sigma\sqrt{\pi c})^m \tag{7.28}$$

$$CY^m(\Delta\sigma)^m \pi^{m/2} \int_0^{N_f} dN = \int_{c_t}^{c_f} \frac{dc}{c^{m/2}} \tag{7.29}$$

$$N_{lcg} = \frac{2}{(m-2)CY^m(\Delta\sigma)^m \pi^{m/2}}\left\{\frac{1}{(c_t)^{(m-2)/2}} - \frac{1}{(c_f)^{(m-2)/2}}\right\} \tag{7.30}$$

where: C & m = Paris regime constants.

Y = geometric configuration factor for a semi-elliptical surface crack.

$\Delta\sigma$ = stress range.

c = surface half-crack length.

N_{lcg} = number of cycles to failure or a predetermined crack length.

c_f = final crack length.

c_t = transition, from SCG to LCG, crack length.

7.4.3.1 Determination of Long Crack Growth Geometric Configuration Factor

The long crack geometric configuration factor, Y, was calculated utilising an analogous approach to that employed in determining the configuration factor used in the calculation of the stress intensity factor range for the SCG rates, as described in Section 6.4.1.2, Stress Intensity Factor Range (page 333), but with the equation[1] modified to take into consideration the pure bending loading applied:

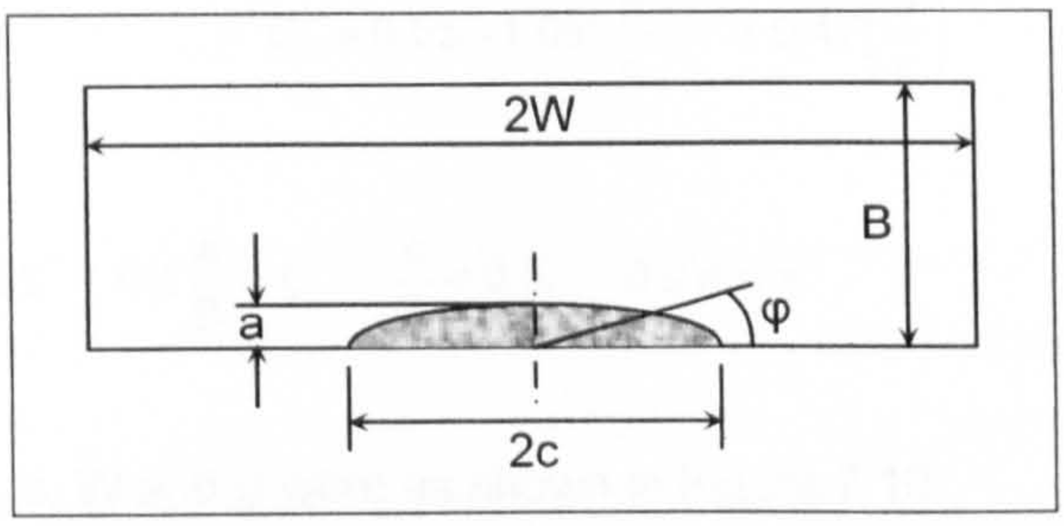

Figure 7.19: Schematic diagram of a semi-elliptical surface flaw.

$$K_I = (\sigma_t + H\sigma_b)\sqrt{\pi \frac{a}{Q}} F\left(\frac{a}{B}, \frac{a}{c}, \frac{c}{W}, \varphi\right) \quad (7.31)$$

$$Q = 1 + 1.464\left(\frac{a}{c}\right)^{1.65} \quad (7.32)$$

$$F = \left[M_1 + M_2\left(\frac{a}{B}\right)^2 + M_3\left(\frac{a}{B}\right)^4\right] f_\varphi g f_w \quad (7.33)$$

$$M_1 = 1.13 - 0.09\left(\frac{a}{c}\right) \quad (7.34)$$

$$M_2 = -0.54 + \frac{0.89}{0.2 + \left(\frac{a}{c}\right)} \quad (7.35)$$

$$M_3 = 0.5 - \frac{1.0}{0.65 + \left(\frac{a}{c}\right)} + 14\left(1.0 - \frac{a}{c}\right)^{24} \quad (7.36)$$

$$g = 1 + \left[0.1 + 0.35\left(\frac{a}{B}\right)^2\right](1 - \sin\varphi)^2 \quad (7.37)$$

$$f_\varphi = \left[\sin^2\varphi + \left(\frac{a}{c}\right)^2 \cos^2\varphi\right]^{0.25} \quad (7.38)$$

[1] Newman, JC; Raju, IS (1981)

$$f_w = \left[\sec\frac{\pi c}{2W}\sqrt{\frac{a}{B}}\right]^{0.5} \tag{7.39}$$

$$H = H_1 + (H_2 - H_1)\sin^p \varphi \tag{7.40}$$

$$p = 0.2 + \frac{a}{c} + 0.6\frac{a}{B} \tag{7.41}$$

$$H_1 = 1 - 0.34\frac{a}{B} - 0.11\frac{a}{c}\left(\frac{a}{B}\right) \tag{7.42}$$

$$H_2 = 1 + G_1\left(\frac{a}{B}\right) + G_2\left(\frac{a}{B}\right)^2 \tag{7.43}$$

$$G_1 = -1.22 - 0.12\frac{a}{c} \tag{7.44}$$

$$G_2 = 0.55 - 1.05\left(\frac{a}{c}\right)^{0.75} + 0.47\left(\frac{a}{c}\right)^{1.5} \tag{7.45}$$

for: $0 < \frac{a}{c} \le 1, \quad 0 \le \frac{a}{B} < 1, \quad \frac{c}{B} < 0.5, \quad 0 \le \varphi \le \pi$

where: a, B, c, W and φ were as shown in Figure 7.19.

σ_t = remote uniform tensile load (= 0 for the loading under consideration).

σ_b = stress in the outer fibre due to pure bending.

Through application of the applied stress ranges, $\Delta\sigma$, equation (7.31) provides the stress intensity factor range, ΔK_I, which is proportional to the crack growth rate:

$$\frac{dc}{dN} = C(Y\Delta\sigma\sqrt{\pi c})^m \tag{7.46}$$

$$\frac{dc}{dN} = C(\Delta K)^m \tag{7.47}$$

$$\Delta K = Y\Delta\sigma\sqrt{\pi c} \tag{7.48}$$

$$\therefore Y = \frac{\Delta K}{\Delta\sigma\sqrt{\pi c}} \tag{7.49}$$

Two problems became apparent with the integration of equation (7.28); a simple integration relies on Y being constant, whereas Y generally varies with the crack length. A simple analysis would also depend on the crack aspect ratio, a/c, remaining constant throughout the fatigue life; semicircular cracks tend to predominate for low a/B ratios (crack depth/material thickness) and attain a value 0.8 - 0.9 for tensile loading as a/B increases, but the application of a bending load generally results in the crack aspect ratio being inversely proportional to the through thickness ratio, $a/c \propto B/a$[1,2].

---

[1] Newman, JC; Raju, IS (1981)
[2] Chell, GG (1984)

Although fractography of the final fracture surfaces of the 40 mm wide S-N specimens suggested that the crack aspect ratios were typically in the range of 0.3 - 0.4, a nominal value of 0.75 was utilised on the basis that a larger percentage of load cycles would be experienced at the greater aspect ratio. This resulted in Y, calculated through employment of equation (7.49), page 429, for crack lengths ranging from 0.25 - 10 mm, ranging from 0.59 - 0.68, with the mean value of 0.61 being employed. A comparison of the value for Y obtained from equation (7.49) was made through utilisation of equation (7.50), the configuration factor for a semi-elliptical surface crack in a semi-infinite plate[1]. Although the analysis related to tensile loading, utilising the same aspect ratio of 0.75 returned a comparable value of 0.57.

$$Y = \left[\left[1+0.12\left(1-\frac{a}{c}\right)\right]^2\left(\frac{a}{c}\right)^2\left[1-0.619\frac{a}{c}\right]\right]^{0.5} \tag{7.50}$$

Due to the change in the nature of the LCG regime in the region of $\Delta K = 9 - 10\ MPa.m^{0.5}$, assumed to be due to the change from predominantly plane strain to plane stress (as detailed in Section 6.4.5, Long Crack Growth Tests, page 341), equation (7.30) was adapted to take into consideration both LCG under predominantly plane strain, equation (7.51), and plane stress, equation (7.52), with the total number of cycles for the crack to propagate to a predetermined length being represented by equation (7.53):

$$N_{lcg_\varepsilon} = \frac{2}{(m_\varepsilon - 2)C_\varepsilon Y^{m_\varepsilon}(\Delta\sigma)^{m_\varepsilon}\pi^{m_\varepsilon/2}}\left\{\frac{1}{(c_t)^{(m_\varepsilon-2)/2}} - \frac{1}{(c_f)^{(m_\varepsilon-2)/2}}\right\} \tag{7.51}$$

$$N_{lcg_\sigma} = \frac{2}{(m_\sigma - 2)C_\sigma Y^{m_\sigma}(\Delta\sigma)^{m_\sigma}\pi^{m_\sigma/2}}\left\{\frac{1}{(c_t)^{(m_\sigma-2)/2}} - \frac{1}{(c_f)^{(m_\sigma-2)/2}}\right\} \tag{7.52}$$

$$N_{lcg_T} = N_{lcg_\varepsilon} + N_{lcg_\sigma} \tag{7.53}$$

where: $N_{lcg\,\varepsilon}$ = number of LCG cycles under predominantly plane strain.

$N_{lcg\,\sigma}$ = number of LCG cycles under predominantly plane stress.

$N_{lcg\,T}$ = total number of LCG cycles.

7.4.3.2 Proportion of the Long Crack Growth Fatigue Life Attributable to Predominantly Plane Strain and Plane Stress States

Due to the change in the nature of the LCG regime in the region of $\Delta K = 9 - 10\ MPa.m^{0.5}$, assumed to be due to the transformation from predominantly plane strain to plane stress (as detailed in Section 6.4.5, Long Crack Growth Tests, page 341), the LCG fatigue lives

---

[1] Gray, TGF (1994)

were determined through the addition of equation (7.54), the number of cycles under predominantly plane strain, and equation (7.55), the number of cycles under predominantly plane stress, resulting in equation (7.56):

$$N_{lcg_\varepsilon} = \frac{2}{(m_\varepsilon - 2) C_\varepsilon Y^{m_\varepsilon} (\Delta\sigma)^{m\varepsilon} \pi^{m_\varepsilon/2}} \left\{ \frac{1}{(c_t)^{(m_\varepsilon - 2)/2}} - \frac{1}{(c_f)^{(m_\varepsilon - 2)/2}} \right\} \tag{7.54}$$

$$N_{lcg_\sigma} = \frac{2}{(m_\sigma - 2) C_\sigma Y^{m_\sigma} (\Delta\sigma)^{m_\sigma} \pi^{m_\sigma/2}} \left\{ \frac{1}{(c_t)^{(m_\sigma - 2)/2}} - \frac{1}{(c_f)^{(m_\sigma - 2)/2}} \right\} \tag{7.55}$$

$$N_{lcg_T} = N_{lcg_\varepsilon} + N_{lcg_\sigma} \tag{7.56}$$

where: $N_{lcg\,\varepsilon}$ = number of LCG cycles under predominantly plane strain.
$N_{lcg\,\sigma}$ = number of LCG cycles under predominantly plane stress.
$N_{lcg\,T}$ = total number of LCG cycles.

Table 7.12 to Table 7.14 depict the number of cycles, for both LCG under the influence of predominantly plane strain and plane stress, for a crack to grow from the SCG to LCG transition length, c_t, to a length, c_f, of 10 mm for various stress ranges (R = 0.1). The crack length of 10 mm being considered the failure length for the 40 mm wide S-N specimens. In reality the crack length at failure would be inversely proportional to the stress range, although the subsequent number of lives in the crack growing from 10 mm to the final failure length, if this was greater than 10 mm, would be small compared to the overall fatigue life and its influence on the LCG fatigue life has been considered to be negligible. The total LCG life values, $N_{lcg\,T}$, resulting from the various stress ranges were then subtracted from the 40 mm wide specimen S-N curves to produce the SCG S-N curves shown in Figure 7.21, for example.

		PP	
		|-	//
SCG to LCG transition length, c_t, (μm)		350	300
ΔK at the change from predominantly plane strain to plane stress (MPa.m$^{0.5}$)		9	9.5
Nominal stress range, outer fibre, R = 0.1, (MPa)		**Load cycles**	
260	$N_{Icg\ \varepsilon}$	14167	18950
	$N_{Icg\ \sigma}$	13473	12041
	N_{IcgT}	**27640**	**30991**
250	$N_{Icg\ \varepsilon}$	16939	22775
	$N_{Icg\ \sigma}$	14268	12689
	N_{IcgT}	**31208**	**35464**
240	$N_{Icg\ \varepsilon}$	20650	27560
	$N_{Icg\ \sigma}$	14824	13294
	N_{IcgT}	**35474**	**40854**
230	$N_{Icg\ \varepsilon}$	24493	33401
	$N_{Icg\ \sigma}$	16086	14057
	N_{IcgT}	**40578**	**47458**
220	$N_{Icg\ \varepsilon}$	30233	40623
	$N_{Icg\ \sigma}$	16577	15000
	N_{IcgT}	**46810**	**55623**
210	$N_{Icg\ \varepsilon}$	36983	50489
	$N_{Icg\ \sigma}$	17446	15079
	N_{IcgT}	**54430**	**65568**
200	$N_{Icg\ \varepsilon}$	45525	61860
	$N_{Icg\ \sigma}$	18343	16605
	N_{IcgT}	**63867**	**78465**

Table 7.12: Parent plate LCG fatigue lives for a crack to grow from the SCG to LCG transition length to a length of 10 mm, determined through integration of the plane strain and plane stress Paris regime equations, (7.54) and (7.55).

				MIG	
				LI	HI
SCG to LCG transition length, c_t, (μm)				300	250
ΔK at the change from predominantly plane strain to plane stress (MPa.m$^{0.5}$)				10	9.5
Stress range, outer fibre, R = 0.1, (MPa),			**Load cycles**		
Weld toe	**Nominal LI**	**Nominal HI**			
300		**231**	**$N_{lcg\,\varepsilon}$ (x 10^6)**		0.14
			$N_{lcg\,\sigma}$(x 10^3)		22.80
			N_{lcgT} (x 10^6)		**0.16**
275		**201**	**$N_{lcg\,\varepsilon}$ (x 10^6)**		0.25
			$N_{lcg\,\sigma}$(x 10^3)		26.73
			N_{lcgT} (x 10^6)		**0.28**
250	**222**	**172**	**$N_{lcg\,\varepsilon}$ (x 10^6)**	1.61	0.47
			$N_{lcg\,\sigma}$(x 10^3)	49.35	30.13
			N_{lcgT} (x 10^6)	**1.66**	**0.50**
240	**211**		**$N_{lcg\,\varepsilon}$ (x 10^6)**	2.12	
			$N_{lcg\,\sigma}$(x 10^3)	52.63	
			N_{lcgT} (x 10^6)	**2.18**	
230	**201**		**$N_{lcg\,\varepsilon}$ (x 10^6)**	2.84	
			$N_{lcg\,\sigma}$(x 10^3)	56.80	
			N_{lcgT} (x 10^6)	**2.89**	
225		**144**	**$N_{lcg\,\varepsilon}$ (x 10^6)**		0.94
			$N_{lcg\,\sigma}$(x 10^3)		34.90
			N_{lcgT} (x 10^6)		**0.97**
220	**190**		**$N_{lcg\,\varepsilon}$ (x 10^6)**	3.84	
			$N_{lcg\,\sigma}$(x 10^3)	58.95	
			N_{lcgT} (x 10^6)	**3.90**	
210	**180**		**$N_{lcg\,\varepsilon}$ (x 10^6)**	5.25	
			$N_{lcg\,\sigma}$(x 10^3)	64.00	
			N_{lcgT} (x 10^6)	**5.32**	
200	**169**	**117**	**$N_{lcg\,\varepsilon}$ (x 10^6)**	7.31	2.03
			$N_{lcg\,\sigma}$(x 10^3)	67.11	39.98
			N_{lcgT} (x 10^6)	**7.37**	**2.07**
190	**159**		**$N_{lcg\,\varepsilon}$ (x 10^6)**	10.33	
			$N_{lcg\,\sigma}$(x 10^3)	72.18	
			N_{lcgT} (x 10^6)	**10.40**	
175		**91**	**$N_{lcg\,\varepsilon}$ (x 10^6)**		4.84
			$N_{lcg\,\sigma}$(x 10^3)		46.03
			N_{lcgT} (x 10^6)		**4.89**
150		**67**	**$N_{lcg\,\varepsilon}$ (x 10^6)**		13.18
			$N_{lcg\,\sigma}$(x 10^3)		50.62
			N_{lcgT} (x 10^6)		**13.23**

Table 7.13: MIG LCG fatigue lives for a crack to grow from the SCG to LCG transition length to a length of 10 mm, determined through integration of the plane strain and plane stress Paris regime equations, (7.54) and (7.55).

		FS		
		SP	DPA	DPR
SCG to LCG transition length, c_t, (μm)		250	250	225
ΔK at the change from predominantly plane strain to plane stress (MPa.m$^{0.5}$)		9	9.5	9
Stress range, outer fibre, R = 0.1, (MPa),	Load cycles			
250	$N_{lcg\,\varepsilon}$ (x 10^3)	21.42		
	$N_{lcg\,\sigma}$(x 10^3)	16.20		
	N_{lcgT} (x 10^3)	**37.62**		
225	$N_{lcg\,\varepsilon}$ (x 10^3)	39.79	45.81	50.64
	$N_{lcg\,\sigma}$(x 10^3)	16.36	14.52	15.96
	N_{lcgT} (x 10^3)	**56.16**	**60.33**	**66.61**
200	$N_{lcg\,\varepsilon}$ (x 10^3)	64.81	76.24	84.57
	$N_{lcg\,\sigma}$(x 10^3)	18.34	16.61	18.16
	N_{lcgT} (x 10^3)	**83.16**	**92.84**	**102.72**
175	$N_{lcg\,\varepsilon}$ (x 10^3)	110.28	134.42	148.74
	$N_{lcg\,\sigma}$(x 10^3)	20.68	18.44	20.89
	N_{lcgT} (x 10^3)	**130.96**	**152.86**	**169.63**
150	$N_{lcg\,\varepsilon}$ (x 10^3)	200.97	254.57	282.48
	$N_{lcg\,\sigma}$(x 10^3)	22.44	20.59	23.20
	N_{lcgT} (x 10^3)	**223.41**	**275.17**	**305.68**
125	$N_{lcg\,\varepsilon}$ (x 10^3)	401.90	536.70	595.78
	$N_{lcg\,\sigma}$(x 10^3)	22.65	20.79	24.17
	N_{lcgT} (x 10^3)	**424.55**	**557.49**	**619.95**

Table 7.14: FS LCG fatigue lives for a crack to grow from the SCG to LCG transition length to a length of 10 mm, determined through integration of the plane strain and plane stress Paris regime equations, (7.54) and (7.55).

7.4.4 Determination of S-N Curves through Short and Long Crack Growth Data

The following section details the prediction of the fatigue life utilising SC and LC growth rates. The SCG rate being considered to be a function of the crack length, stress amplitude, yield or tensile stress and maximum strain, as detailed in equations (7.16) to (7.19), and the LCG rate being modelled through plane strain and plane stress Paris laws.

Due to SCG data only being obtained for a single stress range, typically resulting in a fatigue life in the region of 10^5 cycles, the SC period of growth was determined through subtraction of the LCG S-N curve (determined from Table 7.12 to Table 7.14, these having been calculated through integration of the Paris law equations) from the 40 mm wide specimen S-N curves. The validity of the technique was confirmed through

comparison of the resulting SCG S-N curve with the S-N curve returned by the SCG specimens (the red and dashed black curves respectively in Figure 7.21, page 441, for example) and through comparison of the theoretical SCG rates, $dc/dN = [B.(\sigma_a/\sigma_y)^n.c]$, with the experimental ones (the red and black curves respectively in Figure 7.22, page 442, for example). It would be expected that the SCG specimen S-N curves would have a slightly greater lifespan than that predicted solely by SCG analysis as a small proportion of the fatigue life of the specimen would consist of LCG, SCG was only considered to occur up to a length of ~250 μm and crack lengths at failure in the SCG specimens were greater than this.

Table 7.15 shows the number of cycles to failure for various stress ranges for the AA 5383-H321 parent plate and the proportion of this attributable to LCG and SCG, with N_T being determined from the 40 mm wide specimen S-N curves, N_{lcg} from integration of the Paris equations and N_{scg} through subtraction of N_{lcg} from N_T. The proportion of fatigue crack growth attributable to SCG increased from 0.82 to 0.99 and 0.80 to 0.98 as the stress range decreased from 260 - 200 MPa (R = 0.1) for the PP |- and PP // specimens respectively.

Stress Range, R = 0.1 (MPa)		Specimen	
		PP |-	PP //
260	N_T (x10^3)	156	152
	N_{lcg} (x10^3)	28	31
	N_{scg} (x10^3)	128	121
	N_{scg}/N_T	0.82	0.80
250	N_T (x10^3)	216	183
	N_{lcg} (x10^3)	31	35
	N_{scg} (x10^3)	281	148
	N_{scg}/N_T	0.86	0.81
240	N_T (x10^3)	316	230
	N_{lcg} (x10^3)	35	41
	N_{scg} (x10^3)	281	189
	N_{scg}/N_T	0.89	0.82
230	N_T (x10^3)	501	306
	N_{lcg} (x10^3)	41	47
	N_{scg} (x10^3)	461	258
	N_{scg}/N_T	0.92	0.84
220	N_T (x10^3)	895	452
	N_{lcg} (x10^3)	47	56
	N_{scg} (x10^3)	848	396
	N_{scg}/N_T	0.95	0.88
210	N_T (x10^3)	1957	841
	N_{lcg} (x10^3)	54	66
	N_{scg} (x10^3)	1903	776
	N_{scg}/N_T	0.97	0.92
200	N_T (x10^3)	6579	4340
	N_{lcg} (x10^3)	64	78
	N_{scg} (x10^3)	6515	4261
	N_{scg}/N_T	0.99	0.98

Table 7.15: Fatigue life and proportion represented by LCG and SCG ($N_{scg} = N_T - N_{lcg}$) in the AA 5383-H321 parent material.

Table 7.16 shows the fatigue lives for the MIG and FS welds, with the proportion attributable to LCG and SCG determined as described above for the parent material.

It was apparent that this modelling approach of the MIG welds resulted in negative values for the SCG, the value for the LCG determined through integrations of the plane strain and plane stress Paris equations returning greater values than that returned by the 40 mm wide S-N specimens. This was considered to be due to the influence of the compressive residual stress field in the region of the crack tip in the CT specimens employed for the LCG measurements. Ideally ΔK_{eff} measurements would have provided a more accurate assessment of the MIG weld LCG rates, although these were not available at the time of writing. In an attempt to overcome the problem the LCG rate, with respect to the stress intensity factor range, of the MIG welds was considered to be equal to that observed in the PP |- specimens, although it would generally be considered to be greater. Figure 7.20 shows the PP |- and MIG weld LCG rates, and the difference between the two, with respect to the stress intensity factor range. It was evident for the MIG LI weld that the difference between the stress intensity factor ranges remained relatively constant at a value of 3 $MPa.m^{0.5}$ up to a growth rate of 2×10^{-7} $m.cycle^{-1}$. Greater variability was evident between the stress intensity factor ranges returned by PP |- and MIG HI weld, for comparable growth rates, with a significant deviation being evident as the crack growth in the MIG HI weld changed from predominantly plane strain to plane stress; although the difference between the PP |- and MIG HI weld rates was observed to be less than that for the MIG LI weld with values being less than 2 $MPa.m^{0.5}$. Utilising the PP |- LCG data resulted in the proportion of fatigue crack growth attributable to SCG increasing from 0.90 to 0.98 as the stress range (weld toe) decreased from 250 to 190 MPa in the case of the LI weld. The HI weld exhibited a decrease in the proportion of the fatigue life attributable to SCG, from 0.96 to 0.90, as the stress range (weld toe) decreased from 300 to 150 MPa, when the PP |- LCG data was employed, suggesting that the approach was not appropriate for the HI weld.

The SCG S-N curves for the FS welds were determined in a comparable manner to those employed for the parent material, subtracting the Paris law determined LCG S-N data from the 40 mm wide specimen S-N data. This resulted in the proportion of crack growth attributable to SC increasing from 0.69 to 0.92 as the stress range decreased from 250 to 125 MPa for the SP weld and from 0.75 and 0.73 to 0.96 as the stress range decreased from 225 to 125 MPa for the advancing and retreating sides of the DP weld respectively. Although the residual stresses measured in the FS welds were lower than those in the MIG welds the LCG measurements also suggested that a compressive stress in the region of the crack tip may have influenced the results. As with the MIG welds the SCG S-N curves were also calculated utilising the PP |- LCG data, although the resulting curves were only employed for comparative purposes.

Stress Range (MPa)		Specimen									
		MIG LI		MIG HI		FS SP		FS DPA		FS DPR	
			PP|-		PP|-		PP|-		PP|-		PP|-
300	N_T (x10^3)			167							
	N_{lcg} (x10^3)			162	7						
	N_{scg} (x10^3)			7	162						
	N_{scg}/N_T				0.96						
275	N_T (x10^3)			235							
	N_{lcg} (x10^3)			276	10						
	N_{scg} (x10^3)			-40	226						
	N_{scg}/N_T				0.96						
250	N_T (x10^3)	167		332		122					
	N_{lcg} (x10^3)	1656	17	500	17	38	17				
	N_{scg} (x10^3)	-1489	150	-168	315	84	105				
	N_{scg}/N_T		0.90		0.95	0.69	0.86				
240	N_T (x10^3)	204									
	N_{lcg} (x10^3)	2176	21								
	N_{scg} (x10^3)	-1972	184								
	N_{scg}/N_T		0.90								
230	N_T (x10^3)	259									
	N_{lcg} (x10^3)	2893	24								
	N_{scg} (x10^3)	-2633	235								
	N_{scg}/N_T		0.91								
225	N_T (x10^3)			474		212		243		243	
	N_{lcg} (x10^3)			975	27	56	27	60	27	67	27
	N_{scg} (x10^3)			-501	447	156	185	183	216	176	216
	N_{scg}/N_T				0.94	0.74	0.87	0.75	0.89	0.73	0.89
220	N_T (x10^3)	349									
	N_{lcg} (x10^3)	3896	30								
	N_{scg} (x10^3)	-3547	319								
	N_{scg}/N_T		0.91								
210	N_T (x10^3)	516									
	N_{lcg} (x10^3)	5319	37								
	N_{scg} (x10^3)	-4803	479								
	N_{scg}/N_T		0.93								
200	N_T (x10^3)	916		685		412		422		422	
	N_{lcg} (x10^3)	7375	46	2070	46	83	46	93	46	103	46
	N_{scg} (x10^3)	-6459	870	-1385	640	329	366	329	376	319	376
	N_{scg}/N_T		0.95		0.93	0.80	0.89	0.78	0.89	0.76	0.89
190	N_T (x10^3)	2771									
	N_{lcg} (x10^3)	10398	56								
	N_{scg} (x10^3)	-7626	2715								
	N_{scg}/N_T		0.98		0.92						
175	N_T (x10^3)			1004		936		861		861	
	N_{lcg} (x10^3)			4888	79	131		153		170	
	N_{scg} (x10^3)			-3885	925	805		708		691	
	N_{scg}/N_T				0.92	0.86		0.82		0.80	
150	N_T (x10^3)			1491				2379		2379	
	N_{lcg} (x10^3)			13226	147			275		306	
	N_{scg} (x10^3)			-11736	1344			2104		2074	
	N_{scg}/N_T				0.90			0.88		0.87	
125	N_T (x10^3)					2753		14234		14234	
	N_{lcg} (x10^3)					223		557		620	
	N_{scg} (x10^3)					2530		13676		13614	
	N_{scg}/N_T					0.92		0.96		0.96	

Table 7.16: Fatigue life and proportion represented by LCG and SCG ($N_{scg} = N_T - N_{lcg}$) in the MIG and FS welds.

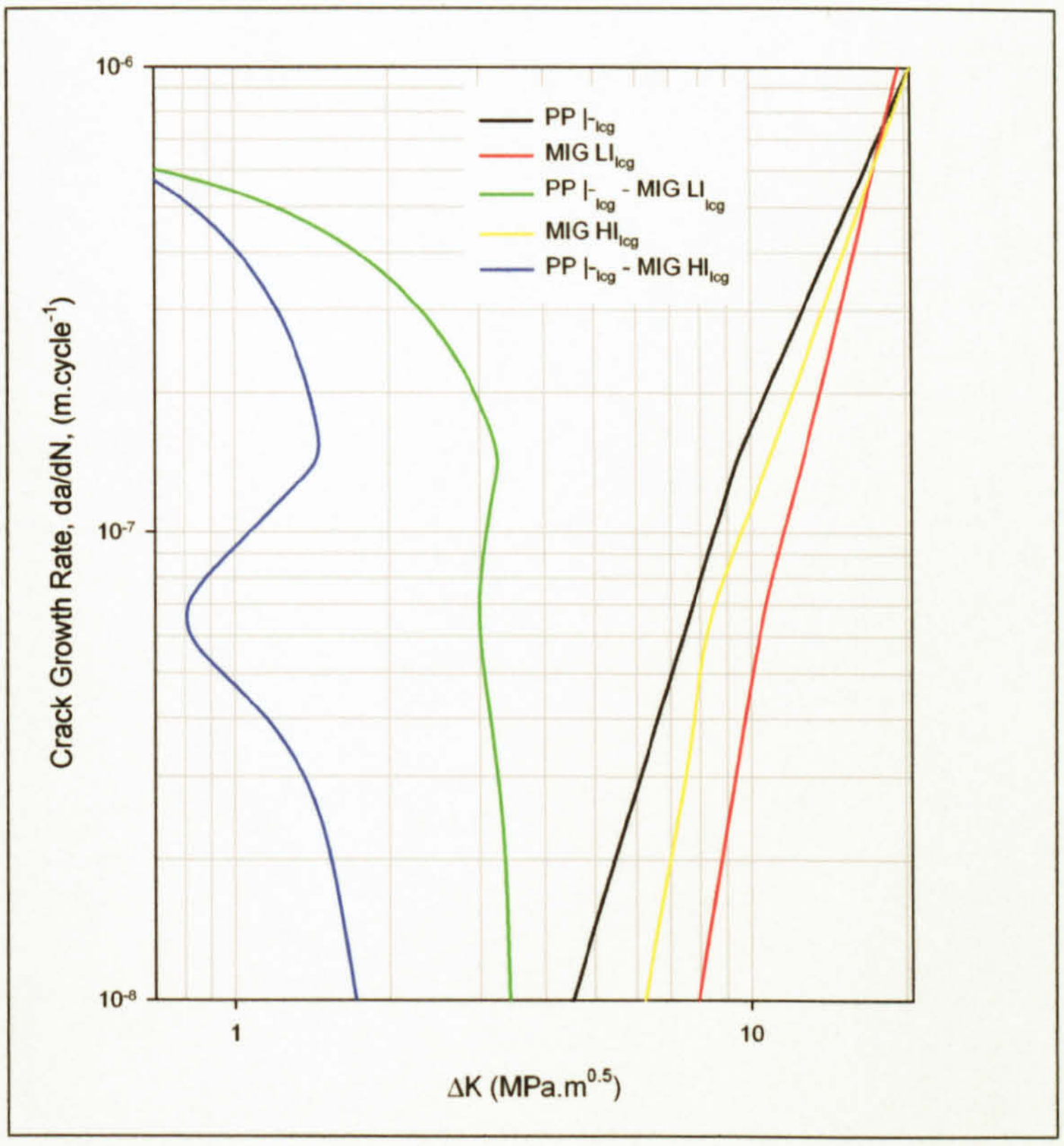

Figure 7.20: PP |- and MIG weld LCG rates, with respect to ΔK, and the difference between the growth rates, PP $|_{-lcg}$ - MIG LI_{lcg} or HI_{lcg}.

Even numbered figures from Figure 7.21 to Figure 7.34 show the experimental and theoretical SCG S-N curves, determined both through subtraction of the Paris equation derived LCG S-N curves from those of the appropriate 40 mm wide specimens (represented by SCG (N_T - N_{lcg})) and utilising equation (7.16) (represented by SCG $(\sigma_a/\sigma_y)^n$) respectively. The S-N curves resulting from the 40 mm wide parent plate or as-welded specimens (as detailed in Section 5.6.1, S-N Test Results, page 289) and those returned by the appropriate SCG specimens (as detailed in Figure 6.42, page 344, Figure 6.59, page 356, and Figure 6.76, page 369), represented by 4 Pt bend S-N curve and SCG specimen S-N curve respectively, are also shown. Plots only exhibit the results from $[B.(\sigma_a/\sigma_y)^n.c]$ analysis due to the various combinations being concomitant; the values of the SCG constants B and n being detailed in Table 7.17 to Table 7.23. Odd numbered figures from Figure 7.21 to Figure 7.34 show both the experimental and theoretical SCG rates with respect to the crack length when the appropriate SCG constants, B and n, were employed, as with the theoretical SCG S-N curves only the $[B.(\sigma_a/\sigma_y)^n.c]$ analyses are shown as the results for the various combinations of equation (7.15) were near identical.

The fatigue life can therefore be described through a combination of the crack initiation period that is not represented by SCG, the SCG period and the LCG period:

$$N_T = N_i + N_{scg} + N_{lcg} \tag{7.57}$$

where: N_T = total fatigue life.
N_i = crack initiation period.
N_{scg} = short crack growth period.
N_{lcg} = long crack growth period.

For the AA 5383-H321 parent material and welds under investigation the initiation period, N_i, was considered to be negligible, with the initial SC length being considered equal to the crack initiator. LC growth was divided into that considered to be occurring predominantly under plane strain and plane stress*, resulting in equation (7.57) being modified to:

$$N_T = N_{scg} + N_{lcg_\varepsilon} + N_{lcg_\sigma} \tag{7.58}$$

where: N_{lcg_ε} = LCG period subjected to predominantly plane strain.
N_{lcg_σ} = LCG period subjected to predominantly plane stress.

The fatigue life can therefore be determined through utilisation of either equation (7.59) or equation (7.60); equation (7.59) employing either the yield or tensile strength whilst equation (7.60) employs either the yield or tensile strength and the maximum applied strain in determining the SCG life:

$$N_T = \left[\frac{1}{B}\left(\frac{\sigma_{y\,or\,TS}}{\sigma_a}\right)^n \ln\frac{c_f}{c_i}\right] + \left[\frac{2}{(m_\varepsilon - 2)C_\varepsilon Y^{m_\varepsilon}(\Delta\sigma)^{m_\varepsilon}\pi^{m_\varepsilon/2}}\left\{\frac{1}{(c_i)^{(m_\varepsilon-2)/2}} - \frac{1}{(c_{f\varepsilon})^{(m_\varepsilon-2)/2}}\right\}\right] + \left[\frac{2}{(m_\sigma - 2)C_\sigma Y^{m_\sigma}(\Delta\sigma)^{m_\sigma}\pi^{m_\sigma/2}}\left\{\frac{1}{(c_{f\varepsilon})^{(m_\sigma-2)/2}} - \frac{1}{(c_{f\sigma})^{(m_\sigma-2)/2}}\right\}\right] \tag{7.59}$$

$$N_T = \left[\frac{1}{B}\left(\left(\frac{\sigma_{y\,or\,TS}}{\sigma_a}\right).\frac{1}{\varepsilon_{max}}\right)^n \ln\frac{c_f}{c_i}\right] + \left[\frac{2}{(m_\varepsilon - 2)C_\varepsilon Y^{m_\varepsilon}(\Delta\sigma)^{m_\varepsilon}\pi^{m_\varepsilon/2}}\left\{\frac{1}{(c_i)^{(m_\varepsilon-2)/2}} - \frac{1}{(c_{f\varepsilon})^{(m_\varepsilon-2)/2}}\right\}\right] + \left[\frac{2}{(m_\sigma - 2)C_\sigma Y^{m_\sigma}(\Delta\sigma)^{m_\sigma}\pi^{m_\sigma/2}}\left\{\frac{1}{(c_{f\varepsilon})^{(m_\sigma-2)/2}} - \frac{1}{(c_{f\sigma})^{(m_\sigma-2)/2}}\right\}\right] \tag{7.60}$$

* If LCG occurs principally under plane strain or stress the corresponding equations can be adjusted accordingly.

where: N_T = number of cycles to failure or a predetermined crack length.

σ_y = yield strength or 0.1% proof stress.

σ_{TS} = tensile strength.

σ_a = stress amplitude.

$\Delta\sigma$ = stress range.

ε_{max} = maximum applied strain.

B = SCG rate constant.

n = SCG rate constant.

c_i = crack initiator size.

c_t = transition from SCG to LCG size.

$c_{f\varepsilon}$ = transition crack length from predominantly plane strain to plane stress.

$c_{f\sigma}$ = final crack size.

m_ε = Paris constant for plane strain.

C_ε = Paris constant for plane strain.

m_σ = Paris constant for plane stress.

C_σ = Paris constant for plane strain.

Y = geometric configuration factor.

7.4.4.1 Parent Plate |-

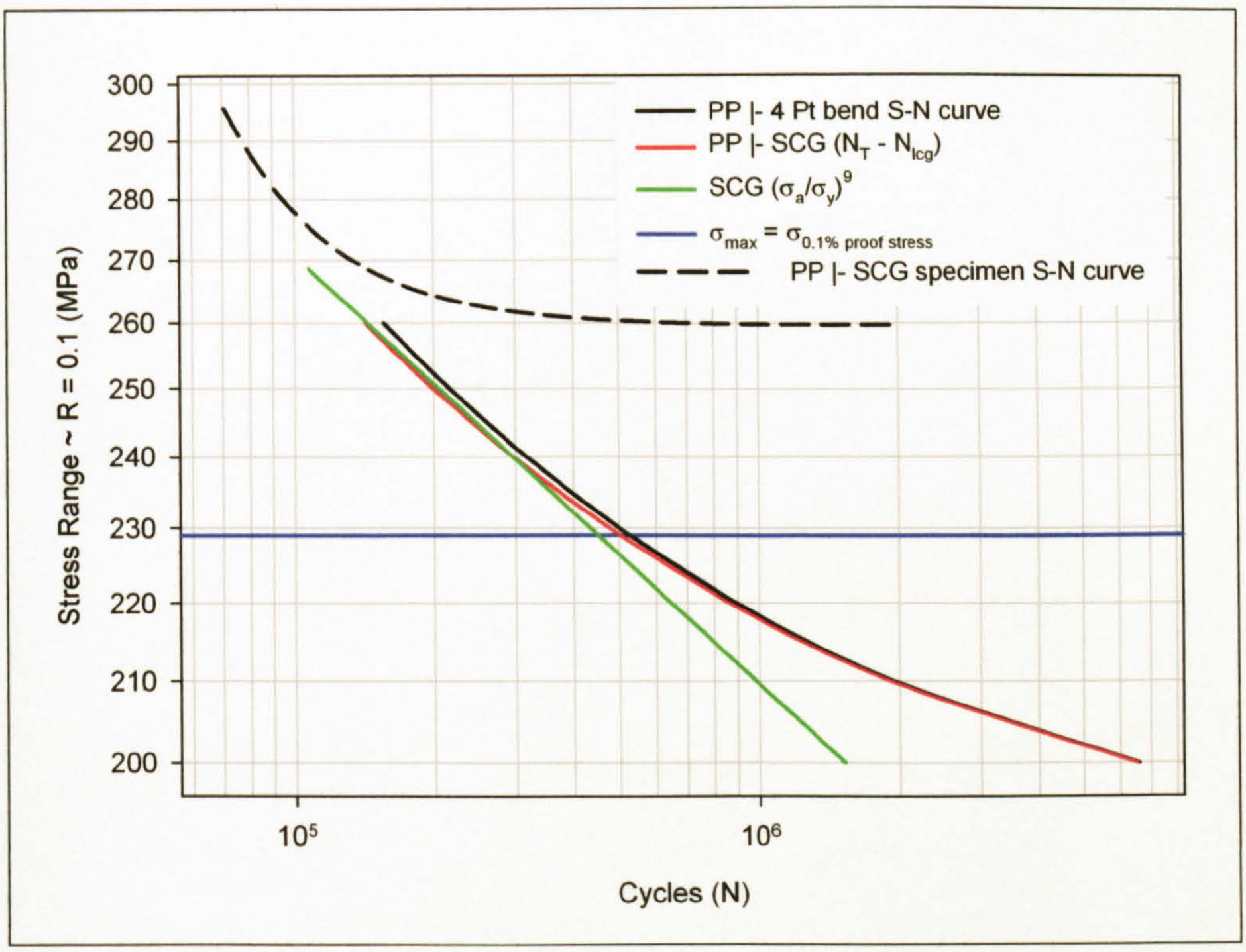

Figure 7.21: PP |- theoretical, $(\sigma_a/\sigma_y)^9$, and experimental $(N_T - N_{Icg})$ SCG S-N curves.

Formulation (value)	B	n
σ_a/σ_y (0.529)	0.01	9
σ_a/σ_{TS} (0.349)	0.42	
$(\sigma_a/\sigma_y).\varepsilon_{max}$ (8.74×10^{-3})	1.09×10^{14}	
$(\sigma_a/\sigma_{TS}).\varepsilon_{max}$ (5.77×10^{-3})	4.60×10^{15}	

Table 7.17: PP |- constants for SCG equations.

From Figure 7.21 it was evident that the theoretical SCG consisted of 87 - 95% of the overall fatigue life when a value of n = 9 was employed for 260 MPa ≥ Δσ ≥ 230 MPa, the values for B being as shown in Table 7.17. For Δσ < 230 MPa the disparity between the predicted values for the SCG period and the experimentally determined values increased as Δσ decreased; at a stress range of 200 MPa the predicted value was 23% of the experimentally determined value. It was evident that the theoretical results were accurate down to a peak applied stress in the region of the yield stress, although due to the relatively low residual stresses in the parent material it was unlikely that these would be influential in explaining the discrepancies observed for stresses below this. Above the yield stress it would be expected that a significant redistribution of the residual stresses would occur resulting in a diminishing of their influence on the fatigue properties. It would be expected that extrapolation of the theoretical PP |- SCG data to increased stress

ranges would result in a comparable response, albeit at slightly reduced values to those returned by the SCG specimen S-N results, as due to the size of the SCG specimens it would be expected that they would consist predominantly of SCG.

$$N_{scg_{PP\,\vdash}} = \frac{1}{0.1}\left(\frac{254}{\sigma_a}\right)^9 \times \ln\left(\frac{350}{13}\right) \tag{7.61}$$

The theoretical value for the SC proportion of the fatigue life of the SCG specimen, calculated utilising the yield stress and stress amplitude, equation (7.61), returned a value of 101955 cycles for the SCG, 90% of the total fatigue life, 112764 cycles, of the specimen.

Figure 7.22 shows the theoretically and experimentally determined SCG rates. Although the two curves were not coincident, with variations in their slopes being evident, they exhibited a common trend with the theoretical predictions being conservative for crack lengths greater than 10^{-4} m and non-conservative for values below this, although the outcome of this would be the opposite with respect to the fatigue life.

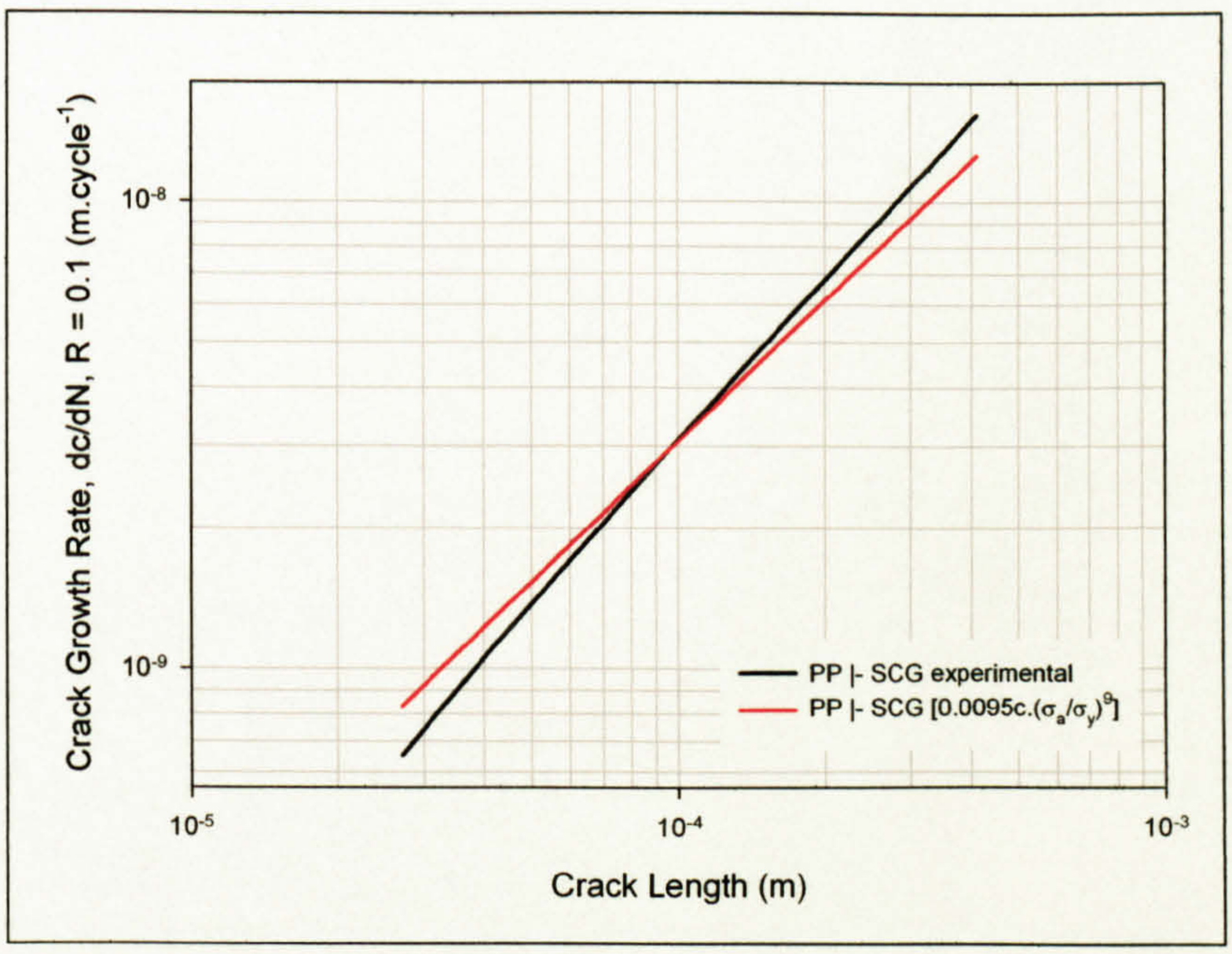

Figure 7.22: Comparison of PP |- experimental and theoretical SCG rates.

On the above evidence the overall fatigue life of a structure could be predicted utilising either equation (7.59) or (7.60) for lives $\leq 5 \times 10^5$ cycles, 230 MPa $\leq \Delta\sigma \leq$ 260 MPa:

N_T = number of cycles to failure or a predetermined crack length, $\leq 5 \times 10^5$ cycles.
σ_y = yield strength or 0.1% proof stress, 254 MPa.
σ_{TS} = tensile strength, 385 MPa.

σ_a = stress amplitude, 115 MPa ≤ $\Delta\sigma$ ≤ 130 MPa (R = 0.1).

$\Delta\sigma$ = stress range, 230 MPa ≤ $\Delta\sigma$ ≤ 260 MPa (R = 0.1).

ε_{max} = maximum applied strain.

B = SCG rate constant, the corresponding value, shown in Table 7.17, depending on the formulation employed.

n = SCG rate constant, 9.

c_i = crack initiator size, 13 μm.

c_t = transition from SCG → LCG size, 350 μm.

$c_{f\varepsilon}$ = transition crack length from predominantly plane strain to plane stress.

$c_{f\sigma}$ = final crack size.

m_ε = Paris constant for plane strain, 3.604.

C_ε = Paris constant for plane strain, 44.24×10^{-12}.

m_σ = Paris constant for plane stress, 2.489.

C_σ = Paris constant for plane strain, 541.80×10^{-12}.

Y = geometric configuration factor for a semi-elliptical surface crack subjected to pure bending, 0.61.

7.4.4.2 Parent Plate //

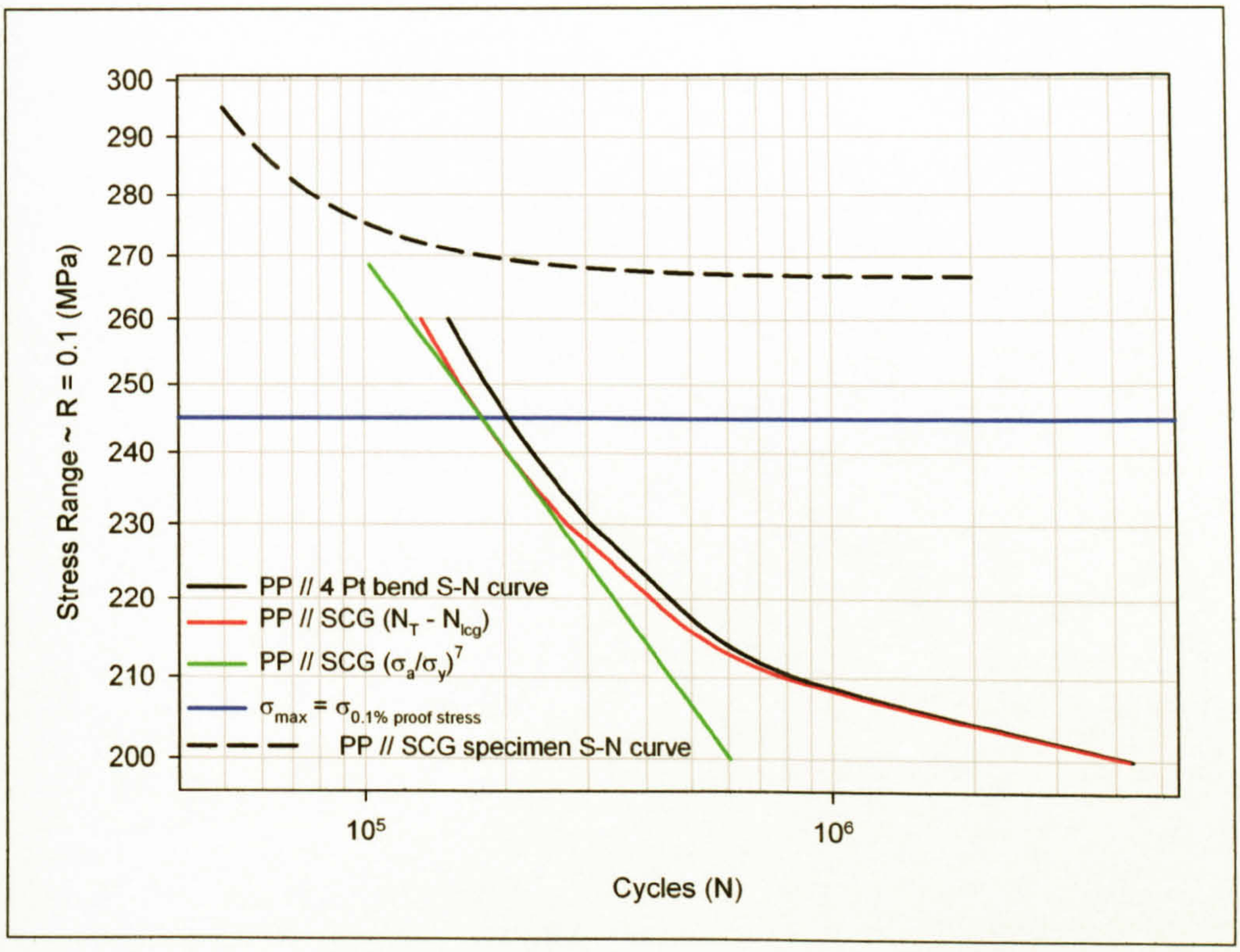

Figure 7.23: PP // theoretical, $(\sigma_a/\sigma_y)^7$, and experimental $(N_T - N_{Icg})$ SCG S-N curves.

Formulation (value)	B	n
σ_a/σ_y (0.492)	0.0021	6
σ_a/σ_{TS} (0.362)	0.0133	
$(\sigma_a/\sigma_y).\varepsilon_{max}$ (8.77×10^{-3})	6.55×10^{7}	
$(\sigma_a/\sigma_{TS}).\varepsilon_{max}$ (6.45×10^{-3})	4.15×10^{8}	

Table 7.18: PP // constants for SCG equations.

From Figure 7.23 it was evident that the SCG consisted of 82 - 88% of the overall fatigue life when a value of n = 6 and B as depicted in Table 7.18 were employed for the SCG equations for 260 MPa ≥ Δσ ≥ 230 MPa. For Δσ < 230 MPa the disparity between the predicted value for the SCG period and the experimentally determined value increased as Δσ decreased; at a stress range of 200 MPa the predicted value was 14% of the experimental. In contrast to the PP |- results, the values were accurate at peak applied stresses below the yield stress, suggesting that residual stresses, although comparatively low in the parent material when compared to those in the welded samples, had minimal influence on the SCG rate. Above the yield stress it may be assumed that a redistribution of the residual stress field would occur, with their influence subsequently being diminished. It would be expected that extrapolation of the theoretical PP // SCG data to higher stress ranges would result in a comparable slope to that returned by the PP // SCG

specimen S-N curve, although in contrast to the PP |- results the values would be slightly greater than those of the S-N curve.

$$N_{scg_{PP\,//}} = \frac{1}{0.021}\left(\frac{272}{\sigma_a}\right)^6 \times \ln\left(\frac{300}{13}\right) \tag{7.62}$$

The theoretical value for the proportion of crack growth attributable to SC for the SCG specimen, utilising the yield stress and stress amplitude, equation (7.62), returned a value of 105493 cycles, 93% of the total fatigue life, 113772 cycles, of the specimen.

Figure 7.24 shows the theoretically and experimentally determined SCG rates. Although the two curves were not coincident, with variations in their slopes being evident, they exhibited a common trend, with the theoretical predictions being conservative for crack lengths greater than 9×10^{-5} m and non-conservative for values below this.

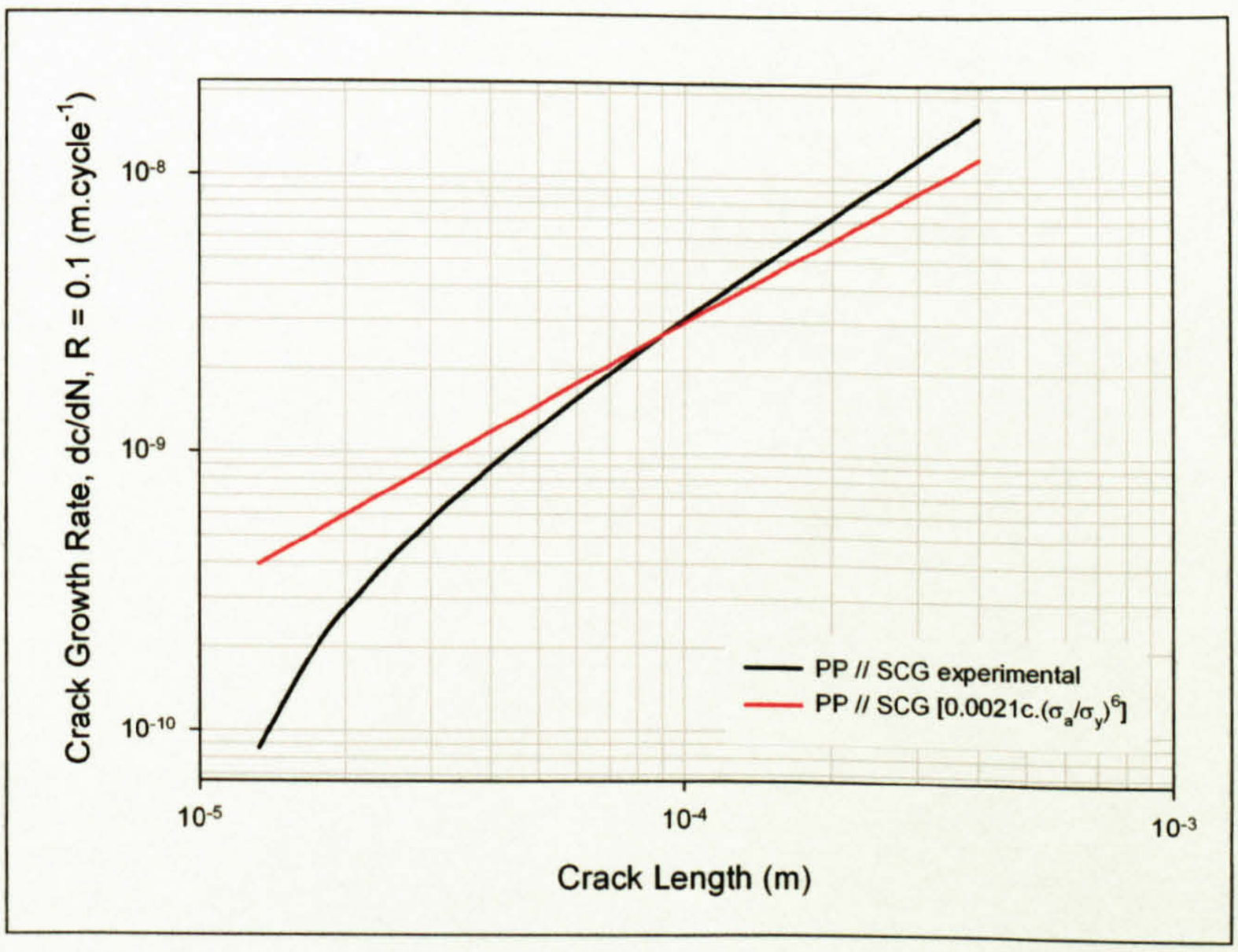

Figure 7.24: Comparison of PP // experimental and theoretical SCG rates.

On the above evidence the overall fatigue life of a structure could be predicted utilising either equation (7.59) or (7.60) for lives $\leq 3.1 \times 10^5$ cycles, 230 MPa $\leq \Delta\sigma \leq$ 260 MPa:

N_T = number of cycles to failure or a predetermined crack length, $\leq 3.1 \times 10^5$ cycles.

σ_y = yield strength or 0.1% proof stress, 272 MPa.

σ_{TS} = tensile strength, 370 MPa.

σ_a = stress amplitude, 115 MPa $\leq \Delta\sigma \leq$ 130 MPa (R = 0.1).

$\Delta\sigma$ = stress range, 230 MPa $\leq \Delta\sigma \leq$ 260 MPa (R = 0.1).

ε_{max} = maximum applied strain.

B = SCG rate constant, the corresponding value, shown in Table 7.18, depending on the formulation employed.

n = SCG rate constant, 6.

c_i = crack initiator size, 13 μm.

c_t = transition from SCG → LCG size, 300 μm.

$c_{f\varepsilon}$ = transition crack length from predominantly plane strain to plane stress.

$c_{f\sigma}$ = final crack size.

m_ε = Paris constant for plane strain, 3.968.

C_ε = Paris constant for plane strain, 21.41×10^{-12}.

m_σ = Paris constant for plane stress, 2.877.

C_σ = Paris constant for plane strain, 198.72×10^{-12}.

Y = geometric configuration factor for a semi-elliptical surface crack subjected to pure bending, 0.61.

7.4.4.3 MIG Low Input

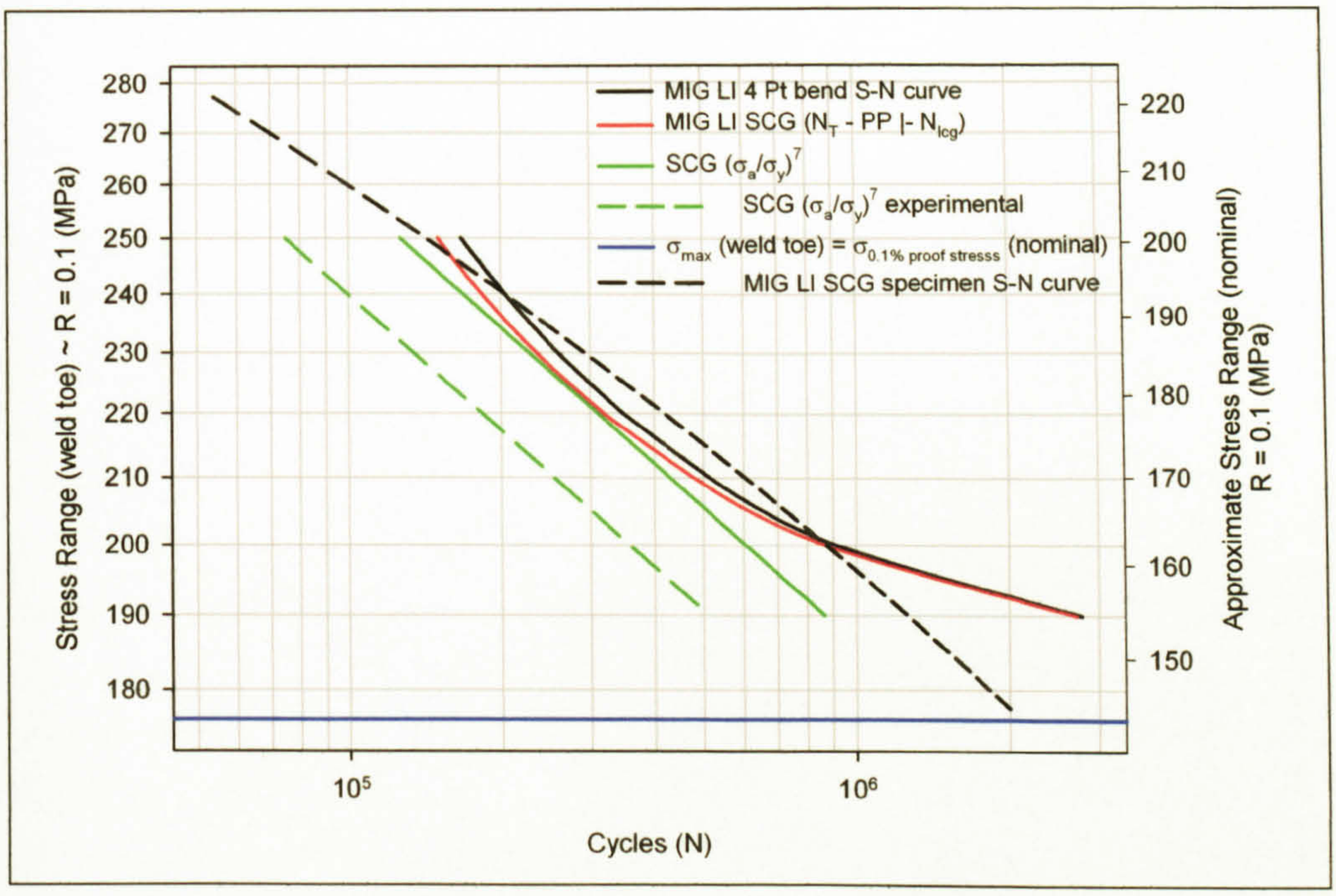

Figure 7.25: MIG LI theoretical, $(\sigma_a/\sigma_y)^7$, and experimental (N_T - N_{lcg}) SCG S-N curves (dashed lines refer to curves predicted through mapping of the theoretical SCG data to the experimental SCG data, see page 448 for details).

Formulation (value)	B		n
	Theoretical	Experimental	
σ_a/σ_y (0.771)	1.18×10^{-4}	2.0×10^{-4}	7
σ_a/σ_{TS} (0.372)	0.0195	0.033	
$(\sigma_a/\sigma_y).\varepsilon_{max}$ (25.05×10^{-3})	3.08×10^{6}	5.23×10^{6}	
$(\sigma_a/\sigma_{TS}).\varepsilon_{max}$ (12.05×10^{-3})	5.10×10^{8}	8.65×10^{8}	

Table 7.19: MIG LI constants for SCG equations.

Due to the fact that the approach of determining the SCG S-N curve by subtracting the LCG period from the overall life returned a negative value*, an attempt at modelling the SCG was made by utilising the PP |- LCG data. The resulting SCG S-N curve, as depicted in Figure 7.25, returned SCG constants with values of n = 7 and the theoretical values for B as shown in Table 7.19. The SCG S-N curve suggested a good correlation between the stress range and SCG fatigue life for 240 MPa ≥ Δσ (weld toe) ≥ 210 MPa, with 80 - 83% of the total fatigue life consisting of SCG. Although subsequent analysis returned an underestimate of the SCG rate, with respect to the crack length, the outcome of this being an overestimate of the fatigue life for the SCG specimen, as shown in Figure

* The fact that the long crack growth and S-N data resulted from different alloys, 5083-H321 and 5383-H321 respectively, the author does not consider that any disparity resulting from this would have been of a great enough magnitude to return the negative values observed.

7.26. The theoretical value for the SCG period of the fatigue life of the SCG specimen, determined through employment of equation (7.63), returned a value of 138839 cycles, 123% of the total fatigue life, 113038 cycles, of the SCG specimen.

$$N_{scg_{MIG\ LI}} = \frac{1}{B}\left(\frac{160}{\sigma_a}\right)^7 \times \ln\left(\frac{300}{21}\right) \qquad (7.63)$$

Assuming that the disparity in the results was related to the employment of the PP |- LCG data, the MIG LI SCG data was reassessed utilising the same value for the SCG constant n, 7, but determining the value of B through mapping of the theoretical SCG data (determined through utilisation of equation (7.63)) to the experimental data, the subsequent result being depicted as the dashed line in Figure 7.25 and Figure 7.26. Values for the SCG constant B are shown as the experimental values in Table 7.19. This approach suggested that SCG consisted of 45 - 52% of the overall fatigue life of the as-welded specimens for 250 MPa ≥ Δσ (weld toe) ≥ 205 MPa, although utilisation of equation (7.63) returned a value of 81915 cycles, 72% of the total life, of the SCG specimen.

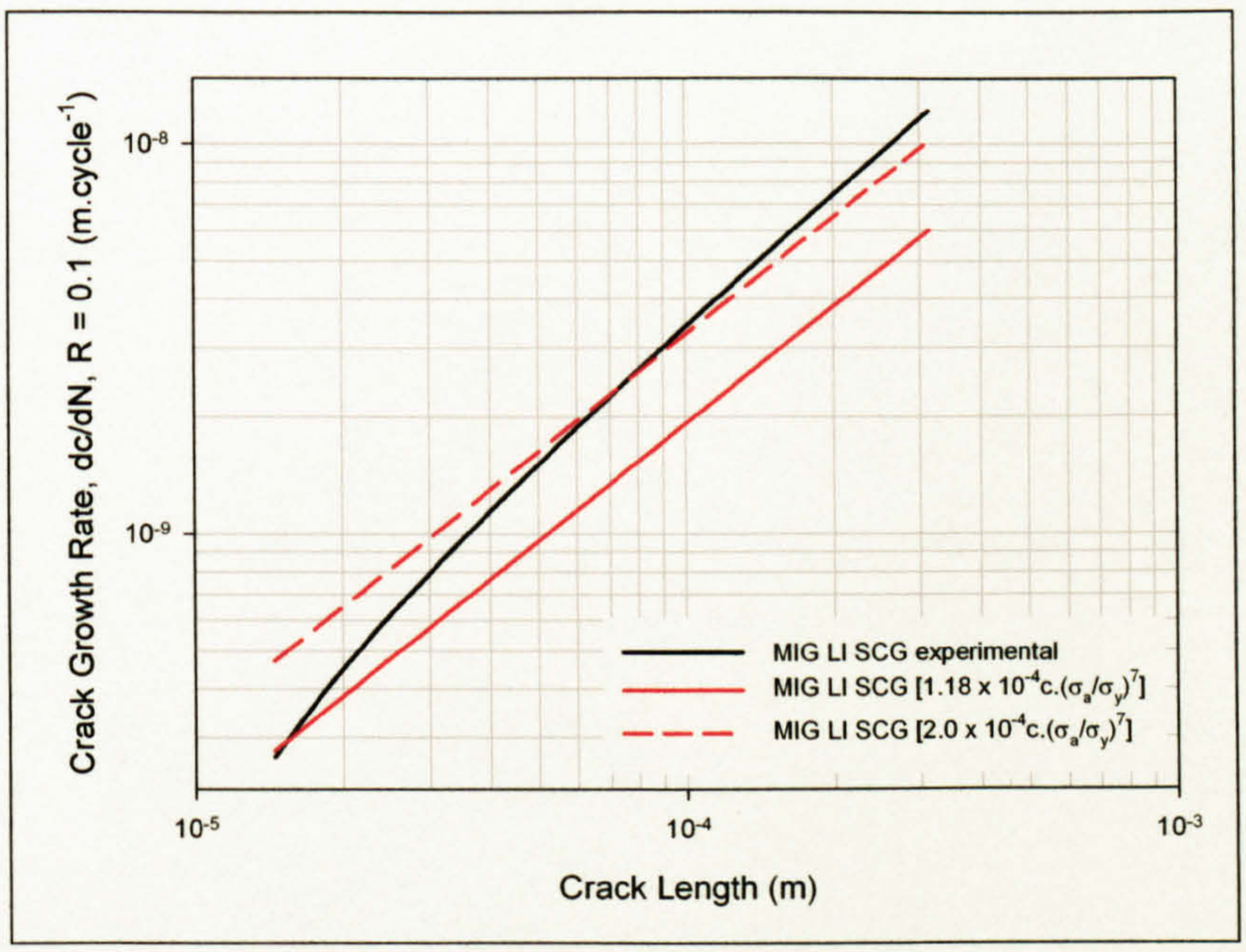

Figure 7.26: Comparison of MIG LI experimental and theoretical SCG rates.

Although the weld induced residual stresses were considered to be influential in the LCG results returned by the MIG LI CT specimens, the maximum applied stresses, for the stress ranges under consideration, were greater than the yield stress, 176 MPa (weld toe). It has therefore been assumed that a subsequent redistribution of the stresses would occur and that their influence on the fatigue strength would be reduced.

The S-N curve returned by the MIG LI SCG specimens had a comparable slope to the theoretical curves, suggesting that the value of n = 7, which determines the slope of the curve, was accurate. As the curve determined through utilisation of the PP |- LCG data lies closer to that from the SCG specimen S-N curve it may be suggested that this was more representative of the SCG than that determined through mapping of theoretical data to the experimental, although further assessment of the MIG LI weld LCG data is required. The geometry of the SCG specimens may also have been influential in the disparity between the results obtained; SCG in the 40 mm wide specimens, and in welded structures, would occur in the region of the plate surface at the weld toe, whereas the geometry of the SCG specimens meant that measurements were being undertaken 2.5 mm below the surface in the HAZ.

On the above evidence the overall fatigue life of a structure could be predicted utilising either equation (7.59) or (7.60) for $2.0 \times 10^5 \leq N_T \leq 5.2 \times 10^5$ cycles, 210 MPa $\leq \Delta\sigma$ (weld toe) $\leq$ 240 MPa, although due to the problems associated with the modelling of the MIG LI results it is suggested that the values detailed below be used only as guidelines until further analysis has been undertaken:

N_T = number of cycles to failure or a predetermined crack length, $2.0 \times 10^5 \leq N_T \leq 5.2 \times 10^5$ cycles.

σ_y = yield strength or 0.1% proof stress, 160 MPa.

σ_{TS} = tensile strength, 332 MPa.

σ_a = stress amplitude, 105 MPa $\leq \Delta\sigma$ (weld toe) $\leq$ 120 MPa (R = 0.1), 85 MPa $\leq \Delta\sigma$ (nominal) $\leq$ 110 MPa .

$\Delta\sigma$ = stress range, 210 MPa $\leq \Delta\sigma$ (weld toe) $\leq$ 240 MPa (R = 0.1), 170 MPa $\leq \Delta\sigma$ (nominal) $\leq$ 220 MPa .

ε_{max} = maximum applied strain.

B = SCG rate constant, the corresponding theoretical value, shown in Table 7.18, depending on the formulation employed.

n = SCG rate constant, 7.

c_i = crack initiator size, 21 μm.

c_t = transition from SCG → LCG size, 300 μm.

$c_{f\varepsilon}$ = transition crack length from predominantly plane strain to plane stress.

$c_{f\sigma}$ = final crack size.

m_ε = Paris constant for plane strain, 6.701.

C_ε = Paris constant for plane strain, 0.01×10^{-12}.

m_σ = Paris constant for plane stress, 4.489.

C_σ = Paris constant for plane strain, 1.610×10^{-12}.

Y = geometric configuration factor for a semi-elliptical surface crack subjected to pure bending, 0.61.

7.4.4.4 MIG High Input

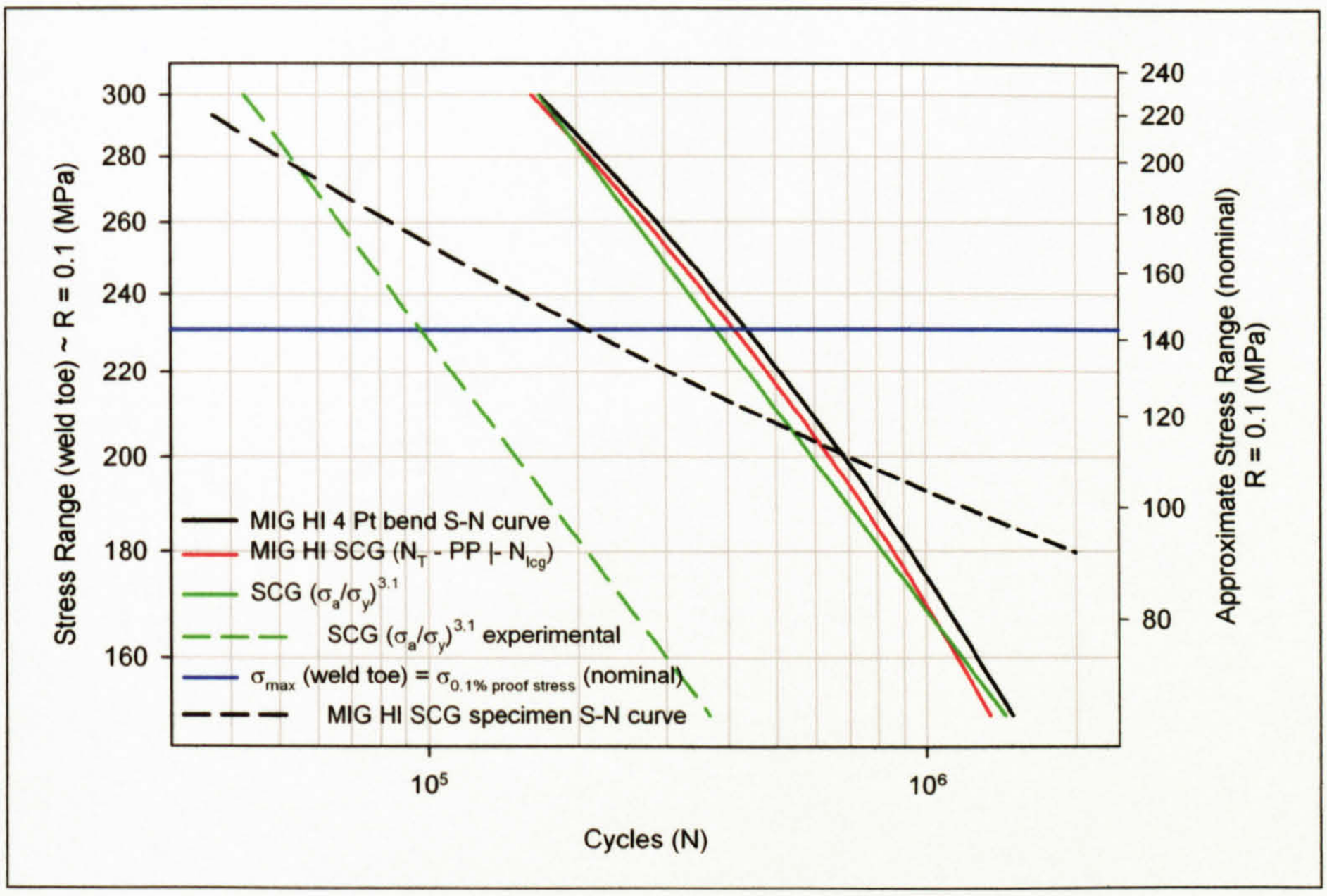

Figure 7.27: MIG HI theoretical, $(\sigma_a/\sigma_y)^{3.1}$, and experimental ($N_T$ - N_{lcg}) SCG S-N curves (dashed lines refer to curves predicted through mapping of the theoretical SCG data to the experimental SCG data, see page 451 for details).

Formulation (value)	B		n
	Theoretical	Experimental	
σ_a/σ_y (0.744)	2.04×10^{-5}	8.00×10^{-5}	3.1
σ_a/σ_{TS} (0.355)	2.03×10^{-4}	7.93×10^{-4}	
$(\sigma_a/\sigma_y).\varepsilon_{max}$ (23.58×10^{-3})	0.91	3.55	
$(\sigma_a/\sigma_{TS}).\varepsilon_{max}$ (11.25×10^{-3})	9.01	35.19	

Table 7.20: MIG HI constants for SCG equations.

In a comparable approach to that employed for the MIG LI weld the MIG HI SCG S-N curve was determined through utilisation of the PP |- LCG data, returning SCG constants of n = 3.1 and the theoretical values shown in Table 7.20 for B. The subsequent SCG curve, shown in Figure 7.27, suggested a good correlation between the stress range and SCG fatigue life for 300 MPa ≥ Δσ (weld toe) ≥ 160 MPa, although it was apparent that the proportion of the fatigue life considered to consist of SCG appeared to decrease as the fatigue life increased, the opposite scenario typically being considered customary. Utilisation of the PP |- LCG data also resulted in an underestimate of the MIG HI SCG rate, with respect to the crack length, when compared to the experimental results, as shown in Figure 7.28, and a subsequent overestimate of the fatigue life. Equation (7.64) returned a SC period of the fatigue life of the SCG specimen of 301151 cycles, 297% of the total fatigue life of 100996 cycles.

As with the MIG LI weld, the MIG HI SCG data was reassessed utilising the value determined through analysis of the PP |- LCG data for the SCG constant n, 3.1, but determining the value of B through mapping of the theoretical SCG data (determined through utilisation of equation (7.64)) to the experimental data, the subsequent result being depicted as the dashed line in Figure 7.27 and Figure 7.28. Values for the SCG constant B are shown as the experimental values in Table 7.20. This approach suggested that the SCG consisted of 22 - 25% of the total fatigue life for 300 MPa ≥ Δσ (weld toe) ≥ 150 MPa. Through this approach employment of the SCG constants and equation (7.64) resulted in a value for the SCG of 76793 cycles, 76% of the overall fatigue life, for the MIG HI SCG specimen.

The MIG HI SCG specimen S-N curve depicted in Figure 7.27 had a gentler gradient than that returned by the theoretical results, suggesting that n should be greater than the value of 3.1 employed, although it was also evident that the SCG specimen S-N curve dissected that resulting from the 40 mm wide as-welded analysis.

$$N_{scg_{MIG\ HI}} = \frac{1}{B}\left(\frac{167}{\sigma_a}\right)^{3.1} \times \ln\left(\frac{250}{21.5}\right) \qquad (7.64)$$

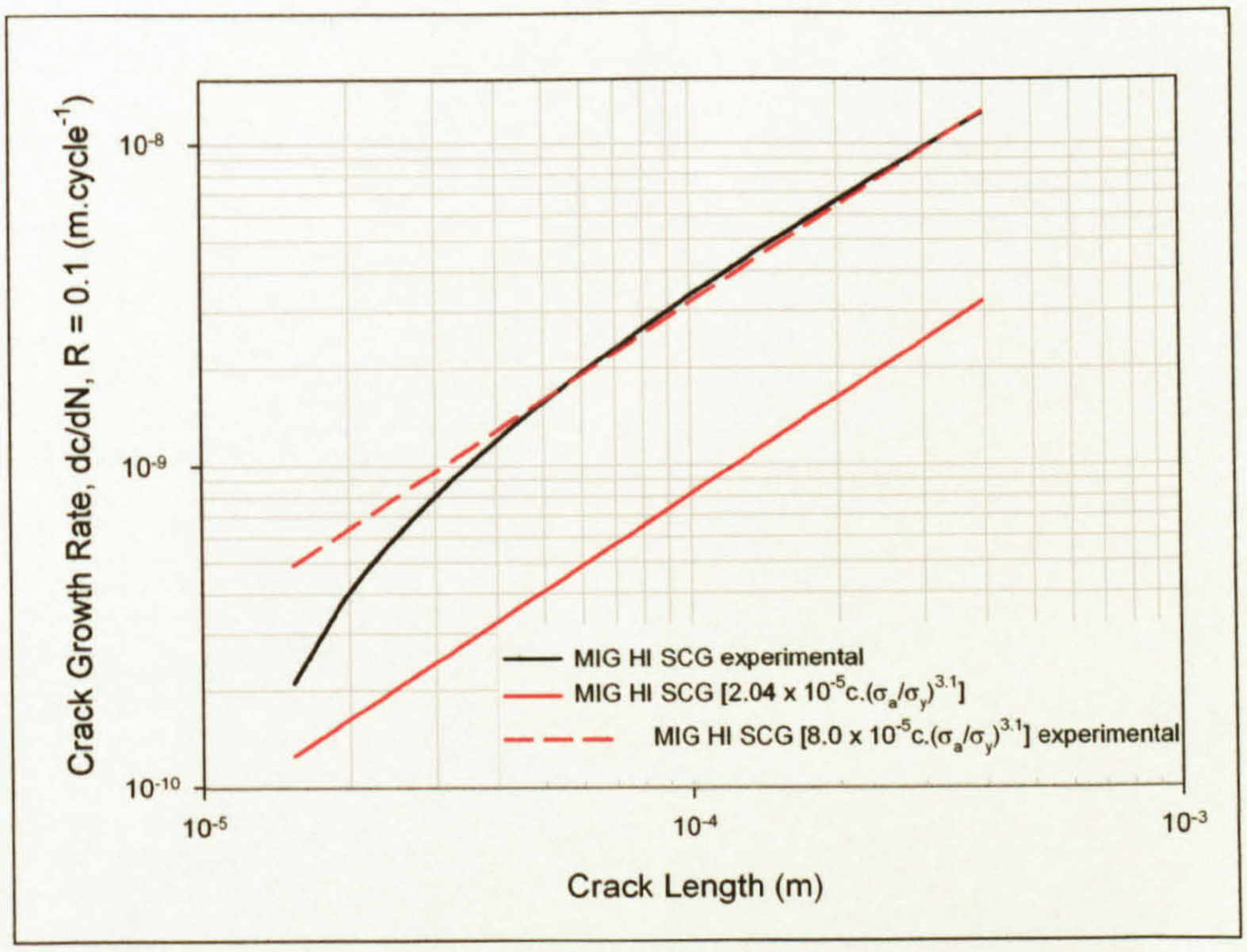

Figure 7.28: Comparison of MIG HI experimental and theoretical SCG rates.

Unlike the MIG LI weld, the maximum stress for a proportion of the stress ranges considered for the HI weld was below the yield stress, suggesting that redistribution of the residual stress field would be incomplete and they would have a subsequent effect on the fatigue properties.

7.4.4.5 FS Single Pass

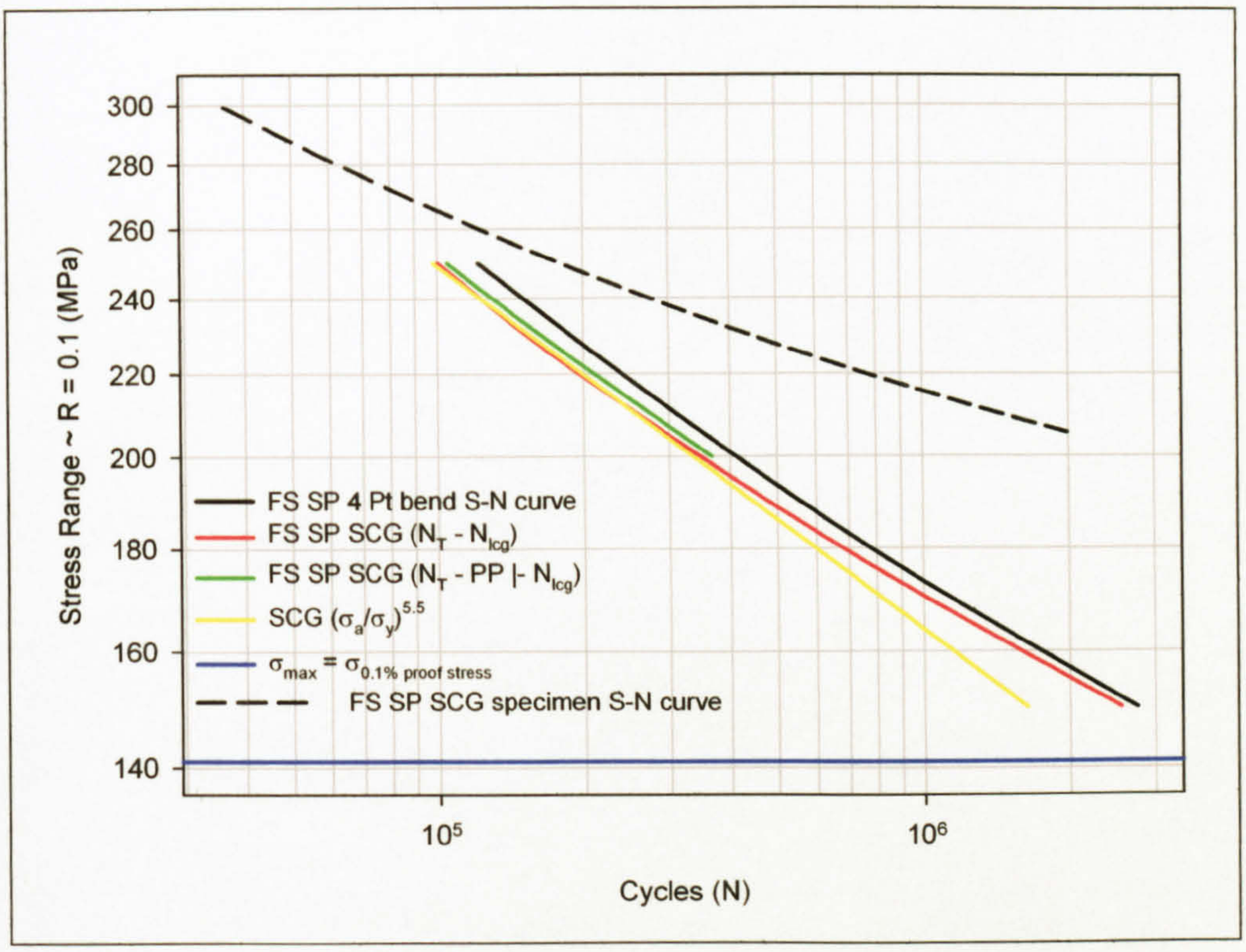

Figure 7.29: FS SP theoretical and experimental SCG S-N.

Formulation (value)	B	n
σ_a/σ_y (0.834)	9.0×10^{-5}	5.5
σ_a/σ_{TS} (0.390)	0.0059	
$(\sigma_a/\sigma_y).\varepsilon_{max}$ (57.07×10^{-3})	229	
$(\sigma_a/\sigma_{TS}).\varepsilon_{max}$ (26.69×10^{-3})	15000	

Table 7.21: FS SP constants for SCG equations.

The theoretical FS SP SCG S-N curve was determined through subtraction of the FS SP LCG from the four point bend S-N data, as shown in Figure 7.29, although the curve resulting from subtraction of the PP |- LCG data has also been included for comparative purposes. From Figure 7.29 the SCG comprised of 78 - 83% of the overall fatigue life when values of n = 5.5 and B as shown in Table 7.21 were employed for the SCG equations with 250 MPa ≥ $\Delta\sigma$ ≥ 185 MPa. For $\Delta\sigma$ < 185 MPa the disparity between the predicted value for the SCG period and the experimentally determined value increased as $\Delta\sigma$ decreased; for a stress range of 150 MPa the predicted value was 64% of the experimental. Determination of the SCG period of the fatigue life of the SCG specimen, utilising the SCG constants detailed in Table 7.21 and equation (7.65), resulted in a value of 105462 cycles, 92% of the fatigue life of 114505 cycles. The S-N curve returned by the FS SP SCG specimens depicts a slightly gentler gradient than that suggested for the

theoretical curve, although extrapolation of the theoretical curve to greater stress ranges suggests that they would be of a comparable magnitude.

$$N_{scg_{FS\ SP}} = \frac{1}{9.0\times10^{-5}}\left(\frac{157}{\sigma_a}\right)^{5.5} \times \ln\left(\frac{250}{7.5}\right) \qquad (7.65)^{*}$$

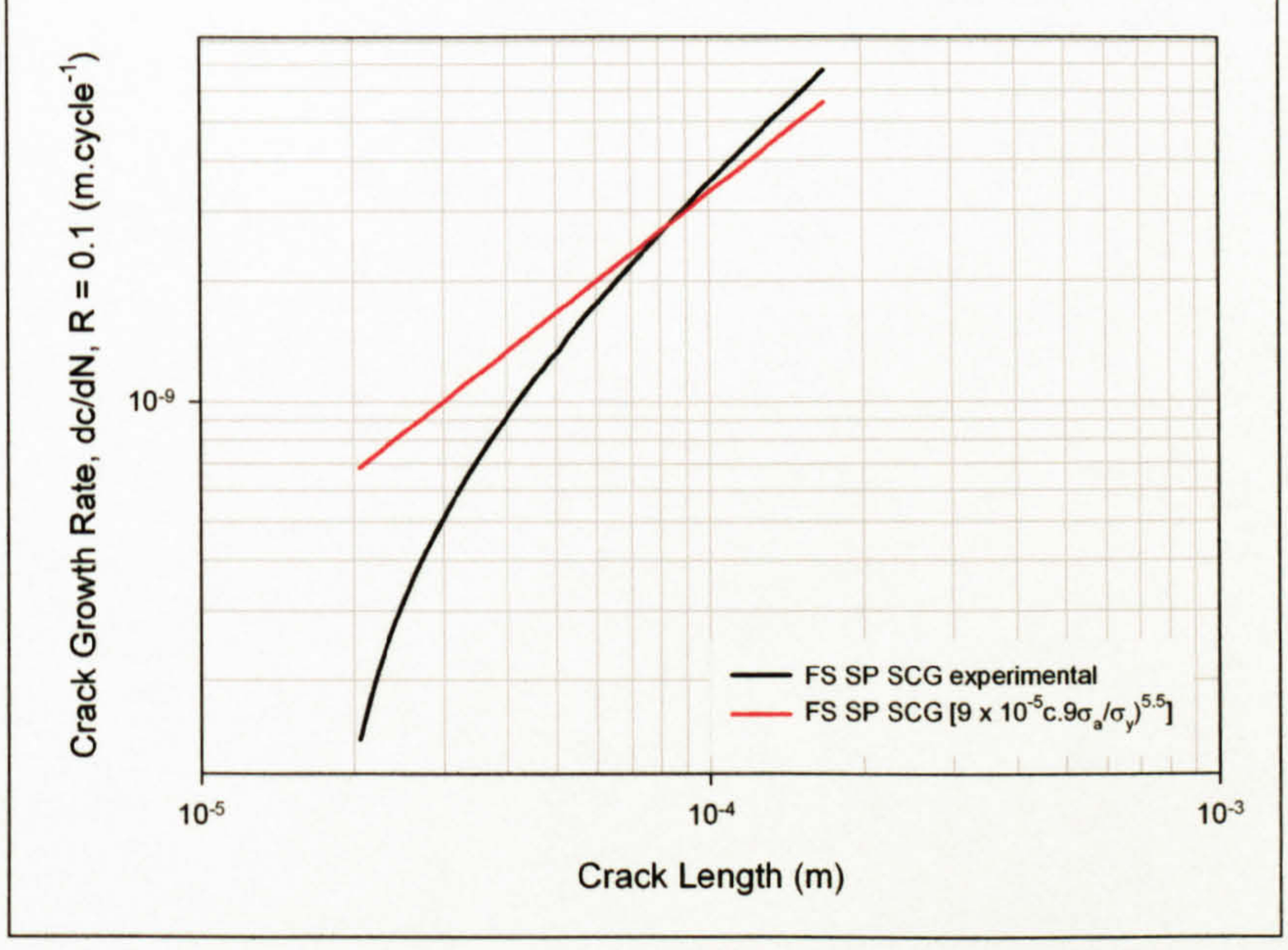

Figure 7.30: Comparison of FS SP experimental and theoretical SCG rates.

Utilising the SCG constants shown in Table 7.21, the SCG rate, with respect to the crack length, exhibited an underestimate for cracks lengths > 8.5×10^{-5} m and an overestimate for lengths < 8.5×10^{-5} m, although the disparity increased at a greater rate for crack lengths < 4×10^{-5} m.

The stress ranges under consideration were greater than the yield stress, suggesting that the effect of any weld induced residual stresses would diminish due to their redistribution.

On the above evidence the overall fatigue life of a structure could be predicted utilising either equation (7.59) or (7.60) for lives ≤ 6.5×10^5 cycles, 185 MPa ≤ $\Delta\sigma$ ≤ 250 MPa:

N_T = number of cycles to failure or a predetermined crack length, ≤ 6.5×10^5 cycles.

σ_y = yield strength or 0.1% proof stress, 157 MPa.

---

* It has been assumed that the maximum crack length that short crack growth would be evident in the FS SP welds would be comparable to that observed in the other specimens, therefore, although the maximum sized SC measured was 169 μm, the maximum crack for determining the number of cycles required to attain long crack growth has been assumed to be comparable to that observed in the other specimens and a nominal value of 250 μm has been employed.

σ_{TS} = tensile strength, 336 MPa.

σ_a = stress amplitude, 92.5 MPa ≤ σ_a ≤ 125 MPa (R = 0.1).

$\Delta\sigma$ = stress range, 185 MPa ≤ $\Delta\sigma$ ≤ 250 MPa (R = 0.1).

ε_{max} = maximum applied strain.

B = SCG rate constant, the corresponding value, shown in Table 7.21, depending on the formulation employed.

n = SCG rate constant, 5.5.

c_i = crack initiator size, 20 μm.

c_t = transition from SCG → LCG size, 250 μm*.

$c_{f\varepsilon}$ = transition crack length from predominantly plane strain to plane stress.

$c_{f\sigma}$ = final crack size.

m_ε = Paris constant for plane strain, 4.219.

C_ε = Paris constant for plane strain, 17.99×10^{-12}.

m_σ = Paris constant for plane stress, 2.159.

C_σ = Paris constant for plane strain, 1.18×10^{-9}.

Y = geometric configuration factor for a semi-elliptical surface crack subjected to pure bending, 0.61.

* It has been assumed that the maximum crack length that short crack growth would be evident in the FS SP welds would be comparable to that observed in the other specimens, therefore, although the maximum sized SC measured was 169 μm, the maximum crack for determining the number of cycles required to attain long crack growth has been assumed to be comparable to that observed in the other specimens and a nominal value of 250 μm has been employed.

7.4.4.6 FS Double Pass Advancing

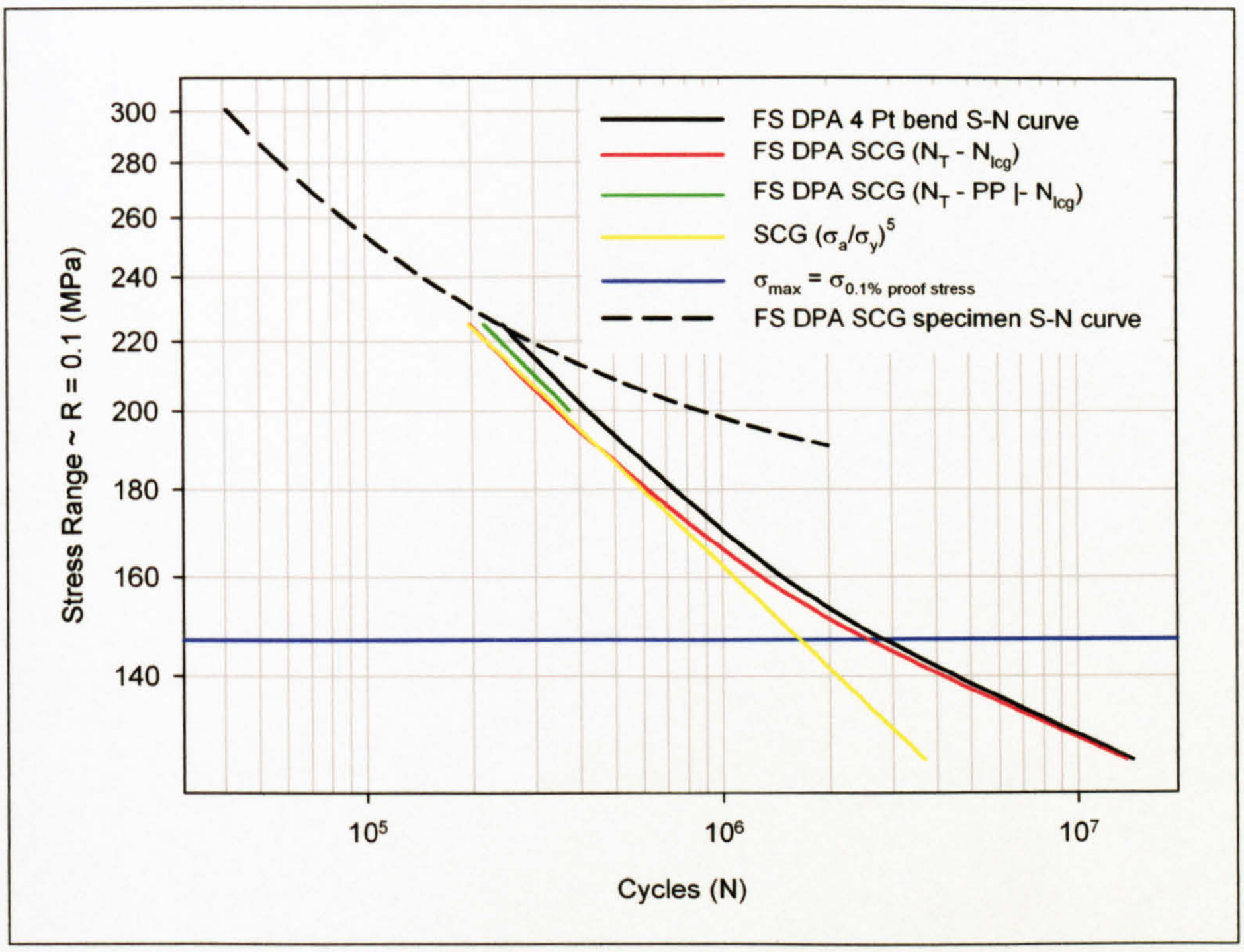

Figure 7.31: FS DPA theoretical and experimental SCG S-N.

Formulation (value)	B	n
σ_a/σ_y (0.746)	1.05×10^{-4}	5
σ_a/σ_{TS} (0.365)	0.00375	
$(\sigma_a/\sigma_y).\varepsilon_{max}$ (34.36×10^{-3})	508	
$(\sigma_a/\sigma_{TS}).\varepsilon_{max}$ (16.81×10^{-3})	18100	

Table 7.22: FS DPA constants for SCG equations.

The theoretical FS DPA SCG S-N curve was determined through subtraction of the FS DPA LCG from the four point bend S-N data, as shown in Figure 7.31, although the curve resulting from subtraction of the PP |- LCG data has also been included for comparative purposes. From Figure 7.31 it was evident that the SCG consisted of 78 - 84% of the overall fatigue life when values of n = 5 and B as shown in Table 7.22 were employed for the SCG equations for 225 MPa ≥ Δσ ≥ 170 MPa. For Δσ < 170 MPa the disparity between the predicted values for the SCG period and the experimentally determined value increased as Δσ decreased; for a stress range of 150 MPa the predicted value was 70% of the experimental. Determination of the SC period of the fatigue life of the SCG specimen, utilising the SCG constants detailed in Table 7.22 and equation (7.66), resulted in a value of 132674 cycles, 133% of the fatigue life of 99420 cycles. Extrapolation of the theoretical curve to greater stress ranges suggested that this would

have a slightly greater slope than that returned by the FS DPA SCG specimen S-N curve and the subsequent values for the SC fatigue life returned by the theoretical curve would be slightly greater, this being evident in the experimental and theoretical values obtained for the SCG specimen.

$$N_{scg_{FS\ DPA}} = \frac{1}{1.05\times10^{-4}}\left(\frac{163}{\sigma_a}\right)^5 \times \ln\left(\frac{250}{10}\right) \qquad (7.66)$$

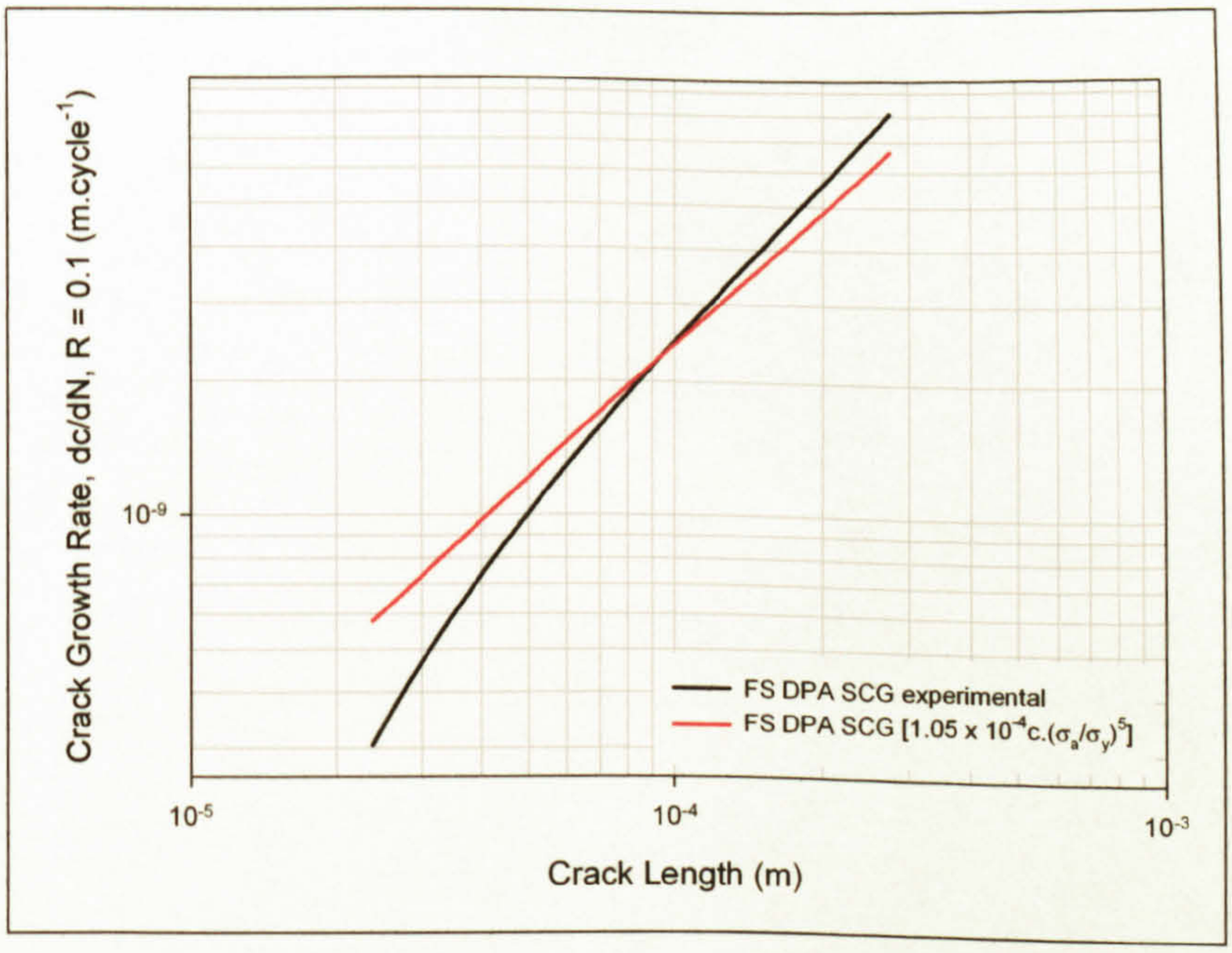

Figure 7.32: Comparison of FS DPA experimental and theoretical SCG rates.

Utilising the SCG constants shown in Table 7.22, the SCG rate, with respect to the crack length, exhibited an underestimate for cracks lengths > 9×10^{-5} m and an overestimate for lengths < 9×10^{-5} m, with the disparity increasing for crack lengths < 5×10^{-5} m.

Although a proportion of the peak stresses in stress ranges under consideration were below the yield strain, the deviation of the theoretical SCG S-N curve from the experimental one commenced at a stress range greater than the yield stress, therefore it is probable that the effect of any residual stresses would be diminished due to redistribution.

On the above evidence the overall fatigue life of a structure could be predicted utilising either equation (7.59) or (7.60) for lives ≤ 10^6 cycles, 170 MPa ≤ $\Delta\sigma$ ≤ 225 MPa:

N_T = number of cycles to failure or a predetermined crack length, ≤ 10^6 cycles.

σ_y = yield strength or 0.1% proof stress, 163 MPa.

σ_{TS} = tensile strength, 333 MPa.

σ_a = stress amplitude, 86.5 MPa ≤ σ_a ≤ 112.5 MPa (R = 0.1).

$\Delta\sigma$ = stress range, 170 MPa ≤ $\Delta\sigma$ ≤ 225 MPa (R = 0.1).

ε_{max} = maximum applied strain.

B = SCG rate constant, the corresponding value, shown in Table 7.21, depending on the formulation employed.

n = SCG rate constant, 5.

c_i = crack initiator size, 20 μm.

c_t = transition from SCG → LCG size, 250 μm.

$c_{f\varepsilon}$ = transition crack length from predominantly plane strain to plane stress.

$c_{f\sigma}$ = final crack size.

m_ε = Paris constant for plane strain, 4.908.

C_ε = Paris constant for plane strain, 1.77×10^{-12}.

m_σ = Paris constant for plane stress, 2.946.

C_σ = Paris constant for plane strain, 138.38×10^{-12}.

Y = geometric configuration factor for a semi-elliptical surface crack subjected to pure bending, 0.61.

7.4.4.7 FS Double Pass Retreating

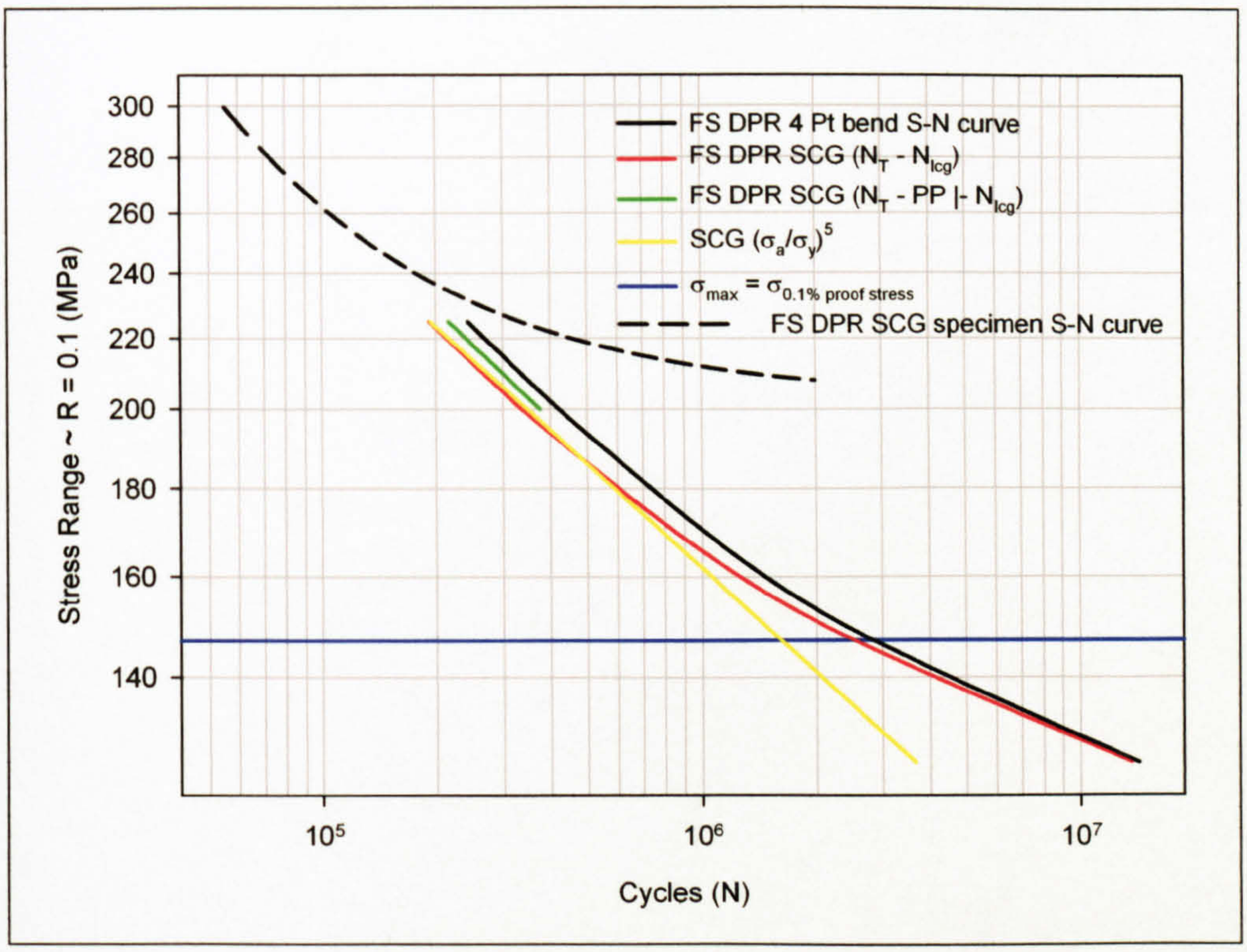

Figure 7.33: FS DPR theoretical and experimental SCG S-N.

Formulation (value)	B	n
σ_a/σ_y (0.796)	1.03×10^{-4}	5
σ_a/σ_{TS} (0.375)	0.00366	
$(\sigma_a/\sigma_y).\varepsilon_{max}$ (42.41×10^{-3})	239.6	
$(\sigma_a/\sigma_{TS}).\varepsilon_{max}$ (19.98×10^{-3})	8525	

Table 7.23: FS DPR constants for SCG equations.

The theoretical FS DPR SCG S-N curve was determined through subtraction of the FS DPR LCG from the four point bend S-N data, as shown in Figure 7.33, although the curve resulting from subtraction of the PP |- LCG data has also been included for comparative purposes. From Figure 7.33 it was evident that the SCG consisted of 77 - 83% of the overall fatigue life when values of n = 5 and B as shown in Table 7.23 were employed for the SCG equations for 225 MPa ≥ Δσ ≥ 170 MPa. For Δσ < 170 MPa the disparity between the predicted values for the SCG period and the experimentally determined value increased as Δσ decreased; for a stress range of 150 MPa the predicted value was 71% of the experimental. Determination of the SC period of the fatigue life of the SCG specimen, utilising the SCG constants detailed in Table 7.23 and equation (7.67), resulted in a value of 94766 cycles, 99% of the fatigue life of 95618 cycles. The S-N curve returned by the FS DPR SCG specimens exhibited a comparable slope and

magnitude to that suggested through extrapolation of the theoretical results to greater stress ranges.

$$N_{scg_{FS\ DPR}} = \frac{1}{1.03\times10^{-4}}\left(\frac{163}{\sigma_a}\right)^5 \times \ln\left(\frac{225}{10}\right) \qquad (7.67)$$

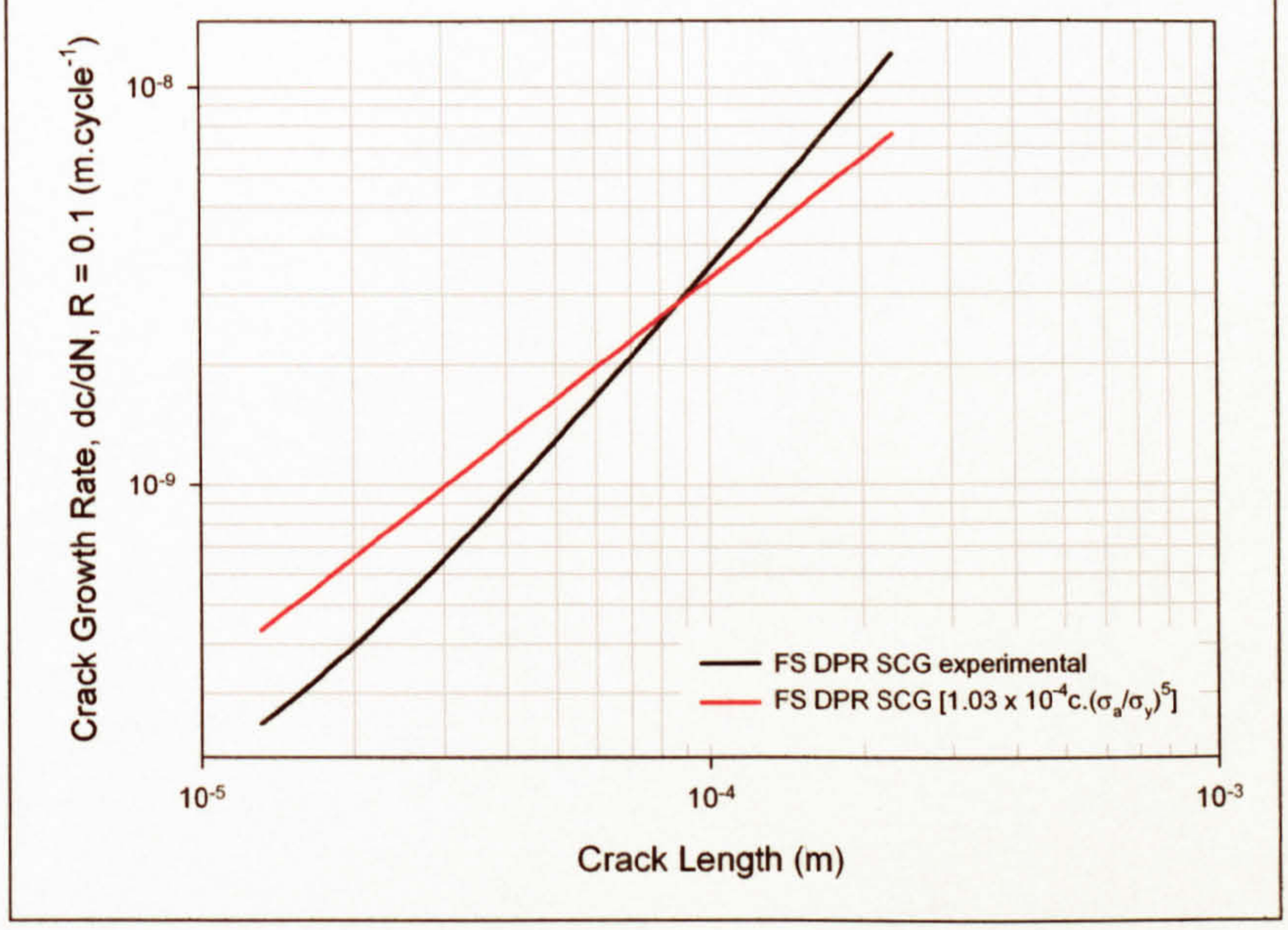

Figure 7.34: Comparison of FS DPR experimental and theoretical SCG rates.

Figure 7.34 details both the experimental and theoretical SCG rates with respect to the crack length, utilising the SCG constants shown in Table 7.23. The theoretical SCG rates exhibited an underestimate for cracks lengths $> 8.5 \times 10^{-5}$ m and an overestimate for lengths $< 8.5 \times 10^{-5}$ m.

Although a proportion of the peak stresses in stress ranges under consideration were below the yield strain, the deviation of the theoretical SCG S-N curve from the experimental one commenced at a stress range greater than the yield stress, where a diminishing of their influence on the fatigue properties would be reduced due to redistribution.

On the above evidence the overall fatigue life of a structure could be predicted utilising either equation (7.59) or (7.60) for lives $\leq 10^6$ cycles, 170 MPa $\leq \Delta\sigma \leq$ 225 MPa:

N_T = number of cycles to failure or a predetermined crack length, $\leq 10^6$ cycles.
σ_y = yield strength or 0.1% proof stress, 163 MPa.
σ_{TS} = tensile strength, 333 MPa.
σ_a = stress amplitude, 85 MPa $\leq \sigma_a \leq$ 112.5 MPa (R = 0.1).

$\Delta\sigma$ = stress range, 170 MPa ≤ $\Delta\sigma$ ≤ 225 MPa (R = 0.1).

ε_{max} = maximum applied strain.

B = SCG rate constant, the corresponding value, shown in Table 7.21, depending on the formulation employed.

n = SCG rate constant, 5.

c_i = crack initiator size, 20 μm.

c_t = transition from SCG → LCG size, 225 μm.

$c_{f\varepsilon}$ = transition crack length from predominantly plane strain to plane stress.

$c_{f\sigma}$ = final crack size.

m_ε = Paris constant for plane strain, 5.147.

C_ε = Paris constant for plane strain, 1.40×10^{-12}.

m_σ = Paris constant for plane stress, 2.713.

C_σ = Paris constant for plane strain, 211.62×10^{-12}.

Y = geometric configuration factor for a semi-elliptical surface crack subjected to pure bending, 0.61.

7.5 Discussion

Regression analysis of the experimental SCG data, as shown in Figure 7.15 to Figure 7.18 (pages 422 - 425), suggested that the SCG rate was proportional to the crack length, a linear response being evident for the log-log plot of the crack growth rate/crack length. A comparable response was also evident when $[(\sigma_a/\sigma_{y\ or\ TS}).c]$ and $[\varepsilon_{max}.(\sigma_a/\sigma_{y\ or\ TS}).c]$ were plotted against the crack length, implying that:

$$\left(\frac{dc}{dN}\right)_{scg} = f\left(\sigma_a, \sigma_y, \sigma_{TS}, \varepsilon_{max}, c\right) \tag{7.68}$$

From the figures it was apparent that the experimental SCG data for both the parent plate and welded specimens, once regression analysis had been undertaken, fell within a narrow range. A comparable response was also evident when σ_a, $\sigma_{y\ or\ TS}$ and the crack length were plotted against the crack length, with a slightly greater disparity being evident when ε_{max} was employed.

Due to SCG data only being available for a stress range resulting in a fatigue life for the SCG specimens in the region of 10^5 cycles it was not possible to determine the constants B and n, as shown in equations (7.69) and (7.70), through normalisation of experimental data, the approach taken by Nisitani et al[1,2] and Caton et al[3,4]. To overcome this problem a LCG S-N curve was developed through integration of the LCG Paris law equations, this was then subtracted from the S-N curve from the 40 mm wide parent plate and as-welded specimens, the result considered to be a S-N curve representative of the SCG. The validity of this approach was verified through comparison of the resulting theoretical SCG rates, with respect to the crack length, when the constants B and n were employed, with those determined experimentally. A good comparison being observed for both the parent plate and FS welds.

$$\left(\frac{dc}{dN}\right)_{scg} = B\left(\frac{\sigma_a}{\sigma_{y\ or\ TS}}\right)^n .c \tag{7.69}$$

$$\left(\frac{dc}{dN}\right)_{scg} = B\left(\frac{\sigma_a}{\sigma_{y\ or\ TS}}\varepsilon_{max}\right)^n .c \tag{7.70}$$

Although the above approach returned a good evaluation when analysing the parent plate and FS welds, the LCG MIG data returned cycles to failure values that were greater than those from the 40 mm wide specimen S-N curves. It has been assumed that this was the

---

[1] Nisitani, H; Goto, M (1986)
[2] Nisitani, H et al (1992)
[3] Caton, MJ et al (1999a)
[4] Caton, MJ et al (1999b)

result of the influence of the weld induced residual stress field on the LCG measurements, with a compressive stress in the region of the crack tip of the CT specimen causing increased crack closure and an apparent increase in the resistance to crack propagation. To overcome this an attempt was made at determining MIG SCG S-N curves by substituting the MIG LCG data with that from the PP |- CT specimens, although when the theoretical crack growth rates, with respect to the crack length, were compared to the experimental ones, as shown in Figure 7.26 and Figure 7.28 (pages 448 and 451), it suggested that the theoretical growth rates were considerably lower than the experimental ones. This outcome would be expected if the PP |- LCG data was consuming a lower proportion of the fatigue life than was attributable in the case of the MIG welds, although this suggests that the LCG rate in the parent material was greater than that of the MIG welds. Adaptation of the theoretical SCG rate through mapping onto the experimental data, changing the value of the constant B, but retaining the value for the constant n, resulted in a SCG rate that was comparable to the experimental values, for both the LI and HI welds. The outcome of this approach was a reduction in the proportion of the fatigue life attributable to SCG, for the SCG specimens this resulted in a reduction from 1.23 to 0.72 and 2.98 to 0.76 for the LI and HI specimens respectively. Subsequent analysis, utilising the mapped values for B, resulted in a shifting of the theoretical SCG S-N curve to a lower number of cycles for the same stress range, which would ultimately result in a conservative assessment of the fatigue life. Further discrepancies between the theoretical and experimental results were evident when considering the S-N curve that resulted from the SCG specimens. The LI weld returned a curve that was comparable to that returned by the 40 mm wide specimens, albeit suggesting a moderate overestimate of the fatigue life, with a slope comparable to that for the theoretical SCG S-N curve. The HI SCG specimens S-N curve had a significantly reduced slope when compared to that of the both the theoretical SCG S-N curve and that returned by the 40 mm wide as-welded specimens. The disparity between the theoretical and experimental results returned by the MIG LI may have been the result of the PP |- LCG data being utilised rather than that of the LI weld as the discrepancies were relatively minor*. The discrepancies observed for the MIG HI weld suggested that more fundamental problems may have arisen, possibly a combination of several variables including the application of the stress concentrating effect of the weld toe, the influence of the residual stress field for peak stresses below the yield stress, as well as the utilisation of the PP |- LCG data.

The values for the constants B and n, determined from the FS weld SCG S-N curves, resulted in theoretical crack growth rates that were comparable to the experimental ones, as shown in Figure 7.30, Figure 7.32 and Figure 7.34. This suggested that the lower

---

* The author does not consider that any disparity resulting from the fact that the long crack growth and S-N data resulted from different alloys, 5083-H321 and 5383-H321 respectively, would have been of a great enough magnitude to return the negative values observed.

residual stresses resulting from the FS welds had a minimal effect on the LCG analysis. SCG S-N curves were also determined through utilisation of the PP |- LCG data in an attempt to compare the response to that attained from the FS SCG specimens and also to ascertain the approach with respect to the MIG welds. Little disparity was evident between the SCG S-N curves determined through application of the appropriate LCG data and those from the PP |- results.

Table 7.24 details the minimum applied stress ranges and maximum number of cycles for which the fatigue life could be relatively accurately predicted, within 10% of the experimentally determined fatigue life, through application of equation (7.71).

$$N_T = \left[\frac{1}{B}\left(\frac{\sigma_{y\ or\ TS}}{\sigma_a}\right)^n \ln\frac{c_f}{c_i}\right] + \left[\frac{2}{(m_\varepsilon - 2)C_\varepsilon Y^{m_\varepsilon}(\Delta\sigma)^{m_\varepsilon}\pi^{m_\varepsilon/2}}\left\{\frac{1}{(c_i)^{(m_\varepsilon-2)/2}} - \frac{1}{(c_{f\varepsilon})^{(m_\varepsilon-2)/2}}\right\}\right] + \left[\frac{2}{(m_\sigma - 2)C_\sigma Y^{m_\sigma}(\Delta\sigma)^{m_\sigma}\pi^{m_\sigma/2}}\left\{\frac{1}{(c_{f\varepsilon})^{(m_\sigma-2)/2}} - \frac{1}{(c_{f\sigma})^{(m_\sigma-2)/2}}\right\}\right] \quad (7.71)$$

A maximum stress level has not been ascertained, except for the MIG LI weld, as reference to the SCG specimen and 40 mm wide S-N curves suggested that extrapolation of the experimental and theoretical results to higher stress ranges would result in comparable values, although further analysis is required to confirm this. A maximum stress range level was detailed for the MIG LI weld as the disparity between the theoretical and experimental values was observed to be increasing as the magnitude increased above 240 MPa, although due to problems in accurate modelling of the MIG welds the values for the LI weld require further analysis, whilst no values are detailed for the HI weld due to the discrepancies between the theoretical and experimental results.

Specimen	$\Delta\sigma \sim R = 0.1$ (MPa)		σ_{max} (MPa)	σ_a (MPa)	σ_y (MPa)	σ_{max}/σ_y (MPa)	Cycles to failure, max (N_T)
	max	min					
PP |-		230	256	115	254	1.00	5.0×10^5
PP //					272	0.94	3.1×10^5
MIG LI weld toe (nominal)	240 (220)	210 (170)	233	105	160	1.46	5.2×10^5
MIG HI	-	-	-	-	167	-	-
FS SP		185	206	92.5	157	1.31	6.5×10^5
FS DPA		170	189	85	163	1.16	10^6
FS DPR							

Table 7.24: Range of values for model suitability.

Table 7.25 details the predicted SCG regimes determined through application of the stress amplitude and yield stress, equation (7.69), and the actual number of cycles to failure of the SCG specimen. Although the applied stresses were relatively high it would be expected that the period of crack growth due to SC would be relatively high due to the geometry of the specimens.

The parent material and FS SP and DPR theoretical predictions all attribute ≥ 90% of the fatigue life of the specimen to SCG, which may be considered acceptable values, although the 99% returned by the FS DPR analysis may be slightly overestimated. The cause of the over prediction of 1/3 returned by the FS DPA analysis is unclear, although the lower stress amplitude and increase in SCG to LCG transition crack length, in comparison to those for the FS DPR analysis, may have had the effect of increasing the number of cycles attributable to SCG. The values for the MIG welds reflect the problems in trying to determine suitable model parameters, with the application of the PP |- LCG data to determine the SCG S-N curve, resulting in a significant overestimate of the period of the fatigue life attributable to SCG, although the effect was more evident for the HI weld. Mapping of the SCG theoretical data to the experimental data resulted in values that may be considered too conservative with regard to the period of SCG, although further analysis is required to verify this.

Specimen	c_l (μm)	c_t (μm)	σ_a	σ_y	Predicted SCG period (N_{scg})	Cycles to failure of SCG specimen (N_{spec})	$\frac{N_{scg}}{N_{spec}}$
PP |-	13	350	134	254	101955	112764	0.90
PP //	13	300		272	105493	113772	0.93
MIG LI	21	300	123	160	138839*/81915**	113038	1.23*/0.72**
MIG HI	21.5	250	124	167	301151*/76793**	100996	2.98*/0.76**
FS SP	20	250***	131	157	105462	114505	0.92
FS DPA	20	250	122	163	132674	99420	1.33
FS DPR	20	225	125		94766	95618	0.99

Table 7.25: Predicted SCG regimes.

* Calculated through utilisation of the PP |- LCG data.
** Calculated through utilisation of the MIG LI or HI SCG data.
*** It has been assumed that the maximum crack length that short crack growth would be evident for in the FS SP welds would be comparable to that observed in the other specimens, therefore, although the maximum sized SC measured was 169 μm, the maximum crack for determining the number of cycles required to attain long crack growth has been assumed to be comparable to that observed in the other specimens and a nominal value of 250 μm has been employed.

Figure 7.35 to Figure 7.37 depict the experimental and theoretical S-N curves for the 40 mm wide specimens and minimum stress range (R = 0.1) values for the theoretical analyses. The minimum stress ranges for the theoretical analyses are comparable to those suggested by Nisitani et al[1,2], for their analysis of a 0.45% C steel and Fe-3% Si alloy, $\sigma_a > \frac{1}{2}\sigma_y$ and $N < 10^6$ cycles. Although the theoretical investigation returned favourable results for the AA 5383-H321 parent material and FS weld S-N curves resulting from the 40 mm wide specimens, further analysis is required to determine whether the approach is suitable for engineering structures. As well as the scaling problem found in fatigue analyses, the residual stresses are also greater in large engineering structures, as shown by the magnitude of those measured in the as-welded (1000 x 500 x 8 mm) plates. Although due to the magnitudes of the applied stresses, $\sigma_{max} > \sigma_y$, a redistribution of the residual stresses within the vicinity of the crack area may be considered to have occurred due to plastic flow and thus their influence would be minimised, as detailed in Sections 4.3.4, Relaxation/Redistribution of Residual Stresses (page 141) and 4.3.5 Effects of Residual Stresses on Fatigue (page 148).

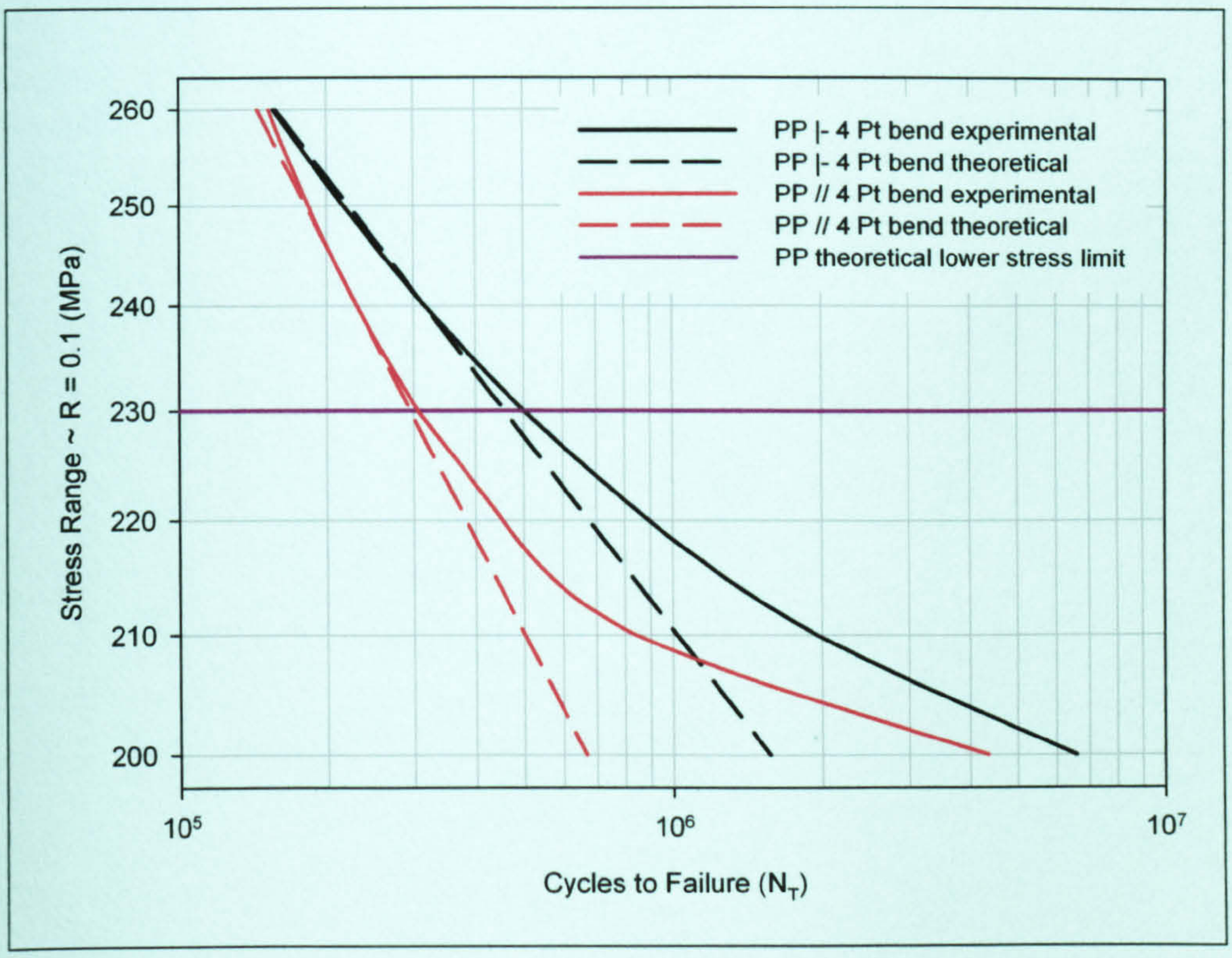

Figure 7.35: AA 5383-H321 parent plate experimental and theoretical S-N curves.

[1] Nisitani, H; Goto, M (1986)
[2] Nisitani, H et al (1992)

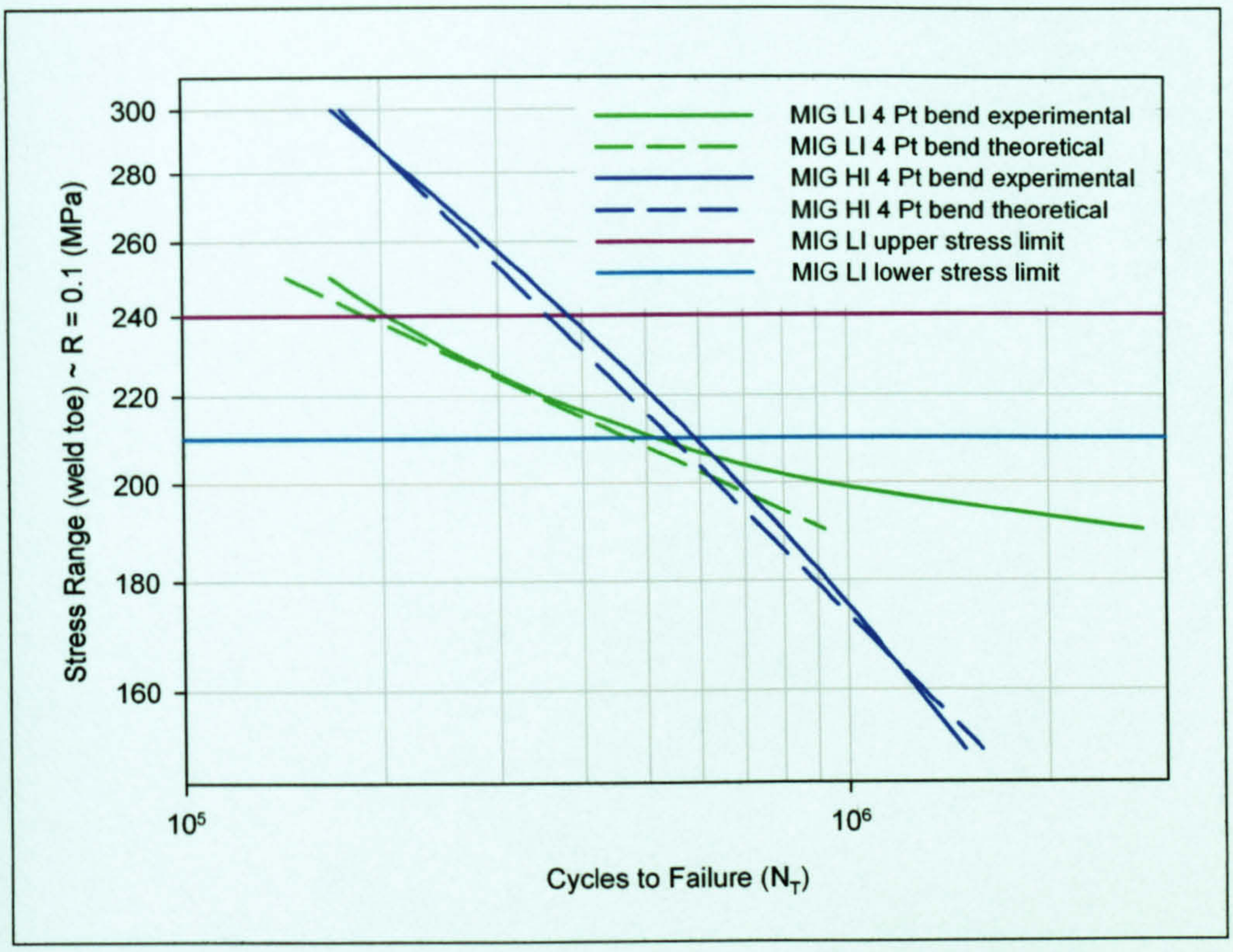

Figure 7.36: MIG LI and HI experimental and theoretical S-N curves (utilising PP |- LCG data to determine the theoretical curves).

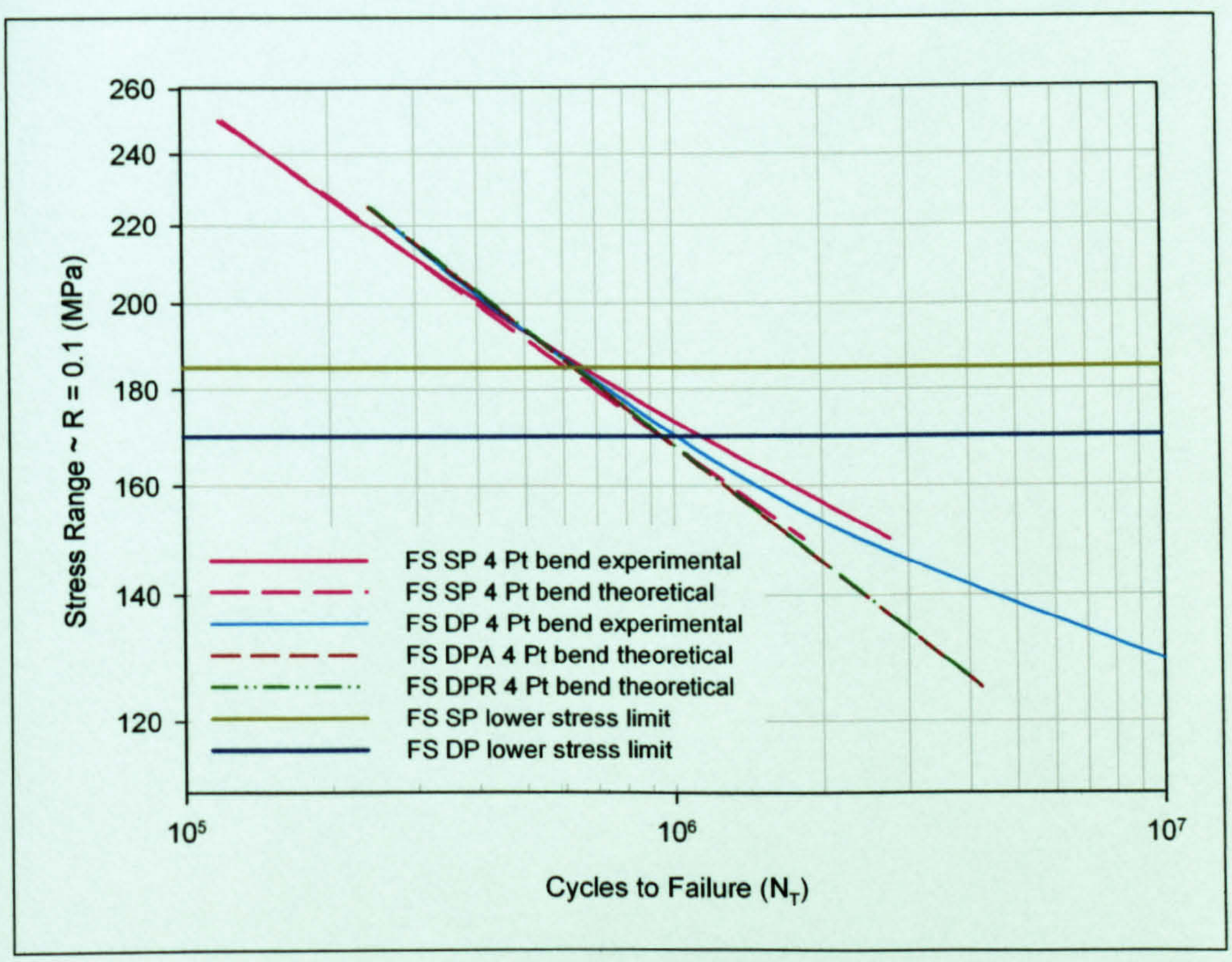

Figure 7.37: FS SP, DPA and DPR experimental and theoretical S-N curves.

8. Discussion

8.1 Abstract

The following section discusses the main parameters employed in the development of a simple defect-tolerant based model for predicting the fatigue life of AA 5383-H321 parent plate and MIG and FS welded butt joints in the same alloy. The main parameters of the model were the crack initiation and short and long crack growth regimes, the effects that the other weld related parameters, the weld geometry, microstructure and residual stresses, had on these and their overall effect on the accuracy of the model are also discussed.

8.2 Weld Geometry and Microstructure

Comparison of the external geometry of the AA 5383-H321 welded butt joints revealed a significant variation, as shown in Figure 8.1, with the MIG welds having a weld bead that acted as a significant stress concentrator in the region of the weld toe, whilst the FS welds had a relatively flat profile, although the circular score marks on the surface, due to the rotational and transverse movement of the tool, would also have had a stress concentrating effect and this was evident in the initiation sites observed in the FS welds.

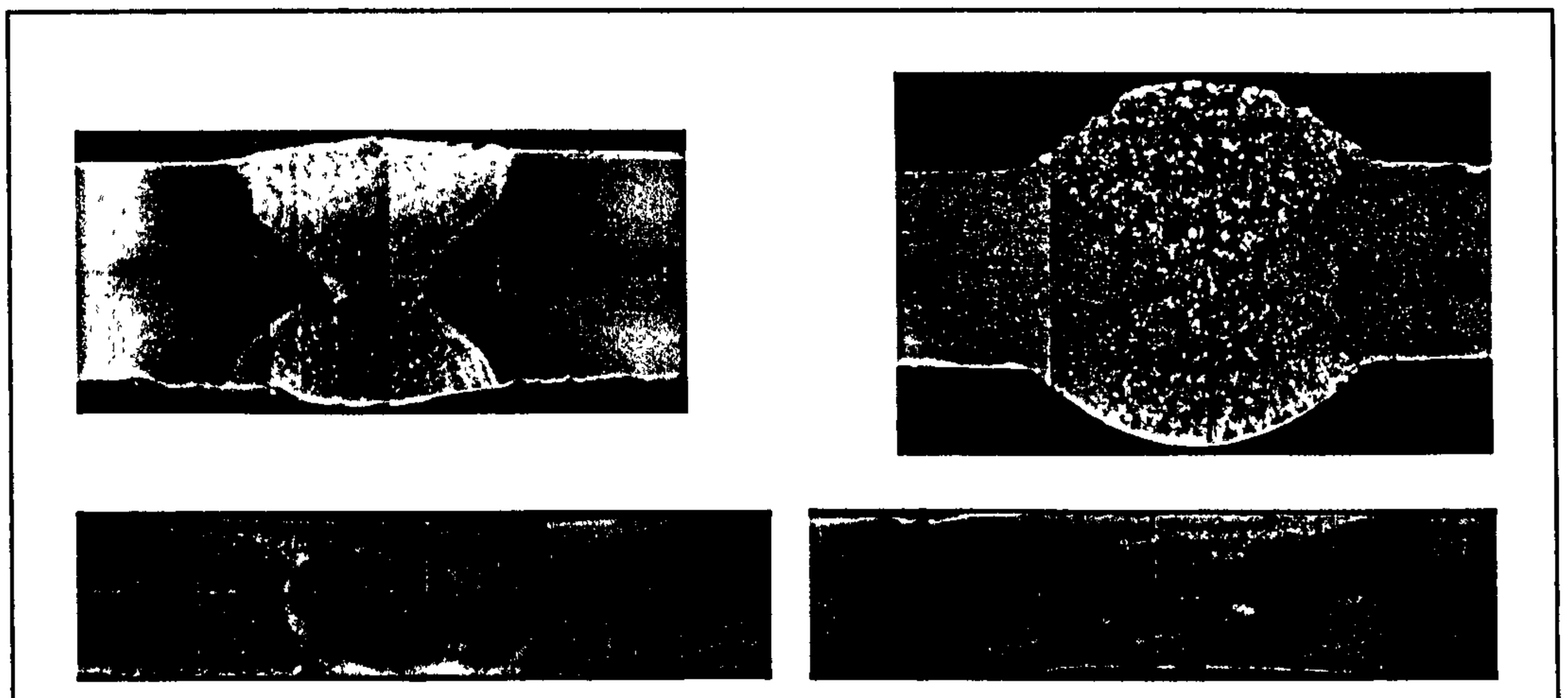

Figure 8.1: External geometry of butt welded joints - MIG LI (upper left), MIG HI (upper right), FS SP (lower left) and FS DP (lower right) (8 mm plate thickness for all welds).

The effect of the weld toe has been well documented, both Saunders et al[1] and Kelsey and Nordmark[2] stated that it was the overriding factor in determining the fatigue life of MIG welded joints, although assessing the magnitude of the SCF has proved more problematic. The weld toe radius and angle are considered to be the influential properties with regards to determining the magnitude of the SCF, with Niu and Glinka[3] considering the toe radius to be influential with respect to crack initiation and the angle to be influential with respect to crack growth.

Due to the range of the measurements obtained when determining the weld toe radii and angles the approach undertaken by the author was to consider the weld bead to be of a fixed radius with the measured weld toe radius intersecting this at a tangent, the toe angle being determined through the parameters employed for the two radii. This approach still resulted in several values for the SCF and it was decided to employ a "worst case scenario" on the basis that each weld toe would contain this combination of

---

[1] Saunders, WW et al (1965)
[2] Kelsey, RA; Nordmark, GE (1979)
[3] Niu, X; Glinka, G (1987)

radii and that theoretically this would be the likely point of crack initiation. Further investigation of crack initiation in the MIG welds suggested that although the weld toe was the region of crack initiation, the actual point of initiation was compounded through the secondary stress concentrating effects of either weld porosity or variations in the toe geometry from effects such as weld spatter.

The stress concentrating effects of the MIG weld toe are evident in S-N curves depicted in Figure 8.2, with the MIG HI weld having the worse fatigue strength of all the welds under examination, although when the stress concentrating effect of the toe was taken into consideration the fatigue strength was superior to that of the FS welds (the stress concentrating effects of the surface marks of the FS welds not being taken into consideration). The MIG LI weld exhibited a comparable response, although for weld toe stresses at the lower stress ranges, when the stress concentrating effect was greatest (at higher stress ranges a reduction occurs due to plasticity effects) the difference in the fatigue strength, when compared to that of the FS welds, increased. The weld toe S-N curves were dependent on the determination of the stress concentration effects of the weld toe, with both the difficulties in obtaining accurate measurements and the variability of these needing to be considered. The approach utilised in determining the stress concentration factor, whether a best, mean or worst case scenario was employed, also has a significant effect on the outcome, the elastic stress concentration factors determined by FEA for the LI weld ranged from 1.22 - 1.45 and from 1.59 - 2.81 for the HI weld. The "worst case scenario" utilised the maximum values for the elastic analysis, although for the weld toe S-N curves shown in Figure 8.2 an elastic-plastic SCF, also determined though FEA, was employed.

The value employed for the SCF of the weld toe had a significant effect on the modelling of the fatigue properties as this is considered to be the local stress for the crack growth regimes. The main influence in the failure of the model to predict the fatigue life of the MIG welds may have been due to choosing the "worst case scenario" for the SCF. Although an elastic-plastic SCF was employed to enhance the SCF at high stress levels no account of the diminishing effect of the SCF as the crack propagated through the material was taken into consideration, a factor which was also likely to have been influential in predicting the fatigue life.

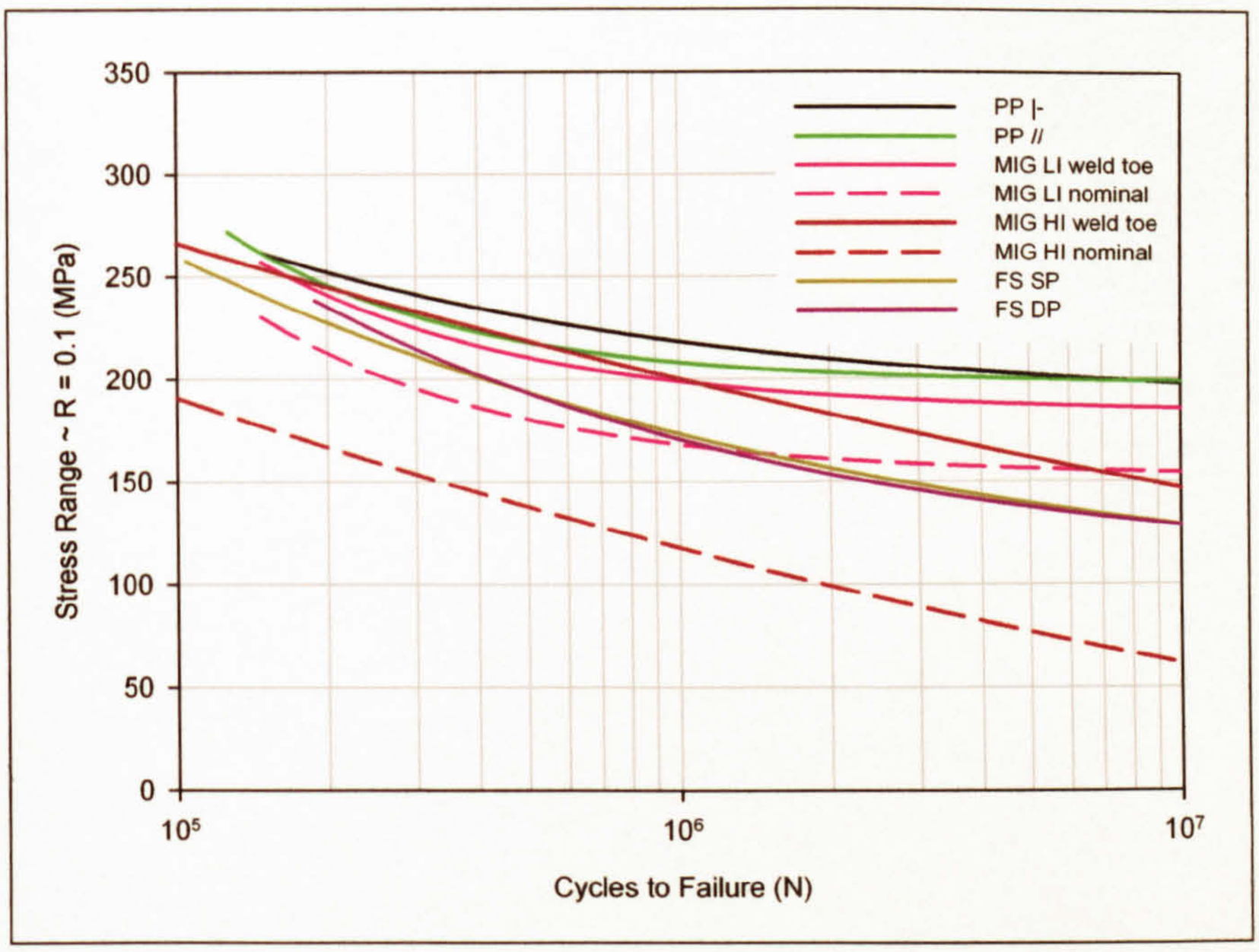

Figure 8.2: Four point loading S-N fatigue curves for AA 5383-H321 parent plate, MIG LI and HI and FS SP and DP welds.

The microstructure of the two welding processes was also notably different, although as crack initiation and growth in the MIG and FS DP welds occurred in comparable regions, the HAZ, similar propagation rates may have been expected for both SCG and LCG if all other variables, such as the magnitude of the residual stress field, were considered equal. Crack growth in the FS SP weld occurred within the TMAZ/weld nugget region and it would have been plausible to have expected the crack growth rates to have been reduced due to the small grain size and thus the greater propensity for crack growth arrest due to the increased number of grain boundary interactions.

Defects within the weld nugget region were observed in the FS SP weld, with these being termed partial fusion defects. Although the PFD appeared to have no effect on the fatigue properties of the as-welded specimens, the SCG specimens, with the centre of the specimen being in the weld nugget region, frequently failed at a substantially lower number of cycles than predicted by the FS SP SCG specimen S-N curve. The reason that the PFD appeared to have no effect on the as-welded fatigue specimens may have been due to the four point loading utilised, only the outer fibres being subjected to the full load, whilst the weld nugget region would have been subjected to a lower load.

8.3 Residual Stresses and Strains

The accuracy of the hole drilling technique to determine the residual strains when they exceed $\sigma_y/3$ for a uniaxial stress field is reduced due to the likelihood of plasticity effects

resulting in an overestimate of the maximum principal strain and a subsequent underestimate of the minimum principal strain. This effect appeared to have occurred in the results returned by the welds, most notably with the MIG welds. The results returned by the MIG welds, for measurements undertaken at the weld toe, suggested that the longitudinal strains were greater than the yield strength of the weld, and frequently that of the parent material, whilst the transverse strains ranged from being compressive to slightly tensile. Considering the results to be qualitative suggested that the greatest longitudinal strains were returned by the MIG LI weld, 4200 – 5500 με, with those from the MIG HI weld being slightly lower, 3000 – 4300 με, subsequently the transverse strains were observed to be lower in the MIG LI weld, -1700 to -600 με, when compared to those returned by the MIG HI weld, -2100 to 750 με. An anticlastic bending effect also appeared apparent, with the transverse strains on the convex side (the convex and concave sides of the welded plates relating to the weld induced distortion along the length of the plates) being lower than those on the concave side, whilst the opposite effect was evident for the longitudinal strains. The FS welds also returned longitudinal residual strains that were greater than the yield strain of the weld, although at the edge of the friction band they returned values that were lower than those returned by the MIG welds, with values ranging from 1500 – 3100 με and 2100 – 3400 με for the SP and DP welds respectively. The transverse strains in the FS welds ranged from -1100 to 1000 με for the SP weld and -1900 to 900 με for the DP weld, with an anticlastic bending effect also being evident.

Synchrotron strain scanning of the friction stir welds also presented problems in that the values of $2\theta_0$, the strain free diffraction angle, returned residual strains that were predominantly compressive in the as-welded samples. The values returned by the fatigue loaded samples exhibited an increase in magnitude, the strains being predominantly tensile, although the overall profile was near-identical to that of the as-welded strains, with little evidence of any redistribution having occurred. The exact cause of these anomalies, by their nature the residual strains must balance throughout the specimen, remained unknown, although it was considered to be either a result of the residual strains in the teeth utilised in determining the values of $2\theta_0$ containing significant strains, or a calibration error occurring between the two sessions when the measurements were performed.

A force and moment balance of the residual strains was undertaken for each specimen in an attempt to determine an "effective" value for $2\theta_0$. The approach resulted in what appeared acceptable, maximum and minimum values equal to or below the yield strain of the weld, values for the transverse strains, although the approach resulted in values that were greater than the yield strain of the parent material for the longitudinal strains. In an attempt to determine suitable values of $2\theta_0$ for the longitudinal strains a force balance

was instigated, but with the strains tending towards zero as the edge of the specimen was approached, this returned values that conformed to the criteria employed for the transverse strains.

A comparison of the residual strains measured by the hole drilling and synchrotron techniques are shown in Figure 8.3 for the 40 mm wide as-welded S-N specimens. The synchrotron measurements returned values that were in the region of 400 – 750 με greater than those returned by the hole drilling approach for the transverse strains, but in the region of 1800 – 2100 greater for the longitudinal strains. The effect may partially be explained by the smaller sized S-N specimens experiencing a greater redistribution of the residual strains than the synchrotron specimens, although further investigations are required to confirm this.

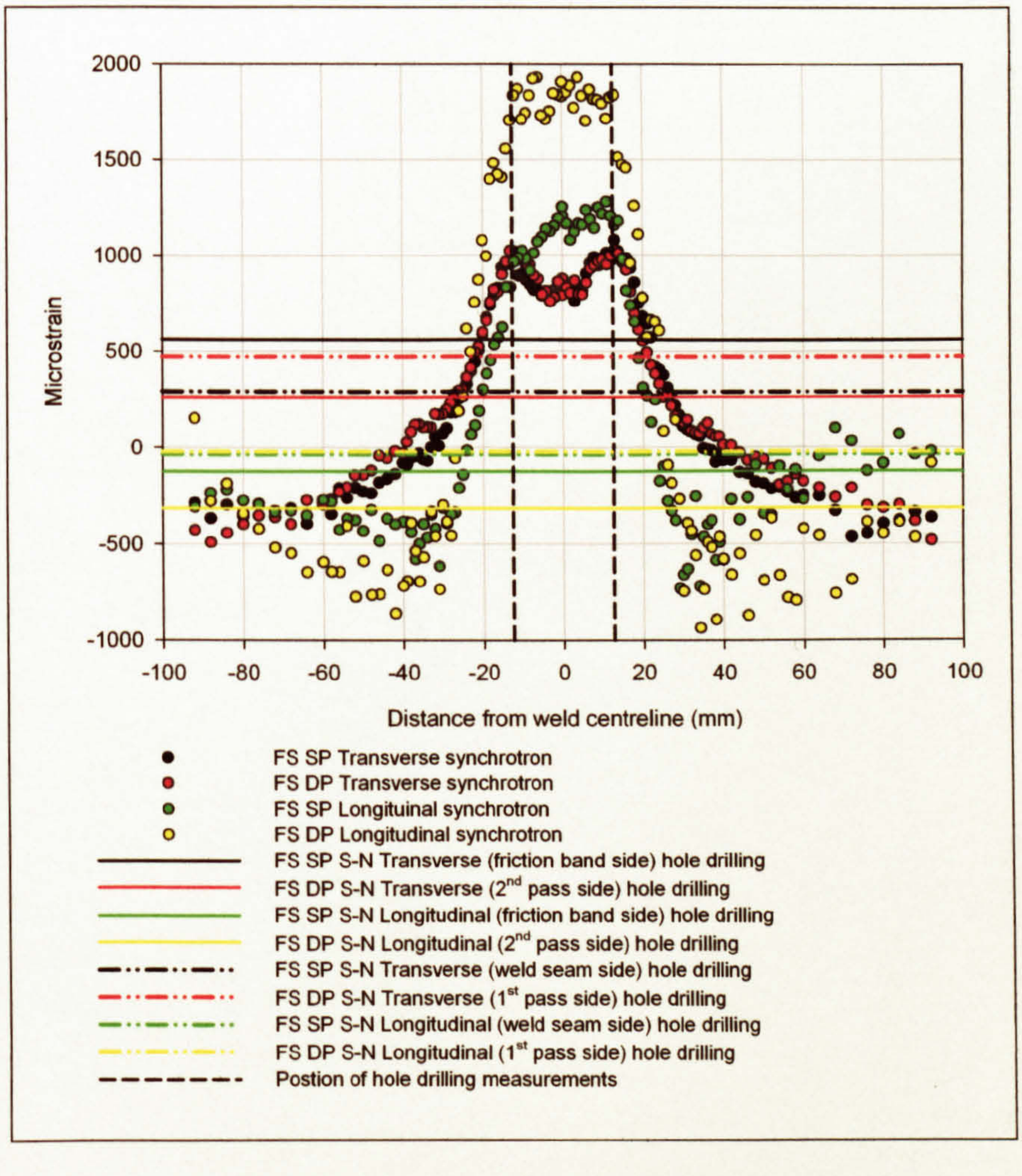

Figure 8.3: Comparison of the transverse and longitudinal residual stresses in FS welds measured by synchrotron radiation (150 mm wide specimens, z = 7 mm) and hole drilling (40 mm wide S-N specimens).

The redistribution of the longitudinal residual strains due to fatigue loading were determined in the same manner to that employed for the as-welded strains, an effective value of $2\theta_0$ being determined for each specimen. From Figure 8.4 the approach suggested that a diminishing in the region of 700 με occurred, although the magnitude and number of cycles appeared to have a minimal effect on the overall redistribution. The redistribution pattern observed may be partially explained by the tensile loading being employed transverse to the weld, the effect of this being a compressive loading in the longitudinal direction. Due to the positions where the synchrotron measurements were undertaken on the fatigue loaded specimens it was not possible to undertake a force and moment balance on the transverse strains.

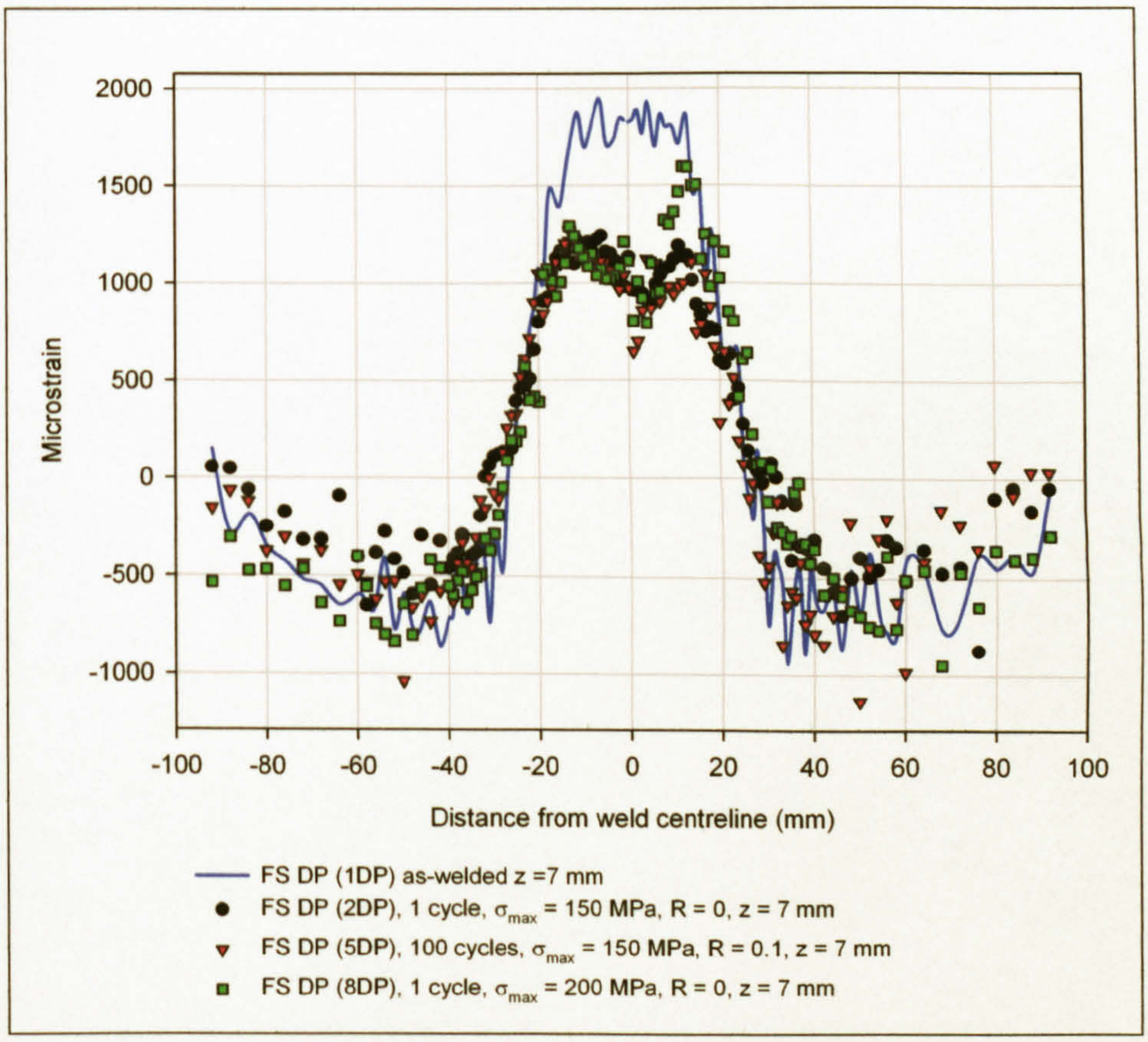

Figure 8.4: The effect of the number and magnitude of load cycles on the distribution of the longitudinal residual strains in a FS DP weld (1 mm below the 2nd pass surface, z = 7 mm, measurements made at the centre of the specimen, x = 0 mm).

The problems encountered in accurately detailing the magnitudes of the as-welded residual strains and their redistribution under loading resulted in difficulties in incorporating these into the fatigue model. The effectiveness of the model was therefore limited to fatigue lives < 10^6 cycles, where the assumption that any residual strains would have redistributed, and their influence diminished, was made, although this was not predicted by the synchrotron measurements.

8.4 Crack Initiation

Welded joints in aluminium are considered to have a significant crack initiation period that can constitute over 90% of the overall fatigue life, although rather than being considered to be crack initiation this can be considered to consist predominantly of short crack growth.

The crack initiation sites of the parent plate were generally the result of the intermetallic phases, although surface marks that had occurred in storage were also observed to have a similar effect. Both the MIG welds investigated exhibited crack initiation at the weld toe, due to its stress concentrating effect, although the actual initiation site was typically the result of a disturbance to the weld toe geometry; frequently porosity, but also due to variations in the toe profile such as weld spatter. The FS welds initiated from surface marks resulting from the motion of the tool in the case of the SP weld and the removal of the weld flash, through grinding, in the case of the DP welds. Both the SP and DP welds exhibited grooves from the motion of the tool and although these were considered to be of a greater magnitude in the case of the SP weld (see Figure 3.76, page 83, and Figure 3.97, page 98), those of the DP weld were of a greater depth than the grooves that resulted from the removal of the weld flash. The difference in the initiation sites for the FS welds was therefore considered to be due to the deeper depth of the grooves in the SP weld, but due a combination of the grooves that occurred due to removal of the weld flash, the increase in the thickness of the weld at the edge of the tool leading to a greater stress when loaded in bending and the peak residual stresses and area of minimum hardness occurring in this region.

Typical crack initiation sizes, which were considered to be short cracks of the same length that were present in the specimens prior to loading, were 13 μm, 21 μm, 20 μm and 10 μm for the parent plate, MIG and FS SP and DP welds respectively.

8.5 Short Crack Growth

Short cracks are generally considered not to conform to the similitude concept; when their growth rates are compared to those in long cracks, with respect to the stress intensity factor range, they are observed to grow at rates below the fatigue threshold and at rates greater than those observed in long cracks as depicted in Figure 6.100 to Figure 6.106 (pages 387 - 390). Due to the various initiation sites the short cracks in the MIG and FS DP welds were growing in a comparable microstructure, the HAZ, whilst those of the FS SP weld grew in the TMAZ and those of the parent material in the as-rolled microstructure. Because of this it may have been expected that their growth rates would be different, although when regression analysis was applied their growth rates fell within a narrow scatter band, as shown in Figure 8.5. The geometry of the SCG specimens

resulted in the SCG measurements for the FS SP weld occurring in the weld nugget. The nugget region is considered to be fully recrystallised, with a grain size in the region of 10 μm, and because of this it would have been expected that there would be a greater predilection for crack growth arrest due to grain boundary interactions. This effect was evident in the FS SP SCG measurements, although regression analysis resulted in an overall SCG rate being comparable to that of the other specimens, as shown in Figure 8.5, suggesting that although crack arrest and deceleration appeared to occur more frequently, during periods of crack advance the growth rate was greater. The geometry of the SCG specimens would also be unrepresentative of the SCG that occurred in the as-welded specimens due to the region of crack growth being in the middle of the specimen, with respect to the thickness, rather than the surface. Fractography of the FS S-N specimens revealed cracks that initially grew along the grooves caused by the motion of the tool and from removal of the weld flash, with this occasionally resulting in cracks propagating in a direction parallel to the applied loading. No account was made for the SCG being measured in a different position to that in which it occurred in the welded specimens.

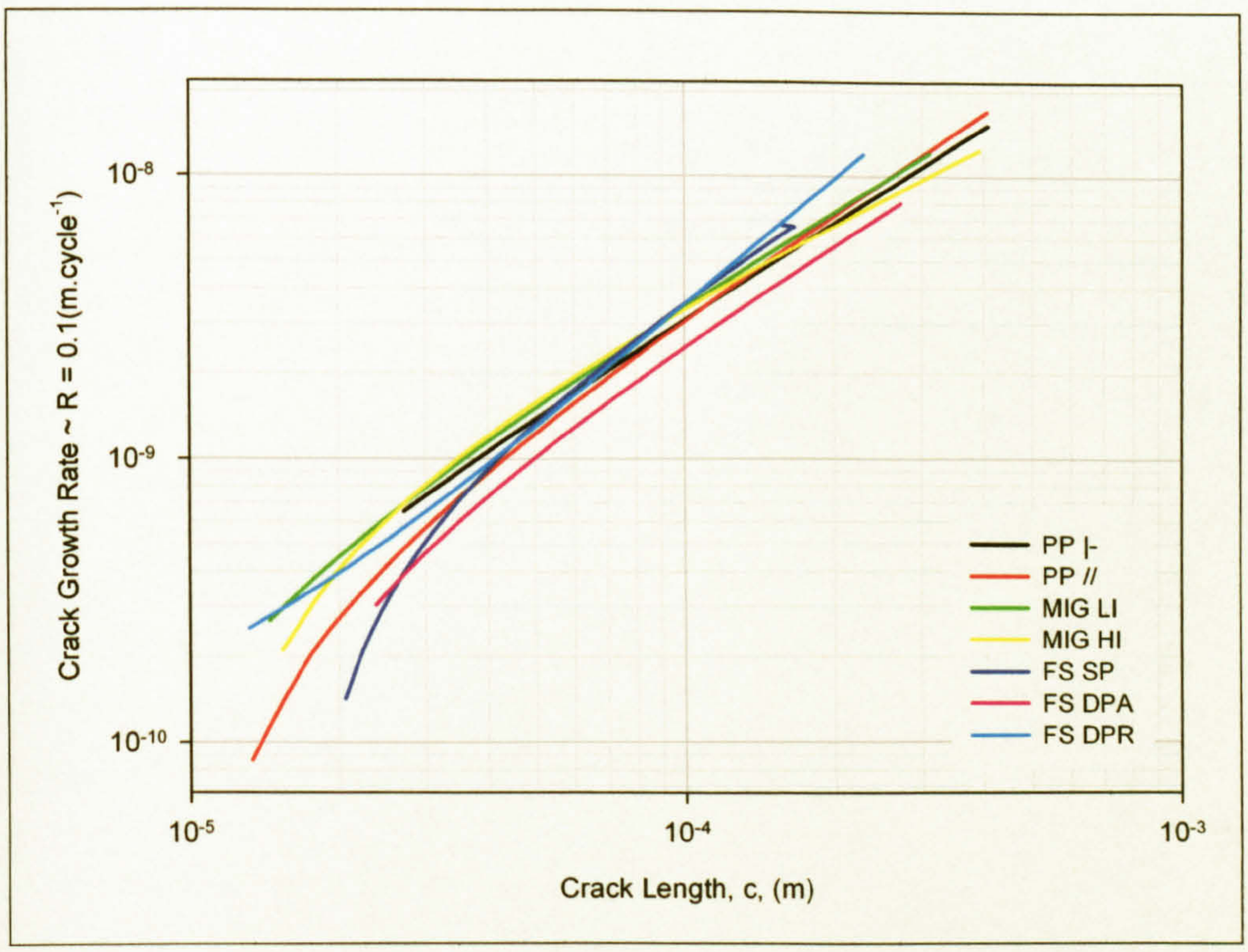

Figure 8.5: SCG rate with respect to crack length, (dc/dN)/c, experimental regression curves.

8.6 Long Crack Growth

All the LCG rate measurements exhibited a point of inflexion in the Paris regime that was attributed to a change in the stress state from predominantly plane strain to predominantly plane stress. The stress state must be taken into consideration when determining the fatigue life as the crack growth rates in the plane stress region were observed to be less than in the plane strain region. Failure to take the stress state into consideration would result in either an underestimate or overestimate of the fatigue life depending on which stress state was employed.

As with the SCG the LCG was determined in the HAZ region for the MIG and FS DP welds, with that of the FS SP welds being measured in the TMAZ/weld nugget region. The LCG measurements undertaken in the HAZ region were all observed to have thresholds greater than that observed in the parent material and it was assumed that this was the result of increased crack closure occurring in the CT specimens employed due to a compressive residual stress field in the region of the crack tip. The residual stresses were considered to have the greatest magnitude in the MIG LI weld, this returning the greatest threshold, with the magnitude decreasing from the MIG HI to the FS DP weld. The FS SP weld was considered to have a comparable residual stress profile to that observed in the DP weld, and, although the measurements were undertaken at the centre of the weld, where a slight reduction in the residual stresses were observed, it was not thought that the reduction was of a magnitude capable of resulting in the increase in the threshold when compared to the FS DP welds. It was therefore thought that the main influence on the increase in the threshold was due to the small grain size of the weld nugget. Although the grain size would result in a greater number of grain boundary interactions the crack tip plastic zone would engulf a significant number of grains diminishing this effect and, combined with the low dislocation density reported for this region, the overall outcome may have resulted in the decrease in the threshold. If the increase in the threshold values was the result of the microstructure it would have been expected that the MIG and FS DP welds would all have exhibited similar threshold values as the cracks were all in a comparable region, the HAZ.

The rate of increase in the LCG rates, up to the change from the predominantly plane strain-stress transition region, was comparable for all the welded specimens and greater than that in the parent plate, suggesting that crack closure resulting from the residual stress field may have been the main cause of the variations in the growth rates. As the crack tip plastic zone size increased it would be expected that the residual stress field would become less influential due to greater plastic flow occurring ahead of the crack tip. In the predominantly plane stress region the crack growth rates, excluding those observed for the MIG LI weld, fell within a narrow band, this may also suggest a further diminishing of the influence of the residual stress field due to plastic flow. The cause of

the rapid increase in the crack growth rate observed in the MIG LI weld when compared to the other welds remained unknown.

Ideally the LCG measurements would be reassessed utilising either a ΔK_{eff} approach that took into consideration the residual stress field in the region of the crack tip or at an increased stress ratio that would result in a reduction in the crack closure effects. Although for the growth to be representative of that in an engineering structure both the local crack geometry and residual stresses would need to be considered, a mid-structure crack would theoretically experience a tensile residual stress at the crack tip, with the expected response being a decrease in the threshold stress intensity factor and an increase in the growth rate. The LCG rate of the welded specimens may also have been influenced by the thickness of the CT specimens being 3 mm less than that of the plate; this being required to produce parallel sided specimens. The outcome of this was that the LCG would have occurred in a slightly different microstructure to that in the 40 mm wide S-N specimens, although as this was still within the HAZ it was thought that any effect would be minimal.

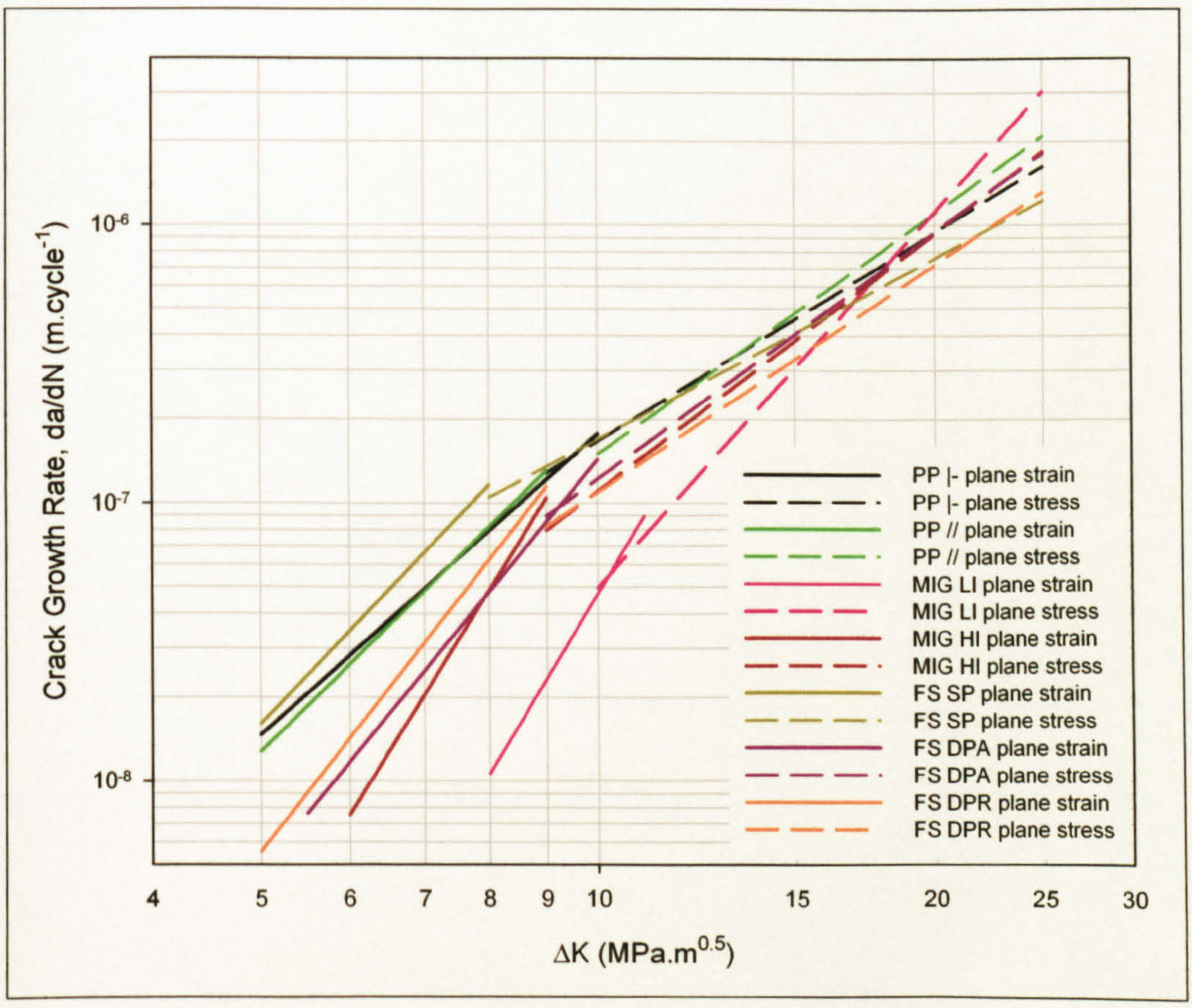

Figure 8.6: Fatigue crack growth rates of AA 5383-H321 parent plate and butt welds (MIG LI AA 5083-H321).

8.7 Modelling

The aim of the modelling was to develop a simple defect-tolerant approach that would predict the fatigue life of AA 5383-H321 plate and MIG and FS butt welded joints in the same alloy by taking into consideration the crack initiation and short and long crack growth regimes, with the effect of the microstructure, geometry and residual stresses also being taken into consideration.

The minimum short crack lengths that were measured were typically in the range of 15 – 25 μm, these being evident after 10,000 - 25,000 cycles of a predicted lifespan of 10^5 cycles. On the assumption that the crack initiation regime consisted solely of SCG, rather than an actual initiation period that did not experience crack growth, the crack initiator (see 8.4 Crack Initiation) was assumed to be a short crack of identical length, this being present prior to fatigue loading, an approach also taken by Newman[1].

The SCG was modelled utilising an technique developed by Nisitani et al[2,3] and subsequently employed by Caton et al[4,5] in cast AA 319, although the technique has not, to the author's knowledge, been employed for defining SCG in welded joints. The approach considered the short crack growth rate to be a function of the stress amplitude, crack length, and yield or tensile stress and maximum strain, equations (8.1) and (8.3), as shown in Figure 8.7 for the stress amplitude and tensile strength. A limitation of the approach is that integration of equations results in a two parameter power law type equation, equations (8.2) and (8.4), which when displayed on a log-log S-N plot results in a straight line, this tends to limit the approach to either the initial or final near linear sections of the S-N curve.

$$\frac{dc}{dN} = B\left(\frac{\sigma_a}{\sigma_{y\ or\ TS}}\right)^n .c \tag{8.1}$$

$$N_{c_i \to c_t} = \frac{1}{B}\left(\frac{\sigma_{y\ or\ TS}}{\sigma_a}\right)^n \ln\frac{c_t}{c_i} \tag{8.2}$$

$$\frac{dc}{dN} = B.\left(\frac{\sigma_a}{\sigma_{y\ or\ TS}}.\varepsilon_{max}\right)^n .c \tag{8.3}$$

$$N_{c_i \to c_t} = \frac{1}{B}\left(\left(\frac{\sigma_{y\ or\ TS}}{\sigma_a}\right).\frac{1}{\varepsilon_{max}}\right)^n \ln\frac{c_t}{c_i} \tag{8.4}$$

---

[1] Newman Jr, JC (1999)
[2] Nisitani, H; Goto, M (1986)
[3] Nisitani, H et al (1992)
[4] Caton, MJ et al (1999a)
[5] Caton, MJ et al (1999b)

It was initially intended that a series of SCG rate measurements would be made at a minimum of two stress ranges, the aim being to observe the effects of varying the stress amplitude on the SCG rate, but difficulties in obtaining results for a life in the region of 10^6 cycles meant that only one series of SCG data was obtained, for a life in the region of 10^5 cycles. The failure to obtain a second set of measurements meant that the SCG equation constants B and n were determined by mapping the resulting curve onto a SCG S-N curve that was determined through subtraction of a LCG S-N curve from the 40 mm wide specimens S-N curve. The accuracy of this approach was then verified through comparing the theoretical SCG values that resulted from the constants B and n with the experimentally determined SCG regression curves, a good correlation being observed for the parent plate and FS welds, but not the MIG welds. The main shortcoming of the technique was that it relied on the LCG rates returned by the CT specimens being identical to those observed in the 40 mm wide S-N specimens. Had a second series of SCG measurements been obtained for another stress amplitude it would have been possible to determine the constants without the development of the SCG S-N curve, the constants B and n being determined through fitting the SCG curve through the two points returned by the stress amplitudes for 10^5 and 10^6 cycles. This would also have had the advantage of verifying the approach of considering the crack growth to be a function of the stress amplitude, crack length, and yield or tensile stress.

Theoretically an enhanced SCG model could be developed that would accurately determine the SCG regime over the full range of stress amplitudes. This could be achieved through a second SCG equation, with a second series of scaling constants, B and n, that represented the low stress amplitude - high life region. Addition of the two SCG equations resulting in an accurate assessment of the fatigue life for the stress ranges under consideration. A more eloquent approach would be to make the scaling constant n, which controls the slope of the curve, a function of the stress amplitude, the resulting curve detailing the SCG regime over the range of stress amplitudes desired, although it is probable that the scaling constant B would also be a function of the stress amplitude or crack length. Although both types of approach are theoretically feasible, an accurate assessment of the residual stress field and its subsequent redistribution under loading would be required for the low stress amplitude – high life region, this then being incorporated into the model as an augmentation to the mean stress.

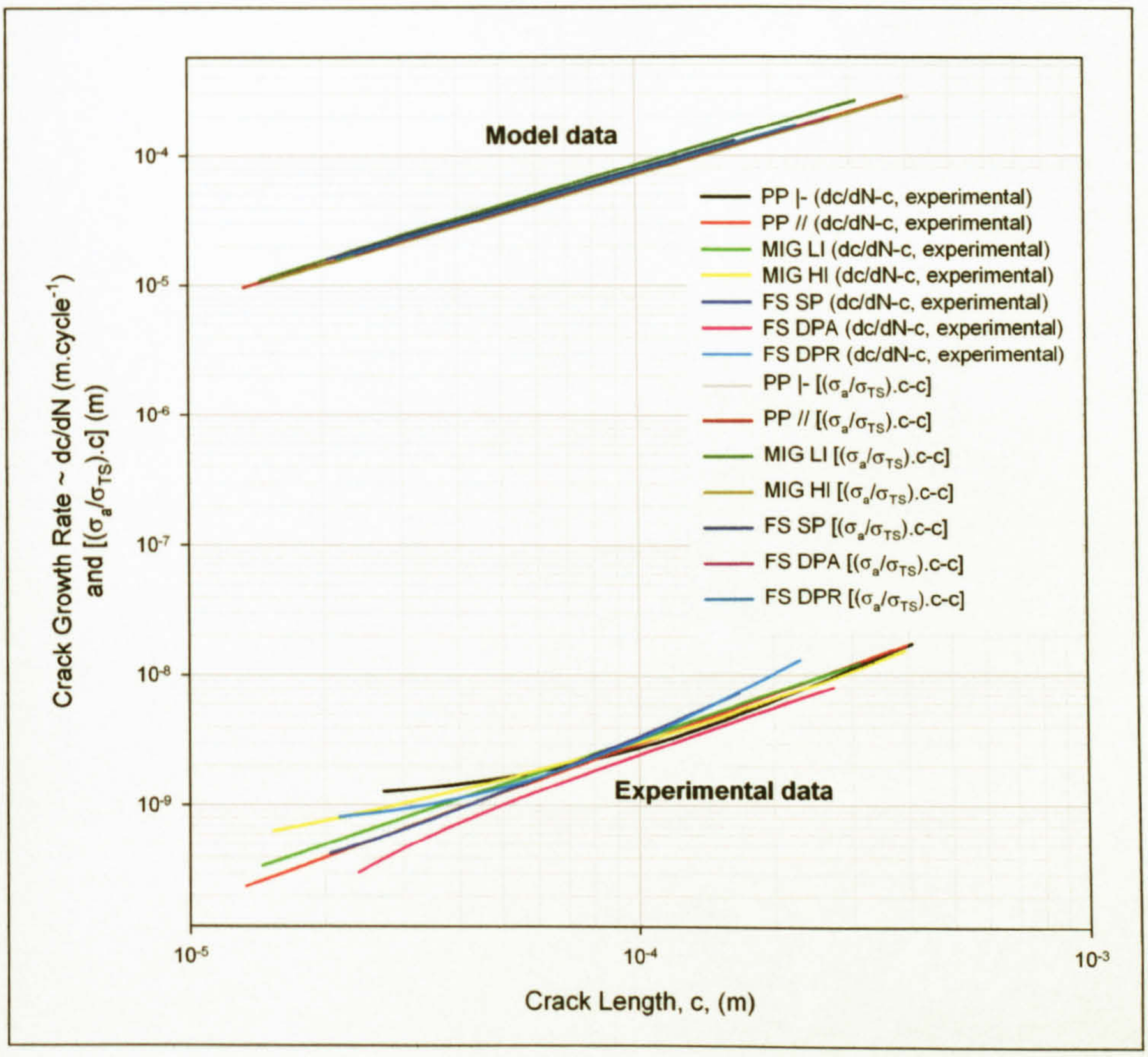

Figure 8.7: Experimentally determined crack growth rate, (dc/dN)/c, regression curves, compared with the growth rate model curves, predicted by $[(\sigma_a/\sigma_{TS}).c]/c$.

The long crack growth was modelled through integrating the equations that described the Paris regime of crack growth, taking into consideration growth under predominantly plain strain and plane stress, the approach typically utilised to predict the fatigue life from crack growth data. Theoretically, the addition of the number of cycles for the crack to grow from the initiation size to the transition from SCG to LCG and the number of cycles from the transition size to a final size should predict the number of cycles to failure for a given stress range on an S-N curve, assuming all other variables, such as the residual stress, stress concentrating effects, etc. are equivalent.

Due to difficulties in accurately determining the residual stress distribution in the as-welded state, and their redistribution under loading, the assumption was made that in the high stress - low life region the influence of any residual stresses would be minimal due to their redistribution and the subsequent reduction in their influence.

The range of values for which the approach returned satisfactory results were as shown in Table 8.1, with the results for the parent plate and friction stir welds being shown in Figure 8.8 and Figure 8.9. The method returned an accurate assessment of the fatigue

lives for values ranging from $0.3 - 1 \times 10^6$ cycles, and maximum stresses ranging from 0.94 – 1.31 of the yield strength. The technique did not appear suitable for determining the fatigue lives of the MIG welds, integration of the LCG equations resulted in fatigue lives that were longer than those returned by the S-N specimens. It was thought that this may have been the result of a combination of the LCG results exhibiting increased crack closure due to the distribution of the residual stress field in the region of the crack tip in the CT specimens and the approach utilised in determining the stress concentrating effect of the weld toe, although verification of these requires further investigation.

Specimen	$\Delta\sigma \sim R = 0.1$ (MPa)		σ_{max} (MPa)	σ_a (MPa)	σ_y (MPa)	σ_{max}/σ_y (MPa)	Cycles to failure, max (N_T)
	max	min					
PP |-		230	256	115	254	1.00	5.0×10^5
PP //					272	0.94	3.1×10^5
FS SP		185	206	92.5	157	1.31	6.5×10^5
FS DPA		170	189	85	163	1.16	10^6
FS DPR							

Table 8.1: Range of values for model suitability.

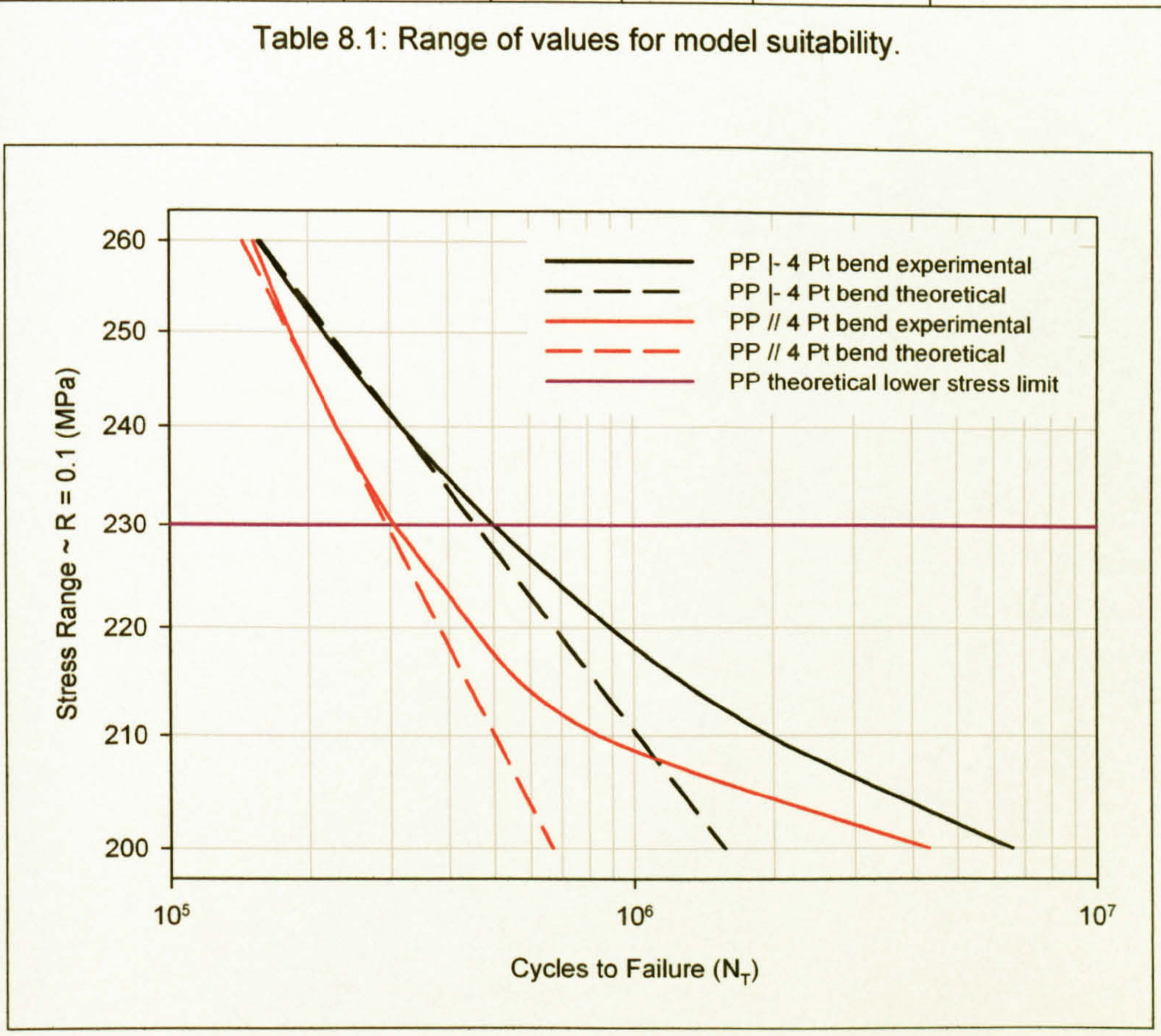

Figure 8.8: AA 5383-H321 parent plate experimental and theoretical S-N curves.

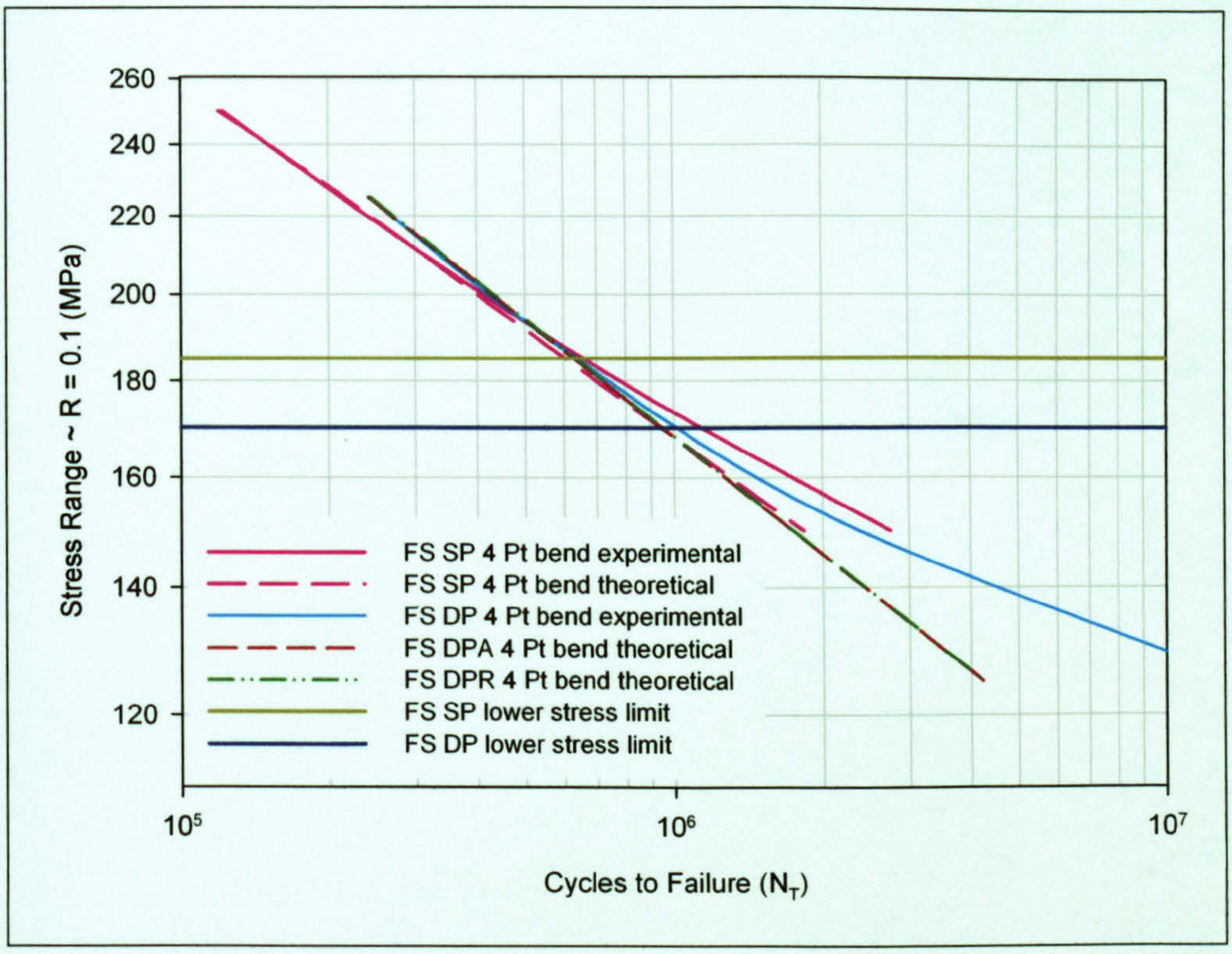

Figure 8.9: FS SP, DPA and DPR experimental and theoretical S-N curves.

9. Conclusion

A defect-tolerant based model for predicting the fatigue life of four-point loaded AA 5383-H321 and butt-welded joints in the same alloy has been developed. Defect-tolerant models are typically based on LEFM, the result of this being that they are restricted to the LCG regime described by the Paris equation, whereas the model developed for the welded butt joints considered both the crack initiation regime, consisting of SCG, and the LCG regime, with both microstructural, macrostructural and residual stress effects being taken into consideration. Accurate predictions of the fatigue life were observed for lives in the region of $10^5 - 10^6$ cycles for both the parent plate and both the FS SP and DP welds, although the approach was less successful at predicting the fatigue life of MIG LI and HI welds.

A detailed analysis of the microstructure and fractography of failed specimens indicated that the crack initiation was the result of secondary intermetallic phases in the case of the parent plate, disturbances to the weld toe profile in the MIG welds and due to weld related surface marks in the FS welds. Comparison of the size of the crack initiators and the minimum short crack lengths measured suggested that any crack initiation period was negligible and that this could be considered to consist of short crack growth. Therefore, with respect to the modelling of the fatigue properties, the crack initiating artefacts were considered to be short cracks that were present prior to fatigue loading. Short crack growth was observed to occur from the crack initiation size, $13 - 22\,\mu m$, up to crack lengths in the region of $225 - 350\,\mu m$, with growth occurring below the long crack threshold and at accelerated rates when quantified through the stress intensity factor range. The microstructure is considered to be influential in SCG and to account for this the SCG rates were determined in a comparable microstructure to that in which they occurred in the as-welded structures, although regression analysis of the SCG returned rates that were comparable for both the parent plate and both weld types. With respect to the defect-tolerance model the SCG rate was considered to be a function of the stress amplitude and the crack length, with a good correlation being observed for both the parent plate and FS welds.

In contrast to the comparable growth rates returned by the short cracks the resistance to LCG was observed to be greatest in the MIG welds, with the FS SP weld returning the lowest resistance, this being below that of the parent material. As with the SCG, the LCG measurements were undertaken in the appropriate microstructure. It was thought that the LCG rates may have been influenced by the effect of weld induced residual stress in the CT specimens causing increased crack closure, although further investigation is required to confirm this. Modelling of the LCG was comparable to that currently employed in defect-tolerant approaches, with the Paris equations being considered representative of the growth rate.

The residual stresses/strains were difficult to quantify accurately, with both the hole drilling and synchrotron strain scanning approaches being employed. The general consensus was that they were in the region of yield magnitude in the longitudinal direction in the MIG welds and lower in the transverse direction, whilst the FS welds were considered to have lower magnitudes than those observed in the MIG welds. Attempts at quantifying the redistribution of the residual strains after fatigue loading suggested that although some diminishing of the peak strains occurred there was no evidence of the number of cycles or the magnitude of the cycle having any influence. Further research into the magnitude of weld induced residual stresses, their redistribution under loading and their influence on the fatigue properties is required.

10. Proposals for Further Research

The author considers the following areas as worthy of further research:

1. Further assessment of the residual stresses fields and their redistribution under loading for both weld types.
2. Determination of effective stress intensity factor ranges, ΔK_{eff}, to attain a more accurate assessment of the long crack growth in the MIG and FS welds.
3. Development of the model to encompass the fatigue properties in the low stress range - high cycle regime.
4. Further assessment of the stress concentrating effect of the MIG weld toe and the FS surface finish.
5. Short crack growth measurements for a series of stress amplitudes.

11. Appendix A ~ Determination of Residual Strains and Stresses by the Hole Drilling Technique ~ Individual Rosette Results

11.1 Parent Plate

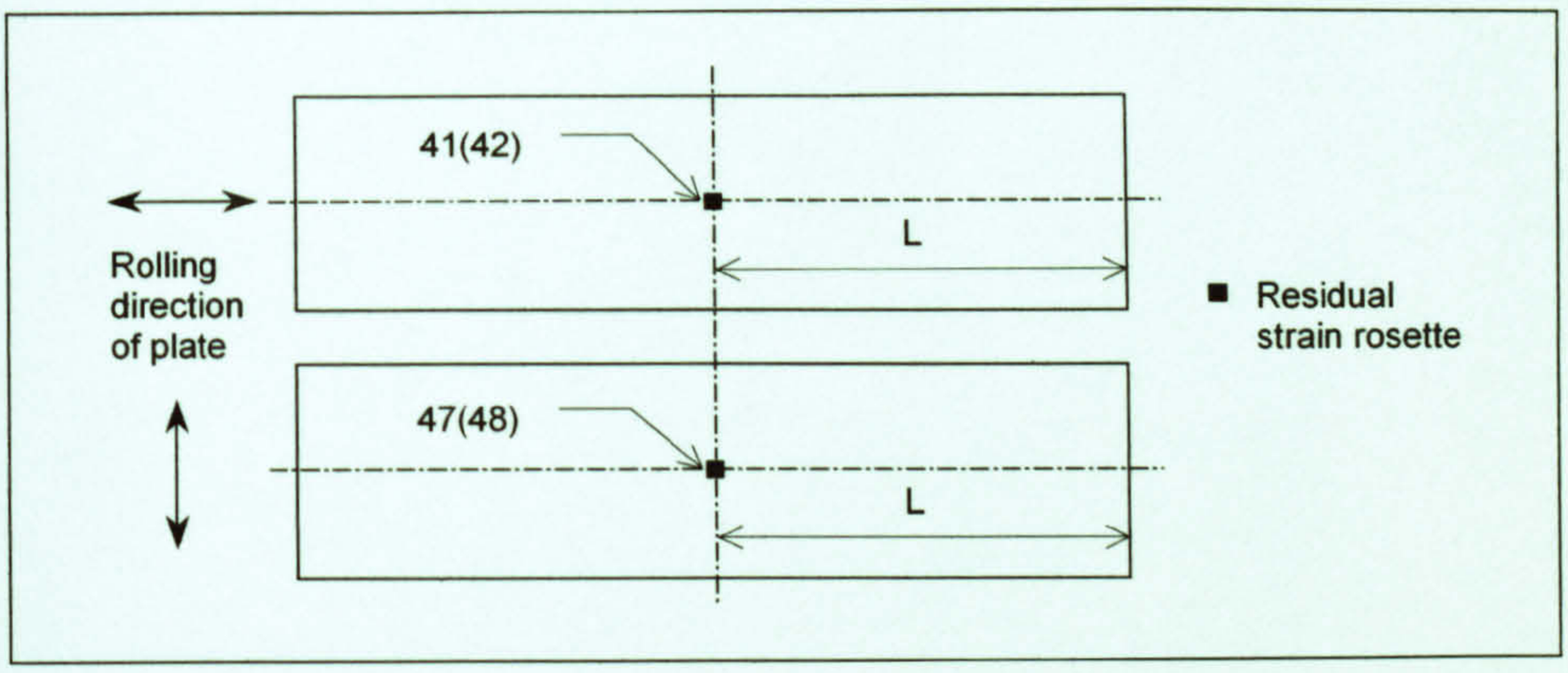

Figure 11.1: Position of residual strain gauge rosettes with respect to the rolling direction of the plate.

11.1.1 Rolling Direction Parallel to Plate Length

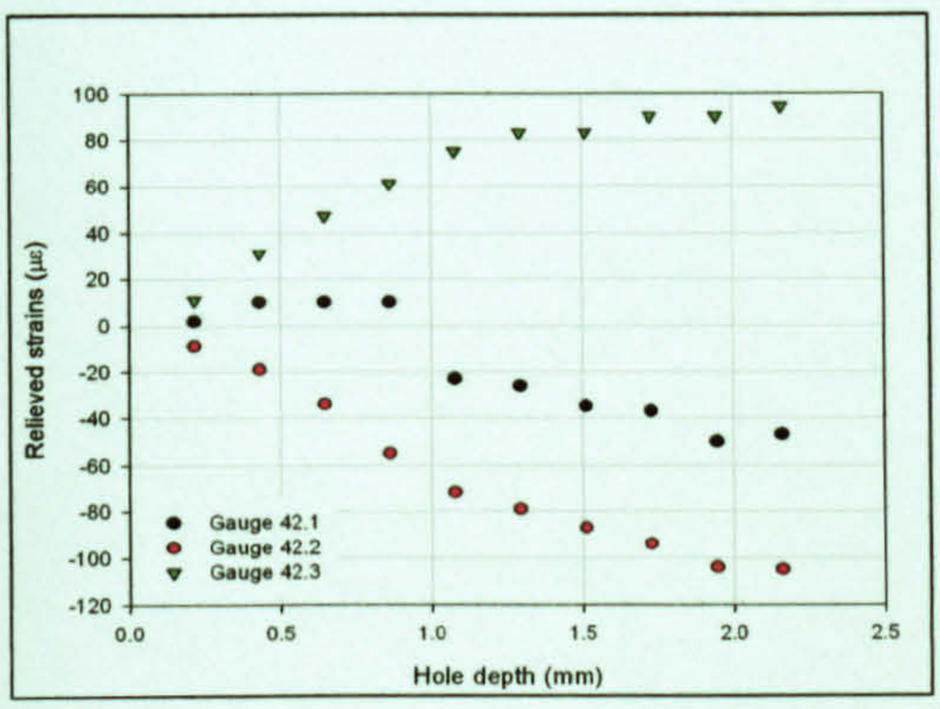

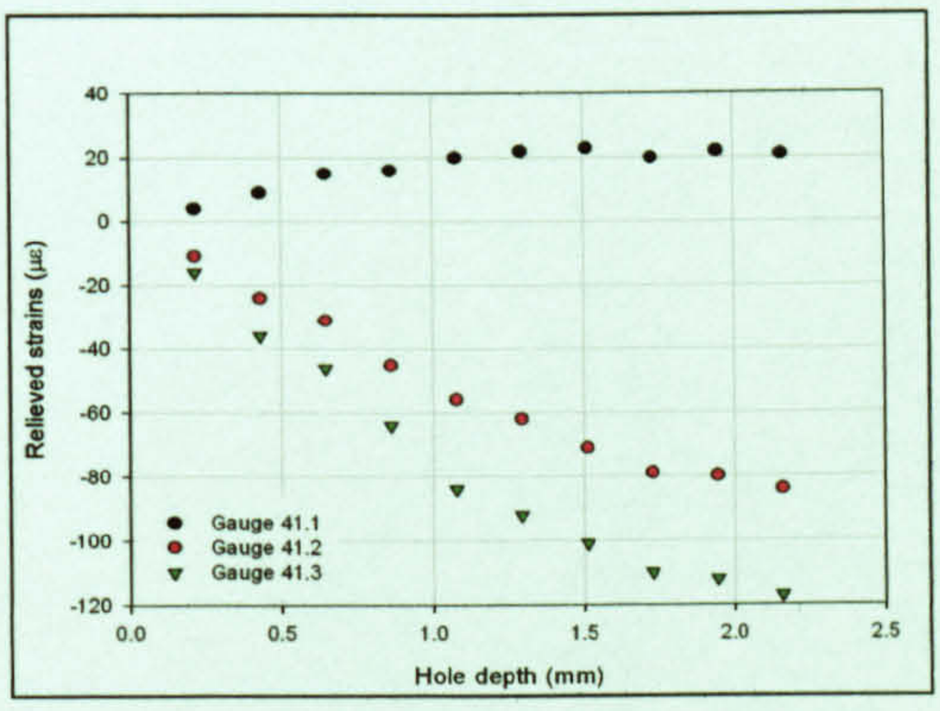

11.1.2 Rolling Direction Transverse to Plate Length

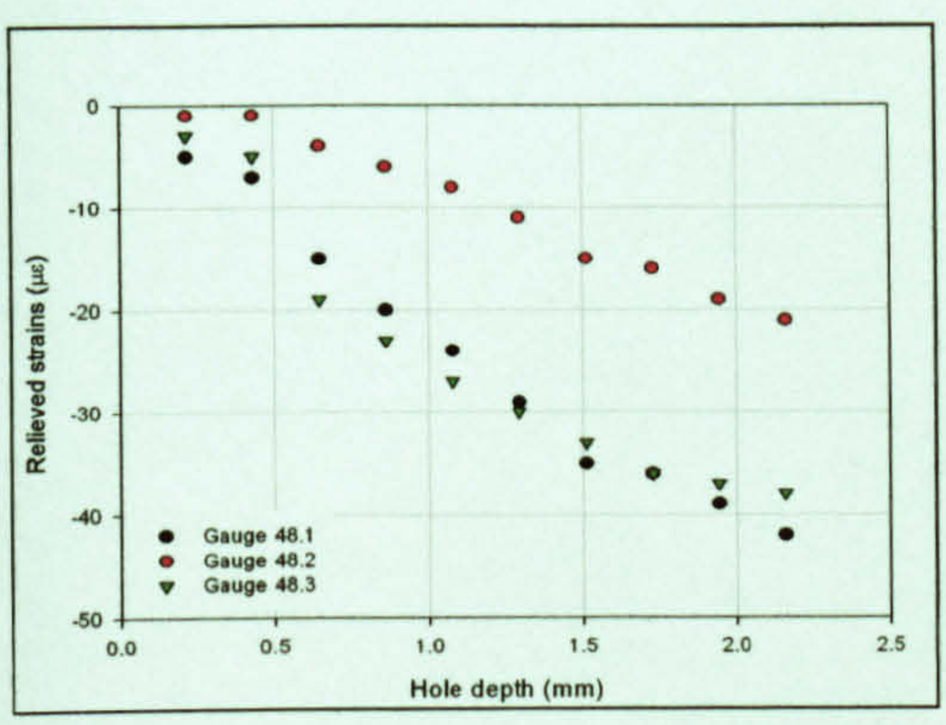

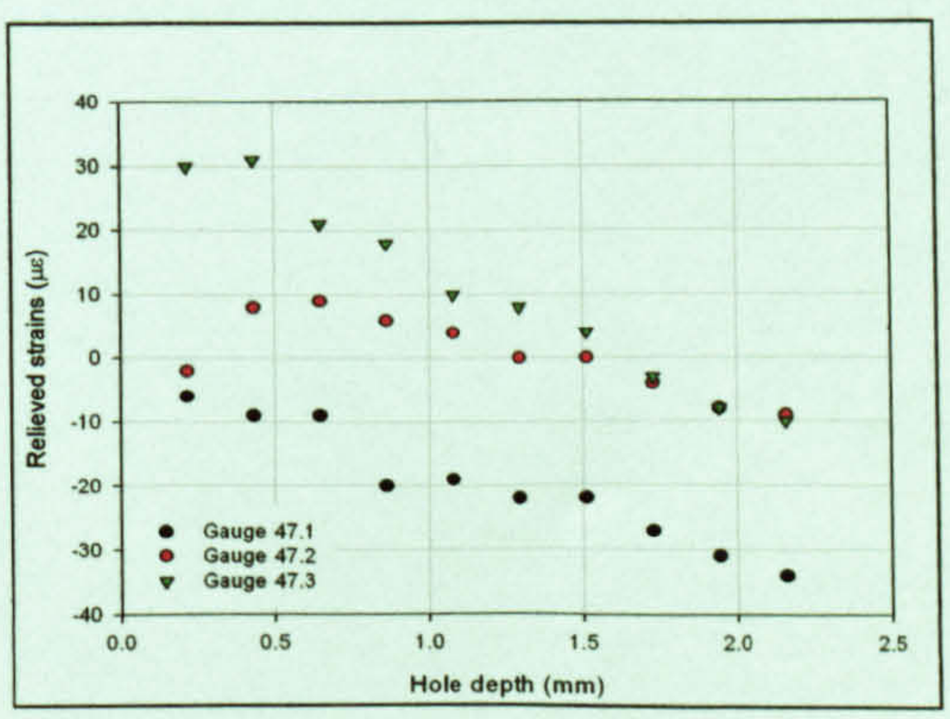

11.2 Metal Inert Gas – Low Input

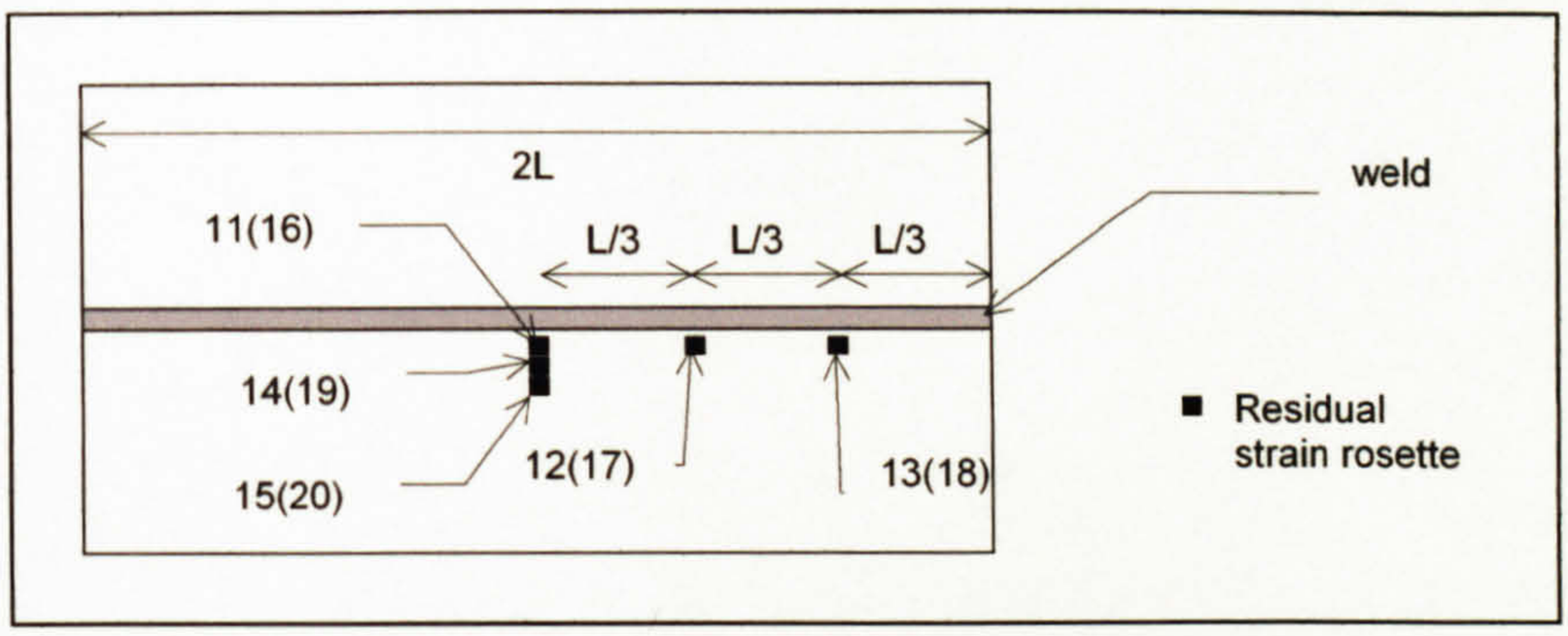

Figure 11.2: Position of residual strain gauge rosettes in relation to the MIG LI weld.

11.2.1 Convex Side

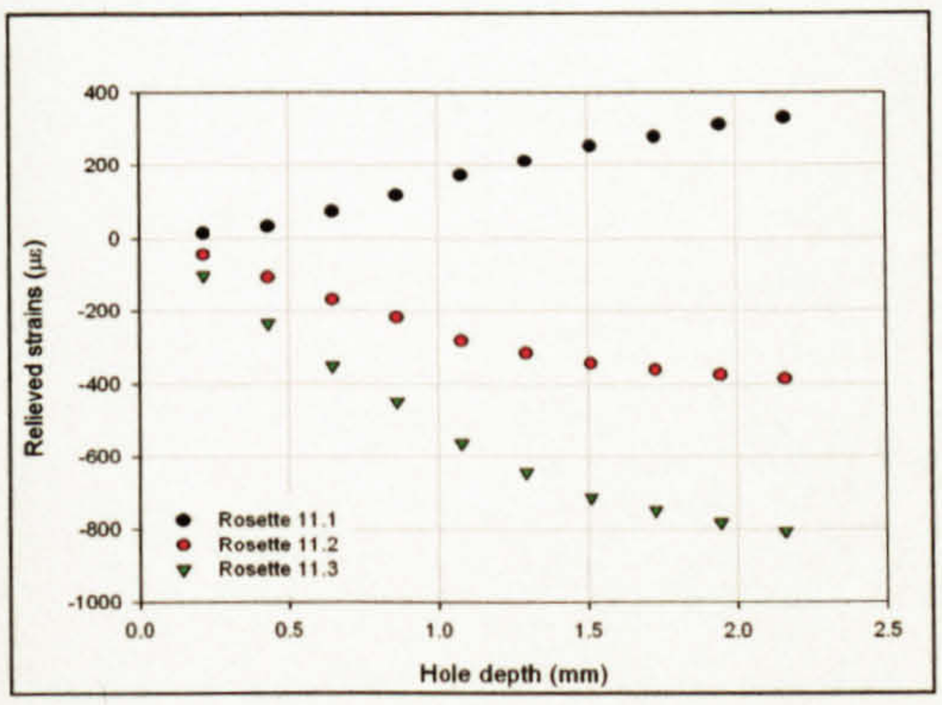

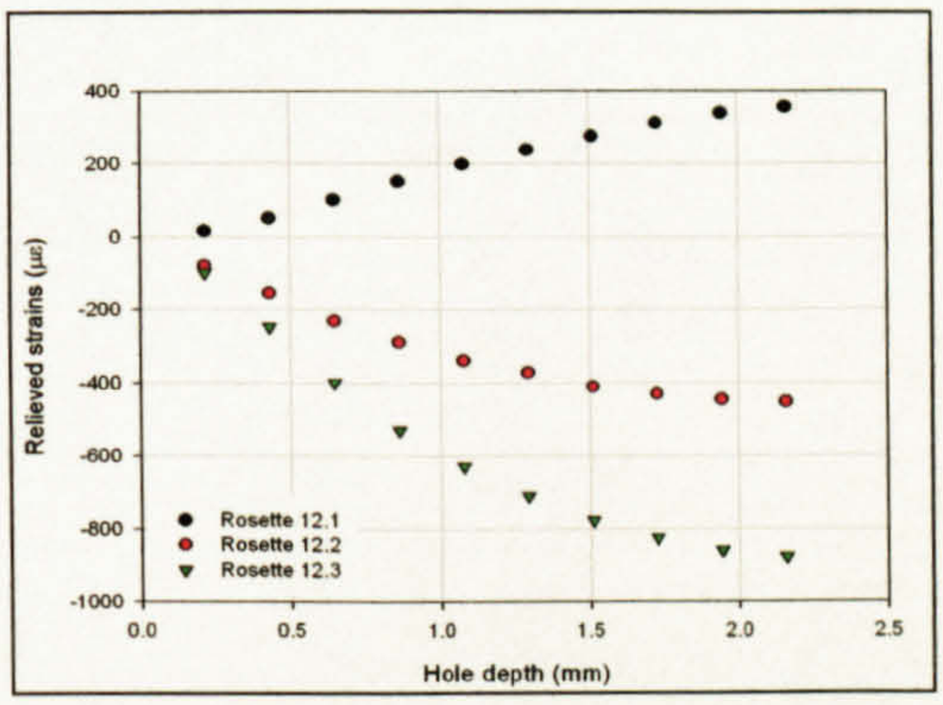

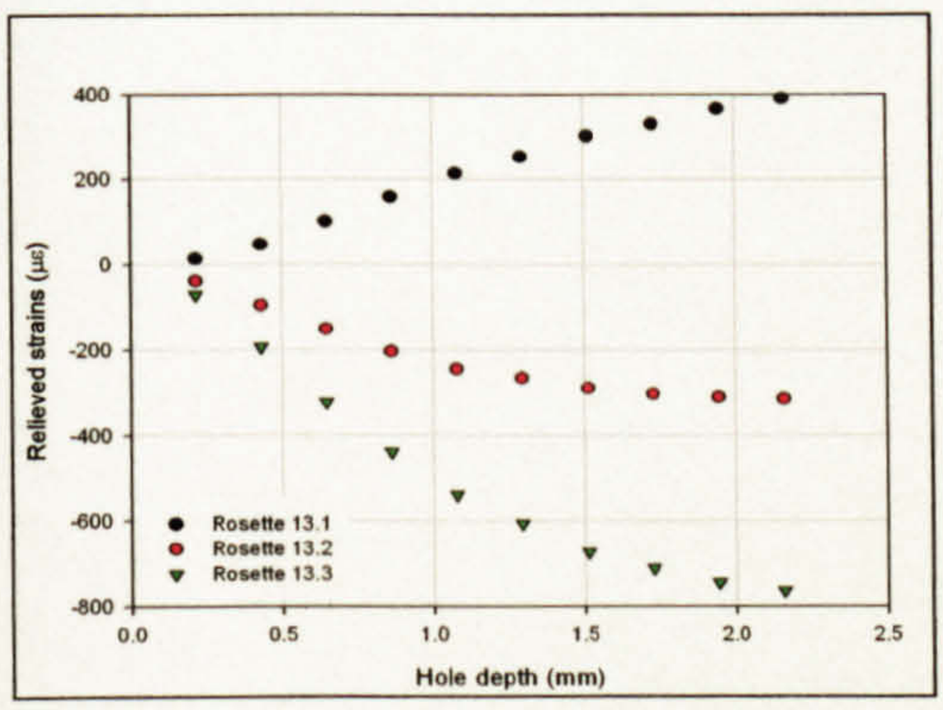

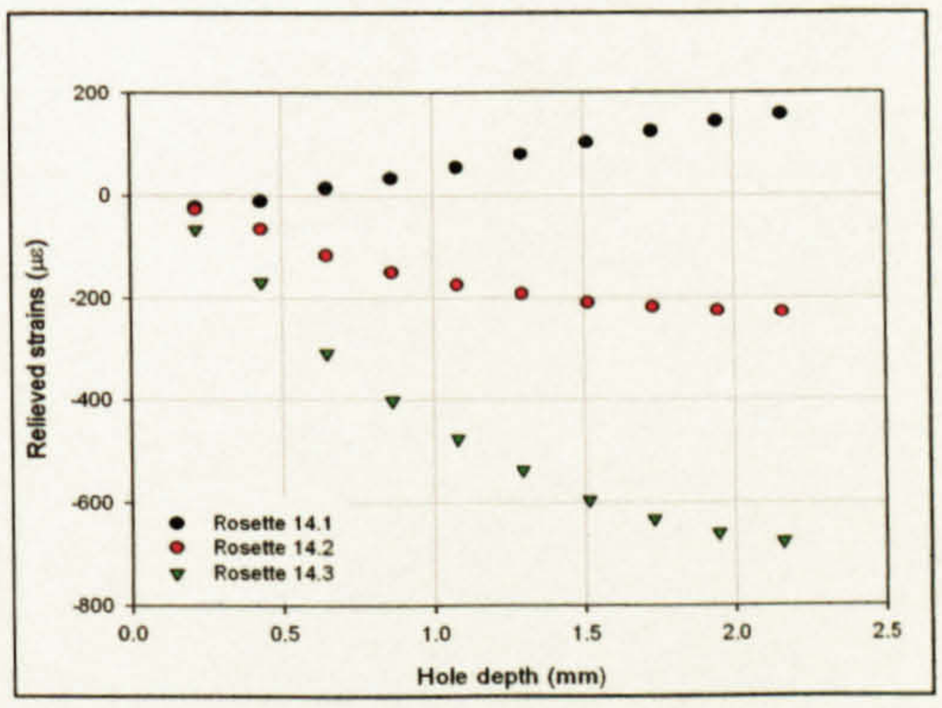

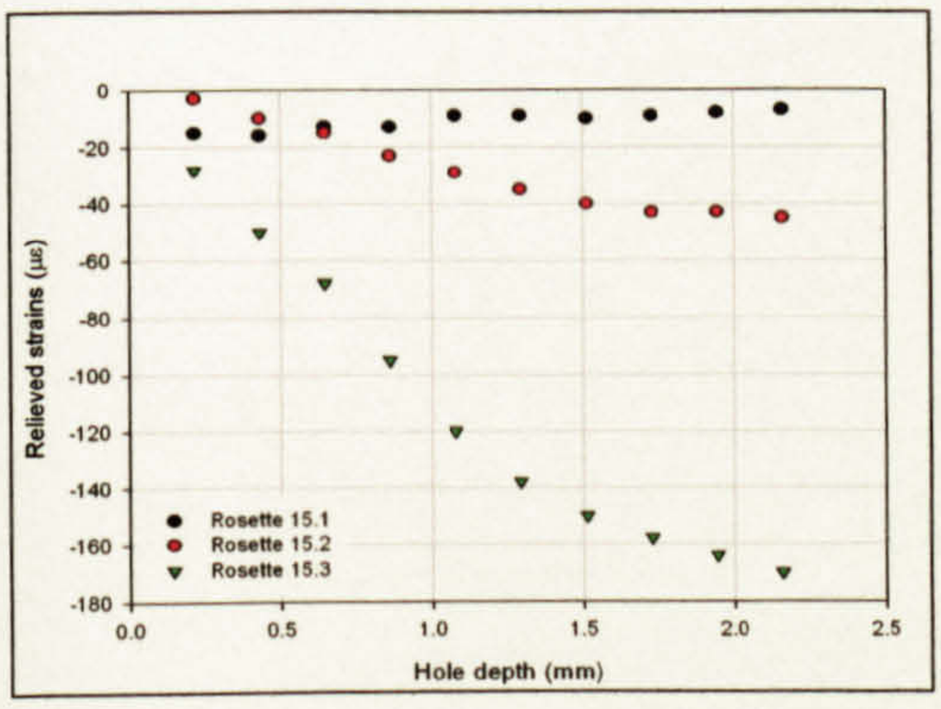

11.2.2 Concave Side

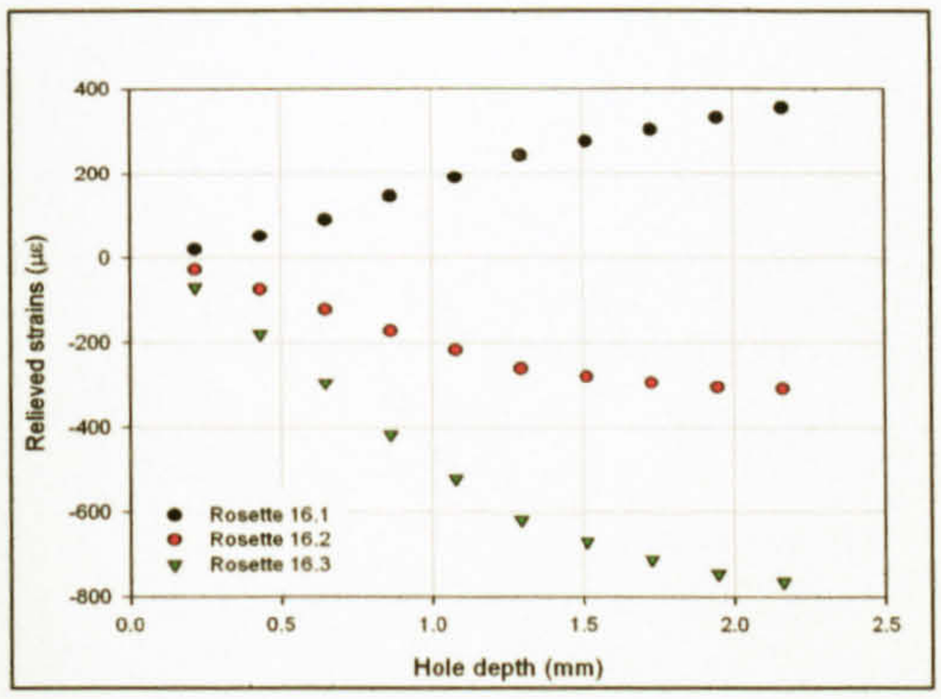

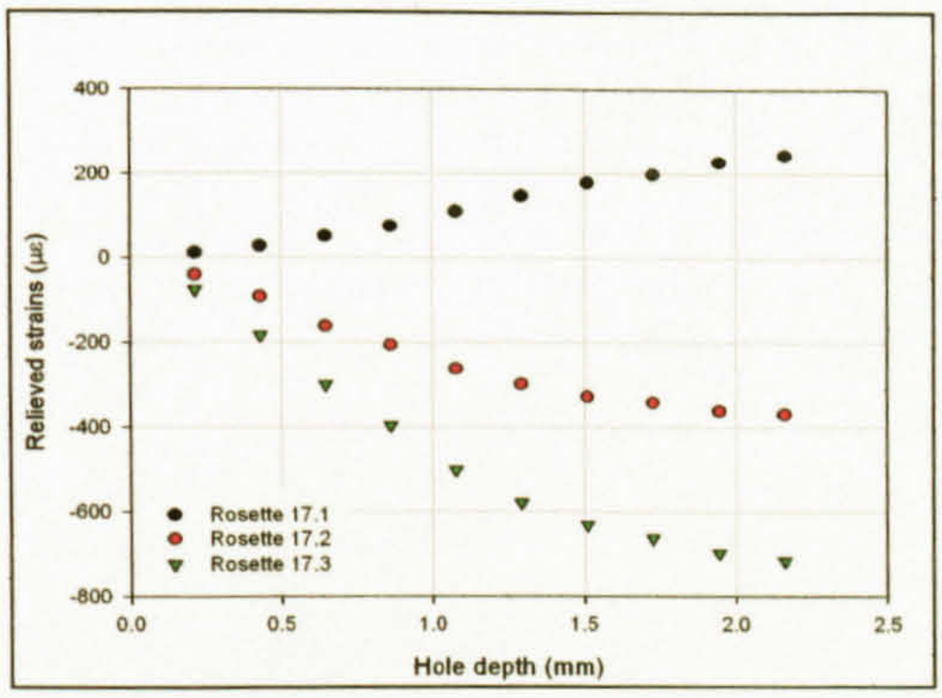

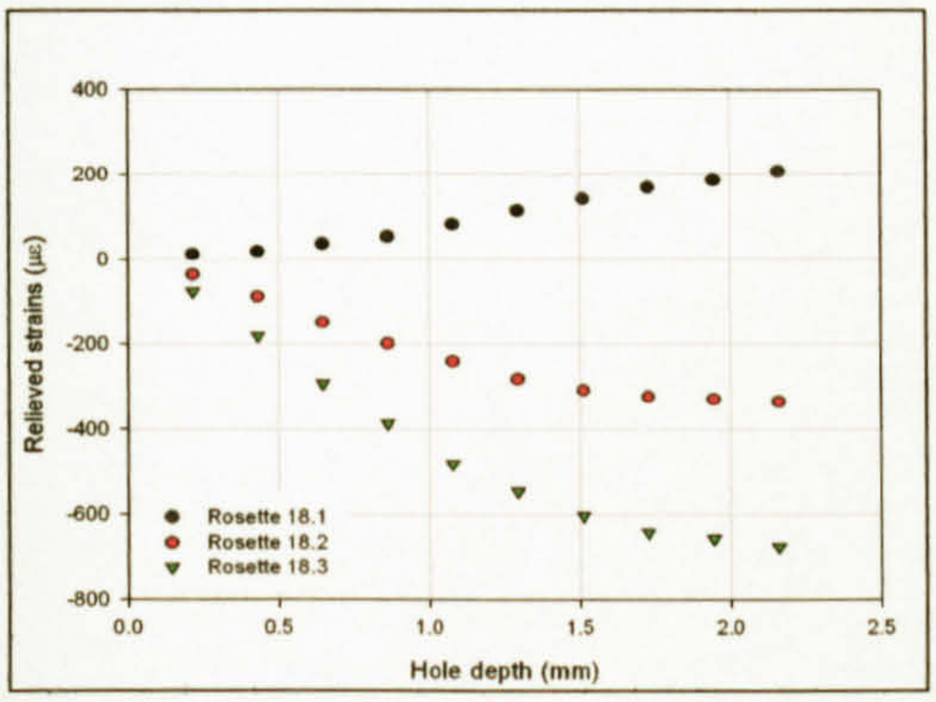

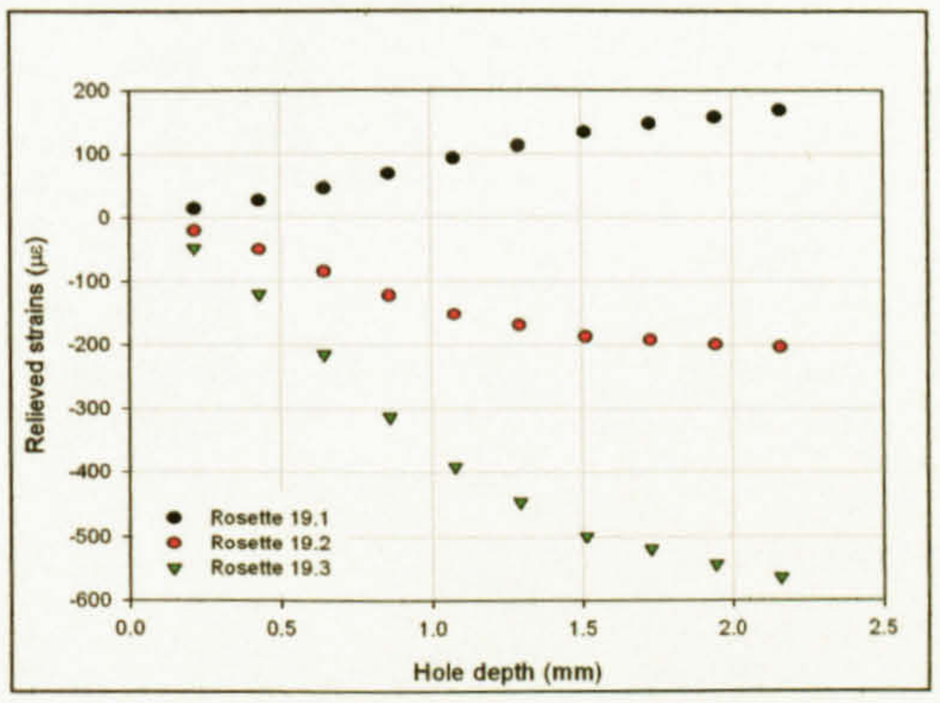

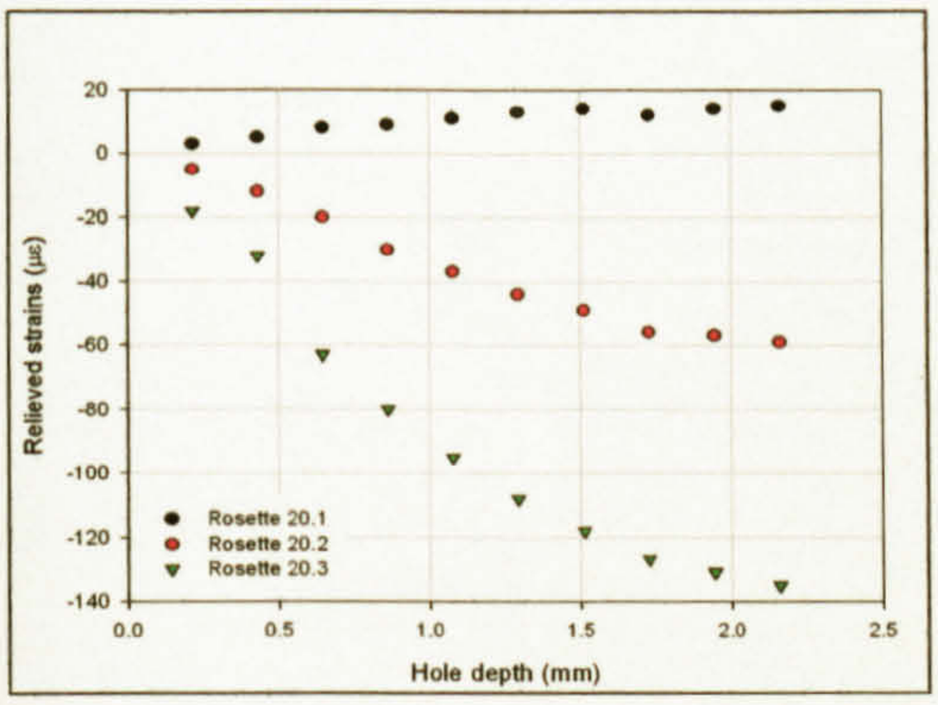

11.2.3 S-N Specimen

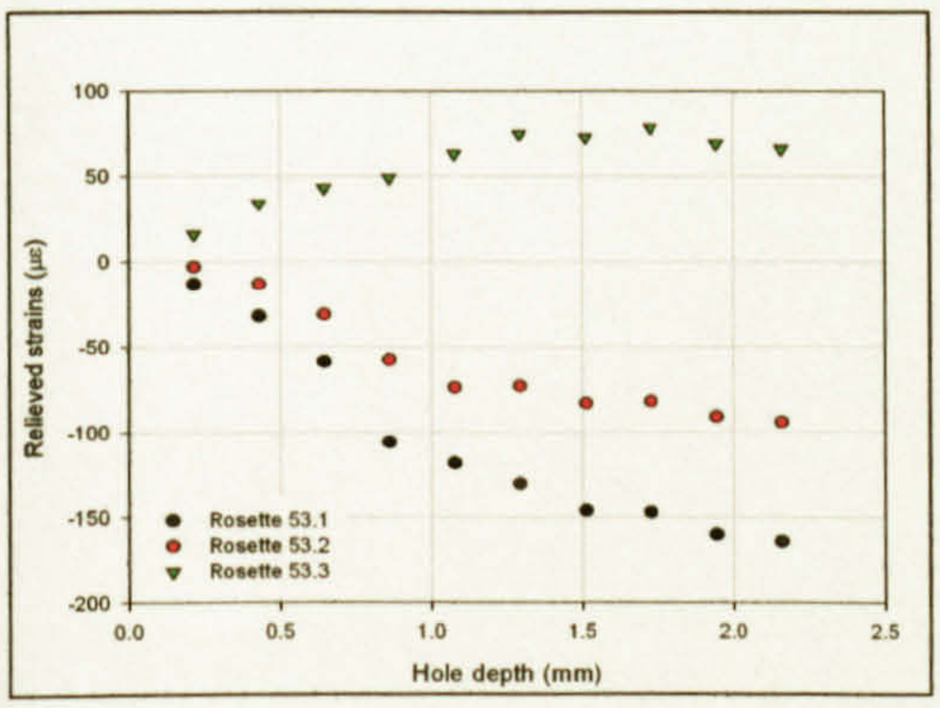

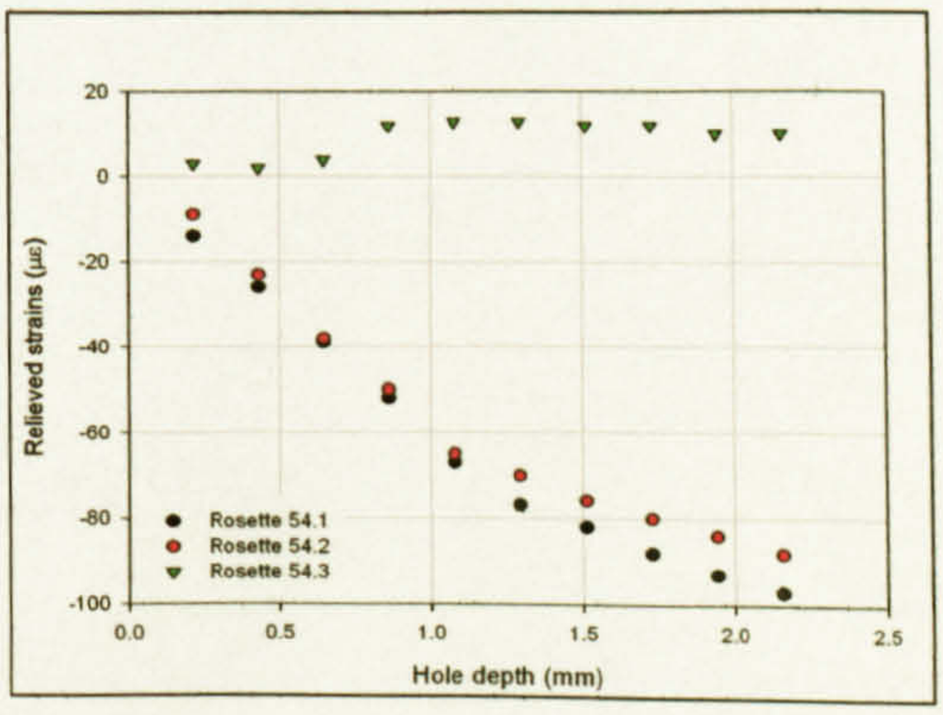

11.3 Metal Inert Gas – High Input

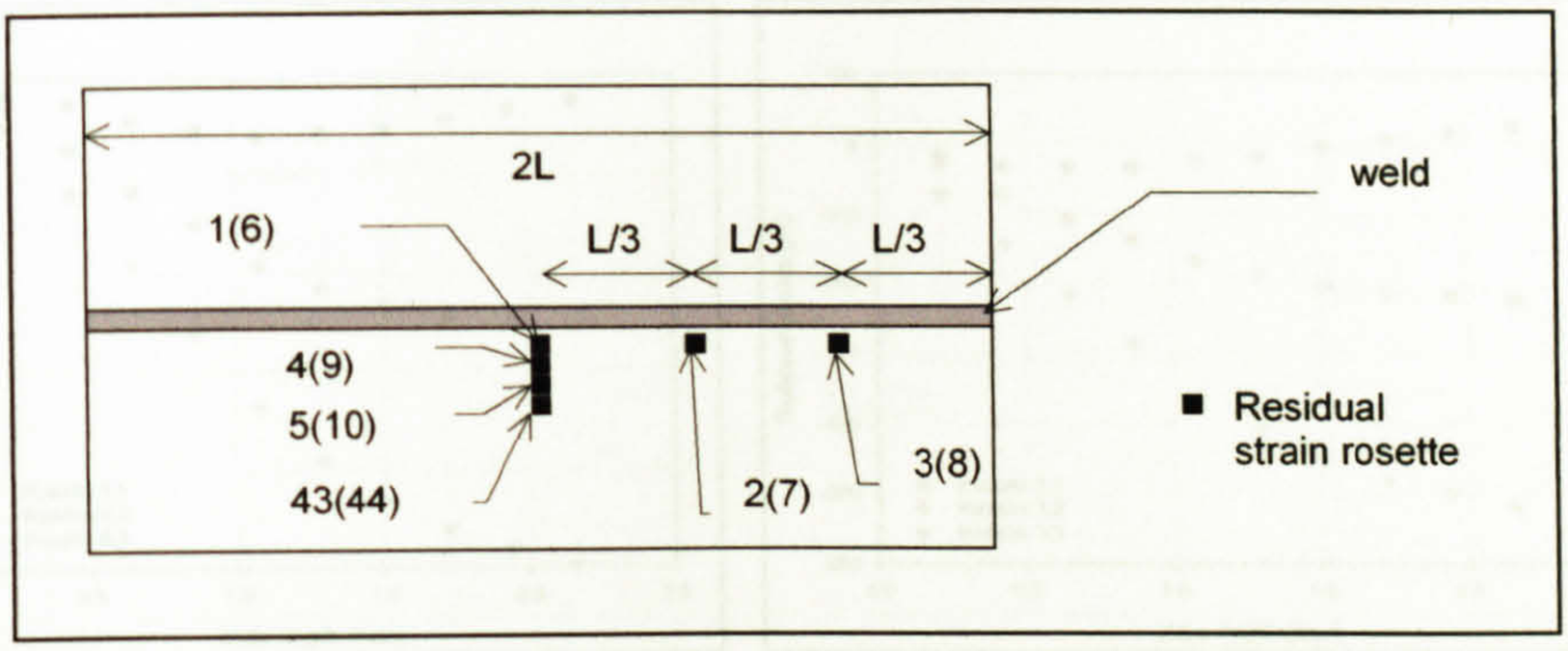

Figure 11.3: Position of residual strain gauge rosettes in relation to the MIG HI weld.

11.3.1 Convex Side

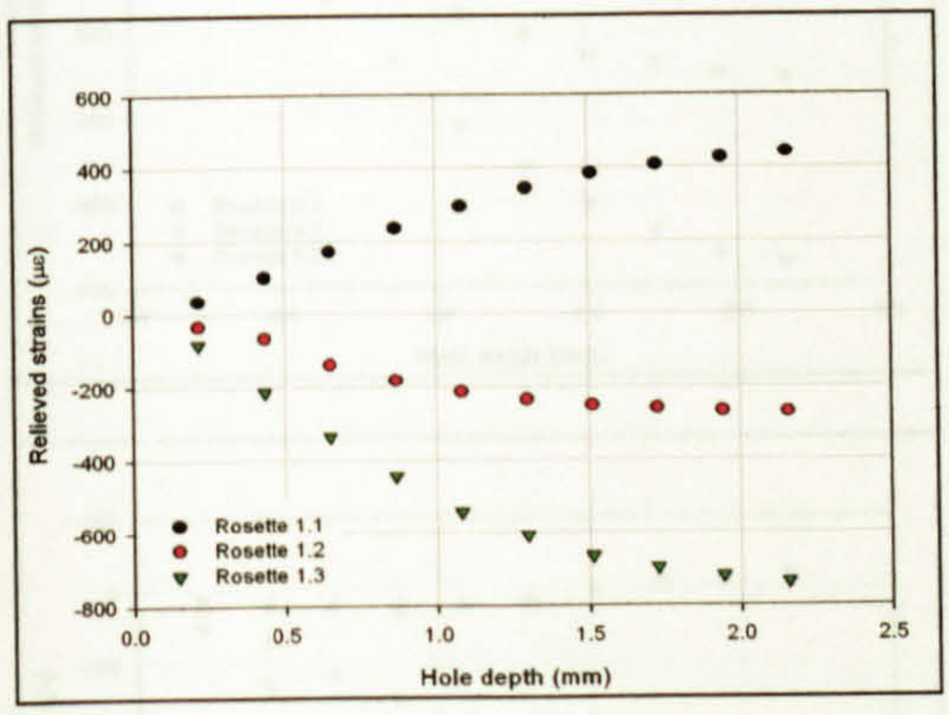

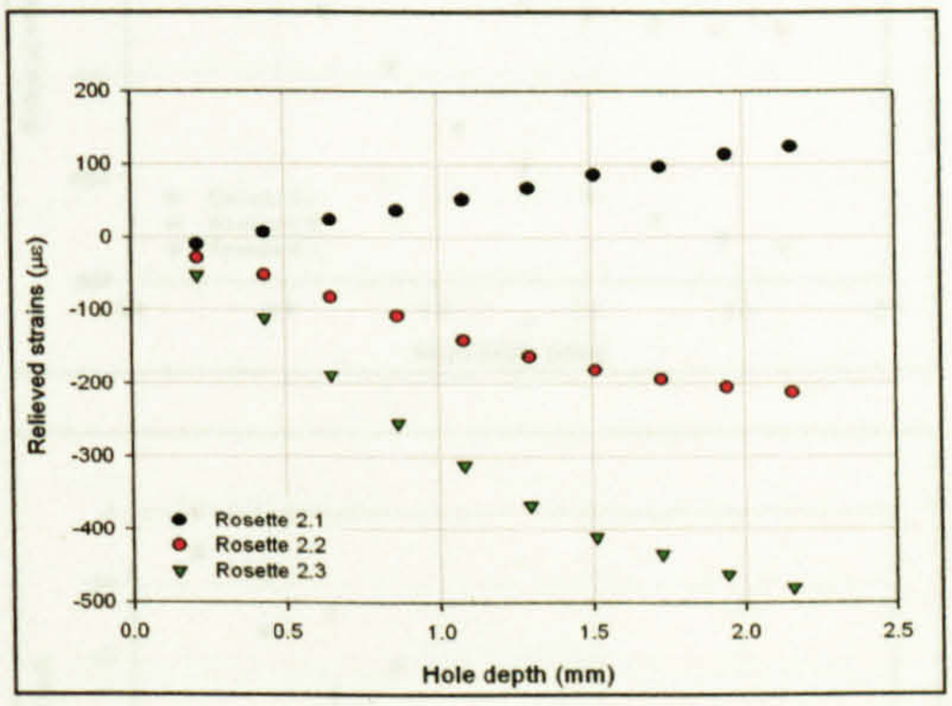

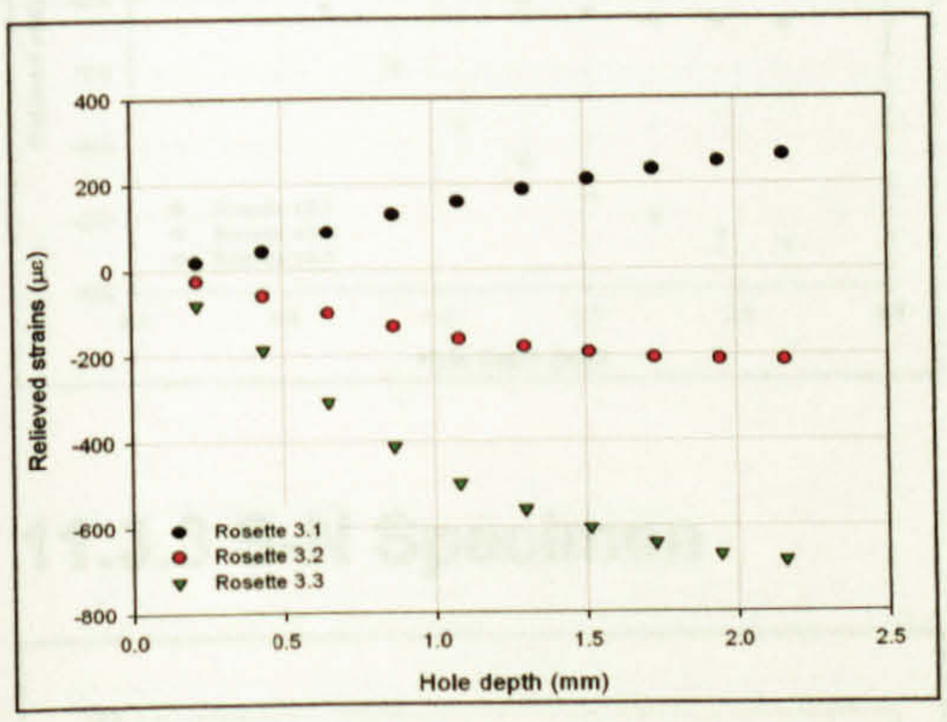

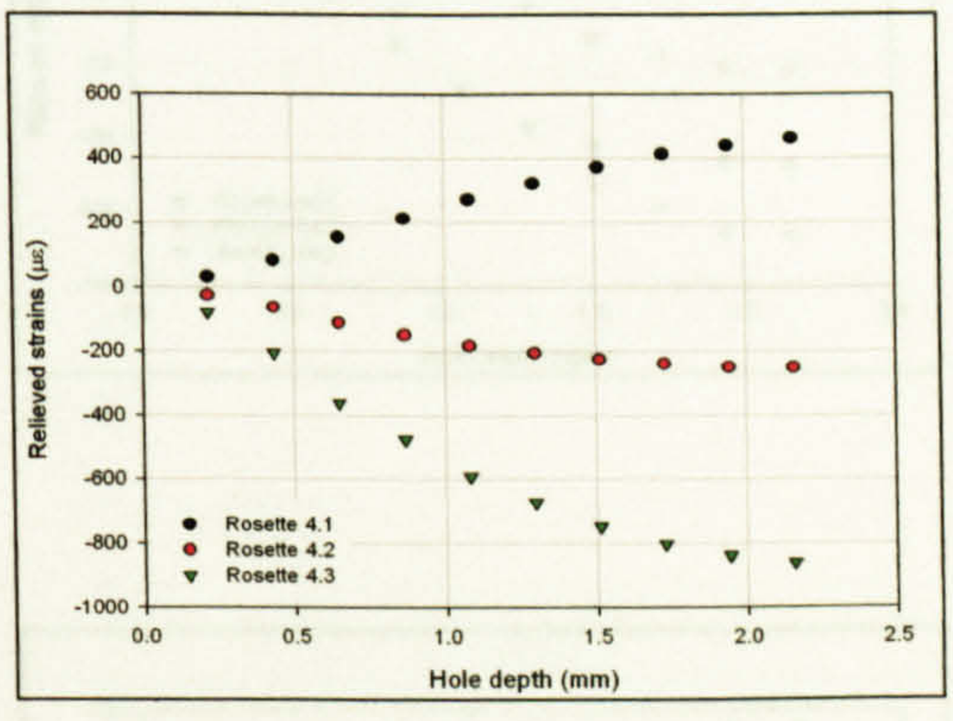

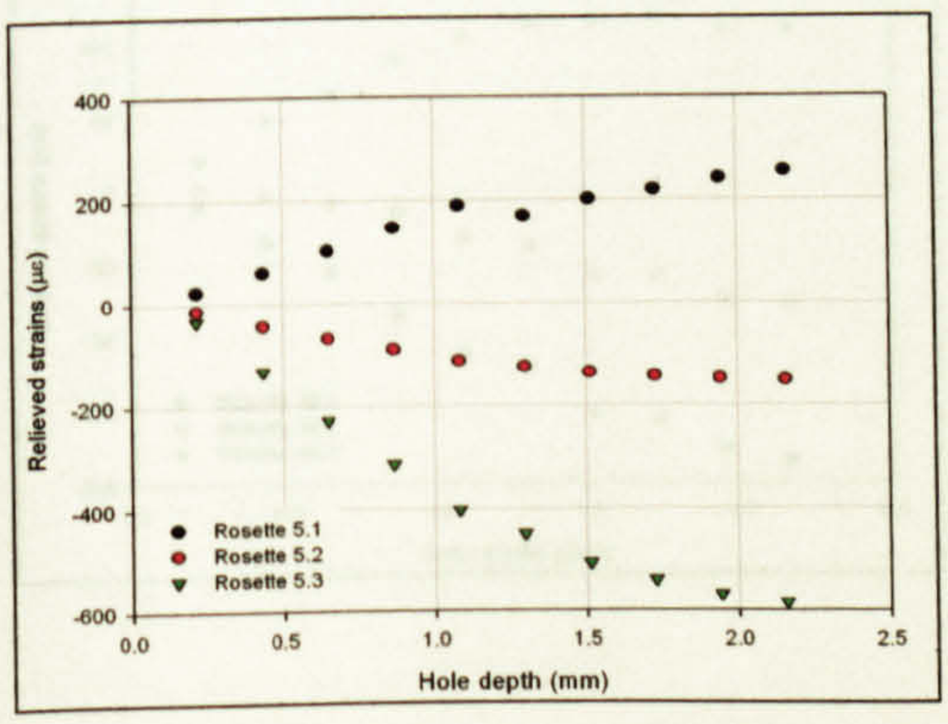

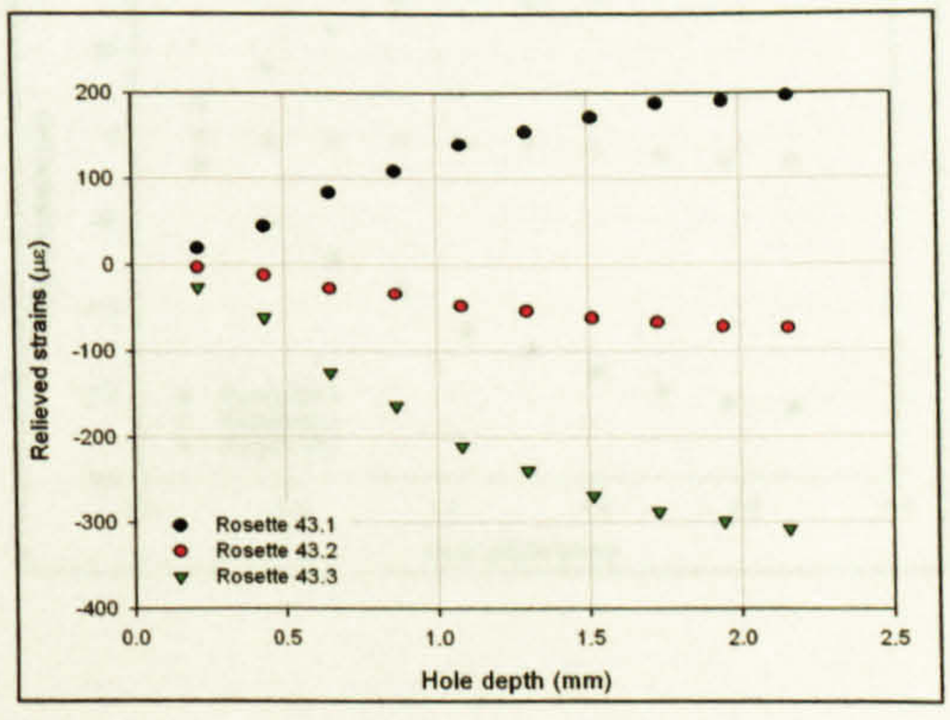

11.3.2 Concave Side

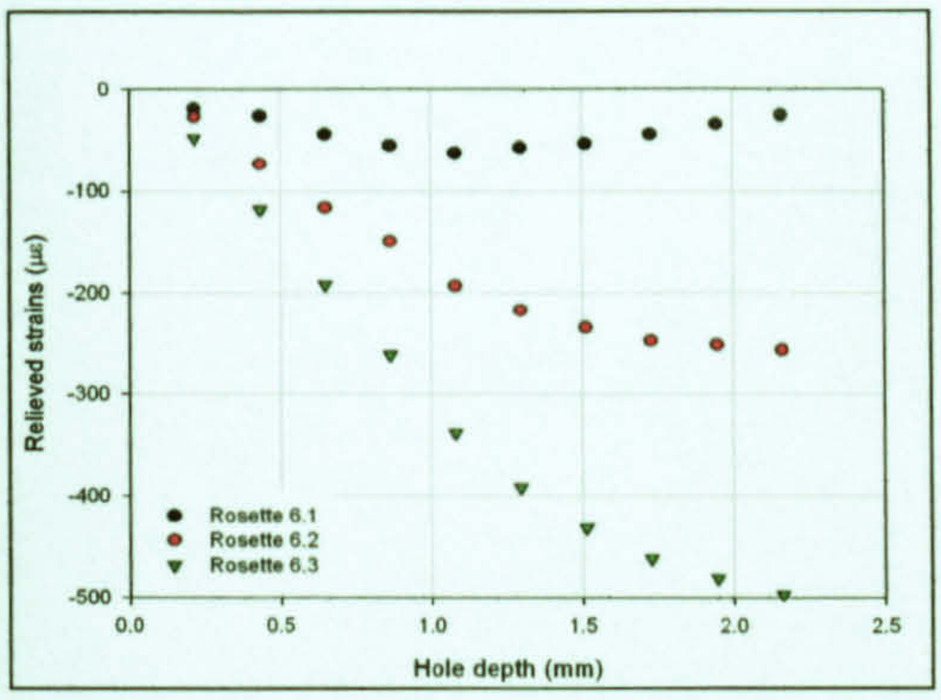

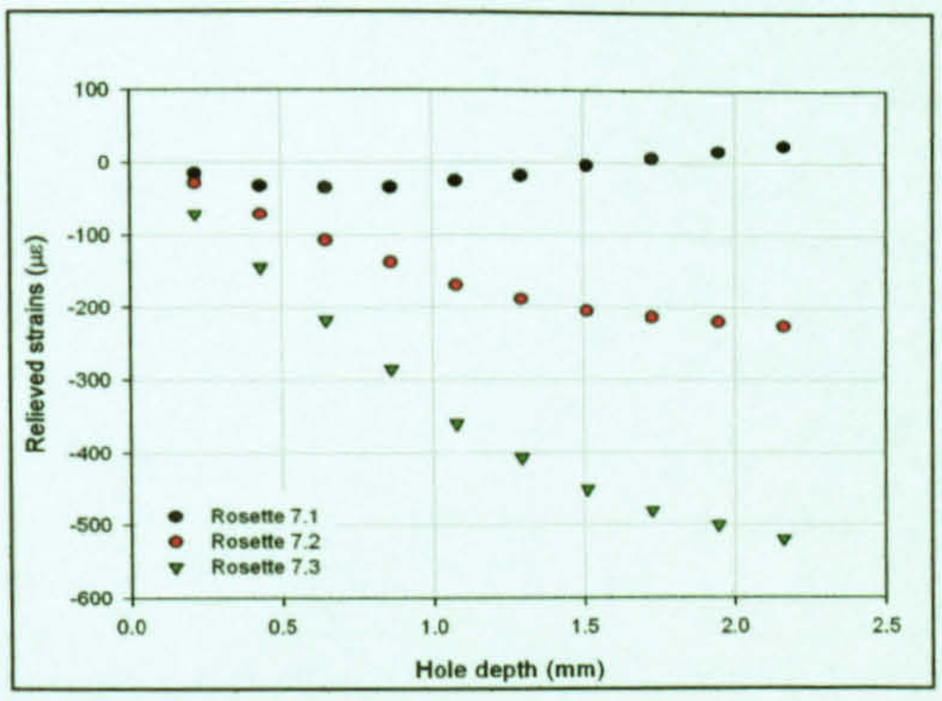

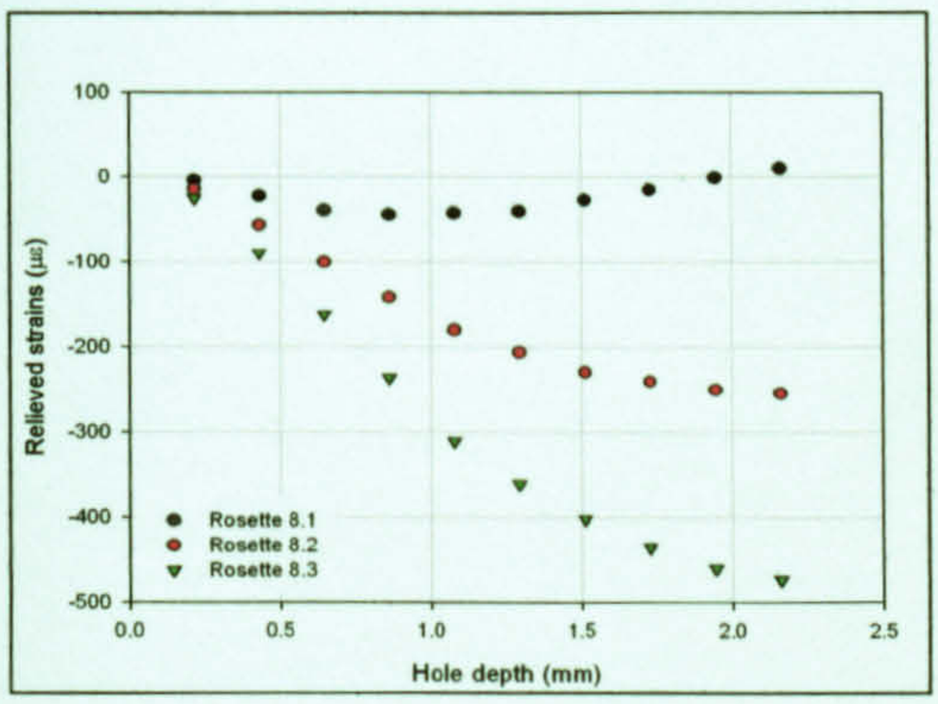

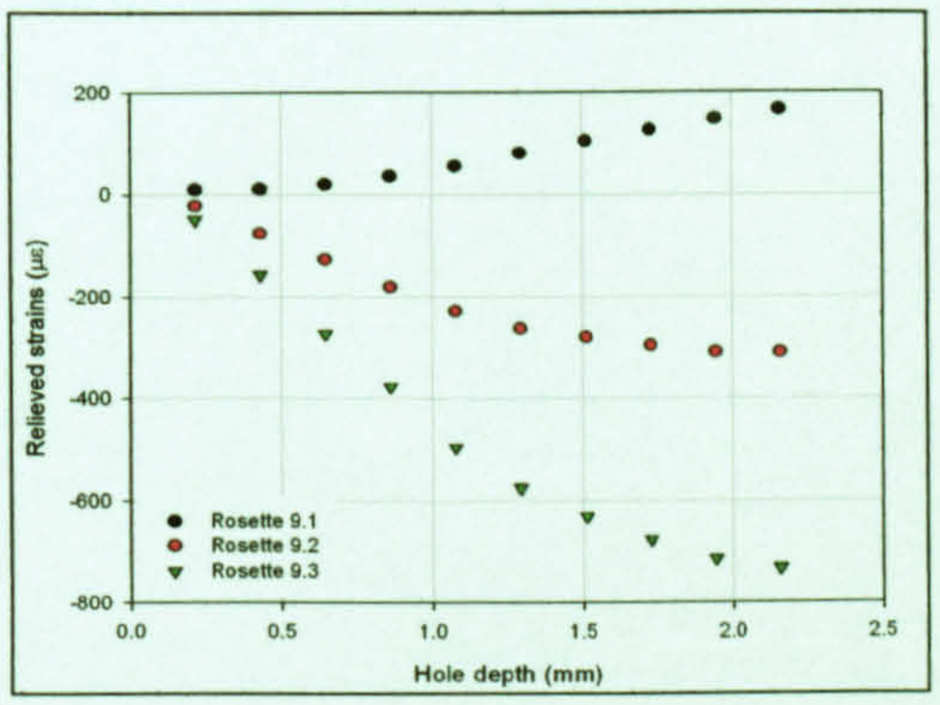

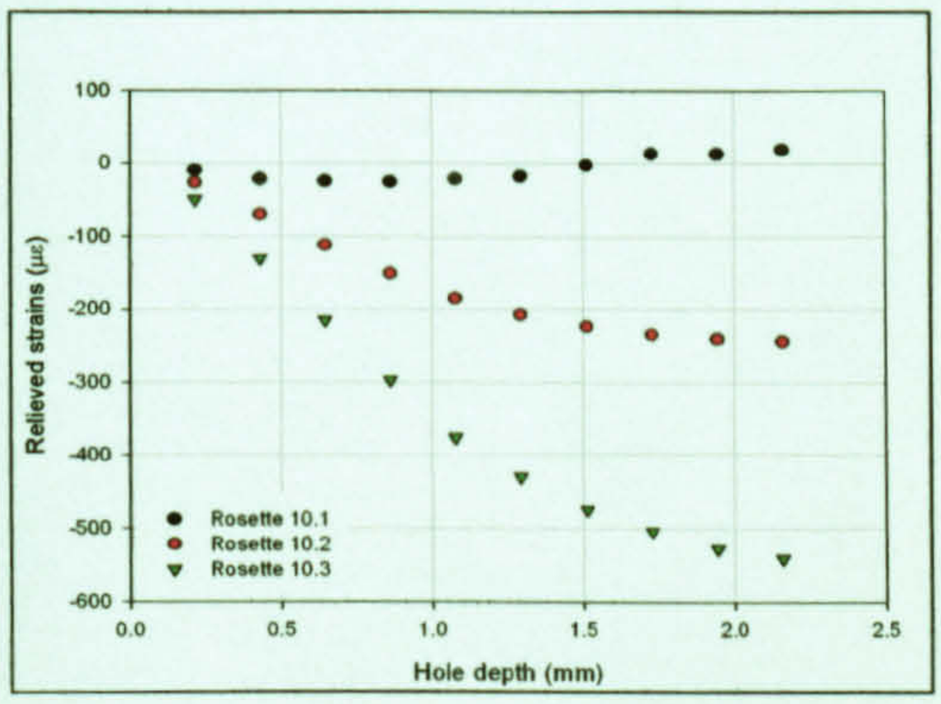

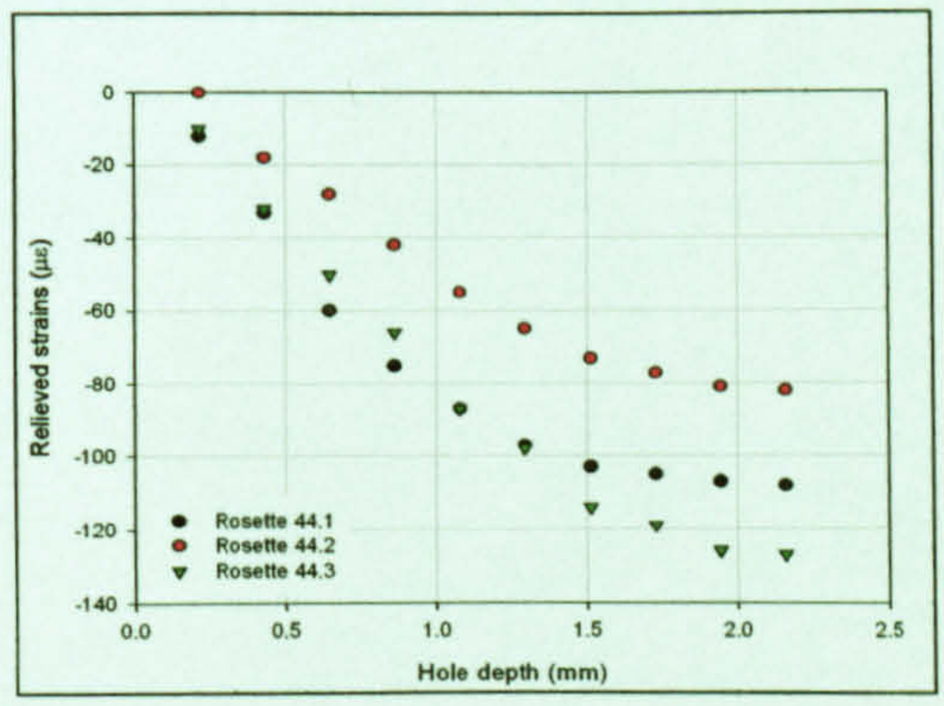

11.3.3 S-N Specimen

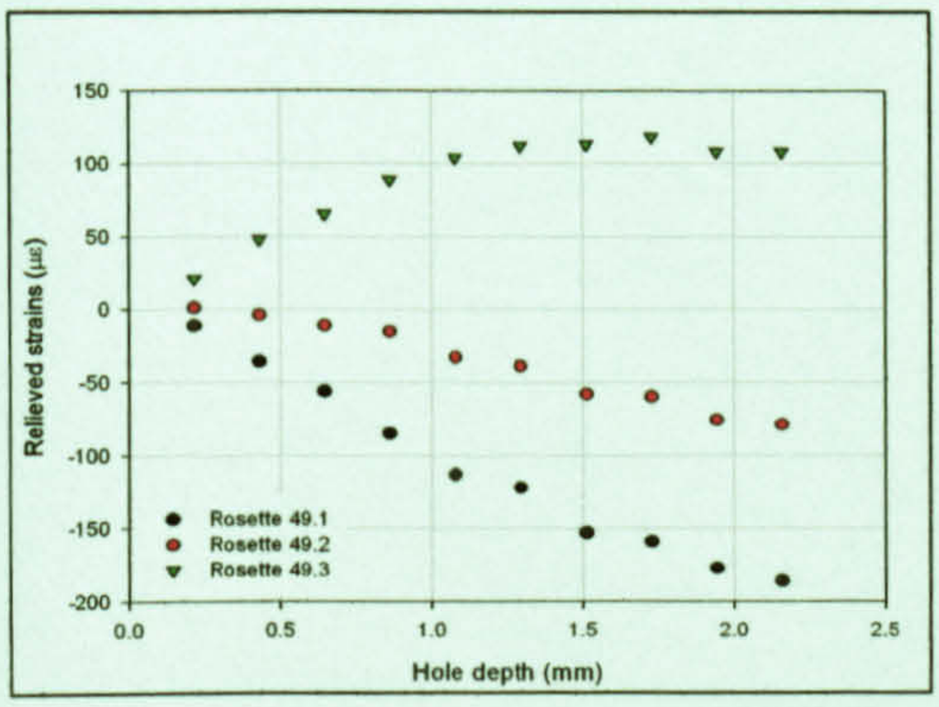

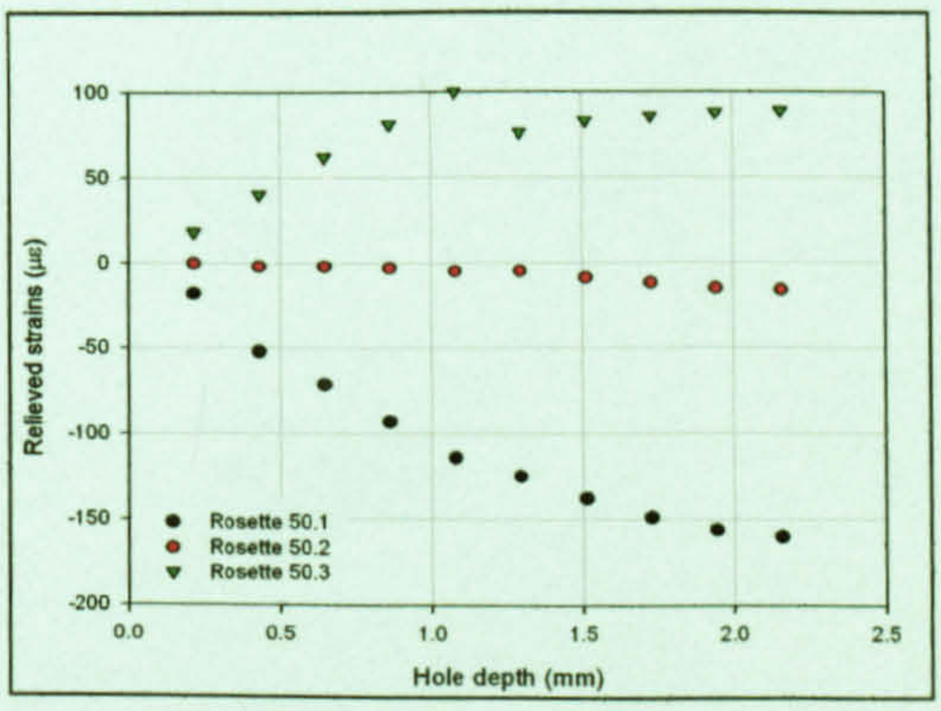

11.4 Friction Stir – Single Pass

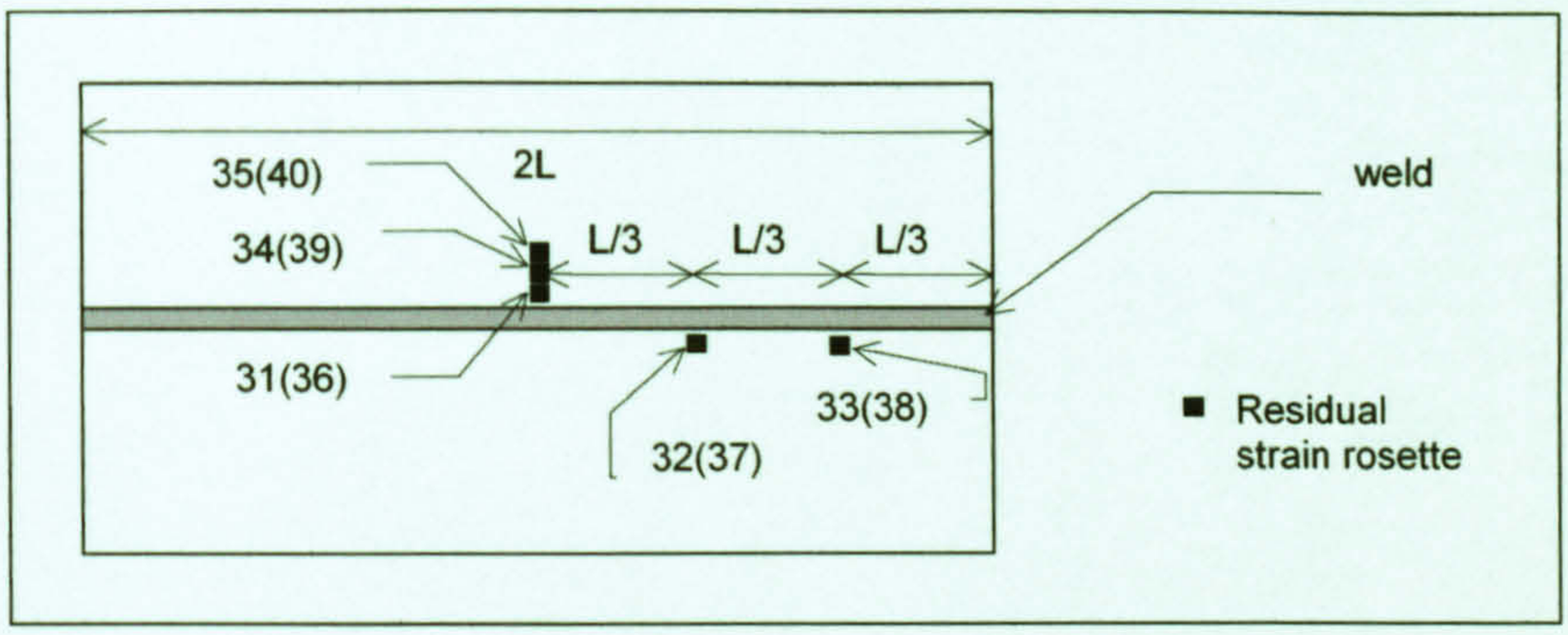

Figure 11.4: Position of residual strain gauge rosettes in relation to FS SP weld.

11.4.1 Friction Band Side (convex)

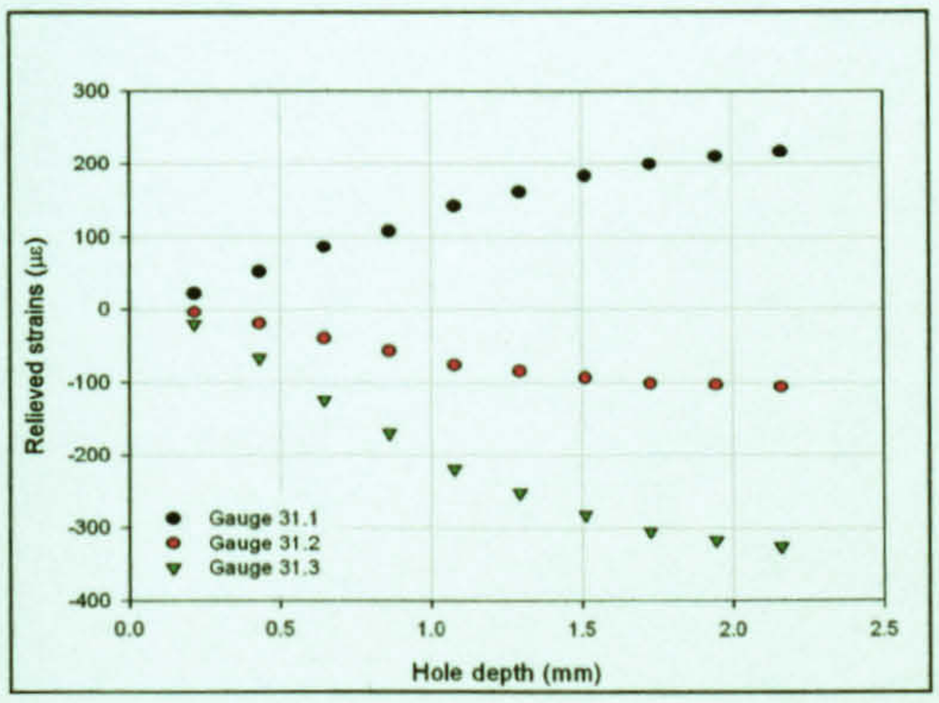

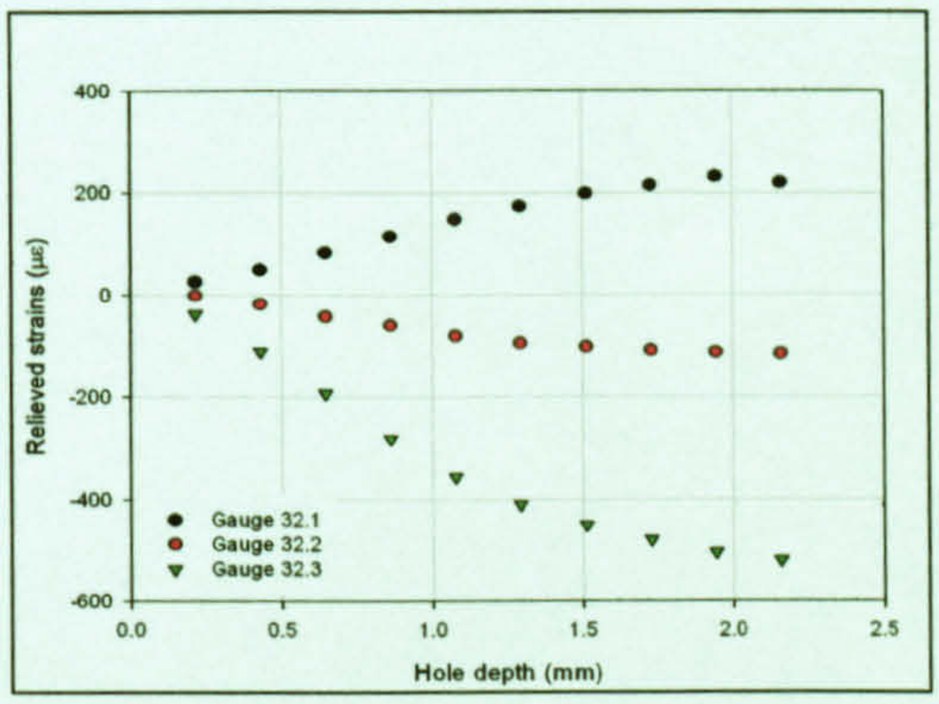

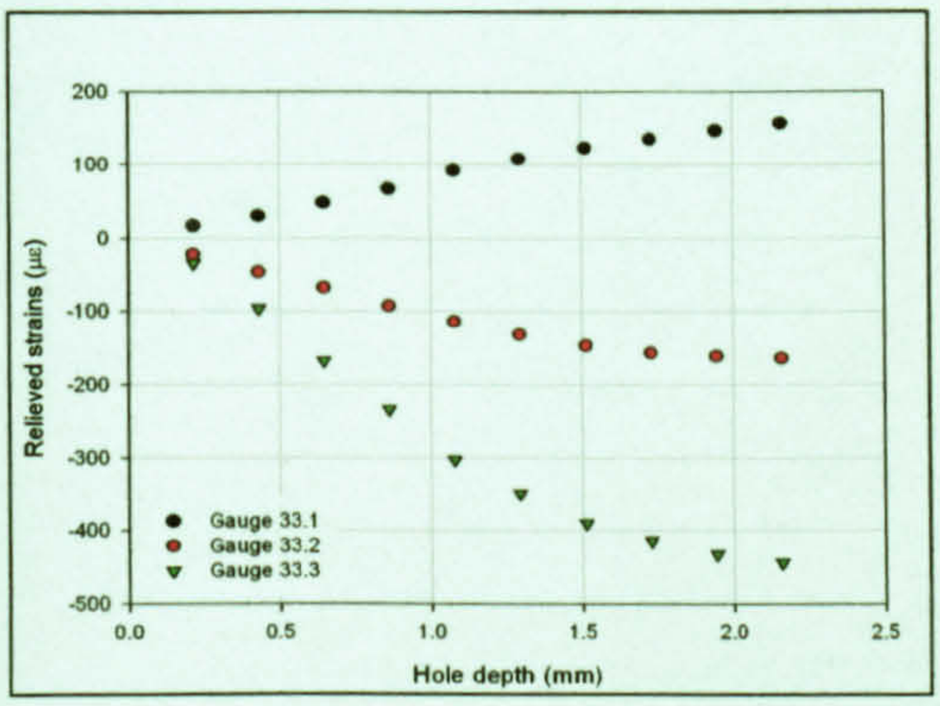

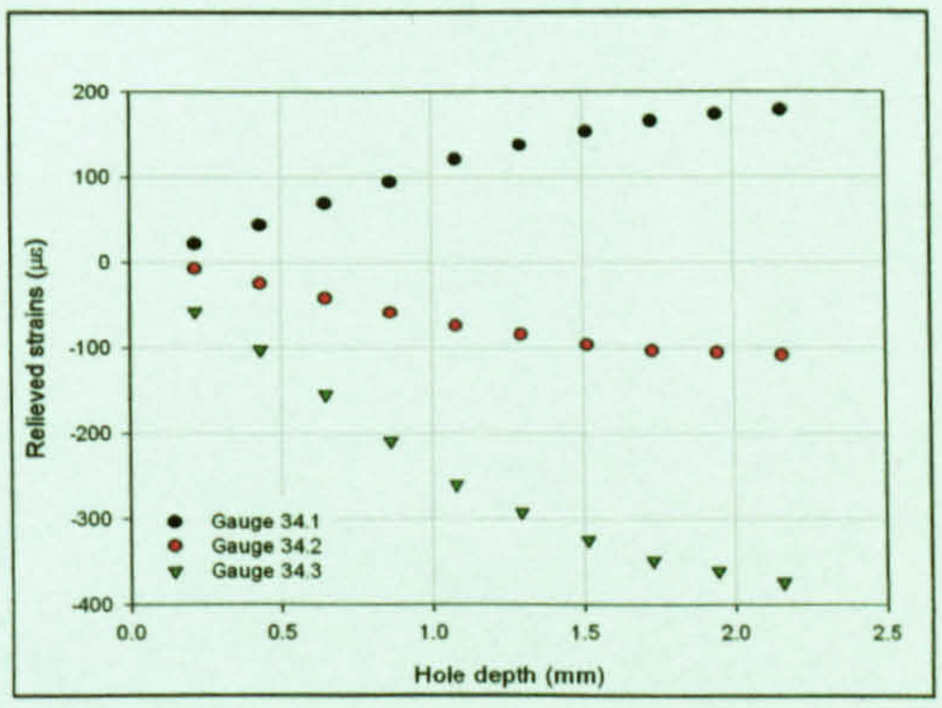

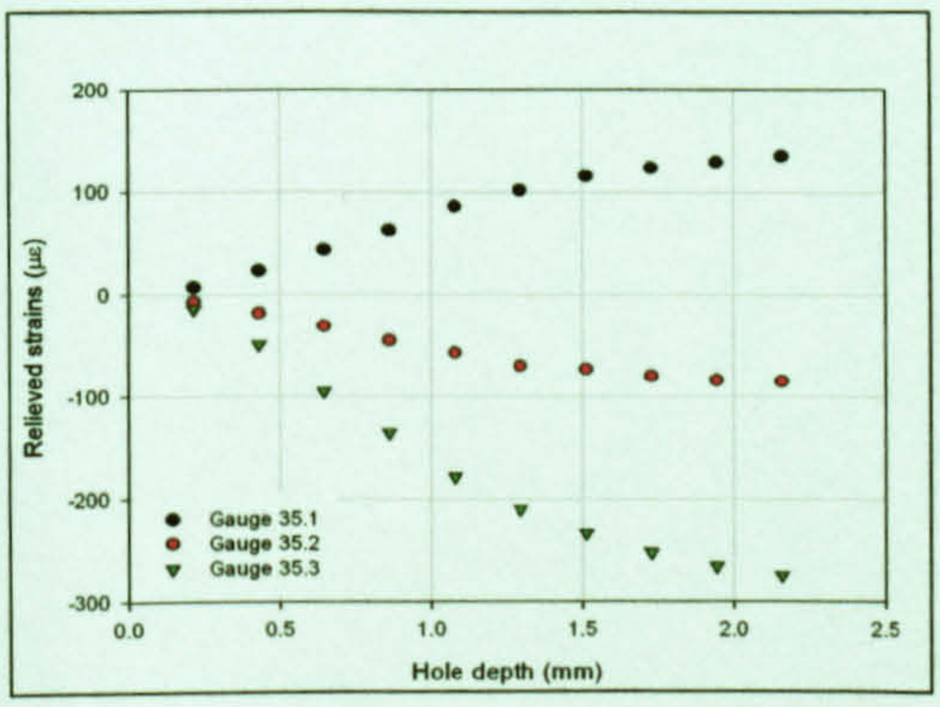

11.4.2 Weld Seam Side (concave)

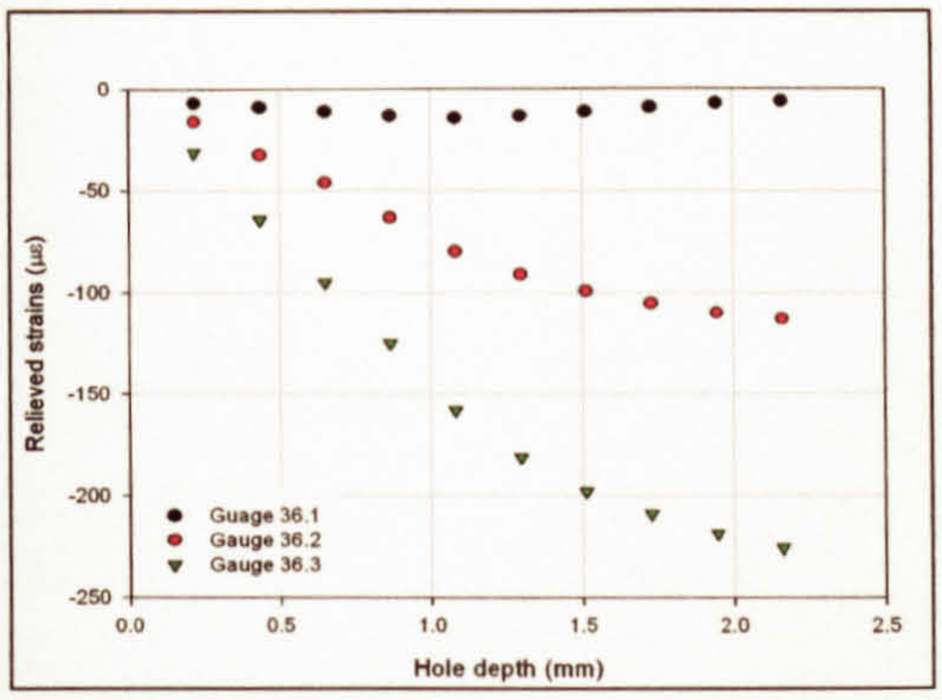

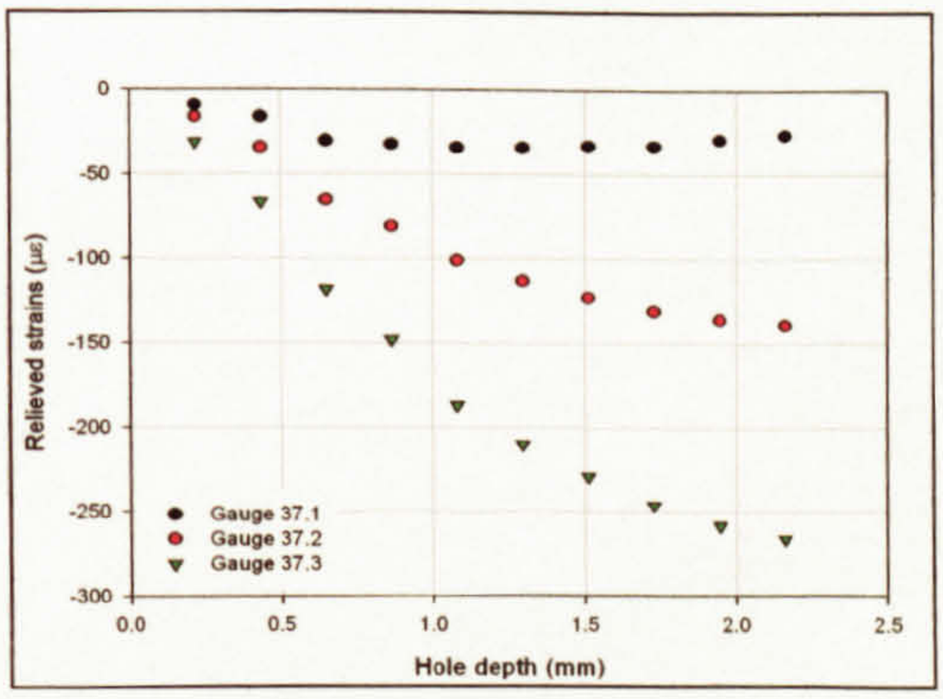

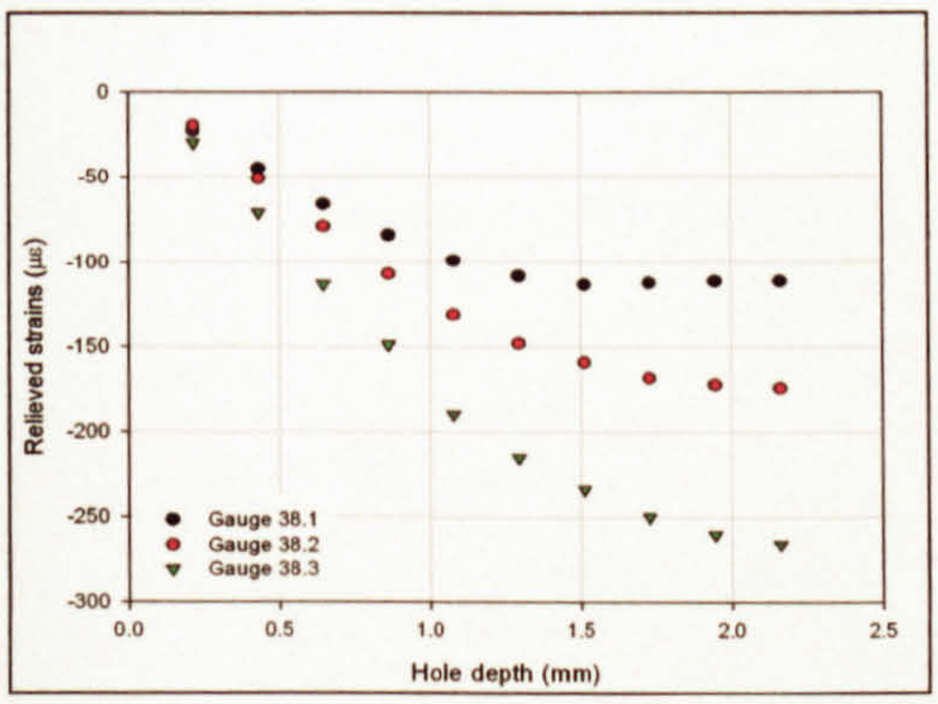

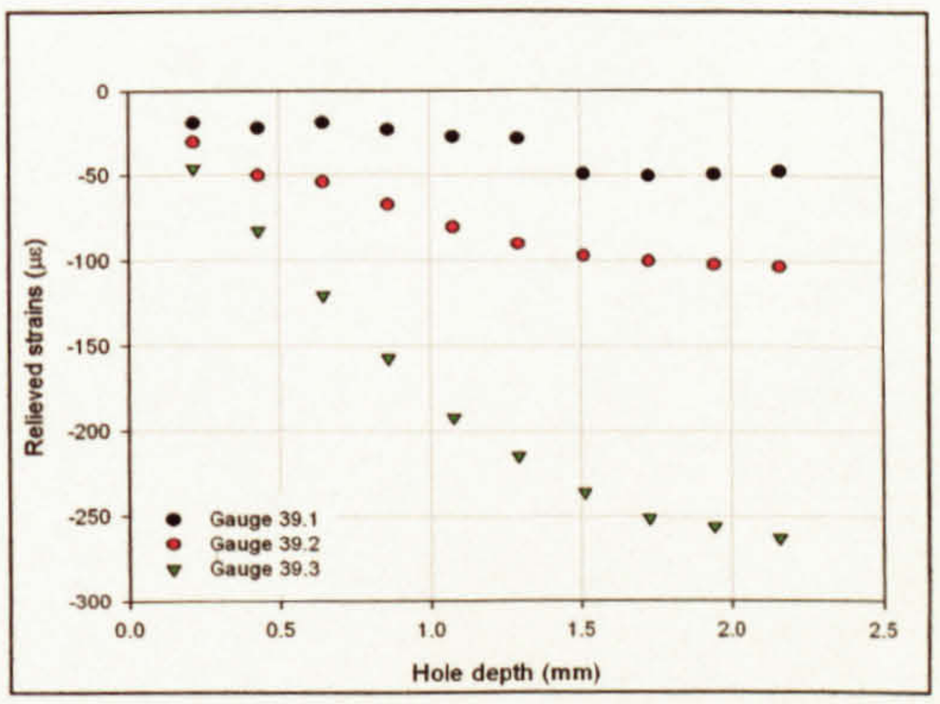

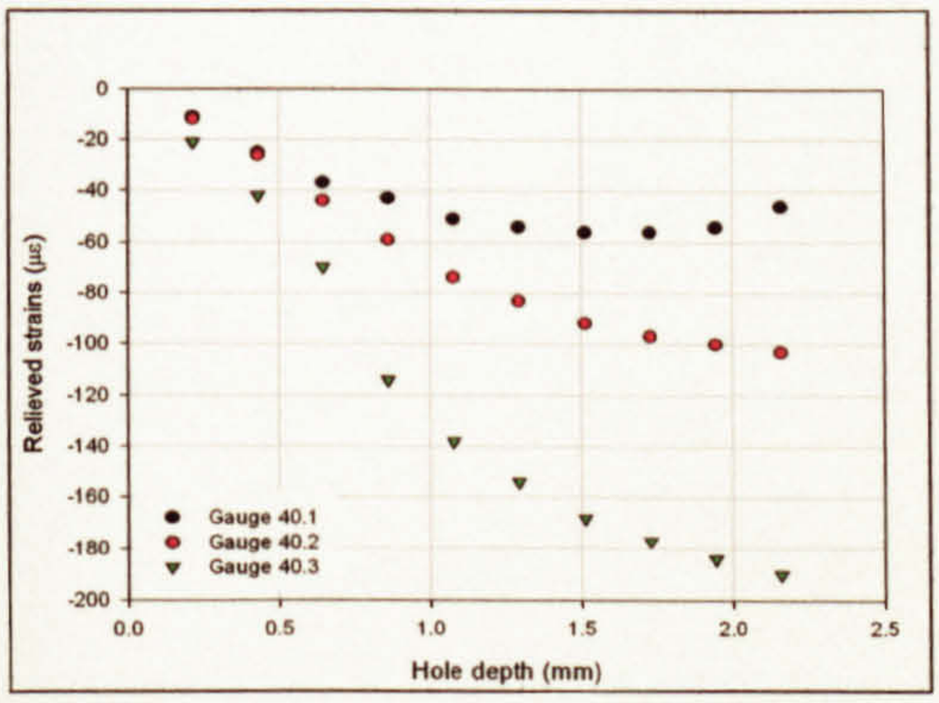

11.4.3 S-N Specimen

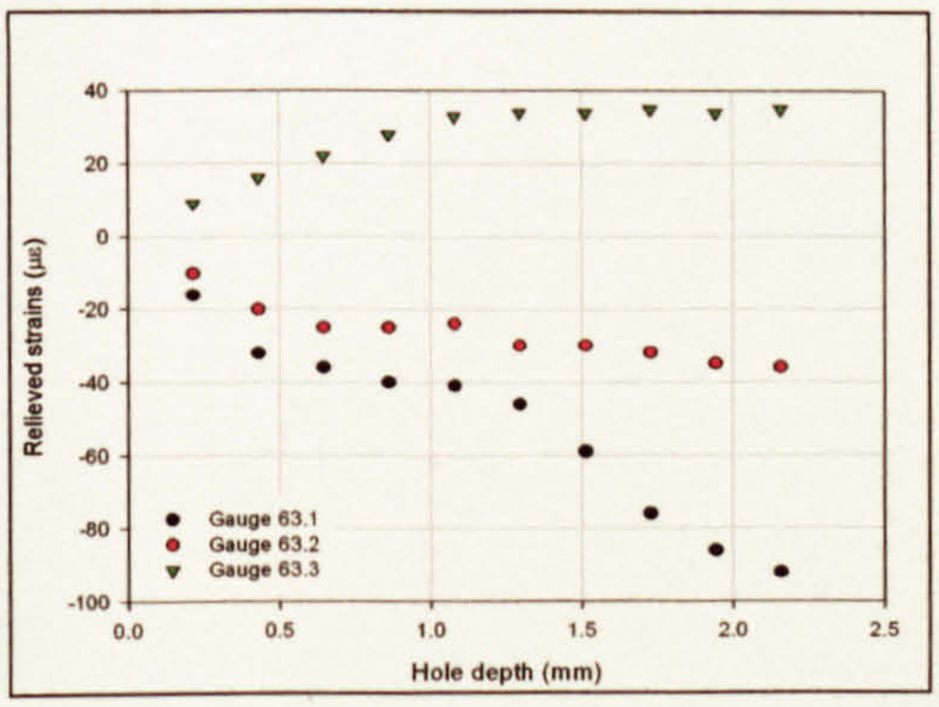

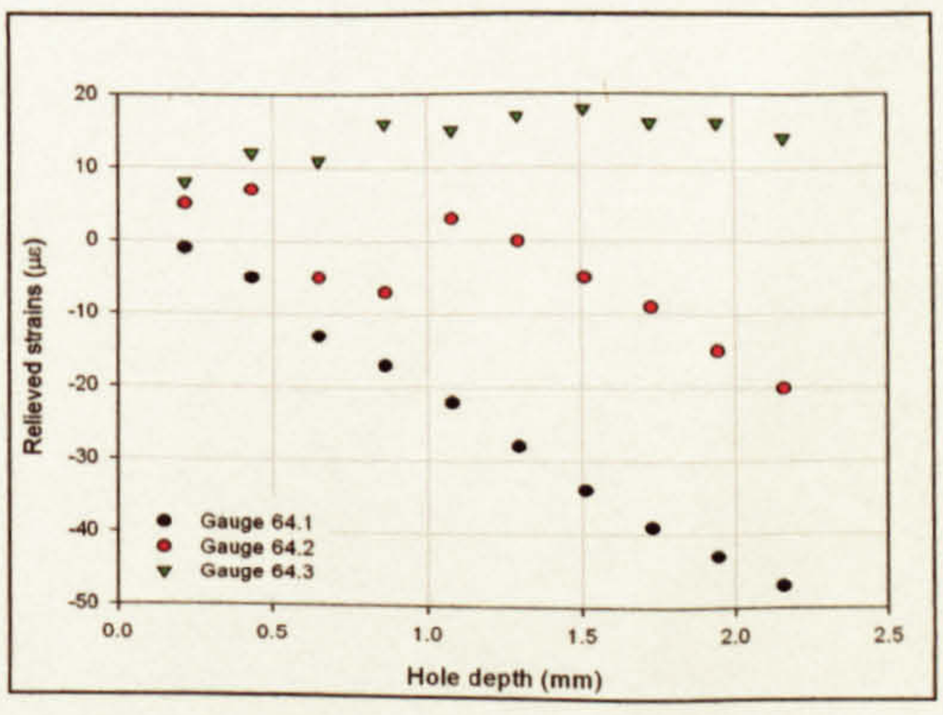

11.4.4 Friction Stir – Double Pass

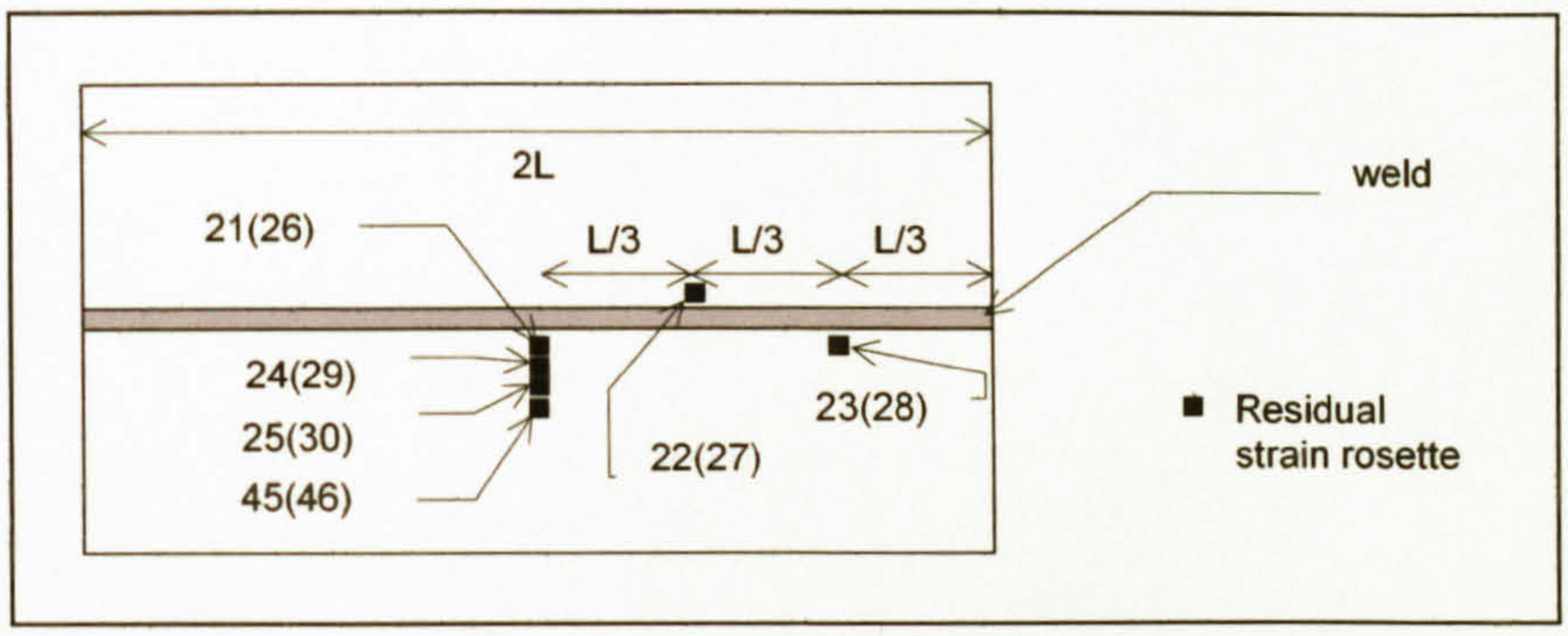

Figure 11.5: Position of residual strain gauge rosettes in relation to FS DP weld.

11.4.5 2nd Pass Side (convex)

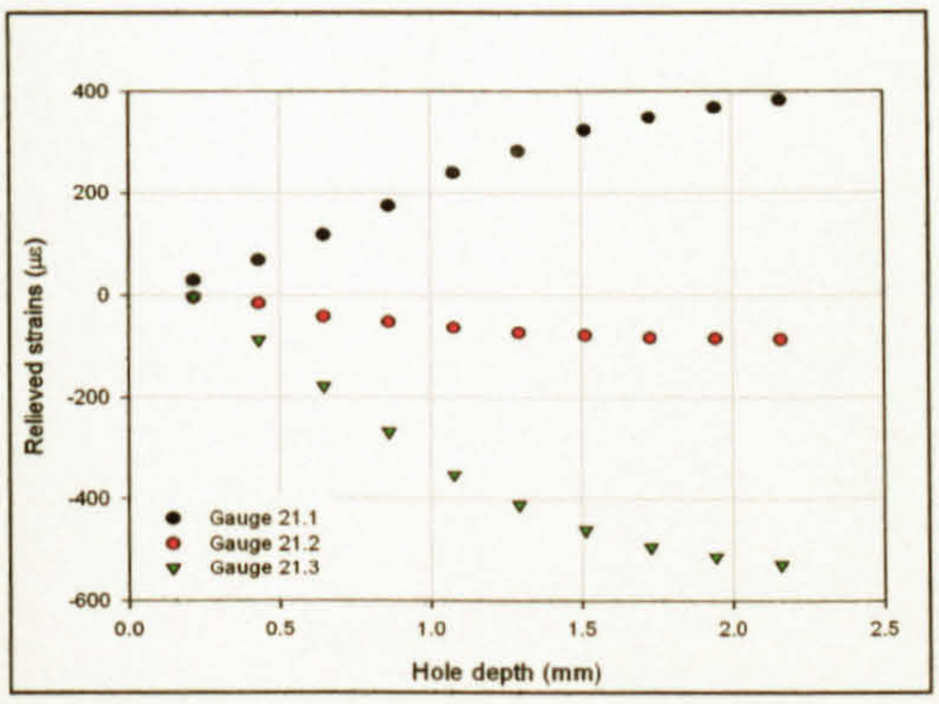

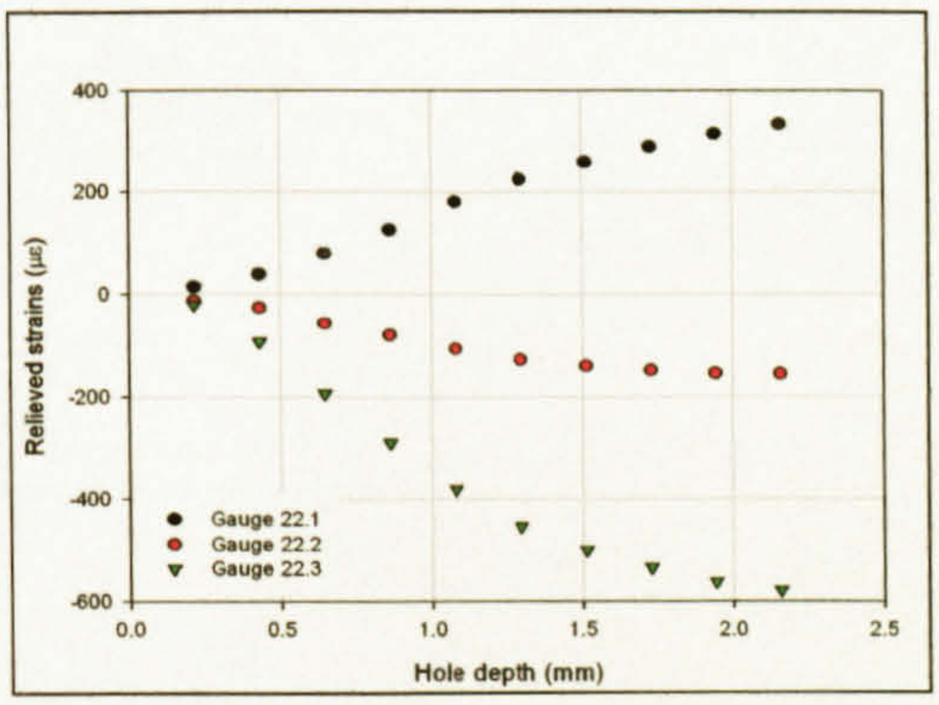

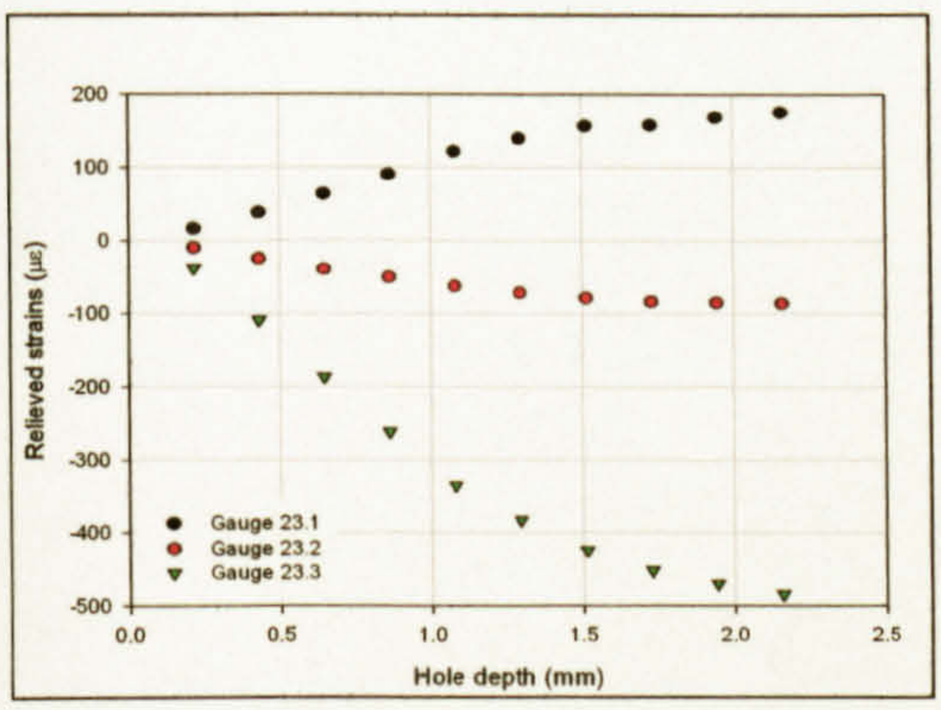

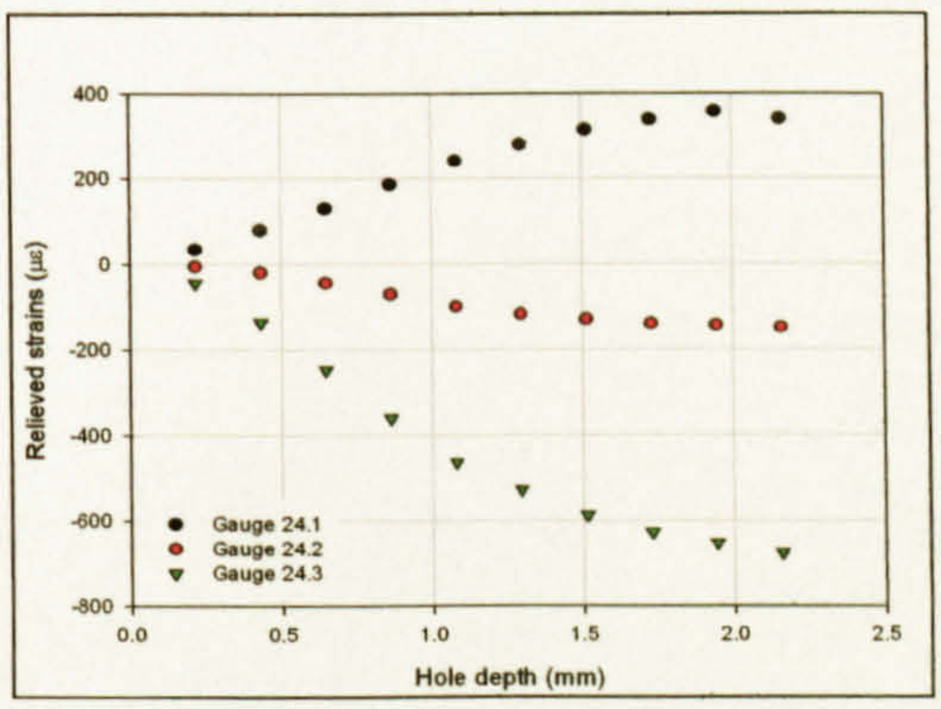

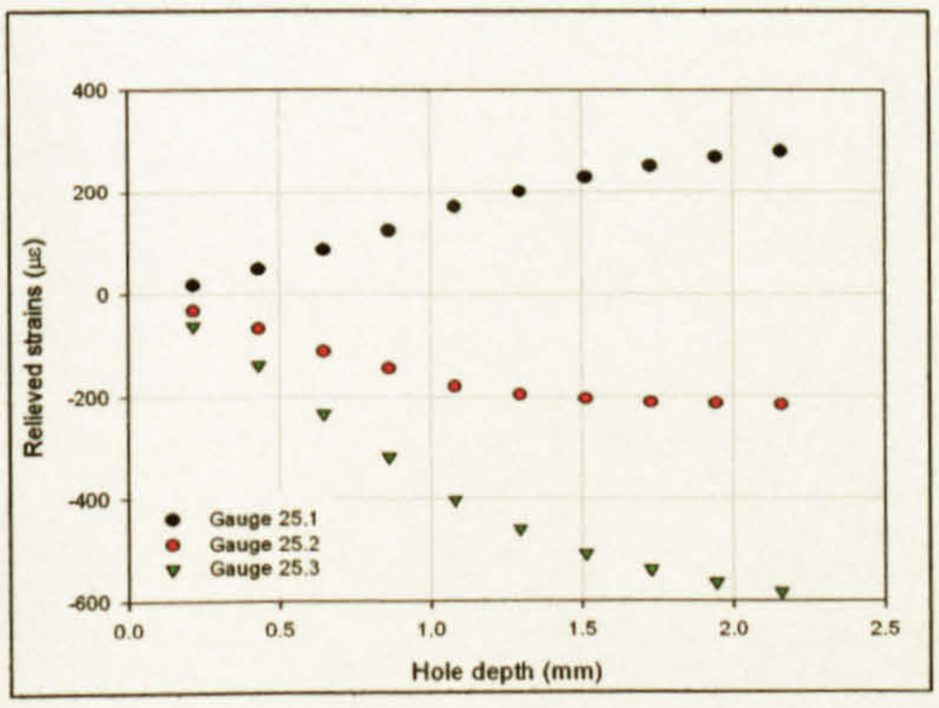

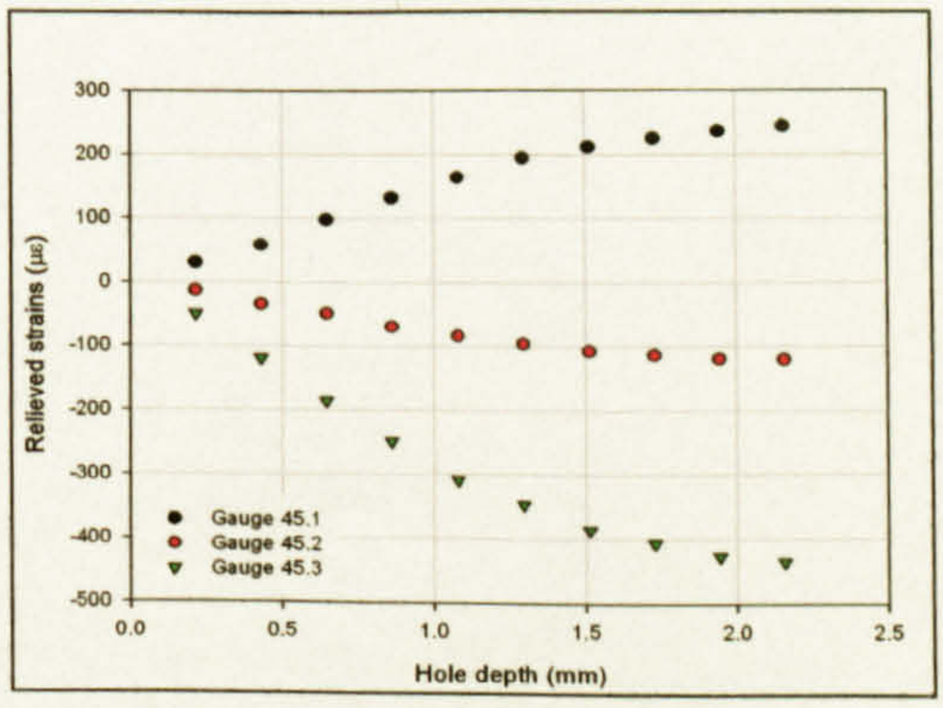

11.4.6 1st Pass Side (concave)

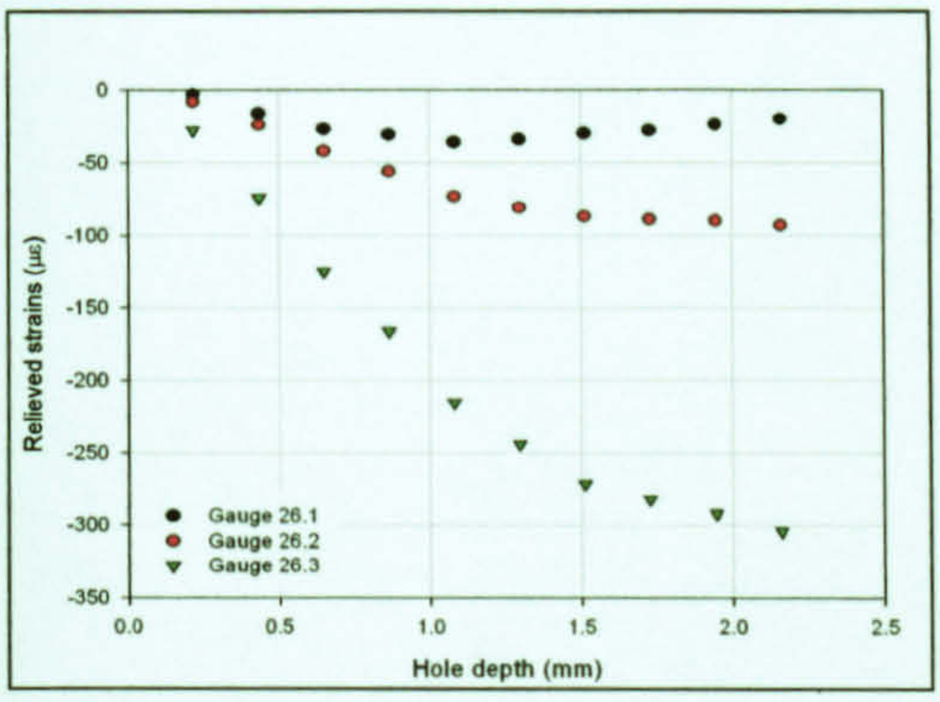

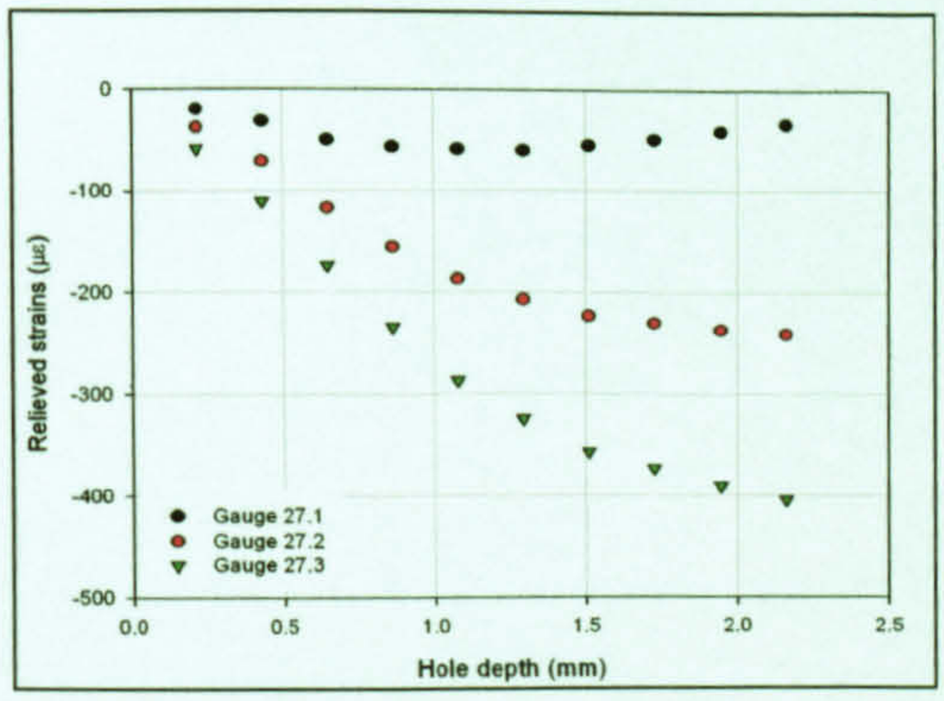

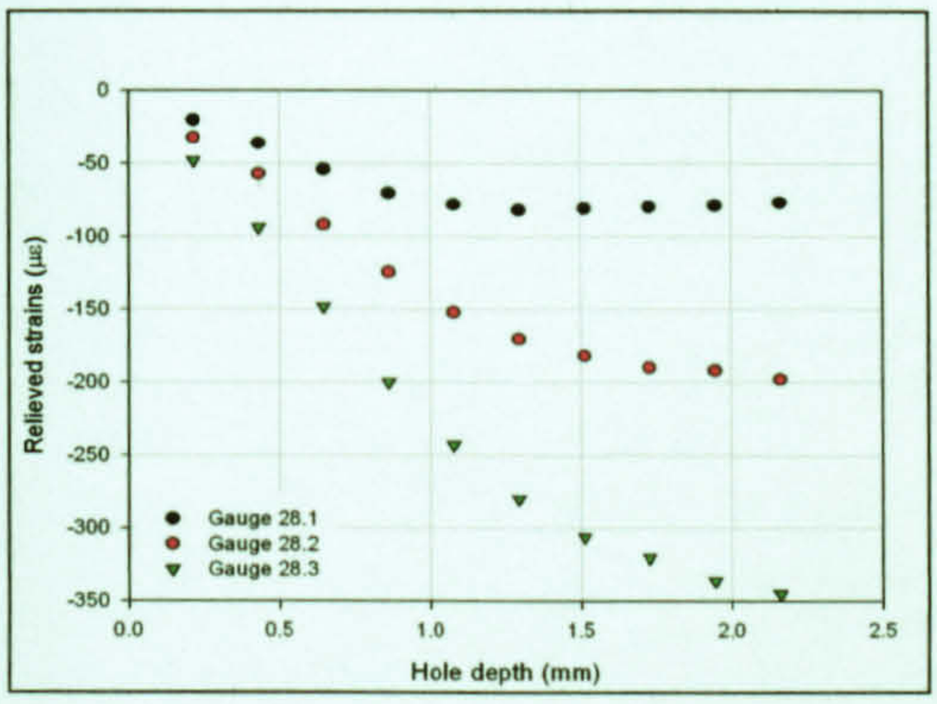

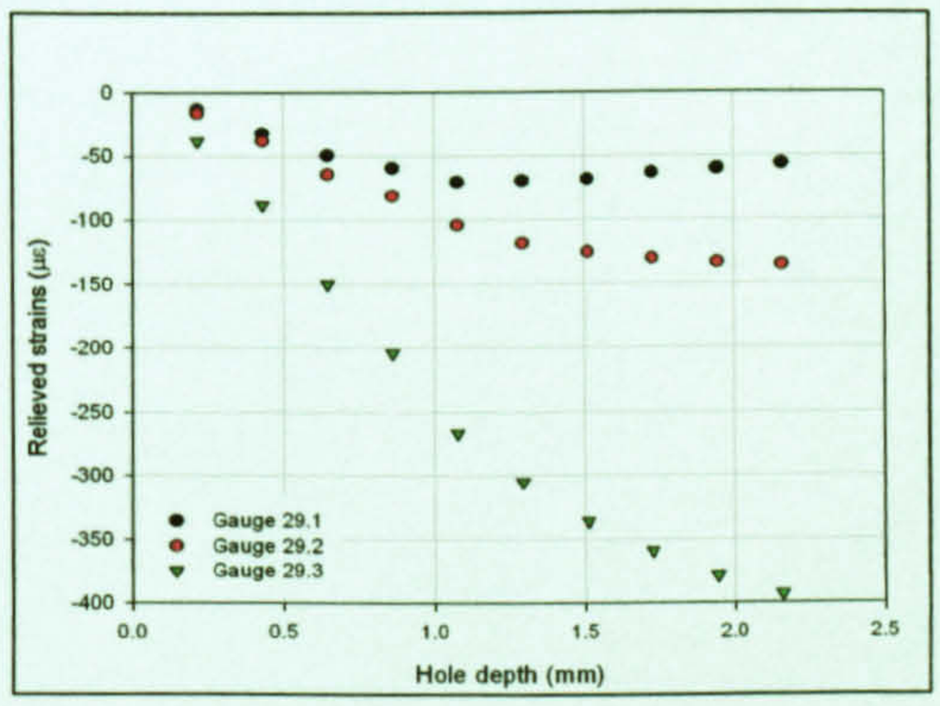

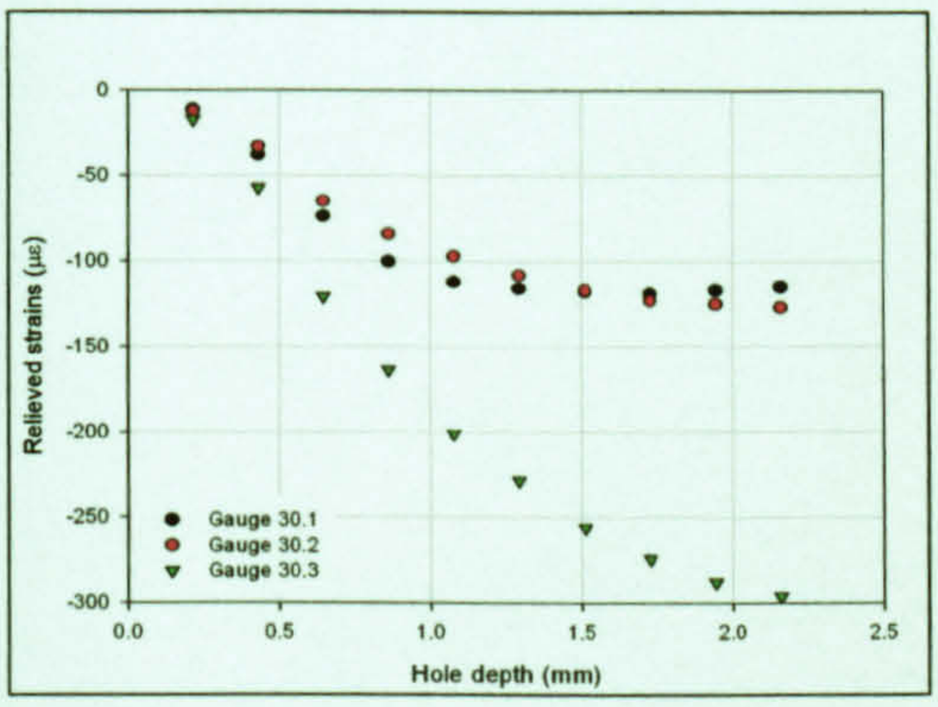

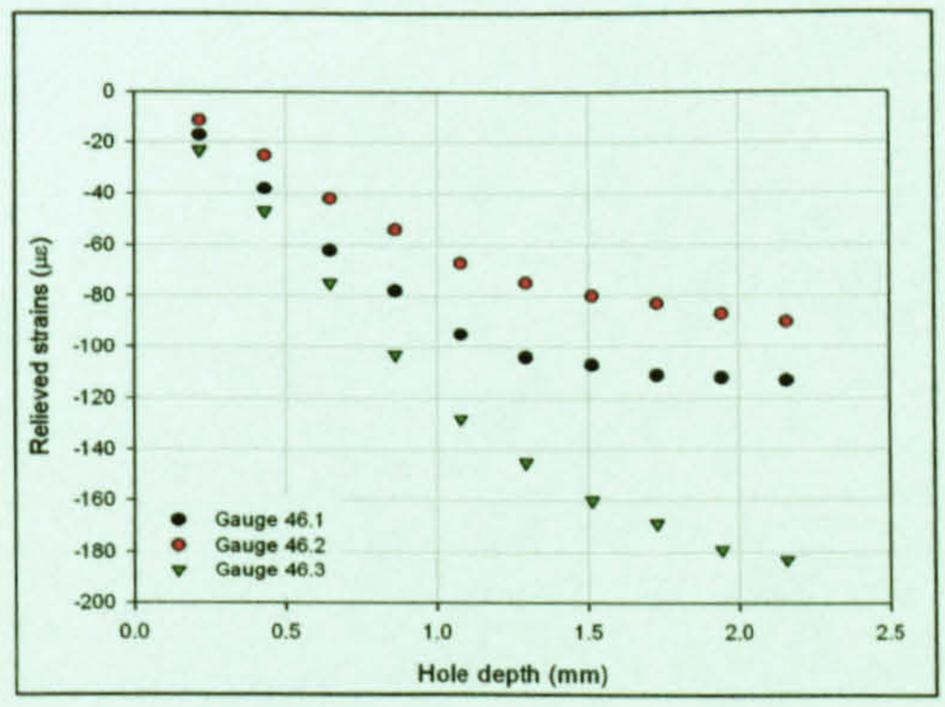

11.4.7 S-N Specimen

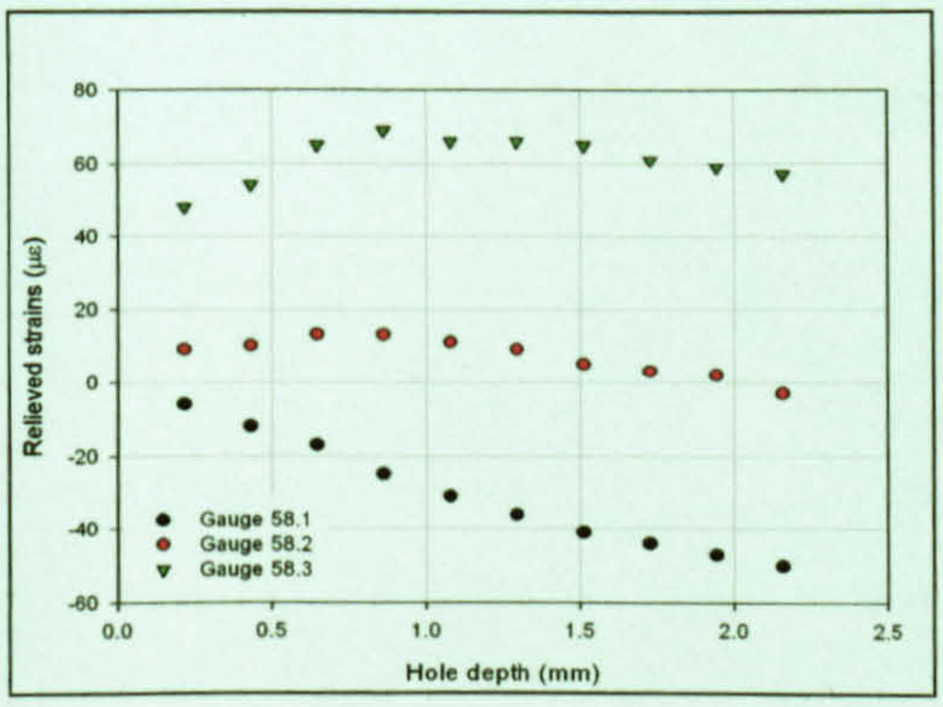

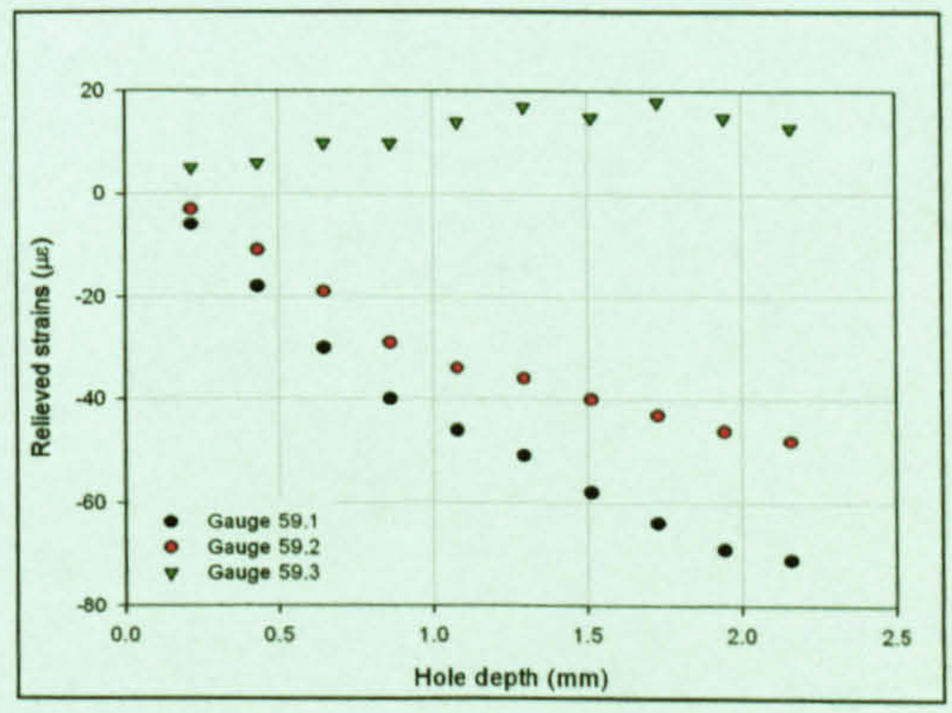

12. Appendix B ~ S-N Test Specimen Results

12.1 Parent Plate ~ Transverse (PP |-)

Specimen number	Δσ (MPa) (R = 0.1)	Cycles to failure (*italics = did not fail*)	Observations
PP |- 1	246.2	599487	Multiple crack initiation and coalescence, main crack probably intermetallic induced. See Figure 5.35.
PP |- 2	233.9	1175334	Multiple crack initiation and coalescence, main crack surface defect and secondary cracks intermetallic induced. See Figure 5.36.
PP |- 3	197.0	1356000	Multiple initiation and coalescence cause of initiation undetermined.
PP |- 4	209.3	8717300	Multiple initiation sites and coalescence, intermetallic induced initiation. See Figure 5.37
PP |- 5	260.4	166716	
PP |- 6	261.6	195614	
PP |- 7	251.0	278393	
PP |- 8	224.3	228276	
PP |- 9	218.0	288343	
PP |- 10	271.5	148720	
PP |- 11	249.7	229299	
PP |- 12	240.2	*2000000*	*Did not fail.*
PP |- 13	243.2	*2000000*	*Did not fail.*
PP |- 14	184.7	*10000000*	*Did not fail.*
PP |- 15	209.3	1083700	*Omitted, failed at support roller.*
PP |- 16	249.1	136424	*Omitted, failed at support roller.*
PP |- 17	284.7	147439	*Omitted, failed at support roller.*
PP |- 18	266.2	155960	*Omitted, failed at support roller.*

Table 12.1: S-N test results for AA 5383-H321 parent plate, rolling direction transverse to the applied load (|-), R = 0.1.

12.2 Parent Plate ~ Parallel (PP //)

Specimen number	Δσ (MPa) (R = 0.1)	Cycles to failure (*italics = did not fail*)	Observations
PP // 1	233.9	267622	Multiple initiation sites and coalescence, main crack possibly surface defect initiated. See Figure 5.41
PP // 2	221.6	369403	Multiple initiation, two main cracks, smaller crack intermetallic initiated, main crack edge initiated. See Figure 5.42.
PP // 3	209.3	771300	Main crack edge initiated, although coalescence also evident.
PP // 4	203.1	349100	Main crack edge initiated, although coalescence also evident.
PP // 5	228.4	358531	
PP // 6	222.6	555805	
PP // 7	272.9	126589	
PP // 8	242.6	389908	
PP // 9	197.0	*2000000*	*Did not fail.*
PP // 10	197.0	*10000000*	*Did not fail.*
PP // 11	249.4	*2000000*	*Did not fail.*
PP // 12	211.7	*2000000*	*Did not fail.*
PP // 13	272.8	119447	*Omitted, failed at support roller.*
PP // 14	260.3	355459	*Omitted, failed at support roller.*
PP // 15	248.5	658536	*Omitted, failed at support roller.*
PP // 16	260.8	143617	*Omitted, failed at support roller.*
PP // 17	250.0	149637	*Omitted, failed at support roller.*
PP // 18	240.7	117959	*Omitted, failed at support roller.*
PP // 19	286.1	155969	*Omitted, failed at support roller.*
PP // 20	261.0	219483	*Omitted, failed at support roller.*
PP // 21	255.4	191464	*Omitted, failed at support roller.*

Table 12.2: S-N test results for AA 5383-H321 parent plate, rolling direction parallel to the applied load (//), R = 0.1.

12.3 Metal Inert Gas ~ Low Input (MIG LI)

Specimen number	Δσ nominal (MPa) (R = 0.1)	Δσ (weld toe) (MPa) (R = 0.1)	Cycles to failure (*italics = did not fail*)	Observations
MIG LI 1	233.9	261.9	147602	Multiple initiation sites, mainly from blow holes and porosity, although not all causes identified. See Figure 5.45 and Figure 5.46.
MIG LI 2	221.6	250.0	226720	Multiple initiation sites, porosity induced and stress concentration of weld toe, some unknown. See Figure 5.47.
MIG LI 3	209.3	238.1	160943	Multiple initiation sites, mainly from porosity, but also one from stress concentrator and some unknown. See Figure 5.48.
MIG LI 4	197.0	226.3	311407	Multiple initiation sites from porosity. See Figure 5.49.
MIG LI 5	123.1	156.9	1738300	Multiple initiation sites from porosity.
MIG LI 6	184.7	214.5	758900	Multiple initiation sites, from porosity, stress concentrators and corner.
MIG LI 7	172.4	202.7	705500	Crack initiation from stress raising spatter on surface and also corner initiated. See Figure 5.49.
MIG LI 8	160.0	191.1	4507700	Multiple initiation sites from porosity.
MIG LI 9	172.4	202.7	*10000000*	*Did not fail.*
MIG LI 10	147.7	179.6	*10000000*	*Did not fail.*
MIG LI 11	135.4	168.1	*10000000*	*Did not fail.*

Table 12.3: S-N test results for AA 5383-H321 MIG LI butt welds, R = 0.1.

12.4 Metal Inert Gas ~ High Input (MIG HI)

Specimen number	Δσ nominal (MPa) (R = 0.1)	Δσ (weld toe) (MPa) (R = 0.1)	Cycles to failure (*italics = did not fail*)	Observations
MIG HI 1	221.6	292.5	34155	Multiple initiation sites from weld toe geometry, possible influence of porosity near to weld toe.
MIG HI 2	197.0	271.6	161846	Multiple initiation sites from weld toe geometry, possible influence of porosity near to weld toe. See Figure 5.52, Figure 5.53 and Figure 5.54.
MIG HI 3	172.6	250.5	279234	Multiple initiation sites from weld toe geometry.
MIG HI 4	147.7	228.6	300091	Porosity and geometry induced fatigue cracks. See Figure 5.55
MIG HI 5	98.5	182.7	1427500	Multiple initiation sites from weld toe geometry and possible influence of porosity near to weld toe. See Figure 5.56.
MIG HI 6	123.1	206.1	1037700	Multiple initiation sites from weld toe geometry, possible influence of porosity near to weld toe.
MIG HI 7	86.2	170.5	1647900	Multiple initiation sites from weld toe geometry, possible corner initiated crack.
MIG HI 8	110.8	194.6	718300	Multiple initiation sites from weld toe geometry, possible influence of porosity near to weld toe.
MIG HI 9	73.9	157.7	*10000000*	*Did not fail.*

Table 12.4: S-N test results for AA 5383-H321 MIG HI butt welds, R = 0.1.

12.5 Friction Stir ~ Single Pass (FS SP)

Specimen number	Δσ (MPa) (R = 0.1)	Cycles to failure (*italics = did not fail)*	Observations
FS SP 1	233.9	265202	Failed due to the coalescence of multiple mid-specimen and edge initiated cracks. The main crack extended from the centre of the weld, in the TMAZ and weld nugget region. Several smaller cracks were evident some that had not coalesced into the main crack and thus remained separate from this. Evidence that the cracks were following score marks in the surface was evident as was a crack running transverse to the applied load. PFD on fast fracture surface. See Figure 5.59, Figure 5.60 and Figure 5.61.
FS SP 2	221.6	333185	Failed due to the coalescence of multiple cracks, both mid-specimen and edge initiated, although the main crack was edge initiated. The edge initiated crack commenced within the TMAZ, whereas others formed on the inner edge of the ridge on the advancing side of the tool shoulder. Several other smaller cracks were evident, both edge and mid-specimen initiated, that had not coalesced into the main crack. These were positioned on the inner edge of the ridge. See Figure 5.62.
FS SP 3	209.3	414766	Failure possibly resulted from an internally initiated crack that occurred due to PFD within the weld nugget/TMAZ region, see Figure 5.63. The crack then grew to outwards to both the upper surface and outer edge of the specimen. Three other edge initiated cracks were also evident, one large one within the TMAZ and two smaller near to the inner edge of the ridge on the advancing side of the tool shoulder. See Figure 5.64.
FS SP 4	246.2	104366	Failed due to coalescence of numerous mid-specimen and edge initiated cracks, with all the cracks being located within the TMAZ. Numerous initiation sites and cracks were visible, with some of the cracks exhibiting evidence of following the score marks on the surface. See Figure 5.68
FS SP 5	197.0	484200	Failed due to the coalescence of multiple cracks. The coalescence resulted in the formation of two mid-specimen cracks forming, although a small edge crack is also evident. All the cracks formed at the inner edge of the ridge produced by the advancing side of the tool shoulder. Most of the cracks exhibited evidence of following the scored marks on the surface prior to coalescence occurring. See Figure 5.69.
FS SP 6	172.4	832700	The main crack appears to have initiated from the edge of the specimen, although PFD on the fatigue fracture surface may have been the origin. Multiple initiation sites from score marks from tool shoulder are also evident. See Figure 5.66.
FS SP 7	147.7	756400	Failed due to a crack that initiated within the TMAZ at the edge of the specimen. Some coalescence of small cracks may have initially occurred, but the overall failure was due to one crack. PFD on fatigue and fast fracture surface. See Figure 5.70.
FS SP 8	135.4	*10000000*	*Did not fail.*
FS SP 9	98.5	*10000000*	*Did not fail.*
FS SP 10	123.1	*10000000*	*Did not fail.*

Table 12.5: S-N test results for friction stir single pass butt welded AA 5383-H321.

12.6 Friction Stir ~ Double Pass (FS DP)

Specimen number	Δσ (MPa) (R = 0.1)	Cycles to failure (*italics = did not fail*)	Observations
FS DP 1	233.9	189007	Failed due to the coalescence of multiple mid-specimen initiated cracks. All the cracks initiated at the retreating side ridge produced by the tool shoulder. The cracks, before coalescence occurred, followed the score marks in the surface. A small crack is also evident slightly inside the ridge caused by the tool shoulder. See Figure 5.71 and Figure 5.72.
FS DP 2	221.6	324027	Failed due to edge crack that eventually coalesced with a mid-specimen crack that resulted from the coalescence of smaller mid-specimen initiated cracks. The mid-specimen cracks were located on the advancing side ridge caused by the tool shoulder. The edge initiated crack originated with in TMAZ and progressed to the ridge. The mid-specimen initiated cracks showed evidence of following the score marks on the surface. See Figure 5.73.
FS DP 3	209.3	379562	Failed due to coalescence of both edge and mid-specimen initiated cracks. The edge crack was located on the inner edge of the advancing side ridge caused by the tool, whereas the mid-specimen cracks were located within the TMAZ.
FS DP 4	197.0	372780	Failed due to coalescence of both edge and mid-specimen initiated cracks. Both the edge and mid-specimen cracks were located on the retreating side ridge caused by the tool. There was evidence of the cracks following the score marks in the surface, although the general pattern of the crack was along the ridge perpendicular to the applied load. See Figure 5.74
FS DP 5	123.1	3431000	Failed from edge initiated crack in the HAZ outside of the advancing side. Some coalescence has occurred with mid-specimen initiated cracks, but the predominating crack resulted from edge initiation. Crack initiation was possibly associated with a small indent on the side of the specimen.
FS DP 6	98.5	6717200	Failed from an edge initiated crack in the HAZ slightly outside the advancing side ridge of the tool shoulder. Some coalescence has occurred with mid-specimen initiated cracks, but the predominating crack resulted from edge initiation. See Figure 5.75 and Figure 5.76.
FS DP 7	172.4	4431900	The main crack was formed from the coalescence of several mid-specimen cracks all located with in small area on the retreating side ridge formed by the tool. This crack then proceeded to coalesce with smaller cracks located near to the edge of the specimen. The crack grew both into the TMAZ and outwards into the HAZ. There was some evidence that the crack followed the score marks present on the surface, although this was as a result of coalescence with the cracks near to the edge. See Figure 5.77 and Figure 5.78.
FS DP 8	147.7	*10000000*	*Did not fail.*
FS DP 9	135.4	*10000000*	*Did not fail.*
FS DP 10	73.9	*10000000*	*Did not fail.*

Table 12.6: S-N test results for friction stir double pass butt welded AA 5383-H321.

13. Appendix C ~ Crack Growth Results

13.1 Parent Plate ~ Transverse (PP |-)

13.1.1 SCG Specimen S-N Results

Specimen number	Δσ (applied) (MPa) (R = 0.1)	Δσ (notch) (MPa) (R = 0.1)	Cycles to failure (*italics = did not fail*)	Comments
PP |- SCG 1	294.8	289.9	72048	
PP |- SCG 2	291.6	286.8	48689	
PP |- SCG 3	288.4	283.7	70694	
PP |- SCG 4	285.2	280.6	91007	
PP |- SCG 5	282.0	277.5	85883	
PP |- SCG 6	278.8	274.4	101705	
PP |- SCG 7	275.6	271.3	89117	
PP |- SCG 8	272.4	268.3	144228	
PP |- SCG 9	269.2	265.2	130358	
PP |- SCG 10	265.9	262.2	151274	
PP |- SCG 11	262.7	259.2	120785	
PP |- SCG 12	259.5	256.1	132444	
PP |- SCG 13	256.3	253.2	112094	
PP |- SCG 14	253.1	250.2	135138	
PP |- SCG 15	249.9	247.3	2.00E+06	*Did not fail.*

Table 13.1: S-N test results for AA 5383-H321 parent plate transverse SCG specimens.

13.1.2 SCG Results

PP	- SCG 21.1									
Cycles (N)	Crack Length (μm)		dc/dN ($m.cycle^{-1}$) x 10^9	N/N_f	Cycles (N)	Crack Length (μm)		dc/dN ($m.cycle^{-1}$) x 10^9	N/N_f
	2c	c				2c	c		
112000	2108	1054	209.02	0.99	79000	338	169	5.76	0.70
111000	1690	845	166.96	0.98	78000	327	163	0.48	0.69
110000	1356	678	120.34	0.98	76000	325	162	9.29	0.67
109000	1115	558	45.16	0.97	75000	306	153	6.13	0.67
108000	1025	513	68.80	0.96	74000	294	147	2.11	0.66
107000	887	444	33.30	0.95	71000	281	141	0.79	0.63
106000	821	410	7.77	0.94	70000	280	140	1.81	0.62
105000	805	403	22.61	0.93	68000	272	136		
104000	760	380	33.60	0.92	Coalescence				
103000	693	346	0.20	0.91	64000	231	116	1.06	0.57
102000	693	346	10.87	0.90	62000	227	114	3.75	0.55
101000	671	335	16.37	0.90	60000	212	106	1.73	0.53
100000	638	319	10.27	0.89	58000	205	103	5.44	0.51
99000	618	309	10.56	0.88	56000	183	92	0.28	0.50
97000	575	288	7.63	0.86	54000	182	91	2.14	0.48
96000	560	280	11.21	0.85	50000	165	83	2.19	0.44
95000	538	269	8.91	0.84	48000	156	78	1.59	0.43
94000	520	260	5.61	0.83	46000	150	75	2.27	0.41
93000	509	254	3.36	0.82	44000	141	70		
92000	502	251	8.60	0.82	Coalescence				
91000	485	242	15.24	0.81	42000	130	65	1.09	0.37
90000	454	227	1.86	0.80	36000	117	59	0.88	0.32
89000	450	225	1.57	0.79	34000	114	57	0.11	0.30
88000	447	224	4.27	0.78	32000	113	57	1.64	0.28
85000	422	211	13.65	0.75	30000	107	53	1.80	0.27
84000	394	197	1.07	0.74	28000	99	50	0.82	0.25
83000	392	196	6.95	0.74	24000	93	46	0.50	0.21
82000	378	189	3.80	0.73	20000	89	44		
80000	363	182	12.53	0.71					

Table 13.2: PP |- SCG specimen, crack 21.1.

PP |- SCG 21.2									
Cycles (N)	Crack Length (μm)		dc/dN (m.cycle^{-1}) x 10^9	N/N_f	Cycles (N)	Crack Length (μm)		dc/dN (m.cycle^{-1}) x 10^9	N/N_f
	2c	c				2c	c		
112000	108	54	10.84	0.99	110000	71	36	2.48	0.98
111000	87	43	7.78	0.98	109000	66	33		

Table 13.3: PP |- SCG specimen, crack 21.2.

PP |- SCG 23.1									
Cycles (N)	Crack Length (μm)		dc/dN (m.cycle^{-1}) x 10^9	N/N_f	Cycles (N)	Crack Length (μm)		dc/dN (m.cycle^{-1}) x 10^9	N/N_f
	2c	c				2c	c		
104000	1845	923	Edge crack		75000	304	152	5.08	0.72
103000	1687	844			72000	273	137	2.52	0.69
102000	1287	643			71000	268	134	4.51	0.68
100000	905	452	74.16	70000	70000	259	130	1.73	0.67
99000	756	378	23.01	0.95	68000	252	126	4.87	0.65
98000	710	355	16.79	0.94	66000	233	116	3.04	0.63
97000	677	338	30.27	0.93	64000	221	110	1.62	0.61
96000	616	308	21.27	0.92	60000	208	104	2.59	0.58
94000	531	266	2.70	0.90	56000	187	93	6.15	0.54
93000	526	263	18.13	0.89	54000	162	81	0.09	0.52
92000	490	245	8.11	0.88	52000	162	81	0.20	0.50
90000	457	229	7.83	0.86	50000	161	81	4.25	0.48
88000	426	213	5.52	0.84	48000	144	72	2.48	0.46
85000	393	196	3.79	0.82	46000	134	67	2.45	0.44
83000	378	189	9.33	0.80	42000	115	57	0.79	0.40
82000	359	179	3.78	0.79	36000	105	53	0.94	0.35
81000	351	176	11.26	0.78	32000	98	49	4.76	0.31
80000	329	164	1.39	0.77	30000	79	39	0.93	0.29
79000	326	163	3.30	0.76	28000	75	37	0.62	0.27
76000	306	153	1.26	0.73	26000	72	36		

Table 13.4: PP |- SCG specimen, crack 23.1.

PP |- SCG 23.2									
Cycles (N)	Crack Length (μm)		dc/dN (m.cycle^{-1}) x 10^9	N/N_f	Cycles (N)	Crack Length (μm)		dc/dN (m.cycle^{-1}) x 10^9	N/N_f
	2c	c				2c	c		
104000	158	79	2.62	1.00	87000	88	44	3.95	0.83
102000	147	74	6.81	0.98	86000	80	40	1.41	0.82
101000	134	67	1.33	0.97	85000	78	39	0.02	0.82
100000	131	65	3.80	0.96	80000	77	39	1.04	0.77
99000	123	62	0.02	0.95	77000	71	36	4.90	0.74
97000	123	62	2.32	0.93	76000	61	31	0.23	0.73
96000	119	59	1.44	0.92	74000	60	30	0.08	0.71
95000	116	58	2.20	0.91	72000	60	30	0.34	0.69
94000	111	56	4.29	0.90	70000	59	29	0.60	0.67
93000	103	51	1.24	0.89	68000	56	28	0.55	0.65
92000	100	50	0.41	0.88	66000	54	27	0.42	0.63
88000	97	48	4.34	0.84	58000	47	24		

Table 13.5: PP |- SCG specimen, crack 23.2.

PP |- SCG 23.3									
Cycles (N)	Crack Length (μm)		dc/dN (m.cycle^{-1}) x 10^9	N/N_f	Cycles (N)	Crack Length (μm)		dc/dN (m.cycle^{-1}) x 10^9	N/N_f
	2c	c				2c	c		
104000	609	305	38.42	1.00	76000	247	123	7.83	0.73
103000	532	266	16.09	0.99	75000	231	116	0.28	0.72
102000	500	250	13.91	0.98	74000	231	115	3.29	0.71

PP |- SCG 23.3									
Cycles (N)	Crack Length (µm)		dc/dN (m.cycle^{-1}) x 10^{9}	N/N$_f$	Cycles (N)	Crack Length (µm)		dc/dN (m.cycle^{-1}) x 10^{9}	N/N$_f$
	2c	c				2c	c		
101000	472	236	24.16	0.97	72000	217	109	2.29	0.69
100000	424	212	10.25	0.96	71000	213	106	3.21	0.68
99000	404	202	1.39	0.95	70000	206	103	2.87	0.67
98000	401	200	6.54	0.94	68000	195	97	3.04	0.65
97000	388	194	8.17	0.93	66000	183	91	3.53	0.63
96000	371	186	5.14	0.92	64000	169	84	2.29	0.61
95000	361	181	2.98	0.91	62000	160	80	0.22	0.59
94000	355	178	3.57	0.90	60000	159	79	2.35	0.58
93000	348	174	1.16	0.89	54000	130	65	3.08	0.52
92000	346	173	13.33	0.88	52000	118	59	1.68	0.50
91000	319	159	0.16	0.87	50000	111	56	0.32	0.48
90000	319	159	3.76	0.86	48000	110	55	0.70	0.46
89000	311	156	1.77	0.85	42000	102	51	0.40	0.40
88000	308	154	2.32	0.84	40000	100	50	2.35	0.38
87000	303	151	3.93	0.83	38000	91	45	1.02	0.36
85000	287	144	8.72	0.82	30000	74	37	1.83	0.29
84000	270	135	1.06	0.81	28000	67	34	0.43	0.27
83000	268	134	1.08	0.80	22000	62	31	0.91	0.21
81000	263	132	1.83	0.78	20000	58	29	1.28	0.19
79000	256	128	4.01	0.76	17500	52	26		
78000	248	124	0.33	0.75					

Table 13.6: PP |- SCG specimen, crack 23.3.

13.1.3 LCG Results

PP |- CT3						
Crack Length (mm)		$\Delta K_{R=0.1}$ (MPa.m$^{0.5}$)			Cycles (N)	da/dN (mm.cycle^{-1}) x 10^{6}
Start	Finish	Start	Finish	Mean		
15.00	19.21	Pre-cracking			950000	Pre-cracking
19.21	19.59	3.96	4.02	3.99	1050000	4
19.59	19.71	4.02	4.05	4.04	1100000	2
19.71	20.27	4.05	4.15	4.10	1200000	6
20.27	20.78	4.15	4.25	4.20	1300000	5
20.78	21.61	4.25	4.42	4.33	1400000	8
21.61	22.02	4.42	4.50	4.46	1450000	8
22.02	22.46	4.50	4.60	4.55	1500000	9
22.46	23.00	4.60	4.72	4.66	1550000	11
23.00	23.63	4.72	4.86	4.79	1600000	13
23.63	24.32	4.86	5.03	4.95	1650000	14
24.32	25.05	5.03	5.21	5.12	1700000	15
25.05	25.86	5.21	5.43	5.32	1750000	16
25.86	26.89	5.43	5.73	5.58	1800000	21
26.89	27.52	5.73	5.93	5.83	1825000	25
27.52	28.19	5.93	6.15	6.04	1850000	27
28.19	29.04	6.15	6.45	6.30	1875000	34
29.04	30.05	6.45	6.84	6.65	1900000	40
30.05	30.62	6.84	7.08	6.96	1910000	57
30.62	31.17	7.08	7.32	7.20	1920000	55
31.17	31.76	7.32	7.60	7.46	1930000	59
31.76	32.53	7.60	8.00	7.80	1940000	77
32.53	33.33	8.00	8.44	8.22	1950000	80
33.33	34.41	8.44	9.11	8.78	1960000	108
34.41	35.04	9.11	9.55	9.33	1965000	126
35.04	35.85	9.55	10.16	9.86	1970000	162
35.85	36.80	10.16	10.97	10.57	1975000	190
36.80	38.02	10.97	12.18	11.58	1980000	244
38.02	38.72	12.18	12.98	12.58	1982500	280
38.72	39.61	12.98	14.12	13.55	1985000	356

PP |- CT3						
Crack Length (mm)		$\Delta K_{R=0.1}$ (MPa.m$^{0.5}$)			Cycles (N)	da/dN (mm.cycle^{-1}) x 10^{6}
Start	Finish	Start	Finish	Mean		
39.61	40.90	14.12	16.10	15.11	1987500	516
40.90	43.09	16.10	20.69	18.40	1990000	876

Table 13.7: PP |- LCG specimen CT3.

PP |- CT4						
Crack Length (mm)		$\Delta K_{R=0.1}$ (MPa.m$^{0.5}$)			Cycles (N)	da/dN (mm.cycle^{-1}) x 10^{6}
Start	Finish	Start	Finish	Mean		
15.00	18.37	Pre-cracking			100000	Pre-cracking
18.37	18.85	6.61	6.75	6.68	110000	48
18.85	19.40	6.75	6.92	6.84	120000	55
19.40	19.93	6.92	7.10	7.01	130000	53
19.93	20.49	7.10	7.28	7.19	140000	56
20.49	21.20	7.28	7.52	7.40	150000	71
21.20	21.91	7.52	7.78	7.65	160000	71
21.91	22.75	7.78	8.09	7.93	170000	84
22.75	23.75	8.09	8.49	8.29	180000	100
23.75	24.35	8.49	8.74	8.61	185000	120
24.35	24.88	8.74	8.97	8.86	190000	106
24.88	25.50	8.97	9.26	9.11	195000	124
25.50	26.25	9.26	9.62	9.44	200000	150
26.25	27.02	9.62	10.02	9.82	205000	154
27.02	27.86	10.02	10.48	10.25	210000	168
27.86	28.82	10.48	11.05	10.77	215000	192
28.82	29.32	11.05	11.38	11.22	217500	200
29.32	29.89	11.38	11.76	11.57	220000	228
29.89	30.50	11.76	12.20	11.98	222500	244
30.50	31.19	12.20	12.73	12.46	225000	276
31.19	32.02	12.73	13.42	13.07	227500	332
32.02	32.85	13.42	14.18	13.80	230000	332
32.85	33.21	14.18	14.53	14.35	231000	360
33.21	33.65	14.53	14.98	14.76	232000	440
33.65	34.12	14.98	15.49	15.23	233000	470
34.12	34.60	15.49	16.04	15.76	234000	480
34.60	35.14	16.04	16.70	16.37	235000	540
35.14	35.73	16.70	17.47	17.09	236000	590
35.73	36.64	17.47	18.79	18.13	237000	910
36.64	37.51	18.79	20.22	19.51	238000	870
37.51	38.04	20.22	21.18	20.70	238500	1060
38.04	38.88	21.18	22.86	22.02	239000	1680
38.88	40.19	22.86	25.97	24.42	239500	2620

Table 13.8: PP |- LCG specimen CT4.

13.2 Parent Plate ~ Parallel (PP //)

13.2.1 SCG Specimen S-N Results

Specimen number	Δσ (applied) (MPa) (R = 0.1)	Δσ (notch) (MPa) (R = 0.1)	Cycles to failure (*italics = did not fail*)	Comments
PP // SCG 1	288.4	282.6	49946	
PP // SCG 2	282.0	276.4	73052	
PP // SCG 3	275.6	270.2	81566	
PP // SCG 4	269.2	264.1	96040	
PP // SCG 5	262.7	258.1	76304	
PP // SCG 6	256.3	252.3	*2000000*	*Did not fail.*

Table 13.9: S-N test results for AA 5383-H321 parent plate parallel SCG specimens.

13.2.2 SCG Results

PP // SCG 8.1 (A + B)									
Cycles (N)	Crack Length (μm)		dc/dN (m.cycle^{-1}) x 10^9	N/N_f	Cycles (N)	Crack Length (μm)		dc/dN (m.cycle^{-1}) x 10^9	N/N_f
	2c	c				2c	c		
112000	591	296	28.93	0.98	106000	439	220	8.35	0.93
111000	534	267	13.50	0.98	105000	422	211	0.82	0.92
110000	507	253	6.20	0.97	104000	421	210	7.12	0.91
109000	494	247	11.33	0.96	103000	407	203		
108000	472	236	8.08	0.95	Coalescence				

Table 13.10: PP // SCG specimen, crack 8.1 (A+B).

PP // SCG 8.1A									
Cycles (N)	Crack Length (μm)		dc/dN (m.cycle^{-1}) x 10^9	N/N_f	Cycles (N)	Crack Length (μm)		dc/dN (m.cycle^{-1}) x 10^9	N/N_f
	2c	c				2c	c		
102000	75	37	3.33	0.90	87000	46	23	1.15	0.77
101000	68	34	1.71	0.90	84000	39	20	0.08	0.74
100000	64	32	0.70	0.89	83000	39	20	0.24	0.74
99000	63	32	2.36	0.88	80000	38	19	0.92	0.71
98000	58	29	1.25	0.87	78000	34	17	0.52	0.69
97000	56	28	0.03	0.86	76000	32	16	0.24	0.67
94000	56	28	1.35	0.83	70000	29	15	0.14	0.62
92000	50	25	0.14	0.82	66000	28	14	0.07	0.59
90000	50	25	0.66	0.80	56000	27	13	0.01	0.50
89000	48	24	0.56	0.79	44000	26	13		

Table 13.11: PP // SCG specimen, crack 8.1A.

PP // SCG 8.1B									
Cycles (N)	Crack Length (μm)		dc/dN (m.cycle^{-1}) x 10^9	N/N_f	Cycles (N)	Crack Length (μm)		dc/dN (m.cycle^{-1}) x 10^9	N/N_f
	2c	c				2c	c		
102000	330	165	3.76	0.90	84000	210	105	0.02	0.74
101000	322	161	0.29	0.89	81000	210	105	7.19	0.71
100000	322	161	1.36	0.88	80000	196	98	0.17	0.70
98000	316	158	4.98	0.86	78000	195	98	1.81	0.69
97000	306	153	0.76	0.85	76000	188	94	2.68	0.67
94000	302	151	6.32	0.83	74000	177	89	1.48	0.65
92000	276	138	4.61	0.81	72000	171	86	0.66	0.63
90000	258	129	6.92	0.79	70000	169	84	1.14	0.62

PP // SCG 8.1B									
Cycles (N)	Crack Length (μm)		dc/dN (m.cycle^{-1}) x 10^{9}	N/N_f	Cycles (N)	Crack Length (μm)		dc/dN (m.cycle^{-1}) x 10^{9}	N/N_f
	2c	c				2c	c		
89000	244	122	6.49	0.78	62000	151	75	1.83	0.54
88000	231	116	3.19	0.77	56000	129	64	0.26	0.49
86000	218	109	2.69	0.76	54000	128	64		
85000	213	107	1.29	0.75					

Table 13.12: PP // SCG specimen, crack 8.1B.

PP // SCG 8.2 (A+B)									
Cycles (N)	Crack Length (μm)		dc/dN (m.cycle^{-1}) x 10^{9}	N/N_f	Cycles (N)	Crack Length (μm)		dc/dN (m.cycle^{-1}) x 10^{9}	N/N_f
	2c	c				2c	c		
112000	602	301	48.51	0.98	96000	234	117	3.23	0.84
111000	505	252	39.38	0.98	95000	227	114	7.13	0.84
110000	426	213	8.63	0.97	94000	213	107	2.99	0.83
108000	391	196	12.90	0.95	93000	207	104	1.03	0.82
106000	340	170	6.01	0.93	92000	205	103	2.46	0.81
105000	328	164	12.27	0.92	89000	190	95	3.37	0.78
104000	303	152	0.94	0.91	87000	177	88	3.77	0.76
103000	301	151	4.31	0.91	86000	169	85	0.38	0.76
102000	293	146	7.48	0.90	84000	168	84	5.09	0.74
101000	278	139	8.19	0.89	83000	158	79	0.85	0.73
100000	261	131	4.44	0.88	80000	153	76	3.11	0.70
98000	244	122	4.41	0.86	78000	140	70		
97000	235	117	0.50	0.85	Coalescence				

Table 13.13: PP // SCG specimen, crack 8.2 (A+B).

PP // SCG 8.2A									
Cycles (N)	Crack Length (μm)		dc/dN (m.cycle^{-1}) x 10^{9}	N/N_f	Cycles (N)	Crack Length (μm)		dc/dN (m.cycle^{-1}) x 10^{9}	N/N_f
	2c	c				2c	c		
74000	112	56	0.82	0.65	62000	101	51	1.48	0.54
68000	103	51	0.10	0.60	56000	84	42		

Table 13.14: PP // SCG specimen, crack 8.2A.

PP // SCG 8.2B									
Cycles (N)	Crack Length (μm)		dc/dN (m.cycle^{-1}) x 10^{9}	N/N_f	Cycles (N)	Crack Length (μm)		dc/dN (m.cycle^{-1}) x 10^{9}	N/N_f
	2c	c				2c	c		
74000	38	19	0.13	0.65	62000	31	16	0.19	0.54
70000	37	18	0.74	0.62	52000	27	14		
68000	34	17	0.20	0.60					

Table 13.15: PP // SCG specimen, crack 8.2B.

PP // SCG 8.3									
Cycles (N)	Crack Length (μm)		dc/dN (m.cycle^{-1}) x 10^{9}	N/N_f	Cycles (N)	Crack Length (μm)		dc/dN (m.cycle^{-1}) x 10^{9}	N/N_f
	2c	c				2c	c		
111000	1009	504	105.46	0.98	86000	270	135	1.57	0.76
110000	798	399	14.47	0.97	85000	267	134	3.38	0.75
109000	769	384	26.66	0.96	84000	260	130	3.27	0.74
108000	716	358	49.69	0.95	83000	254	127	5.26	0.73
107000	616	308	11.12	0.94	81000	233	116	13.20	0.71
106000	594	297	6.51	0.93	80000	207	103	1.99	0.70

PP // SCG 8.3									
Cycles (N)	Crack Length (μm)		dc/dN (m.cycle^{-1}) x 10^{9}	N/N$_f$	Cycles (N)	Crack Length (μm)		dc/dN (m.cycle^{-1}) x 10^{9}	N/N$_f$
	2c	c				2c	c		
105000	581	291	19.40	0.92	78000	199	99	1.39	0.69
104000	542	271	7.89	0.91	76000	193	97	1.19	0.67
103000	526	263	15.10	0.91	70000	179	89	3.68	0.62
101000	466	233	11.58	0.89	68000	164	82	3.74	0.60
100000	443	221	11.54	0.88	66000	149	75	2.38	0.58
98000	397	198	5.75	0.86	64000	139	70	0.47	0.56
97000	385	193	7.76	0.85	62000	138	69	1.11	0.54
96000	370	185	7.01	0.84	56000	124	62	1.48	0.49
95000	356	178	9.01	0.84	52000	112	56	1.28	0.46
94000	338	169	6.87	0.83	48000	102	51	1.51	0.42
93000	324	162	2.33	0.82	40000	78	39	0.92	0.35
91000	315	157	7.92	0.80	36000	71	35	1.27	0.32
90000	299	149	0.29	0.79	32000	60	30	0.20	0.28
89000	298	149	2.51	0.78	28000	59	29	0.64	0.25
88000	293	147	2.64	0.77	24000	54	27	0.70	0.21
87000	288	144	8.80	0.76	20000	48	24		

Table 13.16: PP // SCG specimen, crack 8.3.

13.2.3 LCG Results

PP // CT3						
Crack Length (mm)		$\Delta K_{R=0.1}$ (MPa.m$^{0.5}$)			Cycles (N)	da/dN (mm.cycle^{-1}) x 10^{6}
Start	Finish	Start	Finish	Mean		
15.00	19.03	Pre-cracking			1050000	Pre-cracking
19.03	19.22	3.86	3.89	3.88	1100000	19.22
19.22	19.58	3.89	3.96	3.92	1200000	19.58
19.58	19.94	3.96	4.02	3.99	1300000	19.94
19.94	20.36	4.02	4.10	4.06	1400000	20.36
20.36	20.75	4.10	4.18	4.14	1500000	20.75
20.75	21.25	4.18	4.27	4.23	1600000	21.25
21.25	21.79	4.27	4.38	4.33	1700000	21.79
21.79	22.34	4.38	4.50	4.44	1800000	22.34
22.34	23.13	4.50	4.67	4.58	1900000	23.13
23.13	24.08	4.67	4.89	4.78	2000000	24.08
24.08	24.71	4.89	5.04	4.97	2050000	24.71
24.71	25.44	5.04	5.23	5.14	2100000	25.44
25.44	26.21	5.23	5.44	5.34	2150000	26.21
26.21	27.18	5.44	5.73	5.58	2200000	27.18
27.18	27.79	5.73	5.92	5.82	2225000	27.79
27.79	28.41	5.92	6.12	6.02	2250000	28.41
28.41	29.21	6.12	6.41	6.26	2275000	29.21
29.21	30.17	6.41	6.78	6.59	2300000	30.17
30.17	30.63	6.78	6.97	6.87	2310000	30.63
30.63	31.14	6.97	7.19	7.08	2320000	31.14
31.14	31.69	7.19	7.45	7.32	2330000	31.69
31.69	32.33	7.45	7.76	7.60	2340000	32.33
32.33	33.08	7.76	8.16	7.96	2350000	33.08
33.08	34.07	8.16	8.75	8.45	2360000	34.07
34.07	34.69	8.75	9.15	8.95	2365000	34.69
34.69	35.34	9.15	9.61	9.38	2370000	35.34
35.34	36.03	9.61	10.14	9.88	2375000	36.03
36.03	36.93	10.14	10.91	10.53	2380000	36.93
36.93	37.40	10.91	11.35	11.13	2382500	37.40
37.40	37.99	11.35	11.95	11.65	2385000	37.99
37.99	38.62	11.95	12.65	12.30	2387500	38.62
38.62	39.42	12.65	13.64	13.14	2390000	39.42
39.42	40.65	13.64	15.43	14.53	2392500	40.65
40.65	42.23	15.43	18.36	16.90	2395000	42.23

Table 13.17: PP // LCG specimen CT3.

PP // CT4						
Crack Length (mm)		$\Delta K_{R=0.1}$ (MPa.m$^{0.5}$)			Cycles (N)	da/dN (mm.cycle^{-1}) x 10^{6}
Start	Finish	Start	Finish	Mean		
15.00	18.44	Pre-cracking			110000	Pre-cracking
18.44	18.91	6.67	6.82	6.75	120000	47
18.91	19.17	6.82	6.90	6.86	125000	52
19.17	19.49	6.90	7.00	6.95	130000	64
19.49	19.81	7.00	7.11	7.06	135000	64
19.81	20.13	7.11	7.21	7.16	140000	64
20.13	20.48	7.21	7.33	7.27	145000	70
20.48	20.90	7.33	7.47	7.40	150000	84
20.90	21.39	7.47	7.65	7.56	155000	98
21.39	21.88	7.65	7.82	7.73	160000	98
21.88	22.41	7.82	8.02	7.92	165000	106
22.41	23.00	8.02	8.25	8.13	170000	118
23.00	23.63	8.25	8.50	8.37	175000	126
23.63	24.35	8.50	8.80	8.65	180000	144
24.35	25.12	8.80	9.15	8.98	185000	154
25.12	25.96	9.15	9.55	9.35	190000	168
25.96	26.78	9.55	9.96	9.75	195000	164
26.78	27.60	9.96	10.41	10.18	200000	164
27.60	28.57	10.41	10.98	10.69	205000	194
28.57	29.06	10.98	11.29	11.13	207500	196
29.06	29.57	11.29	11.63	11.46	210000	204
29.57	30.11	11.63	12.00	11.81	212500	216
30.11	30.77	12.00	12.49	12.25	215000	264
30.77	31.42	12.49	13.01	12.75	217500	260
31.42	32.09	13.01	13.58	13.29	220000	268
32.09	33.02	13.58	14.45	14.01	222500	372
33.02	33.99	14.45	15.46	14.95	225000	388
33.99	34.50	15.46	16.04	15.75	226000	510
34.50	35.06	16.04	16.72	16.38	227000	560
35.06	35.71	16.72	17.57	17.15	228000	650
35.71	36.49	17.57	18.70	18.14	229000	780
36.49	37.54	18.70	20.42	19.56	230000	1050
37.54	38.22	20.42	21.68	21.05	230500	1360

Table 13.18: PP // LCG specimen CT4.

13.3 MIG Low Input (MIG LI)

13.3.1 SCG Specimen S-N Results

Specimen number	Δσ (applied at weld toe) (MPa) (R = 0.1)	Δσ (MPa) (R = 0.1)		Cycles to failure (*italics = did not fail/omitted*)	Comments
		Weld metal	Notch (weld toe)		
MIG LI SCG 1	288.4	244.7	286.2	34238	Failed in weld metal.
MIG LI SCG 2	282.0	234.5	279.8	54449	Failed in weld metal.
MIG LI SCG 3	275.6		273.5	69348	Failed at weld toe.
MIG LI SCG 4	269.2		267.2	54146	Failed at weld toe.
MIG LI SCG 5	262.7		260.8	81250	Failed at weld toe.
MIG LI SCG 6	256.3	206.3	254.5	62099	Failed in weld metal.
MIG LI SCG 7	249.9	201.2	248.2	91777	Failed in weld metal.
MIG LI SCG 8	243.5	196.2	241.9	116169	Failed in weld metal.
MIG LI SCG 9	237.1	191.4	235.5	146745	Failed in weld metal.
MIG LI SCG 10	224.3	184.0	222.9	170299	Failed in weld metal.
MIG LI SCG 11	211.5	173.5	210.3	275905	Failed in weld metal.
MIG LI SCG 12	198.7	163.0	197.7	318769	Failed in weld metal.
MIG LI SCG 13	185.8	152.5	185.2	823614	Failed in weld metal.
MIG LI SCG 14	173.0		172.8	*2000000*	*Did not fail.*
MIG LI SCG 15	*249.9*			*39066*	*Failed due to porosity, omitted from S-N curve.*
MIG LI SCG 16	*173.0*			*128899*	*Failed due to porosity, omitted from S-N curve.*

Table 13.19: S-N test results for AA 5383-H321 MIG LI butt welds, short crack growth specimens.

13.3.2 SCG Results

MIG LI SCG 3.1 (A+B)								
Cycles (N)	Crack Length μm)		dc/dN ($m.cycle^{-1}$) x 10^9	N/N_f	Cycles (N)	Crack Length (μm)		dc/dN ($m.cycle^{-1}$) x 10^9	N/N_f
	2c	c				2c	c		
81000	2151	1076	Edge crack		Coalescence				
80000	2089	1044							

Table 13.20: MIG LI SCG specimen, crack 3.1 (A+B).

MIG LI SCG 3.1A								
Cycles (N)	Crack Length (μm)		dc/dN ($m.cycle^{-1}$) x 10^9	N/N_f	Cycles (N)	Crack Length (μm)		dc/dN ($m.cycle^{-1}$) x 10^9	N/N_f
	2c	c				2c	c		
79000	937	468	107.78	0.97	56000	269	135	2.03	0.69
78000	721	361	16.73	0.96	52000	253	126	1.83	0.64
76000	654	327	57.31	0.93	50000	246	123	3.74	0.61
75000	540	270	6.95	0.92	46000	216	108	3.84	0.56
74000	526	263	9.52	0.91	44000	200	100	0.31	0.54
73000	507	253	4.47	0.90	42000	199	100	3.47	0.52
72000	498	249	4.98	0.88	38000	171	86	4.50	0.47
70000	478	239	12.43	0.86	36000	153	77	1.53	0.44
68000	428	214	7.58	0.83	34000	147	74	0.56	0.42

MIG LI SCG 3.1A									
Cycles (N)	Crack Length (μm)		dc/dN ($m.cycle^{-1}$) x 10^9	N/N_f	Cycles (N)	Crack Length (μm)		dc/dN ($m.cycle^{-1}$) x 10^9	N/N_f
	2c	c				2c	c		
66000	398	199	13.05	0.81	32000	145	72	1.67	0.39
64000	346	173	3.39	0.78	30000	138	69	1.20	0.37
62000	332	166	3.18	0.76	28000	133	67	1.50	0.34
60000	319	160	10.26	0.74	26000	128	64		
58000	278	139	2.29	0.71					

Table 13.21: MIG LI SCG specimen, crack 3.1A.

MIG LI SCG 3.1B									
Cycles (N)	Crack Length (μm)		dc/dN ($m.cycle^{-1}$) x 10^9	N/N_f	Cycles (N)	Crack Length (μm)		dc/dN ($m.cycle^{-1}$) x 10^9	N/N_f
	2c	c				2c	c		
79000	928	464	55.75	0.97	48000	160	80	3.60	0.59
78000	817	408	94.89	0.96	46000	145	73	1.39	0.56
77000	627	314	11.78	0.94	44000	140	70	4.60	0.54
76000	604	302	15.18	0.93	42000	121	61	2.27	0.52
75000	573	287	24.97	0.92	40000	112	56	1.58	0.49
74000	523	262	20.70	0.91	38000	106	53	4.78	0.47
73000	482	241	11.01	0.90	36000	87	43	1.28	0.44
72000	460	230	15.24	0.88	34000	82	41	1.11	0.42
70000	399	199	6.19	0.86	32000	77	39	0.43	0.39
68000	374	187	8.54	0.83	30000	76	38	2.67	0.37
66000	340	170	2.75	0.81	28000	65	32	1.16	0.34
64000	329	165	10.77	0.78	26000	60	30	0.44	0.32
62000	286	143	6.34	0.76	24000	58	29	1.65	0.29
58000	235	118	6.68	0.71	22000	52	26	1.19	0.27
56000	208	104	1.34	0.69	20000	47	24	0.79	0.25
52000	198	99	3.44	0.64	12500	35	18		
50000	184	92	6.08	0.61					

Table 13.22: MIG LI SCG specimen, crack 3.1B.

MIG LI SCG 3.2									
Cycles (N)	Crack Length (μm)		dc/dN ($m.cycle^{-1}$) x 10^9	N/N_f	Cycles (N)	Crack Length (μm)		dc/dN ($m.cycle^{-1}$) x 10^9	N/N_f
	2c	c				2c	c		
81000	659	329	55.94	0.99	50000	157	79	5.99	0.61
80000	547	274	53.17	0.98	48000	133	67	3.91	0.59
79000	441	220	4.97	0.97	46000	118	59	2.40	0.56
78000	431	215	14.75	0.96	44000	108	54	0.65	0.54
76000	372	186	9.58	0.93	42000	106	53	1.53	0.52
75000	353	176	14.96	0.92	40000	99	50	3.01	0.49
74000	323	161	1.47	0.91	38000	87	44	2.08	0.47
73000	320	160	5.38	0.90	36000	79	40	0.02	0.44
72000	309	155	6.35	0.88	34000	79	39	1.13	0.42
70000	284	142	4.04	0.86	32000	74	37	0.58	0.39
68000	267	134	3.52	0.83	30000	72	36	0.52	0.37
66000	253	127	3.36	0.81	26000	68	34	1.93	0.32
62000	227	113	4.89	0.76	24000	60	30	2.48	0.29
58000	187	94	0.08	0.71	22000	50	25	1.07	0.27
56000	187	94	4.06	0.69	17500	41	20	2.35	0.21
54000	171	85	2.09	0.66	15000	29	15	0.63	0.18
52000	162	81	1.29	0.64	12500	26	13		

Table 13.23: MIG LI SCG specimen, crack 3.2.

MIG LI SCG 3.3 (A+B)									
Cycles (N)	Crack Length (μm)		dc/dN ($m.cycle^{-1}$) x 10^9	N/N_f	Cycles (N)	Crack Length (μm)		dc/dN ($m.cycle^{-1}$) x 10^9	N/N_f
	2c	c				2c	c		
80000	398	199	9.24	0.98	74000	367	183	3.68	0.91
79000	380	190	4.52	0.97	73000	360	180		
78000	371	185	0.62	0.96	Coalescence				
75000	367	184	0.17	0.92					

Table 13.24: MIG LI SCG specimen, crack 3.3 (A+B).

MIG LI SCG 3.3A									
Cycles (N)	Crack Length (μm)		dc/dN ($m.cycle^{-1}$) x 10^9	N/N_f	Cycles (N)	Crack Length (μm)		dc/dN ($m.cycle^{-1}$) x 10^9	N/N_f
	2c	c				2c	c		
72000	169	84	3.53	0.88	50000	100	50	1.06	0.61
70000	155	77	2.22	0.86	48000	96	48	1.81	0.59
68000	146	73	0.49	0.83	46000	89	44	1.40	0.56
64000	142	71	3.04	0.78	42000	78	39	0.19	0.52
62000	130	65	2.02	0.76	38000	76	38	2.58	0.47
60000	122	61	0.55	0.74	34000	56	28	0.96	0.42
58000	119	60	1.02	0.71	30000	48	24	0.62	0.37
56000	115	58	0.69	0.69	26000	43	22	0.32	0.32
54000	113	56	1.73	0.66	24000	42	21		
52000	106	53	1.33	0.64					

Table 13.25: MIG LI SCG specimen, crack 3.3A.

MIG LI SCG 3.3B									
Cycles (N)	Crack Length (μm)		dc/dN ($m.cycle^{-1}$) x 10^9	N/N_f	Cycles (N)	Crack Length (μm)		dc/dN ($m.cycle^{-1}$) x 10^9	N/N_f
	2c	c				2c	c		
72000	159	79	2.49	0.88	46000	85	42	1.80	0.56
68000	139	69	2.66	0.83	40000	63	31	0.37	0.49
66000	128	64	1.18	0.81	38000	61	31	1.24	0.47
64000	123	62	3.81	0.78	34000	52	26	0.75	0.42
62000	108	54	1.72	0.76	32000	49	24	0.20	0.39
58000	94	47	0.11	0.71	30000	48	24	0.98	0.37
52000	93	47	0.73	0.64	28000	44	22	1.40	0.34
50000	90	45	0.69	0.61	26000	38	19		

Table 13.26: MIG LI SCG specimen, crack 3.3B.

MIG LI SCG 3.4									
Cycles (N)	Crack Length (μm)		dc/dN ($m.cycle^{-1}$) x 10^9	N/N_f	Cycles (N)	Crack Length (μm)		dc/dN ($m.cycle^{-1}$) x 10^9	N/N_f
	2c	c				2c	c		
81000	178.41	89	7.10	0.99	52000	86.70	43	0.68	0.64
80000	164.21	82	2.18	0.98	50000	83.98	42	1.05	0.61
75000	142.37	71	0.58	0.92	46000	75.56	38	0.30	0.56
72000	138.88	69	4.61	0.88	44000	74.37	37	0.16	0.54
71000	129.66	65	2.64	0.87	38000	72.41	36	0.54	0.47
70000	124.38	62	0.24	0.86	34000	68.13	34	0.27	0.42
68000	123.41	62	0.16	0.83	26000	63.79	32	0.12	0.32
64000	122.15	61	1.97	0.78	22000	62.82	31	0.46	0.27
62000	114.29	57	1.53	0.76	17500	58.69	29	0.18	0.21
60000	108.18	54			15000	57.80	29	0.57	0.18
Coalescence					12500	54.96	27	0.43	0.15
56000	89.92	45	0.40	0.69	10000	52.82	26		

Table 13.27: MIG LI SCG specimen, crack 3.4.

13.3.3 LCG Results

MIG LI CT1						
Crack Length (mm)		ΔK (MPa.m$^{0.5}$)			Cycles (N)	da/dN (mm.cycle^{-1}) x 10^{6}
Start	Finish	Start	Finish	Mean		
15.00	19.23	Pre-cracking			90000	Pre-cracking
19.23	19.44	9.74	9.83	9.78	100000	21
19.44	20.04	9.83	10.10	9.97	110000	60
20.04	20.44	10.10	10.29	10.20	115000	80
20.44	20.84	10.29	10.48	10.39	120000	80
20.84	21.12	10.48	10.62	10.55	125000	56
21.12	21.56	10.62	10.84	10.73	130000	88
21.56	21.91	10.84	11.02	10.93	135000	70
21.91	22.41	11.02	11.28	11.15	140000	100
22.41	22.84	11.28	11.51	11.40	145000	86
22.84	23.43	11.51	11.84	11.68	150000	118
23.43	23.97	11.84	12.16	12.00	155000	108
23.97	24.64	12.16	12.56	12.36	160000	134
24.64	25.28	12.56	12.97	12.77	165000	128
25.28	26.10	12.97	13.52	13.25	170000	164
26.10	26.50	13.52	13.81	13.67	172500	160
26.50	27.11	13.81	14.26	14.03	175000	244
27.11	27.79	14.26	14.79	14.53	177500	272
27.79	28.50	14.79	15.38	15.09	180000	284
28.50	29.21	15.38	16.02	15.70	182000	355
29.21	29.73	16.02	16.51	16.26	184000	260
29.73	30.07	16.51	16.84	16.68	185000	340
30.07	30.54	16.84	17.33	17.09	186000	470
30.54	31.04	17.33	17.87	17.60	187000	500
31.04	31.62	17.87	18.53	18.20	188000	580
31.62	32.28	18.53	19.34	18.94	189000	660
32.28	32.98	19.34	20.27	19.80	190000	700
32.98	33.57	20.27	21.11	20.69	190500	1180
33.57	34.37	21.11	22.35	21.73	191000	1600
34.37	35.24	22.35	23.84	23.09	191500	1740
35.24	36.84	23.84	27.07	25.46	192000	3200

Table 13.28: MIG LI (AA 5083-H321) LCG specimen CT1.

MIG LI CT2						
Crack Length (mm)		ΔK (MPa.m$^{0.5}$)			Cycles (N)	da/dN (mm.cycle^{-1}) x 10^{6}
Start	Finish	Start	Finish	Mean		
15.00	23.48	Pre-cracking			3425000	Pre-cracking
23.48	24.15	9.54	9.85	9.69	3450000	27
24.15	24.83	9.85	10.19	10.02	3475000	27
24.83	25.73	10.19	10.66	10.42	3500000	36
25.73	26.18	10.66	10.91	10.78	3510000	45
26.18	26.67	10.91	11.19	11.05	3520000	49
26.67	27.28	11.19	11.56	11.38	3530000	61
27.28	28.05	11.56	12.05	11.81	3540000	77
28.05	28.79	12.05	12.56	12.31	3550000	74
28.79	29.24	12.56	12.89	12.72	3555000	90
29.24	29.91	12.89	13.40	13.15	3560000	134
29.91	30.67	13.40	14.03	13.72	3565000	152
30.67	31.57	14.03	14.84	14.43	3570000	180
31.57	32.17	14.84	15.42	15.13	3572500	240
32.17	32.80	15.42	16.08	15.75	3575000	252
32.80	33.65	16.08	17.05	16.57	3577500	340
33.65	34.92	17.05	18.69	17.87	3580000	508
34.92	35.90	18.69	20.16	19.42	3581000	980
35.90	36.51	20.16	21.16	20.66	3581500	1220
36.51	37.82	21.16	23.64	22.40	3582000	2620

Table 13.29: MIG LI (AA 5083-H321) LCG specimen CT2.

MIG LI CT3						
Crack Length (mm)		ΔK (MPa.m$^{0.5}$)			Cycles (N)	da/dN (mm.cycle^{-1}) x 10^{6}
Start	Finish	Start	Finish	Mean		
15.00	18.39	Pre-cracking			1300000	Pre-cracking
18.39	18.71	7.05	7.16	7.11	1400000	3
18.71	19.12	7.16	7.29	7.23	1500000	4
19.12	19.57	7.29	7.45	7.37	1600000	4
19.57	20.08	7.45	7.62	7.53	1700000	5
20.08	20.85	7.62	7.90	7.76	1800000	8
20.85	21.95	7.90	8.31	8.11	1900000	11
21.95	22.79	8.31	8.65	8.48	1950000	17
22.79	23.96	8.65	9.15	8.90	2000000	23
23.96	24.74	9.15	9.51	9.33	2025000	31
24.74	25.81	9.51	10.03	9.77	2050000	43
25.81	26.34	10.03	10.31	10.17	2060000	53
26.34	26.94	10.31	10.64	10.48	2070000	60
26.94	27.71	10.64	11.09	10.87	2080000	77
27.71	28.65	11.09	11.68	11.39	2090000	94
28.65	29.83	11.68	12.51	12.09	2100000	118
29.83	30.60	12.51	13.10	12.80	2105000	154
30.60	31.50	13.10	13.85	13.47	2110000	180
31.50	32.04	13.85	14.34	14.09	2112500	216
32.04	32.74	14.34	15.02	14.68	2115000	280
32.74	33.63	15.02	15.96	15.49	2117500	356
33.63	34.82	15.96	17.40	16.68	2120000	476
34.82	35.39	17.40	18.16	17.78	2121000	570
35.39	36.20	18.16	19.35	18.76	2122000	810
36.20	37.58	19.35	21.71	20.53	2123000	1380

Table 13.30: MIG LI (AA 5083-H321) LCG specimen CT3.

13.4 MIG High Input (MIG HI)

13.4.1 SCG Specimen S-N Results

Specimen number	Δσ (applied at weld toe) (MPa) (R = 0.1)	Δσ (MPa) (R = 0.1)		Cycles to failure (*italics = did not fail/omitted*)	Comments
		Weld metal	Notch (weld toe)		
MIG HI SCG 1	288.4		286.2	36986	
MIG HI SCG 2	275.6		273.5	39988	
MIG HI SCG 3	262.7		260.8	71197	
MIG HI SCG 4	249.9		248.2	99437	
MIG HI SCG 5	237.1		235.5	152597	
MIG HI SCG 6	224.3		222.9	177597	
MIG HI SCG 7	211.5		210.3	252236	
MIG HI SCG 8	198.7		197.7	393370	
MIG HI SCG 9	185.8		185.2	1254147	
MIG HI SCG 10	173.0		172.8	*2000000*	*Did not fail.*

Table 13.31: S-N test results for AA 5383-H321 MIG HI butt welds, short crack growth specimens.

13.4.2 SCG Results

MIG HI SCG 11.1									
Cycles (N)	Crack Length (μm)		dc/dN ($m.cycle^{-1}$) x 10^9	N/N_f	Cycles (N)	Crack Length (μm)		dc/dN ($m.cycle^{-1}$) x 10^9	N/N_f
	2c	c				2c	c		
100000	404	202	5.15	0.99	71000	205	102	3.48	0.70
99000	394	197	0.61	0.98	70000	198	99	4.45	0.69
98000	392	196	1.28	0.97	68000	180	90	4.59	0.67
97000	390	195	20.63	0.96	66000	161	81	0.20	0.65
96000	349	174	3.79	0.95	64000	161	80	3.38	0.63
95000	341	171	0.42	0.94	62000	147	74	2.46	0.61
92000	339	169	3.92	0.91	58000	128	64	0.93	0.57
90000	323	161	6.41	0.89	52000	116	58	0.29	0.51
89000	310	155	8.03	0.88	50000	115	58	4.18	0.50
88000	294	147	1.51	0.87	48000	99	49	1.79	0.48
86000	288	144	6.40	0.85	46000	91	46	0.22	0.46
85000	275	138	1.59	0.84	42000	90	45	3.01	0.42
83000	269	134	1.10	0.82	40000	78	39	1.48	0.40
81000	264	132	1.86	0.80	36000	66	33	1.19	0.36
80000	261	130	10.22	0.79	32000	56	28	0.13	0.32
79000	240	120	5.91	0.78	30000	56	28	0.86	0.30
78000	229	114	0.84	0.77	28000	52	26	0.39	0.28
76000	225	113	1.28	0.75	24000	49	25	0.53	0.24
75000	223	111	3.19	0.74	22000	47	24	0.16	0.22
74000	216	108	1.45	0.73	20000	46	23	0.41	0.20
73000	213	107	2.19	0.72	12500	40	20	8.04	0.12

Table 13.32: MIG HI SCG specimen, crack 11.1.

MIG HI SCG 11.2 ((A+B)+C)									
Cycles (N)	Crack Length (μm)		dc/dN (m.cycle^{-1}) x 10^9	N/N_f	Cycles (N)	Crack Length (μm)		dc/dN (m.cycle^{-1}) x 10^9	N/N_f
	2c	c				2c	c		
99000	847	424	27.95	0.98	96000	723	361		
98000	791	396	17.06	0.97	Coalescence				

Table 13.33: MIG HI SCG specimen, crack 11.2 ((A+B)+C).

MIG HI SCG 11.2 (A+B)									
Cycles (N)	Crack Length (μm)		dc/dN (m.cycle^{-1}) x 10^9	N/N_f	Cycles (N)	Crack Length (μm)		dc/dN (m.cycle^{-1}) x 10^9	N/N_f
	2c	c				2c	c		
94000	692	346	21.33	0.93	87000	573	287		
92000	607	303	6.88	0.91	Coalescence				
91000	593	296	2.46	0.90					

Table 13.34: MIG HI SCG specimen, crack 11.2 (A+B).

MIG HI SCG 11.2C									
Cycles (N)	Crack Length (μm)		dc/dN (m.cycle^{-1}) x 10^9	N/N_f	Cycles (N)	Crack Length (μm)		dc/dN (m.cycle^{-1}) x 10^9	N/N_f
	2c	c				2c	c		
93000	67	34	3.53	0.92	87000	48	24	0.88	0.86
92000	60	30	2.00	0.91	85000	45	22	2.63	0.84
91000	56	28	2.52	0.90	83000	34	17	0.25	0.82
90000	51	26	0.54	0.89	80000	33	16	0.23	0.79
89000	50	25	0.58	0.88	76000	31	15	0.42	0.75
88000	49	25	0.51	0.87	71000	27	13		

Table 13.35: MIG HI SCG specimen, crack 11.2C.

MIG HI SCG 11.2A									
Cycles (N)	Crack Length (μm)		dc/dN (m.cycle^{-1}) x 10^9	N/N_f	Cycles (N)	Crack Length (μm)		dc/dN (m.cycle^{-1}) x 10^9	N/N_f
	2c	c				2c	c		
84000	312	156	8.09	0.83	56000	131	65	1.57	0.55
83000	296	148	6.12	0.82	54000	125	62	2.59	0.53
80000	259	129	1.66	0.79	50000	104	52	0.99	0.50
78000	252	126	1.49	0.77	46000	96	48	4.08	0.46
77000	249	125	4.60	0.76	44000	80	40	0.36	0.44
76000	240	120	6.54	0.75	42000	78	39	1.66	0.42
75000	227	114	6.47	0.74	40000	72	36	1.19	0.40
74000	214	107	7.14	0.73	36000	62	31	0.00	0.36
73000	200	100	3.24	0.72	34000	62	31	1.39	0.34
72000	193	97	4.08	0.71	32000	57	28	3.28	0.32
71000	185	93	0.36	0.70	30000	44	22	0.96	0.30
70000	184	92	3.46	0.69	28000	40	20	0.57	0.28
64000	143	71	0.60	0.63	24000	35	18	0.06	0.24
58000	136	68	1.21	0.57	20000	35	17		

Table 13.36: MIG HI SCG specimen, crack 11.2A.

MIG HI SCG 11.2B									
Cycles (N)	Crack Length (μm)		dc/dN (m.cycle^{-1}) x 10^9	N/N_f	Cycles (N)	Crack Length (μm)		dc/dN (m.cycle^{-1}) x 10^9	N/N_f
	2c	c				2c	c		
84000	222	111	2.32	0.83	56000	100	50	1.04	0.55
78000	194	97	5.91	0.77	54000	96	48	2.32	0.53
77000	183	91	0.67	0.76	50000	78	39	0.32	0.50

MIG HI SCG 11.2B									
Cycles (N)	Crack Length (μm)		dc/dN (m.cycle^{-1}) x 10^{9}	N/N_f	Cycles (N)	Crack Length (μm)		dc/dN (m.cycle^{-1}) x 10^{9}	N/N_f
	2c	c				2c	c		
76000	181	91	3.66	0.75	46000	75	38	1.61	0.46
74000	167	83	0.31	0.73	44000	69	34	0.24	0.44
72000	165	83	0.81	0.71	42000	68	34	0.13	0.42
71000	164	82	2.30	0.70	40000	67	34	0.47	0.40
70000	159	80	4.11	0.69	34000	62	31	1.13	0.34
68000	143	71	3.19	0.67	32000	57	29	3.16	0.32
66000	130	65	5.33	0.65	30000	44	22	0.66	0.30
64000	109	54	0.72	0.63	28000	42	21	0.08	0.28
60000	103	51	0.61	0.59	20000	41	20		
58000	101	50	0.04	0.57					

Table 13.37: MIG HI SCG specimen, crack 11.2B.

MIG HI SCG 11.3									
Cycles (N)	Crack Length (μm)		dc/dN (m.cycle^{-1}) x 10^{9}	N/N_f	Cycles (N)	Crack Length (μm)		dc/dN (m.cycle^{-1}) x 10^{9}	N/N_f
	2c	c				2c	c		
100000	679	339	75.55	0.99	73000	216	108	4.76	0.72
99000	528	264	18.05	0.98	72000	206	103	11.20	0.71
98000	492	246	14.54	0.97	71000	184	92	1.30	0.70
97000	463	231	9.78	0.96	68000	176	88	4.00	0.67
95000	423	212	10.20	0.94	66000	160	80	2.12	0.65
94000	403	202	5.98	0.93	64000	152	76	3.01	0.63
93000	391	196	7.60	0.92	60000	128	64	2.01	0.59
90000	345	173	7.72	0.89	58000	119	60	1.14	0.57
89000	330	165	3.51	0.88	54000	110	55	3.03	0.53
88000	323	162	15.13	0.87	52000	98	49	0.11	0.51
87000	293	146	4.25	0.86	50000	98	49	1.72	0.50
83000	259	129	0.59	0.82	46000	84	42	2.20	0.46
82000	258	129	5.47	0.81	42000	66	33	1.20	0.42
81000	247	123	1.80	0.80	40000	62	31	2.83	0.40
80000	243	122	1.78	0.79	38000	50	25	0.84	0.38
79000	239	120	4.24	0.78	34000	44	22	0.21	0.34
78000	231	116	1.47	0.77	28000	41	21	0.08	0.28
77000	228	114	2.27	0.76	24000	40	20	1.49	0.24
76000	224	112	0.86	0.75	22000	35	17	0.44	0.22
75000	222	111	2.08	0.74	20000	33	16	0.10	0.20
74000	218	109	0.95	0.73	10000	31	15		

Table 13.38: MIG HI SCG specimen, crack 11.3.

13.4.3 LCG Results

MIG HI CT2						
Crack Length (mm)		$\Delta K_{R=0.1}$ (MPa.m$^{0.5}$)			Cycles (N)	da/dN (mm.cycle^{-1}) x 10^{6}
Start	Finish	Start	Finish	Mean		
15.00	18.53	Pre-cracking			1500000	Pre-cracking
18.53	18.92	4.30	4.38	4.34	1600000	4
18.92	19.32	4.38	4.46	4.42	1700000	4
19.32	19.59	4.46	4.51	4.49	1800000	3
19.59	19.93	4.51	4.58	4.55	1900000	3
19.93	20.29	4.58	4.66	4.62	2000000	4
20.29	20.58	4.66	4.72	4.69	2100000	3
20.58	21.07	4.72	4.83	4.78	2200000	5
21.07	21.15	4.83	4.85	4.84	2300000	1
21.15	21.41	4.85	4.91	4.88	2400000	3
21.41	21.82	4.91	5.00	4.96	2500000	4
21.82	22.14	5.00	5.08	5.04	2600000	3
22.14	22.47	5.08	5.16	5.12	2700000	3

MIG HI CT2						
Crack Length (mm)		$\Delta K_{R=0.1}$ (MPa.m$^{0.5}$)			Cycles (N)	da/dN (mm.cycle^{-1}) x 10^{6}
Start	Finish	Start	Finish	Mean		
22.47	22.92	5.16	5.27	5.21	2800000	5
22.92	23.28	5.27	5.36	5.32	2900000	4
23.28	23.71	5.36	5.47	5.42	3000000	4
23.71	24.21	5.47	5.61	5.54	3100000	5
24.21	24.73	5.61	5.76	5.68	3200000	5
24.73	25.28	5.76	5.92	5.84	3300000	6
25.28	26.00	5.92	6.14	6.03	3400000	7
26.00	27.11	6.14	6.50	6.32	3500000	11
27.11	27.85	6.50	6.77	6.64	3550000	15
27.85	28.97	6.77	7.20	6.99	3600000	22
28.97	29.79	7.20	7.56	7.38	3625000	33
29.79	30.94	7.56	8.10	7.83	3650000	46
30.94	31.52	8.10	8.40	8.25	3660000	58
31.52	32.24	8.40	8.80	8.60	3670000	72
32.24	33.19	8.80	9.38	9.09	3680000	95
33.19	33.75	9.38	9.75	9.56	3685000	112
33.75	34.35	9.75	10.18	9.96	3690000	120
34.35	35.08	10.18	10.74	10.46	3695000	146
35.08	35.96	10.74	11.50	11.12	3700000	176
35.96	36.96	11.50	12.47	11.98	3705000	200
36.96	37.63	12.47	13.20	12.84	3707500	268
37.63	38.51	13.20	14.28	13.74	3710000	352

Table 13.39: MIG HI LCG specimen CT2.

MIG HI CT3						
Crack Length (mm)		$\Delta K_{R=0.1}$ (MPa.m$^{0.5}$)			Cycles (N)	da/dN (mm.cycle^{-1}) x 10^{6}
Start	Finish	Start	Finish	Mean		
15.00	18.81	Pre-cracking			250000	Pre-cracking
18.81	19.32	18.81	19.32	7.32	275000	20
19.32	19.98	19.32	19.98	7.52	300000	26
19.98	20.82	19.98	20.82	7.79	325000	34
20.82	21.88	20.82	21.88	8.14	350000	42
21.88	22.32	21.88	22.32	8.42	360000	44
22.32	22.86	22.32	22.86	8.62	370000	54
22.86	23.60	22.86	23.60	8.89	380000	74
23.60	24.27	23.60	24.27	9.20	390000	67
24.27	25.29	24.27	25.29	9.59	400000	102
25.29	25.83	25.29	25.83	9.97	405000	108
25.83	26.39	25.83	26.39	10.26	410000	112
26.39	26.96	26.39	26.96	10.56	415000	114
26.96	27.66	26.96	27.66	10.92	420000	140
27.66	28.41	27.66	28.41	11.36	425000	150
28.41	29.30	28.41	29.30	11.90	430000	178
29.30	29.77	29.30	29.77	12.37	432500	188
29.77	30.31	29.77	30.31	12.74	435000	216
30.31	30.92	30.31	30.92	13.19	437500	244
30.92	31.56	30.92	31.56	13.71	440000	256
31.56	32.39	31.56	32.39	14.38	442500	332
32.39	33.32	32.39	33.32	15.24	445000	372
33.32	33.87	33.32	33.87	16.03	446000	550
33.87	34.37	33.87	34.37	16.63	447000	500
34.37	34.94	34.37	34.94	17.30	448000	570
34.94	35.71	34.94	35.71	18.20	449000	770
35.71	36.71	35.71	36.71	19.51	450000	1000

Table 13.40: MIG HI LCG specimen CT3.

13.5 FS Single Pass (FS SP)

13.5.1 SCG Specimen S-N Results

Specimen number	Δσ (applied) (MPa) (R = 0.1)	Δσ (notch) (MPa) (R = 0.1)	Cycles to failure (*italics = did not fail/omitted*)	Comments
FS SP SCG 1	288.4	287.5	36427	PFD evident.
FS SP SCG 2	275.6	274.7	73602	
FS SP SCG 3	262.7	261.9	96822	
FS SP SCG 4	249.9	249.2	122699	
FS SP SCG 5	237.1	236.4	222105	
FS SP SCG 6	224.3	223.6	234234	
FS SP SCG 7	211.5	210.8	896292	PFD evident.
FS SP SCG 8	198.7	198.1	*2000000*	*Did not fail.*
FS SP SCG 9	*249.9*	249.2	*44802*	*Failed due to PFD, omitted from S-N curve.*
FS SP SCG 10	*224.3*	223.6	*135773*	*Failed due to edge initiated crack, omitted from S-N curve.*
FS SP SCG 11	*211.5*	210.8	*74445*	*Failed due to edge initiated crack, omitted from S-N curve.*
FS SP SCG 12	*211.5*	210.8	*47102*	*Failed due to PFD, omitted from S-N curve.*
FS SP SCG 13	*211.5*	210.8	*270027*	*Failed due to edge initiated crack, omitted from S-N curve.*
FS SP SCG 14	*211.5*	210.8	*96032*	*Failed due to PFD, omitted from S-N curve.*

Table 13.41: S-N test results for AA 5383-H321 FS SP butt welds, short crack growth specimens.

13.5.2 SCG Results

FS SP SCG 18.1									
Cycles (N)	Crack Length (μm)		dc/dN (m.cycle^{-1}) x 10^9	N/N_f	Cycles (N)	Crack Length (μm)		dc/dN (m.cycle^{-1}) x 10^9	N/N_f
	2c	c				2c	c		
113000	193	97	0.40	0.99	90000	89	45	0.54	0.79
112000	192	96	4.90	0.98	88000	87	44	0.12	0.77
111000	183	91	1.88	0.97	86000	87	43	3.17	0.75
109000	175	88	0.28	0.95	84000	74	37	3.50	0.73
107000	174	87	1.63	0.93	83000	67	34	0.07	0.72
105000	167	84	6.31	0.92	79000	67	33	0.51	0.69
103000	142	71	4.57	0.90	77000	65	32	0.84	0.67
102000	133	67	1.38	0.89	76000	63	31	0.71	0.66
101000	130	65	3.39	0.88	75000	61	31	0.60	0.65
100000	124	62	0.41	0.87	73000	59	30	0.36	0.64
99000	123	61	8.08	0.86	72000	58	29	0.05	0.63
98000	107	53	1.89	0.86	70000	58	29	0.52	0.61
97000	103	51	1.28	0.85	66000	54	27	0.54	0.58
96000	100	50	0.26	0.84	64000	52	26	1.61	0.56
95000	100	50	0.56	0.83	62000	45	23	0.73	0.54
93000	98	49	1.82	0.81	60000	42	21	0.26	0.52
91000	90	45	0.37	0.79	56000	40	20		

Table 13.42: FGS SP SCG specimen, crack 18.1.

FS SP SCG 18.2									
Cycles (N)	Crack Length (μm)		dc/dN (m.cycle^{-1}) x 10^9	N/N_f	Cycles (N)	Crack Length (μm)		dc/dN (m.cycle^{-1}) x 10^9	N/N_f
	2c	c				2c	c		
112000	170	85	1.32	0.98	81000	96	48	0.31	0.71
109000	162	81	9.16	0.95	79000	95	47	0.03	0.69
108000	144	72	3.01	0.94	74000	94	47	0.04	0.65
107000	138	69	0.19	0.93	73000	94	47	0.89	0.64
105000	137	69	0.43	0.92	72000	93	46	1.14	0.63
104000	136	68	2.08	0.91	68000	83	42	0.87	0.59
101000	124	62	4.00	0.88	64000	76	38	1.79	0.56
100000	116	58	1.06	0.87	62000	69	35	0.33	0.54
99000	114	57	0.35	0.86	58000	67	33	0.90	0.51
97000	112	56	0.16	0.85	56000	63	32	0.96	0.49
96000	112	56	0.92	0.84	54000	59	30	0.56	0.47
95000	110	55	0.53	0.83	50000	55	27	0.18	0.44
93000	108	54	1.77	0.81	44000	53	26	0.71	0.38
92000	104	52	0.22	0.80	42000	50	25	0.06	0.37
90000	104	52	1.31	0.79	38000	49	25	0.40	0.33
89000	101	50	0.07	0.78	36000	48	24	0.55	0.31
88000	101	50	1.04	0.77	34000	46	23	0.66	0.30
87000	99	49	0.08	0.76	32000	43	21	0.45	0.28
84000	98	49	0.29	0.73	30000	41	21	0.13	0.26
83000	98	49	0.42	0.72	10000	36	18		

Table 13.43: FGS SP SCG specimen, crack 18.2.

FS SP SCG 18.3									
Cycles (N)	Crack Length (μm)		dc/dN (m.cycle^{-1}) x 10^9	N/N_f	Cycles (N)	Crack Length (μm)		dc/dN (m.cycle^{-1}) x 10^9	N/N_f
	2c	c				2c	c		
113000	338	169	6.22	0.99	78000	150	75	0.56	0.68
112000	325	163	2.45	0.98	77000	149	74	0.20	0.67
111000	320	160	12.86	0.97	74000	148	74	1.01	0.65
109000	269	134	0.59	0.95	70000	139	70	1.25	0.61
108000	268	134	0.19	0.94	66000	129	65	1.76	0.58
107000	267	134	0.99	0.93	62000	115	58	1.47	0.54
104000	261	131	3.37	0.91	60000	110	55	0.46	0.52
101000	241	121	3.28	0.88	58000	108	54	0.20	0.51
96000	208	104	1.66	0.84	54000	106	53	0.39	0.47
95000	205	103	0.16	0.83	50000	103	51	0.61	0.44
93000	205	102	1.05	0.81	48000	101	50	0.35	0.42
92000	202	101	2.28	0.80	44000	98	49	0.71	0.38
90000	193	97	5.99	0.79	36000	86	43	0.04	0.31
89000	181	91	10.00	0.78	30000	86	43	0.34	0.26
88000	161	81	1.18	0.77	24000	82	41	0.61	0.21
87000	159	79			22000	79	40	1.20	0.19
Coalescence					20000	75	37	0.28	0.17
86000	156	78	0.43	0.75	15000	72	36	0.15	0.13
82000	152	76	0.28	0.72	10000	70	35		

Table 13.44: FGS SP SCG specimen, crack 18.3.

FS SP SCG 18.4									
Cycles (N)	Crack Length (μm)		dc/dN (m.cycle^{-1}) x 10^9	N/N_f	Cycles (N)	Crack Length (μm)		dc/dN (m.cycle^{-1}) x 10^9	N/N_f
	2c	c				2c	c		
113000	290	145	16.41	0.99	88000	103	51	2.75	0.77
112000	257	129	2.45	0.98	87000	97	49	0.51	0.76
109000	243	121	11.07	0.95	86000	96	48	0.91	0.75
108000	221	110	3.16	0.94	85000	94	47	0.14	0.74
106000	208	104	6.73	0.93	82000	94	47	1.16	0.72
105000	194	97	7.02	0.92	80000	89	45	2.35	0.70
104000	180	90	1.93	0.91	79000	84	42	1.71	0.69

FS SP SCG 18.4									
Cycles (N)	Crack Length (μm)		dc/dN (m.cycle^{-1}) x 10^{9}	N/N$_f$	Cycles (N)	Crack Length (μm)		dc/dN (m.cycle^{-1}) x 10^{9}	N/N$_f$
	2c	c				2c	c		
102000	173	86	0.34	0.89	78000	81	40	4.08	0.68
101000	172	86	6.82	0.88	77000	73	36	1.64	0.67
100000	158	79	8.11	0.87	76000	69	35	1.85	0.66
99000	142	71	2.05	0.86	75000	66	33	3.14	0.65
98000	138	69	0.09	0.86	74000	60	30	0.62	0.65
97000	138	69	0.01	0.85	72000	57	29	0.02	0.63
96000	138	69	3.59	0.84	70000	57	28	0.34	0.61
95000	131	65	1.26	0.83	66000	54	27	0.87	0.58
93000	126	63	1.51	0.81	64000	51	25	0.81	0.56
91000	120	60	2.37	0.79	62000	48	24	1.02	0.54
90000	115	57	1.41	0.79	58000	39	20		
89000	112	56	4.62	0.78					

Table 13.45: FGS SP SCG specimen, crack 18.4.

13.5.3 LCG Results

FS SP CT2						
Crack Length (mm)		$\Delta K_{R=0.1}$ (MPa.m$^{0.5}$)			Cycles (N)	da/dN (mm.cycle^{-1}) x 10^{6}
Start	Finish	Start	Finish	Mean		
15.00	18.18	Pre-cracking			500000	Pre-cracking
18.88	19.37	6.78	6.94	6.86	510000	49
19.37	19.95	6.94	7.12	7.03	520000	58
19.95	20.59	7.12	7.34	7.23	530000	64
20.59	21.37	7.34	7.61	7.47	540000	78
21.37	22.20	7.61	7.91	7.76	550000	83
22.20	23.13	7.91	8.26	8.09	560000	93
23.13	23.68	8.26	8.49	8.38	565000	110
23.68	24.23	8.49	8.72	8.60	570000	110
24.23	24.83	8.72	8.98	8.85	575000	120
24.83	25.50	8.98	9.29	9.13	580000	134
25.50	26.27	9.29	9.66	9.47	585000	154
26.27	26.68	9.66	9.87	9.76	587500	164
26.68	27.09	9.87	10.08	9.98	590000	164
27.09	27.53	10.08	10.33	10.20	592500	176
27.53	27.97	10.33	10.58	10.45	595000	176
27.97	28.43	10.58	10.85	10.71	597500	184
28.43	28.91	10.85	11.15	11.00	600000	192
28.91	29.44	11.15	11.49	11.32	602500	212
29.44	29.97	11.49	11.85	11.67	605000	212
29.97	30.52	11.85	12.25	12.05	607500	220
30.52	31.15	12.25	12.74	12.49	610000	252
31.15	31.84	12.74	13.31	13.02	612500	276
31.84	32.60	13.31	13.99	13.65	615000	304
32.60	32.96	13.99	14.33	14.16	616000	360
32.96	33.29	14.33	14.66	14.49	617000	330
33.29	33.65	14.66	15.03	14.84	618000	360
33.65	34.06	15.03	15.47	15.25	619000	410
34.06	34.47	15.47	15.94	15.70	620000	410
34.47	34.92	15.94	16.48	16.21	621000	450
34.92	35.40	16.48	17.09	16.78	622000	480
35.40	35.94	17.09	17.82	17.45	623000	540
35.94	36.54	17.82	18.70	18.26	624000	600
36.54	37.16	18.70	19.69	19.19	625000	620
37.16	38.06	19.69	21.28	20.48	626000	900
38.06	38.55	21.28	22.24	21.76	626500	980
38.55	39.17	22.24	23.57	22.91	627000	1240
39.17	40.22	23.57	26.13	24.85	627500	2100

Table 13.46: FS SP LCG specimen CT2.

FS SP CT3						
Crack Length (mm)		$\Delta K_{R=0.1}$ (MPa.m$^{0.5}$)			Cycles (N)	da/dN (mm.cycle^{-1}) x 10^{6}
Start	Finish	Start	Finish	Mean		
15.00	18.82	Pre-cracking			400000	Pre-cracking
18.82	19.48	3.87	3.98	3.92	500000	7
19.48	20.11	3.98	4.10	4.04	600000	6
20.11	20.86	4.10	4.24	4.17	700000	8
20.86	21.63	4.24	4.40	4.32	800000	8
21.63	22.56	4.40	4.60	4.50	900000	9
22.56	23.08	4.60	4.71	4.65	950000	10
23.08	23.64	4.71	4.84	4.78	1000000	11
23.64	24.40	4.84	5.02	4.93	1050000	15
24.40	25.28	5.02	5.25	5.13	1100000	18
25.28	26.45	5.25	5.57	5.41	1150000	23
26.45	27.08	5.57	5.76	5.67	1175000	25
27.08	27.85	5.76	6.00	5.88	1200000	31
27.85	28.77	6.00	6.32	6.16	1225000	37
28.77	29.97	6.32	6.77	6.55	1250000	48
29.97	30.53	6.77	7.01	6.89	1260000	56
30.53	31.24	7.01	7.32	7.16	1270000	71
31.24	32.08	7.32	7.72	7.52	1280000	84
32.08	33.10	7.72	8.27	7.99	1290000	102
33.10	33.67	8.27	8.60	8.43	1295000	114
33.67	34.30	8.60	8.99	8.80	1300000	132
34.30	35.03	8.99	9.49	9.24	1305000	140
35.03	35.87	9.49	10.13	9.81	1310000	168
35.87	36.30	10.13	10.48	10.30	1312500	172
36.30	36.78	10.48	10.90	10.69	1315000	192
36.78	37.32	10.90	11.40	11.15	1317500	216
37.32	37.85	11.40	11.94	11.67	1320000	212
37.85	38.52	11.94	12.68	12.31	1322500	268
38.52	39.29	12.68	13.62	13.15	1325000	308

Table 13.47: FS SP LCG specimen CT3.

13.6 FS Double Pass Advancing (FS DPA)

13.6.1 SCG Specimen S-N Results

Specimen number	Δσ (applied) (MPa) (R = 0.1)	Δσ (notch) (MPa) (R = 0.1)	Cycles to failure (*italics = did not fail/omitted*)	Comments
FS DPA SCG 1	288.4	287.5	40901	
FS DPA SCG 2	275.6	274.7	64259	
FS DPA SCG 3	262.7	261.9	71525	
FS DPA SCG 4	249.9	249.2	95190	
FS DPA SCG 5	237.1	236.4	146233	
FS DPA SCG 6	224.3	223.6	141101	
FS DPA SCG 7	211.5	210.8	215869	
FS DPA SCG 8	198.7	198.1	600724	
FS DPA SCG 9	185.8	185.3	*2000000*	*Did not fail.*
FS DPA SCG 10	*237.1*		*125567*	*Failed outwith notch sections, omitted from S-N curve.*
FS DPA SCG 11	*198.7*		*167613*	*Failed outwith notch sections, omitted from S-N curve.*
FS DPA SCG 12	*185.8*		*188735*	*Failed outwith notch sections, possibly from a machining mark, omitted from S-N curve.*

Table 13.48: S-N test results for AA 5383-H321 FS DPA butt welds, short crack growth specimens.

13.6.2 SCG Results

FS DPA SCG 13.1 (A+B)									
Cycles (N)	Crack Length (μm)		dc/dN ($m.cycle^{-1}$) x 10^9	N/N_f	Cycles (N)	Crack Length (μm)		dc/dN ($m.cycle^{-1}$) x 10^9	N/N_f
	2c	c				2c	c		
99000	2623	1312	158.84	1.00	95000	1457	729	106.95	0.96
98000	2306	1153	285.96	0.99	93000	1029	515		
97000	1734	867	98.34	0.98	Coalescence				
96000	1537	768	39.89	0.97					

Table 13.49: FGS DPA SCG specimen, crack 13.1 (A+B).

FS DPA SCG 13.1A									
Cycles (N)	Crack Length (μm)		dc/dN ($m.cycle^{-1}$) x 10^9	N/N_f	Cycles (N)	Crack Length (μm)		dc/dN ($m.cycle^{-1}$) x 10^9	N/N_f
	2c	c				2c	c		
92000	599	299	24.72	0.93	60000	216	108	2.67	0.60
91000	549	275	13.92	0.92	58000	205	103	1.03	0.58
90000	521	261	15.42	0.91	56000	201	101	0.13	0.56
87000	429	214	6.14	0.88	54000	201	100	0.09	0.54
86000	417	208	11.08	0.87	52000	200	100	4.98	0.52
85000	395	197	7.70	0.85	50000	180	90	3.13	0.50
84000	379	190	6.60	0.84	48000	168	84	0.33	0.48
83000	366	183	5.83	0.83	46000	167	83	2.46	0.46
81000	343	171	0.37	0.81	44000	157	78	0.00	0.44
79000	341	171	14.10	0.79	42000	157	78	1.95	0.42
78000	313	156	5.13	0.78	40000	149	74	0.76	0.40
77000	303	151	2.90	0.77	38000	146	73	0.05	0.38
76000	297	148	2.65	0.76	36000	146	73	1.99	0.36
74000	286	143	0.02	0.74	34000	138	69	1.97	0.34
72000	286	143	9.31	0.72	30000	122	61	6.02	0.30

FS DPA SCG 13.1A									
Cycles (N)	Crack Length (μm)		dc/dN (m.cycle^{-1}) x 10^{9}	N/N$_f$	Cycles (N)	Crack Length (μm)		dc/dN (m.cycle^{-1}) x 10^{9}	N/N$_f$
	2c	c				2c	c		
71000	268	134	2.58	0.71	28000	98	49	0.89	0.28
70000	262	131	3.04	0.70	26000	94	47	1.85	0.26
68000	250	125	1.98	0.68	24000	87	43	0.68	0.24
66000	242	121	4.24	0.66	22000	84	42	1.30	0.22
64000	225	113	0.50	0.64	20000	79	40		
62000	223	112	1.85	0.62					

Table 13.50: FGS DPA SCG specimen, crack 13.1A.

FS DPA SCG 13.1B									
Cycles (N)	Crack Length (μm)		dc/dN (m.cycle^{-1}) x 10^{9}	N/N$_f$	Cycles (N)	Crack Length (μm)		dc/dN (m.cycle^{-1}) x 10^{9}	N/N$_f$
	2c	c				2c	c		
92000	513	257	9.66	0.93	66000	248	124	2.35	0.66
91000	494	247	9.02	0.92	64000	239	120	1.87	0.64
90000	476	238	19.37	0.91	62000	232	116	4.48	0.62
89000	437	219	3.55	0.90	60000	214	107	1.68	0.60
87000	423	211	3.37	0.88	58000	207	103	1.59	0.58
86000	416	208	15.50	0.87	54000	194	97	2.50	0.54
85000	385	193	0.14	0.85	52000	184	92	1.02	0.52
84000	385	192	1.07	0.84	50000	180	90	0.39	0.50
83000	383	191	0.21	0.83	48000	179	89	3.56	0.48
81000	382	191	4.15	0.81	46000	164	82	1.85	0.46
79000	365	183	12.21	0.79	44000	157	79	0.63	0.44
78000	341	170	15.51	0.78	40000	152	76		
77000	310	155	0.93	0.77	Coalescence				
76000	308	154	4.54	0.76	38000	108	54	1.91	0.38
75000	299	149	1.81	0.75	36000	100	50	0.15	0.36
74000	295	148	0.07	0.74	34000	99	50	0.91	0.34
72000	295	148	5.98	0.72	32000	96	48	0.51	0.32
71000	283	142	6.65	0.71	24000	88	44	0.57	0.24
70000	270	135	2.39	0.70	22000	85	43	0.93	0.22
68000	260	130	2.93	0.68	20000	82	41		

Table 13.51: FGS DPA SCG specimen, crack 13.1B.

FS DPA SCG 13.2 (A+B)									
Cycles (N)	Crack Length (μm)		dc/dN (m.cycle^{-1}) x 10^{9}	N/N$_f$	Cycles (N)	Crack Length (μm)		dc/dN (m.cycle^{-1}) x 10^{9}	N/N$_f$
	2c	c				2c	c		
99000	528	264	6.31	1.00	89000	465	232	7.21	0.90
98000	516	258	4.70	0.99	87000	436	218	0.40	0.88
97000	506	253	1.35	0.98	85000	434	217	7.87	0.85
95000	501	250	6.11	0.96	84000	418	209	2.19	0.84
93000	476	238	2.03	0.94	83000	414	207	0.07	0.83
92000	472	236	0.69	0.93	82000	414	207		
91000	471	236	2.88	0.92	Coalescence				
90000	465	233	0.33	0.91					

Table 13.52: FGS DPA SCG specimen, crack 13.2 (A+B).

FS DPA SCG 13.2A									
Cycles (N)	Crack Length (μm)		dc/dN (m.cycle^{-1}) x 10^{9}	N/N$_f$	Cycles (N)	Crack Length (μm)		dc/dN (m.cycle^{-1}) x 10^{9}	N/N$_f$
	2c	c				2c	c		
81000	164	82	1.13	0.81	60000	100	50	2.50	0.60
80000	161	81	1.73	0.80	58000	90	45	0.04	0.58
78000	154	77	1.71	0.78	56000	90	45	0.68	0.56

FS DPA SCG 13.2A									
Cycles (N)	Crack Length (μm)		dc/dN (m.cycle^{-1}) x 10^9	N/N_f	Cycles (N)	Crack Length (μm)		dc/dN (m.cycle^{-1}) x 10^9	N/N_f
	2c	c				2c	c		
77000	151	75	3.52	0.77	54000	87	44	1.83	0.54
76000	144	72	0.56	0.76	52000	80	40	0.29	0.52
75000	143	71	0.49	0.75	48000	78	39	0.37	0.48
73000	141	70	2.38	0.73	46000	76	38	0.01	0.46
72000	136	68	1.58	0.72	42000	76	38	0.00	0.42
71000	133	66	4.57	0.71	40000	76	38	0.05	0.40
70000	124	62	0.77	0.70	38000	76	38	1.71	0.38
68000	121	60	0.36	0.68	36000	69	35	0.87	0.36
66000	119	60	3.12	0.66	32000	62	31	0.47	0.32
64000	107	53	1.61	0.64	28000	58	29	1.30	0.28
62000	100	50	0.05	0.62	24000	48	24		

Table 13.53: FGS DPA SCG specimen, crack 13.2A.

FS DPA SCG 13.2B									
Cycles (N)	Crack Length (μm)		dc/dN (m.cycle^{-1}) x 10^9	N/N_f	Cycles (N)	Crack Length (μm)		dc/dN (m.cycle^{-1}) x 10^9	N/N_f
	2c	c				2c	c		
81000	216	108	4.67	0.81	56000	123	62	1.22	0.56
80000	207	104	11.71	0.80	52000	113	57	0.49	0.52
79000	184	92	0.27	0.79	50000	111	56	1.11	0.50
78000	183	92	2.60	0.78	48000	107	54	0.46	0.48
77000	178	89	0.39	0.77	46000	105	53	2.31	0.46
76000	177	89	0.33	0.76	44000	96	48	0.95	0.44
75000	177	88	1.37	0.75	42000	92	46	0.62	0.42
74000	174	87	1.00	0.74	40000	90	45	0.30	0.40
72000	170	85	0.64	0.72	38000	88	44	0.54	0.38
71000	168	84	0.03	0.71	36000	86	43	0.51	0.36
70000	168	84	2.90	0.70	32000	82	41	1.83	0.32
68000	157	78	0.05	0.68	30000	75	37	0.89	0.30
66000	157	78	2.11	0.66	28000	71	36	0.95	0.28
64000	148	74	0.43	0.64	24000	64	32	1.14	0.24
62000	146	73	0.90	0.62	22000	59	30	0.19	0.22
60000	143	71	3.48	0.60	20000	58	29		
58000	129	64	1.44	0.58					

Table 13.54: FGS DPA SCG specimen, crack 13.2B.

FS DPA SCG 13.3									
Cycles (N)	Crack Length (μm)		dc/dN (m.cycle^{-1}) x 10^9	N/N_f	Cycles (N)	Crack Length (μm)		dc/dN (m.cycle^{-1}) x 10^9	N/N_f
	2c	c				2c	c		
98000	589	294	28.76	0.99	Coalescence				
97000	531	266	3.01	0.98	71000	202	101	0.51	0.71
96000	525	263			68000	199	99	0.42	0.68
Coalescence					64000	195	98	2.27	0.64
95000	441	220	4.49	0.96	62000	186	93	2.26	0.62
93000	423	211	17.03	0.94	60000	177	89	0.04	0.60
92000	389	194	4.57	0.93	58000	177	89	3.81	0.58
91000	380	190	13.79	0.92	56000	162	81	0.31	0.56
90000	352	176	0.50	0.91	52000	159	80	1.01	0.52
89000	351	176	0.37	0.90	50000	155	78	0.10	0.50
88000	350	175	6.51	0.89	48000	155	77	2.87	0.48
87000	337	169	1.25	0.88	46000	143	72	1.42	0.46
86000	335	167	12.00	0.87	44000	138	69	2.55	0.44
85000	311	155	7.10	0.85	40000	117	59		
84000	297	148	0.84	0.84	Coalescence				
83000	295	147	0.42	0.83	38000	78	39	2.15	0.38
82000	294	147	1.86	0.82	36000	69	35	0.36	0.36
81000	290	145	7.28	0.81	34000	68	34	1.07	0.34

FS DPA SCG 13.3									
Cycles (N)	Crack Length (μm)		dc/dN (m.cycle^{-1}) x 10^{9}	N/N_f	Cycles (N)	Crack Length (μm)		dc/dN (m.cycle^{-1}) x 10^{9}	N/N_f
	2c	c				2c	c		
80000	276	138	3.93	0.80	32000	64	32	0.22	0.32
79000	268	134	2.20	0.79	30000	63	31	0.13	0.30
77000	259	130	2.86	0.77	26000	62	31	1.99	0.26
75000	248	124	1.27	0.75	24000	54	27	0.86	0.24
74000	245	123	3.71	0.74	22000	50	25	0.12	0.22
73000	238	119	6.36	0.73	17500	49	25		
72000	225	113							

Table 13.55: FGS DPA SCG specimen, crack 13.3.

FS DPA SCG 13.4									
Cycles (N)	Crack Length (μm)		dc/dN (m.cycle^{-1}) x 10^{9}	N/N_f	Cycles (N)	Crack Length (μm)		dc/dN (m.cycle^{-1}) x 10^{9}	N/N_f
	2c	c				2c	c		
98000	307	154	4.21	0.99	68000	149	75	1.05	0.68
97000	299	149	1.49	0.98	66000	145	72	3.73	0.66
96000	296	148	0.07	0.97	64000	130	65	1.94	0.64
95000	296	148	12.04	0.96	62000	122	61	0.04	0.62
93000	248	124	0.82	0.94	60000	122	61	0.74	0.60
91000	244	122	3.64	0.92	58000	119	60	1.63	0.58
90000	237	119	4.34	0.91	56000	113	56	0.56	0.56
89000	228	114	0.32	0.90	52000	108	54	0.80	0.52
88000	228	114	0.81	0.89	50000	105	52	1.31	0.50
86000	224	112	6.58	0.87	48000	100	50	1.88	0.48
85000	211	106	5.43	0.85	46000	92	46	1.03	0.46
84000	200	100	0.95	0.84	44000	88	44		
82000	197	98	6.36	0.82	Coalescence				
81000	184	92	2.89	0.81	38000	69	34	2.29	0.38
80000	178	89	1.03	0.80	36000	60	30	0.13	0.36
78000	174	87	1.58	0.78	34000	59	30	1.82	0.34
77000	171	85	1.55	0.77	32000	52	26	0.47	0.32
76000	168	84	3.79	0.76	30000	50	25	0.31	0.30
75000	160	80	0.35	0.75	26000	48	24	0.00	0.26
72000	158	79	1.25	0.72	24000	48	24	0.23	0.24
71000	156	78	0.31	0.71	22000	47	23		
70000	155	77	1.47	0.70					

Table 13.56: FGS DPA SCG specimen, crack 13.4.

13.6.3 LCG Results

FS DPA CT2						
Crack Length (mm)		$\Delta K_{R=0.1}$ (MPa.m$^{0.5}$)			Cycles (N)	da/dN (mm.cycle^{-1}) x 10^{6}
Start	Finish	Start	Finish	Mean		
15.00	19.05	Pre-cracking			250000	Pre-cracking
19.05	19.44	3.89	3.96	3.93	300000	8
19.44	19.73	3.96	4.01	3.99	350000	6
19.73	20.05	4.01	4.07	4.04	400000	6
20.05	20.71	4.07	4.20	4.14	500000	7
20.71	21.39	4.20	4.33	4.27	600000	7
21.39	22.09	4.33	4.48	4.40	700000	7
22.09	22.65	4.48	4.60	4.54	800000	6
22.65	23.28	4.60	4.74	4.67	900000	6
23.28	23.78	4.74	4.85	4.79	1000000	5
23.78	24.23	4.85	4.96	4.91	1100000	4
24.23	24.72	4.96	5.08	5.02	1200000	5
24.72	25.21	5.08	5.21	5.14	1300000	5
25.21	25.79	5.21	5.36	5.29	1400000	6
25.79	26.53	5.36	5.57	5.47	1500000	7

FS DPA CT2						
Crack Length (mm)		$\Delta K_{R=0.1}$ (MPa.m$^{0.5}$)			Cycles (N)	da/dN (mm.cycle^{-1}) x 10^{6}
Start	Finish	Start	Finish	Mean		
26.53	26.73	5.57	5.63	5.60	1600000	2
26.73	27.65	5.63	5.91	5.77	1700000	9
27.65	28.77	5.91	6.29	6.10	1800000	11
28.77	29.58	6.29	6.59	6.44	1850000	16
29.58	30.58	6.59	7.00	6.80	1900000	20
30.58	31.23	7.00	7.28	7.14	1925000	26
31.23	32.11	7.28	7.71	7.50	1950000	35
32.11	32.48	7.71	7.90	7.80	1960000	37
32.48	32.93	7.90	8.14	8.02	1970000	45
32.93	33.49	8.14	8.46	8.30	1980000	56
33.49	34.18	8.46	8.88	8.67	1990000	69
34.18	35.02	8.88	9.45	9.16	2000000	84
35.02	36.15	9.45	10.31	9.88	2010000	113
36.15	36.82	10.31	10.89	10.60	2015000	134
36.82	37.68	10.89	11.71	11.30	2020000	172
37.68	38.20	11.71	12.26	11.99	2022500	208
38.20	38.81	12.26	12.97	12.62	2025000	244
38.81	39.57	12.97	13.94	13.45	2027500	304
39.57	40.54	13.94	15.36	14.65	2030000	388

Table 13.57: FS DPA LCG specimen CT2.

FS DPA CT3						
Crack Length (mm)		$\Delta K_{R=0.1}$ (MPa.m$^{0.5}$)			Cycles (N)	da/dN (mm.cycle^{-1}) x 10^{6}
Start	Finish	Start	Finish	Mean		
15.00	18.60	Pre-cracking			320000	Pre-cracking
18.60	18.87	6.73	6.81	6.77	330000	27
18.87	19.18	6.81	6.91	6.86	340000	31
19.18	19.45	6.91	7.00	6.95	350000	27
19.45	19.72	7.00	7.09	7.04	360000	27
19.72	20.04	7.09	7.19	7.14	370000	32
20.04	20.34	7.19	7.29	7.24	380000	30
20.34	20.73	7.29	7.42	7.36	390000	39
20.73	21.10	7.42	7.55	7.49	400000	37
21.10	21.55	7.55	7.71	7.63	410000	45
21.55	22.05	7.71	7.89	7.80	420000	50
22.05	22.57	7.89	8.09	7.99	430000	52
22.57	23.11	8.09	8.30	8.19	440000	54
23.11	23.72	8.30	8.55	8.42	450000	61
23.72	24.52	8.55	8.89	8.72	460000	80
24.52	25.37	8.89	9.27	9.08	470000	85
25.37	26.41	9.27	9.78	9.53	480000	104
26.41	26.96	9.78	10.07	9.92	485000	110
26.96	27.60	10.07	10.42	10.24	490000	128
27.60	28.30	10.42	10.83	10.62	495000	140
28.30	29.05	10.83	11.29	11.06	500000	150
29.05	29.94	11.29	11.89	11.59	505000	178
29.94	30.92	11.89	12.62	12.26	510000	196
30.92	31.53	12.62	13.11	12.87	512500	244
31.53	32.16	13.11	13.66	13.38	515000	252
32.16	32.90	13.66	14.34	14.00	517500	296
32.90	33.79	14.34	15.25	14.80	520000	356
33.79	34.20	15.25	15.71	15.48	521000	410
34.20	34.63	15.71	16.21	15.96	522000	430
34.63	35.08	16.21	16.76	16.48	523000	450
35.08	35.59	16.76	17.43	17.09	524000	510
35.59	36.20	17.43	18.29	17.86	525000	610
36.20	37.03	18.29	19.57	18.93	526000	830
37.03	38.05	19.57	21.37	20.47	527000	1020
38.05	38.60	21.37	22.46	21.92	527500	1100
38.60	39.58	22.46	24.64	23.55	528000	1960

Table 13.58: FS DPA LCG specimen CT3.

13.7 FS Double Pass Retreating (FS DPR)

13.7.1 SCG Specimen S-N Results

Specimen number	Δσ (applied) (MPa) (R = 0.1)	Δσ (notch) (MPa) (R = 0.1)	Cycles to failure (*italics = did not fail/omitted*)	Comments
FS DPR SCG 1	288.4	287.5	55465	
FS DPR SCG 2	275.6	274.7	91342	
FS DPR SCG 3	262.7	261.9	97468	
FS DPR SCG 4	249.9	249.2	100735	
FS DPR SCG 5	237.1	236.4	113420	
FS DPR SCG 6	224.3	223.6	168910	
FS DPR SCG 7	211.5	210.8	754492	
FS DPR SCG 8	198.7	198.1	*2000000*	*Did not fail.*

Table 13.59: S-N test results for AA 5383-H321 FS DPR butt welds, short crack growth specimens.

13.7.2 SCG Results

FS DPR SCG 9.1 (A+B)									
Cycles (N)	Crack Length (μm)		dc/dN (m.cycle^{-1}) x 10^9	N/N_f	Cycles (N)	Crack Length (μm)		dc/dN (m.cycle^{-1}) x 10^9	N/N_f
	2c	c				2c	c		
95000	463	231	10.49	0.99	91000	384	192	5.24	0.95
94000	442	221	3.87	0.98	90000	373	187		
93000	434	217	18.44	0.97	Coalescence				
92000	397	199	6.63	0.96					

Table 13.60: FGS DPR SCG specimen, crack 9.1 (A+B).

FS DPR SCG 9.1A									
Cycles (N)	Crack Length (μm)		dc/dN (m.cycle^{-1}) x 10^9	N/N_f	Cycles (N)	Crack Length (μm)		dc/dN (m.cycle^{-1}) x 10^9	N/N_f
	2c	c				2c	c		
88000	260	130	0.11	0.92	58000	137	69	5.01	0.61
87000	260	130	2.85	0.91	56000	117	59	0.54	0.59
86000	254	127	9.11	0.90	54000	115	57	1.51	0.56
85000	236	118	1.72	0.89	52000	109	54	2.22	0.54
81000	222	111	6.47	0.85	50000	100	50	0.15	0.52
80000	209	105	5.34	0.84	48000	99	50	2.21	0.50
79000	199	99	5.82	0.83	46000	91	45	2.97	0.48
78000	187	94	0.54	0.82	44000	79	39	0.61	0.46
77000	186	93	0.92	0.81	42000	76	38	1.13	0.44
75000	182	91	1.15	0.78	40000	72	36	0.09	0.42
74000	180	90	4.67	0.77	38000	71	36	0.02	0.40
73000	171	85	0.10	0.76	36000	71	36	0.17	0.38
70000	170	85	0.87	0.73	34000	71	35	2.40	0.36
68000	167	83	2.70	0.71	32000	61	31	0.03	0.33
66000	156	78	1.58	0.69	30000	61	30	0.09	0.31
64000	150	75	0.22	0.67	26000	60	30		
62000	149	74	1.45	0.65					

Table 13.61: FGS DPR SCG specimen, crack 9.1A.

FS DPR SCG 9.1B									
Cycles (N)	Crack Length (μm)		dc/dN (m.cycle^{-1}) x 10^9	N/N_f	Cycles (N)	Crack Length (μm)		dc/dN (m.cycle^{-1}) x 10^9	N/N_f
	2c	c				2c	c		
88000	115	57	3.92	0.92	75000	64	32	1.16	0.78
87000	107	53	2.62	0.91	74000	62	31	1.66	0.77
86000	102	51	7.74	0.90	73000	58	29	2.36	0.76
85000	86	43	0.40	0.89	72000	54	27	0.54	0.75
82000	84	42	3.54	0.86	70000	51	26	0.33	0.73
81000	77	38	0.51	0.85	68000	50	25	0.53	0.71
80000	76	38	1.99	0.84	66000	48	24	0.15	0.69
79000	72	36	0.54	0.83	64000	47	24	1.06	0.67
78000	70	35	1.38	0.82	62000	43	22	0.25	0.65
77000	68	34	0.95	0.81	58000	41	21		

Table 13.62: FGS DPR SCG specimen, crack 9.1B.

FS DPR SCG 9.2									
Cycles (N)	Crack Length (μm)		dc/dN (m.cycle^{-1}) x 10^9	N/N_f	Cycles (N)	Crack Length (μm)		dc/dN (m.cycle^{-1}) x 10^9	N/N_f
	2c	c				2c	c		
95000	414	207	18.32	0.99	71000	178	89	0.36	0.74
94000	378	189	4.58	0.98	70000	178	89	4.02	0.73
93000	369	184	12.18	0.97	68000	161	81	0.83	0.71
92000	344	172	15.07	0.96	66000	158	79	3.12	0.69
91000	314	157	3.70	0.95	64000	146	73	1.86	0.67
90000	307	153	2.88	0.94	62000	138	69	2.75	0.65
87000	289	145	6.45	0.91	58000	116	58	1.88	0.61
86000	276	138	7.30	0.90	56000	109	54	0.25	0.59
85000	262	131	2.41	0.89	54000	108	54	1.91	0.56
82000	247	124	8.27	0.86	50000	92	46	1.75	0.52
81000	231	115	2.63	0.85	48000	85	43	0.06	0.50
80000	226	113	4.07	0.84	44000	85	42	0.59	0.46
79000	217	109	1.15	0.83	42000	83	41	1.41	0.44
78000	215	108	1.18	0.82	38000	71	36	1.54	0.40
77000	213	106	4.80	0.81	36000	65	33	2.00	0.38
76000	203	102	4.90	0.79	34000	57	29	0.52	0.36
75000	193	97	0.31	0.78	32000	55	28	0.32	0.33
74000	193	96	5.40	0.77	28000	53	26	0.07	0.29
73000	182	91	0.94	0.76	26000	52	26		
72000	180	90	0.95	0.75					

Table 13.63: FGS DPR SCG specimen, crack 9.2.

FS DPR SCG 9.3 (A+B)									
Cycles (N)	Crack Length (μm)		dc/dN (m.cycle^{-1}) x 10^9	N/N_f	Cycles (N)	Crack Length (μm)		dc/dN (m.cycle^{-1}) x 10^9	N/N_f
	2c	c				2c	c		
95000	2175	1088	289.86	0.99	90000	966	483	45.92	0.94
94000	1596	798	115.04	0.98	89000	874	437	30.02	0.93
93000	1366	683	67.98	0.97	88000	814	407		
91000	1094	547	63.79	0.95	Coalescence				

Table 13.64: FGS DPR SCG specimen, crack 9.3 (A+B).

FS DPR SCG 9.3A									
Cycles (N)	Crack Length (μm)		dc/dN (m.cycle^{-1}) x 10^9	N/N_f	Cycles (N)	Crack Length (μm)		dc/dN (m.cycle^{-1}) x 10^9	N/N_f
	2c	c				2c	c		
87000	379	189	17.20	0.91	66000	175	87	1.64	0.69
86000	344	172	8.53	0.90	62000	162	81	4.85	0.65
84000	310	155	7.79	0.88	60000	142	71	1.24	0.63
83000	295	147	6.59	0.87	58000	137	69	2.09	0.61
82000	281	141	17.59	0.86	54000	121	60	1.48	0.56
81000	246	123	5.99	0.85	52000	115	57	2.09	0.54
80000	234	117	2.01	0.84	50000	106	53	0.05	0.52
79000	230	115	0.87	0.83	48000	106	53	0.13	0.50
78000	229	114	5.74	0.82	46000	106	53	1.86	0.48
77000	217	109	5.19	0.81	44000	98	49	0.12	0.46
76000	207	103	1.59	0.79	36000	96	48		
74000	200	100	3.91	0.77	Coalescence				
73000	193	96	2.37	0.76	32000	70	35	0.02	0.33
72000	188	94	3.80	0.75	30000	70	35	1.57	0.31
71000	180	90	2.66	0.74	28000	63	32		
70000	175	87	0.01	0.73					

Table 13.65: FGS DPR SCG specimen, crack 9.3A.

FS DPR SCG 9.3B									
Cycles (N)	Crack Length (μm)		dc/dN (m.cycle^{-1}) x 10^9	N/N_f	Cycles (N)	Crack Length (μm)		dc/dN (m.cycle^{-1}) x 10^9	N/N_f
	2c	c				2c	c		
87000	478	239	29.31	0.91	64000	173	87	2.25	0.67
86000	419	210	21.75	0.90	62000	164	82	4.04	0.65
85000	376	188	0.70	0.89	60000	148	74	2.26	0.63
83000	373	186	18.13	0.87	58000	139	70	4.92	0.61
82000	336	168	0.21	0.86	56000	119	60	0.21	0.59
81000	336	168	8.62	0.85	54000	119	59	1.79	0.56
80000	319	159	2.40	0.84	52000	111	56	1.12	0.54
79000	314	157	0.63	0.83	48000	102	51	0.91	0.50
78000	313	156	14.73	0.82	46000	99	49	2.11	0.48
77000	283	142	0.24	0.81	44000	90	45	2.81	0.46
76000	283	141	4.77	0.79	42000	79	40	1.47	0.44
74000	264	132	14.64	0.77	40000	73	37	0.97	0.42
73000	234	117	4.39	0.76	38000	69	35	0.93	0.40
72000	226	113	7.17	0.75	36000	66	33	0.67	0.38
71000	211	106	2.21	0.74	32000	60	30	0.98	0.33
70000	207	103	0.72	0.73	28000	52	26		
66000	201	101	6.98	0.69					

Table 13.66: FGS DPR SCG specimen, crack 9.3B.

FS DPR SCG 9.4									
Cycles (N)	Crack Length (μm)		dc/dN (m.cycle^{-1}) x 10^9	N/N_f	Cycles (N)	Crack Length (μm)		dc/dN (m.cycle^{-1}) x 10^9	N/N_f
	2c	c				2c	c		
95000	337	168	3.00	0.99	71000	158	79	0.99	0.74
94000	331	165	9.88	0.98	70000	156	78	3.22	0.73
93000	311	156	5.82	0.97	68000	144	72	2.51	0.71
91000	288	144	5.63	0.95	64000	123	62	0.94	0.67
90000	277	138	0.32	0.94	62000	120	60	0.82	0.65
88000	275	138	2.44	0.92	60000	116	58	2.81	0.63
87000	271	135	6.36	0.91	58000	105	53	5.00	0.61
86000	258	129	12.81	0.90	56000	85	43	0.14	0.59
85000	232	116	2.98	0.89	54000	85	42	0.01	0.56
83000	220	110	4.93	0.87	50000	85	42	1.24	0.52
81000	201	100	2.26	0.85	48000	80	40	0.45	0.50
80000	196	98	6.08	0.84	46000	78	39	0.36	0.48
79000	184	92	0.15	0.83	44000	76	38	0.77	0.46

FS DPR SCG 9.4									
Cycles (N)	Crack Length (μm)		dc/dN (m.cycle^{-1}) x 10^{9}	N/N_f	Cycles (N)	Crack Length (μm)		dc/dN (m.cycle^{-1}) x 10^{9}	N/N_f
	2c	c				2c	c		
77000	183	92	2.85	0.81	40000	70	35	0.98	0.42
76000	178	89	1.82	0.79	36000	62	31	0.82	0.38
74000	170	85	2.71	0.77	32000	56	28	0.39	0.33
72000	159	80	0.55	0.75	28000	53	26		

Table 13.67: FGS DPR SCG specimen, crack 9.4.

13.7.3 LCG Results

FS DPR CT1						
Crack Length (mm)		$\Delta K_{R=0.1}$ (MPa.m$^{0.5}$)			Cycles (N)	da/dN (mm.cycle^{-1}) x 10^{6}
Start	Finish	Start	Finish	Mean		
15.00	19.30	Pre-cracking			75000	Pre-cracking
19.30	20.04	9.84	10.18	10.01	80000	148
20.04	20.27	10.18	10.28	10.23	82000	115
20.27	20.55	10.28	10.42	10.35	84000	140
20.55	20.69	10.42	10.49	10.45	86000	70
20.69	20.98	10.49	10.63	10.56	88000	145
20.98	21.14	10.63	10.71	10.67	90000	80
21.14	21.39	10.71	10.83	10.77	92000	125
21.39	21.64	10.83	10.96	10.90	94000	125
21.64	21.86	10.96	11.07	11.02	96000	110
21.86	22.13	11.07	11.21	11.14	98000	135
22.13	22.48	11.21	11.40	11.31	100000	175
22.48	22.71	11.40	11.52	11.46	102000	115
22.71	23.04	11.52	11.71	11.62	104000	165
23.04	23.31	11.71	11.86	11.78	106000	135
23.31	23.62	11.86	12.04	11.95	108000	155
23.62	23.97	12.04	12.24	12.14	110000	175
23.97	24.33	12.24	12.46	12.35	112000	180
24.33	24.60	12.46	12.63	12.55	114000	135
24.60	24.97	12.63	12.86	12.75	116000	185
24.97	25.38	12.86	13.13	13.00	118000	205
25.38	25.81	13.13	13.42	13.28	120000	215
25.81	26.26	13.42	13.74	13.58	122000	225
26.26	26.77	13.74	14.11	13.92	124000	255
26.77	26.97	14.11	14.26	14.18	126000	100
26.97	27.60	14.26	14.75	14.50	128000	315
27.60	28.18	14.75	15.22	14.98	130000	290
28.18	28.75	15.22	15.71	15.47	132000	285
28.75	29.50	15.71	16.41	16.06	134000	375
29.50	30.33	16.41	17.23	16.82	136000	415
30.33	30.71	17.23	17.63	17.43	137000	380
30.71	31.27	17.63	18.26	17.95	138000	560
31.27	31.81	18.26	18.89	18.58	139000	540
31.81	32.37	18.89	19.60	19.24	140000	560
32.37	33.06	19.60	20.52	20.06	141000	690
33.06	33.54	20.52	21.22	20.87	141500	960
33.54	33.88	21.22	21.73	21.47	142000	680
33.88	34.43	21.73	22.61	22.17	142500	1100
34.43	35.11	22.61	23.78	23.19	143000	1360
35.11	36.01	23.78	25.49	24.63	143500	1800
36.01	37.19	25.49	28.08	26.79	144000	2360

Table 13.68: FS DPR LCG specimen CT1.

FS DPR CT2						
Crack Length (mm)		$\Delta K_{R=0.1}$ (MPa.m$^{0.5}$)			Cycles (N)	da/dN (mm.cycle^{-1}) x 10^{6}
Start	Finish	Start	Finish	Mean		
15.00	18.45	Pre-cracking			800000	Pre-cracking
18.45	18.79	3.80	3.86	3.83	900000	3
18.79	19.11	3.86	3.91	3.88	1000000	3
19.11	19.47	3.91	3.98	3.95	1100000	4
19.47	19.78	3.98	4.03	4.01	1200000	3
19.78	20.19	4.03	4.11	4.07	1300000	4
20.19	20.47	4.11	4.16	4.14	1400000	3
20.47	20.77	4.16	4.22	4.19	1500000	3
20.77	21.18	4.22	4.30	4.26	1600000	4
21.18	21.57	4.30	4.38	4.34	1700000	4
21.57	21.95	4.38	4.46	4.42	1800000	4
21.95	22.34	4.46	4.54	4.50	1900000	4
22.34	22.79	4.54	4.64	4.59	2000000	4
22.79	23.23	4.64	4.74	4.69	2100000	4
23.23	23.70	4.74	4.85	4.79	2200000	5
23.70	24.16	4.85	4.96	4.90	2300000	5
24.16	24.81	4.96	5.12	5.04	2400000	6
24.81	25.44	5.12	5.28	5.20	2500000	6
25.44	26.24	5.28	5.51	5.39	2600000	8
26.24	27.18	5.51	5.78	5.64	2700000	9
27.18	27.74	5.78	5.96	5.87	2750000	11
27.74	28.59	5.96	6.25	6.11	2800000	17
28.59	29.64	6.25	6.64	6.44	2850000	21
29.64	30.40	6.64	6.94	6.79	2875000	30
30.40	31.23	6.94	7.31	7.13	2900000	33
31.23	32.37	7.31	7.86	7.58	2925000	46
32.37	33.04	7.86	8.22	8.04	2935000	67
33.04	33.88	8.22	8.72	8.47	2945000	84
33.88	34.17	8.72	8.90	8.81	2950000	58
34.17	34.67	8.90	9.23	9.07	2955000	100
34.67	35.19	9.23	9.60	9.41	2960000	104
35.19	35.84	9.60	10.09	9.85	2965000	118
35.84	36.49	10.09	10.63	10.36	2970000	130
36.49	37.26	10.63	11.33	10.98	2975000	166
37.26	38.09	11.33	12.18	11.76	2980000	166
38.09	38.69	12.18	12.86	12.52	2982500	240

Table 13.69: FS DPR LCG specimen CT2.

14. Bibliography

Aabø, S; Thuestad, JG (1985)
Effect o he weld profile on fatigue life of aluminium butt and fillet welds.
Aluminium Weldments III, Proceedings of the Third International Conference, Munich, West Germany: pp III.1.1 – III.1.9.

Altenpohl, D (1982)
Aluminium viewed from within - an introduction into the metallurgy of aluminium fabrication (1st edition).
Aluminium-Verlag, Düsseldorf, 1982.
ISBN 3-87017-138-3

Ashby, MF; Jones, DRH (1980)
Engineering materials 1 - An introduction to their properties and applications.
Pergamon Press, Oxford, 1980.
ISBN 0-08-026138-8

Ashton, RF; Wesley, RP; Dixon, CR (1975)
The effect of porosity on 5086-H116 aluminium alloy welds.
Welding Research Supplement, 1975, March, pp. 95s - 98s.

ASM (1993)
In ASM Speciality Handbook - Aluminium and Aluminium Alloys (edited by Davis, JR; Davis and Associates).
ASM International, Ohio; 1993.
ISBN 0-87170-496-X

ASTM (1982)
Standard terminology related to fracture testing - E616.
1986 Annual Book of ASTM Standards Section 3 - Metals Test Methods and Analytical Procedures - Vol. 03.01 Metals - Mechanical Testing; Elevated and Low Temperature Tests; Metallography; pp 674 - 687
American Society for Testing and Materials, Philadelphia (1982).

ASTM (1989)
Standard test method for microhardness of materials - E384.
1997 Annual Book of ASTM Standards Section 3 - Metals Test Methods and Analytical Procedures - Vol. 03.01 Metals - Mechanical Testing; Elevated and Low Temperature Tests; Metallography; pp 386 - 403
American Society for Testing and Materials, Philadelphia (1997).

ASTM (1995a)
Standard test method for determining residual stresses by the hole-drilling strain-gage method - E 837 - 95.
1997 Annual Book of ASTM Standards Section 3 - Metals Test Methods and Analytical Procedures - Vol. 03.01 Metals - Mechanical Testing; Elevated and Low temperature Tests; Metallography; pp 642 - 648.
American Society for Testing and Materials, Philadelphia (1997).

ASTM (1995b)
Standard test methods for measurement of fatigue crack growth rates - E647-95a
1997 Annual Book of ASTM Standards Section 3 - Metals Test Methods and Analytical Procedures - Vol. 03.01 Metals - Mechanical Testing; Elevated and Low Temperature Tests; Metallography; pp 557 - 593
American Society for Testing and Materials, Philadelphia (1997).

ASTM (1996)
Standard test methods for determining average grain size - E112.
1997 Annual Book of ASTM Standards Section 3 - Metals Test Methods and Analytical Procedures - Vol. 03.01 Metals - Mechanical Testing; Elevated and Low Temperature Tests; Metallography; pp 227 - 249
American Society for Testing and Materials, Philadelphia (1997).

Beghini, M; Bertini, L; Raffaelli, P (1994)
Numerical analysis of plasticity effects in the hole-drilling residual stress measurement.
Journal of Testing and Evaluation, 1994, Vol. 22, No. 6, pp. 522 - 529.

Beghini, M; Bertini, L; Raffaelli, P (1995)
An account of plasticity in the hole-drilling method of residual stress measurement.
Journal of Strain Analysis, 1995, Vol. 30, No. 3, pp. 227 - 233.

Berge, S; Eide, OI (1982).
Residual stress and stress interaction in fatigue testing of welded joints.
Residual Stress Effects in Fatigue, ASTM STP 776, pp. 115 - 131.
American Society for Testing and Materials, Philadelphia (1982)

Bertini, L; Fontanari, V; Straffelini, G (1998)
Influence of post weld treatments on the fatigue behaviour of Al-alloy welded joints.
International Journal of Fatigue, 1998, Vol. 20, No. 10, pp. 749 - 755.

Biallas, G; Braun, R; Dalle Donne, C; Staniek, G; Kaysser, WA (1999)
Mechanical properties and corrosion behaviour of friction stir welded 2024-T3
First International Symposium on Friction Stir Welding, Thousand Oaks, California, USA, 14 - 16 June,1999.
Proceedings published (CD ROM) by TWI, Abington (1999).

Bignonnent, A; Lieurade, HP; Picouet, L (1986)
Improvement of the fatigue life for offshore welded connections.
Advances in Surface Treatments: Technology - Applications - Effects. Volume 2: (edited by Niku-Lari, A)
Pergamon Press, Oxford; 1986, pp. 63 - 71.
ISBN 0-08-032535-1

Booth, GS (1983)
A review of fatigue strength improvement techniques.
Improving the fatigue performance of welded joints, Chapter 2, pp. 5 - 10.
The Welding Institute, Cambridge, England (1983)

Brandt, U; Lawrence, FV; Sonsino, CM (2001)
Fatigue crack initiation and growth in AlMg4.5Mn butt weldments.
Fatigue and Fracture of Engineering Materials and Structures, Vol. 24, pp. 117 - 126.

Bussu, G; Irving, PE (1999)
Fatigue performance of friction stir welded 2024-T351 aluminium joints.
First International Symposium on Friction Stir Welding, Thousand Oaks, California, USA, 14 - 16 June,1999.
Proceedings published (CD ROM) by TWI, Abington (1999).

Calcraft, RC; Wahab, MA; Viano, DM; Schumann, GO; Phillips, RH; Ahmed, NU (1999)
The development of the welding procedures and fatigue of butt-welded structures of aluminium-AA5383.
Journal of Materials Processing Technology, 1999, 92 - 93, pp. 60 - 65.

Caton, MJ; Jones, JW; Allison, JE (1999a)
A study of small fatigue crack growth in cast aluminium and prediction of fatigue properties.
Small Fatigue Cracks: Mechanics, Mechanisms and Applications (Editors Ravichandran, KS; Ritchie, RO; Murakami, Y).
Elsevier Science Ltd., 1999, pp. 155 - 166.

Caton, MJ; Jones, JW; Boileau, JM; Allison, JE (1999b)
The effect of solidification rate on the growth of small fatigue cracks in a cast 319-type aluminium alloy.
Metallurgical and Materials Transactions A, 1999, Vol. 30A, No. 12, pp. 3055 - 3068.

Chapetti, MD; Otegui, JL (1997)
Controlled toe waviness as a means to increase fatigue resistance of automatic welds in transverse loading.
International Journal of Fatigue, 1997, Vol. 19, No. 10, pp. 667 - 675.

Chell, GG (1984)
Some subcritical crack growth parameters and their evaluation.
In Subcritical crack growth due to fatigue, stress corrosion and creep (edited by Larsson, LH).
Elsevier Applied Science Publishers, London, 1984, pp. 1 - 29.
ISBN 0-85334-289-X

Costa, JD; Branco, CM; Radon, JC (1997)
Short fatigue crack growth behaviour in Al 5083 alloy.
International Journal of Fatigue, 1997, Vol. 19, No. 2, pp. 161 - 168.

Cross, CE (1993)
Selection and weldability of non-heat treatable aluminium alloys.
Welding of aluminium alloys.
In ASM Handbook, Volume 6 - Welding, Brazing and Soldering, pp 532 - 540.
ASM International, Ohio; 1993.
ISBN 0-87170-382-3

Dalle Donne, C; Biallas, G (1998)
Fatigue and fracture performance of friction stir welded 2024-T3 joints.
Proceedings European Conference on Spacecraft Structures, Materials and Mechanical Testing; Braunschweig, Germany, 4 - 6 November 1998 (ESA SP-428, February 1999) pp 309 - 314.

Dalle Donne, C; Biallas, G; Ghidini, T; Raimbeaux, G (2000)
Effect of weld imperfections and residual stresses on the fatigue crack propagation in friction stir welded joints.
Second International Conference on Friction Stir Welding, 26-28 June, 2000, Gothenburg, Sweden.
Proceedings published (CD ROM) by TWI, Abington (2000).

Davidson, DL; Lankford, J (1992)
Fatigue crack growth in metals and alloys: mechanisms and micromechanics.
International Materials Review, 1992, Vol. 37, No. 2. pp. 45 - 76.

Dawes, C; Thomas, W (1995)
Friction stir joining of aluminium alloys.
Bulletin 6, November/December 1995.
TWI, Reprint 493/6/95.

Dawes, MG; Karger, SA; Dickerson, TL; Przydatek, J (2000)
Strength and fracture toughness of friction stir welds in aluminium alloys.
Second International Conference on Friction Stir Welding, 26 - 28 June, 2000, Gothenburg, Sweden.
Proceedings published (CD ROM) by TWI, Abington (2000).

Devletian, JH; Wood, WE (1983)
Factors affecting porosity in aluminium welds - a review.
Welding Research Council Bulletin 290, pp. 1 - 18.
ISBN 1-58145-289-6

Dickerson, PB (1993)
Welding of aluminium alloys.
In ASM Handbook, Volume 6 - Welding, Brazing and Soldering, pp 722 - 739.
ASM International, Ohio; 1993.
ISBN 0-87170-382-3

Easterling, K (1983).
Introduction to the physical metallurgy of welding.
Butterworths, London (1983).
ISBN 0408 01352 4

ECCS Technical Committee 2 (1992)
European recommendations for aluminium alloy structures fatigue design (1st edition, no. 68).
ECCS, Brussels, Belgium.

Elber, W (1970)
Fatigue crack closure under cyclic tension.
Engineering Fracture Mechanics, 1970, Vol. 2, pp. 37 - 45.

El Haddad, MH; Topper, TH; Topper TN (1981)
Fatigue life predictions of smooth and notched specimens based on fracture mechanics.
Journal of Engineering Materials and Technology, 1981, Vol. 103, pp. 91 - 96.

Ericsson, M; Sandström, R (2002)
Influence of welding speed on the fatigue of friction stir welds and comparison with MIG and TIG.
Accepted for publication in International Journal of Fatigue.

ESDU International (1991)
Static and fatigue strength of butt welded joints in aluminium alloys - ESDU data item 91039.
Engineering Sciences Data Unit (ESDU) International, London.

ESRF (undated)
Seeing things in a different light.
European Synchrotron Radiation Facility (ESRF), Grenoble, France.

Ewalds, HL; Wanhill, RJH (1984)
Fracture Mechanics.
Arnold, London, 1984 (reprinted with corrections 1989).

Flaman, MT (1982).
Brief investigation of induced drilling stresses in the center-hole method of residual-stress measurement.
Experimental Mechanics, Vol. 22, 1982, Jan., pp. 26 - 30.

Frigaard, Ø; Grong, Ø; Hjelen, J; Gulbrandsen-Dahl, S; Midling, OT (1999)
Characterisation of the subgrain structure in friction stir welded aluminium alloys using the SEM-EBSD technique.
First International Symposium on Friction Stir Welding, Thousand Oaks, California, USA, 14 - 16 June,1999.
Proceedings published (CD ROM) by TWI, Abington (1999).

Flores, OV; Kennedy, C; Murr, LE; Brown, D; Pappu, S; Nowak, BM; McClure, JC (1998)
Microstructural issues in a friction-stir-welded aluminium alloy.
Scripta Materialia, 1998, Vol. 38, No. 5, pp. 703 - 708.

Gangloff, RP; Slavik, DC; Piascik, RS; van Stone, RH (1992)
Direct current electrical potential measurement of the growth of small cracks.
Small-Crack Test Methods, ASTM STP 1149 (edited by Larsen, JM; Allison, JE.).
American Society for Testing and Materials, Philadelphia, 1992, pp. 116 - 168.

Gray, TGF (1994)
Fracture & fatigue (course notes for 16566 solid mechanics ~ fracture mechanics)
Department of Mechanical Engineering, University of Strathclyde, 1994.

Gurney, TR (1979)
Fatigue of welded structures (2nd edition).
Cambridge University Press, Cambridge, 1979.
ISBN 0 521 22558 2

Haagensen, PJ (1982)
Improving the fatigue performance of welded joints.
Proceedings of 2nd International Conference on Offshore Welded Structures, The Welding Institute, London, 1982, Paper 36, pp. 36-1 - 36-12.

Haagensen, PJ; Midling, OT; Ranes, M (1995)
Fatigue performance of friction stir butt welds in a 6000 series aluminium alloy.
International conference on computer methods and experimental measurements for surface treatment effects II, Southampton 1995, pp. 225 - 227.

Harrison, JD (1981).
The effect of residual stresses on fatigue behaviour.
Residual stresses and their effect (edited by Parlane, AJA).
The Welding Institute, Abingdon, England; 1981, pp. 9 - 16.

Hashimoto, T; Nishikawa, N; Tazaki, S; Enomoto, M (1998)
Mechanical properties of joints for aluminium alloys with friction stir welding process.
INALCO '98 - Joints in Aluminium, 7th International Conference Pre-prints (Volume 2) - Cambridge, UK, 15th April, 1998; pp 237–247.

Hughes, DJ (2001)
Interim experimental summary for beamtime allocation me282(a).
Personal communication.

Iida, K; Takanashi, M (1998)
Relaxation of welding residual stresses by reversed and repeated loadings.
Welding in the World, 1998, Vol.. 41, No. 4, pp. 27 - 40.

James, M; Mahoney, M; Waldron, D (1999)
Residual stress measurements in friction stir welded aluminium alloys.
First International Symposium on Friction Stir Welding, Thousand Oaks, California, USA, 14 - 16 June,1999.
Proceedings published (CD ROM) by TWI, Abington (1999).

James, MR (1987)
Relaxation of residual stresses.
In Advances in Surface Treatments - Technology - Applications - Effects. Volume 4: Residual Stresses (edited by Niku-Lari, A).
Pergamon Press, Oxford; 1987, pp. 349 - 365.
ISBN 0-08-034062-8.

James, MR; Lu, J (1996)
Chapter 1 - introduction.
Handbook of measurement of residual stresses (edited by Lu, J).
Society for Experimental Mechanics.
The Fairmont Press Inc., Lilburn, GA, USA, pp. 1 - 4.
ISBN 0-13-255738-X

James, MR; Morris, WL (1981)
The relaxation of machining stresses in aluminium alloys during fatigue.
In Residual Stress for Designers and Metallurgists - Proceedings of a conference held 9 - 10 April, 1980, Chicago (Edited by Vande Walle, LJ).
American Society for Metals, Metals Park, Ohio, 1981, pp. 169 - 188.
ISBN 0-87170-106-5

Johnson, R; Kallee, S (1999)
Stirring stuff from friction welding.
Materials World, December 1999, Vol. 7, No. 12, pp. 751 - 753.

Kallee, S (2000)
Application of friction stir welding in the ship building industry.
http://www.twi.co.uk/j32k/protected/band_8/spswkfeb2000.html
TWI, Abington, UK (2000).

Karjalainen, LP (1973)
The effect of grain size on the fatigue of an Al-Mg alloy.
Scripta Metallurgica, 1973, Vol. 7, pp. 43 - 48.

Karlsson, J; Karlsson, B; Larsson, H; Karlsson, L; Svensson, L-E (1998)
Microstructure and properties of friction stir welded aluminium alloys.
INALCO '98 - Joints in Aluminium, 7th International Conference Pre-prints (Volume 2) - Cambridge, UK, 15th April, 1998; pp 221–230.

Kaynak, C; Ankara, A; Baker, TJ (1996)
Effects of short cracks on fatigue life calculations.
International Journal of Fatigue, 1996, Vol. 18, No. 1, pp. 25 - 31.

Kelsey, RA; Nordmark, GE (1979)
Effect of residual stresses on fatigue properties of aluminium butt welds.
Aluminium, 1979, Vol. 55, No. 6 pp. 391 - 394.

Kendall, JM; James, MN; Knott, JF (1986).
The behaviour of physically short fatigue cracks in steels.
The Behaviour of Short Fatigue Cracks (edited by Miller, KJ; Rios, ER de los).
Mechanical Engineering Publications, London (1986), pp 214 - 258.
ISBN 0 85298 615 7

Kosteas, D; Sanders Jr, WW (1987)
Fatigue design format for welded aluminium structures.
Aluminium Structures: Advances, Design and Construction - Proceedings of the International Conference on Steel and Aluminium Structures, Cardiff, UK, 8 - 10 July 1987 (*editor* Narayanan, R).
Elsevier Applied Science Publishers Ltd., 1987, pp. 156 - 161.
ISBN 1-85166-121-2.

Kuitunen, R; Rahka, K (1991)
Fatigue behaviour and design of welded aluminium structures.
Proceedings of the First (1991) International Offshore and Polar Conference, Edinburgh, United Kingdom, 11 - 16 August, 1991.

Lancaster, JF (1999)
Metallurgy of Welding - Sixth edition.
Abington Publishing, Cambridge, England; 1999
ISBN 1 85573 428 1

Larsen, JM; Jira, JR; Ravichandran, KS (1992)
Measurement of small cracks by photomicroscopy: experiments and analysis.
Small Crack Test Methods, ASTM STP 1149.
American Society for Testing and Materials, Philadelphia, PA, 1992, pp. 57 - 80.

Larsson, H; Karlsson, L; Svensson, L-E (1998)
Characteristics of friction stir welds in AA 5083 and AA 6082 aluminium.
Proceedings of International Conference on Aluminium Alloys 6 - Volume 3.
Vol. 3, pp. 1471 - 1476.

Lawrence, FV (1981)
The predicted influence of weld residual stresses on fatigue crack initiation.
Residual Stress for Designers and Metallurgists - Proceedings of a conference held 9 - 10 April 1980 Chicago, Illinois.
American Society for Metals, Ohio (1981).

Lawrence Jr, FV; Burk, JD; Yung, J-Y (1982)
Influence of residual stress on the predicted fatigue life of weldments.
Residual Stress Effects in Fatigue, ASTM STP 776, pp. 33 - 43.
American Society for Testing and Materials, Philadelphia (1982)

Lawrence Jr, FV; Munse, WH; Burk, JD (1975)
Effects of weld porosity on the fatigue properties of 5083 aluminium alloy weldments.
WRC Bulletin 206.
Welding Research Council, June 1975.

Leonard, AJ (2000)
Microstructure and ageing behaviour of FSWs in aluminium alloys 2014A-T651 and 7075-T651.
Second International Conference on Friction Stir Welding, 26 - 28 June, 2000, Gothenburg, Sweden.
Proceedings published (CD ROM) by TWI, Abington (2000).

Li, Y; Murr, LE; McClure, JC (1999)
Flow visualization and residual microstructures associated with the friction-stir welding of 2024 aluminium alloy to 6061 aluminium.
Materials Science and Engineering A, 1999, Vol. 271, No. 1 - 2, pp. 213 - 223.

Liaw, PK (1988)
Overview of crack closure at near-threshold fatigue crack growth levels.
Mechanics of Fatigue Crack Closure, ASTM STP 982 (editors, Newman Jr, JC; Elber, W).
American Society for Testing and Materials., Philadelphia, 1988, pp. 62 - 92.

Link, LR (1990)
Fatigue crack growth of weldments.
Fatigue and fracture testing of weldments - ASTM STP 1058 (editors McHenry, HI; Potter, JM).
American Society for Testing and Materials, Philadelphia, 1990, pp. 16 - 33.

Liu, G; Murr, LE; Niou, C-S; McClure, JC, Vega, FR (1997)
Microstructural aspects of the friction-stir welding of 6061-T6 aluminium.
Scripta Materialia, 1997, Vol. 37, No. 3, pp. 355 - 361.

Macherauch E (1987)
Introduction to residual stress.
In Advances in Surface Treatments - Technology - Applications - Effects. Volume 4: Residual Stresses (edited by Niku-Lari, A).
Pergamon Press, Oxford; 1987, pp. 1 - 36
ISBN 0-08-034062-8.

Maddox, SJ (1982)
Fatigue design of welded aluminium alloy structures.
Second International Conference on Aluminium Weldments, Munich, 24 - 26th May 1982.

Magnusson, L; Källman, L (2000)
Mechanical properties of friction stir welds in thin sheet of aluminium 2024, 6013 and 7475.
Second International Conference on Friction Stir Welding, 26 - 28 June, 2000, Gothenburg, Sweden.
Proceedings published (CD ROM) by TWI, Abington (2000).

Masubuchi, K (1972).
Residual stresses and distortion in welded aluminium structures and their effects on service performance.
Welding Research Council Bulletin 174, 1972, pp. 1 - 30.

Masubuchi, K (1980)
Analysis of welded structures (International series on materials science and technology, vol. 33).
Pergamon Press, Oxford.
ISBN 0-08-022714-7

Masuda, C; Nishijima, S; Shimodaira, M (1983)
Fatigue fractographs for butt-welded joints of A5083-O aluminium alloy.
Transactions of national research institute for metals, 1983, Vol. 25, No. 3, pp. 132 - 142.

Mathar, J (1934)
Determination of initial stresses by measuring the deformations around drilled holes.
Transactions of the American Society of Mechanical Engineers; 1934, Vol. 56, No. 4, pp. 249 - 254.

McEvily, AJ (1988)
On crack closure in fatigue crack growth.
Mechanics of Fatigue Crack Closure, ASTM STP 982 (editors Newman Jr, JC, Elber, W).
American Society for Testing and Materials, Philadelphia, 1988, pp. 35 - 43.

Measurements Group (1988)
Tech Note 503-3 - measurement of residual stresses by the hole-drilling strain gage method.
Measurements Group, Inc. Raleigh.

Moldenhauer, S (1999)
Composition of AA 5383-H321.
Personal communication between Moldenhauer, S and Bradley, GR.
Corus Research and Development (aluminium), IJmuiden, The Netherlands.

Mondolfo, LF (1976)
Aluminium alloys: structures and properties.
Butterworths, London.
ISBN 0-408-70680-5

Mononen, J; Haagensen, PJ (1998)
X-ray and hole-drilling residual stress measurements in friction stir and plasma welds and welds improved by ultrasonic impact treatment.
International Institute of Welding, Commission XIII, Workgroup of fatigue improvement methods, Hamburg, September, 1998.

Morris, WL (1979)
Microcrack closure phenomena for Al 2219-T851.
Metallurgical Transactions A 1979, January, Vol. 10A, pp. 5 - 11.

Morris, WL (1980)
The noncontinuum crack tip deformation behaviour of surface microcracks.
Metallurgical Transactions A 1980, July, Vol. 11A, pp. 1117 - 1123.

Murr, LE; Liu, G; McClure, JC (1997)
Dynamic recrystallization in friction-stir welding of aluminium alloy 1100.
Journal of Materials Science Letters, 1997, Vol. 16, pp. 1801 - 1803.

Murr, LE; Liu, G; McClure, JC (1998a)
A TEM study of precipitation and related microstructures in friction-stir-welded 6061 aluminium.
Journal of Materials Science, 1998, Vol. 33, pp. 1243 - 1251.

Murr, LE; Li, Y; Trillo, EA; Flores, RD; McClure, JC (1998b)
Microstructures in friction-stir welded metals.
Journal of Materials Processing and Manufacturing Science, 1998, Vol. 7, pp. 145 - 161.

Nakai, Y; Ohji, K (1992)
Predictions of growth rate and closure of short fatigue cracks.
Short Fatigue Cracks (edited by Miller, KJ).
Mechanical Engineering Publications, London, 1992, pp. 169 - 189.

Nederlands Normalisatie-instiuut (1998)
Eurocode 9: Ontwerp en berekening van aluminiumconstructies - Deel 2: Constructies gevoelig voor vermoeiing.
Nederlands Normalisatie-instiuut, Delft, The Netherlands.

Newman Jr, JC (1999)
Application of small-crack theory to aircraft materials.
Small Fatigue Cracks: Mechanics, Mechanisms and Applications (edited by Ravichandran, KS; Ritchie, RO; Murakami, Y).
Elsevier Science Ltd. 1999

Newman Jr, JC; Raju, IS (1981)
An empirical stress-intensity factor equation for the surface crack.
Engineering Fracture Mechanics, 1981, Vol. 15, No. 2, pp. 185 - 192.

Newman, JC; Wu, XR; Swain, MH; Zhao, W; Philips, EP; Ding, CF (2000)
Small-crack growth and fatigue life predictions for high-strength aluminium alloys. Part II: crack closure and fatigue analyses.
Fatigue and Fracture of Engineering Materials and Structures, 2000, Vol. 23, pp. 59 - 72.

Nisitani, H; Goto, M (1986)
A small-crack growth law and its application to the evaluation of fatigue life.
The Behaviour of Short Fatigue Cracks, EGF publication 1, (edited by Miller, KJ; Rios, ER de los).
Mechanical Engineering Publications, London, 1986, pp. 461 - 478.
ISBN 0 85298 6157.

Nisitani, H; Goto, M; Kawagoishi, N (1992)
A small-crack growth law and its related phenomena.
Engineering Fracture Mechanics, 1992, Vol. 41, No. 4, pp. 499 - 513.

Niu, X; Glinka, G (1987)
The weld profile effect on stress intensity factors in weldments.
International Journal of Fracture, 1987, Vol. 35, pp. 3–20.

Nordmark, GE; Mueller, LN; Kelsey, RA (1982)
Effect of residual stresses on fatigue crack growth rates in weldments of aluminium alloy 5456 plate.
Residual Stress Effects in Fatigue, ASTM STP 776.
American Society for Testing and Materials, 1982, pp. 44 - 62.

Nosair, S; Jolley, G (1985)
A study of fatigue crack growth rates in welded Al-Mg alloy plate.
Current advances in mechanical design & production, third Cairo University MDP conference, Cairo, Dec. 28 - 30, 1985.

O'Brien, RL (*editor*), (1997)
Jefferson's Welding Encyclopedia
American Welding Society, Miami, 1997
ISBN 0-87171-506-6.

Otegui, JL; Mohaupt, UH; Burns, DJ (1991)
A strain gauge technique for monitoring small fatigue cracks in welds.
Engineering Fracture Mechanics, 1991, Vol. 40, No. 3, pp. 549 - 569

Panasyuk, VV; Andreykiv, OY, Ritchie, RO; Darchuk, OI (2001)
Estimation of the effects of plasticity and resulting crack closure during small fatigue crack growth.
International Journal of Fracture, 2001, Vol. 107, pp. 99 - 115.

Pang, HLJ (1994)
Analysis of weld toe radius effects on fatigue weld toe cracks.
International Journal of Pressure Vessels and Piping, 1994, Vol. 58, pp. 171–177.

Parlane, AJA (1981).
Origin and nature of residual stresses in welded joints.
Residual stresses and their effect (edited by Parlane, AJA).
The Welding Institute, Abingdon, England; 1981, pp. 1 - 4.

Pearson, S (1975)
Initiation of fatigue cracks in commercial aluminium alloys and the subsequent propagation of very short cracks.
Engineering Fracture Mechanics, 1975, Vol. 7, pp. 235 - 247.

Philips, EP; Newman Jr, JC (1989)
Impact of small-crack effects on design-life calculations.
Experimental Mechanics, 1989, Vol. 29, No. 2, pp. 221 - 225.

Pilkey, WD (1997)
Peterson's stress concentration factors - 2nd edition.
John Wiley & Sons, Inc., New York.
ISBN 0-471-53849-3.

Polmear, IJ (1982)
Post-weld treatments to improve fatigue performance of aluminium alloy weldments
30th National Conference - Australian Welding Institute: Welding Technology 82, pp. 115 - 121.
Australian Welding Institute, 1982.
ISBN 0909539243.

Polmear, IJ (1985)
Post-weld surface treatments to improve fatigue performance of aluminium weldments - AWRA document P3-11-85.
Australian Welding Research, 1985, December, pp. 64 - 68.

Proctor, E (1981)
Measurement of residual stresses.
Residual Stresses and their Effect (edited by Parlane, AJA).
The Welding Institute, Abingdon, England; 1981, pp. 34 - 40.

Rhodes, CG; Mahoney, MW; Bingel, WH; Spurling, RA; Bampton, CC (1997)
Effects of friction stir welding on microstructure of 7075 aluminium.
Scripta Materialia, 1997, Vol. 36, No. 1, pp. 69 - 75.

Ritchie, RO (1999)
Mechanisms of fatigue-crack propagation in ductile and brittle solids.
International Journal of Fracture, 1999, Vol. 100, pp. 55 - 83.

Ritchie, RO; Yu, W; Holm, DK; Blom, AF (1988)
Development of fatigue crack closure with extension of long and short cracks in aluminium alloy 2124: a comparison of experimental and numerical results.
Mechanics of Fatigue Crack Closure, ASTM STP 982.
American Society for Testing and Materials, 1988, pp. 300 - 316.

Roy, G; Porter, JF; Holden, TM; Cousineau, EJC; Kiff, D; Fryzuk, P; Root, J; Hosbons, RR (1990)
Determination of residual stress state in HY-80 and HY-100 plates by neutron-diffraction-, x-ray diffraction-,hole drilling- and numerical methods.
Proceedings of the 1990 SEM Spring Conference on Experimental Mechanics, Albuquerque, New Mexico, 4 - 6/6-1990, pp. 255 - 262.

Sanders Jr, WW; Derecho, AT; Munse, WH (1965)
Effect of external geometry on fatigue behaviour of welded joints.
Welding Research - Supplement, 1965, Vol. 30, No. 2, pp.49-s - 55-s.

Saunders, GG (1981)
Methods of stress relief and their efficacy.
Residual Stresses and their Effect (edited by Parlane, AJA).
The Welding Institute, Abingdon, England; 1981, pp. 41 - 47.

Schajer, GS; Flaman, MT; Roy, G; Lu, J (1996)
Hole-drilling and ring core methods
Handbook of measurement of residual stresses / Society for experimental mechanics (editor Lu, J).
The Fairmont Press, Lilburn, US (1996).
ISBN 0-88173-229-X

Schijve, J (1988)
Fatigue crack closure: observations and technical significance.
Mechanics of Fatigue Crack Closure, ASTM STP 982 (editors Newman Jr, JC; Elber, W).
American Society for Testing and Materials, Philadelphia, 1988, pp. 5 - 34.

Scientifics Ltd. (2001)
Certificate No. MTG/01945
Scientifics Ltd., 500 London Road, Derby. DE24 8BQ. England.

Seetharaman, V; Jata, KV, Semiatin, SL (2000)
Plastic flow and microstructure development during high temperature deformation of a friction stir welded 7050 aluminium alloy.
Second International Conference on Friction Stir Welding, 26 - 28 June, 2000, Gothenburg, Sweden.
Proceedings published (CD ROM) by TWI, Abington (2000).

Segal, AM; Tait, RB (1996)
Residual stress evaluation using the air abrasive hole drilling technique.
Research and Development Journal, Vol. 12, No. 2, pp. 54 - 67.

Slatcher, S; Knott, JF (1981)
A comparison of replication and clip-gauge techniques for the determination of the crack-opening-displacement.
International Journal of Fracture, 1981, Vol. 17, pp. R109 - R114.

Smith, DJ; Farrahi, GH; Zhu, WX; McMahon, CA (2001)
Experimental measurement and finite element simulation of the interaction between residual stresses and mechanical loading.
International Journal of Fatigue, 2001, Vol. 23, No. 4, pp. 293 - 302.

Solomon, HD (1993)
Fundamentals of weld solidification.
Welding of aluminium alloys.
In ASM Handbook, Volume 6 - Welding, Brazing and Soldering, pp 45 - 54.
ASM International, Ohio; 1993.
ISBN 0-87170-382-3

Sonsino, CM; Radaj, D; Brandt, U; Lehrke, HP (1999)
Fatigue assessment of welded joints in AlMg 4.5Mn aluminium alloy (AA 5083) by local approaches.
International Journal of Fatigue, 1999, Vol. 21, pp. 985 - 999.

Stevens, RH (chapter revised by) (1985)
ASM Handbook - Volume 9, Metallography and Microstructures, Aluminium Alloys Chapter, pp. 351 - 387.
ASM International, Materials Park, Ohio.
ISBN 0-87170-007-7 (Vol.1)

Strangwood, M; Berry, JE; Cleugh, DP; Leonard, AJ; Threadgill, PL (1999)
Characterisation of the thermo-mechanical effects on microstructural development in friction stir welded age hardening aluminium-based alloys.
First International Symposium on Friction Stir Welding, Thousand Oaks, California, USA, 14 - 16 June,1999.
Proceedings published (CD ROM) by TWI, Abington (1999).

Suresh, S (1983)
Crack deflection: implications for the growth of long and short fatigue cracks.
Metallurgical Transactions A, 1983, Vol. 14A, November, pp. 2375 - 2385.

Suresh, S (1998)
Fatigue of materials (second edition).
Cambridge University Press, Cambridge, 1998.
ISBN 0 521 57046 8.

Suresh, S; Ritchie, RO (1984)
Propagation of short fatigue cracks.
International Metals Reviews, 1984, Vol. 29, pp. 445 - 476.

Swain, MH (1992)
Monitoring small-crack growth by the replication method.
Small-crack test methods, ASTM STP 1149 (Edited by Larsen, JM; Allison, JE).
American Society for Testing and Materials, 1992, pp. 34 - 56.

Talwar, R; Bolser, D; Lederich, RJ; Baumann, J (2000)
Second International Conference on Friction Stir Welding, 26 - 28 June, 2000, Gothenburg, Sweden.
Proceedings published (CD ROM) by TWI, Abington (2000).

Tanaka, K; Nakai, Y; Yamashita, M (1981)
Fatigue growth threshold of small cracks.
International Journal of Fracture, 1981, October, Vol. 17, No. 5, pp. 519 - 533.

Tang, W; Guo, X; McClure, JC; Murr, LE; Nunes, A (1998)
Heat input and temperature distribution in friction stir welding.
Journal of Materials Processing and Manufacturing Science, 1998, October, Vol. 7, No. 2, pp. 163 - 172.

Thomas, WM (1998)
Friction stir welding and related friction process characteristics.
INALCO '98 - Joints in Aluminium, 7th International Conference Pre-prints (Volume 2) - Cambridge, UK, 16th April, 1998; pp S29-1 - S29-18.

Threadgill, P (1997)
Friction stir welds in aluminium alloys - preliminary microstructural assessment.
TWI Bulletin, March/April 1997
TWI, Abington, UK (1997).

Threadgill, P (2000)
Verbal communication between Threadgill, P and James, MN at 2nd Friction Stir Welding Symposium, 26 - 28 June 2000, Gothenburg, Sweden.

Threadgill, P (2002)
Personal communication between Threadgill, P and Bradley, GR.
TWI, Abington, UK (2002).

Threadgill, P (2003)
Personal communication between Threadgill, P and Bradley, GR.
TWI, Abington, UK (2003).

Tokaji, K; Ogawa (1992)
The growth behaviour of microstructurally small fatigue cracks in metals.
Short Fatigue Cracks, ESIS 13 (Edited by Miller, KJ; Rios, ER de los).
Mechanical Engineering Publications, London, 1992, pp. 85 - 99.

Tokyo Sokki Kenkyujo Co., Ltd. (undated a)
Strain gauges -TML Pam E-101l (strain gauge catalogue).
Tokyo Sokki Kenkyujo Co., Ltd., Japan.

Tokyo Sokki Kenkyujo Co., Ltd. (undated b)
Strain gauges -TML Pam E-106 (residual stress measurements by centre-hole drilling method using TML strain gauge type FRS).
Tokyo Sokki Kenkyujo Co., Ltd., Japan.

Turnbull, A; Rios, ER de los (1995)
The effect of grain size on fatigue crack growth in an aluminium magnesium alloy.
Fatigue and Fracture of Engineering Materials and Structures, 1995, Vol. 18, No. 11, pp. 1355 - 1366.

TWI (1998a)
Welding record for metal inert gas low input butt weld.
Catalogue number WPAR1525, Project number 221346
TWI, Abington, UK (1998).

TWI (1998b)
Welding record for metal inert gas high input butt weld.
Catalogue number WPAR1526, Project number 221346
TWI, Abington, UK (1998).

TWI (1999)
Friction stir welding - superior weld quality.
http://www.twi.co.uk/bestprac/datashts/fswqual.html
TWI, Abington, UK (1999).

TWI (2000a)
Classification scheme for microstructural zones in friction stir welds.
Correspondence from Threadgill, P.
TWI, Abington, UK (2000).

TWI (2000b)
Welding details/specification for friction stir single and double pass welds.
Email correspondence to from Threadgill, P.
TWI, Abington, UK (2000).

TWI (2000c)
Welding details/specification for friction stir single and double pass welds.
Email correspondence to Bradley, GR from Threadgill, P.
TWI, Abington, UK (2000).

Vöhringer, O (1987)
Relaxation of residual stresses by annealing or mechanical treatment.
In Advances in Surface Treatments - Technology - Applications - Effects. Volume 4: Residual Stresses (edited by Niku-Lari, A).
Pergamon Press, Oxford; 1987, pp. 367 - 396.
ISBN 0-08-034062-8.

Wanhill, RJH; Hoeven, W van der; Hoeve HJ ten, Ottens, HH (1999)
Fractographic investigation of pressure cabin MSD.
NLR-TP-99265 (This report is based on an article to be published in the proceedings of the ICAF '99 Conference, held in Bellevue, Washington, USA, July 1999)
Division of Structures and Materials, National Aerospace Laboratory NLR, The Netherlands.

Webster, PJ; Oosterkamp, LD; Browne, PA; Hughes, DJ; Kang, WP; Withers, PJ; Vaughan, GBM (2001)
Synchrotron x-ray residual strain scanning of a friction stir weld.
Journal of Strain Analysis for Engineering Design, Vol. 36, No. 1, pp. 61 - 70.

Wohlfahrt, H (1987)
Residual stresses as a consequence of welding.
In Advances in Surface Treatments - Technology - Applications - Effects. Volume 4: Residual Stresses (edited by Niku-Lari, A).
Pergamon Press, Oxford; 1987, pp. 39 - 58.
ISBN 0-08-034062-8.

Wohlfahrt, H; Nitschke-Pagel, TH, Zinn, W (1996)
Improvement of the fatigue strength of welded joints by post-weld treatment methods - a comparison of the results of high strength structural steels and high strength aluminium alloys.
Welding in the World/Le Soudage le Monde, 1996, Vol. 38, pp. 307 - 316.

Woodley, CC (1983)
Practical applications of weld toe grinding.
Improving the fatigue performance of welded joints, Chapter 4, pp. 19 - 22.
The Welding Institute, Cambridge, England, 1983.

Yang, HS (1998)
Microstructural development in friction stir welding of aluminium alloys.
Proceedings of International Conference on Aluminium Alloys 6 - Volume 3.
Vol. 3, pp. 1483 - 1488.

Young, WC (1989)
Roark's formulas for stress and strain - 6th edition.
McGraw-Hill Book Co., New York (1989)
ISBN 0-07-100373-8.

Yung, J-Y; Lawrence, FV (1985)
Analytical and graphical aids for the fatigue design of weldments.
Fatigue and Fracture of Engineering Materials and Structures, 1985, Vol. 8, No. 3, pp. 223 - 241.

Zhao, W; Ding, C; Chen, Y; Yan, M (1986)
Near-threshold fatigue crack propagation and closure behaviour in an aluminium alloy (C247/86).
International Conference on Fatigue of Engineering Materials and Structures - Volume 1; 15 - 16th September 1986, University of Sheffield, England.
IMechE Conference Publications 1986-9, pp. 115 - 120.